

CODEN: JASMAN

The Journal of the Acoustical Society of America

ISSN: 0001-4966

Vol. 111, No. 4

April 2002

ACOUSTICAL NEWS—USA		1491
USA Meetings Calendar		1491
ACOUSTICAL NEWS—INTERNATIONAL		1497
International Meetings Calendar		1497
TECHNICAL PROGRAM SUMMARY		1499
REPORTS OF RELATED MEETINGS		1501
ABSTRACTS FROM ACOUSTICS RESEARCH LETTERS ONLINE		1505
BOOK REVIEWS		1507
REVIEWS OF ACOUSTICAL PATENTS		1509
TUTORIAL PAPER		
Acoustics of friction	Adnan Akay	1525

LETTERS TO THE EDITOR

Incorporating linear viscoelasticity into acoustic scattering theory [20]	Alexander K. Hipp, Laurent P. Adjadj, Giuseppe Storti, Massimo Morbidelli	1549
Comment on “Corrections to Foldy’s effective medium theory for propagation in bubble clouds and other collections of very small scatterers” [J. Acoust. Soc. Am. 105, 2149–2154 (1999)] [30]	C. Feuillade	1552
Reply to “Comment on ‘Corrections to Foldy’s effective medium theory for propagation in bubble clouds and other collections of very small scatterers’ ” [J. Acoust. Soc. Am. 111, 1552–1555 (2002)] [30]	Frank S. Henyey	1556
GENERAL LINEAR ACOUSTICS [20]		
Geoacoustic inversion for fine-grained sediments	Charles W. Holland	1560

(Continued)

CONTENTS—Continued from preceding page

Application of an acoustic backscatter technique for characterizing the roughness of porous soil	Michael L. Oelze, James M. Sabatier, Richard Raspet	1565
NONLINEAR ACOUSTICS [25]		
Theoretical and experimental examination of near-field acoustic levitation	Hideyuki Nomura, Tomoo Kamakura, Kazuhisa Matsuda	1578
An integrated wave-effects model for an underwater explosion bubble	Thomas L. Geers, Kendall S. Hunter	1584
Viscous effects on the interaction force between two small gas bubbles in a weak acoustic field	Alexander A. Doinikov	1602
AEROACOUSTICS, ATMOSPHERIC SOUND [28]		
Efficient calculation of two-dimensional periodic and waveguide acoustic Green's functions	K. V. Horoshenkov, Simon N. Chandler-Wilde	1610
UNDERWATER SOUND [30]		
Coupled-mode solutions in generalized ocean environments	Steven A. Stotts	1623
Comparing Kirchhoff-approximation and boundary-element models for computing gadoid target strengths	Kenneth G. Foote, David T. I. Francis	1644
Coherence of acoustic modes propagating through shallow water internal waves	Daniel Rouseff, Altan Turgut, Stephen N. Wolf, Steve Finette, Marshall H. Orr, Bruce H. Pasewark, John R. Apel, Mohsen Badiy, Ching-sang Chiu, Robert H. Headrick, James F. Lynch, John N. Kemp, Arthur E. Newhall, Keith von der Heydt, Dirk Tielbuerger	1655
ULTRASONICS, QUANTUM ACOUSTICS, AND PHYSICAL EFFECTS OF SOUND [35]		
Determination of elastic moduli of rock samples using resonant ultrasound spectroscopy	TJ Ulrich, K. R. McCall, R. A. Guyer	1667
Saturation of thermoacoustic mixture separation	D. A. Geller, G. W. Swift	1675
Hybrid laser/broadband EMAT ultrasonic system for characterizing cracks in metals	Johanna R. Bernstein, James B. Spicer	1685
TRANSDUCTION [38]		
Performance of a low-frequency, multi-resonant broadband Tonpizl transducer	Dhilsha Rajapan	1692
Generation of an acoustically bright zone with an illuminated region using multiple sources	Joung-Woo Choi, Yang-Hann Kim	1695
STRUCTURAL ACOUSTICS AND VIBRATION [40]		
Experimental study of vibrational behavior of laminated annular disks	Huan Wang	1701
Maximum likelihood estimation of structural wave components from noisy data	Peter J. Halliday, Karl Grosh	1709
Comparison of moments and couple-generating forces near discontinuities in structural-acoustic systems	W. Steve Shepard, Jr.	1718
Global damping of noise or vibration fields with locally synthesized controllers	Jing Yuan	1726

CONTENTS—Continued from preceding page

NOISE: ITS EFFECTS AND CONTROL [50]

Analysis of noise barrier overlap gaps	Lloyd A. Herman, Craig M. Clum	1734
Relationship between low-frequency aircraft noise and annoyance due to rattle and vibration	Sanford Fidell, Karl Pearsons, Laura Silvati, Matthew Sneddon	1743
Synthesis of a robust broadband duct ANC system using convex programming approach	Mingsian R. Bai, Pingshun Zeung	1751
Experimental evaluation of leaky least-mean-square algorithms for active noise reduction in communication headsets	David A. Cartes, Laura R. Ray, Robert D. Collier	1758
Wheel/rail noise generation due to nonlinear effects and parametric excitation	Anders Nordborg	1772

ACOUSTICAL MEASUREMENTS AND INSTRUMENTATION [58]

Acoustic and dynamic mechanical properties of a polyurethane rubber	Peter H. Mott, C. Michael Roland, Robert D. Corsaro	1782
High power ultrasound standard	George S. K. Wong, Lixue Wu	1791

PHYSIOLOGICAL ACOUSTICS [64]

Sources of DPOAEs revealed by suppression experiments, inverse fast Fourier transforms, and SFOAEs in impaired ears	Dawn Konrad-Martin, Stephen T. Neely, Douglas H. Keefe, Patricia A. Dorn, Emily Cyr, Michael P. Gorga	1800
Pure-tone threshold estimation from extrapolated distortion product otoacoustic emission I/O-functions in normal and cochlear hearing loss ears	Paul Boege, Thomas Janssen	1810

PSYCHOLOGICAL ACOUSTICS [66]

Rhythmic masking release: Contribution of cues for perceptual organization to the cross-spectral fusion of concurrent narrow-band noises	Martine Turgeon, Albert S. Bregman, Pierre A. Ahad	1819
Assessing auditory distance perception using virtual acoustics	Pavel Zahorik	1832

SPEECH PRODUCTION [70]

Glottal flow through a two-mass model: Comparison of Navier–Stokes solutions with simplified models	M. P. de Vries, H. K. Schutte, A. E. P. Veldman, G. J. Verkerke	1847
American and Swedish children's acquisition of vowel duration: Effects of vowel identity and final stop voicing	Eugene H. Buder, Carol Stoel-Gammon	1854
Gender differences in vocal fold contact computed from electroglottographic signals: The influence of measurement criteria	Maureen B. Higgins, Laura Schulte	1865

SPEECH PERCEPTION [71]

Toward a model for lexical access based on acoustic landmarks and distinctive features	Kenneth N. Stevens	1872
Auditory normalization of French vowels synthesized by an articulatory model simulating growth from birth to adulthood	Lucie Ménard, Jean-Luc Schwartz, Louis-Jean Boë, Sonia Kandel, Nathalie Vallée	1892
Quantifying the intelligibility of speech in noise for non-native listeners	Sander J. van Wijngaarden, Herman J. M. Steeneken, Tammo Houtgast	1906

SPEECH PROCESSING AND COMMUNICATION SYSTEMS [72]

YIN, a fundamental frequency estimator for speech and music	Alain de Cheveigné, Hideki Kawahara	1917
---	-------------------------------------	------

CONTENTS—*Continued from preceding page***BIOACOUSTICS [80]****Modeling sound transmission through the pulmonary system and chest with application to diagnosis of a collapsed lung**

T. J. Royston, X. Zhang, H. A. Mansy, R. H. Sandler

1931

CUMULATIVE AUTHOR INDEX

1947

ACOUSTICAL NEWS—USA

Elaine Moran

Acoustical Society of America, Suite 1NO1, 2 Huntington Quadrangle, Melville, NY 11747-4502

Editor's Note: Readers of this Journal are encouraged to submit news items on awards, appointments, and other activities about themselves or their colleagues. Deadline dates for news items and notices are 2 months prior to publication.

New Fellows of the Acoustical Society of America



Asbjørn Krokstad—For applications of ray tracing in room acoustics.



David Marsh—For contributions to the application of architectural acoustics and audio design.



Christopher A. Shera—For contributions to the understanding of mechanisms underlying otoacoustic emissions.

USA Meetings Calendar

Listed below is a summary of meetings related to acoustics to be held in the U.S. in the near future. The month/year notation refers to the issue in which a complete meeting announcement appeared.

- 2002**
- 3–7 June 143rd Meeting of the Acoustical Society of America, Pittsburgh, PA [Acoustical Society of America, Suite 1 NO1, 2 Huntington Quadrangle, Melville, NY 11747-4502; Tel.: 516-576-2360; Fax: 516-576-2377; E-mail: asa@aip.org; WWW: asa.aip.org].
- 19–21 Aug. INTER-NOISE 2002, Dearborn, MI [INTER-NOISE 02 Secretariat, The Ohio State University, Department of Mechanical Engineering, 206 West 18th Ave., Columbus, OH 43210-1107, USA or E-mail: hp@internoise2002.org].
- 2–6 Dec. Joint Meeting: 144th Meeting of the Acoustical Society of America, 3rd Iberoamerican Congress of Acoustics, and 9th Mexican Congress on Acoustics, Cancun, Mexico [Acoustical Society of America, Suite 1NO1, 2 Huntington Quadrangle, Melville, NY 11747-4502; Tel.: 516-576-2360; Fax: 516-576-2377; E-mail: asa@aip.org; WWW: asa.aip.org/cancun.html].

- 2003**
- 28 April–2 May 145th Meeting of the Acoustical Society of America, Nashville, TN [Acoustical Society of America, Suite 1NO1, 2 Huntington Quadrangle, Melville, NY 11747-4502; Tel.: 516-576-2360; Fax: 516-576-2377; E-mail: asa@aip.org; WWW: asa.aip.org].
- 10–14 Nov. 146th Meeting of the Acoustical Society of America,

Austin, TX [Acoustical Society of America, Suite 1NO1, 2 Huntington Quadrangle, Melville, NY 11747-4502; Tel.: 516-576-2360; Fax: 516-576-2377; E-mail: asa@aip.org; WWW: asa.aip.org].

- 2004**
- 24–28 May 75th Anniversary Meeting (147th Meeting) of the Acoustical Society of America, New York, NY [Acoustical Society of America, Suite 1NO1, 2 Huntington Quadrangle, Melville, NY 11747-4502; Tel.: 516-576-2360; Fax: 516-576-2377; E-mail: asa@aip.org; WWW: asa.aip.org].
- 29 Nov.–3 Dec. 148th Meeting of the Acoustical Society of America, San Diego, CA [Acoustical Society of America, Suite 1NO1, 2 Huntington Quadrangle, Melville, NY 11747-4502; Tel.: 516-576-2360; Fax: 516-576-2377; E-mail: asa@aip.org; WWW: asa.aip.org].

Cumulative Indexes to the *Journal of the Acoustical Society of America*

Ordering information: Orders must be paid by check or money order in U.S. funds drawn on a U.S. bank or by Mastercard, Visa, or American Express credit cards. Send orders to Circulation and Fulfillment Division, American Institute of Physics, Suite 1NO1, 2 Huntington Quadrangle, Melville, NY 11747-4502; Tel.: 516-576-2270. Non-U.S. orders add \$11 per index.

Some indexes are out of print as noted below.

Volumes 1–10, 1929–1938: JASA and Contemporary Literature, 1937–1939. Classified by subject and indexed by author. Pp. 131. Price: ASA members \$5; Nonmembers \$10.

Volumes 11–20, 1939–1948: JASA, Contemporary Literature, and Patents. Classified by subject and indexed by author and inventor. Pp. 395. Out of print.

Volumes 21–30, 1949–1958: JASA, Contemporary Literature, and Patents. Classified by subject and indexed by author and inventor. Pp. 952. Price: ASA members \$20; Nonmembers \$75.

Volumes 31–35, 1959–1963: JASA, Contemporary Literature, and Patents. Classified by subject and indexed by author and inventor. Pp. 1140. Price: ASA members \$20; Nonmembers \$90.

Volumes 36–44, 1964–1968: JASA and Patents. Classified by subject and indexed by author and inventor. Pp. 485. Out of print.

Volumes 36–44, 1964–1968: Contemporary Literature. Classified by subject and indexed by author. Pp. 1060. Out of print.

Volumes 45–54, 1969–1973: JASA and Patents. Classified by subject and indexed by author and inventor. Pp. 540. Price: \$20 (paperbound); ASA members \$25 (clothbound); Nonmembers \$60 (clothbound).

Volumes 55–64, 1974–1978: JASA and Patents. Classified by subject and indexed by author and inventor. Pp. 816. Price: \$20 (paperbound); ASA members \$25 (clothbound); Nonmembers \$60 (clothbound).

Volumes 65–74, 1979–1983: JASA and Patents. Classified by subject and indexed by author and inventor. Pp. 624. Price: ASA members \$25 (paperbound); Nonmembers \$75 (clothbound).

Volumes 75–84, 1984–1988: JASA and Patents. Classified by subject and indexed by author and inventor. Pp. 625. Price: ASA members \$30 (paperbound); Nonmembers \$80 (clothbound).

Volumes 85–94, 1989–1993: JASA and Patents. Classified by subject and indexed by author and inventor. Pp. 736. Price: ASA members \$30 (paperbound); Nonmembers \$80 (clothbound).

Volumes 95–104, 1994–1998: JASA and Patents. Classified by subject and indexed by author and inventor. Pp. 632. Price: ASA members \$40 (paperbound); Nonmembers \$90 (clothbound).

Revision List

New Associates

Ames, Derek S., UGN, Rieter Automotive Acoustic Lab., 38555 Hills Tech Dr., Farmington Hills, MI 48331

Andersson, Nils-Ake A., Ecophon AB, P.O. Box 500, Hyllinge SE-260 61 Sweden

Bierenbaum, Dan J., 11833 Goshen Ave., Apt. 8, Los Angeles, CA 90049

Bischel, Marsha D., Armstrong World Industries, Inc., Armstrong Bldg. Products Innovation, 2500 Columbia Ave., Lancaster, PA 17603

Bloom, Braham J., 8 LKiege St., Russell Lea, Sydney NSW 2046, Australia

Brennan, Jim, Bollard & Brennan, Inc., 3805 Taylor Rd., Ste. 2, Loomis, CA 95650

Brown, Gordon, The Old School, Ipswich Rd., Gosbeck, Suffolk IP6 9SN, U.K.

Buggy, Niall J., 2 Sussex Court, Roan St., London SE10 9JT, U.K.

Calleja, Christian J., Sparcoustics, Nest Belvedere Str., Gzira GZR02, Malta

Carreras, Francesco, CNUCE/CNR, Via Moruzzi 1, Pisa 56124, Italy

Cassone, Alphonse, Sonic Technologies International, 4171 Moorcroft St., Las Vegas, NV 89147

Cha, Hyungtai, School of Electronic Engineering, Soongsil Univ., 1-1 Sangdo-5 Dong, Dongjak-Ku, Seoul 156-743, South Korea

Chandrasekaran, Kesavan, Flat No. Gb, Old. No. 45, M.G.R. Rd., Kalakshetra Colony, Besant Nagar, Chennai, Tamil Nadu State 600090, India

Chen, Alex C., The Louis Berger Group, Inc., 100 Halsted St., East Orange, NJ 07018

Chisaki, Yoshifumi, 3-10-25 Izumi, Kumamoto 862-0941, Japan

Chowdhury, Sayed, 7/89 Hampden Rd., Lakemba, Sydney NSW 2195, Australia

Corry, Brian P., Arup Acoustics, 2440 South Sepulveda Boulevard, Ste. 180, Los Angeles, CA 90064

Cosgrove, Michael A., 54 Fawn Ridge Rd., Henrietta, NY 14467-9536

Cudahy, Edward A., 6 Oakridge Dr., Gales Ferry, CT 06335

Day, Athol, Day Design Pty. Ltd., Ste. 17, 808 Forest Rd., Peakhurst NSW, Australia

Deguchi, Sachiko, P.O. Box 19706, Stanford, CA 94309

Demoulin, Xavier, 10 alle Kan Ar Mor, Arradon, Bretagne 56610, France

Downing, Marshall W., Aerospace Engineering Dept., Lord Corporation, 2000 West Grandview Blvd., Erie, PA 16514-0038

Drost, Charles E., 34 Main St., Landisville, PA 17538

Fang, Shirley, JMicon, 43 Corporate Park, Ste. 106, Irvine, CA 92606

Fenwick, Alan J., Laurel Cottage, East Farm Osmington, Weymouth, Dorset DT3 6EX, U.K.

Fincham, Adam M., LEGI-Coribus CNRS, 21 Ave Martyrs, Grenoble 38000, France

Fontana, Philip M., 3110 Ann Arbor Court, Sugarland, TX 77478

Fouvy, Charles L., 241 Cotham Rd., Kew VIC 3101, Australia

Garcia-Osuna, Fernando, Schlumberger, Sonic Product Line, 2-2-1 Fuchinobe, Sagamihara, Kanagawa 229-0006, Japan

Garnham, Carolyn W., MED EL, Research and Development, 77a Furstenweg, Innsbruck, Tyrol A6020, Austria

Ghazanfar, Asif A., Max Planck Inst. for Biological Cybernetics, Spemannstrasse 38, Tuebingen 72076, Germany

Hanes, Peter, National Research Council, Inst. of National Measurement Standards, Bldg. M36, 1500 Montreal Rd., Ottawa, ON K1A 0R6, Canada

Harroun, Stuart, 7020 Edith Blvd., NE, Albuquerque, NM 87113

Hasse, Roger D., National Center for Physical Acoustics, Univ. of Mississippi, 1 Coliseum Dr., P.O. Box 1848, University, MS 38677

Hedges, Robert A., Air Force Research Lab., IFGC, 525 Brooks Rd., Rome, NY 13441-4505

Iliev, Alexander I., 2918 Whitehead St., Miami, FL 33133

Jones, David J., Lockheed Martin, ME&SS, 9500 Godwin Dr., Manassas, VA 20110-4157

Jones, David L., Communication Disorders, Univ. of Wyoming, P.O. Box 3311, Laramie, WY 82071-3311

Jung, Wan Jin, Samick, Apt. 3, Dong 206, 1018-1 Bangbae Dong, Secho Gu, Seoul 137-851, Korea

Kastak, David A., Long Marine Lab., 100 Shaffer Rd., Santa Cruz, CA 95060

Katsumi, Nagai, 66-1-B201 Numa, Tsuyama, Okayama 708-0823, Japan

Keiffer, John C., Michael R. Yantis Associates, Inc., 1809 Seventh Ave., Ste. 1609, Seattle, WA 98101

Kemp, Jr., Robert H., Electrical Engineering, Input/Output, Inc., 5200 Toler St., Harahan, LA 70123

Kenbu, Teramoto, A-2 241-17 Akamatsu, Saga 840-0042, Japan

Kenji, Saijyou, Technical Research and Development Inst., Japan Defense Agency, Fifth Res. Ctr., Acoustic Equipment Research Section, First Div., 3-13-1 Nagasetown, Yokosuka, Kanagawa 239-0826, Japan

Khismatullin, Damir B., Dept. of Mathematics, Virginia Polytechnic Inst. and State Univ., 460 McBryde Hall, Blacksburg, VA 24061-0123

Kimmel, Eitan, Technion-Israel Inst. of Technology, Agricultural Eng. & Biomedical Eng., Haifa 32000, Israel

Krajnc, Matjaz, Obala 130, Portoroz S1-6320, Slovenia

Krishnamurthy, Durgasharan, Computer Controls Corporation, 4 S. R. P. Nagar, Saibaba Colony, Coimbatore, Tamil Nadu 641011, India

Kumaresan, Muthiah, 295 Triplican High Rd., Chennai Tamilnadi 600005, India

Lehman, Sean K., 4348 Valley Ave., Pleasanton, CA 94566

Leon, David R., Leon Guitars, P.O. Box 412154, Los Angeles, CA 90041

Linton, Debbie S., Test & Analysis, Buell Motorcycle Company, 2799 Buell Dr., East Troy, WI 53120

Lysaght, Thomas A., National Univ. of Ireland, Maynooth, Computer Science, Callan Bldg., Maynooth, Ireland

Magruder, Steven F., Submarine Technology, Johns Hopkins Univ., Applied Physics Lab., 11100 Johns Hopkins Rd., Laurel, MD 20723-6099

Mann, Thomas L., Weyrcliffe-Century Ltd., 37863 Melrose Dr., Cathedral City, CA 92234

Marrin Nakra, Teresa, 381 Farrwood Dr., Ward Hill, MA 01835

Marshall, Gordon B., Ramsey Coote Instruments Pty. Ltd., 18 Edward St., Sandringham VIC 3191, Australia

Martin, Stephen W., 26034 Bellemore Dr., Ramona, CA 92065

McAloon, Kevin P., Champion Technologies, Inc., Resonator Development, 2553 North Edgington St., Franklin Park, IL 60131

McArthur, Rod L., 1123 Jade Wind Dr., Ballwin, MO 63011

McKay, T. Niel, 687 6th Ave. North, Naples, FL 34102

- McLachlan, Neil M., 11 Brockenshire St., Clifton Hill, VIC 3068, Australia
 Meghezzi, Fatiha, 15 Rue A Cie Emir Abdelkaber, Constantine 25000, Algeria
 Miller, Cheryl J., Geo-Marine, Inc., Marine Biology, 11846 Rock Landing Dr., Ste. C, Newport News, VA 23606
 Miller, Jeffrey D., Sound Technology Consultants, Inc., 2707 Via Viejas, Alpine, CA 91901
 Minor, Michael A., Michael Minor & Associates, 2535 NE 22nd Ave., Portland, OR 97212
 Moenssen, David, Visteon Corporation, 15200 Commerce Dr. North, MD 83, Cube C-144, Dearborn, MI 48120
 Mohl, Bertel, Zoophysiology, Arhus Univ., Bygn. 131, C. F. Mollers Alle, Arhus DK-8000C, Denmark
 Montgomery, T. C., Applied Research Lab., Pennsylvania State Univ., P.O. Box 30, State College, PA 16804
 Moran, Mark L., ERDC-CCREL, 72 Lyme Rd., Hanover, NH 03755
 Morcillo, Miguel A., Fundacion Cidaut, Parque tecnologico de Boecillo P209, Boecillo, Valladolid 47151, Spain
 Murdoch, Jay, Owens Corning, 6209 44th Ave., Riverdale Park, MD 20737
 Murray, Todd W., Aerospace and Mechanical Eng., Boston Univ., 110 Cummington St., Boston, MA 02215
 Nakayama, Kaoru T., Faculty of Literature and Social Science, Yamagata Univ., 1-4-12 Kojirakawa, Yamagata 990-8560, Japan
 Nash, Amy A., 1009 Tony Place, Longmont, CO 80501
 Ogoli, David M., Architecture, Judson College, 1151 North State St., Elgin, IL 60123
 Olsen, Henrik, ATCO Noise Management, 1243 McKnight Blvd. NE, Calgary, AB T2E 5T1, Canada
 Oppegaard, Brian R., 40 Acacia Tree Ln., Irvine, CA 92612
 Piazza, Timothy W., CAE Ultrasonics, Precision Cleaning, 9 North Main St., Jamestown, NY 14701
 Pinezich, John D., Advanced Acoustic Concepts, Systems Engineering, 200 13th Ave., Ronkonkoma, NY 11779
 Pope, Ernest D., 500 Oak Garden Dr., Kernersville, NC 27284
 Posey, Roger D., Ascent Noise Control, Inc., P.O. Box 396, Sykesville, MD 21784
 Poterek, Thomas J., 4620 Crestway Dr., Austin, TX 78731
 Prasad, Satya, Satyu Associates, 176/25 4th Main Rd., Bangalore, Karnataka 560003, India
 Pristera, Jessica L., Cerami & Associates, Inc., 317 Madison, Ste. 220, New York, NY 10017
 Querol, Jose M., Querol Consultors Acustics S.L., Rambia 109-C, 5-2, Sabadell, Barcelona 08202, Spain
 Rackley, Ronald D., du Treil, Lundin & Rackley, Inc., 201 Fletcher Ave., Sarasota, FL 34237
 Rampone, Joseph C., 600 Meridian St. Ext., Apt. 709, Groton, CT 06340
 Raney, Jill J., CREC Soundbridge, Audiology, 123 Progress Dr., Wethersfield, CT 06109
 Reis, Luiz A. C., Rua do Progresso 368/32, Recife PE 50070-020, Brazil
 Requena, Rodmara, UNIJAC, Av. Nicolau Mercadante #48, Sao Paulo 12327-680, Brazil
 Reyes, Carlos H., Wilson, Ihrig & Associates, Inc., 5776 Broadway, Oakland, CA 94618
 Roberts, Simona P., NOAA Fisheries, Office of Protected Resources, 1315 East-West Highway, 13th Fl., Silver Spring, MD 20910
 Robinson, Carlos J., Ecologia de Pesquerias, UNAM, Inst. de Ciencias Del Mar, Ciudad Univ., Mexico DF 04500, Mexico
 Rocchesso, Davide, Dipt. di Informatica, Universita' di Verona, Strada Le Grazie 15 Verona VR 34134, Italy
 Rosen, Kristin M., 5002 Sheboygan Ave., 308, Madison, WI 53705
 Ryan, Thomas N., GPD Group, 520 South Main St., Akron, OH 44311
 Samuels, Ruth E., 7080 High Sierra Circle, West Palm Beach, FL 33411
 Sawicki, Katharine, 102 Easton Ave., New Brunswick, NJ 08901
 Sawyer, Eric, 40 Wilmot St., Manchester, NH 03103
 Schwartz, Reva, Forensic Services Div., U. S. Secret Service, 950 "H" St. NW, Ste. 4200, Washington, DC 20223
 Scott, Dan W., 901 East Hazel Ave., Ponca City, OK 74601
 Sheplak, Mark, Aerospace Engineering, Univ. of Florida, 231 Aerospace Bldg., P.O. Box 11, Gainesville, FL 32611-6250
 Sheridan, Ted M., Ryall Porter Architects, 135 Fifth Ave., 2nd Fl., New York, NY 10010
 Shuttari, Syed B., S. B. S. & Associates, Ajek Chamber, 1st Fl., 4 Kushal Nagar, Jalna Rd., Aurangabad, Maharashtra 431005, India
 Silvia, Manuel T., Sittel Corporation, Research and Business Development, 1206 Foothill Rd., Ojai, CA 93023-1727
 Skowbo, Eric, 3481 Monarch St., Melbourne, FL 32934
 Smith, Robert W., Physical Acoustics Group, Penn State Univ., Applied Research Lab., P.O. Box 30, North Atherton St., State College, PA 16804
 Soares de Brito, Alexandre, Rua Etelvina 262, Sao Paulo 03616-100, Brazil
 Sodal, Audun, Acoustics and Cables, Petroleum Geo-Sciences, Inc., 16010 Barkers Point Ln., Houston, TX 77079
 Tibbitts, Jo T., Brainwaves: A Step Ahead Pty. Ltd., Forensic Sound Lab., P.O. Box 740, Katoomba NSW 2780, Australia
 Tuomainen, Jyrki, Lab. of Computational Engineering, Helsinki Univ. of Technology, Miestentie 3, Espoo FIN-02015 HUT, Finland
 Van Dijk, Bas, Cochlear Technology Centre Europe, Research Team, Drie Eikestraat 661, Edegem 2650, Belgium
 Van Trees, Harry L., C3I Center, 4400 University Dr., Fairfax, VA 22030
 Venditti, Jennifer J., P.O. Box 452, Providence, NJ 07974
 Vertegeal, Han, Acoustics Engineering, Groenling 43, Boxmeer NB 5831 MZ, The Netherlands
 Viator, John A., Univ. of California, Irvine, Beckman Laser Inst. and Medical Clinic, 1002 Health Sciences Rd. East, Irvine, CA 92612
 Wang, Chao, Lab. for Computer Science, MIT, 200 Technology Square, Room 639, Cambridge, MA 02139
 Wangpattanamongkol, Kiinon, 50/251 Bangna Trad Rd., Bangkaew, Bangplee, Samutprakarn 10540, Thailand
 Wartzok, Douglas, Dept. of Biology, Florida International Univ., University Graduate School, Univ. Park PC 236, Miami, FL 33199
 Witton, Carolina, Neurosciences Research Inst., Aston Univ., Birmingham B4 7ET, U.K.
 Xiaorui, Shi, Dept. of Otolaryngology, Head & Neck Surgery, Oregon Health Hearing Research Center, 3181 SW Sam Jackson Park Rd., Portland, OR 97201-3098
 Zhu, Wenhao, Inst. for Microstructural Sciences, National Research Council, Ottawa, ON K1A 0R6, Canada
 Zu, Yiqing, Motorola Labs., Motorola China Research Center, 1168 Nanjing Rd., W. 38F, Shanghai 200041, China

New Students

- Alvarenga, Andre V., COPPE/Federal Univ. of Rio de Janeiro, Biomedical Engineering, Center of Technology, Room H327, Caixa Postal 68510, Rio de Janeiro 21945-970, Brazil
 Anderson, Brian E., 421 North 800 East, Provo, UT 84606
 Armstrong, Kristen A., Speech and Hearing Science, Univ. of North Texas, P.O. Box 305010, Denton, TX 76203-5010
 Aziz, Asim, H. No. 522/10 St. No. 27, Rawalpindi, Punjab 46000, Pakistan
 Baughman, Jason R., 1809 A Morgan Ln., Redondo Beach, CA 90278
 Bello, Ryan M., 415 South Atherton St., Apt. C6, State College, PA 16801
 Beltran, Alicia, Oceanographic Center, Nova Southeastern Univ., 8000 North Ocean Dr., Dania Beach, FL 33004
 Bemis, Jeremy, 740 Phillips, South Haven, MI 49090
 Biziorek, Ryan B., Box 85 Hicks Center, 1200 Academy St., Kalamazoo, MI 49006
 Blodgett, Benjamin D., 18 East Congress Parkway, #604D, Chicago, IL 60605
 Bolin, Michael J., 206½ South St., West Lafayette, IN 47906
 Bowden, Erica E., Architectural Engineering, Univ. of Nebraska, 245 Peter Kiewit Inst., 1110 S. 67th St., Omaha, NE 68182
 Brown, Christopher A., Parnly Hearing Inst., Loyola Univ. Chicago, 6525 North Sheridan Rd., Chicago, IL 60626
 Callen, Peter A., Mechanical Engineering, Univ. of Wollongong, Wollongong NSW 2522, Australia
 Carter, Benjamin A., 415 West College Ave., #507, State College, PA 16801
 Ceperley, Daniel P., 107B Carrollton Terrace, Charlottesville, VA 22903-3514
 Chilcote, Elizabeth A., 11526 Clipper Circle, Frisco, CA 75034
 Cooper, Huw R., Audiology Dept., Univ. Hospital Birmingham, Selly Oak Hospital, Raddlebarn Rd., Birmingham B29 6JD, England
 Couture, Olivier, Medical Biophysics, Univ. of Toronto, 2075 Bayview, S-Wing, Toronto, ON M4N 3M5, Canada
 Davis, Donald P., 14 Chauret, Montreal, PQ H9A 1M7, Canada

- de la Vaux, Steven K., Psychology Dept., Emory Univ., 532 North Kilgo Circle, Atlanta, GA 30322
- Devore, Sasha, 66 Pleasant St., #1, Cambridge, MA 02139
- Dibazar, Alireza A., Biomedical Engineering, Univ. of Southern California, OHE 500, 2650 McClintock St., Los Angeles, CA 90089-1451
- Dooley, Benjamin D., 12 Oakwood Rd., Simsbury, CT 06070
- Doolittle, Daniel F., 1595 Angus Rd., Hayes, VA 23072
- Dunkley, Kathleen T., 3226 Cowley Way, #2, San Diego, CA 92117
- Escudero, Paola, McGill Univ., School of Communication Sciences, 1266 Pine Ave. West, Montreal, PQ H3G 1A8, Canada
- Fenech, Benjamin A., 97 Guze Ellul Mercer St., Dingli RB1 11, Malta
- Fitzgerald, Erin C., SMC 986, P.O. Box 3210, Pittsburgh, PA 15230
- Fox, Jesse R., Bates College, Box 179, Lewiston, ME 04240
- Freeman, Smith A. M., Dickinson College, HUB 636, Colege and Louthier St., Carlisle, PA 17013
- George, Mathew M., 3000 Kings Court, Apt. C, Raleigh, NC 27606
- Gertner, Alan B., 1280 Rolls Court, Toms River, NJ 08755
- Glenn, Christopher D., 8 East Galloway Dr., Hillsdale, MI 49242
- Gonzalez, Carolina, Linguistics, Univ. of Southern California, 3601 Watt Way, GFS 301, Los Angeles, CA 90089-1693
- Gramann, Mark R., 803 South Pugh St., #1, State College, PA 16801
- Grube, Manon, Dept. of Zoology-Neurobiology, Univ. of Leipzig, Talstr. 33, Leipzig, Saxony 04103, Germany
- Gupta, Navarun, Dept. of Electrical and Computer Eng., Florida International Univ., 10555 West Flagler St., DSP Lab., Room EAS 3970, Miami, FL 33174
- Guthrie, Oneil W., 5519 Wellesley Ave., Pittsburgh, PA 15206
- Gutierrez, Remy, Univ. of Rochester, CPU Box 271491, Rochester, NY 14627
- Haroon, Muhammad, 271 South River Rd., Apt. 20, West Lafayette, IN 47906
- Hayes, Rachel L., Linguistics Dept., Univ. of Arizona, Douglass Bldg. 200-E, Tucson, AZ 85721
- Henderson, Paul D., 15817 Thompson Rd., Charlotte, NC 28227
- Hozsan, Vladimir, Strocsa Vas 83, Lsutomer 9240, Slovenia
- Hyeong-Seok, Kim, 2917 SW 13th St., #85, Gainesville, FL 32608-3044
- Inacio, Octavio J., ESMAE, Polytechnic School of Music and Performing Arts, Rua da Alegria 503, Porto 4000-045, Portugal
- Jambrosic, Kristian, Faculty of EE and Computing, Dept. of Electroacoustics, Unska 3, Zagreb HR 1000, Croatia
- Jing, Yuan, 14 Buswell St., #615, Boston, MA 02215
- Johnson, Shawn F., 606 St. Paul St., Campus Box 166, Baltimore, MD 21202
- Kelly, Thomas P., Edinburgh Univ., Adam Ferguson Bldg., George Square, Edinburgh, Midlothian EH8 9YL, Scotland
- Kim, Moonseok, Mathematics Dept., Pohang Univ. of Sci. and Tech., San 31, Hyoja dong, Nam gu, Pohang, Kyunbuk 790784, Korea
- Kiran, Konde K., National Center for Physical Acoustics, Univ. of Mississippi, Room 1093, University, MS 38677
- Kolodziej, Martin P., 4349 N Neva, Norridge, IL 60706
- Kopco, Norbert, Cognitive and Neural Systems, Boston Univ., 677 Beacon St., Boston, MA 02215
- Kottke, Nelson J., Graduate Program in Acoustics, Penn State Univ., Applied Science Bldg., P.O. Box 30, State College, PA 16804
- Kwern, Ohgoo, Chango Elementary 646, Pohang, Kyunbuk 791-250, South Korea
- Leonard, Taryn M., 2411 South I-35E, Apt. 1916, Denton, TX 76210
- Lewis, Dawna E., Audiology, BTNRH, 555 North 30th St., Omaha, NE 68131
- Li, Yaoyu, Mechanical Engineering, Purdue Univ., Room 76, Herrick Labs., West Lafayette, IN 47907-1077
- Liao, Kuo Chih, 1197 West 36th St., Apt. C, Los Angeles, CA 90007
- Libbey, Bradley W., Mechanical Engineering, Georgia Inst. of Technology, Atlanta, GA 30324-0405
- Lin, Calvin, Room L-507, Tsui Nam House, Tsui Ping Rd., Kwun Tonh, Kowloon, Hong Kong
- Man Lung Stanley, Cheung, Flat F, 18/F, Tower 4, Park Belvedere, MaOn Shan, Shatin, Hong Kong
- Martis, Emily L., Beloit College, Box 866, 700 College St., Beloit, WI 53511
- McDuffee, Matthew R., Columbia College Chicago, 600 South Michigan Ave., Chicago, IL 60605-1996
- Megerson, Susan C., 14212 West 72nd St., Shawnee Mission, KS 66216
- Meinke, Deanna K., Associates in Acoustics, Inc., Audiology, 1112 73rd Ave., Greeley, CO 80634
- Menezes, Pedro L., Rua Prudente de Moraes 352-Carmo, Olinda PE 53020-140, Brazil
- Mensing, David J., 1007 Arrowhead Dr., Apt. 23C, Oxford, OH 45056
- Micallef, Cynthia F., Kjellmansgatan 13-314, Gothenburg GTB 41318, Sweden
- Michal, Pakula, Environmental Mechanics and Computer Science, Bydgoszcz Univ., ul. Chodkiewicza 30, Bydgoszcz 85-064, Poland
- Miller, Denise M., Univ. of Hartford, Box 2017, 299 Bloomfield Ave., West Hartford, CT 06117
- Mirman, Daniel, Psychology, Carnegie Mellon Univ., 5000 Forbes Ave., Pittsburgh, PA 15213
- Mossbridge, Julia A., Communication Sciences & Disorders, Northwestern Univ., 2229 North Campus Dr., Evanston, IL 60208
- Na, Won-Bae, 3636 North Campbell Ave., #4109, Tucson, AZ 85719
- Nagy, Attila B., 17 Etele UT, Budapest 1119, Hungary
- Namarvar, Hassan H., Dept. of Biomedical Engineering, Univ. of Southern California, OHE 500, 3650 McClintock St., Los Angeles, CA 90007
- Norville, Pelham D., Georgia Inst. of Technology, Electrical Engineering, 324852 Georgia Tech Station, Atlanta, GA 30332-1030
- Ochs, Robert A., RR7 Box 152, Spencer, IN 47460
- Oh, Sunyoung, Linguistics Dept., Univ. of British Columbia, E270-1866 Main Mall, Vancouver, BC B6T 1Z1, Canada
- Ohkawa, Keiichi, RSMAS, AMP, Univ. of Miami, 4600 Rickenbacker Causeway, Miami, FL 33149
- Oliveira, Leonardo C. F., Lab. de Fonetica e Psicolinguistica, Inst. de Estudos da Linguagem, UNICAMP, CP 6045, Campinas SP 13084-971, Brazil
- Osterhoudt, Curtis, Physics Dept., Washington State Univ., Pullman, WA 99164-2814
- Owens, Andrew D., 2020 Hollywood Parkway, York, PA 17403-4214
- Paeng, Dong-Guk, Pennsylvania State Univ., 315 Hallowell Bldg., University Park, PA 16802
- Paes, Edward, Physics Dept., Univ. of Rhode Island, 2 Lippitt Rd., Kingston, RI 02881-0817
- Park, Chang-Mok, Industrial Engineering, Ajou Univ., San 5, Wonchun, Paldal-gu, Suwon, Kyonggi 442-749, South Korea
- Parks, Susan E., Biology, Woods Hole Oceanographic Inst., Redfield 132, MS#34, Woods Hole, MA 02543
- Pincon, Herve B., Georgia Inst. of Technology, Mechanical Engineering, 873 Ferst Dr., Atlanta, GA 30332
- Prasad, Kunal, Electrical and Computer Engineering, Univ. of Massachusetts, Dartmouth, 285 Old Westport Rd., North Dartmouth, MA 02747
- Roby, Joshua L., Mechanical Engineering, Virginia Commonwealth Univ., 601 West Main St., Richmond, VA 23284
- Sarda, Alexandra A. P., Dept. of Ocean Engineering, Florida Atlantic Univ., 101 North Beach Rd., Dania Beach, FL 33004
- Schultz, Todd, Aerospace Engineering, Univ. of Florida, P.O. Box 116250, Gainesville, FL 32611-6250
- Shiraiwa, Hiroko, Dept. of Electronics Engineering, Univ. of Electro-Communications, 1-5-1 Chofugaoka, Chofu, Tokyo 182-8585, Japan
- Sladen, Douglas P., Hearing and Speech Sciences, Vanderbilt Bill Wilkerson Center, 1114 19th Ave. South, Nashville, TN 37215
- Smith, Jason L., 153 Pleasant St., Watertown, MA 02472
- Stephens, Joseph D., Psychology Dept., Carnegie Mellon Univ., 5000 Forbes Ave., Pittsburgh, PA 15213
- Sun, Lei, Bioengineering Dept., Pennsylvania State Univ., 205 Hallowell Bldg., University Park, PA 16802
- Taiwo, Michael, Bestway Recording Studio, G.P.O. Box 17525 Dugbe Ibadan, Ibadan, Oyo State 30667, Nigeria
- Tlumak, Abreena I., 235 Edgewood Ave., #B-12, Pittsburgh, PA 15218
- Tucker, Beth E., 303 Westbrook Hills Dr., Syracuse, NY 13215
- Valentine, Andrew S., 94 Campden Crescent, Dagenham, Essex RM8 2SA, England
- Vodila, Benjamin J., P.O. Box 4389, West Point, NY 10997
- Walker, Natasha M., 483 North Pine Island Rd., C103, Plantation, FL 33324
- Watkinson, Rebecca K., 21 Waterside, Brighthelmsea, Essex CO7 0AY, U.K.
- Weber, Thomas C., Pennsylvania State Univ., Graduate Program in Acoustics, 2045 Applied Science Bldg., University Park, PA 16802
- White, Brian R., Rear 4 Harrison, Carbondale, PA 18407
- Willt, Ben D., 1601 Hillcrest Dr., Apt. Y30, Manhattan, KS 66502

Wohlgemuth, Tara A., 9 Prospect Ave., Roslindale, MA 02131
 Wrigley, Stuart N., Dept. of Computer Science, Univ. of Sheffield, Regent Court, 211 Portobello St., Sheffield South Yorkshire S1 4DP, U.K.
 Wu, Tianming, Electrical and Computer Eng., Univ. of Massachusetts, Dartmouth, 285 Oldwesport Rd., North Dartmouth, MA 02747
 Yang, Wonyoung, 710 South Atherton St., #405, State College, PA 16801
 Yim, Geun-Tae, ISVR, Univ. of Southampton, Tizard Bld., Southampton SO17 1BJ, U.K.
 Yoon, Heakyung, Carnegie Mellon Univ., Dept. of Architecture, 5000 Forbes Ave., Pittsburgh, PA 15213
 Zook, Thomas C., 7109 Pluribus St., Long Beach, CA 90808

Members Elected Fellows

K. W. Commander, P. H. Dahl, B. H. Houston, P. M. Hurdle, D. R. Ketten, A. Krokstad, D. E. Marsh, A. Rakowski, W. J. Richardson, N. Rott, C. Shera, L. H. Sibul, A. M. Simmons, D. C. Swanson, L. A. Werner, G. Zweig

Associates Elected Members

M. F. Cheesman, T. Connelly, R. J. Cruz, C. L. Fouvy, R. D. Godfrey, M. C. Goody, L. C. Gray, D. P. Joiner, K. Q. Kay, L. LoPresti, R. Panuszka, D. W. Sawnz, S. A. Sansone, X. Serra, G. R. Stanley, M. R. Sydorenko, M. Veidt, D. M. Warren

Students to Associates

J. E. Ament, P-P. Beaujean, F. J. Blonigen, A. R. Bontomase, P. Bouchilloux, E. F. Brittan-Powell, S. C. Burnett, B. S. Cazzolato, R-L. Chen, S-L. K. Chi, L. M. T. De Jesus, M. L. Dent, L. A. Drake, M. R. Dungan, G. Emadi, P. E. Guise, J. E. Huber, W. Hui, M. Kitahara, J. S. Krueger, D. O. Ludwigsen, J. S. Madison, M. F. McKinney, M. E. Nilsson, K. S. Olson, P. H. Ressler, B. M. Sabol, Z. Shi, K. M. Steinhauer, G. S. Stickney, P-C. Torng, R. R. Torres, F-M. Tsao, E. J. Tucholski, Y. Wang, A. Weber, W. Xu

Associates to Students

T. Pham, A. Sarampalis

Reinstated

W. G. Richarz—*Fellow*
 D. J. Burr—*Member*
 P. Case—*Associate*

Resigned

C. W. Horton, Sr., P. Leehey, F. D. Tappert—*Fellows*
 W. L. Braun, M. Brooke, L. M. Cross, B. R. B. Garrett, M. A. Hayes, S. Kawamura, R. Makarewicz, J.F. Mills—*Members*
 J-L. M. Berton, K. Chittayil, P. A. Davidson, D. Frederick, T. Hattori, W. Holliday, J. M. Hudig, D. Lohse, J. C. Machado, R. E. McClocklin, Y. K. Pong, B. Prager, G. Schouten, S. D. Teitzel, P. Temerli, D. S. G. Vine, J. Wilhelm, M. L. Yaeger-Dror—*Associates*
 B. Lanctot—*Student*

Deceased

E. H. Brown, J. A. Kessler, H. R. Mull, M. Schulkin—*Fellows*
 A. B. Anderson, R. Goldstein, G. B. Henry, H. G. McMichael—*Members*
 C. Y. Kapper—*Associate*

Fellows	997
Members	2714
Associates	2627
Students	961
	<hr/> 7299

ACOUSTICAL NEWS—INTERNATIONAL

Walter G. Mayer

Physics Department, Georgetown University, Washington, DC 20057

New Officers of the International Commission for Acoustics (ICA)

The International Commission for Acoustics (ICA) General Assembly elected new Members of the Board at their meeting in Rome on 6 September 2001: Gilles Daigle (Canada), President; Suk Wang Yoon (Korea), Secretary-General; Volker Mellert (Germany), Treasurer; Lawrence A. Crum (USA), Past-President.

The following were elected to Designated Seats: Sonoko Kuwano (Japan); Ren-He Zhang (China); Claude Legros (France); Giovanni Brambilla (Italy); Nikolai A. Dubrovsky (Russia); Philip A. Nelson (UK). The following were elected to Open Seats: Charles G. Don (Australia); Samir N. Y. Gerdes (Brazil); Juan A. Gallego-Juarez (Spain); Antoni Śliwiński (Poland); Ewald Benes (Austria); George Dodd (New Zealand).

In addition, the ICA chose Madrid as their meeting location in 2007. The next International Congress on Acoustics will be held in Kobe, Japan, 5–9 April 2004.



ICA officers (left to right): Volker Mellert, Treasurer; Gilles Daigle, President; Adriano Allipi, Chair Rome Congress; Lawrence A. Crum, Past-President; Suk Wang Yoon, Secretary-General.

Stanley Ehrlich receives Mira Paul Memorial Award

At the recent joint meeting of the Acoustical Society of India and the Madras Chapter of ASA in Vellore, India, Stanley Ehrlich received the first Mira Paul Memorial Award. This award, which is granted by the Indian organization, the Acoustical Foundation, Educational, and Charitable Trust (AFECT), is given annually to an outstanding acoustician whose achievements exemplify the ideals of AFECT, which is based in Madras and which has programs to help deafened individuals.



Stanley L. Ehrlich (I) receives Mira Paul Award.

International Meetings Calendar

Below are announcements of meetings to be held abroad. Entries preceded by an * are new or updated listings with full contact addresses given in parentheses. *Month/year* listings following other entries refer to meeting announcements, with full contact addresses, which were published in previous issues of the *Journal*.

April 2002

8–11

6th Congress of the French Acoustical Society, joint with the Belgian Acoustical Society, Lille. (Web: www.isen.fr/cfa2002) 8/01

22–24

International Meeting on Acoustic Pollution in Cities, Madrid. (Fax: +34 1 559 74 11; e-mail: dccimad8@viajeseci.es) 12/01

May 2002

27–30

Joint Meeting: Russian Acoustical Society and Conference on Ocean Acoustics, Moscow. (Fax: +7 095 124 5983; Web: rav.sio.rssi.ru/Ixconf.html) 6/01

28–31

6th International Conference on Applied Technologies of Hydroacoustics and Hydrophysics, St. Petersburg. (Fax: +7 812 320 8052; e-mail: mfp@mail.wplus.net) 2/02

29–1

Nonlinear Waves in Microstructured Solids (Euro-mech 436), Tallinn. (Fax: +371 645 1805; e-mail: je@ioc.ee) 10/01

30–1

2nd International Conference on Newborn Hearing Screening, Diagnosis, and Intervention, Villa Erba/Como. (Fax: +1 303 764 8220; Web: <http://www.biomed.polimi.it/nhs2002>) 12/01

June 2002

- 1–3 ***AES 21st International Conference on Architectural Acoustics and Sound Reinforcement**, St. Petersburg, Russia. (Conference Secretariat, P.O. Box 08A9, 1st Krasnoarmeyskaya Street 1, 198005 St. Petersburg, Russia; Fax: +7 812 316 1559; Web: <http://www.aes.org/events/21>)
- 4–6 **6th International Symposium on Transport Noise and Vibration**, St. Petersburg. (Fax: +7 812 127 9323; Web: webcenter.ru/~eeaa/tn/eng/tn2002) 2/01
- 10–14 **Acoustics in Fisheries and Aquatic Ecology**, Montpellier. (Web: www.ices.dk/symposia/) 12/00
- 24–27 **6th European Conference on Underwater Acoustics**, Gdańsk. (Fax: +48 58 347 1535; Web: www.ecua2002.gda.pl/) 10/01
- 24–28 **11th Symposium of the International Society for Acoustic Remote Sensing**, Rome. (Fax: +39 06 20660291; Web: ISARS2002.ifa.rm.cnr.it/) 10/01
- 24–28 **11th International Symposium on Nondestructive Characterization of Materials**, Berlin. (Fax: +49 30 678 07129; Web: www.cnde.com) 2/02

July 2002

- 2–7 **ClarinetFest 2002**, Stockholm. (e-mail: kkoons@pegasus.cc.ucf.edu) 10/01
- 15–17 **International Symposium on Active Control of Sound & Vibration (Active 2002)**, Southampton. (Fax: +44 23 8059 3190; Web: <http://www.isvr.soton.ac.uk/active2002>) 10/01
- 17–21 **7th International Conference on Music Perception and Cognition (7th ICMPC)**, Sydney. (Fax: +61 2 9772 6736; Web: www.uws.edu.au/marcs/icmpc7) 2/02
- 19–21 **Auditorium Acoustics: historical and contemporary design and performance**, London. (Fax: +44 1225 826691; e-mail: m.barron@bath.ac.uk) 2/02

August 2002

- 19–23 **16th International Symposium on Nonlinear Acoustics (ISNA16)**, Moscow. (Fax: +7 095 126 8411; Web: acs366b.phys.msu.su/isna16/) 12/00
- 26–28 **2nd Biot Conference on Poromechanics**, Grenoble. (Web: geo.hmg.inpg.fr/biot2001) 8/01
- 26–28 **Joint Baltic-Nordic Acoustical Meeting 2002**, Lyngby. (Fax: +45 45 88 05 77; Web: www.dat.dtu.dk/~bnam/) 10/01

September 2002

- 10–12 ***32nd International Acoustical Conference—EAA Symposium**, Banská Štiavnica, Slovakia. (M. Čulik, Physics and Applied Mechanics Department, TU Zvolen, Masarykova 24, 96001 Zvolen, Slovakia; Fax: +421 45 532 1811; Web: <http://alpha.tuzvo.sk/skas/acoustics>)
- 11 ***Dutch and Belgian Acoustical Societies Joint Meeting**, Utrecht, The Netherlands. (NAG-Secretariat, P.O. Box 480, 6200 AL Maastricht, The Netherlands; e-mail: info@nag-acoustics.nl)
- 11–13 **10th International Meeting on Low Frequency Noise and Vibration**, York. (Fax: +44 1277 223 453; Web: <http://www.lowfrequency2002.org.uk>) 12/01
- 16–18 **International Conference on Noise and Vibration Engineering**, Leuven. (Fax: +32 1632 2987; Web: www.isma.isaac.be) 2/02
- 16–21 **Forum Acusticum 2002 (Joint EAA-SEA-ASJ Meeting)**, Sevilla. (Fax: +34 91 411 7651; Web: www.cica.es/aliens/forum2002) 2/00
- 26–28 **Autumn Meeting of the Acoustical Society of Japan**, Akita. (Fax: +81 3 5256 1022; Web: <http://wwwsoc.nacsis.ac.jp/asj/>) 12/01

October 2002

- 9–11 ***Acoustics Week in Canada**, Charlottetown, PE, Canada. (A. Cohen, Department of Psychology, University of Prince Edward Island, 550 University Avenue, Charlottetown, PE C1A 4P3, Canada; Fax: +1 902 628 4359; Web: <http://caa-aca.ca/PEI-2002.html>)
- 26–28 ***6th National Congress of the Turkish Acoustical Society**, Kars, Turkey. (Türk Akustik Derneği, YTÜ Mimarlık Fakültesi, 80750 Beşiktaş-Istanbul, Turkey; Fax: +90 212 261 0549; Web: <http://www.takder.org/kongre-2002/kongre2002.html>)

November 2002

- 21–22 ***New Zealand Acoustical Society 16th Biennial Conference**, Auckland, New Zealand. (New Zealand Acoustical Society, PO Box 1181, Auckland, New Zealand; e-mail: graham@marshallday.co.nz)
- 30–6 **Joint Meeting: 9th Mexican Congress on Acoustics, 144th Meeting of the Acoustical Society of America, and 3rd Iberoamerican Congress on Acoustics**, Cancún. (Web: asa.aip.org/cancun.html) 10/00

December 2002

- 9–13 **International Symposium on Musical Acoustics (ISMA Mexico City)**, Mexico City. (Fax: +52 55 5601 3210; Web: <http://www.unam.mx/enmusica/ismamexico.html>) 2/02

March 2003

- 17–20 **German Acoustical Society Meeting (DAGA2003)**, Aachen. (Fax: +49 441 798 3698; e-mail: dega@aku-physik.uni-oldenburg.de) 2/02

April 2003

- 7–9 **WESPAC8**, Melbourne, Australia. (Web: www.wespac8.com) 10/01

June 2003

- 8–13 **XVIII International Evoked Response Audiometry Study Group Symposium**, Puerto de la Cruz. (Web: www.ierasg-2003.org) 8/01
- 16–18 ***ACOUSTICS—Modeling & Experimental Measurements**, Cadiz, Spain. (Acoustics03, Wessex Institute of Technology, Ashurst Lodge, Ashurst, Southampton SO40 7AA, UK; Fax: +44 238 029 2853; Web: www.wessex.ac.uk/conference/2003/acoustics/index.html)
- 29–3 ***8th Conference on Noise as a Public Health Problem**, Amsterdam-Rotterdam, The Netherlands. (Congress Secretariat, P.O. Box 1558, 6501 BN Nijmegen, The Netherlands; Fax: +31 24 360 1159; e-mail: office.nw@prompt.nl)

July 2003

- 7–10 ***10th International Congress on Sound and Vibration**, Stockholm, Sweden. (Fax: +46 88 661 9125; Web: www.congex.com/icsv10)

August 2003

- 6–9 ***Stockholm Music Acoustics Conference 2003 (SMAC03)**, Stockholm, Sweden. (SMAC Secretariat, Department of Speech, Music, and Hearing, Royal Institute of Technology (KTH), Dr. Kristinas Väg 31, 10044 Stockholm, Sweden; Web: <http://www.speech.kth.se/music/smac03>)
- 25–27 ***Inter-Noise 2003**, Jeju Island, Korea. (Dept. of Mechanical Engineering KAIST, 373-1, Kusong-dong, Yusong-gu, Taejon 305-701, Korea; Fax: +82 42 869 8220; Web: www.icjeju.co.kr)

September 2003

- 1–4 **Eurospeech 2003**, Geneva. (Web: www.symporg.ch/eurospeech2003) 8/01

April 2004

- 5–9 **18th International Congress on Acoustics (ICA2004)**, Kyoto. (Web: <http://www.ica2004.or.jp>) 4/01

REPORTS OF RELATED MEETINGS

This Journal department provides concise reports of meetings that have been held by other organizations concerned with acoustical subjects; and of meetings co-sponsored by the Acoustical Society but planned primarily by other co-sponsors.

First International Workshop on Thermoacoustics

s'Hertogenbosch, The Netherlands

INTRODUCTION

The First International Workshop on Thermoacoustics in s'Hertogenbosch, The Netherlands, held 23–25 April 2001 brought together people in academia, industry, and government who specialize in the field of thermoacoustics for the exchange of scientific and technical information (see Fig. 1). The workshop focused on technical discussions rather than commercial activities.

Primary sponsors and organizers were the Technical University of Eindhoven and the Acoustical Society of America (ASA), with numerous other sponsors, including sponsorship and participation by the Office of Naval Research International Field Office Europe. The primary organizer was Jos Zeegers from the Technical University of Eindhoven, assisted by Charles Schmid, Executive Director of ASA, and Robert Keolian, Chair of the ASA Technical Committee on Physical Acoustics. The 78 participants were from the US, The Netherlands, United Kingdom, Japan, France, Russia, Germany, Ukraine, Australia, China, Mexico, Canada, and Italy.

The workshop was divided into six focus sessions (A–F), which are discussed below. Copies of the full agenda, abstracts of presentations, and attendees list are available from either the author or the Acoustical Society of America.

Thermoacoustics usually refers to the science and technology of heat transport in a sound field, e.g., a thermoacoustic cooler for Navy shipboard or other cooling requirements, to the generation of sound from heat, and to heat-driven thermoacoustic coolers. The scope of the First International Workshop on Thermoacoustics was somewhat broader to include topics such as thermoacoustics in relation to combustion processes and thermoacoustics and flame noise amplification and control.

TECHNICAL PRESENTATIONS

Session A: Thermoacoustics component

All papers in this session were concerned with detailed description and measurement of basic thermoacoustic phenomena, such as temperature and flow distribution.

The session began with an interesting paper by Phillip Blanc-Benon [Ecole Centrale de Lyon] that addressed particle image velocimetry for flow measurement in thermoacoustic fields. Basically, he uses laser imaging and a charge coupled device (CCD) camera to capture the motion of particle packets and then charts the particle packets' motion by cross correlating packets as a function of time. This technique clearly images the flow and vortex motion across the stack plates. He also uses arrays of thermocouples to accurately track temperature distributions.

The next paper on temperature distribution modeling was by Haruko Ishikawa [University of Queensland], and was followed by two papers by Pierrick Lotton [Université du Maine] and Mamoru Ozawa [Kansai University], which were concerned with temperature distribution across the stack. Ralph Muehleisen [University of Colorado] described the measurement of thermoviscous functions of various pore density sections of reticulated vitreous carbon (RVC) stacks.

This session closed with a well-researched review paper by Nicholas Rott [Stanford University], which was distributed to the participants. Professor Rott reported that our current knowledge of thermoacoustic phenomenon began in the early 1900s when unexplained acoustic emissions were noted by people who first liquified helium.

A member of the audience subsequently noted that thermoacoustic instability has been a major concern in spacecraft design due to the use of cryogenic liquid fuels. Kramers solved the helium emission mystery in a

1949 paper. Professor Rott traced the understanding of the phenomenon back to Kirchhoff and then via an historical tour through the additions to our understanding provided by Maxwell, Stokes, Prandtl, Langevin, Rayleigh, Joule, and Lighthill. Rott himself published extensively on the topic in the 1960s and 1970s and is the originator of the Rott functions, which are used to characterize viscous and thermal properties of the working gas in a thermoacoustic device.

Session B: Streaming and nonlinearities

Streaming is a second-order acoustic effect caused by nonzero average mass transport within the gas. It is usually undesirable because it generally works against the heat-flow action in the thermoacoustic device. That is, it literally blows the heat in the wrong direction.

The session began with an overview of acoustics research at the National Center for Physical Acoustics at the University of Mississippi, delivered by Richard Raspet. Raspet noted that thermoacoustic processes are very complex, with many degrees of freedom which cannot be easily separated for analysis.

John McHugh [University of New Hampshire] followed with a computer modeling paper that considered the effect of viscosity in a thermoacoustic resonator. He began with the full Navier–Stokes equations. Victor Sparrow [Penn State University (PSU)] then presented a second computer modeling paper. Sparrow's PSU team has assembled a 32-processor computing capability. He noted that commercially available computational fluid dynamics (CFD) codes are inadequate to handle thermoacoustic problems. Hence, they have developed their own codes. He uses these sophisticated numerical modeling methods to investigate streaming flows and minor losses in thermoacoustic devices. Their long-term goal is the development of full three-dimensional simulations of thermoacoustic refrigerators.

Vitali Gusev [Université du Maine] presented work on asymptotic models for nonlinear phenomena. He considered streaming, nonlinear wave steepening, the use of active suppression to remove second harmonics (and hence the subsequent chain of higher-order harmonics), and some near-field edge effects.

Nobumasa Sugimoto [Osaka University] then presented work on thermoacoustic effects on nonlinear propagation of pulse waves in a gas-filled tube with an array of Helmholtz resonators. The surprise in this theoretical work was the appearance of an acoustic soliton. The last two papers by S. Job [Université de Maine] and André Petculescu [Ohio University] respectively, considered streaming in an annular (traveling wave) device and the use of jet pumps (flow restrictors) for streaming suppression.

Session C: Driven refrigerators

After a full day of theory and modeling results, it was with anticipation that we began a session on actual applications. Steve Garrett of Penn State University was the lead speaker and he did not disappoint any of the listeners, as he is one of the strongest promoters of thermoacoustics.



FIG. 1. Workshop organizer Jos Zeegers with workshop participants Nicholas Rott and F. de Waele.



FIG. 2. Matthew Poese demonstrating a small, regenerator-based, thermoacoustic refrigerator.

Garrett's major current interest is in thermoacoustic refrigerators. In general, he favors the use of high-intensity electrodynamic loudspeakers as prime movers for his devices. He prefers these drivers because they have good frequency and amplitude control, robust high-temperature design, and are readily available. He also favors placing the magnet on the armature and the coil on the stator. He traced the development of these coolers from Greg Swift's 1983 patent and showed several current devices that he has designed and delivered. He and his Penn State University team are currently building a 10-KW (3-ton) chiller. Garrett closed by noting that these chillers are still niche devices.

Matthew Poese, one of Garrett's Ph.D. students, followed with a demonstration of a small, regenerator-based, thermoacoustic refrigerator (see Fig. 2). This device is a standing wave tube with a short stack at the half-wavelength location. This regenerator stack is cylindrical and of smaller diameter than the standing wave tube. Hence, some gas leaks around the regenerator and back into the tube. The portion beyond the regenerator is then a two-port Helmholtz resonator (one port through the leak path and the other through the higher impedance regenerator). This device has some potential efficiency advantage over the standing wave chiller. Matthew switched on the drive to this device and, sure enough, the resonator end quickly turned cold.

The session closed with a paper by Pablo Mayzys [University of Calgary], which covered some computer simulations of pulse tube regenerator designs. The pulse tube regenerators are used in cryocoolers because of their ability to reach a few degrees Kelvin. Their heat removal capacity is small but they can reach lower temperatures than other thermoacoustic designs.

Session D: Transducers, drivers, and outside the gas topics

Yoichi Matsubara [Nihon University] presented a paper on the performance of a thermal compressor for a pulse tube cryocooler. This complex device is basically a thermoacoustic Stirling cycle compressor where the piston in a conventional Stirling engine is replaced by a "slug" of moving

gas. The working gas is helium and Matsubara has been able to reach 8–9° K. The device has multiple cooling stages and, while it reaches very low temperatures, its heat capacity is small.

Robert Smith of Garrett's group at Penn State University then presented a detailed design for a high-efficiency, 2-KW acoustic source for a thermoacoustic refrigerator. This device used a permanent magnet armature and the design focus was on optimizing performance by carefully controlling variables such as electrical and mechanical resistance, eddy currents, magnetic field leakage, etc.

John Corey, who runs a small company called the Clever Fellows Innovation Company (CFIC), closed this session. He noted that he is neither an acoustician nor a physicist; instead, he is a very innovative engineer who is working hard to make devices that can economically outperform internal combustion engines. He pointed out that most of the problems of loss and inefficiency in Stirling and thermoacoustic devices are "on the edges," i.e., in the heat exchangers, burners, and other secondary devices. Corey also lamented the fact that these thermoacoustic devices cannot take advantage of the isothermal heat absorption/rejection that occurs in other engine types with change of phase. In his words, "The whole issue is the search for devices that outperform internal combustion engines." CFIC has built a number of ingenious devices and currently has a 3-ton (10-KW) cooler almost ready to market.

Session E1: Spontaneous oscillators: Combustion

This session was devoted to explaining the spontaneous acoustic emissions that occur in furnaces and other combustors. In general, these emissions are troublesome and sometimes destabilizing and need to be controlled. Ann Dowling [University of Cambridge] led this session.

A principal objective in modern combustors is to achieve a very lean operation in order to minimize nitrous oxide. Unsteady combustion is a problem at these lean burn temperatures, and this unsteadiness can lead to acoustic emissions which, in turn, can feed the instability of the flame, occasionally leading to flame extinguishment. Rayleigh first identified the general phenomenon as "singing flames." Control of the problem, while maintaining the desired lean burn, is the focus of Dowling's group's research. Their technique is to determine the acoustic modes (eigenvalues) in the complex burner geometry and then try to alleviate those modes that show instability or a tendency to grow via burner design changes. They use computational fluid dynamics techniques for this purpose. Several other speakers explored aspects of this problem following Dowling's talk.

The last of these papers by F. Einsiger [Foster Wheeler Energy Corporation] discussed 300-MW fossil fired plants with furnace dimensions of 10 meters on a side that can vibrate at 40–50 Hz in an extreme manner due to acoustic effects. He concluded how this effect can be avoided with stable Sondhauss or Rijke tubes.

Session E2: Spontaneous oscillators: Engines

Greg Swift [Los Alamos National Laboratory (LANL)] gave the invited presentation for this session. If there is one person who has championed this technology internationally over the last 20 years, it is Dr. Swift. He possesses the rare but important combination of theoretician and experimentalist, and has provided the inspiration and guidance to the small community of people currently working in this field.

He reported on progress achieved by a joint LANL/Chart Denver (formerly Cryogen, Inc.) project, funded by the U.S. Department of Energy to build a "500-gallon/day" cryocooler. The objective is to use methane (CH₄) to power a traveling wave thermoacoustic engine that in turn powers three cryocoolers. The purpose of the cryocoolers is to cool the methane to 111 K, at which point it liquefies. The liquid natural gas (LNG) can then be transported in tank trucks. The market for such a device is a gas field, which is remotely located, so that transport of the LNG by boat or trucks has an economic advantage over the use of pipelines.

The cryocooler device, photos of which were shown, is about 40 ft. long and stands vertically (to take advantage of convective forces) with the burner on the top. It operates at 40 Hz and uses 30 MPa (about 450 PSI) helium as the working gas. Streaming and thermal expansion stress are key problems with this device. The ultimate goal is to attain 20 tons (about 60 KW) of cooling power. The current device achieves about 40% of Carnot

efficiency, which means that 40 KW of acoustic power results in about 8 KW of cooling. Hence, the scale up to 60 KW is very dependent on the solution of these problems.

Mark Hamilton of The University of Texas concluded this session with a discussion of a numerically efficient algorithm to solve the full nonlinear gas dynamic equations in a thermoacoustic engine.

Session F: Visions of the future

W. C. van Wijngaarden, of the Dutch firm IHC Gusto Engineering, presented an economic analysis of the use of a TASHER (a combination of a thermoacoustic Stirling heat engine and an acoustic Stirling hybrid refrigerator). This is basically the device that Greg Swift is building to produce liquid natural gas. A second potential future application is in the area of using very small thermoacoustic refrigerators as on-circuit-board coolers for use in computers. Reh-Lin Chen and Ya-Chi Chen [Rockwell Science Center], and Orest Symko [University of Utah] and his students are developing devices for this application.

CONCLUSION

The basic thermoacoustic processes are now well understood to at least first order (the introduction of ever louder acoustic sources brings nonlinear wave steepening and this area is still not fully characterized), but major engineering problems in improving device efficiency still exist.

The ultimate success of thermoacoustics as an economically viable alternative to more conventional energy cycles depends on the solution of these difficult problems. Device physical configuration, working gases, material selection, peripheral component design, and working pressures and temperatures all interact in ways that make device optimization difficult. If these problems are solved and thermoacoustic devices of efficiencies approaching more conventional devices are produced, they then promise to provide powerful, safe, and environmentally friendly power sources that can be used in remote and difficult situations. The ultimate goal, in this case, is worth the small but intense effort now being expended. The First International Workshop on Thermoacoustics served as part of this effort, and anyone interested in organizing the next workshop should contact Jos Zeegers (j.c.h.zeegers@tue.nl) or Charles Schmid (asa@aip.org)

F. Michael Pestorius

Office of Naval Research International Field Office

Electronic mail: mpestorius@onrifo.navy.mil

BOOK REVIEWS

P. L. Marston

Physics Department, Washington State University, Pullman, Washington 99164

These reviews of books and other forms of information express the opinions of the individual reviewers and are not necessarily endorsed by the Editorial Board of this Journal.

Editorial Policy: *If there is a negative review, the author of the book will be given a chance to respond to the review in this section of the Journal and the reviewer will be allowed to respond to the author's comments. [See "Book Reviews Editor's Note," J. Acoust. Soc. Am. 81, 1651 (May 1987).]*

Boundary Element Acoustics Fundamentals and Computer Codes

T. W. Wu, Editor

WIT Press, Billerica, MA, 2001.

256 pp. Price: \$149.00 ISBN: 1853125709.

As stated in the preface, this book is intended to be used as a "tutorial book on the fundamentals of BEM in acoustics with some simple source codes." Hence, the book starts with basic aspects of prediction and simulation of acoustics fields by means of the boundary element method (BEM). But it also leads the reader to more advanced topics such as the indirect variational boundary element method, time domain analysis, and the boundary element technique for moving sources.

The editor, T. W. Wu, has written four of the nine chapters of the book. The remaining five chapters are written by other researchers. Hence, some overlapping could not be avoided, especially when defining basic equations and boundary conditions in several chapters. However, this has not disturbed me at all, since a certain degree of repetition makes the text more readable.

A few similar books exist for the same subject. Some of the books were published nearly 10 years ago, and therefore it seems to be a good time for publishing a new book about the boundary element method. Surprisingly, the same publisher announces on the back cover a second new book on *Boundary Elements in Acoustics* (edited by O. von Estorff), which covers just the same subject. The reader will judge if both books will supplement and complete each other in a suitable way.

The book includes a CD-ROM containing the FORTRAN code for 2-D BEM, 3-D BEM, indirect BEM, eigenvalue BEM, and transient BEM.

The book is organized into nine chapters.

In Chap. 1 (Fundamentals of linear acoustics, by A. F. Seybert), a short introduction is given into the theory of linear acoustics by explaining some important topics such as the wave equation, velocity potential, acoustics intensity, etc. This chapter is useful for a reader, who has only little knowledge in acoustics and will use the book for learning the first steps in acoustics and boundary elements simultaneously. However, some care is needed, since the time conventions $\exp(+i\omega t)$ [Eq. (4)] and $\exp(-i\omega t)$ [Eq. (10)] are mixed up.

In Chap. 2 (The Helmholtz integral equation, by T. W. Wu), the fundamental solution of the Helmholtz equation and the integral equations for the interior and the exterior problems are derived in a very clear and comprehensible manner. Furthermore, scattering and half-space problems are treated. The nonuniqueness difficulty at the eigenfrequencies of the adjoint problem is especially well explained. The presentation by T. W. Wu is successful in concentrating on the main ideas of the theory without using a big machinery of mathematics which sometimes hides the primary ideas by a lot of equations. Also, the explanation of the coefficient $C(P)$ is done with great care. On the other hand, the famous CHIEF method for overcoming the nonuniqueness problem is treated very briefly, so that additional literature likely has to be used for going deeper into details.

Chapter 3 (Two-dimensional problems) and Chap. 4 (Three-dimensional problems) are written by T. W. Wu, too. They focus on the computational aspects of the boundary element method and show how to transform the Helmholtz integral equation into a system of linear equations which can be solved numerically. Both chapters handle the two- and three-dimensional case in a very similar fashion. First, the discretization procedure

is described by introducing different kinds of elements (linear, quadratic, and cubic elements). Then it is shown how to transform general elements to a master element and how shape functions for the nodal variables should be chosen. Second, for the numerical integration, the standard Gaussian quadrature is recommended. The special treatment of the singular elements at the diagonal of the matrix is explained very carefully. Finally, the implementation of the CHIEF method by solving an overdetermined system by means of least square fitting is given. The accompanying FORTRAN programs for the 2-D and 3-D BEM are extremely helpful, and the source code can be found on the CD-ROM included with the book. All subroutines are carefully described at the ends of both chapters, and files with input and output data for two examples are provided. I could compile and execute the programs in a few minutes without any problems for the 2-D case, and I obtained the output results reported in the book. The compilation of the 3-D case took some more time due to the presence of two small errors in the program code. First, one line in the code was longer than 72 characters, which was easy to find. The second bug was more difficult to discover. An output file for both prepared examples was generated (one-dimensional plane wave in a box and pulsating sphere), but surprisingly it did not contain any of the results promised at the end of Chap. 4. The solution of the riddle was that an "END" statement was missing at the end of both input data files (in "example1.dat" and "example2.dat" after the "SOLVE" statement). Having added the "END," I just got the expected results in the output file.

Chapter 5 is devoted to the normal derivative of the Helmholtz integral equation. This equation is of high importance for practical applications, since a suitable combination of the surface Helmholtz integral equation and its normal derivative is free from critical frequencies. Such an approach is called the Burton–Miller method, which is often used, especially in the high-frequency domain, where the CHIEF method mostly fails to give good results due to many interior nodal surfaces appearing at higher frequencies. While the Burton–Miller approach is treated very briefly, the so-called "thin-body difficulty" is outlined in greater detail and explained thoroughly. The example given for the direct mixed formulation is very succinct, and I missed the FORTRAN code for these advanced methods. However, I am aware that it is impossible to address all aspects of the BEM in the same great detail.

In Chap. 6, the indirect variational boundary element method is treated by N. Vlahoupoulos. Subchapters 1–3 contain a clear description of the theory of the indirect formulation including its numerical formulation based on a variational principle. However, I had some problems understanding the content of subchapter 4 concerning the treatment of irregular frequencies with the so-called "simultaneous velocity and unequal impedance boundary condition" and the handling of multiple connections. Furthermore, I could not recognize the three curves in Fig. 3 (analytical solution, IBEM computation with and without treatment) on p. 103. But here again, it is very useful that the author has provided the source code of a large FORTRAN program, and I was able to compile and run the program without problems.

Normally, a dynamical analysis of a structural or an acoustical system is performed by using the finite element method (FEM). An interesting alternative for determining the eigenvalues and eigenmodes is the boundary element method as described in Chap. 7 (Acoustic eigenvalue analysis by boundary element methods, by E. de Mesquita Neto, E. R. Carvalho, J. R. de Franca Arruda, and R. Pavanello). Starting with the Helmholtz integral equation, the implicit acoustic eigenvalue problem is derived very clearly. Then, three strategies for determining the eigenfrequencies and eigenmodes are described. The direct search method can be easily understood. However,

the description of modal parameter estimation from frequency response functions is very compact and can only be fully understood if the reader possesses some background knowledge about the method. If not, the presentation given on pp. 136–138 may be somewhat dark and might be complemented by additional literature. The third strategy, the multiple reciprocity method, is clearly presented. For me, it was a new and fascinating idea to consider the Helmholtz equation as a Poisson equation with forcing term k^2u on the right-hand side. This procedure allows deriving a formulation for the eigenvalue problem, where the wave number k appears explicitly in the system of equations. Hence, this method is computationally less expensive, and it is compared with a FEM calculation for determining the eigenfrequencies of the interior of a two-dimensional model vehicle. Also, a 2-D FORTRAN code for the multiple reciprocity method is provided. All subroutines are very well documented, and it was a pleasure for me to reconstruct the numerical example described in the book and given in the input data file.

While in all other chapters of the book the boundary element analysis is performed in the frequency domain, only Chap. 8 describes the BEM in the time domain (Time domain three-dimensional analysis, by F. C. de Araujo, W. J. Mansur, and J. A. Carrer). Thus, it seems to be justified that it is the longest chapter with nearly 60 pages and covers approximately a quarter of the complete book. The time-dependent integral representation and the Kirchhoff integral representation for the scalar wave equation are derived by using a reciprocal relationship and the fundamental solution in the time domain. This presentation is mathematically very elegant, and it is clearly and comprehensibly formulated. Furthermore, all topics of the process of numerical implementation are precisely described. One of the most important issues, how to implement the method, seems to be the time-marching process. However, I had difficulties understanding this algorithm fully by going through the equations. Perhaps, it is needed to perform some numerical experiments with the programs included to get a “feeling” for time-based algorithms, if one is more familiar with the frequency domain. For this reason, the attached FORTRAN programs will be surely a great help, if the reader likes to understand the numerical implementation and corresponding algorithms more deeply. Curiously enough, the FORTRAN code on the CD-ROM is delivered as a Word-document (Prog1.doc), and both input files (App1_2.dat, K1.dat) are not documented in the book—perhaps I have overlooked such explanations (?).

The book ends with Chap. 9, where an important extension of the Helmholtz integral equation is described (Extended Kirchhoff integral formulations, by S. F. Wu). The extension is done for calculating acoustic radiation from a vibrating structure in motion. Such an extension is very important from a practical point of view, since the simulation of traffic noise with moving sources is often needed. The derivation of the extended formu-

lation is likely not easy to read for someone who is not well acquainted with the underlying theory of flow acoustics, since it is a very advanced subject. In addition, the presentation is very condensed, because the theory given in subchapters 2 and 3 is a short version of an earlier paper of X.-F. Wu and A. Akay (published in JASA 1992: “Sound radiation from vibrating bodies in motion,” JASA **91**, 2544–2555). Also, the nonuniqueness at critical frequencies is discussed. Two examples without flow and one example with flow are considered where critical frequencies appear. No formal proof of the existence of critical frequencies for the extended integral equation is given, but the examples of dilating and oscillating spheres in motion show the shifting effect of the flow (or the corresponding movement) on the critical frequencies in an impressive manner. The last subchapter is devoted to the practically important simulation of vehicle pass-by noise radiation. The sound radiation from a simplified vehicle at different Mach numbers is studied. This is a very interesting example, and it is a pity that no program code is included for providing an easier entrance to the numerical modeling of sound radiation from moving structures.

In summary, the book gives an excellent introduction and a good overview over the boundary element method in acoustics. Also, advanced topics of the method are treated, and the enclosed boundary element codes are particularly valuable.

One possible improvement of the layout of the book would be the following: On the top of every page, only the same general title is given. This makes the orientation for the reader difficult, especially if one would like to jump from a certain chapter to another. Hence, for the convenience of the reader, it would be useful to write, for example, the title of the current chapter into the header line on the left and the title of the corresponding subchapter into the header line on the right.

At present, I am responsible for a project, which has the aim to develop a special boundary element code for the purpose of improved noise protection. For the beginning and as a first step, I have recommended my students read the book and look at the FORTRAN code to gain a better understanding of the boundary element method. For this reason, it is very helpful to have the source code itself and not only executable programs. However, this suggestion is not limited to novices in the sector of the boundary element method. I highly recommend the book for all acousticians interested in theory, numerical implementation, and applications of the boundary element method in acoustics.

MARTIN OCHMANN

*TFH Berlin—University of Applied Sciences
Faculty of Mathematics, Physics, and Chemistry
Luxenburger Strasse 10 D-13353 Berlin, Germany*

REVIEWS OF ACOUSTICAL PATENTS

Lloyd Rice

11222 Flatiron Drive, Lafayette, Colorado 80026

The purpose of these acoustical patent reviews is to provide enough information for a Journal reader to decide whether to seek more information from the patent itself. Any opinions expressed here are those of reviewers as individuals and are not legal opinions. Printed copies of United States Patents may be ordered at \$3.00 each from the Commissioner of Patents and Trademarks, Washington, DC 20231. Patents are available via the Internet at <http://www.uspto.gov>.

Reviewers for this issue:

GEORGE L. AUGSPURGER, *Perception, Incorporated, Box 39536, Los Angeles, California 90039*

ALIREZA DIBAZAR, *Department of BioMed Engineering, University of Southern California, Los Angeles, California 90089*

HASSAN NAMARVAR, *Department of BioMed Engineering, University of Southern California, Los Angeles, California 90089*

DAVID PREVES, *4 Deerfield Drive, Princeton Junction, New Jersey 08550*

DANIEL R. RAICHEL, *2727 Moore Lane, Fort Collins, Colorado 80526*

CARL J. ROSENBERG, *Acentech, Incorporated, 33 Moulton Street, Cambridge, Massachusetts 02138*

KEVIN P. SHEPHERD, *Mail Stop 463, NASA Langley Research Center, Hampton, Virginia 23681*

WILLIAM THOMPSON, JR., *Pennsylvania State University, University Park, Pennsylvania 16802*

ERIC E. UNGAR, *Acentech, Incorporated, 33 Moulton Street, Cambridge, Massachusetts 02138*

6,278,656

43.20.Gp MANIPULATION OF ACOUSTIC WAVES USING A FUNCTIONALLY GRADED MATERIAL AND PROCESS FOR MAKING THE SAME

Vineet Tyagi and David A. Tinch, assignors to LightPath Technologies, Incorporated

21 August 2001 (Class 367/138); filed 2 September 1999

Manipulation (e.g., focusing, dispersing, steering, guiding) of acoustic waves is achieved by use of materials that have suitable gradients in their acoustic velocities. Such a gradient may be obtained as the result of a gradient in a material's elastic modulus, Poisson's ratio, and/or density. Suitable materials may be made, for example, by vapor deposition, by sol-gel processes, or by fusing together of sections with different acoustic properties.—EEU

6,256,263

43.30.Vh ACOUSTIC SENSING COUNTERMEASURE DEVICE AND METHOD OF DETERMINING A THREAT DIRECTION

Gerald T. Stevens, assignor to the United States of America as represented by the Secretary of the Navy

3 July 2001 (Class 367/1); filed 28 February 2000

An underwater acoustic receiving array is comprised of segmented vertical staves mounted around a vertical cylindrical housing. The staves are grouped to form directional acoustic beams across the entire horizontal plane. The direction of a threat is indicated by the output of the directional acoustic beams and the device relates this direction to a known reference direction, such as a compass heading or the heading to a vessel or other countermeasure device.—EEU

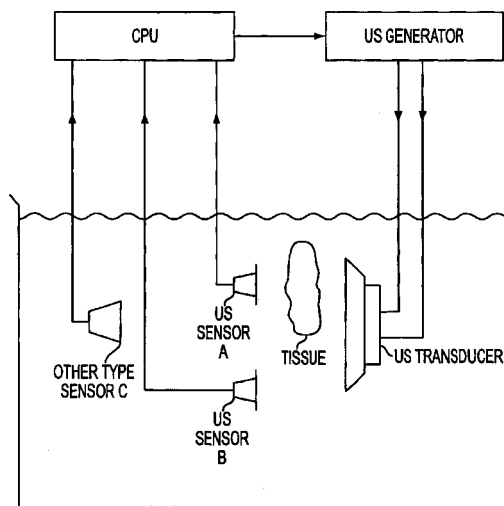
6,291,180

43.35.Wa ULTRASOUND-MEDIATED HIGH-SPEED BIOLOGICAL REACTION AND TISSUE PROCESSING

Wei-Sing Chu, assignor to American Registry of Pathology

18 September 2001 (Class 435/6); filed 29 September 1999

The fixation process for tissues prevents or arrests autolysis and putrefaction, coagulates and stabilizes soluble and structural proteins, fortifies the tissues against deleterious effects of subsequent processing, and facilitates staining. This patent points out that exposing tissues to ultrasound can elevate the rates of biological processes. Ultrasound in the frequency range of 0.1–50 MHz is applied and the sample tissue receives 0.1–200 W/cm² of



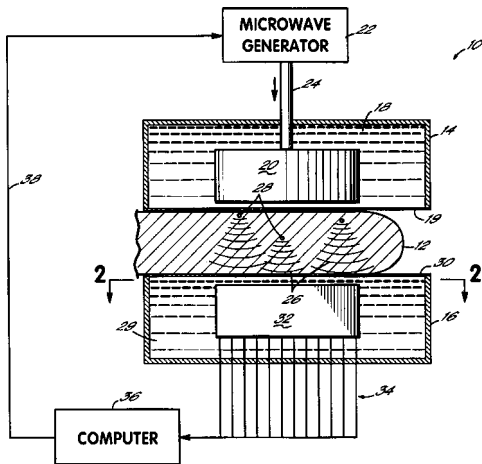
ultrasound intensity. One or more transducers produce ultrasound radiation under the control of a central processing unit. Sensors are provided to measure the tissue temperature. The system is said to provide accurate and optimum tissue fixation and processing without overfixation or tissue damage. The system is also said to permit completion of antigen–antibody reactions or nucleic acid hybridization in a very short time.—DRR

6,292,682

43.35.Wa PHOTOACOUSTIC BREAST SCANNER

Robert A. Kruger, assignor to Optosonics, Incorporated
18 September 2001 (Class 600/407); filed 4 October 1996

United States Patent 4,385,634 pointed out that ultrasonic signals could be induced in soft tissue whenever pulsed radiation is absorbed within the tissue. These signals can be detected by a transducer outside the body. The present patent discloses a way to produce multidimensional images from the detected signals. Multiple acoustic transducers are acoustically coupled to the surface of the tissue to measure acoustic waves produced



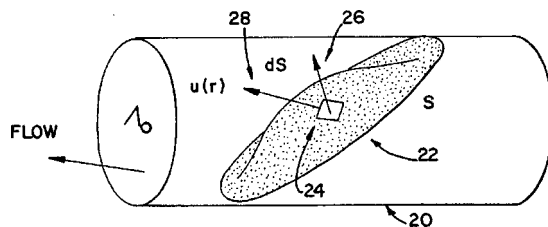
when the tissue is exposed to a pulse of electromagnetic radiation. The multiple transducer signals are then combined to yield an image of the absorptivity of the tissue, thus proving a means of medical diagnosis. Mathematical reconstruction procedures are described for producing images from the transducer signals.—DRR

6,293,914

43.35.Yb ULTRASONIC SYSTEM AND METHOD FOR MEASUREMENT OF FLUID FLOW

Thilaka S. Sumanaweera and Patrick J. Phillips, assignors to Acuson Corporation
25 September 2001 (Class 600/465); filed 31 August 1998

This is another Doppler effect detection device for measuring fluid flow in an enclosed system. Velocities are obtained along two or more different scan lines in a first ultrasonic scan plane to establish an angle of flow within the enclosed structure. A Doppler spectrum parameter is measured from a transmission in a second scan plane substantially perpendicular to the



first scan plane. Volume flow is computed from the flow angle and the parameter. The scan planes are generated through rotation of a linear array of transducers or holding a multi-dimensional transducer in place. A C-scan method with a linear transducer may also be used.—DRR

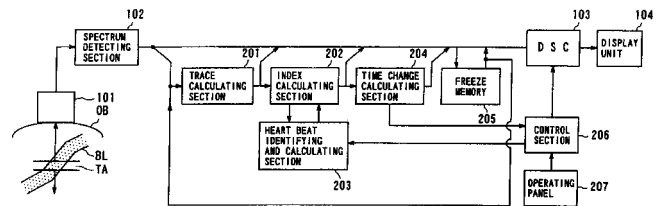
6,293,913

43.35.Yb DOPPLER ULTRASONIC DIAGNOSIS APPARATUS

Hiroyuki Tsujino and Takuya Sasaki, assignors to Kabushiki Kaisha Toshiba

25 September 2001 (Class 600/450); filed in Japan 10 February 1999

The device is intended to diagnose fluid motion such as blood flow *in vivo* through the well-known Doppler effect of ultrasonic waves. The device displays an image of the real time Doppler spectrum arising from ultrasonic echoes from the fluid motion. The embodiment is said to be capable of selecting a Doppler spectrum from this generated image, automatically rec-



ognizing the heartbeat range in the selected Doppler spectrum, and measuring an index value for Doppler diagnosis of every heartbeat range thus recognized. The patent cites benefits of simplified manual operation and reduced diagnostic time.—DRR

6,253,618

43.35.Zc APPARATUS AND METHOD FOR SYNTHETIC PHASE TUNING OF ACOUSTIC GUIDED WAVES

Shi-Chang Wooh, assignor to Massachusetts Institute of Technology

3 July 2001 (Class 73/602); filed 8 December 1999

This patent relates generally to nondestructive evaluation using a method for synthetically tuning multi-mode waves to a singular wave mode. The method is based on transmitting a multi-mode wave from each of a plurality of transmitters, receiving the plurality of transmitted waves with a receiver, shifting the received waves by an amount which reinforces a selected wave mode, and summing the received shifted waves to obtain a wave that is synthetically tuned to the selected wave mode.—EEU

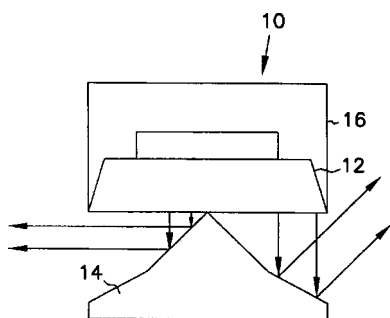
6,257,365

43.38.Ja CONE REFLECTOR/COUPLER SPEAKER SYSTEM AND METHOD

Alan Dwight Hulsebus II, assignor to Mediaphile AV Technologies, Incorporated

10 July 2001 (Class 181/155); filed 30 August 1996

Every few years someone patents the all too familiar combination of a downward-firing loudspeaker 12 and a conical reflector 14. This variant uses



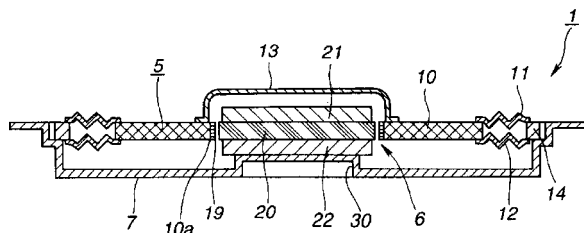
two or more conical sections to control the coverage pattern. Nineteen patent claims were granted.—GLA

6,259,800

43.38.Ja SPEAKER AND SPEAKER APPARATUS

Takahisa Tagami, assignor to Sony Corporation
10 July 2001 (Class 381/412); filed in Japan 11 March 1998

An improved, panel-type, gapless loudspeaker is disclosed. Voice coil 19 is attached directly to panel 5. A “double doughnut” field is produced by



the combination of magnetic plate 20 sandwiched between magnets 21 and 22.—GLA

6,263,083

43.38.Ja DIRECTIONAL TONE COLOR LOUSPEAKER

Gabriel Weinreich, assignor to The Regents of the University of Michigan
17 July 2001 (Class 381/97); filed 11 April 1997

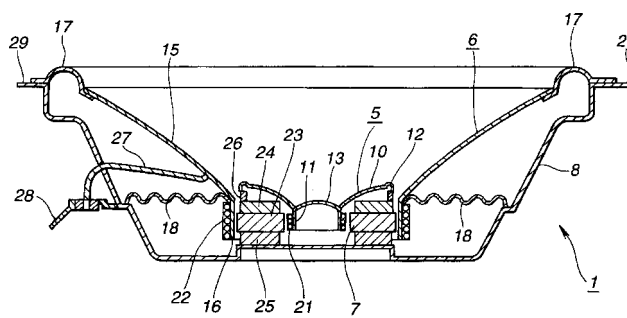
Sophisticated loudspeaker arrays employ complex signal processing to maintain a desired directional pattern, independent of frequency. This interesting invention does just the opposite. Complicated, frequency-specific directional patterns are developed to mimic the directionality of musical instruments.—GLA

6,269,168

43.38.Ja SPEAKER APPARATUS

Takahisa Tagami, assignor to Sony Corporation
31 July 2001 (Class 381/412); filed in Japan 25 March 1998

This coaxial loudspeaker is the gapless equivalent of the JBL LE14C



(circa 1970), which used a single magnet to energize high- and low-frequency voice coil gaps.—GLA

6,278,790

43.38.Ja ELECTROACOUSTIC TRANSDUCERS COMPRISING VIBRATING PANELS

Gillian Margaret Davis *et al.*, assignors to NCT Group, Incorporated
21 August 2001 (Class 381/398); filed 18 June 1999

A loudspeaker according to this patent consists in essence of a panel that forms one face of a box, the other faces being relatively rigid. The panel is provided with one or more piezoelectric actuators that induce flexural oscillations in it, and its edges are sealed to a frame, so as to eliminate the effect of sound radiated from the back of the panel. More complex embodiments make use of several parallel panels with suitable apertures to permit the passage of sound.—EEU

6,282,298

43.38.Ja ACOUSTIC DEVICE

Henry Azima *et al.*, assignors to New Transducers Limited
28 August 2001 (Class 381/423); filed 3 September 1996

This patent pertains essentially to acoustic radiators with nonuniform mass and stiffness distributions, selected to provide bending mode shapes and natural frequencies that result in desired radiation characteristics. The intent appears to be the achievement of loudspeakers with good acoustic properties, although their shapes may be unfavorable.—EEU

6,272,227

43.38.Si SIMULTANEOUS TWO-WAY COMMUNICATION APPARATUS USING EAR MICROPHONE

Hiroaki Yanagisawa, assignor to Temco Japan Company, Limited
7 August 2001 (Class 381/104); filed 24 September 1998

Several recent patents have been devoted to voice communication techniques utilizing in-the-ear bone conduction microphones. This invention is a relatively simple combination of gain switching and dynamic low-pass filtering to increase gain before feedback.—GLA

6,282,176

43.38.Si FULL-DUPLEX SPEAKERPHONE CIRCUIT INCLUDING A SUPPLEMENTARY ECHO SUPPRESSOR

Nariankadu D. Hemkumar, assignor to Cirrus Logic, Incorporated
28 August 2001 (Class 370/276); filed 20 March 1998

This speech processing integrated circuit is designed for speakerphone use, primarily due to the addition of echo cancellation circuitry. Separate detectors provide echo cancellation for both local (room) and far (network) conditions. The arrangement allows full-duplex communication, that is, simultaneous speech in both directions.—DLR

6,259,795

43.38.Vk METHODS AND APPARATUS FOR PROCESSING SPATIALIZED AUDIO

David Stanley McGrath, assignor to Lake DSP Pty Limited
10 July 2001 (Class 381/310); filed in Australia 12 July 1996

For computer games and virtual reality systems a synthesized, dynamic soundfield can be created via headphones by tracking the head motions of the user. A substantial amount of prior art already exists in this specialized field. But suppose that a computer game involves more than one user—what then? The patent describes a method of dealing with this situation. The description is quite technical and relies on a fair amount of math, but is well written and interesting.—GLA

6,263,085

43.38.Vk SURROUND SOUND HEADPHONES

Sergio W. Weffer, Provo, Utah
17 July 2001 (Class 381/371); filed 1 July 1999

Some earlier inventions have attempted to reproduce surround sound via headphones, not through electronic signal processing but by simply installing multiple transducers in each ear cup. This patent goes a step further. Each ear cup contains four teeny two-way systems mounted on the faces of a pyramidal baffle.—GLA

6,269,166

43.38.Vk THREE-DIMENSIONAL ACOUSTIC PROCESSOR WHICH USES LINEAR PREDICTIVE COEFFICIENTS

Naoshi Matsuo and Kaori Suzuki, assignors to Fujitsu Limited
31 July 2001 (Class 381/310); filed in Japan 8 September 1995

The patent document consists of 55 pages of illustrations followed by 12 pages of text. It describes a computationally efficient method of generating a dynamic, three-dimensional sound field via headphones or a pair of loudspeakers. The explanation is not always easy to follow, but includes useful information for those interested in this field.—GLA

6,278,657

43.38.Zp FOLDED SAGNAC SENSOR ARRAY

Benjamin A. Vakoc, assignor to The Board of Trustees of the Leland Stanford Junior University
21 August 2001 (Class 367/149); filed 3 April 1998

A fiber optic acoustic sensor array for use in detecting acoustic signals in water is described. The design is based on the operating principles of a Sagnac interferometer rather than the more common Mach–Zehnder inter-

ferometer. Consequently, the system has a more stable, temperature-independent bias point, has reduced phase noise, and allows for the use of a broadband, rather than narrowline, laser light source.—WT

6,289,143

43.38.Zp FIBER OPTIC ACOUSTIC EMISSION SENSOR

John W. Berthold and Garry W. Roman, assignors to McDermott Technology, Incorporated
11 September 2001 (Class 385/12); filed 12 July 1996

The “Extrinsic Fabry Perot Interferometer” described in this patent was developed initially as an optical strain gage. Two optical fibers are mounted in a cylindrical support structure with their ends a known small distance apart. These ends are coated with partial reflectors, so that the changes in the distance between these ends can be determined from the interference between direct and reflected coherent light propagating through the fibers. In order to make this system more sensitive to vibrations at the high frequencies of interest in acoustic emission sensing, the structure that supports the fiber ends is designed to resonate in the frequency range of concern.—EEU

6,250,163

43.40.Le EMATS FOR SPOT WELD EXAMINATION

Daniel T. MacLauchlan and Wayne M. Latham, assignors to McDermott Technology, Incorporated
26 June 2001 (Class 73/643); filed 9 March 1999

An EMAT (Electro-Magnetic Acoustic Transducer) permits nondestructive ultrasonic evaluation without the use of a fluid coupling medium. Radio frequency currents flowing in a flat coil placed near a metal surface induce eddy currents in the metal. A magnetic field also applied to the metal surface results in the eddy currents being subjected to Lorentz forces, causing a mechanical disturbance in the metal. Sensing of these disturbances takes place in a reciprocal manner—that is, an elastic wave in a conductor in the presence of a magnetic field induces currents in a receiving coil. In one approach to inspection of spot welds, an EMAT is placed on the weld and generates shear waves that travel normal to the surfaces of the plates that are welded together. The shear wave travels through the weld to the opposite surface and is reflected there, then travels back to the surface where the transducer is located and is detected by that transducer. The wave continues to reverberate between the top and bottom surfaces of the welded plates, taking a certain time between successive arrivals at the transducer. If the two plates are unbonded, then the shear wave reverberates between the two surfaces of only the plate on which the transducer is positioned, resulting in much shorter intervals between successive arrivals.—EEU

6,253,616

43.40.Le METHOD AND SYSTEM FOR DETECTING THE VIBRATION SIGNATURE OF A SAFETY INSERT FITTED IN A TIRE

Alfred Permuy and Laurent Breneol, assignors to Valeo Electronique
3 July 2001 (Class 73/579); filed in France 2 October 1998

This patent deals with evaluation of a safety insert (i.e., a secondary inner tube) in a tire that is running on the safety insert. In order to detect a mode of resonance of the insert in the presence of vibrations induced by the road surface, the insert’s vibrations are measured in a narrow and in a wide frequency band centered on the natural frequency of the mode of concern. The ratio of the two resulting signals, which is claimed to be independent of the vibrations due to the road, is compared to a corresponding warning detection threshold.—EEU

6,256,275

43.40.Le DISK REPRODUCING APPARATUS AND METHOD OF DETECTING VIBRATION

Toyokazu Eguchi *et al.*, assignors to Kabushiki Kaisha Toshiba
3 July 2001 (Class 369/44.32); filed in Japan 1 May 1998

The mass eccentricity of a disk is determined without the use of a contacting sensor by counting the number of tracks crossed by the beam spot of an optical pickup as the disk is spun at low and high speeds. At high speeds, the vibration is taken to be due to the sum of the eccentricities of the disk and of the driver, whereas at low speeds the contribution of the disk's eccentricity is negligible. Thus, the eccentricity of the disk is determined by subtracting the vibration observed at high speed from that observed at low speed.—EEU

6,257,065

43.40.Le STRAIN GAUGE VIBRATION SENSOR

Christos T. Kyrtos, assignor to Meritor Heavy Systems, Limited Liability Corporation
10 July 2001 (Class 73/654); filed 24 March 1999

This sensor, intended for monitoring the axial vibrations of rotating shafts, is preferably to be fabricated as an integrated circuit chip using micro-machining technology. A mass is arranged in a housing so that the mass—a sphere in one embodiment—can travel axially with minimal friction and thus is little affected by radial vibrations. The mass bears axially on strain gages, which provide a signal proportional to the axial force that acts on them.—EEU

6,257,066

43.40.Le PORTABLE VIBRATION MONITORING DEVICE

Jon K. Chandler and Orris L. Dent, assignors to Reid Asset Management Company
10 July 2001 (Class 73/660); filed 21 May 1998

A quick indication of machinery condition, generally useful as part of a predictive maintenance program, is obtained from an accelerometer signal that is processed to display bargraphs (a series of vertically arranged lights) of overall vibration displacement, velocity, and acceleration levels, and/or other vibration characteristics. The monitoring device includes circuitry for scaling the measurands relative to each other according to predetermined relationships.—EEU

6,263,738

43.40.Le VIBRATION PHASOR MONITORING SYSTEM FOR ROTATING MEMBERS

Joseph A. Hogle, assignor to General Electric Company
24 July 2001 (Class 73/593); filed 25 August 1999

Monitoring in real time of the vibration phasor at the fundamental frequency of a rotating shaft is accomplished without sensors installed on the rotating elements. The phasor's magnitude and angle with respect to a reference point on the rotating member are obtained with the aid of two displacement sensors mounted on the nonrotating part of the machine. One of these sensors is arranged to provide a signal when a key or notch in the shaft passes by, and thus indicates the occurrence of a complete revolution. The other sensor provides a signal indicative of the shaft's radial vibration. A clocking arrangement is used to ascertain the shaft angle at which the vibration signal is read. The sine and cosine of the shaft angle then are used to determine the phasor angle and magnitude.—EEU

6,285,629

43.40.Ng METHOD FOR PREVENTING DETERIORATION OF SUBMARINE STRUCTURE AND ULTRASONIC VIBRATION UNIT USED FOR THE METHOD

Takanori Shigihara and Masaki Kobayashi, assignors to Richter Corporation; Erocia Corporation
4 September 2001 (Class 367/139); filed in Japan 19 November 1997

A system is discussed for simultaneously vibrating and applying a voltage to a submerged marine structure for the purpose of retarding marine growth and rust corrosion of the structure.—WT

6,241,062

43.40.Tm NESTED DAMPING DEVICE WITH RELATIVE MOTION

John J. Enright, assignor to The B. F. Goodrich Company
5 June 2001 (Class 188/378); filed 16 November 1995

The device described in this patent is intended for the suppression of torsional oscillations such as may occur when the brakes in aircraft landing gear are activated. The device in essence consists of a tubular element that is located within a load-bearing tubular structure and that is in frictional contact with that structure. As the load-bearing structure vibrates torsionally, it is damped due to friction between the inner surface of that structure and the outer surface of the tubular element.—EEU

6,251,493

43.40.Tm VIBRATION AND SHOCK ATTENUATING ARTICLES AND METHOD OF ATTENUATING VIBRATIONS AND SHOCKS THEREWITH

Gordon G. Johnson *et al.*, assignors to 3M Innovative Properties Company
26 June 2001 (Class 428/71); filed 8 April 1996

This patent describes a variety of configurations consisting of a resilient material or materials enclosed in a film that is nontacky, with a layer of adhesive covering some portion of the film. These devices are intended to be adhered to various items, so as to provide these items with vibration isolation. Potential applications include disk drives, actuator voice coils, drawers, doors, etc.—EEU

6,257,067

43.40.Tm VERTICAL DIRECTION SPACECRAFT VIBRATION TEST SYSTEM WITH PSEUDO-FREE BOUNDARY CONDITIONS

Mark E. Ankrom *et al.*, assignors to Hughes Electronics Corporation
10 July 2001 (Class 73/663); filed 28 April 1999

In order to subject a spacecraft to purely vertical vibrations, a vertically acting shaker is disposed under the test item and its supports. This shaker acts on the test item via a spherical joint, such as a hydraulic ball joint. The test item's weight is supported on isolators, and the item is prevented from moving horizontally and from rotating about its vertical axis by means of an arrangement of flexures and/or vibration isolation mounts.—EEU

6,267,361

43.40.Tm DYNAMIC REACTION REDUCER FOR ISOLATED VIBRATORY EQUIPMENT

Bo Richard Rosenstrom, assignor to Carrier Vibrating Equipment, Incorporated
31 July 2001 (Class 267/140.11); filed 21 September 2000

The arrangement described in this patent is intended for reduction of the vibrations that act on the supporting structures of vibratory conveyors, feeders, and the like. These machines, which typically are actuated by eccentric-mass shakers that are fastened to them, generally are mounted on their supporting structures via springs. The present patent in essence pertains to a dynamic absorber that acts in conjunction with each such spring. The absorber—a spring-mass system tuned to the operating frequency of concern—is attached to a plate on which the spring rests, which plate is mounted on resilient elements (such as rubber pads) atop the supporting structure. The arrangement is said to be not extremely sensitive to changes in the operating speed of the machines, to require little space, and to be relatively inexpensive.—EEU

6,246,638

43.40.Yq FIBER-OPTIC VIBRATION SENSOR BASED ON FREQUENCY MODULATION OF LIGHT-EXCITED OSCILLATORS

J. David Zook *et al.*, assignors to Honeywell International, Incorporated
12 June 2001 (Class 367/140); filed 30 March 1999

This sensor makes use of a mechanical resonator whose natural frequency changes with the strain to which the resonator is subjected due to acceleration. In a preferred embodiment, a microchip has a microbeam mounted on a thin silicon cantilever such that deflection of the beam perpendicular to the plane of the microchip changes the tension on the microbeam to change its natural frequency. In the preferred embodiment, the oscillator is powered optically by means of an optical fiber and the output is in the form of light with intensity modulation at the frequency of the strain-sensitive resonator.—EEU

6,271,924

43.40.Yq NONCONTACT ACOUSTIC OPTIC SCANNING LASER VIBROMETER FOR DETERMINING THE DIFFERENCE BETWEEN AN OBJECT AND A REFERENCE SURFACE

Bryan Kok Ann Ngoi and Krishnan Venkatakrishnan, both of Singapore, Singapore
7 August 2001 (Class 356/489); filed 29 December 1998

An acousto-optic scanning laser vibrometer is the major element of this noncontact system for measuring the dynamic parameters of hard disk drives and the like. The patent clearly describes the invention and its advantages over a mechanically driven scanning mirror.—GLA

6,286,361

43.40.Yq METHOD AND APPARATUS FOR REMOTELY DETECTING PRESSURE, FORCE, TEMPERATURE, DENSITY, VIBRATION, VISCOSITY AND SPEED OF SOUND IN A FLUID

Alan R. Jones *et al.*, assignors to Rolls-Royce plc
11 September 2001 (Class 73/24.05); filed 5 January 1998

This patent is directed primarily at the inspection of hollow fan blades in gas turbine engines and the like, improving on the tedious process of attaching a transducer and measurement system to each blade in succession. A magnetostrictive transducer is located in a subvolume of each fan blade and is actuated by the oscillatory magnetic field produced by an electromagnet located in the engine casing, remote from the transducer. The fan blade's resulting vibrations are detected by means of a noncontacting transducer and their frequencies, amplitudes, phase, and/or damping are analyzed to identify changes in the blade's dynamics. Similar arrangements, with somewhat different constraints on the transducer and test items, may be used to detect changes in pressure and in the properties of a fluid contained in a hollow article.—EEU

6,260,658

43.50.Gf SILENCER FOR A GAS TURBINE

Jahn D. Darrell *et al.*, assignors to Donaldson Company, Incorporated
17 July 2001 (Class 181/224); filed 23 October 1998

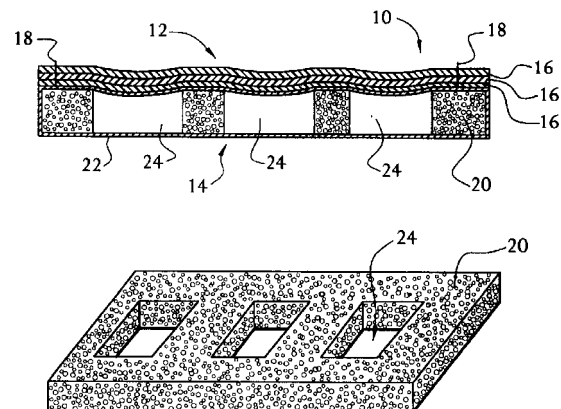
Details are given for a splitter-type silencer for application to industrial gas turbines. The splitters are oriented parallel to the intake or exhaust flow direction and consist of sound-absorbing material compressed between perforated plates.—KPS

6,260,660

43.50.Gf AIRCRAFT CABIN INTERIOR NOISE TREATMENT

Charles A. Yoerkie, Jr. and Bryan T. Wadey, assignors to Sikorsky Aircraft Corporation
17 July 2001 (Class 181/290); filed 18 December 1998

An acoustic blanket for application to aircraft fuselage sidewalls consists of a foam core 20 encased in a vapor barrier 22. Sheets of mass-loaded vinyl 16 are attached to the foam layer. Voids 24 are formed in the acoustic foam, the dimensions of which are determined by the primary frequency requiring attenuation. Another interesting aspect of this design is that the



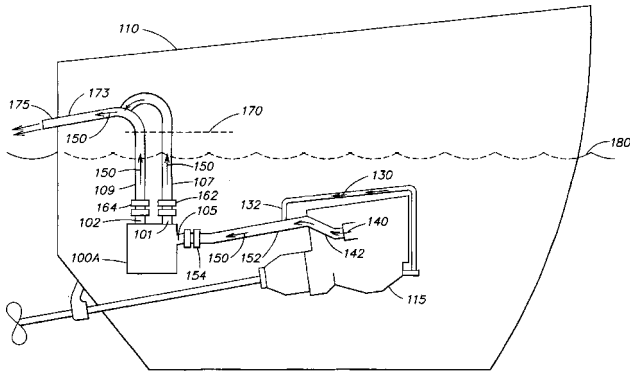
layers of vinyl are free to move with respect to one another, providing enhanced damping. Interior noise measurements for a Sikorsky S-76 helicopter equipped with this blanket design demonstrate reduced levels relative to those obtained with a more conventional, heavier design.—KPS

6,273,772

43.50.Gf APPARATUS AND METHOD FOR MULTI-CONDUIT WATERLIFT ENGINE SILENCING

Joseph I. Smullin, assignor to Smullin Corporation
14 August 2001 (Class 440/89); filed 8 July 1999

A muffler is described for use in marine applications in which cooling water is mixed with the engine exhaust gases. Furthermore, this muffler is intended for use in situations where the engine is below the water line, a so-called waterlift silencer. The key aspect of this design is the employment



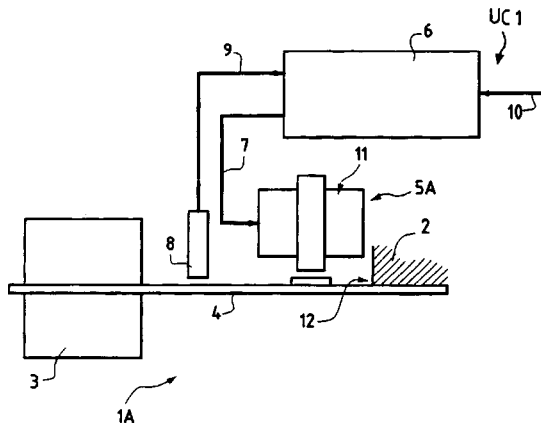
of multiple exhaust pipes which are arranged so that they operate sequentially through the range of engine operating speeds, thus maintaining sufficient exhaust gas flow to expell the water with minimal backpressure. Numerous geometrical arrangements are described.—KPS

6,279,704

43.50.Ki DEVICE FOR REDUCING THE VIBRATION GENERATED ON THE STRUCTURE OF A ROTARY-WING AIRCRAFT

Thomas Pierre Louis Manfredotti, assignor to Eurocopter
28 August 2001 (Class 188/378); filed in France 12 October 1998

Intended primarily for helicopter applications, this active vibration control system is designed to reduce tail shake, aerodynamically induced vibration of the tail boom which typically occurs at a few Hertz. The system consists of a flapping mass 3 attached to the primary structure 2, an electro-



magnetic actuator 5A capable of causing the mass to flap, a sensor 8, and a feedback control unit UC1. Several actuation arrangements are described.—KPS

6,274,216

43.55.Ev HONEYCOMB STRUCTURE, PARTICULARLY FOR ABSORBING SOUND AND ITS PRODUCTION PROCESS

Patrick Gonidec and Jean Adam Roger Treger, assignors to Hispano Suiza Aerostructures
14 August 2001 (Class 428/116); filed in France 30 July 1998

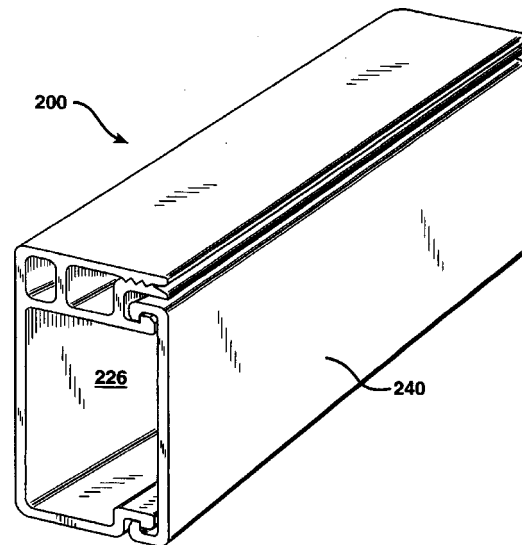
In this patent, internal, vertical membranes are added to a conventional honeycomb structure. This compartmentalizes the cells and gives them increased mechanical strength and high damping properties as Helmholtz resonators intended to trap sound waves impinging on a perforated face.—CJR

6,283,247

43.55.Ev FABRIC RETAINER FOR ACOUSTIC STRUCTURE AND METHODS OF INSTALLATION

Ralph D. McGrath and Frank C. O'Brien-Bernini, assignors to Owens Corning Fibreglas Technology, Incorporated
4 September 2001 (Class 181/295); filed 6 April 1999

Sound-absorbing treatments are often covered over by a fabric that is stretched and held in place by mechanical retainers. In this patent, the fabric retainers have a chase or a raceway for running wires within the interior of



the retainers. The chase has an open side that allows for the insertion of wires into the chase. There is a removable cover to secure and conceal the wiring.—CJR

6,284,351

43.55.Ev PLAIN SURFACE ACOUSTICAL PRODUCT AND COATING THEREFOR

Darryl L. Sensenig, assignor to Armstrong World Industries, Incorporated
4 September 2001 (Class 428/206); filed 1 September 1995

This patent describes two products, both with a plain, fine-textured, nonperforated painted surface. One product has a fiberboard substrate to which the finished painted surface is applied directly. The other has a perforated fiberboard substrate, where the hole perforations improve its sound

absorptive properties. In this latter case, a laminated, porous, nonwoven scrim is added, and then the finished surface is painted. In both cases, the painted surface must remain acoustically transparent to retain the sound absorption properties of the fiberboard substrate.—CJR

6,289,284

43.60.Rw METHOD OF IMAGING THE PERMEABILITY AND FLUID CONTENT STRUCTURE WITHIN SEDIMENT

Tokuo Yamamoto, assignor to Yamamoto Engineering Corporation; Kawasaki Steel Corporation
11 September 2001 (Class 702/14); filed 30 June 1998

In this method for cross-well tomography to image geological structures, such as uncemented sediments, a pseudo-random acoustic signal is transmitted into the medium to be measured and is received by a plurality of hydrophones. As summarized in the patent's abstract, the received signal is processed to obtain an image of the velocity and attenuation and the result is used to determine a universal geoacoustic model of the medium. The model is then solved to obtain permeability-porosity results.—EEU

6,275,596

43.66.Ts OPEN EAR CANAL HEARING AID SYSTEM

Robert J. Fretz et al., assignors to GN ReSound Corporation
14 August 2001 (Class 381/321); filed 10 January 1997

Persons with mild hearing loss frequently require amplification only in the higher frequency range. A very small behind-the-ear hearing aid module with a compression amplifier is described. The module is coupled to the ear canal with a small tubing, the diameter of which is such that the ear canal is left substantially open, allowing sound energy to enter and leave naturally. This type of hearing aid system provides a mild amount of amplification only at the high frequencies, since the open ear canal acts as a high-pass filter and allows low frequencies to both enter and leak out. The tube can be retained in the ear by attaching a plastic barb which lodges behind the tragus.—DAP

6,285,771

43.66.Ts DIRECTIONAL MICROPHONE ASSEMBLY

Mead C. Killion et al., assignors to Etymotic Research, Incorporated
4 September 2001 (Class 381/313); filed 31 December 1996

A small capsule is described that contains directional and omni-directional microphone cartridges and their acoustic couplings, and an electrical equalization network to provide the same frequency response in directional and omni-directional modes. A second acoustic resistor may be added to the front inlet of the directional microphone to provide adequate damping of its resonant peak for a smooth frequency response, while still providing the appropriate time delay between front and rear ports. A molded manifold optionally provides the acoustic inertance and volume compliance required for good directivity in the high frequencies. An effective wind screen may be added that does not affect directivity.—DAP

6,289,310

43.70.Dn APPARATUS FOR ENHANCING PHONEME DIFFERENCES ACCORDING TO ACOUSTIC PROCESSING PROFILE FOR LANGUAGE LEARNING IMPAIRED SUBJECT

Steven L. Miller et al., assignors to Scientific Learning Corporation
11 September 2001 (Class 704/268); filed 7 October 1998

This patent is another in a long series concerning devices and methods for diagnosing and treating the developmental disorder known as specific language impairment. In this example, the device generates acoustic stimuli with "varying amplitude emphasis of selected frequency envelopes, time stretching of selected portions, and phase adjustment of selected portions relative to a base frequency." Testing with the device reveals the nature of the impairment and suggests specific types of acoustical therapy which might be most effective in treating the disorder.—DLR

6,278,974

43.72.Ja HIGH RESOLUTION SPEECH SYNTHESIZER WITHOUT INTERPOLATION CIRCUIT

James J. Y. Lin, assignor to Winbond Electronics Corporation
21 August 2001 (Class 704/267); filed 5 May 1995

The patented speech playback technology was recently purchased from the original designer by the present assignee. A newly added twist allowed a new patent to be filed. The device stores undigitized, analog speech samples as analog values in standard EPROM cells. In the new circuit, multiple cells are used to store each time sample, yielding better analog value accuracy than could be achieved by digitizing the sample and storing the bits. Various forms of signal coding may also be applied, such as analog variations of DPCM (digital pulse code modulation) and ADPCM (adaptive DPCM).—DLR

6,283,367

43.72.Ja IC CARD READER WITH SYNTHESIZED VOICE OUTPUT

Kerry Ray Matthew and Paul Waihung Chau, assignors to Info Telecom
4 September 2001 (Class 235/380); filed 29 September 1995

An IC card, as the term is used here, is any card containing an IC chip. These are used as credit or debit cards, phone cards, vending machine cards, and transportation fare cards. The patent describes a hand-held card reader which will scan the card and uses speech output to describe the current card contents.—DLR

6,285,862

43.72.Ja RDS-TMC RADIO RECEIVER INCLUDING A SPEECH SEGMENT MEMORY

Hans-Wilhelm Rühl et al., assignors to U.S. Philips Corporation
4 September 2001 (Class 455/186.1); filed in Germany 29 April 1997

RDS-TMC is a European system for broadcasting traffic advisory messages to drivers in various language areas. The transmissions include words

as well as codes for cities, routes, and other installations of the highway system. RDS-TMC receivers contain permanent memory to decode the various items and stored speech to speak certain items in several languages. A particular received signal may include items for visual display on a screen in the vehicle, items to be spoken, or both.—DLR

6,289,304

43.72.Ja TEXT SUMMARIZATION USING PART-OF-SPEECH

Gregory Grefenstette, assignor to Xerox Corporation
11 September 2001 (Class 704/9); filed in the United Kingdom 23 March 1998

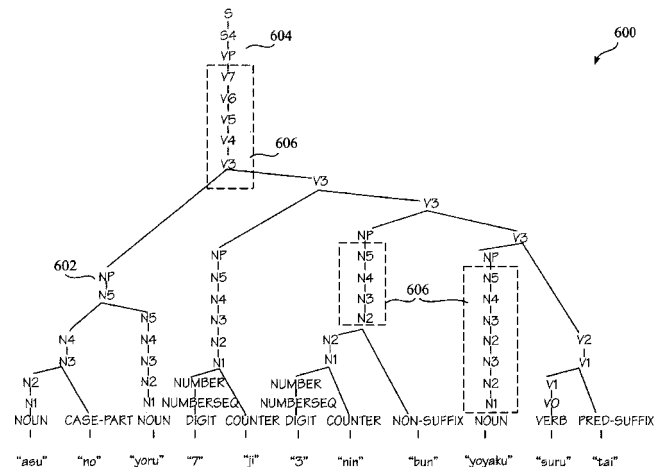
The patent reviews several prior linguistic and word processing methods of summarizing text for use in a reading machine. The patented method involves a lexical access to determine a part-of-speech for each word. A syntactic analysis then provides criteria for deleting words or phrases while retaining the essential content of the text.—DLR

6,282,507

43.72.Kb METHOD AND APPARATUS FOR INTERACTIVE SOURCE LANGUAGE EXPRESSION RECOGNITION AND ALTERNATIVE HYPOTHESIS PRESENTATION AND SELECTION

Keiko Horiguchi and Alexander M. Franz, assignors to Sony Corporation; Sony Electronics, Incorporated
28 August 2001 (Class 704/3); filed 29 January 1999

This spoken language translation system uses a typical speech recognition system and a generalized left-to-right parser, which may be combined with various methods of statistical analysis to achieve a high-quality parse. Information available to the parser includes feedback from semantic and



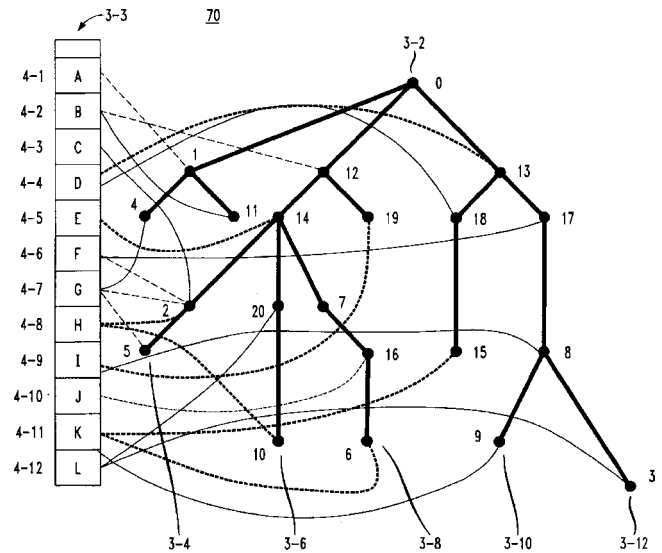
pragmatic analyses, which help narrow the field of alternative parses. The best-fitting result is presented to the sender for confirmation before the translation proceeds.—DLR

6,272,455

43.72.Ne METHOD AND APPARATUS FOR UNDERSTANDING NATURAL LANGUAGE

Joseph Hoshen *et al.*, assignors to Lucent Technologies, Incorporated
7 August 2001 (Class 704/1); filed 22 October 1997

The patent describes a syntactic processor designed to identify spoken words or phrases as meaningful entries to a telephone menu-type information interface. Words are individually identified and then discarded if not



found in the prespecified vocabulary. In the figure, qualified words are listed on the left and linked to nodes of the tree. The most nearly completed path from the root 3-2 to a terminal node, such as 3-8, represents the decoded meaning of the phrase.—DLR

6,278,973

43.72.Ne ON-DEMAND LANGUAGE PROCESSING SYSTEM AND METHOD

Pi-Yu Chung *et al.*, assignors to Lucent Technologies, Incorporated
21 August 2001 (Class 704/257); filed 12 December 1995

This patent represents a slight improvement upon the augmented transition network (ATN) parser developed by Woods in the 1970s. This system accepts speech rather than the word strings for which ATNs were originally planned. As a result, the unit recognized at a node may be smaller than a word, such as a phone or other phonetic unit. At certain nodes, the state may be "pushed" and a lower-level subnetwork entered to parse a nested portion of the input. The top level parses word sequences, much like an ATN.—DLR

6,292,776

43.72.Ne HIERARCHICAL SUBBAND LINEAR PREDICTIVE CEPSTRAL FEATURES FOR HMM-BASED SPEECH RECOGNITION

Rathinavelu Chengalvarayan, assignor to Lucent Technologies, Incorporated
18 September 2001 (Class 704/219); filed 12 March 1999

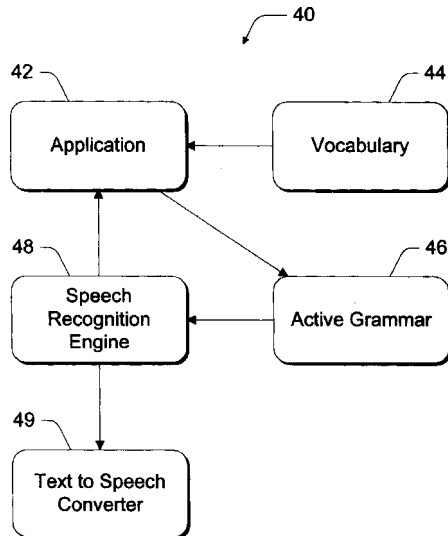
This patent presents a hierarchical subband linear predictive cepstral (HSLPC) feature extraction method for use in HMM-based speech recognition systems. The method uses two levels of subbands. The first level is the speech signal band (e.g., 0–4000 Hz) and the second level has two equally spaced subbands (e.g., 0–2000 and 2000–4000 Hz). The HSLPC feature extraction process includes preemphasis, blocking speech into frames with windowing functions, and Fourier transformation in each level. Finally, a linear predictive cepstral analysis is performed. According to the patent, the use of these features improves the overall recognition performance.—AAD

6,298,324

43.72.Ne SPEECH RECOGNITION SYSTEM WITH CHANGING GRAMMARS AND GRAMMAR HELP COMMAND

Sarah E. Zuberec *et al.*, assignors to Microsoft Corporation
2 October 2001 (Class 704/251); filed 5 January 1998

This patent describes a speech recognition system with a help system interface to assist the user at any time in navigating new or changing grammars. The system consists of a discrete speech recognition system 40 that recognizes words or phrases, an application 42, a vocabulary 44, an active grammar 46, a speech recognition engine 48, and a text-to-speech converter 49.



49. The active grammar includes a help command. When the help command is detected, the system interacts with the user verbally. For example, by asking "What can I say?" the user receives a spoken list of the commands currently available in the active grammar.—HHN

6,301,559

43.72.Ne SPEECH RECOGNITION METHOD AND SPEECH RECOGNITION DEVICE

Hiroshi Shinotsuka and Noritoshi Hino, assignors to Oki Electric Industry Company, Limited
9 October 2001 (Class 704/239); filed in Japan 14 November 1997

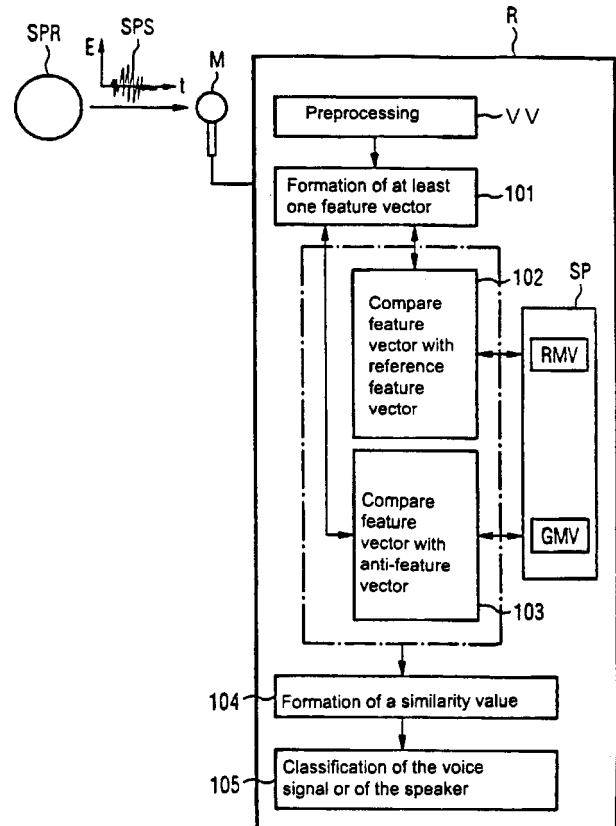
This patent relates to a speech recognition method which improves isolated-word recognition performance by using template matching. The system employs templates of prestored features of words to be recognized. The stored features include those of sudden ambient sounds, such as the sound of a door opening and closing, as well as continuous sounds, such as the sound of an air conditioner, etc. In the recognition phase, the system measures the degree of similarity between existing templates and features derived from a word spoken by an unspecified speaker.—AAD

6,298,323

43.72.Pf COMPUTER VOICE RECOGNITION METHOD VERIFYING SPEAKER IDENTITY USING SPEAKER AND NON-SPEAKER DATA

Bernhard Kaemmerer, assignor to Siemens Aktiengesellschaft
2 October 2001 (Class 704/246); filed in Germany 25 July 1996

This patent describes a method for verifying a speaker's identity on the basis of a brief voice sample. An acoustic feature vector is formed by extracting the vocal tract shape and a typical time sequence of the articulatory motions from stationary frames of the speech signal. The feature vector is compared to at least one reference feature vector and at least one anti-



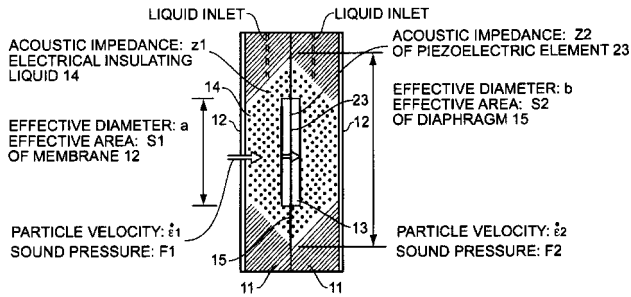
feature vector 103. A two-class, multi-layer perceptron, neural network classifier performs classification by forming and evaluating a similarity value 104. The tolerance range for the decision depends on the required security demands and can be changed during the test phase.—HHN

6,295,365

43.80.Ev ACOUSTIC SENSOR AND ELECTRIC STETHOSCOPE DEVICE INCORPORATING THE SAME THEREIN

Haruyoshi Ota, Tokorozawa-shi, Saitama-ken, Japan
25 September 2001 (Class 381/114); filed in Japan 6 November 1998

This electronic stethoscope consists of an acoustic sensor exhibiting an ideally homomorphous relation with an object or body to be examined. The goal is to reduce the amount of acoustic reflection and resist changes in ambient temperature and mixing of ambient noise, while operating over a wide range of frequencies with highly sensitive, flat frequency characteristics. The acoustic sensor includes a piezoelectric element with at least one



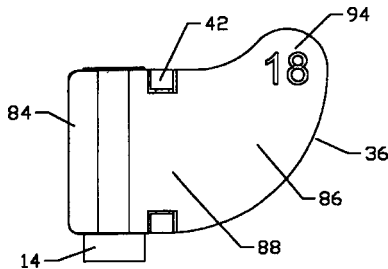
embedded electrode, a diaphragm on which the piezoelectric material is supported, a membrane capable of vibrating and facing the diaphragm, and a horn-shaped frame which provides an interior space enlarged from the edge of the membrane to the edge of the diaphragm. A cell formed by the frame houses the diaphragm, exposing the membrane to the outside and enclosing an electrically insulating hermetically sealed liquid.—DRR

6,296,614

43.80.Gx NEEDLE GUIDE FOR ATTACHMENT TO ULTRASOUND TRANSDUCER PROBE

Rick L. Pruter, Iowa City, Iowa
2 October 2001 (Class 600/461); filed 8 April 1999

In the medical field, procedures may be done to obtain biopsy samples or to place drainage tubes within the body. To facilitate such procedures, an ultrasound image may be obtained to guide the biopsy needle or drainage tube into the proper position. The aim of this device is to provide a needle



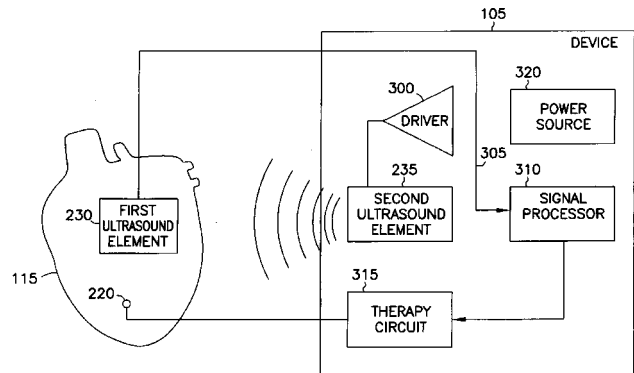
guide that permits easy release of a biopsy needle from an ultrasonic transducer probe after the needle has been guided into place by visualization of ultrasound images generated by the ultrasound transducer probe.—DRR

6,298,269

43.80.Gx CARDIAC RHYTHM MANAGEMENT SYSTEM WITH ULTRASOUND FOR AUTOCAPTURE OR OTHER APPLICATIONS

Robert J. Sweeney, assignor to Cardiac Pacemakers, Incorporated
2 October 2001 (Class 607/28); filed 19 April 1999

Some people suffer irregular cardiac rhythms, referred to as cardiac arrhythmias. If drug therapy is not effective, then some kind of cardiac rhythm management system must be tried, one of which is the well-known pacemaker. A pacemaker initiates heart contractions by pacer pulses. This is referred to as “capturing” the heart. This patent documents a cardiac rhythm management system with ultrasound autocapture capability for determining whether a stimulation has evoked a desired response from the heart, and for



adjusting the stimulation energy based on the observed response from the heart. One ultrasound element is placed on a lead in the heart, while a second is positioned elsewhere in the heart or in the implanted device. An autocapture determination circuit detects a contraction in response to the stimulation and adjusts the stimulation energy to ensure reliable capture. This is said to increase the life of the implanted device and reduce the risk and expense of early replacement.—DRR

Acoustics of friction^{a)}

Adnan Akay

Mechanical Engineering Department, Carnegie Mellon University, Pittsburgh, Pennsylvania 15213

(Received 20 July 2001; revised 7 January 2002; accepted 10 January 2002)

This article presents an overview of the acoustics of friction by covering friction sounds, friction-induced vibrations and waves in solids, and descriptions of other frictional phenomena related to acoustics. Friction, resulting from the sliding contact of solids, often gives rise to diverse forms of waves and oscillations within solids which frequently lead to radiation of sound to the surrounding media. Among the many everyday examples of friction sounds, violin music and brake noise in automobiles represent the two extremes in terms of the sounds they produce and the mechanisms by which they are generated. Of the multiple examples of friction sounds in nature, insect sounds are prominent. Friction also provides a means by which energy dissipation takes place at the interface of solids. Friction damping that develops between surfaces, such as joints and connections, in some cases requires only microscopic motion to dissipate energy. Modeling of friction-induced vibrations and friction damping in mechanical systems requires an accurate description of friction for which only approximations exist. While many of the components that contribute to friction can be modeled, computational requirements become prohibitive for their contemporaneous calculation. Furthermore, quantification of friction at the atomic scale still remains elusive. At the atomic scale, friction becomes a mechanism that converts the kinetic energy associated with the relative motion of surfaces to thermal energy. However, the description of the conversion to thermal energy represented by a disordered state of oscillations of atoms in a solid is still not well understood. At the macroscopic level, friction interacts with the vibrations and waves that it causes. Such interaction sets up a feedback between the friction force and waves at the surfaces, thereby making friction and surface motion interdependent. Such interdependence forms the basis for friction-induced motion as in the case of ultrasonic motors and other examples. Last, when considered phenomenologically, friction and boundary layer turbulence exhibit analogous properties and, when compared, each may provide clues to a better understanding of the other. © 2002 Acoustical Society of America. [DOI: 10.1121/1.1456514]

PACS numbers: 43.10.Ln, 43.40.At, 43.40.Ga [ADP]

I. INTRODUCTION

Friction develops between sliding surfaces regardless of the magnitude of relative motion between them. Always acting as a resistance to relative motion, friction fulfills a dual role by transmitting energy from one surface to the other and by dissipating energy of relative motion. The physical processes that contribute to friction have a wide range of length and time scales. At the length scale that corresponds to the interatomic distance in solids, which forms the upper limit of acoustics, friction acts as a dissipation mechanism, converting kinetic energy to thermal energy. This means of conversion, arguably the most fundamental aspect of friction, is an acoustical process that involves oscillations of atoms and relates to the first principles.

In practice, at longer length scales, the dual roles of friction, both transmitting and dissipating energy, almost always coexist. The conditions under which friction provides more energy to a system than that system can dissipate constitute the basis for most of the instabilities observed in friction-excited vibrations and a prime source of resulting sound radiation.

Examples of sounds that result from friction-excited vibrations and waves appear frequently. They include squeaks and squeals in the interior of automobiles, the squeal of sneakers on parquet floors, the squeak of snow when walking on it, door hinges, chalk on a blackboard, turkey friction calls that hunters use, aircraft and automotive brake squeals, belts on pulleys, rail-wheel noise, and retarders in rail yards. These and many others typify the annoying aspects of friction sounds. String instruments exemplify the musical dimensions of friction sounds.

The acoustics of friction extends beyond noise and music and includes such phenomena as friction damping, friction-assisted assembly, and friction motion. Contact damping of inserted blades in gas turbines and braided wires exemplify friction dampers. In manufacturing assembly processes, friction has an important role, such as in vibratory conveyors and in reducing friction during the cold drawing of wires by vibrating them. Friction motion refers to vibration devices such as the ultrasonic motor that relies on bending waves and friction to develop precise motion. A historical example demonstrated by Tyndall¹ shown in Fig. 1 suggests that rubbing a glass tube along its length can break off rings at its free end. (Admittedly, the author has been unsuccessful trying to re-enact this experiment.) These examples and others involve both acoustics and friction. This article considers acoustics

^{a)}A portion of the contents of this article was presented as the 1999 Rayleigh Lecture on 19 November 1999 at the International Mechanical Engineering Conference in Nashville, Tennessee.

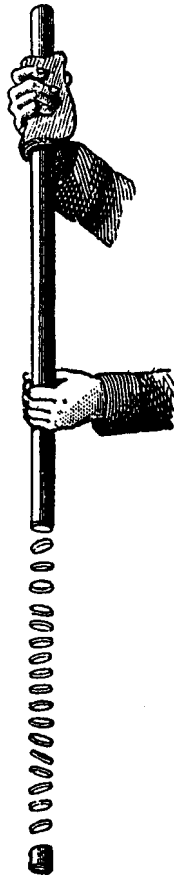


FIG. 1. Tyndall's experiment breaking rings off a glass tube by friction. From Ref. 1.

and friction each in its broader meaning, rather than their conventional engineering implications, while keeping the focus narrow to consider aspects of friction relevant to acoustics. As such, the article leaves out many rigid-body oscillation problems associated with friction-induced instabilities.

A major challenge in studying the acoustics of friction relates to the ability to predict sound and vibration responses of systems subject to friction. The challenge rests with the modeling of friction as well as the modeling of real boundary conditions that often involve friction. A friction force interacts with and often depends on the response of the system within which it develops. Such interaction sets up a feedback between the friction force and the waves on the surfaces, making them interdependent. In addition to such dynamic effects with short time scales, friction also undergoes changes over a longer time that correspond to, for example, the deformation and wear of surfaces. Consequently, friction, when acting on even a simple and an otherwise linear system, can still produce very complicated responses.

This paper treats several aspects of the acoustics of friction. The next section describes friction-induced vibrations and sounds starting with several pedagogical examples to illustrate fundamental concepts. It follows these with detailed descriptions of two engineering applications that involve complex friction and vibration interaction, namely bowed string and brake noise. The second section concludes with examples of sounds in nature. The third section of the paper treats macroscopic interactions between friction and

vibrations to demonstrate friction-induced motion, followed in Sec. IV by a description of friction-induced damping phenomena. The paper then presents a brief review of the issues pertinent to measuring and modeling of friction in dynamic systems, followed by a description of friction and its components which includes a description of friction dissipation in terms of atomic oscillations. The final part of the paper draws an analogy between two little-understood phenomena: friction-excited vibrations in solid mechanics and boundary-layer turbulence in fluid mechanics.

II. FRICTION-EXCITED VIBRATIONS AND SOUNDS

The range of sounds a bow and a string can produce bespeaks the extent of the many different forms friction sounds may take. Friction sounds are rarely, if at all, ergodic and stationary. Rather, they are mostly unsteady or transient. Sounds emanate from either one or both components of the friction pair or from other parts of the system to which the friction pair transmits unsteady forces. In some cases, transient radiation originates from sudden deformation of the surfaces near the contact areas, which may also be accompanied by waves that develop within the components under friction excitation. Rubbing of viscoelastic materials often exhibits a transient sound radiation, as in the case of the heel of a sneaker sliding on a polished parquet floor. Rubbing an inflated balloon with a finger also produces a transient sound from near the contact area, in this case, followed by a pseudo-steady-state radiation. Similarly, rubbing the surface of a small ($D=1$ cm) steel ball with a moist finger also demonstrates radiation from local acceleration near a contact. Since the fundamental natural frequency of the ball is in the ultrasonic range, the sound produced in the sonic range results solely from the rapid movement of the contact area of the finger and rigid-body radiation of the ball.

Sliding, whether through a continuous or transient contact, is an unsteady process. Transient sliding, the source of many squeaks and squeals, develops intermittently or cyclically, as in *spiccato* bowing of violin that requires a sliding stroke of a bow onto and off a string. Continuous sliding, on the other hand, can produce a broad range of responses including transient response, for example, by a slight variation in the normal contact load.

For a particular friction pair, the differences in the sounds they radiate, and their governing vibrations, largely arise from the variation of contact forces at the interface where the sliding surfaces meet. In turn, contact forces depend on the interface properties and the external forces that maintain the sliding contact. In cases where the friction pair is attached to other components, the response of the entire system can also modify the interface behavior and thus the resulting acoustic response.

The strength of contact governs the type of waves and oscillations that develop during sliding. Weak contacts, with effects localized to the interface region, produce response in each component at its own natural frequencies, nearly independently of other components. Weak contacts that involve rough surfaces can produce light impulses as asperities come into contact, and again produce a response at the natural frequencies of each component. Such sliding conditions of-

ten produce sounds, referred to here as roughness noise or surface noise. For example, two pieces of sandpaper, when rubbed against each other, produce a random sound from the vibrating paper that results from the interaction among the granules on opposing surfaces. Another example of surface or roughness noise involves bending waves of a rod with a rough surface when lightly rubbed against another rough surface. Similarly, corrugated surfaces sliding over each other under light normal loads produce impulsive contact forces that develop at the “corrugation frequency” with components in both tangential and normal directions to the interface. Such contact forces produce response in each direction at a combination of corrugation frequency and natural frequencies of each component.

When sliding takes place under strong contact conditions, the influence of the contact force reaches beyond the interface and friction; the friction pair becomes a coupled system and produces a more complex and often nonlinear response. Under such conditions, instabilities develop and frequently lead to a condition called mode lock-in, where the coupled system responds at one of its fundamental frequencies and its harmonics.² Development of mode lock-in and the selection of the mode at which the system responds depends on the normal load, sliding velocity, and the contact geometry.

The external normal force that maintains contact between surfaces not only influences the strength of the contact, and thus the friction force, but it can also modify the dynamic response of the components under friction. As discussed later, the splitting of modes in beams and disks is but one example that also exhibits the influence of the normal force.

A. Pedagogical examples

The following examples present a hierarchy of friction sounds that helps illustrate the fundamental concepts associated with friction-excited vibrations and the ensuing sound radiation described above. They start with the simple cases involving only two components with distinctly different impedances followed by those that have comparable impedances. In the former cases, response of the system is closer to the component with “weaker” impedance, whereas in the latter, system response is different than that of either component.

1. Wineglass

It is well-known that rubbing the rim of a glass, preferably with a moist finger, makes it radiate sound from its bending waves at one of its natural frequencies and its harmonics.^{3,4} In cases of crystal glasses with very small internal damping, even light rubbing of the glass surface produces a sound. Friction, although applied to the rim in the circumferential direction, excites bending waves. When approximated as a cylinder of height H and radius R that has a rigid base, its fundamental vibration frequency is given as⁵

$$\omega_0 = \frac{h_g}{R} \sqrt{\frac{3E_g}{5\rho_g}} \left[1 + \frac{4}{3} \left(\frac{R}{H} \right)^4 \right]^{1/2}, \quad (1)$$

where h_g , ρ_g , and E_g represent the thickness, density, and Young’s modulus of glass cylinder, respectively. Rubbing a glass around its perimeter can also excite the torsional oscillations of the wine glass about its axis of symmetry, but at a much higher frequency than the bending natural frequencies.⁵

A different mechanism takes place when the rim of a glass is gently rubbed in the radial direction by a dry finger. This light radial application of friction to the edge of the glass primarily excites the bending waves of the glass wall by light impulses. Impulses develop at a corrugation frequency corresponding to the speed and the spacing between ridges on the fingertip, and sometimes described as the “picket fence” or “washboard” effect. As illustrated in Fig. 2, such impulses excite the natural frequencies of the glass.

A more complex response results from exciting a wineglass with a violin bow applied radially to its rim. The response usually, but not always, shows a dominance by only one of the natural frequencies of the glass and its harmonics. Frequently, the first or the second mode appears depending on the application of the bow. By imposing a nodal point on the surface of the glass, for example with a finger tip, even the third mode and its integer harmonics can result from a seemingly identical application of the bow. This behavior, where the bow and the glass respond, in this case, at or near a particular natural frequency of the glass to the exclusion of its other modes, illustrates the concept of mode lock-in described earlier.²

The presence of water in the glass helps demonstrate the corresponding mode shapes of the glass, similar to Galileo’s observations⁶ (cited in Ref. 7). Under high excitation amplitudes, water in the glass shoots up, similar to the Chinese sprouting fish basin, which consists of a pot, usually bronze, that fountains the water it is filled with when rubbed at its handles.

2. Cantilever beam and plate

Another demonstration of mode lock-in results from applying a violin bow to the free edge of a cantilever beam or a plate. Chladni also happened to demonstrate mode lock-in^{8,9} when presenting the first visualization of mode shapes in 1787 by sprinkling sand on a plate and bowing its free edge to create different mode shapes.

Similarly, bowing the free end of a cantilever beam can also produce mode lock-in. Depending on the application of the bow, the spectra of bending vibrations and radiated sound display either the first, the second, or even the third natural frequency of the beam and its harmonics. In these experiments, only infrequently does more than one natural frequency appear simultaneously. Mostly, the bow and beam lock into a particular mode and oscillate in a rather stable manner. Because bow impedance in the direction of excitation differs significantly from that of the beam, the dynamics of the two does not critically interact, and the beam responds at one of its natural frequencies with corresponding harmonics, as shown in the radiation spectrum given in Fig. 3.

3. Cuica

The cuica, the Brazilian friction drum, presents an example of a friction system in which friction excitation takes

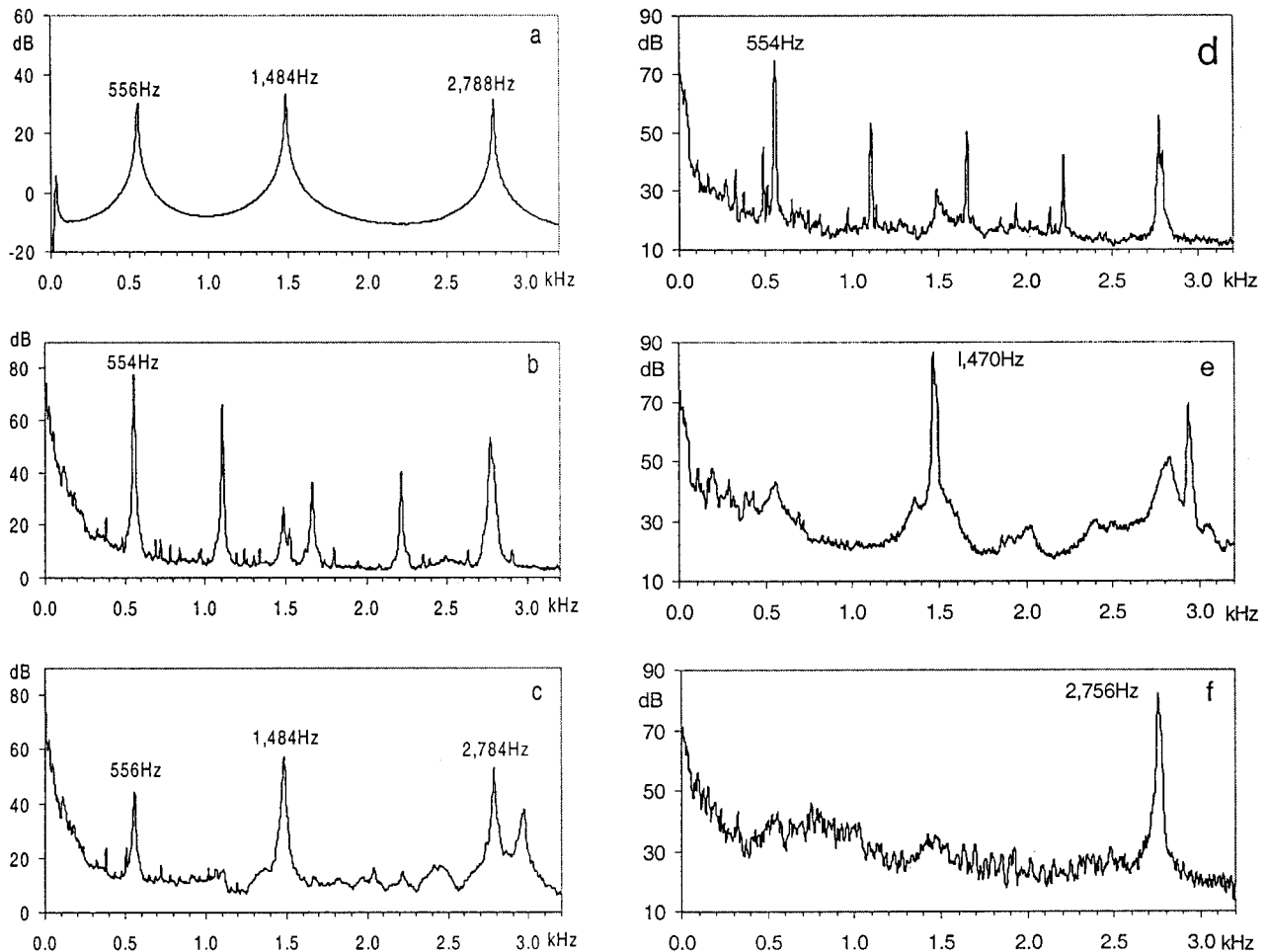


FIG. 2. Demonstration of mode lock-in with a wine glass half-filled with water. (a) Frequency response; (b) response to excitation to a finger rubbed along its edge; (c) excitation by dry finger across its rim; (d)–(f) response to excitation with a bow; (e)–(f) show the effect of placing a finger on different positions on the glass to suppress the other modes thus creating a mode lock-in.

place away from the radiation source. The cuica consists of a cylindrical metal shell covered at one end with a membrane, as in a drum. Inside the cylinder, a thin bamboo stick suspends from the center of the membrane where one end of the stick is tied with a knot. The player continuously strokes the stick with a piece of moist cloth, thereby exciting the membrane at its center with the resulting stick–slip motion. The player produces music by controlling the radiation response by judiciously placing a finger on various spots on the membrane.

Mechanically, the operation of the cuica has similarities to that of a bowed string instrument. In the case of the cuica, the bamboo stick vibrates the membrane as a bow does with a string, and the player’s finger on the membrane selects the mode of vibration as does placing a finger on the string.

4. Extraction of a nail from wood

Extracting a nail from a plank of wood presents another instructive example of friction, stick-and-slip, and friction sounds. Pulling a nail exhibits stick–slip if it is extracted from hard wood. Both the hardness of the wood and the average diameter of the nail determines the pressure, and thus the friction force, on the surface of the nail. Larger-size nails produce more friction force and sounds. Speed with

which a nail is extracted also affects the dynamic response, but probably because of the temperature effects. Rapid extraction of a nail can easily char the adjacent surface of the wood and change the characteristics of friction.

5. Smooth versus corrugated surfaces

Two simple experiments using polished and corrugated surfaces can demonstrate the effects of surface texture on sound radiation from friction excitation. Rubbing along the length of a steel bar with a smooth surface produces longitudinal vibrations and radiates sound at its fundamental frequencies as determined by the position at which the bar is constrained. Friction dominates the dynamic component of the contact force without a significant perturbation of its normal component. The friction force, in this case, travels along the rod and gives rise to longitudinal waves, modeled as

$$-E \frac{\partial^2 u}{\partial x^2} + \rho \frac{\partial^2 u}{\partial t^2} = \frac{1}{A} \mu F_N \delta(x - Vt). \quad (2)$$

The use of a smooth rod excited by friction dates back to 1866, when it became the excitation source in what is now known as the Kundt’s tube to measure the speed of sound. In that experiment, longitudinal waves in the stroked rod vi-

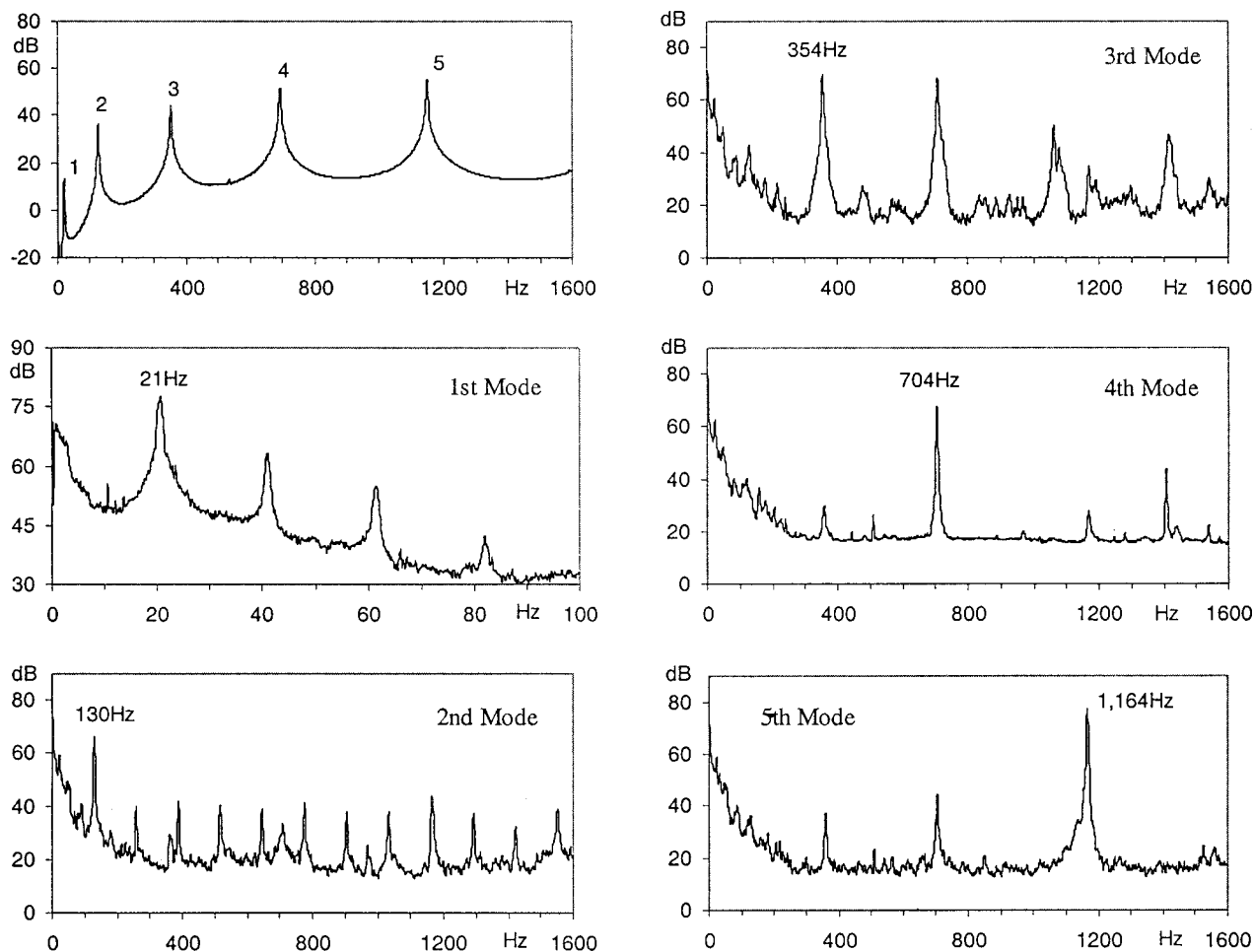


FIG. 3. Demonstration of mode lock-in obtained by applying friction to a clamped-free beam using a violin bow. Response lock-in to each of the natural frequencies separately, although higher modes require suppression of lower modes.

brates a disk attached to its end, which acts like a loudspeaker inside a tube.

A rod with a corrugated surface, such as a threaded bar, when rubbed along its length with a rough surface, produces both longitudinal and bending vibrations of the bar. Unlike the case for a smooth rod, forces that develop at the corrugations have an impulsive character with components both in tangential and normal directions, thus simultaneously exciting longitudinal and bending waves in the rod. Assuming that impulsive contact forces dominate over friction forces, the longitudinal response of a rod with corrugations Δx apart is governed by

$$-E \frac{\partial^2 u}{\partial x^2} + \rho \frac{\partial^2 u}{\partial t^2} = \frac{1}{A} \sum_{n=1}^m F_n \cos \phi_n \prod [(n\Delta x - Vt)/b] \delta(x - n\Delta x), \quad (3)$$

where $n = \text{integer}(L/\Delta x)$, and m represents the number of simultaneous contacts that have a length b traveling at a sliding velocity V . The function $\prod [(n\Delta x - Vt)/b]$ represents a rectangle of width b positioned at $n\Delta x$ and traveling at a velocity V . F_n represents the discrete impulsive point forces that develop during motion at an angle ϕ with the axis of the

rod. Similarly, the bending vibrations of the rod can be described by

$$EI \frac{\partial^4 w}{\partial x^4} + \rho A \frac{\partial^2 w}{\partial t^2} = \sum_{n=1}^n F_n \sin \phi_n \prod [(n\Delta x - Vt)/b] \delta(x - n\Delta x), \quad (4)$$

where ρ , E , I , and A represent the density, Young's modulus, the cross-sectional moment of inertia, and the cross-sectional area of the beam, respectively.

A reed rubbed along a guitar string presents another example in which both bending and longitudinal vibrations are excited. The contact force characteristics again involve primarily the spatial period of the winding on the string and the speed, V , with which the reed moves along the string

$$-c_s^2 \frac{\partial^2 u}{\partial x^2} + \frac{\partial^2 u}{\partial t^2} = F_N \delta(x - n\Delta x), \quad (5)$$

where $n = \text{Integer}(V \cdot t / \Delta x)$ indicates the position of excitation at time t , $c_s = \sqrt{T/\rho}$ represents the speed of sound for a string of density ρ and under tension T , and $F_N = F_i \cos \phi$ corresponds to the normal component of the contact force. This "picket-fence effect," where the reed excites the string with impulses at the corrugation frequency, has a similar

mechanism as friction sounds from insects (described later), but is a simpler form of what occurs among the asperities between rough surfaces in sliding contact. In the latter case, impulses arising from impacts of asperities have more complex spatial and temporal distributions.

6. Rod on rotating pulleys

A rod placed in the grooves of two pulleys, set apart a distance of $2a$ and rotating toward each other, oscillates along its axis with a frequency that depends on the friction coefficient between the pulleys and the rod, $\Omega = \sqrt{\mu g/a}$. In addition to this rigid-body response, the rod develops bending and axial vibrations and radiates sound as the pulleys slip at their respective contacts with the rod. The average intensity of sound reaches a maximum as the oscillatory motion of the rod on the pulleys diminishes and energy from slipping pulleys feeds the rod vibrations. Sound from the rod radiates from its bending vibrations and from longitudinal vibrations through its flat ends. The fundamental longitudinal natural frequency of the rod dominates the sound spectrum, which indicates that, as described earlier, for smooth surfaces excitation is predominantly in a tangential direction. The spatial distribution of sound intensity has a peak along the axis of the rod, in part, because it radiates from its ends due to longitudinal vibrations. When any of its natural frequencies in longitudinal and bending directions coincide, the corresponding modes readily couple thereby increasing sound radiation from bending waves of the rod. This result suggests the significance of in-plane waves in rotating disks where they couple with and promote bending waves under tangential (friction) forces.

As the rigid-body oscillations of the bar cease, its axial vibrations that develop from friction excitation at the two supports can be described with

$$-E \frac{\partial^2 u}{\partial x^2} + \rho \frac{\partial^2 u}{\partial t^2} = [F_N(t)\mu]_{-a} \delta(x+a) - [F_N(t)\mu]_{+a} \delta(x-a), \quad (6)$$

where $F_N(t)$ represents the normal component of the contact force and $\mu_{\pm a}$ represent the coefficients of friction at the contacts the rod makes with the pulleys.

Although the nominal direction of friction excitation is tangential (parallel to the rod axis), surface roughness gives rise to transverse excitation of the rod due to light impacts among the asperities on the surfaces, described by

$$EI \frac{\partial^4 w}{\partial x^4} + \rho A \frac{\partial^2 w}{\partial t^2} = F_N^-(t) \delta(x+a) - F_N^+(t) \delta(x-a), \quad (7)$$

where $F_N^\pm(x,t)$ represent the impulsive normal forces that develop where the rod rests on the pulleys. For elastic contacts, Hertz formulation provides a convenient approximation for $F_N^\pm(t)$.

As surface roughness increases, the transverse component of the excitation also increases. Higher rotation speeds often cause contact loss and exacerbate the development of impacts. On the other hand, high normal loads imposed on the beam can inhibit its transverse motion while maintaining tangential excitation. Under such conditions response of the

rod primarily consists of axial vibrations. Thus, the partitioning of energy between bending and axial waves in the rod depends on the texture of the rod and pulley surfaces as well as the contact load in the normal direction.

A rod in the V-grooves of a double-pulley system also experiences torsional vibrations that result from the difference in the friction it experiences at its contact areas on the walls of the V-grooves. In this case, sound radiation at torsional frequencies accompanies the rotation of the rod about its axis.

Friction in the grooves also develops waves within the pulleys. However, in the absence of any coupling mechanisms such as impacts due to asperities, these waves confine themselves to in-plane vibrations and produce very little sound radiation. In most systems, however, coupling mechanisms always exist as discussed in the next section.

B. Beam and rotating disk

Friction between the free end of a cantilever beam and a rotating disk provides an example that engenders the different modes of friction behavior and system response, including mode lock-in and surface noise. Different configurations of sliding contact between a beam and disk generate different combinations of waves within each. For instance, in the seemingly simple case where the flat tip of a beam rubs against a planar side of a rotating disk, the friction force, acting tangentially on the disk surface, excites the in-plane waves of the disk. Also, as expected, friction at its tip simultaneously develops bending waves of the beam. As a result of these bending vibrations the beam undergoes, the contact force at the interface develops a fluctuating component normal to the surface of the disk and easily excites the disk-bending vibrations. (The impulses due to the surface texture discussed earlier further contribute to the bending wave excitation of the disk.) This type of geometric coupling that results from the dynamic response of the beam and disk, a potential cause for instabilities, is exacerbated when the beam contacts the disk surface at an acute angle against the direction of motion. Furthermore, should the disk have its in-plane and bending vibration frequencies in close proximity, energy transfer through friction becomes enhanced, thus making it easier to generate bending waves. The examples described below present evidence of different friction sounds that can develop from the sliding contact of a beam tip and a disk and the relationship such sounds have with the disk and beam natural frequencies.

1. Experiments

The demonstrations described here consist of a stationary clamped beam with its free end in sliding contact with the flat surface of a rotating disk during which both the beam and disk simultaneously respond to contact forces. Figures 4(a) and (b) show a free vibration response of the beam and disk, respectively. Figure 4(c) shows the transfer function of the disk when in stationary contact with the beam. Note the splitting of frequency that corresponds to the (0,2) mode of the disk when in contact with the beam. The spectrum of sound during sliding contact of the beam tip and disk, shown in Fig. 4(d), exhibits a mode lock-in at the higher of the split

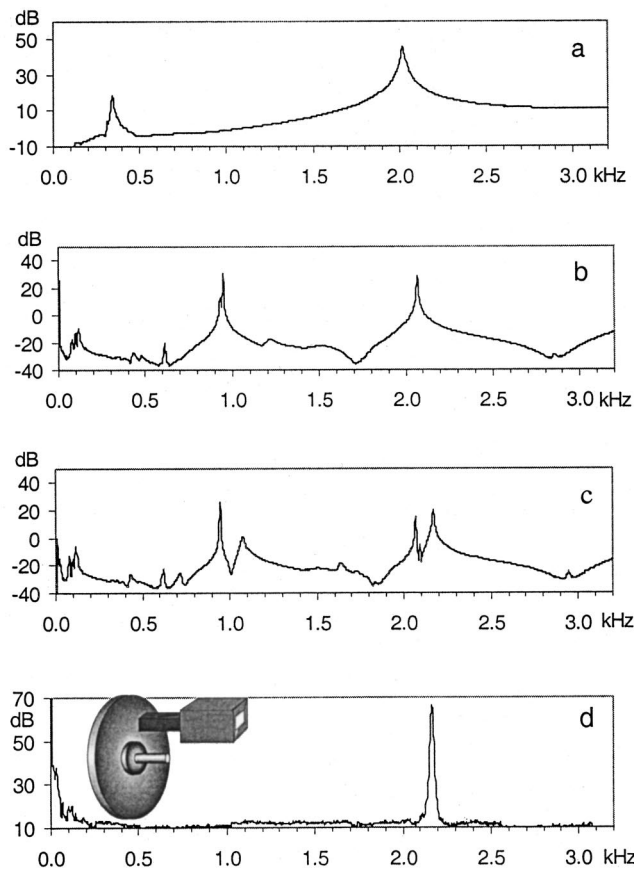


FIG. 4. Development of mode lock-in between a beam and a disk (a) transfer function of disk; (b) transfer function of beam; (c) transfer function of beam and disk in stationary contact; (d) response during sliding contact.

frequencies, which represents the cosine mode, whereas the lower of the pair corresponds to the sine mode for which the beam contact takes place at its nodal line.

Figure 5 demonstrates the diversity of examples of sound radiation from the same beam–disk system. The conditions that lead to sound spectra shown in Figs. 5(a) and (b) differ from each other only by the direction of the disk rotation and produce these very different sounds. Although in both cases the frequency of the second mode of the beam coincides with the (0,2) mode natural frequency of the disk, the first one represents a mode lock-in, but the second does not. For cases shown in Figs. 5(c) and (d), the second natural frequency of the beam coincides with the (0,3) mode natural frequency of the disk. The conditions that lead to the responses shown in Figs. 5(c) and (d) have very little difference between them except for a slight change in the normal pressure. Yet, one produces a pure mode lock-in, Fig. 5(c), and the other, Fig. 5(d) leads to beats (when observed over a longer time than shown here).

2. Models

In general, response of systems to friction, such as those illustrated above for a beam and disk, can be described as forced vibrations, resonant vibrations, or instabilities. Instabilities in the presence of friction usually develop through one of four mechanisms: (i) geometric instabilities (*viz.*, Refs. 10 and 11); (ii) material nonlinearities; (iii) thermoelas-

tic instabilities^{12,13} and (iv) instabilities due to decreasing friction with increasing velocity. In the first two types of instabilities, friction has a passive role. For example, in geometric instabilities, such as brush and commutator contact in electric motors, friction has a necessary but passive role.¹⁰ Friction also has a passive role in instabilities caused by system nonlinearities, e.g., in cases where material properties exhibit nonlinear contact stresses (*viz.*, Refs. 14 and 15). On the other hand, friction has an active role in instabilities caused, for example, by a decreasing friction force with increasing velocity that lead to mode lock-in.²

A thorough review of unstable vibrations of disks by frictional loading given by Mottershead¹⁶ includes an analysis of instabilities due to frictional follower forces and friction-induced parametric resonances, and their extension to the case with a negative friction-velocity slope.^{17–22} Using a distributed frictional load, Mottershead and Chan¹⁷ showed that follower friction force led to flutter instability indicated by the coalescing of eigenvalues, and they compared their results with previous studies.^{23,24} Mottershead *et al.*¹⁸ also investigated parametric resonances under a sector load with friction rotating on an annular disk and identified combination resonances and how they change when friction has a negative slope with respect to velocity. Other studies also address the propensity of a disk to generate noise when the natural frequencies of in-plane and bending vibrations exist close to each other^{18,25–28} as well as self-excited vibrations of a circular plate with friction forces acting on its edge to model squeal in railway brakes and drum brakes in automobiles.^{34,35} Studies addressing friction-induced rigid-body instabilities, such as those encountered in braking systems, are adequately covered elsewhere (*viz.*, Refs. 7, 29–33).

Because different configurations and operating conditions of a clamped beam and a rotating disk can produce the different responses cited above, they provide a useful benchmark for investigating friction sounds and vibrations. As depicted in Fig. 6, considering a beam that makes an angle φ with the normal to the surface of the disk and neglecting the effects of shear and rotatory inertia, its bending and longitudinal vibrations are governed by^{36–40}

$$EI \frac{\partial^4 w}{\partial x^4} + \rho A \frac{\partial^2 w}{\partial t^2} + C \frac{\partial w}{\partial t} = F_N(t) [\mu(v_r) \cos \varphi + \sin \varphi] \delta(x-L), \quad (8)$$

$$EA \frac{\partial^2 u}{\partial x^2} - \rho A \frac{\partial^2 u}{\partial t^2} - C' \frac{\partial u}{\partial t} = F_N(t) [-\mu(v_r) \sin \varphi + \cos \varphi] \delta(x-L), \quad (9)$$

where the beam properties ρ , E , I , and A are as defined before. C and C' are representative damping constants proportional to bending and longitudinal vibration velocities, respectively. The contact force develops at the tip of the beam of length L .

Bending vibrations of a disk excited at a point (r_0, θ_0) on its flat surface are described by

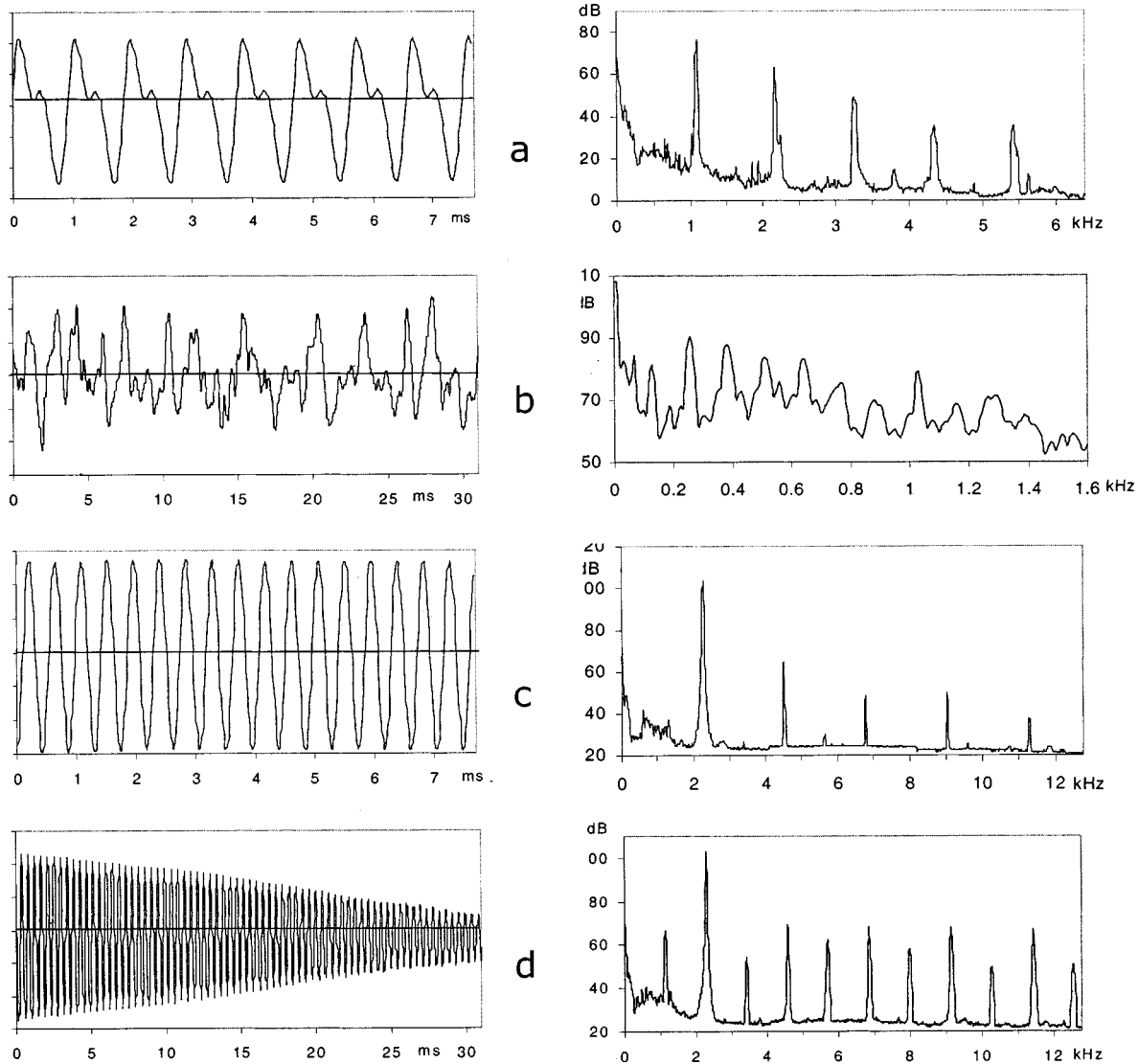


FIG. 5. Time history and spectrum for sounds generated by beam and disk friction. Beam length in (a)–(b) 200 mm, in (c)–(d) 135 mm. (a) CW rotation shows mode lock-in of (0,2) mode of disk; (b) CCW rotation does not generate a lock-in; (c) CW rotation lock-in to (0,3) mode of disk, but a slight change of normal load shows beating in (d).

$$D\nabla^4\eta + \rho_d h_d \frac{\partial^2 \eta}{\partial t^2} + C'' \frac{\partial \eta}{\partial t} = -F_N(t) \delta(r-r_0) \delta(\theta-\theta_0), \quad (10)$$

where $D = E_d h_d^3 / 12(1 - \nu^2)$ represents the bending rigidity of the disk, and h_d and ρ_d are its thickness and density, respectively. C'' represents an equivalent damping proportional to velocity.

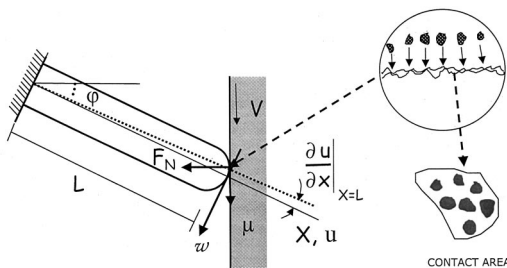


FIG. 6. Schematic of contact of a beam with a flat surface and depiction of the magnified contact area.

Assuming that friction force can be represented with a constant coefficient, $\mu(v_r)F_N(t)$ represents the friction force as a function of the relative sliding velocity, v_r , between the disk and rod tip under a normal contact force $F_N(t)$. The two primary sources of nonlinearities in the equations given above come from the coefficient of friction expressions and the contact forces.

3. Contact force

In the cases described in this section, the normal component of the contact forces relates to the deformation of the contact areas. For instance, in the case of a beam in contact with a disk, the normal contact force $F_N(t)$ can be expressed as one that results from the combined deformation, α , of the beam and disk at the contact area, referred to as the approach. In addition to an initial approach α_0 that results from a static normal load applied to the beam–disk system, the combined deformation between the bending and longitudinal deformations of the beam and the bending deformation of the

disk gives rise to a fluctuating contact force that changes with the vibration of the beam and disk.

For example, in case of Eqs. (8)–(10), for perfectly smooth surfaces the combined approach can be expressed as

$$\alpha_H = \alpha_0 + u \cos \varphi - w \sin \varphi + \eta. \quad (11)$$

In cases where surface has a texture that alters the contact force, the approach can include an additional term that describes surface topography which considers both its roughness and waviness.

The Hertz theory describes the contact force $F_N(t)$ that results from elastic deformation in terms of approach α

$$F_N(t) = k_H \alpha_H^{3/2}(t), \quad (12)$$

where for a spherical surface, with radius a , in contact with a planar surface of similar material, $k_H = 2E\sqrt{a/3}(1-\nu^2)$.

When $\alpha_H < 0$, contact ceases and the ensuing impacts lead to a highly nonlinear behavior. A common approach to solving Eqs. (8)–(10) assumes that contact is maintained between the beam and the disk. Under conditions where the friction force linearly depends on the normal load, but independent of sliding velocity, the coupling of Eqs. (8)–(10) eliminates the normal load, leaving only its ratio to friction force, or the coefficient of friction, as a parameter. This model also permits the friction force to follow the displacement and act as a follower force. However, as noted earlier, a normal load more than only modifies the friction force F_f . Within certain regimes of $|F_f/F_N|$, modes of the system coalesce and develop instability. This particular type of instability, sometimes referred to as a flutter instability, is one of the mechanisms that leads to mode lock-in described earlier.

Improvements to this model include consideration of the in-plane vibrations of the disk and an accurate model of the friction force at contact. Just as in the case of longitudinal and bending waves of a beam, in-plane natural frequencies of the disk can have a significant role, particularly when they fall in the neighborhood of its bending wave natural frequencies.

A friction coefficient that increases with decreasing velocity also produces instabilities that generate mode lock-in. Phenomenological expressions for a friction force lead to qualitative results that help bring out the underlying physical phenomena, but not the accuracy required in some applications. Such expressions take several forms, for example^{36,2}

$$\mu(v_r) = \alpha_1 e^{\alpha_2 v_r^2} + \alpha_3 v_r + \alpha_4, \quad (13)$$

$$\mu(v_r) = \text{sgn}(v_r)(1 - e^{-\beta_v |v_r|})[1 + (f_r - 1)e^{-\alpha_v |v_r|}], \quad (14)$$

where α_1 , α_2 , α_3 , α_4 in Eq. (13) and α_v and β_v in (14) are constants with f_r representing the ratio of the static to kinetic friction coefficients.

The foregoing equations follow the conventional approach which relies on representing friction as an external contact force. In most cases this approach gives satisfactory answers, but not in all. Some cases require a more detailed and more accurate representation of friction to better predict

system response and the development of instabilities. Numerically obtained results of the models described above support the experimental observations, suggesting that at light contact loads, sound sources are confined to the surfaces.^{36–40} Other studies also relate sound radiation to the effects of surface roughness, *viz.*, Refs. 41–44.

Analyses of friction sounds that appear in other mechanical systems present different challenges, as in the case of thermally induced noise in roofs,^{45,46} roller bearings,^{47–50} gear noise,⁵¹ belts,⁵² and band brakes.^{53,54} Adams,^{55–60} in a series of studies that involved friction between elastic half-spaces, discussed instability mechanisms between two half-spaces and showed that the steady sliding generates self-excited waves due to destabilization of slip waves. He also showed that, as a result of unstable sliding, the apparent coefficient of friction measured away from the interface can differ from the interface friction coefficient. Similarly, Ruina and Rice showed the existence of flutter instability during the steady sliding of surfaces where shear stress depends on slip velocity.⁶¹

The effort required to analyze response to friction in simple systems described above increases with an increase in the dimension of the system. The two examples reviewed below, bowed strings and brakes (both subjects of continuing investigations), represent different but equally complex sources of friction sounds.

C. Bowed string—violin sounds

A bowed string presents a particularly useful example because of the seemingly simple configuration of a bow and a string. Yet, its very complex dynamic response makes it a challenge to accurately predict sound radiation from a string instrument. Such predictions necessitate a high degree of accuracy because the narrow frequency intervals between musical notes (tones) make errors as little as 1% unacceptable.⁶² The factors that contribute to the complexity of string dynamics result from the combined interaction among the string, the (violin) structure, the bow, and the friction between the bow and string.

A nondimensional coupling constant was shown to characterize the classical stick–slip example that consists of a mass, m , restrained by a spring of constant k on a conveyor belt that moves at a speed V ⁶²

$$\Gamma = \frac{F_0/k}{V_0/\omega_0}, \quad (15)$$

where F_0 represents the maximum static friction force and $\omega_0 = \sqrt{k/m}$. The larger the value of Γ , the longer the sticking period of the mass and the longer the period of its oscillation. However, since the frequency of vibration of a bowed string remains the same as for its free vibrations, the coupling function does not correctly describe the bowed-string oscillations. As pointed out earlier,⁶² string, and by extension other friction-excited systems, should be considered not as having a single degree of freedom, but as continuum systems with many degrees of freedom. Also, the mode lock-in seen in

other examples is not so obvious in the case of a string, for harmonics of a string coincide with its natural frequencies.

The bowing action divides a string into two approximately straight-line sections, on either side of the “corner,” caused by the bow contact. During bowing, the string moves with the bow until the tension in the string exceeds the friction force, at which time the string separates from the bow until they reconnect. The corner travels along the string at the transverse speed of string waves, and follows a parabolic path between the two fixed ends of the string. This behavior of the string, named after Helmholtz,⁶³ who first studied it prior to Raman,⁶⁴ describes the free vibrations of the string. At each instant, the string maintains the two approximately straight-line segments between the corner and the fixed ends. Thus, the complete motion of the string during bowing consists of the classic circulating corner of the Helmholtz motion, which is the homogeneous solution of the equations of motion, superposed on the particular integral that describes a stationary corner at the bow contact.

The structure of the violin often modifies the pure Helmholtz motion, i.e., the transverse motion of the string under ideal conditions, through the compliance of pegs at one end and the triangular tailpiece at the other end. As the pegs and tailpiece deform, the tension and length of the string change to make the string vibrations anharmonic. In addition to such nonlinearities, the torsional and longitudinal vibrations of the string, as well as the vibration of the bow, also participate in the transmission of structure-borne sounds through the bridge, thereby adding to the complexity of the problem.

An example of how sound quality depends on the interaction of friction and vibration appears in the phenomenon called *double slip*. Double slip occurs when the actual bowing force falls below the minimum bowing force necessary for “playability.” Double slip manifests itself by splitting the fundamental frequency and producing the “wolf tone.”^{65–67}

The difficulties associated with predicting sound radiation from musical instruments with bowed strings, particularly the violin, fall beyond the scope of this paper. Studies continue to uncover the details of what makes one violin sound better than another. Additional references summarizing some of the previous research can be found in *viz.*, Refs. 68–79.

D. Brake noise

Aircraft, rail, and automotive brakes have qualities opposite those of the violin in terms of their structures, purposes, and, albeit unintentionally, the sounds they produce. Within brakes all possible vibrations and classes of waves may develop through several instability mechanisms and the forced vibrations described earlier. Responses range from roughness noise to mode lock-in, which on occasion develops with more than one fundamental frequency. Such a wide range of responses stems from the number of components in a brake system, the range of braking conditions, and the large amount of energy transmitted by friction, compared to a violin or a door hinge.

Records show that as early as 1930 brake noise emerged as one of the top-10 noise problems in a survey conducted in New York City, and it still continues to be a source of an-

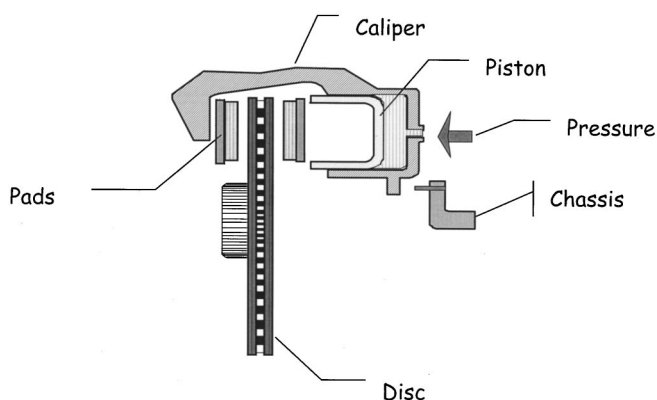


FIG. 7. Components of an automotive brake.

noyance. Industry sources suggest that the warranty costs in North America for brake noise, vibration, and harshness reaches one billion dollars each year.

Braking action in an automobile takes place between the rotors and brake pads. A rotor or disk, attached to an axle and usually made of cast iron, carries the wheel (Fig. 7). Each brake pad, one on each side of a rotor, moves freely in a caliper and consists of a layer of friction material attached to a steel backplate. Braking takes place by pushing the pads against the rotor under hydraulic pressure. A steering knuckle attaches the caliper to the frame of the automobile and carries the torque.

Braking converts most of the kinetic energy of a vehicle to thermal energy primarily within the pads and rotors.⁸⁰ However, a small fraction of the energy finds its way to vibrational energy within the braking system which can even travel to the suspension of the vehicle. The vibratory energy follows a complex path, and the resulting sound radiation may involve any number of components of the brake system. Aircraft brakes tend to respond at lower frequencies. They “walk” (5–20 Hz), chatter (50–100 Hz), and squeal (100–1000 Hz), and sometimes the dynamic instabilities lead to a “whirl” (200–300 Hz) of the landing system. Automotive and rail brake noises often reach much higher frequencies. In an effort to display the vibratory energy path (and the types of waves and radiation) braking produces, the following summary presents the sound and vibration sources in a brake in terms of a hierarchy of causes and effects.^{81–83}

1. Brake noise generation mechanisms

An idealized brake consists of a pair of pads that squeezes a rotating disk with a constant friction coefficient, with each component having perfect geometry and uniform material properties. Under such conditions, the rotor and the pads experience normal and tangential forces at their interface. These forces, while uniformly distributed during stationary contact, develop a nonuniform distribution during relative motion.

Under a constant normal load, tangential forces acting on the surfaces of a rotor develop in-plane vibrations within it.^{25,27,28} A combination of in-plane vibrations, through consequent surface deformations, alters the contact area, thereby changing the presumed constant behavior of the friction force. Even under assumed constant-friction properties at the

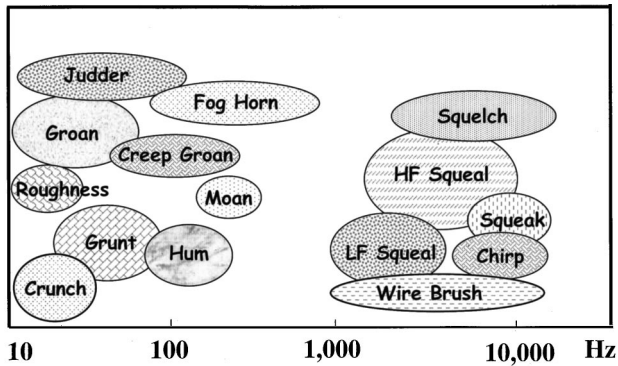


FIG. 8. Different brake noises and their approximate spectral contents.

interface, a friction force induces a moment arm about the supports of the pads that leads to oscillations of the pads. Consequently, oscillatory normal force components always accompany the friction force even in an otherwise ideal braking system, and easily excite bending waves in the rotor and pads.

Geometric instabilities can result in cases where the contact between pads and rotor is not uniform. These instabilities usually lead to rigid-body oscillations of the pads, but they can also cause vibrations within the pads. Pad vibrations, in turn, can have sufficient energy to easily travel to the brake caliper and beyond, and cause caliper resonances, providing yet another source of excitation for the bending waves in the rotor. Rail⁸⁴⁻⁸⁸ and aircraft^{14,15,89-92} brakes have different but analogous designs that also yield geometric instabilities.

In addition to the above, numerous other parameters afford an abundant set of possible sources for brake-noise generation. Examples include the time-dependent nature of friction properties, manufacturing tolerances with respect to flatness and parallelism of rotor surfaces, and variability of material properties. These different noise sources manifest themselves by a variety of brake-noise types described below.

Twenty-five or so different designations describe automotive brake noise and vibrations. Some refer to their alleged mechanisms, and others describe the characteristics of the sounds. Figure 8 shows their approximate distribution in the frequency spectrum. Grunt, hum, groan, and moan have lower frequency content than the family of squeals. Not surprisingly, some of these sounds have similar generation mechanisms. For example, *squeak* describes a short-lived squeal, *wire brush* describes a randomly modulated squeal, and *squelch* describes an amplitude-modulated version of squeak noise.⁸³ The following sections give synopses of a few of the brake-noise mechanisms.

2. High-frequency squeal

A high-frequency squeal typically involves the higher-order disk modes, with 5 to 10 nodal diameters. Their frequencies range between 5–15 kHz. Nodal spacing between the excited modes is comparable to or less than the length of brake pads. Holograms usually show unconstrained disk mode shapes associated with high-frequency squeal sounds,

thus suggesting that the pads do not act as constraints everywhere within their nominal contact areas. Mode shapes, however, remain stationary with respect to the ground, thereby indicating some constraining effect by the pads, although not excessive enough to alter the mode shapes. Furthermore, the spectra show one or more fundamental frequencies closely associated with disk natural frequencies, and their harmonics, whereby exhibiting the mode lock-in phenomenon described earlier.^{82,83}

3. Low-frequency squeal

A low-frequency squeal involves modes with 1, 2, 3, or 4 nodal diameters (ND) each with nodal spacing larger than the pad length. Holograms of rotating disks show that squeal occurs at a frequency other than a natural frequency of the rotor. Furthermore, the displacement of the rotor has a fixed shape usually resembling a 2.5-ND mode shape with respect to the laboratory coordinates. Analyses show that this shape is comprised of first, second, third, and fourth modes, and the mode with 3 nodal diameters contributes the most at nearly 50%.^{82,83,93}

4. Groan

A typical groan has a spectrum between 10 to 30 Hz, with harmonics reaching 500 Hz. It occurs at low speeds and under moderate braking conditions. A groan appears to result from a geometric instability of pads that gives rise to stick-slip which, in turn, excites the low-frequency resonances in a brake system. In particular, resonances of the rigid-body rotation mode of the caliper and the local suspension parts develop and radiate sound without the participation of the rotor. The position of the pads with respect to the rotor has a significant role: the higher the relative tilt between them, the higher the propensity for groan generation.^{83,94}

5. Judder

Judder develops from continuous pulsations between the rotor and pads and manifests itself as a low-frequency vibration with frequencies that are integer multiples of the rotational speed of the wheel. Judder, transmitted through the brake to the chassis and steering, falls into the category of vibration and harshness rather than noise. The conditions that lead to judder generally result from nonuniform friction force between the rotor and pads. The nonuniformity may result from any one or a combination of circumferential thickness variation, uneven coating by friction material, and variation in surface finish.^{95,83}

6. Some solutions to brake noise

The engineering solutions to reduce brake noise described below give a few examples that demonstrate methods to prevent waves from developing within a rotor that make it unable to radiate sound. Each of these solutions, however, has obvious drawbacks in terms of its implementation.

Radial slits in a rotor reduce its propensity to radiate sound by preventing the circumferential waves from fully developing. In Fig. 9, the short solid lines on the disks indicate radial slits with numbers referring to the length of each

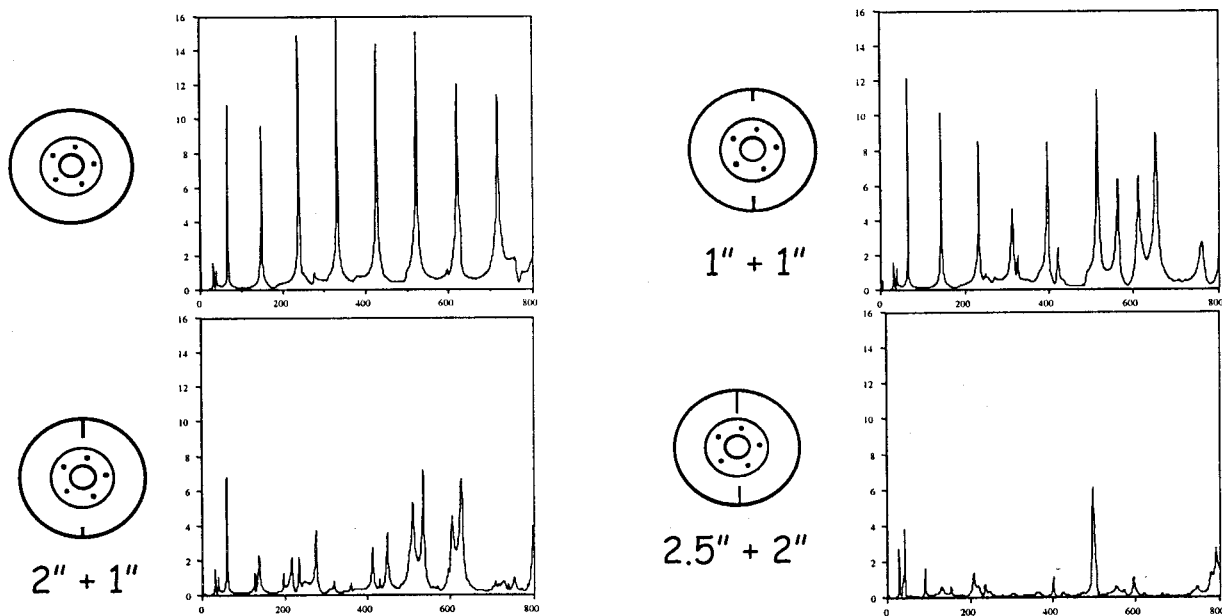


FIG. 9. Transfer functions of a typical automotive rotor with radial slits. The numbers next to lines describing slit locations indicate their lengths in inches.

slit. The corresponding transfer functions of the rotor show a reduction of peak amplitudes with increasing slit length.

The insertion of a metal piece into a radial slit nearly eliminates the sharpness of the peaks in the transfer function of the rotor, thus making it an effective method to reduce high-frequency squeal.

The use of ring dampers around the circumference of a rotor, as shown in Fig. 10, can completely eliminate the peaks in the bending-wave transfer function of a brake rotor. Ring dampers reduce vibrations by means of friction between the ring and the rotor.⁹⁶

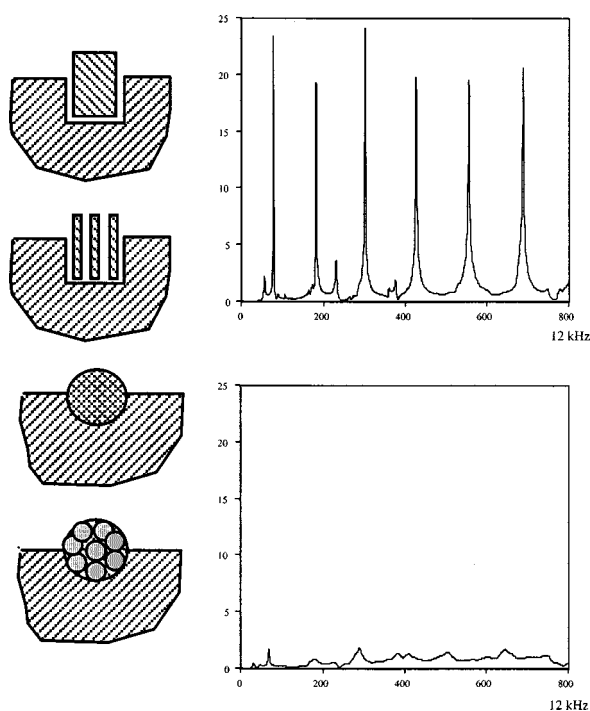


FIG. 10. Transfer function of a rotor with and without ring dampers. The lower figures show the different types of ring cross sections that can be used.

E. Friction sounds in nature

Nature offers its own friction sounds that have developed through evolution, in this case, for the purpose of communication among the animals such as fish, crustacea, and insects. One of the mechanisms by which invertebrates, such as crickets, locusts, and cicadas,^{97,98} produce sounds is through friction of differential parts, ordinarily termed stridulation.

1. Stridulatory sounds by insects

The stridulatory apparatus of an insect body has two parts as shown in Figs. 11 and 12. One part, named *pars stridens* (or file), has a surface with ridges, the composition and size of which vary (hairs, spines, tubercles, teeth, ridges, ribs, etc.). The second part, called the *plectrum* (scraper), is a hard ridge or a knob. Morphology and location of *pars stridens* and *plectrum* differ widely with the insects. The *plectrum*, in some cases, is a protrusion with a sharp edge while in others it is composed of the tapering edge of an appendage or a joint. Their locations may be just as varied, on the sides of their heads, under their torso, or at one of many other places, depending on the type of insect.

Insects stridulate by rubbing the scraper (*plectrum*) on the file (*pars stridens*), or vice versa. Stridulation commonly refers to sounds that result from the rubbing of two special bodily structures. However, in some cases, the mechanism by which insects generate sounds may also be described as a succession of impacts made by the rubbing of the scraper and the file, not unlike sounds that result from friction between two periodically rough surfaces exhibiting the "picket-fence effect." As an insect draws the scraper across the file, each tooth impact produces a vibration of the body surface, and generates percussive sounds. Such a series of impact sounds almost always contains many frequencies with complex harmonics. However, in some species (acrid-

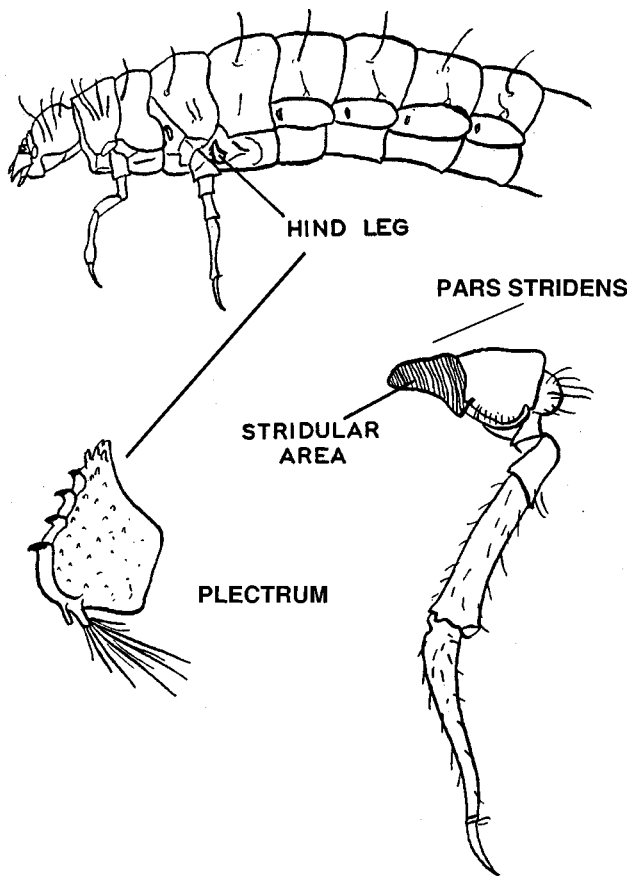


FIG. 11. Drawings that describe stridulatory components of an insect. (a) adult larva; (b) modified hind leg; (c) *pars stridens* on the inner leg [from P. T. Haskell (Ref. 97). After G. C. Schiodte, *Nat. Tidsskr.* 9, 227–376 (1874)].

ids), sound emission evokes more of a rubbing sound than a succession of percussions.

In insects with hard exoskeleton, a certain amount of vibrational energy will be transmitted to large resonant surfaces and radiated, even when the actual site of frictional mechanisms is remote and localized, as in the case of insects that produce sound by rubbing their antennae. This transmission is reminiscent of sounds from the cuica and some types of brake noise discussed earlier.

Some of the parameters that affect the emission of sound from insects are inherent in the physical nature of the stridulatory apparatus, for example the spatial distribution of ridges on *pars stridens*. Others concern more the manner by which the insect uses its apparatus: duration, speed of displacement of the parts, and differences in the spacing of movements. During stridulation, the displacement of the point of contact between the file and the scraper excites and produces resonance of various portions of the elytron, thereby modifying the frequency, intensity, modulation, and transients in the sounds insects produce.

Frequency content of friction sounds in insects range from 1–2 kHz up to 90–100 kHz. The breadth of the sound spectrum for a given species is highly variable; for example, some can cover 90 kHz while others are limited to 500 Hz. Often the lower end of the spectrum is used for calling, and the upper end is used for courtship. Warning songs have

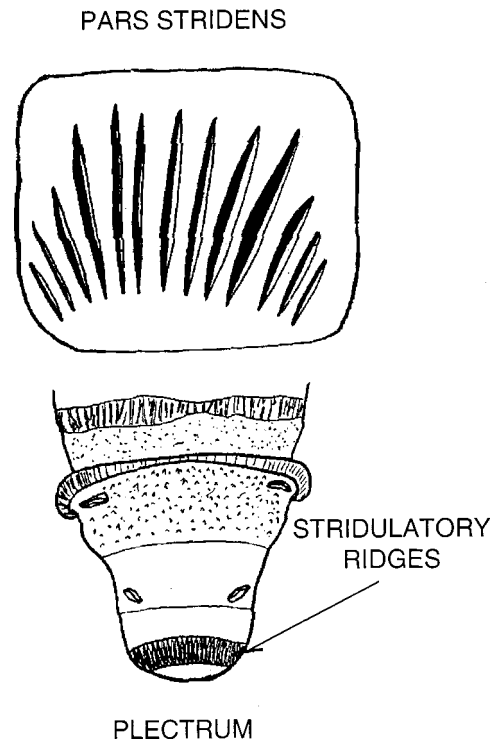


FIG. 12. Stridulatory ridges of a silken cocoon *Eligma hypsoides* with ridges (above) and end of abdomen (below) [from P. T. Haskell (Ref. 97)].

about 30–35-dB amplitude, whereas calling songs can reach up to more than 50 dB.

To generate sound, an insect moves its limbs back and forth. While observations suggest that sound radiation corresponds to the closing movement, in some cases sound emission occurs in both directions. Some insects employ more complex motions that involve rapid oscillations. It appears that no single law rules the sound emission procedure in insects, not unlike the case for other friction sounds.

Similar sound generation mechanisms exist in ants.⁹⁹ Spiny lobsters, however, rub a soft-tissue plectrum over a file, generating a stick-and-slip motion, without the impacts associated with the picket-fence or washboard action described above.¹⁰⁰

Different groups of fish generate sounds by using skeletal stridulatory mechanisms which are magnified by resonance of the air bladder. An example is stridulation of *pharyngeal* teeth adjacent to the air bladder that amplifies the faint friction sounds. Other underwater insects, such as the water bug, have long been known to generate sounds through stridulation. *Microvelia diluta*, for example, when disturbed, produces a “shrill scraping sound” by stridulation.⁹⁸

2. Pleural and pericardial friction sounds

Friction sounds also develop in humans. Two common forms, pleural and pericardial friction sounds or friction rubs, result from an inflammation of tissues that surround the lungs and the heart, respectively. Pleural friction sounds develop during respiration when inflamed visceral and pulmonary surfaces that cover the lungs and line the thoracic cavity come together. Pericardial friction sounds or friction rubs are caused by an inflammation in the pericardial space or peri-

cardial sac, the fibroserous sac which surrounds the heart, that leads to the parietal (outer) and visceral (inner) surfaces of the roughened pericardium rubbing against each other. A pericardial friction rub produces an extra cardiac sound with both systolic and diastolic components. Up to three components of a pericardial friction rub may be audible. Pericardial friction sounds are said to resemble those of squeaky leather and are often described as grating or scratching.

III. FRICTION AND MOTION

Friction-induced motion, in this paper, refers to flight-free transport of an object on a surface by means of inducing vibrations to the surface and utilizing the friction between the two. The examples described below represent two very different friction motion mechanisms. Flight-free motion, or transportation of objects over a surface without losing contact, represents a useful example of friction-induced motion that involves oscillation of at least one of the surfaces. A flight-free conveyance has uses in the transportation of fragile materials and in motion control that requires accuracy, such as a camera lens. Other forms of motion and force conveyance by friction, such as clutches and belts, do not fall within this category, for they do not require vibration of their components.

The essential elements of flight-free motion involve friction and oscillatory relative motion between the transported object and the platform. Motion results from a nonzero average friction force that develops during oscillatory movements. Such a force and the consequent motion develop through either a rigid-body movement of the platform, or track, or by means of traveling- or standing waves in it. As described below, many of the classical vibratory conveyors rely on the first mechanism, and the ultrasonic motors rely on the second.

A. Analysis of vibratory conveyance

A simple vibratory conveyor consists of a planar platform at an angle α with the horizontal and a mass m placed on it. For conveyance, a throw force vibrates the platform in a direction ψ to the axis of the platform at a frequency ω and amplitude ξ_0 . Maintaining a positive contact force N normal to the track, or satisfying the condition $\xi_0 \omega^2 \sin \psi / g \cos \alpha < 1$, ensures continuous contact or flight-free motion. Motion of the mass along the track that results from the combined vibration and friction force is governed by

$$m\ddot{x} + \text{sign}(\dot{x})\mu N = -mg \sin \alpha, \quad (16)$$

where x describes the relative displacement of the mass on the track. Substituting in Eq. (16) for the normal force on the mass $N = m(g \cos \alpha - \xi_0 \omega^2 \sin \omega t \sin \psi)$ explicitly describes the motion of the mass as

$$\ddot{x} = -g \sin \alpha \mp \mu(g \cos \alpha - \xi_0 \omega^2 \sin \omega t \sin \psi), \quad (17)$$

where minus and plus signs indicate slip in the negative and positive directions, respectively. During the stick phase the particle, \dot{x} will have a value between the two slip accelerations.^{101,102} However, conveyors sometimes exhibit nonperiodic, and possibly chaotic, motion of the mass on a

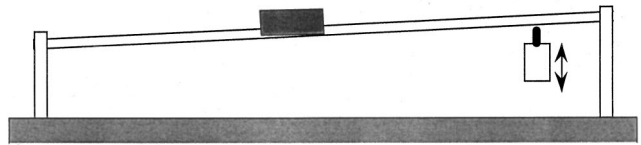


FIG. 13. Description of a flight-free motion of a mass on a beam.

track that cannot be explained with the conventional friction models.^{103–107}

B. Vibratory conveyance: An experiment

A simple laboratory demonstration of friction motion consists of a mass that can move freely on an inclined beam supported at both ends, and a shaker that vibrates the beam and its supports, as shown in Fig. 13. Under a suitable combination of excitation frequency and amplitude, the mass can move up or down the inclined beam without losing contact. The frequencies at which conveyance takes place correspond to a natural frequency of the beam and its supports, whereby each point on the beam surface follows an elliptical trajectory. During oscillations, the mass on the beam experiences a larger contact force, hence a larger friction force, during one-half of the cycle. Such uneven friction forces during each half of a cycle of oscillations produce a nonzero average force on the mass along the beam. This example of flight-free conveyance points to the significance of system dynamics in friction problems and suggests a reconsideration of the classical definition of the coefficient of friction which does not account for the presence of vibrations within the system. A similar demonstration shows a wheel in contact with the beam rotating clockwise or counterclockwise as a result of changing the frequency of excitation that changes the direction of the phasor of surface vibrations.

C. Ultrasonic motors

The principle of motion in ultrasonic motors also relies on elliptical motion of each material point on the surface of the driver that leads to a nonzero average friction force. Ultrasonic motors, whether linear or rotary, produce elliptical motion by utilizing either standing or traveling waves within or on the surface of the driver. Those that rely on standing waves require only one exciter, but without directional control, and operate similarly to the traditional vibratory conveyors described above.^{108–115}

Rotating ultrasonic motors normally use traveling bending waves in a circular driver. The method to generate traveling waves involves inducing two standing waves, of equal amplitude that differ in space and in time by $\pi/2$

$$w(r, \theta, t) = W_0 R(r) \cos m \theta \cos \omega t,$$

$$w(r, \theta, t) = W_0 R(r) \cos(m \theta - \pi/2) \cos(\omega t - \pi/2),$$

where the radial component of the displacement given by $R(r)$ represents Bessel functions and θ describes the circular coordinate. Two such standing waves combine to produce a traveling wave

$$w(r, \theta, t) = W_0 R(r) \cos(m \theta - \cos \omega t), \quad (18)$$

that travels at an angular speed of ω/m .

The expression in Eq. (13) describes the motion of the middle plane of the driver disk in the normal direction. The

actual displacement of a point on the surface of the disk follows an elliptical path in the $z-\theta$ plane and can be obtained by projecting a surface point onto the midplane.

A rotor placed on such a driver that has traveling waves described above rotates with a speed in the opposite direction to the bending waves¹⁰⁸

$$\dot{\theta} = -\omega(h_d/2r)m[R(r)/r], \quad (19)$$

which differs from the speed of the traveling waves. By appropriate choice of modes of vibration and disk geometry, the ultrasonic motors rotate at much reduced speeds.¹⁰⁸

In advanced ultrasonic motors, excitation is usually provided by using an array of piezoelectric transducers distributed near the perimeter of the disk with a spatial distribution that matches the desired mode shape. Alternative methods include use of two thin piezoelectric membranes below the disk, each excited at one of its own resonant frequencies.

D. Granular flow

A different type of friction motion develops with granular materials when they behave like a liquid under vibratory excitation. For example, glass granules of 2–3-mm diameter that fill a cylindrical container move in a regular and coherent manner when the container is vibrated vertically. The granular material flows downward adjacent to and near the wall of the cylindrical container and upward along its center, together forming a toroidal pattern with an axis that coincides with that of the cylinder. The flow originates at the wall of the container where, as a result of wall friction, the granules develop a nonzero average velocity. The downward flow at and near the wall has a narrow thickness reminiscent of a boundary layer. Objects buried among the granules come up to the surface following the flow in the center of the container. But, they cannot follow the boundary layer flow if their size exceeds the layer thickness, a phenomenon which explains the reasons behind size segregation in cylindrical containers (*viz.*, Refs. 116–123). As discussed in the next section, the flow generated in a container of granular materials can have a significant effect on their damping properties.

E. Friction reduction by vibration

Just as vibrations can loosen bolted joints, they can be used to reduce friction. For example, during the cold drawing of wires, vibrations assist in reducing friction between the wire and die. The underlying mechanism of friction reduction is similar to friction-induced motion in the sense that contact forces are manipulated to reduce the average friction force during a cycle of oscillation.^{124–126}

IV. FRICTION DAMPING

Friction damping refers to the conversion of kinetic energy associated with the relative motion of vibrating surfaces to thermal energy through friction between them (*viz.*, Refs. 127–148). Applications of friction damping range from damper rings in gears to beanbag dampers consisting of granular materials. Friction damping devices such as the Lanchester damper¹⁴⁹ effectively reduce torsional vibrations.

Significant structural damping can also result from friction at joints and connections as well as within braided wire ropes.

A. Granular materials

Granular materials provide an effective mechanism of vibration damping by dissipating energy primarily through inelastic collisions and friction among the granules.¹⁴⁵ For example, sand¹⁵⁰ and lead grains absorb energy largely through inelastic collisions among the grains. On the other hand, low-density granular materials packed adjacent to beam or plate surfaces form a very effective dissipation mechanism mostly due to friction among the particles to which the bending waves of the structure provide the motion.^{146,147}

Elastic granules, such as ball bearings, also absorb vibration energy but become effective only when exposed to a vibration field collectively, as in beanbag absorbers. Although each ball bearing may rebound upon impact, when collected in a flexible container such as a bag they behave inelastically, due to friction among them and due to diffusion of the direction of vibratory forces. This collective behavior strongly depends on the packing force that holds them together. If the packing force severely limits relative motion, damping decreases.

A demonstration of applying friction damping to structural vibrations by using granular media consists of a steel tube welded to a beam, illustrated in Fig. 14. A spring-loaded cap adjusts the relative motion among the granules in the tube. Thus, as illustrated in Fig. 15, by changing the pressure (packing force) on the granules through the end cap, damping properties can be adjusted as desired. In the experiments described here, granular materials reduce the response of second and higher modes.¹⁴⁶ Experiments also show that the amplitude of vibrations influences the dynamic behavior of the granules in the container, ranging from a collective plug-like motion to a liquid-like flow. The different behaviors of granules produce different damping effects, thus making granular damping nonlinear and amplitude dependent.¹⁴⁸ Damping properties of granules and optimum packing forces can be evaluated directly by impact tests using a container described above. However, effective impact tests do not address liquefaction that develops during continuous vibrations.

B. Conforming surfaces

Contacts that generate friction damping generally fall into two groups: (a) contact between nominally conforming surfaces that do not have a relative rigid-body motion between the surfaces as in the case of bolted or riveted joints, braided wire ropes, and gas turbine blades, and (b) contacting surfaces that also have a relative whole-body motion as in the case of damper rings in gears and Lanchester dampers. In the first case, relative motion, sometimes referred to as micromotion, may not reach slip conditions, and friction remains in the “static” range associated with tangential stiffness. In the second case, full slip can develop between the surfaces.

In any type of contact, friction damping has a preferred range of contact force within which it becomes most effective. Below such an optimum range, excess relative motion

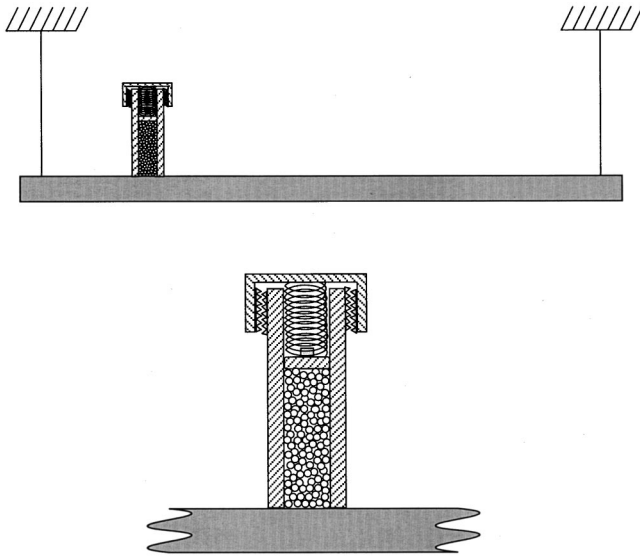


FIG. 14. Granular material in a cylindrical container when oscillated vertically generates a flow within the container.

at the interface develops without significant energy dissipation. Above it, excess pressure limits the development of relative motion for friction to act as an effective damper. Den Hartog¹⁵¹ provided the case of a simple oscillator with a friction damper solving $m\ddot{x} + kx = F_0 \cos \omega t - \mu N \text{sgn}(\dot{x})$. More on the specific mechanisms and models of friction damping can be found elsewhere (*viz.*, Refs. 127–148).

The transition from low to high contact forces and the corresponding changes in friction damping and system response can be demonstrated with a simple setup that consists of a cantilever beam with its free end positioned against another surface. Exciting bending vibrations of the beam with a shaker induces the relative motion between the free end of the beam and the opposite surface.¹⁵² The frequency-

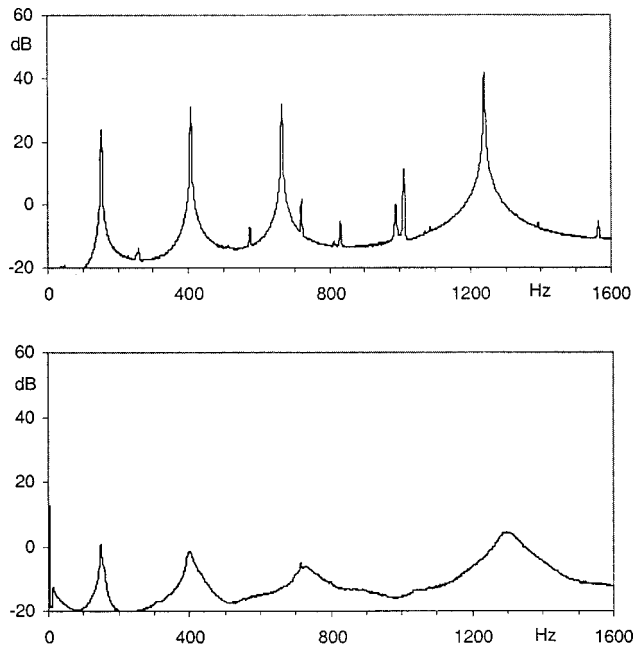


FIG. 15. Transfer functions of a beam with a container carrying granular materials under different pressures show damping of higher frequencies under optimum pressure.

response functions measured at the tip of the beam, shown in Fig. 16, illustrate the effects of varying normal contact load. The first figure displays the response without friction and clearly shows the clamped–free vibration frequencies. With increased normal load, amplitudes at these frequencies decrease, thus demonstrating damping due to friction. However, at higher normal loads, the response transitions to a different set of frequencies than the clamped–free frequencies and does so without the influence of friction damping. The new frequencies correspond to the clamped–constrained beam natural frequencies, illustrating that, beyond a critical normal load, friction turns into a constraint. Between these two extreme contact forces, the tip of the beam undergoes stick–slip motion. In frequency-domain terms, during stick–slip, both clamped–free and clamped–constrained boundary conditions coexist within each cycle of motion. Such time-dependent boundary conditions form the basis of nonlinearities in systems that involve friction.¹⁵²

Using thin inserts in the contact area to alter friction makes it possible to isolate the influence of friction from that of the system dynamics. Such inserts do not otherwise affect the system response. In Fig. 17, the measured responses clearly show the significance of friction, regardless of system dynamics or normal load.

V. FRICTION MEASUREMENT AND IDENTIFICATION

A. Measurement of friction

A friction force that results from the sliding contact of two surfaces depends strongly upon the dynamics of the system within which it develops. Since a friction force can only be inferred from measurements of its dynamic effects on a system, the need to also consider the influence of other forces within the system becomes unavoidable. The simplest case of friction force measurement involves an idealized mass on a flat surface moved to and fro by a force F . Under such ideal conditions, the friction force becomes the difference between the force applied to the mass and the resulting inertial force of the mass

$$F_f = F - m\ddot{x}. \quad (20)$$

Friction force relates to a normal load, N , through the conventional coefficient of friction that describes the average friction characteristics of an interface: $F_f = \mu N$. However, in most dynamic systems contact parameters between two sliding surfaces continually change, and the normal contact force does not stay constant. As a result, friction force becomes time dependent, and its estimate requires detailed measurements of the system response and an understanding of the system dynamics.

Figure 18 displays a simple demonstration of friction measurement in a dynamic system that uses a cantilever beam excited harmonically by a shaker similar to that described earlier. The free end of the beam rubs against the spherical surface of a rigid mass attached to a platform that can move freely. A force transducer placed between the rigid mass and the freely moving platform measures the force on

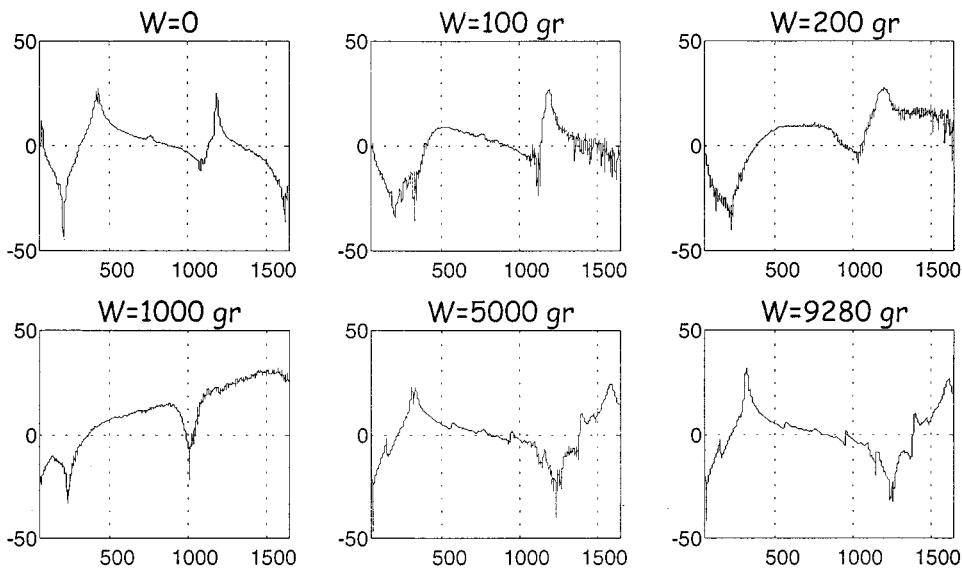


FIG. 16. Transfer function of a clamped-free beam subject to friction at its free end. As normal load increases, response transitions from one of clamped-free to a damped beam and eventually to a clamped beam with a constrained end (Ref. 152).

the mass effected by friction. The sum of the measured force and the inertial force of the mass (obtained by measuring its acceleration) yields the friction force.

B. Identification of friction

Most analyses of dynamic systems represent friction with a constant coefficient or with a function that depends on such parameters as velocity or, infrequently, temperature. The use of such phenomenological expressions gives acceptable results, particularly when modeling a continuous relative motion, as in rotating machinery. In cases of oscillatory relative motion, in particular those with small amplitudes, modeling requires further details of the friction force in terms of its variation with both displacement and velocity. During an oscillatory motion, characteristics of friction change, particularly where relative velocity at the extrema of displacement vanishes. Specifically, in cases where relative motion is very small, as in the contact dampers for turbine blades, an accurate characterization of friction becomes nec-

essary to model system response. The use of the measurement technique described above provides a convenient method to characterize the friction force. As displayed in Fig. 19, an examination of the friction force with respect to time, displacement, and velocity can lead to expressions that fully characterize it.

Considering the change of friction with displacement in Fig. 19, the measurements show that the friction force remains largely constant during sliding, but changes with displacement during each reversal of direction. The slope of the change with displacement represents the tangential stiffness associated with contact, usually represented by a constant in friction expressions

$$F_f = \begin{cases} k(d \mp X_0) \pm \mu N & |k(x - X_0)| < \mu N \\ \mu N \operatorname{sign}(v) & \text{otherwise} \end{cases}, \quad (21)$$

where X_0 is the maximum amplitude displacement x reaches during the oscillatory motion.

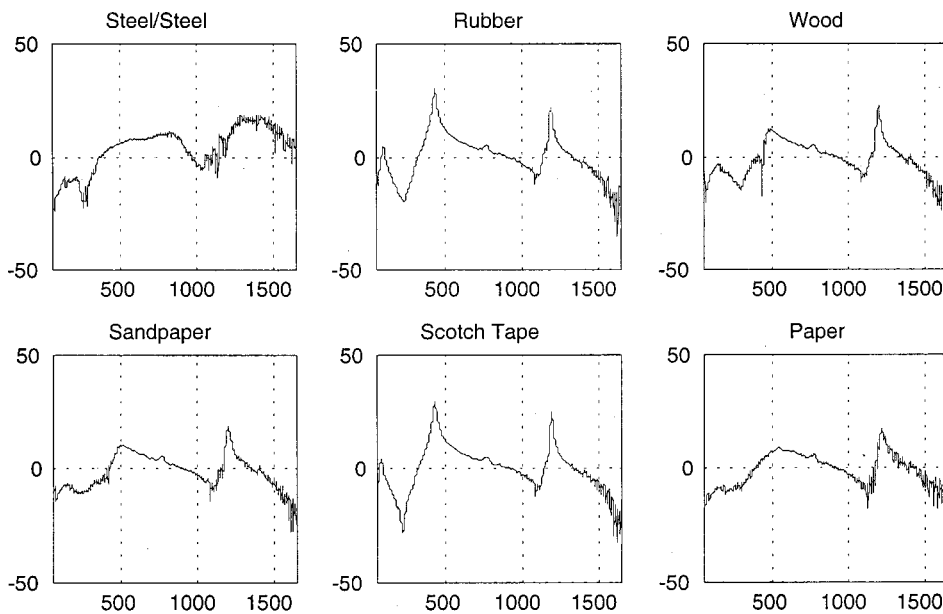


FIG. 17. Transfer functions of a clamped-free beam under a normal load of $N=9280$ gr with different inserts at the contact area shows how friction affects the dynamic response of the beam (Ref. 152).

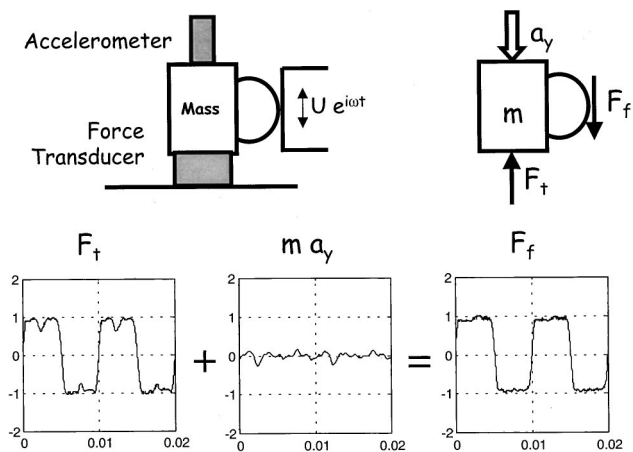


FIG. 18. Description and results of friction measurements between the oscillating tip of a cantilever beam and spherical surface attached to a rigid mass that can move freely.

Similarly, when examined with respect to relative velocity, the friction force remains unchanged during most of the sliding regime, but it shows an exponential dependence on velocity during a reversal of its direction. This velocity dependence can be expressed as

$$F_f = \mu N [1 - e^{-\beta |v \pm V_0|}] \text{sign}(v \pm V_0), \quad (22)$$

where V_0 represents the relative velocity at which the friction force vanishes and β relates to the slope at V_0 .

The characteristic coefficients, k and β , that describe the measurements shown here in a sense represent the number of different processes that contribute to friction between two surfaces. The following brief review describes the constitu-

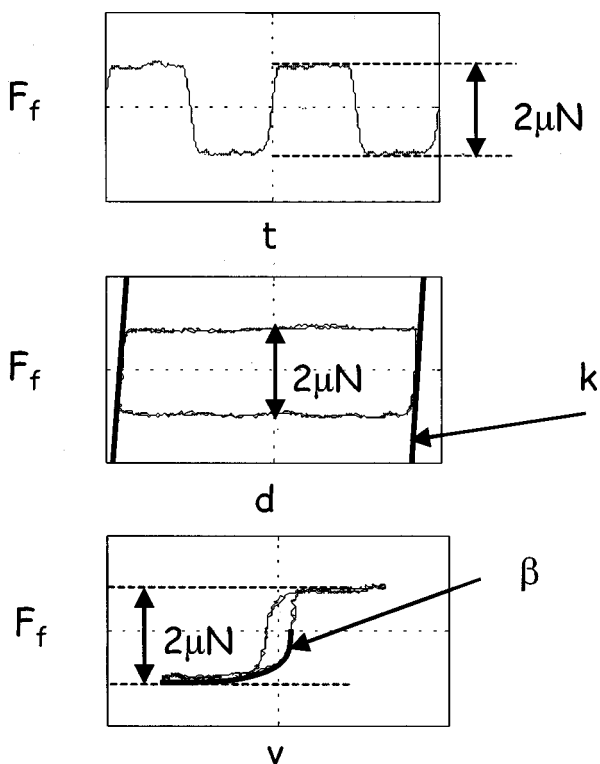


FIG. 19. Variation of a typical friction force with time, displacement, and velocity that shows the constants that characterize it (Ref. 152).

ents of friction and relates some of the fundamental aspects of friction in terms of acoustical phenomena.

VI. FRICTION

A closer look at a contact area, as depicted in Fig. 6, shows that the true contact between the disk and beam consists of a distribution of small contacts that takes place between asperities of the surfaces. During motion, such true contacts develop at different locations between new asperity pairs, thus making the distribution of the contact area time dependent. The nonuniformity and the resulting time dependence confound accurate modeling of friction. The computation of true contact between surfaces can be modeled through direct numerical simulation (*viz.*, Refs. 153 and 154). However, such detailed simulations have prohibitive computational requirements, at least for now (*viz.*, Refs. 155 and 156). In addition, friction still has aspects that require further understanding before it can be modeled accurately. Consequently, the unavailability of definitive friction models prevents accurate prediction of acoustic response of those friction-excited systems that are sensitive to friction parameters.

A. Friction components

The chart in Fig. 20 describes the processes by which “dc” kinetic energy of a relative motion converts into “ac” oscillations that represent thermal energy that eventually dissipates to the surroundings. During sliding contact, part of the kinetic energy produces waves and oscillations in the bodies, and part of it leads to plastic and anelastic deformation of asperity tips. Some energy expends through viscous dissipation, and the balance through adhesion, fracture, chemical reactions, and photoemission. Distribution of energy conversion through these processes varies for different applications. Each of these processes provides a mechanism for converting the original kinetic energy to an interim one in the form of vibration and sound, deformation energy, surface energy, tribo-chemical energy, and other tribo-emissions. In the end, part of the initial energy remains stored as potential energy, and part of it converts to thermal energy, eventually dissipating to the surroundings. Thus, friction can be viewed as a combination of processes that transforms ordered kinetic energy into either potential energy or a disordered, or thermalized, state of kinetic energy. It then follows that the friction force can be considered as a combination of forces that resist motion during each of these energy conversion processes

$$F_f = F_{\text{elastic deformation}} + F_{\text{plastic deformation}} + F_{\text{fracture}} + F_{\text{adhesion}} + \dots \quad (23)$$

The schematic depiction in Fig. 21 summarizes contributions to friction at different scales. The events that take place at each scale and contribute to the unsteady nature of friction require different models. The difficulty continues to center around integration of these length scales, each of which, by necessity, requires expertise from different disciplines of science and engineering. However, each scale of friction involves acoustics. Friction sounds and vibrations

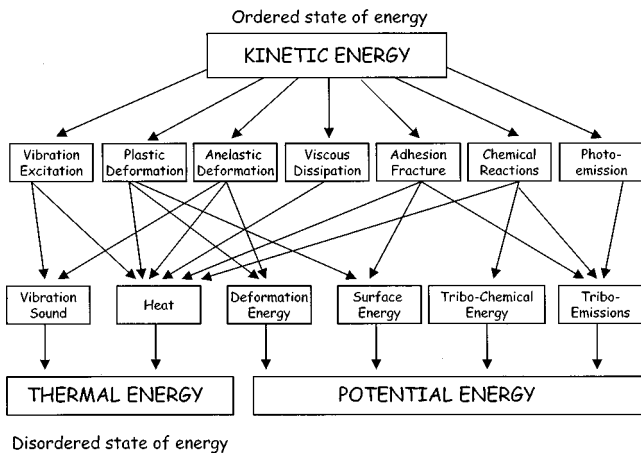


FIG. 20. A description of energy path during friction.

described earlier have engineering time and length scales. Near the interface, however, a continuum scale becomes more suitable for modeling, and the corresponding acoustical phenomena include, for example, ultrasonic emissions from contact areas. At the atomic scale, the primary issues relate to the dissipation and oscillation of atoms that describe thermal energy, examined later in this section.

Many of the current efforts to model friction start at the continuum scale, relating surface roughness to friction (*viz.*, Refs. 155–157). As depicted in Fig. 20, the obvious mechanisms that contribute to friction in such models include elastic/plastic contacts, viscous dissipation, fracture, and adhesion. Each of these processes develops at each true contact region between the surfaces. And, the true contacts take place between asperities on the surfaces or on particles between them. Computational resources required to compute a model that includes all the processes that contribute to friction at each asperity, for the time being, make it prohibitive. Also, in cases where inertial effects and elastic waves may not be ignored, the motion of the surfaces adds one more complication to the modeling of friction.

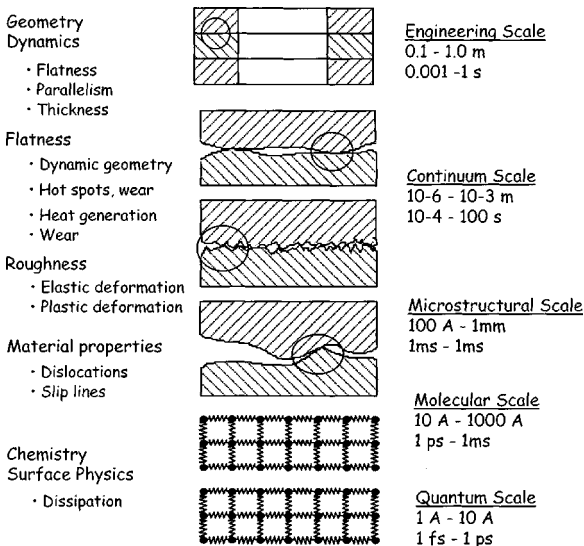


FIG. 21. Length and time scales associated with friction and examples of different events that accompany each.

B. Friction–vibration interaction

A significant, but often overlooked, aspect of friction and the waves and oscillations it causes relates to the feedback relationship between friction and the resulting structure-borne acoustic field. During a sliding contact, whether caused by friction or other forces, waves and oscillations modify the distribution of the true contact areas. This interaction of vibration and friction at the continuum scale forms the basis for a feedback loop between friction and vibrations.

Because friction is an intrinsic part of a dynamic system, accurate models to describe friction-excited vibrations must account for the coupling of system dynamics and the simultaneous development of friction during relative motion. One approach that combines system dynamics with the development of friction relates reactions at asperities (continuum scale) to relative motion (engineering scale) in terms of the deformation of asperities and their resistance to adhesion.^{157,158} Forces at each asperity contact depend on the area of that contact which, in turn, depends on the nominal relative position of the surfaces. Such dependence between the individual true contact areas and relative position of surfaces relates friction to the motion of the surfaces. This approach also assumes that contacts take place at asperity slopes. Consequently, normal oscillations develop, even though the nominal motion takes place in the tangential direction.^{159,160} Considering the classical case of an oscillator on a conveyor, equations that describe its response in tangential and normal directions to the conveyor couple with equations that, in this case, describe the true area of contact, A , which changes during sliding

$$m\ddot{x} + c\dot{x} + kx = \mathcal{F}_t, \quad m\ddot{y} = -N + \mathcal{F}_n,$$

$$\dot{A}_n^{(r)} + \mathcal{G}(\dot{x}, \dot{y}, Z, \dot{Z}, v) A_n^{(r)} = 0,$$

$$\dot{A}_n^{(a)} + \mathcal{G}'(\dot{x}, \dot{y}, Z, \dot{Z}, v) A_n^{(a)} = 0.$$

The first two equations above describe the dynamics of a simple oscillator on a conveyor configuration subject to tangential and normal forces ($\mathcal{F}_t, \mathcal{F}_n$) that result from sliding friction. Both components of the contact forces relate to the instantaneous properties of the footprint of the total true contact area, A_n , on a plane parallel to the interface.^{2,158} The second set of equations, using functions \mathcal{G} and \mathcal{G}' , describe the variation of the true contact area as a function of the motion of the system in both tangential and normal directions, relative velocity v , average slope Z of the asperities on the surface, as well as time rate of change of slope, \dot{Z} . The superscripts (r, a) identify the slopes of asperities that resist or assist sliding. Such an approach to modeling friction together with system response simultaneously yields the friction force and system response that affect each other.¹⁵⁸

One missing element in friction models relates to friction at the atomic level, sometimes referred to as microfriction. Presently, efforts to simulate materials at the atomic scale continue, but with a different emphasis than those presented here where the focus is on the oscillatory behavior of atoms.

C. Dissipation and atomic level friction

Friction in its most fundamental form occurs at the atomic level. During friction between two atomically flat surfaces, some of the kinetic energy associated with the relative motion propagates (as phonons) beyond the surfaces into the bodies and dissipates. Dissipation here refers to conversion of kinetic energy to thermal energy. The same phenomenon occurs during passage of a sound wave in a solid when some of its energy converts to thermal energy.

Thermal energy relates to the vibrations of atoms in a solid. In solids atoms are held in equilibrium with respect to each other by means of electrostatic forces or interatomic potentials, often described as bonds between atoms. As external forces such as a sound wave or friction on a surface excite atoms, their energy levels increase as represented by their vibration amplitudes. Models that study thermal energy consider vibrations of atoms in a solid as an idealized lattice which has a periodic structure of identical mass-spring cells. In such a lattice, nonlinear springs link the masses together.

Proposed relationships between the kinetic energy of atoms and temperature in a solid assume that vibrations of atoms are in statistical (or thermal) equilibrium and that energy absorption is irreversible. Investigations of thermalization in a lattice look for conditions leading to energy equipartitioning among its modes of vibration. Studies on deterministic models of lattice dynamics point to chaos, instead of ergodicity as believed earlier, as an indicator of thermalization and the means of energy equipartitioning.

If the lattice does not respond chaotically, energy absorbed by the system remains coherent, and periodically returns to the external source. Thus, chaotic behavior ensures both equipartitioning and irreversibility of energy absorbed by a lattice. Although a model based on first principles that describes the mechanism by which this conversion takes place continues to be a research topic, a one-dimensional array of atoms can help elucidate the behavior of the response of atoms. Considering an array of oscillators connected with identical nonlinear springs with a spring constant

$$K(x) = 2bD[e^{-b(x-a)} - e^{-2b(x-a)}], \quad (24)$$

which can be derived by representing the interatomic potential between atoms by the Morse potential¹⁶¹

$$V(x) = D[e^{-2b(x-a)} - 2e^{-b(x-a)}]. \quad (25)$$

The equations that describe the response of the array can be expressed as

$$m\ddot{x}_i = 2bD[e^{-2b(x_i - x_{i-1} - a)} - e^{-b(x_i - x_{i-1} - a)}] - 2bD[e^{-2b(x_{i+1} - x_i - a)} - e^{-b(x_{i+1} - x_i - a)}], \quad (26)$$

where $i = 1, \dots, n-1$. The equation describing the motion of the atom at its free end is

$$m\ddot{x}_n = 2bD[e^{-2b(x_n - x_{n-1} - a)} - e^{-b(x_n - x_{n-1} - a)}] + A \cos \omega t. \quad (27)$$

Numerically solving these equations allows examination of conditions under which energy becomes thermalized. A detailed explanation of the conditions that lead to dissipation is given in Ref. 162.

VII. FRICTION AND BOUNDARY-LAYER TURBULENCE

The purpose of this section is to describe analogies between solid friction and boundary-layer turbulence. Although friction and boundary-layer turbulence occur in dissimilar continua, they possess notable phenomenological similarities between many of the attributes that describe them. The following analogies assume motion of a solid or a fluid continuum over a semi-infinite solid body (*viz.*, Refs. 163–165).

A. Generation mechanisms

Consider the boundary between the two media having a perfectly flat surface. In a flow over a smooth plane near the leading edge, a laminar boundary layer develops. At higher speeds and large distances downstream, after a region of transition, a turbulent boundary layer fully develops. [Such development depends on the Reynolds number (Re) and the amount of turbulence present in the free stream.] While not commonly addressed, surface friction has a significant role in the development of boundary-layer turbulence, particularly over a perfectly flat surface. An analogous configuration for solids consists of friction between flat surfaces of half-spaces where interface or Stoneley waves develop. In cases of finite-size bodies, the friction force leads to the development of a moment and other types of vibratory behavior as a result of nonuniform contact force distribution.

For rough surfaces, the nature of contact of a fluid flow over a surface differs from that between two solids. In solids, actual contact takes place at the true contact areas, usually between crests of waves or tips of asperities. At the fluid interface, contact develops everywhere. In the case of solids under light loads, stress waves develop locally around the asperities. As long as the contact load stays light, stress distribution is confined to an area near the interface. At higher contact loads, the stress field around each true contact spreads and starts to interact with the stress fields of the other contacts, eventually developing into a full stress field in the body. Because the system is dynamic, these contact stresses lead to waves in the bodies and transport some of the energy away from the contact areas. (In some cases, the response can rigidly move the entire body.)

Fluid flow over a rough surface exhibits an analogous behavior where local pressure fields develop around the protuberances (asperities) on a surface. At low Reynolds numbers, the influence of pressure fields remains local. As Re increases, the pressure field around each asperity spreads and starts to interact with the pressure fields around the others.

In the case of solids, interactions between asperities of opposite surfaces generate waves which then transmit energy into the body of the solids. In the case of a fluid, eddies develop and carry momentum into the free-stream flow. In both cases, the mean motion of the main body of the solid or the fluid may be unaffected by its behavior at the boundary.

B. Analogies

1. Dissipation

Analogous to friction, turbulent flows also have dual roles. Turbulence transmits energy from the flow to the boundary as well as dissipates the kinetic energy of the tur-

bulent flow as viscous shear stresses perform work increasing the internal energy of the fluid. Consequently, turbulence needs a continuous supply of energy to make up for these viscous losses. Without a continuous energy supply, turbulence decays rapidly. As proposed by Kolmogorov, and explained further by Batchelor, any large-scale individual motion in a fluid cannot persist as such indefinitely, but sooner or later breaks down into smaller eddies. However, as the energy progressively passes on to smaller length scales, Re becomes too low to permit the formation of yet smaller eddies. The energy is then directly converted into heat as it is absorbed into the random motion of the molecules by viscosity. In summary, kinetic energy moves from the mean flow into the large, or energy-containing scales, and from them into the next smaller eddies, and so on until it reaches the scales at which dissipation takes place in terms of increased thermal energy. This process is reminiscent of what takes place during solid friction. As discussed in the earlier sections, while friction also has the role of transferring energy from one body to the other, it also dissipates energy. Unless a constant source of energy makes up for the losses, the relative motion will not last.

2. Continuum

The equations of fluid mechanics govern turbulence as a continuum phenomenon. Except in certain circumstances, even the smallest turbulent length scales (the Kolmogorov microscale) are very much larger than molecular scales. Friction, while commonly treated as a continuum concept, also develops at the molecular scale. In this manner, friction differs from the current understanding of boundary layer turbulence and suggests that turbulence may also have molecular scale events, similar to friction.

3. Inertia versus stiffness

Turbulence is an inertial phenomenon. It has statistically indistinguishable characteristics on energy-containing scales in gases, liquids, slurries, foams, and many non-Newtonian media. These media have markedly different fine structures, and their mechanisms for dissipation of energy are quite different. Friction, in contrast, exhibits stiffness characteristics at low velocities and damping at higher velocities, as discussed earlier.

4. Irregularity

Irregularity and randomness that characterize turbulence make deterministic approaches impossible and necessitate statistical methods. As pointed out earlier, due to the computational requirements required for deterministic simulations of friction, statistical approaches are often used to describe such characteristics as surface roughness.

5. Diffusivity

Diffusivity, another important feature of turbulence, causes rapid mixing and increased rates of momentum, heat, and mass transfer. The diffusivity of turbulence prevents boundary-layer separation on airfoils at large angles of attack. It increases heat transfer rates in machinery and the

source of resistance of flow in pipelines. It also increases momentum transfer between winds and ocean waves.

During friction, momentum and heat transfer also take place. Equally important, friction generates heat.

6. Boundary layer turbulence and friction as features of system dynamics

Turbulence originates as an instability of laminar flow as Re becomes large. The instabilities stem from interactions of viscous terms and the nonlinear inertia terms in the equations of motion. Thus, turbulence is a feature not of fluids but of fluid flows. Most of the dynamics of turbulence is common to all fluids if Re of turbulence is large enough. According to current thinking, molecular properties of the fluid in which the turbulence occurs do not control the major characteristics of turbulent flows. Since the equations of motion are nonlinear, each individual flow pattern has certain unique characteristics associated with its initial and boundary conditions.

Analogously, friction is neither a property of a material nor of a surface, but it is a property of a dynamic system. The waves generated at the interface emanate from contact areas into the solid bodies which then change the contact configuration. Their wave numbers range from molecular distance to correlation lengths between material impurities, and to the size of the surface on which friction develops.

VIII. CONCLUDING REMARKS

This paper attempts to bring together acoustics and friction by exposing many of the topics that are common to both fields. When treated as a tangential force acting on a surface, friction becomes the source of all imaginable types of waves within solids, the cause of music or noise, and the source of damping for resonant and unstable vibrations. Conversely, through the use of acoustic perturbations, the influence of friction can be modified, mostly to reduce friction and, when managed, to produce precisely controlled motion. The ultimate intersection of friction and acoustics takes place at the atomic level, where oscillations of atoms provide the mechanism by which the kinetic energy associated with friction converts to thermal energy. This paper excludes many other topics related to the acoustics of friction, such as acoustic emission from contact regions and friction-excited rigid-body behavior. However, the author hopes that this review adequately covers the most common aspects of acoustics and friction, and reaffirms that, like many other dynamic phenomena, even friction down to the atomic level has its foundation in acoustics.

ACKNOWLEDGMENTS

The author gratefully acknowledges the work of his current and former students. Particular acknowledgement goes to Mr. Zhaoshun Xu for his contributions to our discoveries over the years. Special thanks go to the sponsors of the re-

search, among which The National Science Foundation, AlliedSignal, and Chrysler are prominent. The author expresses his appreciation to Professor Allan Pierce for his encouragement to develop this paper for the Journal.

- ¹ J. Tyndall, *Sound* (Appleton, New York, 1903) or (Greenwood Press, Westport, CT, 1970).
- ² M. T. Bengisu and A. Akay, "Stability of friction-induced vibrations in multi-degree-of-freedom systems," *J. Sound Vib.* **171**, 557–570 (1994).
- ³ J. W. S. Rayleigh, *The Theory of Sound*, 2nd ed. (Dover, New York, 1894).
- ⁴ R. T. Spurr, "The ringing of wine glasses," *Wear* **4**, 150–153 (1961).
- ⁵ A. P. French, "In vino veritas: A study of wineglass acoustics," *Am. J. Phys.* **51**, No. 8, 688–694 (1983).
- ⁶ G. Galileo, *Dialogues Concerning Two New Sciences*, translated by H. Crew and A. DeSalvo (Northwestern University Press, Chicago, 1946).
- ⁷ B. Feeny, A. Guran, N. Hinrichs, and K. Popp, "A historical review on dry friction and stick-slip phenomena," *Appl. Mech. Rev.* **51**, 321–341 (1998).
- ⁸ E. F. F. Chladni, *Entdeckungen über die Theorie des Klanges* (Breitkopf und Härtel, Leipzig, 1787).
- ⁹ E. F. F. Chladni, *Die Akustik* (Breitkopf und Härtel, Leipzig, 1802 and 1830).
- ¹⁰ J. Swayze and A. Akay, "Effects of system dynamics on friction-induced oscillations," *J. Sound Vib.* **173**, 599–610 (1994).
- ¹¹ E. J. Berger, C. M. Krousgrill, and F. Sadeghi, "Stability of sliding in a system excited by a rough moving surface," *J. Tribol.* **119**, 673–680 (1997).
- ¹² Y.-B. Yi, S. Du, J. R. Barber, and J. W. Fash, "Effect of geometry on thermoelastic instability in disk brakes and clutches," *J. Tribol.* **121**, 661–666 (1999).
- ¹³ K. Lee, "Frictionally excited thermoelastic instability in automotive drum brakes," *J. Tribol.* **122**, 849–855 (2000).
- ¹⁴ S. Y. Liu, J. T. Gordon, and M. A. Ozbek, "Nonlinear model for aircraft brake-squeal analysis: Model description and solution methodology," *J. Aircr.* **35**, 623–630 (1998).
- ¹⁵ J. T. Gordon, S. Y. Liu, and M. A. Ozbek, "Nonlinear model for aircraft brake squeal analysis: Stability analysis and parametric studies," *J. Aircr.* **35**, 631–636 (1998).
- ¹⁶ J. E. Mottershead, "Vibration- and friction-induced instability in disks," *Shock Vib. Dig.* **30**, 14–31 (1998).
- ¹⁷ J. E. Mottershead and S. N. Chan, "Flutter instability of circular discs with frictional follower loads," *J. Vibr. Acoust.* **117**, 161–163 (1995).
- ¹⁸ H. Ouyang, J. E. Mottershead, M. P. Cartmell, and M. I. Friswell, "Friction-induced parametric resonances in discs: Effect of a negative friction-velocity relationship," *J. Sound Vib.* **209**, 251–264 (1998).
- ¹⁹ H. Ouyang, J. E. Mottershead, M. P. Cartmell, and D. J. Brookfield, "Friction-induced vibration of an elastic slider on a vibrating disc," *Int. J. Mech. Sci.* **41**, 325–336 (1999).
- ²⁰ S. N. Chan, J. E. Mottershead, and M. P. Cartmell, "Parametric resonances at subcritical speeds in discs with rotating frictional loads," *Proc. Inst. Mech. Engrs. Part C (J. Mech. Eng. Sci.)* **208**, 417–425 (1994).
- ²¹ H. Ouyang, J. E. Mottershead, D. J. Brookfield, S. James, and M. P. Cartmell, "A methodology for the determination of dynamic instabilities in a car disc brake," *Int. J. Veh. Des.* **23**, 241–262 (2000).
- ²² H. Ouyang, S. N. Chan, J. E. Mottershead, M. I. Friswell, and M. P. Cartmell, "Parametric vibrations in discs: Point-wise and distributed loads, including rotating friction," *Des. Eng. Tech. Conf., Part A, DE-Vol 84-1 (3-A)*, 1125–1133 (1995).
- ²³ J. S. Chen and D. B. Bogy, "Effects of load parameters on the natural frequencies and stability of a flexible spinning disk with a stationary load system," *J. Appl. Mech.* **59**, 5230–5235 (1992).
- ²⁴ D. Lee and A. M. Waas, "Stability analysis of a rotating multi-layer annular plate with a stationary frictional follower load," *Int. J. Mech. Sci.* **39**, 1117–1138 (1997).
- ²⁵ K. I. Tzou, J. A. Wickert, and A. Akay, "In-plane vibration modes of arbitrarily thick disks," *J. Vibr. Acoust.* **120**, 384–391 (1998).
- ²⁶ K. I. Tzou, J. A. Wickert, and A. Akay, "Frequency clusters in the spectrum of annular cylinders," *J. Appl. Mech.* **65**, 797–803 (1998).
- ²⁷ Y. Gui-Lan and W. Yue-Sheng, "In-plane motion induced by an SH pulse at a frictional contact surface," *Mech. Res. Commun.* **25**, 203–210 (1998).
- ²⁸ M. Matsuzaki and T. Izumihara, "Brake noise caused by longitudinal vibration of the disc rotor," *SAE Paper 930804* (1993).
- ²⁹ V. Aronov, A. F. D'Souza, S. Kalpakjian, and I. Shareef, "Interactions among frictions, wear and system stiffness, Part 1: Effect of normal load and system stiffness," *J. Tribol.* **106**, 55–58 (1984).
- ³⁰ V. Aronov, A. F. D'Souza, S. Kalpakjian, and I. Shareef, "Interactions among frictions, wear, and system stiffness, Part 2: Vibrations induced by dry friction," *J. Tribol.* **106**, 59–64 (1984).
- ³¹ V. Aronov, A. F. D'Souza, S. Kalpakjian, and I. Shareef, "Interactions among frictions, wear, and system stiffness, Part 3: Wear model," *J. Tribol.* **106**, 65–69 (1984).
- ³² N. Hinrichs, M. Oestreich, and K. Popp, "On the modeling of friction oscillators," *J. Sound Vib.* **216**, 435–459 (1998).
- ³³ B. Feeny and F. C. Moon, "Chaos in a forced dry-friction oscillator: Experiments and numerical modelling," *J. Sound Vib.* **170**, 303–323 (1994).
- ³⁴ A. Sueoka, Y. Yoshitake, H. Tamura, and K. Horita, "Self-excited vibration of a circular plate subjected to frictional forces exerted in two regions on its outer circumference. Part I. The case of a circular plate without effect of internal resonances," *Bull. JSME* **29**, No. 255, 3019–3057 (1986).
- ³⁵ A. Sueoka, Y. Yoshitake, H. Tamura, and K. Horita, "Self-excited vibration of a circular plate subjected to frictional forces exerted in two regions on its outer circumference. Part II. The case of a circular plate with effect of internal resonances," *Bull. JSME* **29**, No. 255, 3058–3065 (1986).
- ³⁶ M. Yokoi and M. Nakai, "A fundamental study on frictional noise, 1st report: The generating mechanism of rubbing noise and squeal noise," *Bull. JSME* **22**, No. 173, 1665–1671 (1979).
- ³⁷ M. Yokoi and M. Nakai, "A fundamental study on frictional noise, 2nd report: The generating mechanism of squeal noise of higher modes," *Bull. JSME* **23**, No. 186, 2118–2124 (1980).
- ³⁸ M. Yokoi and M. Nakai, "A fundamental study on frictional noise, 3rd report: The influence of periodic surface roughness on frictional noise," *Bull. JSME* **24**, No. 194, 1470–1476 (1981).
- ³⁹ M. Yokoi and M. Nakai, "A fundamental study on frictional noise, 4th report: The influence of angle of inclination of the rod on frictional noise," *Bull. JSME* **24**, No. 194, 1477–1483 (1981).
- ⁴⁰ M. Yokoi and M. Nakai, "A fundamental study on frictional noise, 5th report: The influence of random surface roughness on frictional noise," *Bull. JSME* **25**, No. 203, 827–833 (1982).
- ⁴¹ C. H. Wang and A. Soom, "Interpretation of rubbing noise radiated from a pin-on-disc configuration," *ASME 83-WA-NCA-41-6* (1983).
- ⁴² F. Bergman, M. Eriksson, and S. Jacobson, "Influence of disk topography on generation of brake squeal," *Wear* **225–229**, 621–628 (1999).
- ⁴³ T. Ananthapadmanaban and V. Radhakrishnan, "An investigation of the role of surface irregularities in the noise spectrum of rolling and sliding contacts," *Wear* **83**, 399–409 (1982).
- ⁴⁴ V. M. Baranov, E. M. Kuddryavtsev, and G. A. Sarychev, "Modeling of the parameters of acoustic emission under sliding friction of solids," *Wear* **202**, 125–133 (1997).
- ⁴⁵ C. H. Ellen, C. V. Tu, and W. Y. D. Yuen, "Thermally induced roof noise," *J. Appl. Mech.* **52**, 494–496 (1985).
- ⁴⁶ C. H. Ellen, C. V. Tu, and W. Y. D. Yuen, "Theory for thermally induced roof noise," *J. Struct. Eng.* **111**, 2302–2319 (1985).
- ⁴⁷ M. Nakai, M. Yokoi, M. Inue, and K. Kawakami, "Squealing of cylindrical roller bearing," *JSME Int. J.* **34**, 72–81 (1991).
- ⁴⁸ D. G. Evseev, B. M. Medvedev, G. G. Grigoryan, and O. A. Ermolin, "Description of the rolling friction process by acoustic modeling," *Wear* **167**, 33–40 (1993).
- ⁴⁹ A. I. Krauter, "Generation of squeal/chatter in water-lubricated elastomeric bearings," *J. Lubr. Technol.* **103**, 406–413 (1981).
- ⁵⁰ B. Bhushan, "Stick-slip induced noise generation in water-lubricated compliant rubber bearings," *J. Lubr. Technol.* **102**, 201–212 (1980).
- ⁵¹ S. M. A. Aziz and A. Seireg, "A parametric study of frictional noise in gears," *Wear* **176**, 25–28 (1994).
- ⁵² H. Tokoro, M. Nakamura, N. Sugiura, H. Tani, K. Yamamoto, and T. Shuku, "Analysis of high frequency noise in engine timing belt," *JSAE Paper 9830037* (1998).
- ⁵³ M. Nakai, and M. Yokoi, "Band brake squeal," *J. Vibr. Acoust.* **118**, 190–197 (1996).
- ⁵⁴ M. Oya, T. Masamura, S. Hattori, and T. Ohoki, "Squealing of band brake for bicycle," *Trans. Jpn. Soc. Mech. Eng. (Preprint)*, no. 780-14, 151–153 (1978).
- ⁵⁵ G. G. Adams, "Self-excited oscillations of two elastic half-spaces sliding

- with a constant coefficient of friction," *J. Appl. Mech.* **62**, 867–872 (1995).
- ⁵⁶G. G. Adams, "Self-excited oscillations in sliding with a constant friction coefficient—A simple model," *J. Tribol.* **118**, 819–823 (1996).
- ⁵⁷G. G. Adams, "Dynamic instabilities in the sliding of two layered elastic half-spaces," *J. Tribol.* **120**, 289–295 (1998).
- ⁵⁸G. G. Adams, "Steady sliding of two elastic half-spaces with friction reduction due to interface stick-slip," *J. Appl. Mech.* **65**, 470–475 (1998).
- ⁵⁹G. G. Adams, "Self-excited oscillations in sliding with a constant friction coefficient," *ASME Des. Eng. Tech. Conf., Part A, DE-Vol 84-1*, 3, 1171–1177 (1995).
- ⁶⁰L. Johansson, "Model and numerical algorithm for sliding contact between two elastic half-planes with frictional heat generation and wear," *Wear* **160**, 77–93 (1993).
- ⁶¹J. R. Rice and A. L. Ruina, "Stability of steady frictional slipping," *J. Appl. Mech.* **50**, 343–349 (1983).
- ⁶²G. Weinreich, "What science knows about violins—And what it does not know," *Am. J. Phys.* **61**, 1067–1077 (1993).
- ⁶³H. v. Helmholtz, *On the Sensations of Tone* (Dover, New York, 1954) (English translation of the German edition, 1877).
- ⁶⁴*Scientific Papers of C. V. Raman: Acoustics*, edited by S. Ramaseshan (Oxford University Press, Oxford, 1989).
- ⁶⁵J. C. Schelleng, "The violin as a circuit," *J. Acoust. Soc. Am.* **35**, 326–338 (1963).
- ⁶⁶C. V. Raman, "On the 'wolf-note' in bowed stringed instruments," *Philos. Mag.* **32**, 391–395 (1916).
- ⁶⁷M. E. McIntyre and J. Woodhouse, "The acoustics of stringed musical instruments," *Interdisciplinary Sci. Rev.* **3**, 157–173 (1978).
- ⁶⁸J. Woodhouse, "On the playability of violins, Part I: Reflection functions," *Acustica* **78**, 125–136 (1993).
- ⁶⁹J. Woodhouse, "On the playability of violins, Part II: Minimum bow force and transients," *Acustica* **78**, 137–153 (1993).
- ⁷⁰M. E. McIntyre, R. T. Schumacher, and J. Woodhouse, "On the oscillations of musical instruments," *J. Acoust. Soc. Am.* **74**, 1325–1345 (1983).
- ⁷¹M. E. McIntyre and J. Woodhouse, "On the fundamentals of bowed-string dynamics," *Acustica* **43**, No. 2, 93–108 (1979).
- ⁷²M. E. McIntyre, "Aperiodicity in bowed-string motion," *Acustica* **50**, 294–295 (1982).
- ⁷³M. E. McIntyre, R. T. Schumacher, and J. Woodhouse, "Aperiodicity in bowed-string motion," *Acustica* **49**, 13–32 (1981).
- ⁷⁴R. T. Schumacher, "Self-sustained oscillations of the bowed string," *Acustica* **43**, 109–120 (1979).
- ⁷⁵G. Weinreich and R. Caussé, "Elementary stability considerations for bowed-string motion," *J. Acoust. Soc. Am.* **89**, 887–895 (1991).
- ⁷⁶J. Woodhouse, R. T. Schumacher, and S. Garoff, "Reconstruction of bowing point friction force in a bowed string," *J. Acoust. Soc. Am.* **108**, 357–368 (2000).
- ⁷⁷G. Essl and P. R. Cook, "Measurements and efficient simulations of bowed bars," *J. Acoust. Soc. Am.* **108**, 379–388 (2000).
- ⁷⁸L. Cremer, *The Physics of the Violin* (MIT Press, Cambridge, 1984).
- ⁷⁹C. M. Hutchins and V. Benade, *Research Papers in Violin Acoustics 1975–1993* (ASA, New York, 1997), Vols. I and II.
- ⁸⁰A. J. Day and T. P. Newcomb, "The dissipation of friction energy from the interface of annular disc brake," *Proc. Inst. Mech. Eng., Part D (J. Automob. Eng.)* **198D**, No. 11, 201–209 (1984).
- ⁸¹M. Nishiwaki, "Generalized theory of brake noise," *Proc. Inst. Mech. Eng. Part D (J. Automob. Eng.)* **207**, 195–202 (1993).
- ⁸²M. Nishiwaki, "Review of study on brake squeal," *Jap. Soc. Automob. Eng. Rev.* **11(4)**, 48–54 (1990).
- ⁸³A. M. Lang and H. Smales, "An approach to the solution of disc brake vibration problems," *IMEChE Paper C37/83*, 223–230 (1983).
- ⁸⁴P. J. Remington, "Wheel/rail squeal and impact noise: What do we know? What don't we know? Where do we go from here?," *J. Sound Vib.* **116**, 339–353 (1987).
- ⁸⁵P. J. Remington and J. D. Stahr, "The effects on noise of changes in wheel/rail system parameters," *J. Sound Vib.* **87**, 221–229 (1983).
- ⁸⁶M. Nakai and M. Yokoi, "Railway wheel squeal—3rd report: Squeal of a disk simulating a wheel in internal resonances," *Bull. JSME* **28**, 500–507 (1985).
- ⁸⁷M. Nakai and S. Akiyama, "Railway wheel squeal (squeal of disk subjected to random excitation)," *JSME Int. J., Ser. C* **41(3)**, 608–615 (1998).
- ⁸⁸M. Nakai, M. Yokoi, and M. Sugiura, "Railway wheel squeal (squeal of a rotating disk)," *JSME Int. J., Ser. III* **32**, No. 3, 406–412 (1989).
- ⁸⁹J. T. Gordon, "A perturbation analysis of nonlinear squeal vibrations in aircraft braking systems," *Proc. ASME Des. Eng. Tech. Conf., DETC97/VIB-4163* (1997).
- ⁹⁰M. A. Ozbek, S. Y. Liu, J. T. Gordon, and D. S. Newman, "Chaotic vibration in aircraft braking systems," *Proc. ASME Des. Eng. Tech. Conf., Part A, DE-Vol84-1* 3, 1233–1240 (1995).
- ⁹¹D. J. Feld and D. J. Fehr, "Complex eigenvalue analysis applied to an aircraft brake vibration problem," *ASME Des. Eng. Tech. Conf., Part A, DE-Vol 84-1*, 3:1135–1142 (1995).
- ⁹²M. H. Travis, "Nonlinear transient analysis of aircraft landing gear brake whirl and squeal," *ASME Des. Eng. Tech. Conf., Part A, DE-Vol. 84-1*, 3, 1209–1216 (1995).
- ⁹³I. Kido, T. Kurahachi, and M. Asai, "A study on low-frequency brake squeal noise," *SAE Paper 960993* (1996).
- ⁹⁴M. Gouya and M. Nishiwaki, "Study on disc brake groan," *SAE Trans. Paper 900007* (1990).
- ⁹⁵T. K. Kao, J. W. Richmond, and M. W. Moore, "The application of predictive techniques to study thermo elastic instability of braking," *SAE Paper 942087* (1994).
- ⁹⁶J. A. Wickert and A. Akay, "Damper for Brake Noise Reduction," U.S. Patent No. 5,855,257 (1999), and "Damper for Brake Noise Reduction (brake drums)," U.S. Patent No. 6,112,865 (2000).
- ⁹⁷P. T. Haskell, *Insect Sounds* (Witherby, London, 1961).
- ⁹⁸R.-G. Busnell, *Acoustic Behavior of Animals* (Elsevier, New York, 1963).
- ⁹⁹R. Hickling and R. L. Brown, "Analysis of acoustic communication by ants," *J. Acoust. Soc. Am.* **108**, 1920–1929 (2000).
- ¹⁰⁰S. N. Patek, "Spiny lobsters stick and slip to make sound," *Nature (London)* **411**, 153–154 (2000).
- ¹⁰¹R. M. Nedderman and G. H. L. Harding, "The flight-free vibrating conveyor: Part I. Basic theory and performance analysis," *Trans. Inst. Chem. Eng., Part A* **68**, 123–130 (1990).
- ¹⁰²G. H. L. Harding and R. M. Nedderman, "The flight-free vibrating conveyor: Part II. Stability analysis and criteria for optimal design," *Trans. Inst. Chem. Eng., Part A* **68**, 131–138 (1990).
- ¹⁰³Y. Hashimoto, Y. Koiki, and S. Ueha, "Transporting objects without contact using flexural traveling waves," *J. Acoust. Soc. Am.* **103**, 3230–3233 (1998).
- ¹⁰⁴P. Vielsack and H. Spiess, "Sliding of a mass on an inclined driven plan with randomly varying coefficient of friction," *J. Appl. Mech.* **67**, 112–116 (2000).
- ¹⁰⁵E. C. Miranda and J. J. Thomsen, "Vibration induced sliding: Theory and experiment for a beam with a spring-loaded mass," *Nonlinear Dyn.* **16**, 167–186 (1998).
- ¹⁰⁶Y. G. Long, K. Nagaya, and H. Niwa, "Vibration conveyance in spatial-curved tubes," *J. Vib. Acoust.* **116**, 38–46 (1994).
- ¹⁰⁷T. Sashida and T. Kenjo, *An Introduction to Ultrasonic Motors* (Clarendon, Oxford, 1993).
- ¹⁰⁸P. Hagedorn and J. Wallashek, "Travelling wave ultrasonic motors. Part I. Working principle and mathematical modeling of the stator," *J. Sound Vib.* **155**, 31–46 (1992).
- ¹⁰⁹J. Wallashek, P. Hagedorn, and W. Konrad, "Travelling wave ultrasonic motors. Part II. A numerical method for the flexural vibrations of the stator," *J. Sound Vib.* **168**, 115–122 (1993).
- ¹¹⁰K. Adachi, K. Kato, and Y. Sasatani, "The micro-mechanism of friction drive with ultrasonic wave," *Wear* **194**, 137–142 (1996).
- ¹¹¹S. Ueha and Y. Tomikawa, *Ultrasonic Motors—Theory and Applications* (Clarendon, Oxford, 1993).
- ¹¹²T. Sashida, "Motor device utilizing ultrasonic oscillation," U.S. Patent No. 4,562,374.
- ¹¹³A. Kumada, "Piezoelectric revolving resonator and ultrasonic motor," U.S. Patent No. 4,868,446 (1989).
- ¹¹⁴T. Nakashima, M. Yishizawa, H. Kuno, M. Tsukui, K. Takatsuka, and T. Akuto, "Driving characteristics of traveling wave ultrasonic motor (Effect of rotor vibration)," *Proc. ASME Design Eng. Tech. Conf., Pittsburgh, PA*, 9–12 September 2001. DETC2001/VIB-21653.
- ¹¹⁵A. Kumada, T. Iochi, and M. Okada, "Piezoelectric revolving resonator and single-phase ultrasonic motor," U.S. Patent No. 5,008,581 (1991).
- ¹¹⁶H. M. Jaeger and S. R. Nagel, "Physics of the granular state," *Science* **255**, 1523–1531 (1992).
- ¹¹⁷H. M. Jaeger and S. R. Nagel, "Dynamics of granular material," *Am. Sci.* **85**, 540–545 (1997).

- ¹¹⁸H. M. Jaeger, S. R. Nagel, and R. P. Behringer, "The physics of granular materials," *Phys. Today* **49**(4), 32–38 (1996).
- ¹¹⁹J. B. Knight, H. M. Jaeger, and S. R. Nagel, "Vibration-induced size separation in granular media: The convection connection," *Phys. Rev. Lett.* **70**, No. 24, 3728–3731 (1993).
- ¹²⁰J. M. Montanero, V. Garzo, A. Santos, and J. J. Brey, "Kinetic theory of simple granular shear flows of smooth hard spheres," *J. Fluid Mech.* **389**, 391–411 (1999).
- ¹²¹I. Peterson, "Dry sand, wet sand—digging into the physics of sandpiles and sand castles," *Sci. News* (Washington, D. C.) **152**, 186–187 (1997).
- ¹²²P. Evesque and J. Rajchenbach, "Instability in a sand heap," *Phys. Rev. Lett.* **62**, No. 1, 44–46 (1989).
- ¹²³A. Rosato, K. J. Strandburg, F. Prinz, and R. H. Swendsen, "Why the Brazil nuts are on top: Size segregation of particulate matter by shaking," *Phys. Rev. Lett.* **58**, No. 10, 1038–1040 (1987).
- ¹²⁴R. I. Zadoks and X. Yu, "An investigation of the self-loosening behaviour of bolts under transverse vibration," *J. Sound Vib.* **208**, 189–209 (1997).
- ¹²⁵D. P. Hess and K. Davis, "Threaded components under axial harmonic vibration. Part I. Experiments," *J. Vibr. Acoust.* **118**, 417–429 (1996).
- ¹²⁶D. P. Hess, "Vibration-induced loosening and tightening of threaded fasteners," *Des. Eng. Tech. Conf., Part A, DE-Vol 84-1, 3*, 1165–1170 (1995).
- ¹²⁷S. Thomas, "Vibrations damped by solid friction," *Philos. Mag.* **9**, 329 (1930).
- ¹²⁸J. H. Griffin, "Friction damping of resonant stresses in gas turbine engine airfoils," *J. Eng. Power* **102**, 329–333 (1980).
- ¹²⁹C. H. Menq and J. H. Griffin, "A comparison of transient and steady state finite element analyses of the forced response of a frictionally damped beam," *J. Vib., Acoust., Stress, Reliability Design* **107**, 19–25 (1985).
- ¹³⁰A. Sinha and J. H. Griffin, "Effects of static friction on the forced response of frictionally damped turbine blades," *J. Eng. Power* **106**, 65–69 (1984).
- ¹³¹L. Gaul and J. Lenz, "Nonlinear dynamics of structures assembled by bolted joints," *Acta Mech.* **125**, 169–181 (1997).
- ¹³²M. Groper, "Microslip and macroslip in bolted joints," *Exp. Mech.* **42**, 171–174 (1985).
- ¹³³P. R. Dahl, "Solid friction damping of mechanical vibrations," *AIAA J.* **14**, 1675–1682 (1976).
- ¹³⁴K. Yamanaka, T. Kakubari, A. Yamada, and M. Kano, "Study on the dynamic characteristic of a contact surface (the logarithmic decrement and natural frequency dependent on an amplitude of vibration)," *No.* 85-194A.
- ¹³⁵W. Sextro, "The calculation of the forced response of shrouded blades with friction contacts and its experimental verification," *Proceedings of the International Gas Turbine & Aeroengine Congress, Munich (2000-GT-540)* (2000).
- ¹³⁶T. Berruti, S. Filippi, M. M. Gola, and S. Salvano, "Friction damping of interlocked vane segments: Experimental results," *Proceedings of the International Gas Turbine & Aeroengine Congress, Munich, 2001-GT-0432* (2001).
- ¹³⁷E. H. Dowell, "Damping in beams and plates due to slipping at the support boundaries," *J. Sound Vib.* **105**, 243–253 (1986).
- ¹³⁸D. M. Tang and E. H. Dowell, "Damping in beams and plates due to slipping at the support boundaries. Part 2: Numerical and experimental study," *J. Sound Vib.* **108**, 509–522 (1986).
- ¹³⁹E. H. Dowell and H. B. Schwartz, "Forced response of a cantilever beam with a dry friction damper attached. Part I: Theory," *J. Sound Vib.* **91**, 255–267 (1983).
- ¹⁴⁰E. H. Dowell and H. B. Schwartz, "Forced response of a cantilever beam with a dry friction damper attached. Part II: Experiment," *J. Sound Vib.* **91**, 269–291 (1983).
- ¹⁴¹A. A. Ferri, "Friction damping and isolation systems," *J. Vibr. Acoust.* **117**, 196–206 (1995).
- ¹⁴²W. E. Whiteman and A. A. Ferri, "Displacement-dependent dry friction damping of a beam-like structure," *J. Sound Vib.* **198**, 313–329 (1996).
- ¹⁴³W. E. Whiteman and A. A. Ferri, "Displacement-dependent dry friction damping of a beam-like structure," *J. Sound Vib.* **207**, 403–418 (1997).
- ¹⁴⁴K. Y. Sanliturk and D. J. Ewins, "Modeling two-dimensional friction contact and its application using harmonic balance method," *J. Sound Vib.* **193**, 511–523 (1996).
- ¹⁴⁵N. Popplewell and S. E. Semercigil, "Performance of the bean bag impact damper for a sinusoidal external force," *J. Sound Vib.* **133**, 193–223 (1989).
- ¹⁴⁶D. Warwick and D. Feit, "An evaluation of polyethylene beads as a damping treatment for tubular truss structures," *Carderock Division Naval Surface Warfare Center, CDNSWC-SIG-94-146-7250*, October 1994.
- ¹⁴⁷J. R. Fricke, "Lodengraf damping—An advanced vibration damping technology," *Sound Vib.* **34**, 22–27 (July 2000).
- ¹⁴⁸G. Tomlinson, "Recent developments in particle dampers," *Proceedings of the 6th National Turbine Engine High Cycle Fatigue Conference* (Jacksonville, FL, 5–8 March 2001).
- ¹⁴⁹J. N. Macduff and J. R. Curreri, *Vibration Control* (McGraw-Hill, New York, 1958).
- ¹⁵⁰S. R. Nagel and H. M. Jaeger, "Sound propagation in sand," *Echoes* **8**, No. 3, 1, 4 (1998).
- ¹⁵¹J. P. Den Hartog, *Mechanical Vibrations*, 3rd ed. (McGraw-Hill, New York, 1947).
- ¹⁵²C. E. Celik, "Modeling and Identification of Friction in Dynamic Systems," Ph.D. thesis, Carnegie Mellon University (2000).
- ¹⁵³J. T. Oden and J. A. C. Martins, "Models and computational methods for dynamic friction phenomena," *Comput. Methods Appl. Mech. Eng.* **52**, 527–634 (1985).
- ¹⁵⁴J. A. C. Martins, J. T. Oden, and F. F. Simões, "A study of static and kinetic friction," *Int. J. Eng. Sci.* **28**, 29–92 (1990).
- ¹⁵⁵Y. Karpenko and A. Akay, "A numerical model of friction between rough surfaces," *Tribol. Int.* **34**, 531–545 (2001).
- ¹⁵⁶Y. Karpenko and A. Akay, "A numerical method for analysis of extended rough wavy surfaces in contact," *J. Tribol.* (July 2002).
- ¹⁵⁷M. T. Bengisu and A. Akay, "Relation of dry-friction to surface roughness," *J. Tribol.* **119**, 18–25 (1997).
- ¹⁵⁸M. T. Bengisu and A. Akay, "Stick–slip oscillations: Dynamics of friction and surface roughness," *J. Acoust. Soc. Am.* **105**, 194–205 (1999).
- ¹⁵⁹A. Soom and C. Kim, "Interactions between dynamic normal and frictional forces during unlubricated sliding," *J. Lubr. Technol.* **105**, 221–229 (1983).
- ¹⁶⁰P. E. Dupont and P. S. Kasturi, "Experimental investigation of friction dynamics associated with normal load," *Des. Eng. Tech. Conf., Part A, DE-Vol 84-1 3:1109–1115*, 1995.
- ¹⁶¹K. U. Ingard, *Fundamentals of Waves and Oscillations* (Cambridge University Press, New York, 1993).
- ¹⁶²C. E. Celik and A. Akay, "Dissipation in solids: Thermal oscillations of atoms," *J. Acoust. Soc. Am.* **108**, 184–191 (2000).
- ¹⁶³U. Frisch, *Turbulence* (Cambridge University Press, Cambridge, 1995).
- ¹⁶⁴P. Holmes, J. L. Lumley, and G. Berkooz, *Turbulence, Coherent Structures, Dynamical Systems and Symmetry* (Cambridge University Press, Cambridge, 1996).
- ¹⁶⁵M. T. Landahl and E. Mollo-Christensen, *Turbulence and Random Processes in Fluid Mechanics* (Cambridge University Press, Cambridge, 1986).

Incorporating linear viscoelasticity into acoustic scattering theory (L)

Alexander K. Hipp^{a)}, Laurent P. Adjadj, Giuseppe Storti, and Massimo Morbidelli^{b)}
ETH Zürich, Department of Chemical Engineering (LTC), HCI, CH-8093 Zürich, Switzerland

(Received 20 August 2001; revised 18 December 2001; accepted 7 January 2002)

The scattering theory of Epstein and Carhart [J. Acoust. Soc. Am. **25**, 553–565 (1953)] and Allegra and Hawley [J. Acoust. Soc. Am. **51**, 1545–1564 (1972)] is a well-established approach for the prediction of the acoustic attenuation and sound speed in suspensions and emulsions. The original theory assumes that each phase is either an elastic solid or a Newtonian liquid; incorporation of other rheological behavior generally requires rederivation of the model equations. An exception is the case of linear viscoelasticity: using a suitable stress–strain relation, the original model equations also hold for this case. In this work, it is shown that $\bar{G}^* = G' - iG''$, where G' and G'' are the storage and loss moduli of a viscoelastic material, is analogous to the shear modulus G (elastic solids) and $-i\omega\eta$ (Newtonian liquids). Viscoelasticity can thus be introduced simply by using \bar{G}^* in place of G . © 2002 Acoustical Society of America. [DOI: 10.1121/1.1455022]

PACS numbers: 43.20.Hq, 43.20.Bi, 43.35.Mr [MO]

I. INTRODUCTION

Ultrasonic techniques are becoming increasingly popular for the analysis of disperse systems, for example as a means for the on-line monitoring of the dispersed-phase volume fraction and particle size.¹ Typically, such measurements rely on a mathematical model which enables one to translate between the acoustic signal, for example, an attenuation spectrum, and the properties of interest.

A popular model for this purpose is that of Epstein and Carhart² and Allegra and Hawley,³ often referred to as “ECAH model.” This is a comprehensive model based on the conservation of mass, momentum, and energy, which are used to derive a set of wave equations. By means of appropriate boundary conditions, this framework can be used to describe a single particle in a continuous medium. The ECAH model involves only a small number of assumptions, notably harmonic oscillations, a linear stress–strain relation, and Fourier’s law for the heat conduction, which makes this model applicable to a wide range of particle sizes and material types.

A limiting factor with respect to the allowable types of dispersions may be the description of the rheological material properties. When the model was first introduced in 1953, Epstein and Carhart² restricted themselves to Newtonian liquids. Almost 20 years later, Allegra and Hawley^{3,4} extended the original concept to elastic solids. Based on the assumption that the time dependence of all involved dynamic variables is described by $e^{-i\omega t}$, where i is the imaginary unit and ω the angular frequency ($2\pi f$), Allegra and Hawley derived a unified stress–strain relation for both solids and liquids:^{4,5}

$$\tau_{ij} = p \delta_{ij} - 2\mu \left[\gamma_{ij} - \frac{1}{3} \delta_{ij} \varepsilon_v \right]. \quad (1)$$

This equation gives the overall stress tensor τ_{ij} including the portion due to the hydrodynamic pressure p ; δ_{ij} is the Kro-

necker delta. The symbols γ_{ij} and ε_v are detailed below. Allegra and Hawley showed that in the case of harmonic oscillations, this relation represents elastic solids as well as Newtonian liquids, simply by attributing a different meaning to μ :

elastic solids: $\mu = G$ where G is the shear modulus (2a)

Newtonian liquids: $\mu = -i\omega\eta$ where η is the shear viscosity. (2b)

In Eq. (1), γ_{ij} stands for the strain tensor, a geometrical quantity giving the j -directed strain in the i -plane (corresponding to S'_{ij} in Ref. 4). In Cartesian coordinates, it is equal to $\gamma_{ij} = 1/2 [\partial\xi_i/\partial x_j + \partial\xi_j/\partial x_i]$, where ξ_i is the displacement in the i direction at a given position [$x_1 \ x_2 \ x_3$]. Expressions in other coordinate systems are available in the literature. The volume expansion ε_v is a related quantity, $\varepsilon_v = \nabla \cdot \xi$, that is, ε_v is equal to the divergence of the displacement field ξ .

By utilizing an identical type of stress tensor for elastic solids and Newtonian liquids, Allegra and Hawley were able to derive a single set of model equations for both types of materials, and to thus create a unified modeling concept. The purpose of this work is to point out that the applicability of this concept spans any material behavior which can be expressed in the form of Eq. (1). The example addressed here is linear viscoelasticity.

II. LINEAR VISCOELASTICITY

In general, a change of the basic rheological behavior requires rederivation of the model equations of the ECAH theory. This approach was followed by Verdier and Piau,⁶ who were the first to incorporate a linear viscoelastic stress–

^{a)}Current address: Dow Europe, CH-8810 Horgen (Zurich), Switzerland.

^{b)}Author to whom correspondence should be addressed.

strain relation into this theory. This resulted in a similar but different set of model equations compared to the original ones. However, by a sensible choice of stress–strain relation, it is possible to incorporate linear viscoelastic behavior into the ECAH framework *without rederivation* of the model equations, therefore taking advantage of the original solution of Epstein, Carhart, Allegra, and Hawley. The starting point is the following general stress–strain relation:⁷

$$\tau_{ij}(t) = -\delta_{ij} \int_{-\infty}^t \left[B^t(t-t') - \frac{2}{3} G^t(t-t') \right] \dot{\varepsilon}_v(t') dt' - 2 \int_{-\infty}^t G^t(t-t') \dot{\gamma}_{ij}(t') dt'. \quad (3)$$

The hydrostatic pressure can be obtained from the stress tensor for the case of pure isotropic compression (no shearing mode, $G^t=0$):⁷

$$p(t) = \frac{1}{3} \text{trace} \tau_{ij}(t) \Big|_{G^t=0} = - \int_{-\infty}^t B^t(t-t') \dot{\varepsilon}_v(t') dt'. \quad (4)$$

In these equations, $B^t(s)$ and $G^t(s)$ are the real, time-dependent (indicated by the superscript t) bulk and shear relaxation moduli. By integrating the products of these moduli and the deformation rates ($\dot{\varepsilon}_v, \dot{\gamma}_{ij}$) over time, the history of deformation is incorporated: $B^t(0)$ and $G^t(0)$ are used to weigh the current deformation rates, while $B^t(s)$ and $G^t(s)$ are used to weigh the rates which were present s seconds in the past. If B^t and G^t are constant, all events are weighted equally, and viscoelastic relaxation is absent. In this case, ideal elastic behavior is recovered [Eqs. (1) and (2a); using $\varepsilon_v = \int \dot{\varepsilon}_v dt$, $\gamma_{ij} = \int \dot{\gamma}_{ij} dt$].

In the case of harmonic oscillatory shear, the time dependence of all dynamic variables is sinusoidal. In rheological applications, it is customary to describe this dependence by $e^{i\omega t}$. However, with respect to the incorporation into the ECAH framework, it is important to adhere to the ECAH convention of $e^{-i\omega t}$. To establish a link between rheological and ECAH parameters, both approaches are pursued in parallel in the following. For this purpose, the volume expansion can be written as $\varepsilon_v = \varepsilon_v^0 e^{\pm i\omega t}$, and thus $\dot{\varepsilon}_v = d\varepsilon_v/dt = \pm i\omega \varepsilon_v^0 e^{\pm i\omega t}$ (analogous for $\dot{\gamma}_{ij}$). By introducing a new variable $s = t - t'$, Eqs. (3) and (4) can be brought into the following forms:

using $e^{i\omega t}$ for the time dependence

$$\tau_{ij} = p \delta_{ij} - 2G^* \left[\gamma_{ij} - \frac{1}{3} \delta_{ij} \varepsilon_v \right], \quad (5a)$$

using $e^{-i\omega t}$ for the time dependence

$$\tau_{ij} = p \delta_{ij} - 2\bar{G}^* \left[\gamma_{ij} - \frac{1}{3} \delta_{ij} \varepsilon_v \right], \quad (5b)$$

with

$$G^* = i\omega \int_0^\infty G^t(s) e^{-i\omega s} ds, \quad (6a)$$

$$\bar{G}^* = -i\omega \int_0^\infty G^t(s) e^{i\omega s} ds. \quad (6b)$$

Note that the bulk modulus $B^t(s)$ has been written in terms of pressure using Eq. (4), and thus does not show up in these relations. Equations (5a) and (5b) have the same form as the standard ECAH stress–strain relation [Eq. (1)], which enables one to a straightforward incorporation of linear viscoelastic behavior into the ECAH framework. The complex moduli G^* and \bar{G}^* are (Fourier-type) integral transforms of the time-dependent real modulus $G^t(s)$. By separating real and imaginary parts in the integrand of Eqs. (6a) and (6b), and noting that $G^t(s)$ is a real quantity, it can be shown that G^* and \bar{G}^* are complex conjugates of each other. This is marked by the usual bar over \bar{G}^* . The role of both moduli is discussed in the following.

A. Experimental interpretation of G^*

G^* as defined by Eq. (6a) is the complex shear modulus commonly known in rheology, which describes the behavior of any kind of linear viscoelastic material under harmonic oscillatory strain. It is usually written as the sum of its real and imaginary part, $G^* = G' + iG''$, where G' is the “storage modulus” and G'' the “loss modulus.” This allows one to characterize a viscoelastic material by means of quantities such as the “loss angle” δ , with $\tan \delta = G''/G'$, which is a measure for the delay between stress and strain. For an elastic solid ($G''=0$), stress and strain are in phase, and $\delta = 0$ degrees. For Newtonian liquids ($G'=0$), the stress is 90 degrees ahead of the strain, and $\delta = 90$ degrees. Experimental techniques for the measurement of G' and G'' are readily available. An example for direct measurements is given in Ref. 8, where different techniques are combined to cover a wide frequency range.

B. The role of \bar{G}^* in the ECAH theory

The stress–strain relation (5b) is derived under the same assumption of harmonic time dependence ($e^{-i\omega t}$) as throughout the ECAH framework. The complex modulus \bar{G}^* of Eq. (6b) is therefore the direct analog to the shear modulus G [elastic solids, Eq. (2a)] and $-i\omega\eta$ [Newtonian liquids, Eq. (2b)], which means that viscoelastic behavior can be specified as follows:

$$\boxed{\mu = \bar{G}^*} \quad \text{or} \quad \boxed{\mu = G' - iG''}. \quad (7)$$

This way, arbitrary linear viscoelastic behavior (determined experimentally through G' and G'') can be introduced into the ECAH theory. Note that this does not require rederivation of any model equation.

It is important to realize that $\bar{G}^* = G' - iG''$ is the complex modulus relevant for the ECAH framework, *not* $G^* = G' + iG''$. Even though both moduli are derived from the same constitutive relation [Eq. (3)], and even though both lead to the same type of stress-strain relation [Eqs. (5a) and (5b)], the time dependence used in the derivation of G^* is incompatible with that of the ECAH treatment ($e^{i\omega t}$ versus $e^{-i\omega t}$).

The same considerations as made for the shear modulus G^* (or \bar{G}^*) also hold for the bulk modulus $B^* = B' + iB''$ (or $\bar{B}^* = B' - iB''$). However, this variable does not appear in our model equations as bulk relaxation was expressed in terms of pressure using Eq. (4). Note that the definition of B^* (or \bar{B}^*) is different from that of the modulus \tilde{K}^* (or $\bar{\tilde{K}}^*$) in Verdier and Piau's model.⁶ The two models become identical for \tilde{K}^* equal to zero.

III. CONCLUSIONS

In this contribution, the extension of the classic ECAH scattering theory to linear viscoelastic behavior was discussed. By introducing complex moduli into a standard viscoelastic stress–strain relation, this equation could be rewritten in the form of the standard ECAH stress–strain relation. Therefore, the original ECAH model equations [e.g., Allegra and Hawley's³ equations (8a)–(8f)] remain valid also in the viscoelastic case, and viscoelasticity can be introduced by means of the complex (conjugate) shear modulus $\bar{G}^* = G' - iG''$. \bar{G}^* plays the same role as G and $-i\omega\eta$ in the elastic and Newtonian case, respectively.

ACKNOWLEDGMENTS

The financial support by the Swiss National Science Foundation (Grant NF 20-61883.00) is gratefully acknowledged.

- ¹A. K. Hipp, B. Walker, M. Mazzotti, and M. Morbidelli, "In-situ monitoring of batch crystallization by ultrasound spectroscopy," *Ind. Eng. Chem. Res.* **39**(3), 783–789 (2000).
- ²P. S. Epstein and R. R. Carhart, "The absorption of sound in suspensions and emulsions. I. Water fog in air," *J. Acoust. Soc. Am.* **25**, 553–565 (1953).
- ³J. R. Allegra and S. A. Hawley, "Attenuation of sound in suspensions and emulsions: Theory and experiments," *J. Acoust. Soc. Am.* **51**, 1545–1564 (1972).
- ⁴J. R. Allegra, "Theoretical and Experimental Investigation of the Attenuation of Sound in Suspensions and Emulsions," Ph.D. thesis, Department of Physics, Harvard University, 1971.
- ⁵A. K. Hipp, "Acoustic Characterization of Particulate Systems," Ph.D. thesis, Department of Chemical Engineering, ETH Zürich, Switzerland, 2001.
- ⁶C. Verdier and M. Piau, "Acoustic wave propagation in two-phase viscoelastic fluids: The case of polymer emulsions," *J. Acoust. Soc. Am.* **101**, 1868–1876 (1997).
- ⁷N. W. Tschoegl, *The Phenomenological Theory of Linear Viscoelastic Behavior* (Springer, Berlin, 1989).
- ⁸R. S. Marvin, "The dynamic mechanical properties of polyisobutylene," in *Proceedings of the Second International Congress on Rheology*, edited by V. G. W. Harrison (Butterworths, London, 1954), p. 156.

Comment on “Corrections to Foldy’s effective medium theory for propagation in bubble clouds and other collections of very small scatterers” [J. Acoust. Soc. Am. 105, 2149–2154 (1999)] (L)

C. Feuillade

Naval Research Laboratory, Stennis Space Center, Mississippi 39529-5004

(Received 1 July 1999; revised 14 September 2001; accepted 26 October 2001)

Criticisms made by Henyey of my article “The attenuation and dispersion of sound in water containing multiply interacting air bubbles” [J. Acoust. Soc. Am. 99, 3412–3430 (1996)] are refuted. The first two criticisms are based upon misunderstandings and misreadings of my article. The third criticism, based upon an unjustifiable comparison between theories designed for dissimilar physical cases, is irrelevant. My theory is designed to apply to high volume fraction, strong resonator cases where Foldy’s scattering theory has been unable to satisfactorily explain experimental data. Henyey notes that his theory is applicable to low volume fraction and/or weak scatterer cases. Any overlap in the ranges of the two theories appears negligible for practical purposes. © 2002 Acoustical Society of America. [DOI: 10.1121/1.1430688]

PACS numbers: 43.30.Es, 43.30.Ft, 43.30.Jx, 43.30.Ky [SAC-B]

I. INTRODUCTION

It is known that Foldy’s classic theory of propagation in bubbly water¹ may fail to give an accurate description of high volume fraction media when the acoustic frequency is such as to excite the individual bubble resonances. A helpful background to this issue is given by Commander and Prosperetti.²

Figure 1 shows the variation of the attenuation coefficient in bubbly water, as a function of frequency, for one of the experimental cases of Silberman,³ who used high volume fractions varying between about 0.025% and 1.0% in his work. The data points labeled “ \diamond ” apply to water containing bubbles of radius 1.77 mm (resonance frequency = 1.84 kHz), with a volume fraction $\beta=0.22\%$. Comparison of the dashed line, which shows the attenuation coefficient predicted by the Foldy theory for bubbles of this size, with the corresponding data shows that the theory overestimates the attenuation coefficient in the resonance region by a factor of 2–3 in this case. Below the resonance frequency, the Foldy theory fits the data well, even when the actual radius of the bubbles differs from that used to draw the theoretical curve. The disparity between theory and data in the resonance region was ascribed by Silberman to experimental errors associated with the difficulty of measuring very high attenuation levels, but has been widely attributed subsequently to failures in the theory to correctly account for multiple scattering processes between bubbles.^{2,4}

The theory described in my article “The attenuation and dispersion of sound in water containing multiply interacting air bubbles” (Ref. 5) (“FP”) is specifically intended to remedy the limitations of the Foldy theory in this physically interesting regime, i.e., in dense media of strongly resonating bubbles. The solid line in Fig. 1 shows the corresponding fit to Silberman’s $\beta=0.22\%$ data obtained with my theory.

The theory presented in FP has previously been applied, in modified form, to the interpretation of sound scattering from, and transmission through, schools of fish.^{6,7} In FP, it provides a consistent interpretation of Silberman’s data. Notwithstanding its successes, Henyey⁸ contends that the ex-

pression I propose for the speed of sound in bubbly water is “incorrect,” and that my approach, which is a formal development (not based on “intuitive arguments,” as stated by Henyey) of the self-consistent approach of Twersky⁹ and Weston,¹⁰ contains multiple “errors.” His claims, which are based purely on propositional theorizing, are not supported by any computations projected from his analysis, or by comparisons with data.

My theory, and that of Henyey, represent two distinct approaches to two different problems. The intention of FP was to develop a theory applicable to high gas volume fractions (typically $\beta>\sim 0.01\%$) of strong scatterers in the resonance region. Henyey uses a perturbation method which is restricted, as he notes in his article, to low volume fraction and/or weak scatterer cases (for bubbles of the size used by Silberman, his approach is limited to $\beta\leq 0.021\%$). Any overlap in the ranges of the two theories appears negligible for practical purposes.

My purposes in writing these comments on Henyey’s paper are twofold. First, I will defend my work by providing a detailed refutation of his criticisms. Second, by performing data comparisons based upon his analysis, I want to illustrate the differences between my approach and his, and clarify the very different physical environments to which they are meant to apply.

II. RESPONSE TO HENYEY’S CRITICISMS

In his article, Henyey claims three “specific identifications” of errors in FP. First (and “most significantly”), he argues that I have been inconsistent in the way I have determined the compressibility of bubbly water when the additional field due to bubble scattering is present. I have confused, he implies, the external pressure field with the total pressure field (i.e., the external field plus the scattered field). In fact, the total pressure field is never quantified or used in my work at all, but is mistakenly attributed to it by Henyey himself. It is helpful to quote his exact words here: “... p is defined below his [i.e., my] equation (11) [i.e., in FP] as the set of values of the external pressure at each bubble (the aggregate of the scattered fields is added to get the total

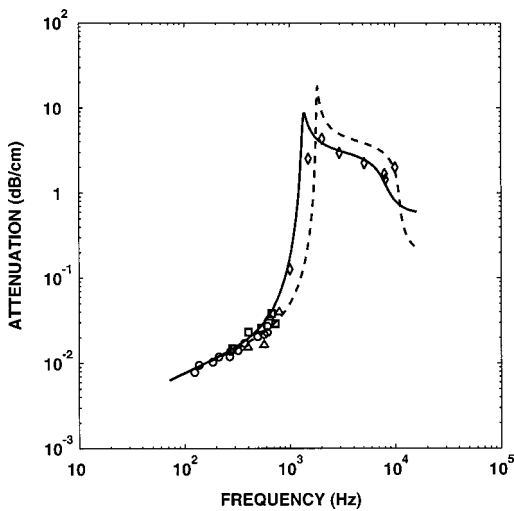


FIG. 1. Attenuation coefficient as a function of frequency. Note the logarithmic scales on the axes. The data are from Silberman (Ref. 3). The volume fraction $\beta=0.22\%$. The data points are for bubbles of radius: 1.77 mm (\diamond); 1.83 mm (\circ); 2.07 mm (\square); and 2.44 mm (\triangle). The dashed line shows the attenuation coefficient predicted for bubbles of radius 1.77 mm using the Foldy theory. The solid line shows the corresponding attenuation coefficient predicted by FP (Ref. 5), which explains the data analysis procedure used.

pressure)...” The underlined words indicate where his mistake is made. A careful reading¹¹ of Eq. (11) in FP and the section following [especially Eq. (12)], reveals that the radiative interactions between bubbles (i.e., scattering), represented by the second terms on the rhs of the coupled equations, are incorporated into the lhs of the matrix equation $\mathbf{M}\mathbf{v}=\mathbf{p}$ as the off-diagonal terms of \mathbf{M} . They are definitely not added to \mathbf{p} , which is, and remains throughout, the external field only. The procedure of incorporating the interactions on the lhs, rather than the rhs, is the essence of the self-consistent approach to multiple scattering which makes the method applicable to strong scatterers. Furthermore, the compressibility of bubbly water is always calculated as the fractional change in volume divided by the change in *external* field pressure, which is how compressibility is macroscopically defined. The first sentence below my Eq. (29) again identifies p_n (an element of \mathbf{p}) as the external field for one of the bubbles; and the contextual statement which immediately follows, interpreting the quantity $(1/N)\sum_n p_n$ as the average pressure field experienced by the bubbles, says and implies nothing about adding the scattering field to the external field. It simply recognizes that within a group of bubbles the individual external p_n values will usually vary [e.g., due to attenuation in the original (i.e., nonbubbly) medium], and that an average must be taken to determine the typical bubble response.

Second (but “less significantly”), Henyey raises the issue of what the wave number k appearing in the exponents of the radiation coupling terms on the rhs of Eqs. (11) in FP should be. He asserts that it must be the wave number in the original medium (i.e., water), and also wrongly reports that I intend it to be the effective wave number in bubbly water. In fact, nothing in my formalism necessitates that k represent either of these quantities. I believe that in the dense ensembles of strongly resonating bubbles for which my theory was designed (e.g., as in Silberman’s experiments), the scat-

tered field from any one bubble is rapidly absorbed and rescattered by its near neighbors. To ensure the consequent local nature and small interactive range of the scattered radiation, k must necessarily contain an attenuation component to describe the decay of the field as it propagates through neighboring bubbles. While the definition of k given by Eq. (5) in FP explicitly allows for the introduction of general complex values to incorporate an attenuation effect, there is no requirement that k must correspond to the complex wave number of the effective medium. Indeed, using the formalism to analyze Silberman’s data has convinced me that it does not. Likewise, there is no requirement that k should necessarily be the wave number of the original medium. Although much of the data analysis performed in FP does substitute k_w (the wave number in water) for k , this is a special approximation used for data fitting which also requires truncating the spatial integral at a finite upper bound R (instead of ∞). This procedure carries no general implications.

Henyey’s third criticism is his contention that my expression for the wave number in the effective medium must be incorrect, because when it is expanded in a Taylor series it gives an order f^2 correction to the Foldy expression (f is the scattering function for a single bubble), “...whereas Ye and Ding¹² have rigorously shown the leading correction to be of order f^3 ...” While this claim is also wrong, because (as I will show) it rests on an unjustifiable comparison, it raises an important topic, i.e., the distinction between perturbation-series approaches (as advocated by Henyey, and Ye and Ding) and self-consistent approaches (as used in FP) to multiple scattering problems.

Figure 2 shows data and theoretical curves for the same Silberman case as Fig. 1. This time only the central resonance portion of the response is plotted, using a logarithmic scale for frequencies between 10^3 and 10^4 Hz, and a linear scale for the attenuation axis. The points denoted “ \diamond ” are the same data shown in Fig. 1 (two points are omitted here, since they lie outside the frequency range plotted). The dashed line again represents the attenuation coefficient predicted by the Foldy theory for uniform bubbles of radius 1.77 mm and volume fraction $\beta=0.22\%$, but shows only a small bump at the resonance frequency in this depiction. The solid line represents the attenuation coefficient predicted by the theory of Ye and Ding [as derived from Eq. (17) of Ref. 12, or using the scattering function from Eq. (7) of Henyey’s article^{8,13}] for the same parameters. The reason why a linear scale has been used for the attenuation axis in this example is clear from Fig. 2. The theory of Ye and Ding predicts *negative* values for the attenuation over large portions of the frequency range!

Why does the theory of Ye and Ding predict such physically unlikely behavior? The answer is that perturbation-series approaches to multiple scattering of this type are essentially applicable only to weakly scattering media. Whether or not the specific scattering schemas proposed by Ye and Ding, or Henyey, are correct (and I leave this particular matter open), the power expansions in ascending orders of f that result from them can only be meaningfully applied if the series converges, i.e., so that the higher-order terms form a small correction to the first-order term. If the void fraction

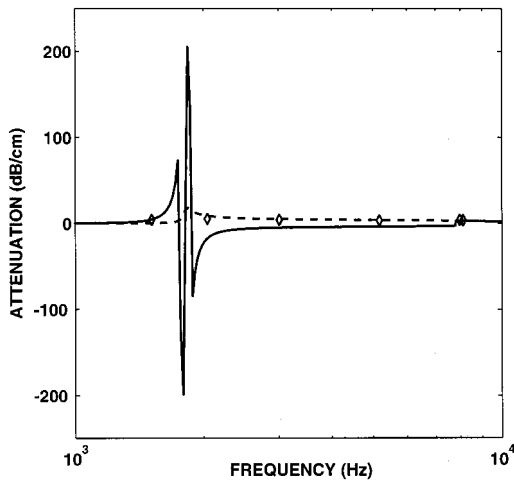


FIG. 2. Attenuation coefficient as a function of frequency. This figure shows data and theoretical curves for the same Silberman $\beta=0.22\%$ case shown in Fig. 1. Only the central resonance region is plotted using a logarithmic frequency scale, and a linear scale for the attenuation axis. The points denoted “ \diamond ” are the data for 1.77-mm bubbles. All other data are outside the frequency range plotted. The dashed line represents the attenuation coefficient predicted by the Foldy theory for bubbles of radius 1.77 mm. The solid line represents the corresponding attenuation coefficient predicted by the theory of Ye and Ding.

is high (so the bubbles are closely spaced), or if the individual bubble damping is low (so $|f|$ at resonance is large, making the bubbles strong scatterers), the perturbation series may diverge.¹⁴ Recognizing this, Henry restricts the results presented in his article to the regime $N|f|^3 \ll 1$, where N is the number of bubbles per unit volume. For the largest bubbles in Silberman’s experiment (3.17 mm radius), this restriction yields an equivalent condition for the volume fraction: $\beta \ll 0.01\%$, in order for the perturbation-series method to be applicable. For the smallest bubbles in the experiment (0.994 mm radius) the condition is $\beta \ll 0.021\%$. The smallest volume fraction used in Silberman’s experiments is actually $\beta=0.025\%$, so that, according to Henry’s limitation, the perturbation-series approach he advocates is not applicable to this data set. This explains the aberrant prediction of the solid line in Fig. 2. It is due to the divergence of the f^3 term, in the Ye and Ding series expansion of the scattering function, because of the large volume fraction.

While the Silberman data suggest that deviations from the Foldy theory may occur, to analyze these data it is necessary to develop a theory of multiple scattering which is applicable to strongly resonating scatterers and high volume fractions. The theory in FP uses a self-consistent procedure, incorporating approximations consistent with the microscopic physical behavior of high-volume fraction bubbly water containing resonating bubbles, and is specifically designed for these cases (see FP,⁵ and also Ref. 15, for further details). Adjusting the notation to correspond to Henry’s paper, it yields the following expression for the effective wave number K in bubbly water:

$$K^2 = k_w^2 + \frac{4\pi Nf}{1 - 4\pi NfI}, \quad (1)$$

where $I = \int_0^\infty r e^{ikr} dr$. Here, k represents a complex wave number whose imaginary component describes attenuation in bubbly water, but not necessarily the macroscopic effective

wave number for bubbly water. As before, k_w is the wave number for pure water. Henry’s criticism of (1) derives from his observation that an expansion of the denominator in a Taylor series predicts that the lowest-order correction to the Foldy expression is of order f^2 while, based upon comparison with the Ye and Ding expression, he argues that it should be of order f^3 . However, if $|4\pi NfI| > 1$ (as, indeed, it is for the cases for which my theory is designed, as I shall show), a Taylor expansion is not analytically justified. If we let $k \equiv \kappa + i\gamma$ and perform the integral, we find $4\pi NfI = -4\pi Nf/k^2$. If we put $\kappa = k_w$, and make γ very small, then $4\pi NfI = -4\pi Nf/k_w^2$. Now, as Henry states, it is specifically those cases where $4\pi Nf/k_w^2$ is large that are expected to lead to deviations from the Foldy theory. For the largest bubbles in Silberman’s experiment (3.17 mm radius) at the resonance frequency, $4\pi Nf/k_w^2 > 1$ for $\beta > 0.00018\%$; while for the smallest bubbles (0.994 mm radius), $4\pi Nf/k_w^2 > 1$ for $\beta > 0.00023\%$ (Silberman’s volume fractions varied from 0.025% to 1.0%). The assumption of reasonable nonzero values for γ will cause these lower limits to increase, but still remain much smaller than the actual experimental values. In FP, where Silberman’s data were analyzed via a truncated integral approximation, $|4\pi NfI| \gg 1$ for all the cases examined. An estimate based upon the requirement that the wavelength of the external field at resonance should be much greater than the nearest-neighbor spacing of bubbles in the medium, which is an approximation used in FP, leads to a limit for application of the theory of FP of $\beta > \sim 0.01\%$. All of the data cases examined in FP satisfy this condition. For small oceanic bubbles ($\sim 10 \mu\text{m}$ radius), $4\pi Nf/k_w^2 > 1$ for $\beta > \sim 0.001\%$.

This attempt to criticize FP by comparing power series terms fails because $|4\pi NfI| > 1$ (and, typically, $|4\pi NfI| \gg 1$) in the resonant bubble, high-volume fraction cases for which the theory is designed. The Taylor expansion cannot be performed, and the comparison is meaningless. However, the fact that $|4\pi NfI|$ is large for these cases is not a fortuitous accident. It is the failure of perturbation-series methods in these cases which originally necessitated a self-consistent approach. The motivation for using a self-consistent method is to derive an expression for the modified scattering function *in closed form* [as in Eq. (1)], and thereby avoid a divergent power series. In other words, the self-consistent methodology is useful specifically because it can often be applied to strong interaction cases (e.g., where N and/or $|f|$ is large) where a power series would diverge.

III. HENY’S FORMALISM

Henry’s analysis is developed beyond the approach of Ye and Ding, to derive his own new expression for the modified scattering function in the presence of other bubbles (but restricted to the regime $N|f|^3 \ll 1$). In water, the damping of a single noninteracting bubble of radius a is described by a parameter¹⁶ $\delta = \delta_r + \delta_i + \delta_v$, where $\delta_r = k_w a$ is the damping due to acoustic radiation from the bubble¹³ (also called the scattering loss), and δ_i and δ_v are the thermal and viscous damping components, respectively. In bubbly water, Henry argues, the scattering loss must be evaluated in the effective medium, and the result of his analysis is to replace the radia-

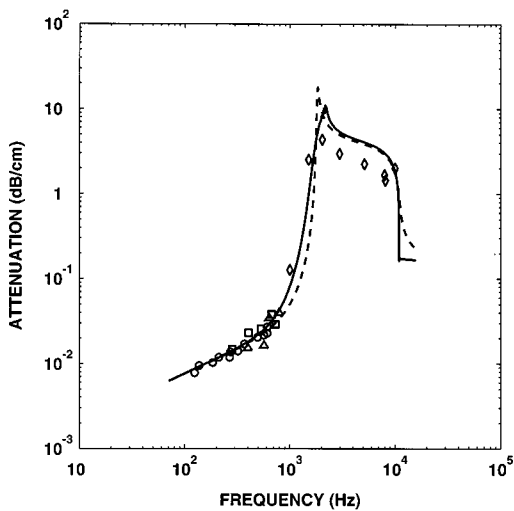


FIG. 3. Attenuation coefficient as a function of frequency. This figure shows data and theoretical curves for the same Silberman $\beta=0.22\%$ case shown in Fig. 1. The dashed line again shows the attenuation coefficient predicted by the Foldy theory for bubbles of radius 1.77 mm. The solid line shows the corresponding attenuation coefficient predicted by Henyey's formalism, evaluated using a recursive algorithm. Note that Henyey's formalism continues to overestimate the attenuation in the resonance region.

tion damping component of δ by $\delta_r = Ka$, where K is the wave number for the effective medium. To investigate this idea, Fig. 3 represents the same Silberman case shown in Fig. 1. The dashed line again shows the attenuation coefficient predicted by the Foldy theory for bubbles of radius $a = 1.77$ mm. This time, the solid line is the corresponding prediction for the attenuation coefficient obtained by using $\delta_r = Ka$ (rather than $\delta_r = k_w a$) as the radiative damping in the scattering function, as prescribed by Henyey. (A recursive algorithm was used to solve the resulting cubic equation for K .)

As we saw earlier, Henyey's formalism cannot strictly be applied to any of Silberman's data. Its employment here, however, serves to illuminate the type of resonant bubble, high-volume fraction cases for which the theory of FP is designed. Inspection of the solid line in Fig. 3 shows that evaluating the scattering loss in the effective medium does not lead to any substantive differences from the Foldy theory, and does not solve the problem of the overestimation of attenuation in the resonance region. To understand what is happening, it is instructive to look carefully at the *experimental data points* in the resonance region in Fig. 3. Silberman measured attenuations from about 1.4–4 dB/cm in this region. Since the average nearest-neighbor distance between 1.77-mm bubbles, for $\beta=0.22\%$, is about 2.2 cm, this indicates an acoustic attenuation here of about 3–8 dB per bubble spacing length. This high attenuation value implies a very short range of influence for interactions between bubbles (i.e., \sim one spacing). Under these conditions, it appears unlikely that the scattering loss is determined by the macroscopic effective medium. In FP, these same data were analyzed by assuming (as the data suggest) that the bubbles interact strongly only with their near neighbors (which dominate the scattering loss), with water as the coupling medium. The resulting analysis led to the data fit shown by the solid line in Fig. 1.

IV. SUMMARY

A refutation of criticisms made by Henyey of my article "The attenuation and dispersion of sound in water containing multiply interacting air bubbles" [J. Acoust. Soc. Am. **99**, 3412–3430 (1996)] has been presented. The first two criticisms are based upon misunderstandings of my theory, and misreadings of my article. The third criticism, which relies on comparing power series terms from the theory of Ye and Ding with my theory, is based upon an unjustifiable comparison between theories designed for dissimilar physical cases.

My theory is specifically designed to apply to high-volume fraction, strong resonator cases where Foldy's scattering theory¹ has been unable to satisfactorily explain data, as exemplified by the experimental work of Silberman.³ When Henyey's theory was applied to this data set, it was shown that the scattering loss is not determined by the effective medium as Henyey claims and that his formalism fails to give a useful correction to the Foldy theory. Application of the theory of Ye and Ding.¹² (which is cited and attested by Henyey) to Silberman's data gives anomalous results.

ACKNOWLEDGMENTS

This work was supported by the US Office of Naval Research.

- ¹L. L. Foldy, "The multiple scattering of waves. I. General theory of isotropic scattering by randomly distributed scatterers," Phys. Rev. **67**, 107–119 (1945); E. L. Carstensen and L. L. Foldy, "Propagation of sound through a liquid containing bubbles," J. Acoust. Soc. Am. **19**, 481–501 (1947).
- ²K. W. Commander, and A. Prosperetti, "Linear pressure waves in bubbly liquids: Comparison between theory and experiments," J. Acoust. Soc. Am. **85**, 732–746 (1989).
- ³E. Silberman, "Sound velocity and attenuation in bubbly mixtures measured in standing wave tubes," J. Acoust. Soc. Am. **29**, 925–933 (1957).
- ⁴A. Prosperetti, private communication (1999).
- ⁵C. Feuillade, "The attenuation and dispersion of sound in water containing multiply interacting air bubbles," J. Acoust. Soc. Am. **99**, 3412–3430 (1996).
- ⁶C. Feuillade, R. W. Nero, and R. H. Love, "A low frequency acoustic scattering model for small schools of fish," J. Acoust. Soc. Am. **99**, 196–208 (1996).
- ⁷O. Diachok, "Effects of absorptivity due to fish on transmission loss in shallow water," J. Acoust. Soc. Am. **105**, 2107–2128 (1999).
- ⁸F. S. Henyey, "Corrections to Foldy's effective medium theory for propagation in bubble clouds and other collections of very small scatterers," J. Acoust. Soc. Am. **105**, 2149–2154 (1999).
- ⁹V. Twersky, "Multiple scattering of waves and optical phenomena," J. Opt. Soc. Am. **52**, 145–171 (1962).
- ¹⁰D. E. Weston, "Acoustic interaction effects in arrays of small spheres," J. Acoust. Soc. Am. **39**, 316–322 (1966).
- ¹¹Equation (11) in FP may be straightforwardly derived by combining Eqs. (2) and (5) for an ensemble system of coupled bubbles, while referring to Fig. 1. See Ref. 6 for another explanation.
- ¹²Z. Ye, and L. Ding, "Acoustic dispersion and attenuation relation in bubbly mixture," J. Acoust. Soc. Am. **98**, 1629–1636 (1995).
- ¹³Henyey adopts a $-i$ phase convention in his work, whereas Ye and Ding, and this work, use $+i$. A consistent application of either convention yields exactly the same results.
- ¹⁴C. Feuillade, "Acoustically coupled gas bubbles in fluids: Time domain phenomena," J. Acoust. Soc. Am. **109**, 2606–2615 (2001).
- ¹⁵C. Feuillade, "Response to 'Comments on 'The attenuation and dispersion of sound in water containing multiply interacting air bubbles' [J. Acoust. Soc. Am. **99**, 3412–3430 (1996)]," J. Acoust. Soc. Am. **102**, 1242–1245 (1997).
- ¹⁶C. Devin, "Survey of thermal, radiation, and viscous damping of pulsating air bubbles in water," J. Acoust. Soc. Am. **31**, 1654–1667 (1959).

Reply to “Comment on ‘Corrections to Foldy’s effective medium theory for propagation in bubble clouds and other collections of very small scatterers’” [J. Acoust. Soc. Am. 111, 1552–1555 (2002)] (L)

Frank S. Henyey

Applied Physics Laboratory, University of Washington, Seattle, Washington 98105

(Received 16 March 2000; revised 9 October 2001; accepted 26 October 2001)

Response is made to Feuillade’s comments [J. Acoust. Soc. Am. **111**, 1552–1555 (2002)]. After discussing the care needed in formulating self-consistent physical theories to avoid multiple counting of scattering contributions, I show that Feuillade [J. Acoust. Soc. Am. **99**, 3412–3430 (1996)] did not avoid that multiple counting, and made a number of further mistakes. I show (as Foldy showed over half a century ago) that by making the primary assumption made by Feuillade, and avoiding the multiple counting, the theory can be solved with no further assumptions, and Foldy’s result is obtained. My paper [J. Acoust. Soc. Am. **105**, 2149–2154 (1999)] constructed a self-consistent method which avoids an expansion in a parameter that is often large, and results in an expansion in a parameter which is large much less often. I showed that the lowest order of the resulting expansion duplicates Foldy, and the next order gives an expression which Sangani previously obtained, but in a less rigorous way. © 2002 Acoustical Society of America. [DOI: 10.1121/1.1430689]

PACS numbers: 43.30.Es, 43.30.Ft, 43.20.Bi [SAC-B]

I. INTRODUCTION

The formulation and interpretation of self-consistent physical theories has frequently been incorrectly carried out. Schiff¹ issues a warning about the incorrect use of the Hartree theory of electrons surrounding an atom. Self-consistent calculations of elastic properties of rocks with many cracks were also originally done incorrectly; the correct treatment was given by Bruner,² and later by Henyey and Pomphrey.³ These difficulties are avoided by being careful as to the meanings of the quantities involved. The collective behavior of the acoustics of a large collection of bubbles can be treated as such a self-consistent theory; both Feuillade^{4,5} (F1 and F2) and I⁶ adopt this approach, as did Foldy⁷ in his classic paper on this subject. However, F1 and F2 arrive at very different results than I do. This comment first shows what care needs to be taken, shows that F1 and F2 do not take that care, and then identifies an unnecessary incorrect approximation in F1. A version of the calculation in F1 without that approximation is sketched, giving Foldy’s result.

II. SELF-CONSISTENT THEORIES

Terms such as “the wave number” of the acoustics, or “the field scattered by” a particular bubble are ambiguous in a self-consistent theory. They should only be used in the presence of a precise definition. I shall avoid using these terms, and provide definitions of the terms I use. “The wave number in the water,” denoted by k , is defined as the frequency divided by the sound speed in water. “The effective wave number” denoted by K , is defined, following Foldy,⁷ in terms of an ensemble of configurations of the positions of the bubbles by

$$\nabla^2 \langle P \rangle = -K^2 \langle P \rangle, \quad (1)$$

where $\langle P \rangle$ is the ensemble average of the field. Instead of “the field scattered by” a particular bubble, the carefully defined quantities are “the field last scattered by” a particular bubble and “the extra field due to a bubble” of a certain size at a certain position. Each of these terms requires a bit of discussion to make the definitions clear. Consider a region between the outside of a bubble and a concentric sphere that does not quite reach the closest other bubble to the one under consideration. This region is entirely in the water. The general solution of the wave equation in this region is given by a uniformly convergent series

$$P = \sum_{l,m} Y_{lm}(a_{lm} j_l(kr) + b_{lm} h_l^{(1)}(kr)), \quad (2)$$

where Y_{lm} is the spherical harmonic function of the polar angles of a coordinate system centered on the bubble, r is the radius in that system, and j and h are spherical Bessel functions. If there were no bubble inside the sphere, only the a terms would occur. Therefore, the sum of the b terms defines the field last scattered by bubble A . This expression involves k , the wave number in the water, not K , the effective wave number. It can be continued to arbitrarily large distances, unlike the sum of the a terms. Foldy showed that the field at any point is the incident field plus the sum of the fields last scattered by each bubble. In the region surrounding bubble A where Eq. (2) applies, the sum of the a terms is the total field P minus the field last scattered by A , i.e., the incident field plus the sum of the fields last scattered by each bubble with the exception of bubble A itself.

For a spherically symmetric bubble, each (l,m) combination can be studied independently of the remainder. The coefficient b_{lm} is related to a_{lm} by a scattering amplitude

$$b_{lm} = f_l a_{lm}. \quad (3)$$

Foldy makes the approximation that only f_0 is nonzero, and denotes it by f . This is a good approximation for bubbles except at very high frequency because nonspherical oscillations of the bubble couple very weakly to acoustics. The value of f is independent of what contributes to a_{00} , so it can be evaluated ignoring the other bubbles. It depends on frequency and on the size of the bubble.

Combining Eq. (3) for $l=0$ with the fact that a_{00} is the incident field plus the sum of the fields last scattered by each bubble with the exception of bubble A itself, Foldy derives a matrix equation relating the a_{00} values for each bubble. The size of the matrix is $n \times n$, where n is the number of bubbles. The field is the inverse of that matrix applied to the incident field contribution to the a_{00} values, multiplied by the propagation through water to the point where the field is to be evaluated.

Foldy's matrix equation involves the propagation factors $g = e^{ikr}/r$ between each pair of bubbles, involving k , the wave number in water. It is important to emphasize that there is absolutely no assumption of weak scattering or low density in Foldy's derivation of the matrix equation. The appearance of k , rather than K , is because it is the fields last scattered by each bubble that are added together. If some portion of the field is scattered by bubble A , and later scattered by bubble B , it is attributed to B , not A . If it were attributed to both, and these were added together, that contribution would be counted twice.

We now consider "the extra field due to a bubble." For each configuration of bubbles, we consider the possibility of adding an extra bubble at some fixed position. Without the extra bubble, the field is P , and with it, the field is $P + dP$. Then "the extra field due to a bubble" is defined to be dP . If we take the ensemble average, and we assume the ensemble to be statistically homogeneous so that K is a constant over space, the extra field due to a bubble at the origin is proportional to $G = e^{iKr}/r$, at least at large R , as a result of Eq. (1).

The common mistake is to assume that it is better to use G in the matrix equation, rather than g . After all, the thinking goes, isn't it better to use the actual extra field due to a bubble than the field that would be there if there were no other bubbles (but with the same a_{00})? This assumption ignores the fact that the matrix equation was derived, not guessed, and it commits the double counting mentioned earlier. The difference between G and g is due to the subsequent scattering of the wave emitted from the bubble under consideration by other bubbles. According to one possible correct bookkeeping, that subsequent scattering should be assigned to the last bubble it scattered from, rather than the one we may have wanted to concentrate on. Feuillade's comment, F2, states that k is neither the wave number in water nor the effective wave number, but does not state what it is. F2 asserts that it "must necessarily contain an attenuation component to describe the decay of the field as it propagates through neighboring fields." In doing so, the rescattering that is responsible for the attenuation is counted twice.

III. FEUILLADE'S THEORY

F1 presents a matrix equation [his Eq. (11)] without a reference, a derivation, or a definition of the quantities. Of concern are the definition of the pressures P_n and the wave number k used in e^{ikr}/r . The equation is equivalent to Foldy's only if k is the wave number in water, and P_n is the incident wave (in Foldy's terminology) which obeys the wave equation in water. The incident wave does not solve Eq. (1) with the effective wave number, in order to avoid double counting; it is the contribution which never scattered off any bubble. F2 claims I made a mistake in stating "(the aggregate of the scattered fields is added to get the total pressure);" however, my parenthetical comment was meant as a paraphrase of "The total field incident on any one of the bubbles is the external field and the aggregate of the scattered fields from all the other bubbles" in F1. In other words, I was asserting that F1 used the correct identification at this point. This contrasts with Foldy's use of the term "external field," which refers to a_{00} . My objection was that in F1 the meaning of "external field" is changed by the time of the discussion following F1 Eq. (29). Let us focus on a mathematical manipulation in F1, rather than word meanings. F1 replaces (\bar{v}/P) in Eq. (7) by an average v divided by an average P_n . However, P in Eq. (7) is the total pressure, not the incident pressure.

Finally, we turn to an approximation in F1 that I did not mention in my earlier work. The purpose is to be able to carry out a correct calculation, as close to that of F1 as is possible. F1 states "all of the bubbles in any given local neighborhood...experience essentially the same driving phase." In the equations that follow, the magnitude as well as the phase is assumed equal. This is a very reasonable assumption; I shall impose it in the calculation which follows. In a parenthetical comment in the middle of the quoted passage F1 asserts that it is these nearby bubbles "that interact strongly with each other." While it is true that any given bubble interacts more strongly the closer it is, there are many more bubbles farther away. Which of these effects is more important? F1 actually provides the answer, although without mention that it contradicts the assertion. The spatial structure of the interaction is contained in an integral (where I change from the convention in F1 to mine):

$$\int_0 r e^{ikr} dr. \quad (4)$$

It is clearly the large r part of the integral which dominates; the interaction with the distant bubbles is most important. F1 treats this assumed behavior of the driving as if it were an eigenfunction. Such a treatment is unjustified, but a correct calculation can be done avoiding this issue altogether.

We are now in a position to carry out a correct calculation under the assumption that locally the exciting field is constant. We will use Foldy's matrix, which is the matrix of F1 times the inverse of its diagonal part; this transformation simply consists of writing the equation in terms of the force (i.e., the sum of the alm terms in Eq. (2), in this work) rather than the velocity.

The matrix equation is

$$A_j = P_0(\mathbf{r}_j) + f \sum_{k \neq j} g_{jk} A_k, \quad (5)$$

where A_j is the value of a_{00} for the j th bubble, $P_0(\mathbf{r}_j)$ is the incident field at the position of the j th bubble, and g_{jk} is g evaluated at the distance between the j th and k th bubbles. The ensemble average of this equation is

$$\langle A_j \rangle = P_0(\mathbf{r}_j) + f \left\langle \sum_{k \neq j} g_{jk} A_k \right\rangle. \quad (6)$$

For a Poisson process (which means that the probabilities of the positions of nearby bubbles are independent), $\langle A_j \rangle = \langle P(\mathbf{r}_j) \rangle$. The assumption that the driving is locally constant lets us also replace A_k by $\langle A_k \rangle = \langle P(\mathbf{r}_k) \rangle$ on the right-hand side of Eq. (6), obtaining

$$\langle P(\mathbf{r}_j) \rangle = P_0(\mathbf{r}_j) + f \left\langle \sum_{k \neq j} g_{jk} P(\mathbf{r}_k) \right\rangle. \quad (7)$$

In order to have a specific problem, assume a unit point source at the origin,

$$P_0(\mathbf{r}_j) = \frac{e^{ikr}}{r}. \quad (8)$$

The reader is reminded that, in order to avoid double counting, the k in Eqs. (5)–(8) is the wave number in water.

For a statistically homogeneous bubble field

$$\langle P(\mathbf{r}) \rangle = \alpha \frac{e^{iKr}}{r}. \quad (9)$$

Since each bubble is positioned independently, the sum in Eq. (7) simply gives a factor of $n-1$, where n is the number of bubbles. We assume n is large, and the difference between n and $n-1$ is ignored. The ensemble averaging is just an average over position, the integral over position divided by the volume. Finally n/volume is the density of bubbles, N .

We obtain

$$\alpha \frac{e^{iKr}}{r} = \frac{e^{ikr}}{r} + Nf \frac{e^{ikr}}{r} * \alpha \frac{e^{iKr}}{r}, \quad (10)$$

where $*$ denotes a spatial convolution. If we were to believe that only nearby interactions were important, we could treat $\alpha e^{iKr}/r$ in the convolution as a constant. We would then be left with $4\pi \int_0^r e^{ikr} dr$, the integral in F1. In that case, Eq. (10) would not have a solution, and further approximation would be required. However, the convolution as it stands is easily evaluated:

$$\frac{e^{ikr}}{r} * \frac{e^{iKr}}{r} = \frac{4\pi}{K^2 - k^2} \left(\frac{e^{iKr}}{r} - \frac{e^{ikr}}{r} \right). \quad (11)$$

Inserting this expression into Eq. (10), one finds a solution by matching the coefficients of e^{ikr}/r and e^{iKr}/r , finding

$$\alpha = 1, \quad (12)$$

$$K^2 = k^2 + 4\pi Nf. \quad (13)$$

Equation (13) is exactly Foldy's result, which is not surprising because F1 made the same assumption that Foldy did.

Corrections to Foldy's result require refraining from replacing A_k by its average in Eq. (6). It is the deviation of A_k from its average which is only important for nearby bubbles.

IV. MY THEORY

There is a historical misunderstanding in F2 describing my result. The result I obtain was earlier obtained by Sangani,⁸ my contribution was to show how that expression followed from a self-consistent resummation of the multiple scattering series. Sangani [his equation (5.23), and the discussion following it] obtained a term that, when combined with Foldy's term, are the first two terms of a geometric series. He then replaced the first two terms by the entire series. He gave the interpretation "the acoustic damping based on the pure-liquid wavenumber is replaced by the effective-medium wavenumber." Clearly, he realizes that the entire geometric series need not follow just because of its first two terms, for he says "it is *perhaps* more accurate to solve...in a self-consistent manner"[emphasis added]. What I added is showing that the rest of the terms in that geometric series are indeed present. For Sangani, the interpretation that the radiation loss should be evaluated in the effective medium is an argument for a result obtained in a nonrigorous way; for my calculations this is an *a posteriori* description of the result obtained, not, as F2 implies, an argument necessary in obtaining the result.

There are two expansion parameters in the multiple scattering series. One is the ratio of the second term in Eq. (13) to the first. An expansion in this term cannot be truncated in many cases, because the second term can be much larger than the first. Neither Foldy nor I truncated in this parameter. Ye and Ding did truncate in that parameter, which was the basis of my objection to their result. F2 incorrectly attributes to me a claim that Foldy's result depends on that parameter being small. My article presented a method for analytically carrying out the sum over this possibly large parameter to all orders, leaving a series in the second parameter. The second parameter can be identified in a number of ways. In my article, I made an identification which was not optimum for two reasons: (1) I identified the square of the actual expansion parameter. (2) My identification required Foldy's approximation, Eq. (13), to be accurate. My method makes use of a quantity F which has the property that the equation

$$K^2 = k^2 + 4\pi Nf \quad (14)$$

is exact. To lowest order, $F = f$, which leads me to name this quantity the "effective scattering amplitude" in analogy with K being the effective wave number. I obtain the next term, and show how additional terms can be obtained. The additional terms involve F and K , leading to algebraic equations to be solved in a self-consistent way. Whenever possible without double counting, propagation with e^{iKr}/r is used, and scattering with F instead of f is used. In all low-order contributions, at most one propagation with e^{iKr}/r is needed, and at most one scattering with f is needed; it is likely that the same holds for arbitrarily high order. Assuming that to be the case, the second expansion parameter is $|KF|$. Thus, in Eq. (10) [with the replacement leading to Eq. (11)] of my article, the ratio of the second term in F to the first is $i(K$

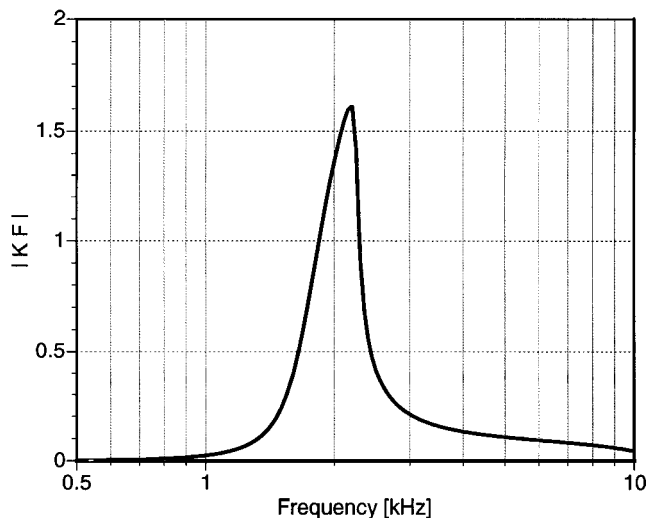


FIG. 1. The expansion parameter $|KF|$ of the self-consistent expansion, evaluated at the order carried out in my article. There truncation of this expansion is justified except when this parameter exceeds unity, which occurs between 1.8 and 2.3 kHz. However, the region of comparison with data extends up to 8 kHz, where the truncation is justified.

$-k)F$, whose magnitude is smaller than that of KF .

F2 claims that the theory in F1 only works at high density, even though the assumption of local constancy of the forcing is best at low densities. The second parameter grows with density, so a truncation of the series may fail at high enough density. In connection with data of Silberman,⁹ F2 claims the density is too high for my considerations. To examine this claim, in Fig. 1 I show a graph of KF , evaluated to the order K^2F^3 for the conditions given in F2.

It can be seen that $|KF| > 1$ only for frequencies between 1.8 and 2.3 kHz. The deviation between the expression of Sangani that I derived and Silberman's data, as shown in Fig. 3 of Feuillade's comment, extends well outside this region (especially at higher frequencies, up to 8 kHz), where $|KF|$ is very small, and the curve nearly coincides with Foldy's. The shape of Silberman's data fits the shape of the curve quite well, but the resonant frequency and level are not in agreement. It is possible that the bubbles in the experiment were larger than the size used in the theory, and that the number of bubbles was smaller.

The fit in F1 looks better, but an arbitrary parameter is adjusted to obtain that fit. The k in the integral $\int_0^r e^{ikr} dr$ is

undetermined in spite of its occurrence in Eq. (11) of F1, which was asserted as accepted. F1 uses the wave number in water as k , and changes the upper limit of integration from infinity to some very small adjusted value.

V. SUMMARY

F1 and F2 contain many mistakes, and are not consistent with careful developments of self-consistent theories in many branches of physical theory. It is a hallmark of these theories that care is taken not to multiply count one contribution. F1 makes the same assumption as Foldy, that the field felt by each bubble is independent of the detailed positions of nearby bubbles. With this one assumption, no further assumptions are required to get Foldy's result. True corrections to Foldy require improvements on Foldy's assumption, by dealing with deviations at the position of a bubble from the average field that survive the averaging over positions of nearby bubbles.

ACKNOWLEDGMENT

This work was supported by the office of Naval Research.

- ¹L. I. Schiff, *Quantum Mechanics*, 3rd ed. (McGraw-Hill, New York, 1968), pp. 431–433.
- ²W. M. Bruner, "Comment on 'Seismic velocities in dry and saturated cracked solids' by Richard J. O'Connell and Bernard Budiansky," *J. Geophys. Res.* **81**, 2573–2576 (1976).
- ³F. S. Henyey and N. Pomphrey, "Self-consistent elastic moduli of a cracked solid," *Geophys. Res. Lett.* **9**, 903–906 (1982).
- ⁴C. Feuillade, "The attenuation and dispersion of sound in water containing multiply interacting air bubbles," *J. Acoust. Soc. Am.* **99**, 3412–3430 (1996).
- ⁵C. Feuillade, "Comments on 'Corrections to Foldy's effective medium theory for propagation in bubble clouds and other collections of very small scatterers' [J. Acoust. Soc. Am. **105**, 2149–2154 (1999)]," *J. Acoust. Soc. Am.* **111**, 1552–1555 (2002).
- ⁶F. S. Henyey, "Corrections to Foldy's effective medium theory for propagation in bubble clouds and other collections of very small scatterers," *J. Acoust. Soc. Am.* **105**, 2149–2154 (1999).
- ⁷L. L. Foldy, "The multiple scattering of waves. I. General theory of isotropic scattering by randomly distributed scatterers," *Phys. Rev.* **67**, 107–119 (1945).
- ⁸A. S. Sangani, "A pairwise interaction theory for determining the linear acoustic properties of dilute bubbly liquids," *J. Fluid Mech.* **232**, 221–284 (1991).
- ⁹E. Silberman, "Sound velocity and attenuation in bubbly mixtures measured in standing wave tubes," *J. Acoust. Soc. Am.* **29**, 925–933 (1957).

Geoacoustic inversion for fine-grained sediments

Charles W. Holland^{a)}

SACLANT Undersea Research Centre, Viale San Bartolomeo 400, 19138 La Spezia, Italy

(Received 6 March 2001; revised 12 October 2001; accepted 14 January 2002)

Fine-grained water saturated sediments like silty clays have the curious property that the speed of sound through its bulk medium is lower than that of the interstitial pore fluid. When a fine-grained sediment is at the water–sediment interface, classical theory predicts that there is an angle at which the reflection coefficient is zero, and there is total transmission of sound into the seabed. This angle is called the angle of intromission and has been directly observed at the seafloor only rarely. Data from a new measurement technique show this phenomenon with remarkable clarity. The presence of the angle of intromission creates an opportunity for a direct (i.e., without search) inversion for the sediment sound speed and density. Though acoustic techniques generally do not estimate sediment density very precisely, this technique is quite sensitive to density. Geoacoustic inversion results from reflection measurements in the Straits of Sicily compare very favorably with independent “ground truth” data indicating that the method is robust. [DOI: 10.1121/1.1461836]

PACS numbers: 43.20.Ef, 43.30.Pc, 43.30.Ma [DLB]

I. INTRODUCTION

Sound propagation and reverberation in coastal areas is often controlled by the properties of the seabed. A common sediment type in shallow water is silty-clay that typically originates from terrestrial sources. Silty-clay and other fine-grained sediment types can have a profound influence on sound propagation (e.g., Eller and Gershfeld, 1985). These sediments exhibit densities greater than, but sound speeds less than, water.

Classical theory (Rayleigh, 1896) predicts for this sediment that, at a certain angle, the reflection coefficient goes to zero, and there is complete transmission of sound into the seafloor. In practice, not all of the energy is completely transmitted due to sediment attenuation. The bottom reflection loss ($-20 \log_{10} |\mathbf{R}|$, where \mathbf{R} is the Rayleigh reflection coefficient) for a silty-clay sediment is shown in Fig. 1. The angle of near complete transmission, called angle of intromission, is apparent at a grazing angle of 16 degrees.

While there are copious published results showing the effects of low-velocity sediments, there is a marked dearth of direct measurements of the angle of intromission phenomenon itself. The reason for this is that the direct observation of the angle of intromission is hindered by the presence of ubiquitous subbottom higher speed layers, or sound speed gradients, which tend to “fill in” the reflection coefficient so that the intromission phenomenon is obscured. Therefore, in order to observe the angle of intromission, some kind of time windowing generally needs to be applied in order to eliminate deeper reflections.

One of the only clear examples of the angle of intromission was published by Winokur and Bohn (1968) in deep water, who processed reflection data using peak amplitude over just the first few cycles of the reflected waveform. The angle of intromission was apparent at about 11 degrees at 1 and 2 kHz. Bucker *et al.* (1965) present bottom reflection

loss data from several areas that exhibit a large peak, having the appearance of an angle of intromission. However, the reflection loss values appear to be too low (with the possible exception of Area II at 3 kHz) or the peak occurs at too high an angle to suggest an angle of intromission. Christensen *et al.* (1975), using SUS charges in the deep ocean, observed that the reflected arrival in the time series data was small enough to be “not discernable” between grazing angles of 13 and 21 degrees.¹ The angle of intromission presumably fell in that range but could not be clearly identified.

Other researchers using similar measurement techniques in deep water have processed the data for the reflection coefficient (e.g., Chapman, 1983) but without direct observation of the intromission phenomenon. Shallow water propagation measurements (e.g., Rubano, 1980; Hermand, 1999) have also shown effects of the low sound speeds of silty-clay, however, without direct measure of the angle of intromission.

A new experimental and layer-stripping processing technique allows measurement of the reflection coefficient at the boundary of the water–sediment interface. This permits direct observations of the angle of intromission. The observation of the intromission angle provides a unique “window” (or perhaps more appropriately a “lens” since the sound

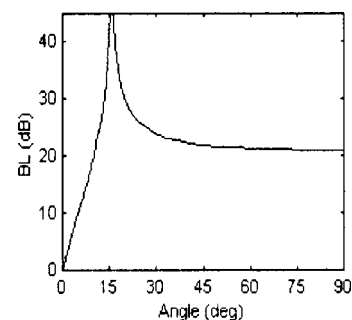


FIG. 1. Theoretical reflection loss for a seabed whose sound speed is smaller than that of the water. Sound speed and density ratios are 0.9822 and 1.2174, respectively.

^{a)}Present address: Pennsylvania State University, Applied Research Lab, P.O. Box 30, State College, PA 16804.

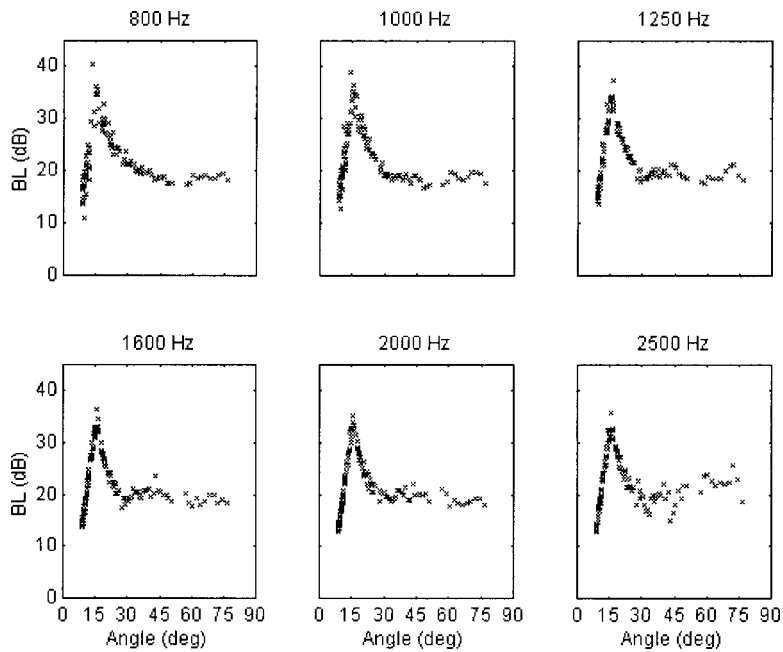


FIG. 2. Bottom reflection loss from first sediment layer on the Malta Plateau. Water depth is 101 m and the source/receiver depths are 0.35 and 85 m, respectively. The salient feature in the data is the peak at 15 degrees corresponding to the angle of intromission.

speed contrast introduces refraction) through which sediment geoacoustics can be probed. Following the presentation of the measurements, a simple but robust geoacoustic inversion technique is presented whereby the sediment sound speed and density are obtained unambiguously. These results are confirmed by independent “ground truth” measurements.

II. REFLECTION MEASUREMENTS

The reflection measurement employs a broadband source (Boomer) opening in range (angle) and a single fixed hydrophone. The processing uses the direct arrival and the bottom reflected path in a self-calibrating method to compute the reflection coefficient. A key feature of the processing is that the reflection coefficient is processed for multiple, cumulative depths into the sediment. Reflection coefficients for the water–sediment interface include reflection from the uppermost several meters of the sediment column. Further de-

tails of the measurement and processing techniques can be found in Holland and Osler (2000) who analyzed data acquired in the Capraia basin.²

Figure 2 shows reflection loss measurements on the Malta Plateau (see Fig. 3) for the upper 2.5 m of the seabed. The salient feature of the reflection data is the presence of the angle of intromission at about 15 degrees. One of the remarkable aspects of this kind of sediment is the nearly complete acoustic transparency. Even up to 5 kHz, the data (not shown) indicate that above 10 degrees grazing angle, 99% of the energy is transmitted into the seafloor. At the angle of intromission, 99.95% is transmitted. The implication is that the sediments below the first layer will largely control the reflection and scattering characteristics. The silty-clay layer acts largely as a lens, modifying the angle of incidence on the subbottom strata.

Another remarkable aspect of these data is the similarity to sites on the Tuscany shelf more than 900 km away. Figure 4 shows 2000 Hz measurements in the Malta Plateau and in

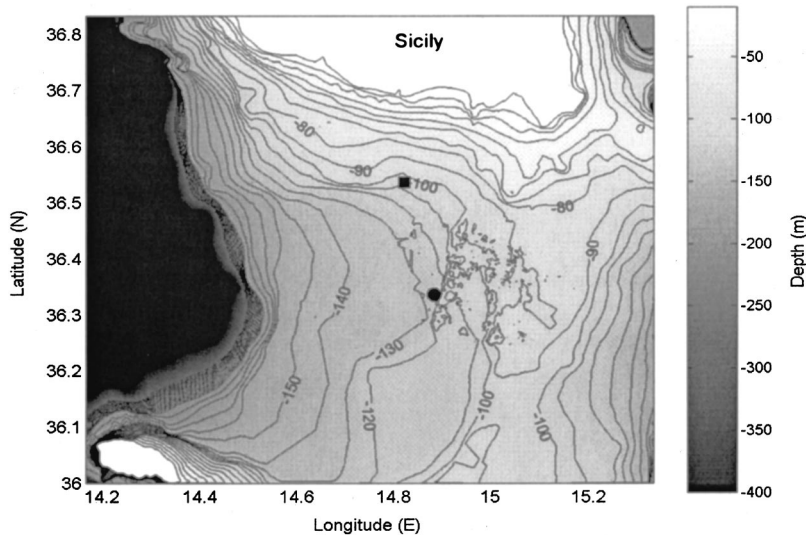


FIG. 3. Map of experimental area in the Straits of Sicily. Measurements were conducted on the flat lying shelf between Sicily and Malta (the island in the southwest corner of the map) known as the Malta Plateau. Acoustic data and core data were collected at the site marked with a box; more core data were collected at the site marked with a circle.

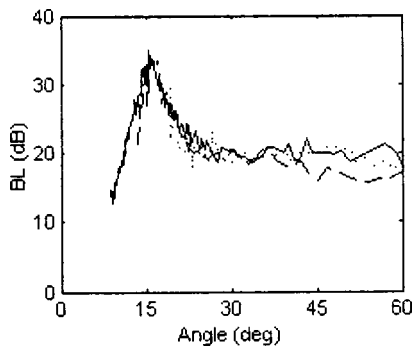


FIG. 4. Comparison of measured reflection coefficient at 2000 Hz in the Malta Plateau (solid) at a water depth of 101 m and at two sites in the North Elba area (dashed, dotted) at 102-m water depth.

the Tuscany shelf area. It appears that the surficial sediments in both areas are almost identical. This is surprising given the notorious geoacoustic variability that characterizes shallow water sediments and the distinct riverine environments feeding both regions. The silty clay sediment properties likewise appear to be quite uniform across the entire Malta Plateau.

III. GEOACOUSTIC INVERSION USING THE ANGLE OF INTROMISSION

Measurement of the angle of intromission presents an opportunity to probe the sediment geoacoustic properties. In this section a simple but robust geoacoustic inversion method is described, then applied to the data. The resulting geoacoustic properties are compared with ground truth.

The angle of intromission, δ , is a function of the ratio of the bulk density, ρ , and velocity, c , contrasts at the interface and is given by

$$\cos \delta = (1 - (\rho_1 c_1 / \rho_2 c_2)^2)^{1/2} (1 - (\rho_1 / \rho_2)^2)^{-1/2}, \quad (1)$$

where the subscript refers to layer number. By measuring the reflection coefficient versus angle, two parameters can easily be extracted: the angle of intromission, δ , and the normal

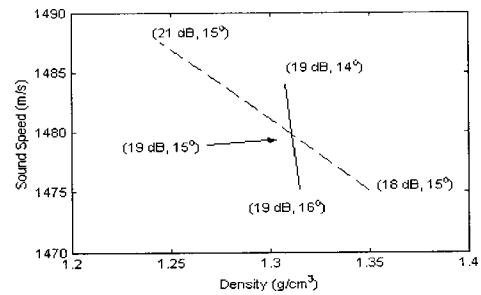


FIG. 5. The sensitivity between the sediment properties and the measured parameters ($-20 \log_{10} \nu, \delta$). The plot is a graphical solution of Eq. (3), showing that sediment sound speed.

incidence pressure reflection coefficient ν . Those two parameters (along with ρ_1 and c_1 in the water) are sufficient to unambiguously obtain the sediment density and sound speed from the following equations:

$$\rho_2 = \rho_1 (1 - 4\nu / (\cos \delta (1 + \nu))^2)^{-1/2}, \quad (2)$$

$$c_2 = \rho_1 c_1 / \rho_2 (1 + \nu) / (1 - \nu). \quad (3)$$

As with any inversion problem, it is important to understand the sensitivity of the solution (in this case sediment density and sound speed) to the input parameters. Figure 5 shows the sensitivity between the parameters δ and ν and the sediment properties ρ_2 and c_2 ; c_1 and ρ_1 are 1511 m/s and 1.092 g/cm³, which are the conditions of the Malta Plateau site. The solid line shows the effect on sediment properties from changes in δ with ν being fixed. The dashed line shows the effect on sediment properties from changes in ν with δ fixed. The salient aspect of the figure is that the sediment properties are very sensitive to the two measured parameters. In particular, note the high sensitivity to density, which is usually not a sensitive parameter in geoacoustic inversions. Measurable changes in δ (of order 1 degree) lead to velocity estimates within about ± 2 m/s and density estimates within $2e-3$ g/cm³. Measurable changes in ν (of order 2 dB) lead to

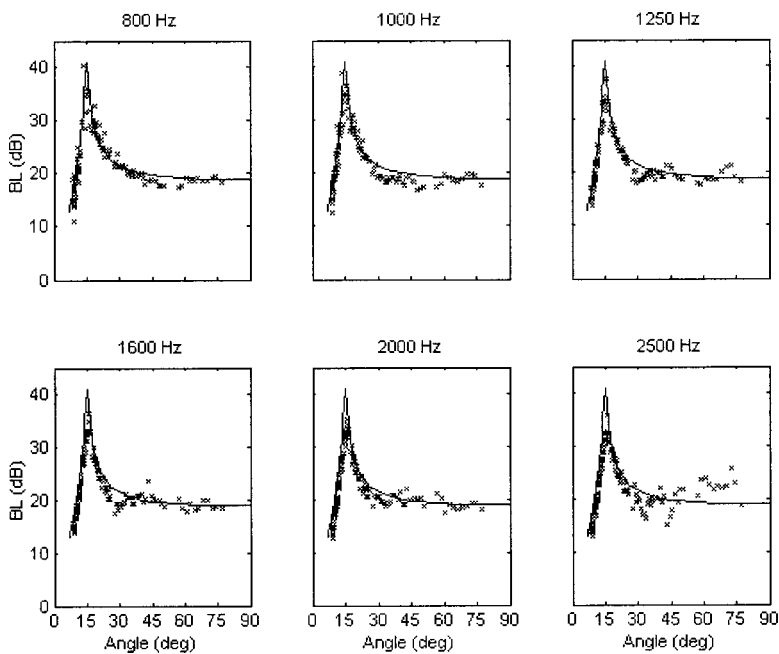


FIG. 6. Measured bottom reflection loss (x) from the first layer of sediment with the model results from the geoacoustic inversion (line).

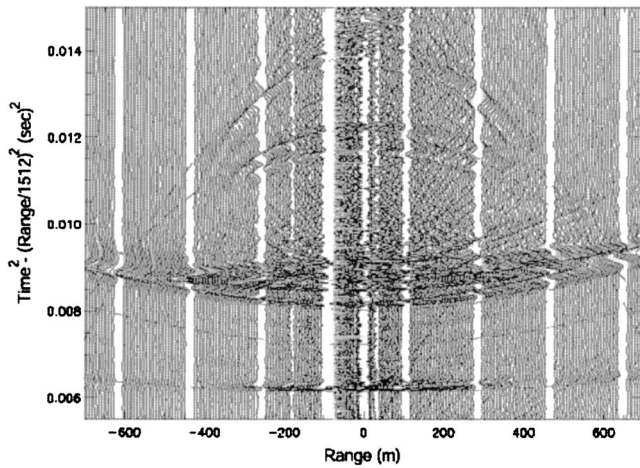


FIG. 7. Time domain data with horizon picks (dashed hyperbolae) on the Malta Plateau. The reflection from the silty-clay interface is the first arrival (at about 0.006 s^2). Note the decrease in amplitude and change of phase due to the angle of intromission at about 440-m range, corresponding to 15 degrees. The reflection data of Figs. 2 and 6 were calculated using a time window of $5e-4 \text{ s}^2$ around the silty-clay interface.

velocity estimates within about $\pm 4 \text{ m/s}$ and density estimates within $4e-2 \text{ g/cm}^3$.

It would be desirable to also estimate the sediment attenuation from the measurements. In a perfectly homogeneous medium, the magnitude of the reflection coefficient at δ could be used to estimate sediment attenuation. However, $|\mathbf{R}(\delta)|$ is also controlled by micro-scale layering, shear waves, scattering from volume inhomogeneities, and scattering from interface roughness.³ Since these effects almost certainly dominate $|\mathbf{R}(\delta)|$ (and are unknown), we do not attempt to extract the attenuation coefficient. However, fitting an effective attenuation to the data can provide an upper bound to the intrinsic sediment absorption.

IV. GEOACOUSTIC INVERSION RESULTS AND GROUND TRUTHING

By picking off the angle of intromission and the normal incidence reflection coefficient from the data of 15 degrees and 19 dB, respectively, Eqs. (2) and (3) immediately give the silty clay sound speed and density of 1480 m/s and 1.32 g/cm^3 . Model-to-data comparisons using those inputs (and a fitted effective attenuation of 0.07 dB/m/kHz) are shown in Fig. 6. The slight frequency dependence and the fluctuations around the model results are indicative of the presence of fine-scale (centimeter scale) layering, volume inhomogeneities, and/or surface roughness.⁴ Modeling indicates [see Appendix A of Holland (2002)] that fine-scale layering is the mechanism causing the frequency dependence in these data. The effective attenuation value is useful in defining the absolute upper bound for intrinsic attenuation, which for this sediment type is expected to be one order of magnitude smaller⁵ than 0.07 dB/m/kHz.

A. Ground truthing using wide angle reflection data

The time domain data provide the opportunity to “ground-truth” the sound speed estimates from the geoa-

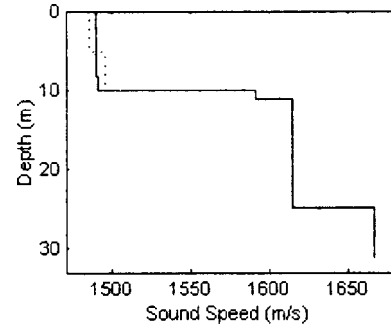


FIG. 8. Sediment sound speed from time domain analysis. The solid line represents interval velocities from the main reflecting horizons, the dashed line includes a very weak layer at 4.9 m subbottom in order to obtain a better estimate of the sound speed at the water–sediment interface.

coustic inversion method. The Bryan (1980) technique was used as described in Holland and Osler (2000).

Wide-angle reflection data and the associated hyperbolic picks (dashed lines) are shown in Fig. 7. Figure 8 provides the resulting interval velocity associated with main reflecting horizons (solid line). The average sound speed in the top 10 m is 1490 m/s. Using the 1.5 s^{-1} sound speed gradient observed in the core data (see Fig. 9) the interface sound speed of 1482.5 m/s agrees well with the intromission inversion of 1480 m/s.

Another way to estimate the sound speed gradient is to use the very weak reflecting horizons observed in the upper 10 m. A very weak horizon was found at 4.9 m subbottom and the solution obtained including that pick is shown in Fig. 8 in the dotted line. The average sound speed over the first 5 m was 1485 m/s, giving 1481 m/s at the water–sediment interface, essentially again identical to the value obtained from the angle of intromission analysis.

B. Ground truthing from core data

Sound speed measurements on cores (see Fig. 9) from this site could not be calibrated because (1) there was insufficient seawater above the core and (2) there was a multipath problem in the measurement system. Although the absolute values of the sound speed are not known, the data indicate the presence of a sound speed gradient, estimated at 1.5 s^{-1} (as shown in the dotted black line).

Figure 10 shows the nearest (see Fig. 3) high-quality core data. The sound speed and density from this core are

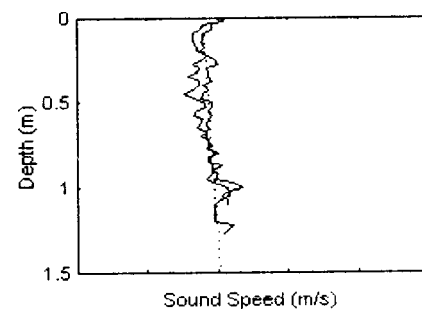


FIG. 9. Uncalibrated sound speed measurements from two gravity cores separated by about 60 m. The tick marks are at 10-m/s intervals and the dashed line is a fit to the data with a gradient of 1.5 s^{-1} .

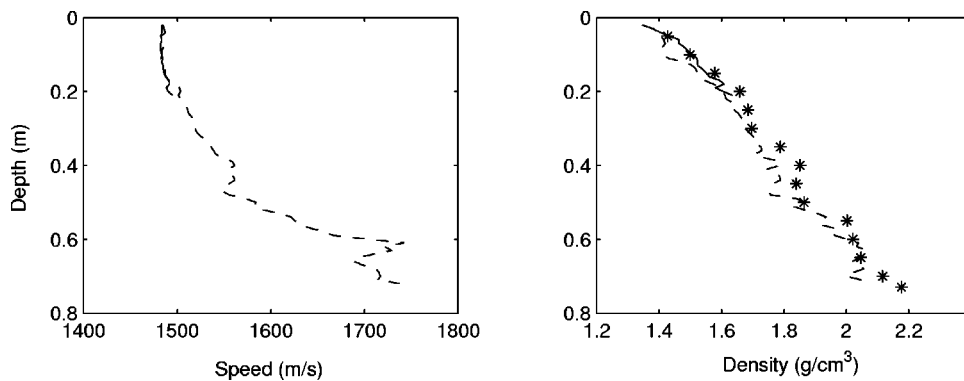


FIG. 10. Core analyses (solid and dashed lines) from the nearest high-quality samples. The asterisks were measured using standard laboratory methods as a crosscheck. The cores were separated by approximately 130 m.

1483 m/s and 1.346 g/cm^3 at the top of the core (2 cm depth). The expected errors in velocity and density measurements are approximately $\pm 2 \text{ m/s}$ and $\pm 0.013 \text{ g/cm}^3$. These values are in excellent agreement with the geoaoustic inversion results of 1480 m/s and 1.32 g/cm^3 . Thus, despite the spatial separation between this core and the acoustic measurements, there is evidence that the interface properties are uniform across scales of the entire plateau.

V. SUMMARY AND CONCLUSIONS

New seabed reflection measurements clearly show the phenomenon of the intromission angle. The measurement of this phenomenon opens several doors for probing sediment geoaoustics. A simple method was demonstrated by which to recover the sediment sound speed and bulk density. The sediment properties derived from this method agree well with those from independent measurements (wide angle reflection and cores). Initial indications show that the fine-grained sediments blanketing shallow water regions around the coastal region of Italy are surprisingly homogeneous.

Conducting the geoaoustic inversion over various frequency bands could be a powerful tool for examining frequency dependence of the material properties. Also, the unique “window” provided by the angle of intromission creates an opportunity to measure fine-scale geoaoustic fluctuations that are ordinarily impossible to measure via reflectivity but whose effects become measurable at the angle of intromission. The technique described is applicable to marine as well as riverine and lake sediments.

ACKNOWLEDGMENTS

The NATO SAACLANT Undersea Research Center and the Office of Naval Research supported this research. The captain, officers, crew, and the scientific crew aboard the NRV Alliance are also gratefully acknowledged, who contributed to the success of the data collection effort.

¹Christensen *et al.* indicate that the angle of intromission is 10 degrees, however, this is inconsistent with the observed 13–21-degree angular range. Furthermore, a 10-degree angle of intromission is also inconsistent with their estimate of a sound speed ratio of 0.974 (from the travel time difference analysis) which gives an estimated angle of intromission of about 14–16 degrees using a reasonable density ratio range of 1.3–1.4 g/cm^3 .

²The site in the Capraia basin described in Holland and Osler (2000) is in 150-m water depth and is in quite a different kind of sedimentary environment than that considered in this paper. In that environment there were a

series of random high-speed sediment layers close to the water–sediment interface so that isolation of the angle of intromission was not possible.

³There are yet other practical difficulties with trying to extract information at the angle of intromission. One is that it requires infinitely fine angular resolution. Yet another practical difficulty is that the small attenuations associated with these kinds of sediments require a very wide dynamic range in the data acquisition system in addition to a high source level and low noise.

⁴Sidescan and bottom video recordings show that the seafloor is very flat and featureless except for centimeter-scale holes from biologies. It is hypothesized that the fluctuations in the reflectivity data are caused by fine-scale layering and volume inhomogeneities. ν was chosen at the lowest frequency (800 Hz) where the effects of fine-scale layering/volume inhomogeneities are least significant.

⁵See, for example, Mitchell and Focke (1980), Frisk *et al.* (1981), and Holland and Neumann (1998, Fig. 8). Evidence is mounting that Hamilton’s (1980) attenuation prediction for fine-grained, high-porosity sediments (which in this case gives 0.065 dB/m/kHz) is far too high.

Bachman, R. T. (1985). “Acoustic and physical property relationships in marine sediments,” *J. Acoust. Soc. Am.* **78**, 616–621.

Bucker, H. P., Whitney, J. A., Yee, G. S., and Gardner, R. R. (1965). “Reflection of low frequency sonar signals from a smooth ocean bottom,” *J. Acoust. Soc. Am.* **37**, 1037–1051.

Bryan, G. M. (1980). “The hydrophone-pinger experiment,” *J. Acoust. Soc. Am.* **68**, 1403–1408.

Chapman, N. R. (1983). “Modeling ocean-bottom reflection loss measurements with the plant-wave reflection coefficient,” *J. Acoust. Soc. Am.* **73**, 1601–1607.

Christensen, R. E., Frank, J. A., and Geddes, W. H. (1975). “Low-frequency propagation via shallow refracted paths through deep ocean unconsolidated sediments,” *J. Acoust. Soc. Am.* **57**, 1421–1426.

Eller, A. I., and Gershfeld, D. A. (1985). “Low frequency acoustic response of shallow water ducts,” *J. Acoust. Soc. Am.* **78**, 622.

Frisk, G., Douthett, J., and Hayes, E. (1981). “Bottom interaction of low-frequency acoustic signals at small grazing angles in the deep ocean,” *J. Acoust. Soc. Am.* **69**, 84–94.

Hamilton, E. L. (1980). “Geoacoustic modeling of the seafloor,” *J. Acoust. Soc. Am.* **68**, 1313–1339.

Hermund, J. P. (1999). “Broad-band geoacoustic inversion in shallow water from waveguide impulse response. Measurements on a single hydrophone: theory and experimental results,” *IEEE J. Ocean. Eng.* **24**, 41–66.

Holland, C. W. (2002). “Shallow water coupled scattering and reflection measurements,” *IEEE J. Ocean. Eng.*, in press.

Holland, C. W., and Neumann, P. (1998). “Sub-bottom scattering: A modeling approach,” *J. Acoust. Soc. Am.* **104**, 1363–1373.

Holland, C. W., and Osler, J. (2000). “High resolution geoacoustic inversion in shallow water: A joint time and frequency domain technique,” *J. Acoust. Soc. Am.* **107**, 1263–1279.

Mitchell, S. K., and Focke, K. (1980). “New measurements of compressional wave attenuation in deep ocean sediments,” *J. Acoust. Soc. Am.* **67**, 1582–1589.

Baron Rayleigh (John William Strutt) (1896). *The Theory of Sounds*, 2nd ed.; republished (Dover, New York, 1945), Vol. II, p. 81.

Rubano, L. A. (1980). “Acoustic propagation in shallow water over a low-velocity bottom,” *J. Acoust. Soc. Am.* **67**, 1608–1613.

Winokur, R. S., and Bohn, J. (1968). “Sound reflection from a low-velocity bottom,” *J. Acoust. Soc. Am.* **44**, 1130–1138.

Application of an acoustic backscatter technique for characterizing the roughness of porous soil

Michael L. Oelze,^{a)} James M. Sabatier, and Richard Raspet
*National Center for Physical Acoustics and Department of Physics and Astronomy,
University of Mississippi, University, Mississippi 38677*

(Received 11 October 2001; revised 12 January 2002; accepted 18 January 2002)

An acoustic backscatter technique proposed by Oelze *et al.* [J. Acoust. Soc. Am. **109**, 1826–1832 (2001)] was used to characterize the roughness of porous soil surfaces. Roughness estimation errors are minimized when the effective flow resistivity of the porous soil is high, e.g., above 300 000 mks Rayls/m. Four soil plots were constructed by roughening soil with farming implements. Three plots were sealed using Saran powder dissolved in methyl ethyl ketone (MEK) and then covered to prevent further weathering. A fourth plot was left in the open and exposed to rainfall, which also acted to seal the surface and further change the roughness. In sealing the surface the effective flow resistivity of the surface was increased above 300 000 mks Rayls/m, which is typical for weathered agricultural surfaces. The roughness power spectra of the soil surfaces were measured by acoustic backscatter and alternatively by a laser profiler. Regression analysis was used to approximate each roughness power spectrum versus roughness wave number with a best-fit line. The best-fit line was used to calculate the rms height and the correlation length of the rough surface by integrating the approximate roughness power spectrum over a range of roughness wave number values. The range of roughness wave number values defines the roughness length scales used in the statistical calculations. High-roughness wave numbers correspond to smaller length scales of roughness and low-roughness wave numbers correspond to larger length scales of roughness. Over certain ranges of roughness wave number values the statistics from the acoustic backscatter and laser profiler measurements is in good agreement. However, as the low-cutoff roughness wave number is decreased and the high-cutoff roughness wave number is increased, agreement between the laser and acoustic techniques diminishes. © 2002 Acoustical Society of America.
[DOI: 10.1121/1.1459462]

PACS numbers: 43.20.Fn, 43.30.Hw [LLT]

I. INTRODUCTION

Quantifying the roughness of agricultural surfaces is important to determine the degree of local soil erosion through erosion models and evaluate the effects of tillage processes. Roughness is important to erosion control of agricultural surfaces since it impedes water run-off. If a fallow agricultural field is left with no roughness, rainfall can wash away the topsoil into local rivers and streams. Topsoil is vital to growing crops and once the topsoil is washed away, it is difficult if not impossible to replace. Roughness prevents the washing away of topsoil because the valleys and dips on a rough surface allow the water from rainfall to pool.

Much work has been done to examine the effects of roughness on soil erosion.^{1–4} For soil conservation use it is important to have the ability to rapidly quantify the roughness of agricultural lands. Relating the roughness statistics to erosion allows for farmers or other soil conservationists to keep fallow agricultural surfaces sufficiently roughened to prevent soil erosion.

Several instruments have been used in the past to obtain the surface roughness statistical characterizations. Contact-type microreliefmeters have been used to measure surface

roughness.^{5,6} Contact methods tend to be time-consuming, cumbersome, and have the great disadvantage of disturbing or damaging the soil surface. Römken and Wang first described the use of a noncontact, laser microreliefmeter at the Fourth Federal Interagency Sedimentation Conference.⁷ A subsequent paper described in detail the operation and performance of the laser microreliefmeter.⁸ The laser profiler has been used to study the relationship of roughness to soil erosion and profile evolution with increased rainfall and tillage.^{4,7,9} A diagram of the laser microreliefmeter is shown in Fig. 1.

The laser microreliefmeter effectively measures the surface statistics of rough soil surfaces without disturbing the soil surface. However, the equipment is expensive, somewhat bulky, and scan times can take several hours for a plot of 60×60 cm. An alternate noncontact method was proposed by Oelze *et al.* using acoustic backscatter techniques to measure surface roughness statistics.¹⁰ The goal was to find a quick and economical means to noninvasively evaluate surface roughness statistics.

Surface roughness characterization by the use of acoustic backscatter has been used for many years in the underwater acoustics community. A review of acoustic backscatter to characterize surface roughness in underwater sound is presented in Jackson *et al.*¹¹ Use of an acoustic backscatter technique to measure surface roughness offers the possibility of

^{a)}Current address: Bioacoustics Research Laboratory, Department of Electrical and Computer Engineering, University of Illinois at Urbana-Champaign, 405 North Mathews Avenue, Urbana, IL 61801.

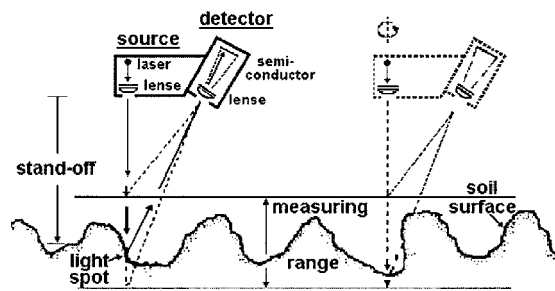


FIG. 1. Diagram of the laser microprofiler showing the laser and detector apparatus (Ref. 8).

an inexpensive and quick method of determining surface roughness statistics.

Acoustic backscatter techniques were proposed because of the limitations of acoustic forward-propagation techniques. Previous models of acoustic forward-propagation techniques did not allow the measurement of the roughness of porous soil independently from the effects of the pore properties of the soil. Acoustic forward-propagation techniques have been used invasively and noninvasively to measure the pore properties of soils. Invasive techniques, like the probe microphone technique, examine sound as it propagates through soil by measuring the magnitude and phase of sound.¹²⁻¹⁶ From the phase and magnitude of the sound as it propagates, the complex acoustic wave numbers for the porous material are obtained. Measured propagation wave numbers are related to pore properties of the soil.

Noninvasive techniques, such as the level difference technique, look at sound as it reflects from the porous surface.^{12,13,17,18} Impedance values measured by the reflection coefficient from the surface at different frequencies are used to estimate pore property values. The level difference technique was able to quantify the pore properties of porous soil surfaces over smooth, flat ground. Roughness of the soil surface complicated measurements of the pore properties by mimicking the impedance contribution of the pore properties.^{19,20} Previous models showed that separating the roughness effect from the pore property effect was impossible.^{20,21} Combining the probe microphone technique with the forward-scattering technique allowed the separation of pore property effects from roughness effects. The previous models used to describe the roughness effect on acoustic forward-propagation measurements combined vertical and horizontal roughness statistics into an effective ground impedance. According to the previous theory, however, horizontal (spatial) and vertical (height) roughness statistics could not be separately obtained with acoustic forward-propagation techniques.

Recent models of acoustic forward-propagation techniques describe the roughness with separable horizontal and vertical roughness parameters.^{22,23} Furthermore, the recent models suggest that the roughness parameters may be separable from the pore property effects of the soil. The recent acoustic forward-propagation models are sensitive to the porosity of the surface. Inversion of the new forward-propagation models to extract roughness parameters from pore properties (porosity) is possible but has not been done. If the measurement is more sensitive to porosity than to the

roughness, estimation of roughness parameters may be inaccurate. The recent models allow for separation of the roughness effects from the pore property effects, but the accurate estimation of these parameters using the model still needs to be tested.

The acoustic backscatter technique does not suffer from the same limitations as the acoustic-forward propagation techniques. Oelze *et al.* showed theoretically that acoustic backscatter could independently measure roughness from pore property effects in typical weathered agricultural surfaces.¹⁰ The acoustic backscatter also gives two independent parameters describing the roughness. The first parameter describes roughness on the vertical scales (rms height) and the other parameter describes the spatial distribution of roughness (correlation length of the roughness). Experiments were conducted that showed the sensitivity of acoustic backscatter to different roughness sizes and determined the rms height and correlation length statistics.²⁴

In this paper the results of further acoustic backscatter experiments are examined for their ability to accurately predict roughness statistics of typical weathered agricultural surfaces. The calculated roughness statistics are affected by the choice of roughness wave number range used. The low-cutoff roughness wave number determines the largest scales of roughness that will be incorporated in the statistical calculation. The high-roughness wave number limits the smallest roughness scales that will be included in the statistical calculations. Actual acoustic measurements are examined to determine the effects of low- and high-roughness wave number cutoff choices on the statistical calculation. Section II describes the acoustic backscatter and laser profiler devices and preparation of the experimental roughness plots. Section III describes the theory used to obtain the roughness statistics from the acoustic and laser measurements. Section IV lists the experimental results of measurements of rough surfaces by the acoustic backscatter and laser profiler technique and examines the choice of roughness wave number cutoff on the statistical calculations of the rms height and correlation length.

II. ACOUSTIC BACKSCATTER AND LASER PROFILER DEVICE

A. Acoustic backscatter device

Acoustic backscatter techniques relate measurements of the intensity of backscattered sound from a rough surface to models describing the surface properties. Figure 2 shows a typical experimental setup for an acoustic backscatter measurement from a rough surface. A transducer is positioned at some height, h , above a rough surface directed at a grazing angle, θ_g , towards the surface. The graze angle, θ_g , is measured from a plane parallel to the surface. A pulse or tone burst of sound is emitted from the transducer and propagates towards the surface. The transducer is operated in pulse/echo mode so that it is used not only as the transmitter but also as the receiver. The sound that scatters back towards the transducer is called the backscatter. When the size of the transducer aperture is large relative to the wavelength of sound, the sound emitted is in an acoustic beam. A beam enables the

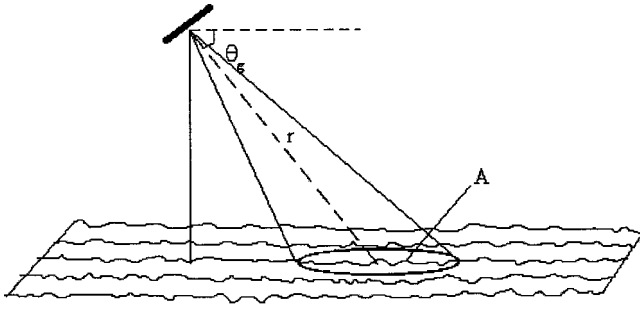


FIG. 2. Typical backscatter experimental setup with graze angle, θ_g , distance on transducer axis from transducer to surface, r , and area of ensounded surface, A .

sound to be localized to a specific spot on the surface. In Fig. 2, A is the area ensounded on the surface and is the projection of the acoustic beam on the surface.

Acoustic backscatter is measured in terms of the scatter strength, with units in decibels (dB). The backscatter strength is defined as²⁵

$$S_s = 10 \log(\sigma), \quad (1)$$

where σ is the backscattered cross section. The backscattered cross section is given by

$$\sigma = \frac{r^2 I_s}{I_0 A}, \quad (2)$$

where I_s is the intensity of the field scattered back towards the source, r is the axial distance from the source to the ensounded area, I_0 is the incident intensity, and A is the area of the ensounded surface.

When sound is incident on a rough soil surface with graze angle, θ_g , most of the sound is reflected away from the transducer at an angle, θ_g . If the graze angle is large, some of the sound will be received by the transducer beam. For very low graze angles, the transducer will receive none of the sound reflected from the surface. As shown in Fig. 3, a small portion of the sound is scattered from the roughness in all directions. The sound level of the source must be large enough so that the portion of sound scattered from the surface back to the transducer is detectable above the noise. The sound intensity level (SIL) is a decibel scale, and is defined as²⁶

$$\text{SIL} = 10 \log_{10} \frac{I_s}{I_{\text{ref}}}, \quad (3)$$

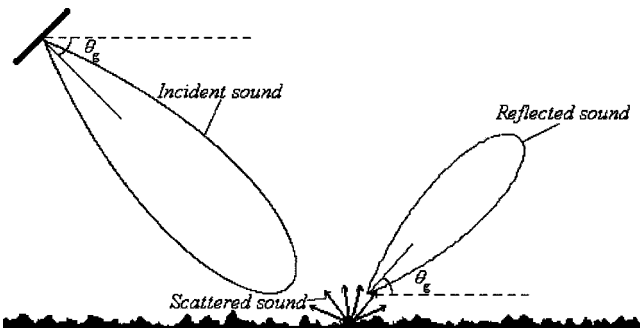


FIG. 3. Reflection and scattering of incident sound from a rough surface.

where I_s is the intensity of the sound source at 1 m and I_{ref} is a reference intensity for sound in air equal to 10^{-12} W/m^2 . Since the scattering returns are usually on the order of 20 to 30 dB less than the incident sound intensity level, it is necessary to have a source level at least 40 dB above the noise at the surface. Noise levels of sound outdoors are typically between 50–70 dB for the frequency ranges of 1–10 kHz, the frequencies used in the experiments. The source levels of transducers used for roughness characterization of porous soils outdoors should be at least 100 dB in order to discern the scattered signal.

The scattered intensities are measured and inserted into Eq. (2) to calculate the backscatter cross section. The effect of the equipment (i.e., the magnitude of the output and receiving sensitivity of the transducer) on the scattered returns is taken out by the substitution method. The same transducer used in the scattering experiment is used to measure the reflection of the pulse from a planar surface at normal incidence. The planar surface in this work was a large sheet of Plexiglas that was assumed to be a perfect reflector. The reflected pulse is used as a reference for the incident pulse. Since the same equipment and settings were used for the incident and scattered intensities, the effect of the equipment on the measured cross section is canceled out.

For the acoustic backscatter measurements taken on the four roughness plots, a capacitor style transducer with grooved backplate covered by Mylar film was used.²⁷ The transducer was circular, with a diameter of around 25 cm and a flat frequency response over the range of 1 to 10 kHz. The transducer was used in pulse/echo mode through a diode clamp over the frequency range of 1.5 to 10 kHz. Two- or three-cycle tone bursts were generated by an HP model 3314A function generator and amplified to the desired voltage (100–150 Vp-p) by means of a Khrone-Hite amplifier. A 200-V dc bias was placed on the transducer using a Heathkit model IP-2717A power supply. Backscatter signals were received by the same transducer and filtered and amplified by an SRS 650 filter. The resulting signals were displayed on an HP model 54540C oscilloscope and saved to a disk for post-processing.

For the measurements the transducer was mounted to a movable cart. The mounting bar could be adjusted to change the elevation of the transducer element with respect to the surface. The screw attaching the transducer to the mounting bar could adjust the graze angle of the transducer. Figure 4 shows a diagram of the cart used to mount the transducer. The cart was rolled down the length of a soil plot, allowing measurements to be taken at different points on the surface for averaging.

B. Laser profiler technique

The roughness of the soil plots were also measured by a laser profiler (see Fig. 1).⁸ The laser profiler has been used in the past to measure the roughness of soils. The laser profiler is a nonacoustic technique and is not affected by the pore properties of the soil.

The laser profiler works by focusing a laser beam on the rough surface. A lens attached to the laser box passes light to a detector that converts the light to a voltage. The higher up

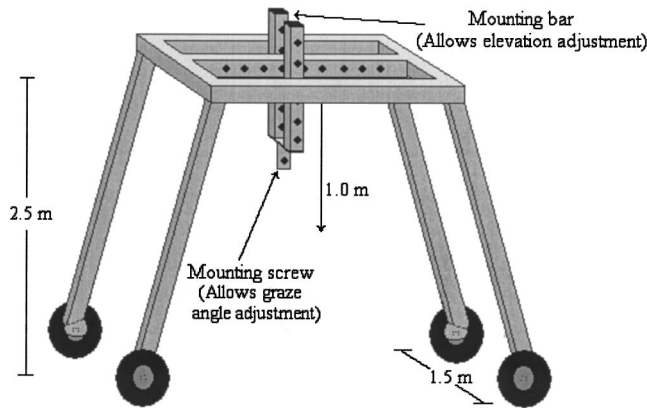


FIG. 4. The cart used to mount the transducers at various heights and graze angles.

the light appears on the detector screen, the lower the voltage, which in turn corresponds to a lower roughness height. The laser profiler works by converting the voltage level to a roughness height. For the detector used in the experiment, 1 volt corresponded to $\frac{1}{4}$ cm. Potential for errors occur with the laser profiler if the rough surface blocks the laser spot from the detector. The larger the roughness, the greater the potential for the roughness to block the view of the detector. Measurements with error due to rough surface blockage were not included in the data.

The laser profiler was mounted on a table situated on a metal cage that sat on tracks attached to an aluminum frame. Figure 5 shows a diagram of the laser profiler mount. The tracks allowed the laser profiler to translate in one horizontal direction. The table mount was attached to rails and a screw that went across the length of the cage. The screw was attached to a step motor that allowed for the laser/detector apparatus to translate in a horizontal direction perpendicular to the direction of the tracks. The aluminum frame sat on six legs that allowed for the level of the frame to be adjusted. Leveling is done in order to take out any slant that would be detected as long wavelength roughness.

Transects 60 cm in length were measured from the surface in the horizontal direction perpendicular to the tracks (x direction). Each transect was taken by recording the laser profiler readings at certain time intervals as the motor translated the profiler in the x direction. The motor was controlled by a computer program that read in the values obtained by the laser profiler. After a full translation in the x direction, the

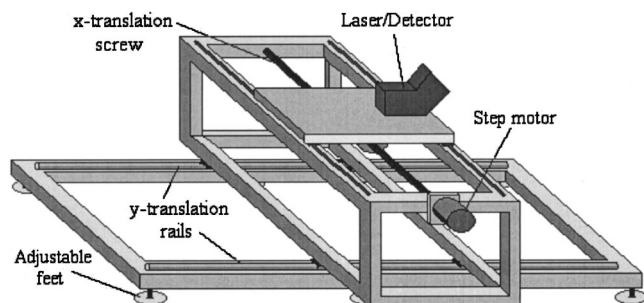


FIG. 5. Diagram of the laser profiler mount with adjustable feet for leveling and the rails and step motor/screw bar to translate the profiler in both x - and y directions.

laser profiler was then translated 3 mm in the y direction by physically moving the cage on the aluminum frame tracks forward by 3 mm. Once the cage and laser profiler were translated forward, the motor then translated the profiler in the x direction another full turn, 60 cm. The process was repeated until a profile with area of 60×60 cm was measured.

Data acquisition was accomplished by use of a PC, an HP 3478A multimeter, a GP-IB interface card and cable, and an optocator. The optocator delivers a dc voltage from the laser detector to the multimeter that in turn is sent to the computer through the GP-IB interface. The value measured by the multimeter is sent to the computer, which saves the value in a sequential array to the PC's hard drive. The spacing between each point is determined by the speed of the motor, i.e., the slower the motor the more points are obtained. The distance between each point can be calculated by dividing the total translated distance by the total number of recorded points. After measuring each transect, a matrix of $N_x \times N_y$ height values is obtained. This matrix or area profile, $h(x, y)$, can be broken into separate x and y transects.

From a height profile transect in the x - or y direction obtained by the laser profiler, the 1D power spectrum can be calculated through the equation

$$W(k) = \frac{1}{2\pi L} \left| \int_0^L h(x_i) e^{ikx_i} dx_i \right|^2, \quad (4)$$

where L is the length of the transect and x_i represents the 1D transect direction. The total 1D power spectrum is calculated by averaging the 1D power spectra from transects recorded in the x - and y directions. Averaging allows for the total 1D power spectrum to be smoothed and to decrease the effects of anomalous roughness.

If the surface is isotropic in the x - and y -directions, then the roughness power spectra from the x - and y -transects will have approximately the same form. For truly random rough surfaces, the assumption of isotropy will be true. In order to compare the total 1D power spectrum measured by the laser profiler with the 2D power spectrum obtained by the acoustic backscatter technique, the total 1D power spectrum is converted to a 2D power spectrum. Under the assumption of isotropy and that the roughness power spectrum for soil surfaces is a power law and fractal in nature, the 1D power spectrum can be related to the 2D power spectrum.¹⁰ Assuming a power-law form and fractal nature of the surface, then the 2D power spectrum is given by

$$W(k_x, k_y) = \frac{\beta}{(k_x^2 + k_y^2)^{\gamma/2}}, \quad (5)$$

where β is the 2D intercept and γ is the power-law exponent with the constraint $2 < \gamma < 4$. The 2D power spectrum intercept and exponent can be related to the intercept and exponent of the 1D power spectrum by integrating Eq. (5) over one variable. Integrating Eq. (5) over one variable gives²⁸

$$W(k)dk = \beta \frac{\sqrt{\pi}}{(2\pi)^{2-\gamma}} \frac{\Gamma\left(\frac{\gamma-1}{2}\right)}{\Gamma\left(\frac{\gamma}{2}\right)} k^{1-\gamma} dk. \quad (6)$$

Relating Eq. (6) to the power-law 1D roughness power spectrum

$$W(k)dk = \phi k^{-m} dk, \quad (7)$$

yields

$$\beta = \frac{(2\pi)^{\gamma-2} \phi \Gamma\left(\frac{\gamma}{2}\right)}{\sqrt{\pi} \Gamma\left(\frac{1-\gamma}{2}\right)} \quad \text{and} \quad m = \gamma - 1. \quad (8)$$

From a 1D power-law power spectrum that is isotropic, the approximate 2D roughness power spectrum can be obtained by converting the 1D intercept and power exponent into the 2D intercept and power exponent through Eq. (8).

C. Plot preparation

Acoustic backscatter experiments were conducted *in situ* on rough soil surfaces. The 1.5-m \times 4-m plots were constructed by breaking up the soil with various farming implements, i.e., a hoe and rake. Clods with radius up to 8 cm were present on the surfaces after preparation. The first three soil surfaces were coated with powder Saran dissolved in MEK to decrease the acoustic permeability, and then covered with wooden shelters to prevent further weathering. The three plots were made with different roughness sizes. The largest roughness-sized plot was made by randomly breaking up the ground with a hoe and rake. The medium-sized roughness plot was made the same way except that the clods were further broken down with the hoe and rake. The smallest roughness plot was constructed again by breaking up and smoothing clods with a hoe and then further smoothing with a rake. Random cross-sectional transects of the roughness plots are given in Fig. 6.

The fourth plot was constructed in a similar fashion to the medium-sized roughness plot. Figure 7 shows a random cross-sectional transect of the fourth roughness plot. Unlike the first three plots, the fourth plot was left open and exposed to a rainstorm. The rain served two purposes in that it further broke down the roughness clods and decreased the acoustic permeability (raised the effective flow resistivity). After being exposed to the rainstorm, the surface was covered to prevent further erosion while the experiment was being conducted. The flow resistivity was measured independently by a Leonard's apparatus and shown to be above 3×10^5 mks Rayls/m for each plot.²⁹

III. THEORY

In this work, the roughness of a soil surface is modeled as a smooth surface with small perturbations. The perturbation theory for a rough surface assumes the roughness and local slope is small compared to the acoustic wavelength. Acoustic backscatter from rough surfaces can be modeled

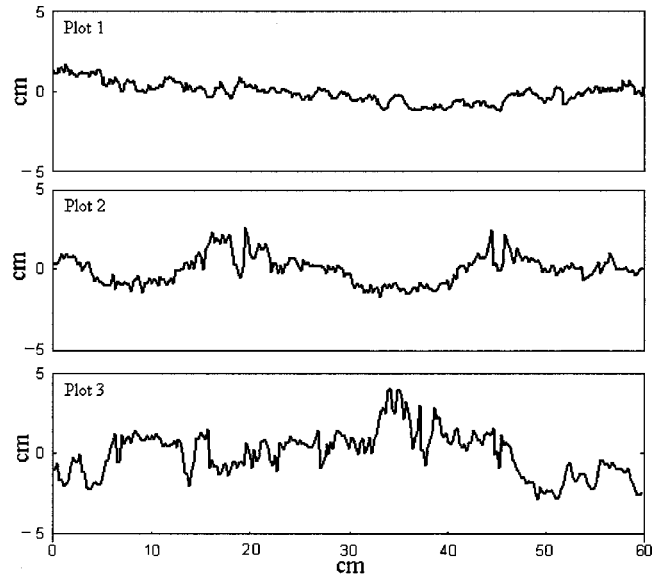


FIG. 6. Random transects of the three roughness soil plots coated with Saran powder dissolved in MEK as measured by the laser profiler.

using first-order perturbation theories at a rough fluid–fluid interface. First-order perturbation theory is valid under the constraints that³⁰

$$k_a h \sin \theta_g < 0.5. \quad (9)$$

where h is the rms height of the surface, k_a is the acoustic wave number, and θ_g is the graze angle. The first-order backscatter cross section is given by

$$\sigma_p(\theta_g) = 4k_a^4 \sin^4 \theta_g |Y(k_a, \theta_g)|^2 W(2k_a \cos \theta_g, 0), \quad (10)$$

where $W(2k_a \cos \theta_g, 0)$ is the 2D roughness power spectrum evaluated at the Bragg wave number.²⁸ The 2D roughness power spectrum, $W(\mathbf{K})$, represents the scattered power at a roughness wave number defined by $|\mathbf{K}| = 2k_a \cos \theta_g$ in Eq. (10). The middle term in Eq. (10)

$$Y(k_a, \theta_g) = \frac{(\rho - 1)^2 \cos^2 \theta_g + \rho^2 - \kappa^2}{[\rho \sin \theta_g + \sqrt{\kappa^2 - \cos^2 \theta_g}]^2}, \quad (11)$$

is a modified reflection coefficient, ρ is the ratio of the density of the surface material to the density of air, and κ is the ratio of rough surface wave numbers to air wave numbers.³¹ Substituting the complex wave number and complex density from Attenborough's analysis of rigid frame porous materials yields the modified reflection coefficient in terms of the surface impedance³²

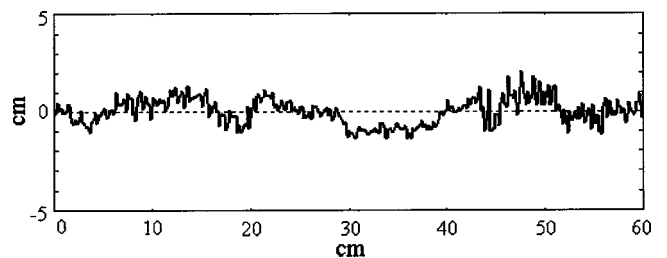


FIG. 7. Random transect of the roughness plot sealed by rainfall as measured by the laser profiler.

$$Y(k_a, \theta_g) = \frac{\left[Z - \frac{k_a}{k_b} \right]^2 \cos^2 \theta_g + Z^2 - 1}{\left[Z \sin \theta_g + \sqrt{1 - \left(\frac{k_a \cos \theta_g}{k_b} \right)^2} \right]^2}, \quad (12)$$

where k_b is the complex wave number of the porous soil surface and Z is the complex acoustic impedance of the soil surface.

The acoustic surface impedance and complex wave number describing a porous soil are functions of the frequency of sound and the pore properties of the soil surface. The acoustic impedance and complex wave number describe the interaction of sound with the soil. For very large surface impedance the sound will be perfectly reflected from the surface. For a finite surface impedance the amount of sound absorbed by the surface will depend on the frequency of sound and pore properties of the soil.

The pore properties that influence the propagation of sound into and through the soil are the porosity, tortuosity, and effective flow resistivity. The porosity is a unitless parameter and is the ratio of the open space in the soil relative to the overall soil volume. The tortuosity is the effective length of the pore per unit depth and describes the amount of crinkle and interconnectivity of the pore pathways in the soil.¹³ The effective flow resistivity measures the permeability of the soil to sound. A high flow resistivity means that the surface becomes more impenetrable to sound, or acoustically harder. The value of porosity is always less than 1, the tortuosity is less than 10, and the effective flow resistivity can range from 100 to 10×10^6 (mks Rayls/m). For acoustically harder surfaces (effective flow resistivity greater than 3×10^5 mks Rayls/m) the impedance is dominated by the flow resistivity term and the other pore properties have negligible effect. Furthermore, the response of the complex surface impedance to changes in flow resistivity for acoustically harder surfaces is very small.¹⁰

For acoustically harder surfaces, such as weathered agricultural surfaces, assuming a value for the effective flow resistivity of 1×10^6 yields the complex surface impedance and wave number with minimal error. The contribution of the modified reflection coefficient to the acoustic backscatter measurement can be calculated from the approximated values of the complex surface impedance and wave number. The 2D roughness power spectrum can then be determined at a particular frequency and graze angle by relating an acoustic backscatter strength measurement with the theoretical perturbation cross section, Eq. (10)

$$10 \log W(2k_a \cos \theta_g, 0) = S_s(k_a, \theta_g) - 10 \log [4k_a^4 \sin^4 \theta_g |Y(k_a, \theta_g)|^2]. \quad (13)$$

By varying the frequency of operation (acoustic wave number) and graze angle, different portions of the roughness power spectrum, $W(k_a, \theta_g)$, may be mapped out.

Random rough surfaces tend to have roughness power spectra with power-law dependence.^{33,34} Soil plots broken up with farming implements were also shown to have power-law dependence.¹⁰ When plotting a power spectrum that is a

power law in log-log space, the power spectrum is a line whose slope is the power-law exponent. All that is needed to describe a line is two points, which means that relatively few measurements are needed to approximate the roughness power spectrum. Assuming the roughness power spectrum will be a power law, the acoustic backscatter technique can give the approximate roughness power spectrum quickly with just a few measurements.

The acoustic backscatter technique measures the 2D power spectrum of an area of the rough surface. The power spectrum of an area of rough surface with height profile $h(x, y)$ is defined as

$$W(k_x, k_y) = |F\{h(x, y)\}|^2, \quad (14)$$

the magnitude squared of the Fourier transform of the height profile. The power spectrum leads to important statistical descriptions of the rough surface. From the 2D roughness power spectrum, two independent parameters describing both horizontal and vertical scales of roughness can be calculated. The rms height, which describes the variation of heights about some mean height, can be found by the equation

$$h_{\text{rms}}^2 = 2\pi \int_{k_L}^{k_H} W(k) k dk, \quad (15)$$

where k represents the magnitude of the two-dimensional wave vector, \mathbf{k} , and the factor of 2π comes from integrating over the unit circle. Likewise, the autocorrelation function for the surface profile, $h(x, y)$, describes the spatial arrangement of roughness on the surface, and is given by

$$C(x) = \frac{2\pi}{h_{\text{rms}}^2} \int_{k_L}^{k_H} W(k) e^{-ikx} k dk. \quad (16)$$

The statistical values are found by integrating the roughness power spectrum over the range of roughness wave number values k_L to k_H , the low- and high-cutoff roughness wave numbers, respectively. The correlation length, L_c , is defined as the length at which the correlation function drops to $1/e$ of its initial value. The correlation length value describes the spatial arrangement of roughness on the surface. A surface with roughness that changes rapidly, i.e., smaller clods, will have a shorter correlation length than a surface that has slow, undulating roughness.

The low- and high-cutoff roughness wave numbers are important to the statistical description of the roughness. The low-cutoff roughness wave number, k_L , is chosen based on the size of the surface being measured. If the low-cutoff roughness wave numbers were chosen corresponding to a wavelength of several kilometers, then the roughness of larger scale valleys and hills would be included in the roughness calculation. Likewise, a high-cutoff roughness wave number, k_H , should also be chosen. A high-cutoff roughness wave number of infinity corresponds to adding infinitesimal scaled roughness into the roughness statistics calculation. The higher the value for the high-cutoff roughness wave number that is chosen, the smaller the roughness scales that will be included in the statistical calculations. Cutoff wave numbers should be chosen with respect to the surface length being considered. For agricultural surfaces a low cutoff on

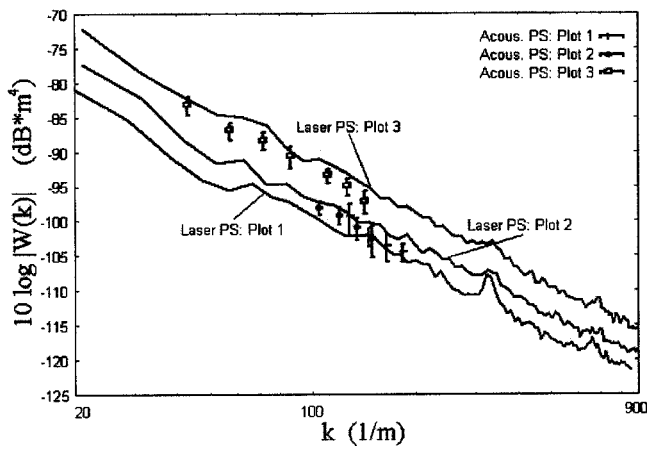


FIG. 8. Power spectra of rough surfaces coated with Saran powder dissolved in MEK as measured by laser profiler and the acoustic backscatter.

the scale of meters should be chosen. In this work, a low cutoff corresponding to 60 cm was chosen because it was the length of the transects measured by the laser profiler. The high-cutoff wave number was chosen corresponding to a wavelength of 3 mm, the approximate sampling length of the laser profiler. All roughness statistics should be referenced to the cutoff wave numbers used in calculation.³⁵ In order to compare roughness parameter estimations between the laser profiler and acoustic measurements, the same cutoff wave numbers were used for both.

IV. RESULTS

A. General results and interpretation

Measurements by the laser profiler showed that the slope and intercept parameters for the power spectrum in the x - and y -directions were approximately the same for each plot. The similarity between the 1D power spectra measured for the x - and y -directions showed that the random rough surfaces were approximately isotropic. Conversion of the 1D power spectra from the x - and y -transects to 2D power spectra could occur, according to Eq. (8), since the surfaces were isotropic.

Measurements of the roughness power spectra by the laser profiler and acoustic backscatter for the soil plots coated with Saran powder dissolved in MEK are shown in Fig. 8. The error bars on the acoustic data points represent

one standard deviation about the mean value of 15 acoustic measurements taken at different points on the rough soil surface. Acoustic points measured at different roughness wave number values were obtained by changing the frequency of the tone burst or by changing the graze angle.

The difference in the three soil plots can immediately be seen by viewing Fig. 8. The largest roughness plot has the greatest overall scattering power and the smaller-sized roughness plots can be seen in descending order of scattered power. Both the laser profiler and the acoustic backscatter measurements differentiate between the different-sized roughness plots. However, the acoustic technique appears to show less distinction between the two smallest roughness plots than the laser profiler technique.

The slope and intercept of the best-fit line to the three plots are listed in Table I. The intercept is defined where $k = 1 \text{ m}^{-1}$. Since the measurements from the laser profiler spanned a larger bandwidth of values, the slope and intercept values were also deduced from different bandwidths. The laser profiler slope and intercept values were obtained over a larger bandwidth than the acoustic values. From Table I it is seen that agreement between slope values from the laser profiler and acoustic backscatter becomes better when a greater number of acoustic data points is taken. The standard errors are also listed with the values of slope and intercept for the best-fit line and show that measurements of the laser profiler and acoustic backscatter are within error of each other.

Slope and intercept values of the roughness power spectrum of the rain-sealed soil plot (plot 4) were also measured and are given in Table I. The power spectra evaluated from measurements by the laser profiler and acoustic backscatter are seen in Fig. 9. The data points represent an average of 30 measurements taken at a particular roughness wave number from different points on the surface. The error bars represent one full standard deviation about the average value of 30 measurements.

From the slope and intercept values, the rms height and correlation length are calculated over the chosen roughness wave number range. The values for the rms height and correlation length are shown in Table II. The low-cutoff wave number used in these calculations was 10 1/m, corresponding to a wavelength of approximately 60 cm, the length of the transects measured by the laser profiler. The high-cutoff

TABLE I. Slope and intercept values of best-fit line to the laser profiler and acoustic data along with the standard errors.

	Slope			Intercept		
	Laser	Acoustic	% Diff.	Laser	Acoustic	% Diff.
Soil plots coated by Saran powder dissolved in MEK						
Plot 1	-2.41 ±0.027	-2.29 ±0.065	5.0	-51.2 ±0.69	-52.7 ±1.43	2.9
Plot 2	-2.42 ±0.019	-2.10 ±0.44	13.2	-48.0 ±0.495	-56.0 ±9.16	16.7
Plot 3	-2.58 ±0.017	-2.58 ±0.104	0.0	-39.7 ±0.45	-40.6 ±2.02	2.3
Soil plot sealed by rainfall						
	-2.20 ±0.039	-2.25 ±0.245	2.3	-54.4 ±0.88	-23.2 ±4.48	2.2

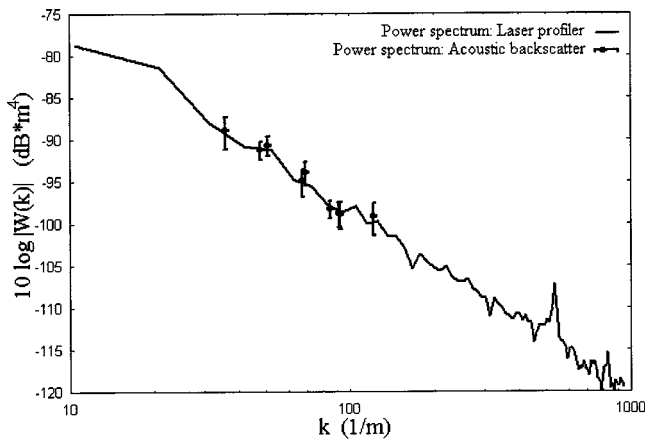


FIG. 9. Power spectra of rough surface sealed and weathered by rainfall as measured by the laser profiler and acoustic backscatter.

wave number was 2100 1/m, corresponding to a wavelength of approximately 3 mm, the sampling length of the laser profiler.

When the power spectrum is a power law over a range of roughness wave numbers, as is assumed for random rough surfaces, the correlation length does not depend on the intercept value but only on the slope (exponent) of the log of the power spectrum. The range of roughness wave numbers for which the power law is valid depends on the largest and smallest clod sizes existing on the rough surface. As the percent difference between the laser profiler and acoustic backscatter slope estimations increases, the percent difference between the correlation length also increases. Good estimates of the slope and intercept values are important to obtaining reliable statistical parameters describing the roughness of the surface. The slope and intercept values of the roughness power spectrum are determined by fitting a line to a series of data points. The fewer the data points, the greater the chance for error. The error inherent in any one measurement has more effect on the approximation when the number of data points is few as opposed to many. Fewer acoustic measurements were taken on the first two plots than on the last two plots. Comparing the values of the slope and intercept with the statistical values of rms height and correlation length shows that better results were obtained by taking more acoustic measurements. The results show that many acoustic data points (greater than 6) should be taken to map out an adequate portion of the roughness power spectrum, or else

TABLE II. rms height and correlation length statistics calculated from the slope and intercept values measured by the laser profiler and acoustic backscatter technique on the four roughness soil plots.

	rms height			Corr. length		
	From best-fit line			From best-fit line		
	Laser	Acoustic	% Diff	Laser	Acoustic	% Diff
Soil plots coated by Saran powder dissolved in MEK						
Plot 1	6.34 mm	6.85 mm	8.0	4.1 cm	3.2 cm	22
Plot 2	8.98 mm	7.2 mm	19.8	4.3 cm	1.8 cm	58
Plot 3	1.70 cm	1.55 cm	8.8	5.4 cm	5.4 cm	0.0
Soil plot sealed by rainfall						
	6.88 mm	7.06 mm	2.6	2.6 cm	2.9 cm	12

the estimations of correlation length for the rough surface will not be valid.

B. The effects of roughness wave number cutoff choice

A further consideration of the statistical characterization of the roughness from porous soil surfaces is the effect of choosing a cutoff roughness wave number. The low-cutoff roughness wave number is chosen to limit the largest roughness scales that will be included in the statistical calculations. The high-cutoff roughness wave number is chosen to limit the smallest scales of roughness that will be included in the statistical estimations. Jackson *et al.* have previously used a high-cutoff roughness wave number of infinity for measurements of the roughness statistics for underwater surfaces.¹¹ Likewise, their criterion for choosing the low-cutoff roughness wave number is that it be on the order of the lowest acoustic wave number used. In Jackson *et al.* the high-cutoff roughness wave number is specific and the low-cutoff roughness wave number is somewhat arbitrary and limited by the extent of the acoustic measurement.

An important question to examine is whether extrapolating the approximate power spectra beyond the roughness wave numbers measured is feasible or if calculations from the power spectra should be limited to measured values. The power-law assumption will hold over a particular range of frequencies up to a certain maximum clod size (low-roughness cutoff wave number). An immediate consequence is that extrapolating the data above the range where the power-law assumption holds would give inaccurate estimates of roughness. The power spectra are approximated by a finite number of data points over a specific range of roughness wave numbers from both the laser profiler measurements and acoustic backscatter measurements. The following paragraphs will examine the choice of different cutoff roughness wave numbers, both high and low, on the calculation of the surface roughness statistics, and the assumption that the power spectra are power law. First, the rms height and correlation length are calculated from the approximated power spectra for various roughness wave number ranges for both the laser profiler data and the acoustic backscatter data of plot 4 and compared. The first set of calculations is made to determine the magnitude of errors introduced by choosing various low- and high-cutoff roughness wave numbers. Second, the power spectra from plot 4 are approximated by limiting the analysis data over the acoustic measurements and the laser profiler measurements. By examining the roughness statistics from power spectra approximated over different wave number bandwidths, the assumption of a power-law form for the power spectrum is tested.

Examination of the effects of the choice of cutoff roughness wave numbers to the estimation of the rms height value is straightforward. Solving Eq. (15) for the case of a power law

$$W(\mathbf{k}) = \beta k^{-\gamma}, \quad (17)$$

yields

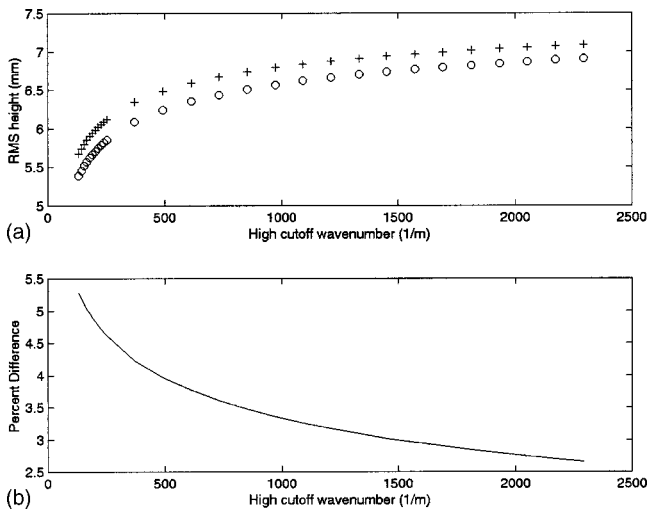


FIG. 10. (a) rms height values obtained from slope and intercept values measured for the fourth rough surface plot versus different values of high wave number cutoff (+—acoustic backscatter; O—laser profiler). (b) Percent difference between the rms height values obtained by the laser profiler and acoustic backscatter technique.

$$h_{\text{rms}}^2 = \frac{2\pi\beta(k_L^{-\gamma+2} - k_H^{-\gamma+2})}{\gamma - 2}. \quad (18)$$

Since the exponent variable, γ , is constrained between 2 and 4, the rms height is proportional to the inverse of the low- and high-cutoff roughness wave number values raised to some positive power. Changes in the high-cutoff roughness wave number have little to negligible effect on the value of the rms height as long as the high-cutoff value is large enough. Figure 10 shows the rms height calculation, as the high-cutoff roughness wave number is increased (low cutoff remains 10 l/m) for the slope and intercept values obtained from plot 4. The high-cutoff roughness wave numbers graphed start from 130 l/m (the limit of roughness wave numbers measured by the acoustic technique) and extrapolate beyond the high-roughness wave number measured by the laser profiler (2100 l/m). As the high-cutoff wave number value increases to infinity, the rms height asymptotically approaches a certain value, around 8 mm for plot 4. In Eq. (18) it can also be seen that in the limit of k_H goes to infinity, the k_H term vanishes from the calculation. It is always better to have a specific cutoff value as opposed to an arbitrary value. Since the value of the rms height does not appear to change much as the high-cutoff roughness wave number becomes large and the value asymptotically approaches a specific value, the statistical measurement can be standardized by assuming the value for the high cutoff to be infinity.

Changes in the low-cutoff roughness wave number will have a more dramatic effect on the rms height value. Decreasing the low-cutoff wave number value will increase the value of the rms height while increasing the value of the low cutoff will decrease the value of the rms height. Decreasing the low-cutoff roughness wave number is the same as including larger scales of roughness in the statistical calculation. Figure 11 shows the effect of decreasing the low-cutoff roughness wave number (high cutoff remains 2100 l/m). The smaller the low-cutoff value is, the larger the rms height

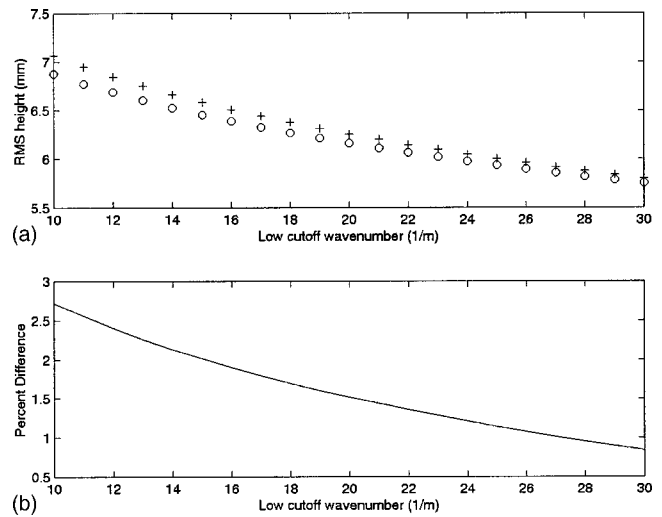


FIG. 11. (a) rms height values obtained from slope and intercept values measured for the fourth rough surface plot versus different values of low wave number cutoff (+—acoustic backscatter; O—laser profiler). (b) Percent difference between the rms height values obtained by the laser profiler and acoustic backscatter technique.

value estimation and the larger the percent difference between values obtained by the acoustic backscatter method and the laser profiler method. Choosing the low-cutoff roughness wave number based on the lowest wave number values measured by the laser profiler and acoustic backscatter techniques (about 10 l/m and 30 l/m, respectively) shows an increase of 20% in the rms height. As the low-cutoff roughness wave number decreases the rms height does not asymptotically approach a particular value. No absolute low-cutoff value can be chosen, but rather the low-cutoff roughness wave number should be chosen based on the lowest roughness wave number obtained by the measurement technique. If the power-law assumption is seen to break down above the lowest roughness wave number measured, a cutoff should be chosen before the power-law assumption broke down.

Similar effects for the choice of high- and low-roughness wave number cutoff can be seen for the calculation of the correlation length of the rough surface. Figure 12 shows a graph of the correlation length versus the changing high-roughness wave number cutoff (low cutoff remains 10 l/m). The percent differences between the laser profiler and acoustic backscatter values are also shown. As the high-cutoff roughness wave number is increased, smaller scales of roughness are included in the overall statistical calculation. By lining up the rough surface profile with itself, the inclusion of smaller scales of roughness means that the surface would become more uncorrelated at a shorter distance. Figure 12 shows the effect of decreasing the correlation length by including smaller scales of roughness. The absolute differences between the acoustic backscatter and laser profiler values do not change much by increasing the high-roughness wave number cutoff. However, since the overall correlation length becomes less with the inclusion of smaller scales of roughness, the relative percent difference increases significantly. As the high-cutoff roughness wave number is increased to infinity, the correlation lengths appear to asymp-

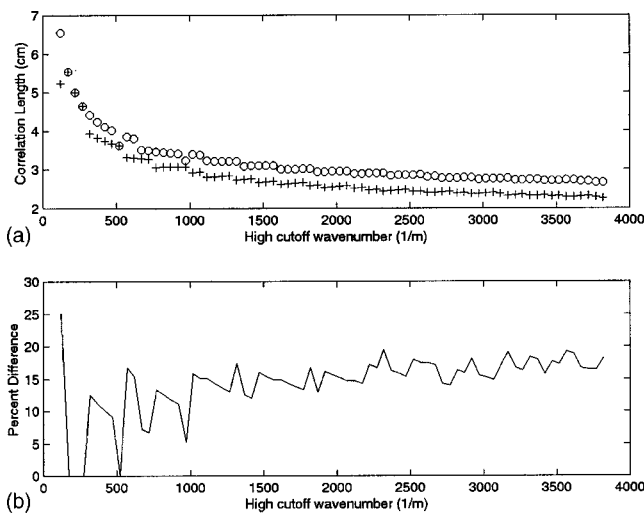


FIG. 12. (a) Correlation length values obtained from slope and intercept values measured for the fourth rough surface plot versus different values of high wave number cutoff (+—acoustic backscatter; O—laser profiler). (b) Percent difference between the correlation length values obtained by the laser profiler and acoustic backscatter technique.

totically approach a certain value. Furthermore, since the absolute difference between the acoustic and laser profiler values for correlation length remains small, choosing the high cutoff at infinity for the correlation length statistic is preferable.

Examination of the effects of the low-cutoff roughness wave number choice on the estimation of the correlation length shows the opposite trend as the effect of the high-cutoff choice. Figure 13 shows the effect of changing the low-cutoff roughness wave number (high cutoff remains 2100 l/m) on the correlation length. The percent differences between the laser profiler and acoustic backscatter values are also shown. As the low-cutoff roughness wave number is decreased, larger roughness scales are incorporated into the statistical calculation. The low-cutoff roughness wave number going from 30 l/m to 10 l/m means that the area of rough surface would increase from a 20- \times 20-cm plot to a 60- \times 60-cm plot. The effect of correlating a longer profile that includes larger scales of roughness with itself is to increase

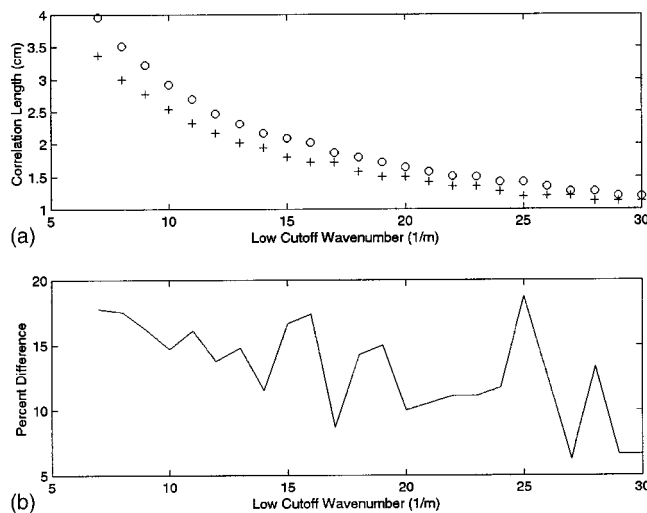


FIG. 13. (a) Correlation length values obtained from slope and intercept values measured for the fourth rough surface plot versus different values of low wave number cutoff (+—acoustic backscatter; O—laser profiler). (b) Percent difference between the correlation length values obtained by the laser profiler and acoustic backscatter technique.

the distance at which the profile becomes uncorrelated with itself. As the low-cutoff roughness wave number gets smaller, the correlation length becomes large. The absolute error between estimates made by the laser profiler and the acoustic backscatter technique increases dramatically, as does the relative percent difference. In going from a low-cutoff value of 30 l/m to 10 l/m, the correlation length increases by almost 150%. The dramatic increase in correlation length value with decreasing low-cutoff choice means that the choice of low-cutoff value should not extrapolate far beyond the actual measured roughness wave numbers.

The effects of the choice of low- and high-cutoff roughness wave numbers appear to follow a general trend for the case examined. Table III shows the values of rms height and correlation length for plot 4 using specific values for the low- and high-cutoff roughness wave numbers. Values for slope and intercept were also obtained for the laser profiler data of plot 4 using only the roughness wave number bandwidth measured by the acoustic backscatter technique (30 l/m to

TABLE III. rms height and correlation length values for plot 4 with different values of high and low cutoff roughness wave number.

	Cutoff		% difference	Corr. length	% difference
	wave number	rms height			
(1) Acoustic technique	lo—10 l/m	6.88	(1) & (2)=1	2.9	(1) & (2)=11.9
(2) Laser profiler (BW—A) ^a		6.95	(1) & (3)=2.5	3.29	(1) & (3)=11.5
(3) Laser profiler (BW—L) ^b	hi—2100 l/m	7.06	(2) & (3)=1.6	2.6	(2) & (3)=26.5
(1) Acoustic technique	lo—10 l/m	8.23	(1) & (2)=5.5	1.89	(1) & (2)=21.3
(2) Laser profiler (BW—A)		7.8	(1) & (3)=3	2.4	(1) & (3)=39.0
(3) Laser profiler (BW—L)	hi— ∞	8.48	(2) & (3)=8	1.36	(2) & (3)=76.5
(1) Acoustic technique	lo—30 l/m	3.97	(1) & (2)=1	3.93	(1) & (2)=0.0
(2) Laser profiler (BW—A)		3.93	(1) & (3)=3.7	3.93	(1) & (3)=0.0
(3) Laser profiler (BW—L)	hi—130 l/m	3.83	(2) & (3)=2.6	3.93	(2) & (3)=0.0
(1) Acoustic technique	lo—30 l/m	7.2	(1) & (2)=9	0.65	(1) & (2)=21.7
(2) Laser profiler (BW—A)		6.6	(1) & (3)=5.3	0.83	(1) & (3)=38.3
(3) Laser profiler (BW—L)	hi— ∞	7.6	(2) & (3)=13	0.47	(2) & (3)=76.6

^aBW—A= values obtained from slope and intercept estimated over acoustic measurement bandwidth.

^bBW—L= values obtained from slope and intercept estimated over laser profiler measurement bandwidth.

130 l/m). Using the acoustic backscatter bandwidth (BW—A) of roughness wave numbers yielded a slope and intercept for the laser profiler power spectrum of -2.3 ± 0.11 and -52.4 ± 2.15 , respectively. Table III shows that the rms height and correlation length values obtained from the laser profiler power spectrum (BW—A) do not give better agreement to the acoustic measurements than the values obtained using the power spectrum approximation from the full laser bandwidth (BW—L). If the power spectrum deviates from the power-law form outside of a particular bandwidth, comparing results obtained from two different analysis bandwidths should yield significantly different results. The fact that the roughness statistics from the laser profiler data is in good agreement between the narrowly defined bandwidth (BW—A) and the larger bandwidth (BW—L) show the power law is a good approximation to the power spectrum for the rough surface.

A comparison of correlation length values using different low-and high-cutoff roughness wave numbers corresponding to the laser profiler sampling and the wave number ranges corresponding to the acoustic measurements seems to indicate the latter gives better estimates. However, comparisons of the table values with Fig. 12 show that on average the absolute difference remains the same. Overall, choosing cutoff ranges as sampled by the laser profiler and the acoustic technique does not yield better agreement. The percent difference between the laser profiler and acoustic backscatter technique for the rms height does not change much for choice of high-cutoff value of infinity. The correlation length has a larger percent difference for high cutoff of infinity but a small absolute difference. Extrapolating the wave number range to infinity for the high-cutoff value is acceptable since it removes the arbitrariness of the choice without sacrificing a proper description of the surface by the roughness statistics.

When the cutoff wave numbers are chosen such that they are an extrapolation far beyond the maximum length of the sampled area (decreased low-cutoff value), the reliability of the estimation decreases. The percent difference between the values estimated by the acoustic backscatter technique and the laser profiler technique increases dramatically as the low-cutoff roughness wave number is decreased. Minor differences in the calculated best-fit slope and intercept propagate into large errors at the lower roughness wave numbers. Special care needs to be taken when choosing the low-cutoff roughness wave number for estimating the roughness statistics. In order to decrease the error introduced into the estimation of roughness statistics for a surface, the low-cutoff roughness wave number should not be chosen far beyond the lowest roughness wave number actually sampled by the measurement technique.

The construction of the rough surfaces explains the need to limit the low-cutoff value to the measured ranges. The rough surface plots were constructed by breaking the soil into large clods. These larger clods were further broken down into smaller and smaller clods, depending on the roughness sizes desired for a particular plot. It has been noted by Kolmogorov that the breaking of particles into smaller and smaller particles yields a fractal-like structure.³⁶

In the case of a rough surface this means similar roughness on all scales. The power-law form of the power spectrum describes the fractal behavior of the rough surface. Only the smallest-sized clods that are broken off from larger clods limit the smallest scales of roughness (high-roughness wave numbers). The largest clods initially used to construct the rough surface limit the largest scales of roughness (low-roughness wave numbers). Therefore, it is reasonable to assume that the power-law structure of the rough surface would extend to infinitely high-roughness wave numbers but would not extend to infinitesimally small-roughness wave numbers. The roughness power spectrum will begin to deviate from the power-law form as the roughness wave number is sampled below the maximum clod size. The low-cutoff roughness wave number should be chosen at the point of deviation if sampled by the measurement. If the deviation from the power law is not seen in the roughness wave numbers sampled, the lowest sampled wave number should be chosen for the cutoff. Any expansion below the minimum sampled roughness wave number may give erroneous statistical results since the power-law form of the roughness power spectrum may not hold far below the sampled roughness wave numbers.

V. SUMMARY AND CONCLUSION

Theory that was previously developed to measure the roughness of porous soil surfaces from acoustic backscatter was tested through experiments.¹⁰ Four soil plots were constructed by simple farming implements. The first three plots were constructed with varying degrees of roughness and sealed with Saran powder dissolved in MEK. The fourth plot was constructed and left out in the elements (rain) for weathering. The four plots were created to mimic the kind of soil surfaces one might expect to find on real agricultural lands.

The rms height and the correlation length of rough soil surfaces were estimated by measuring the roughness power spectra of the surfaces through acoustic backscatter. The rms height describes roughness on vertical scales and the correlation length describes the spatial arrangement of the roughness on the surface. The results of the acoustic backscatter technique were then compared with measurements made by a laser profiler. Good agreement was obtained between the acoustic backscatter technique and the laser profiler technique. Both techniques were able to distinguish between surfaces with different-sized roughness.

Calculation of the roughness statistics, rms height, and correlation length is done by integrating the roughness power spectrum, approximated as a power law, over a range of roughness wave numbers. The high-cutoff roughness wave number describes the smallest sampling length used in the estimation of the roughness statistics. The low-cutoff roughness wave number corresponds to the overall length of the plot used in the statistical calculation. Good agreement was found between the laser profiler and acoustic backscatter when the low-cutoff roughness wave number was chosen to correspond to the length of 60 cm and the high-cutoff roughness wave number was chosen to correspond to a sampling length of 3 mm. The laser profiler measured the surface pro-

file in transects of length 60 cm with an average sampling distance of about 3 mm between measurements.

The roughness power spectra were calculated from the profile transects measured by the laser profiler. Different points on the roughness power spectra were also mapped out by the acoustic backscatter technique for each surface. From these data values, the roughness power spectra were approximated as a power law for both the acoustic technique and the laser profiler technique. Approximating the roughness power spectra as a power law enabled the values of the roughness power spectra to be extrapolated beyond the measured values. Examination of the effects of including different roughness wave number ranges on the roughness statistics was made by choosing different low- and high-cutoff roughness wave number values. The percent difference between the laser profiler and acoustic backscatter values for rms height and correlation length increased as the low- and high-cutoff roughness wave numbers were expanded. A dramatic increase in the percent difference in values for rms height and correlation length was seen as the low-cutoff roughness wave number was decreased. In making estimates of roughness statistics for a surface it is important to choose the appropriate roughness scales to incorporate in the final calculation. Especially important is not to extrapolate the low-cutoff roughness wave number far below the actual sampled values. Using a low-cutoff roughness wave number corresponding to a length of 3 m when the maximum length sampled was only 50 cm may lead to large errors in the estimation of the roughness statistics. In most cases, a high-cutoff roughness wave number of infinity (no high-cutoff value) can be chosen since the roughness statistics approaches a specific value as the high-cutoff value approaches infinity. Choosing the high-cutoff value to be infinity gives uniqueness to the statistics (the asymptotic value at infinity) and provides a standard for the statistical description. Examination of the low- and high-cutoff roughness wave numbers values shows the importance of describing the surface with roughness statistics referenced to the incorporated wave number ranges.

ACKNOWLEDGMENTS

This research was supported by grants from the USDA through the National Sedimentation Laboratory. Thanks to Matt Römken and Jine Wang for assistance with the laser profiler. Thanks to Matt Römken, Craig Hickey, Jim Chambers, and Keith Attenborough for their helpful discussions on roughness of porous soils.

- ¹A. R. Dexter, "Effect of rainfall on the surface micro-relief of tilled soil," *J. Terramech.* **14**(1), 11–22 (1977).
- ²J. K. Mitchell and B. A. Jones, "Micro-relief surface depression storage: Analysis of models to describe the depth-storage function," *Water Resour. Bull.* **12**(6), 1205–1222 (1976).
- ³J. K. Mitchell and B. A. Jones, "Micro-relief surface depression storage: Changes during rainfall events and their application to rainfall-runoff models," *Water Resour. Bull.* **14**(4), 777–802 (1978).
- ⁴M. J. M. Römken and J. Y. Wang, "Soil roughness changes from rainfall," *Trans. ASAE* **30**(1), 101–107 (1987).
- ⁵J. K. Radke, M. A. Otterby, R. A. Young, and C. A. Onstad, "A micro-processor automated rillmeter," *Trans. ASAE* **24**(2), 401–404, 408 (1981).

- ⁶T. H. Podmore and L. F. Huggins, "An automated profile meter for surface roughness measurements," *Trans. ASAE* **24**(3), 663–665, 669 (1981).
- ⁷M. J. M. Römken and J. Y. Wang, "Sediment redistribution by raindrop impact," *Proceedings of the Fourth Federal Interagency Sedimentation Conference*, **1**(3), pp. 10–17, Las Vegas, NV (1986).
- ⁸M. J. M. Römken, J. Y. Wang, and R. W. Darden, "A laser microrelief-meter," *Trans. ASAE* **31**(2), 408–413 (1988).
- ⁹M. J. M. Römken and J. Y. Wang, "Effect of tillage on surface roughness," *Trans. ASAE* **29**(2), 429–433 (1986).
- ¹⁰M. L. Oelze, J. M. Sabatier, and R. Raspet, "Roughness characterization of porous soil with acoustic backscatter," *J. Acoust. Soc. Am.* **109**, 1826–1832 (2001).
- ¹¹D. R. Jackson, D. P. Winebrenner, and A. Ishimaru, "Application of the composite roughness model to high-frequency bottom backscattering," *J. Acoust. Soc. Am.* **79**, 1410–1422 (1986).
- ¹²H. M. Hess, K. Attenborough, and N. W. Heap, "Ground characterization by short-range propagation measurements," *J. Acoust. Soc. Am.* **87**, 1975–1986 (1990).
- ¹³J. M. Sabatier, H. Hess, W. P. Arnott, K. Attenborough, and M. J. M. Römken, "In situ measurements of soil physical properties by acoustical techniques," *Soil Sci. Soc. Am. J.* **54**, 68–72 (1990).
- ¹⁴K. Attenborough, J. M. Sabatier, H. E. Bass, and L. N. Bolen, "The acoustical transfer function at the surface of a layered poroelastic soil," *J. Acoust. Soc. Am.* **79**, 1353–1358 (1986).
- ¹⁵H. M. Moore and K. Attenborough, "Acoustic determination of air-filled porosity and relative air permeability of soils," *J. Soil Sci.* **43**, 211–228 (1992).
- ¹⁶J. M. Sabatier, D. C. Sokol, C. K. Fredrickson, M. J. M. Römken, E. H. Grissinger, and J. C. Shipp, "Probe microphone instrumentation of determining soil physical properties: Testing in model porous materials," *Soil Tech.* **8**, 259–274 (1996).
- ¹⁷C. Glaretas, "A new method for measuring the acoustic impedance of the ground," Ph.D. thesis, Pennsylvania State University, PA (1981).
- ¹⁸K. Attenborough, S. I. Hayek, and J. M. Lawther, "Propagation of sound above a porous half space," *J. Acoust. Soc. Am.* **68**, 1493–1501 (1980).
- ¹⁹K. Attenborough, "Review of ground effects on outdoor sound propagation from continuous broadband sources," *Appl. Acoust.* **24**, 289–319 (1988).
- ²⁰K. Attenborough and S. Taherzadeh, "Propagation from a point source over a rough finite impedance boundary," *J. Acoust. Soc. Am.* **98**, 1717–1722 (1995).
- ²¹J. P. Chambers, R. Raspet, and J. M. Sabatier, "Incorporating the effects of roughness in outdoor sound propagation models," in *Proceedings of Noise-Con '96* (Conference on Noise Control Engineering, Seattle) (1996), pp. 905–910.
- ²²P. Boulanger, K. Attenborough, S. Taherzadeh, T. Waters-Fuller, and K. M. Li, "Ground effect over hard rough surfaces," *J. Acoust. Soc. Am.* **104**, 1474–1482 (1998).
- ²³K. Attenborough and T. Waters-Fuller, "Effective impedance of rough porous ground surfaces," *J. Acoust. Soc. Am.* **108**, 949–956 (2000).
- ²⁴M. L. Oelze, J. M. Sabatier, and R. Raspet, "Roughness measurements of soil surfaces by the laser microreliefmeter and acoustic backscatter," *Soil Sci. Soc. Am. J.* (submitted).
- ²⁵R. J. Urick, *Principles of Underwater Sound* (McGraw-Hill, New York, 1983).
- ²⁶L. E. Kinsler, A. R. Frey, A. B. Coppens, and J. V. Sanders, *Fundamentals of Acoustics* (Wiley, New York, 1982).
- ²⁷F. D. Shields, H. E. Bass, and L. N. Bolen, "Tube method of sound-absorption measurement extended to frequencies far above cutoff," *J. Acoust. Soc. Am.* **62**, 346–353 (1977).
- ²⁸D. R. Jackson, K. B. Briggs, K. L. Williams, and M. D. Richardson, "Tests of models for high-frequency seafloor backscatter," *IEEE J. Ocean. Eng.* **21**(4), 458–470 (1996).
- ²⁹R. W. Leonard, "Simplified flow resistance measurements," *J. Acoust. Soc. Am.* **17**, 240–241 (1946).
- ³⁰A. Ishimaru, *Wave Propagation and Scattering in Random Media* (Academic, New York, 1978), Vol. 2.
- ³¹E. Y. T. Kuo, "Wave scattering and transmission at irregular surfaces," *J. Acoust. Soc. Am.* **36**, 2135–2142 (1964).
- ³²K. Attenborough, "Acoustical characteristics of rigid fibrous absorbent and granular materials," *J. Acoust. Soc. Am.* **73**, 785–799 (1983).

- ³³K. B. Briggs, "Microtopographical roughness of shallow-water continental shelves," *IEEE J. Ocean. Eng.* **14**(4), 360–367 (1989).
- ³⁴C. G. Fox and D. E. Hayes, "Quantitative methods for analyzing the roughness of the sea bottom," *Rev. Geophys.* **23**, 1–48 (1985).
- ³⁵J. M. Bennett and L. Mattson, *Introduction to Surface Roughness and Scattering* (Opt. Soc. Am., Washington, D.C., 1989).
- ³⁶A. N. Kolmogorov, "On the logarithmic normal distribution rules of dimensions of particles by grinding," *Mathematika* **31**, 99–101 (1971).

Theoretical and experimental examination of near-field acoustic levitation

Hideyuki Nomura^{a)} and Tomoo Kamakura

The University of Electro-Communications 1-5-1, Chofugaoka, Chofu-shi 182-8585, Japan

Kazuhisa Matsuda

Koganei Technical High School 6-8-9, Honmachi, Koganei-shi 184-8551, Japan

(Received 5 February 2001; accepted for publication 3 January 2002)

A planar object can be levitated stably close to a piston sound source by making use of acoustic radiation pressure. This phenomenon is called near-field acoustic levitation [Y. Hashimoto *et al.*, J. Acoust. Soc. Am. **100**, 2057–2061 (1996)]. In the present article, the levitation distance is predicted theoretically by numerically solving basic equations in a compressible viscous fluid subject to the appropriate initial and boundary conditions. Additionally, experiments are carried out using a 19.5-kHz piston source with a 40-mm aperture and various aluminum disks of different sizes. The measured levitation distance agrees well with the theory, which is different from a conventional theory, and the levitation distance is not inversely proportional to the square root of the surface density of the levitated disk in a strict sense. © 2002 Acoustical Society of America.

[DOI: 10.1121/1.1453452]

PACS numbers: 43.25.Qp, 43.25.Uv [MFH]

I. INTRODUCTION

In 1975, Whymark reported that a brass planar disk of 50 mm in diameter and 0.5 mm in thickness was levitated extremely close to a 74-mm-diameter piston source that was driven harmonically at a frequency of 20 kHz.¹ In his experiment, the disk itself acted as a wave reflector. Recently, Hashimoto *et al.* applied this levitation phenomenon to a new, noncontact actuator to transport a planar object of a few kilograms, and referred to it as near-field acoustic levitation.^{2–4} In addition, a theory is provided in their report, assuming that plane waves only exist in a gap between the source face and the disk and acoustic energy never leaks out of the gap. With some speculation, they conclude that the levitation distance is inversely proportional to the square root of the weight per unit area of the levitated object, and is proportional to the vibrational velocity of the source. Experiments using a piston-like radiator driven by a bolt-clamped Langevin transducer and many planar specimens made of Bakelite and Duralumin support the effectiveness of their theory. Unfortunately, however, the experimental data for the distance are about two times smaller than the theoretical data.² Later, they extended their theory to the case where a rectangular Duralumin plate that is vibrating in flexural modes is employed in place of the piston radiator, still leaving the theory inconsistent with experiments in detail.^{3,4}

The present study is concerned with the theoretical and experimental examination of near-field acoustic levitation to understand fully its essential mechanism. The theory begins with numerically solving basic equations in fluid dynamics via MacCormack's finite-difference scheme, imposing the appropriate initial and boundary conditions. To demonstrate

the validity of the present theory, careful comparison is made with experiments using a 19.5-kHz piston source and different kinds of aluminum disks.

II. THEORY

We consider now a piston sound source of radius R_1 to be vibrating uniformly along the vertical axis z at an angular frequency of ω and a velocity amplitude of U_1 , and an acoustically rigid disk with radius R_2 ($\leq R_1$) remaining levitated in a steady state (see Fig. 1). The levitation distance L is extremely close to the source face, being of several tens to a few hundred micrometers away, in general. It is assumed that the thus-levitated disk never moves even if the source vibrates greatly. In an actual situation, however, any disk vibrates more or less in response to the source motion, as will be shown later.

The gap distance is so very small that fluid properties such as viscosity must be included in the theory to describe rigorously a sound field in the gap.⁵ Basic governing equations in hydrodynamics are found elsewhere, and are summarized in the following compact form:^{5,6}

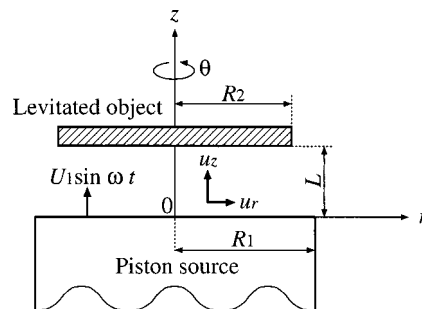


FIG. 1. Theoretical model for the near-field acoustic levitation.

^{a)}Current address: Faculty of Engineering, Kanazawa University, 2-40-20, Kodatsuno, Kanazawa-shi 920-8667, Japan. Electronic mail: nomu@t.kanazawa-u.ac.jp

$$\frac{\partial \tilde{\mathbf{Q}}}{\partial \tilde{t}} + \frac{\partial \tilde{\mathbf{F}}_1}{\partial \tilde{z}} + \frac{\partial \tilde{\mathbf{F}}_2}{\partial \tilde{r}} + \frac{\partial \tilde{\mathbf{G}}_1}{\partial \tilde{z}} + \frac{\partial \tilde{\mathbf{G}}_2}{\partial \tilde{r}} + \tilde{\mathbf{H}} = 0, \quad (1)$$

where $\tilde{t} = \omega t$ is dimensionless time in terms of actual time t and the angular frequency ω of the wave radiated from the source. $\tilde{r} = r/R_1$ and $\tilde{z} = z/L$ are both dimensionless spatial variables. Other dependent variables with the tilde notation are all dimensionless, and are expressed for an axis-symmetric sound field

$$\begin{aligned} \tilde{\mathbf{Q}} &= \begin{bmatrix} \tilde{e} \\ \tilde{\rho} \\ \tilde{\rho} \tilde{u}_z \\ \tilde{\rho} \tilde{u}_r \end{bmatrix}, \quad \tilde{\mathbf{F}}_1 = \frac{1}{kL} \begin{bmatrix} \tilde{u}_z(\tilde{e} + \tilde{P}) \\ \tilde{\rho} \tilde{u}_z \\ \tilde{\rho} \tilde{u}_z^2 + \tilde{P} \\ \tilde{\rho} \tilde{u}_z \tilde{u}_r \end{bmatrix}, \\ \tilde{\mathbf{F}}_2 &= \frac{1}{kR_1} \begin{bmatrix} \tilde{u}_r(\tilde{e} + \tilde{P}) \\ \tilde{\rho} \tilde{u}_r \\ \tilde{\rho} \tilde{u}_z \tilde{u}_r \\ \tilde{\rho} \tilde{u}_r^2 + \tilde{P} \end{bmatrix}, \\ \tilde{\mathbf{G}}_1 &= \frac{1}{kL} \frac{1}{\text{Re}} \begin{bmatrix} \tilde{u}_z \tilde{f}_z - \tilde{u}_r \tilde{\tau} \\ 0 \\ \tilde{f}_z \\ -\tilde{\tau} \end{bmatrix}, \quad (2) \\ \tilde{\mathbf{G}}_2 &= \frac{1}{kR_1} \frac{1}{\text{Re}} \begin{bmatrix} \tilde{u}_r \tilde{f}_r - \tilde{u}_z \tilde{\tau} \\ 0 \\ -\tilde{\tau} \\ \tilde{f}_r \end{bmatrix}, \\ \tilde{\mathbf{H}} &= \frac{1}{kR_1} \frac{1}{\tilde{r}} \begin{bmatrix} \tilde{u}_r(\tilde{e} + \tilde{P}) + (\tilde{u}_r \tilde{f}_r - \tilde{u}_z \tilde{\tau})/\text{Re} \\ \tilde{\rho} \tilde{u}_r \\ \tilde{\rho} \tilde{u}_z \tilde{u}_r - \tilde{\tau}/\text{Re} \\ \tilde{\rho} \tilde{u}_r^2 - \tilde{\alpha}/\text{Re} \end{bmatrix}. \end{aligned}$$

Dimensionless variables are also introduced in these equations: $\tilde{P} = P/(\rho_0 c_0^2)$, $\tilde{\rho} = \rho/\rho_0$, $\tilde{u}_z = u_z/c_0$, $\tilde{u}_r = u_r/c_0$, where P is the pressure, ρ the medium density, u_z the axial component of the particle velocity, u_r the radial component, and $k = \omega/c_0$ the wave number. The subscript 0 in the variables designates the quantities at atmospheric pressure 1 atm and at temperature 20°C. c_0 is the sound speed of infinitesimal amplitude.

The dimensionless total energy density \tilde{e} is given as

$$\tilde{e} = \frac{\tilde{P}}{\gamma - 1} + \frac{1}{2} \tilde{\rho} (\tilde{u}_z^2 + \tilde{u}_r^2), \quad (3)$$

where γ is the specific heat ratio. For air, $\gamma = 1.4$. Viscosity-induced drag forces in Eq. (2) are written as

$$\begin{aligned} \tilde{f}_z &= -\frac{2}{3} \tilde{\eta} \left\{ 2 \frac{\partial \tilde{u}_z}{\partial \tilde{z}} - \frac{L}{R_1} \left(\frac{\partial \tilde{u}_r}{\partial \tilde{r}} - \frac{\tilde{u}_r}{\tilde{r}} \right) \right\}, \\ \tilde{f}_r &= -\frac{2}{3} \tilde{\eta} \left\{ \frac{L}{R_1} \left(2 \frac{\partial \tilde{u}_r}{\partial \tilde{r}} - \frac{\tilde{u}_r}{\tilde{r}} \right) - \frac{\partial \tilde{u}_z}{\partial \tilde{z}} \right\}, \quad (4) \\ \tilde{\tau} &= \tilde{\eta} \left(\frac{\partial \tilde{u}_r}{\partial \tilde{z}} + \frac{L}{R_1} \frac{\partial \tilde{u}_z}{\partial \tilde{r}} \right), \quad \tilde{\alpha} = 2 \tilde{\eta} \frac{L}{R_1} \left(\frac{\partial \tilde{u}_r}{\partial \tilde{r}} - \frac{\tilde{u}_r}{\tilde{r}} \right). \end{aligned}$$

Here, $\tilde{\eta} = \eta/\eta_0$, η is the shear viscosity, $\text{Re} = c_0 L/\nu_0$ is the Reynolds number, and $\nu_0 = \eta_0/\rho_0$ is the kinematic viscosity. Additionally, an adiabatic relation for a compressible fluid is used to connect absolute temperature $\tilde{T} = T/T_0$ and the pressure

$$\tilde{P} = \tilde{\rho} \tilde{T} / \gamma. \quad (5)$$

The viscosity in air depends primarily on temperature; then, the semiempirical formula proposed by Sutherland

$$\tilde{\eta} = \frac{T_0 + T_S}{T_0 \tilde{T} + T_S} \tilde{T}^{3/2}, \quad (6)$$

is utilized, where $T_S = 110.4$ K.⁵

Suppose that the piston source begins to vibrate sinusoidally at $\tilde{t} = 0$ with a uniform velocity amplitude U_1 . The initial conditions are readily given in all the space of the gap

$$\tilde{u}_z = \tilde{u}_r = 0, \quad \tilde{\rho} = 1, \quad \tilde{P} = 1/\gamma \quad (\tilde{t} = 0). \quad (7)$$

The boundary conditions for $\tilde{t} \geq 0$ must be determined in accordance with a realistic situation. At the source face, the radial component \tilde{u}_r of the particle velocity vanishes due to the existence of viscosity

$$\tilde{u}_r = 0 \quad (\tilde{z} = 0, 0 \leq \tilde{r} \leq 1). \quad (8)$$

Whereas, the axial component \tilde{u}_z must be imposed according to the source vibration

$$\tilde{u}_z = M \sin \tilde{t} \quad (\tilde{z} = 0, 0 \leq \tilde{r} \leq 1), \quad (9)$$

where $M = U_1/c_0$ is the acoustic Mach number and is usually less than unity. Strictly speaking, Eq. (9) does not correctly describe the sinusoidal motion at $\tilde{z} = 0$ because the piston source is vibrating with finite displacement around the equilibrium position $\tilde{z} = 0$. The piston motion should be specified in a Lagrange sense, and the expression of Eq. (9) is insufficient for describing the actual velocity at $\tilde{z} = 0$ in an Euler sense.⁷ However, as long as the displacement amplitude is smaller than the wavelength and the gap dimension, we may safely ignore the second-order smallness of difference between the Lagrange and Euler descriptions for quantitative evaluation of dc components in the pressure P . Incidentally, the displacement amplitude is no more than 8 μm at $f = 20$ kHz even for an intense excitation of $U_1 = 1$ m/s. The thickness of the viscous boundary layer that is typically defined as $\sqrt{2\nu_0/\omega}$ becomes about 15 μm ($\nu_0 \approx 1.5 \times 10^{-5}$ m²/s),⁵ larger than the displacement amplitude. In any case, further investigation is needed to clarify such boundary nonlinearities.

Since the disk is assumed to always be in a motionless state, the particle velocity on the bottom surface of the disk vanishes due to viscosity

$$\tilde{u}_r = 0, \quad \tilde{u}_z = 0 \quad (\tilde{z} = 1, 0 \leq \tilde{r} \leq R_2/R_1). \quad (10)$$

On the outer line indicated in dots (c–d–e–f) in Fig. 2, we adopt a nonreflection condition of waves,⁸ taking account of the acoustic energy leakage. Nonleakage of the energy permitting hypothetically a pressure-release condition of $\tilde{P}|_{\tilde{r}=1} = 1/\gamma$, is specifically imposed over the line of $0 \leq \tilde{z} \leq 1$.

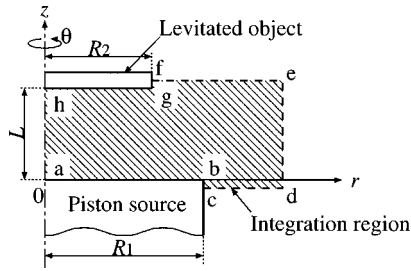


FIG. 2. Integration region.

There are two more requirements to determine a unique solution

$$\begin{aligned} \tilde{u}_r|_{\tilde{r}=1} = \tilde{u}_z|_{\tilde{r}=1} = 0 \quad (\text{b-c}) \\ \tilde{u}_r|_{\tilde{r}=R_2/R_1} = \tilde{u}_z|_{\tilde{r}=R_2/R_1} = 0 \quad (\text{f-g}). \end{aligned} \quad (11)$$

Solving the above nonlinear hydrodynamic equations analytically subject to the initial and boundary conditions is extremely involved. Instead, we employ a numerical computation method, MacCormack's finite-difference scheme that has a fourth-order accuracy in space and a second-order accuracy in time.⁹

For numerical integration, the gap is typically divided at regular grid spacing into 50 grids in the axial direction and 80 grids in the radial direction. For $L=200 \mu\text{m}$ and $R_1=20 \text{ mm}$, the grid sizes become $\Delta z=4 \mu\text{m}$ and $\Delta r=0.25 \text{ mm}$. These sizes are much smaller than the wavelength 17 mm when the source is excited at 20 kHz ($c_0=340 \text{ m/s}$). In the present numerical analysis, $\text{b-c}=\text{f-g}=0.4L$, $\text{c-d}=0.5R_1$, and $\text{e-f}=(1.5-R_2/R_1)R_1$ are set, where b-c means the side length of b-c .

Finite-difference equations derived from Eq. (1) are solved explicitly with respect to time, in which the time is discretized at a regular interval of $\Delta \tilde{t}=2 \times 10^{-3}$. The Courant-Friedrichs-Lewy (CFL) condition for numerical convergence of the difference equations is satisfied because the CFL number become 0.1, which is less than unity. The steady-state solutions are almost established in no more than ten periods, i.e., $\tilde{t}=20\pi$. All the numerical data in the following figures are, therefore, taken at that time. More information on numerical accuracy and comments on the features of the field in the gap are found in an accompanying article.¹⁰

Acoustic levitation is maintained by equal and oppositely directed forces; one is the radiation force and the other the gravity, applied to the disk surface

$$\sigma \mathbf{g} + \mathbf{F}_a/S_0 = 0, \quad (12)$$

where σ is the surface density $\sigma=m/S_0$ of the disk (m is the mass and $S_0=\pi R_2^2$ is the bottom area of the disk), and \mathbf{g} is the gravitational acceleration. \mathbf{F}_a in Eq. (12) is the radiation force acting on the disk bottom, and is estimated by time averaging of the stress tensor T_{zz}

$$\begin{aligned} \mathbf{F}_a = \int \int_{S_0} \langle T_{zz}|_{z=L} \rangle \mathbf{n} dS, \\ T_{zz} = -P + \frac{2}{3} \eta \left[\frac{1}{r} \frac{\partial}{\partial r} (r u_r) + \frac{\partial u_z}{\partial z} \right] + 2\mu \frac{\partial u_z}{\partial z}, \end{aligned} \quad (13)$$

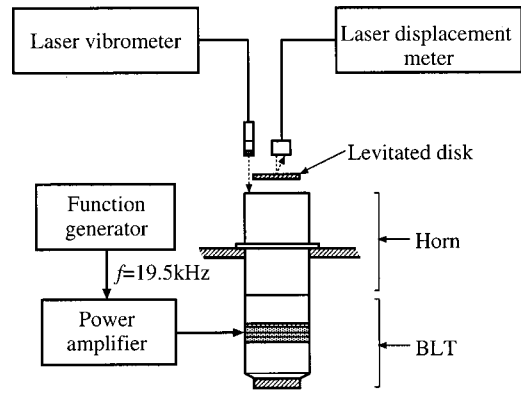


FIG. 3. Arrangement of the experiment setup.

where the notation $\langle \rangle$ denotes time averaging over one period and \mathbf{n} is the normal unit vector on the surface. In the present levitation system, \mathbf{n} is pointing in the minus- z direction.

Even if $u_r=u_z=0$ everywhere on the disk from the boundary conditions of Eq. (10), all the viscous terms in the expression of T_{zz} do not necessarily vanish and $\mathbf{F}_a \neq -\int \langle P \rangle \mathbf{n} dS$. The term $\partial(r u_r)/\partial r$ vanishes on the disk, indeed. However, another term $\partial u_z/\partial z$ does not vanish. These viscous terms are three orders of magnitude smaller than the first term $-P$ in the present theoretical and experimental model, then, T_{zz} may be replaced by $-P$ in practice.

III. EXPERIMENTS AND DISCUSSION

A. Experiment setup

In order to validate the theory proposed here, we carried out experiments in a way similar to Hashimoto *et al.*²

Figure 3 shows the experiment setup, where the piston sound source is a straight horn with a flat face of radius $R_1=20 \text{ mm}$, and is joined with a bolt-clamped Langevin transducer (BLT). The transducer is driven at a frequency of 19.5 kHz. It is preliminarily ascertained that the piston source is vibrating uniformly over its radiating face.

Several kinds of circular and planar aluminum disks were used as specimens to be levitated. The radii of the disks are $R_2=10, 15, \text{ and } 20 \text{ mm}$, and their thicknesses were $t=0.5, 1, 1.5, \text{ and } 2 \text{ mm}$. The surface density for each disk is determined by its mass m and surface area $S_0=\pi R_2^2$; i.e., $\sigma=m/S_0$. For a representative surface density, the disk of $R_2=20 \text{ mm}$ and $t=1 \text{ mm}$ takes a value of $\sigma=2.80 \text{ kg/m}^2$.

The velocity amplitude U_1 of the piston source was accurately measured by a laser Doppler vibrometer (model AT1100, Graphteck). Additionally, we had to pay much attention to the measurement of the levitation distance. This was accomplished by another precision instrument, a laser displacement meter (model LC2400, Keyence).

B. Results and discussion

Levitating disks vibrate more or less in synchronization with the source motion. In particular, disks vibrate significantly when the source-driving frequency approaches their resonance frequencies of transverse bending motion. For example, an aluminum disk of 15 mm in radius and 0.5 mm in

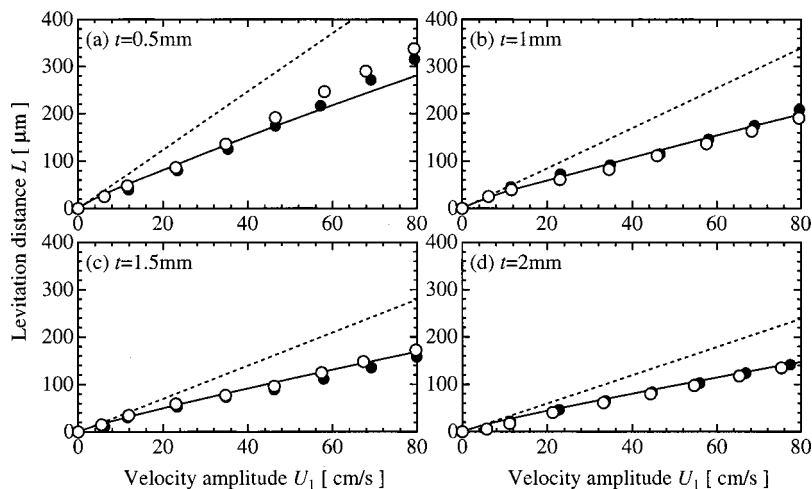


FIG. 4. Levitation distance L as a function of the source velocity U_1 . $f=19.5$ kHz, $R_1=20$ mm, $R_2=10$ mm. Solid curves denote the numerical solutions based on the present theory, and dotted lines are Hashimoto *et al.*'s theoretical prediction, Eq. (14).

thickness under free-circumference support has a theoretical natural resonance frequency of 21.3 kHz, which is nearly equal to the source frequency of 19.5 kHz. In fact, it has been experimentally found that the disk vibrates greatly at a velocity amplitude of more than twice the source velocity. To ensure that the disk was exactly motionless, we selected only disks whose vibration velocity was less than one tenth of the source velocity. A brief discussion on the synchronizing vibration of the disk is provided in the Appendix.

Figure 4 shows the relationship between the levitation distance L and velocity amplitude U_1 for the 10-mm radius disks. Open and closed circles denote the measured data under two different trials, and solid lines, the numerically computed results. As can be seen, the present theory agrees fairly well with the experiment except for the disk of $t=0.5$ mm. The main reason such a discrepancy appears for the 0.5-mm disk seems to be that the disk tilts somewhat when it is highly levitated.

Hashimoto *et al.* proposed a simple expression for the levitation distance under the assumption that only plane waves exit in the gap and acoustic energy never leaks out of the gap. For comparison, their prediction²

$$L = \frac{1}{k} \sqrt{\frac{\rho_0}{2\sigma g}} U_1, \quad (14)$$

is also plotted in dots. Obviously the prediction is about twice as large as the present experiment and theory. It seems doubtful whether their theoretical assumptions are actually realized in near-field levitation.

Another comparison is made in Fig. 5 for the disks of $R_2=20$ mm, the same diameter as the source. Overall, no noticeable differences are seen in the levitation curves between the disks of $R_2=10$ and 20 mm because their surface densities are nearly identical. However, the curves of the disks $R_2=20$ mm bend slightly more than those of $R_2=10$ mm as the source velocity is increased. Dotted curves are the numerically obtained results for the boundary condition of the pressure release at $\tilde{r}=1$ under otherwise unchanged conditions. It should be noted that the experiment results are in overall good agreement with the numerical solutions, including rather than excluding the energy leakage.

In most cases, the radiation force is defined as a Langevin-type pressure and is given by the following integration over the surface of an object:¹¹

$$\mathbf{F}_a = \int \int_{S_0} \{ \langle \mathcal{L} \rangle \mathbf{n} - \rho_0 \langle \mathbf{u}(\mathbf{u} \cdot \mathbf{n}) \rangle \} dS, \quad (15)$$

where $\mathcal{L}=T-U$, T is the kinetic energy density, U is the potential energy density, and \mathbf{u} is the particle velocity. Since $\mathbf{u}=0$ on the disk, the integration is equivalently performed

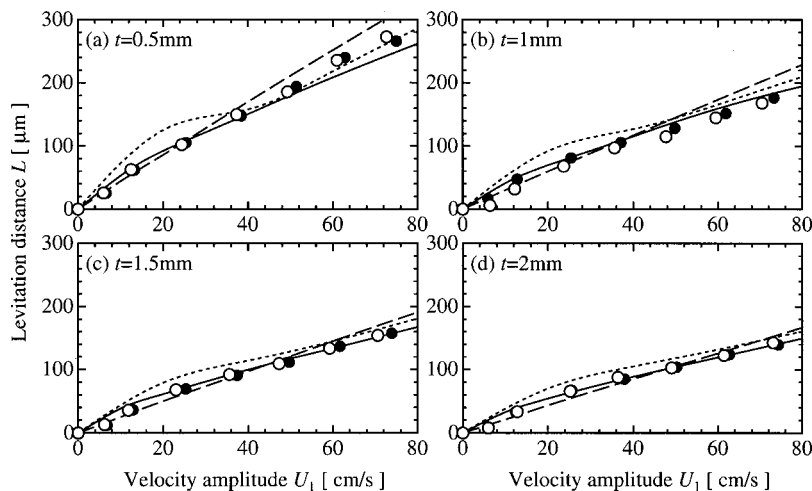


FIG. 5. Same as in Fig. 4 except for $R_2=20$ mm. Solid curves show the numerically computed results including the energy leakage, and dotted curves the results excluding it (pressure-release boundary condition). Dashed lines are based on Eq. (15).

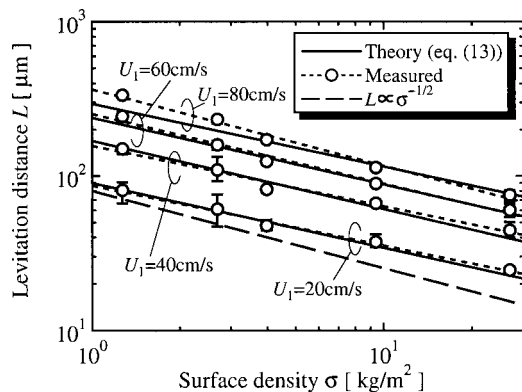


FIG. 6. Levitation distance L as a function of surface density σ for the disk $R_2 = 10$ mm.

by removing the second term of the integrand. Dashed curves in Fig. 5 are the theoretical prediction based on Eq. (15). The effect of the energy leakage on the levitation distance is included in the theory. In contrast to the characteristics of solid and dotted curves, the distance L increases linearly with the source velocity U_1 , exhibiting the same tendency as Eq. (14)'s prediction, although these three curves in the figure are not separated too much from each other. However, the numerical results obtained from Eq. (13) still agree well with the experiment data compared with other theories.

Figure 6 shows the relationship between the levitation distance and surface density for the disks of $R_2 = 10$ mm with various thicknesses. The disks with surface density exceeding 9.3 kg/m^2 were obtained by piling up several lighter disks. The source velocity amplitude was kept at $U_1 = 20, 40, 60,$ and 80 cm/s . A series of levitation measurements was repeated five times for each disk, and the mean values obtained by averaging the measured data are plotted as circles. Error bars denote the confidence of the data and the deviation along the curves. The theory based on Eq. (13) is given in solid curves, and experimentally best-fit straight lines are plotted as dots. The slopes of the theoretical and experimental curves are both gentle compared with the dashed line, whose characteristic is predicted to be inversely proportional to the square root of the surface density; i.e., $L \propto \sigma^{-1/2}$, just as Eq. (14) shows.

The fact that the levitation distance does not obey the $-1/2$ power-law dependence of σ is confirmed in Table I, where the data for $R_2 = 20$ mm are included. Except for the

TABLE I. Relationship between the levitation distance L and the surface density σ .

R_2 [mm]	U_1 [cm/s]	Theory	Experiment
10	20	$L \propto \sigma^{-0.42}$	$L \propto \sigma^{-0.39}$
	40	$L \propto \sigma^{-0.44}$	$L \propto \sigma^{-0.39}$
	60	$L \propto \sigma^{-0.43}$	$L \propto \sigma^{-0.45}$
	80	$L \propto \sigma^{-0.41}$	$L \propto \sigma^{-0.50}$
20	20	$L \propto \sigma^{-0.38}$	$L \propto \sigma^{-0.38}$
	40	$L \propto \sigma^{-0.35}$	$L \propto \sigma^{-0.37}$
	60	$L \propto \sigma^{-0.38}$	$L \propto \sigma^{-0.39}$
	80	$L \propto \sigma^{-0.39}$	$L \propto \sigma^{-0.43}$

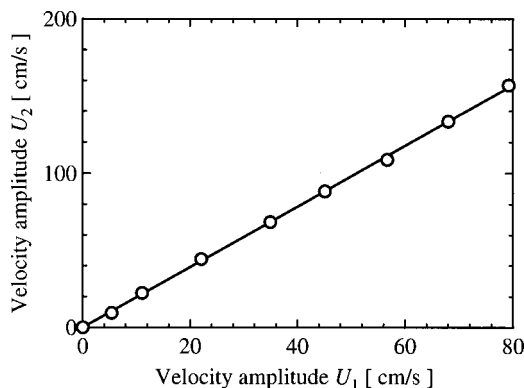


FIG. 7. Synchronizing vibration of the disk with 15-mm radius and 0.5-mm thickness. The velocity amplitude of the disk U_2 is almost proportional to the driving velocity amplitude U_1 .

experiment prediction for the case of $R_2 = 10$ mm and $U_1 = 80 \text{ m/s}$, the power numbers are all less than $-1/2$.

IV. CONCLUSION

We have theoretically and experimentally examined near-field acoustic levitation. The theoretical examination begins with numerically solving basic equations in a viscous fluid by means of MacCormack's finite-difference scheme. Although this approach requires numerical integration, it is capable of readily including viscosity and acoustic energy leakage in the theory.

We have also conducted experiments in air to precisely measure the levitation distances of aluminum disks with various surface densities by increasing the velocity amplitude of a 19.5-kHz piston sound source. Within the framework of a source velocity less than 80 cm/s , theory and experiment were in good agreement. The relationship between the levitation distance and surface density was carefully examined. It was found that the levitation distance is not inversely proportional to the square root of the surface density, but changes depending upon the source velocities and disk radii.

ACKNOWLEDGMENTS

The authors gratefully acknowledge Dr. Yoshikazu Koike of Shibaura Institute of Technology for his very valuable and fruitful discussions.

APPENDIX:

A pronounced synchronization of vibration with the piston source was noted for some of the disks used here, in particular, for the disk of $R_2 = 15$ mm in radius and of $t = 0.5$ mm in thickness. We measured the vibration amplitude U_2 at the center of the disk while varying the source velocity amplitude U_1 . Figure 7 shows the results. As can be seen, the disk vibration increases almost linearly with the source velocity at the rate of a factor of 2.

The amplitudes of the vibrational velocity U_2 and their phases were measured on the surface of the disk. The source velocity was set $U_1 = 12 \text{ cm/s}$. Open and closed circles in Fig. 8 are the measured data along the radial lines that are at

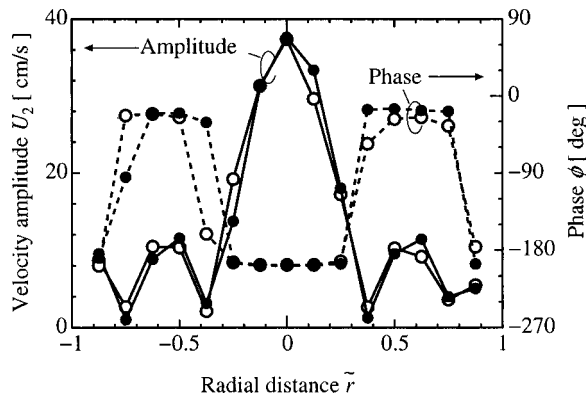


FIG. 8. Amplitude and phase distributions for the vibrational velocity of the disk with 15-mm radius and 0.5-mm thickness. $U_1 = 12$ cm/s.

right angles to each other. The phase was evaluated as the difference angle relative to the source phase. Around the center of the disk, the greatest vibration occurs out of phase by -180° . Approaching the circumference, we can observe that the amplitude decreases and vanishes near $\tilde{r} = 0.38$, and the first nodal circle appears there. Beyond that circle, the phase turns out to be almost in-phase, and a second nodal circle appears at $\tilde{r} = 0.75$.

The positions of these nodal circles are estimated by the following transverse vibration equations of a uniform circular plate:¹²

$$(\nabla^4 - k'^4)\xi = 0, \quad k'^4 = \frac{12\rho'(1 - \sigma'^2)}{Et^2} \omega^2, \quad (\text{A1})$$

where ξ is the transverse displacement of the plate, t is the thickness, ρ' is the density, σ' is the Poisson's ratio, and E is the Young's modulus. Since the disk interestingly is levitated without support, free vibration of the disk is presumably realized around its circumference. Imposing the corresponding boundary conditions yields natural resonance frequencies

$$f_i = \frac{x_i t}{R_2^2} \sqrt{\frac{E}{\rho'(1 - \sigma'^2)}} \quad (i = 1, 2, \dots), \quad (\text{A2})$$

where the parameter x_i depends on the number of the nodal circles i . For example, $x_1 = 0.412$ for a circle, $x_2 = 1.76$ for two circles, and so on. The physical properties of aluminum are $\rho' = 2.69 \times 10^3$ kg/m³, $\sigma' = 0.345$, $E = 7.03 \times 10^{10}$ N/m²; thus, the resonance frequencies of the disk with $R_2 = 15$ mm and $t = 0.5$ mm are calculated to be 5.03 and 21.3 kHz for x_1 and x_2 , respectively. Actually, the latter resonance frequency is close to the driving frequency of 19.5 kHz.

In a similar manner, the positions of the nodal circles are theoretically determined after performing some arithmetical

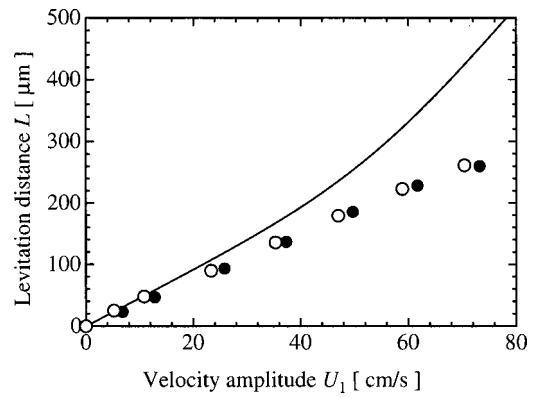


FIG. 9. Levitation distance L vs source velocity U_1 for the greatly vibrating disk of 15-mm radius and 0.5-mm thickness. The theory represented in the solid line overestimates the experimental data in circles.

arrangement. When the disk is excited at 19.5 kHz, two nodal circles should appear at $\tilde{r} = 0.39$ and $\tilde{r} = 0.84$. From Fig. 8, the experimental circles are located at $\tilde{r} = 0.38$ and $\tilde{r} = 0.75$. Thus, they are in relatively good agreement with the theoretical prediction.

As Fig. 9 demonstrates, the present proposed levitation model does not allow the use of strongly vibrating disks because the objects to be levitated are initially assumed to be motionless, even if the piston source vibrates greatly.

¹R. R. Whymark, "Acoustic field positioning for containerless processing," *Ultrasonics* **13**, 251–261 (1975).

²Y. Hashimoto, Y. Koike, and S. Ueha, "Acoustic levitation of planar objects using a longitudinal vibration mode," *J. Acoust. Soc. Jpn. (E)* **16**, 189–192 (1995).

³Y. Hashimoto, Y. Koike, and S. Ueha, "Near-field acoustic levitation of planar specimens using flexural vibration," *J. Acoust. Soc. Am.* **100**, 3230–3233 (1996).

⁴Y. Hashimoto, Y. Koike, and S. Ueha, "Transporting objects without contact using flexural traveling waves," *J. Acoust. Soc. Am.* **103**, 3230–3233 (1998).

⁵A. D. Pierce, *Acoustics* (ASA, New York, 1991), Chap. 10.

⁶J. D. Anderson, "Governing equations of fluid dynamics," in *Computational Fluid Dynamics*, edited by J. F. Wendt (Springer, Berlin, 1992), Chap. 2.

⁷P. M. Morse and K. U. Ingard, *Theoretical Acoustics* (Princeton University Press, Princeton, 1986), pp. 234–238.

⁸K. W. Thompson, "Time dependent boundary conditions for hyperbolic systems," *J. Comput. Phys.* **68**, 1–24 (1987).

⁹E. Turkel, "On the practical use of high-order methods for hyperbolic systems," *J. Comput. Phys.* **35**, 319–340 (1980).

¹⁰H. Nomura and T. Kamakura, "Effect of acoustic energy leakage on the near-field acoustic levitation," *J. Acoust. Soc. Jpn.* **57**, 200–209 (2001).

¹¹T. G. Wang and C. P. Lee, "Radiation Pressure and Acoustic Levitation," in *Nonlinear Acoustics*, edited by M. F. Hamilton and D. T. Blackstock (Academic, CA, 1998), Chap. 6.

¹²P. M. Morse and K. U. Ingard, *Theoretical Acoustics* (Princeton University Press, Princeton, 1986), Sec. 5.3.

An integrated wave-effects model for an underwater explosion bubble^{a)}

Thomas L. Geers^{b)} and Kendall S. Hunter

Department of Mechanical Engineering, University of Colorado, Boulder, Colorado 80309

(Received 28 June 2001; revised 31 December 2001; accepted 14 January 2002)

A model for a moderately deep underwater explosion bubble is developed that integrates the shock wave and oscillation phases of the motion. A hyperacoustic relationship is formulated that relates bubble volume acceleration to far-field pressure profile during the shock-wave phase, thereby providing initial conditions for the subsequent oscillation phase. For the latter, equations for bubble-surface response are derived that include wave effects in both the external liquid and the internal gas. The equations are then specialized to the case of a spherical bubble, and bubble-surface displacement histories are calculated for dilational and translational motion. Agreement between these histories and experimental data is found to be substantially better than that produced by previous models. © 2002 Acoustical Society of America. [DOI: 10.1121/1.1458590]

PACS numbers: 43.25.Yw [ADP]

I. INTRODUCTION

The early work on bubble dynamics focused on underwater explosions [Lamb (1923); Herring (1941); Kirkwood and Bethe (1942); Penney and Price (1942); Taylor (1942); Shiffman and Friedman (1943); Ward (1943)]; this work is well covered in Cole (1948). Since the 1940s, the field has expanded to encompass such areas as medical ultrasonics, sonochemistry, and oceanography [Leighton (1994)]. In recent years, there has been a resurgence of interest in underwater explosion bubbles, driven by the increasing use of computational methods to predict the response of marine structures to underwater explosions [see, e.g., Atkatsch *et al.* (1983); DeRuntz (1989); Schittke *et al.* (1989)].

A. Bubble phenomena

The sequence of events in the motion of an underwater explosion bubble is depicted in Fig. 1 [Snay (1956)], where the snapshots are continuously offset to the right for clarity. When the detonation wave in a spherical charge reaches the charge's wet surface, the highly compressed gas in the small bubble propels the surrounding liquid radially outward, generating an outward-propagating shock wave. The shock-wave pressure profile is step-exponential in nature; 10 m from a 100-kg charge of TNT, the maximum pressure is approximately 20 MPa (3000 psi) and the time constant is about 1/2 ms. Unlike a cavitation bubble generated by an acoustic transducer or a ship's propeller, the bubble produced by an explosive charge is dirty, containing a mixture of explosion products.

As the dilating bubble continues to expand, the pressure inside decreases until it is below the ambient (hydrostatic plus atmospheric) pressure, and soon (at about 100 ms for a 100-kg charge at a depth of 100 m) the bubble reaches its maximum radius (of 3 m or so for the 100-kg/100-m case) and begins to contract. The contraction proceeds until the

bubble collapses on itself (at about 200 ms for the 100-kg/100-m case) and then rebounds; the duration of the collapse-rebound segment (roughly 10 ms for the 100-kg/100-m case) is much shorter than the time to first collapse/rebound. During this segment, a second outward-propagating wave is generated, which carries nearly as much impulse as that carried by the shock wave; the pressure profile of this wave at a point of interest in the field is called the first bubble pulse. Following rebound, the bubble expands again to a second maximum and then contracts until it collapses and rebounds again. This expansion-contraction-collapse-rebound sequence can repeat several times, each time with reduced amplitude.

Accompanying dilation is translation, in which the bubble migrates upward under the force of buoyancy. Eventually the bubble breaches, and the viewer is sometimes treated to a spectacular plume that shoots many meters skyward. In addition to dilation and translation, there is deformation. While the surface of the bubble remains essentially spherical when the bubble is large, it approaches a mushroom-cap profile as it collapses. In many cases, the deformation is so large that the bubble becomes a torus with a water jet shooting upward through the hole.

As just described, bubble motion well beneath the surface is characterized by three different time scales, with the times between dramatic events (shock-wave generation and bubble collapse/rebound) being one to two orders of magnitude greater than the duration of the events themselves. Also, there is a long list of possible energy repositories (kinetic and potential energy of the liquid, kinetic and potential energy of the bubble gas, gravitational potential energy due to buoyancy, potential energy due to surface tension) and loss mechanisms (acoustic radiation into the liquid, chemical reactions, molecular relaxation in the gas, heat and mass transfer at the bubble surface). As seen below, some of these are primary, some are secondary, and some are negligible. Finally, there are extensive experimental data available with which to compare theoretical predictions produced by various models. Much of these data are decades old, but are

^{a)}Presented at the 142nd Meeting of the Acoustical Society of America and the 72nd Shock and Vibration Symposium.

^{b)}Electronic mail: geers@spot.colorado.edu

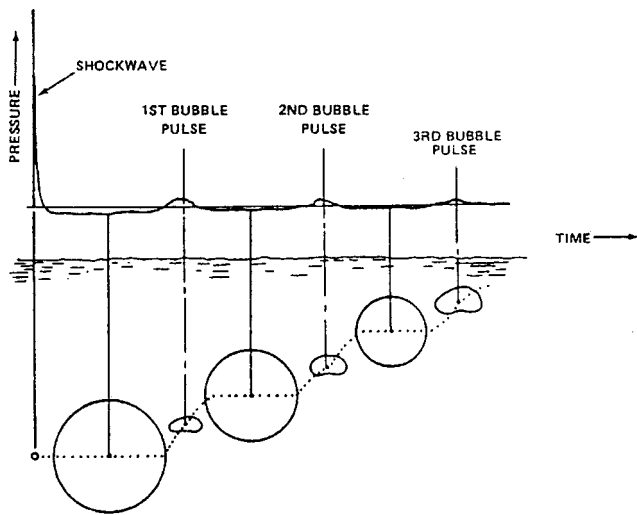


FIG. 1. Typical bubble motion and free-field pressure history [Snay (1956)].

often the product of great skill and care. However, as discussed in Sec. V C, gaps remain.

B. This study

Shock-wave generation and bubble oscillation have often been treated separately. Here, we treat them comprehensively as two phases of a single phenomenon, with the first phase providing initial conditions to the second.

As discussed above, the shock-wave phase is short, typically less than a few milli-seconds. Extensive far-field pressure-profile data have been obtained for the shock wave [Coles *et al.* (1946); Farley and Snay (1978); Price (1979)], but the authors know of no data that pertain to the inside or the surface of the highly compressed bubble. Recently, hydrocode simulations of detonation and initial bubble dynamics have been performed [Wardlaw and Mair (1998)]. Here, we employ a simple volume-acceleration model [Strasberg (1956); Frost and Harper (1975)] to determine shockwave-phase bubble motion from a similitude relation for the far-field pressure profiles [Price (1979)].

Previous treatments of *general bubble motion* in the oscillation phase model the unbounded liquid as incompressible [Blake and Gibson (1987); Duncan and Zhang (1991a, b); Chahine and Kalumuck (1998)]. Here, we account for wave effects in the liquid by means of a first-order *external doubly asymptotic approximation* [Geers (1978); Geers and Zhang (1994a)]. The previous treatments of general bubble motion also ignore wave effects in the internal gas. We include such effects here through the use of a first-order *internal doubly asymptotic approximation*. Many equations of state have been developed for explosive gas products [Dobratz (1981)]. Two have been found suitable for the bubble oscillation phase [Jones and Miller (1948); Lee, Hornig, and Kurry (1968)], and have been consolidated into a single adiabatic equation of state for bubble oscillation.

The new bubble model is specialized to a *spherical geometry* for which only dilation and translation are considered. As discussed below, at least six equations exist for pure dilation of a spherical bubble in the oscillation phase [Lamb

(1923); Herring (1941); Kirkwood and Bethe (1942); Keller and Kolodner (1956); Prosperetti and Lezzi (1986); Moss *et al.* (2000)]. The first treats the unbounded liquid as incompressible, while the next four introduce external wave effects through various means. The last addresses wave effects in both the external liquid and the internal gas. Extensions to modes beyond dilation have treated the liquid as incompressible [Penney and Price (1942); Taylor (1942); Ward (1943); Kolodner and Keller (1953); Hicks (1970)]. Here, we formulate equations for dilation plus translation that account for wave effects in both the liquid and the gas. The spherical-bubble equations for the new model are numerically integrated in time to produce dilation and translation histories. Agreement between these histories and previously obtained experimental data [Swift and Decius (1948); Snay (1962); Snay and Tipton (1962); Hicks (1970)] is substantially better than that produced by previous models.

II. SHOCK-WAVE PHASE

A dilational model of the bubble is appropriate for this brief, but important, phase. Extensive far-field pressure data have been obtained [Coles *et al.* (1946); Farley and Snay (1978); Price (1979)], and analytical models have been developed and validated against those data [Kirkwood and Bethe (1942); Cole (1948)]. The models are complicated and focus on far-field quantities; bubble-motion calculations are neither straightforward nor validated. Eulerian simulations have recently been performed [Wardlaw and Mair (1998)], but have not been validated by experimental data. To the authors' knowledge, close-in experimental data are not available, apparently because of the inhospitable environment. We employ here a surprisingly useful volume-acceleration model to determine shock-wave-phase bubble motion from far-field pressure data.

A. Similitude relations

An accurate representation of far-field shock-wave pressure profiles is the *similitude relation* [Coles *et al.* (1946); Farley and Snay (1978); Price (1979)]

$$P(R, t) = P_c [a_c / R]^{1+A} f([a_c / R]^B v_c t / a_c), \quad (1)$$

in which R is the distance from the center of the explosive charge with radius a_c , and P_c , v_c , A , and B are constants associated with the charge material. Some recommended values for these constants appear in Table I. Two good choices for $f(\tau)$ are

$$f(\tau) = e^{-\tau}, \quad \tau \leq 1, \\ f(\tau) = 0.8251e^{-1.338\tau} + 0.1749e^{-0.1805\tau}, \quad \tau \leq 7. \quad (2)$$

The single-exponential fit does not extend to the start of the oscillation phase (Sec. III), so here we employ the double-exponential fit, which extends to the time when the pressure is down to about 5% of its peak.

A representative comparison of Eqs. (1) and (2) with a measured pressure profile is shown in Fig. 2 for the constants of Coles *et al.* (1946) in Table I. The fits within their respective ranges are good, with the exception of the small oscillation in the experimental profile. This oscillation is a mani-

TABLE I. Material constants for shock-wave similitude equations; the units of P_c and v_c are GPa and km/s respectively.

Material	Source	P_c	v_c	A	B
TNT (1.52 g/cc)	Coles <i>et al.</i> (1946)	1.42	0.992	0.13	0.18
TNT (1.60 g/cc)	Farley and Snay (1978)	1.45	1.24	0.13	0.23
TNT (1.60 g/cc)	Price (1979)	1.67	1.01	0.18	0.185
Pentolite (1.71 g/cc) (50/50 PETN/TNT)	Thiel (1961)	1.65	1.22	0.14	0.23
Pentolite (1.71 g/cc) (unknown comp.)	Price (1979)	1.92	1.29	0.194	0.257
HBX-1 (1.72 g/cc) (40/38/17/5 RDX/TNT/A1/D-2 Wax)	Swisdak (1978)	1.71	1.47	0.15	0.29
HBX-1 (1.72 g/cc) (unknown comp.)	Price (1979)	1.58	1.17	0.144	0.247

festation of wave effects in the bubble gas [Cole (1948); Wardlaw and Mair (1998)]. We constructed a high-order polynomial fit to the oscillation, but the effect on subsequent bubble motion was negligible. Hence, we regard Eq. (2b) as satisfactory for $\tau \leq 7$.

B. Volume-acceleration model

Now, we seek to use the far-field pressure profile given by Eq. (1) with $f(\tau)$ given by Eq. (2b) to determine the motion of the bubble surface during the shock-wave phase. If the fields in the liquid were acoustic during this phase, we could use an equation proposed by Strasberg (1956), systematically formulated by Frost and Harper (1975), and discussed by Pierce (1989). This equation relates the far-field pressure profile to bubble motion as

$$P(R,t) = (\rho_l/4\pi R)\dot{V}(t), \quad (3)$$

where ρ_l is the mass density of the liquid and V is the bubble volume. Note that this profile expression does not contain the speed of sound in the liquid, c_l , and is therefore independent of liquid compressibility. This is because the width of the wave in the liquid is substantially greater than the radius of the charge.

In our “hyperacoustic” situation, the bubble surface produces nonlinear wave propagation at speeds somewhat greater than c_l . But, because Eq. (3) exhibits no dependence on c_l , we might also expect negligible liquid-compressibility effects here. This is supported by the fact that A and B are both substantially less than 1, and that Eq. (1) describes acoustic wave propagation when $A=B=0$. Hence, by comparison of Eqs. (1) and (3), we find that the appropriate extension of Eq. (3) to the hyperacoustic case is

$$P(R,t) = \frac{\rho_l}{4\pi R} \left[\frac{a_c}{R} \right]^A \dot{V}([a_c/R]^B t). \quad (4)$$

Equating Eqs. (4) and (1) with $f(\tau)$ given by Eq. (2b), we obtain for volume acceleration

$$\begin{aligned} \dot{V}(t) = & \frac{4\pi a_c}{\rho_l} P_c [0.8251 \exp(-1.338t/T_c) \\ & + 0.1749 \exp(-0.1805t/T_c)], \end{aligned} \quad (5)$$

where $T_c = a_c/v_c$. Integration with $\dot{V}(0)=0$ and further integration with $V(0) = (4/3)\pi a_c^3$ then yield

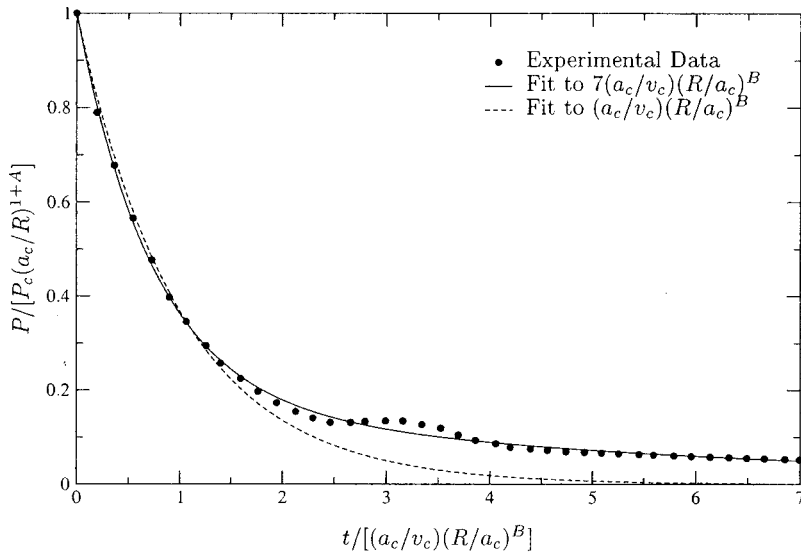


FIG. 2. Fit of Eqs. (1) and (2) to a typical shock-wave pressure profile.

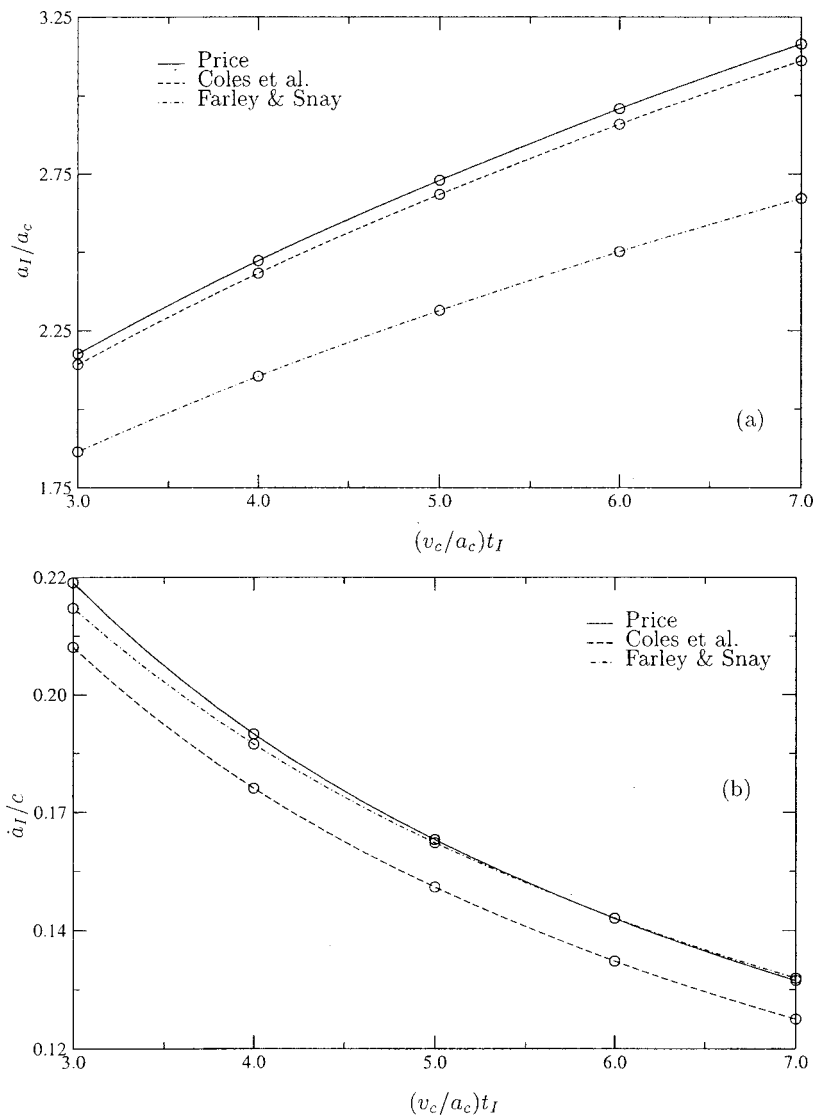


FIG. 3. Initial displacement and velocity as functions of the initial time selected for the oscillation phase, and as determined from three sets of charge constants.

$$\dot{V}(t) = \frac{4\pi a_c}{\rho_l} P_c [1.5857 - 0.6167 \exp(-1.338t/T_c) - 0.9690 \exp(-0.1805t/T_c)], \quad (6)$$

$$V(t) = \frac{4}{3} \pi a_c^3 + \frac{4\pi a_c}{\rho_l} P_c [1.5857t - 5.8293 + 0.4609 \exp(-1.338t/T_c) + 5.3684 \exp(-0.1805t/T_c)],$$

and radial displacement and velocity follow as

$$a(t) = [3V(t)/4\pi]^{1/3}, \quad \dot{a}(t) = \dot{V}(t)/4\pi a^2(t). \quad (7)$$

C. Initial conditions for the oscillation phase

An arbitrary aspect of partitioning underwater-explosion-bubble phenomenology into shock-wave and oscillation phases is defining their time of connection. From Eq. (2b) at $R = a_c$, this time should fall somewhere between $3T_c$, where the pressure has fallen to less than 10% of its peak value, to $7T_c$, which is the time limit for Eq. (2b) at $R = a_c$. The selected connection time determines the initial

conditions for subsequent bubble-response calculations during the oscillation phase and is given the symbol t_I . Success of the partitioning concept depends, of course, on the insensitivity of subsequent response calculations to the choice of t_I .

Figure 3 shows initial conditions computed from Eqs. (6) and (7) for $t_I/T_c = 3, 4, 5, 6,$ and 7 , and for three sets of charge constants [Coles *et al.* (1946); Farley and Snay (1978); Price (1979)], all pertaining to TNT. We see that a_I increases and \dot{a}_I decreases with increasing t_I , as one would expect. It is shown below that these dependencies are such that, for a single set of charge constants, all pairs of initial-condition values for values of t_I between $3T_c$ and $7T_c$ produce essentially the same bubble response during the oscillation phase. This validates the partitioning concept.

III. OSCILLATION PHASE: GENERAL MOTION

In view of the time scales mentioned in Sec. IA, we would expect to see incompressible flow of the unbounded liquid during the expansion-contraction segments of this phase and wave effects during the collapse-rebound segments. However, the earliest dilational bubble models as-

sumed *only* incompressible flow [Besant (1859); Lord Rayleigh (1917); Lamb (1923)], as did those for combined dilation and translation [Taylor (1942); Hicks (1970)], and those for general bubble motion [Penney and Price (1942); Ward (1943); Kolodner and Keller (1953)].

Even modern boundary-element models based on inviscid, irrotational flow of the liquid assume incompressible flow [Blake and Gibson (1987); Duncan and Zhang (1991a, b); Chahine and Kalumuck (1998)]. However, certain components of those models do not rely on that assumption. With $\mathbf{R}_l(t)$ as the position vector for a liquid particle at the bubble's surface, and $\phi_l(\mathbf{R}_l)$ as the velocity potential at the particle's location, and with an overdot denoting the material derivative, these components produce the following Lagrangian-description equations at each point on the bubble surface S :

Kinematic compatibility:

$$\dot{\mathbf{R}}_l = \nabla \phi_l(\mathbf{R}_l), \quad (8a)$$

Gradient in local coordinates:

$$\nabla \phi_l(\mathbf{R}_l) = \mathbf{e}_N \phi'_l + \mathbf{e}_1 \phi_{l,1} + \mathbf{e}_2 \phi_{l,2}, \quad (8b)$$

Bernoulli's equation:

$$\dot{\phi}_l = \frac{1}{2} \nabla \phi_l(\mathbf{R}_l) \cdot \nabla \phi_l(\mathbf{R}_l) - \rho_l^{-1} [p_l - (p_{\text{atm}} + p_l g d)]. \quad (8c)$$

The first of these matches the velocity of the bubble surface to the velocity of the liquid at that surface. The second defines the gradient of the velocity potential in local coordinates, where the tangential derivatives $\phi_{l,1}$ and $\phi_{l,2}$ may be obtained by surface differentiation. Clearly, ϕ'_l cannot be obtained in this way, so recourse is made to a boundary relation, as discussed below.

Equation (8c) relates the material time derivative of the liquid's velocity-potential field at the bubble surface to the square of the liquid velocity and the net pressure. The pressure p_l is regarded as a known surface pressure, p_{atm} is atmospheric pressure, g is the acceleration due to gravity, and d (defined positive downward) is the current depth of the liquid particle in question. If $\phi_l=0$, Eq. (8c) requires that $p_l = p_{\text{atm}} + \rho_l g d$, which is the condition for static equilibrium.

To the authors' knowledge, no previous model for general bubble motion accounts for wave effects in the internal gas. Here, the gas is modeled at a level consistent with that characterizing the liquid model. Hence, the gas equations corresponding to Eq. (8) are

Kinematic compatibility:

$$\dot{\mathbf{R}}_g = \nabla \phi_g(\mathbf{R}_g), \quad (9a)$$

Gradient in local coordinates:

$$\nabla \phi_g(\mathbf{R}_g) = \mathbf{e}_N \phi'_g + \mathbf{e}_1 \phi_{g,1} + \mathbf{e}_2 \phi_{g,2}, \quad (9b)$$

Bernoulli's equation:

$$\dot{\phi}_g = \frac{1}{2} \nabla \phi_g(\mathbf{R}_g) \cdot \nabla \phi_g(\mathbf{R}_g) - \rho_g^{-1} \{ p_g - [P_g + \rho_g g (d - d_{cg})] \}, \quad (9c)$$

where $\mathbf{R}_g(t)$ is the position vector for a gas particle at the bubble's surface, $\phi_g(\mathbf{R}_g)$ is the velocity potential at the particle's location, ρ_g is the mass density of the internal gas, p_g is regarded as a known surface pressure, P_g is the uniform internal pressure defined by the equation of state, and d_{cg} is the depth of the bubble's center of gravity. If $\phi_g=0$, Eq. (9c) requires that $p_g = P_g + \rho_g g (d - d_{cg})$, which is the condition for static equilibrium.

The liquid and gas fields are linked at the bubble surface in two ways. First, compatibility of normal velocity requires that $\mathbf{R}_g \cdot \mathbf{e}_N = \mathbf{R}_l \cdot \mathbf{e}_N$, i.e., $\phi'_g = \phi'_l$, at every point on the surface. Second, pressure equilibrium requires that $p_l = p_g - \sigma \kappa$ at every surface point, where σ is the surface tension and κ is the mean curvature. The effects of surface tension are negligible for underwater-explosion bubbles, so we take $\sigma=0$.

We now formulate two bubble models. The *first* ignores wave phenomena by treating the external liquid as incompressible and the internal gas as having zero density. The *second* incorporates wave effects in both the liquid and the gas by means of first-order doubly asymptotic approximations.

A. Waveless model

A three-dimensional *boundary integral equation (BIE)* that, for inviscid, irrotational, incompressible flow of the unbounded liquid, relates the velocity potential to its normal derivative over a smooth internal surface is [see, e.g., Banerjee and Butterfield (1981)]

$$\phi'_l = -H_l \phi_l, \quad (10)$$

in which $H_l = B_l^{-1} \Gamma_l$, where the geometry-dependent, boundary-integral operators B_l and Γ_l are defined by

$$B_l \xi(\mathbf{R}_l) \equiv \int_S |\mathbf{R}'_l - \mathbf{R}_l|^{-1} \xi(\mathbf{R}'_l) dS(\mathbf{R}'_l), \quad (11)$$

$$\Gamma_l \xi(\mathbf{R}_l) \equiv \int_S |\mathbf{R}'_l - \mathbf{R}_l|^{-3} (\mathbf{R}'_l - \mathbf{R}_l) \cdot \mathbf{n}_l(\mathbf{R}'_l) \xi(\mathbf{R}'_l) dS(\mathbf{R}'_l).$$

Here, \mathbf{n}_l is the unit normal to the surface S , defined positive going into the liquid.

For $\rho_g=0$, Eq. (9c) yields $p_g = P_g$, so, for negligible surface tension, $p_l = P_g$. Introducing Eq. (10) into Eq. (8b) and the result into Eq. (8a), and introducing $p_l = P_g$ into Eq. (8c), we obtain the BIE-consolidated kinematic-compatibility and Bernoulli equations

$$\dot{\mathbf{R}}_l = -\mathbf{e}_N H_l \phi_l + \mathbf{e}_1 \phi_{l,1} + \mathbf{e}_2 \phi_{l,2}, \quad (12a)$$

$$\dot{\phi}_l = \frac{1}{2} \dot{\mathbf{R}}_l \cdot \dot{\mathbf{R}}_l - \rho_l^{-1} [P_g - (p_{\text{atm}} + \rho_l g d)]. \quad (12b)$$

These equations are well suited to numerical computation by boundary-element semidiscretization and explicit time integration.

Concerning initial conditions at time t_l , we regard the bubble as spherical and centered at the origin. Hence,

$\mathbf{R}_l(t_l) = \mathbf{e}_r a_l$ and, from Sec. VA below, $\phi_l(t_l) = -a_l \dot{a}_l$, where $a_l = a(t_l)$ and $\dot{a}_l = \dot{a}(t_l)$ are determined from Eqs. (7) and (6).

B. DAA model

Now, Eq. (10) is quite accurate during the relatively slow expansion and contraction of the bubble. However, a boundary relation that is more applicable to bubble collapse and rebound is the plane-wave-radiation equation $c_l \phi_l' = -\phi_{l,t}$ [Felippa (1980)], where $\phi_{l,t}$ is the partial derivative of ϕ_l with respect to time. The first-order differential equation that uniquely reduces to these two equations in their appropriate limits is the first-order external doubly asymptotic approximation (EDAA₁) [Geers and Zhang (1994a)]

$$\phi_l' = -H_l \phi_l - c_l^{-1} \phi_{l,t}. \quad (13)$$

With $\phi_{l,t} = \dot{\phi}_l - \nabla \varphi_l(\mathbf{R}_l) \cdot \nabla \varphi_l(\mathbf{R}_l) = \dot{\phi}_l - \dot{\mathbf{R}}_l \cdot \dot{\mathbf{R}}_l$, Eq. (13) becomes

$$\phi_l' = -H_l \phi_l - c_l^{-1} (\dot{\phi}_l - \dot{\mathbf{R}}_l \cdot \dot{\mathbf{R}}_l). \quad (14)$$

This equation constitutes a simple means by which to include wave effects in the liquid during the bubble's oscillation phase.

DAAs have been formulated in acoustics [Geers (1971, 1978); Nicolas-Vullierme (1991); Geers and Zhang (1994a, b); Geers and Toothaker (1997, 2000)]; electromagnetics [Geers and Zhang (1988)]; elastodynamics [Underwood and Geers (1981); Geers and Lewis (1997)]; and poroelastodynamics [Qi and Geers (1997)]. First-order DAAs were obtained by inspection [Geers (1971); Underwood and Geers (1981)]. Higher-order DAAs have been formulated by modal analysis [Geers (1978)] and by operator matching [Nicolas-Vullierme (1991); Geers and Zhang (1994a); Geers and Lewis (1997); Qi and Geers (1997); Geers and Toothaker (1997, 2000)]. Operator matching is akin to the method of matched asymptotic expansions [see, e.g., Van Dyke (1964)]. The formulation of a DAA for the present problem has been done by inspection.

Wave effects may be included in the gas model by means of the first-order internal doubly asymptotic approximation (IDAA₁) [Geers and Zhang (1994a)]

$$\phi_g' = H_g \phi_g + c_g^{-1} \phi_{g,t}, \quad (15)$$

in which $H_g = B_g^{-1} \Gamma_g$, where B_g and Γ_g are given by Eqs. (11) with $l \rightarrow g$ and \mathbf{n}_g defined positive going into the gas. As discussed in Geers and Zhang (1994a), one may write $\phi_g = \phi_g^d + \phi_g^e$, where ϕ_g^d , which is uniform over the bubble surface, pertains to dilational motion and ϕ_g^e , which has no uniform component, pertains to equivoluminal motion. It is shown by Geers and Zhang that $H_g \phi_g^d = 0$; hence, the second term in Eq. (15) is essential to admitting nonzero dilation. With $\phi_{g,t} = \dot{\phi}_g - \nabla \varphi_g(\mathbf{R}_g) \cdot \nabla \varphi_g(\mathbf{R}_g) = \dot{\phi}_g - \dot{\mathbf{R}}_g \cdot \dot{\mathbf{R}}_g$, Eq. (15) becomes

$$\phi_g' = H_g \phi_g + c_g^{-1} (\dot{\phi}_g - \dot{\mathbf{R}}_g \cdot \dot{\mathbf{R}}_g). \quad (16)$$

To obtain the DAA-consolidated kinematic-compatibility equations, we eliminate ϕ_l' in Eq. (8b) by employ-

ing Eq. (14) and introduce the result into Eq. (8a), and then eliminate ϕ_g' in Eq. (9b) by employing Eq. (16) and introduce the result into Eq. (9a). This yields

$$\dot{\mathbf{R}}_l = -\mathbf{e}_N [H_l \phi_l + c_l^{-1} (\dot{\phi}_l - \dot{\mathbf{R}}_l \cdot \dot{\mathbf{R}}_l)] + \mathbf{e}_1 \phi_{l,1} + \mathbf{e}_2 \phi_{l,2}, \quad (17a)$$

$$\dot{\mathbf{R}}_g = \mathbf{e}_N [H_g \phi_g + c_g^{-1} (\dot{\phi}_g - \dot{\mathbf{R}}_g \cdot \dot{\mathbf{R}}_g)] + \mathbf{e}_1 \phi_{g,1} + \mathbf{e}_2 \phi_{g,2}. \quad (17b)$$

We obtain the DAA-consolidated Bernoulli equations in four steps. In Eqs. (8c) and (9c), we eliminate $\nabla \varphi_l(\mathbf{R}_l)$ and $\nabla \varphi_g(\mathbf{R}_g)$ by means of Eqs. (8a) and (9a), respectively. Next, we solve the modified Eq. (8c) for p_l and the modified Eq. (9c) for p_g , and equate the right sides of the resulting equations. Then, we enforce $\phi_g' = \phi_l'$ by equating the right side of Eq. (16) to the right side of Eq. (14). Finally, we solve the resulting coupled algebraic equations for $\dot{\phi}_l$ and $\dot{\phi}_g$ to get

$$\begin{aligned} \dot{\phi}_l = (1 + \zeta)^{-1} & \left[\left(\frac{1}{2} + \zeta \right) \dot{\mathbf{R}}_l \cdot \dot{\mathbf{R}}_l + \frac{1}{2} \left(\frac{\rho_g}{\rho_l} \right) \dot{\mathbf{R}}_g \cdot \dot{\mathbf{R}}_g - \zeta c_l (H_l \phi_l \right. \\ & \left. + H_g \phi_g) \right] - [(1 + \zeta) \rho_l]^{-1} \\ & \times [P_g - (p_{\text{atm}} + \rho_l g d_{cg}) - (\rho_l - \rho_g) g (d - d_{cg})], \\ \dot{\phi}_g = (1 + \zeta)^{-1} & \left[\left(1 + \frac{1}{2} \zeta \right) \dot{\mathbf{R}}_g \cdot \dot{\mathbf{R}}_g + \frac{1}{2} \left(\frac{c_g}{c_l} \right) \dot{\mathbf{R}}_l \cdot \dot{\mathbf{R}}_l \right. \\ & \left. - c_g (H_l \phi_l + H_g \phi_g) \right] + [(1 + \zeta) \rho_l]^{-1} \left(\frac{c_g}{c_l} \right) \\ & \times [P_g - (p_{\text{atm}} + \rho_l g d_{cg}) - (\rho_l - \rho_g) g (d - d_{cg})], \end{aligned} \quad (18)$$

where $\zeta = \rho_g c_g / \rho_l c_l$ is the specific-acoustic-impedance ratio. The right sides of Eqs. (18) are used for $\dot{\phi}_l$ and $\dot{\phi}_g$ on the right sides of Eq. (17). Equations (17) and (18) are new; they are amenable to numerical solution by boundary-element semidiscretization and explicit time integration, with iteration keyed to the dot products $\dot{\mathbf{R}}_l \cdot \dot{\mathbf{R}}_l$ and $\dot{\mathbf{R}}_g \cdot \dot{\mathbf{R}}_g$.

Regarding initial conditions at time t_l , we again consider the bubble at t_l as spherical and centered at the origin. Then, the initial values are $\mathbf{R}_l(t_l) = \mathbf{R}_g(t_l) = \mathbf{e}_r a_l$, $\dot{\mathbf{R}}_l(t_l) = \dot{\mathbf{R}}_g(t_l) = \mathbf{e}_r \dot{a}_l$, and, from Sec. VB below, $\phi_l(t_l) = \phi_{l0}(t_l) + \phi_{l1}(t_l) \cos \theta$ and $\phi_g(t_l) = \phi_{g1}(t_l) \cos \theta$, where $\phi_{l0}(t_l)$, ϕ_{l1} and $\phi_{g1}(t_l)$ are given by Eq. (72).

C. Properties of the internal gas

There is a large body of work on the equation of state (EOS) for explosive gas products [Dobratz (1981)]. We excluded most EOS from consideration here, however, primarily because they do not consider explosives pertinent to underwater shock, and secondarily because we desired an adiabatic EOS for the gas. The retained EOS are due to Jones and Miller (1948), who produced adiabatic dense-gas EOS in tabular form, and to Lee, Hornig, and Kury (1968), who produced their dense-gas EOS by fitting an empirical relation to experimental data. The two EOS provide consistent models for the adiabatic expansion of TNT with mass densities in

TABLE II. Values of K_c and γ appearing in the consolidated adiabatic EOS.

Material	Source	K_c [MPa]	γ
TNT (1.00 g/cc)	Jones and Miller (1948)	556.2	1.20
TNT (1.50 g/cc)	Jones and Miller (1948)	839.6	1.27
TNT (1.63 g/cc)	Lee <i>et al.</i> (1973)	1045	1.30
Pentolite (1.70 g/cc)	Lee and Walton (1975)	1033	1.35

the range 1.00–1.63 g/cm³ and at pressures below 100 MPa. Hence, we shall use here the *consolidated adiabatic equation of state*

$$P_g = K_c (V_c/V)^\gamma, \quad (19)$$

where K_c is the adiabatic charge constant for the explosive material, V_c is the volume of the charge, V is the current volume of the bubble, and γ is the (constant) ratio of specific heats for the gas. Values of K_c and γ for TNT and Pentolite are given in Table II.

Wave effects in the gas constitute small perturbations (except in a small region surrounding the bubble center), so the material properties of the gas may be considered uniform throughout the volume of the bubble. Hence, conservation of mass yields for mass density

$$\rho_g = \rho_c (V_c/V). \quad (20)$$

The bulk modulus of the gas is defined by $B_g = -\Delta P_g / (\Delta V/V)$. But, $B_g = \rho_g c_g^2$ and, from Eq. (19), $\Delta P_g = -\gamma K_c (V_c/V)^\gamma (\Delta V/V)$. Hence,

$$c_g = c_c (V_c/V)^{(1/2)(\gamma-1)}, \quad (21)$$

where $c_c = \sqrt{\gamma K_c / \rho_c}$.

IV. OSCILLATION PHASE: DILATION OF A SPHERICAL BUBBLE

For this simplest of cases, $\mathbf{R}(t) = a(t)\mathbf{e}_r$ and $\varphi(\mathbf{r}, t) = \varphi(r, t)$ for both the liquid and the gas, where the origin of the coordinate system is at the center of the bubble, $\mathbf{r}(t)$ is the position vector for a particle, and $\varphi(\mathbf{r}, t)$ is the velocity potential at the particle's position. Hence, Eqs. (8a), (8b), (9a), and (9b) yield

$$\dot{a} = \phi'_l, \quad \dot{a} = \phi'_g, \quad (22)$$

and the averages of Eqs. (8c) and (9c) over the bubble surface give

$$\begin{aligned} \dot{\phi}_l &= \frac{1}{2}(\phi'_l)^2 - \rho_l^{-1}(p_l - p_l), \\ \dot{\phi}_g &= \frac{1}{2}(\phi'_g)^2 - \rho_g^{-1}(p_g - P_g), \end{aligned} \quad (23)$$

in which $p_l = p_{\text{atm}} + \rho_l g d_l$, where d_l is the fixed depth of the bubble's center. Compatibility of normal velocity requires that $\phi'_g = \phi'_l$, which is also mandated by Eq. (22). Pressure equilibrium, for negligible surface tension, requires that $p_l = p_g$.

A. Waveless model

For dilation of a spherical surface with radius a , the BIE, Eq. (10) becomes

$$\phi'_l = -a^{-1}\phi_l, \quad (24)$$

which is readily verified by noting that the pertinent solution to Laplace's equation is $\varphi(r) = \phi \cdot a/r$. Furthermore, Eq. (23b) with $\rho_g = 0$ yields $p_g = P_g$, so $p_l = P_g$. Employing this and Eq. (22a) in Eq. (23a) and introducing Eq. (24) in Eq. (22a), we obtain

$$\dot{a} = -a^{-1}\phi_l, \quad \dot{\phi}_l = \frac{1}{2}\dot{a}^2 - \rho_l^{-1}(P_g - p_l), \quad (25)$$

where, from Eq. (19), $P_g = K_c (a_c/a)^{3\gamma}$. These equations correspond to Eq. (12). The initial conditions are $a(t_I) = a_I$ and, from Eq. (25a), $\phi_l(t_I) = -a_I \dot{a}_I$.

We can eliminate ϕ_l as a variable by multiplying Eq. (25a) through by a , differentiating, and equating the resulting expression for $\dot{\phi}_l$ to the right side of Eq. (25b). This produces the following *equation of motion* (EOM) for the bubble radius:

$$a\ddot{a} + \frac{3}{2}\dot{a}^2 = \rho_l^{-1}(P_g - p_l). \quad (26)$$

This is widely known as the Rayleigh–Plesset equation, but it was actually first derived by Lamb in 1923. We shall avoid misattribution and refer to it as the *Lamb EOM*. The initial conditions are simply $a(t_I) = a_I$ and $\dot{a}(t_I) = \dot{a}_I$.

B. DAA model

With $H_l \phi_l$ producing $a^{-1}\phi_l$ for this case [see Eqs. (10) and (24)], and with $H_g \phi_g = 0$ for dilation, EDAA₁, Eq. (14), and IDAA₁, Eq. (16), become

$$\phi'_l = -a^{-1}\phi_l - c_l^{-1}(\dot{\phi}_l - \dot{a}^2), \quad \phi'_g = c_g^{-1}(\dot{\phi}_g - \dot{a}^2). \quad (27)$$

The introduction of Eq. (22) then gives

$$\dot{a} = -a^{-1}\phi_l - c_l^{-1}(\dot{\phi}_l - \dot{a}^2), \quad \dot{a} = c_g^{-1}(\dot{\phi}_g - \dot{a}^2), \quad (28)$$

which correspond to Eq. (17). Proceeding as described between Eqs. (17) and (18) with Eq. (8a)→Eq. (22a), Eq. (8c)→Eq. (23a), Eq. (9a)→Eq. (22b), Eq. (9c)→Eq. (23b), Eq. (14)→Eq. (27a), and Eq. (16)→Eq. (27b), we find

$$\begin{aligned} \dot{\phi}_l &= (1 + \zeta)^{-1} \left\{ \left[\frac{1}{2} + \zeta + \frac{1}{2} \left(\frac{\rho_g}{\rho_l} \right) \right] \dot{a}^2 - \zeta \frac{c_l}{a} \phi_l \right. \\ &\quad \left. - \rho_l^{-1}(P_g - p_l) \right\}, \\ \dot{\phi}_g &= (1 + \zeta)^{-1} \left\{ \left[1 + \frac{1}{2}\zeta + \frac{1}{2} \left(\frac{c_g}{c_l} \right) \right] \dot{a}^2 - \frac{c_g}{a} \phi_l \right. \\ &\quad \left. + \rho_l^{-1} \frac{c_g}{c_l} (P_g - p_l) \right\}, \end{aligned} \quad (29)$$

which correspond to Eq. (18). The right sides of Eq. (29) are used for $\dot{\phi}_l$ and $\dot{\phi}_g$ on the right sides of Eq. (28). Actually, there is no need to consider $\dot{\phi}_g$ because Eqs. (28a) and (29a) are sufficient to calculate $a(t)$.

Three initial values are required by Eqs. (28a) and (29a). The first two are again $a(t_I) = a_I$ and $\dot{a}(t_I) = \dot{a}_I$. To calculate $\phi_l(t_I)$, we solve Eq. (28a) for $\dot{\phi}_l$ and equate the right side of the result to the right side of Eq. (29a); or, we solve Eq. (28b) for $\dot{\phi}_g$ and equate the right side of that result to the right side of Eq. (29b). Either procedure yields

TABLE III. Dilational equations of motion for a compressible liquid; $p_l = p_{\text{atm}} + \rho_l g d_l$ and $0 \leq \lambda \leq 1$.

Herring (1941):	$a\ddot{a}\left(1 - 2\frac{\dot{a}}{c_l}\right) + \frac{3}{2}\dot{a}^2\left(1 - \frac{4\dot{a}}{3c_l}\right) = \rho_l^{-1}\left(P_g - p_l + \frac{a}{c_l}\dot{P}_g\right)$
Kirkwood and Bethe (1942):	$a\ddot{a}\left(1 - \frac{\dot{a}}{c_l}\right) + \frac{3}{2}\dot{a}^2\left(1 - \frac{\dot{a}}{3c_l}\right) = \rho_l^{-1}\left(P_g - p_l + \frac{a}{c_l}\dot{P}_g\right)\left(1 + \frac{\dot{a}}{c_l}\right)$
Keller and Kolodner (1956):	$a\ddot{a}\left(1 - \frac{\dot{a}}{c_l}\right) + \frac{3}{2}\dot{a}^2\left(1 - \frac{\dot{a}}{3c_l}\right) = \rho_l^{-1}\left[(P_g - p_l)\left(1 + \frac{\dot{a}}{c_l}\right) + \frac{a}{c_l}\dot{P}_g\right]$
Prosperetti and Lezzi (1986):	$a\ddot{a}\left[1 - (\lambda + 1)\frac{\dot{a}}{c_l}\right] + \frac{3}{2}\dot{a}^2\left[1 - \frac{1}{3}(3\lambda + 1)\frac{\dot{a}}{c_l}\right]$ $= \rho_l^{-1}\left\{(P_g - p_l)\left[1 + (1 - \lambda)\frac{\dot{a}}{c_l}\right] + \frac{a}{c_l}\dot{P}_g\right\}$

$$\phi_l = -a\ddot{a}\left[1 + \zeta - \frac{1}{2}(1 - \rho_g/\rho_l)\frac{\dot{a}}{c_l}\right] + \frac{a}{\rho_l c_l}(P_g - p_l), \quad (30)$$

which we evaluate at $t = t_l$. If interested, we may calculate ϕ_g from Eq. (29b), with $\phi_g(t_l)$ specified as any constant, zero being the most convenient.

Here too, we can eliminate ϕ_l as an unknown. We introduce Eq. (30) into Eq. (29a) to get

$$\phi_l = \frac{1}{2}(1 + \rho_g/\rho_l)\dot{a}^2 + \zeta c_l \dot{a} - \rho_l^{-1}(P_g - p_l). \quad (31)$$

Then, we differentiate Eq. (30) and equate the right side of the result to the right side of Eq. (31). This yields the DAA EOM

$$a\ddot{a}\left[1 + \zeta - \left(1 - \frac{\rho_g}{\rho_l}\right)\frac{\dot{a}}{c_l}\right] + \frac{3}{2}\dot{a}^2\left[1 + \frac{2}{3}\zeta - \frac{1}{3}\left(\frac{\dot{a}}{c_l}\right)\right]$$

$$+ \frac{1}{3}\left(\frac{\rho_g}{\rho_l}\right)\left(1 + \frac{\dot{a}}{c_l} + \frac{a}{c_l} \cdot \frac{\dot{\rho}_g}{\rho_g}\right) + (\zeta c_l + \zeta a)\dot{a}$$

$$= \rho_l^{-1}\left[(P_g - p_l)\left(1 + \frac{\dot{a}}{c_l}\right) + \frac{a}{c_l}\dot{P}_g\right], \quad (32)$$

with initial conditions $a(t_l) = a_l$ and $\dot{a}(t_l) = \dot{a}_l$. This new equation of motion accounts for wave effects in both the liquid and the gas, and reduces to Eq. (26) for $c_l \rightarrow \infty$, $\rho_g \rightarrow 0$.

Equation (32) provides greater insight if it is ‘‘normalized’’ to Eq. (26) with, from Eqs. (19)–(21)

$$\dot{P}_g = -3\rho_g c_g^2 \frac{\dot{a}}{a}, \quad \dot{\rho}_g = -3\rho_g \frac{\dot{a}}{a}, \quad \zeta = -\frac{3}{2}(\gamma + 1)\zeta \frac{\dot{a}}{a}. \quad (33)$$

Introducing these into Eq. (32) and neglecting terms in $(\dot{a}/c_l)^2$, we obtain

$$a\ddot{a}\left[1 + \zeta - \left(2 - \frac{\rho_g}{\rho_l}\right)\frac{\dot{a}}{c_l}\right] + \frac{3}{2}\dot{a}^2\left[1 - (\gamma + 1)\zeta - \left(\frac{4}{3} + \frac{\rho_g}{\rho_l}\right)\frac{\dot{a}}{c_l}\right]$$

$$+ \frac{1}{3}\left(\frac{\rho_g}{\rho_l}\right)\left(1 + \frac{\dot{a}}{c_l}\right) + \zeta(c_l + 3c_g)\dot{a}$$

$$= \rho_l^{-1}(P_g - p_l). \quad (34)$$

Comparing this with Eq. (26), we see that wave effects introduce modest response dependence into the coefficients of

$a\ddot{a}$ and \dot{a}^2 . However, their principal impact is to introduce two damping terms, with waves in the gas and liquid producing the coefficients $\zeta c_l = (\rho_g/\rho_l)c_g$ and $3\zeta c_g = 3\rho_g c_g^2/\rho_l c_l$, respectively. It is seen below that these a -dependent coefficients are comparable in size. Finally, it is interesting to note that, from Eq. (33c), the term $\zeta a \dot{a}$ in Eq. (32) produces an \dot{a}^2 term in Eq. (34), and, from Eq. (33a), the term $\rho_l^{-1}(a/c_l)\dot{P}_g$ in Eq. (32) produces the term $3\zeta c_g \dot{a}$ plus an \dot{a}^2 term in Eq. (34).

C. Mixed and previous models

There are two models that lie between the waveless and DAA models. The first accounts for wave effects in the liquid but not in the gas; the pertinent EOM is Eq. (32) with $\rho_g = \dot{\rho}_g = \zeta = \dot{\zeta} = 0$. The second accounts for wave effects in the gas but not in the liquid; the pertinent EOM is Eq. (32) with $\zeta = 0$, $c_l \rightarrow \infty$, and $\zeta c_l = (\rho_g/\rho_l)c_g$.

Table III shows some earlier dilational EOM that account for wave effects in the liquid but not in the gas. We see that the EOM for our first mixed model is identical to that of Keller and Kolodner (1956). In fact, if we divide each of the equations in Table III through by the coefficient of $a\ddot{a}$, we obtain the generic EOM

$$a\ddot{a} + \frac{3}{2}\dot{a}^2\left[1 + \frac{2}{3}\left(\frac{\dot{a}}{c_l}\right) + O_2\right]$$

$$= \rho^{-1}\left[(P_g - p_l)\left(1 + 2\frac{\dot{a}}{c_l} + O_2\right) + \frac{a}{c_l}\dot{P}_g(1 + O_1)\right], \quad (35)$$

where O_1 and O_2 denote terms in first and second powers, respectively, of the dilational Mach number \dot{a}/c_l . In the following, we refer to the EOM for the first mixed model as the K&K EOM and refer to the EOM for the second mixed model as the NPC (not previously considered) EOM.

It is informative to observe the effect of taking $\phi_{l,t} \approx \dot{\phi}_l$ in EDAA₁, i.e., neglecting \dot{a}^2 in Eq. (28a). The resulting EOM is the K&K EOM with the signs of the Mach-number terms on the left side reversed. Although this EOM performs satisfactorily in response computations, it is not consistent with the generic EOM, Eq. (35).

In 2000, Moss, Levatin, and Szeri (MLS) published a model for internal wave effects in a spherical bubble that

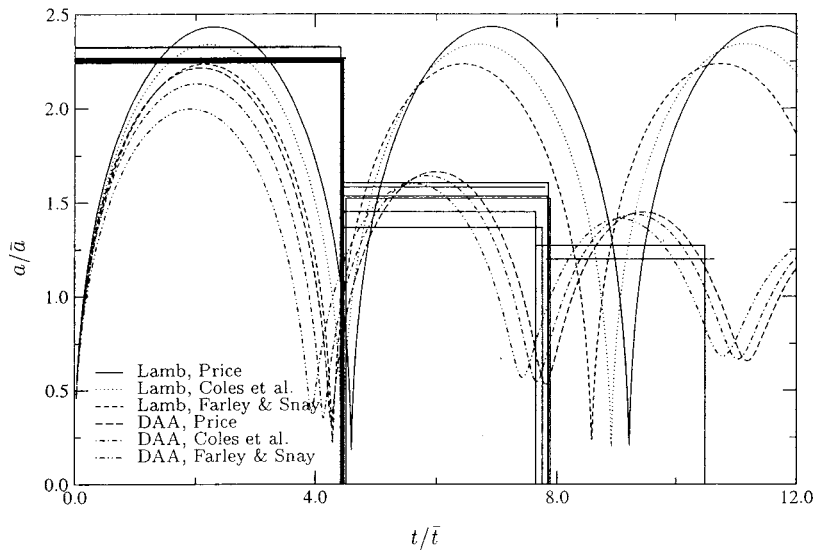


FIG. 4. Dilational displacement histories from the Lamb EOM, Eq. (26) and the DAA EOM, Eq. (32) for three sets of shock-wave ICs and the consolidated adiabatic EOS, Eq. (19); $t_1/T_c=7$.

calls for merely replacing P_g with $P_g + (a/3c_g)\dot{P}_g$. With $V_c/V = (a_c/a)^3$ in Eqs. (19)–(21), it is easily found that $(a/3c_g)\dot{P}_g = -\rho_g c_g \dot{a}$. Hence, the MLS modification corresponds to neglecting the convection terms in both Bernoulli's equation, Eq. (23b), and IDAA₁, Eq. (28b), for the gas, which yields $p_g = P_g - \rho_g c_g \dot{a}$. Introduction of the MLS replacement into the K&K EOM yields

$$a\ddot{a} \left(1 + \zeta - \frac{\dot{a}}{c_l} \right) + \frac{3}{2} \dot{a}^2 \left[1 - \left(\gamma + \frac{1}{3} \right) \zeta - \frac{1}{3} \left(\frac{\dot{a}}{c_l} \right) \right] = \rho_l^{-1} \left[(P_g - p_l) \left(1 + \frac{\dot{a}}{c_l} \right) + \left(\frac{1}{c_l} + \frac{1}{3c_g} \right) a \dot{P}_g \right], \quad (36)$$

to which Eq. (32) reduces if $(\rho_g/\rho_l)|\dot{a}/c_l| \ll 1$ and $\rho_g/3\rho_l \ll 1$. If one accepts these restrictions in order to simplify Eq. (32), one might also take $\zeta=0$ in Eq. (36), which yields a very simple equation. However, we prefer to stay with Eq. (32), which imposes no restrictions beyond those underlying the systematic formulation.

D. Computational versus experimental results for dilation

In this section we show nondimensional bubble-radius histories computed with the shock-wave ICs of Sec. II C, various equations of motion, and the equation of state given by Eq. (19). Pressure is normalized to p_l , and length and time are normalized to

$$\bar{a} = a_c (K_c/p_l)^{1/3\gamma}, \quad \bar{t} = \bar{a} / \sqrt{p_l/\rho_l}. \quad (37)$$

Based on $P_g = K_c (a_c/a)^{3\gamma}$, \bar{a} is the adiabatic equilibrium radius, i.e., the static radius at which $P_g = p_l$. With this parametrization, the nondimensional Lamb EOM [see Eq. (26)] is

$$\hat{a}\hat{a}'' + \frac{3}{2}(\hat{a}')^2 = \hat{a}^{-3\gamma} - 1, \quad (38)$$

where $\hat{a} = a/\bar{a}$ and a prime denotes differentiation with respect to $\hat{t} = t/\bar{t}$.

In 1948, Swift and Decius reported results from an extensive array of underwater explosion tests, among which were nine shots, each for a nominally 300-g charge of TNT

with mass density 1.50 g/cm³ detonated at a depth of 92 m. This depth was sufficiently large that each bubble remained essentially spherical and translated less than $\frac{1}{2}\%$ of its depth over three bubble periods. We shall use this ensemble of nearly identical shots as our *benchmark test*.

Shown in Fig. 4 are bubble-radius histories produced for the benchmark test by the Lamb and DAA EOM for $t_1/T_c = 7$, the 1.50 g/cm³ TNT constants from Table II, and the shock-wave-phase charge constants of Price (1979); Farley and Snay (1978); and Coles *et al.* (1946). Also shown as horizontal (vertical) lines are the maximum radii (times of minimum radii) measured by Swift and Decius. First, we note that the Lamb EOM erroneously produces no response decay and the DAA EOM correctly produces substantial response decay. Second, we observe that the DAA EOM predicts within 10% the first radial maximum and first minimum-radius time for the shock-wave-phase charge constants of Price and of Coles *et al.*, but not for the constants of Farley and Snay.

We investigated the charge-constant discrepancies by examining post-shock-wave energy associated with DAA-EOM calculations at time t_1 for the five choices $t_1/T_c = 3, 4, 5, 6,$ and 7 . As mentioned above, the flow at these times is nearly lossless; hence, we can calculate the total energy at the beginning of the oscillation phase from Cole (1948)

$$E_I = 2\pi\rho_l a_l^3 \dot{a}_l^2 + \frac{4}{3}\pi p_l a_l^3 + \frac{4}{3}\pi(\gamma-1)^{-1} K_c (a_c/a_l)^{3\gamma} a_l^3. \quad (39)$$

The first term on the right is the kinetic energy of incompressible liquid, the second is potential energy due to buoyancy, and the third is potential energy in the bubble gas. Table IV shows statistical data from the five calculations for

TABLE IV. Post-shock-wave energy from three sets of TNT charge constants.

Data set	Average (Kj)	Std. deviation (% of average)	Percent of original
Coles <i>et al.</i> (1946)	604	1.86%	42.2%
Farley and Snay (1978)	550	3.10%	38.4%
Price (1979)	661	1.25%	46.2%

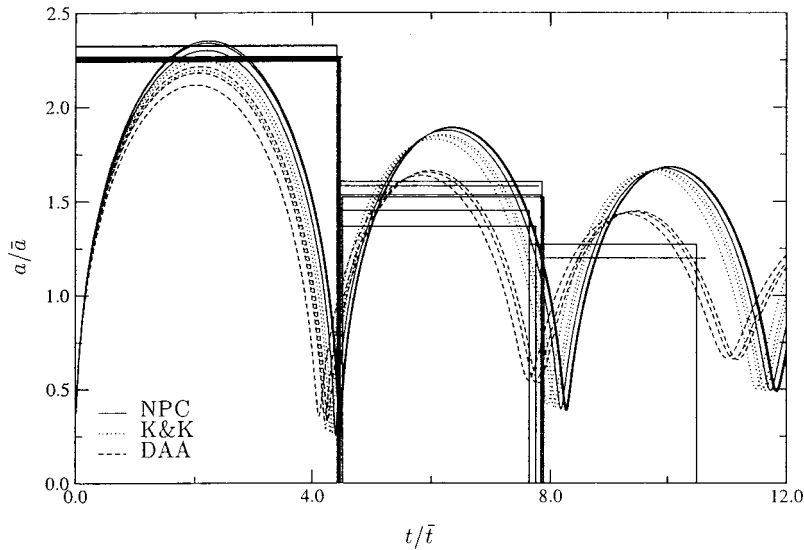


FIG. 5. Dilational displacement histories produced by the NPC EOM, the K&K EOM, and the DAA EOM, for $t_1/T_c=3, 5,$ and 7 .

each set of shock-wave-phase charge constants: P_c , ν_c , A , and B . The small standard deviations demonstrate that the choice of t_1 over the range considered is unimportant. For a detonation energy of 4770 J/g for TNT of density 1.5 g/cm^3 [Cook (1968)], the three charge-constant sets yield the entries in the last column of the table. Only Price's set yields a value for the percent of original energy left for the oscillation phase that lies within the range of previous estimates, *viz.*, $45\% - 50\%$ [Taylor (1942), Arons and Yennie (1948)], although the set of Coles *et al.* comes close. We use Price's shock-wave-phase charge constants in all subsequent calculations.

Figure 5 shows computed bubble-radius histories for the benchmark test produced by the DAA, K&K, and NPC EOM for $t_1/T_c=3, 5,$ and 7 . Also shown are the measured maximum radii and minimum-radius times from Fig. 4. The closeness of each trio of curves for a specified EOM again demonstrates the insensitivity of bubble response to t_1 values within the range $3T_c \leq t_1 \leq 7T_c$. We see in the figure that all the histories exhibit values for first bubble maximum and first minimum-radius time that agree satisfactorily with the

experimental data. However, the K&K and NPC histories do not exhibit satisfactory values for the second bubble maximum, in contrast to the DAA histories. The DAA EOM also outperforms the K&K and NPC EOM in predicting the third bubble maximum and minimum-radius time, but the DAA histories do not produce particularly accurate values. The NPC and K&K histories show energy loss in the gas as comparable to energy loss in the liquid, as mentioned in the discussion following Eq. (34). We also computed response histories with Eq. (36); they are barely distinguishable from the DAA histories. Finally, the nearly coincident K & K histories in Fig. 5 resemble closely a corresponding history presented in Fig. 5 of Chisum and Shin (1997), which was generated with a hydrocode.

It is informative to examine the ratios ρ_g/ρ_l , c_g/c_l , ζ , \dot{a}/c_g , and \dot{a}/c_l over the three bubble periods of Fig. 5. These ratios are shown in Fig. 6 as produced by the DAA EOM for $t_1/T_c=7$. We see that all five ratios remain substantially smaller than unity. That $(\dot{a}/c_g)^2 \ll 1$ and $(\dot{a}/c_l)^2 \ll 1$ is reassuring, because the DAA EOM is accurate only when both of these limitations hold, just as the EOM

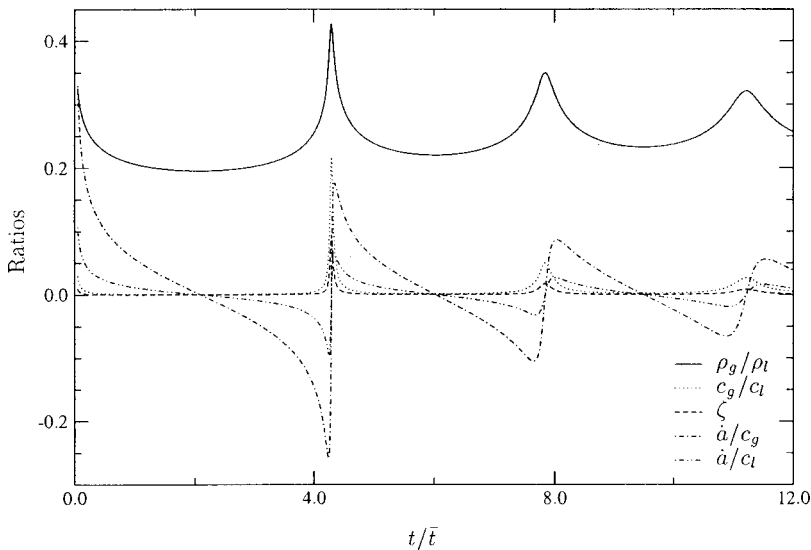


FIG. 6. Ratios pertinent to external and internal wave effects; $t_1/T_c=7$.

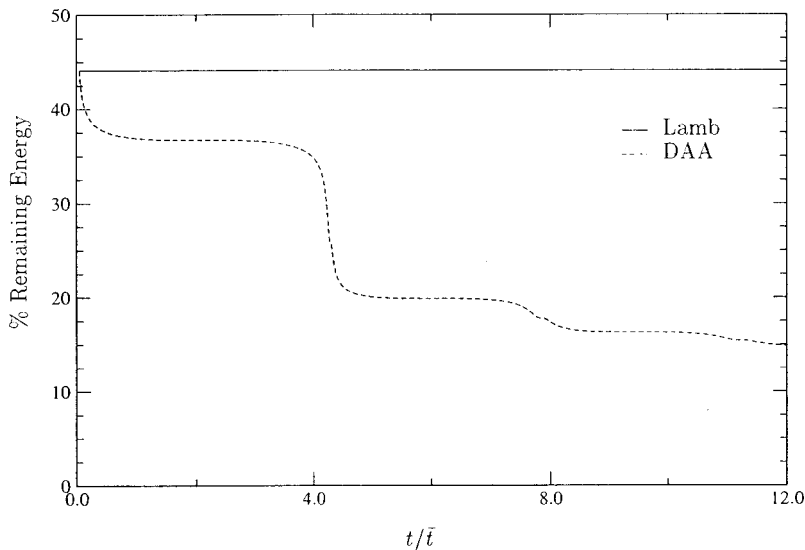


FIG. 7. Total energy as a function of time as calculated from Eq. (39) with $a_I \rightarrow a(t)$, the Lamb EOM, Eq. (26), and the DAA EOM, Eq. (32), for the benchmark test; $t_I/T_c = 7$.

listed in Table III are accurate only for $(\dot{a}/c_l)^2 \ll 1$ [Prosperetti and Lezzi (1986)]. Figure 6 shows that the largest value of $(\dot{a}/c_g)^2$ occurs at $t = t_I$; that value is 0.11. The same holds true for $t_I = 5T_c$, but the largest value is 0.19. Hence, the best available selection for t_I is $7T_c$, which is the value for which the DAA EOM performs best in Fig. 5.

E. Energy-loss mechanisms

Figure 5 implies that wave effects in the external liquid and the internal gas are the primary energy-loss mechanisms involved. It's obvious that the wave energy in the liquid is lost by acoustic radiation to the far field. But, the wave energy in the gas is internal, and can be lost only by transmission into the liquid for subsequent radiation or by conversion into another form. We consider the transmission mechanism first.

Figure 7 shows total energy as a function of time calculated from Eq. (39) with a_I replaced by $a(t)$. For the Lamb EOM, Eq. (26), $E(t)$ is constant because there is no energy-loss mechanism. There are two such mechanisms, however, for the DAA EOM, Eq. (32), so $E(t)$ decreases with time. As one would expect, however, the decrease is not steady, but consists of abrupt drops at times when the radial velocity is high. At each of these times, two spherical acoustic pulse waves are generated, one propagating outward and one propagating inward. Roughly speaking, the inward-propagating pulse has the pressure profile of a sine wave with a duration of one period T_P , and the outward-propagating pulse has the negative of that profile. Let us examine the propagation of the internal pulse wave generated by the bubble's first collapse/rebound. Because \dot{a} is always substantially smaller than c_g (Fig. 6), we neglect Doppler effects.

The internal pulse wave propagates with velocity c_g , which, from Eq. (21), varies in accordance with time-dependent bubble volume. The pulse travels inward until it reaches the bubble center and then returns to the bubble surface at time $t_{m1} + t_1$, where t_{m1} is the time of first collapse/rebound and t_1 is determined from

$$\int_{t_{m1}}^{t_{m1}+t_1} c_g(t) dt = a(t_{m1}) + a(t_{m1} + t_1). \quad (40)$$

Upon reaching the bubble surface, the pulse undergoes reflection and transmission, with energy fraction f_1 being reflected back into the bubble gas. The reflected pulse travels inward with variable velocity c_g , returns when it reaches the bubble center, and reaches the bubble surface at the time $t_{m1} + t_1 + t_2$, where t_2 is determined from

$$\int_{t_{m1}+t_1}^{t_{m1}+t_1+t_2} c_g(t) dt = a(t_{m1} + t_1) + a(t_{m1} + t_1 + t_2). \quad (41)$$

At this time, a second reflected pulse with energy fraction f_2 travels inward, and the events repeat. Let us follow the process through time t_J determined by

$$t_{m1} + \sum_{j=1}^J t_j < t_{M2} \quad \text{and} \quad t_{m1} + \sum_{j=1}^{J+1} t_j > t_{M2}, \quad (42)$$

where t_{M2} is the time of second bubble maximum. The fraction of first-collapse/rebound wave energy remaining at the time of second bubble maximum is then

$$F_J = \prod_{j=1}^J f_j. \quad (43)$$

If the characteristic wavelength, $\bar{c}_g T_P$, were much smaller than \bar{a} , where \bar{c}_g is a characteristic value of c_g during $t_{m1} \leq t \leq t_{M2}$, then transmission and reflection at the bubble surface would be nearly planar. This would produce an energy fraction reflected back into the bubble at time t_j of approximately [Kinsler *et al.* (1982)]

$$f_j = \left[\frac{1 - \zeta(t_{m1} + t_j)}{1 + \zeta(t_{m1} + t_j)} \right]^2. \quad (44)$$

However, the DAA-EOM calculations for the benchmark test produced a characteristic wavelength greater than \bar{a} , in which case the reflected energy fractions produced by Eq. (44) constitute lower bounds. Equation (42) for the benchmark test gives $J = 8$, and Eq. (43) with Eq. (44) yields $F_J = 0.91$. Hence, the transmission of internal wave energy out

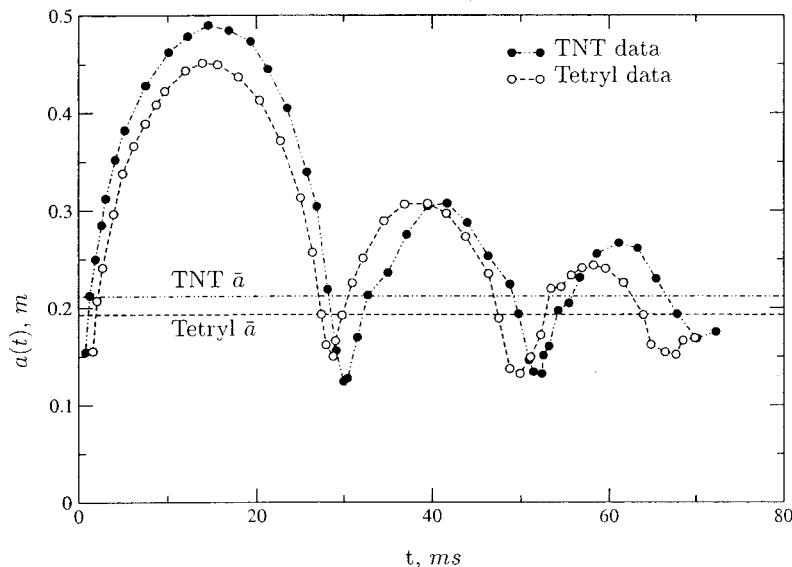


FIG. 8. Experimental radius histories for 300 g of TNT and 225 g of Tetryl, both detonated at a depth of 91.5 m; calculated equilibrium radii (\bar{a}) appear as horizontal lines at about 0.2 m [Swift and Decius (1948)].

to the liquid is an insignificant loss mechanism. This is because, as seen in Fig. 6, the specific-acoustic-impedance ratio ζ is very small at all times.

Regarding internal wave-energy loss by conversion to another form, we recall the convergence of an internal spherical pulse wave at the bubble center. Theoretically, the energy density in the pulse wave becomes unbounded there; actually, the transient pressures and temperatures approach levels far in excess of those characterizing the waveless gas model. These levels admit energy-loss mechanisms other than acoustic, such as gas dissociation and chemical reaction [Suslick (1990); Colussi *et al.* (1998)]. Although a study of such mechanisms is beyond the scope of this paper, it is clear that wave convergence offers ample opportunity for the loss of internal wave energy.

Even though the DAA radial-displacement histories in Fig. 5 indicate that wave effects in the external liquid and the internal gas are the primary energy-loss mechanisms, the histories do display a rate of decay that is somewhat slower than that seen in the tests, which implies that there is at least one other secondary mechanism at work. One secondary mechanism, heat and/or mass transfer at the bubble surface, would invalidate the adiabatic equation of state, Eq. (19) [see, e.g., Hentschel and Lauterborn (1982)]. A symptom of this type of energy loss is a bubble-radius history that settles down to a late-time asymptotic radius a_∞ smaller than the equilibrium radius \bar{a} . However, this symptom is not observed in Fig. 8, which shows measured bubble-radius histories for TNT and Tetryl charges [Swift and Decius (1948)] that are settling down nicely to their respective equilibrium radii. A contrary conclusion would be drawn from Fig. 8.1 in Cole (1948), which shows a measured bubble-radius history approaching a late-time asymptote of about 8 in., one-third smaller than the equilibrium-radius value drawn on the figure. However, we calculated for this experiment a value for equilibrium radius of 8 in., not 12 in.

Another possible energy-loss mechanism is the transfer of dilational energy to deformational modes of response. This has been considered by Penney and Price (1942); Ward (1943); Kolodner and Keller (1953); and recently by

Longuet-Higgins (1992), Feng and Leal (1993), Mao *et al.* (1995), and McDonald and Holland (2000). These researchers have shown that deformation can grow rapidly during bubble contraction, with computations typically failing at collapse. On the other hand, experiments have shown the bubble regaining its sphericity during subsequent expansion. This complex behavior is presently a topic of active research.

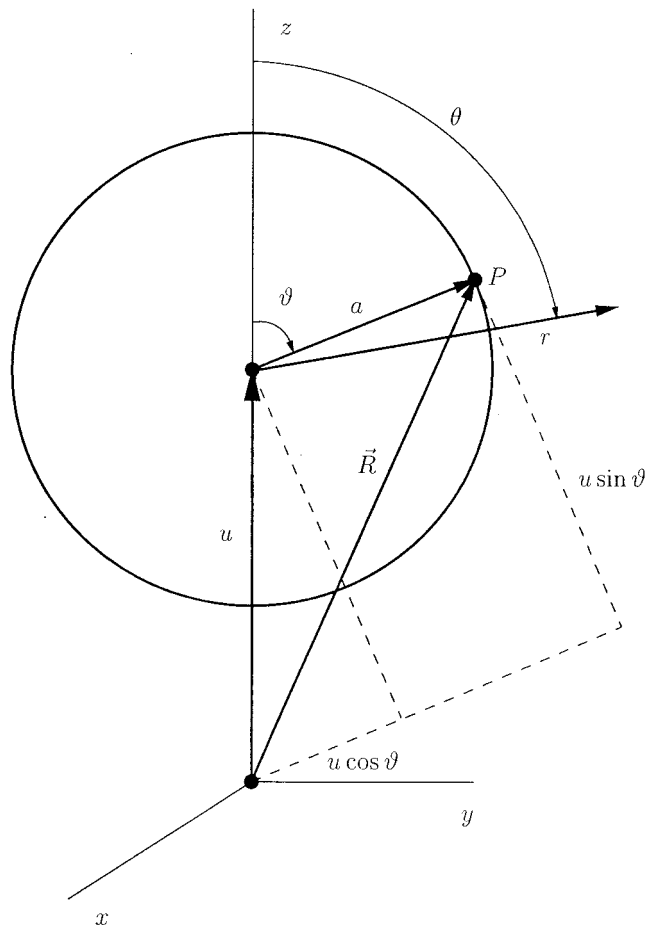


FIG. 9. Geometry for analysis of a dilating and translating bubble.

V. OSCILLATION PHASE: DILATION PLUS TRANSLATION OF A SPHERICAL BUBBLE

From Fig. 9, the position of an azimuthal ring of liquid particles on the spherical bubble surface may be described as

$$\mathbf{R}_l(t) = [a(t) + u(t)\cos\vartheta_l(t)]\mathbf{e}_r[\vartheta_l(t)] - u(t)\sin\vartheta_l(t)\mathbf{e}_\theta[\vartheta_l(t)]. \quad (45)$$

Hence,

$$\dot{\mathbf{R}}_l(t) = (\dot{a} + \dot{u}\cos\vartheta_l)\mathbf{e}_r(\vartheta_l) + [a\dot{\vartheta}_l(\vartheta_l) - \dot{u}\sin\vartheta_l]\mathbf{e}_\theta(\vartheta_l), \quad (46)$$

where the arguments of the time-dependent functions on the right have been dropped. From symmetry, we write $a\dot{\vartheta}_l(\vartheta_l) = \dot{\nu}_l \sin\vartheta_l$, so that Eq. (46) becomes

$$\dot{\mathbf{R}}_l = (\dot{a} + \dot{u}\cos\vartheta_l)\mathbf{e}_r(\vartheta_l) + (\dot{\nu}_l - \dot{u})\sin\vartheta_l\mathbf{e}_\theta(\vartheta_l). \quad (47)$$

Now at any instant, the velocity potential in the liquid, and its gradient, may be expressed in axisymmetric spherical coordinates for $r \geq a(t)$ as (Fig. 9)

$$\varphi_l(r, \theta, t) = \varphi_{l0}(r, t) + \varphi_{l1}(r, t)\cos\theta, \quad (48a)$$

$$\nabla\varphi_l(r, \theta, t) = [\varphi_{l0,r}(r, t) + \varphi_{l1,r}(r, t)\cos\theta]\mathbf{e}_r(\theta) - r^{-1}\varphi_{l1}(r, t)\sin\theta\mathbf{e}_\theta(\theta). \quad (48b)$$

Therefore, we can enforce Eq. (8a) by equating the right side of Eq. (47) to the right side of Eq. (48b) expressed at $r = a(t)$, $\theta = \vartheta_l(t)$, which yields

$$\dot{a} + \dot{u}\cos\vartheta_l = \dot{\phi}'_{l0} + \dot{\phi}'_{l1}\cos\vartheta_l, \quad (49a)$$

$$(\dot{\nu}_l - \dot{u})\sin\vartheta_l = -a^{-1}\dot{\phi}'_{l1}\sin\vartheta_l, \quad (49b)$$

where $\phi_{lm}(t) = \varphi_{lm}(a, t)$ and $\phi'_{lm}(t) = [(\partial/\partial r)\varphi_{lm}(r, t)]_{r=a(t)}$.

Now, the functions 1 and $\cos\vartheta_l$ are, with weight-function $\sin\vartheta_l$ for the spherical geometry, mutually orthogonal over the domain $0 \leq \vartheta_l \leq \pi$. Hence, we project Eq. (49a) onto each of those functions by multiplying both sides, first by $\sin\vartheta_l$ and then by $\sin\vartheta_l\cos\vartheta_l$, and integrating the two resulting equations over $0 \leq \vartheta_l \leq \pi$. Then, we project Eq. (49b) onto the function $\sin\vartheta_l$ by multiplying both sides by $\sin^2\vartheta_l$ and integrating the resulting equation over $0 \leq \vartheta_l \leq \pi$. This yields

$$\dot{a} = \dot{\phi}'_{l0}, \quad \dot{u} = \dot{\phi}'_{l1}, \quad \dot{\nu}_l = \dot{\phi}'_{l1} - a^{-1}\dot{\phi}'_{l1}. \quad (50)$$

Next, using Eq. (48) expressed at $r = a(t)$, $\theta = \vartheta_l(t)$, we write Bernoulli's equation at the bubble surface, Eq. (8c), as

$$\begin{aligned} \dot{\phi}'_{l0} + \dot{\phi}'_{l1}\cos\vartheta_l - \dot{\phi}'_{l1}\dot{\vartheta}_l(\vartheta_l)\sin\vartheta_l \\ = \frac{1}{2}[(\dot{\phi}'_{l0} + \dot{\phi}'_{l1}\cos\vartheta_l)^2 + (-a^{-1}\dot{\phi}'_{l1})^2\sin^2\vartheta_l] \\ - \rho_l^{-1}\{p_{l0} + p_{l1}\cos\vartheta_l \\ - [p_{\text{atm}} + \rho_l g(d_l - u - a\cos\vartheta_l)]\}. \end{aligned} \quad (51)$$

From $a\dot{\vartheta}_l(\vartheta_l) = \dot{\nu}_l \sin\vartheta_l$ and Eq. (50c), we find $\dot{\vartheta}_l(\vartheta_l) = a^{-1}(\dot{\phi}'_{l1} - a^{-1}\dot{\phi}'_{l1})\sin\vartheta_l$, which we introduce into Eq. (51). Then, we project the resulting equation, first onto the function 1 (dilatational projection) and then onto the function $\cos\vartheta_l$ (translational projection), to obtain

$$\begin{aligned} \dot{\phi}'_{l0} = \frac{1}{2}(\dot{\phi}'_{l0})^2 + \frac{1}{6}(\dot{\phi}'_{l1})^2 + \frac{1}{3}a^{-1}\dot{\phi}'_{l1}(2\dot{\phi}'_{l1} - a^{-1}\dot{\phi}'_{l1}) \\ - \rho_l^{-1}(p_{l0} - p_l + \rho_l g u), \end{aligned} \quad (52)$$

$$\dot{\phi}'_{l1} = \dot{\phi}'_{l0}\dot{\phi}'_{l1} - \rho_l^{-1}p_{l1} - g a.$$

Proceeding similarly with $r \leq a(t)$ for the internal gas, we obtain

$$\dot{a} = \dot{\phi}'_{g0}, \quad \dot{u} = \dot{\phi}'_{g1}, \quad \dot{\nu}_g = \dot{\phi}'_{g1} - a^{-1}\dot{\phi}'_{g1}, \quad (53)$$

and

$$\begin{aligned} \dot{\phi}'_{g0} = \frac{1}{2}(\dot{\phi}'_{g0})^2 + \frac{1}{6}(\dot{\phi}'_{g1})^2 + \frac{1}{3}a^{-1}\dot{\phi}'_{g1}(2\dot{\phi}'_{g1} - a^{-1}\dot{\phi}'_{g1}) \\ - \rho_g^{-1}(p_{g0} - P_g), \end{aligned} \quad (54)$$

$$\dot{\phi}'_{g1} = \dot{\phi}'_{g0}\dot{\phi}'_{g1} - \rho_g^{-1}p_{g1} - g a.$$

The velocity-compatibility and pressure-equilibrium conditions are $[\dot{\phi}'_{g0} + \dot{\phi}'_{g1}\cos\vartheta_g]_{\vartheta_g=\vartheta_l} = \dot{\phi}'_{l0} + \dot{\phi}'_{l1}\cos\vartheta_l$ and $[p_{g0} + p_{g1}\cos\vartheta_g]_{\vartheta_g=\vartheta_l} = p_{l0} + p_{l1}\cos\vartheta_l$, respectively. Projection then yields $\dot{\phi}'_{g0} = \dot{\phi}'_{l0}$, $\dot{\phi}'_{g1} = \dot{\phi}'_{l1}$, $p_{l0} = p_{g0}$, and $p_{l1} = p_{g1}$.

A. Waveless model

For dilation plus translation of a spherical surface with radius a , the BIE, Eq. (10), becomes

$$\dot{\phi}'_{l0} + \dot{\phi}'_{l1}\cos\vartheta_l = -a^{-1}(\dot{\phi}'_{l0} + 2\dot{\phi}'_{l1}\cos\vartheta_l), \quad (55)$$

which is readily verified by noting that the pertinent solution to Laplace's equation is $\varphi(r, \theta, t) = \phi_0(t) \cdot a/r + \phi_1(t) \cdot (a/r)^2 \cos\theta$. Dilational and translational projection of Eq. (55) gives

$$\dot{\phi}'_{l0} = -a^{-1}\dot{\phi}'_{l0}, \quad \dot{\phi}'_{l1} = -2a^{-1}\dot{\phi}'_{l1}. \quad (56)$$

Using Eqs. (50a) and (50b) to eliminate $\dot{\phi}'_{l0}$ and $\dot{\phi}'_{l1}$ from these relations, we find

$$\dot{a} = -a^{-1}\dot{\phi}'_{l0}, \quad \dot{u} = -2a^{-1}\dot{\phi}'_{l1}, \quad (57)$$

which correspond to Eq. (12a).

With $p_{g0} = P_g$ and $p_{g1} = 0$, pressure equilibrium yields $p_{l0} = P_g$ and $p_{l1} = 0$. Introducing these and Eqs. (56) into Eqs. (52), we obtain

$$\dot{\phi}'_{l0} = \frac{1}{2}(a^{-1}\dot{\phi}'_{l0})^2 - (a^{-1}\dot{\phi}'_{l1})^2 - \rho_l^{-1}(P_g - p_l + \rho_l g u), \quad (58a)$$

$$\dot{\phi}'_{l1} = 2(a^{-1}\dot{\phi}'_{l0})(a^{-1}\dot{\phi}'_{l1}) - g a, \quad (58b)$$

which correspond to Eq. (12b). The initial conditions for Eqs. (57) and (58) are $a(t_I) = a_I$, $u(t_I) = 0$, $\phi_{l0}(t_I) = -a_I \dot{a}_I$, and $\phi_{l1}(t_I) = 0$, the latter pair coming from Eq. (57) and $\dot{u}(t_I) = 0$.

We can eliminate ϕ_{l0} and ϕ_{l1} as variables in three steps. First, employ Eq. (57) to eliminate them on the right sides of Eq. (58). Second, multiply Eq. (57a) through by a , differentiate to get an expression for $\dot{\phi}'_{l0}$, and equate that expression to the right side of the modified Eq. (58a). Third, multiply Eq. (57b) through by a , differentiate to get an expression for $\dot{\phi}'_{l1}$, and equate that expression to the right side of the modified Eq. (58b). This yields the following waveless EOM for dilation plus translation:

$$a\ddot{a} + \frac{3}{2}\dot{a}^2 - \frac{1}{4}\dot{u}^2 - gu = \rho_l^{-1}[P_g - (p_{\text{atm}} + \rho_l g d_l)], \quad (59)$$

$$a\ddot{u} + 3\dot{a}\dot{u} - 2ga = 0.$$

These agree closely with previous equations obtained by different means. Penney and Price (1942) and Ward (1943) obtained equations that differ from Eq. (59) only in the absence of the term $\frac{1}{4}\dot{u}^2$. Hicks (1970) used Lagrange's equation to obtain Eq. (59) in its entirety. Hence, we shall refer to them as the Hicks EOM. The initial conditions for Eq. (59) are $a(t_l) = a_l$, $\dot{a}(t_l) = \dot{a}_l$, $u(t_l) = 0$, and $\dot{u}(t_l) = 0$. The last of these, when introduced into Eq. (59b), leads to $u(t) \approx g(t - t_l)^2$ at very early time.

It is informative to consider Eq. (59) from the standpoint of generalized momenta and forces. The former are defined as $P_q \equiv \partial T / \partial \dot{q}$, where T is system kinetic energy and q is a generalized displacement [Meirovitch (1997)]. Here, the momenta are given by

$$P_a = 4\pi\rho_l a^3 \dot{a}, \quad P_u = \frac{2}{3}\pi\rho_l a^3 \dot{u}, \quad (60)$$

i.e., each is the product of an "added mass" of liquid [Milne-Thomson (1960)] and its associated velocity. We may write Eq. (59) in terms of these quantities as

$$\dot{P}_a = F_{\text{gas}} - F_{\text{amb}} + F_{\text{exp}}, \quad \dot{P}_u = F_{\text{buoy}}, \quad (61)$$

where the (always positive) gas, ambient, expansion, and buoyancy forces are given by

$$F_{\text{gas}} = 4\pi a_c^2 K_c (a_c/a)^{3\gamma-2},$$

$$F_{\text{amb}} = 4\pi a^2 [p_{\text{atm}} + \rho_l g (d_l - u)], \quad (62)$$

$$F_{\text{exp}} = \pi\rho_l a^2 (6\dot{a}^2 + \dot{u}^2), \quad F_{\text{buoy}} = \frac{4}{3}\pi\rho_l g a^3.$$

Figure 10 shows nondimensional histories for P_a , P_u , F_{gas} , F_{amb} , F_{exp} , and F_{buoy} over the first $2\frac{1}{2}$ response cycles for the benchmark test defined in Sec. IV D. We observe that P_a is oscillatory while P_u increases monotonically. When a is large, P_u is the product of a large translational added mass and a small translational velocity; the reverse holds when a is small, however, which produces rapid bubble translation at each collapse/rebound. Because P_u at second collapse/rebound is essentially double that at first collapse/rebound, the second jump in translational velocity is essentially twice as large as its predecessor; similarly, the n th translational jump is essentially n times as large as the first jump. With regard to the dilational generalized forces, F_{amb} is dominant when a is large, while F_{gas} and F_{exp} are dominant when a is small. F_{gas} is a dominant force only at collapse/rebound, whereas F_{exp} is a dominant force over much of a cycle. Note that F_{exp} suffers extremely rapid variation as \dot{a} passes through zero during collapse/rebound.

B. DAA model

From Eqs. (14), (55), and (48a) expressed at $r = a(t)$, $\theta = \vartheta_l(t)$, and from Eq. (47), EDAA₁ for dilation plus translation of a spherical surface is

$$\begin{aligned} \phi'_{l0} + \phi'_{l1} \cos \vartheta_l &= -a^{-1}(\phi_{l0} + 2\phi_{l1} \cos \vartheta_l) \\ &\quad - c_l^{-1}[\dot{\phi}_{l0} + \dot{\phi}_{l1} \cos \vartheta_l - \phi_{l1} \dot{\vartheta}_l(\vartheta_l) \sin \vartheta_l \\ &\quad - (\dot{a} + \dot{u} \cos \vartheta_l)^2 - (\dot{v}_l - \dot{u})^2 \sin^2 \vartheta_l]. \end{aligned} \quad (63)$$

Introducing $\dot{\vartheta}_l(\vartheta_l) = a^{-1}\dot{v}_l \sin \vartheta_l$ and Eqs. (50b) and (50c) in the right side of this equation, and then projecting the result, we obtain the modal EDAA₁ equations

$$\begin{aligned} \phi'_{l0} &= -a^{-1}\phi_{l0} - c_l^{-1}(\dot{\phi}_{l0} - \dot{a}^2 - \frac{1}{3}\dot{u}^2 - \frac{2}{3}\dot{u}a^{-1}\phi_{l1}), \\ \phi'_{l1} &= -2a^{-1}\phi_{l1} - c_l^{-1}(\dot{\phi}_{l1} - 2\dot{a}\dot{u}). \end{aligned} \quad (64)$$

As discussed in Sec. III B, $H_g \phi_g$ vanishes for dilational motion. $H_g \phi_g$ produces $a^{-1}\phi_{g1} \cos \vartheta_g$ for translational motion, which is readily verified from Eq. (10) by noting that the pertinent solution to Laplace's equation is $\varphi_1(r, \vartheta) = (\phi_1 \cdot r/a) \cos \vartheta$. Hence, from Eq. (16), Eq. (48a) with $l \rightarrow g$ expressed at $r = a(t)$, $\theta = \vartheta_g(t)$, and Eq. (47) with $l \rightarrow g$, IDAA₁ for dilation plus translation of a spherical surface is [cf. Eq. (63)]

$$\begin{aligned} \phi'_{g0} + \phi'_{g1} \cos \vartheta_g &= a^{-1}\phi_{g1} \cos \vartheta_g \\ &\quad + c_g^{-1}[\dot{\phi}_{g0} + \dot{\phi}_{g1} \cos \vartheta_g - \phi_{g1} \dot{\vartheta}_g(\vartheta_g) \sin \vartheta_g \\ &\quad - (\dot{a} + \dot{u} \cos \vartheta_g)^2 - (\dot{v}_g - \dot{u})^2 \sin^2 \vartheta_g]. \end{aligned} \quad (65)$$

Employing $\dot{\vartheta}_g(\vartheta_g) = a^{-1}\dot{v}_g \sin \vartheta_g$ and Eqs. (53b) and (53c) in the right side of this equation, and then projecting the result, we obtain the modal IDAA₁ equations [cf. Eq. (64)]

$$\begin{aligned} \phi'_{g0} &= c_g^{-1}(\dot{\phi}_{g0} - \dot{a}^2 - \frac{1}{3}\dot{u}^2 - \frac{2}{3}\dot{u}a^{-1}\phi_{g1}), \\ \phi'_{g1} &= a^{-1}\phi_{g1} + c_g^{-1}(\dot{\phi}_{g1} - 2\dot{a}\dot{u}). \end{aligned} \quad (66)$$

The substitution of \dot{a} for ϕ'_{l0} and \dot{u} for ϕ'_{l1} in Eq. (64) yields the following DAA-consolidated kinematic-compatibility equations that correspond to Eq. (17a):

$$\dot{a} = -a^{-1}\phi_{l0} - c_l^{-1}(\dot{\phi}_{l0} - \dot{a}^2 - \frac{1}{3}\dot{u}^2 - \frac{2}{3}\dot{u}a^{-1}\phi_{l1}), \quad (67a)$$

$$\dot{u} = -2a^{-1}\phi_{l1} - c_l^{-1}(\dot{\phi}_{l1} - 2\dot{a}\dot{u}). \quad (67b)$$

The substitution of \dot{a} for ϕ'_{g0} and \dot{u} for ϕ'_{g1} in Eq. (66) yields the following equations that correspond to (17b):

$$\dot{a} = c_g^{-1}(\dot{\phi}_{g0} - \dot{a}^2 - \frac{1}{3}\dot{u}^2 - \frac{2}{3}\dot{u}a^{-1}\phi_{g1}), \quad (68a)$$

$$\dot{u} = a^{-1}\phi_{g1} + c_g^{-1}(\dot{\phi}_{g1} - 2\dot{a}\dot{u}). \quad (68b)$$

A procedure parallel to that described between Eqs. (17) and (18) yields the following DAA-consolidated Bernoulli equations that correspond to Eqs. (18):

$$\begin{aligned} \dot{\phi}_{l0} &= (1 + \zeta)^{-1} \left\{ \left[\frac{1}{2} + \frac{1}{2} \left(\frac{\rho_g}{\rho_l} \right) + \zeta \right] (\dot{a}^2 + \frac{1}{3}\dot{u}^2) \right. \\ &\quad \left. - \frac{\rho_g}{\rho_l} c_g a^{-1} \phi_{l0} + \frac{2}{3} (1 + \zeta) \dot{u} a^{-1} \phi_{l1} - Z \right\}, \end{aligned} \quad (69a)$$

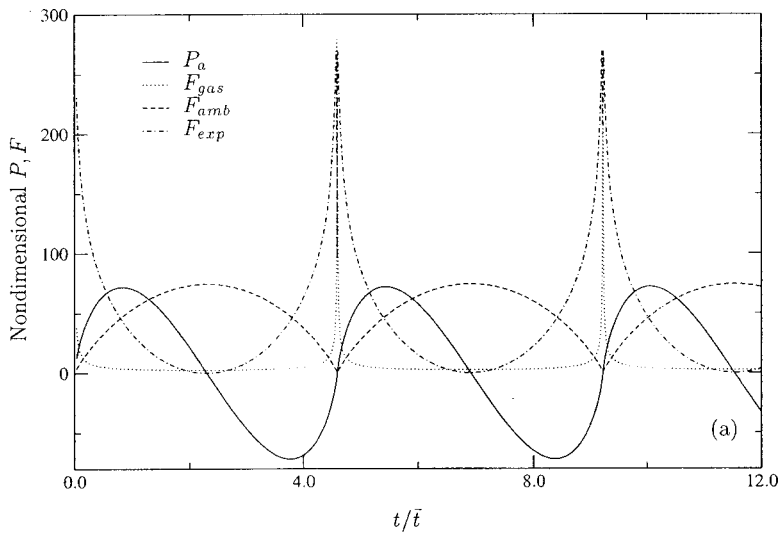
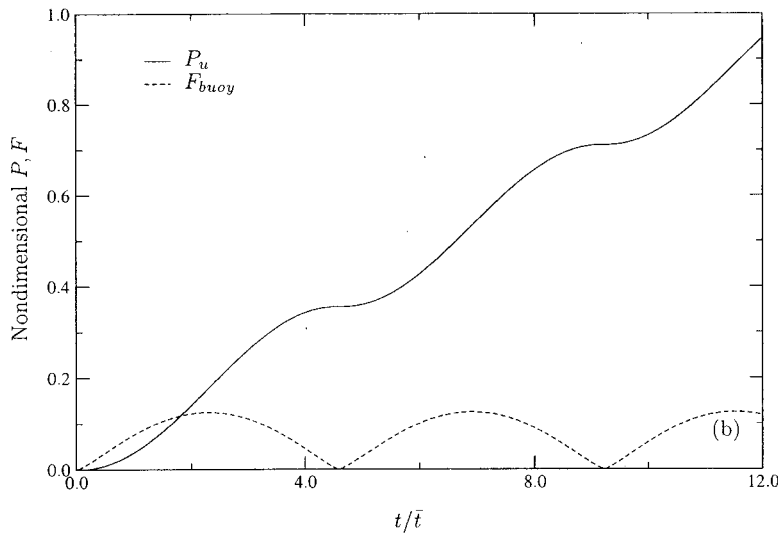


FIG. 10. Momentum, Eq. (60), and force, Eq. (62), histories for the Hicks EOM, Eq. (59); $t_I/T_c=7$.



$$\begin{aligned} \phi_{g0} = (1 + \zeta)^{-1} & \left[\left[1 + \frac{1}{2} \left(\frac{c_g}{c_l} \right) + \frac{1}{2} \zeta \right] (\dot{a}^2 + \frac{1}{3} \dot{u}^2) \right. \\ & \left. - c_g a^{-1} \phi_{l0} + \frac{2}{3} (1 + \zeta) \dot{u} a^{-1} \phi_{g1} + \frac{c_g}{c_l} Z \right], \quad (69b) \end{aligned}$$

$$\begin{aligned} \phi_{l1} = (1 + \zeta)^{-1} & \left[\left(1 + \frac{\rho_g}{\rho_l} + 2\zeta \right) \dot{a} \dot{u} - \frac{\rho_g}{\rho_l} c_g (2a^{-1} \phi_{l1} \right. \\ & \left. + a^{-1} \phi_{g1}) - \left(1 - \frac{\rho_g}{\rho_l} \right) g a \right], \quad (69c) \end{aligned}$$

$$\begin{aligned} \phi_{g1} = (1 + \zeta)^{-1} & \left[\left(2 + \frac{c_g}{c_l} + \zeta \right) \dot{a} \dot{u} - c_g (2a^{-1} \phi_{l1} \right. \\ & \left. + a^{-1} \phi_{g1}) + \frac{c_g}{c_l} \left(1 - \frac{\rho_g}{\rho_l} \right) g a \right], \quad (69d) \end{aligned}$$

where $Z = \rho_l^{-1} (P_g - p_l + \rho_l g u) + 1/3 [(a^{-1} \phi_{l1})^2 - (\rho_g/\rho_l) \times (a^{-1} \phi_{g1})^2]$. The right sides of Eq. (69) are used for ϕ_{l0} , ϕ_{g0} , ϕ_{l1} , and ϕ_{g1} on the right sides of Eqs. (67) and (68). Equations (67)–(69) are new; they lend themselves to numerical solution by explicit time integration with iteration keyed to $(a^{-1} \phi_{l1})^2$ and $(a^{-1} \phi_{g1})^2$. Again, there is no need to consider ϕ_{g0} because Eqs. (67) and (69a), (69c), and (69d)

are sufficient to calculate $a(t)$ and $u(t)$. Thus, we have five equations for five unknowns.

Seven initial values are needed; the first two are $a(t_I) = a_I$, $\dot{a}(t_I) = \dot{a}_I$ and the second two are $u(t_I) = 0$, $\dot{u}(t_I) = 0$. To determine $\phi_{l0}(t_I)$, we may either solve Eq. (67a) for $\dot{\phi}_{l0}$ and equate the right side of the result to the right side of Eq. (69a), or solve Eq. (68a) for $\dot{\phi}_{g0}$ and equate the right side of that result to the right side of Eq. (69b). Either way gives

$$\phi_{l0} = -a \dot{a} \left[1 + \zeta - \frac{1}{2} \left(1 - \frac{\rho_g}{\rho_l} \right) \frac{\dot{a}}{c_l} \right] + \frac{1}{6} \left(1 - \frac{\rho_g}{\rho_l} \right) \frac{\dot{u}}{c_l} + \frac{a}{c_l} Z, \quad (70)$$

which we must evaluate at $t = t_I$. To determine $\phi_{g1}(t_I)$, we may either solve Eq. (67b) for $\dot{\phi}_{l1}$ and equate the right side of the result to the right side of Eq. (69c), or solve Eq. (68b) for $\dot{\phi}_{g1}$ and equate the right side of that result to the right side of Eq. (69d). Either procedure yields

$$\phi_{g1} = \zeta^{-1} \left\{ \left[1 + \zeta - \left(1 - \frac{\rho_g}{\rho_l} \right) \frac{\dot{a}}{c_l} \right] a \dot{u} - \left(1 - \frac{\rho_g}{\rho_l} \right) \frac{g}{c_l} a^2 + 2 \phi_{l1} \right\}, \quad (71)$$

which we also must evaluate at $t = t_I$.

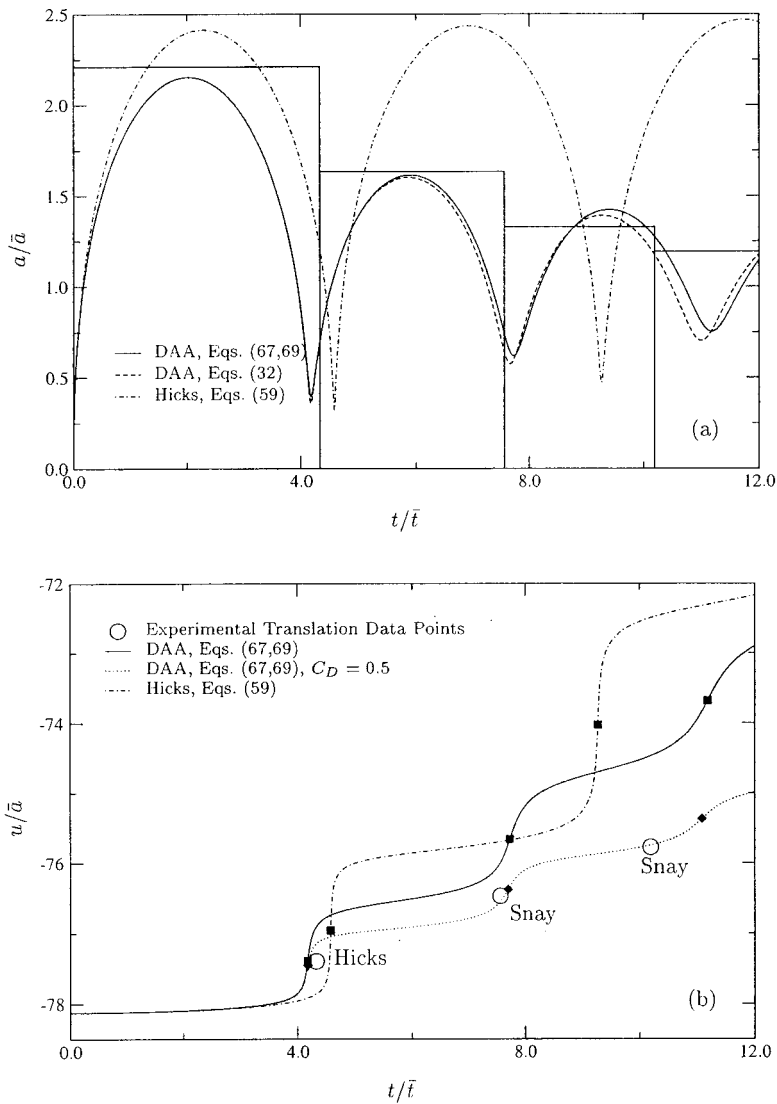


FIG. 11. Dilational and translational displacement histories from the DAA-consolidated equations, Eqs. (67) and (69a), (69c), and (69d), the Hicks EOM, Eq. (59), and the DAA-dilational EOM, Eq. (32), compared with experimental data from Snay (1962) and Hicks (1970); $t_I/T_c=7$.

In order to evaluate Eqs. (70) and (71) at $t=t_I$, we require $\phi_{11}(t_I)$. This may be found by first determining $\dot{\phi}_{11}(t_I)$ for the waveless model with Eqs. (58b) and (57b); the result is $\dot{\phi}_{11}(t_I) = -g a_I$. Introducing this relation into Eq. (67b) expressed at $t=t_I$, solving for $\phi_{11}(t_I)$, and introducing the result into Eqs. (71) and (70), we obtain the initial values

$$\begin{aligned} \phi_{11}(t_I) &= \frac{1}{2}(g/c_l)a_I^2, & \phi_{g1}(t_I) &= (g/c_g)a_I^2, \\ \phi_{10}(t_I) &= -a_I \left\{ \dot{a}_I \left[1 + \zeta_l - \frac{1}{2} \left(1 - \frac{\rho_{gl}}{\rho_l} \right) \frac{\dot{a}_I}{c_l} \right] - (\rho_l c_l)^{-1} \right. \\ & \quad \left. \times (P_{gl} - p_l) + \frac{1}{3} \left(\frac{\rho_{gl}}{\rho_l} c_{gl}^{-2} - \frac{1}{4} c_l^{-2} \right) c_l^{-1} (g a_I)^2 \right\}. \end{aligned} \quad (72)$$

Note that the introduction of Eqs. (72a) and (72b) into Eq. (69c) yields $\dot{\phi}_{11}(t_I) = -g a_I$, as found from the waveless model.

As mentioned at the end of Sec. III B, Eq. (72) can also be used to define the initial conditions for general bubble motion, inasmuch as deformation results only from parametric forcing [Penney and Price (1942); Ward (1943); Kolodner

and Keller (1953)]. This is in contrast to dilation, which is driven by bubble pressure, and translation, which is driven by buoyancy.

Unfortunately, Eqs. (67) and (69a), (69c) and (69d) do not lend themselves to the formulation of EOM for dilation plus translation. This matters little, however, as the first-order equations integrate quite readily.

C. Computational versus experimental results for dilation plus translation

Figure 11 shows computed dilation and translation histories for a case in which experimental data pertaining to both motions exist [Snay (1962); Hicks (1970)]. The data pertain to a detonation of 227 kg of 1.5 g/cc TNT at a depth of 137 m. The histories come from the DAA-consolidated equations, Eqs. (67) and (69a), (69c), and (69d), the Hicks EOM, Eq. (59), and the DAA EOM for dilation only, Eq. (32). The solid symbols on the translational histories mark calculated bubble positions at calculated radial minima, and the circles mark measured bubble positions at measured radial minima.

Figure 11(a) shows very good agreement between the

DAA bubble-radius histories and the experimental data through the first two bubble periods; it shows satisfactory agreement between the Hicks history and the data through the first bubble period. The proximity of the two DAA histories indicates that, at this depth, the effect of translation on dilation is small. For the third bubble period, the DAA-calculated maximum radius is close to its experimental counterpart, but the associated period is too large. The comparison does not extend beyond three bubble periods because Snay characterizes the measurements of later periods as “sparse and uncertain.”

Figure 11(b) implies good DAA prediction of translation until just beyond the first bubble minimum, fair prediction from that time to just beyond the second bubble minimum, and poor prediction thereafter. It implies fair Hicks prediction until just beyond the first period and poor prediction after that. Regarding the experimental data points, Snay (1962) discusses the “rather approximate nature of the information.” To improve his prediction of translation, Hicks introduced form drag with an exaggerated drag coefficient of 2.25. We introduced a drag coefficient of 0.5 into our DAA model to produce the history marked with diamonds. The corresponding dilation history lies between the two DAA histories in Fig. 11(a).

VI. CONCLUSION

In this paper, we have introduced the following new constituents into a boundary model of an underwater-explosion bubble located well below the free surface.

- (1) A treatment of shock-wave-phase phenomena that relates volume acceleration to an empirical far-field pressure profile, thereby connecting the shock-wave and oscillation phases of bubble motion by means of initial conditions for the latter;
- (2) DAA-based response equations for oscillation-phase bubble motion that account for wave effects in both the liquid and the gas; equations are given for general motion, pure dilation of a spherical bubble, and dilation plus translation of a spherical bubble.

The result is an integrated bubble model that, when specialized to the spherical geometry, produces calculated responses in much better agreement with experimental data than those produced by waveless and mixed models.

However, as seen in Fig. 11, the DAA-based spherical model has its deficiencies. The deficiency in dilation prediction may be addressed through artificial reductions of c_l and/or c_g so as to fit existing bubble-maximum and bubble-period experimental data, at least through the third bubble period. The deficiency in translation prediction may then be addressed through the introduction of a drag coefficient adjusted to fit bubble-translation experimental data, although the existing data are not highly reliable.

A more satisfying strategy would employ a dilation/translation/deformation model for the oscillation phase that incorporates wave effects in both the liquid and the gas [Eqs. (17) and (18)], as well as jetting effects at bubble collapse/rebound [Best (1993); Zhang *et al.* (1993)]. Boundary-

element bubble codes based on Eq. (12), when applied to the spherical bubble in Fig. 9, surely produce the Hicks histories in Fig. 11.

Finally, it would be worthwhile to explore the physical phenomena underlying the wave-energy sink implied in the internal doubly asymptotic approximation, Eq. (16). Bubble calculations with hydrocodes that don't account for such energy loss overpredict bubble response as a matter of course.

ACKNOWLEDGMENTS

This work was supported under Contract No. DNA001-94-C-0004 with the Defense Threat Reduction Agency, Alexandria, VA, and Contract Nos. N00014-94-1-0796 and N00014-01-1-0154 with the Office of Naval Research, Arlington, VA. The authors thank Mr. Douglas Bruder and Mr. Michael Giltrud of DTRA, Dr. Roshdy Barsoum, Dr. Luise Couchman, and Mr. Steven Schreppler of ONR, Mr. Michael Riley and Mr. Gregory Harris of the Naval Surface Warfare Center, and Mr. Austin Alvarez of Electric Boat Corporation.

- Arons, A. B., and Yennie, D. R. (1948). “Energy partition in underwater explosion phenomena,” *Rev. Mod. Phys.* **20**, 519–536.
- Atkatsch, R. S., Bieniek, M. P., and Baron, M. L. (1983). “Dynamic elastoplastic response of shells in an acoustic medium—EPSA code,” *Int. J. Numer. Methods Eng.* **19**(6), 811–824.
- Banerjee, P. K., and Butterfield, R. (1981). *Boundary Element Methods in Engineering Science* (McGraw-Hill, New York).
- Besant, W. H. (1859). *Hydrostatics and Hydromechanics* (Bell, London).
- Best, J. P. (1993). “The formation of toroidal bubbles upon the collapse of transient cavities,” *J. Fluid Mech.* **251**, 79–107.
- Blake, J. R., and Gibson, D. C. (1987). “Cavitation bubbles near boundaries,” *Annu. Rev. Fluid Mech.* **19**, 99–123.
- Chahine, G. L., and Kalumuck, K. M. (1998). “BEM software for free surface flow simulation including fluid structure interaction effects,” *Int. J. Comput. Appl. Tech.* **11**(3/4/5), 177–198.
- Chisum, J. E., and Shin, Y. S. (1997). “Explosion gas bubbles near simple boundaries,” *Shock Vibration* **4**(1), 11–25.
- Cole, R. H. (1948). *Underwater Explosions* (Princeton University Press, Princeton).
- Coles, J. S., Christian, E. A., Slifko, J. P., Niffenegger, C. R., and Rogers, M. A. (1946). “Shock-wave parameters from spherical TNT charges detonated underwater,” in *Underwater Explosion Research* (Office of Naval Research, Washington, D.C., 1950), Vol. 1, pp. 1085–1105.
- Colussi, A. J., Weavers, L. K., and Hoffmann, M. R. (1998). “Chemical bubble dynamics and quantitative sonochemistry,” *J. Phys. Chem. A* **102**, 6927–6934.
- Cook, M. A. (1968). *The Science of High Explosives* (Reinhold, New York), Chap. 12.
- DeRuntz, J. A. (1989). “The Underwater Shock Analysis Code and its applications,” in *Proceedings 60th Shock and Vib. Symposium*, pp. 89–107, SAVIAC.
- Dobratz, B. M. (1981). LLNL Explosives Handbook. Technical Report UCRL-52997, Lawrence Livermore National Laboratory, Livermore, CA.
- Duncan, J. H., and Zhang, S. (1991a). “Numerical calculations on the growth and collapse of a vapor cavity in the vicinity of a compliant wall,” in *Mathematical Approaches to Hydrodynamics*, edited by T. Miloh (SIAM), pp. 68–87.
- Duncan, J. H., and Zhang, S. (1991b). “On the interaction of a collapsing cavity and a compliant wall,” *J. Fluid Mech.* **226**, 401–423.
- Farley, T. E., and Snay, H. G. (1978). “Unclassified data from classified source,” in *Explosion Effects and Properties: Part II—Explosion Effects in Water*, edited by M. M. Swisdak, NSWC/WOL TR 76-116, NSWC.
- Felippa, C. A. (1980). “A family of early time approximations for fluid-structure interaction,” *J. Appl. Mech.* **47**, 703–708.
- Feng, Z. C., and Leal, L. G. (1993). “Energy transfer mechanism in coupled bubble oscillations,” *Phys. Lett. A* **5**(4), 826–836.
- Frost, P. A., and Harper, E. Y. (1975). “Acoustic radiation from surfaces oscillating at large amplitude and small mach number,” *J. Acoust. Soc. Am.* **58**, 318–325.

- Geers, T. L. (1971). "Residual potential and approximate methods for three dimensional fluid-structure interaction problems," *J. Acoust. Soc. Am.* **49**, 1505-1510.
- Geers, T. L. (1978). "Doubly asymptotic approximations for transient motions of submerged structures," *J. Acoust. Soc. Am.* **64**, 1500-1508.
- Geers, T. L., and Lewis, B. A. (1997). "Doubly asymptotic approximations for transient elastodynamics," *Int. J. Solids Struct.* **34**(11), 1293-1305.
- Geers, T. L., and Tothaker, B. J. (1997). "Evaluation of doubly asymptotic approximations for boundary element analysis in transient acoustics," in *Fundamental Solutions in Boundary Elements*, edited by F. G. Benitez (University of Sevilla, SAND (Camas)), pp. 139-156.
- Geers, T. L., and Tothaker, B. J. (2000). "Third-order doubly asymptotic approximations for computational acoustics," *J. Comput. Acoust.* **8**(1), 101-120.
- Geers, T. L., and Zhang, P. (1988). "Doubly asymptotic approximations for electromagnetic scattering problems," in *Boundary Element Methods in Applied Mechanics*, edited by M. Tanaka and T. A. Cruse (Pergamon, Oxford, U.K.), pp. 357-369.
- Geers, T. L., and Zhang, P. (1994a). "Doubly asymptotic approximations for submerged structures with internal fluid volumes: Formulation," *J. Appl. Mech.* **61**(4), 893-899.
- Geers, T. L., and Zhang, P. (1994b). "Doubly asymptotic approximations for submerged structures with internal fluid volumes: Evaluation," *J. Appl. Mech.* **61**(4), 900-906.
- Hentschel, W., and Lauterborn, W. (1982). "Acoustic emission of single laser-produced cavitation bubbles and their dynamics," *Appl. Sci. Res.* **38**, 225-230.
- Herring, C. (1941). "Theory of the pulsations of the gas bubble produced by an underwater explosion," in *Underwater Explosion Research* (Office of Naval Research, Washington, D.C., 1950), Vol. 2, pp. 35-131.
- Hicks, A. N. (1970). "Effect of bubble migration on explosion-induced whipping in ships," Technical Report 3301, Naval Ship Research and Development Center, Bethesda, MD.
- Jones, H., and Miller, A. R. (1948). "The detonation of solid explosives," *Proc. R. Soc. London, Ser. A* **194A**, 480-507.
- Keller, J. B., and Kolodner, I. I. (1956). "Damping of underwater explosion bubble oscillations," *J. Appl. Phys.* **27**, 1152-1161.
- Kinsler, L. E., Frey, A. R., Coppens, A. B., and Sanders, J. V. (1982). *Fundamentals of Acoustics*, 3rd ed. (Wiley, New York), pp. 125-126.
- Kirkwood, J. G., and Bethe, H. (1942). "The pressure wave produced by an underwater explosion I. (OSRD no. 588)," in *Shock and Detonation Waves*, edited by W. W. Wood (Gordon and Breach, New York, 1967), pp. 1-34.
- Kolodner, I. I., and Keller, J. B. (1953). "Underwater explosion bubbles II: The effect of gravity and the change of shape," Technical Report IMM-NYU 197, Institute for Mathematics and Mechanics, New York University.
- Lamb, H. (1923). "The early stages of a submarine explosion," *Philos. Mag.* **45** (Ser. 6), 257-265.
- Lee, E. L., Finger, M., and Collins, W. (1973). "JWL equation of state coefficients for high explosives," Technical Report UCID-16189, Lawrence Livermore National Laboratory, Livermore, CA.
- Lee, E. L., Hornig, H. C., and Kury, J. W. (1968). "Adiabatic expansion of high explosive detonation products," Technical Report UCRL-50422, Lawrence Livermore National Laboratory, Livermore, CA.
- Lee, E. L., and Walton, J. R. (1975). "Equation of state for pentolite," Technical Report UCID-16953, Lawrence Livermore National Laboratory, Livermore, CA.
- Leighton, T. G. (1994). *The Acoustic Bubble* (Academic, New York).
- Longuet-Higgins, M. S. (1992). "Nonlinear damping of bubble oscillations by resonant interaction," *J. Acoust. Soc. Am.* **91**, 1414-1422.
- Lord, Rayleigh (1917). "On the pressure developed in a liquid during the collapse of a spherical cavity," *Philos. Mag.* (Ser. 6), **34**, 94-98.
- Mao, Y., Crum, L. A., and Roy, R. A. (1995). "Nonlinear coupling between the surface and volume modes of an oscillating bubble," *J. Acoust. Soc. Am.* **98**, 2764-2771.
- McDonald, B. E., and Holland, C. (2000). "Decay of large underwater bubble oscillations," *J. Acoust. Soc. Am.* **107**, 3084-3088.
- Meirovitch, L. (1997). *Principles and Techniques of Vibrations* (Prentice Hall, Englewood Cliffs, NJ), p. 92.
- Milne-Thomson, L. M. (1960). *Theoretical Hydrodynamics*, 4th ed. (Macmillan, New York).
- Moss, W. C., Levatin, J. L., and Szeri, A. J. (2000). "A new damping mechanism in strongly collapsing bubbles," *Proc. R. Soc. London, Ser. A* **456**, 2983-2994.
- Nicolas-Vullierme, B. (1991). "A contribution to doubly asymptotic approximations: An operator top-down approach," *J. Vibr. Acoust.* **113**, 409-415.
- Penney, W. G., and Price, A. T. (1942). "On the changing form of a nearly spherical submarine bubble," in *Underwater Explosion Research* (Office of Naval Research, Washington, D.C., 1950), Vol. 2, pp. 145-161.
- Pierce, A. D. (1989). *Acoustics*, 2nd ed. (Acoustical Society of America, New York).
- Price, R. S. (1979). "Similitude equations for explosives fired underwater," Technical Report NSWC TR 80-299, NSWC.
- Prosperetti, A., and Lezzi, A. (1986). "Bubble dynamics in a compressible liquid. I. First-order theory," *J. Fluid Mech.* **168**, 457-478.
- Qi, Q. A., and Geers, T. L. (1997). "Doubly asymptotic approximations for transient poroelastodynamics," *J. Acoust. Soc. Am.* **102**, 1361-1371.
- Schittke, H. J., Mohr, W., Lutje, H., and Pirang, W. (1989). "The program DYSMAS/ELC and its application to underwater shock loading of vessels," in *Proceedings of 60th Shock and Vib. Symposium*, pp. 55-78, SAVIAC.
- Shiffman, M., and Friedman, B. (1943). "Studies on the gas bubble resulting from underwater explosions—on the best location of a mine near the sea bed," in *Underwater Explosion Research*, Vol. 2, pp. 245-320 (Office of Naval Research, Washington, D.C., 1950).
- Snay, H. G. (1956). "Hydrodynamics of underwater explosions," in *Symposium on Naval Hydrodynamics* (National Academy of Sciences, Washington, D.C.), pp. 325-352.
- Snay, H. G. (1962). "Underwater explosion phenomena: The parameters of migrating bubbles," Technical Report NAVORD 4185, U.S. Naval Ordnance Laboratory, White Oak, MD.
- Snay, H. G., and Tipton, R. V., (1962). "Charts for the parameters of Migratory explosion bubbles," Technical Report NOLTR 62-184, U. S. Naval Ordnance Laboratory, White Oak, MD.
- Strasberg, M. (1956). "Gas bubbles as sources of sound in liquids," *J. Acoust. Soc. Am.* **28**, 20-26.
- Suslick, K. S. (1990). "Sonochemistry," *Science* **247**, 1439-1445.
- Swift, E., and Decius, J. C. (1948). "Measurements of bubble pulse phenomena. III. Radius and period studies," in *Underwater Explosion Research* (Office of Naval Research, Washington, D.C., 1950), Vol. 2, pp. 553-599.
- Swisdak, M. M., editor (1978). *Explosion Effects and Properties: Part II—Explosion Effects in Water*, NSWC/WOL TR 76-116, NSWC.
- Taylor, G. I. (1942). "Vertical motion of a spherical bubble and the pressure surrounding it," in *Underwater Explosion Research* (Office of Naval Research, Washington, D.C., 1950), Vol. 2, pp. 131-144.
- Thiel, M. A. (1961). "Revised similitude equations for the underwater shock wave performance of pentolite and HBX-1," Technical Report 7380, NAVWEPS.
- Underwood, P., and Geers, T. L. (1981). "Doubly asymptotic, boundary-element analysis of dynamic soil-structure interaction," *Int. J. Solids Struct.* **17**(7), 687-697.
- Van Dyke, M. (1964). *Perturbation Methods in Fluid Mechanics* (Academic, New York).
- Ward, A. B. (1943). *Undex 20*, pp. in Cole (1948), Chap. 8, pp. 308-312.
- Wardlaw, A. B., and Mair, H. U. (1998). "Spherical solutions of an underwater explosion bubble," *Shock Vibration* **5**(2), 89-102.
- Zhang, S., Duncan, J. H., and Chahine, G. L. (1993). "The final stage of the collapse of a cavitation bubble near a rigid wall," *J. Fluid Mech.* **257**, 147-181.

Viscous effects on the interaction force between two small gas bubbles in a weak acoustic field

Alexander A. Doinikov

Institute of Nuclear Problems, Byelorussian State University, 11 Bobruiskaya Street, Minsk 220050, Belarus

(Received 15 March 2001; revised 2 January 2002; accepted 14 January 2002)

The relative motion of two gas bubbles in an acoustic field is investigated by calculating the time-averaged interaction force known as the secondary Bjerknes force. The surrounding medium is assumed to be an incompressible viscous liquid and the separation distance between the bubbles much larger than their radii. A refined formula for the interaction force is derived, which allows for translational oscillations of the bubbles, the vorticity of the linear scattered field, and acoustic streaming. The boundary condition of slippage on the gas–liquid interface is assumed. It is shown that viscous effects can cause small bubbles, driven well below resonance, to repel each other within a relatively wide parameter range. This result discloses a significant boundedness of the classical Bjerknes theory according to which bubbles of this sort are capable of mutual attraction alone.

© 2002 Acoustical Society of America. [DOI: 10.1121/1.1459466]

PACS numbers: 43.25.Yw, 43.35.Ei [MAB]

I. INTRODUCTION

This article concerns the relative translational motion of two gas bubbles in an acoustically driven liquid. This motion results from the mutual interaction force, normally called the secondary Bjerknes force, which is exerted between the bubbles due to the action of an applied acoustic field. The literature on this subject is quite extensive and the reader interested in a detailed discussion of the previous work is referred to Refs. 1–8.

According to the classical Bjerknes theory,⁹ two interacting bubbles can only behave in the following fashion: If the driving frequency is in between their natural frequencies, then the bubbles repel each other; otherwise mutual attraction occurs, which should eventually result in coalescence of the bubbles. However, as experiments show, real bubbles do not always follow this scenario. Under certain conditions, both big bubbles, driven above their natural frequencies, and small bubbles, driven below resonance, exhibit behavior that is inconsistent with the Bjerknes theory. Instead of coalescing, the big bubbles form stable clusters known as “bubble grapes,”^{10–14} and the small ones group themselves in strong fields in branched filamentary structures called “acoustic streamers.”^{15–17} Such phenomena prompt researchers to improve the Bjerknes theory with the purpose of revealing reasons of the anomalous bubble behavior. While the origin of the bubble grapes created by big bubbles is now clear enough,^{12–14} causes that inhibit coalescence of small bubbles are still incomprehensible. Everything seems to indicate that there are several mechanisms that can make small bubbles repel one another. One such mechanism has been suggested by Oguz and Prosperetti.¹⁸ They investigated numerically the interaction of two bubbles, maintaining all the restrictions of the Bjerknes theory but assuming that the bubble oscillations were slightly nonlinear. (The Bjerknes theory is known to neglect nonlinear effects.) It was found that two bubbles driven below their fundamental resonance could undergo repulsion nevertheless if twice the driving frequency was in between their fundamental resonance frequencies and the

forcing was high enough, on the order of 0.5 bar at a static pressure of 1 bar. Oguz and Prosperetti conjectured that this effect resulted from the second harmonic of the bubble oscillation. This hypothesis was then verified analytically by Doinikov.⁸ Another possible mechanism has been found by Mettin *et al.*,⁷ who have examined even stronger fields, with driving pressure amplitudes exceeding 1 bar, for bubble pairs with resonant frequencies far above twice the driving frequency. They showed that for such bubbles the interaction force could also be repulsive. In this case, the changeover of the force is caused by a nonlinear resonancelike response of bubbles that occurs in very strong fields if the equilibrium bubble radius is a little larger than the dynamical Blake threshold, which is typically equal to a few microns. The common shortcoming of both theories is that the range of bubble radii where repulsion is predicted is quite narrow. Therefore they, even in combination, cannot explain fully the fact that coalescence is not a dominant event in collective bubble phenomena such as acoustic streamers.

The purpose of this article is to show that repulsion of small bubbles can also be caused by effects stemming from the viscosity of the surrounding liquid, even if the forcing is weak. The viscosity gives rise to vortical motion in the host liquid. In a weak acoustic field, this motion can be separated into two components, namely, a linear one that is generated by the translational and shape oscillations of the bubbles, and the nonlinear one known as acoustic streaming, which is a stationary vortical flow quadratic in the acoustic pressure amplitude. Both of these processes make contributions of the same order to the interaction force between the bubbles, rendering under certain conditions the net effect repulsive. The approach used in this article is similar to that used in Ref. 19, with the exception of the boundary conditions at the bubble surfaces. In Ref. 19, the boundary condition of adhesion of liquid particles to the bubble surface is applied, which corresponds to bubbles with coating. Here, the boundary condition that assumes slippage is taken, which corresponds to clean gas bubbles.²⁰ There is a superposition that it is clean

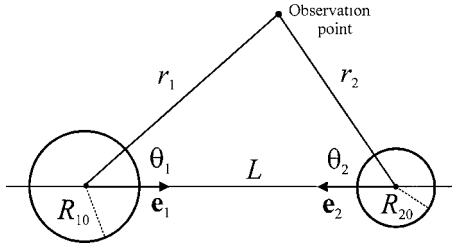


FIG. 1. Geometry of the system.

bubbles that dominate medium- and high-intensity fields because violent oscillations break down surface bubble films even if they initially exist.¹ The replacement of boundary conditions leads to a very significant change in the final results. In particular, whereas in Ref. 19 it is predicted that at high viscosity the interaction force can only decrease in magnitude, remaining attractive, the present study reveals that the force can be repulsive in a fairly wide range of bubble radii.

II. THEORY

Let two gas bubbles with mean radii R_{10} and R_{20} and a distance L between their equilibrium centers be in a liquid exposed to an acoustic wave field. The geometry of the system is shown in Fig. 1. Suppose that the wavelength of sound is much larger than L and that $L \gg R_{10}, R_{20}$. Then we can ignore the compressibility of the liquid and the shape deviations of the bubbles from sphericity and restrict our consideration only to volume and translational oscillations of the bubbles. It is also assumed that the imposed field is weak and therefore nonlinear effects, such as super- and subharmonics, can as well be disregarded.

The motion of the surrounding liquid is described by the following equations:

$$\nabla \cdot \mathbf{v} = 0, \quad (1)$$

$$\rho \frac{\partial \mathbf{v}}{\partial t} + \rho(\mathbf{v} \cdot \nabla) \mathbf{v} = \eta \Delta \mathbf{v} - \nabla p, \quad (2)$$

where \mathbf{v} is the liquid velocity, ρ is the liquid density, η is the liquid viscosity, and p is the liquid pressure. Equation (2) is known as the Navier–Stokes equation for incompressible fluid.²¹

The time-averaged acoustic radiation force on the j th bubble ($j=1,2$) can be represented as²²

$$\mathbf{F}_j = \int_{S_{j0}} \langle 2\eta(\mathbf{n}_j \cdot \nabla) \mathbf{v}^{(2)} + \eta \mathbf{n}_j \times (\nabla \times \mathbf{v}^{(2)}) - \mathbf{n}_j p^{(2)} - \rho \mathbf{v}^{(1)}(\mathbf{v}^{(1)} \cdot \mathbf{n}_j) \rangle dS_{j0}, \quad (3)$$

where S_{j0} is the surface of the j th bubble at rest, \mathbf{n}_j is the unit outward normal to S_{j0} , the superscripts (1) and (2) denote quantities of first and second order in the acoustic pressure amplitude, and $\langle \rangle$ means the time average.

The next two subsections are devoted to calculating, respectively, the linear and quadratic quantities appearing in Eq. (3).

A. Linear field

Linearizing Eqs. (1) and (2), one obtains

$$\nabla \cdot \mathbf{v}^{(1)} = 0, \quad (4)$$

$$\rho \frac{\partial \mathbf{v}^{(1)}}{\partial t} = \eta \Delta \mathbf{v}^{(1)} - \nabla p^{(1)}. \quad (5)$$

The linear liquid velocity $\mathbf{v}^{(1)}$ can be expressed as

$$\mathbf{v}^{(1)} = \nabla \varphi^{(1)} + \nabla \times \boldsymbol{\psi}^{(1)}, \quad (6)$$

where $\varphi^{(1)}$ and $\boldsymbol{\psi}^{(1)}$ are the scalar and vorticity velocity potentials, which can be written as

$$\varphi^{(1)} = \varphi_I + \varphi_1^{(1)} + \varphi_2^{(1)}, \quad (7)$$

$$\boldsymbol{\psi}^{(1)} = \boldsymbol{\psi}_1^{(1)} + \boldsymbol{\psi}_2^{(1)} \quad (8)$$

with $\varphi_I = A \exp(-i\omega t)$ the incident potential and $\varphi_j^{(1)}$ and $\boldsymbol{\psi}_j^{(1)}$ the scattered potentials of the j th bubble. As $L \gg R_{j0}$, $\varphi_j^{(1)}$ can be taken to be

$$\varphi_j^{(1)} = A e^{-i\omega t} a_j R_{j0} / r_j, \quad (9)$$

where a_j is a nondimensional coefficient to be determined by the boundary conditions at the bubbles' surface and the meaning of r_j is clear from Fig. 1.

The axial symmetry of the problem suggests that $\boldsymbol{\psi}_j^{(1)}$ should be of the form $\boldsymbol{\psi}_j^{(1)} = \psi_j(r_j, \theta_j, t) \mathbf{e}_\varepsilon$, where $\psi_j(r_j, \theta_j, t)$ is some function and \mathbf{e}_ε is the unit azimuth vector that is used in both coordinate systems shown in Fig. 1. It follows that $\nabla \cdot \boldsymbol{\psi}_j^{(1)} = 0$. Using this fact and applying the curl operator to Eq. (5), one finds

$$(\Delta^2 + \alpha^2 \Delta) \boldsymbol{\psi}_j^{(1)} = 0, \quad (10)$$

where $\alpha^2 = i\omega/\nu$ and $\nu = \eta/\rho$ is the kinematic viscosity. Let us further refine the form of $\boldsymbol{\psi}_j^{(1)}$. The curl of $\boldsymbol{\psi}_j^{(1)}$, as a part of the liquid velocity $\mathbf{v}^{(1)}$, must be a polar vector. Therefore $\boldsymbol{\psi}_j^{(1)}$ should be an axial vector. It follows that $\boldsymbol{\psi}_j^{(1)}$ should be the curl of the polar vector. In view of the symmetry of the problem involved that polar vector should be of the form $f_j(r_j) \mathbf{e}_j$, where $f_j(r_j)$ is a certain function to be found and \mathbf{e}_j is the unit vector directed from the j th bubble to the other bubble as shown in Fig. 1. Thus $\boldsymbol{\psi}_j^{(1)}$ can be represented as

$$\begin{aligned} \boldsymbol{\psi}_j^{(1)} &= A e^{-i\omega t} \nabla \times [f_j(r_j) \mathbf{e}_j] \\ &= A e^{-i\omega t} \nabla f_j(r_j) \times \mathbf{e}_j \\ &= -A e^{-i\omega t} f_j'(r_j) \mathbf{e}_\varepsilon \sin \theta_j \end{aligned} \quad (11)$$

with $f_j'(r_j) = df_j(r_j)/dr_j$ and $\mathbf{e}_j = \mathbf{e}_{rj} \cos \theta_j - \mathbf{e}_{\theta j} \sin \theta_j$, where \mathbf{e}_{rj} and $\mathbf{e}_{\theta j}$ are the unit vectors of the spherical coordinates related to the j th bubble.

Substituting Eq. (11) into Eq. (10) and exploiting the fact that $\mathbf{v}^{(1)} \rightarrow 0$ and $r_j \rightarrow \infty$, one obtains

$$(\Delta + \alpha^2) \Delta f_j(r_j) = 0. \quad (12)$$

Solution to this equation is given by

$$\Delta f_j(r_j) = C \frac{e^{i\alpha r_j}}{r_j}, \quad (13)$$

where C is some constant. Because viscous waves should die out as $r_j \rightarrow \infty$, α is chosen to be $\alpha = (1+i)/\delta_v$, where $\delta_v = (2\nu/\omega)^{1/2}$ is the viscous penetration depth in the host liquid. Integration of Eq. (13) yields

$$f_j'(r_j) = b_j \frac{e^{i\alpha r_j}}{(\alpha r_j)^2} (1 - i\alpha r_j) + c_j \left(\frac{R_{j0}}{r_j} \right)^2, \quad (14)$$

where b_j and c_j are nondimensional coefficients to be determined by the boundary conditions at the bubbles' surfaces. Note that, as is seen from Eq. (11), there is no need to calculate the function $f_j(r_j)$ itself.

We now proceed to find the linear liquid pressure $p^{(1)}$. It can be represented as

$$p^{(1)} = p_l + p_1^{(1)} + p_2^{(1)}, \quad (15)$$

where $p_l = -\rho \partial \phi_l / \partial t$ and $p_j^{(1)}$ is the pressure produced by the j th bubble. From Eq. (5), using Eqs. (4), (6)–(9), (11), and (12), one obtains

$$p_j^{(1)} = A e^{-i\omega t} [i\omega \rho a_j (R_{j0}/r_j) + \eta(\mathbf{e}_j \cdot \nabla)(\Delta + \alpha^2)f_j(r_j)]. \quad (16)$$

To calculate the coefficients a_j , b_j , and c_j , the linearized boundary conditions for the normal and tangential stresses of the liquid as well as the normal liquid velocity are applied to the surface of the j th bubble. The redundant boundary condition for the tangential liquid velocity is dropped, which implies slippage on the liquid-gas interface. The boundary conditions for the normal velocity is given by

$$\dot{R}_j(t) + U_j(t) \cos \theta_j = \mathbf{e}_{r_j} \cdot \mathbf{v}^{(1)}|_{r_j=R_{j0}}, \quad (17)$$

where $R_j(t)$ and $U_j(t)$ are, respectively, the instantaneous radius and the linear translational velocity of the j th bubble, and the dot over $R_j(t)$ denotes the time derivative. Upon substitution of Eqs. (6)–(9) and (11), Eq. (17) yields

$$a_j A e^{-i\omega t} = -R_{j0} \dot{R}_j(t), \quad (18)$$

$$U_j(t) = A e^{-i\omega t} \left[\frac{R_{3-j0}}{L^2} a_{3-j} - \frac{2}{R_{j0}} f_j'(R_{j0}) \right]. \quad (19)$$

These equations are accurate up to terms of second order in R_{j0}/L , assuming that a_j is of zeroth order and b_j and c_j of second order. It will be seen below that this is indeed so.

The boundary condition for the tangential stress is given by

$$\sigma_{r\theta}^{(1)}|_{r_j=R_{j0}} = \eta \left(\frac{1}{r_j} \frac{\partial v_{r_j}^{(1)}}{\partial \theta_j} + \frac{\partial v_{\theta_j}^{(1)}}{\partial r_j} - \frac{v_{\theta_j}^{(1)}}{r_j} \right)_{r_j=R_{j0}} = 0, \quad (20)$$

where $\sigma_{r\theta}^{(1)}$ is the tangential component of the linear stress tensor of the liquid in the spherical coordinates related to the j th bubble.²¹ Substituting all the necessary quantities into Eq. (20), one finds

$$f_j'''(R_{j0}) = 0, \quad (21)$$

which, on substitution of Eq. (14), gives c_j in terms of b_j :

$$c_j = -b_j \frac{e^{iz_j}}{6z_j^2} (iz_j^3 - 3z_j^2 - 6iz_j + 6), \quad (22)$$

where $z_j = \alpha R_{j0}$.

Let us now apply the boundary condition for the normal stress:

$$P_0 - \sigma_{rr}^{(1)}|_{r_j=R_{j0}} + \frac{2\sigma}{R_j(t)} = P_{gj} \left(\frac{R_{j0}}{R_j(t)} \right)^{3\gamma_j}, \quad (23)$$

where P_0 is the hydrostatic pressure of the liquid, σ is the surface tension, P_{gj} is the equilibrium pressure of the gas inside the j th bubble, $\sigma_{rr}^{(1)}$ is the radial component of the linear stress tensor of the liquid, given by²¹

$$\sigma_{rr}^{(1)} = -p^{(1)} + 2\eta \frac{\partial v_{r_j}^{(1)}}{\partial r_j}, \quad (24)$$

the complex exponent $\gamma_j = \gamma(\beta_j - id_j)$ allows for departures from the adiabatic law due to heat losses, γ is the specific heat ratio of the gas, and β_j and d_j are defined as²³

$$\beta_j = \left[\left(1 + \frac{d_j^2}{\beta_j^2} \right) \left(1 + \frac{3(\gamma-1)(\sinh X_j - \sin X_j)}{X_j(\cosh X_j - \cos X_j)} \right) \right]^{-1}, \quad (25)$$

$$\frac{d_j}{\beta_j} = 3(\gamma-1) \times \frac{X_j(\sinh X_j + \sin X_j) - 2(\cosh X_j - \cos X_j)}{X_j^2(\cosh X_j - \cos X_j) + 3(\gamma-1)X_j(\sinh X_j - \sin X_j)}. \quad (26)$$

Here, $X_j = R_{j0}(2\omega/\chi_j)^{1/2}$, $\chi_j = \kappa/(c_p \rho_{j0})$ is the thermal diffusivity of the gas inside the j th bubble, κ is the thermal conductivity, c_p is the specific heat at constant pressure, and ρ_{j0} is the equilibrium density of the gas within the j th bubble, defined as $\rho_{j0} = \rho_A P_{gj}/P_A$, where ρ_A is the gas density at the atmospheric pressure P_A .

Substituting all the necessary quantities into Eq. (24) and keeping up to the second-order terms in R_{j0}/L , one obtains

$$\sigma_{rr}^{(1)}|_{r_j=R_{j0}} = -i\omega \rho A e^{-i\omega t} \left\{ 1 + a_j(1 - 4z_j^{-2}) + a_{3-j} \frac{R_{3-j0}}{L} \left(1 + \frac{R_{j0}}{L} \cos \theta_j \right) + \frac{\cos \theta_j}{z_j^2} \times [6R_{j0} f_j''(R_{j0}) + (z_j^2 - 6)f_j'(R_{j0})] \right\}. \quad (27)$$

The time-varying radius of the j th bubble can be written as

$$R_j(t) = R_{j0} + x_j^{(1)}(t), \quad (28)$$

where, as follows from Eq. (18), the linear change $x_j^{(1)}(t)$ is given by

$$x_j^{(1)}(t) = -iA e^{-i\omega t} a_j / (\omega R_{j0}). \quad (29)$$

Substituting Eqs. (27)–(29) into Eq. (23), with an accuracy up to the second-order terms in R_{j0}/L , one has

$$\left(\frac{\omega_j^2}{\omega^2} - 1 - i\delta_j\right) a_j - \frac{R_{3-j0}}{L} a_{3-j} = 1, \quad (30)$$

$$(6z_j^{-2} - 1)f_j'(R_{j0}) - 6z_j^{-2}R_{j0}f_j''(R_{j0}) = \frac{R_{10}R_{20}}{L^2} a_{3-j}, \quad (31)$$

where ω_j is the monopole resonance frequency of the j th bubble, given by

$$\omega_j = \frac{1}{R_{j0}} \left[\frac{1}{\rho} \left(3\gamma\beta_j P_{gj} - \frac{2\sigma}{R_{j0}} \right) \right]^{1/2}, \quad (32)$$

and δ_j is the nondimensional damping constant due to viscous and heat losses, defined as

$$\delta_j = \frac{4\nu}{\omega R_{j0}^2} + \frac{3\gamma d_j P_{gj}}{\rho \omega^2 R_{j0}^2}. \quad (33)$$

Solving Eq. (30) for a_j , one obtains

$$a_j = \frac{1}{D} \left(\frac{\omega_{3-j}^2}{\omega^2} - 1 - i\delta_{3-j} + \frac{R_{3-j0}}{L} \right) \quad (34)$$

with

$$D = \left(\frac{\omega_1^2}{\omega^2} - 1 - i\delta_1 \right) \left(\frac{\omega_2^2}{\omega^2} - 1 - i\delta_2 \right) - \frac{R_{10}R_{20}}{L^2}. \quad (35)$$

On substitution of Eqs. (14) and (22), Eq. (31) yields

$$b_j = \frac{6z_j^2 \exp(-iz_j)}{18 - 18iz_j - 3z_j^2 + iz_j^3} \frac{R_{10}R_{20}}{L^2} a_{3-j}, \quad (36)$$

$$c_j = -\frac{6 - 6iz_j - 3z_j^2 + iz_j^3}{18 - 18iz_j - 3z_j^2 + iz_j^3} \frac{R_{10}R_{20}}{L^2} a_{3-j}. \quad (37)$$

Finally, from Eq. (19), one has

$$U_j(t) = \frac{3Ae^{-i\omega t}}{R_{j0}} \frac{6 - 6iz_j - 3z_j^2 + iz_j^3}{18 - 18iz_j - 3z_j^2 + iz_j^3} \frac{R_{10}R_{20}}{L^2} a_{3-j}. \quad (38)$$

The linear solution is obtained and we can now proceed to solve equations of acoustic streaming.

B. Acoustic streaming

By averaging Eqs. (1) and (2) over time, the time average being taken over an integral number of acoustic cycles, and keeping up to the second order in the acoustic pressure amplitude, one obtains the so-called equations of acoustic streaming²⁴

$$\nabla \cdot \langle \mathbf{v}^{(2)} \rangle = 0, \quad (39)$$

$$\eta \Delta \langle \mathbf{v}^{(2)} \rangle - \nabla \langle p^{(2)} \rangle = \rho \langle (\mathbf{v}^{(1)} \cdot \nabla) \mathbf{v}^{(1)} \rangle. \quad (40)$$

The velocity $\langle \mathbf{v}^{(2)} \rangle$ can be expressed as

$$\langle \mathbf{v}^{(2)} \rangle = \nabla \times \Psi. \quad (41)$$

Substituting this equation into Eq. (40) and applying the curl operator, one has

$$\Delta^2 \Psi = -\nu^{-1} \nabla \times \langle (\mathbf{v}^{(1)} \cdot \nabla) \mathbf{v}^{(1)} \rangle. \quad (42)$$

Using Eq. (6), after some manipulation, one finds

$$\Delta^2 \Psi = \nu^{-1} \nabla \times \langle \Delta \psi^{(1)} \times (\nabla \varphi^{(1)} + \nabla \times \psi^{(1)}) \rangle. \quad (43)$$

To calculate the force on the j th bubble, it will suffice to know the leading term of Ψ in the vicinity of that bubble. Let us denote this term by Ψ_j . It can be seen from Eq. (43) that Ψ_j is of second order in R_{j0}/L and adheres to the following equation:

$$\Delta^2 \Psi_j = \nu^{-1} \nabla \times \langle \Delta \psi_j^{(1)} \times \nabla \varphi_j^{(1)} \rangle. \quad (44)$$

Upon substitution of Eqs. (9), (11), and (14), Eq. (44) yields

$$\Delta^2 \Psi_j = \frac{|A|^2 R_{j0} \sin \theta_j \mathbf{e}_s}{2\nu r_j^5} \text{Re} \{ a_j^* b_j e^{i\alpha r_j} (3 - 3i\alpha r_j - \alpha^2 r_j^2) \}, \quad (45)$$

where Re means “the real part of” and the asterisk indicates the complex conjugate. Equation (45) shows that Ψ_j can be represented as

$$\Psi_j = \frac{|A|^2 R_{j0}}{2\nu} \sin \theta_j \mathbf{e}_s \text{Re} \{ a_j^* b_j g_j(r_j) \}. \quad (46)$$

Substituting Eq. (46) into Eq. (45), one finds that the function $g_j(r_j)$ is to obey the following equation:

$$g_j^{IV}(r_j) + 4r_j^{-1} g_j'''(r_j) - 4r_j^{-2} g_j''(r_j) = r_j^{-5} e^{i\alpha r_j} (3 - 3i\alpha r_j - \alpha^2 r_j^2). \quad (47)$$

This equation is solved by using the standard Lagrange method. The result is

$$g_j(r_j) = C_1(r_j) r_j^{-2} + C_2(r_j) + C_3(r_j) r_j + C_4(r_j) r_j^3, \quad (48)$$

where the functions $C_n(r_j)$ are given by

$$C_1(r_j) = D_1 - \frac{e^{i\alpha r_j}}{30i\alpha} (8 - 5i\alpha r_j - \alpha^2 r_j^2), \quad (49)$$

$$C_2(r_j) = D_2 + \frac{i\alpha}{6} e^{i\alpha r_j} + \frac{1}{2} \int_{R_{j0}}^{r_j} r^{-2} e^{i\alpha r} (1 - i\alpha r) dr, \quad (50)$$

$$C_3(r_j) = D_3 - \frac{1}{6} \int_{R_{j0}}^{r_j} r^{-3} e^{i\alpha r} (3 - 3i\alpha r - \alpha^2 r^2) dr, \quad (51)$$

$$C_4(r_j) = D_4 + \frac{1}{30} \int_{R_{j0}}^{r_j} r^{-5} e^{i\alpha r} (3 - 3i\alpha r - \alpha^2 r^2) dr. \quad (52)$$

The constants D_n are determined from the boundary conditions at infinity and at the surface of the j th bubble. From the condition that $\nabla \times \Psi_j \rightarrow 0$ as $r_j \rightarrow \infty$, one has

$$D_3 = \frac{1}{6} \int_{R_{j0}}^{\infty} r^{-3} e^{i\alpha r} (3 - 3i\alpha r - \alpha^2 r^2) dr$$

$$= \frac{1}{2R_{j0}^2} \left[E_3(-iz_j) - iz_j E_2(-iz_j) - \frac{1}{3} z_j^2 E_1(-iz_j) \right], \quad (53)$$

$$D_4 = -\frac{1}{30} \int_{R_{j0}}^{\infty} r^{-5} e^{i\alpha r} (3 - 3i\alpha r - \alpha^2 r^2) dr$$

$$= \frac{1}{10R_{j0}^4} \left[\frac{1}{3} z_j^2 E_3(-iz_j) + iz_j E_4(-iz_j) - E_5(-iz_j) \right], \quad (54)$$

where $E_m(z)$ denotes the integral exponential of order m as defined in Ref. 25.

To find D_1 and D_2 , the boundary conditions for the tangential stress and normal velocity are used, which are now applied to the perturbed surface of the j th bubble and averaged over time, keeping up to the second order in the acoustic pressure amplitude. The perturbed surface of the j th bubble can be represented as

$$\mathbf{r}_j = \xi_j(t) \mathbf{e}_j + [R_{j0} + x_j^{(1)}(t)] \mathbf{n}_j, \quad (55)$$

where the displacement of the center of the bubble $\xi_j(t)$ is defined by the following relationship: $\dot{\xi}_j(t) = U_j(t)$. By expanding the shear stress of the liquid $\sigma_{r\theta}$ at this surface in a Taylor series up to the second order in the acoustic pressure amplitude and averaging over time, one obtains

$$\langle \sigma_{r\theta}|_{S_j(t)} \rangle \approx \langle \sigma_{r\theta}^{(2)} \rangle_{r_j=R_{j0}} + \langle [\xi_j(t) \mathbf{e}_j + x_j^{(1)}(t) \mathbf{e}_{r_j}] \cdot \nabla \sigma_{r\theta}^{(1)} \rangle_{r_j=R_{j0}} = 0, \quad (56)$$

where $S_j(t)$ denotes the perturbed surface of the j th bubble and $\langle \sigma_{r\theta}^{(2)} \rangle_{r_j=R_{j0}}$ is given by

$$\langle \sigma_{r\theta}^{(2)} \rangle_{r_j=R_{j0}} = \eta \left\langle \frac{1}{r_j} \frac{\partial v_{r_j}^{(2)}}{\partial \theta_j} + \frac{\partial v_{\theta_j}^{(2)}}{\partial r_j} - \frac{v_{\theta_j}^{(2)}}{r_j} \right\rangle_{r_j=R_{j0}}. \quad (57)$$

From Eq. (46), one finds

$$\langle \mathbf{v}_j^{(2)} \rangle = \nabla \times \boldsymbol{\Psi}_j = \frac{|A|^2 R_{j0}}{2\nu r_j} \text{Re} \{ a_j^* b_j [2g_j(r_j) \cos \theta_j \mathbf{e}_{r_j} - (g_j(r_j) + r_j g_j'(r_j)) \sin \theta_j \mathbf{e}_{\theta_j}] \}, \quad (58)$$

where $\langle \mathbf{v}_j^{(2)} \rangle$ denotes the leading term of the velocity field of acoustic streaming near the j th bubble. Substitution of Eq. (58) into Eq. (57) yields

$$\langle \sigma_{r\theta}^{(2)} \rangle_{r_j=R_{j0}} = -\frac{1}{2} \rho |A|^2 R_{j0} \sin \theta_j \text{Re} \{ a_j^* b_j g_j''(R_{j0}) \}. \quad (59)$$

Substituting Eq. (59) along with all the necessary equations from the preceding subsection into Eq. (56), with an accuracy up to the second order in R_{j0}/L , one has

$$g_j''(R_{j0}) = R_{j0}^{-3} \exp(iz_j). \quad (60)$$

Finally, by using Eqs. (48)–(52), one obtains

$$D_1 = \frac{iR_{j0} \exp(iz_j)}{30z_j} (z_j^2 - 8) - R_{j0}^5 D_4. \quad (61)$$

In a similar manner, the liquid velocity at $S_j(t)$ can be written as

$$\langle \mathbf{v}|_{S_j(t)} \rangle \approx \langle \mathbf{v}^{(2)} \rangle_{r_j=R_{j0}} + \langle [(\xi_j \mathbf{e}_j + x_j^{(1)} \mathbf{e}_{r_j}) \cdot \nabla] \mathbf{v}^{(1)} \rangle_{r_j=R_{j0}}. \quad (62)$$

Since the time-averaged motion of the bubbles is just caused by the very forces we are searching for, we can neglect this motion when calculating the forces as such. Then Eq. (62) gives, with an accuracy up to the second order in R_{j0}/L ,

$$\mathbf{e}_{r_j} \cdot (\nabla \times \boldsymbol{\Psi}_j)_{r_j=R_{j0}} + \mathbf{e}_{r_j} \cdot \left\langle \xi_j (\mathbf{e}_j \cdot \nabla) \nabla \varphi_j^{(1)} + x_j^{(1)} \frac{\partial}{\partial r_j} (\nabla \varphi_j^{(1)} + \nabla \times \boldsymbol{\psi}_j^{(1)}) \right\rangle_{r_j=R_{j0}} = 0. \quad (63)$$

Using Eq. (58) and the linear solutions, one finds

$$g_j(R_{j0}) = \frac{\exp(iz_j)}{2R_{j0}z_j^4} (6 - 6iz_j - 2z_j^2), \quad (64)$$

which yields

$$D_2 = \frac{\exp(iz_j)}{6R_{j0}z_j^4} (18 - 18iz_j - 6z_j^2 - z_j^4 - iz_j^5) - R_{j0} D_3. \quad (65)$$

We proceed to calculate the pressure field of acoustic streaming, $\langle p^{(2)} \rangle$. Let us denote the leading term of this field in the vicinity of the j th bubble by $\langle p_j^{(2)} \rangle$. According to Eq. (40), this term must obey the equation:

$$\begin{aligned} \nabla \langle p_j^{(2)} \rangle &= \eta \Delta (\nabla \times \boldsymbol{\Psi}_j) - \rho \langle (\mathbf{v}^{(1)} \cdot \nabla) \mathbf{v}^{(1)} \rangle \\ &= \eta \Delta (\nabla \times \boldsymbol{\Psi}_j) - \rho \langle \frac{1}{2} \nabla (v^{(1)})^2 + (\nabla \times \mathbf{v}^{(1)}) \times \mathbf{v}^{(1)} \rangle \\ &= \eta \Delta (\nabla \times \boldsymbol{\Psi}_j) - \frac{\rho}{2} \nabla \langle (v^{(1)})^2 \rangle - \rho \langle \nabla \varphi_j^{(1)} \times \Delta \boldsymbol{\psi}_j^{(1)} \rangle, \end{aligned} \quad (66)$$

where terms are kept accurate up to R_{j0}^2/L^2 .

For subsequent calculations it is convenient to represent $\boldsymbol{\Psi}_j$ as

$$\boldsymbol{\Psi}_j = \nabla \times [\chi(r_j) \mathbf{e}_j] = \nabla \chi(r_j) \times \mathbf{e}_j = -\chi'(r_j) \sin \theta_j \mathbf{e}_\theta, \quad (67)$$

where, as is seen from comparison with Eq. (46),

$$\chi'(r_j) = -\frac{|A|^2 R_{j0}}{2\nu} \text{Re} \{ a_j^* b_j g_j(r_j) \}. \quad (68)$$

Substitution of Eq. (67) into Eq. (66) gives

$$\begin{aligned} \nabla \langle p_j^{(2)} \rangle &= \eta \nabla (\mathbf{e}_j \cdot \nabla) \Delta \chi(r_j) - \frac{\rho}{2} \nabla \langle (v^{(1)})^2 \rangle \\ &\quad - \eta \mathbf{e}_j \Delta^2 \chi(r_j) + \rho \langle \Delta \boldsymbol{\psi}_j^{(1)} \times \nabla \varphi_j^{(1)} \rangle. \end{aligned} \quad (69)$$

Let us transform the last two terms on the right-hand side of this equation, denoting their sum by \mathbf{T} . Using Eqs. (48) and (68), one finds

$$\Delta^2 \chi(r_j) = -15\nu^{-1}|A|^2 R_{j0} \operatorname{Re}\{a_j^* b_j C_4(r_j)\}. \quad (70)$$

Substituting Eq. (70) along with Eqs. (9) and (11) into \mathbf{T} and using Eq. (14), one obtains

$$\mathbf{T} = 15|A|^2 R_{j0} \rho \operatorname{Re} \left\{ a_j^* b_j \left[C_4(r_j) \cos \theta_j \mathbf{e}_{rj} + \left(\frac{e^{i\alpha r_j}}{30r_j^4} (i\alpha r_j - 1) - C_4(r_j) \right) \sin \theta_j \mathbf{e}_{\theta j} \right] \right\}. \quad (71)$$

It is easy to verify that

$$\mathbf{T} = \nabla[Q(r_j) \cos \theta_j], \quad (72)$$

where

$$Q(r_j) = 15|A|^2 R_{j0} \rho \operatorname{Re} \left\{ a_j^* b_j \left[r_j C_4(r_j) + \frac{e^{i\alpha r_j}}{30r_j^3} (1 - i\alpha r_j) \right] \right\}. \quad (73)$$

Substituting Eq. (72) into Eq. (69), one finds

$$\langle p_j^{(2)} \rangle = \eta(\mathbf{e}_j \cdot \nabla) \Delta \chi(r_j) - \frac{\rho}{2} \langle (v^{(1)})^2 \rangle + Q(r_j) \cos \theta_j, \quad (74)$$

which, after some manipulation, yields

$$\begin{aligned} \langle p_j^{(2)} \rangle = & \frac{1}{2} \rho |A|^2 R_{j0} \cos \theta_j \operatorname{Re} \{ a_j^* b_j [20r_j C_4(r_j) \\ & + 2r_j^{-2} C_2(r_j) + r_j^{-3} e^{i\alpha r_j} (1 - i\alpha r_j)] \} \\ & - \frac{\rho}{4} \operatorname{Re} \{ \nabla \varphi_j^{(1)*} (\nabla \varphi_j^{(1)} + 2\nabla \varphi_{3-j}^{(1)} + 2\nabla \times \boldsymbol{\psi}_j^{(1)}) \}. \end{aligned} \quad (75)$$

We are now fully prepared to arrive at the interaction force.

C. Interaction force

Retaining in Eq. (3) only the leading terms in R_{j0}/L , one has

$$\begin{aligned} \mathbf{F}_j = & R_{j0}^2 \int_0^{2\pi} d\varepsilon \int_0^\pi \sin \theta_j d\theta_j \left[2\eta \frac{\partial}{\partial r_j} (\nabla \times \boldsymbol{\Psi}_j) - \eta \mathbf{e}_{rj} \right. \\ & \left. \times \Delta \boldsymbol{\Psi}_j - \mathbf{e}_{rj} \langle p_j^{(2)} \rangle - \rho \langle \mathbf{v}^{(1)} \cdot (\mathbf{e}_{rj} \cdot \mathbf{v}^{(1)}) \rangle \right]_{r_j=R_{j0}}. \end{aligned} \quad (76)$$

Integration of this equation using the results of the two preceding subsections yields

$$\mathbf{F}_j = \frac{2\pi\rho|A|^2 R_{10} R_{20}}{L^2} \mathbf{e}_j \operatorname{Re} \{ a_j^* a_{3-j} [1 + \tau(z_j)] \}, \quad (77)$$

where the function $\tau(z_j)$ is given by

$$\tau(z_j) = -\frac{6z_j^2(1 + 2R_{j0}e^{-iz_j}D_2)}{18 - 18iz_j - 3z_j^2 + iz_j^3}. \quad (78)$$

Substituting Eq. (34) into Eq. (77), Eqs. (53) and (65) into Eq. (78), and applying recurrence formulas for $E_m(z)$,²⁵ one finally obtains

$$\begin{aligned} \mathbf{F}_j = & \frac{2\pi\rho|A|^2 R_{10} R_{20}}{|D|^2 L^2} \mathbf{e}_j [(T_1 T_2 + \delta_1 \delta_2)(1 + \operatorname{Re}\{\tau(z_j)\}) \\ & + \operatorname{Im}\{\tau(z_j)\}(\delta_j T_{3-j} - \delta_{3-j} T_j)], \end{aligned} \quad (79)$$

$$\tau(z_j) = \frac{z_j^6 e^{-iz_j} E_1(-iz_j) - 36 + 36iz_j + 12z_j^2 - z_j^4 - iz_j^5}{z_j^2(18 - 18iz_j - 3z_j^2 + iz_j^3)}, \quad (80)$$

where

$$T_j = \frac{\omega_j^2}{\omega^2} - 1 + \frac{R_{j0}}{L} \quad (81)$$

and Im means ‘‘the imaginary part of.’’

In the limit of low viscosity, where $R_{j0} \gg \delta_v$ and $|z_j| \rightarrow \infty$, the function $\tau(z_j)$ is approximated by

$$\tau(z_j) \approx -2z_j^{-2} = i(\delta_v/R_{j0})^2, \quad (82)$$

and Eq. (79) is reduced to the well-known expression^{12,13}

$$\mathbf{F}_{Bj} = \frac{2\pi\rho|A|^2 R_{10} R_{20}}{|D|^2 L^2} (T_1 T_2 + \delta_1 \delta_2) \mathbf{e}_j. \quad (83)$$

In the reverse limiting case of high viscosity, where $R_{j0} \ll \delta_v$ and $|z_j| \rightarrow 0$,

$$\tau(z_j) \approx \frac{1}{3} + i(\delta_v/R_{j0})^2, \quad (84)$$

which indicates that strong viscous effects should result in a considerable departure from the Bjerknes theory.

D. Relative motion

To determine when the interaction force leads to attraction and when to repulsion, one needs to obtain an equation of the time-averaged relative motion of the bubbles. The equation of the time-averaged motion of the j th bubble can be written as

$$\frac{2}{3} \pi \rho R_{j0}^3 \frac{d\mathbf{W}_j}{dt} = \mathbf{F}_j - 4\pi\eta R_{j0} \mathbf{W}_j, \quad (85)$$

where \mathbf{W}_j is the time-averaged translational velocity of the j th bubble, the term on the left-hand side is the added mass force, and the second term on the right-hand side is the viscous drag force. Note that the numerical factor of the drag force depends on the Reynolds number $\operatorname{Re}_j = 2R_{j0}|\mathbf{W}_j|/\nu$ that is related to the translational motion of the j th bubble. For $\operatorname{Re}_j \gg 1$ the factor is equal to 12, whereas if $\operatorname{Re}_j \ll 1$ it is 4.²⁶ In the next section it is shown that in situations of interest to us $\operatorname{Re}_j \ll 1$. Therefore, the factor is chosen to be equal to 4.

Let us now estimate the ratio of the added mass force to the viscous drag force:

$$\left| \frac{\mathbf{F}_{am}}{\mathbf{F}_{vd}} \right| = \frac{R_{j0}^2 |dW_j/dt|}{6\nu |W_j|} = \frac{R_{j0} |dW_j/dt|}{12 |W_j|^2} \text{Re} j. \quad (86)$$

The order of magnitude of W_j is R_{j0}/T_c , where T_c is some characteristic time. Accordingly, $dW_j/dt \approx R_{j0}/T_c^2$. It follows that

$$\left| \frac{\mathbf{F}_{am}}{\mathbf{F}_{vd}} \right| \approx \frac{\text{Re} j}{12} \ll 1. \quad (87)$$

Hence we can neglect the added mass force and set that

$$\mathbf{F}_j - 4\pi\eta R_{j0} \mathbf{W}_j = 0. \quad (88)$$

Physically, this implies that the motions of the bubbles are quasistationary. Subtracting Eq. (88) with $j=1$ from that with $j=2$, one obtains the equation of the relative motion of the bubbles:

$$\frac{dL}{dt} = - \frac{|A|^2 G}{2\nu |D|^2 L^2}, \quad (89)$$

where

$$\begin{aligned} G = & (T_1 T_2 + \delta_1 \delta_2) [R_{10} + R_{10} \text{Re}\{\tau(z_2)\} + R_{20} \\ & + R_{20} \text{Re}\{\tau(z_1)\}] + (\delta_2 T_1 - \delta_1 T_2) [R_{10} \text{Im}\{\tau(z_2)\} \\ & - R_{20} \text{Im}\{\tau(z_1)\}]. \end{aligned} \quad (90)$$

It is seen that for $G > 0$ the separation distance between the bubbles, L , is reduced, while for $G < 0$ it is increased. The regions of attraction and repulsion are determined in the next section.

III. NUMERICAL RESULTS

As mentioned above, new phenomena should be expected under conditions of high viscosity. Therefore, as an example, the physical parameters corresponding to air bubbles in glycerine were set: $\rho = 1260 \text{ kg m}^{-3}$, $\eta = 1.48 \text{ Pa s}$, $\sigma = 0.0657 \text{ N m}^{-1}$, $\rho_A = 1.29 \text{ kg m}^{-3}$, $P_0 = P_A = 1 \text{ bar}$, $\kappa = 0.034 \text{ J (s m K)}^{-1}$, $c_p = 1009 \text{ J (kg K)}^{-1}$, and $\gamma = 1.4$. The results of the calculations are presented in Fig. 2. The latter is a set of contour plots showing the regions of attraction and repulsion in the range of bubble radii from 1 to 20 μm for three values of the driving frequency $f = 10, 20,$ and 40 kHz. Under the indicated conditions, with the acoustic pressure amplitude equal to $0.1P_0$, the Reynolds numbers are found to be on the order of $10^{-10} - 10^{-9}$, which confirms the validity of Eq. (88). In all three cases the bubbles are driven far below resonance and thus, according to the Bjerknes theory, must undergo mutual attraction. However, Fig. 2 displays that because of viscous effects there are quite wide areas of repulsion, which enlarge with decreasing the driving frequency and increasing the difference in size between the bubbles. The reason for the repulsion of the bubbles is still unclear. The most likely conjecture is that the vortical motion

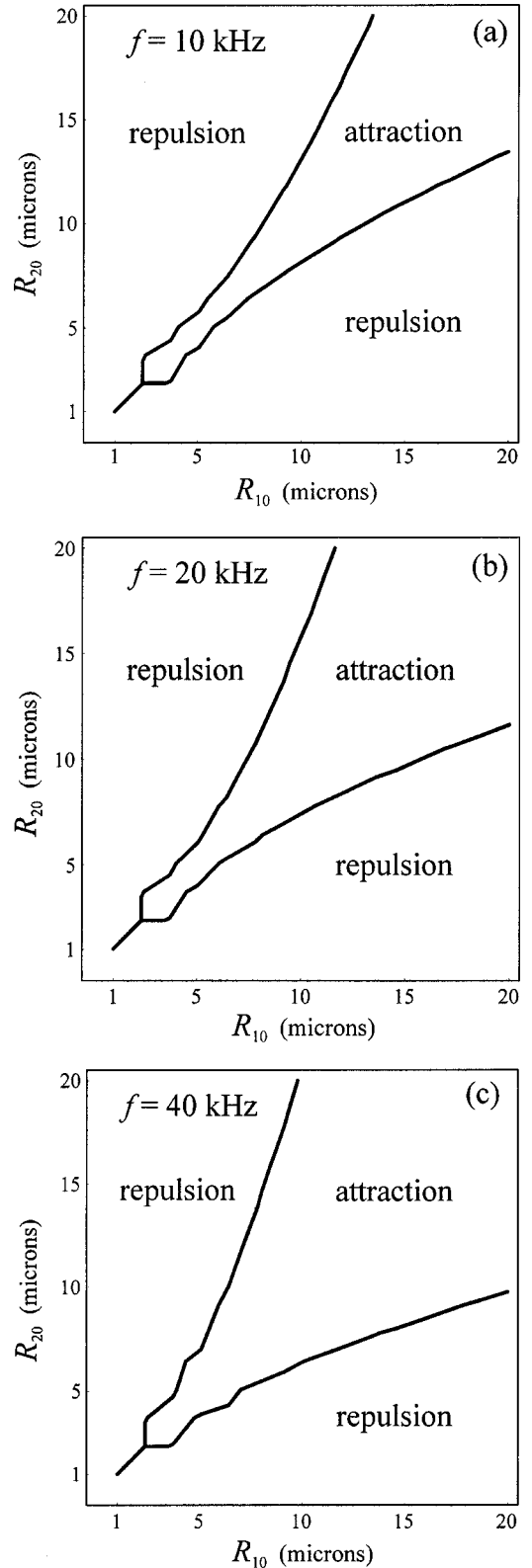


FIG. 2. Regions of attraction and repulsion for two bubbles driven well below resonance under conditions of high viscosity. The ranges of resonance frequencies corresponding to the range of bubble radii depicted (1–20 μm) are (a) 126.33 kHz–3.38 MHz; (b) 126.61 kHz–3.38 MHz; and (c) 127.63 kHz–3.38 MHz.

and acoustic streaming developing around either bubble lead to viscous drag forces on the other bubble that counteract the Bjerknes attraction and thus prevents the bubbles from being brought close together.

IV. CONCLUSION

A refined formula for the time-averaged interaction force between two gas bubbles in an acoustically driven liquid has been derived that improves the Bjerknes theory by allowing for the translational oscillations of the bubbles, the linear vortical motion of the liquid, and acoustic streaming around the bubbles. The boundary condition of slippage on the gas–liquid interface has been applied, which corresponds to gas bubbles free from organic impurities on the surface. It has been shown that by virtue of viscous effects there is a fairly wide parameter range where small bubbles, driven below resonance, are capable of repelling each other contrary to the classical Bjerknes theory.

ACKNOWLEDGMENT

This research was supported by the European Commission under the INCO Copernicus program.

- ¹L. A. Crum, “Bjerknes forces on bubbles in a stationary sound field,” *J. Acoust. Soc. Am.* **57**, 1363–1370 (1975).
- ²N. A. Pelekasis and J. A. Tsamopoulos, “Bjerknes forces between two bubbles. Part 1. Response to a step change in pressure,” *J. Fluid Mech.* **254**, 467–499 (1993).
- ³N. A. Pelekasis and J. A. Tsamopoulos, “Bjerknes forces between two bubbles. Part 2. Responses to an oscillatory pressure field,” *J. Fluid Mech.* **254**, 501–527 (1993).
- ⁴T. G. Leighton, *The Acoustic Bubble* (Academic, London, 1994).
- ⁵X. Zheng and R. E. Apfel, “Acoustic interaction forces between two fluid spheres in an acoustic field,” *J. Acoust. Soc. Am.* **97**, 2218–2226 (1995).
- ⁶A. A. Doinikov and S. T. Zavtrak, “Radiation forces between two bubbles in a compressible liquid,” *J. Acoust. Soc. Am.* **102**, 1424–1431 (1997).
- ⁷R. Mettin, I. Akhatov, U. Parlitz, C. D. Ohl, and W. Lauterborn, “Bjerknes forces between small cavitation bubbles in a strong acoustic field,” *Phys. Rev. E* **56**, 2924–2931 (1997).
- ⁸A. A. Doinikov, “Effects of the second harmonic on the secondary Bjerknes force,” *Phys. Rev. E* **59**, 3016–3021 (1999).
- ⁹V. F. K. Bjerknes, *Fluids of Force* (Columbia U. P., New York, 1906).
- ¹⁰Y. A. Kobelev, L. A. Ostrovskii, and A. M. Sutin, “Effect of self-clearing for acoustic waves in a liquid with gas bubbles,” *Pis'ma Zh. Eksp. Teor. Fiz.* **30**, 423–425 (1979).
- ¹¹P. L. Marston, E. H. Trinh, J. Depew, and J. Asaki, “Response of bubbles to ultrasonic radiation pressure: Dynamics in low gravity and shape oscillations,” in *Bubble Dynamics and Interface Phenomena*, edited by J. R. Blake, J. M. Boulton Stone, and N. H. Thomas (Kluwer Academic, Dordrecht, 1994), pp. 343–353.
- ¹²E. A. Zabolotskaya, “Interaction of gas bubbles in a sound field,” *Sov. Phys. Acoust.* **30**, 365–368 (1984).
- ¹³A. A. Doinikov and S. T. Zavtrak, “On the mutual interaction of two gas bubbles in a sound field,” *Phys. Fluids* **7**, 1923–1930 (1995).
- ¹⁴A. A. Doinikov and S. T. Zavtrak, “On the ‘bubble grapes’ induced by a sound field,” *J. Acoust. Soc. Am.* **99**, 3849–3850 (1996).
- ¹⁵I. Akhatov, U. Parlitz, and W. Lauterborn, “Pattern formation in acoustic cavitation,” *J. Acoust. Soc. Am.* **96**, 3627–3635 (1994).
- ¹⁶I. Akhatov, U. Parlitz, and W. Lauterborn, “Towards a theory of self-organization phenomena in bubble-liquid mixtures,” *Phys. Rev. E* **54**, 4990–5003 (1996).
- ¹⁷W. Lauterborn and C. D. Ohl, “Cavitation bubble dynamics,” *Ultrason. Sonochem.* **4**, 65–75 (1997).
- ¹⁸H. Oguz and A. Prosperetti, “A generalization of the impulse and virial theorems with an application to bubble oscillations,” *J. Fluid Mech.* **218**, 143–162 (1990).
- ¹⁹A. A. Doinikov, “Bjerknes forces between two bubbles in a viscous fluid,” *J. Acoust. Soc. Am.* **106**, 3305–3312 (1999).
- ²⁰G. K. Batchelor, *An Introduction to Fluid Dynamics* (Cambridge U. P., Cambridge, 1979), pp. 148–151.
- ²¹L. D. Landau and E. M. Lifshitz, *Fluid Mechanics* (Pergamon, New York, 1959).
- ²²A. A. Doinikov, “Acoustic radiation pressure on a compressible sphere in a viscous fluid,” *J. Fluid Mech.* **267**, 1–21 (1994).
- ²³C. S. Clay and H. Medwin, *Acoustical Oceanography. Principles and Applications* (Wiley, New York, 1977).
- ²⁴M. J. Lighthill, “Acoustic streaming,” *J. Sound Vib.* **24**, 471–492 (1978).
- ²⁵*Handbook of Mathematical Functions*, edited by M. Abramowitz and I. A. Stegun (Dover, New York, 1972).
- ²⁶J. Magnaudet and D. Legendre, “The viscous drag force on a spherical bubble with a time-dependent radius,” *Phys. Fluids* **10**, 550–554 (1998).

Efficient calculation of two-dimensional periodic and waveguide acoustic Green's functions

K. V. Horoshenkov^{a)}

School of Engineering, University of Bradford, Bradford BD7 1DP, United Kingdom

Simon N. Chandler-Wilde^{b)}

Department of Mathematical Sciences, Brunel University, Uxbridge UB8 3PH, United Kingdom

(Received 9 April 2001; revised 6 October 2001; accepted 17 January 2002)

New representations and efficient calculation methods are derived for the problem of propagation from an infinite regularly spaced array of coherent line sources above a homogeneous impedance plane, and for the Green's function for sound propagation in the canyon formed by two infinitely high, parallel rigid or sound soft walls and an impedance ground surface. The infinite sum of source contributions is replaced by a finite sum and the remainder is expressed as a Laplace-type integral. A pole subtraction technique is used to remove poles in the integrand which lie near the path of integration, obtaining a smooth integrand, more suitable for numerical integration, and a specific numerical integration method is proposed. Numerical experiments show highly accurate results across the frequency spectrum for a range of ground surface types. It is expected that the methods proposed will prove useful in boundary element modeling of noise propagation in canyon streets and in ducts, and for problems of scattering by periodic surfaces. © 2002 Acoustical Society of America. [DOI: 10.1121/1.1460920]

PACS numbers: 43.28.Mw, 43.20.El, 43.50.Jh [ANN]

I. INTRODUCTION

In the last 10 to 20 years the popularity of numerical modeling of sound propagation has received a substantial impetus as a result of the continuous increase in computer speed and storage capacity. The boundary element method has emerged as a powerful numerical technique for modeling sound propagation in the presence of multiple scattering and diffracting objects with complex shapes. In outdoor acoustics two-dimensional versions of the boundary element method have been exploited to predict the efficiency of noise barriers (e.g., Refs. 1–3) and the effect of building façades.⁴ In principle, the method is not limited by the extent of the acoustic region of interest. However, restrictions are imposed by the size of the available computer memory and execution times can be unacceptably slow if the discretization of larger boundaries at shorter wavelengths is required.

The number of boundary elements required can be reduced drastically by using a Green's function in the boundary integral equation formulation which incorporates analytically many of the physical boundary conditions of the problem. In this paper we propose methods for computation of the Green's function for sound propagation in a two-dimensional canyon/waveguide, occupying the part of the Oxy plane, $0 < x < h$, $y > 0$, with rigid or sound soft boundary conditions on $x = 0$ and $x = h$ for $y > 0$ and an impedance boundary condition on $y = 0$, $0 < x < h$. It is envisaged that this Green's function will prove useful for the efficient investigation by boundary element simulations of noise propagation in city streets. In this application the infinitely high walls at $x = 0$ and $x = h$ would represent high rise building

facades and the impedance boundary condition at $y = 0$ a reflecting or sound absorbing road surface. Boundary element discretization would only be required for additional structures, e.g., balconies and building features, sound absorbing treatments to building elements, noise barriers, etc. The actual finite height of building facades could be modeled accurately by imposing an absorbing boundary condition (requiring boundary element discretization) on sections of the walls at $x = 0$ and $x = h$, starting at the heights where the buildings finish. The point of using the canyon/waveguide Green's function is that, rather than discretizing the whole of the physical boundary, only those parts of the boundary which are perturbations from the boundary conditions for the Green's function need be discretized, leading to much smaller storage and computational requirements. Use of a two-dimensional Green's function implies that the geometry must be a two-dimensional one, invariant in the horizontal z direction. For a completely 2D problem the sound sources must also be invariant in the z direction, so that the sources of sound are coherent line sources. The applicability of 2D boundary element models can, however, be extended to more general sound sources by partial Fourier transform techniques. These are discussed, for example, in Refs. 2 and 3, and predictions of outdoor sound propagation are made in Ref. 2 for point and incoherent line sources of sound using a 2D boundary element code. There has been considerable recent interest in making predictions of noise levels, using mathematical and experimental models, for the type of urban configuration described in this paragraph—see, e.g., Refs. 4–8. In particular, work by Tang⁸ illustrates that the acoustic field near a finitely high building facade at a low receiver position can be predicted accurately using a model which assumes that the facade is infinitely high, so that the technique proposed above to model finitely high facades accu-

^{a)}Electronic mail: k.horoshenkov@bradford.ac.uk

^{b)}Electronic mail: simon.chandler-wilde@brunel.ac.uk

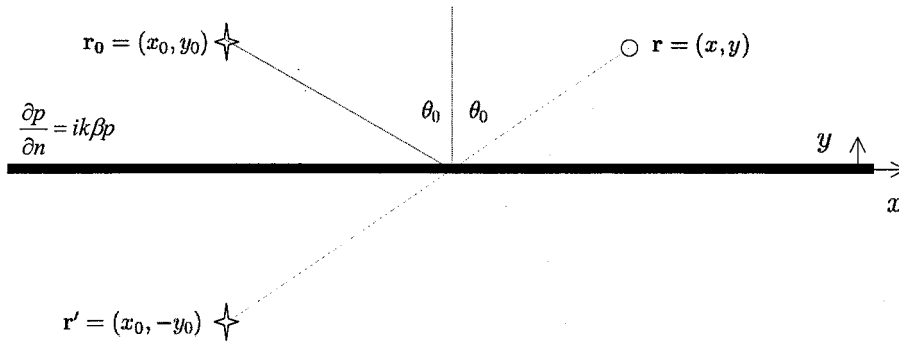


FIG. 1. Sound propagation above an impedance plane.

rately may be unnecessary. Tang's results are supported by close agreement between his theory and scale model experiments.⁸

Computing the canyon/waveguide Green's function requires calculation of the combined effect of the multiple reflections in the vertical rigid or sound soft walls at $x=0$ and $x=h$. This leads to an initial study of computation of the field due to an infinite array of periodically spaced point sources above a flat impedance boundary. The field due to such a periodic array of sources, extending to infinity in both directions, is usually termed the periodic Green's function. This function is utilized widely in the solution by integral equation methods of problems of acoustic and electromagnetic scattering by structures which are periodic in one dimension only. It is usual to utilize, in the numerical solution of such problems, the *free field periodic Green's function*, the solution to the calculation of the field due to an infinite periodic source array in free space, and there is a large literature on the computation of this function, reviewed recently in Ref. 9. In Secs. III and IV we discuss the computation of what may be termed the two-dimensional periodic Green's function for propagation above an impedance plane. The efficient calculation of this periodic Green's function appears not to have been discussed previously, although its use (and the use of other half-plane periodic Green's functions) in place of the free field periodic Green's function has been recommended recently for problems of scattering by one-dimensional periodic surfaces.^{10,11} In particular, use of the impedance periodic Green's function in place of the free field function leads to integral equation formulations which are well-defined for all periods of the scattering surface. As is well known and discussed in Sec. III, the free field periodic Green's function is undefined for a sequence of values of the periodicity.

The method described for computing the impedance periodic Green's function, proposed in the thesis of the first author,¹² is to compute a finite number of the source contributions explicitly and represent the contributions from the remaining (infinite number of) source contributions as a single Laplace-type integral. This technique, with just a single source contribution computed explicitly, has been proposed for the much simpler free field periodic Green's function in Ref. 13 (and see Refs. 14, 15, and 9). The analysis presented here derives, for the first time, integral representations for the infinite sum of source contributions for the im-

pedance case. It is also shown, adapting methods for the case of a single source above an impedance boundary,¹⁶ how parts of the integral, corresponding to poles of the integrand lying near the path of integration, can be evaluated explicitly in terms of the complementary error function, leaving a much smaller and smoother integrand to evaluate numerically. Finally, an explicit numerical integration scheme is proposed and its error analyzed, and it is shown how to select the number of source contributions to be computed explicitly so as to ensure high accuracy of calculation for the integral terms using only a 22-point quadrature rule. This attention to efficient evaluation is essential for the successful use of this Green's function in boundary element calculations. The accuracy and efficiency of the calculation method is illustrated by comparison with an alternative solution to the problem using normal mode decomposition.

II. THE GREEN'S FUNCTION FOR SOUND PROPAGATION ABOVE AN IMPEDANCE BOUNDARY

Consider the fundamental situation in which a monofrequency line source ($e^{-i\omega t}$ time dependence) is elevated above a flat boundary with normalized surface admittance β . Let $G_\beta(\mathbf{r}, \mathbf{r}_0)$ denote the acoustic pressure at $\mathbf{r}=(x, y)$ when the source is at $\mathbf{r}_0=(x_0, y_0)$. We note that $\beta=0$ if the boundary is rigid, while $\text{Re } \beta > 0$ if the boundary is an energy-absorbing surface. In the case $\beta=0$ the sound field can be found, as the combination of a direct wave and a wave reflected by the surface (Fig. 1), to be

$$G_0(\mathbf{r}, \mathbf{r}_0) = -\frac{i}{4} H_0^{(1)}(k|\mathbf{r}_0 - \mathbf{r}|) - \frac{i}{4} H_0^{(1)}(k|\mathbf{r}_0 - \mathbf{r}'|), \quad (1)$$

where $\mathbf{r}'=(x_0, -y_0)$ is the position vector of the image of the source in the plane $y=0$, and $H_0^{(1)}$ is the Hankel function of the first kind of order zero.

In the more general case when $\beta \neq 0$, the total field G_β can be written as

$$G_\beta(\mathbf{r}, \mathbf{r}_0) = G_0(\mathbf{r}, \mathbf{r}_0) + P_\beta(\mathbf{r}, \mathbf{r}_0), \quad (2)$$

where $P_\beta(\mathbf{r}, \mathbf{r}_0)$ is a perturbation term, accounting for the effect of nonzero admittance. Clearly $P_\beta=0$ if $\beta=0$. To determine the perturbation term P_β , for $\text{Re } \beta > 0$, it is necessary to solve the Helmholtz equation

$$(\Delta + k^2)P_\beta = 0, \quad (3)$$

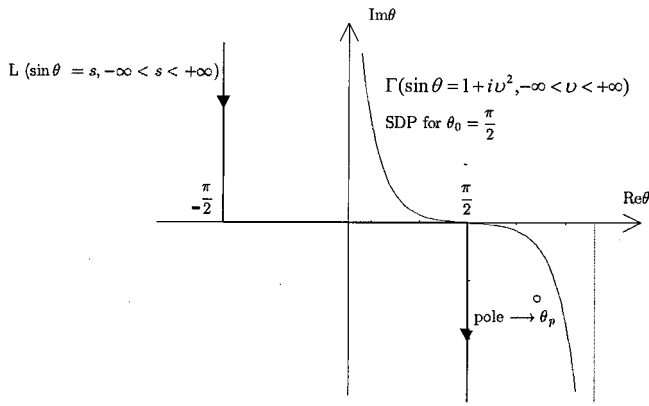


FIG. 2. The transformation of the integration path.

with the impedance boundary condition on $y=0$,

$$\begin{aligned} \frac{\partial}{\partial y} P_\beta(\mathbf{r}, \mathbf{r}_0) + ik\beta P_\beta(\mathbf{r}, \mathbf{r}_0) \\ = -ik\beta G_0(\mathbf{r}, \mathbf{r}_0) = -\frac{k\beta}{2} H_0^{(1)}(k\sqrt{(x-x_0)^2 + y_0^2}). \end{aligned} \quad (4)$$

This can be accomplished by Fourier transform methods, as discussed, for example, in Ref. 16. The solution to (3) and (4) which also satisfies the Sommerfeld radiation condition,

$$\lim_{r \rightarrow \infty} r^{1/2} \left(\frac{\partial P_\beta(\mathbf{r}, \mathbf{r}_0)}{\partial r} - ikP_\beta(\mathbf{r}, \mathbf{r}_0) \right) = 0, \quad (5)$$

is¹⁶

$$P_\beta(\mathbf{r}, \mathbf{r}_0) = \frac{i\beta}{2\pi} \int_{-\infty}^{+\infty} \frac{e^{i\eta_+ \sqrt{1-s^2}}}{\sqrt{1-s^2}(\sqrt{1-s^2} + \beta)} e^{-is|\xi_-|} ds, \quad (6)$$

where $\xi_- = k(x-x_0)$, $\eta_+ = k(y+y_0)$, and the square root is taken with $\text{Re}(\sqrt{1-s^2}) \geq 0$ and $\text{Im}(\sqrt{1-s^2}) \geq 0$.

The representation (6) for $P_\beta(\mathbf{r}, \mathbf{r}_0)$ is not suitable for evaluation by numerical integration as the integrand becomes increasingly oscillatory as $k|\mathbf{r}-\mathbf{r}_0| \rightarrow \infty$. A standard first step to a more suitable representation is to substitute $s = \sin \theta$. This change of variable transforms expression (6) into

$$P_\beta(\mathbf{r}, \mathbf{r}_0) = \frac{i\beta}{2\pi} \int_L \frac{e^{i(\eta_+ \cos \theta + |\xi_-| \sin \theta)}}{\cos \theta + \beta} d\theta. \quad (7)$$

Here L is the path of integration from $(-\pi/2 + i\infty) \rightarrow -\pi/2 \rightarrow \pi/2 \rightarrow (\pi/2 - i\infty)$ which is shown in Fig. 2. The integrand has an infinite number of simple poles which occur at

$$\theta = \pm \theta_p + 2\pi n, \quad n \in \mathbb{Z}, \quad (8)$$

where θ_p denotes the unique solution of $\cos \theta + \beta = 0$ in $\pi/2 < \text{Re} \theta < \pi$. The point θ_p lies above or below the real axis, depending on whether $\text{Im} \beta > 0$ or $\text{Im} \beta < 0$, respectively.

In Ref. 16, starting from Eq. (7), representations for P_β are derived which can be evaluated accurately and efficiently by Gauss-Laguerre quadrature rules. The method employed is to deform the path of integration to the steepest descent path, which connects $-\pi/2 + i\infty$ to $\pi/2 - i\infty$, passing

through $\theta = \theta_0$, where θ_0 is the angle of incidence as shown in Fig. 1. This path is given by $\cos(\theta - \theta_0) = 1 + iv^2$, $-\infty < v < \infty$. Then a pole subtraction technique is employed to smooth the behavior of the integrand on this path.

The methods proposed in Sec. III will make use of this representation, but a further representation for P_β will also be required. To develop this expression the choice is made to deform the path of integration to what is the steepest descent path in the case that the angle of incidence is $\theta_0 = \pi/2$. This transformed path of integration Γ connects $i\infty$ to $(\pi - i\infty)$, cutting the real axis at $\theta = \pi/2$, and is defined by

$$\sin \theta = 1 + iv^2, \quad v \in \mathbb{R}, \quad (9)$$

with $0 < \text{Re} \theta < \pi/2$ for $v < 0$, $\pi/2 < \text{Re} \theta < \pi$ for $v > 0$, so that $\cos \theta = -v\sqrt{v^2 - 2i}$, with $\text{Re} \sqrt{v^2 - 2i} > 0$. The path Γ and the direction of integration as v increases from $-\infty$ to $+\infty$ are shown in Fig. 2. Making the deformation of the path of integration we obtain that

$$P_\beta^{(L)} = P_\beta^{(\Gamma)} + P_s, \quad (10)$$

where $P_\beta^{(\Gamma)}$ is the integral (7) with the path of integration changed from L to Γ and P_s is the contribution accounting for the residue at the pole θ_p , the only one which can be crossed in the deformation. Explicitly, where $\sqrt{1-\beta^2}$ denotes the square root with positive real part,

$$P_s = \begin{cases} \beta \frac{e^{-i\eta_+ \beta}}{\sqrt{1-\beta^2}} e^{i|\xi_-| \sqrt{1-\beta^2}} & \text{if } \text{Im} \beta < 0 \text{ and } \text{Re} \sqrt{1-\beta^2} > 1, \\ \frac{\beta}{2} \frac{e^{-i\eta_+ \beta}}{\sqrt{1-\beta^2}} e^{i|\xi_-| \sqrt{1-\beta^2}} & \text{if } \text{Im} \beta < 0 \text{ and } \text{Re} \sqrt{1-\beta^2} = 1, \\ 0 & \text{otherwise.} \end{cases} \quad (11)$$

Physically, this term is a surface wave which decays exponentially with height above the surface.

The first term on the right-hand side of Eq. (10) can be represented, via the parametrization (9), as the integral

$$P_\beta^{(\Gamma)} = \frac{\beta e^{i|\xi_-|}}{\pi} \int_{-\infty}^{+\infty} \frac{e^{-i\eta_+ \sqrt{v^2 - 2i}}}{\sqrt{v^2 - 2i}(\beta - v\sqrt{v^2 - 2i})} e^{-|\xi_-|v^2} dv. \quad (12)$$

Splitting the range of integration in (12) and changing the sign of the variable of integration in the second integral, it is seen that, defining $w = v\sqrt{v^2 - 2i}$,

$$\begin{aligned} P_\beta^{(\Gamma)} &= \frac{\beta e^{i|\xi_-|}}{\pi} \left[\int_0^\infty \frac{e^{-i\eta_+ v \sqrt{v^2 - 2i}}}{\sqrt{v^2 - 2i}(\beta - v\sqrt{v^2 - 2i})} e^{-|\xi_-|v^2} dv \right. \\ &\quad \left. + \int_0^\infty \frac{e^{i\eta_+ v \sqrt{v^2 - 2i}}}{\sqrt{v^2 - 2i}(\beta + v\sqrt{v^2 - 2i})} e^{-|\xi_-|v^2} dv \right] \\ &= \frac{2\beta e^{i|\xi_-|}}{\pi} \int_0^\infty \frac{\beta \cos(\eta_+ w) - iw \sin(\eta_+ w)}{\sqrt{v^2 - 2i}(\beta^2 - w^2)} e^{-|\xi_-|v^2} dv. \end{aligned} \quad (13)$$

To finish this section, a similar representation for the total field from a line monopole placed above the impedance surface is obtained. The total field is given as

$$G_\beta(\mathbf{r}, \mathbf{r}_0) = G_0(\mathbf{r}, \mathbf{r}_0) + P_\beta^{(\Gamma)} + P_s. \quad (14)$$

Further, in terms of the variables ξ_- and η_\pm , where $\eta_- = k(y - y_0)$, it holds that

$$G_0(\mathbf{r}, \mathbf{r}_0) = -\frac{i}{4} \{H_0^{(1)}(\sqrt{\xi_-^2 + \eta_+^2}) + H_0^{(1)}(\sqrt{\xi_-^2 + \eta_-^2})\}. \quad (15)$$

Using a representation for the Hankel function as a Laplace-type integral (Ref. 17 formulas 2.13.52 and 2.13.60), the function G_0 can be represented in a similar form to (13), as

$$G_0(\mathbf{r}, \mathbf{r}_0) = -\frac{e^{i|\xi_-|}}{\pi} \int_0^\infty \frac{\cos(\eta_+ w) + \cos(\eta_- w)}{\sqrt{v^2 - 2i}} e^{-|\xi_-|v^2} dv. \quad (16)$$

Combining (13), (14), and (16), it is seen that

$$G_\beta(\mathbf{r}, \mathbf{r}_0) = \frac{e^{i|\xi_-|}}{\pi} \int_0^\infty \left[\frac{w^2(\cos(\eta_+ w) + \cos(\eta_- w)) - 2i\beta w \sin(\eta_+ w)}{\sqrt{v^2 - 2i(\beta^2 - w^2)}} + \frac{\beta^2(\cos(\eta_+ w) - \cos(\eta_- w))}{\sqrt{v^2 - 2i(\beta^2 - w^2)}} \right] e^{-|\xi_-|v^2} dv + P_s. \quad (17)$$

III. PROPAGATION OF SOUND FROM AN INFINITE NUMBER OF PERIODICALLY SPACED SOURCES

Consider the problem of an infinite number of equidistantly spaced sources elevated at the same height above an impedance plane as shown in Fig. 3, at positions $\mathbf{r}_l = (x_l, y_0)$, $l=0, 1, \dots$, where $x_l = x_0 + 2hl$ and $2h$ is the distance between adjacent sources. Suppose that the sources have the same unit strength but allow the possibility that there is a phase shift of $2H\alpha$ between adjacent sources, where $H = kh$ and α is some fixed real number. Using the same notation as in Sec. II, the resultant field at an arbitrary observation point $\mathbf{r} = (x, y)$ can be written as the superposition of the contributions from all the sources as

$$G_\beta^P(\mathbf{r}, \mathbf{r}_0; \alpha) = \sum_{l=0}^{\infty} e^{-2il\alpha H} G_\beta(\mathbf{r}, \mathbf{r}_l). \quad (18)$$

Provided $\text{Re } \beta > 0$ (the boundary is energy absorbing) and the source and receiver remain close to the ground surface, $G_\beta(\mathbf{r}, \mathbf{r}_l)$ decays, as the distance between source and receiver increases, at a rate which is faster than in free-field conditions. A full far-field asymptotic expansion for G_β , quantifying this behavior, is given in Ref. 18. The leading asymptotic behavior can also be seen directly from (17). Note first that P_s decays exponentially as $|x - x_0| \rightarrow \infty$. The integral in (17) has the form

$$\int_0^\infty Q(v^2) e^{-|\xi_-|v^2} dv = \frac{1}{2} \int_0^\infty s^{-1/2} Q(s) e^{-|\xi_-|s} ds,$$

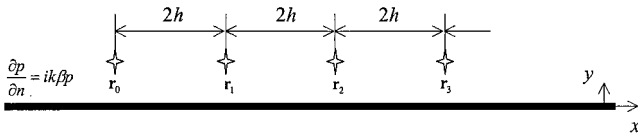


FIG. 3. The set of periodically spaced sources above the impedance boundary.

where the function Q has the asymptotic behavior $Q(s) \sim as$ as $s \rightarrow 0$, where

$$a = \frac{\sqrt{-2i}}{2\beta^2} [4 - 4i\beta\eta_+ + \beta^2(\eta_+^2 - \eta_-^2)].$$

It follows from Watson's lemma (e.g., Ref. 19 p. 263) that

$$G_\beta(\mathbf{r}, \mathbf{r}_l) = O(|x - x_l|^{-3/2})$$

as $|x - x_l| \rightarrow \infty$ with y and y_0 fixed. This rate of decay ensures that the infinite series (18) is absolutely convergent, which in turn ensures that the validity of the interchange of integration and infinite summation in the manipulations below is valid, at least for the case $\text{Re } \beta > 0$.

The summation corresponding to (18) in the free-field case is studied extensively in the literature: this work has been clearly reviewed by Linton.⁹ This summation is

$$G_f^P(\mathbf{r}, \mathbf{r}_0; \alpha) = \sum_{l=0}^{\infty} e^{-2il\alpha H} G_f(\mathbf{r}, \mathbf{r}_l), \quad (19)$$

where G_f is the standard free-field Green's function, defined by $G_f(\mathbf{r}, \mathbf{r}_l) = -(i/4) H_0^{(1)}(k|\mathbf{r} - \mathbf{r}_l|)$. In contrast to (18), in the case $\text{Re } \beta > 0$, the series (19) is only conditionally convergent, since the Hankel function has the asymptotic behavior $H_0^{(1)}(t) \sim \sqrt{2/\pi t} e^{i(t - \pi/4)}$ as $t \rightarrow \infty$. Indeed, if $\alpha = 0$, (19) is divergent to infinity if the wavelength divides the period, i.e., if H is an integer multiple of π . More generally, for an arbitrary value of α , the series (19) diverges if $H(1 - \alpha)$ is an integer multiple of π . The same restriction, that the series is only conditionally convergent, or divergent in the case that $H(1 - \alpha)$ is a multiple of π , carries over to (18) in the case $\beta = 0$. Physically, this divergence corresponds to cases where the contributions from far source points are all in phase, and combine to give an infinite pressure field at the receiver position.

The first N terms can be extracted from the sum (18) to

be evaluated explicitly, using the efficient calculation method proposed in Ref. 16. The remaining sum, from N to infinity, can be expressed as a single infinite integral by replacing G_β by its integral representation (17), reversing the order of summation and integration, and finally evaluating the summation under the integral sign, which is now a geometric series. Provided N is chosen large enough so that $x_N > x$, the resulting expression is

$$G_\beta^P(\mathbf{r}, \mathbf{r}_0; \alpha) = \sum_{l=0}^{N-1} e^{-2il\alpha H} G_\beta(\mathbf{r}, \mathbf{r}_l) + \frac{2e^{i(\xi_N - 2N\alpha H)}}{\pi} \int_0^\infty f(v^2) e^{-\xi_N v^2} dv + P_s^P, \quad (20)$$

where $\xi_N = k(x_N - x)$, the function f is defined implicitly by

$$f(v^2) = \frac{w^2 \cos(\eta_0 w) \cos(\eta w) - \beta^2 \sin(\eta_0 w) \sin(\eta w) - i\beta w \sin(\eta_+ w)}{\sqrt{v^2 - 2i(\beta^2 - w^2)}(1 - e^{-2H(v^2 - i(1 - \alpha))})}, \quad (21)$$

with $\eta_0 = ky_0$ and $\eta = ky$, and P_s^P is the sum of the surface wave contributions, given by

$$P_s^P = \begin{cases} \beta \frac{e^{-i\eta_+ \beta} e^{i(\xi_N \sqrt{1 - \beta^2} - 2N\alpha H)}}{\sqrt{1 - \beta^2}} [1 - e^{2iH(\sqrt{1 - \beta^2} - \alpha)}]^{-1} & \text{if } \text{Im } \beta < 0 \text{ and } \text{Re } \sqrt{1 - \beta^2} > 1, \\ \frac{\beta}{2} \frac{e^{-i\eta_+ \beta} e^{i(\xi_N \sqrt{1 - \beta^2} - 2N\alpha H)}}{\sqrt{1 - \beta^2}} [1 - e^{2iH(\sqrt{1 - \beta^2} - \alpha)}]^{-1} & \text{if } \text{Im } \beta < 0 \text{ and } \text{Re } \sqrt{1 - \beta^2} = 1, \\ 0 & \text{otherwise.} \end{cases} \quad (22)$$

A discussion of the choice of N in (20) follows in Sec. III B.

A. Pole subtraction

As mentioned already, in the representation (20) for $G_\beta^P(\mathbf{r}, \mathbf{r}_0; \alpha)$ the contributions from the terms $G_\beta(\mathbf{r}, \mathbf{r}_l)$ in the finite summation can be evaluated using the method proposed in Ref. 16. This method represents $G_\beta(\mathbf{r}, \mathbf{r}_l)$ as the sum of an expression involving the complementary error function of complex argument and a Laplace-type integral which, as shown in Ref. 16, can be evaluated accurately and efficiently using a 22-point Gauss–Laguerre quadrature rule. To evaluate $G_\beta^P(\mathbf{r}, \mathbf{r}_0; \alpha)$ using Eq. (20), it remains to consider the evaluation of the integral on the right-hand side of that equation, for which a similar integration scheme will be developed.

It is necessary first to examine the singularities of the function $f(z)$ and their proximity to the path of integration (the positive real axis). This is important because the accuracy of numerical integration methods is seriously affected if a singularity in the integrand lies on or near the integration path. It will become apparent that the only singularities which may lie close to the path of integration are poles. Further, a method of subtraction of the poles nearest to the positive real axis will be described leading to alternative representations of the integral in (20) as the sum of a Laplace-type integral and expressions involving the complementary

error function of complex argument. In these expressions, in contrast to the original integral in (20), the integrand is a smooth function for all values of β and H .

Substituting $t = \xi_N v^2$ in the integral in (20), this equation becomes

$$G_\beta^P(\mathbf{r}, \mathbf{r}_0; \alpha) = \sum_{l=0}^{N-1} e^{-2il\alpha H} G_\beta(\mathbf{r}, \mathbf{r}_l) + \frac{e^{i(\xi_N - 2N\alpha H)}}{\pi \sqrt{\xi_N}} I + P_s^P, \quad (23)$$

where

$$I = \int_0^\infty f(t/\xi_N) t^{-1/2} e^{-t} dt. \quad (24)$$

This integral can be approximated by Gaussian quadrature with weight function $t^{-1/2} e^{-t}$, in other words, by generalized Gauss–Laguerre quadrature,²⁰ and this will be accurate, using a rule with a small number of points, provided $f(t/\xi_N)$ is smooth as a function of t on the interval of integration, $0 \leq t < \infty$. This will be the case provided $f(t/\xi_N)$ does not have singularities close to the positive real axis.

From (21), the function f is given explicitly by

$$f(z) = \frac{F(z)}{\sqrt{z - 2i(\beta^2 + 2iz - z^2)}(1 - e^{-2H(z - i(1 - \alpha))})}, \quad (25)$$

where

$$F(z) = z(z - 2i) \cos(\eta_0 \sqrt{z(z - 2i)}) \cos(\eta \sqrt{z(z - 2i)}) - \beta^2 \sin(\eta_0 \sqrt{z(z - 2i)}) \sin(\eta \sqrt{z(z - 2i)}) - i\beta \sqrt{z(z - 2i)} \sin(\eta_+ \sqrt{z(z - 2i)}). \quad (26)$$

The function F , the numerator in (25), is an entire function, i.e., is analytic in the whole complex plane. Provided the square root in (25) is chosen with $\text{Re } \sqrt{z - 2i} > 0$, $\sqrt{z - 2i}$ is analytic in the half-plane $\text{Im } z < 2$, which includes the positive real axis. The remaining singularities of f are poles at the points z which are the solutions of the equations

$$z^2 - 2iz - \beta^2 = 0 \quad (27)$$

and

$$1 - qe^{-2Hz} = 0, \quad (28)$$

where $q = e^{2iH(1 - \alpha)}$.

The solutions of (27) are $z=i(1\pm\sqrt{1-\beta^2})$. One of these solutions lies in the half-plane $\text{Im } z \geq 1$. Choosing the square root so that $\text{Re } \sqrt{1-\beta^2} \geq 0$, the other solution, in $\text{Im } z \leq 1$, is

$$z_a = i(1 - \sqrt{1 - \beta^2}) = i\beta^2 / (1 + \sqrt{1 - \beta^2}). \quad (29)$$

Noting that $|z_a| \leq |\beta|^2$, it becomes clear that this root may lie on or arbitrarily close to the positive real axis, though $z_a \neq 0$ provided $\beta \neq 0$. In the numerical results reported in this paper, the effect of this pole will be ignored if $|\text{Re } \sqrt{1 - \beta^2}| \geq 0.75$ or $\text{Im}(1 - \sqrt{1 - \beta^2}) \geq 0.75$, in which case z_a lies at least distance 0.75 from the positive real axis. Otherwise the effect of this pole will be subtracted, i.e., the integral I will be rewritten as

$$I = \int_0^\infty g_a(t/\xi_N) t^{-1/2} e^{-t} dt + \epsilon_a \int_0^\infty \frac{t^{-1/2} e^{-t}}{t/\xi_N - z_a} dt, \quad (30)$$

where

$$g_a(z) = f(z) - \frac{\epsilon_a}{z - z_a} \quad (31)$$

and

$$\begin{aligned} \epsilon_a &:= \text{Res}_{z=z_a} f(z) \\ &= - \frac{F(z_a)}{2\sqrt{z_a - 2i(z_a - i)(1 - e^{-2H(z_a - i(1 - \alpha))})}}, \end{aligned} \quad (32)$$

with

$$\begin{aligned} F(z_a) &= \beta^2 [\cos(\eta_0 \beta) \cos(\eta \beta) - \sin(\eta_0 \beta) \sin(\eta \beta) \\ &\quad - i \sin(\eta + \beta)]. \end{aligned} \quad (33)$$

The point of the pole subtraction in (30) is that the second integral can be evaluated exactly. From Ref. 21, Eqs. (7.1.3) and (7.1.4), it follows, for arbitrary complex $z \neq 0$, that

$$\int_0^\infty \frac{t^{-1/2} e^{-t}}{t/\xi_N - z} dt = -i\pi \frac{\xi_N}{\sqrt{\xi_N z}} e^{-\sqrt{z\xi_N}} [\text{erfc}(-i\sqrt{z\xi_N}) - \Psi(z)], \quad (34)$$

where, if z is not on the positive real axis, then the square roots in (34) are to be taken with positive imaginary part. In Eq. (34), erfc is the complementary error function of complex argument, defined by $\text{erfc } w = (2/\sqrt{\pi}) \int_w^\infty e^{-t^2} dt$, and

$$\Psi(z) = \begin{cases} 1, & z > 0, \\ 0, & \text{otherwise.} \end{cases} \quad (35)$$

Note that $\Psi(z) = 1$ if and only if $\text{Im } \beta < 0$ and $\text{Re } \sqrt{1 - \beta^2} = 1$, which is the same condition as selects the second alternative in Eq. (22).

The solutions of (28), which are the other poles of f , are

$$z = i \frac{\arg q + 2\pi n}{2H}, \quad n \in \mathbb{Z}, \quad (36)$$

where $\arg q$ denotes the principal argument of q , in the range $-\pi < \arg q \leq \pi$. The closest of these poles to the positive real axis is that at

$$z_b = i \frac{\arg q}{2H}. \quad (37)$$

The other poles have imaginary parts satisfying $|\text{Im } z| \geq \pi/(2H)$, and so lie at least this distance from the real axis. In the numerical results shown below the pole at $z = z_b$ is subtracted if $0 < \arg q \leq \pi/4$, in which case $0 < |\text{Im } z_b| \leq \pi/(8H)$. [If $\arg q = 0$, then the apparent singularity, at $z = z_b = 0$, is removable since $F(0) = 0$.] The same technique for removing the pole is utilized as has been described above for the pole at $z = z_a$, noting that

$$\epsilon_b := \text{Res}_{z=z_b} f(z) = \frac{F(z_b)}{2\sqrt{z_b - 2i(\beta^2 - z_b^2 + 2iz_b)H}}. \quad (38)$$

If only the pole at $z = z_b$ is to be subtracted, the resulting expression for the integral, Eq. (44), is similar to (30), but with $g_a(t/\xi_N)$ replaced by $g_b(t/\xi_N)$, where the function g_b is defined by

$$g_b(z) = f(z) - \frac{\epsilon_b}{z - z_b}. \quad (39)$$

In the case that both the poles at z_a and z_b are to be subtracted, then $g_a(t/\xi_N)$ is replaced by $g_{ab}(t/\xi_N)$, where

$$g_{ab}(z) = f(z) - \frac{\epsilon_a}{z - z_a} - \frac{\epsilon_b}{z - z_b}. \quad (40)$$

To sum up, the following expressions for the integral I are proposed for $\text{Re } \beta > 0$, the different expressions below depending on whether the poles z_a and z_b are, or are not, ‘‘close’’ to the positive real axis, where, as mentioned above, it is proposed to treat z_a as lying close to the positive real axis if $\text{Re } z_a > -0.75$ and $|\text{Im } z_a| < 0.75$, i.e., if $\text{Im}(1 - \sqrt{1 - \beta^2}) > 0.75$ and $|\text{Re } \sqrt{1 - \beta^2}| < 0.75$, and z_b as lying close to the real axis if $|\text{Im } z_b| < \pi/(8H)$, i.e., if $|\arg q| < \pi/4$. In each of the cases the integral to be calculated takes the form $\int_0^\infty g(t/\xi_N) t^{-1/2} e^{-t} dt$, for some function g . The pole subtraction carried out ensures that, in each case, the integrand $g(t/\xi_N)$ is bounded and analytic, as a function of t , in a neighborhood of the positive real axis, namely the strip $\text{Re } t > -3\xi_N/4$, $|\text{Im } t| \leq \min(\frac{3}{4}, \pi/(8H))\xi_N$. Thus it can be ensured that in each case singularities of the integrand do not lie closer than distance $\frac{3}{4}$ from the positive real axis by choosing N so that $\xi_N \geq \max(1, 6H/\pi)$. In other words, since $\xi_N = \xi_0 - \xi + 2HN$, where $\xi_0 = kx_0$ and $\xi = kx$, N is to be chosen in the range

$$N \geq \max\left(\frac{1}{2H}, \frac{3}{\pi}\right) - \frac{\xi_0 - \xi}{2H}. \quad (41)$$

The four cases to be considered and the respective integral representations to be used for numerical evaluation are as follows. Recall that, in Eqs. (43)–(45), the square roots $\sqrt{z_a \xi_N}$ and $\sqrt{z_b \xi_N}$ are to be taken with argument in the range $[0, \pi)$.

I. Neither of the poles are close to the positive real axis (or $z_b = 0$ and z_a is not close to the positive real axis):

$$I = \int_0^\infty f(t/\xi_N) t^{-1/2} e^{-t} dt. \quad (42)$$

II. The pole z_a is close to the positive real axis and either $z_b=0$ or z_b is not close to the real axis:

$$I = \int_0^\infty g_a(t/\xi_N) t^{-1/2} e^{-t} dt + \frac{i\epsilon_a \pi \xi_N}{\sqrt{z_a \xi_N}} e^{-z_a \xi_N} \times [\operatorname{erfc}(-i\sqrt{z_a \xi_N}) - \Psi(z_a)]. \quad (43)$$

III. Only the pole z_b is close to the real axis (but $z_b \neq 0$):

$$I = \int_0^\infty g_b(t/\xi_N) t^{-1/2} e^{-t} dt + \frac{i\epsilon_b \pi \xi_N}{\sqrt{z_b \xi_N}} e^{-z_b \xi_N} \times \operatorname{erfc}(-i\sqrt{z_b \xi_N}). \quad (44)$$

IV. Both the poles z_a and z_b are close to the positive real axis (but $z_b \neq 0$ and $z_a \neq z_b$):

$$I = \int_0^\infty g_{ab}(t/\xi_N) t^{-1/2} e^{-t} dt + i\pi \xi_N \times \left[\frac{\epsilon_a}{\sqrt{z_a \xi_N}} e^{-z_a \xi_N} [\operatorname{erfc}(-i\sqrt{z_a \xi_N}) - \Psi(z_a)] + \frac{\epsilon_b}{\sqrt{z_b \xi_N}} e^{-z_b \xi_N} \operatorname{erfc}(-i\sqrt{z_b \xi_N}) \right]. \quad (45)$$

The above formulas apply if $\operatorname{Re} \beta > 0$ (the boundary is energy absorbing). An important special case not covered above is that of a rigid boundary with $\beta=0$. In this case, as noted earlier, the series (19) is divergent if $H(1-\alpha)$ is a multiple of π , in other words, if $q=1$. If $q \neq 1$, then it can be shown, via arguments similar to those used to derive the representation (20), that the summation (19) is (conditionally) convergent, and has the value given by (23) and (24), with the function f simplifying in this case to

$$f(z) = -\frac{\cos(\eta_0 \sqrt{z(z-2i)}) \cos(\eta \sqrt{z(z-2i)})}{\sqrt{z-2i} (1 - e^{-2H(z-i(1-\alpha))})}.$$

B. Numerical integration and choice of the parameter N

As indicated earlier, it is proposed to evaluate each of the integrals in Eqs. (42)–(45) by generalized Gauss–Laguerre quadrature. Let $x_{1,n}, x_{2,n}, \dots, x_{n,n}$ denote the abscissae and $w_{1,n}, w_{2,n}, \dots, w_{n,n}$ the weights of the n -point Gauss–Laguerre quadrature rule for the weight function $t^{-1/2} e^{-t}$. These weights and abscissae are tabulated for $n=1, 2, \dots, 15$ in Ref. 20 and for $n=1, 2, 3$ in Ref. 16, or can be calculated using a standard subroutine library.²² Let g denote one of the functions f , g_a , g_b , or g_{ab} . Then the numerical integration method employed will be to approximate

$$J := \int_0^\infty g(t/\xi_N) t^{-1/2} e^{-t} dt \approx J_{m,n} := \sum_{j=1}^m w_{j,n} g(x_{j,n}/\xi_N). \quad (46)$$

For $m=n$ the approximation, $J_{m,n}$, is the n -point Gauss–Laguerre rule approximation to the integral J . For $1 \leq m$

$< n$, $J_{m,n}$ is an approximation to the Gauss–Laguerre rule obtained by neglecting the last $n-m$ weights and abscissae. Since the weights $w_{j,n}$ become extremely small for j and n large, $J_{m,n}$ can be just as accurate as $J_{n,n}$ while needing fewer terms in the summation (46) and thus being cheaper to evaluate.

The error in the numerical integration scheme proposed will now be examined. For brevity this error will be estimated only for the integral (42) in case I, where $g=f$ and z_a is at least distance $\pi/(8H)$ and z_b is at least distance 0.75 from the positive real axis. However, a similar analysis and nearly identical criteria for accuracy apply in the other three cases—cf. Ref. 16, Appendix B, and Ref. 23.

The error, $|J - J_{m,n}|$, in the numerical integration method has two components. One component arises from the neglect of the last $n-m$ weights and abscissae. The effect of this is equivalent to setting the integrand to zero beyond the m th abscissa, $x_{m,n}$. For this to be accurate it is necessary that the integrand $f(t/\xi_N) t^{-1/2} e^{-t}$ be small for $t > x_{m,n}$. To simplify the task of bounding f the assumption will be made that $|\beta| \leq 1$, which range of β includes the values usually of interest in applications of the impedance boundary condition in outdoor sound propagation, where β is the relative surface impedance of the ground surface. Recalling that the case considered is that in which z_a and z_b are not close to the positive real axis, it then follows that, for $z \geq 0$,

$$|1 - e^{-2H(z-i(1-\alpha))}| \geq \frac{1}{\sqrt{2}}, \quad |\sqrt{z-2i}| \geq \sqrt{2},$$

$$|\beta^2 + 2iz - z^2| \geq \frac{3}{4},$$

and, where $\phi = |z(z-2i)|$,

$$|z(z-2i)/(\beta^2 + 2iz - z^2)| \leq \frac{\phi}{\max(\frac{3}{4}, \phi-1)} \leq \frac{7}{3}.$$

Further,

$$|\cos(\eta_0 \sqrt{z(z-2i)})| \leq e^{\eta_0 p(z)},$$

where $p(z) = |\operatorname{Im} \sqrt{z(z-2i)}|$. The same bound applies to $|\sin(\eta_0 \sqrt{z(z-2i)})|$, and analogous bounds apply to the other sine and cosine terms in (26). Applying the above inequalities to f defined by (25), it follows that

$$|f(z)| \leq 6e^{\eta_+ p(z)}, \quad (47)$$

for $z \geq 0$ and $|\beta| \leq 1$, with

$$p(z) = |\operatorname{Im} \sqrt{z(z-2i)}| = \left\{ \frac{2z}{z + \sqrt{z^2 + 4}} \right\}^{1/2} \leq \min(1, z^{1/2}).$$

Thus, for $t > 0$,

$$|f(t/\xi_N) t^{-1/2} e^{-t}| \leq 6t^{-1/2} \exp(\eta_+ \min(1, \sqrt{t/\xi_N}) - t).$$

If ξ_N is chosen such that $\xi_N \geq \eta_+^2/x_{m,n}$, it then follows that

$$|f(t/\xi_N) t^{-1/2} e^{-t}| \leq 6x_{m,n}^{-1/2} \exp(\eta_+ \min(1, \sqrt{x_{m,n}/\xi_N}) - x_{m,n}), \quad (48)$$

for $t \geq x_{m,n}$.

In the numerical results the values

$$n=40, \quad m=22, \quad (49)$$

are chosen, for which $x_{m,n}=30.26$. Then the criterion (48) ensures that

$$|f(t/\xi_N)t^{-1/2}e^{-t}| \leq 10^{-9},$$

for $t \geq x_{m,n}$, provided $\eta_+ \leq 9.4$ or

$$\xi_N \geq 0.34\eta_+^2. \quad (50)$$

The other contribution to the error, $|J - J_{m,n}|$, is that inherent in the Gauss–Laguerre quadrature formula. In the case $y = y_0 = 0$, when $\eta = \eta_0 = \eta_+ = 0$, provided the criterion (41) is satisfied so that the integrand is analytic within at least distance 0.75 of the positive real axis, it is not difficult to apply Ref. 16, Theorem 3(i), to show that the error in the n -point Gauss–Laguerre rule, $|J - J_{n,n}|$, tends to zero as $n \rightarrow \infty$, uniformly with respect to N and β , for $|\beta| \leq C$, where $C > 0$ is a positive constant. As remarked above, we adopt the values of n and m given by (49), whose values proved accurate in Ref. 16 for very similar integrands.

When $\eta_+ > 0$, the integrand has additional oscillatory terms: a typical such term is $\sin(\eta_+ \sqrt{z(z-2i)})$, the oscillatory behavior of which is determined, for $z \geq 0$, by

$$q(z) := \operatorname{Re} \sqrt{z(z-2i)} = z^{1/2} \sqrt{\frac{z + \sqrt{z^2 + 4}}{2}}.$$

As η_+ increases the integrand becomes more oscillatory and a greater density of quadrature points is needed to sample this oscillation. A heuristic criterion for the choice of N is to insist that ξ_N be chosen large enough so that the Nyquist sampling criterion is amply satisfied in an average sense. The abscissae, sampling the integrand in (42), are distributed on the interval $[0, x_{m,n}/\xi_N]$ and the number of oscillations in this interval is $\eta_+ q(x_{m,n}/\xi_N)/(2\pi)$. Choosing ξ_N so that there are, on average, at least 11 integration points per oscillation leads to the heuristic criterion for the choice of ξ_N that

$$\tilde{c}q(x_{m,n}/\xi_N) \leq 1, \quad (51)$$

where $\tilde{c} = 11\eta_+/(2\pi m)$. Now, for $z \geq 0$,

$$z^{1/2} \max(1, z^{1/2}) \leq q(z) \leq \tilde{q}(z) \leq 1.5z^{1/2} \max(1, z^{1/2}),$$

where $\tilde{q}(z) := z^{1/2}(z^2 + 4)^{1/4}$. Thus a simpler and only slightly stricter criterion is obtained by replacing the function q by \tilde{q} in (51). This slightly stricter criterion holds if and only if

$$\xi_N \geq \xi^* := x_{m,n} \tilde{c} \sqrt{2\tilde{c}^2 + \sqrt{1 + 4\tilde{c}^4}}. \quad (52)$$

Clearly $\xi^* > 2x_{m,n}\tilde{c}^2$. With the values of n and m proposed in Eq. (49), $x_{m,n} = 30.26$ so that $\xi^* > 2x_{m,n}\tilde{c}^2 = 0.38\eta_+^2$. Thus (50) is satisfied if (52) holds. Therefore, for the values $n=40$ and $m=22$ suggested, the various proposed criteria for the choice of N , Eqs. (41), (50), and (52), are all satisfied by choosing

$$N \geq 1 + \frac{1}{2H} \max(1, \xi^*) - \frac{\xi_0 - \xi}{2H}. \quad (53)$$

IV. THE PERIODIC AND CANYON GREEN'S FUNCTIONS

The previous section details formulas and a numerical scheme for computing the field due to the infinite array of sources (18). As discussed in the Introduction, it is much more frequently of interest to be able to compute the field due to an array of sources extending to infinity in both directions, that is, to be able to compute the function

$$G_{\beta}^{DP}(\mathbf{r}, \mathbf{r}_0; \alpha) = \sum_{l=-\infty}^{\infty} e^{-2il\alpha H} G_{\beta}(\mathbf{r}, \mathbf{r}_l). \quad (54)$$

Of course, the summation (54) can be written as two sums of the form (18). Precisely, let $\tilde{x}_l := 2x - x_{-l}$ and $\tilde{\mathbf{r}}_l := (\tilde{x}_l, y_0) = (2x - x_{-l}, y_0)$, for $l=0, 1, \dots$, so that $\tilde{\mathbf{r}}_l$ is the reflection of \mathbf{r}_{-l} in the vertical line through \mathbf{r} . Then

$$\begin{aligned} G_{\beta}^{DP}(\mathbf{r}, \mathbf{r}_0; \alpha) &= -G_{\beta}(\mathbf{r}, \mathbf{r}_0) + \sum_{l=0}^{\infty} e^{-2il\alpha H} G_{\beta}(\mathbf{r}, \mathbf{r}_l) \\ &\quad + \sum_{l=0}^{\infty} e^{2il\alpha H} G_{\beta}(\mathbf{r}, \tilde{\mathbf{r}}_l) \\ &= -G_{\beta}(\mathbf{r}, \mathbf{r}_0) + G_{\beta}^P(\mathbf{r}, \mathbf{r}_0; \alpha) + G_{\beta}^P(\mathbf{r}, \tilde{\mathbf{r}}_0; -\alpha). \end{aligned} \quad (55)$$

Without loss of generality it will be supposed in the remainder of this section that \mathbf{r}_0 is the closest of the sources \mathbf{r}_l , $l=0, \pm 1, \dots$, to \mathbf{r} , so that

$$|\xi - \xi_0| \leq H. \quad (56)$$

Then $x_1 > x$ and $\tilde{x}_1 > x$, so that, for $N=1, 2, \dots$, $G_{\beta}^P(\mathbf{r}, \mathbf{r}_0; \alpha)$ and $G_{\beta}^P(\mathbf{r}, \tilde{\mathbf{r}}_0; -\alpha)$ have the representations given by (23) and (24). The calculation of the integral (24) in the four different cases, using Gauss–Laguerre quadrature, has been discussed in the last two subsections. [Of course, for the computation of $G_{\beta}^P(\mathbf{r}, \tilde{\mathbf{r}}_0; -\alpha)$, ξ_N must be replaced with $\tilde{\xi}_N := k(\tilde{x}_N - x) = \xi - \xi_0 + 2HN$ and α with $-\alpha$.] Given that (56) holds, the criterion (53) proposed for the choice of N is satisfied for the computation of both $G_{\beta}^P(\mathbf{r}, \mathbf{r}_0; \alpha)$ and $G_{\beta}^P(\mathbf{r}, \tilde{\mathbf{r}}_0; -\alpha)$ if N is chosen so that

$$N \geq 1.5 + \frac{1}{2H} \max(1, \xi^*). \quad (57)$$

The function $G^{DP}(\mathbf{r}, \mathbf{r}_0; \alpha)$ may be termed the *periodic impedance Green's function* for the Helmholtz equation in the upper half-plane, since it satisfies the impedance boundary condition on the ground surface and, clearly, has the periodicity property that

$$G^{DP}(\mathbf{r} + 2H\mathbf{i}, \mathbf{r}_0; \alpha) = e^{-2i\alpha H} G^{DP}(\mathbf{r}, \mathbf{r}_0; \alpha),$$

where \mathbf{i} is a unit vector in the x direction. The periodic Green's function, $G^{DP}(\mathbf{r}, \mathbf{r}_0; \alpha)$, has applications in its own right, notably to problems of plane wave scattering by periodic structures (in which application α is the sine of the angle of incidence), but can also be used to construct solutions to problems of sound propagation in waveguides.

Consider the sound field generated by a point source of sound at \mathbf{r}_0 in the canyon formed by two parallel vertical rigid walls emerging from an impedance ground surface.

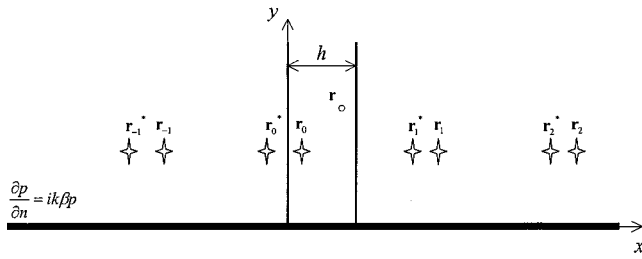


FIG. 4. The 2-D canyon/waveguide, showing the source and its images in the vertical walls.

Clearly (see Fig. 4), the problem can be solved by computing the positions of the infinite array of image sources formed by reflection in the rigid walls. It can be seen in Fig. 4 that these images form two doubly infinite periodic arrays, so that the effect of the rigid walls is to introduce additional sources at \mathbf{r}_l , $l = \pm 1, \pm 2, \dots$, and at \mathbf{r}_l^* , for $l = 0, \pm 1, \pm 2, \dots$, where $\mathbf{r}_l^* = \mathbf{r}_0^* + 2hl\mathbf{i}$ and \mathbf{r}_0^* is the image of \mathbf{r}_0 in the wall at $x = 0$, i.e., $\mathbf{r}_0^* = (-x_0, y_0)$. Thus the solution to this problem of noise propagation in a canyon can be given in terms of the periodic Green's function, $G_\beta^{DP}(\mathbf{r}, \mathbf{r}_0; \alpha)$, with $\alpha = 0$, as

$$G_\beta^{can}(\mathbf{r}, \mathbf{r}_0) = G_\beta^{DP}(\mathbf{r}, \mathbf{r}_0; 0) + G_\beta^{DP}(\mathbf{r}, \mathbf{r}_0^*; 0). \quad (58)$$

In the case where the vertical walls are sound soft (i.e., the sound field vanishes on the vertical surfaces), the solution can be given in terms of the periodic Green's function, G_β^{DP} , as

$$G_\beta^{DP}(\mathbf{r}, \mathbf{r}_0; 0) - G_\beta^{DP}(\mathbf{r}, \mathbf{r}_0^*; 0),$$

and, in the case when one wall is rigid (that at $x = 0$) and the other sound soft, the solution is

$$G_\beta^{DP}(\mathbf{r}, \mathbf{r}_0; \pi/(2H)) - G_\beta^{DP}(\mathbf{r}, \mathbf{r}_0^*; \pi/(2H)).$$

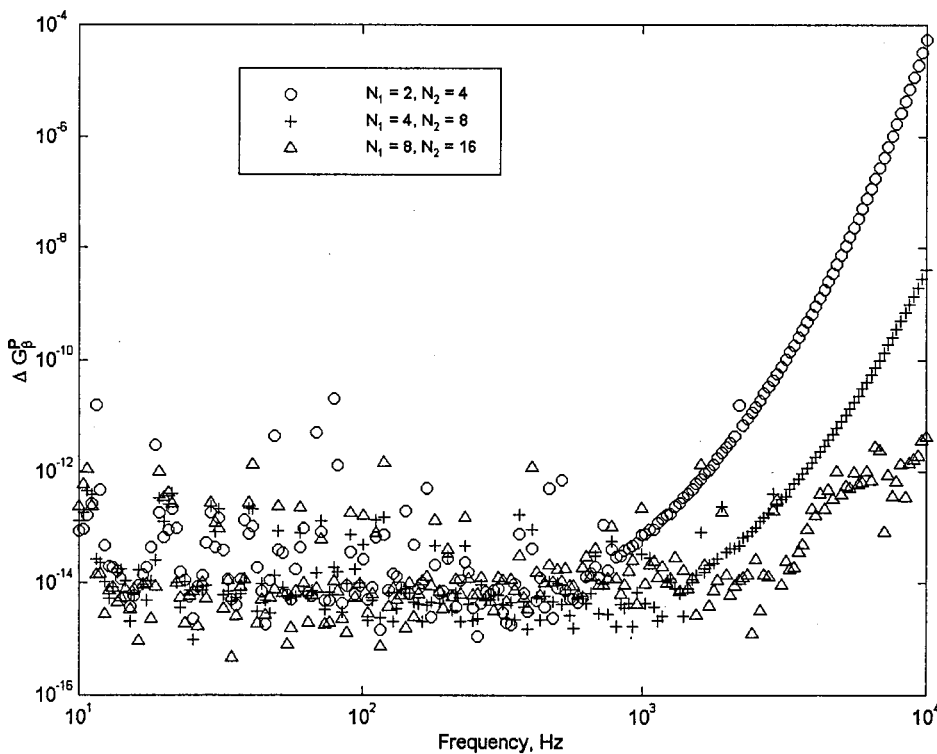


FIG. 5. Absolute error as a function of the parameter N calculated for sound propagation above 100-mm layer of porous road surface.

To sum up, to compute the solution, $G_\beta^{can}(\mathbf{r}, \mathbf{r}_0)$, to the canyon problem, the Green's function is expressed in terms of the periodic Green's function via Eq. (58). The periodic Green's function is, in turn, expressed in terms of G_β^P through Eq. (55). Provided (56) holds, the terms $G_\beta^P(\mathbf{r}, \mathbf{r}_0; \alpha)$ and $G_\beta^P(\mathbf{r}, \mathbf{r}_0^*; -\alpha)$ in (55) can be calculated using Eqs. (23) and (24), with the Green's function G_β in (23) calculated using the method of Ref. 16. The calculation of the integral (24) is carried out via four different representations, discussed in Sec. III A. Specifically, it has been proposed that the representations (42)–(45) be used in the four different cases, with the integrals in these formulas evaluated using the Gauss–Laguerre quadrature rule (46), with n and m given by (49), and the parameter N chosen to be the smallest positive integer satisfying (57).

V. NUMERICAL RESULTS

Results are presented first of all illustrating the effect of the choice of N , the number of source contributions to be evaluated explicitly in Eq. (20), on the accuracy of the calculations. The field $G_\beta^P(\mathbf{r}, \mathbf{r}_0; \alpha)$ due to an infinite array of sources is evaluated using Eq. (23), with the integral I evaluated using Eqs. (42)–(45), the evaluation carried out as proposed in Sec. III B by the numerical integration formula (46) with the choices (49) for m and n . Results are shown for the case $\alpha = 0$. Plotted in Fig. 5 is ΔG_β^P , the absolute value of the difference between two calculations of $G_\beta^P(\mathbf{r}, \mathbf{r}_0; \alpha)$ using different values for N ($N = N_1$ and $N = N_2$). Having in mind applications in outdoor sound propagation, the surface impedance β is chosen to be that appropriate to a rigidly backed 100-mm layer of porous road surface. The acoustical properties of the porous layer as a function of frequency are calculated using the Attenborough model.^{24,25} This model speci-

TABLE I. Values of the nonacoustic parameters used in the calculations.

Material	Flow resistivity, R_b (Pa s m ⁻²)	Porosity, Ω	Tortuosity, q^2	Shape factor, s_p	Thickness, d (m)
Reflective ground	2×10^7	0.1	1.06	0.5	0.1
Porous road surface	3500	0.335	1.91	0.21	0.1
Highly absorbing ground	2×10^4	0.9	1.06	0.5	0.1

fies the acoustical admittance (β_b) and wave number (k_b) of the porous layer in terms of its porosity (Ω), tortuosity (q^2), flow resistivity (R_b), and a pore shape factor (s_p), giving²⁵

$$\beta_b = \frac{\Omega}{q} g_\beta(\sqrt{-i}\lambda_A), \quad k_b = qk g_\beta(\sqrt{-i}\lambda_A),$$

where $\lambda_A = (1/2s_p)(8\rho_0q^2\omega/\Omega\sigma)^{1/2}$ and ρ_0 is the air density. The functions g_β and g_k are defined by $g_\beta(z) := \sqrt{g_c(z)/g_\rho(z)}$ and $g_k(z) := \sqrt{g_c(z)g_\rho(z)}$, in terms of the auxiliary functions $g_\rho(z) := [1 - S(z)]^{-1}$ and $g_c(z) := 1 + (\gamma - 1)S(N_{Pr}^{1/2}z)$. In these last expressions $\gamma = 1.4$ is the ratio of specific heats and $N_{Pr} = 0.708$ is the Prandtl number, while S is the function defined by

$$S(z) := \frac{2J_1(iz)}{izJ_0(iz)} = \frac{2I_1(z)}{zI_0(z)},$$

with J_n the Bessel function of order n and I_n the corresponding modified Bessel function. In terms of β_b and k_b the impedance of the layer is

$$\beta = \beta_b \tanh(-ik_b d),$$

and the values of the nonacoustical parameters for the porous road surface are given in Table I. The positions of the source and the receiver were chosen to be $x_0 = 5.75$ m, $y_0 = 2.0$ m, $x = 1.5$ m, and $y = 1.5$ m. The value of h was set to 17 m, so that there is a spacing of 34 m between adjacent sources.

The error in Fig. 5 is mainly confined to the range $10^{-14} < \Delta G_\beta^P < 10^{-12}$, but increases at high frequency where $\eta_+ = k(y + y_0)$ is large ($\eta_+ \approx 640$ at 10 000 Hz). Results accurate to 10^{-12} are obtained at almost all frequencies up to 2000 Hz with $N = 2$, at frequencies up to 5000 Hz with $N = 4$, and across the frequency range with $N = 8$. At the highest frequency each doubling of N reduces the error by a factor of about 1000. The criterion proposed to ensure high accuracy, (20), suggests that N should increase approximately in proportion to $\eta_+^2/H = k(y + y_0)^2/h$. Specifically it recommends, for this geometry, $N \geq 5.9$ at 2000 Hz, $N \geq 13.5$ at 5000 Hz, and $N \geq 26.2$ at 10000 Hz.

The remaining figures show calculations of the canyon/waveguide Green's function $G_\beta^{can}(\mathbf{r}, \mathbf{r}_0)$. A method for computing G_β^{can} efficiently has been proposed in Sec. IV. An alternative expression for G_β^{can} can be obtained as a normal mode decomposition (NMD),^{26,27} namely,

$$G_\beta^{can}(\mathbf{r}, \mathbf{r}_0) = \frac{1}{2iH} \sum_{n=0}^{\infty} \frac{\chi_n}{\zeta_n} \cos(k_n x_0) \cos(k_n x) \times [e^{ik\zeta_n|y-y_0|} + R_n e^{ik\zeta_n(y+y_0)}], \quad (59)$$

where $\chi_n = 1$ when $n = 0$, $\chi_n = 2$ for all other values of n , $k_n = n\pi/h$, and $\zeta_n = \sqrt{1 - k_n^2/k^2}$, with $\text{Im } \zeta_n > 0$ for $k_n > k$. In Eq. (59) R_n is the reflection coefficient for mode n from the impedance ground, given by

$$R_n = \frac{\zeta_n - \beta}{\zeta_n + \beta}. \quad (60)$$

Values of $G_\beta^{can}(\mathbf{r}, \mathbf{r}_0)$ calculated using the method described in Sec. IV, with n and m given by (49), and N selected according to the criterion (57), are compared in Figs. 6–8 with the predictions of normal mode decomposition calculations, using the first 2000 terms in (59). Precisely, what is plotted in these figures is a sound pressure level given by

$$L = 20 \log_{10}(\sqrt{k} |G_\beta^{can}(\mathbf{r}, \mathbf{r}_0)|). \quad (61)$$

(The factor \sqrt{k} ensures that the sound pressure level close to the source is approximately constant across the frequency range.) The three figures show predictions for different ground types (and so different variations of β with frequency), namely a reflecting boundary, a porous road surface, and a highly absorbing ground, with parameter values as shown in Table I. The positions of the source and the receiver were chosen to be $x_0 = 5.75$ m, $y_0 = 2.0$ m, $x = 1.5$ m and $y = 1.5$ m and the width of the canyon was set to $h = 17$ m. Figures 6–8 demonstrate excellent agreement between the results of the two methods throughout the spectral range considered.

Regarding the relative computational efficiency of the two methods the following comments can be made. In Sec. IV a specific quadrature rule for numerical integration has been suggested, with $m = 22$ (m is the number of evaluations of the integrand required). With m fixed the cost of the calculation method depends only on N , the number of source contributions calculated explicitly. The criterion (57), for selecting N to ensure a high accuracy, forces N to increase approximately in proportion to $\eta_+^2/H = k(y + y_0)^2/h$, although with a small constant of proportionality, and we have seen in Fig. 5 that with $N = 8$ very accurate results (error 10^{-12}) are obtained at even the highest frequency when $y + y_0 \approx 100$ wavelengths and $k(y + y_0)^2/h \approx 130$.

The representation (59) as a normal mode decomposition is to some extent complementary. For accurate results all the propagating modes (those for which $k_n \leq 1$) and at least some of the evanescent modes ($k_n > 1$) must be included in the summation. There are $\approx kh/\pi$ propagating modes so that this is the minimum number of mode contributions to be included, and so the cost is at least proportional to kh . In addition, when $k|y - y_0|$ is small the series converges slowly:

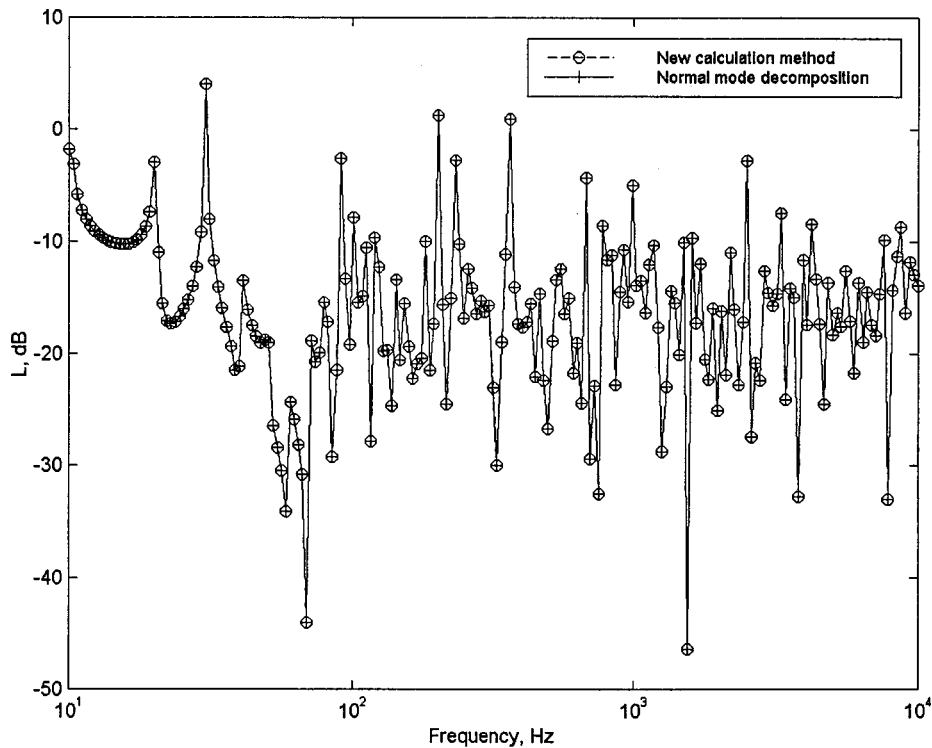


FIG. 6. Comparison of predictions using the method proposed in Sec. IV and the method of normal mode decomposition for sound propagation over reflective ground.

when $k|y - y_0| = 0$ this convergence is very slow so that a very large number of evanescent modes need to be included in the summation, though this additional difficulty can be ameliorated by applying a Kummer's transformation⁹ which accelerates the convergence of the series and reduces substantially the number of evanescent modes that need to be summed explicitly.^{9,27}

The new representation proposed has a cost linearly dependent on N while the cost of evaluating the normal mode

decomposition representation is proportional to the number of normal modes required for accurate results. Thus the new method will be faster when the ratio $N/(\text{No. of normal modes required})$ is small enough. In view of the above remarks, this ratio is $\leq C[k(y + y_0)^2/h]/[kh] = C[(y + y_0)/h]^2$, for some positive constant C , so that the new method of Sec. IV should be more effective for problems where h is large compared to $y + y_0$. To illustrate this, computational times required by the two methods are given in

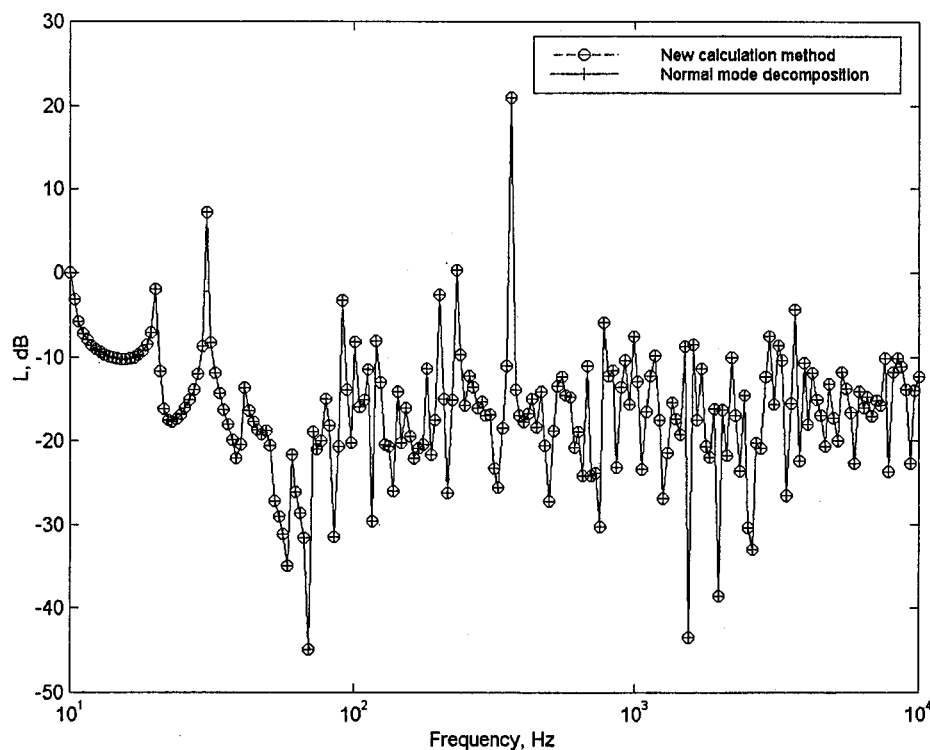


FIG. 7. Comparison of predictions using the method proposed in Sec. IV and the method of normal mode decomposition for sound propagation over a porous road surface.

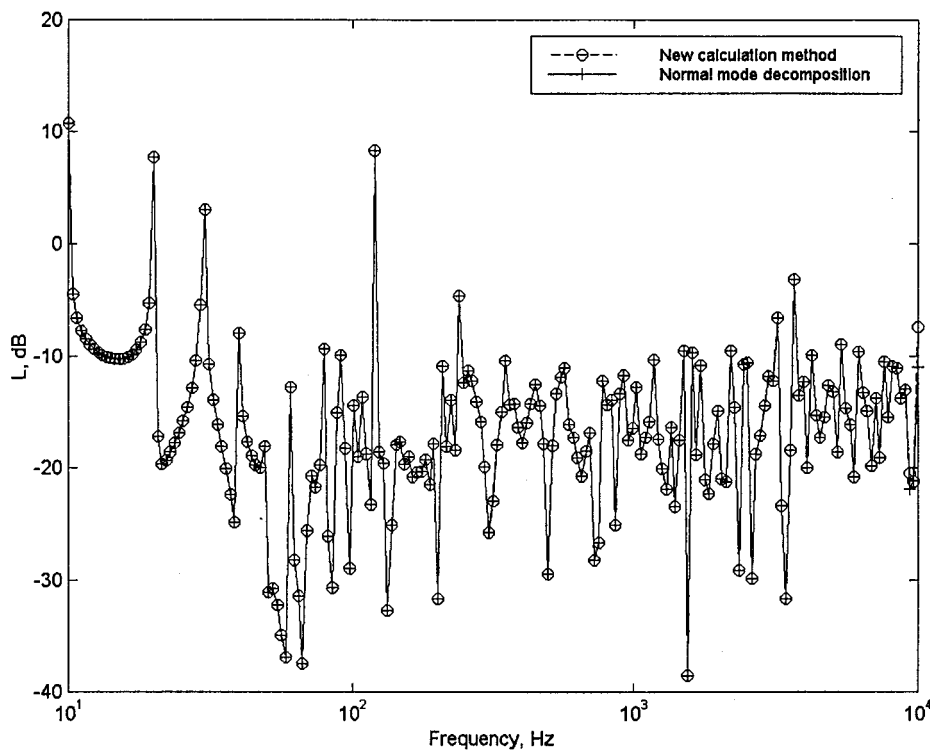


FIG. 8. Comparison of predictions using the method proposed in Sec. IV and the method of normal mode decomposition for sound propagation over a highly absorbing porous surface.

Table II. The CPU times tabulated are for the same geometry as for Fig. 5, i.e., $x_0=5.75$ m, $y_0=2.0$ m, $x=1.5$ m, $y=1.5$ m, and $h=17$ m. As indicated above, the normal mode decomposition requires calculation of all the propagating modes and at least some of the evanescent modes for accurate calculations, how many depending on the size of $k|y-y_0|$ and on the acceleration procedure used. The third column shows CPU times for normal mode decomposition calculations using the same number of evanescent as propagating modes, so that approximately $2kh/\pi$ modes are computed and thus the CPU time increases approximately linearly with frequency. The remaining columns show the CPU times required for the method described in Sec. IV, with n and m given by (49). Specifically, the fourth column shows calculations with $N=2$, which was found in Fig. 5 to give errors at most 10^{-12} for frequencies up to 2000 Hz, and the fifth column shows results with $N=4$, which gave errors at most 10^{-12} up to 5000 Hz. It can be seen that, for this geometry, which has a small value of $[(y+y_0)/h]^2$ of approximately 0.04, and at higher frequencies where a large number

of modes is required, the new calculation method does indeed require less CPU time to compute accurate results.

VI. CONCLUSIONS

In this paper mathematical expressions for two-dimensional calculations of the sound field due to a mono-frequency point source in a canyon/waveguide have been derived, the canyon occupying the strip $0 < x < H$, $y > 0$ in the Oxy plane, and having rigid or sound soft walls at $x=0$ and $x=H$ and an impedance boundary condition on $y=0$. In the expressions proposed for this Green's function, and for the related periodic Green's function, the infinite sums of source contributions due to the multiple reflections from the walls are reduced to single integral terms. Further representations are proposed in which poles close to the integration path are removed and their contributions evaluated analytically, which greatly improves the accuracy of numerical integration. The error in numerical integration has been examined carefully, a specific 22-point quadrature rule has

TABLE II. CPU times for the canyon problem of Fig. 5, with $x_0=5.75$ m, $y_0=2.0$ m, $x=1.5$ m, $y=1.5$ m, $h=17$ m, and a 100-mm layer of porous road surface.

Frequency (Hz)	Normal mode decomposition		New calculation method	
	No. modes	CPU time (ms)	$N=2$ CPU time (ms)	$N=4$ CPU time (ms)
125	25	1.46	2.93	3.91
250	50	1.95	2.83	3.91
500	100	2.68	2.92	3.91
1000	200	4.15	2.93	3.90
2000	400	6.83	2.93	3.90
4000	800	12.21	2.93	3.91
8000	1600	38.08	2.92	3.90

been proposed, and a criterion for selection of the parameter N (the number of source contributions to be treated explicitly) has been suggested. Numerical experiments show that, choosing N according to this criterion, the 22-point quadrature rule proposed gives extremely accurate results. The calculation procedure to be followed is summarized at the end of Sec. IV.

The numerical results include comparisons with an alternative representation of the function via normal mode decomposition. The new calculation procedure proposed complements this representation which becomes expensive to compute when kh is large (k the wave number and h the width of the waveguide) and/or when $k|y - y_0|$ is small ($|y - y_0|$ the difference in heights of source and receiver). By contrast, since the cost of the new method depends mainly on N which increases in proportion to $k(y + y_0)^2/h$, the new representations proposed are computationally efficient as long as $k(y + y_0)^2/h$ is not too large. The results presented show that very small absolute errors (10^{-12}) are obtained with $k(y + y_0)^2/h$ as large as 130 with $N = 8$.

As discussed in the Introduction, it is expected that these new representations for the canyon/waveguide Green's function and the related periodic Green's function will prove useful in boundary element modeling of sound propagation in city streets and in waveguides, and for problems of scattering by periodic structures. For all these boundary element applications very efficient calculation procedures for the Green's function are crucial.

ACKNOWLEDGMENTS

The authors are grateful to Professor D. C. Hothersall and Dr. I. Belinskaya-Abnizova for their constructive comments on this manuscript.

- ¹D. C. Hothersall, S. N. Chandler-Wilde, and M. N. Hajmirzae, "Efficiency of single noise barriers," *J. Sound Vib.* **146**, 303–322 (1991).
- ²D. Duhamel, "Efficient calculation of the 3-dimensional sound pressure field around a noise barrier," *J. Sound Vib.* **197**, 547–571 (1996).
- ³S. N. Chandler-Wilde, "Tyndall medal lecture: The boundary element method in outdoor noise propagation," *Proc. Inst. Acoust.* **19**(8), 27–50 (1997).
- ⁴D. C. Hothersall, K. V. Horoshenkov, and S. E. Mercy, "Numerical modelling of the sound field near a tall building with balconies near a road," *J. Sound Vib.* **198**, 507–515 (1996).
- ⁵K. V. Horoshenkov, D. C. Hothersall, and S. E. Mercy, "Scale modelling of sound propagation in a city street canyon," *J. Sound Vib.* **223**, 795–819 (1999).
- ⁶J. Kang, "Sound propagation in street canyons: Comparison between diffusely and geometrically reflecting boundaries," *J. Acoust. Soc. Am.* **107**, 1394–1404 (2000).

- ⁷E. Walerian, R. Janczur, and M. Czechowicz, "Sound level forecasting for city-centres. part 1: sound level due to a road within an urban canyon," *Appl. Acoust.* **62**, 359–380 (2001).
- ⁸S. H. Tang and K. M. Li, "The prediction of facade effects from a point source above an impedance ground," *J. Acoust. Soc. Am.* **110**, 278–288 (2001).
- ⁹C. M. Linton, "The Green's function for the two-dimensional Helmholtz equation in periodic domains," *J. Eng. Math.* **33**, 377–402 (1998).
- ¹⁰S. N. Chandler-Wilde, C. R. Ross, and B. Zhang, "Scattering by infinite one-dimensional rough surfaces," *Proc. R. Soc. London, Ser. A* **455**, 3767–3787 (1999).
- ¹¹A. Meier, T. Arens, S. N. Chandler-Wilde, and A. Kirsch, "A Nyström method for a class of integral equations on the real line with applications to scattering by diffraction gratings and rough surfaces," *J. Integral Eq. Appl.* **12**, 281–321 (2000).
- ¹²K. V. Horoshenkov, "Control of road traffic noise in city streets," Ph.D. thesis, School of Engineering, University of Bradford, 1996.
- ¹³M. E. Veysoglu, H. A. Yueh, R. T. Shin, and J. A. Kong, "Polarimetric passive remote sensing of periodic surfaces," *J. Electromagn. Waves Appl.* **5**, 267–280 (1991).
- ¹⁴A. W. Mathis and A. F. Pearson, "A comparison of acceleration procedures for the two-dimensional periodic Green's function," *IEEE Trans. Microwave Theory Tech.* **41**, 567–571 (1996).
- ¹⁵J. DeSanto, G. Erdmann, W. Hereman, and M. Misra, "Theoretical and computational aspects of scattering from rough surfaces: one-dimensional perfectly reflecting surfaces," *Waves Random Media* **8**, 385–414 (1998).
- ¹⁶S. N. Chandler-Wilde and D. C. Hothersall, "Efficient calculation of the Green function for acoustic propagation above a homogeneous impedance plane," *J. Sound Vib.* **180**, 705–724 (1995).
- ¹⁷T. Oberhettinger and L. Baddi, *Tables of Laplace Transforms* (Springer, Berlin, 1973).
- ¹⁸S. N. Chandler-Wilde and D. C. Hothersall, "A uniformly valid far field asymptotic expansion for the Green function for two-dimensional propagation above a homogeneous impedance plane," *J. Sound Vib.* **182**, 665–675 (1995).
- ¹⁹C. M. Bender and S. A. Orszag, *Advanced Mathematical Methods for Scientists and Engineers* (McGraw-Hill, Tokyo, 1978).
- ²⁰P. Concus, D. Cassatt, G. Jaehrig, and E. Melby, "Tables for the evaluation of $\int_0^x x^\beta e^{-x} f(x) dx$, by Gauss-Laguerre quadrature," *Math. Comput.* **17**, 245–256 (1963).
- ²¹M. Abramowitz and I. Stegun, *Handbook of Mathematical Functions* (Dover, New York, 1964).
- ²²*Document D01BBF NAGFLIB: 1594/0:Mk 7:Dec 78 in NAG FORTRAN Library Manual, Mark 9* (Numerical Algorithms Group Ltd., Oxford, 1981).
- ²³S. N. Chandler-Wilde and D. C. Hothersall, "On the Green function for two-dimensional acoustic propagation above a homogeneous impedance plane," Research Report, Department of Civil Engineering, University of Bradford, November 1991.
- ²⁴K. Attenborough, "Acoustical impedance models for outdoor ground surfaces," *J. Sound Vib.* **99**, 521–544 (1985).
- ²⁵S. N. Chandler-Wilde and K. V. Horoshenkov, "Padé approximants for the acoustical characteristics of rigid frame porous media," *J. Acoust. Soc. Am.* **98**, 1119–1129 (1995).
- ²⁶P. M. Morse and K. U. Ingard, *Theoretical Acoustics* (Princeton U.P., Princeton, NJ, 1986).
- ²⁷P. M. Morse and H. Feshbach, *Methods of Theoretical Physics* (McGraw-Hill, Tokyo, 1953).

Coupled-mode solutions in generalized ocean environments

Steven A. Stotts^{a)}

Applied Research Laboratories, The University of Texas at Austin, P. O. Box 8029, Austin, Texas 78713-8029

(Received 13 April 1999; revised 26 October 2001; accepted 7 December 2001)

This paper presents the application of the differential equation approach to solving the second-order coupled-mode equations in inhomogeneous ocean environments. The model incorporates sound velocity profile points to construct depth-dependent, piecewise linear, ocean and bottom environments along a range grid. Modal solutions are evaluated in terms of Airy functions. The formalism to evaluate analytically the mode-coupling coefficients is presented. Comparisons to conventional expressions of the coefficients are made. The integro-differential form of the coupled equations is solved using an approach developed in nuclear theory that incorporates the Lanczos method [Knobles, *J. Acoust. Soc. Am.* **96**, 1741–1747 (1994)]. Demonstration of the practicality of this approach is made by applying the results in actual calculations with realistic ocean environments. The formalism to evaluate analytically the mode-coupling coefficients is presented. Several benchmark examples were examined in order to validate the model and are discussed, including propagation over a hill, benchmark wedge problems, and a range-varying sound speed profile benchmark. The importance of this model is also demonstrated by the physical insight gained in having a coupled-mode approach to solving range-dependent problems. © 2002 Acoustical Society of America. [DOI: 10.1121/1.1448316]

PACS numbers: 43.30.Bp, 43.20.Mv [SAC-B]

I. INTRODUCTION

Problems involving a dynamical system are often solved in terms of states or modes that characterize the important properties of the system. Often, the exchange of energy between these states must be taken into account to reach a proper solution. This is the basis of coupled-mode theory.

In ocean acoustics, coupled-mode theory was introduced by Pierce¹ in 1965 and again by Milder² in 1969 to describe this energy exchange in the context of a nonseparable Helmholtz equation, but they did not solve the coupled-mode equations. Rutherford and Hawker^{3,4} applied the coupled-mode theory to range-variable ocean environments, with an emphasis on ocean bottom range variations. They introduced a first-order correction to the modal amplitudes and depth functions in Pierce and Milder's theory to properly account for sloping bottoms. This satisfied the requirement for energy conservation to first order. Fawcett⁵ introduced a coupled-mode theory that took into account conservation of energy to all orders. This was achieved by the introduction of boundary layer coupling terms at sloping layer interfaces. Gillette⁶ also solved the coupled-mode equations for a rigid bottom in such a way that the proper boundary conditions were satisfied. A stair-step coupled-mode approach was introduced by Evans⁷ as a good approximation to range-dependent environments, although the solution by this method can pose practical limitations if the complexity of the problem increases, especially for two-way calculations in general environments. Recently, Porter⁸ developed an efficient one-way marching coupled-mode scheme in a stair-step method. More recently, Godin⁹ presented a first-order coupled-mode theory similar to Boyles,¹⁰ also using a differential equation approach and re-

iterated the importance of solving energy-conserving coupled-mode equations, as pointed out by Fawcett.⁵

Paralleling these developments, the concept of coupled channels was introduced in nuclear theory.¹¹ Tamura^{12,13} developed a coupled-channel formalism and successfully applied this method to explain the observed inelastic scattering cross section for hadrons with a variety of nuclei. The drawback to this original formalism was that the computation time of the calculation was proportional to N^3 , where N corresponded to the number of channels. A technique recently developed and applied to problems in nuclear theory^{14–17} reformulated this approach and solved the ensuing coupled-channel equations by incorporating the Lanczos routine¹⁸ in a method referred to here as the Udagawa–Kim (UK) formalism. Since its introduction, the UK method has been extensively applied to large shell-model calculations in nuclear structure problems. The computation time is greatly reduced because the calculation is proportional to $N^2 \times M$, where N is the number of channels or modes, and M corresponds to the number of Lanczos vectors, M being $\ll N$. Recently, the UK approach was used by Knobles¹⁹ to demonstrate the efficiency of solving the ocean acoustic coupled-mode equations for simplistic environments.

The ability to solve the Sturm–Liouville problem for the depth equation on a range grid, in a timely fashion, is essential to solving the coupled-mode equations in general environments. In addition, the coupling matrices must also be computed accurately in a practical time span. Both of these goals have been achievable with the advent of fast and efficient normal-mode models that are based on Airy functions.^{20–23}

This paper presents an exact solution to the two-way coupled-mode equations in differential form for generalized

^{a)}Electronic mail: stotts@arlut.utexas.edu

environments. A major limitation of performing such calculations involves the evaluation of the mode coupling coefficients, where overlap integrals of the mode function with the range derivative of the mode function must be evaluated as a function of depth at each range step. The main emphasis of this paper is in obtaining analytic expressions for these coupling coefficients. The efficiency of this coupled-mode approach is greatly increased by reducing the large memory storage requirements and thereby making realistic computations more practical.

The coupling coefficients are shown to be solvable by analytic expressions. Also, the examples presented demonstrate that only a few Lanczos vectors are needed to solve these benchmark problems, making the method of solution practicable. Similar to the nuclear problem, the limited number of Lanczos vectors is in contrast to the number of modes (degrees of freedom), which can be much larger, depending on the environment and/or frequency.

The model presented here allows arbitrary bathymetry and sound velocity profile (SVP) variations with range. The SVP points are assumed to vary analytically with depth, locally, within each layer of the ocean environment. The profiles are also allowed to vary with range, and the bottom boundary conditions can be range dependent, as well. The main emphasis of this paper is again on the demonstration of the use of the mode coupling coefficient method, independent of the particular Airy-based local-mode model used. Once the coupling coefficients are obtained, the method given in Ref. 19 is used to solve the coupled equations. Although most of the examples shown are solved using real mode functions, the formalism can be generalized to modal solutions in the complex k -plane.²⁴

Section II presents the generalized coupled-mode approach, including the use of two different methods to derive analytic expressions for the mode-coupling coefficients. The first method is presented in detail in Sec. II A and is referred to as the Airy form. An alternate method is presented in Sec. II B and in Appendix D. In addition, a review is given of how the coupled equations are solved. Example calculations are presented in Sec. III. This paper is concluded in Sec. IV.

II. COUPLED-MODE MODEL

A summary of the key steps in obtaining the coupled-mode equations is presented in this section. The coupling coefficients are defined, followed by presentation of the analytic expressions for their solution, which may be calculated accurately and efficiently. Finally, the method used to solve the coupled-mode equations is reviewed at the end of this section.

The two-dimensional inhomogeneous wave equation for a point source may be written in Cartesian coordinates as

$$\left\{ \frac{\partial^2}{\partial x^2} + \frac{\partial^2}{\partial z^2} - \frac{1}{\rho(z)} \frac{d\rho}{dz} \frac{\partial}{\partial z} + k^2(x, z) \right\} p(x, z) = -\delta(x-x_0)\delta(z-z_0), \quad (1)$$

where x and z correspond to the horizontal component and vertical depth, respectively, and the right-hand side defines a

point source located at x_0, z_0 . A symmetry of the waveguide with respect to the y axis has been assumed to reduce the three-dimensional propagation to two dimensions. The pressure field solution may then be assumed to vary as

$$p(x, z) = \sum_{n=1}^{\infty} R_n(x) \psi_n(x, z). \quad (2)$$

Substitution of Eq. (2) into Eq. (1) yields a local depth evaluation for $\psi_n(x, z)$ and a coupled equation in the range-dependent amplitude, $R_n(x)$.

The depth equation is given by

$$-\frac{1}{\rho} \frac{d\rho}{dz} \frac{\partial \psi_n}{\partial z} + \frac{\partial^2 \psi_n}{\partial z^2} + k^2(x, z) \psi_n \equiv k_n^2(x) \psi_n(x, z), \quad (3)$$

where the separation constant, corresponding to the mode eigenvalues, has been defined as $k_n(x)$. The mode functions satisfy the orthonormality condition

$$\int_0^{\infty} \frac{1}{\rho(z)} \psi_m(x, z) \psi_n(x, z) dz = \delta_{mn}, \quad (4)$$

and are assumed to be normalizable by this expression. They also satisfy the completeness relation

$$\sum_{m=1}^{\infty} \frac{1}{\rho} \psi_m(x, z) \psi_m(x, z') = \delta(z-z'). \quad (5)$$

The range equation in Cartesian form is given by

$$\left\{ \frac{d^2}{dx^2} + k_m^2(x) \right\} R_m(x) = -\psi_m(x, z_0) \frac{1}{\rho(z_0)} \delta(x-x_0) - \sum_{n=1}^N \left\{ \bar{B}_{mn}(x) \frac{d}{dx} + \bar{C}_{mn}(x) \right\} R_n(x), \quad (6)$$

where N corresponds to the number of modes in the system and the bar above the B and C coefficients implies that interface terms are included in this definition.

Mode-coupling coefficients between the m th and n th modes are written as

$$\bar{B}_{mn}(x) = 2 \int_0^{\infty} \frac{1}{\rho(z)} \psi_m(x, z) \frac{\partial}{\partial x} \psi_n(x, z) dz + I_{mn}^B(x) \equiv \tilde{B}_{mn} + I_{mn}^B, \quad (7)$$

$$\bar{C}_{mn}(x) = \int_0^{\infty} \frac{1}{\rho(z)} \psi_m(x, z) \frac{\partial^2}{\partial x^2} \psi_n(x, z) dz + I_{mn}^C(x) \equiv \tilde{C}_{mn} + I_{mn}^C, \quad (8)$$

where \tilde{B}_{mn} and \tilde{C}_{mn} are referred to as the first and second coupling coefficients, respectively, and where I_{mn}^B and I_{mn}^C are the interface coupling coefficients introduced by Fawcett⁵ to ensure conservation of energy. They arise from the required boundary condition that the normal derivative of the pressure field, not the vertical derivative, is continuous

across a boundary. The integral and interface coupling coefficients are discussed in Sec. II A.

Locally, the ocean environment is divided into horizontally stratified layers.¹⁰ Within a given layer, l , the density is assumed constant and is written as

$$\rho(z) = \rho_l, \quad z_l < z < z_{l+1}, \quad (9)$$

where z_l and z_{l+1} correspond to the depths at the upper and lower interface, respectively. Also, within each layer the square of the index of refraction and inverse square of the sound speed depend linearly on depth as

$$n^2(x, z) = \frac{1}{c_l^2(x, z)} = a_l(x) + b_l(x)(z - z_l(x)). \quad (10)$$

The terms $a_l(x)$ and $b_l(x)$ are defined by

$$a_l(x) = \frac{1}{c_{T,l}^2(x)}, \quad (11)$$

$$b_l(x) = \frac{1}{h_l(x)} \left(\frac{1}{c_{B,l}^2(x)} - \frac{1}{c_{T,l}^2(x)} \right), \quad (12)$$

with the layer thickness being $h_l(x) = z_{l+1}(x) - z_l(x)$, and $c_{T,l}$ and $c_{B,l}$ being the sound speeds at the top and bottom of the l th layer, respectively.

The depth equation, Eq. (3), simplifies to

$$\frac{d^2 \psi_{n,l}}{dZ_{n,l}^2} - Z_{n,l} \psi_{n,l} = 0 \quad (13)$$

for the l th layer, where

$$Z_{n,l}(x, z) = \eta_l^{-2}(x) \{k_n^2(x) - \omega^2 a_l(x)\} - \eta_l(x) \{z - z_l(x)\}. \quad (14)$$

Here, η_l is defined by

$$\eta_l(x) \equiv \{\omega^2 b_l(x)\}^{1/3}, \quad (15)$$

with the corresponding range derivative

$$\frac{d\eta_l(x)}{dx} = \frac{1}{3} \eta_l^{-2}(x) \omega^2 \dot{b}_l(x) \equiv g_l(x). \quad (16)$$

Several of the examples presented in Sec. III are solved in the cylindrical coordinate system, due to their symmetry. The coupled equation in cylindrical coordinates for a point source located at range, r_0 , and depth, z_0 , is given by

$$\begin{aligned} & \left\{ \frac{d^2}{dr^2} + \frac{1}{r} \frac{d}{dr} + k_m^2(r) \right\} R_m(r) \\ &= -\psi_m(r, z) \frac{1}{\rho(z)} \frac{\delta(r - r_0) \delta(z - z_0)}{r} \\ & - \sum_{n=1}^N \left\{ \bar{B}_{mn}(r) \frac{d}{dr} + \tilde{B}_{mn}(r) \frac{1}{2r} + \bar{C}_{mn}(r) \right\} R_n(r), \end{aligned} \quad (17)$$

where the coupling coefficients are defined in Eqs. (7) and (8), by replacing x with r . The coupling coefficients are evaluated next and then the range equation is solved.

Two methods are used to obtain the coupling coefficients so that comparisons between them can be made with respect to the efficiency of the calculation and to the stability of the coupling coefficient evaluation. The first method is referred to as the Airy integral formalism and is discussed in Sec. II A. Layer indices are first introduced following the notation presented and consistent with the formalism given by Levinson²⁰ as adapted from Boyles.¹⁰ This description gives a layer-by-layer evaluation of the coupling coefficients and is the main point of this paper.

The second method, referred to as the Rutherford formalism,³ is included for comparison, and is generalized here to include multiple layers. The Rutherford approach requires an evaluation of the range derivative of the wave number, $k(r, z)$, which, in general, may not be in a convenient form for evaluation of the coupling coefficients. Further, to evaluate the coefficients in the Rutherford form, the range derivative of the wave function needs to be computed. This part of the calculation is done analytically, using the part of the Airy formalism presented in Sec. II A 1, making the usefulness of the Airy approach apparent even in this form of evaluation. The generalized Rutherford form of the coupling coefficients is presented in Sec. II B.

Finally, in Sec. II C the key steps of the solution to the coupled mode equation are presented. The methods used in evaluating the coupling coefficients for each example are presented in Sec. III.

A. Coupling coefficients—Airy form

In the Airy integral form, using the explicit expressions for the wave functions, the range and depth dependence of the integrands in the mode-coupling coefficients are separated so that the depth derivatives can be carried out analytically. Section II A 1 gives the explicit form of the coupling coefficients by defining the reference integrals to be evaluated. Diagonal and nondiagonal coefficients are evaluated separately. Results for $\tilde{B}_{mn,l}$ are presented here, whereas the details for $\tilde{C}_{mn,l}$ are given in Appendix C. In Sec. II A 2 the coefficients are evaluated. The range derivatives of the wave functions' explicit terms are first evaluated. This step is given in Appendix B. These include the range derivatives of several quantities including the eigenvalues, the propagator matrices, the mode functions evaluated at layer interfaces, and the depth derivative of the mode functions evaluated at layer interfaces. Once these terms are obtained, the coupling integrals are written in the form of the reference integrals presented in Sec. II A 1.

The first coupling coefficient integral for the l th layer is defined as

$$\tilde{B}_{mn,l}(x) = 2 \int_{z_l}^{z_{l+1}} \frac{1}{\rho(x, z)} \psi_{m,l}(x, z) \frac{\partial}{\partial x} \psi_{n,l}(x, z) dz, \quad (18)$$

where a tilde refers to the first term of the mode-coupling coefficient in Eq. (7), and the layer index l has been introduced. The interface coupling coefficient for the l th layer are given by⁵

$$I_{mn,l}^B(x) = \psi_{m,l}[x, z_{l+1}(x)] \frac{dz_{l+1}(x)}{dx} \times \psi_{n,l}[x, z_{l+1}(x)] \left\{ \frac{1}{\rho_l} - \frac{1}{\rho_{l+1}} \right\}, \quad (19)$$

$$I_{mn,l}^C(x) = \psi_{m,l}[x, z_{l+1}(x)] \frac{dz_{l+1}(x)}{dx} \times \left\{ \frac{1}{\rho_l} \frac{\partial}{\partial x} \psi_{n,l}(x, z_{l+1}^-) - \frac{1}{\rho_{l+1}} \frac{\partial}{\partial x} \psi_{n,l+1}(x, z_{l+1}^+) \right\}, \quad (20)$$

where z_{l+1}^- and z_{l+1}^+ are the depths just above and below the lower l th interface. The first derivative coupling coefficient is then obtained by summing over the layers,

$$\bar{B}_{mn}(x) = \sum_{l=1}^L (\bar{B}_{mn,l}(x) + I_{mn,l}^B(x)), \quad (21)$$

where L corresponds to the final layer. The $\bar{C}_{mn}(x)$ coefficients are obtained similarly. Details for calculating the mode-coupling coefficients in the Airy integral form are presented in Sec. II A 1. The steps are shown for Cartesian coordinates, however, the results for cylindrical coordinates are obtained by simply substituting r for x .

1. Formalism

The normalized mode function solutions to the depth equation are written in the form

$$\psi_{n,l}(x, z) = A_{n,l}(x) \text{Ai}[Z_{n,l}(x, z)] + B_{n,l}(x) \text{Bi}[Z_{n,l}(x, z)], \quad (22)$$

where the mode coefficients $A_{n,l}(x)$ and $B_{n,l}(x)$ are evaluated locally at each horizontal coordinate, x , using a range-independent normal-mode model. The Ai and Bi are the Airy function solutions to the Airy differential equation given in Eq. (13).

To evaluate the mode-coupling coefficients, first and second derivatives of the mode functions with respect to range, x , are required. The first derivative is given by

$$\begin{aligned} \frac{\partial \psi_{n,l}(x, z)}{\partial x} &= \dot{A}_{n,l}(x) \text{Ai}[Z_{n,l}(x, z)] + \dot{B}_{n,l}(x) \text{Bi}[Z_{n,l}(x, z)] \\ &+ A_{n,l}(x) \frac{\partial Z_{n,l}(x, z)}{\partial x} \text{Ai}'[Z_{n,l}(x, z)] \\ &+ B_{n,l}(x) \frac{\partial Z_{n,l}(x, z)}{\partial x} \text{Bi}'[Z_{n,l}(x, z)], \end{aligned} \quad (23)$$

where the dot implies a partial derivative with respect to x and the prime denotes a derivative with respect to $Z_{n,l}$. The term, $\partial Z_{n,l} / \partial x$, is linear in z and is defined to be

$$\frac{\partial Z_{n,l}(x, z)}{\partial x} \equiv f_{n,l}(x) - g_l(x)z, \quad (24)$$

with $f_{n,l}$ defined as

$$\begin{aligned} f_{n,l}(x) &= -2\eta_l^{-3}(x)g_l(x)[k_n^2(x) - \omega^2 a_l(x)] \\ &+ g_l(x)z_l(x) + \eta_l(x)\dot{z}_l(x) \\ &+ \eta_l^{-2}(x)[2k_n(x)\dot{k}_n(x) - \omega^2 \dot{a}_l(x)], \end{aligned} \quad (25)$$

and $g_l(x)$ is defined in Eq. (16). Therefore, the first derivative of the mode function is written analytically in terms of quantities easily calculated:

$$\begin{aligned} \frac{\partial \psi_{n,l}(x, z)}{\partial x} &= \dot{A}_{n,l}(x) \text{Ai}[Z_{n,l}(x, z)] + \dot{B}_{n,l}(x) \text{Bi}[Z_{n,l}(x, z)] \\ &+ [f_{n,l}(x) - g_l(x)z] \{ A_{n,l}(x) \text{Ai}'[Z_{n,l}(x, z)] \\ &+ B_{n,l}(x) \text{Bi}'[Z_{n,l}(x, z)] \}. \end{aligned} \quad (26)$$

Following the work of Gordon,²⁵ the mode functions and their derivatives are grouped in terms of linear combinations of the two Airy functions, Ai and Bi, or argument derivatives of these two functions. The mode function then becomes

$$\begin{aligned} \psi_{n,l}(x, z) &= A_{n,l}(x) \text{Ai}[\delta_l(z + \beta_{n,l})] + B_{n,l}(x) \text{Bi}[\delta_l(z + \beta_{n,l})] \\ &\equiv \mathcal{A}[\delta_l(z + \beta_{n,l})], \end{aligned} \quad (27)$$

where the explicit x dependence on δ_l and $\beta_{n,l}$ has been suppressed, and where Eq. (14) has been rewritten in the convenient form

$$Z_{n,l}(x, z) = \delta_l(x)(z + \beta_{n,l}(x)), \quad (28)$$

with

$$\delta_l(x) = -\eta_l(x), \quad (29)$$

and

$$\beta_{n,l}(x) = -\eta_l^{-3}(x)[k_n^2(x) - \omega^2 a_l(x)] - z_l(x). \quad (30)$$

Similarly, the first derivative of the mode function becomes

$$\begin{aligned} \frac{\partial \psi_{n,l}(x, z)}{\partial x} &= \mathcal{B}[\delta_l(z + \beta_{n,l})] + f_{n,l}(x) \mathcal{A}'[\delta_l(z + \beta_{n,l})] \\ &- z g_l(x) \mathcal{A}'[\delta_l(z + \beta_{n,l})], \end{aligned} \quad (31)$$

where \mathcal{B} and \mathcal{A}' are defined by

$$\begin{aligned} \mathcal{B}[\delta_l(z + \beta_{n,l})] &= \dot{A}_{n,l}(x) \text{Ai}[\delta_l(z + \beta_{n,l})] \\ &+ \dot{B}_{n,l}(x) \text{Bi}[\delta_l(z + \beta_{n,l})], \\ \mathcal{A}'[\delta_l(z + \beta_{n,l})] &= A_{n,l}(x) \text{Ai}'[\delta_l(z + \beta_{n,l})] \\ &+ B_{n,l}(x) \text{Bi}'[\delta_l(z + \beta_{n,l})]. \end{aligned} \quad (32)$$

The $\tilde{B}_{mn,l}$ coefficient integral, defined in Eq. (18), will next be evaluated for the diagonal and nondiagonal terms.

a. Nondiagonal coefficient. For simplicity, the density is assumed constant within a given layer and can be removed from the mode-coupling coefficient integrals. Substituting Eqs. (31)–(33) into Eq. (18) yields

$$\begin{aligned}\tilde{B}_{mn,l}(x) &= \frac{2}{\rho_l} \left[\int \mathcal{A}[\delta_l(z + \beta_{m,l})] \mathcal{B}[\delta_l(z + \beta_{n,l})] dz \right. \\ &\quad + f_{n,l}(x) \int \mathcal{A}[\delta_l(z + \beta_{m,l})] \\ &\quad \times \mathcal{A}'[\delta_l(z + \beta_{n,l})] dz - g_l(x) \\ &\quad \left. \times \int z \mathcal{A}[\delta_l(z + \beta_{m,l})] \mathcal{A}'[\delta_l(z + \beta_{n,l})] dz \right] \quad (34)\end{aligned}$$

$$\equiv \frac{2}{\rho_l} [\mathcal{B}I_1 + f_{n,l}(x) \mathcal{A}I_2 - g_l(x) \mathcal{A}I_4], \quad (35)$$

for the nondiagonal coupling coefficients, where the integration limits have been suppressed for convenience. The integral designations $\mathcal{B}I_1$, $\mathcal{A}I_2$, and $\mathcal{A}I_4$ defined in Eq. (35) contain a left subscript which designates the second argument inside the integral, whereas the right subscript designates the integral type. Explicitly, the integral $\mathcal{B}I_1$ is given by

$$\begin{aligned}\mathcal{B}I_1 &\equiv \int \mathcal{A}[\delta_l(z + \beta_{m,l})] \mathcal{B}[\delta_l(z + \beta_{n,l})] dz \\ &= \frac{1}{\delta_l^2[\beta_{m,l} - \beta_{n,l}]} \{ \mathcal{A}'[\delta_l(z + \beta_{m,l})] \mathcal{B}[\delta_l(z + \beta_{n,l})] \\ &\quad - \mathcal{A}[\delta_l(z + \beta_{m,l})] \mathcal{B}'[\delta_l(z + \beta_{n,l})] \}. \quad (36)\end{aligned}$$

Appendix A contains the general evaluation of the higher order integrals along with the solutions for $\mathcal{A}I_2$ and $\mathcal{A}I_4$.

b. Diagonal coefficient. Reference 25 contains some of the integrals needed to evaluate the diagonal coupling coefficient integrals. Higher order integrals can also be derived for $\beta_{m,l} = \beta_{n,l} \equiv \beta_l$, by taking derivatives with respect to β_l of the integral expression:

$$\begin{aligned}\mathcal{B}I_1 &= \int \mathcal{A}[\delta_l(z + \beta_l)] \mathcal{B}[\delta_l(z + \beta_l)] dz \\ &= (z + \beta_l) \mathcal{A}[\delta_l(z + \beta_l)] \mathcal{B}[\delta_l(z + \beta_l)] \\ &\quad - \mathcal{A}'[\delta_l(z + \beta_l)] \mathcal{B}'[\delta_l(z + \beta_l)] / \delta_l. \quad (37)\end{aligned}$$

For purposes of discussion, \mathcal{A} and \mathcal{B} are defined as linear combinations of the Airy functions,

$$\begin{aligned}\mathcal{A} &= a \text{Ai}[\delta_l(z + \beta_l)] + b \text{Bi}[\delta_l(z + \beta_l)], \\ \mathcal{B} &= c \text{Ai}[\delta_l(z + \beta_l)] + d \text{Bi}[\delta_l(z + \beta_l)]. \quad (38)\end{aligned}$$

The symmetric term ($\mathcal{A}\mathcal{B}' + \mathcal{A}'\mathcal{B}$) appears in the higher order integral expressions. The latter quantity in this term, $\mathcal{A}'\mathcal{B}$ is not desired in the coupling coefficient solution since the range derivative only acts on the second argument of the integrand. This quantity is eliminated by using the relation

$$\mathcal{A}\mathcal{B}' - \mathcal{A}'\mathcal{B} = \frac{1}{\pi} (ad - bc), \quad (39)$$

which is derived from the Wronskian of the Airy functions. The values for a , b , c , and d depend on which integral is being evaluated. Some of these coefficients are given explicitly in Eqs. (32) and (33), while other values are given in

Appendix C. Recurrence relations for the diagonal integrals are also given in Appendix A.

c. Second coefficient. The nondiagonal coefficient which involves the second derivative of the mode function is written as

$$\tilde{C}_{mn,l}(x) = \int_{z_l}^{z_{l+1}} \frac{1}{\rho(x,z)} \psi_{m,l}(x,z) \frac{\partial^2}{\partial x^2} \psi_{n,l}(x,z) dz \quad (40)$$

$$\begin{aligned}&= \frac{1}{\rho_l} [cI_1 + \delta_l \beta_{n,l} f_{n,l}^2(x) \mathcal{A}I_1 + \delta_l f_{n,l}(x) (f_{n,l}(x) \\ &\quad - 2g_l(x) \beta_{n,l}) \mathcal{A}I_3 + \delta_l g_l(x) (\beta_{n,l} g_l(x) \\ &\quad - 2f_{n,l}(x)) \mathcal{A}I_5 + \delta_l g_l^2(x) \mathcal{A}I_7 + \mathcal{D}I_2 - \mathcal{E}I_4]. \quad (41)\end{aligned}$$

Appendix C lists the values of the coefficients \mathcal{C} , \mathcal{D} , and \mathcal{E} , along with other terms to be calculated involving the second derivative with respect to range.

2. Integral equation

The integrals in Eqs. (7) and (8) are written in terms of the integral expressions introduced by Gordon.²⁵ The outlines of these procedures are discussed in this section. More details of the calculations are presented in the appendices.

To evaluate the coupling coefficient integrals, it is required that $A_{n,l}$ and $B_{n,l}$ be computed. Taking the derivative with respect to depth of the mode function, Eq. (22) gives

$$\begin{aligned}\frac{\partial \psi_{n,l}(x,z)}{\partial z} &= -\eta_l(x) A_{n,l}(x) \text{Ai}'[Z_{n,l}(x,z)] \\ &\quad - \eta_l(x) B_{n,l}(x) \text{Bi}'[Z_{n,l}(x,z)], \quad (42)\end{aligned}$$

where the chain rule has been used so that the derivative of the Airy functions is evaluated with respect to $Z_{n,l}(x,z)$ and is denoted by a prime. Equations (22) and (42) are evaluated at the layer interfaces, $z = z_l$, and are inverted to obtain

$$\begin{aligned}A_{n,l} &= \pi \left(\text{Bi}'[Z_{n,l}(x,z_l)] \psi_{n,l}(x,z_l) \right. \\ &\quad \left. + \frac{1}{\eta_l} \text{Bi}[Z_{n,l}(x,z_l)] \frac{\partial \psi_{n,l}(x,z_l)}{\partial z} \right), \quad (43)\end{aligned}$$

$$\begin{aligned}B_{n,l} &= -\pi \left(\text{Ai}'[Z_{n,l}(x,z_l)] \psi_{n,l}(x,z_l) \right. \\ &\quad \left. + \frac{1}{\eta_l} \text{Ai}[Z_{n,l}(x,z_l)] \frac{\partial \psi_{n,l}(x,z_l)}{\partial z} \right). \quad (44)\end{aligned}$$

Range derivatives of $A_{n,l}$ and $B_{n,l}$ are needed to calculate the coupling integrals and are given by

$$\begin{aligned} \frac{\partial A_{n,l}}{\partial x} = & \pi \left[Z_{n,l}(x, z_l) \frac{\partial Z_{n,l}(x, z_l)}{\partial x} \psi_{n,l}(x, z_l) - \frac{1}{\eta_l^2} \frac{d\eta_l}{dx} \right. \\ & \times \left. \frac{\partial \psi_{n,l}(x, z_l)}{\partial z} + \frac{1}{\eta_l} \frac{\partial^2 \psi_{n,l}(x, z_l)}{\partial x \partial z} \right] \text{Bi}[Z_{n,l}(x, z_l)] \\ & + \pi \left[\frac{\partial \psi_{n,l}(x, z_l)}{\partial x} + \frac{1}{\eta_l} \frac{\partial Z_{n,l}(x, z_l)}{\partial x} \frac{\partial \psi_{n,l}(x, z_l)}{\partial z} \right] \\ & \times \text{Bi}'[Z_{n,l}(x, z_l)], \end{aligned} \quad (45)$$

$$\begin{aligned} \frac{\partial B_{n,l}}{\partial x} = & -\pi \left[Z_{n,l}(x, z_l) \frac{\partial Z_{n,l}(x, z_l)}{\partial x} \psi_{n,l}(x, z_l) - \frac{1}{\eta_l^2} \frac{d\eta_l}{dx} \right. \\ & \times \left. \frac{\partial \psi_{n,l}(x, z_l)}{\partial z} + \frac{1}{\eta_l} \frac{\partial^2 \psi_{n,l}(x, z_l)}{\partial x \partial z} \right] \text{Ai}[Z_{n,l}(x, z_l)] \\ & - \pi \left[\frac{\partial \psi_{n,l}(x, z_l)}{\partial x} + \frac{1}{\eta_l} \frac{\partial Z_{n,l}(x, z_l)}{\partial x} \frac{\partial \psi_{n,l}(x, z_l)}{\partial z} \right] \\ & \times \text{Ai}'[Z_{n,l}(x, z_l)]. \end{aligned} \quad (46)$$

Each term inside the brackets must be evaluated at the l th layer interface. The range derivatives of each of these bracketed terms are given in Appendix B.

The second derivative terms, $\ddot{A}_{n,l}(x)$ and $\ddot{B}_{n,l}(x)$, are calculated from these first derivative terms in order to evaluate the second coupling coefficient integrals. The final results are presented in Appendix C.

An important point concerning the range-derivative calculations (such as for the eigenvalues) is that performing them analytically instead of numerically obtains the values at each range step, which avoids having to store many variables for later use. Also, many of the range-dependent functions require fine mesh points for derivative evaluation, which may increase computation time considerably.

B. Coupling coefficients—generalized Rutherford form

The method of Ref. 3 has been generalized to a multilayer environment. In this form, the coupling coefficients are derived by taking the range derivative of the depth equation, multiplying the result by ψ/ρ , integrating from with respect to z from 0 to ∞ , and then simplifying the expressions using the boundary conditions. Several of these steps are given in Appendix D. The range variable is represented here as r , since the application of this method was carried out in cylindrical coordinates. The result for the non-diagonal \bar{B}_{mn} coefficient is

$$\begin{aligned} \bar{B}_{mn} = & \frac{2}{(k_n^2 - k_m^2)} \left\{ 2 \int_0^\infty \frac{1}{\rho} k(x, z) \dot{k}(r, z) \psi_m(r, z) \psi_n(r, z) dz \right. \\ & \left. + \sum_{l=1}^L \frac{\partial z_{l+1}}{\partial r} \bar{\sigma}_{mn,l} - \sum_{l=1}^L \frac{\partial z_{l+1}}{\partial r} \bar{v}_{mn,l} \right\} + I_{mn,l}^B(r), \end{aligned} \quad (47)$$

where

$$\begin{aligned} \bar{\sigma}_{mn,l} = & \psi_{m,l}(r, z_{l+1}) \psi_{n,l}(r, z_{l+1}) \\ & \times \left[\frac{1}{\rho_{l+1}} (k_n^2 - k_{l+1}^2(r)) - \frac{1}{\rho_l} (k_n^2 - k_l^2(r)) \right], \quad (48) \\ \bar{v}_{mn,l} = & \frac{\rho_{l+1}}{\rho_l} \frac{\partial \psi_{m,l}(r, z_{l+1})}{\partial z} \frac{\partial \psi_{n,l}(r, z_{l+1})}{\partial z} \left[\frac{1}{\rho_l} - \frac{1}{\rho_{l+1}} \right]. \end{aligned} \quad (49)$$

$I_{mn,l}^B(r)$ is given in Eq. (19). Note that, in general, the depth integral over the wave number and its range derivative must be carried out when this method is used. This integral may or may not be analytic, and numerical derivatives may require fine sampling.

The second coupling coefficient in the Rutherford form, $\bar{C}_{mn,l}$, is obtained by taking the range derivative of the first coefficient. The result, summed over all the layers, is

$$\begin{aligned} \tilde{C}_{mn} = & \frac{\dot{\bar{B}}_{mn}}{2} - \sum_p E_{mp} E_{np} - \sum_{l=1}^L \frac{dz_{l+1}}{dr} \psi_{m,l}(r, z_{l+1}) \\ & \times \dot{\psi}_{n,l}(r, z_{l+1}) \left(\frac{1}{\rho_l} - \frac{1}{\rho_{l+1}} \right), \end{aligned} \quad (50)$$

where

$$\begin{aligned} E_{mp} = & \frac{\tilde{B}_{mp}}{2} - \sum_{l=1}^L \frac{dz_{l+1}}{dr} \left(\frac{1}{\rho_l} - \frac{1}{\rho_{l+1}} \right) \\ & \times \psi_{m,l}(r, z_{l+1}) \psi_{p,l}(r, z_{l+1}) \end{aligned} \quad (51)$$

and the factors of 1/2 are included in Eqs. (50) and (51) because of the definition of \tilde{B}_{mp} .

Further details of this calculation are given in Appendix D, including a discussion of the diagonal term, \bar{B}_{mm} .

C. Solution of range equation

Reference 19 presented details of the UK method that was used to transform the system of differential equations into a set of coupled integro-differential equations involving the adiabatic Green's function. A key step in the solution of this transformed problem is the introduction of an auxiliary function to express the range-dependent modal amplitudes. Performing this step changes the unbound problem into a bound state calculation. By expanding this auxiliary range-dependent modal amplitude function in terms of an orthonormal set of basis functions, i.e., Lanczos vectors, the solutions are obtained.

The solutions of the coupled equations are repeated here for completeness in both Cartesian and cylindrical coordinates. Also, a discussion of the Green's function in both Cartesian and cylindrical coordinates is included in this section.²⁶ In Cartesian coordinates, Eq. (6) is first put into an integro-differential form by operating on it with the adiabatic Green's function and then integrating the resulting equation over all space. The result is

$$R_m(x) = \int_{-\infty}^{\infty} dx' g_m(x, x') S_m(x') + \sum_{n=1}^N \left[\int_{-\infty}^{\infty} dx' g_m(x, x') \times \left(\bar{B}_{mn}(x') \frac{d}{dx'} + \bar{C}_{mn}(x') \right) R_n(x') \right]. \quad (52)$$

Note that Eq. (52) is a corrected form of Eq. (7) in Ref. 19, which contained a typographical error in the Green's function index. Also, the source function in Eq. (52) has been defined as $S_m(x, x_0, z_0) = \psi_m(x, z_0) \times [1/\rho_0(z_0)] \delta(x - x_0)$, with the source located at (x_0, z_0) .

Also, $g_m(x, x')$ is the adiabatic Green's function, and is evaluated by neglecting the coupling terms so that it satisfies

$$\left\{ \frac{d^2}{dx^2} + k_m^2(x) \right\} g_m(x, x') = -\delta(x - x'). \quad (53)$$

The Green's function solution has the form

$$g_m(x, x') = \frac{-y_{1m}(x_{>})y_{2m}(x_{<})}{W(x')}, \quad (54)$$

where $x_{>} = \max(x, x')$, $x_{<} = \min(x, x')$, and y_{1m} and y_{2m} are two independent solutions to the homogeneous adiabatic equation that satisfy the proper boundary conditions at $\pm\infty$.

The two independent solutions of the homogeneous adiabatic equation are obtained by one of two methods for either the Cartesian or cylindrical coordinate solution. Namely, by either using a modified Numerov method or Wentzel-Kramers-Brillouin (WKB) approximation. Initially, the Numerov method was used to obtain the first example presented in Sec. III, which was solved in Cartesian coordinates. For the examples solved in cylindrical coordinates, the WKB approximation was compared to the Numerov solution and gave excellent agreement, so that this method was used for evaluating the homogeneous Green's function for the remaining examples.

An auxiliary function, λ , is introduced next and is defined as

$$R_m(x) = \int_{-\infty}^{\infty} dx' g_m(x, x') [\lambda_m(x') + S_m(x')], \quad (55)$$

where the source term S_m has been added for convenience to remove the explicit source dependence from λ_m . This form, a slightly different transformation than that introduced in Ref. 19, avoids the difficulty associated with specifying a starting vector in the Lanczos technique for a delta-function source.

Equation (55) is then substituted into Eq. (52) so that a coupled integro-differential equation is now obtained. The result is

$$\lambda_m(x) = \sum_{n=1}^N \left(\bar{C}_{mn}(x) + \bar{B}_{mn}(x) \frac{d}{dx} \right) \times \int_{-\infty}^{\infty} dx' g_n(x, x') [\lambda_n(x') + S_n(x')]. \quad (56)$$

The key result of this step is that the integration is bounded to the region where coupling takes place. The coupling operator in Eq. (56) acts on the remaining integral on the right-hand side of Eq. (56) to confine it to this region; i.e., $R_m(x)$ corresponds to a scattered wave function, whereas $\lambda_m(x)$ is a bounded wave function.

In cylindrical coordinates the coupled equation becomes

$$R_m(r) = \frac{1}{2\pi\rho(z_0)} \int_0^{\infty} g_m(r, r') \psi_m(r', z_0) \frac{\delta(r')}{r'} r' dr' + \sum_{n=1}^N \int_0^{\infty} g_m(r, r') \left[\bar{C}_{mn}(r') + \bar{B}_{mn}(r') \frac{d}{dr'} + \tilde{B}_{mn}(r') \frac{1}{2r'} \right] R_n(r') r' dr', \quad (57)$$

where the Green's function satisfies

$$\left\{ \frac{d^2}{dr^2} + \frac{1}{r} \frac{d}{dr} + k_m^2(r) \right\} g_m(r, r') = -\frac{\delta(r - r')}{r}. \quad (58)$$

The resulting Green's function is given by

$$g_m(r, r') = \frac{-y_m^0(k_m r_{<}) y_m^\infty(k_m r_{>})}{r' W[y_m^0, y_m^\infty]_{r=r'}}, \quad (59)$$

where W corresponds to the Wronskian.

In the Numerov method the cylindrical form assumes the initial starting values are given by the asymptotic forms near the source and end range values. For a source located at $r' = 0$, the field near $r = 0$ is assumed to be range independent, which implies the boundary conditions should be given by

$$y_m^0(r, r') \rightarrow J_0(k_m r), \quad r \rightarrow 0, \quad (60)$$

$$y_m^\infty(r, r') \rightarrow H_0^{(1)}(k_m r), \quad r \rightarrow \infty. \quad (61)$$

For the WKB approximation the solution becomes

$$y_m^0(r, r' = 0) = \sqrt{\frac{2}{k_m(r)r}} \exp i \left(\int k_m(r) dr - \frac{\pi}{4} \right), \quad (62)$$

$$y_m^\infty(r, r' = 0) = \sqrt{\frac{2}{k_m(r)r}} \cos \left(\int k_m(r) dr - \frac{\pi}{4} \right), \quad (63)$$

with the Wronskian given by $r' W = 2i/\pi$.

One difficulty in using these methods near the origin is that the solutions diverge. To avoid this problem the initial point is taken slightly offset from $r = 0$. Also, for small range steps on the order of 1 m, the environment very near the source is assumed to be range independent to obtain the starting values. With these adjustments, either method for constructing the Green's function gives good results in reproducing the transmission loss for the examples presented in Sec. III.

Equation (56) is expressed in matrix form to facilitate the solution. This can be written as

$$|\lambda\rangle = |\bar{S}\rangle + \mathbf{VG}|\lambda\rangle, \quad (64)$$

where $|\lambda\rangle = [\lambda_1(x), \dots, \lambda_N(x)]^T$, and $|\bar{S}\rangle \equiv \mathbf{VG}|S\rangle = [\bar{S}_1(x), \dots, \bar{S}_N(x)]^T$. Also, \mathbf{V} and \mathbf{G} are $N \times N$ matrices with elements given by $[B_{mn}(x)(d/dx) + C_{mn}(x)]$ and $g_m \delta_{mn}$, respectively.

The Lanczos method is now applied to Eq. (64) by expanding $|\lambda\rangle$ in a set of $I+1$ orthonormal basis functions, $|F_i\rangle = [f_1^i(x), \dots, f_N^i(x)]^T$, ($i=0, 1, \dots, I$). Explicitly,

$$|\lambda\rangle = \sum_{i=0}^I C_i |F_i\rangle. \quad (65)$$

The orthonormality condition for the expansion wave functions $|F_i\rangle$ is given by

$$\langle F_j | F_i \rangle = \sum_{n=1}^N \int_{-\infty}^{\infty} dx f_n^j(x)^* \times f_n^i(x) = \delta_{j,i}, \quad (66)$$

where $\langle F_j |$ are defined as the conjugate states to $|F_j\rangle$, and the asterisk denotes complex conjugation.

The Lanczos routine is an iterative method with a starting vector usually chosen as the source term, $|F_0\rangle = (1/N_0)|\bar{S}\rangle$. The remaining expansion functions are generated by

$$|F_{i+1}\rangle = \frac{1}{N_i} \left\{ \mathbf{VG}|F_i\rangle - \sum_{j=0}^i |F_j\rangle \alpha_{ji} \right\}, \quad (67)$$

with

$$\alpha_{ji} = \langle F_j | \mathbf{VG} | F_i \rangle \quad \text{if } j \leq i+1 \quad \text{but } 0 \text{ otherwise.} \quad (68)$$

The normalization constant, N_i , is defined so that $\langle F_i | F_i \rangle = 1$. Also, by substituting Eq. (65) into Eq. (64) and using the orthonormality condition, Eq. (66), the inhomogeneous linear equation for the expansion coefficients, C_i , can be written

$$\sum_j (\delta_{ij} - \alpha_{ij}) C_j = N_0 \delta_{0i}. \quad (69)$$

The α_{ji} are recognized as being determined by the standard Gram–Schmidt orthogonalization procedure, and since $\alpha_{ji} = 0$ for $j > i$, the solution of Eq. (67) is more easily obtained. Also, the Lanczos method is very efficient if the number of Lanczos vectors needed to solve the equations is much smaller than the number of modes in the system. Approximately 10–15 vectors are needed for the examples presented here, whereas the number of modes can be on the order of 100, depending on the example. The criterion for convergence is calculated by monitoring the ratio of the current Lanczos vector to the first vector, C_i/C_1 . When this value approaches a small number, $< 1 \times 10^{-6}$ for example, the solution has converged.

The first two examples presented in Sec. III demonstrate the usefulness of this formalism. For the third example, the Rutherford form of the coupling coefficients is used. The basic derivations given in Ref. 3 are repeated in Appendix D for the multilayer case. An advantage of this form is that the coupling coefficients are given in terms of the local wave functions or their depth derivatives. Furthermore, the second-

order coupling coefficient is written in terms of the range derivative of the first-order coefficient and some additional terms. As shown in Eq. (50), the latter additional term involves evaluating $\partial \psi_{n,l}(x, z_{l+1}) / \partial x$ by using Eqs. (B10) and (B14). One drawback to this form is that an additional integral over $k(x)$ must be performed for sound speeds that depend on range.

III. EXAMPLE CALCULATIONS

In this section four examples are presented which validate the model calculations. Each example isolates certain aspects of the formalism and is used as an aid in model development. The first example is a single layer with a constant sound speed which has a perfectly reflecting hill along the bottom.⁵ The second and third examples are benchmark wedge problems,^{27,28} and the fourth example is a benchmark flat waveguide with a range-varying SVP.²⁸

For the first two examples, the reflecting hill and perfect wedge, the Airy form of the coefficients was used. The Rutherford form of the coefficients was used for the penetrable wedge. A combination of these two formalisms was used for the flat waveguide. Explicitly, \bar{B}_{mn} was calculated using the Airy integral method, and \bar{C}_{mn} was evaluated with the Rutherford form. Even though either method could be used for the \bar{C}_{mn} coefficient, the Rutherford form required less computation to evaluate. Also, for a range-varying SVP, a non-trivial integral for \bar{B}_{mn} must be evaluated for the Rutherford form, which makes the Airy form the best choice for this example.

A. Reflecting hill

In the first example, a single layer waveguide, i.e., ($l = 1$), was chosen with a constant sound speed of $c = 1500$ m/s. The bottom of the waveguide contained a perfectly reflecting hill with the local ocean-bottom depth given by

$$z_{l+1}(x) = H(x) = \left\{ h - \frac{\sigma}{2} \left[1 + \cos \frac{2\pi x}{100} \right] \right\} \quad (70)$$

in the range region $-50 \text{ m} < x < 50 \text{ m}$. Otherwise, $z_{l+1}(x) = h$, where $h = 200 \text{ m}$. The hill parameter was $\sigma = 12.4 \text{ m}$.

Analytic expressions for this example given in Ref. 19 were evaluated using the trigonometric expressions for the mode functions. A slight gradient was introduced to allow the use of the Airy solution to this problem. This example was for a single layer with $g_l(r) = 0$, one of the simplest cases to consider.

For the chosen frequency of 10 Hz, three propagating modes were obtained and were all above mode cutoff throughout the region. For a constant sound speed overlying a rigid bottom, the eigenvalues and mode functions are given analytically by

$$k_m(x) = \sqrt{\left(\frac{\omega}{c}\right)^2 - \gamma_m^2(x)} \quad (71)$$

and

$$\psi_m(x, z) = \sqrt{\frac{2}{H(x)}} \sin[\gamma_m(x)z], \quad (72)$$

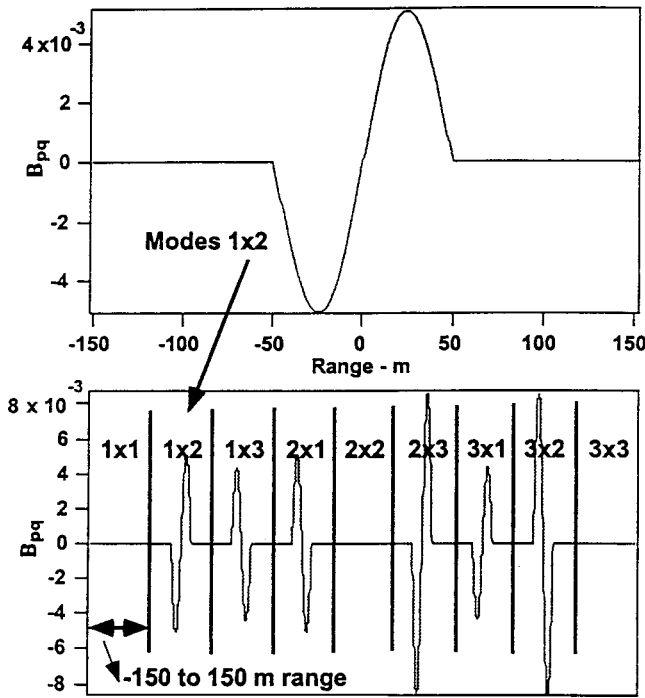


FIG. 1. Coupling coefficients as a function of range. Vertical bars separate each pair as labeled.

respectively, where

$$\gamma_m(x) = \frac{(m + 1/2)\pi}{H(x)}. \quad (73)$$

Here, m corresponds to the mode index, and the ω dependence on quantities is understood.

Several of the most involved steps of the calculations were verified for validity. First, the range derivatives of the eigenvalues were calculated analytically and agreed well with the numerical derivatives, to within five orders of magnitude. For the benchmark problems the eigenvalues had a smooth range variation so the numerical derivatives could be used. Use of the analytic derivative would be advantageous for problems where a rapid range variation would require a finer range grid.

Next, the range derivatives of $d\psi_{n,1}(r, z_1)/dz$ were calculated analytically and were compared to the numerical range derivatives, and again agreed to within five orders of magnitude. These terms accounted for some of the most difficult steps in obtaining the range derivatives of the mode function amplitudes.

The coupling coefficient integrals were evaluated analytically using the eigenvalues and mode functions from Eqs. (71) and (72). These coefficients were then compared to the analytic coupling coefficients for the Airy solutions to validate the program. The range dependence for each pair 1×1 , 1×2 , ... is shown in Fig. 1, where the pair values are separated by vertical bars for convenience. The surface term evaluated at the ocean-bottom interface exactly corresponded to minus the coupling coefficient integral for the diagonal terms, making the total diagonal coupling coefficient identically zero, satisfying the requirement mentioned in Sec. II.

Figure 2 shows the pressure field solutions as functions

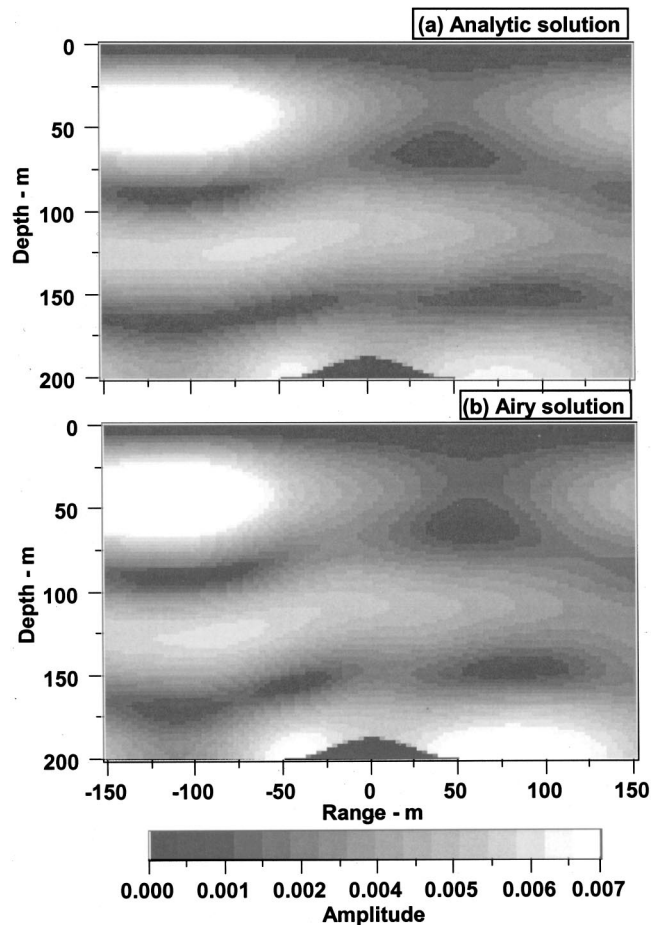


FIG. 2. Pressure field solutions comparison for the reflecting hill; the top figure corresponds to the analytic solution, the bottom to the Airy solution.

of range and depth for this example. A point source was assumed at $x = -100$ m at a depth of 50 m. The top figure corresponds to the trigonometric case and the bottom figure to the Airy solution. Excellent agreement was obtained for the two solutions. Note that the introduction of the gradient for the Airy solution precluded exact agreement. Also, the energy exchange between modes as a function of range was apparent because of the presence of the hill, as shown in the modal amplitude plots in Fig. 3.

The difference between the Airy and analytic solutions for the coupling coefficients was between 10^{-6} and 10^{-7} for the B_{mn} coefficient, which was approximately three to four orders of magnitude smaller than the value of this coefficient. These differences are dependent on the size of the gradient introduced for the Airy solutions presented here. For this comparison both forms of the coupling coefficients, Airy and Rutherford, were evaluated; both gave comparable results.

Range derivatives of a_l and b_l , and terms involving these variables, were zero since the sound speed and the gradient, b_l , were held constant in this example. This isolated several of the range-dependent terms for model validation. To test the multilayer capability of the model, a few imaginary layers were introduced on top of the hill so that the sound speed gradient remained constant throughout the layers. This change tested terms involving range derivatives

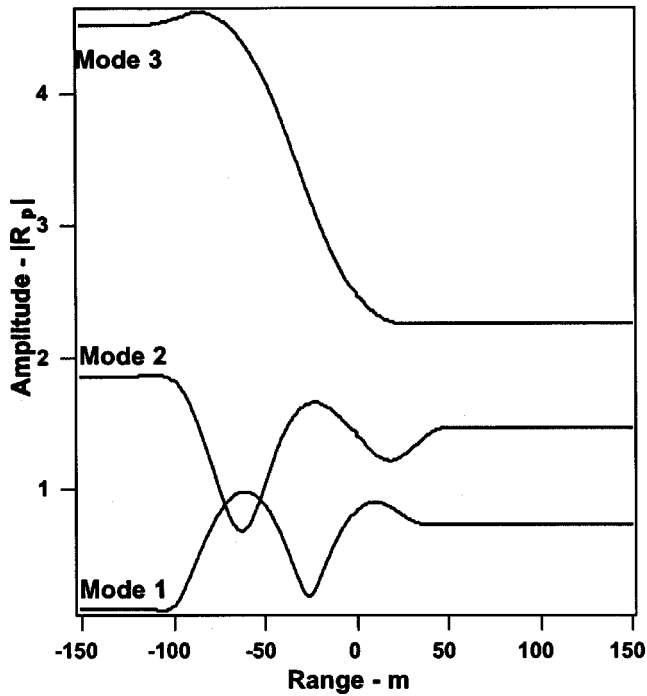


FIG. 3. Range dependence of the mode amplitudes for a receiver located at a depth of 100 m.

of the propagator matrices across multiple layers, along with coupling coefficients which must be summed over the layers. The test required that the resulting pressure solution obtained be the same as the pressure solution for the single layer overlying the hill.

B. Ideal wedge

The second example was a benchmark case with a point source located in an ideal wedge with a pressure-release top. Two bottom types were considered, a pressure-release bottom and a rigid bottom. An isospeed environment was used in this example. The exact analytic expression was compared to the trigonometric and Airy solutions for the pressure-release and rigid bottom examples. This analytic expression was obtained from the inhomogeneous Helmholtz equation by first performing a finite Fourier sine transform in the angle variable, θ , and then applying a Hankel transform in the range variable, r . The potential can be written²⁹

$$\Psi(r, r', \theta, \theta') = (i\pi/\theta_0) \sum_{m=1}^{\infty} J_\nu(kr_<) H_\nu^{(1)}(kr_>) \times \sin(\nu\theta) \sin(\nu\theta'), \quad (74)$$

where $r_< = \min(r, r')$, $r_> = \max(r, r')$, and $H_\nu^{(1)}$ is the Hankel function of order ν with

$$\nu = \begin{cases} m\pi/\theta_0 & \text{pressure-release bottom} \\ (m - \frac{1}{2})\pi/\theta_0 & \text{rigid bottom} \end{cases}. \quad (75)$$

The source and receiver depths were $z_s = 100$ m and $z_r = 30$ m, respectively. The source range was $r = 4000$ m from the wedge apex, and the range increments were $\Delta r = 4$ m. Figure 4 contains the transmission loss as a function of range for

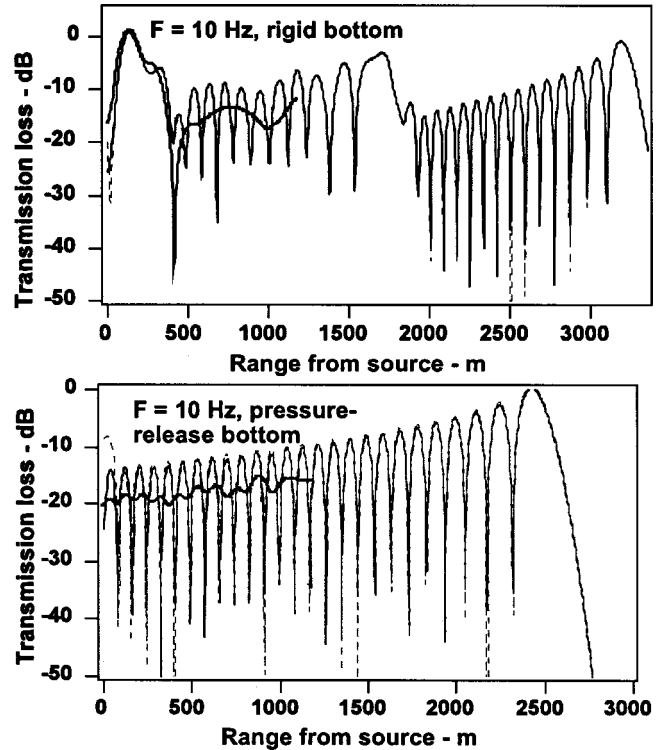


FIG. 4. Transmission loss as a function of range in ideal wedge problems for the analytic (solid line) and trigonometric (dashed line) solutions. The short 1200 m range solid curves demonstrate the importance of backscattered energy.

both solutions at a frequency of 10 Hz. The wedge angle was taken to be $\theta_0 = \arctan(200/4000) \approx 2.86^\circ$.

The trigonometric solutions for the eigenvalues and mode functions were given in Eqs. (71) and (72) for the rigid bottom wedge. Initially, there were three real modes for ranges near the source. As the receiver was moved closer to the apex, first mode 3 was cut off, and then mode 2 was cut off.

The range dependencies of the coupling coefficients were compared for the Airy and trigonometric calculations and agreed very well. Also, the range dependence of each modal amplitude displayed an oscillatory behavior that increased with range until the mode cutoff region was approached, and then abruptly ceased.

The transmission loss calculations shown in Fig. 4 were first obtained with the trigonometric wave functions. The solution converged rapidly for this problem, with only a few Lanczos vectors needed, which demonstrated the usefulness of the UK method in solving wedge problems. Coupling coefficient calculations were repeated for the Airy form for modes above cutoff, and the results were virtually the same. For modes past cutoff, the wave functions and eigenvalues are complex.

Backscattered energy is important for the ideal wedge example, as illustrated in Fig. 4 where the range integration was performed only up to 1200 m from the source. Major differences between the full solution and this shorter range solution were apparent even at very close ranges from the source, which demonstrated that in this case a global integra-

tion had to be performed to allow the energy to propagate up the length of the wedge and reflect back.

C. Penetrable wedge

For the penetrable wedge, a false bottom was introduced to transform this example into a proper Sturm–Liouville problem. Comparisons were made between the trigonometric solution in a constant sound speed environment, the Airy solution, and the benchmark solution for the unattenuated bottom type. For the trigonometric and Airy solutions, 86 mode eigenvalues and eigenfunctions were used.

The previous examples were based on solutions written in terms of Cartesian coordinates. For this example, and the last example shown in Sec. III D, cylindrical coordinates were used and a point source was assumed.

The analytic expression for a two-layer problem with sound speeds and densities c_1, ρ_1 , and c_2, ρ_2 , respectively, overlying a perfectly reflecting infinite half space is given by¹⁰

$$\begin{aligned} \phi_m(z) &= \frac{1}{N_m} \sin(\gamma_{1m}z), \quad z \leq H \\ &= \frac{1}{N_m} \frac{\sin(\gamma_{1m}H)}{\cos(\gamma_{2m}(L-H))} \cos(\gamma_{2m}(z-L)), \quad H \leq z \leq L, \end{aligned} \quad (76)$$

with H and L corresponding to the depths of the water-bottom interface and the depth of the false bottom layer, respectively. Also, $\gamma_{1m} = (k_1^2 - k_m^2)^{1/2}$, $\gamma_{2m} = (k_2^2 - k_m^2)^{1/2}$, $k_1 = \omega/c_1$, $k_2 = \omega/c_2$, and the normalization is given by¹⁰

$$\begin{aligned} N_m &= \left\{ \frac{1}{2\rho_1} \left[H - \frac{\sin(2\gamma_{1m}H)}{2\gamma_{1m}} \right] \right. \\ &\quad \left. + \frac{\sin^2(\gamma_{1m}H)[(L-H) + \sin(2\gamma_{2m}(L-H))/2\gamma_{2m}]}{2\rho_2 \cos^2(\gamma_{2m}(L-H))} \right\}. \end{aligned} \quad (77)$$

For the Airy solution, a slight gradient was introduced into the problem and the Rutherford form of the coupling coefficients was used to solve this problem. To evaluate the second coupling coefficient boundary term, the range derivative of the wave function is needed. For the trigonometric solution, the partial derivative with respect to range evaluated at the bottom of the wedge is given by

$$\frac{\partial \phi_m(r)}{\partial r} = \frac{-1}{N_m} \dot{N}_m \sin(\gamma_{1m}z) + \frac{\dot{\gamma}_{1m}}{N_m} \cos(\gamma_{1m}z), \quad z \leq H, \quad (78)$$

which was compared with Eq. (23) (The Airy solution) and showed excellent agreement. A numerical evaluation of this derivative would require many range steps, since this is a partial, not a total, derivative with respect to range. This further demonstrates the usefulness of the analytic approach developed in Sec. II A.

Figure 5 shows the transmission loss for the lossless penetrable wedge for a receiver depth of 30 m, at a frequency

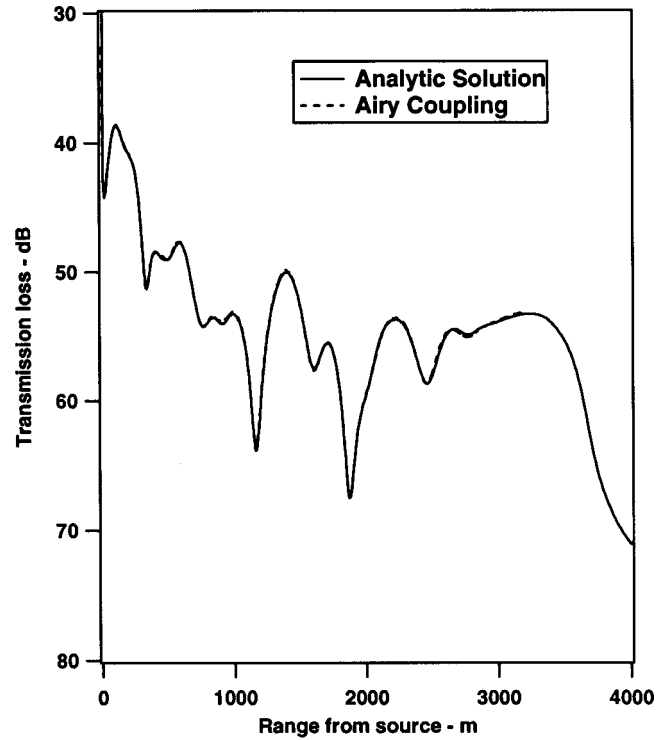


FIG. 5. Transmission loss for a lossless penetrable wedge with a receiver located at a depth of 30 m. The source is located at a depth of 100 m.

of 25 Hz. The constant sound speed trigonometric solution, as well as the Airy solution obtained from ORCA, are shown. Excellent agreement compared to the benchmark results was obtained, the difference in the calculations being at most a few hundredths of a dB for the 30 m receiver depth. For the Airy solution, the sound speed was set to 1500.01 m/s, and the bottom sound speed was adjusted at each range point to ensure a constant gradient. The range dependence of the first three eigenvalues, which were above cutoff starting from the source, showed a monotonic decrease as the apex was approached. The cutoff ranges were approximately 800 m for mode 3 and 2100 m for mode 2. To avoid false bottom reflections, the solution corresponding to 35 source modes was obtained for ranges greater than 1400 m, although coupling was allowed between all 86 modes.

The range dependence of several of the B_{mn} coupling coefficients was also examined. For the modes above cutoff, monotonic variations with range were seen; however, near the transition regions abrupt changes in the coefficients occurred. This ensured energy conservation within the system. Note that the surface integrals canceled the coupling integrals for the diagonal coefficients, $\bar{B}_{mm} = 0$, but there still existed a diagonal coupling coefficient contribution multiplying the $1/r$ term in Eq. (17). Also, by symmetry, $\bar{B}_{mn} = -\bar{B}_{nm}$ for the benchmark wedge problem.

One point concerning these wedge calculations is that coupling is important when solving the problem using the false bottom approach, where the coupling effects of many modes must be included to reproduce the correct results. This was demonstrated by calculating the adiabatic solution with the false bottom which did not reproduce the correct results shown in Fig. 5.

D. Waveguide with range-varying SVP

The last example considered was a flat waveguide with a range- and depth-dependent sound speed profile, a pressure-release top, and a rigid bottom. This was the second benchmark problem where an analytic expression for the sound speed profile was given as a function of range and depth in Ref. 28. Here, $a_l(r)$ and $g_l(r)$ were nonzero, so that the remaining terms not tested by examples A–C were verified. The range variation was shown to be in an analytic form so that $\dot{a}_l(r)$ and $\dot{b}_l(r)$, as well as the second range derivative terms, were obtained analytically.

The waveguide was 500 m deep and the profile was designed in such a way that most of the range variation occurred within the first 400–500 m from the source. Initially, the sound speed at the top of the waveguide was 1877 m/s, which decreased to a minimum of 1346 m/s near the midpoint of the waveguide. The SVP then increased to approximately 1500 m/s at the bottom. As the range from the source increased, the depth dependence of the SVP became increasingly uniform, so that the SVP approached a constant speed of 1500 m/s at a range of 400 m. Also, the SVP was represented using a total of 20 layers, each 25 m thick, which were summed to evaluate the coupling coefficients.

This example further tested multiple-layer calculations and also had $a_l(r)$, $b_l(r)$, and $g_l(r)$ nonzero, so that all aspects of the model were validated. The sound speed profile is given by

$$\frac{c^2(r,z)}{c_0^2} = \mathcal{L}^{-1}(r,z), \quad (79)$$

with

$$\begin{aligned} \mathcal{L}(r,z) \equiv & \left\{ 1 + \left(\frac{\pi h_1}{H} \right)^2 e^{-2\pi r/H} + \left(\frac{2\pi h_2}{H} \right)^2 e^{-4\pi r/H} - \frac{2\pi h_1}{H} \right. \\ & \times \left[1 - \left(\frac{2\pi h_2}{H} \right) e^{-2\pi r/H} \right] \cos(\pi z/H) e^{-\pi r/H} \\ & \left. - \frac{4\pi h_2}{H} \cos(2\pi z/H) e^{-2\pi r/H} \right\}, \quad (80) \end{aligned}$$

where $c_0 = 1500$ m/s, which is a reference sound speed, $H = 500$ m is the waveguide depth, $h_1/H = 0.032$, and $h_2/H = 0.016$.

The sound speed parameters are given by

$$a_l(r) = \frac{1}{c_{T,l}^2} = \mathcal{L}(r, z_l) / c_0^2, \quad (81)$$

$$b_l(r) = \frac{1}{h_l c_0^2} [\mathcal{L}(r, z_{l+1}) - \mathcal{L}(r, z_l)], \quad (82)$$

$$\frac{da_l}{dr} = \frac{1}{c_0^2} \frac{d\mathcal{L}(r, z_l)}{dr}, \quad (83)$$

$$\frac{db_l}{dr} = \frac{1}{h_l c_0^2} \left[\frac{d\mathcal{L}(r, z_{l+1})}{dr} - \frac{d\mathcal{L}(r, z_l)}{dr} \right], \quad (84)$$

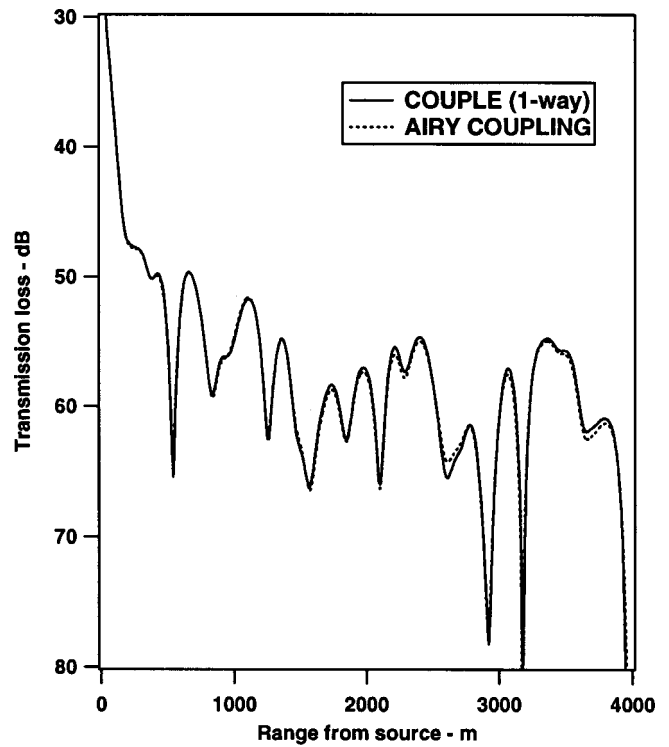


FIG. 6. Transmission loss for the flat waveguide, with a range- and depth-varying SVP, at 25 Hz for source and receiver depths of 250 m, using ten source modes.

$$\frac{d^2 a_l}{dr^2} = \frac{1}{c_0^2} \frac{d^2 \mathcal{L}(r, z_l)}{dr^2}, \quad (85)$$

$$\frac{d^2 b_l}{dr^2} = \frac{1}{h_l} \left[\frac{1}{c_0^2} \frac{d^2 \mathcal{L}(r, z_{l+1})}{dr^2} - \frac{d^2 a_l}{dr^2} \right], \quad (86)$$

where $h_l = z_{l+1} - z_l$.

Transmission loss results, obtained in cylindrical coordinates, were calculated at a frequency of 25 Hz. Source and receiver depths were both set at 250 m. The SVP was shown to be flat after approximately 400 m, so that the SVP was approximated at 1500 m/s (plus a slight gradient for the Airy solution) well beyond this range value. Range increments were chosen to be 1 m for this example. Also, since most of the coupling occurred only in this region, the integration was carried out to a range near 1000 m. After this range value the adiabatic solution was assumed, which significantly reduced the computer time needed to evaluate this example.

The comparisons to the benchmark are shown in Figs. 6 and 7 for two different cases. Ten source modes were assumed in the calculations shown in Fig. 6, while the curve in Fig. 7 included all 17 modes in the calculation. The ten-source mode result shows very good agreement with the COUPLE one-way result. The 17-mode curve again shows an overall good fit to within about 1 dB for the local maximums in the transmission loss curve, although the minimum points do not always agree in magnitude. The overall phase shows good agreement, however.

The lack of agreement at some ranges may exist because the results are being compared to a one-way calculation; however, the model presented here is a two-way model

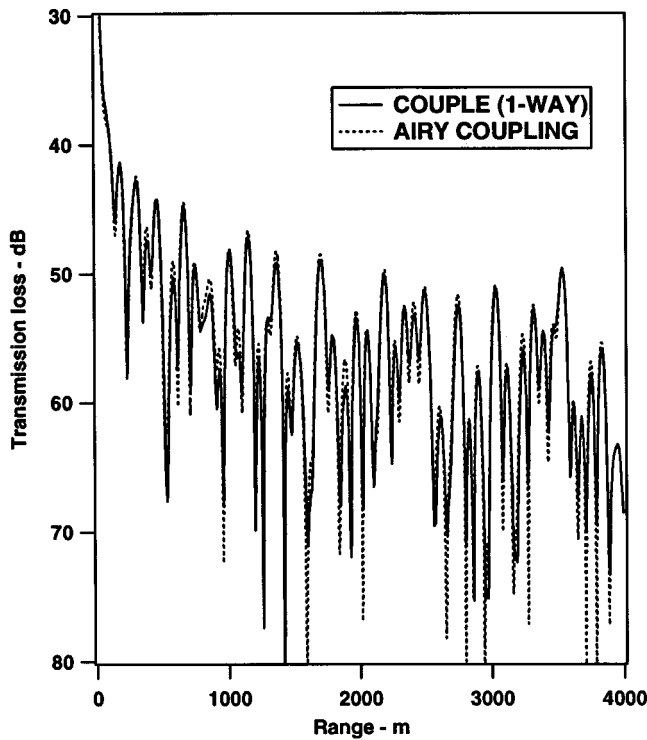


FIG. 7. Transmission loss for the same configuration as shown in Fig. 6, but including all 17 source modes.

which includes backscatter. The rapid variation in the SVP near the source may cause the backscatter component to be significant.

For this example the \bar{B}_{mn} coefficient was obtained using the formulas (derived in Sec. II A) for the Airy integral form. In the Rutherford form, \bar{B}_{mn} has only the depth integral over the eigenvalues as nonzero for flat layer examples such as these, since $dz_{l+1}(r)/dr=0$. Thus, the second term of the coupling coefficient given in Eq. (47), as well as the surface contributions at each layer interface, are zero. The analytic coupling coefficient was compared to the result

$$\bar{B}_{mn} = \frac{-4}{(k_m^2 - k_n^2)} \int_0^L \frac{1}{\rho(z)} k \dot{k} \psi_m(x, z) \psi_n(x, z) dz. \quad (87)$$

Using Eq. (79), the integrand in Eq. (87) can be written as

$$\begin{aligned} k \dot{k} &= \frac{\omega^2}{2c_0^2} \frac{\partial \mathcal{L}(r, z)}{\partial r} \\ &= \frac{\omega^2}{2c_0^2} \left(f_1(r) + f_2(r) \cos\left(\frac{\pi z}{H}\right) + f_3(r) \cos\left(\frac{2\pi z}{H}\right) \right), \end{aligned} \quad (88)$$

where

$$f_1(r) = \frac{-2\pi}{H} \left(\frac{\pi h_1}{H} \right)^2 e^{-2\pi r/H} - \frac{4\pi}{H} \left(\frac{2\pi h_2}{H} \right)^2 e^{-4\pi r/H}, \quad (89)$$

$$f_2(r) = \frac{-2\pi h_1}{H} \left\{ \frac{-\pi}{H} + \frac{3\pi}{H} \left(\frac{2\pi h_2}{H} \right) e^{-2\pi r/H} \right\} e^{-\pi r/H}, \quad (90)$$

$$f_3(r) = \frac{2\pi}{H} \left(\frac{4\pi h_2}{H} \right) e^{-2\pi r/H}. \quad (91)$$

The integral in Eq. (87), with $\rho(z)=1 \text{ g/cm}^3$, is written in the convenient form

$$\begin{aligned} \bar{B}_{mn} &= \frac{-2}{(k_m^2 - k_n^2)} \frac{\omega^2}{c_0^2} \left[f_1(r) \int_0^H \psi_m \psi_n dz \right. \\ &\quad + f_2(r) \int_0^H \cos\left(\frac{\pi z}{H}\right) \psi_m \psi_n dz \\ &\quad \left. + f_3(r) \int_0^H \cos\left(\frac{2\pi z}{H}\right) \psi_m \psi_n dz \right]. \end{aligned} \quad (92)$$

By using numerical integration, this result was compared to the exact layer-by-layer evaluation of the coupling coefficients by Eq. (35) and gave very good agreement, the difference being on the order of 10^{-4} or less for the B_{mn} coefficient. Note also that the diagonal term, B_{mm} , was zero for this example, as seen by Eq. (D17), since $dz_{l+1}/dr=0$.

An important point concerning the Airy method of calculating the coupling coefficients is that $\Delta Z=25 \text{ m}$ Airy layers were used to sample the SVP, as mentioned previously. The Airy coupling coefficient evaluations were performed in a very short time, as compared to the numerical integration which was evaluated on a $\Delta z=2.5 \text{ m}$ depth grid spacing.

The second coupling coefficient was calculated using Eq. (50), which simplifies for this example to

$$\tilde{C}_{mn} = \frac{\dot{\bar{B}}_{mn}}{2} - \sum_p E_{mp} E_{np}. \quad (93)$$

Comparisons were not made explicitly for these coefficients, since they were weaker than the first derivative coefficient by at least an order of magnitude. Note that the second term in Eq. (93) makes the diagonal term C_{mm} nonzero.

IV. CONCLUSIONS

Details were presented for a coupled-mode model in differential form developed to solve multilayer sound speed profiles where $1/c^2$ varies linearly with depth. The local mode solutions were expressed in terms of Airy functions whose coupling integrals were shown to be solvable analytically. The coupling coefficients were first evaluated and then were used in the UK method to solve the coupled equations efficiently. It was demonstrated that only a few Lanczos vectors were needed to obtain convergence. Several example transmission loss calculations were presented to validate the model in increasingly complex environments. All of the results shown were for environments where the eigenvalues and eigenfunctions are real.

Extensions to the model are in progress. This includes generalizing the model to include continuum effects via leaky modes. A substantial savings in computer time can, in

principle, be achieved by using a coupled-leaky-mode solution as compared to the false-bottom coupled-mode solution, due to a large reduction in the number of modes needed to represent the field. This approach has also been demonstrated for solving the penetrable wedge benchmark, although it was not reported here. Preliminary results demonstrate that an accurate representation of the field near mode transitions is important to obtain the best result in this type of coupled-mode calculation. In evanescent regions, a similar procedure, presented in Ref. 20, of separating large exponents from the propagators may need to be carried out in order to avoid numerical overflow. This approach is currently under investigation.

ACKNOWLEDGMENTS

The author wishes to thank Dr. David P. Knobles, Dr. Scott J. Levinson, Dr. Robert A. Koch, and Dr. Evan K. Westwood for many helpful discussions and suggestions. This work was supported by the Independent Research and Development Program of Applied Research Laboratories, The University of Texas at Austin.

APPENDIX A: MODE-COUPLING COEFFICIENT INTEGRALS

1. Nondiagonal terms

The appendix in Ref. 25 contains the expressions for ${}_xI_1$ and ${}_xI_3$. As mentioned in Ref. 25, by taking higher derivatives with respect to $\beta_{m,l}$ or $\beta_{n,l}$ and using the Airy differential equation $\mathcal{B}''(x) = x\mathcal{B}(x)$, higher order integrals can be generated. They satisfy the recurrence relations

$$\begin{aligned} {}_B I_{2j+1} &\equiv \int z^j \mathcal{A}[\delta_l(z + \beta_{m,l})] \mathcal{B}'[\delta_l(z + \beta_{n,l})] dz \\ &= \frac{1}{\delta_l^3} \frac{\partial^2}{\partial \beta_{n,l}^2} {}_B I_{2j-1} - \beta_{n,l} ({}_B I_{2j-1}), \quad j = 1 \sim \infty, \end{aligned} \quad (\text{A1})$$

$$\begin{aligned} {}_B I_{2j} &\equiv \int z^{j-1} \mathcal{A}[\delta_l(z + \beta_{m,l})] \mathcal{B}'[\delta_l(z + \beta_{n,l})] dz \\ &= \frac{1}{\delta_l} \frac{\partial ({}_B I_{2j-1})}{\partial \beta_{n,l}}, \quad j = 1 \sim \infty. \end{aligned} \quad (\text{A2})$$

The last two integrals needed to evaluate the B_{mn} coefficients are given explicitly by

$$\begin{aligned} {}_A I_2 &= \frac{1}{\delta_l^3 (\beta_{m,l} - \beta_{n,l})^2} \{ \mathcal{A}'[1] \mathcal{A}[2] - \mathcal{A}[1] \mathcal{A}'[2] \} \\ &\quad + \frac{1}{\delta_l^2 (\beta_{m,l} - \beta_{n,l})} \\ &\quad \times \{ \mathcal{A}'[1] \mathcal{A}'[2] - Z_{n,l}(r, z) \mathcal{A}[1] \mathcal{A}[2] \}, \end{aligned} \quad (\text{A3})$$

where, symbolically, $1 = \delta_l(z + \beta_{m,l})$ and $2 = \delta_l(z + \beta_{n,l})$. Similarly,

$$\begin{aligned} {}_A I_4 &= x_1 \mathcal{A}[1] \mathcal{A}[2] + x_2 \mathcal{A}[1] \mathcal{A}'[2] + x_3 \mathcal{A}'[1] \mathcal{A}[2] \\ &\quad + x_4 \mathcal{A}'[1] \mathcal{A}'[2], \end{aligned} \quad (\text{A4})$$

where

$$\begin{aligned} x_1 &= \frac{-3(\beta_{m,l} + \beta_{n,l} + 2z)}{\delta_l^4 (\beta_{m,l} - \beta_{n,l})^3} - \frac{z(z + \beta_{n,l})}{\delta_l (\beta_{m,l} - \beta_{n,l})}, \\ x_2 &= \frac{-(\beta_{m,l} + \beta_{n,l} + 3z)}{\delta_l^3 (\beta_{m,l} - \beta_{n,l})^2} - \frac{6}{\delta_l^6 (\beta_{m,l} - \beta_{n,l})^4}, \\ x_3 &= \frac{(2\beta_{n,l} + 3z)}{\delta_l^3 (\beta_{m,l} - \beta_{n,l})^2} + \frac{6}{\delta_l^6 (\beta_{m,l} - \beta_{n,l})^4}, \\ x_4 &= \frac{z}{\delta_l^2 (\beta_{m,l} - \beta_{n,l})} + \frac{6}{\delta_l^5 (\beta_{m,l} - \beta_{n,l})^3}. \end{aligned} \quad (\text{A5})$$

2. Diagonal terms

The second diagonal integral I_2 as derived from Eqs. (37) and (39) is shown to be

$$\begin{aligned} {}_B I_2 &= \int \mathcal{A}[\delta_l(z + \beta_l)] \mathcal{B}'[\delta_l(z + \beta_l)] dz \\ &= \frac{1}{2\delta_l} \mathcal{A}[\delta_l(z + \beta_l)] \mathcal{B}[\delta_l(z + \beta_l)] + \frac{(ad - bc)}{2\pi} z. \end{aligned} \quad (\text{A6})$$

Note that for ${}_A I_2$, the last expression in Eq. (A6) vanishes.

The diagonal integrals have recurrence relations similar to the nondiagonal integrals. The odd integral terms I_1 , I_3 , and I_5 are given in the appendix of Ref. 25. The second derivative coupling coefficient involves I_7 and is easily calculated by assuming a form similar to the previous odd integral expressions.

The recurrence relation for the even integral terms is given by

$${}_B I_{2j} = \frac{1}{2\delta_l} \frac{\partial {}_B I_{2j-1}}{\partial \beta_l} + \frac{(ad - bc)}{2\pi} \frac{z^j}{j}, \quad j = 1 \sim \infty. \quad (\text{A7})$$

APPENDIX B: FIRST-ORDER DERIVATIVES

This section contains the range derivative terms needed to evaluate $\dot{A}_{n,l}$ and $\dot{B}_{n,l}$ in Eqs. (45) and (46). These terms include $\dot{k}_n(x)$ and $(\partial/\partial x)\Psi_l(x)$, where the normalized displacement potential-state vector for the l th layer is defined by $\Psi_l = [\psi_l \partial\psi_l/\partial z]$, henceforth referred to as the ‘‘wave function.’’

These terms are evaluated by using the propagator matrices described in Ref. 20 and repeated here. The elements of the propagator matrix, D_l , for the l th layer are given by

$$\begin{aligned} d_{l,11} &= \begin{pmatrix} \rho_l \\ \rho_{l+1} \end{pmatrix} e_{l,11} = \begin{pmatrix} \rho_l \\ \rho_{l+1} \end{pmatrix} [\text{Ai}(Z_{\text{bot}}) \text{Bi}'(Z_{\text{top}}) \\ &\quad - \text{Bi}(Z_{\text{bot}}) \text{Ai}'(Z_{\text{top}})] / W, \end{aligned} \quad (\text{B1})$$

$$d_{l,12} = \left(\frac{\rho_l}{\rho_{l+1}} \right) e_{l,12} = \left(\frac{\rho_l}{\rho_{l+1}} \right) [\text{Ai}(Z_{\text{bot}})\text{Bi}(Z_{\text{top}}) - \text{Bi}(Z_{\text{bot}})\text{Ai}(Z_{\text{top}})]/(\eta_l W), \quad (\text{B2})$$

$$d_{l,21} = e_{l,21} = [-\text{Ai}'(Z_{\text{bot}})\text{Bi}'(Z_{\text{top}}) + \text{Bi}'(Z_{\text{bot}})\text{Ai}'(Z_{\text{top}})]\eta_l/W, \quad (\text{B3})$$

$$d_{l,22} = e_{l,22} = [-\text{Ai}'(Z_{\text{bot}})\text{Bi}(Z_{\text{top}}) + \text{Bi}'(Z_{\text{bot}})\text{Ai}(Z_{\text{top}})]/W, \quad (\text{B4})$$

where the Airy arguments, Z_{top} and Z_{bot} have been defined as

$$Z_{\text{top}} \equiv Z_{n,l}(x, z_l(x)), \quad (\text{B5})$$

$$Z_{\text{bot}} \equiv Z_{n,l}(x, z_{l+1}(x)), \quad (\text{B6})$$

except when calculating the eigenvalue range derivatives, where $Z_{\text{top}} \equiv Z_{T,l}$ and $Z_{\text{bot}} \equiv Z_{B,l}$, which signifies that the Airy arguments contain k as a free parameter rather than $k(x)$. Also, the Wronskian $W = 1/\pi$.

1. Range derivative of Airy argument

The range derivative of the Airy function argument at the top of the layer, Eq. (24), reduces to

$$\frac{\partial Z_{n,l}(x, z_l(x))}{\partial x} \equiv \tilde{f}_{n,l}(x), \quad (\text{B7})$$

with $\tilde{f}_{n,l}$ defined by

$$\tilde{f}_{n,l}(x) = -2\eta_l^{-3}(x)g_l(x)[k_n^2(x) - \omega^2 a_l(x)] + \eta_l^{-2}(x) \times [2k_n(x)\dot{k}_n(x) - \omega^2 \dot{a}_l(x)]. \quad (\text{B8})$$

The corresponding derivative at the bottom of layer l is given by

$$\frac{\partial Z_{n,l}(x, z_{l+1}(x))}{\partial x} \equiv \tilde{f}_{n,l}(x) - g_l(x)[z_{l+1}(x) - z_l(x)] - \eta_l(x)[\dot{z}_{l+1}(x) - \dot{z}_l(x)]. \quad (\text{B9})$$

2. Range derivative of the wave function

The propagation of the wave function from the top to the bottom of layer l is defined by

$$\Psi_{n,l}(x, z_{l+1}) = E_{n,l}\Psi_{n,l}(x, z_l). \quad (\text{B10})$$

The matrix E_l involves the sums of products of Airy functions and their derivatives with respect to Airy arguments. The elements of E_l are listed in the following. Similarly, the propagation of the wave function from the top of layer l to the top of layer $l+1$ is given by

$$\Psi_{n,l+1}(x, z_{l+1}) = \tilde{D}_{n,l}\Psi_{n,l}(x, z_l) = \tilde{D}_{n,l}\Phi_{n,l}(x, z_l)/N_n(x), \quad (\text{B11})$$

where $N_n(x)$ is the normalization factor, written explicitly to show its range dependence, and $\Phi_{n,l}$ is the unnormalized wave function. The normalization factor is also given in Appendix B 3. All expressions involving the wave function are

written in terms of normalized wave functions. The normalization factor is used for evaluating parts of Eqs. (45) and (46), as discussed subsequently. The propagator matrix $\tilde{D}_{n,l}$ is defined here by

$$\tilde{D}_{n,l} \equiv D_{n,l} \exp(|X_l|) = \begin{bmatrix} \rho_l/\rho_{l+1} & 0 \\ 0 & 1 \end{bmatrix} E_l \quad (\text{B12})$$

$$\equiv \begin{bmatrix} d_{l,11} & d_{l,12} \\ d_{l,21} & d_{l,22} \end{bmatrix}. \quad (\text{B13})$$

The mode index n is implied for the individual propagator matrix elements, as in Eq. (B13), but is not explicitly shown for brevity. For numerical stability the exponent term, X_l , in Eq. (B12) factors out the large magnitudes associated with these functions and provides numerical stability when solving for the mode functions. However, the derivations given here can be evaluated in terms of \tilde{D} , eliminating the need for evaluating derivatives of the exponent term explicitly.

The value of the wave function at the top of the l th layer is written in terms of the mode function at the ocean surface, $z_1 = 0$, by combining the propagator matrices:

$$\Psi_{n,l}(x, z_l) = \tilde{D}_n^- \Psi_{n,1}(x, z_1), \quad (\text{B14})$$

where the negative superscript signifies that the propagation is from the l th layer to the surface and is given by

$$\tilde{D}_n^- = \tilde{D}_{n,l-1} \times \tilde{D}_{n,l-2} \times \cdots \times \tilde{D}_{n,2} \times \tilde{D}_{n,1} = \prod_{i=1}^{l-1} \tilde{D}_{n,l-i}, \quad l > 1, \quad (\text{B15})$$

and

$$\tilde{D}_n^- = I, \quad l = 1. \quad (\text{B16})$$

The total propagator from the top of the substrate is written

$$\tilde{D}_n = \tilde{D}_{n,L} \times \tilde{D}_{n,L-1} \times \cdots \times \tilde{D}_{n,l} \times \tilde{D}_n^-, \quad L > 1 = \begin{bmatrix} d_{11} & d_{12} \\ d_{21} & d_{22} \end{bmatrix}, \quad (\text{B17})$$

where

$$\tilde{D}_n = \tilde{D}_{n,1}, \quad L = l = 1. \quad (\text{B18})$$

The range derivative of the wave function given in Eq. (B14) is needed to evaluate Eqs. (45) and (46). This is given by

$$\frac{\partial \Psi_{n,l}(x, z_l)}{\partial x} = \frac{\partial \tilde{D}_n^-}{\partial x} \Psi_{n,1}(x, z_1) + \tilde{D}_n^- \frac{\partial \Psi_{n,1}(x, z_1)}{\partial x}. \quad (\text{B19})$$

The partial product of the propagator matrices is given by

$$\tilde{D}_n^- \equiv \begin{bmatrix} \tilde{D}_{11}^- & \tilde{D}_{12}^- \\ \tilde{D}_{21}^- & \tilde{D}_{22}^- \end{bmatrix}, \quad (\text{B20})$$

where the product is understood to be from layers 1 to $l-1$ and the elements have been designated by \tilde{D}_{ij}^- , instead of a lower case d_{ij}^- designation, to avoid confusion with the total matrix product elements d_{ij} . Equation (B19) can then be expressed in component form as

$$\begin{aligned} \frac{\partial \psi_{n,l}(x, z_l)}{\partial x} &= \frac{\partial \tilde{D}_{11}^-}{\partial x} \psi_{n,1}(x, z_1) + \frac{\partial \tilde{D}_{12}^-}{\partial x} \left[\frac{\partial \psi_{n,1}(x, z_1)}{\partial z} \right] \\ &+ \tilde{D}_{12}^- \frac{\partial}{\partial x} \left[\frac{\partial \psi_{n,1}(x, z_1)}{\partial z} \right], \end{aligned} \quad (\text{B21})$$

and

$$\begin{aligned} \frac{\partial}{\partial x} \left[\frac{\partial \psi_{n,l}(x, z_l)}{\partial z} \right] &= \frac{\partial \tilde{D}_{21}^-}{\partial x} \psi_{n,1}(x, z_1) + \frac{\partial \tilde{D}_{22}^-}{\partial x} \left[\frac{\partial \psi_{n,1}(x, z_1)}{\partial z} \right] \\ &+ \tilde{D}_{22}^- \frac{\partial}{\partial x} \left[\frac{\partial \psi_{n,1}(x, z_1)}{\partial z} \right], \end{aligned} \quad (\text{B22})$$

where the boundary conditions at the top of the ocean make $\partial \psi_{n,1}(x, z_1)/\partial x = 0$.

The matrix elements and their derivatives can be calculated layer by layer using the chain rule. For the j th product, corresponding to the j th layer, this is given by

$$\begin{aligned} &\begin{bmatrix} \partial \tilde{D}_{11}^-(j) & \partial \tilde{D}_{12}^-(j) \\ \partial \tilde{D}_{21}^-(j) & \partial \tilde{D}_{22}^-(j) \end{bmatrix} \\ &= \begin{bmatrix} d_{j,11} & d_{j,12} \\ d_{j,21} & d_{j,22} \end{bmatrix} \begin{bmatrix} \partial \tilde{D}_{11}^-(j-1) & \partial \tilde{D}_{12}^-(j-1) \\ \partial \tilde{D}_{21}^-(j-1) & \partial \tilde{D}_{22}^-(j-1) \end{bmatrix} \\ &+ \begin{bmatrix} \partial d_{j,11} & \partial d_{j,12} \\ \partial d_{j,21} & \partial d_{j,22} \end{bmatrix} \begin{bmatrix} \tilde{D}_{11}^-(j-1) & \tilde{D}_{12}^-(j-1) \\ \tilde{D}_{21}^-(j-1) & \tilde{D}_{22}^-(j-1) \end{bmatrix}, \end{aligned} \quad (\text{B23})$$

where the derivative has been designated by a ∂ and refers to either the range derivatives described in Eqs. (B21) and (B22) or the derivatives of the propagators with respect to k that are needed in calculating \dot{k}_n and \ddot{k}_n . The individual layer elements $d_{j,11}, \dots$ are given in the following, along with their derivatives with respect to k and x .

The remaining unknown term in Eqs. (45) and (46) is

$$\frac{\partial}{\partial x} \left[\frac{\partial \psi_{n,1}(x, z_1)}{\partial z} \right], \quad (\text{B24})$$

and is calculated from the normalization given by Eq. (B28) in Appendix B 3. By dividing both sides of Eq. (B28) by $N_n^2(x)$, expressing all normalized wave functions in terms of $\psi_{n,1}(x, z_1)$ and $\partial \psi_{n,1}(x, z_1)/\partial z$, and then taking the range derivative of the resulting equation, the unknown term can be written as

$$\frac{\partial}{\partial x} \left[\frac{\partial \psi_{n,1}(x, z_1)}{\partial z} \right] = \frac{\mathcal{N}}{\mathcal{D}}, \quad (\text{B25})$$

where

$$\begin{aligned} \mathcal{N} &= - \left[Y_{L+1} + \sum_{l=1}^L \left\{ \gamma_l + \left(\Omega_l \frac{\partial \tilde{D}_{11}^-}{\partial x} + \prod_l \frac{\partial \tilde{D}_{21}^-}{\partial x} \right) \psi_{n,1}(x, z_1) \right. \right. \\ &\quad \left. \left. + \left(\Omega_l \frac{\partial \tilde{D}_{12}^-}{\partial x} + \prod_l \frac{\partial \tilde{D}_{22}^-}{\partial x} \right) \frac{\partial \psi_{n,1}(x, z_1)}{\partial x} \right\} \right], \end{aligned} \quad (\text{B26})$$

and

$$\begin{aligned} \mathcal{D} &= \left[\frac{\rho_{L+1} d_{12}}{\sqrt{k_n^2 - (\omega/c_{L+1})^2}} \left(d_{11} \psi_{n,1}(x, z_1) + d_{12} \frac{\partial \psi_{n,1}(x, z_1)}{\partial z} \right) \right. \\ &\quad \left. + \sum_{l=1}^L \left(\Omega_l \tilde{D}_{12}^- + \prod_l \tilde{D}_{22}^- \right) \right]. \end{aligned} \quad (\text{B27})$$

The definitions of Y_{L+1} , γ_l , Ω_l , and Π_l are given in Appendix B 4, where the eigenvalue range derivative is evaluated.

3. Normalization

Calculations of wave function normalizations can be performed analytically.²⁰ The normalization is given by

$$N_n^2(x) = \sum_{l=1}^L \rho_l I_{n,l}(x, z_l(x), z_{l+1}(x)) + N_{n\infty}^2(x), \quad (\text{B28})$$

with the integral evaluated by the expression³⁰

$$I_{n,l}(x, z_l(x), z_{l+1}(x)) \equiv \int_{z_l}^{z_{l+1}} \phi_{n,l}^2(x, z) dz. \quad (\text{B29})$$

This integral is evaluated to yield

$$\begin{aligned} I_{n,l} &= \left[\eta_l(x)^{-3} \left[\frac{\partial \phi_{n,l}(x, z)}{\partial z} \right]^2 - \eta_l(x)^{-1} Z_{n,l}(x, z) \right. \\ &\quad \left. \times [\phi_{n,l}(x, z)]^2 \right]_{z_l}^{z_{l+1}}, \end{aligned} \quad (\text{B30})$$

where L is the index of the last layer above the lower half-space. The lower half-space contribution is given by

$$N_{n\infty}^2(x) = \frac{\rho_{L+1} \phi_{n,L+1}^2(x, z_{L+1}(x))}{2 \sqrt{k_n^2(x) - (\omega/c_{L+1})^2}}. \quad (\text{B31})$$

4. Eigenvalue range derivative

The first-order range derivative of the eigenvalues, $\dot{k}_n(x)$, is evaluated using the eigenvalue dispersion function given by

$$\epsilon(k, \eta_l(x), Z_{T,l}, Z_{B,l}) = d_{22} + \sqrt{k^2 - (\omega/c_{L+1})^2} d_{12}, \quad (\text{B32})$$

where the matrix elements d_{12} and d_{22} correspond to the product propagator matrix given in Eq. (B17), and c_{L+1} corresponds to the lower half-space sound speed. The Airy arguments $Z_{T,l}$ and $Z_{B,l}$ are defined at the top and bottom of the l th layer, respectively.

The range derivative of the eigenvalues is calculated by

$$\frac{dk}{dx} = - \left(\frac{D\epsilon}{Dx} \right)_k \bigg/ \left(\frac{D\epsilon}{Dk} \right)_x \bigg|_{\epsilon=0}, \quad (\text{B33})$$

where $\epsilon=0$ implies $k=k_n$, and the numerator or denominator on the right-hand side is evaluated at fixed k or x , respectively. This necessarily implies that $\partial Z_{T,l}/\partial x$ and $\partial Z_{B,l}/\partial x$ are evaluated at fixed k . The explicit calculation of dk/dx is given in the following; Appendix C contains the second derivative d^2k/dx^2 .

The denominator in Eq. (B33) is given explicitly by

$$\left(\frac{D\epsilon}{Dk} \right)_x = \frac{\partial d_{22}(k)}{\partial k} + \frac{\partial d_{12}(k)}{\partial k} \sqrt{k^2 - (\omega/c_{L+1})^2} + \frac{kd_{12}(k)}{\sqrt{k^2 - (\omega/c_{L+1})^2}}, \quad (\text{B34})$$

where the $Z_{T,l}$, $Z_{B,l}$, and $\eta_l(r)$ dependence on the right-hand side is implicit.

For the l th layer, the derivatives of the propagator matrix elements with respect to k are calculated by the chain rule

$$\frac{\partial \vec{d}_l}{\partial k} = \frac{\partial \vec{d}_l}{\partial Z_{T,l}} \frac{\partial Z_{T,l}}{\partial k} + \frac{\partial \vec{d}_l}{\partial Z_{B,l}} \frac{\partial Z_{B,l}}{\partial k}, \quad (\text{B35})$$

where the vector \vec{d}_l has been defined as

$$\vec{d}_l \equiv [d_{l,11} \ d_{l,12} \ d_{l,21} \ d_{l,22}]^T \quad (\text{B36})$$

for compactness, and the derivatives of the Airy arguments with respect to k are given by

$$\left(\frac{\partial Z_{T,l}}{\partial k} \right)_x = \left(\frac{\partial Z_{B,l}}{\partial k} \right)_x = 2\eta_l^{-2}(x)k. \quad (\text{B37})$$

For convenience, the 2×2 submatrices \bar{T} , \bar{B} , and \bar{C} are defined as follows:

$$\bar{T} = \begin{bmatrix} 0 & Z_{T,l} \\ \frac{1}{\eta_l^2} & 0 \end{bmatrix}, \quad (\text{B38})$$

$$\bar{B} = \frac{-1}{\eta_l^2} \begin{bmatrix} \rho_l & \\ & \rho_{l+1} \end{bmatrix} \bar{I}, \quad (\text{B39})$$

$$\bar{C} = \frac{-\rho_{l+1}}{\rho_l} Z_{B,l} \bar{I}, \quad (\text{B40})$$

where \bar{I} corresponds to the 2×2 identity matrix

$$\bar{I} = \begin{bmatrix} 1 & 0 \\ 0 & 1 \end{bmatrix}. \quad (\text{B41})$$

The derivatives with respect to $Z_{T,l}$ and $Z_{B,l}$ in Eq. (B35) are expressed as

$$\frac{\partial \vec{d}_l}{\partial Z_{T,l}} = \eta_l(x) \begin{bmatrix} \bar{T} & \bar{0} \\ \bar{0} & \bar{T} \end{bmatrix} \vec{d}_l, \quad (\text{B42})$$

$$\frac{\partial \vec{d}_l}{\partial Z_{B,l}} = \eta_l(x) \begin{bmatrix} \bar{0} & \bar{B} \\ \bar{C} & \bar{0} \end{bmatrix} \vec{d}_l, \quad (\text{B43})$$

therefore, Eq. (B35) can be written compactly as

$$\frac{\partial \vec{d}_l}{\partial k} = \frac{2k}{\eta_l} \begin{bmatrix} \bar{T} & \bar{B} \\ \bar{C} & \bar{T} \end{bmatrix} \vec{d}_l. \quad (\text{B44})$$

The numerator of Eq. (B33) is given more explicitly by

$$\left(\frac{D\epsilon}{Dx} \right)_k = \frac{\partial d_{22}(k,x)}{\partial x} + \frac{\partial d_{12}(k,x)}{\partial x} \sqrt{k^2 - (\omega/c_{L+1})^2}. \quad (\text{B45})$$

The range derivatives of $Z_{T,l}$ and $Z_{B,l}$ at fixed k are given by

$$\left(\frac{\partial Z_{T,l}}{\partial x} \right)_k = -2\eta_l^{-3}(x) \frac{d\eta_l}{dx} [k^2 - \omega^2 a_l(x)] - \omega^2 \eta_l^{-2}(x) \frac{da_l(x)}{dx}, \quad (\text{B46})$$

$$\left(\frac{\partial Z_{B,l}}{\partial x} \right)_k = \left(\frac{\partial Z_{T,l}}{\partial x} \right)_k - \frac{d\eta_l(x)}{dx} [z_{l+1}(x) - z_l(x)] - \eta_l(x) \left[\frac{dz_{l+1}}{dx} - \frac{dz_l}{dx} \right], \quad (\text{B47})$$

where the eigenvalue, k , is considered a range-independent parameter in evaluating these terms.

The range derivatives of the propagator matrices are needed for both the wave function derivatives and the eigenvalue derivatives. Using the definitions of Z_{top} and Z_{bot} given in Eqs. (B5) and (B6), they can be written as

$$\frac{\partial \vec{d}_l}{\partial x} = \begin{bmatrix} \bar{G} & \bar{J} \\ \bar{H} & \bar{F} \end{bmatrix} \vec{d}_l, \quad (\text{B48})$$

where

$$\bar{F} = \begin{bmatrix} f_{11} & f_{12} \\ f_{21} & f_{22} \end{bmatrix}, \quad (\text{B49})$$

with matrix elements given by

$$f_{11} = \frac{1}{\eta_l(x)} \frac{d\eta_l}{dx}, \quad f_{12} = \eta_l Z_{\text{top}} \frac{\partial Z_{\text{top}}}{\partial x}, \quad (\text{B50})$$

$$f_{21} = \frac{1}{\eta_l(x)} \frac{\partial Z_{\text{top}}}{\partial x}, \quad f_{22} = 0,$$

and the remaining 2×2 matrices are given by

$$\bar{G} = \bar{F} - \frac{1}{\eta_l(x)} \frac{d\eta_l}{dx} \bar{I}, \quad (\text{B51})$$

$$\bar{H} = -\eta_l(x) \frac{\rho_{l+1}}{\rho_l} Z_{\text{bot}} \frac{\partial Z_{\text{bot}}}{\partial x} \bar{I}, \quad (\text{B52})$$

$$\bar{J} = -\frac{1}{\eta_l(x)} \frac{\rho_l}{\rho_{l+1}} \frac{\partial Z_{\text{bot}}}{\partial x} \bar{I}. \quad (\text{B53})$$

Equations (B26) and (B27), corresponding to the range derivative of the mode function's depth derivative (which

has been evaluated at the top of the waveguide), contain several definitions. They are listed here for reference:

$$\begin{aligned}
Y_{L+1} = & \frac{-\rho_{L+1} k_n \dot{k}_n}{2(k_n^2 - (\omega/c_{L+1})^2)^{3/2}} \\
& \times \left(d_{11} \psi_{n,1}(x, z_1) + d_{12} \frac{\partial \psi_{n,1}(x, z_1)}{\partial z} \right)^2 \\
& + \frac{\rho_{L+1}}{\sqrt{k_n^2 - (\omega/c_{L+1})^2}} \\
& \times \left(d_{11} \psi_{n,1}(x, z_1) + d_{12} \frac{\partial \psi_{n,1}(x, z_1)}{\partial z} \right) \\
& \times \left[\frac{\partial d_{11}}{\partial x} \psi_{n,1}(x, z_1) + \frac{\partial d_{12}}{\partial x} \frac{\partial \psi_{n,1}(x, z_1)}{\partial z} \right], \quad (B54)
\end{aligned}$$

$$\begin{aligned}
\Omega_l = \rho_l \left[\frac{2}{\eta_l^3} (e_{l,21} \chi_1 + e_{l,22} \chi_2) e_{l,21} + \frac{2}{\eta_l} \chi_1 Z_{n,l}(x, z_l) \right. \\
\left. - \frac{2}{\eta_l} Z_{n,l}(x, z_{l+1}) (e_{l,11} \chi_1 + e_{l,12} \chi_2) e_{l,11} \right], \quad (B55)
\end{aligned}$$

$$\begin{aligned}
\Pi_l = \rho_l \left[\frac{2}{\eta_l^3} (e_{l,21} \chi_1 + e_{l,22} \chi_2) e_{l,22} - \frac{2\chi_2}{\eta_l^3} \right. \\
\left. - \frac{2}{\eta_l} Z_{n,l}(x, z_{l+1}) (e_{l,11} \chi_1 + e_{l,12} \chi_2) e_{l,12} \right], \quad (B56)
\end{aligned}$$

$$\begin{aligned}
\gamma_l = \rho_l \left\{ \frac{-3}{\eta_l^4} \frac{d\eta_l}{dx} [(e_{l,21} \chi_1 + e_{l,22} \chi_2)^2 - \chi_2^2] \right. \\
+ \frac{1}{\eta_l^2} \frac{d\eta_l}{dx} [Z_{n,l}(x, z_{l+1}) (e_{l,11} \chi_1 + e_{l,22} \chi_2)^2 \\
- Z_{n,l}(x, z_l) \chi_1^2] + \frac{2}{\eta_l^3} (e_{l,21} \chi_1 + e_{l,22} \chi_2) \\
\times \left(\frac{\partial e_{l,21}}{\partial x} \chi_1 + \frac{\partial e_{l,22}}{\partial x} \chi_2 \right) - \frac{1}{\eta_l} \left[\frac{\partial Z_{n,l}(x, z_{l+1})}{\partial x} \right. \\
\times (e_{l,11} \chi_1 + e_{l,12} \chi_2)^2 - \frac{\partial Z_{n,l}(x, z_l)}{\partial x} \chi_1^2 + 2Z_{n,l}(x, z_{l+1}) \\
\left. \times (e_{l,11} \chi_1 + e_{l,12} \chi_2) \left(\frac{\partial e_{l,11}}{\partial x} \chi_1 + \frac{\partial e_{l,12}}{\partial x} \chi_2 \right) \right] \left. \right\}, \quad (B57)
\end{aligned}$$

where χ_1 and χ_2 are the components of the wave function at the top of the layer:

$$\chi_1 = \psi_{n,l}(x, z_l), \quad (B58)$$

$$\chi_2 = \frac{\partial \psi_{n,l}(x, z_l)}{\partial z}. \quad (B59)$$

APPENDIX C: SECOND-ORDER DERIVATIVES

1. Mode function range derivatives

The second derivative with respect to range, x , of the mode function can be written

$$\begin{aligned}
\frac{\partial^2 \psi_{n,l}(x, z)}{\partial x^2} = \mathcal{C} [\delta_l(z + \beta_{n,l})] + \delta_l(z + \beta_{n,l}) \\
\times [f_{n,l}(x) - z g_l(x)]^2 \mathcal{A} [\delta_l(z + \beta_{n,l})] \\
+ \mathcal{D}' [\delta_l(z + \beta_{n,l})] - z \mathcal{E}' [\delta_l(z + \beta_{n,l})]. \quad (C1)
\end{aligned}$$

The coefficients \mathcal{C} , \mathcal{D} , and \mathcal{E} are given by

$$\begin{aligned}
\mathcal{C} [\delta_l(z + \beta_{n,l})] = \ddot{A}_{n,l}(x) \text{Ai} [\delta_l(z + \beta_{n,l})] \\
+ \ddot{B}_{n,l}(x) \text{Bi} [\delta_l(z + \beta_{n,l})], \quad (C2)
\end{aligned}$$

$$\begin{aligned}
\mathcal{D} [\delta_l(z + \beta_{n,l})] = [2f_{n,l}(x) \dot{A}_{n,l}(x) + \dot{f}_{n,l}(x) A_{n,l}(x)] \\
\times \text{Ai} [\delta_l(z + \beta_{n,l})] + [2f_{n,l}(x) \dot{B}_{n,l}(x) \\
+ \dot{f}_{n,l}(x) B_{n,l}(x)] \text{Bi} [\delta_l(z + \beta_{n,l})], \quad (C3)
\end{aligned}$$

$$\begin{aligned}
\mathcal{E} [\delta_l(z + \beta_{n,l})] = [2g_l(x) \dot{A}_{n,l}(x) + \dot{g}_l(x) A_{n,l}(x)] \\
\times \text{Ai} [\delta_l(z + \beta_{n,l})] + [2g_l(x) \dot{B}_{n,l}(x) \\
+ \dot{g}_{n,l}(x) B_{n,l}(x)] \text{Bi} [\delta_l(z + \beta_{n,l})], \quad (C4)
\end{aligned}$$

where again the dot implies a derivative with respect to range. The coefficients \mathcal{D} and \mathcal{E} are also expressed in terms of the \mathcal{A} and \mathcal{B} coefficients by

$$\mathcal{D} = 2f_{n,l}(x) \mathcal{B} + \dot{f}_{n,l}(x) \mathcal{A} \quad (C5)$$

and

$$\mathcal{E} = 2g_l(x) \mathcal{B} + \dot{g}_l(x) \mathcal{A}, \quad (C6)$$

respectively.

The second derivative with respect to range of the mode coefficients A_l and B_l is given by

$$\frac{\partial^2}{\partial x^2} \begin{bmatrix} A_{n,l} \\ -B_{n,l} \end{bmatrix} = \pi \begin{bmatrix} \text{Bi}(Z_{\text{top}}) & \text{Bi}'(Z_{\text{top}}) \\ \text{Ai}(Z_{\text{top}}) & \text{Ai}'(Z_{\text{top}}) \end{bmatrix} \begin{bmatrix} X_1(x, z_l(x)) \\ X_2(x, z_l(x)) \end{bmatrix}, \quad (C7)$$

where Z_{top} was defined in Eq. (B5) and X_1 and X_2 are calculated using Eqs. (45) and (46).

Second-order range derivatives of the Airy arguments are calculated using Eqs. (16), (B7), and (B10). For example,

$$\frac{\partial^2 Z_{n,l}(x, z_l(x))}{\partial x^2} = \frac{\partial \tilde{f}_{n,l}(x)}{\partial x}. \quad (C8)$$

The second derivative with respect to range of the wave function is obtained from Eq. (B19). Explicit components are easily obtained from the resulting equation or from taking the range derivative of Eqs. (B21) and (B22) and noting that

$$\frac{\partial^2}{\partial x^2} \psi_{n,1}(x, z_1) = 0. \quad (\text{C9})$$

The range derivative of Eq. (B25) is also needed to evaluate this second derivative of the wave function, and is given by

$$\begin{aligned} & \frac{\partial^2}{\partial x^2} \left[\frac{\partial \psi_{n,1}(x, z_1)}{\partial z} \right] \\ &= - \frac{(\partial \mathcal{N}(x)/\partial x) \mathcal{D}(x) - (\partial \mathcal{D}(x)/\partial x) \mathcal{N}(x)}{[\mathcal{D}(x)]^2}, \end{aligned} \quad (\text{C10})$$

where $\partial \mathcal{N}(x)/\partial x$ and $\partial \mathcal{D}(x)/\partial x$ are evaluated using Eqs. (B26) and (B27), respectively.

The derivative terms $\partial Y_{L+1}/\partial x$, $\partial \Omega_l/\partial x$, $\partial \Pi_l/\partial x$, and $\partial \gamma_l/\partial x$, which are needed to calculate Eq. (C10), can be calculated in a straightforward manner from Eqs. (B54) to (B59).

2. Eigenvalue range derivative

The second derivative of the eigenvalue with respect to range is calculated from

$$\begin{aligned} \frac{d^2 k}{dx^2} &= \frac{d}{dx} \left(\frac{d\epsilon}{dx} \bigg/ \frac{d\epsilon}{dk} \right) \\ &= \left(\left(\frac{d\epsilon}{dk} \right)_x \left(\frac{d^2 \epsilon}{dx^2} \right)_k - \left(\frac{d\epsilon}{dx} \right)_k \left(\frac{d^2 \epsilon}{dx dk} \right)_{x,k} \right) \bigg/ \left[\frac{d\epsilon}{dk} \right]_x^2, \end{aligned} \quad (\text{C11})$$

where the x, k subscript implies a derivative with respect to k at fixed x , then with respect to x at fixed k . The first-order derivatives were evaluated using Eqs. (B34) and (B45). Second-order derivative terms can be written explicitly from Eqs. (B44) and (B48). The result for the mixed derivative term is

$$\begin{aligned} \frac{\partial^2 \vec{d}_l}{\partial x \partial k} &= \left\{ \frac{-2k}{\eta_l^2} \frac{d\eta_l}{dx} \begin{bmatrix} \bar{T} & \bar{B} \\ \bar{C} & \bar{T} \end{bmatrix} + \frac{2k}{\eta_l} \frac{\partial}{\partial x} \left[\begin{bmatrix} \bar{T} & \bar{B} \\ \bar{C} & \bar{T} \end{bmatrix} \right] \right. \\ &\quad \left. + \frac{2k}{\eta_l} \begin{bmatrix} \bar{T} & \bar{B} \\ \bar{C} & \bar{T} \end{bmatrix} \begin{bmatrix} \bar{G} & \bar{J} \\ \bar{H} & \bar{F} \end{bmatrix} \right\} \vec{d}_l, \end{aligned} \quad (\text{C12})$$

where \vec{d}_l was defined in Eq. (B36) and where $\partial \bar{T}/\partial x$, $\partial \bar{B}/\partial x$, and $\partial \bar{C}/\partial x$ are evaluated straightforwardly from Eqs. (B38), (B39), and (B40), respectively. Similarly, from Eq. (B48), the second range derivative is

$$\frac{\partial^2 \vec{d}_l}{\partial x^2} = \left\{ \frac{\partial}{\partial x} \left[\begin{bmatrix} \bar{G} & \bar{J} \\ \bar{H} & \bar{F} \end{bmatrix} \right] + \begin{bmatrix} \bar{G} & \bar{J} \\ \bar{H} & \bar{F} \end{bmatrix}^2 \right\} \vec{d}_l, \quad (\text{C13})$$

and $\partial \bar{F}/\partial x$, $\partial \bar{G}/\partial x$, $\partial \bar{H}/\partial x$, and $\partial \bar{J}/\partial x$ are evaluated from Eqs. (B49), (B51), (B52), and (B53), respectively.

APPENDIX D: GENERALIZED RUTHERFORD COEFFICIENTS

In this section the key steps to obtain the Rutherford form of the coupling coefficients are presented. First, the

B_{mn} coefficient is obtained by differentiating with respect to range, r , the depth equation written in the form

$$\frac{\partial^2 \psi_n}{\partial z^2} + (k^2 - k_n^2) \psi_n = 0. \quad (\text{D1})$$

The result is

$$\frac{\partial^2 \dot{\psi}_n}{\partial z^2} + 2(k\dot{k} - k_n \dot{k}_n) \psi_n + (k^2 - k_n^2) \dot{\psi}_n = 0, \quad (\text{D2})$$

where the dot designates the range derivative. This equation is multiplied by $(1/\rho(z)) \psi_m$ and then integrated over the z coordinate from 0 to ∞ . The result is given by

$$\begin{aligned} J_1 + \int_0^\infty \frac{1}{\rho} \psi_m \dot{\psi}_n (k^2 - k_n^2) dz \\ = 2k_n \dot{k}_n \delta_{m,n} - 2 \int_0^\infty \frac{1}{\rho(z)} k \dot{k} \psi_m \psi_n dz, \end{aligned} \quad (\text{D3})$$

where

$$J_1 \equiv \int_0^\infty \frac{1}{\rho} \psi_m \frac{\partial^2 \dot{\psi}_n}{\partial z^2} dz. \quad (\text{D4})$$

Next, the first term of this resulting equation, J_1 , is twice integrated by parts, to yield

$$J_1 = \sum_{l=1}^{L+1} \left[\int_{z_l}^{z_{l+1}} \frac{1}{\rho_l} \dot{\psi}_{n,l} \frac{\partial^2 \psi_{m,l}}{\partial z^2} \right] + J_2 - J_3, \quad (\text{D5})$$

where

$$J_2 = \sum_{l=1}^{L+1} J_{2,l}, \quad J_{2,l} = \frac{1}{\rho_l} \psi_{m,l} \frac{\partial \dot{\psi}_{n,l}}{\partial z} \bigg|_{z_l}^{z_{l+1}}, \quad (\text{D6})$$

$$J_3 = \sum_{l=1}^{L+1} J_{3,l}, \quad J_{3,l} = \frac{1}{\rho_l} \dot{\psi}_{n,l} \frac{\partial \psi_{m,l}}{\partial z} \bigg|_{z_l}^{z_{l+1}}, \quad (\text{D7})$$

and the $L+1$ layer corresponds to the integral evaluated from z_{L+1} to ∞ .

The boundary conditions are given by

$$\psi_{m,1}(z=z_1=0) = \dot{\psi}_{m,1}(z=z_1=0) = 0, \quad (\text{D8})$$

$$\psi_{m,\infty}(z=\infty) = \dot{\psi}_{m,\infty}(z=\infty) = 0, \quad (\text{D9})$$

$$\psi_{m,l} = \psi_{m,l+1} \big|_{z=z_{l+1}}, \quad (\text{D10})$$

$$\frac{1}{\rho_l} \frac{\partial \psi_{m,l}}{\partial z} = \frac{1}{\rho_{l+1}} \frac{\partial \psi_{m,l+1}}{\partial z} \bigg|_{z=z_{l+1}}, \quad (\text{D11})$$

and are used to evaluate $J_{2,l}$ and $J_{3,l}$ by grouping together terms that are evaluated at each layer interface, $z=z_{l+1}$. The result is

$$J_2 = \sum_{l=1}^L J_{2,l} = \sum_{l=1}^L \psi_{m,l} \left[\frac{1}{\rho_l} \frac{\partial \dot{\psi}_{n,l}}{\partial z} - \frac{1}{\rho_{l+1}} \frac{\partial \dot{\psi}_{n,l+1}}{\partial z} \right] \bigg|_{z_{l+1}}, \quad (\text{D12})$$

$$J_3 = \sum_{l=1}^L J_{3,l} = \sum_{l=1}^L \frac{1}{\rho_l} \frac{\partial \psi_{m,l}}{\partial z} [\dot{\psi}_{n,l} - \dot{\psi}_{n,l+1}]|_{z_{l+1}}, \quad (\text{D13})$$

where the sum now runs only up to the L th layer.

These expressions are further simplified by taking the total range derivative of the boundary conditions, substituting into the depth equation, and again using the boundary conditions. The final form for these expressions is given by

$$J_2 = \sum_{l=1}^L \frac{\partial z_{l+1}}{\partial r} (\psi_{m,l} \psi_{n,l})_{z=z_{l+1}} \times \left[\frac{1}{\rho_{l+1}} (k_n^2(r) - k_{l+1}^2(r)) - \frac{1}{\rho_l} (k_n^2(r) - k_l^2(r)) \right], \quad (\text{D14})$$

$$J_3 = \sum_{l=1}^L \frac{\partial z_{l+1}}{\partial r} \frac{\rho_{l+1}}{\rho_l} \left(\frac{\partial \psi_{m,l}}{\partial z} \frac{\partial \psi_{n,l}}{\partial z} \right)_{z=z_{l+1}} \left[\frac{1}{\rho_l} - \frac{1}{\rho_{l+1}} \right]. \quad (\text{D15})$$

The resulting nondiagonal coupling coefficient was given in Eq. (47).

The diagonal terms \bar{B}_{mm} are identically zero since the contributions from the coupling coefficient, $2\bar{B}_{mm}$, are equal to minus the boundary integral contribution. This can be shown by taking the range derivative of the orthonormality relation for the mode functions. Written in terms of layers, this derivative is given by

$$\begin{aligned} \frac{d}{dr} \left[\sum_{l=1}^{L+1} \left\{ \int_{z_l}^{z_{l+1}} \frac{1}{\rho_l} \psi_{m,l} \psi_{n,l} dz \right\} \right] \\ = \sum_{l=1}^{L+1} \int_{z_l}^{z_{l+1}} \frac{1}{\rho_l} (\dot{\psi}_{m,l} \psi_{n,l} + \psi_{m,l} \dot{\psi}_{n,l}) dz \\ + \sum_{l=1}^{L+1} \frac{1}{\rho_l} \left(\frac{dz_{l+1}}{dr} \psi_{m,l}(r, z_{l+1}) \psi_{n,l}(r, z_{l+1}) \right. \\ \left. - \frac{dz_l}{dr} \psi_{m,l}(r, z_l) \psi_{n,l}(r, z_l) \right) = 0. \end{aligned} \quad (\text{D16})$$

The first term on the right-hand side of Eq. (D16) corresponds to the coupling coefficients and the second term can be grouped by recombining the terms with similar depths, z_{l+1} . The result after applying the layer boundary conditions on the wave functions is

$$\begin{aligned} \frac{1}{2} \bar{B}_{mn} + \frac{1}{2} \bar{B}_{nm} \\ = \bar{B}_{mn}^{(s)} \\ = - \sum_{l=1}^{L+1} \frac{dz_{l+1}}{dr} \left(\frac{1}{\rho_l} - \frac{1}{\rho_{l+1}} \right) \psi_{m,l}(r, z_{l+1}) \psi_{n,l}(r, z_{l+1}), \end{aligned} \quad (\text{D17})$$

which cancels out the contributions from I_{mn}^B given in Eq. (19).

The second coupling coefficient is derived from the range derivative of the first coupling coefficient, $\bar{B}_{mn} = 2 \int_0^\infty (1/\rho) \psi_m \dot{\psi}_n dz$. To evaluate this term, the integral is

again divided into layers, and the range derivatives over the layers are grouped in terms of similar z_{l+1} depth evaluations. The result is given by

$$\begin{aligned} \frac{\dot{\bar{B}}_{mn}}{2} = \bar{C}_{mn} + \int_0^\infty \frac{1}{\rho} \dot{\psi}_m \dot{\psi}_n dz + \sum_{l=1}^L \left[\frac{dz_{l+1}}{dr} \psi_{m,l}(r, z_{l+1}) \right. \\ \left. \times \dot{\psi}_{n,l}(r, z_{l+1}) \left(\frac{1}{\rho_l} - \frac{1}{\rho_{l+1}} \right) \right]. \end{aligned} \quad (\text{D18})$$

The last step is to simplify the integral on the right-hand side of Eq. (D18). The method used, which was given in Ref. 3, begins by differentiating the completeness relation, Eq. (5), with respect to range, and then uses the completeness relation in the result. Explicitly,

$$\begin{aligned} \sum_p \dot{\psi}_p(r, z) \psi_p(r, z') + \sum_p \psi_p(r, z) \dot{\psi}_p(r, z') \\ = \dot{\rho} \delta(z - z') = \dot{\rho} \sum_p \frac{1}{\rho(z)} \psi_p(r, z) \psi_p(r, z'). \end{aligned} \quad (\text{D19})$$

Next, Eq. (D19) is multiplied by $(1/\rho) \psi_m(r, z)$ and integrated over z . This result is further simplified by using the orthonormality relation and also by evaluating the range derivative of the density function by the relation

$$\dot{\rho}(r, z) = \frac{dz_{l+1}}{dr} [\rho_l \delta(z - z_{l+1}^-) - \rho_{l+1} \delta(z - z_{l+1}^+)], \quad (\text{D20})$$

where z^- corresponds to just above the $(l+1)$ th interface, and z^+ corresponds to just below it. After rearranging the terms and changing the arbitrary variable z' to z , Eq. (D19) becomes

$$\begin{aligned} \sum_p \delta_{mp} \dot{\psi}_p(r, z) = \dot{\psi}_m(r, z) \\ = - \sum_p \left\{ \frac{\bar{B}_{mp}}{2} - \sum_{l=1}^L \frac{dz_{l+1}}{dr} \left(\frac{1}{\rho_l} - \frac{1}{\rho_{l+1}} \right) \right. \\ \left. \times \psi_m(r, z_{l+1}) \psi_p(r, z_{l+1}) \right\} \psi_p(r, z). \end{aligned} \quad (\text{D21})$$

Defining the term in the curly braces in Eq. (D21) as E_{mp} , and using the orthonormality of the wave functions, yields

$$\int_0^\infty \frac{1}{\rho} \dot{\psi}_m(r, z) \dot{\psi}_n(r, z) dz = \sum_p E_{mp} E_{np}. \quad (\text{D22})$$

Solving for \bar{C}_{mn} in Eq. (D18) gives Eq. (50).

¹A. D. Pierce, "Extension of the method of normal modes to sound propagation in an almost-stratified medium," J. Acoust. Soc. Am. **37**, 19–27 (1965).

²D. M. Milder, "Ray and wave invariants for SOFAR channel propagation," J. Acoust. Soc. Am. **46**, 1259–1263 (1969).

³S. R. Rutherford, "An examination of coupled mode theory as applied to underwater sound propagation," ARL:UT Technical Report No. ARL-TR-79-44, Applied Research Laboratories, The University of Texas at Austin, 1979.

⁴S. R. Rutherford and K. E. Hawker, "Consistent coupled mode theory of sound for a class of non separable problems," J. Acoust. Soc. Am. **70**, 554–564 (1981).

- ⁵J. A. Fawcett, "A derivation of the differential equations in coupled-mode propagation," J. Acoust. Soc. Am. **92**, 290–295 (1992).
- ⁶G. Gillette, "Coupled modes in a waveguide with a range-dependent rigid basement," J. Acoust. Soc. Am. **95**, 187–200 (1994).
- ⁷R. B. Evans, "A coupled mode solution for acoustic propagation in a waveguide with stepwise variations of a penetrable bottom," J. Acoust. Soc. Am. **74**, 188–195 (1983).
- ⁸M. B. Porter, C. M. Ferla, and F. B. Jensen, "Coupled modes for rapid range-dependent modeling," *Proceedings of the Second Parabolic Equation Workshop*, 6–9 May 1991, Slidell, Louisiana (Naval Research Laboratory, Stennis Space Center, MS, 1993), NRL/BE/7181-93-0001, pp. 271–281.
- ⁹O. A. Godin, "A note on differential equations of coupled-mode propagation in fluids," J. Acoust. Soc. Am. **103**, 159–168 (1998).
- ¹⁰C. Allan Boyles, *Acoustic Waveguides: Applications to Ocean Science* (Wiley, New York, 1984), Chap. 4.
- ¹¹A. Bohr and B. R. Mottelson, "Collective and individual-particle aspects of nuclear structure," K. Dan. Vidensk. Selsk. Mat. Fys. Medd. **27**, 1–169 (1953).
- ¹²T. Tamura, "Analyses of the scattering of nuclear particles by collective nuclei in terms of the coupled channel calculation," Rev. Mod. Phys. **37**, 679–708 (1965).
- ¹³T. Tamura, "Computer program Jupiter-1 for coupled-channel calculations," Oak Ridge National Laboratories Technical Report No. 4152, UC-32-Mathematics and Computers, Oak Ridge, Tennessee, 1967.
- ¹⁴T. Udagawa and B. T. Kim, "Random-phase-approximation calculations of nuclear response in the continuum," Phys. Rev. C **40**, 2271–2275 (1989).
- ¹⁵B. T. Kim and T. Udagawa, "Method of nonlocal optical model calculations," Phys. Rev. C **42**, 1147–1149 (1990).
- ¹⁶T. Udagawa, S. W. Hong, and F. Osterfeld, "Delta excitations in nuclei," Phys. Lett. B **245**, 1–6 (1990).
- ¹⁷D. P. Knobles and T. Udagawa, "Random-phase approximation calculations of the nuclear response in the continuum using a finite-range interaction," Nucl. Phys. A **533**, 189–214 (1991).
- ¹⁸R. R. Whitehead, A. Watt, B. J. Cole, and I. Morrison, "Computational methods for shell-model calculations," Adv. Nucl. Phys. **9**, 123–176 (1977).
- ¹⁹D. P. Knobles, "Solutions of coupled-mode equations with a large dimension in underwater acoustics," J. Acoust. Soc. Am. **96**, 1741–1747 (1994).
- ²⁰S. J. Levinson *et al.*, "An efficient and robust method for underwater acoustic normal mode computations," J. Acoust. Soc. Am. **97**, 1576–1585 (1994).
- ²¹R. A. Koch and D. P. Knobles, "A practical application of the Galerkin method to the broadband calculation of normal modes for underwater acoustics," J. Acoust. Soc. Am. **98**, 1682–1698 (1995).
- ²²J. E. Lemond, R. A. Koch, and R. Patterson, "NAUTILUS, A broadband normal mode modeling package beta version 0.6," Applied Research Laboratories, The University of Texas at Austin, 1997, Tech. Lett., ARL-TL-EV-97-21.
- ²³E. K. Westwood, C. T. Tindle, and N. R. Chapman, "A normal mode model for multilayered acoustoelastic ocean environments based on an analytic reflection coefficient method," J. Acoust. Soc. Am. **95**, 2908 (1994).
- ²⁴C. T. Tindle and Z. Y. Zhang, "Continuous modes and shallow water sound propagation," *OCEANS '93: Engineering in Harmony with the Ocean, Proceedings I, 18–21 October*, Victoria, British Columbia, Canada (IEEE, New York, 1993), pp. 81–86.
- ²⁵R. G. Gordon, "New method for constructing wave functions for bound states and scattering," J. Chem. Phys. **51**, 14–25 (1969).
- ²⁶P. M. Morse and H. A. Feshbach, *Methods of Theoretical Physics* (McGraw-Hill, New York, 1953), Chap. 7, pp. 825–832.
- ²⁷G. V. Frisk, *Ocean and Seabed Acoustics* (Prentice-Hall, Englewood Cliffs, NJ, 1994), Appendix B, pp. 275–280.
- ²⁸F. B. Jensen and C. M. Ferla, "Numerical solutions of range-dependent benchmark problems in ocean acoustics," J. Acoust. Soc. Am. **87**, 1499–1510 (1990).
- ²⁹M. J. Buckingham and A. Tolstoy, "An analytical solution for benchmark problem. 1. The 'ideal' wedge," J. Acoust. Soc. Am. **87**, 1511–1513 (1990).
- ³⁰H. P. Bucker, "Sound propagation in a channel with lossy boundaries," J. Acoust. Soc. Am. **48**, 1187–1194 (1970).

Comparing Kirchhoff-approximation and boundary-element models for computing gadoid target strengths

Kenneth G. Foote^{a)}

Woods Hole Oceanographic Institution, Woods Hole, Massachusetts 02543

David T. I. Francis

School of Electronic and Electrical Engineering, University of Birmingham, Edgbaston, Birmingham B15 2TT, United Kingdom

(Received 16 April 2001; revised 4 December 2001; accepted 14 January 2002)

To establish the validity of the boundary-element method (BEM) for modeling scattering by swimbladder-bearing fish, the BEM is exercised in several ways. In a computation of backscattering by a 50-mm-diam spherical void in sea water at the four frequencies 38.1, 49.6, 68.4, and 120.4 kHz, agreement with the analytical solution is excellent. In computations of target strength as a function of tilt angle for each of 15 surface-adapted gadoids for which the swimbladders were earlier mapped, BEM results are in close agreement with Kirchhoff-approximation-model results at each of the same four frequencies. When averaged with respect to various tilt angle distributions and combined by regression analysis, the two models yield similar results. Comparisons with corresponding values derived from measured target strength functions of the same 15 gadoid specimens are fair, especially for the tilt angle distribution with the greatest standard deviation, namely 16°. © 2002 Acoustical Society of America. [DOI: 10.1121/1.1458939]

PACS numbers: 43.30.Gv, 43.30.Sf [DLB]

I. INTRODUCTION

Knowledge of fish target strength has long been recognized to be vitally important in acoustic measurements of fish density, witnessed by the bibliographies in Refs. 1–5. In the echo integration method, it appears through the backscattering cross section as a divisor of the area backscattering coefficient or like proportional quantity.⁶ In the echo counting method, it appears in the expression for the acoustic sampling volume.⁷

There is a multiplicity of methods to determine target strength. The 20 or so methods cited in a 1991 study³ have since been augmented significantly by a number of new techniques, including both empirical methods^{8,9} and theoretical models, especially those based on the deformed-cylinder model¹⁰ and boundary-element method.¹¹ These have been accompanied by novel applications, for example, to salmon and trout,^{8,9} cod (*Gadus morhua*),¹² orange roughy (*Hoplostethus atlanticus*),¹³ and pollack (*Pollachius pollachius*).^{14,15}

Modeling fish target strength, in particular, offers opportunities of investigation that may otherwise be unrealizable or exceedingly cumbersome, as in the case of orange roughy, a fish that resides at 700–1500 m depth.¹⁶ At the same time, models generally have a domain of applicability that must be defined and respected in applications.

A number of distinct scattering models have been applied to fish. These have been based principally on simple shapes such as the sphere at low frequencies^{17–19} and prolate ellipsoid,^{20–22} or the actual shape,^{14,15,23–26} called “mapping” method by McClatchie *et al.*²⁵ Only the first two models have exact solutions in general, thus the matter of approxi-

mation must be addressed, at least for realistic shapes at relatively high frequencies, where the wavelength is not very long compared to the size of significant scattering organs.^{23,24}

The deformed fluid-cylinder model^{10,27–29} has been very popular and has been the object of a major study.³⁰ Essentially, it reduces an observed shape to a series of axisymmetric cylinders. The method has been realized by Clay and Horne for Atlantic cod,¹² McClatchie and Ye for orange roughy,¹³ McClatchie *et al.* for barracouta (*Thyrstites atun*), red cod (*Pseudophycis bachus*), and southern blue whiting (*Micromesistius australis*),²⁵ and Sawada *et al.* for walleye pollock (*Theragra chalcogramma*).²² Excepting the cited case of Atlantic cod, each model has been based entirely on the swimbladder as a deformed cylinder. The swimbladder is important in the Atlantic cod model, but this includes other parts of the fish too, again represented as finite cylinders.¹²

The exact shape of the swimbladder has also been considered more directly in the Kirchhoff-approximation model for pollack and saithe (*Pollachius virens*),²³ walleye pollock,²⁴ and southern blue whiting.²⁶

All of the high-frequency models cited so far are similar in their neglect of diffraction. To remedy this, the boundary-element method (BEM)¹¹ has begun to be applied in modeling scattering by swimbladder-bearing fish.^{14,15}

In addition to treating diffraction, the BEM allows use of general conditions on the swimbladder boundary surface, with explicit representation of the internal fluid. Thus the BEM can also be used to study pressure-dependent effects, which are otherwise precluded by the standard Kirchhoff-approximation model. Establishing the validity of the BEM for a pressure-release surface is important for the larger program being introduced.

The present aim is to describe the two basic models that

^{a)}Electronic mail: kfoote@whoi.edu

represent the swimbladder by its actual shape, namely the Kirchhoff-approximation model and the BEM, but both assuming a pressure-release boundary condition. Application of these to historical swimbladder morphometric data is described. Independent validation of the two methods is addressed, and computations with the two models are compared.

II. KIRCHHOFF-APPROXIMATION MODEL

In the Kirchhoff approximation, the field on the scattering surface is assumed to be known *a priori*. For a swimbladder-bearing fish at rather high frequencies, or wavelengths which are rather small compared to the maximum length of the swimbladder, the fish is represented by a pressure-release surface conforming to the inner wall of the swimbladder.^{23,24} The normal component of particle velocity on the scattering surface is assumed to be equal to that of the incident field on the directly insonified part of the surface, and zero on the geometrically shadowed part of the surface.

Mathematically, the farfield backscattering amplitude in this approximation is

$$f = \lambda^{-1} \oint_S \exp(2i\mathbf{k} \cdot \mathbf{r}) \mathcal{H}(\hat{\mathbf{k}} \cdot \hat{\mathbf{n}}) \hat{\mathbf{k}} \cdot \hat{\mathbf{n}} dS, \quad (1)$$

where λ is the acoustic wavelength, \mathbf{k} is the wave vector in the source or backscattering direction $\hat{\mathbf{k}} = \mathbf{k}/k$, \mathbf{r} is the position vector of the surface element with infinitesimal area dS , $\hat{\mathbf{n}}$ is the unit normal to dS at \mathbf{r} , and $\mathcal{H}(x)$ is the Heaviside step function with values 1 for $x > 0$, $\frac{1}{2}$ for $x = 0$, and 0 for $x < 0$.

The integration in Eq. (1) is performed numerically using Gauss quadrature over curvilinear surface elements on which the position vector \mathbf{r} is interpolated quadratically from nodal values. The integrand is evaluated at each integration, or Gauss, point using the interpolated value of \mathbf{r} . A good representation of the phase, as given by the factor $\exp(2i\mathbf{k} \cdot \mathbf{r})$, depends on the separation of these points. If the integration were to be performed by primitive Riemann summation, then the points should be closer than about $\lambda/16$. However, the point-separation condition is undoubtedly relaxed by the use of Gauss quadrature. If the polynomial fit assumed by Gauss quadrature is of order 2 or higher, a good representation of the wave form should be obtained for a point separation up to $\lambda/6$. For seven-point quadrature on six-node triangular elements, with nodes at the corners and midsides of the elements, the Gauss point separation is at most 0.8 times the nodal separation. A similar relationship exists for eight-node quadrilateral elements using 3×3 or more Gauss points. A condition for validity of the numerical integration, that the nodal separation should be less than $\lambda/5$, is therefore tentatively suggested. This translates to a condition that the element side-to-wavelength ratio should be less than $2/5$. In order to give commonality with the corresponding condition in the case of the boundary-element method, to be discussed in Sec. III, the slightly stricter ratio of $1/3$ is adopted in this paper for assessing the frequency range of validity of a given mesh. The element meshes are described in Sec. IV.

The backscattering cross section is

$$\sigma = 4\pi |f|^2. \quad (2)$$

The target strength is the logarithmic expression of σ ,

$$\text{TS} = 10 \log \left[\frac{\sigma}{4\pi r_0^2} \right], \quad (3)$$

where r_0 is a reference distance, assumed here to be 1 m.

III. BOUNDARY-ELEMENT METHOD

To develop the acoustic boundary-element method (BEM), the wave equation for the pressure p is reduced to the Helmholtz form by assuming the harmonic time dependence $\exp(i\omega t)$, where ω is the angular frequency in radians per second, hence $\nabla^2 p + k^2 p = 0$, where $k = \omega/c$ is the wave number. This is rewritten in integral form, in which the pressure at any point is expressed in terms of the acoustic pressure and normal displacement u on the scattering surface S . This surface is subdivided into elements, and the pressure and displacement distributions on S are represented by discrete values, p_i and u_i , respectively, at each node i associated with these elements. The standard Helmholtz integral equation suffers from singularities at certain critical frequencies, which are dense at high frequencies. To overcome this problem, the integral is combined with a second integral developed from the first by differentiating with respect to the normal direction at the surface.³¹ In principle, the two equations are combined by adding the standard form evaluated at each node of each element to a multiple α of the normal-derivative form evaluated at the centroid of that element in the local coordinate system.¹¹ The resulting equation can be written thus:

$$\mathbf{A}\mathbf{p} = \mathbf{B}\mathbf{u} - \mathbf{p}_{\text{inc}} - \alpha \frac{\partial \mathbf{p}_{\text{inc}}}{\partial n}. \quad (4)$$

If the swimbladder is assumed to be ideally pressure-releasing, $p_i = 0$ for all i , and Eq. (4) can be solved directly for the nodal normal displacements:

$$\mathbf{u} = \mathbf{B}^{-1} \left(\mathbf{p}_{\text{inc}} + \alpha \frac{\partial \mathbf{p}_{\text{inc}}}{\partial n} \right). \quad (5)$$

The coefficients of the matrix \mathbf{B} are assembled from local matrices pertaining to each element of the mesh. With the calculation point of the Helmholtz integral taken at node i , with position \mathbf{r}_i , integration over element m provides the following coefficients in the standard formulation:

$$b_{mn}^{(1)}(\mathbf{r}_i) = \rho \omega^2 \int_{S_m} N_n(\mathbf{q}) \cos \theta_{mn} G(\mathbf{r}_i, \mathbf{q}) dS_q, \quad (6)$$

where ρ is the fluid density, \mathbf{q} is the position vector of the integration point on the element surface S_m , G is the Green's function, given by $G(\mathbf{r}_i, \mathbf{q}) = e^{-ik|\mathbf{r}_i - \mathbf{q}|} / 4\pi |\mathbf{r}_i - \mathbf{q}|$, n is the local nodal label, and $N_n(\mathbf{q})$ ($n = 1, 2, \dots, 6$ for triangular elements, $n = 1, 2, \dots, 8$ for quadrilateral elements) are the shape functions, which are of the standard second-order (quadratic) form.³² The factor $\cos \theta_{mn}$ is included to allow for the deviation θ_{mn} of the normal to the element m at local node n from the mean normal at that node. The mean normal at a node is

TABLE I. Properties of the 15 specimens whose swimbladder surfaces have been remapped, based on the original mapping (Ref. 23) with n_{tri} small triangular facets, by n_{elem} curvilinear elements with n_{nodes} nodes. The nodal separation distance such that 99% of neighboring separations are smaller and the maximum nodal separation are both specified.

Fish No.	Species	Length (cm)	Mass (g)	Ref. 23 n_{tri}	New meshes		Swimbladder		Nodal separation	
					n_{elem}	n_{nodes}	Surface area (cm ²)	Volume (cm ³)	99% limit (mm)	Max (mm)
201	Pollack	31.5	195	5 546	1168	3364	33.01	6.91	1.20	2.21
202	Pollack	44.0	533	9 965	1389	4041	58.83	16.33	1.37	1.77
204	Pollack	35.5	321	6 562	1078	3116	42.39	10.03	1.41	1.72
205	Pollack	39.0	380	7 171	1107	3181	45.75	11.34	1.43	1.93
206	Pollack	35.0	287	5 379	1159	3347	31.37	7.75	1.17	1.46
207	Pollack	44.5	635	8 695	1487	4363	65.24	19.15	1.34	1.61
209	Saithe	38.5	385	6 762	1501	4387	43.29	10.08	1.06	1.39
213	Pollack	34.5	259	10 192	1039	2935	34.11	7.83	1.33	1.61
214	Pollack	39.0	406	7 649	1164	3362	44.14	10.15	1.34	1.53
215	Pollack	37.0	332	5 265	1076	3092	38.89	8.75	1.34	1.74
216	Pollack	36.5	343	6 436	1062	3060	43.33	10.85	1.40	1.64
217	Pollack	34.5	253	5 500	962	2764	34.61	7.11	1.32	1.46
218	Pollack	32.5	257	4 689	1327	3879	29.75	6.27	1.00	1.39
219	Pollack	35.5	292	5 106	1039	3005	35.74	8.15	1.27	1.53
220	Saithe	38.0	406	8 968	1321	3857	44.32	10.46	1.13	1.32

defined as the average of the normals at the node on all contiguous elements weighted by the respective differential surface area.

The normal-derivative form of the Helmholtz integral equation, calculated at the centroids $\bar{\mathbf{r}}_l$ of the elements, similarly provides coefficients as follows:

$$b_{mn}^{(2)}(\bar{\mathbf{r}}_l) = \rho \omega^2 \int_{S_m} N_n(\mathbf{q}) \cos \theta_{mn} \frac{\partial G(\bar{\mathbf{r}}_l, \mathbf{q})}{\partial n_r} dS_q, \quad (7)$$

where the normal derivative is evaluated at the centroid. These are combined with the previous coefficients by adding a multiple of $b_{mn}^{(2)}(\bar{\mathbf{r}}_l)$ for all elements l on which global node i lies, i.e.,

$$b_{mn}(\mathbf{r}_i) = b_{mn}^{(1)}(\mathbf{r}_i) + \alpha_i \sum_{l:i \in S_l} b_{mn}^{(2)}(\bar{\mathbf{r}}_l), \quad (8)$$

where the combination factor α_i is taken to be $-i/kM_i$, where M_i is the number of elements meeting at node i .^{11,33,34}

The use of the centroids, rather than the nodes, as the calculation points for the normal-derivative form is found to be sufficient to overcome the problem of the critical frequencies while not increasing the computational effort unduly.¹¹

The integrals are evaluated numerically using Gauss quadrature.

The coefficients $b_{mn}(\mathbf{r}_i)$ are assembled into the global matrix \mathbf{B} by summing the coefficients that correspond to the same global node, thus

$$B_{ij} = \sum_{m,n:C(m,n)=j} b_{mn}(\mathbf{r}_i), \quad (9)$$

where $C(m,n)$ is the global node label of local node n on element m . The source terms in Eq. (4) are evaluated thus:

$$\mathbf{p}_{\text{inc}}(\mathbf{r}_i) + \alpha_i \sum_{l:i \in S_l} \frac{\partial \mathbf{p}_{\text{inc}}(\bar{\mathbf{r}}_l)}{\partial n_r}$$

Given the solution for \mathbf{u} from Eq. (5), the scattered pressure at any exterior point \mathbf{r} is obtained from the standard

integral equation by calculating coefficients similar to $b_{mn}^{(1)}(\mathbf{r}_i)$ but with \mathbf{r}_i replaced by the position vector \mathbf{r} :

$$b_j^{(3)}(\mathbf{r}) = \rho \omega^2 \sum_{m,n:C(m,n)=j} \int_{S_m} N_n(\mathbf{q}) \cos \theta_{mn} G(\mathbf{r}, \mathbf{q}) dS_q \quad (10)$$

and then

$$p(\mathbf{r}) = -\mathbf{b}^{(3)}(\mathbf{r}) \cdot \mathbf{u}. \quad (11)$$

The backscattering amplitude at finite range r is

$$f(r) = \frac{r|p(\mathbf{r})|}{|p_{\text{inc}}|}. \quad (12)$$

The farfield backscattering amplitude f is the limit of $f(r)$ as r approaches infinity. Expressions for the backscattering cross section and target strength are derived by substituting $f(r)$, or f , in Eqs. (2) and (3), respectively.

The elements used here are quadrilaterals and triangles of the quadratic isoparametric type, in which both the geometric and acoustic quantities are interpolated from the nodal values using quadratic shape functions, the nodes being situated at the vertices and midsides.³² As a general guide, good representation of the acoustic variables is obtained if the lengths of the sides of the elements are less than one-third of a wavelength. The accuracy of geometrical representation depends on the degree of undulation of the surface, but it should be noted that the quadratic interpolation allows the elements to be curved. Further details of the formulation and equations can be found in Ref. 11.

IV. SWIMBLADDER MORPHOMETRY

The origin of the morphometric data is a study performed in 1980³⁵ on surface-adapted specimens of pollack and saithe, described briefly in Table I. Each specimen was anesthetized, tethered, and acoustically measured at each of four frequencies, nominally 38, 50, 70, and 120 kHz, prior to shock-freezing and microtoming in the sagittal plane, hence

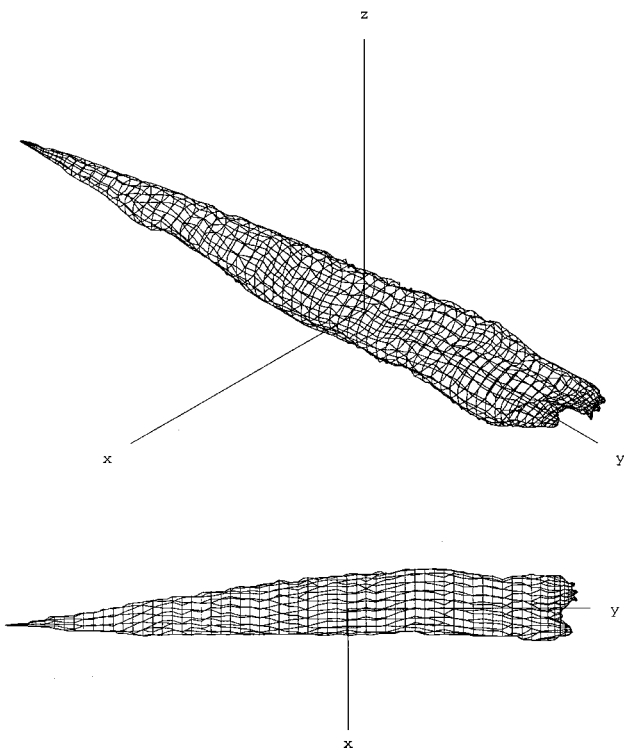


FIG. 1. Boundary-element mesh of the swimbladder to specimen No. 205 of Ref. 23, shown in both oblique and dorsal views. The model has 1107 elements and 3181 nodes. The meshed swimbladder length is 141 mm.

parallel to the main axis, according to the method of Ona.³⁶ The thickness of successive photographed sections was 100 μm . Each swimbladder section was digitized as a set of coordinates describing the outline of the swimbladder, and the surface of each swimbladder was represented by a mesh consisting of flat triangular facets.²³

Because of the use of curvilinear quadrilaterals and triangles in the BEM, new meshes have been produced for each of the specimens using a semiautomatic process. First, the contours of the swimbladder in planes perpendicular to the major axis of the fish, and hence perpendicular to the microtomed sections, are determined at intervals along the major axis, by finding the points of intersection of each plane with the original digitized sections. Quadrilateral and triangular elements are then fitted between neighboring contours. Where required, nodes are interpolated using cubic splines. This method allows the fineness of the mesh to be controlled by the choice of the separation between the contours and the nodal separation on each contour. Some manual fitting of elements is required where the swimbladder branches into separate lobes.

A further reason for the remapping exercise was to reduce the number of nodes in order to facilitate matrix operations inherent to the BEM. The resulting meshes have fewer elements than the original triangular meshes,²³ but this is offset by the allowance for curvature of the surface. An example of one of the meshes is visualized in Fig. 1. The new meshes have been used in computations with the Kirchhoff-approximation model in parallel with the BEM.

Details of the meshes are listed in Table I. For each mesh, the maximum distance between neighboring nodes is

shown in the final column, column 11; however, a better indication of the degree of fineness of each mesh is given in column 10, namely the limit of nodal spacing which is satisfied by 99% of the distances between pairs of neighboring nodes. At 120.4 kHz the nodal spacing, to satisfy the $\lambda/6$ condition for accuracy of the BEM and Kirchhoff-approximation model, should be less than 2.03 mm. All of the meshes except that for specimen 201 are well within this limit even on the basis of the maximum nodal spacing found in the mesh. Detailed analysis of the mesh for specimen 201 reveals that the $\lambda/6$ condition is satisfied for all but two pairs of neighboring nodes out of 4530 such pairs.

V. INDEPENDENT VALIDATION OF MODELS

A cogent form of validation of the Kirchhoff-approximation model is the direct comparison of model computations and measurement results for the same fish specimens used in the morphometry. This work is documented in detail in Ref. 23 but in which the integration in Eq. (1) is performed by the primitive Riemann summation, with evaluation of the integrand at the centroid of each triangular facet.

Validation of the BEM has already been documented for a series of cases in which analytical solutions are available. Three of those described in Ref. 11 are cited. (1) The forward scattered pressure for a plane wave incident on a rigid sphere has been computed. The agreement over the ka range from 0 to 10 is excellent, without discrepancies at the critical frequencies that arise in the standard formulation, which lacks the normal component included in Eq. (4). (2) The backscattered pressure from a rigid sphere has been computed under similar conditions, again with excellent agreement, while avoiding discrepancies at the critical frequencies. (3) As an illustration, the radiation impedance of a uniformly vibrating circular piston of radius a in the end face of a cylinder of radius $2a$ and height $4a$ over the ka range from 0 to 5 has been computed and compared with the analytical solution for a piston in an infinite baffle. With allowance for the difference between the two problems, the agreement is quite good.

An additional trial of the BEM has been designed specifically for the present study. A spherical void of radius 25 mm is assumed to be immersed in sea water of sound speed 1470 m/s and density 1025 kg/m^3 . The size has been chosen for having an area of 7854 mm^2 , which is roughly 20% greater than the area of the mesh spanning the surface of the largest swimbladder, No. 207, as represented by 1487 elements (4363 nodes), with an area of 6524 mm^2 . Meshes have been generated by subdividing each spherical triangle of a geodesic icosahedron into four subtriangles, subdivided again to get a mesh of 320 elements (642 nodes) and subdivided once more to get a mesh of 1280 elements (2562 nodes). The latter mesh has a maximum nodal separation of 2.06 mm, which is just outside the limit of 2.03 mm required by the $\lambda/6$ condition at 120.4 kHz.

The same example provides a trial for the Kirchhoff approximation, since the integration in Eq. (1) can be performed analytically for the spherical shape:

$$f = (4k)^{-1} \{-1 + \cos(2ka) + 2ka \sin(2ka) + i[\sin(2ka) - 2ka \cos(2ka)]\}, \quad (13)$$

where a is the sphere radius. Comparison of the numerical and closed-form analytic solutions at the frequencies 38.1, 49.6, 68.4, and 120.4 kHz demonstrates agreement to within 0.01 dB for the 2562-node sphere. Further exercise of the Kirchhoff model reveals significant divergence of the numerical solution from the exact solution at about 180 kHz for the 2562-node sphere and at about 90 kHz for the 642-node sphere. The truth of this last statement is evident in the target strength spectrum in Fig. 2, which also compares the results of the Kirchhoff approximation with the exact series solution and BEM solution for the 642-node mesh. The observed deviation of the BEM solution from the exact series solution at about 90 kHz corresponds to a nodal spacing of $\lambda/4$, which is coarser than the nominal criterion for validity of the BEM, namely neighboring-point separations within $\lambda/6$.

Numerical computations have been performed for both the BEM and Kirchhoff-approximation model for each of the two meshes. The computations have been repeated at each of the four measurement frequencies, 38.1, 49.6, 68.4, and 120.4 kHz, hence with $ka = 4.07, 5.30, 7.31, \text{ and } 12.87$. The results have been compared against the well-known analytical solution for scattering by a spherical void, with perfectly soft boundary condition, in a homogeneous fluid with given sound speed and density values.³⁷ In one set of computations, the effect of orientation of the axis of the meshed void is examined by comparing the backscattered pressure amplitude at infinity for the Kirchhoff-approximation model and at 1000-m range for the BEM. The results are shown in Table II. In a second set of computations, the same backscattered pressure amplitude for a single orientation is compared directly against the amplitude derived with the analytical solution. The results of these computations, as well as those for the forward scattered amplitude by the analytical solution and BEM, are presented in Table III. Corresponding target strengths and forward-scattering strengths are presented in Table IV.

It is noted that, for certain frequencies and mesh sizes, the condition for the nodal spacing discussed in Secs. II and III, namely that this should be less than $\lambda/6$, is violated. The results for these cases are included in Tables II–IV but are shown in italics. The limit is only just exceeded by the finer mesh at 120.4 kHz.

VI. COMPARISON OF MODEL COMPUTATIONS

The target strength for an immersed void with the shape of the swimbladder shown in Fig. 1 has been computed as a function of tilt angle for both the dorsal and ventral aspects at each of four frequencies. Both the Kirchhoff-approximation model and BEM have been examined. The computational results are shown with the measured functions in Fig. 3.

The same computations have been repeated for the mapped swimbladder shapes of all 15 gadoid specimens listed in Table I. In order to reduce these to manageable

proportions, the several functions have been averaged with respect to normal distributions $g(\theta)$ of tilt angle θ , with mean $\bar{\theta}$ and standard deviation s_θ :

$$\bar{\sigma} = \int g(\theta) \sigma(\theta) d\theta / \int g(\theta') d\theta', \quad (14)$$

where the integration has been performed over the range $[\bar{\theta} - 3s_\theta, \bar{\theta} + 3s_\theta]$. For the measured target strength functions, values at tilt angles outside the range $[-45^\circ, 45^\circ]$ were not available, and for such angles the value of σ at the nearest angle limit has been used.

Computations have been performed for each of four normal distributions of tilt angle. The paired values $(\bar{\theta}, s_\theta)$ are $(0^\circ, 0^\circ)$, $(0^\circ, 5^\circ)$, $(0^\circ, 10^\circ)$, and $(-4.4^\circ, 16^\circ)$. Because of the effect of perspective, by which the apparent tilt angle of a fish changes as it is observed at different positions in the plane transverse to the acoustic axis,³⁸ the effective values of s_θ are larger than the nominal ones. The values shown above have been adjusted for the perspectival effect for a circular beam of 5° beamwidth measured between the half-power points. The effective standard deviations for the four cases are $2.5^\circ, 5.5^\circ, 10.2^\circ, \text{ and } 16^\circ$.²³

The target strength corresponding to each averaged backscattering cross section, denoted TS, has been computed by substituting the value of $\bar{\sigma}$ from Eq. (14) in Eq. (3). The values of TS have been regressed on fish length l in centimeters according to the regression equation,

$$\overline{\text{TS}} = 20 \log l + b, \quad (15)$$

where the regression coefficient b is expressed in decibels. The standard error of the regression has been computed for each derived regression equation. The results are shown in Tables V and VI.

VII. DISCUSSION

A. Model validation computations

To validate the BEM for application to the gadoid swimbladder, a 25-mm-radius spherical void in sea water has been chosen as a test case in order to have a shape for which a rather simple analytical solution exists and whose surface area is greater than that of the largest swimbladder in the data set. Finite-element representation of the sphere by a subdivided icosahedron has allowed both the BEM and Kirchhoff approximation to be computed according to Eqs. (12) and (1), respectively.

Because of the finiteness of the facets, there is an effect due to axial orientation, which is indicated in Table II. The BEM is seen to be quite accurate for the two meshes that were chosen. Sensitivity to axial orientation is negligible as long as the maximal nodal separation does not exceed $\lambda/6$. The Kirchhoff-approximation model is exercised with the identical meshes but performs less well than the BEM; it is inherently different, as is proved by the difference in respective exact and analytical solutions for the two models for this special shape. The variability with orientation is notable for the coarser mesh.

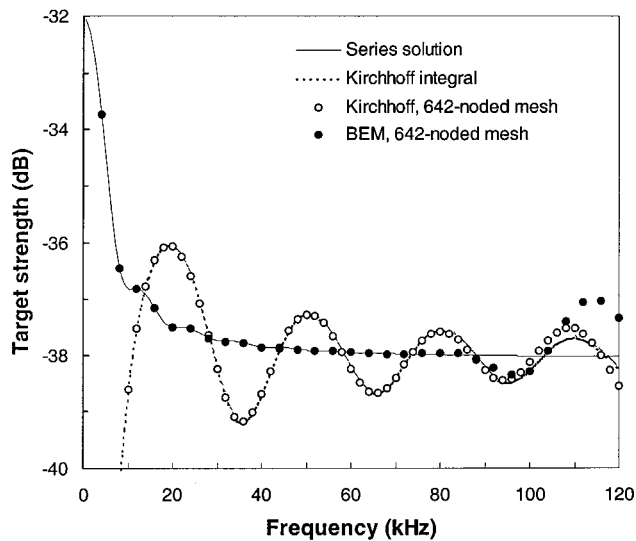


FIG. 2. Frequency dependence of a spherical void of radius 25 mm immersed in water of density 1025 kg/m^3 and sound speed 1470 m/s, as given by the series solution, Kirchhoff integral through the closed-form expression in Eq. (13), numerical Kirchhoff approximation using a surface mesh with 642 nodes, and boundary-element method using the same 642-node surface mesh.

Both backscattering and forward-scattered pressure amplitudes for the same boundary-element meshes are shown in Table III for the BEM, with close agreement with the analytical result except for the coarser mesh at the highest frequency of 120.4 kHz, where the nodal spacing greatly exceeds $\lambda/6$. Again, the Kirchhoff approximation performs less well. Differences in the two models are also evident in the logarithmic measures presented in Table IV.

The apparent improvement in performance of the Kirchhoff approximation at the highest frequency of 120.4 kHz is illusory, since, as noted previously, the closed-form analytic solution for the Kirchhoff-approximation model for the spherical void differs from the exact series solution. In fact, the approximation solution given by Eq. (13) oscillates about the analytical solution with a cycle frequency of about 30 kHz, corresponding to the condition $2\Delta ka = \pi$, where Δk describes the change in wave number that satisfies the equality, as shown in Fig. 2. The corresponding Kirchhoff-approximation model results for the two meshes agree well with each other except at the highest frequency, where the

separation in neighboring Gauss points for the coarser mesh, using seven-point integration, is about $\lambda/4$, thus exceeding $\lambda/6$. The nodal spacing for the same mesh is about $\lambda/3$, also exceeding both the $\lambda/5$ and $\lambda/6$ conditions mentioned in Secs. II and III, respectively.

The Kirchhoff approximation, since it requires only a direct integration, is computationally much faster than the BEM, which requires the inversion of a complex matrix of size equal to the square of the number of nodes. Above about 4000 nodes, the BEM becomes cumbersome, at least on current desk-type workstation-level computers. In contrast, the Kirchhoff approximation could be exercised with far more elements than used here and thus, in principle, could be more amenable to computation at higher frequencies. However, the approximation has inherent limitations, such as the neglect of diffraction over the surface of the scattering shape or body, if most serious at relatively low frequencies.

To summarize, the BEM results agree well with the analytical results for the cases of 2562 and 642 nodes, deviating significantly only for nodal separations exceeding $\lambda/6$. The Kirchhoff approximation fares relatively poorly in comparison; nonetheless, it agrees to within about 1.2 dB at 38.1 kHz and within about 0.6 dB at the three highest frequencies.

B. Swimbladder-shape-based computations

The detailed computations of target strength as a function of tilt angle are shown for a single specimen, No. 205, in Fig. 3. Both the Kirchhoff-approximation model and BEM results are shown for the swimbladder as represented in Fig. 1. The respective measured target strength functions are also shown.

Both similarities and deviations are observed. Significantly for this work, the Kirchhoff-approximation and BEM results are quite similar. Comparisons against the measured function reveal similarities in overall structure, but with sizable discrepancies over certain angular regions, both in amplitude and degree of structure. Nonetheless, in the displayed case of specimen No. 205, it can be imagined that some average backscattering cross sections will be similar in magnitude.

Statistical combination of the individual averages in the regression analysis described by Eq. (15) reveals strong similarities, especially for the tilt angle distribution with largest

TABLE II. Backscattered pressure amplitude relative to the incident pressure amplitude in units of 1×10^{-6} for a 50-mm-diam spherical void immersed in sea water, calculated at 1000 m range for the analytical series-expressed solution and BEM, and scaled to 1000 m for the farfield Kirchhoff approximation. The effect on the amplitude of the orientation of the subdivided icosahedron used to represent the void in the BEM and Kirchhoff approximation is expressed through the parenthetical quantity, which is the maximum percentage deviation from the mean observed over a wide range of axial orientations. Values in italics indicate that the model has a nodal separation exceeding $\lambda/6$ at the specified frequency.

Frequency (kHz)	38.1	49.6	68.4	120.4
ka	4.071	5.300	7.309	12.866
Analytical solution	12.850	12.721	12.634	12.545
BEM, 2562 nodes	12.846	12.716	12.630 (0.1)	<i>12.541 (0.3)</i>
BEM, 642 nodes	12.839 (0.1)	12.710 (0.4)	<i>12.616 (1.6)</i>	<i>12.587 (28.4)</i>
Kirchhoff, 2562 nodes	11.199 (0.6)	13.692 (0.8)	11.801 (1.0)	<i>12.219 (1.4)</i>
Kirchhoff, 642 nodes	11.187 (2.5)	13.707 (3.7)	<i>11.784 (4.8)</i>	<i>12.060 (29.1)</i>

TABLE III. Back- and forward-scattered pressure amplitudes relative to the incident pressure amplitude in units of 1×10^{-6} for a 50-mm-diam spherical void at 1000-m range for the analytical series-expressed solution and BEM, and scaled to 1000 m for the farfield Kirchhoff approximation. A single, fixed orientation is assumed for the axis of the subdivided icosahedron used to represent the void in the BEM and Kirchhoff approximation. The percentage deviation relative to the analytical solution is given.

Frequency (kHz)	38.1		49.6		68.4		120.4	
	Back	Forward	Back	Forward	Back	Forward	Back	Forward
Analytical solution	12.850	78.658	12.721	95.306	12.634	122.240	12.545	195.700
BEM, 2562 nodes	12.847	78.644	12.716	95.290	12.629	122.225	12.542	195.695
Percentage error	-0.026	-0.018	-0.038	-0.017	-0.036	-0.012	-0.026	-0.003
BEM, 642 nodes	12.839	78.625	12.707	95.269	12.617	122.204	13.511	195.544
Percentage error	-0.088	-0.042	-0.106	-0.039	-0.135	-0.030	7.696	-0.080
Kirchhoff, 2562 nodes	11.203		13.686		11.808		12.228	
Percentage error	-12.817		7.586		-6.538		-2.527	
Kirchhoff, 642 nodes	11.206		13.677		11.820		11.769	
Percentage error	-12.794		7.515		-6.443		-6.186	

standard deviation, $N(-4.4^\circ, 16^\circ)$. This distribution, in fact, is the first and possibly only one of a gadoid, cod (*Gadus morhua*), determined photographically *in situ*.³⁹ In this case, in dorsal aspect, the Kirchhoff approximation agrees with measurement to within 0–1 dB over all four frequencies, while the BEM results differ by 0.7–1.5 dB, as documented in Table V. For the tilt angle distribution with nominal standard deviation of 10° , the difference between the Kirchhoff and measured TS functions is 0.1–1.5 dB. The difference between the BEM and measured TS functions is 1.2–2 dB. For the narrower tilt angle distributions, differences are larger, reflecting differences in structure of the modeled backscattering amplitude at central angles.

For the ventral aspect, with results presented in Table VI, differences are smaller. The difference between Kirchhoff and measured results at the broadest tilt angle distribution is 0.7–1.9 dB. For the BEM and measured results, the difference is 0.4–1.1 dB.

The BEM and Kirchhoff-approximation results are quite similar except at the lowest frequency, 38.1 kHz, where the greatest discrepancy in regression coefficient is 1.3 dB. At this frequency, the Kirchhoff-approximation result is closer to the result based on measurement in dorsal aspect for all four tilt angle distributions. In ventral aspect, the BEM result is closer.

At 49.6 kHz, the greatest difference in Kirchhoff-approximation and BEM results is 0.7 dB, with average difference about 0.4 dB. At 68.4 kHz, the greatest difference is

0.4 dB, with average difference about 0.2 dB. At 120.4 kHz, the respective numbers are 0.8 and 0.5 dB.

A survey of the overall results in Tables V and VI may suggest some systematic differences with the regression coefficient b and standard error. Caution is advised in the interpretation of apparent systematic differences, however, because the computational results are not all independent. While 16 sets of computations are presented for each aspect, they apply to a total of only four frequencies, which is closer to the number of degrees of freedom for the respective aspect. Were data available at other frequencies, the possible presence of systematic differences among measurements and models might reveal the influence of other parts of the fish in modifying backscattering by the swimbladder alone.

A further internal comparison is possible for the Kirchhoff approximation. The mapping of the swimbladder is derived from the original mapping by flat triangular facets.²³ The new mapping, for consistency with the BEM, contains fewer but curvilinear elements spanning the swimbladder surface. A detailed comparison of corresponding values for the regression coefficient b in Eq. (15) reveals a greatest discrepancy of 0.2 dB, with median discrepancy of 0.1 dB, for the dorsal aspect. In ventral aspect the greatest discrepancy is 0.1 dB, with median discrepancy less than 0.05 dB.

C. Summary of comparisons

Earlier validation exercises with the BEM have been supplemented by a new example, that of a spherical void for

TABLE IV. Back- and forward-scattered pressure amplitudes shown in Table III, but expressed in decibels relative to 1-m range and incident wave amplitude.

Frequency (kHz)	38.1		49.6		68.4		120.4	
	Back	Forward	Back	Forward	Back	Forward	Back	Forward
Analytical solution	-37.822	-22.085	-37.910	-20.418	-37.969	-18.256	-38.031	-14.168
BEM, 2562 nodes	-37.824	-22.087	-37.913	-20.419	-37.972	-18.257	-38.033	-14.168
BEM, 642 nodes	-37.830	-22.089	-37.919	-20.241	-37.981	-18.258	-37.387	-14.175
Kirchhoff, 2562 nodes	-39.013		-37.274		-38.556		-38.253	
Kirchhoff, 642 nodes	-39.011		-37.280		-38.547		-38.585	

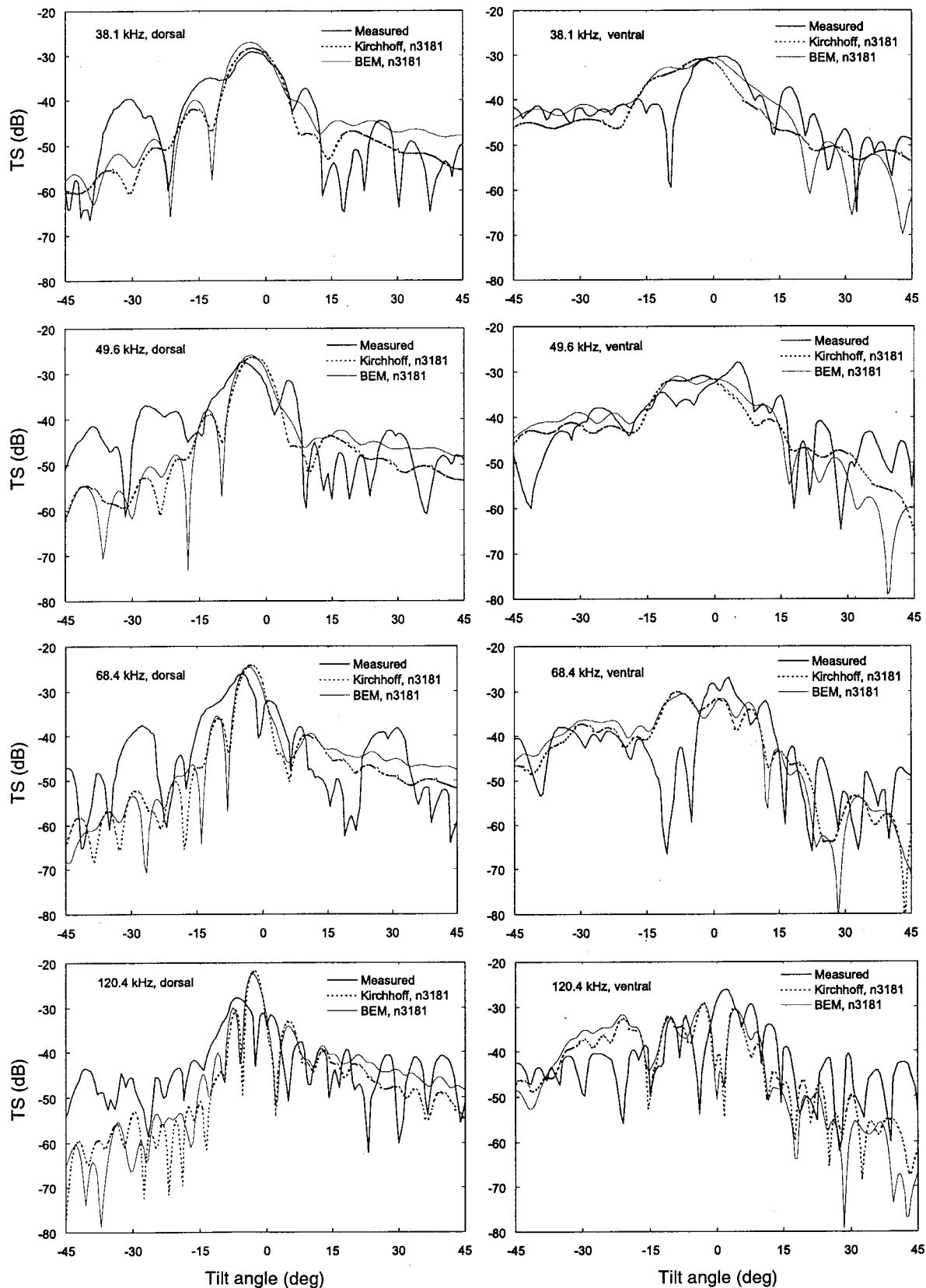


FIG. 3. BEM and Kirchhoff-approximation-model computations of target strength as a function of tilt angle compared against direct measurements for specimen No. 205. The functions are shown for both dorsal and ventral aspects at each of four frequencies.

which a simple analytical solution is known. Results with the Kirchhoff approximation are poorer. Nonetheless, in the case of the swimbladder-shape-based computations, the Kirchhoff

approximation, when exercised with the curvilinear elements used in the BEM, yields results that agree well with earlier computations carried out using meshes with larger numbers

TABLE V. Regression coefficient for the target strength–fish length relationship based on computations or measurements of each of 15 specimens in dorsal aspect when averaged over four distinct distributions of tilt angle θ , characterized by the mean $\bar{\theta}$ and standard deviation s_θ , abbreviated s.d. The coefficient b is that shown in Eq. (15). The associated standard error of the regression, SE, is also shown.

Frequency (kHz)	Tilt angle distribution (deg)		BEM		Kirchhoff		Measured TS functions	
	Mean	s.d.	b	SE	b	SE	b	SE
38.1	0.0	0.0	-61.3	1.0	-62.3	1.2	-63.5	1.3
38.1	0.0	5.0	-62.3	0.6	-63.6	0.9	-64.3	0.6
38.1	0.0	10.0	-64.1	0.4	-65.4	0.7	-65.7	0.4
38.1	-4.4	16.0	-65.7	0.4	-67.0	0.6	-66.9	0.4
49.6	0.0	0.0	-60.8	1.1	-61.1	1.3	-64.8	1.1
49.6	0.0	5.0	-61.9	0.6	-62.4	0.8	-64.1	0.7
49.6	0.0	10.0	-63.8	0.4	-64.4	0.7	-65.0	0.6
49.6	-4.4	16.0	-65.4	0.4	-66.1	0.6	-66.1	0.6
68.4	0.0	0.0	-60.2	1.3	-60.0	1.4	-64.7	1.2
68.4	0.0	5.0	-61.4	0.7	-61.5	0.8	-63.9	1.0
68.4	0.0	10.0	-63.3	0.5	-63.5	0.7	-64.8	0.7
68.4	-4.4	16.0	-65.0	0.5	-65.2	0.6	-65.9	0.6
120.4	0.0	0.0	-59.3	1.6	-59.8	1.8	-64.8	1.6
120.4	0.0	5.0	-60.7	1.2	-61.2	1.3	-63.8	1.3
120.4	0.0	10.0	-62.7	1.1	-63.2	1.2	-64.7	1.1
120.4	-4.4	16.0	-64.4	1.0	-64.9	1.2	-65.9	0.9

of flat elements.

While use of the BEM does not improve the earlier agreement of Kirchhoff-approximation computations with the measured target strength functions,²³ the two models do show a basic agreement. Differences in predictions, as expressed through the regression coefficient in Eq. (15), are less than 1 dB in all cases except at 38.1 kHz where the greatest difference is 1.3 dB. There is some expectation that the discrepancy might be largest at the lowest frequency, for the Kirchhoff approximation assumes high frequencies. An

offsetting factor, however, is the effective element side-to-wavelength ratio, which increases with frequency, decreasing the applicability, hence accuracy, of the approximation.

D. Future work

The BEM performs similarly to the Kirchhoff approximation for the frequencies and swimbladder sizes considered here. This is reassuring, since both models have the great

TABLE VI. Regression coefficient for the target strength–fish length relationship based on computations or measurements of each of 15 specimens in ventral aspect when averaged over four distinct distributions of tilt angle θ , characterized by the mean $\bar{\theta}$ and standard deviation s_θ , abbreviated s.d. The coefficient b is that shown in Eq. (15). The associated standard error of the regression, SE, is also shown.

Frequency (kHz)	Tilt angle distribution (deg)		BEM		Kirchhoff		Measured	
	Mean	s.d.	b	SE	b	SE	b	SE
38.1	0.0	0.0	-64.8	1.9	-65.2	1.8	-63.7	1.5
38.1	0.0	5.0	-65.0	1.2	-65.7	1.2	-64.3	0.9
38.1	0.0	10.0	-65.8	0.7	-66.7	0.8	-65.7	0.7
38.1	-4.4	16.0	-66.7	0.4	-67.8	0.7	-67.1	0.7
49.6	0.0	0.0	-65.7	2.5	-65.2	2.2	-62.7	1.4
49.6	0.0	5.0	-65.4	1.4	-65.3	1.4	-63.4	0.8
49.6	0.0	10.0	-65.9	0.7	-66.2	0.9	-64.6	0.6
49.6	-4.4	16.0	-66.7	0.5	-67.2	0.7	-66.0	0.6
68.4	0.0	0.0	-66.0	2.5	-65.6	2.6	-62.3	1.3
68.4	0.0	5.0	-65.7	1.5	-65.5	1.7	-63.0	0.7
68.4	0.0	10.0	-66.0	0.8	-66.1	0.9	-64.3	0.5
68.4	-4.4	16.0	-66.6	0.6	-67.0	0.8	-65.8	0.5
120.4	0.0	0.0	-66.0	1.9	-66.4	2.2	-62.5	1.2
120.4	0.0	5.0	-65.6	1.2	-66.0	1.4	-62.8	0.7
120.4	0.0	10.0	-66.0	0.9	-66.6	1.2	-64.0	0.5
120.4	-4.4	16.0	-66.6	0.9	-67.4	1.2	-65.5	0.5

advantage over other models in being able to treat a complicated shape without compromise, in principle, based on a finite-element representation of the surface.

The BEM can, however, do much more than the Kirchhoff-approximation model. (1) It can, for example, treat lower frequencies, for diffraction is addressed in a fundamental manner through the integral-equation solution of the wave equation described in Sec. III. (2) The BEM can also treat the case of a gas-filled swimbladder under the influence of hydrostatic pressure without having to make assumptions about the applicable boundary conditions. (3) A third advantage of the model is its capacity to treat heterogeneous structures, as long as the heterogeneities can be demarked by surfaces within which the acoustic properties are uniform. Thus, the BEM can predict scattering by a swimbladder-bearing fish in which the swimbladder and other structures, e.g., liver, reproductive products, and fish tissue surrounding the swimbladder, are explicitly represented. (4) It is noted that the BEM can address finite-scattering-range effects, without having to assume an infinite range, as is done in typical farfield-only models.

The applicability of the BEM to organisms other than swimbladder-bearing fish is evident. Thus the BEM can address scattering by the organisms conveniently classified by Stanton as deformed fluid cylinders, deformed elastic-shelled spheres, and bubble plus tissue, as represented, for example, by euphausiids, gastropods, and siphonophores, respectively.⁴⁰ Significantly, there is no need to approximate shape or boundary conditions, for the model is numerical.

Some of the effects mentioned here may be addressed in a future work. These may also include bistatic scattering, which is allowed by both the BEM and Kirchhoff-approximation model, as well as other models, such as the deformed-cylinder model.¹⁰

ACKNOWLEDGMENTS

This work began with sponsorship by the European Commission through its RTD-program, Contract No. MAS3-CT95-0031 (BASS). A Norton is thanked for much valued assistance in the technical editing. This is Woods Hole Oceanographic Institution Contribution No. 10437.

¹R. H. Love, "Measurements of fish target strength: A review," *Fish. Bull.* **69**, 703–715 (1971).

²L. Midttun, "Fish and other organisms as acoustic targets," *Rapp. P.-V. Reun.-Cons. int. Explor. Mer.* **184**, 25–33 (1984).

³K. G. Foote, "Summary of methods for determining fish target strength at ultrasonic frequencies," *ICES J. mar. Sci.* **48**, 211–217 (1991).

⁴S. McClatchie, G. Macaulay, R. F. Coombs, P. Grimes, and A. Hart, "Target strength of an oily deep-water fish, orange roughy (*Hoplostethus atlanticus*). I. Experiments," *J. Acoust. Soc. Am.* **106**, 131–142 (1999).

⁵K. G. Foote, "Target strength of fish," in *Encyclopedia of Acoustics*, edited by M. J. Crocker (Wiley, New York, 1997), pp. 493–500.

⁶D. N. MacLennan, "Acoustical measurement of fish abundance," *J. Acoust. Soc. Am.* **87**, 1–15 (1990).

⁷K. G. Foote, "Acoustic sampling volume," *J. Acoust. Soc. Am.* **90**, 959–964 (1991).

⁸J. B. Hedgepeth, V. F. Gallucci, F. O'Sullivan, and R. E. Thorne, "An expectation maximization and smoothing approach for indirect acoustic estimation of fish size and density," *ICES J. mar. Sci.* **56**, 36–50 (1999).

⁹A. Stepnowski, and M. Moszinski, "Inverse problem solution techniques

as applied to indirect *in situ* estimation of fish target strength," *J. Acoust. Soc. Am.* **107**, 2554–2562 (2000).

¹⁰T. K. Stanton, "Sound scattering by cylinders of finite length. III. Deformed cylinders," *J. Acoust. Soc. Am.* **86**, 691–705 (1989).

¹¹D. T. I. Francis, "A gradient formulation of the Helmholtz integral equation for acoustic radiation and scattering," *J. Acoust. Soc. Am.* **93**, 1700–1709 (1993).

¹²C. S. Clay and J. K. Horne, "Acoustic models of fish: The Atlantic cod (*Gadus morhua*)," *J. Acoust. Soc. Am.* **96**, 1661–1668 (1994).

¹³S. McClatchie, and Z. Ye, "Target strength of an oily deep-water fish, orange roughy (*Hoplostethus atlanticus*). II. Modeling," *J. Acoust. Soc. Am.* **107**, 1280–1285 (2000).

¹⁴D. T. I. Francis and K. G. Foote, "Boundary-element-model predictions of acoustic scattering by swimbladder-bearing fish," *Proceedings of the Fourth European Conference on Underwater Acoustics*, edited by A. Alippi and G. B. Cannelli (CNR-IDAC, Rome, Italy, 1998), Vol. I, pp. 255–260.

¹⁵K. G. Foote and D. T. I. Francis, "Target strength spectra of swimbladder-bearing fish," *J. Acoust. Soc. Am.* **105**, 1111 (1999).

¹⁶R. I. C. C. Francis and M. R. Clark, "Inferring spawning migrations of orange roughy (*Hoplostethus atlanticus*) from spawning oöives," *Mar. Freshwater Res.* **49**, 103–108 (1998).

¹⁷I. Andreeva, "Scattering of sound by air bladders of fish in deep sound scattering ocean layers," *Sov. Phys. Acoust.* **10**, 17–20 (1964).

¹⁸D. E. Weston, "Sound propagation in the presence of bladder fish," in *Underwater Acoustics*, edited by V. M. Albers (Plenum, New York, 1967), Vol. 2, pp. 55–88.

¹⁹R. H. Love, "Resonant acoustic scattering by swimbladder-bearing fish," *J. Acoust. Soc. Am.* **64**, 571–580 (1978).

²⁰M. Furusawa, "Prolate spheroidal models for predicting general trends of fish target strength," *J. Acoust. Soc. Jpn. (E)* **9**, 13–24 (1988).

²¹L. Ding and Z. Ye, "A method for acoustic scattering by slender bodies. II. Comparison with laboratory measurements," *J. Acoust. Soc. Am.* **102**, 1977–1981 (1997).

²²K. Sawada, Z. Ye, R. Kieser, G. A. McFarlane, Y. Miyahana, and M. Furusawa, "Target strength measurements and modeling of walleye pollock and Pacific hake," *Fish. Sci.* **65**, 193–205 (1999).

²³K. G. Foote, "Rather-high-frequency sound scattering by swimbladder-bearing fish," *J. Acoust. Soc. Am.* **78**, 688–700 (1985).

²⁴K. G. Foote and J. J. Traynor, "Comparison of walleye pollock target strength estimates determined from *in situ* measurements and calculations based on swimbladder form," *J. Acoust. Soc. Am.* **83**, 9–17 (1988).

²⁵S. McClatchie, J. Alsop, Z. Ye, and R. F. Coombs, "Consequence of swimbladder model choice and fish orientation to target strength of three New Zealand fish species," *ICES J. mar. Sci.* **53**, 847–862 (1996).

²⁶S. McClatchie, G. Macaulay, S. Hanchet, and R. F. Coombs, "Target strength of southern blue whiting (*Micromesistius australis*) using swimbladder modelling, split beam and deconvolution," *ICES J. mar. Sci.* **55**, 482–493 (1998).

²⁷T. K. Stanton, "Sound scattering by cylinders of finite length. I. Fluid cylinders," *J. Acoust. Soc. Am.* **83**, 55–63 (1988).

²⁸T. K. Stanton, "Sound scattering by cylinders of finite length. II. Elastic cylinders," *J. Acoust. Soc. Am.* **83**, 64–67 (1988).

²⁹T. K. Stanton, "Sound scattering by spherical and elongated shelled bodies," *J. Acoust. Soc. Am.* **88**, 1619–1633 (1990).

³⁰C. Partridge and E. R. Smith, "Acoustic scattering from bodies: Range of validity of the deformed cylinder method," *J. Acoust. Soc. Am.* **97**, 784–795 (1995).

³¹A. J. Burton and G. F. Miller, "The application of integral equation methods to the numerical solutions of some exterior boundary problems," *Proc. R. Soc. London, Ser. A* **323**, 201–210 (1971).

³²O. C. Zienkiewicz and R. L. Taylor, *The Finite Element Method*, 4th ed. (McGraw-Hill, London, 1989), Vol. 1, pp. 121–132.

³³W. L. Meyer, W. A. Bell, M. P. Stallybrass, and B. T. Zinn, "Prediction of the sound field radiated from axisymmetric surfaces," *J. Acoust. Soc. Am.* **65**, 631–638 (1979).

³⁴T. Terai, "On calculation of sound fields around three dimensional objects by integral equation methods," *J. Sound Vib.* **69**, 71–100 (1980).

³⁵K. G. Foote, "Linearity of fisheries acoustics, with addition theorems," *J. Acoust. Soc. Am.* **73**, 1932–1940 (1983).

³⁶E. Ona, "Physiological factors causing natural variations in acoustic target strength of fish," *J. Mar. Biol. Assoc. U.K.* **70**, 107–127 (1990).

³⁷R. R. Goodman and R. Stern, "Reflection and transmission of sound by elastic spherical shells," *J. Acoust. Soc. Am.* **34**, 338–344 (1962).

³⁸K. G. Foote, "Averaging of fish target strength functions," *J. Acoust. Soc. Am.* **67**, 504–515 (1980).

³⁹K. Olsen, "Orientation measurements of cod in Lofoten obtained from underwater photography, and their relation to target strength," Council

Meeting of the International Council on Explor. Sea 1971/B, 17, 8 pp.

⁴⁰T. K. Stanton, "Simple approximate formulas for backscattering of sound by spherical and elongated objects," *J. Acoust. Soc. Am.* **86**, 1499–1510 (1989).

Coherence of acoustic modes propagating through shallow water internal waves

Daniel Rouseff

Applied Physics Laboratory, College of Ocean and Fishery Sciences, University of Washington, Seattle, Washington 98105

Altan Turgut, Stephen N. Wolf, Steve Finette, Marshall H. Orr, and Bruce H. Pasewark

Naval Research Laboratory, Washington DC 20375-5350

John R. Apel^{a)}

Global Ocean Associates, PO Box 12131, Silver Spring, Maryland 20908

Mohsen Badiey

Ocean Acoustic Laboratory, Graduate College of Marine Studies, University of Delaware, Newark, Delaware 19716

Ching-sang Chiu

Naval Postgraduate School, Monterey, California 93943

Robert H. Headrick, James F. Lynch, John N. Kemp, Arthur E. Newhall, and Keith von der Heydt

Woods Hole Oceanographic Institution, Woods Hole, Massachusetts 02543

Dirk Tielbuerger

Forschungsanstalt der Bundeswehr für Wasserschall und Geophysik, Klausdorfer Weg 2-24, -24148 Keil, Germany

(Received 30 October 2000; revised 25 September 2001; accepted 14 January 2002)

The 1995 Shallow Water Acoustics in a Random Medium (SWARM) experiment [Apel *et al.*, *IEEE J. Ocean. Eng.* **22**, 445–464 (1997)] was conducted off the New Jersey coast. The experiment featured two well-populated vertical receiving arrays, which permitted the measured acoustic field to be decomposed into its normal modes. The decomposition was repeated for successive transmissions allowing the amplitude of each mode to be tracked. The modal amplitudes were observed to decorrelate with time scales on the order of 100 s [Headrick *et al.*, *J. Acoust. Soc. Am.* **107**(1), 201–220 (2000)]. In the present work, a theoretical model is proposed to explain the observed decorrelation. Packets of intense internal waves are modeled as coherent structures moving along the acoustic propagation path without changing shape. The packets cause mode coupling and their motion results in a changing acoustic interference pattern. The model is consistent with the rapid decorrelation observed in SWARM. The model also predicts the observed partial recorelation of the field at longer time scales. The model is first tested in simple continuous-wave simulations using canonical representations for the internal waves. More detailed time-domain simulations are presented mimicking the situation in SWARM. Modeling results are compared to experimental data. © 2002 Acoustical Society of America. [DOI: 10.1121/1.1461837]

PACS numbers: 43.30.Re, 43.30.Bp, 43.30.Ft, 43.30.Zk [DLB]

I. INTRODUCTION

The 1995 Shallow Water Acoustics in a Random Medium (SWARM) experiment was conducted off the New Jersey coast. The primary objective was to study the interaction of sound with internal waves in the ocean waveguide. To better characterize the propagation regime, detailed oceanographic and geophysical data were taken concurrently with the acoustical measurements. An overview of the experiment, along with initial results, is presented by Apel *et al.*¹

The experiment featured moored sources transmitting 16- and 100-Hz BW pseudorandom noise sequences at respective center frequencies 224 and 400 Hz. Vertical receive-

ing arrays were located at ranges 32 and 42 km from the source (see Fig. 1). The arrays were well populated, having 16 and 32 elements, respectively, permitting the measured acoustic field to be decomposed into its normal modes. The decomposition was repeated for successive transmissions, allowing the amplitude of each mode to be tracked. An interesting result of this analysis was that the transient mode amplitudes decorrelated more rapidly than expected. A typical decorrelation time was on the order of 100 s but varied about 50 s.^{2,3} The observed rapid decorrelation and its variability are presumably due to internal waves.

Internal waves come in two general varieties. When there are many uncorrelated sources for the waves, a statistical representation is appropriate. This is the usual situation in deep water.⁴ In shallow water, there is often another type

^{a)}Deceased.

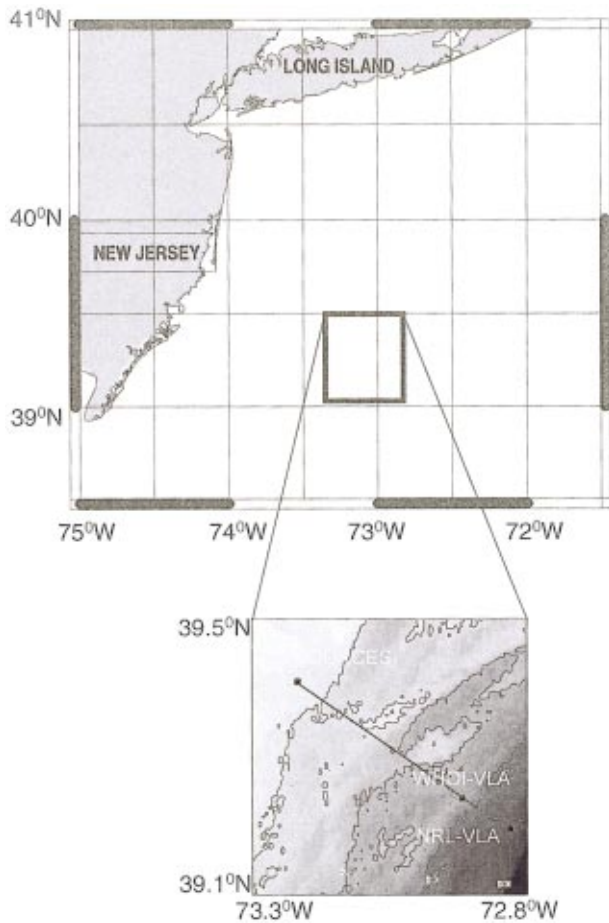


FIG. 1. Location of acoustic sources and VLA receivers used in the SWARM95 experiment.

of internal wave. Driven by tidal interaction with topographic features, packets of intense internal waves can be generated. Satellite images have shown that these waves can remain coherent over multiple tidal cycles.⁵ Because of the borelike nature of these solitary waves, the term “solibore” has been coined.⁶ This type of internal wave is more deterministic in nature, and so is the model presented here. Internal wave packets are known to always be present somewhere in the long propagation paths during the SWARM experiment.

In the present work, a simple model is proposed to explain the observed decorrelation of the acoustic modes. Internal wave packets are treated as structures that cause acoustic mode coupling. These modeled solitary waves are allowed to move shoreward along the acoustic propagation track toward the acoustic sources. The amplitude of an acoustic mode measured downrange is shown to depend on the location of the packet. As a packet moves, the mode amplitude changes. Even if the packet’s shape is unchanging as it propagates, it induces time dependence in the received acoustic field.

The proposed model takes an essentially deterministic view of acoustic propagation through internal wave packets. The details of how they induce mode coupling may, in some sense, be random, but the primary experimental observable—the fluctuations in the received acoustic

intensity—can be explained as consequence of the deterministic motion of this mode coupling structure. This deterministic model does not preclude the existence of other, possibly stochastic, sources of variability such as background internal waves. Rather, it shows in a simple setting how a deterministic effect, known to be present during SWARM, can produce temporal variability on the time scales observed in the experiment. An additional, intriguing feature of this model is that it also predicts a partial recorelation of the field at longer time scales. This recorelation effect will be analyzed in the present work both through simulation and SWARM data analysis.

Other attempts to model the effects of solitary waves on shallow water acoustic propagation are available in the literature. By using data from experiments in the Yellow Sea together with simple numerical models, Zhou and colleagues^{7,8} initiated studies in this area. Tielbürger *et al.* included both solitons and random background internal waves in their parabolic equation (PE) simulations conducted in preparation for SWARM.⁹ Also using PE calculations, Preisig and Duda studied how individual acoustic modes coupled as they propagated through canonical representations of a single soliton.¹⁰ In a follow-up paper they also studied fluctuation of continuous wave (CW) acoustic signals propagating through internal solitary wave packets.¹¹ Taking the decorrelation time observed in SWARM as representative,^{2,3} Yoo and Yang examined the feasibility of doing broadband source localization.¹² In this paper, modal coherence of both CW and broadband acoustic signals is investigated as they propagated through both canonical and realistic solitary wave packets measured during the SWARM experiment.

In Sec. II, the model is outlined. For ease in development, a continuous wave approach is adopted. Evolution of the mode amplitude is shown to be a direct consequence of coupling and soliton motion. A simple formula is derived by relating the harmonics of the mode amplitude to the modal wave numbers and the velocity of the packets. Properties of the model are examined for three scenarios: adiabatic propagation, and both weak and strong mode coupling. Sample calculations in Sec. III are for a canonical environment. The development is extended to consider broadband ensonification in Sec. IV. The evolution of the acoustic mode structure is quantified in terms of the modal correlation coefficient. Realistic broadband simulations are presented that include sound speed profiles, bathymetry, and bottom properties that were measured in the SWARM experiment. Finally, in Sec. V, SWARM acoustic data are analyzed to look at both the short- and long-time correlation properties of the field. The results are consistent with both the theory developed for continuous waves and the broadband simulations.

II. MODEL

A time-harmonic $\exp(-i\omega t)$ acoustic point source is located at depth $z=z_s$ in an ocean waveguide. Initially, the sound speed profile is $c_0(z)$ and assumed independent of range x . A convenient representation for the pressure is in

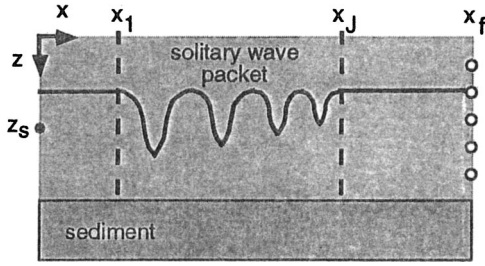


FIG. 2. Range-dependent environment. Heavy line represents contour of constant sound speed. A packet of solitary internal waves lies in the region $x_1 < x < x_j$.

terms of normal modes. Using an asymptotic representation for the Hankel function, the familiar expression for the pressure $p(x, z)$ is¹³

$$p(x, z) = \sum_m (\xi_m x)^{-1/2} \Psi_m(z_s) \Psi_m(z) e^{i\xi_m x}. \quad (1)$$

Here, Ψ_m is the pressure eigenfunction (normal mode) and ξ_m is the eigenvalue (horizontal wavenumber) associated with the discrete mode m . The wave numbers ξ_m are complex if loss is included in the model. Scaling terms such as those from the Hankel function expansion have been suppressed.

If the medium varies in range, the simple decomposition of Eq. (1) no longer applies. Consider the situation shown in Fig. 2. Both the water depth and bottom properties are still independent of range, but the sound speed in the water column is allowed to vary. The heavy line shows a contour of constant sound speed. The region $x_1 < x < x_j$ contains a packet of solitary ocean internal waves. These waves are characterized by deep depressions in the thermocline with resulting strong range dependence in the sound speed profile. The medium is taken to be range independent from the source to the leading edge of the packet at x_1 , and again from the trailing edge at x_j to the receiving array at x_f . Let $c_0(z)$ be the sound speed profile in the water column in these range-independent sections.

The concept of normal modes can be generalized for the range-dependent environment. Let the region $x_1 < x < x_j$ be subdivided into $J-1$ slabs. Within each slab, the medium is approximated as being range independent and local modes and wave numbers are calculated. Boundary conditions are applied at the interfaces between slabs to yield the transmission and reflection coefficients. We use a one-way coupled-mode model,¹³ an approximation to full coupling, thereby considering only outward propagating energy. The pressure within the j th slab (which lies between x_{j-1} and x_j) is written as a combination of the local modes Ψ_m^j weighted by the coefficients a_m^j

$$p^j(x, z) = (z_{j-1}/x)^{1/2} \sum_m a_m^j h_m^j(x) \Psi_m^j(z), \quad (2)$$

where for this slab $x_{j-1} < x \leq x_j$. The propagator within the j th slab is

$$h_m^j(x) = \exp [i\xi_m^j (x - x_{j-1})]. \quad (3)$$

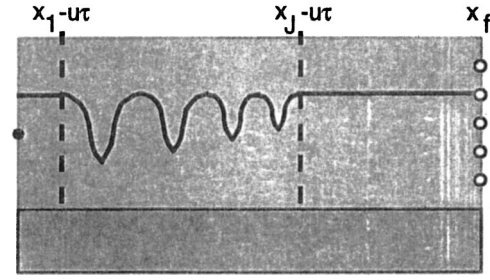


FIG. 3. Time evolution in the medium. Shown is the same medium as in Fig. 1 but at a later time τ . The packet of solitary waves have traveled towards the acoustic source with speed u .

For the special case of the first slab, where $x < x_1$ and $j=1$, the mode coefficient within this region is then found by comparing Eqs. (1) and (2):

$$a_m^1 = (\xi_m^1 x_0)^{-1/2} \Psi_m^1(z_s) \exp(i\xi_m^1 x_0). \quad (4)$$

It remains to quantify the mode coefficient in Eq. (2) for an arbitrary range. Let \mathbf{a}^{j+1} be a vector containing the amplitudes of the M modes near x_j within slab $j+1$. Within the one-way coupled mode formulation, these coefficients are related to those in the preceding slab by

$$\mathbf{a}^{j+1} = (x_{j-1}/x_j)^{1/2} \mathbf{C}^j \mathbf{H}^j(x_j) \mathbf{a}^j. \quad (5)$$

The matrix \mathbf{H}^j is diagonal with elements defined by Eq. (3). The definition of the coupling matrix \mathbf{C}^j is less straightforward. Strictly speaking, boundary conditions on both the pressure and the normal component of velocity must be satisfied at the j th interface. Because only one-way propagation is allowed in the present model, only one of these conditions can be satisfied. Jensen *et al.*¹³ note how a coupling matrix can be defined that is a compromise between the two conditions. In the present context, one-way coupled modes are used as a theoretical formalism rather than a computational approach; subtleties in approximating the boundary condition are irrelevant. For simplicity, only the condition on pressure is used and the elements of \mathbf{C}^j are

$$c_{lm}^j = \int_0^D \rho^{-1}(z) \Psi_l^{j+1}(z) \Psi_m^j(z) dz, \quad (6)$$

where $\rho(z)$ the depth-dependent density and the depth D extends sufficiently far into the sediment for the field to be extinguished. The modal coefficients at the array are determined by recursion

$$\mathbf{a}^{J+1} = (x_1/x_J)^{1/2} \mathbf{P} \mathbf{a}^1, \quad (7)$$

with the transmission matrix

$$\mathbf{P} = \mathbf{C}^J \mathbf{H}^J(x_J) \mathbf{C}^{J-1} \mathbf{H}^{J-1}(x_{J-1}) \cdots \mathbf{C}^1 \mathbf{H}^1(x_1). \quad (8)$$

Substituting into Eq. (2) yields the result

$$p(x_f, z) = \sum_m \Psi_m^J(z) \exp [i\xi_m^J (x_f - x_J)] \times \sum_n (\xi_n^1 x_f)^{-1/2} P_{mn} \Psi_n^1(z_s) \exp(i\xi_n^1 x_1). \quad (9)$$

Equation (9) can be readily interpreted. The acoustic field propagates as if in a range-independent environment from

the source to the leading edge of the wave packet at x_1 . From there, the transmission matrix describes any mode coupling that occurs while traveling through the solitons. The field then propagates without coupling from the trailing edge at x_J to the receiving array. In the following discussion we assume the environment is the same for the regions $x < x_1$ and $x > x_J$, so we have $\Psi_m^1 = \Psi_m^J$ and $\xi_m^1 = \xi_m^J$, and drop the superscripts 1 and J for convenience.

A solitary internal wave is nonlinear; its group velocity depends on its amplitude. A packet of several waves, as suggested in Fig. 2, may disperse as it propagates. The dispersion is small, however, over time scales comparable to the acoustic decorrelation time observed in SWARM. As a reasonable approximation, the packet can be modeled as a disturbance that simply moves through the region of acoustic propagation without changing shape. Figure 3 shows the geometry of Fig. 2 at some later time τ . The packet is assumed to travel with constant speed u towards the acoustic source. In this initial analysis, questions regarding packets traveling at an angle to the x - z propagation plane or other three-dimensional effects are ignored.

Generalizing Eq. (9) to include packet motion is straightforward. Inspection of the defining equations shows the transmission matrix \mathbf{P} to be independent of the absolute position of the mode coupling region. Neglecting any changes in the packet over the time separations of interest, Eq. (9) is generalized to

$$p(x_f, z; \tau) = \sum_m \Psi_m(z) \exp[i \xi_m(x_f - x_J + u\tau)] \\ \times \sum_n (\xi_n x_f)^{-1/2} P_{mn} \Psi_n(z_s) \exp[i \xi_n(x_1 - u\tau)]. \quad (10)$$

If the receiving array is well populated and spans the water column, in principle the received wavefront can be decomposed into its normal modes. In practice, a variety of techniques have been used to perform this decomposition. One method is to multiply the received wavefront by the calculated local mode shape and then approximate the modal orthogonality integral by numerical quadrature.² The coefficients of the local modes can also be determined by a least-squares analysis.¹⁴ In the present context, the details of implementation are unimportant; it is simply assumed that the decomposition can be accomplished. Using the orthogonality condition of the normal modes and the shorthand of continuous integrals, the amplitude of the observed mode m at time τ is

$$A_m(\tau) = \int_0^D \rho^{-1}(z) p(x_f, z; \tau) \Psi_m(z) dz \\ = \exp[i \xi_m(x_f - x_J)] \sum_n (\xi_n x_f)^{-1/2} P_{mn} \Psi_n(z_s) \\ \times \exp[i(\xi_n x_1 + \omega_{mn} \tau)], \quad (11)$$

where

$$\omega_{mn} = (\xi_m - \xi_n)u. \quad (12)$$

Equations (11) and (12) represent the primary modeling result. The amplitude of mode m is a linear combination of all excited modes. The observed linear combination depends on how the modes are excited at the source and on how the modes couple as the field propagates through the solitary wave packet. The individual terms in Eq. (11) are each multiplied by a different complex exponential. Inspection of Eq. (12) shows that the primary time dependence in the problem resides in the phases

$$\phi_{mn} \equiv \text{Re}(\omega_{mn} \tau) = \text{Re}[(\xi_m - \xi_n)u\tau]. \quad (13)$$

Each ϕ_{mn} represents the relative phase difference between two modes after propagating a distance $u\tau$. This time variability is related explicitly to the packet velocity u . The behavior of the mode amplitude $A_m(\tau)$ is now examined for three distinct propagation scenarios: adiabatic propagation, weak- and strong-mode coupling.

A. Adiabatic propagation

In the adiabatic approximation, interaction between modes is neglected. All of the off-diagonal terms in the transmission matrix are zero and Eq. (11) collapses to

$$A_m(\tau) = \exp[i \xi_m(x_f - x_J + x_1)] (\xi_m x_f)^{-1/2} P_{mm} \Psi_m(z_s), \quad (14)$$

which implies that the mode amplitude does not change in time. This can be understood as follows. In the adiabatic approximation, the phase of each mode reduces to an integral over range of the corresponding wave number. The contribution to the integral is the same regardless of the location of the internal wave. Consequently, if the propagation is adiabatic, then the mode amplitude will not change. The contraposition—if the mode amplitude changes, then there is mode coupling—is not necessarily true as the physical picture of a time-invariant internal wave packet may not be correct. Still, the experimentally observed fluctuations in the modal amplitudes imply at least the plausibility that mode coupling is the cause. Similarly, Headrick *et al.*³ showed how the effects of adiabatic variability were primarily manifest in the wander of the mode arrivals.

B. Weak mode coupling

If the mode coupling is weak, the primary interaction is often between consecutive mode orders. A typical quantity of interest is

$$\phi_{m+1,m}(\tau) = \text{Re}[(\xi_{m+1} - \xi_m)u\tau]. \quad (15)$$

To a good approximation, it can be shown that the difference between adjacent modal wavenumbers is inversely proportional to the cycle length of the corresponding ray.¹⁵ Consequently, the phase retardation between the coupled components becomes significant as the distance the internal wave packet moves, $u\tau$, becomes an appreciable fraction of the ray cycle length.

C. Strong mode coupling

If the coupling is strong, the transmission matrix \mathbf{P} will be fully populated. All of the terms in Eq. (11) can poten-

TABLE I. Parameters of soliton packet model.

i	a_i (m)	b_i (m)	d_i (m)
1	15	100	900
2	12	125	1400
3	10	150	2000

tially contribute to $A_m(\tau)$. The diagonal term P_{mm} provides a constant bias to the mode amplitude. The other terms will oscillate with periods given by $2\pi/\omega_{mn}$. Closely spaced mode pairs (in mode order) cause a relatively slow oscillation, while more widely spaced mode pairs will contribute more rapid fluctuations. The sum of the many components would produce a rich temporal structure in the mode amplitude. Like the transmission matrix, the harmonics described by Eq. (12) are independent of the internal wave packet's position and the depth of the source. The weighting of these harmonics, though, will depend on the location of the packet. In their numerical study, Duda and Preisig studied this effect in detail.¹¹ Modal attenuation caused by bottom loss generally increases with mode number. Consequently, if the packet is near the acoustic source, the higher-order modes are disproportionately attenuated, leaving only the lower-order modes present at the receiver. The amplitudes of the low-order modes will be affected by energy coupled from the higher-order modes when the internal wave packet is near the source.¹⁶ The lower harmonics in Eq. (12) will dominate and the modal amplitude changes relatively slowly. If the packet is near the acoustic receiver, coupling will repopulate the higher-order modes and weight the higher harmonics. It would be difficult to isolate this effect definitively, however, in the SWARM data at the NRL array. Multiplying the period of the M2 tide driving the internal waves by the best estimate of the packet velocity, $u=0.62$ m/s, yields packets separated by 27 km. Since the NRL array was 42 km downrange, whenever one packet is near the source another is by the

receiver. In the numerical studies that follow, the emphasis is on scenarios where there is a single packet located near the middle of the acoustic path.

III. CONTINUOUS WAVE SIMULATIONS

A numerical example illustrates the model. We begin by defining a coordinate system moving with the unchanging soliton packet. Let d be the distance coordinate in the moving frame relative to the leading edge of the packet; in fixed space, the leading edge is at $x=x_1-u\tau$. The vertical depression $\eta(d)$ within the packet is modeled as the sum of three solitary waves:

$$\eta(d) = \sum_{i=1}^3 a_i \operatorname{sech}^2[(d-d_i)/b_i], \quad (16)$$

where the numerical values used for a_i , b_i , and d_i are listed in Table I. The range-dependent sound speed profile (in m/s) in the water column $c(z,d)$ is modeled as being piecewise linear,

$$c(z,d) = \begin{cases} 1522, & 0 < z < z_U + \eta, \\ 1522 + \Delta(z - (z_U + \eta)), & z_U + \eta < z < z_L + \eta, \\ 1494, & z_L + \eta < z < z_B, \end{cases} \quad (17)$$

where the sound-speed gradient $\Delta = 28/(z_L - z_U)$. In our numerical calculations, we chose $z_U = 15$ m and $z_L = 30$ m with water depth $z_B = 60$ m. The ocean sediment has constant sound speed 1573 m/s, density 1.8 g/cm³, and attenuation 0.04 dB/ λ . The water-column model described by Eqs. (16) and (17) is identical to the one used by Duda and Preisig¹¹ in their numerical studies. The sediment model has been changed, however, to more accurately represent the situation in the SWARM experiment.

Equation (11) is primarily a theoretical result showing how the mode amplitude changes in time as the soliton

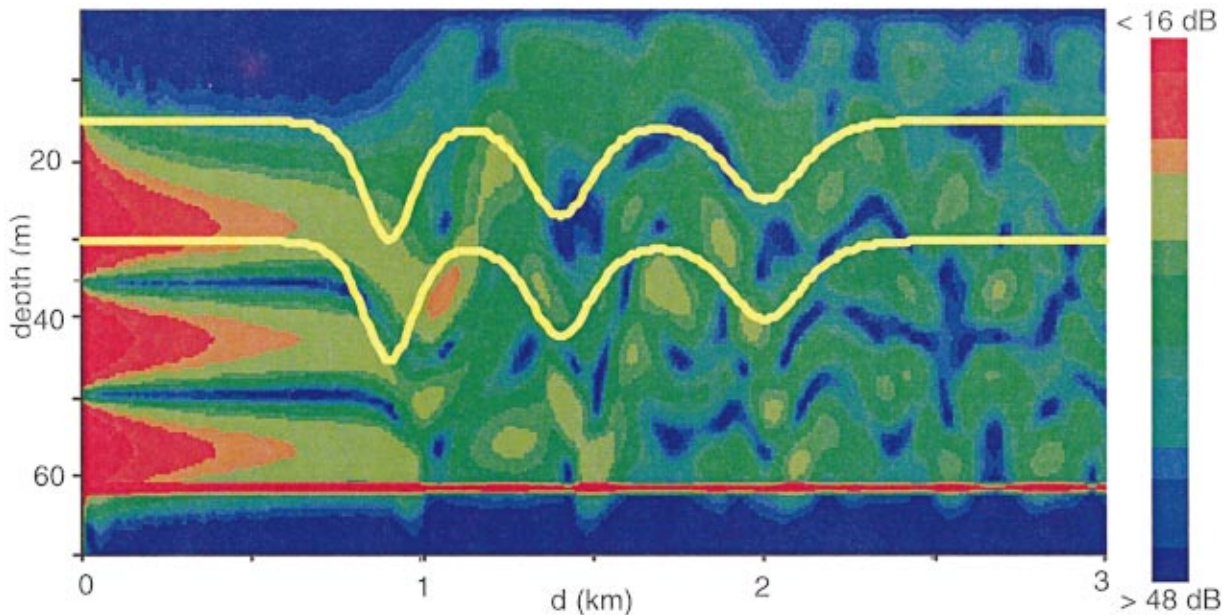


FIG. 4. Transmission loss for 400-Hz mode 3 starting field.

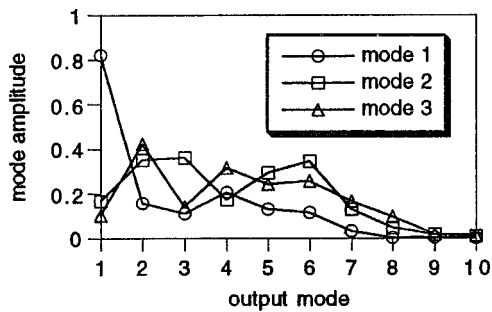


FIG. 5. Magnitude of elements in 400-Hz transmission matrix. Unit amplitude input mode couples into other modes after propagating through soliton packet. Environment described in text.

packet propagates. It can also, however, be used as the basis for a computationally efficient algorithm. Once \mathbf{P} is calculated, the remaining parameters—time, source depth, ranges to the soliton and the receiving array—can be easily varied. The matrix itself can be calculated by propagating individual modes through the range-dependent part of the medium using a parabolic equation routine.¹⁰

Figure 4 shows transmission loss associated with a 400-Hz mode 3 starting field propagating through the environment described by Eqs. (16) and (17). The yellow lines show contours of constant sound speed at the top and bottom of the thermocline. The red line indicates the sea bottom. The strong coupling of mode 3 into the other modes is apparent from the acoustic field at ranges beyond 2.5 km. The associated complex (i.e., including phase) field at the final range $d=3000$ m gives a column of the matrix \mathbf{P} . Repeating the simulation for other modes as the starting field fills the matrix. Magnitudes of elements in the matrix \mathbf{P} is plotted in Fig. 5 which shows how the first three modes couple into other modes as they propagate through the range-dependent environment described above. A through analysis¹⁰ of coupling behavior of a single solitary wave indicated that the energy will shift between normal modes at the steep faces of the internal solitary waves. For the solitary wave packet considered here (unevenly spaced solitons with different amplitudes), the elements of matrix \mathbf{P} are complex functions of signal frequency, packet geometry, water depth, and the degree of sound-speed variation. For example, note in Fig. 5 that the packet effectively shifts the second and third mode energy to other modes while keeping the adiabatic component of the first mode at relatively higher levels.

In the ensuing simulations, acoustic propagation is simulated at both 400 and 224 Hz. As was the case in the SWARM experiment, the 400-Hz source is located at $z_s = 29$ m, just below the unperturbed thermocline, while the 224-Hz source is positioned 2 m above the bottom. The receiving array is fixed at $x_r = 40$ km. The packet of solitary waves moves at 0.6 m/s, similar to what was observed in the SWARM experiment. Ten modes are used in all calculations.

Figure 6 shows results from the 400-Hz simulations. The amplitudes of the first three modes as observed at the receiving array are plotted over a 1-h time interval. Initially, at time $\tau=0$, the leading edge of the packet is at 20 km, midway between the source and receiver. The plot is normalized such that mode one has unit amplitude at $\tau=0$. Viewed over the

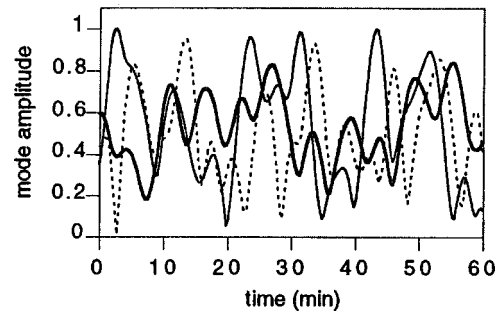


FIG. 6. Mode amplitude A_m for mode 1 (thick solid line), mode 2 (thin solid line), and mode 3 (dotted line). 400-Hz source located at $z_s = 29$ m. Environment described in text.

entire hour, the mode amplitudes display a rich structure. The amplitude of any particular mode varies over a range of time scales. In examining the 400-Hz SWARM data, Headrick reported an average modal decorrelation time of less than 2 min.² Results reported in Ref. 2 over individual 2-min windows, however, could vary significantly. The simple continuous wave simulation of Fig. 6 shows similar qualitative features if one focuses only on isolated 2-min time windows. For 2-min windows selected near local maxima, for example, the amplitude of a mode may exhibit slight variability. For other sections, the change in amplitude can be substantial. Time windows where one mode may change rapidly can occur when another mode is nearly constant. These results can be interpreted as a time-varying interference effect caused by mode coupling.

Figure 7 shows results from the 224-Hz simulations. In comparison to the 400-Hz calculations, the mode amplitudes exhibit a more slowly varying structure. This must be due to the relatively stronger coupling between more closely spaced mode pairs at 224 Hz which will cause large interference distances, hence relatively slow oscillations as the internal packet moves [see Eq. (13)]. Also, at 400 Hz, there are more modes excited and hence more widely separated mode pairs contribute to the high-frequency oscillations. At 224 Hz, the situation is closer to the weak-coupling case considered in the previous section; the amplitude of a given mode is more clearly dominated by a small number of harmonics.

The simple CW scenarios considered in this section serve to illustrate the model. The modal amplitudes display temporal variability on the time scales observed in the SWARM experiment. The experiment, however, used broad-

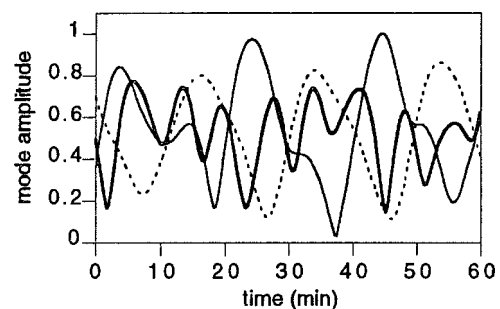


FIG. 7. Mode amplitude A_m for mode 1 (thick solid line), mode 2 (thin solid line), and mode 3 (dotted line). 224-Hz source located at $z_s = 58$ m. Environment described in text.

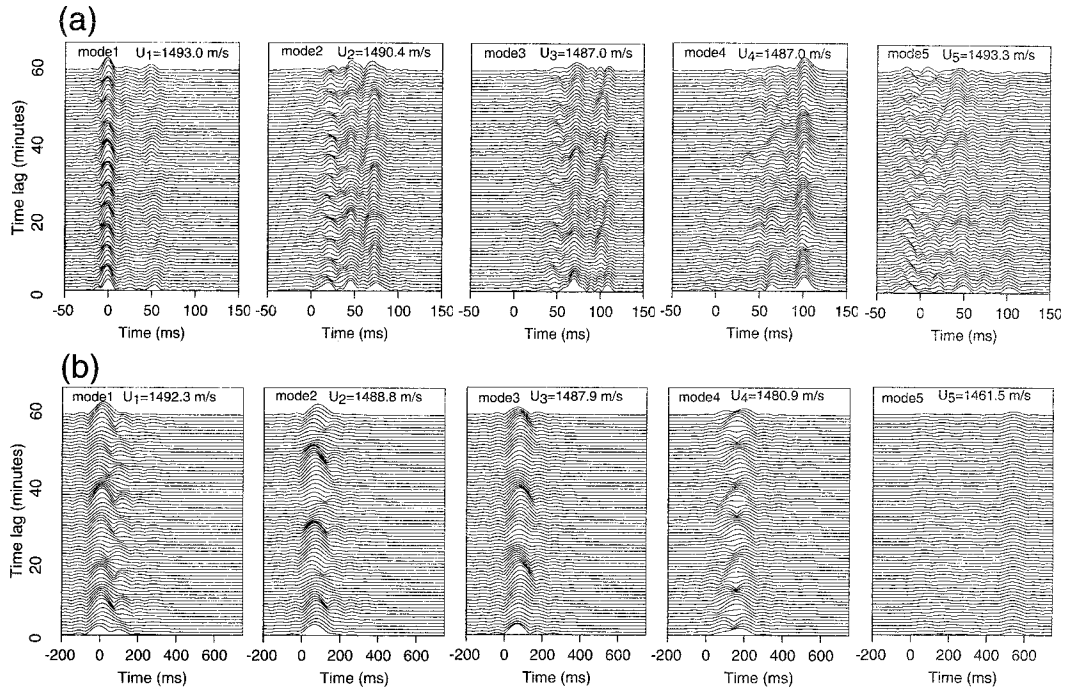


FIG. 8. Transient mode amplitudes $A_m(t; \tau)$ of (a) 350–450 Hz and (b) 216–232 Hz signals as the soliton packet moved from 20-km range to 17.84-km range. Environment is the same as that of the CW case described in Sec. IV.

band sources. Broadband simulations are considered in the following section.

IV. BROADBAND SIMULATIONS

Time-domain results for acoustic pulse propagation are obtained by Fourier synthesis of single-frequency runs. Corresponding to the bandwidths of the two sources used in SWARM, the single-frequency calculations were performed over two bands: 350–450 Hz and 216–232 Hz. The frequency intervals used for the band centered at 400 Hz was 1 Hz, while a 0.25-Hz interval was used for the 224-Hz band. This provided 1- and 4-s duration time windows which were long enough to minimize the wrap-around effects at the 40-km propagation range. Transient acoustic mode coefficients were obtained by broadband depth-projection mode filtering.² The short-term temporal coherence of individual modes was then studied by calculating the correlation coefficients between transient mode amplitudes of a reference signal and subsequent signals as the sound-speed field was varied due to internal wave propagation.

A. Simulations for a simple environment

For the simple environment of Eqs. (16) and (17), the calculations are again conveniently performed in terms of the transmission matrix \mathbf{P} . The matrix is constructed by propagating individual modes through the range-dependent part of the environment. The single frequency calculations are performed at each frequency bin to obtain the now frequency-dependent transmission matrix \mathbf{P} . For a band-limited transient signal, noting the frequency dependency of the pressure eigenfunction Ψ_m and the eigenvalue in Eq. (10), the transient pressure amplitude can be obtained from the CW pressure amplitude by Fourier synthesis as

$$p(x_f, z, t; \tau) = \int_{f_0}^{f_0 + \Delta f} S(f) p(x_f, z, f; \tau) e^{-i2\pi f t} df, \quad (18)$$

where $S(f)$ is the source spectrum defined within a frequency band Δf . Here, τ is lag-time, corresponding to when a pulse was transmitted. Similarly, the transient mode amplitudes can be obtained from frequency-dependent mode amplitudes defined in Eq. (11) as

$$A_m(t; \tau) = \int_{f_0}^{f_0 + \Delta f} S(f) A_m(f; \tau) e^{-i2\pi f t} df. \quad (19)$$

Figure 8 shows moduli of the first five transient mode amplitudes for 350–450-Hz and 216–232-Hz signals as the soliton packet moved from 20-km range to 17.84-km range. This range interval corresponds to a time interval of 1 h where again a constant propagation speed of 0.6 m/s for the internal wave packet has been assumed. The environmental parameters used in the calculation are same as those used in the CW simulations. In Fig. 8, the adiabatic travel time for mode 1 signal was arbitrarily chosen to be zero. If the acoustic propagation is entirely adiabatic, each panel shown in Fig. 8 would show a sequence of pulses each having constant amplitude and travel time as the soliton packet moves along the propagation path. Consider single-scattering components of mode m in the received field. The time difference of arrival of adiabatic mode m and scattered mode m will be determined by the propagation distance that scattered mode traveled in “donor mode” n and the difference in the group speeds of mode m and n . This behavior has been observed in model calculations (not shown here) as the arrival time of scattered component of mode m approaching that of the adiabatic component of donor mode n when the soliton packet moves closer to the receiver. If the soliton packet moves closer to the source, the arrival time of the scattered mode m

approaches to the adiabatic component of mode m . If the group speeds of donor and receiving modes are nearly equal, as in the case with modes 1 and 5 at 400 Hz, then the interference pattern will exhibit oscillations in amplitude at constant delay [see Fig. 8(a) for mode 1 at time 0 ms]. Each transient mode amplitude structure exhibits a quasi-periodic behavior as a function of time-lag, as observed in the CW mode amplitudes (see Figs. 6 and 7). Similar to the CW simulations, the periods of oscillations are larger for the 216–232-Hz signal than those for the 350–450-Hz signal. One interesting feature is that coupled transient mode peaks can be easily identified for the 350–450-Hz signal since the modes are well separated in time. Considering the group speeds given in Fig. 8, the calculated travel-time differences (relative to first mode) for 40-km range are -47 , -108 , -108 , and 5 ms for the second, third, fourth, and fifth modes, respectively. The peaks of adiabatic components of each mode can be identified in Fig. 8(a) based on the travel-time differences. Since the coupling occurs at the mid-range of propagation track, other peaks corresponding to the coupled transient modes can be also identified. For example, mode 2 peak at ~ 20 ms is coupled from mode 1 which traveled with relatively higher group speed in the first 20 km of the propagation track. Note also that the adiabatic component of mode 5 arrives earlier than the adiabatic component of mode 1. Similarly, for the 216–232-Hz signal, the calculated travel-time differences referred to mode 1 are -63 , -79 , -206 , and -565 ms. The relatively narrow bandwidth of the 216–232-Hz signal would prevent clearly identifying the adiabatic and coupled transient mode peaks for the first four modes. Note, however, that the adiabatic component of the mode 5 peak is clearly identified since its group speed is significantly lower and therefore temporally resolved.

To quantify the effects of a changing medium on pulse propagation, it is convenient to define a correlation coefficient for the transient mode amplitudes. For his analysis of the SWARM data, Headrick calculated the decorrelation time of individual modes.² Similarly, we define the normalized correlation coefficient of a particular mode m as

$$\rho_m(\tau) = \frac{|\int A_m(t;0)A_m(t;\tau) dt|}{(\int |A_m(t;0)|^2 dt)^{1/2}(\int |A_m(t;\tau)|^2 dt)^{1/2}}, \quad (20)$$

in which the integrals are evaluated over the width of the observed pulses.

Figures 9(a) and (b) show corresponding normalized mode correlation coefficients for the 350–450-Hz and 216–232-Hz signals, respectively. Notice the significant decay of the correlation coefficients within the first-2 min for both cases. Decorrelation of the 216–232-Hz signals is usually less than that of the 350–450-Hz signal for time lags larger than 5 min. This difference is due to the relatively smaller off-diagonal terms of the coupling matrix. The size of the coupling matrix is also smaller for the 216–232-Hz signals since a relatively fewer number of modes are generated at lower frequencies. Notice also that recorrelation at longer time-lags is observed in both cases. As will be shown in Sec. V, recorrelation was also observed in the SWARM data.

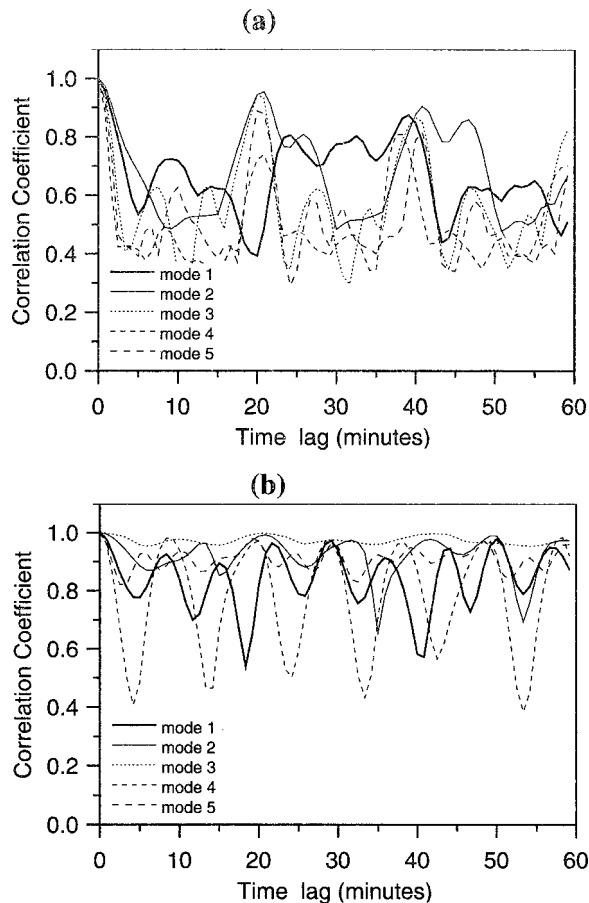


FIG. 9. Normalized mode correlation coefficients $\rho_m(\tau)$ for (a) 350–450 Hz and (b) 216–232 Hz signals with the transient mode amplitudes depicted in Fig. 8.

B. Simulations in the SWARM environment

Even if internal waves were not present, the SWARM environment would be range-dependent. Range-dependence is introduced by the varying bathymetry as well as by variability in the water column. Consequently, the computational short cut of propagating individual modes through the relatively small range-dependent part of the environment is no longer suitable. Propagation through the entire SWARM environment was simulated using Range-dependent Acoustic Model (RAM).¹⁷ Fourier techniques were again used for pulse propagation.

In this section, we first outline how the assorted environmental measurements made during SWARM were integrated to produce a semi-deterministic environmental model. Broad band acoustic simulations are then presented.

As detailed in Apel *et al.*,¹ extensive oceanographic and geophysical data were taken at the SWARM site concurrently with the acoustic measurements. To construct a model, 19 representative CTD profiles measured along the 42 km acoustic propagation track were used to provide a weakly range-dependent background sound-speed field. High-frequency acoustic backscatter measurements¹ provided a detailed structure of pycnocline depression with approximately 1 m horizontal resolution. The weakly range-dependent sound-speed field was modified by using the particle motion defined by the pycnocline depression and depth

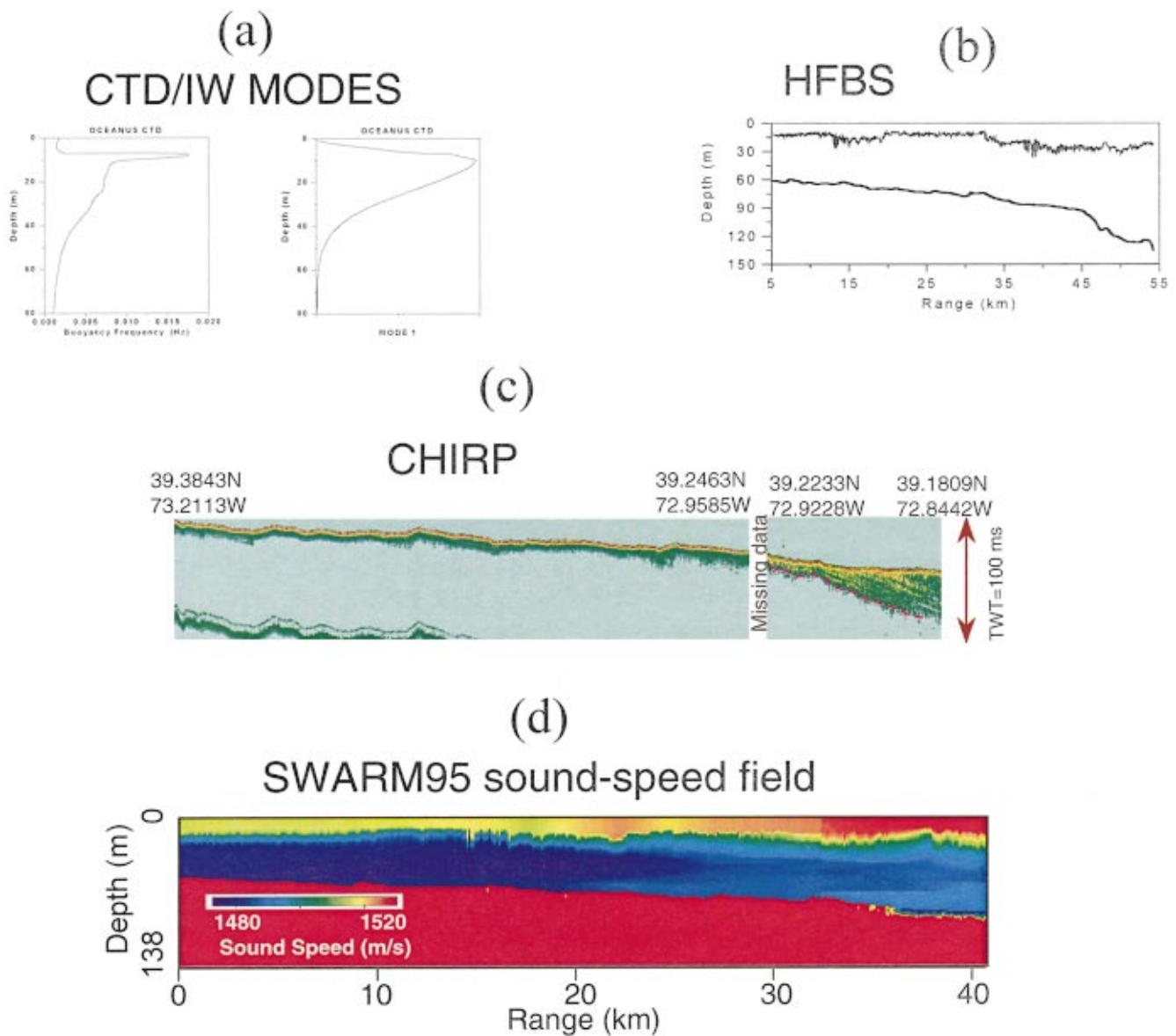


FIG. 10. Data from (a) CTD, (b) high-frequency backscatter, and (c) chirp sonar used for (d) environmental construction.

dependence of the first mode of internal wave field (calculated from CTD data). To obtain the range dependence of the internal field for a given time of the experiment, the high-frequency backscatter data set (approximately 6 h covering 42-km range) was adjusted in range by using the recorded ship speed of approximately 2 m/s and an internal-wave speed of 0.6 m/s. Detailed bathymetric data and bottom geoacoustic properties were obtained from chirp sonar data with 10-m range intervals.¹ Figure 10 shows the process of environmental construction using the yo-yo CTD, high-frequency backscatter, and chirp sonar data.

To simulate environmental time dependence, the sound-speed field in the water column was translated in range by assuming a constant internal wave propagation speed of 0.6 m/s. Since the internal wave packets are expected to be slowly varying, the assumption of nondispersive solitary wave propagation is justified for the calculation of temporal coherence at the time scales of interest here, namely a few tens of minutes. Rubenstein and Brill¹⁸ have used a similar approach by propagating measured “thermistor string” data

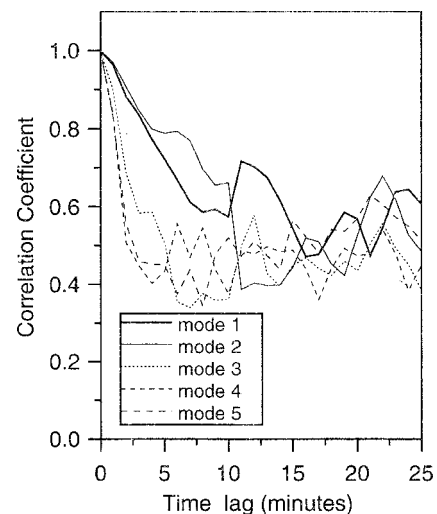


FIG. 11. Normalized mode correlation coefficients $\rho_m(\tau)$ of 350–450 Hz signal in the SWARM95 simulated environment at ($\tau=0$ is at 06:30:20 on JD210, 1995 as the reference).

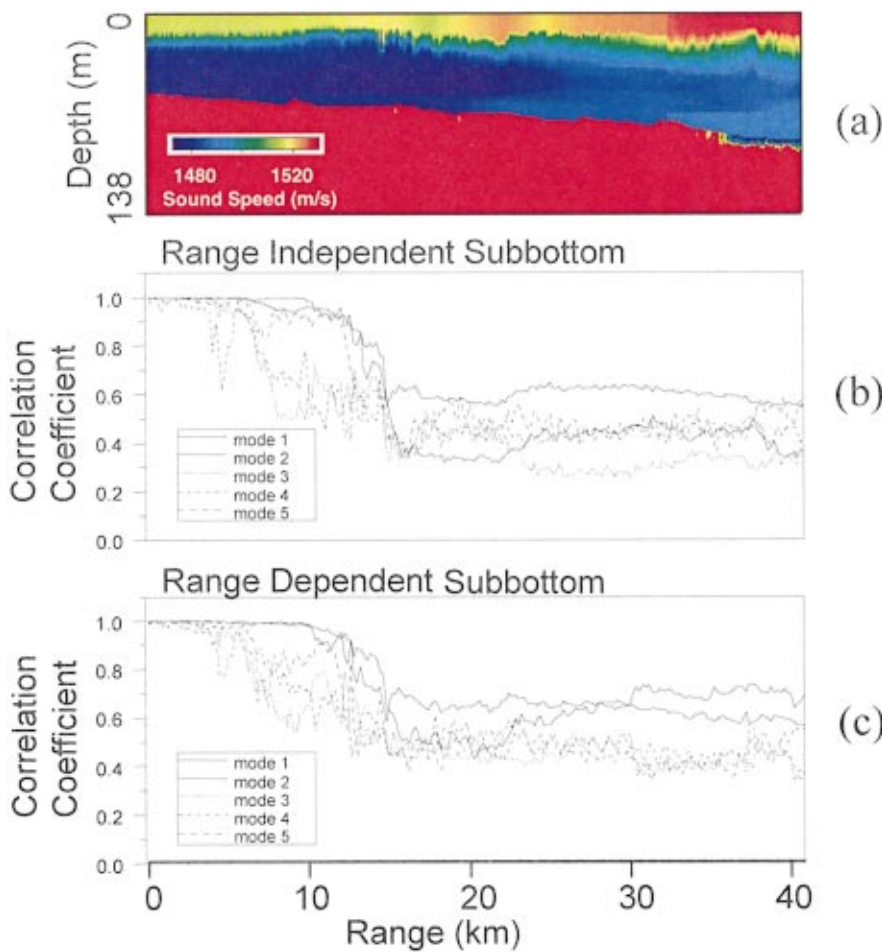


FIG. 12. Normalized mode correlation coefficients $\rho_m(r; \tau)$ of 350–450 Hz signal as a function of range r in the SWARM95 simulated environment ($\tau = 0$ is at 06:30:20 on JD210, 1995 as the reference) for $\tau = 10$ min using (a) range-dependent bottom and (b) range-independent bottom.

to explain measured high acoustic variability by obliquely propagating internal waves.

Figure 11 shows mode correlation coefficients of the calculated 350–450-Hz signal for up to 25 min time-lag using the signal for the simulated environment at 06:30:20 on JD210, 1995 as the correlation reference. Calculations were performed only for the 350–450-Hz signal due to the significant computational requirements. Correlation coefficients of all the modes considered decay to a level of 0.5 within 10 min. Similar to the SWARM experimental results shown below, the decay is more rapid for higher-order modes (e.g.,

mode orders 3–5 reach 0.5 level within the first 2 min). Also, the limiting values of the correlation coefficients are relatively smaller for the higher-order modes. This mode-order dependence might be due to the scattered portion of the mode energy dominating the received higher-order modal energy as a result of the strong attenuation of the adiabatic portion. Notice the partial recorelation peaks of first few modes at 11- and 22-min time lags which is also consistent with the SWARM experimental results.

Figures 12(b) and (c) show the mode correlation coefficients of the 350–450-Hz signal as a function of range (τ

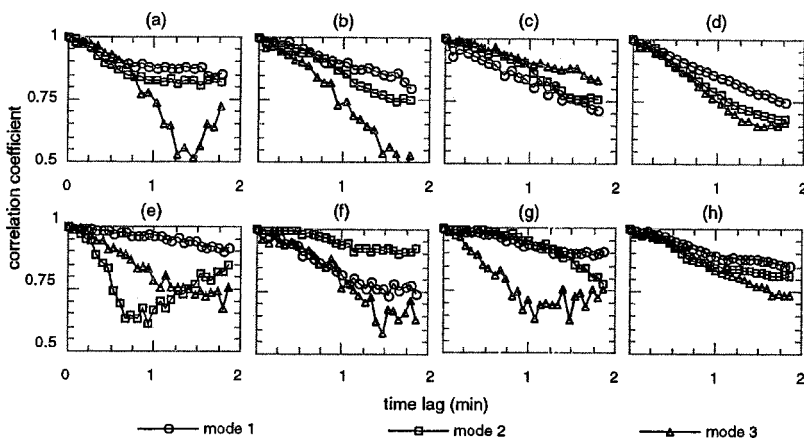


FIG. 13. Short-time lag mode correlation coefficients. Results from SWARM 95. (a)–(d) for 400 Hz data, (e)–(h) for 224 Hz. Time lag in (a) and (e) relative to JD 210 04:25:26. (b) and (c) look at 2-min windows 6 and 12 min later, respectively. (f) and (g) look at 2-min windows 5 and 10 min later, respectively. (d) and (h) are averages over 2 h.

$=0$ is at 06:30:20 on JD210 1995 as the reference and $\Delta\tau = 10$ min) for both SWARM range-dependent [Fig. 12(a)] and a range-independent bottom with average geoacoustic profiles. In using the range-independent bottom, the true bathymetry is replaced by one with a constant slope, where that slope is determined by the water depths at the source and receiver positions. Although the same decorrelation of the bottom interacting high-order modes is seen near the source, significant decorrelation of mode orders 1 and 2 starts at range ~ 14 km where the soliton packet is located. Both range-dependent and range-independent bottom simulations yield similar range dependency of correlation coefficients. This indicates that for the SWARM environment the bottom roughness and subbottom inhomogeneities have little effect on the temporal mode coherence. This result is probably due to the intrusion of warmer, more saline water near the bottom in the vicinity of the receiver. This upward-refracting part of the sound-speed profile near the bottom creates a duct and reduces the bottom/subbottom interaction. This intrusion is seen in the positive gradient of the near-bottom sound-speed profile near the receiver in Fig. 12(a).

V. EXPERIMENTAL RESULTS

Since the details of SWARM95 experiment have been reported in a previous overview paper,¹ only a brief description of experimental geometry and acoustic data is given here. The experiment took place between 20 July 1995 and 12 August 1995 in the Mid-Atlantic Bight continental shelf region off the coast of New Jersey. Extensive environmental data were collected concurrently with the acoustic propagation measurements using moored and ship-towed acoustic sources and moored vertical receiving arrays. The data reported in this paper are from two acoustic sources (center frequencies 224 and 400 Hz) moored at a common site in approximately 55 m of water. The source depths for the 224- and 400-Hz sources were 53 and 29 m, respectively. Both sources transmitted acoustic waveforms obtained from pseudo-random binary sequences using a programmed transmission schedule for two weeks. The 224-Hz source repeatedly transmitted 31 3.9375-s duration pulses (224 Hz center frequency and 16-Hz bandwidth) providing approximately a “two minutes on, three minutes off” schedule. The 400-Hz source repeatedly transmitted 23 5.11-s duration pulses (400 Hz center frequency and 100 Hz bandwidth) providing approximately a “two minutes on, four minutes off” schedule.

Acoustic data were collected using two well-populated vertical receiving arrays arranged on a line directly seaward of the sources at distances of 32 and 42 km from the source site. The data from the 32-km array have been analyzed by Headrick² and Headrick *et al.*³ The results reported here are for the 42-km array. This array was deployed in 88 m of water. It featured 32 hydrophones, spaced 2 m apart, spanning depths from 20 to 82 m. Note that all the hydrophones were below the nominal thermocline.

The received wavefront was decomposed into its constituent normal modes by spatial filtering. The mode filter coefficients were calculated using a sound-speed profile obtained from a CTD cast made near the array. Note that this

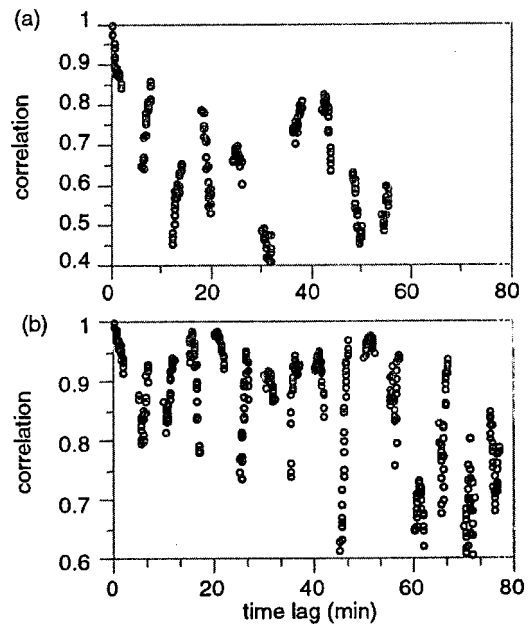


FIG. 14. Long-time-lag mode correlation coefficients (mode one) for SWARM 95 (a) 350–450 Hz and (b) 216–232 Hz data.

profile was not updated during processing. The use of the same profile for 2 h does seriously hamper the analysis; numerical results confirmed that low-order modes processed here are not particularly sensitive to the details of the sound speed profile. (This would not be true when a packet of internal waves is in the vicinity of the array.^{2,8} Such periods are not considered here.) The short-time lag coherence analysis suggested by Eq. (20) was performed using the pulse sequences received during the 2-min periods when a source was transmitting.

Figure 13 shows the short-time lag mode correlation coefficients for the first three modes. The top row shows results for the 400-Hz transmissions. Figures 13(b) and (c) show the correlation over 2-minute windows starting 6 and 12 min, respectively, after Fig. 13(a). Notice the significant variability between the different panels. For example, while the third mode decorrelates the most rapidly in Figs. 13(a) and (b), it remains the most correlated 6 min later. Figure 13(d) shows the average of several 2-minute windows taken over 2 h. The results are comparable to those presented by Headrick² for the 32-km array. Similarly, Figs. 13(e)–(h) show results for the 224-Hz transmissions. The decorrelation is typically more rapid for the 400 Hz data than it is for 224 Hz.

Figure 14 shows the long-time-lag correlation coefficients for both frequencies. Because of uncertainty in the assumed sound-speed profile, only the first mode is shown. The transmission schedule used in the experiment leaves gaps in the two time series. As a result, it is difficult to make definitive statements about a possible recorrelation effect, particularly at 400 Hz. The 224-Hz results do suggest a regular recorrelation at time scales of 6 min and longer.

VI. DISCUSSION AND CONCLUSIONS

In this paper, the observed rapid decorrelation of acoustic modes in shallow water has been studied. We have hypothesized that this is a direct consequence of the motion of

internal wave packets. A simple model has been proposed that treats the packets as mode coupling structures that move through the acoustic propagation regime. We showed that broadband acoustic simulations consistent with this model can produce decorrelation times consistent with those observed in the SWARM experiment.

It remains an open research question as how to best model propagation through solitary internal waves. Both deterministic and stochastic approaches have been proposed.^{19,20} The model we have formulated takes an essentially deterministic viewpoint. While the details of the internal waves may be random, the simple motion of the waves explains the observed decorrelation of the acoustics. In this model, the motion of a mode coupling structure is the key ingredient. If the effects of the solitary waves were so benign as to produce only adiabatic changes in the acoustics, there would be no decorrelation for CW signals. Our model does not preclude the additional presence of other random sources of variability such as background internal waves. No attempt has been made here to rank the relative importance of discrete solitary waves and random background waves. Other effects, such as soliton motion at an angle to the vertical plane established by the source and receiver,¹⁰ have also been neglected.

An interesting feature of the proposed model is that it predicts a partial recorelation of the acoustic field. This occurs as the relative phase retardation between dominant mode pairs approaches 2π . This is an important result as it suggests that the fading and reemergence of a signal may occur in a predictable way. This is the subject of continued research.

ACKNOWLEDGMENTS

This work was supported by the Office of Naval Research. Dr. Rouseff spent the summer of 1997 visiting NRL and working on this project as an American Society for Engineering Education—U.S. Navy Senior Faculty Fellow. A preliminary version of this research was presented at the 136th Meeting of the Acoustical Society of America.

¹J. R. Apel, M. Badiéy, C.-S. Chiu, S. Finette, R. Headrick, J. Kemp, J. F. Lynch, A. Newhall, M. H. Orr, B. H. Pasewark, D. Tielbuerger, A. Turgut, K. von der Heydt, and S. Wolf, "An Overview of the 1995 SWARM shallow-water internal wave acoustic scattering experiment," *IEEE J. Ocean. Eng.* **22**(3), 445–464 (1997).

²R. H. Headrick, "Analysis of internal wave induced mode coupling effects on the 1995 SWARM experiment acoustic transmissions," Ph.D. dissertation, MIT, 1997.

³R. H. Headrick, J. F. Lynch, J. Kemp, A. Newhall, K. von der Heydt, J. R. Apel, M. Badiéy, C.-S. Chiu, S. Finette, M. Orr, B. Pasewark, A. Turgut, S. Wolf, and D. Tielbuerger, "Acoustic normal mode fluctuation statistics in the 1995 SWARM internal wave scattering experiment," *J. Acoust. Soc. Am.* **107**, 201–220 (2000).

⁴W. H. Munk, "Internal waves and small-scale processes," in *Evolution of Physical Oceanography*, edited by B. A. Warren and C. Wunsch (MIT, Cambridge, MA, 1981), pp. 264–291.

⁵A. K. Liu, "Analysis of nonlinear internal waves in the New York Bight," *J. Geophys. Res.* **93**, 12317–12329 (1988).

⁶F. S. Henyey, and A. Hoering, "Energetics of borelike internal waves," *J. Geophys. Res.* **102**, 3323–3330 (1997).

⁷J. X. Zhou, X. Z. Zhang, and P. H. Rogers, "Resonant interaction of sound with internal solitons in the coastal zone," *J. Acoust. Soc. Am.* **90**, 2042–2054 (1991).

⁸J. X. Zhou, X. Z. Zhang, P. H. Rogers, D. Wang, and E. Luo, "Anomalous sound propagation in shallow water due to internal wave solitons," *Proc. Oceans '93*, I87–I92 (1993).

⁹D. Tielbuerger, S. Finette, and S. Wolf, "Acoustic propagation through an internal wave field in a shallow water waveguide," *J. Acoust. Soc. Am.* **101**, 789–808 (1997).

¹⁰J. C. Preisig, and T. F. Duda, "Coupled acoustic mode propagation through continental-shelf internal solitary waves," *IEEE J. Ocean. Eng.* **22**, 256–269 (1997).

¹¹T. F. Duda, and J. C. Preisig, "A modeling study of acoustic propagation through moving shallow-water solitary wave packets," *IEEE J. Ocean. Eng.* **24**, 16–32 (1999).

¹²K. Yoo, and T. C. Yang, "Broadband source localization in shallow water in the presence of internal waves," *J. Acoust. Soc. Am.* **106**, 3255–3269 (1999).

¹³F. B. Jensen, W. A. Kuperman, M. B. Porter, and H. Schmidt, *Computational Ocean Acoustics* (American Institute of Physics, New York, 1994).

¹⁴T. C. Yang, "Effectiveness of mode filtering: A comparison of matched-field and matched mode processing," *J. Acoust. Soc. Am.* **87**, 2072–2084 (1990).

¹⁵L. M. Brekhovskikh and Y. P. Lysanov, *Fundamentals of Ocean Acoustics* (Springer-Verlag, New York, 1991), pp. Sec. 6.7.1.

¹⁶S. Finette, M. H. Orr, A. Turgut, J. R. Apel, M. Badiéy, C.-S. Chiu, R. H. Headrick, J. N. Kemp, J. F. Lynch, A. E. Newhall, K. von der Heydt, B. Pasewark, S. N. Wolf, and D. Tielbuerger, "Acoustic field variability induced by time evolving internal wave fields," *J. Acoust. Soc. Am.* **108**, 957–972 (2000).

¹⁷M. D. Collins, R. J. Cederberg, D. B. King, and S. A. Chin-Bing, "Comparison of algorithms for solving parabolic wave equations," *J. Acoust. Soc. Am.* **100**, 178–182 (1996).

¹⁸D. Rubenstein and M. H. Brill, "Acoustic variability due to internal waves and surface waves in shallow water," in *Ocean Variability and Acoustic Propagation* (Kluwer, Dordrecht, 1991), pp. 215–228.

¹⁹R. H. Headrick, J. F. Lynch, J. Kemp, A. Newhall, K. von der Heydt, J. R. Apel, M. Badiéy, C.-S. Chiu, S. Finette, M. Orr, B. Pasewark, A. Turgut, S. Wolf, and D. Tielbuerger, "Modeling mode arrivals in the 1995 SWARM experiment acoustic transmissions," *J. Acoust. Soc. Am.* **107**, 221–236 (2000).

²⁰J. F. Lynch, "Report of the Office of Naval Research Shallow-Water Acoustic Workshop, 1–3 October 1996," Woods Hole Oceanographic Institution Technical Report WHOI-97-12 (1997).

Determination of elastic moduli of rock samples using resonant ultrasound spectroscopy

TJ Ulrich and K. R. McCall

Department of Physics, University of Nevada, Reno, Nevada 89557

R. A. Guyer

Department of Physics, University of Massachusetts, Amherst, Massachusetts 01003

(Received 28 December 2000; revised 20 January 2002; accepted 28 January 2002)

Resonant ultrasound spectroscopy (RUS) is a method whereby the elastic tensor of a sample is extracted from a set of measured resonance frequencies. RUS has been used successfully to determine the elastic properties of single crystals and homogeneous samples. In this paper, we study the application of RUS to macroscopic samples of mesoscopically inhomogeneous materials, specifically rock. Particular attention is paid to five issues: the scale of mesoscopic inhomogeneity, imprecision in the figure of the sample, the effects of low Q , optimizing the data sets to extract the elastic tensor reliably, and sensitivity to anisotropy. Using modeling and empirical testing, we find that many of the difficulties associated with using RUS on mesoscopically inhomogeneous materials can be mitigated through the judicious choice of sample size and sample aspect ratio. © 2002 Acoustical Society of America. [DOI: 10.1121/1.1463447]

PACS numbers: 43.35.Cg, 43.35.Yb, 43.20.Ks [SGK]

I. INTRODUCTION AND BACKGROUND

In this paper, we explore the application of resonant ultrasound spectroscopy (RUS) to macroscopic (e.g., $L_{\text{macro}} = 0.1 \text{ cm} - 10 \text{ cm}$) samples of rock in order to learn the elastic tensor. Rocks are consolidated materials, typically assembled from aggregates of mesoscopic sized pieces (e.g., $L_{\text{meso}} = 10 \mu\text{m} - 100 \mu\text{m}$) of microscopically uniform material (length scale L_{μ}). They are mesoscopically inhomogeneous, that is, inhomogeneous on a scale small compared to the sample size but large compared to the microscopic length scale ($L_{\text{macro}} \gg L_{\text{meso}} \gg L_{\mu}$). Rocks are not easily machined to precise shapes. While the microscopic scale symmetry is homogenized by the process of their assembly, these samples may have macroscopic symmetry of great importance. For example, rock samples commonly have symmetry due to bedding planes or other features related to their construction. Our goal is to proscribe the conditions necessary for the successful use of RUS on rock and rocklike materials. These conditions include constraints on sample preparation and constraints on the set of reasonable questions that can be answered with RUS.

The success of RUS derives from the sensitivity of the normal mode frequencies of a sample to its elastic structure.¹ The elastic structure affecting resonance frequencies has three components: the figure of the sample; the homogeneity of the sample; and the elastic tensor of the sample, including symmetry and orientation. Given a perfectly homogeneous sample with a precise figure, the elastic tensor can be derived to a very high degree of accuracy.²

The definition of the elastic tensor C_{ijkl} comes from an expansion of the free energy of an elastic system to second order in the strain field,³

$$\mathcal{E} = \mathcal{E}_0 + \frac{1}{2} C_{ijkl} \epsilon_{ij} \epsilon_{kl}, \quad (1)$$

where

$$\epsilon_{ij} = \frac{1}{2} \left(\frac{\partial u_i}{\partial x_j} + \frac{\partial u_j}{\partial x_i} \right) \quad (2)$$

is the $ij = ji$ component of the strain tensor, and u_i is the i th component of the displacement field. We use notation in which repeated indices are summed. The equation of motion for the displacement field is

$$\rho \frac{\partial^2 u_i}{\partial t^2} = \frac{\partial \sigma_{ij}}{\partial x_j}, \quad (3)$$

where

$$\sigma_{ij} = \frac{\partial \mathcal{E}}{\partial (\partial u_i / \partial x_j)} \quad (4)$$

is the stress field.

For a finite sample, the elastic equations of motion are complemented by the requirement that the normal components of internal stresses balance the external stresses at the surface of the sample. That is,

$$\sigma_{ik}(\mathbf{x}) n_k(\mathbf{x}) = P_i(\mathbf{x}), \quad (5)$$

where \mathbf{n} is the normal to the surface at \mathbf{x} , and P_i is the normal component of the external stress applied to the sample at \mathbf{x} .

For linear systems, the elastic tensor C_{ijkl} relates the stress field to the strain field, $\sigma_{ij} = C_{ijkl} \epsilon_{kl}$. Because both stress and strain are symmetric, $\sigma_{ij} = \sigma_{ji}$ and $\epsilon_{ij} = \epsilon_{ji}$, the notation is commonly contracted such that stress and strain are six-component rank-one tensors, and the elastic tensor is a 6×6 rank-two tensor.⁴ In the contracted notation,

$$\sigma_{\alpha} = c_{\alpha\beta} \epsilon_{\beta}, \quad (6)$$

where $x = 1, y = 2, z = 3, \epsilon_{11} = \epsilon_1, \epsilon_{22} = \epsilon_2, \epsilon_{33} = \epsilon_3, \epsilon_{23} = \epsilon_4, \epsilon_{31} = \epsilon_5, \epsilon_{12} = \epsilon_6$, and similarly for the stresses. For an isotropic sample, the symmetry of the system allows further

reductions of the elastic tensor until only two elements are independent,

$$c_{\alpha\beta} = \begin{pmatrix} \lambda + 2\mu & \lambda & \lambda & 0 & 0 & 0 \\ \lambda & \lambda + 2\mu & \lambda & 0 & 0 & 0 \\ \lambda & \lambda & \lambda + 2\mu & 0 & 0 & 0 \\ 0 & 0 & 0 & \mu & 0 & 0 \\ 0 & 0 & 0 & 0 & \mu & 0 \\ 0 & 0 & 0 & 0 & 0 & \mu \end{pmatrix}, \quad (7)$$

or $c_{11} = \lambda + 2\mu$, $c_{12} = \lambda$, and $c_{44} = \mu = (c_{11} - c_{12})/2$. The constants λ and μ are called the Lamé coefficients; c_{11} is the compressional modulus, and c_{44} is the shear modulus (μ). Other sets of two independent coefficients are also common, such as the bulk modulus and shear modulus ($K = \lambda + 2\mu/3, G = \mu$), or Young's modulus and Poisson's ratio [$E = \mu(3\lambda + 2\mu)/(\lambda + \mu), \nu = \lambda/2(\lambda + \mu)$].

In terms of the Lamé coefficients, the equation of motion, Eq. (3), for an isotropic sample is

$$\rho \ddot{u}_i = (\lambda + \mu) \frac{\partial}{\partial x_i} \nabla \cdot \mathbf{u} + \mu \nabla^2 u_i, \quad (8)$$

and the boundary condition on the surface of the sample is

$$\lambda \nabla \cdot \mathbf{u} n_i + 2\mu \frac{\partial u_i}{\partial x_k} n_k = P_i; \quad (9)$$

$P_i = 0$ for a free standing sample.

Historically, the elements of the elastic tensor of macroscopic inhomogeneous materials have been found using mechanical testing⁵ or ultrasonic time-of-flight measurements.⁶ In mechanical testing the strain in response to stress, the inverse of Eq. (6), is measured between ambient conditions and failure in order to determine material strength and toughness. Components of the elastic tensor are found from mechanical testing data as the slope of stress versus strain extrapolated to low strain. For example, $c_{11} = \sigma_1 / \epsilon_1$, for low strain. A mechanical test is typically quasistatic, i.e., the stress is varied slowly (e.g., 0 MPa to 10 MPa in 1000 s). Mechanical tests are inherently high amplitude tests. The great disadvantage to using such tests to determine the low strain elastic tensor is that the sample is often altered or destroyed as a result of the test. Thus results cannot be confirmed for a given sample and only part of the elastic tensor can be determined for each run. In addition, mechanical testing often probes the sample at strains that activate its hysteretic elastic response. Thus extrapolation of such data to low strain is not reliable.⁷ Our primary interest is in the elastic tensor for low amplitude disturbances that is related to the propagation of acoustic waves. Generally, elements of the elastic tensor found from mechanical testing have lower value than elements of the elastic tensor inferred from time-of-flight measurements. In other words, the quasistatic modulus is less than the dynamic modulus.

Time-of-flight determinations of the elements of the elastic tensor are measurements of the velocity of an acoustic pulse propagating in the sample. The displacement caused by the acoustic pulse obeys Eq. (8), but the constraints set by Eq. (9) at the sample surface are not met, as transducers must

be bonded to the surfaces of the sample. The boundary condition can be ignored if the pulse width is small compared to the sample width. The transmission time t of an ultrasonic pulse across the sample is measured. Given the distance from source to receiver L , and density of the sample ρ , the wave velocities and elastic tensor can be determined. From $v = L/t$, $c_{11} = \lambda + 2\mu = \rho v_c^2$, and $c_{44} = \mu = \rho v_s^2$, where v_c and v_s are the compressional wave velocity (wave vector parallel to displacement) and shear wave velocity (wave vector perpendicular to displacement) respectively. To determine both compressional and shear velocities, transducers that produce compressional and shear waves are bonded to the sample in a variety of orientations.

Resonant ultrasound spectroscopy is an alternative technique for determining the elements of the elastic tensor of a sample. In RUS the frequencies of N low-lying modes of a free standing sample are measured. These measured frequencies are compared to N frequencies found by solving Eq. (8), while satisfying the free boundary condition set by Eq. (9) with $P_i = 0$. The modes of the sample are not simply compressional or shear waves, as is the case for pulse propagation, but are complicated entities having both compressional and shear character. Thus in RUS the problem of solving Eqs. (8) and (9) for the n th model resonance frequency f_n^M , has equal prominence with the problem of measuring the n th experimental resonance frequency f_n^X . The elements of the elastic tensor are found by minimizing

$$df^2 = \sum_{n=1}^N (f_n^X - f_n^M(c_{\alpha\beta}))^2 \quad (10)$$

with respect to $c_{\alpha\beta}$.

In Sec. II, several issues pertaining to using RUS on inhomogeneous samples are discussed. In most cases, numerical modeling was used to explore ways to optimize experimental chances for success. In Sec. III, the results of RUS experiments on a variety of samples are displayed and discussed as well as a summary of our findings, describing the bounds on RUS applicability to inhomogeneous materials found empirically and through modeling.

II. MODELING AND EXPERIMENTAL DEVELOPMENT

In this section we will apply the methods described in Visscher *et al.*⁸ to model and analyze experiments performed on macroscopic samples of rock. The assumptions inherent in the analysis will be discussed, as well as ways in which to maximize the success of RUS on samples whose properties do not superficially satisfy these assumptions. Since rocks are not single crystals, or even polycrystals, but are usually aggregates of multiple materials with different symmetry properties, we do not expect to be able to study detailed properties of specific modes of the sample, or to probe the sophisticated symmetries that may be present in the constituents of the samples. Our goal is to characterize the aggregate material. To this end, we will focus our attention on average frequency changes over multiple modes, i.e., we begin by answering the broadest questions, such as whether there is a good isotropic approximation to the elastic tensor of the rock. If we have a satisfactory answer to this question, we

may ask whether there is a possible transverse isotropic approximation to the elastic tensor. In this work, we do not attempt to answer refined questions that focus on the behavior of particular modes of a particular symmetry.

The experiment, measurement of resonance frequencies, and numerical inversion is performed using hardware and software developed by Dynamic Resonance Systems (DRS), a commercial provider of RUS measurement systems. Numerical inversion, i.e., determination of $c_{\alpha\beta}$ from Eq. (10), is based on the Visscher *et al.*⁸ variational technique. The analysis software finds model resonance frequencies using a model of the elastic system in which it is (A) free standing, (B) spatially homogeneous, and (C) a rectangular parallelepiped. Departure of the experimental system or sample from these three conditions can introduce shifts in the experimentally measured frequencies that will introduce errors in the derived elastic tensor. How well our system and samples conform to (A), (B), and (C), and estimates of the error induced by nonconformity are discussed below.

Rock and similar type samples, e.g., concrete, have relatively high acoustic attenuation, or low Q . Thus several very practical issues arise. (D) What can we do to make the resonance peaks distinct from one another and therefore well defined? (E) How do we acquire the most information out of the low-lying resonance peaks, the ones we can see clearly? That is, how do we maximize the dependence of the low-lying resonances on the full elastic tensor? Finally, (F) how sensitive are we to anisotropy in the sample? We will show here, that by altering the sample geometry, while maintaining a rectangular parallelepiped shape, these practical issues can be addressed.

A. Free boundaries

The variational technique used to find model frequencies, f_n^M , is based on recognizing that the displacement field satisfying the elastic wave equation with free boundaries on the sample surface, Eq. (8) and Eq. (9) with $P_i=0$, also makes the elastic Lagrangian of the sample stationary.⁸ To approximate free boundaries in the experiment, the source and detector are most often placed at vertices of the parallelepiped, delicately supporting the sample. The sample is nearly free standing. Holding the sample at vertices has the further advantage of keeping the transducers away from the expected node lines of the resonant modes. When the full resonance spectrum is complicated, transducers may be placed purposely at expected nodes, such as the center of a face, to temporarily simplify the spectrum. Using transducers for support limits the sample size. Our transducers are PZT-5 piezoelectric pinducers. We have limited our samples to less than 100 cm³, and 250 g.

B. Homogeneity

The elastic behavior of a consolidated material is primarily determined by a macroscopic average over the bonds between constituents (grains in a rock), rather than by the elastic properties of the constituents themselves. For example, the elastic behavior of sandstone, a quartz conglomerate, is more a function of grain-to-grain bond properties than of SiO₂ properties. We are interested in the elastic prop-

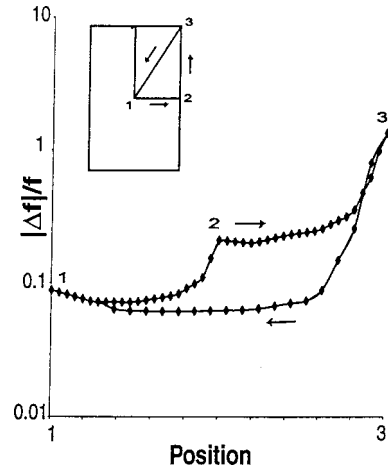


FIG. 1. Percentage frequency shift as a function of mass perturbation placement. The perturbation is moved through a two-dimensional rectangle as shown in the inset.

erties of consolidated materials, i.e., materials that are mesoscopically inhomogeneous. We want to be able to regard these materials as homogeneous. We adopt the rule of thumb that an inhomogeneous material looks homogeneous to a propagating wave when the wavelength of the wave is much greater than the length scale of the inhomogeneity.

A simple calculation for a one-dimensional system with free boundaries results in resonance wavelengths $\lambda = 2l/n$, where l is the length of the sample and n is an integer number of nodes. Assuming that we need the first ten resonance frequencies to accurately determine two elastic constants with RUS,¹ we want the maximum size of an inhomogeneity $\xi \ll l_{\min}/5$, where l_{\min} is the length of the smallest side of the sample. This estimate is very conservative, since it is highly unlikely that all of the first ten resonant modes in a three-dimensional sample will have nodes along a single direction. We use the ratio ξ/l_{\min} to characterize the inhomogeneity of our samples, where ξ is crudely determined by measuring the diameter of the largest area of color variation on the surface of a sample, e.g., the diameter of the largest black spot on a sample of Sierra white granite.

C. Sample geometry, the figure of the sample

Samples of consolidated materials are difficult to machine without chipping, and often do not have perfectly parallel sides. How ideal must the figure of a sample be? This question can be examined using the perturbation treatment of the elasticity problem sketched in the Appendix. To simulate the effect of an error in the figure of a sample, a localized mass is carried around a two-dimensional rectangular membrane, and the frequency shift caused by this mass is calculated. The frequency shift for mode n is given by

$$\frac{\omega_n^2 - \omega_{n0}^2}{\omega_{n0}^2} \approx 2 \frac{\delta f_n}{f_n} = \langle u_n | \frac{\delta \rho}{\rho_0} | u_n \rangle, \quad (11)$$

where u_n and ω_{n0} are the n th eigenmode and eigenfrequency of a perfectly shaped sample and $\delta \rho$ is the localized mass perturbation being carried around the sample (see the Appendix). In Fig. 1, the average frequency shift of the lowest 20

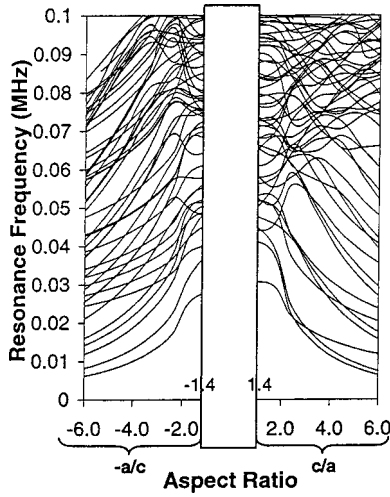


FIG. 2. Calculated resonance frequencies as a function of aspect ratio. The sample is at a constant volume of 4.8 cm^3 , $b = 1.1a$, and the aspect ratio is c/a on the right side, $-a/c$ on the left side. The elastic constants are $c_{11} = 86.6 \text{ GPa}$ and $c_{44} = 31.9 \text{ GPa}$.

resonances of the membrane,

$$\delta F = \frac{1}{20} \sqrt{\sum_{n=1}^{20} \left(\frac{\delta f_n}{f_n} \right)^2}, \quad (12)$$

is shown as a function of the perturbation placement. The perturbation is carried along the sample edge and into the sample interior as shown in the inset in the figure. When the perturbation is at an interior point it is essentially a 1% mass distortion, when it is along the perimeter it is a 1% distortion of the figure. Distortions in the figure of the sample are much more important than equivalent mass distortions in the sample interior. A 1% chip out of the corner of a sample can produce a 1% change in the frequency. A 1% mass distortion at the sample center produces less than 0.2% change in frequency.

The test calculation was performed on a two-dimensional membrane. In three dimensions we expect small mass distortions to cause smaller frequency shifts than in two dimensions. Given the number of other contributors to error in RUS measurements on consolidated materials, the contribution due to a mass or figure distortion is rather small. This conclusion was confirmed empirically by making RUS measurements on samples before and after chipping, and on various samples of the same size.

D. Distinct resonance peaks

Consolidated materials are often found to have a low quality factor Q , i.e., a high attenuation. At fixed amplitude, low Q materials have fewer observable resonance frequencies than high Q materials. Additionally the broader resonance peaks of low Q materials overlap nearby peaks and complicate peak picking. However, the geometry of a sample sets the frequency difference between peaks. For example, a sample that is a cube of an isotropic material has a three-fold degeneracy in all of its resonance frequencies. Thus we can use geometry to minimize peak overlap due to a low Q .

In Fig. 2, calculated resonance frequencies are plotted

for a parallelepiped sample as a function of the aspect ratio, c/a . The volume of the sample is fixed, $a \times b \times c = 4.8 \text{ cm}^3$, and $b = 1.1a$. Aspect ratios greater than one correspond to rodlike samples and are characterized by the number c/a in Fig. 2. Aspect ratios less than one correspond to platelike samples and are characterized by the number $-a/c$ in Fig. 2. A homogeneous, isotropic sample with elastic constants appropriate to basalt was assumed. As the aspect ratio is increased, the low-lying modes separate. For example, at $b = 1.1a$, $c/a = 4$, we expect to be able to pick out 14 distinct resonances before mode overlap becomes a serious problem for a RUS experiment.

Increasing the aspect ratio further might allow us to pick out even more distinct peaks. However, the RUS inversion code uses a fixed order polynomial to variationally fit modes.⁸ As one side of a sample becomes disproportionately large, a disproportionate number of nodes in the normal modes will be in that direction, and the inversion code will lose fitting accuracy in that direction. We have chosen to keep samples at $1/4 \leq c/a \leq 4$ (-4 to 4 in Fig. 2).

E. c_{11} dependence

A rule of thumb¹ is that five resonance frequencies are needed to accurately determine each independent component of the elastic tensor. Thus for an isotropic material described by two independent components, c_{11} and c_{44} , we need to experimentally determine at least ten resonance frequencies. Certainly the confidence with which the two independent components of the elastic tensor can be determined is influenced by the involvement of each component in the first ten modes of the sample.

The dependence of mode n on c_{11} or c_{44} is given by the derivative of the n th model frequency with respect to the modulus,

$$D_{in} = \frac{2c_{ii}}{f_n^M} \frac{\partial f_n^M}{\partial c_{ii}}, \quad (13)$$

where $i = 1$, or 4 . The derivatives are normed such that $D_{1n} + D_{4n} = 1$. Since $c_{44} \approx c_{11}/2$, i.e., $v_s < v_c$, we expect low frequency modes to be more highly dependent on c_{44} than on c_{11} (in analogy to the frequencies of the modes of a soft spring versus a stiff spring network). Indeed, for a cube of basalt, the first eight modes have an average dependence on c_{11} of less than 15%. That is, most low-lying modes are shear modes, involving very little compression. However, the geometry of the sample influences the dependence of a mode on c_{11} . Platelike and rodlike samples will have low-lying bending or flexural modes that are compressional in nature.

In Fig. 3, the mode dependence on c_{11} , D_{1n} , is shown as a function of the ratio of the longest side to the shortest side of the sample, c/a , for the first ten modes of a parallelepiped. The third side of the sample is held fixed with respect to the shortest side, $b = 1.1a$. Positive aspect ratios denote rodlike samples (the aspect ratio c/a on the right side); negative aspect ratios denote platelike samples (the aspect ratio $-a/c$ on the left side). A homogeneous, isotropic sample with elastic tensor appropriate to basalt was used. As the aspect ratio is increased, sensitivity to c_{11} increases. For ex-

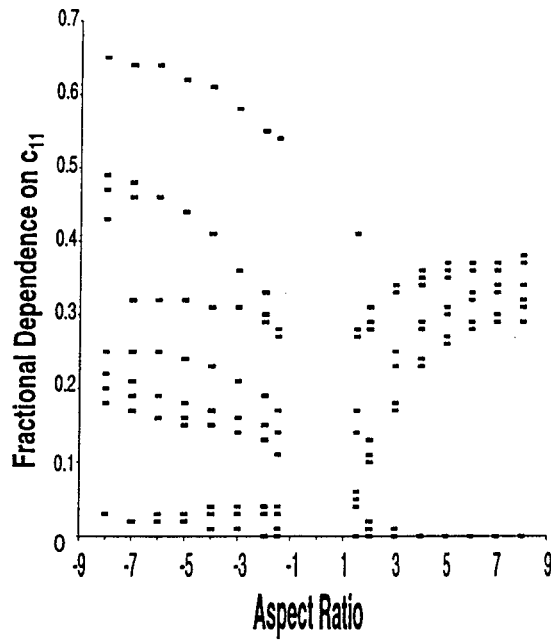


FIG. 3. c_{11} dependence as a function of aspect ratio. The sample is at a constant volume of 4.8 cm^3 ; $b = 1.1a$, and the aspect ratio is c/a on the right side, $-a/c$ on the left side. The elastic constants are $c_{11} = 86.6 \text{ GPa}$ and $c_{44} = 31.9 \text{ GPa}$.

ample, for a sample with $c/a = 4$, seven of the first ten modes have a c_{11} dependence over 20%, as opposed to only two modes for $c/a = 1$.

F. Anisotropy

If isotropic symmetry is broken in a single direction, the sample has hexagonal symmetry and is called transversely isotropic. Many consolidated materials, such as sedimentary rock and laminar systems, are transversely isotropic. The elastic tensor of a system with hexagonal symmetry has five independent elements: c_{11} , c_{33} , c_{13} , c_{44} , and c_{66} . Thus in order to determine the elastic tensor for a system with hexagonal symmetry, we might expect to need 25 resonance frequencies. This is a prohibitively large number for low Q samples. Can we detect anisotropy with the lowest 10 modes? The following is a test of the sensitivity of RUS to anisotropy.

Consider a hexagonal elastic tensor

$$M = \begin{pmatrix} c_{11} & c_{12} & c_{13} & 0 & 0 & 0 \\ c_{12} & c_{11} & c_{13} & 0 & 0 & 0 \\ c_{13} & c_{13} & c_{33} & 0 & 0 & 0 \\ 0 & 0 & 0 & c_{44} & 0 & 0 \\ 0 & 0 & 0 & 0 & c_{44} & 0 \\ 0 & 0 & 0 & 0 & 0 & c_{66} \end{pmatrix}, \quad (14)$$

where

$$c_{11} = (1 + \epsilon)C_0, \quad (15)$$

$$c_{12} = 0.4(1 - 2\epsilon)C_0, \quad (16)$$

$$c_{13} = 0.4(1 + \epsilon)C_0, \quad (17)$$

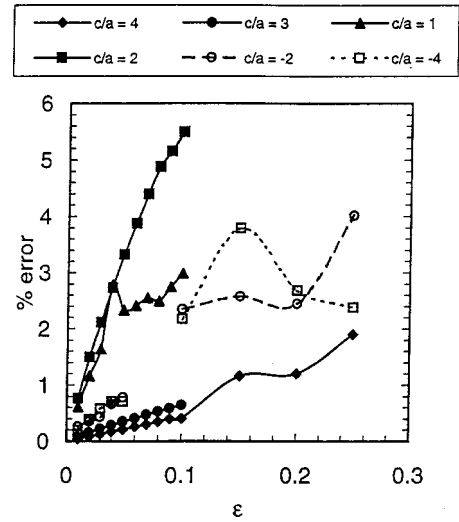


FIG. 4. Root-mean-square error for an isotropic fit to anisotropic sample resonances. Anisotropy is characterized by the parameter ϵ . RUS fits are performed for $c/a = -4, -2, 1, 2, 3, 4$.

$$c_{33} = (1 - 2\epsilon)C_0, \quad (18)$$

$$c_{44} = 0.3(1 - 1.5\epsilon)C_0, \quad (19)$$

$$c_{66} = 0.3(1 + 3\epsilon)C_0. \quad (20)$$

As ϵ varies from 0 to 0.25, the elastic tensor varies from isotropic to hexagonal. Independent of ϵ , $c_{11} + c_{22} + c_{33} = 3C_0$; $c_{12} + c_{13} + c_{23} = 1.2C_0$; and $c_{44} + c_{55} + c_{66} = 0.9C_0$. For $\epsilon = 0.25$ the elements of the elastic tensor have relative values approximately that of zinc.⁹

Sensitivity to anisotropy is calculated as follows: (1) Choose values of c/a , and ϵ . (2) Calculate the lowest 10 resonance frequencies of the hexagonal system, using the elastic tensor in Eqs. (14)–(20), and call these frequencies the experimentally measured frequencies f_n^X . (3) Fit these frequencies f_n^X with an isotropic model, i.e., minimize Eq. (10) assuming that the f_n^M depend only on c_{11} and c_{44} .

In Fig. 4 the rms frequency error,

$$\text{rms error} = \sqrt{\frac{1}{10} \sum_{n=1}^{10} \left(\frac{f_n^X - f_n^M}{f_n^X} \right)^2}, \quad (21)$$

is shown as a function of ϵ , for various aspect ratios c/a , and $b/a = 1.1$. In the figure, aspect ratios less than one are represented as negative reciprocals, e.g., $c/a = 1/4$ is represented as $c/a = -4$. For $c/a = 4$, the rms error is less than 1% for $\epsilon < 0.22$. If we choose 1% error as the threshold between a good fit and a bad fit, we do not have enough information about the elastic properties of the system to recognize that it is anisotropic if we are given only the first ten modes. For $c/a = 2$, the rms error rises fastest as the degree of anisotropy increases. This implies that the $c/a = 2$ aspect ratio provides the best detection of anisotropy. However, the ability to accurately determine the elastic tensor for an anisotropic sample will still depend on having a data set with 20 or more resonance frequencies.

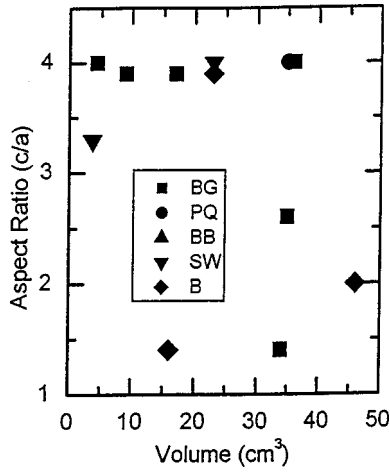


FIG. 5. Aspect ratio as a function of volume for the 13 samples studied. Samples are black gabbro (BG), pink quartzite (PQ), Berkeley blue granite (BB), Sierra white granite (SW), and basalt (B).

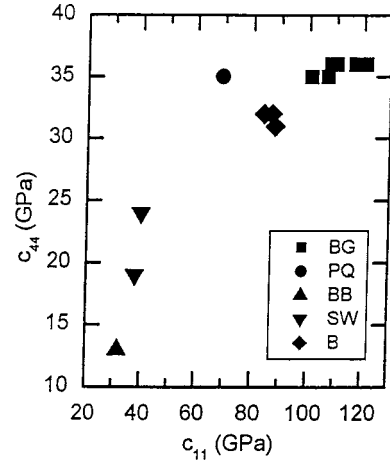


FIG. 6. c_{11} versus c_{44} for the 13 samples studied. Samples are black gabbro (BG), pink quartzite (PQ), Berkeley blue granite (BB), Sierra white granite (SW), and basalt (B).

III. RESULTS AND CONCLUSIONS

The previous section has provided a foundation for the investigation of real samples. RUS experiments and analysis were performed on five rock types. The sample set consists of 13 parallelepipeds: 6 of Berkeley blue granite, 1 of pink quartzite, 1 black gabbro, 2 of Sierra white granite, and 3 of basalt. Multiple samples of the same rock type were cut from a single large specimen. Figure 5 shows the aspect ratios and volumes spanned by the sample set.

For each sample, an estimate of the expected isotropic elastic tensor was used to calculate the expected (model) resonance frequencies for the sample. These model frequencies were used to guide the experimental search for resonances. RUS scans were performed for each sample to find the first ten experimental resonance frequencies. The first ten visible experimental resonant modes are not always the first ten modes as predicted by the model, i.e., some modes are missing in the experiment. Thus while the data analysis was always performed with ten experimentally measured resonance frequencies, the mode identities are not necessarily the same from sample to sample.

Table I contains the RUS derived elements of the isotropic elastic tensors of the 13 samples. The reported value of Q is the average quality factor for the lowest ten measured resonance frequencies,

$$Q = \frac{1}{10} \sum_{n=1}^{10} \frac{f_n^X}{\Delta f_n^X}, \quad (22)$$

where Δf_n^X is the full-width at half-maximum of the resonance intensity centered at f_n^X . The error in the right-most column is given by Eq. (21). The isotropic moduli derived for each sample, c_{11} and c_{44} are also shown in Fig. 6.

Notice that for all black gabbro samples, the shear modulus (c_{44}) is consistently 35–36 GPa, while the compressional modulus (c_{11}) varies by 20%. As indicated in the percent c_{11} column of the table, the compressional modulus varies because it is not heavily involved in the resonant modes used for the fits (Sec. II E). The smallest aspect ratio black gabbro sample has the largest rms frequency error, as expected. However, there is no direct correlation between rms frequency error and aspect ratio. Too many other factors play a role, such as volume and the presence of inhomoge-

TABLE I. Sample set 1. Samples are black gabbro (BG), pink quartzite (PQ), Berkeley blue granite (BB), Sierra white granite (SW), and basalt (B). The samples are characterized by smallest side a , aspect ratio c/a , volume V , relative size of inhomogeneity ξ/a , quality factor Q , compressional modulus c_{11} , percentage of compressional modulus involvement in the ten modes used for the fit, shear modulus c_{44} , and rms error in the RUS fit to resonance frequencies.

Sample	a (cm)	c/a	V (cm ³)	ξ/a	Q	c_{11} (GPa)	% c_{11}	c_{44} (GPa)	% error
BG-1	2.8	1.4	34	0.23	350	101	14	35	1.23
BG-2	2.3	2.6	35	0.28	350	108	12	36	0.27
BG-3	1.0	4.0	4.4	0.32	350	121	14	36	0.48
BG-4	1.3	3.9	9.1	0.24	350	107	16	35	0.39
BG-5	1.6	3.9	17	0.31	350	117	10	36	0.71
BG-6	2.0	4.0	36	0.21	350	110	16	36	0.31
PQ	2.0	4.0	35	1.7	250	69	42	35	1.4
BB	2.0	4.0	35	0.20	230	32	26	13	13
SW-1	0.96	3.3	3.7	0.46	150	40	51	24	15
SW-2	1.7	4.0	23	0.17	140	38	54	19	0.61
B-1	2.1	1.4	16	0.29	275	88	13	31	0.69
B-2	2.8	2.0	46	0.04	255	84	14	32	0.47
B-3	1.7	3.9	23	0.06	335	87	20	32	0.31

neity. An important factor in RUS experiments, that cannot be easily quantified, is user confidence. While the results of a RUS fit may not provide direct evidence that a high aspect ratio sample gives better results than a low aspect ratio sample, the picking of the resonance peaks (accomplished primarily by hand and eye) is easier for high aspect ratios, since the peaks are more spread out (Fig. 2).

If we require that the rms frequency error in the RUS fits be less than 1%, the results from BG-1, BB, and SW-1 would be considered invalid. Notice that the elastic tensors derived for the two Sierra white granite samples are within 20% of each other, even though the rms frequency errors are wildly different. Again, the rms frequency error is not a reliable test of the validity of results. Indeed, the commonly accepted values of the moduli of Berkeley blue granite are $c_{11} = 30$ GPa and $c_{44} = 13$ GPa. Given inherent variability in samples, and the low dependence of the measured resonant modes on c_{11} , the results for Berkeley blue granite are remarkably good. The rms frequency error is not directly correlated with any of the variables we studied, i.e., aspect ratio, volume, Q , or relative inhomogeneity. However, it is still a measure of how well our experimental RUS results can be modeled.

The modeling in Sec. II and the results shown in Table I indicate that RUS is a viable technique for characterizing the average elastic behavior of inhomogeneous materials. Although larger rms errors can be expected for inhomogeneous materials than those acceptable for homogeneous samples (less than 0.5%¹), our results are generally close for different samples of the same material, and consistent with accepted values.¹⁰ We have found that high aspect ratio samples are easier to work with than low aspect ratio samples, although our results indicate that this is primarily a user preference issue, rather than an accuracy issue. A hypothesis that remains untested is whether anisotropy is more likely to be detected with low aspect ratio samples than with high aspect ratio samples.

The future of RUS as a characterization tool for inhomogeneous materials may be more connected to the sensitivity of resonant modes to changes in the elastic state of a system, than to the ability of the RUS inversion technique to accurately predict the elastic tensor. Preliminary measurements of resonances of Berea sandstone as a function of temperature, show that the elastic behavior of Berea sandstone at low temperature (less than 200 K) is repeatably hysteretic.^{11,12} These measurements also indicate that the elastic tensor is softening, rather than hardening, as the temperature is lowered. RUS may prove to be a useful technique for probing changes in elastic state under extreme conditions.

ACKNOWLEDGMENTS

The authors acknowledge useful discussions with T. W. Darling, A. Migliori, and P. A. Johnson. This work was sponsored by the Department of the Navy, Office of Naval Research, and the Institute for Geophysics and Planetary Physics, Los Alamos National Laboratory.

APPENDIX: PERTURBATION THEORY FOR NONIDEAL SAMPLE GEOMETRY

The elastic energy of a solid body, in steady state at frequency ω , is described by the Lagrangian

$$L = \int d\mathbf{x} \phi(\mathbf{x}) \left(\frac{\omega^2}{2} \rho(\mathbf{x}) u_i^2 - \frac{1}{2} c_{ijkl}(\mathbf{x}) \frac{\partial u_i}{\partial x_j} \frac{\partial u_k}{\partial x_l} \right), \quad (\text{A1})$$

where \mathbf{u} is the displacement vector at position \mathbf{x} , c_{ijkl} is the elastic tensor, ρ the mass density, repeated indices are summed over the Cartesian coordinates, and ϕ describes the extent or figure of the sample,

$$\phi(\mathbf{x}) = \begin{cases} 1, & \mathbf{x} \text{ inside the sample} \\ 0, & \mathbf{x} \text{ outside the sample.} \end{cases} \quad (\text{A2})$$

Equation (A1) is quite general, allowing for: (1) an arbitrary sample figure $\phi(\mathbf{x})$; (2) a nonuniform density $\rho(\mathbf{x})$; and (3) a nonuniform elastic tensor $c_{ijkl}(\mathbf{x})$.

The equation of motion for the normal modes is found by varying L with respect to u_i . If the traction on the surfaces defined by $\phi(\mathbf{x})$ vanishes, u_i satisfies a wave equation in the form

$$\rho(\mathbf{x}) \omega^2 u_i + \frac{\partial}{\partial x_j} \left(c_{ijkl}(\mathbf{x}) \frac{\partial u_k}{\partial x_l} \right) = 0 \quad (\text{A3})$$

for \mathbf{x} inside the sample. The condition that the traction on the surfaces vanish is enforced by holding the sample so that it is effectively free standing.

The equation of motion for u_i , Eq. (A3), can be cast in the form of a variational problem.¹¹ That is, the quantity $\omega^2[u_i]$, where

$$\omega^2[u_i] = \frac{\int d\mathbf{x} \phi(\mathbf{x}) c_{ijkl}(\mathbf{x}) \frac{\partial u_i}{\partial x_j} \frac{\partial u_k}{\partial x_l}}{\int d\mathbf{x} \phi(\mathbf{x}) \rho(\mathbf{x}) u_i^2}, \quad (\text{A4})$$

must be stationary subject to arbitrary variations of u_i consistent with traction free boundaries. Using this form for the normal mode frequencies it is possible to make a systematic study of the consequences of change in $\phi(\mathbf{x})$, $\rho(\mathbf{x})$, and $c_{ijkl}(\mathbf{x})$. Assume the ideal sample is a rectangular parallelepiped specified by ϕ_0 , has uniform density ρ_0 , and has uniform elastic constants c_{ijkl}^0 . Then variations in these quantities are given by $\delta\phi(\mathbf{x}) = \phi(\mathbf{x}) - \phi_0$, $\delta\rho(\mathbf{x}) = \rho(\mathbf{x}) - \rho_0$, and $\delta c_{ijkl}(\mathbf{x}) = c_{ijkl}(\mathbf{x}) - c_{ijkl}^0$. To first order in $\delta\phi$, $\delta\rho$, and δc we have

$$\omega^2 = \frac{N_0}{D_0} \left[1 + \frac{\delta N_c}{N_0} + \frac{\delta N_\phi}{N_0} - \frac{\delta D_\rho}{D_0} - \frac{\delta D_\phi}{D_0} \right], \quad (\text{A5})$$

where

$$N_0 = c_{ijkl}^0 \int d\mathbf{x} \phi_0 \frac{\partial u_i}{\partial x_j} \frac{\partial u_k}{\partial x_l}. \quad (\text{A6})$$

$$D_0 = \rho_0 \int d\mathbf{x} \phi_0 u_i^2, \quad (\text{A7})$$

$$\delta N_c = \int d\mathbf{x} \phi_0 \delta c_{ijkl}(\mathbf{x}) \frac{\partial u_i}{\partial x_j} \frac{\partial u_k}{\partial x_l}, \quad (\text{A8})$$

$$\delta N_\phi = c_{ijkl}^0 \int d\mathbf{x} \delta\phi(\mathbf{x}) \frac{\partial u_i}{\partial x_j} \frac{\partial u_k}{\partial x_l}, \quad (\text{A9})$$

$$\delta D_p = \int d\mathbf{x} \phi_0 \delta \rho(\mathbf{x}) u_i^2, \quad (\text{A10})$$

$$\delta D_\phi = \rho_0 \int d\mathbf{x} \delta \phi(\mathbf{x}) u_i^2. \quad (\text{A11})$$

Using the variational technique of Visscher *et al.*, we can find the eigenvalues $\omega_{v,0}^2 = N_0/D_0$ and eigenfunctions $u_{i,v}^0 = \psi_v(\mathbf{x})$ associated with the ideal sample. Thus the lowest order contribution to the frequency shift due to a perturbation is

$$\frac{\omega_v^2 - \omega_{v,0}^2}{\omega_{v,0}^2} = \frac{\delta N_c}{N_0} + \frac{\delta N_\phi}{N_0} - \frac{\delta D_p}{D_0} - \frac{\delta D_\phi}{N_0}, \quad (\text{A12})$$

where $u_i = \psi_v(\mathbf{x})$. For the example of an inhomogeneous mass density, we would have

$$\frac{\omega_v^2 - \omega_{v,0}^2}{\omega_{v,0}^2} = - \frac{\int d\mathbf{x} \phi_0 \delta \rho(\mathbf{x}) |\psi_v|^2}{\rho_0 \int d\mathbf{x} \phi_0 |\psi_v|^2}, \quad (\text{A13})$$

where

$$\omega_{v,0}^2 = \frac{c_{ijkl}^0 \int d\mathbf{x} \phi_0 \partial \psi_v / \partial x_j \partial \psi_v / \partial x_l}{\rho_0 \int d\mathbf{x} \phi_0 |\psi_v|^2}. \quad (\text{A14})$$

Equation (A13) is used in Sec. IIC for the case of a mass defect to illustrate the consequences of a mass inhomogeneity on resonant mode frequencies of a two-dimensional membrane.

¹A. Migliori and J. L. Sarrao, *Resonant Ultrasound Spectroscopy* (Wiley, New York, 1997).

²J. L. Sarrao, D. Mandrus, A. Migliori, Z. Fisk, I. Tanaka, H. Kojima, P. C. Canfield, and P. D. Kodali, "Complete elastic moduli of $\text{La}_{2-x}\text{Sr}_x\text{CuO}_4$ ($x=0.00$ and 0.14) near the tetragonal-orthorhombic structural phase transition," *Phys. Rev. B* **50**, 13125–13131 (1994).

³L. D. Landau and E. M. Lifshitz, *Theory of Elasticity*, 3rd ed. (Pergamon, Oxford, 1986), pp. 9–11.

⁴R. E. Green, Jr., *Treatise on Materials Science and Technology, Vol. 3, Ultrasonic Investigation of Mechanical Properties* (Academic, New York, 1973), pp. 76–78.

⁵F. Birch, "Compressibility; Elastic Constants," in *Handbook of Physical Constants*, edited by S. P. Clark (Geological Society of America, New York, 1966), Vol. 97, pp. 97–106.

⁶T. Bourbie, O. Coussy, and B. Zinszner, *Acoustics of Porous Media* (Gulf Publishing, Houston, 1987), pp. 145–169.

⁷R. A. Guyer, K. R. McCall, G. N. Boitnott, L. B. Hilbert, Jr., and T. J. Plona, "Quantitative implementation of Preisach–Mayergoyz space to find static and dynamic elastic moduli in rock," *J. Geophys. Res.* **102**, 5281–5293 (1997).

⁸W. M. Visscher, A. Migliori, T. M. Bell, R. A. Reinert, "On the normal modes of free vibration of inhomogeneous and anisotropic elastic objects," *J. Acoust. Soc. Am.* **90**, 2154–2162 (1991).

⁹K. Lau, and A. K. McCurdy, "Elastic anisotropy factors for orthorhombic, tetragonal, and hexagonal crystals," *Phys. Rev. B* **58**, 8980–8984 (1998).

¹⁰N. I. Christensen, "Seismic Velocities," in *Handbook of Physical Properties of Rocks*, edited by R. S. Carmichael (CRC Press, Boca Raton, FL, 1982), Vol. 2, pp. 1–228.

¹¹A. L. Fetter and J. D. Walecka, *Theoretical Mechanics of Particles and Continua* (McGraw-Hill, New York, 1980), pp. 226–244.

¹²T. J. Ulrich, and T. W. Darling, "Observation of anomalous elastic behavior in rock at low temperatures," *Geophys. Res. Lett.* **28**, 2293–2296 (2001).

Saturation of thermoacoustic mixture separation

D. A. Geller and G. W. Swift

Condensed Matter and Thermal Physics Group, Los Alamos National Laboratory, Los Alamos, New Mexico 87545

(Received 19 January 2001; revised 27 November 2001; accepted 17 December 2001)

The theory for thermoacoustic mixture separation is extended to include the effects of a nonzero concentration gradient. New data are presented, which are in excellent agreement with this theory. The maximum concentration gradient which may be achieved in a binary mixture of gases through this separation process is intrinsically limited by the fractional pressure amplitude, by the tidal displacement, and by the size of the thermal diffusion ratio. Ordinary diffusion further detracts from the attainable final concentration gradient and can become the dominant remixing process as the cross section of the duct is increased. Rayleigh streaming also works against thermoacoustic separation, and an estimate of the molar flux from streaming is given. © 2002 Acoustical Society of America. [DOI: 10.1121/1.1453449]

PACS numbers: 43.35.Ud, 43.20.Mv, 43.35.Ty [SGK]

I. INTRODUCTION

Recently, Swift and Spoor¹ (S&S) showed theoretically how the propagation of acoustic waves through a mixture of gases in a duct can cause the time-averaged separation of light and heavy molecules along the wave-propagation direction by means of processes occurring at the boundary layer. The separation is second order in the dynamical variables and can lead to large separation rates and concentration gradients. The strength of this separation mechanism depends both on the properties of the gas mixture and on the phasing of the acoustic field. Spoor and Swift² experimentally found that the separation saturates exponentially, and they were able to generate final concentration gradients as large as 7% per meter for 50–50 He–Ar starting mixtures in a tube of approximately 5 mm diameter. However, the focus of their attention was on the initial rate of separation, before significant concentration gradients had developed, because the theory of S&S was limited to that situation.

In this paper, we investigate the separation process in the presence of a nonzero concentration gradient in order to understand the saturation separation. Several processes work against the separation mechanism of S&S to determine the final gradient. Our most important new result is that the separation in a duct is intrinsically limited by the square of the amplitude of displacement of the gas in the acoustic wave. In addition, the remixing arising from concentration-gradient-driven mutual diffusion is typically a large effect. Although we do not study the effect thoroughly here, Rayleigh streaming may also contribute a substantial remixing flux, depending on the shape of the duct and on the intensity of the acoustic field.

In what follows, we first introduce and define the important physical and mathematical parameters in this problem. We then present a heuristic argument, assuming standing-wave phasing, for the intrinsic limitation of the separation process. In the next few sections we extend the S&S theory to lowest order in the concentration gradient and find the expression determining the saturation of the separation pro-

cess. We conclude by describing our experiments supporting this more complete theory.

II. IMPORTANT QUANTITIES

Since early in the last century,³ it has been understood that application of a thermal gradient to a binary mixture of gases can yield a gradient in the molar concentrations of the constituent gases. Ordinary mutual diffusion opposes this thermal diffusion process; and for a closed, isobaric volume of a mixture, the steady state is reached when

$$\nabla n_H = -k_T \nabla \ln T, \quad (1)$$

where n_H is, by convention, the mole fraction of the heavier of the two gases and k_T is called the thermal diffusion ratio. Frequently—but not always—thermal diffusion drives the heavier gas toward the lower temperature region, so these conventions normally lead to positive values for k_T . For He–Ar, the binary mixture used in our experiments, we use $k_T = 0.38 (1 - n_H)^{1.2} n_H^{0.8}$ based on a fit to the data of Atkins *et al.*⁴

Following S&S, our analysis is based on the notation of Landau and Lifshitz,⁵ which accounts for the concentrations of gases by mass fraction instead of mole fraction. Hence, we define the heavy mass fraction c by

$$c = n_H m_H / m_{\text{avg}}, \quad (2)$$

where the molar-average mass m_{avg} can be expressed in either of two ways

$$m_{\text{avg}} = n_H m_H + (1 - n_H) m_L, \quad (3)$$

$$m_{\text{avg}}^{-1} = c m_H^{-1} + (1 - c) m_L^{-1}, \quad (4)$$

and m_L and m_H are the molar masses of the light and heavy gases, respectively. In order to write the mass flux density from diffusion in terms of c rather than n , we must use the scaled thermal diffusion ratio

$$k'_T = k_T m_L m_H / m_{\text{avg}}^2, \quad (5)$$

which is Eq. (44) in S&S, in place of k_T .

The effect in which we are interested occurs via acoustic processes within the thermal and viscous boundary layers. To study this analytically, we consider the gas in an acoustic duct, with sound of a single frequency f propagating along the axis of the duct. The wavelength $\lambda = a/f$, where a is the speed of sound in the gas mixture, is taken to be much larger than all other length scales in the system, including the transverse dimensions of the duct characterized by r_h , the hydraulic radius.⁶ The thermoacoustic variables can be expanded in harmonics to first order

$$\begin{aligned} p &= p_m + \Re[p_1(x)e^{i\omega t}], \\ T &= T_m + \Re[T_1(x,r)e^{i\omega t}], \\ \rho &= \rho_m(x) + \Re[\rho_1(x,r)e^{i\omega t}], \\ u &= \Re[u_1(x,r)e^{i\omega t}], \\ c &= c_m(x) + \Re[c_1(x,r)e^{i\omega t}], \end{aligned} \quad (6)$$

where $\omega = 2\pi f$ is the angular frequency of the acoustic field and x is the longitudinal coordinate along the acoustic duct. The parameter r stands for the radial coordinate if the duct is a circular tube, for the coordinate y normal to the duct's wall in the boundary-layer approximation, or for both coordinates perpendicular to x in ducts of lower symmetry. Symbols p , T , ρ , u , and c are the pressure, temperature, mass density, x component of velocity, and concentration of the heavy component, respectively. The thickness of the thermal boundary layer is the thermal penetration depth

$$\delta_\kappa = \sqrt{2k/\omega\rho c_p} = \sqrt{2\kappa/\omega}, \quad (7)$$

where k is the thermal conductivity of the gas, c_p is the isobaric heat capacity per unit mass, and κ is the thermal diffusivity. Similarly, the viscous boundary layer is defined by the viscous penetration depth

$$\delta_\nu = \sqrt{2\mu/\omega\rho} = \sqrt{2\nu/\omega}, \quad (8)$$

where μ is the viscosity and ν is the kinematic viscosity. Another fundamental length scale involved in the mixture system is the mass diffusion length

$$\delta_D = \sqrt{2D/\omega}, \quad (9)$$

where $D = D_{12}$ is the mutual diffusion coefficient for the binary mixture.

It is convenient to define two ratios of the length scales that appear repeatedly in the analysis. The Prandtl number is defined as

$$\sigma = (\delta_\nu/\delta_\kappa)^2, \quad (10)$$

and describes the relative extent of the viscous and thermal effects. This ratio is $\leq 2/3$ for binary mixtures of monatomic ideal gases. A second ratio is

$$L = (\delta_\kappa/\delta_D)^2, \quad (11)$$

which compares the relative importance of thermal conduction to mass diffusion.

III. A SIMPLE BUCKET-BRIGADE MODEL

S&S showed that the time-averaged separation flux along x is due to oscillating motion and concentration, with suitable time phasing, in the gas about a thermal penetration depth from the wall of the duct. These phased oscillations constitute a bucket-brigade shuttling of one component in the x direction and the other component in the $-x$ direction. In order to depict this process it was useful to consider the behavior of the gas at a fixed location in a duct, but for describing saturation qualitatively in this section it is easier to follow the processes in moving parcels of the gas. To gain intuition about the most interesting mechanism that causes saturation of the time-averaged concentration gradient in the duct, we consider the caricature of oscillations with standing-wave phasing shown in Fig. 1.

In this crude approximation, the time-averaged separation flux may be carried by the gas parcel approximately δ_κ from the wall, because this parcel may experience both oscillating concentration and oscillating motion (with suitable phasing). Hence, the time-averaged separation flux will stop when the concentration oscillation $|c_1|$ is zero in the gas parcel approximately δ_κ from the wall. This will occur when the oscillating diffusion between that parcel and those adjacent to the wall, indicated by the wide arrows, is also zero.

According to Eq. (58.11) from Landau and Lifshitz,⁵ the diffusive mass-flux density vector is

$$\mathbf{i} = -\rho D \left[\nabla c + \frac{k'_T}{T} \nabla T \right]. \quad (12)$$

Using Fig. 1 to estimate the values on the right-hand side of Eq. (12) when the transverse component of the flux $i_y = 0$, and hence $|c_1| = 0$, for the parcel a distance δ_κ from the wall yields

$$0 = \frac{c_m - (c_m + |x_1| dc_m/dx)}{\delta_\kappa} + \frac{k'_T}{T_m} \frac{|T_1|}{\delta_\kappa}, \quad (13)$$

so that

$$\left(\frac{dc_m}{dx} \right)_{\text{sat}} \sim \frac{k'_T}{T_m} \frac{|T_1|}{|x_1|}. \quad (14)$$

Finally, using $T_1 = p_1/\rho_m c_p$ and $x_1 = \langle u_1 \rangle / i\omega$, where $\langle \rangle$ denotes the spatial average over the duct's cross section, this becomes⁷

$$\left(\frac{dc_m}{dx} \right)_{\text{sat}} \sim \frac{\gamma - 1}{\gamma} k'_T \frac{|p_1|}{p_m} \frac{\omega}{|\langle u_1 \rangle|}. \quad (15)$$

We can expect that the quantitative theory developed in the next sections will be in qualitative agreement with Eq. (15), so that the thermoacoustic mixture separation can only occur when the concentration gradient is less than approximately $(dc_m/dx)_{\text{sat}}$. For future convenience, then, let us define $(dc_m/dx)_{\text{sat}}$ exactly according to Eq. (15), and we also define

$$\Gamma_c = \frac{dc_m/dx}{(dc_m/dx)_{\text{sat}}}. \quad (16)$$

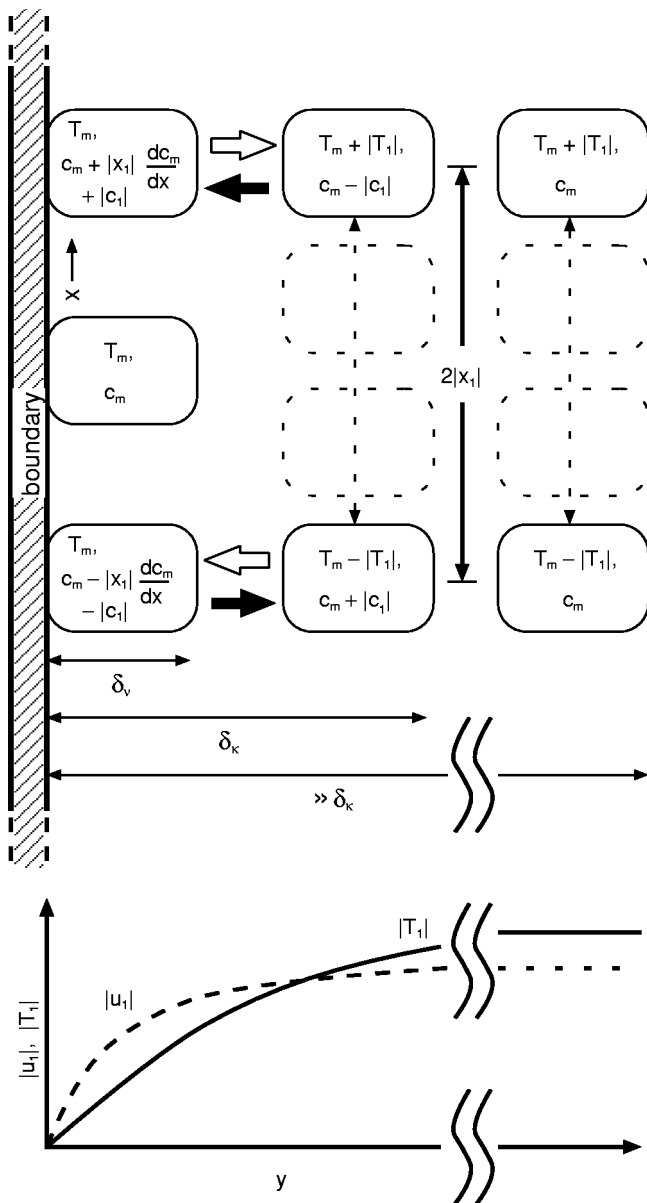


FIG. 1. Illustration of five typical parcels of gas, to guide the intuition about the saturation concentration difference. The three parcels abutting the wall are immobilized by viscosity. The parcel farthest from the wall, shown at the two extremes of its motion, is too far from the wall to experience oscillating temperature gradients or oscillating concentrations. The intervening parcel, also shown at the two extremes of its motion, *might* experience concentration oscillations $|c_1|$ due to oscillating thermal diffusion, indicated by the wide arrows. The filled wide arrows represent diffusion of the heavy component, while the open arrows represent diffusion of the light component. The thermal diffusion ratio k_T is assumed to be positive, as for the He–Ar mixtures in our experiments. The heavy component diffuses toward the isothermal boundary during compression, provided that the longitudinal concentration gradient dc_m/dx is not too large. In this boundary-layer picture, we denote the transverse coordinate by y in place of r .

Γ_c is always real and may loosely be regarded as a figure of merit for the progress of the separation process toward saturation.⁸

IV. THE FIRST-ORDER THEORY

We can derive the lowest-order theory for the saturation of thermoacoustic separation by preserving terms containing the longitudinal concentration gradient dc_m/dx in the equa-

tions of two-component fluid dynamics. We will continue to assume $dT_m/dx=0$ as in S&S, because our result will be complicated enough even in the absence of a temperature gradient.

From S&S Eqs. (17)–(18) for the convection and diffusion of c ,

$$\frac{\partial c}{\partial t} + \mathbf{u} \cdot \nabla c = -\frac{1}{\rho} \nabla \cdot \mathbf{i} = \nabla \cdot \left[D \nabla c + \left(\frac{Dk'_T}{T} \right) \nabla T \right], \quad (17)$$

we now obtain

$$c_1 + \frac{u_1}{i\omega} \frac{dc_m}{dx} = \frac{\delta_D^2}{2i} \left[\nabla_r^2 c_1 + \frac{k'_T}{T_m} \nabla_r^2 T_1 \right], \quad (18)$$

to first order in the oscillating quantities, where ∇_r^2 denotes the parts of the Laplacian belonging to the transverse coordinates.

We now write Eq. (20) from S&S for the first-order oscillating heat transfer (or diffusion of entropy) in the gas mixture

$$\begin{aligned} \rho_m T_m \left(i\omega s_1 + u_1 \frac{ds_m}{dx} \right) \\ = k \nabla_r^2 T_1 - \left[k'_T \left(\frac{\partial g}{\partial c} \right)_{p,T} - T_m \left(\frac{\partial g}{\partial T} \right)_{p,c} \right] \nabla \cdot \mathbf{i}_1, \end{aligned} \quad (19)$$

where g is the Gibbs free energy per unit mass, and with the divergence of the first-order oscillating mass flux

$$\nabla \cdot \mathbf{i}_1 = -i\omega \rho_m c_1 - \rho_m u_1 \frac{dc_m}{dx}, \quad (20)$$

according to Eqs. (17) and (18) above. We cannot discard the ds_m/dx term, as the gradient in entropy will not be negligible when there is a concentration gradient along the duct. Instead, we use the identity (22) from S&S to write

$$\frac{ds_m}{dx} = \frac{c_p}{T_m} \frac{dT_m}{dx} - \left(\frac{\partial g}{\partial T} \right)_{p,c} \frac{dc_m}{dx} - \frac{1}{\rho_m T_m} \frac{dp_m}{dx}. \quad (21)$$

The first term on the right-hand side is zero, because of our assumption at the outset of zero temperature gradient. The last term is zero too, because we assume that the mean pressure is constant throughout the duct. If we eliminate s_1 from (19) by means of S&S's (22), substitute our (21) into (19), and define for future convenience the dimensionless quantity

$$\varepsilon \equiv \frac{(k'_T)^2}{c_p T_m} \left(\frac{\partial g}{\partial c} \right)_{p,T} = \frac{\gamma - 1}{\gamma} \frac{k_T^2}{n_H (1 - n_H)}, \quad (22)$$

as in S&S Eqs. (24) and (45), we finally obtain

$$T_1 = \frac{p_1}{\rho_m c_p} + \frac{\varepsilon T_m}{k'_T} c_1 + \frac{\delta_k^2}{2i} \nabla_r^2 T_1 + \frac{\varepsilon T_m}{i\omega k'_T} \frac{dc_m}{dx} u_1. \quad (23)$$

This differential equation differs from (23) of S&S only through the appearance of the new, final term on the right.

Up to this point we have avoided specifying our duct geometry, and we can proceed a bit further in that mode. First, note that we can write u_1 in terms of its average over the cross-sectional area $\langle u_1 \rangle$ as

$$u_1 = \frac{\langle u_1 \rangle}{1 - f_\nu} (1 - h_\nu), \quad (24)$$

where $(1 - h_\nu)$ describes the velocity profile as a function of position on the cross section, and $f_\nu \equiv \langle h_\nu \rangle$. Equations (18) and (23) constitute two coupled partial differential equations in T_1 and c_1 . Solving Eq. (23) for c_1 , inserting the result in (18), and using Eq. (24) yields

$$T_1 = \frac{p_1}{\rho_m c_p} + \frac{1}{2i} [\delta_\kappa^2 + \delta_D^2 (1 + \varepsilon)] \nabla_r^2 T_1 + \frac{\delta_\kappa^2 \delta_D^2}{4} \nabla_r^4 T_1 + \frac{\delta_D^2}{2i} \frac{\langle u_1 \rangle}{1 - f_\nu} \frac{\varepsilon T_m}{i \omega k'_T} \frac{dc_m}{dx} \nabla_r^2 h_\nu, \quad (25)$$

which is similar to Eq. (27) of S&S. This can now be solved for T_1 as a function of the coordinates. Because of the new term appearing on the right, this inhomogeneous differential equation for T_1 is driven by the concentration gradient and u_1 , as well as by p_1 .

To determine a solution for T_1 , we must apply appropriate boundary conditions to our fourth-order differential equation. One boundary condition is provided by assuming the wall of the duct to be isothermal, so that $T_1 = 0$ at the wall. The wall is generally isothermal because the solid has a much higher heat capacity and thermal conductivity than the gas. A second boundary condition can be taken by requiring that there be no net flux of concentration into the wall

$$i_r|_{\text{wall}} \propto \left[\nabla_r c_1 + \frac{k'_T}{T_m} \nabla_r T_1 \right]_{\text{wall}} = 0. \quad (26)$$

Inserting (23) and (24), this becomes

$$0 = \left[(1 + \varepsilon) \nabla_r T_1 - \frac{\delta_\kappa^2}{2i} \nabla_r^3 T_1 + \frac{\langle u_1 \rangle}{1 - f_\nu} \frac{\varepsilon T_m}{i \omega k'_T} \frac{dc_m}{dx} \nabla_r h_\nu \right]_{\text{wall}}. \quad (27)$$

For some duct geometries, such as the infinite slab, these two boundary conditions specify four equations, so that the solution is uniquely defined. For the boundary-layer and circular-tube geometries we consider, though, these conditions provide only two equations and it is necessary to impose the additional restriction that the solution be finite everywhere inside the duct.

To proceed further, one must now specify a geometry for the duct. The boundary-layer solution is of limited practical interest, but it yields a relatively simple expression for the separation flux and demonstrates the main features of thermoacoustic separation which are present in any geometry. In the boundary-layer limit (transverse duct dimensions $\gg \delta_\nu$), we have $\nabla_r^2 \equiv \partial^2 / \partial y^2$, with y the direction perpendicular to the boundary. We will also investigate the problem for a circular tube of arbitrary diameter: the algebraic manipulations are almost identical, except for the presence of some normalization factors that prevent simplifications from occurring. In the circular tube, $\nabla_r \rightarrow \partial / \partial r$ and $\nabla_r^2 \rightarrow (1/r) \partial / \partial r (r \partial / \partial r)$, and we ignore the ϕ derivatives because of cylindrical symmetry.⁹ In Eqs. (25) and (27), we

also interpret the higher-order differential operators as $\nabla_r^3 \rightarrow \nabla_r \nabla_r^2$ and $\nabla_r^4 \rightarrow \nabla_r^2 \nabla_r^2$, consistent with the derivation of these equations.

For the boundary-layer limit

$$h_\nu = e^{-(1+i)y/\delta_\nu} \quad \text{and} \quad f_\nu = \frac{(1-i)\delta_\nu}{2r_h}, \quad (28)$$

while for a circular tube of radius R , the oscillating velocity u_1 of Eq. (24) is expressed in terms of

$$h_\nu = \frac{J_0[(1-i)r/\delta_\nu]}{J_0[(1-i)R/\delta_\nu]}, \quad (29)$$

$$f_\nu = \frac{2J_1[(1-i)R/\delta_\nu]}{J_0[(1-i)R/\delta_\nu](1-i)R/\delta_\nu},$$

where the J_i are cylindrical Bessel functions. Direct substitution shows that the solution to Eq. (25) must be of the form

$$T_1 = \frac{p_1}{\rho_m c_p} [1 - B h_\nu - C h_{\kappa D} - (1 - B - C) h_{D\kappa}], \quad (30)$$

with the same length scales for the y or r dependence as found by S&S

$$\delta_{\kappa D}^2 = \frac{1}{2} \delta_\kappa^2 [1 + (1 + \varepsilon)/L + \sqrt{[1 + (1 + \varepsilon)/L]^2 - 4/L}], \quad (31)$$

$$\delta_{D\kappa}^2 = \frac{1}{2} \delta_\kappa^2 [1 + (1 + \varepsilon)/L - \sqrt{[1 + (1 + \varepsilon)/L]^2 - 4/L}]. \quad (32)$$

For the boundary-layer calculation, we choose all the δ s to be positive, in order to satisfy the aforementioned requirement that the solution remain finite as $y \rightarrow \infty$. For the cylindrical tube, we can choose the δ s to be positive because the functions J_0 are even; the Y_0 solutions to Eq. (25) have been discarded because they diverge at the center of the tube. The final coefficient $1 - B - C$ in Eq. (30) has been chosen so that the isothermal boundary condition, $T_1|_{\text{wall}} = 0$, is explicitly obeyed. Substitution into Eq. (25) leads to

$$B = \frac{i e^{-i\theta} \varepsilon}{1 - f_\nu} \frac{\sigma}{(1 - \sigma)(1 - \sigma L) - \varepsilon \sigma} \Gamma_c, \quad (33)$$

where θ is the phase of the acoustic impedance, i.e., the phase by which p_1 leads U_1 . Next, substitution into the unusual ‘‘zero transverse flux’’ boundary condition (27) yields

$$C = \frac{f_{D\kappa} (\delta_\kappa^2 / \delta_{D\kappa}^2 - 1) - B [f_\nu (\sigma - 1) / \sigma + f_{D\kappa} (\delta_\kappa^2 / \delta_{D\kappa}^2 - 1)]}{f_{D\kappa} (\delta_\kappa^2 / \delta_{D\kappa}^2 - 1) - f_{\kappa D} (\delta_\kappa^2 / \delta_{\kappa D}^2 - 1)}. \quad (34)$$

In the boundary-layer approximation, this simplifies further to

$$C_{\text{BL}} = C_{\text{S\&S}} \left[1 - B \left(1 + \frac{\sigma - 1}{\sqrt{\sigma}} \frac{\delta_\kappa}{\sqrt{L} \delta_{\kappa D} - \delta_{D\kappa}} \right) \right], \quad (35)$$

where $C_{\text{S\&S}}$ is defined as in Eq. (33) of S&S

$$C_{\text{S\&S}} = \frac{\sqrt{L} \delta_{\kappa D} - \delta_{D\kappa}}{(1 + \sqrt{L})(\delta_{\kappa D} - \delta_{D\kappa})}. \quad (36)$$

One sees immediately that for $dc_m/dx \rightarrow 0$,

$$B \rightarrow 0 \quad \text{and} \quad C_{\text{BL}} \rightarrow C_{\text{S\&S}}. \quad (37)$$

So, our expression returns the results of S&S when the concentration gradient is zero. Whether or not the concentration gradient is zero, Eq. (30) for the complex temperature T_1 reduces to the ordinary thermoacoustic result as the thermal diffusion ratio is reduced to zero, just like the expression (30) of S&S. When $k'_T \rightarrow 0$ and, therefore, $\varepsilon \rightarrow 0$, it follows that $B \rightarrow 0$; and, as before (i) if $L \geq 1$, then $\delta_{\kappa D} \rightarrow \delta_\kappa$, $\delta_{D\kappa} \rightarrow \delta_D$, and $C \rightarrow 1$, and (ii) if $L < 1$, then $\delta_{\kappa D} \rightarrow \delta_D$, $\delta_{D\kappa} \rightarrow \delta_\kappa$, and $C \rightarrow 0$.

Finally, the complex concentration c_1 can be determined by inserting Eq. (30) for T_1 into Eq. (23), with (24) and either (28) or (29)

$$\begin{aligned} c_1 = & -\frac{p_1}{\rho_m c_p} \frac{k'_T}{\varepsilon T_m} \left[C \left(1 - \frac{\delta_\kappa^2}{\delta_{\kappa D}^2} \right) h_{\kappa D} \right. \\ & + (1 - B - C) \left(1 - \frac{\delta_\kappa^2}{\delta_{D\kappa}^2} \right) h_{D\kappa} + B \left(1 - \frac{1}{\sigma} \right) h_\nu \\ & \left. + \frac{\rho_m c_p}{p_1} \frac{\langle u_1 \rangle}{1 - f_\nu} \frac{\varepsilon T_m}{i \omega k'_T} \frac{dc_m}{dx} (1 - h_\nu) \right]. \quad (38) \end{aligned}$$

Notice in particular the fourth term in this equation, which is proportional to $(-u_1/i\omega) \cdot dc_m/dx = -x_1 \cdot dc_m/dx$ where x_1 denotes the complex first-order oscillating particle displacement (i.e., the tidal displacement). In other words, this term describes the change in concentration inside a stationary control volume due to the flow of gas into this volume from a point about x_1 away along the axis of the tube, where the mean concentration will generally be different when $dc_m/dx \neq 0$. This portion of the oscillating local concentration, call it c_{x1} , becomes comparable to the other terms as the concentration gradient approaches its saturation value. However, c_{x1} does not ultimately contribute to the time-averaged transport of concentration, because it is exactly 90° out of phase from the conjugate velocity \tilde{u}_1 .

V. THE SEPARATION FLUX THROUGH SECOND ORDER

Next, we seek the time-averaged mole flux of the heavy component along the x axis, through second order. From Landau and Lifshitz,⁵ the mass-flux densities are $\rho c u + i$ and $\rho(1-c)u - i$ for the heavy and light components, respectively; this is necessary in order to preserve the definition of u as equal to the momentum of a unit mass of the gas. The mole fluxes of the two components are therefore

$$\dot{N}_H = A \overline{\langle \rho c u + i \rangle} / m_H, \quad (39)$$

and

$$\dot{N}_L = A \overline{\langle \rho(1-c)u - i \rangle} / m_L, \quad (40)$$

where i is the x component of \mathbf{i} and the overbar denotes the time average. For the equimolar process of interest to us, $\dot{N}_H = -\dot{N}_L$. Expanding Eq. (39) yields

$$\dot{N}_H = \dot{N}_{H,m} + \dot{N}_{H,2} + \dot{N}_{H,4} + \dots, \quad (41)$$

where the odd-order terms are zero because the time average of a periodic function is zero.

Setting $\dot{N}_{H,m} = -\dot{N}_{L,m}$ yields a mean velocity

$$u_m = \frac{m_{\text{avg}}(m_H - m_L)}{m_H m_L} \frac{i_m}{\rho_m}. \quad (42)$$

Formally, this should have been included in Eq. (6), but we argue here that it is negligible. There are three ways in which u_m could potentially modify the results of acoustics as derived here. The first-order continuity equation (18) would, in principle, gain a term $(u_m/i\omega)dc_1/dx$, but this contribution is of order δ_D/λ smaller than all the other terms in that approximate equation and can be ignored, as long as λ is much larger than any other length scale in the system. The equation for heat transfer (19) would also gain a new first-order term $\rho_m T_m u_m (ds_1/dx)$, but this contribution is again of order δ_D/λ smaller than the other terms in that equation. Finally, in our expression below for the second-order mole flux (45) there would emerge a new term $(A/2)u_m \Re[\langle \tilde{\rho}_1 c_1 \rangle]$, but this portion of the flux is approximately u_m/a times smaller than the main term $(A/2)\rho_m \Re[\langle c_1 \tilde{u}_1 \rangle]$. In our experiments, we always had $u_m/a < 5 \times 10^{-8}$ so that the $u_m \langle \tilde{\rho}_1 c_1 \rangle$ contribution to the flux was negligible. We thus can safely ignore this u_m from steady diffusion, a mean flow which the experimenter does not directly adjust, in our harmonic expansion of the velocity $u(x, r)$ in Eq. (6). Further, we note that the arguments above hold identically for an externally imposed steady flow velocity u_m . In that case, an arbitrary u_m will not affect the mole fluxes associated with the acoustics, provided that $u_m \ll a$. Only the zeroth-order mole fluxes Eqs. (39) and (40) will change through the addition of this imposed u_m to the mean velocity from Eq. (42), and the mole fluxes measured in a frame moving with velocity u_m are the same as the mole fluxes when the applied $u_m = 0$.

Using Eqs. (42) and (12) (with $dT_m/dx = 0$) in Eq. (39) yields

$$\dot{N}_{H,m} = -\rho A D \frac{dc_m}{dx} \frac{m_{\text{avg}}}{m_L m_H} \quad (43)$$

for the zeroth-order diffusive molar flux of the heavy component. Using Eqs. (2) and (3), this can be recast in the more familiar form

$$\dot{N}_{H,m} = -N A D \frac{dn_H}{dx}, \quad (44)$$

where N is the total number of moles per unit volume. Unlike the thermal diffusion ratio k_T [cf. Eq. (5)], the diffusion constant D is the same for either measure of concentration, n_H or c . This ordinary diffusion, driven by the concentration gradient along x but independent of the acoustic field, always works against the molar flux of thermoacoustic mixture separation derived next.

Using Eq. (39) to write all possible second-order terms for $\dot{N}_{H,2}$ yields a sum of many terms, each of which can have factors with subscripts m , 1, and 2. The terms containing u_m are negligible at this order, as argued above. The i_2 term,

proportional to Ddc_2/dx , is negligible compared to $\dot{N}_{H,m}$ for the non-negligible dc_m/dx of interest to us. This leaves us with simply

$$\dot{N}_{H,2} = \frac{A\rho_m}{2m_H} \Re[\langle c_1 \tilde{u}_1 \rangle] + \frac{c_m}{m_H} \dot{M}_2, \quad (45)$$

where $\dot{M}_2 = A \Re[\langle \rho_1 \tilde{u}_1 \rangle]/2 + A\rho_m \langle u_{2,0} \rangle$ is the net second-order mass flux, and A is the cross-sectional area of the duct. Using $\dot{N}_H = -\dot{N}_L$ again, this time at second order, and again neglecting i_2 gives

$$\dot{M}_2 = \dot{M}_{H,2}(1 - m_L/m_H). \quad (46)$$

Combining Eqs. (45) and (46), we finally have for the second-order mole flux of the heavier component

$$\dot{N}_{H,2} = \frac{m_{\text{avg}}}{m_H m_L} \frac{A\rho_m}{2} \Re[\langle c_1 \tilde{u}_1 \rangle]. \quad (47)$$

Using Eqs. (38) and (24), along with the definition of volumetric velocity $U_1 = A\langle u_1 \rangle$, we can write

$$\begin{aligned} \frac{A\rho_m}{2} \Re[\langle c_1 \tilde{u}_1 \rangle] &= \frac{\delta_\kappa}{4r_h} \frac{k'_T/\varepsilon}{c_p T_m} \Re \left\{ \frac{p_1 \tilde{U}_1}{1 - \tilde{f}_v} \left[C_{\text{BL}} \left(1 - \frac{\delta_{\kappa D}^2}{\delta_\kappa^2} \right) \frac{(\delta_{\kappa D}/\delta_\kappa - \sqrt{\sigma}) - i(\delta_{\kappa D}/\delta_\kappa + \sqrt{\sigma})}{(\delta_{\kappa D}^2/\delta_\kappa^2 + \sigma)} \right. \right. \\ &\quad \left. \left. + (1 - B - C_{\text{BL}}) \left(1 - \frac{\delta_{D\kappa}^2}{\delta_\kappa^2} \right) \frac{(\delta_{D\kappa}/\delta_\kappa - \sqrt{\sigma}) - i(\delta_{D\kappa}/\delta_\kappa + \sqrt{\sigma})}{(\delta_{D\kappa}^2/\delta_\kappa^2 + \sigma)} - B \frac{1}{i} \left(\frac{\sigma - 1}{\sqrt{\sigma}} \right) \right] \right\} \end{aligned} \quad (49)$$

in place of S&S's intermediate result (48). If we take $r_h \gg \delta_\kappa$, this portion of the mass flux can again be coerced into a compact form similar to S&S's (49) to first order in δ/r_h

$$\begin{aligned} \frac{A\rho_m}{2} \Re[\langle c_1 \tilde{u}_1 \rangle] &= \frac{\delta_\kappa}{4r_h} \frac{k'_T}{c_p T_m} \{ F_{\text{trav}} \Re[p_1 \tilde{U}_1] \\ &\quad + F_{\text{stand}} \Im[p_1 \tilde{U}_1] + F_{\text{grad}} |p_1| |U_1| \Gamma_c \}, \end{aligned} \quad (50)$$

$$F_{\text{grad}} = \frac{\sqrt{\sigma L}(1 - \sigma^2)(1 + \sqrt{L}) + \varepsilon \sqrt{\sigma}(\sqrt{L} - 1) + [(\sigma^2 - 1)L + \varepsilon \sigma \sqrt{L}](\delta_{\kappa D}/\delta_\kappa + \delta_{D\kappa}/\delta_\kappa)}{(1 + \sqrt{L})[(1 + \sigma)(1 + \sigma L) + \varepsilon \sigma][(1 - \sigma)(1 - \sigma L) - \varepsilon \sigma]/\sigma}, \quad (53)$$

representing the effect of the building gradient. We finally arrive at

$$\begin{aligned} \dot{N}_{H,2} &= \frac{\delta_\kappa}{4r_h} \frac{\gamma - 1}{\gamma} \frac{k_T}{R_{\text{univ}} T_m} |p_1| |U_1| \\ &\quad \times [F_{\text{trav}} \cos \theta + F_{\text{stand}} \sin \theta + F_{\text{grad}} \Gamma_c] \end{aligned} \quad (54)$$

in the boundary-layer limit, where R_{univ} is the universal gas constant. S&S plotted $k_T F_{\text{trav}}$ and $k_T F_{\text{stand}}$ vs mole fraction

$$\begin{aligned} &\frac{A\rho_m}{2} \Re[\langle c_1 \tilde{u}_1 \rangle] \\ &= \frac{1}{2} \frac{k'_T/\varepsilon}{c_p T_m} \Re \left\{ \frac{p_1 \tilde{U}_1}{1 - \tilde{f}_v} \left[C \left(\frac{\delta_\kappa^2}{\delta_{\kappa D}^2} - 1 \right) \langle h_{\kappa D}(1 - \tilde{h}_v) \rangle \right. \right. \\ &\quad \left. \left. + (1 - B - C) \left(\frac{\delta_\kappa^2}{\delta_{D\kappa}^2} - 1 \right) \langle h_{D\kappa}(1 - \tilde{h}_v) \rangle \right. \right. \\ &\quad \left. \left. + B \frac{\sigma - 1}{\sigma} \langle h_v(1 - \tilde{h}_v) \rangle \right] \right\}. \end{aligned} \quad (48)$$

The thermoacoustic mole flux from Eqs. (47) and (48), plus the mole flux from diffusion given above in Eq. (44), was integrated using the Bessel-function forms for the h_i , and is compared with the data in Sec. VII.

Further progress can be made in the boundary-layer approximation. Making use of the integral identity (47) from S&S, we calculate

where

$$F_{\text{trav}} = \frac{\sigma \sqrt{\sigma L} - \sqrt{\sigma} - \sigma \sqrt{L}(\delta_{\kappa D}/\delta_\kappa + \delta_{D\kappa}/\delta_\kappa)}{(1 + \sqrt{L})[(1 + \sigma)(1 + \sigma L) + \varepsilon \sigma]}, \quad (51)$$

$$F_{\text{stand}} = \frac{-\sigma \sqrt{\sigma L} + \sqrt{\sigma} - \sigma \sqrt{L}(\delta_{\kappa D}/\delta_\kappa + \delta_{D\kappa}/\delta_\kappa)}{(1 + \sqrt{L})[(1 + \sigma)(1 + \sigma L) + \varepsilon \sigma]}, \quad (52)$$

as before, and we additionally define

$$\Gamma_c = - \frac{F_{\text{trav}} \cos \theta + F_{\text{stand}} \sin \theta}{F_{\text{grad}}}, \quad (55)$$

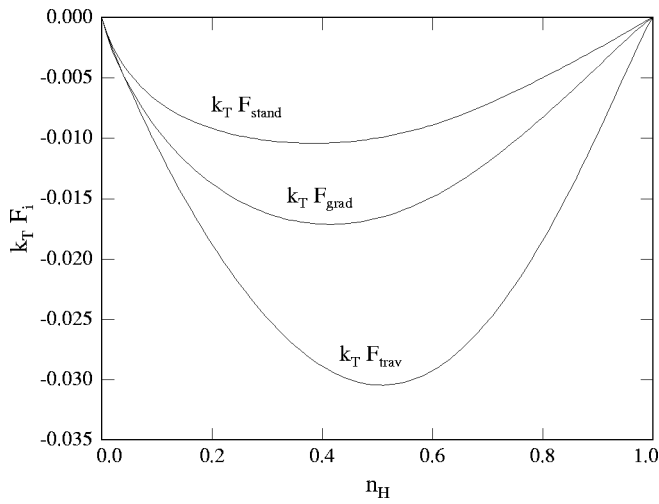


FIG. 2. Comparison of the three geometrical prefactors describing the separation flux for He–Ar.

which is of order 1 as we came to expect at the end of Sec. III, with details shown in Fig. 3.

Simply by substituting in the definition (16) for Γ_c , Eq. (54) can also be written as

$$\begin{aligned} \dot{N}_{H,2} = & \frac{\delta_\kappa}{4r_h} \frac{\gamma-1}{\gamma} \frac{k_T}{R_{\text{univ}} T_m} |p_1| |U_1| [F_{\text{trav}} \cos \theta + F_{\text{stand}} \sin \theta] \\ & + \frac{\delta_\kappa}{4r_h} \frac{\rho_m |U_1|^2}{m_{\text{avg}} \omega A} F_{\text{grad}} \frac{dn_H}{dx}. \end{aligned} \quad (56)$$

In this form, it is apparent that the new effect always opposes mixture separation, because $F_{\text{grad}} < 0$, and hence this term's contribution to $\dot{N}_{H,2}$ always opposes dn_H/dx . Being independent of p_1 , this term represents a mixing phenomenon occurring in any laminar oscillating flow of a mixture in a duct. Watson¹⁰ studied this problem in great detail, giving results for arbitrary r_h/δ_v in circular and two-dimensional “slab” ducts. In our notation, Watson's boundary-layer result is

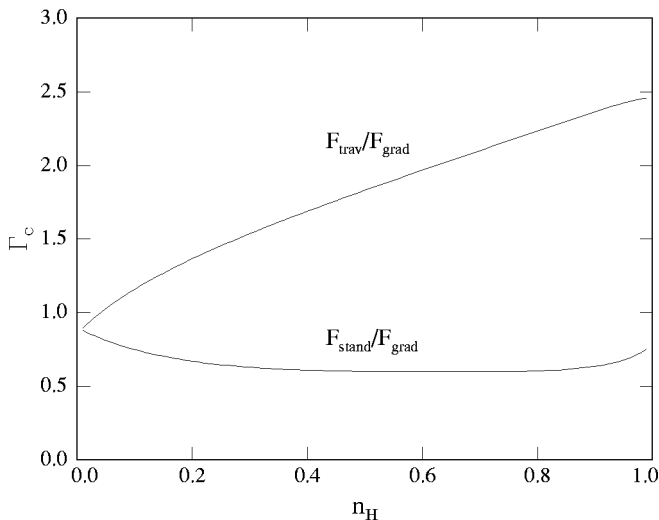


FIG. 3. The figure of merit for separation Γ_c for $\dot{N}_{H,2}=0$, as a function of Ar mole fraction in He–Ar mixtures for $\theta=180^\circ$ and $\theta=270^\circ$.

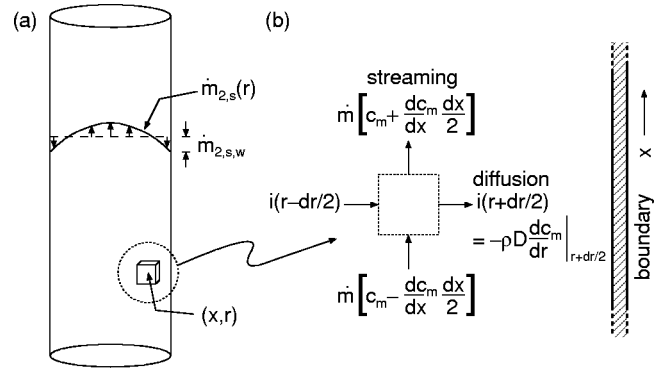


FIG. 4. (a) For laminar flow, the streaming mass-flux density is parabolic in the tube, except within the viscous boundary layer (negligibly thin in this figure), where it must approach zero at the wall. For a duct closed on both ends, the mass-flux density $\dot{m}_{2,s}(r)$ averages to zero over the cross section. (b) In the steady state, the net streaming flux of the heavy component into a fixed volume in space, centered on coordinates (x,r) , is balanced by the flux of heavy mass out of this volume by diffusion.

$$\dot{N}_{H,2} = - \frac{\delta_v}{4r_h} \frac{\rho_m |U_1|^2}{m_{\text{avg}} \omega A} \frac{\sqrt{\sigma L}}{(1 + \sqrt{\sigma L})(1 + \sigma L)} \frac{dn_H}{dx}. \quad (57)$$

This is identical to the $|U_1|^2$ term in Eq. (56), if our F_{grad} is evaluated with $\varepsilon=0$. Although ε is often small, Watson's neglect of it is not strictly valid. Mass diffusion and heat flux are inextricably linked in mixtures, as is most easily seen in our Eq. (23) with $p_1=0$, and so oscillating temperature should not necessarily be neglected in the problem Watson considered.

VI. REMIXING BY RAYLEIGH STREAMING

Rayleigh streaming¹¹ provides another mixing process that can work against thermoacoustic mixture separation. The steady circulation of Rayleigh streaming within the duct will tend to carry heavy-enriched gas in one direction in one part of the duct's cross section and light-enriched gas in the other direction in another part of the duct's cross section, as illustrated in Fig. 4, thereby mixing the separated gases. Fortunately, lateral diffusion of mass between these counter-flowing streams will tend to reduce the net mixing, and will be most effective at doing so in small ducts.

We have found no citations in the literature regarding Rayleigh streaming in a gas mixture, including the effect of nonzero ε on T_1 , and indeed this calculation appears very challenging. Hence, here we will provide only an order-of-magnitude estimate in boundary-layer approximation, in a circular tube, to get a rough idea of the magnitude of this effect and its dependence on key variables. The order of magnitude¹¹ of the second-order, streaming mass-flux density $\dot{m}_{2,s,w}$ just outside the boundary layer at the wall of the tube is

$$\dot{m}_{2,s,w} \sim |p_1| |\langle u_1 \rangle| / a^2. \quad (58)$$

This mass-flux density typically has a periodic dependence on the phase between p_1 and $\langle u_1 \rangle$, and hence will be zero for some phasing, but we ignore this issue here. For laminar flow, the mass-flux-density distribution over most of the tube is then given by

$$\dot{m}_{2,s}(r) = \dot{m}_{2,s,w}(2r^2/R^2 - 1), \quad (59)$$

if we ignore the complicated details of how $\dot{m}_{2,s}$ goes to zero from the edge of the boundary layer to the wall itself and insist that $\langle \dot{m}_{2,s} \rangle = 0$ for our closed system. This distribution of mass-flux density will tend to carry gas enriched in one component in one direction in the center of the tube, where $r < R/\sqrt{2}$, and gas enriched in the other component in the other direction in the rest of the tube.

In the absence of mitigating factors, these two counterflowing enriched-gas streams could be imagined as flowing independently along the entire length of the tube, effectively carrying light-enriched gas all the way from the “light” reservoir at one end of the tube to the “heavy” reservoir at the other end of the tube, and vice versa. Such mixing might be catastrophically large. Fortunately, for the experimental conditions of interest to us here, these two counterflowing streams have plenty of time to exchange significant mass with each other via diffusion, very analogous to the way heat is exchanged between fluid streams in a counterflow heat exchanger, so the remixing effect is greatly reduced. The characteristic transit time for streaming the full length l of the tube, $\rho_m l / \dot{m}_{2,s,w}$, is 10 to 100 times larger than the lateral diffusion time R^2/D . For a quantitative estimate of the magnitude of the mixing under these conditions, we consider the steady-state concentration $c_m(x, r)$ in a control volume at some fixed location (x, r) in the tube. The steady-state concentration is maintained by the competition between axial streaming flow along the concentration gradient and radial diffusion, obeying the equation

$$\dot{m}_{2,s}(r) \frac{dc_m(x, r)}{dx} = \rho_m D \frac{1}{r} \frac{d}{dr} r \frac{dc_m(x, r)}{dr}. \quad (60)$$

We assume that the diffusion is effective enough that dc_m/dx can be regarded as independent of r , so that this equation can easily be integrated when Eq. (59) is substituted for $\dot{m}_{2,s}(r)$. The result is

$$c_m(x, r) = E + \frac{dc_m}{dx} \left[x + \frac{\dot{m}_{2,s,w}}{\rho_m D} \left(\frac{r^4}{8R^2} - \frac{r^2}{4} \right) \right], \quad (61)$$

with E an r -independent constant of integration that we have no need to evaluate. Then, the mixing flux can easily be obtained by integrating the product of Eqs. (59) and (61)

$$\dot{N}_{H,4,\text{stream}} = \frac{1}{m_H} \int_0^R c_m \dot{m}_{2,s} 2\pi r dr \quad (62)$$

$$= - \frac{\pi}{48} \frac{dc_m}{dx} \frac{\dot{m}_{2,s,w}^2 R^4}{m_H \rho D} \quad (63)$$

$$\sim - \frac{\pi}{48} \frac{dn_H}{dx} \frac{m_L}{m_{\text{avg}}^2} \frac{|p_1|^2 \langle |u_1| \rangle^2 R^4}{a^4 \rho D}, \quad (64)$$

where the r -independent terms in Eq. (61) disappear in the integration, and the final step simply requires substitution of Eqs. (2) and (58).

To judge the seriousness of the threat imposed by this fourth-order effect, we can take the ratio of $\dot{N}_{H,4,\text{stream}}$ to the

intrinsic remixing described by the $|U_1|^2$ term at the end of Eq. (56). Using the simple identities $\rho_m a^2 = \gamma p_m$ and $A = \pi R^2$, we obtain

$$\frac{\dot{N}_{H,4,\text{stream}}}{\dot{N}_{\text{intrinsic}}} \sim \frac{1}{12} \frac{m_L}{m_{\text{avg}}} \frac{R^3}{F_{\text{grad}} \delta_\kappa \delta_D^2} \frac{|p_1|^2}{\gamma^2 p_m^2}. \quad (65)$$

With F_{grad} and m_L/m_{avg} of order unity and, typically, $|p_1|/p_m$ no larger than approximately 0.1, we see that it is probably necessary to keep R less than 10δ if we want to keep the mixing effect of streaming acceptably small. For the experiments described below, we always have $R \leq 4.8 \delta_\kappa$ and $R \leq 4.5 \delta_D$, and $|p_1|/p_m \leq 0.03$, so we anticipate no significant contribution from streaming. However, we must keep in mind the approximate nature of Eq. (58). This is only a rough estimate, and other circumstances can easily violate the approximations leading to Eq. (65).

VII. COMPARISON WITH EXPERIMENT

The mole flux expanded to second order in the acoustic variables is seen from Eqs. (41), (44), and (56) to be linear in the concentration gradient dn_H/dx . The contribution from streaming is also proportional to dn_H/dx , but it was estimated above to be too small to detect under our experimental conditions. Considering terms through second order, then, we can calculate the saturation gradient easily by setting $\dot{N}_H = 0$. For example, if the duct is so narrow that ordinary diffusion can be neglected, one finds from Eq. (56) that the final separation in the boundary-layer limit is a sinusoidal function of the phasing

$$\frac{dn_H}{dx} = - \frac{\gamma - 1}{\gamma} \frac{\omega k_T A}{p_m} \frac{|p_1|}{|U_1|} \frac{F_{\text{trav}} \cos \theta + F_{\text{stand}} \sin \theta}{F_{\text{grad}}}. \quad (66)$$

Although the boundary-layer approximation yields the most compact expression for the separation flux, the expression remains qualitatively the same regardless of the duct geometry. We have therefore used our circular-tube calculation from Sec. V to calculate the expected final separations corresponding to the two tubes studied in our experiment. The narrower of the two tubes described below was chosen so that $\dot{N}_{H,m}$ and $\dot{N}_{H,4,\text{stream}}$ would be small and the new term from Sec. V proportional to $|U_1|^2$ would be emphasized. The wider tube, in contrast, was selected in order to demonstrate the convergence of the exact, circular-tube calculation to that of the boundary-layer limit derived in Sec. V.

In order to test our theory experimentally, we used the apparatus presented in Ref. 2. The acoustic field inside the tube was provided by the compressions of metal bellows housed in closed reservoirs at either end. The bellows were driven by independent linear motors, so that we could create arbitrary phasings and amplitudes in the sound field. Two ducts were studied, the first of which was a copper tube 4.75 mm in diameter and $l = 0.914$ m long, driven at 10 Hz with pressure amplitudes as high as 2.5 kPa. The second, wider duct was a stainless-steel tube of 1.52 cm diameter and 0.912 m length, driven at 15 Hz at amplitudes up to 1.25 kPa. The sample was a 50–50 mixture of helium and argon at room

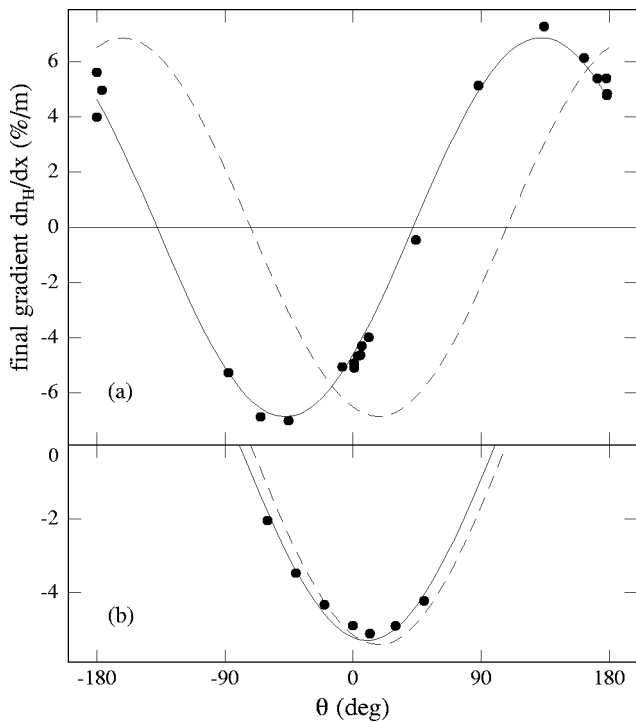


FIG. 5. Dependence of final separation on the phasing between p_1 and U_1 . (a) Data for the 4.75-mm tube are scaled to $|Z|=70 \text{ MPa}\cdot\text{s}/\text{m}^3$. The solid curve is generated from an exact calculation for this circular tube and includes the effect of steady diffusion from Eq. (44). The dashed curve is the boundary-layer limit calculation for the narrow tube and also includes the remixing from steady diffusion. The boundary-layer expression is inappropriate for the 4.75-mm tube, because the radius of the tube is not much greater than the boundary-layer thickness. Although the boundary-layer calculation deviates greatly from the exact calculation and from the data in its periodic phase dependence, it still yields a reasonable value for the magnitude of the maximum separation. (b) For the 1.52-cm tube, all data were taken with $|Z|=10 \text{ MPa}\cdot\text{s}/\text{m}^3$ and $|p_1||U_1|=0.1 \text{ W}$. The solid curve is again the result of a circular-tube calculation, while the dashed curve is the boundary-layer limit calculation. For the 1.52-cm tube, $R\sim 5\delta$ and the boundary-layer calculation is fairly accurate.

temperature and at a mean pressure of 80 kPa, which is approximately the local atmospheric pressure. Complex pressure amplitudes $p_{1,\text{top}}$ and $p_{1,\text{bottom}}$ were measured in the two reservoirs using piezoresistive transducers and lock-in amplifiers. From these measurements we inferred the wave in the tube to be

$$p_1(x) = p_{1,\text{bottom}} \frac{\sin k(l-x)}{\sin kl} + p_{1,\text{top}} \frac{\sin kx}{\sin kl}, \quad (67)$$

and

$$U_1(x) = \frac{i(1-f_\nu)A}{\omega\rho_m} \frac{dp_1}{dx}, \quad (68)$$

where $x=0$ at the bottom end of the tube and the complex wave number is given by

$$k = \frac{\omega}{a} \sqrt{\frac{1+(\gamma-1)f_\kappa}{1-f_\nu}}. \quad (69)$$

We evaluate a , ρ_m , f_ν , and f_κ using properties of the 50–50 mixture (ignoring their x dependence for $dc_m/dx \neq 0$), and we use the Bessel-function expressions for f_ν and f_κ . For the display of data here, we use p_1 and U_1 at $x=l/2$.

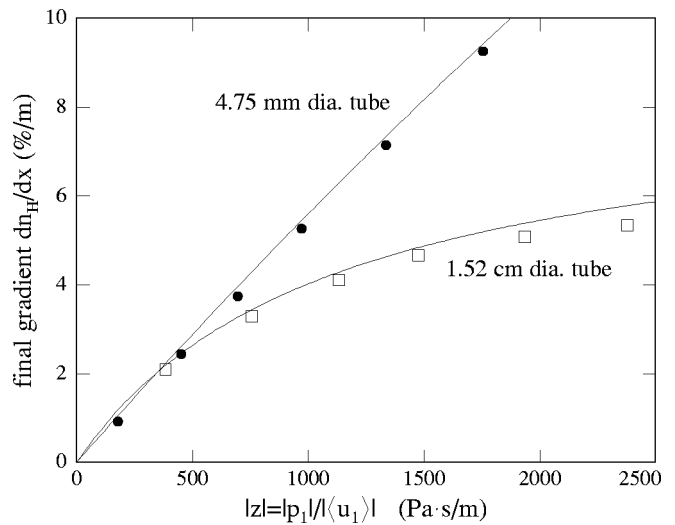


FIG. 6. The saturation value of the concentration gradient as a function of specific acoustic impedance $|z|$ for fixed $|p_1||U_1|$ and fixed phasing θ . For the 4.75-mm tube, $|p_1||U_1|=0.05 \text{ W}$ and $\theta=-45^\circ$, while for the 1.52-cm tube $|p_1||U_1|=0.1 \text{ W}$ and $\theta=12^\circ$. Points are measurements, and lines are circular-tube calculations.

The first verification of our circular-tube calculation for an arbitrary-diameter tube was in experimentally demonstrating the calculated dependence on phase θ for the narrow cylindrical tube. The data are compared against our theory, both in the boundary-layer limit and in the exact case for our geometry, in Fig. 5(a). Not all the data for the 4.75-mm tube in this figure were taken at the exact same value of $|p_1||U_1|$ or of acoustic impedance $Z=p_1/U_1$. Because the values of $|Z|$ varied over an order of magnitude among the data, the fractional separation for each point was normalized to an intermediate value of $|Z|$ by multiplying by $(70 \text{ MPa}\cdot\text{s}/\text{m}^3)/|Z|$, as suggested by Eq. (66). This scaling is valid if $\dot{N}_{H,m}$ and $\dot{N}_{H,4,\text{stream}}$ are much smaller than $\dot{N}_{H,2}$. Neverthe-

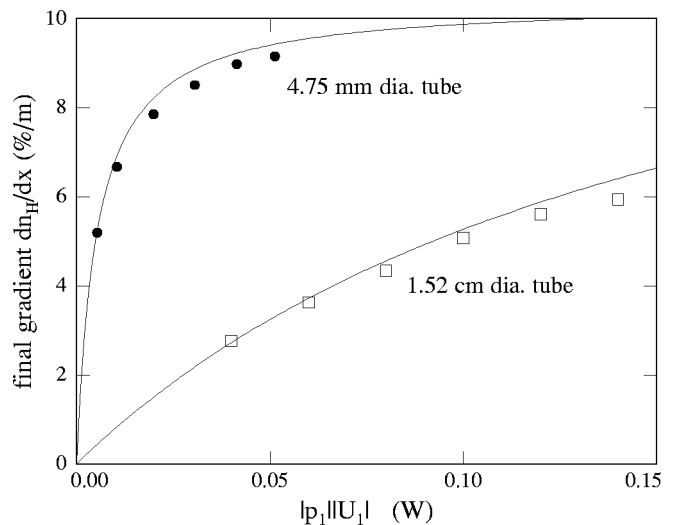


FIG. 7. The saturation gradient with varying $|p_1||U_1|$ and with $|Z|$ now held fixed. For the narrow tube, $|Z|=100 \text{ MPa}\cdot\text{s}/\text{m}^3$ and $\theta=-45^\circ$, and for the wide tube, $|Z|=10 \text{ MPa}\cdot\text{s}/\text{m}^3$ and $\theta=12^\circ$. Points are measurements, and lines are circular-tube calculations. In the absence of ordinary diffusion or acoustic streaming, each curve would be a horizontal line with dn_H/dx at its asymptotic value for $|p_1||U_1|\rightarrow\infty$.

less, there are small ($\sim 15\%$) deviations in $|p_1||U_1|$ between the points, which cause some of the scatter in the data through the presence of the $\dot{N}_{H,m}$ term. Several data points are also shown in Fig. 5(b) for the phase dependence of separation in the 1.52-cm tube. In this case, the boundary-layer and circular-tube calculations give quite similar results, although the circular-tube calculation is still in better agreement with the data.

In view of Eqs. (41), (44), and (56), one is able to demonstrate the effect of each remixing term by varying $|p_1||U_1|$ and $|Z|$ independently, while maintaining a fixed phasing of the acoustic field in the tube. In order to minimize errors arising from small deviations in the experimental phasing, and to maximize the resolution of our separation measurement, we chose that value of θ that yielded the greatest final separation for each tube. As seen in Fig. 5, for the narrow tube this angle was approximately -45° , whereas for the wide tube the maximum was at 12° ; the boundary-layer calculation gives the largest gradient at saturation for $\theta \sim 18^\circ$. Figure 6 shows the nearly linear relationship between final gradient and specific acoustic impedance for the narrow tube, which is in very good agreement with our calculations. The deviation of the filled circles and their associated curve from a linear relationship is almost entirely due to the flux from ordinary diffusion, $\dot{N}_{H,m}$: had we held $|U_1|^2$ constant instead of $|p_1||U_1|$, the function would be a straight line.

The small deviations of the data from the calculated curves may derive from several sources. First, the saturation gradient $(dn_H/dx)_{\text{sat}}$ depends on n_H , which itself varies along the length of the tube. We have not calculated the exact profile of n_H along the tube, although one can in principle do so for our apparatus using the fact that the system is closed so that the total number of moles of each gas is conserved. Second, the thermophysical properties of the gas mixture are calculated as in Giacobbe¹² and may contain errors of a few percent at our operating pressure and temperature for the 50–50 mixture. Finally, no effort was made to accurately control the temperature of the apparatus, and the ambient temperature of the laboratory varied by as much as 5°C over the course of an experiment.

Data for the wide tube are also shown in Fig. 6. The nonlinearity of the saturation gradient vs specific acoustic impedance is much more pronounced in this case than for the narrow tube. Although $|p_1||U_1|$ for these data is twice that of the narrow-tube data, the area of the wide tube is ten times greater, so that the remixing flux from steady diffusion is proportionately higher.

In Fig. 7, we show the effect of the diffusion term more clearly by varying $|p_1||U_1|$ at constant $|Z|$. Steady diffusion competes more effectively with the separation process when the separation rate is made small. In view of Eq. (64), the saturation gradient should begin to decrease again at higher values of $|p_1||U_1|$ due to streaming. However, we are not able to attain such large values of $|p_1||U_1|$ in our apparatus, and other nonlinear effects may set in that limit the applicability of our analysis for such operating conditions.

ACKNOWLEDGMENTS

This work was supported by the Office of Basic Energy Sciences in the U.S. Department of Energy under contract No. W-7405-ENG-36. The authors are grateful to Phil Spoor and Scott Backhaus for several useful discussions.

¹G. W. Swift, and P. S. Spoor, "Thermal diffusion and mixture separation in the acoustic boundary layer," *J. Acoust. Soc. Am.* **106**, 1794 (1999); **107**, 2299(E) (2000); **109**, 1261(E) (2001).

²P. S. Spoor and G. W. Swift, "Thermoacoustic separation of a He–Ar mixture," *Phys. Rev. Lett.* **85**, 1646 (2000).

³Thermal diffusion was first discovered theoretically from the kinetic theory of gases by D. Enskog and S. Chapman independently. An account including the original references can be found in K. E. Grew and T. L. Ibbs, *Thermal Diffusion in Gases* (Cambridge University Press, Cambridge, 1952).

⁴B. E. Atkins, R. E. Bastick, and T. L. Ibbs, "Thermal diffusion in mixtures of inert gases," *Proc. R. Soc. London, Ser. A* **172**, 142–158 (1939).

⁵L. D. Landau and E. M. Lifshitz, *Fluid Mechanics* (Pergamon, New York, 1982).

⁶The hydraulic radius r_h of a tube or duct is defined as the ratio of its cross section to its perimeter. For a right circular cylinder, the hydraulic radius is equal to one half of the cylinder radius.

⁷Readers who are familiar with standing-wave thermoacoustic engines and refrigerators will recognize that the above discussion is similar to the description of the critical temperature gradient, which differs from $(dc_m/dx)_{\text{sat}}$ by the factor k'_T/T_m .

⁸Note that Eqs. (15) and (16) may equally well be expressed in terms of the mole fraction. Use of Eqs. (2) and (5) shows that these are equivalent to

$$\left(\frac{dn_H}{dx}\right)_{\text{sat}} = \frac{\gamma-1}{\gamma} k_T \frac{|p_1|}{p_m} \frac{\omega}{|u_1|}, \quad \text{and} \quad \Gamma_c = \frac{dn_H/dx}{(dn_H/dx)_{\text{sat}}}.$$

⁹For consistency with the prior literature, we denote the longitudinal direction along the tube by x . Where we refer to cylindrical coordinates, then, we consider the set to be (x, r, ϕ) .

¹⁰E. J. Watson, "Diffusion in oscillating pipe flow," *J. Fluid Mech.* **133**, 233–244 (1983).

¹¹W. L. M. Nyborg, "Acoustic Streaming," in *Physical Acoustics*, edited by W. P. Mason (Academic, New York, 1965), Vol. II B, pp. 265–331.

¹²F. W. Giacobbe, "Estimation of Prandtl numbers in binary mixtures of helium and other noble gases," *J. Acoust. Soc. Am.* **96**, 3568–3580 (1994).

Hybrid laser/broadband EMAT ultrasonic system for characterizing cracks in metals

Johanna R. Bernstein^{a)} and James B. Spicer

Department of Materials Science and Engineering, The Johns Hopkins University, Baltimore, Maryland 21218

(Received 25 June 2001; revised 24 January 2002; accepted 25 January 2002)

Detection and characterization of defects in metal parts in industrial and commercial settings has typically been carried out by nondestructive ultrasonic inspection systems. Correct measurement of crack size is critical for lifetime prediction inspections. Normally, measurements are made based on far-field ultrasonic diffraction models and time-of-flight reflection signals making accurate measurements for parts less than approximately 25 mm in thickness impossible. In this work a hybrid noncontacting laser generation/broadband electromagnetic acoustic transducer (EMAT) detection system is used to characterize ideal cracks in aluminum in which the far-field condition for ultrasonic diffraction cannot be met. Time domain signals show that diffracted energy is measured in the geometrical shadow zone of the crack. Fourier transform methods are used to show that the frequency content of the diffracted signals is different than those from the waves that do not interact with the crack. Crack size measurements are made by using the frequency content of the ultrasonic signal rather than time-of-flight information. © 2002 Acoustical Society of America.

[DOI: 10.1121/1.1462640]

PACS numbers: 43.35.Zc, 43.20.Ye [YHB]

I. INTRODUCTION

Conventional ultrasonic testing for the detection and characterization of defects in metals has relied on systems using contact piezoelectric transducers for both generation and detection of the ultrasonic field.¹ The standard inspection configurations include pulse-echo, through-transmission, and tandem.² In a pulse-echo configuration, a single transducer is used for both generating and receiving the ultrasonic signal. For through transmission and tandem configurations, two transducers are used, one for generation and one for detection.

These ultrasonic inspection systems work well for room temperature applications when the defects are not too small, no less than about 5 mm, and the surface of the material to be interrogated is readily accessible.³ Contact transducers also require the use of a couplant, usually a water soluble gel, between the surface of the sensor and the surface of the material. If the application is at high temperatures, or on surfaces where a couplant cannot be used, such as a moving surface, the use of contact transducers is no longer practical. For these applications, a noncontacting system is generally desirable. This report describes a noncontacting system for use in the characterization of cracks in metals.

As a research tool, optical generation and detection,^{4,5} and generation and detection by other electromagnetic methods⁶ have been among the more successful noncontact ultrasonic inspection systems. In an all-optical system, generation of ultrasound can be achieved readily using a pulsed laser source. The pulsed laser provides a broadband signal in which both shear and longitudinal wave fields are produced.⁴ An interferometer can be used as a broadband receiver to

detect displacements normal to the surface on both metallic or nonmetallic systems. However, an optically reflective surface is required for efficient detection. This is a major drawback for on-line monitoring and detection at rough surfaces.

Alternatively, electromagnetic acoustic transducers (EMAT) can also be used to generate or detect ultrasound.⁶ Shear or longitudinal wave fields can be produced depending on the transducer design, however, the generation efficiency is rather low. EMATs are generally considered to be better receivers than generators of ultrasound. An EMAT receiver can be designed to sense particle motion either parallel or perpendicular to the surface of the material, but not both. EMATs are technically noncontact sensors since a stand-off up to approximately 1 mm can be tolerated for detection, although, a wear plate or thin barrier film is usually placed between the sensing coils and the surface to be examined. An EMAT does not require the use of a couplant, and has been shown to be effective on rough, corroded or "dirty" surfaces. In addition, EMATs can be tuned to detect a narrow-band or wide-band signal depending on the design of the receiver coil, although they can only be used on conducting surfaces.

In this work, a noncontacting system is designed that couples the generation efficiency of a laser source with the superior detection capabilities of an EMAT receiver. The use of a hybrid ultrasonic inspection system is demonstrated that combines a pulsed laser line source with a broadband EMAT receiver sensitive to ultrasonic shear waves. Similar hybrid systems have been used previously for thickness gauging applications, high temperature measurements, and weld inspections.⁷⁻⁹ However, in all previously reported hybrid systems, a laser point source has been used^{7,9} or a narrow-band EMAT receiver.⁸ In addition, these systems have concentrated on crack detection rather than sizing. Our modifi-

^{a)}Current address: Corrosion and Protection Centre, University of Manchester Institute of Science and Technology, Manchester M60 1QD, United Kingdom. Electronic mail: j.r.bernstein@umist.ac.uk

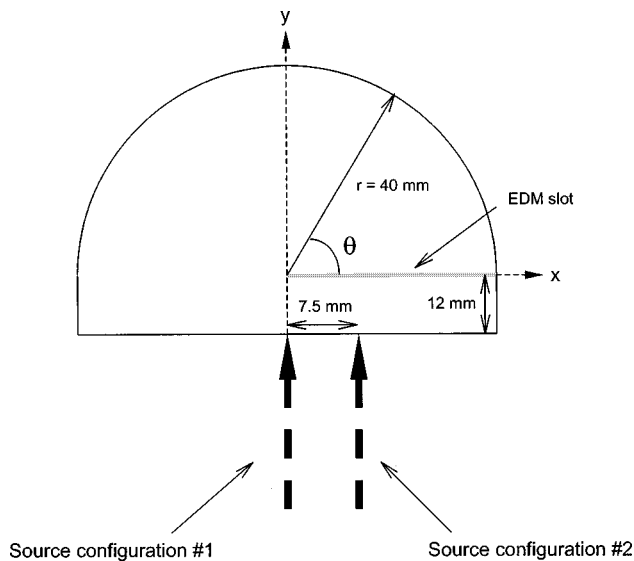


FIG. 1. Diagram of aluminum half-cylinder with two laser line source configurations.

cations to the hybrid laser/broadband EMAT system is used to investigate the nature of acoustic diffraction at an ideal crack (semi-infinite half-plane) in aluminum samples in order to gain an understanding of issues related to both crack detection and sizing.

A laser line source operating in the thermoelastic regime produces an ultrasonic shear wave in the sample with a sharp peak in amplitude at a particular angle without the use of a mode conversion wedge.¹⁰ The angle of the resulting ultrasonic wave is dependent on the material properties of the sample. The laser line also provides a noncontact and non-destructive source. The use of a line rather than a point for generation allows more energy to be deposited at the surface without damaging the sample. The EMAT receiver does not need a couplant and can be used on unprepared surfaces, unlike a contact transducer or an interferometer that requires

optical polishing for efficient detection. Design flexibility for the receiver coil also allows the EMAT detector area to be made very small while maintaining reasonable sensitivity. The EMAT receiver can have a small detection area, theoretically as small as the width of a very fine single wire. In practice, the footprint of the smallest EMAT receivers are on the order of 0.5–1 mm.

Standard ultrasonic transducer methods that have traditionally been used to characterize cracks have relied on geometric ray tracing methods, where the incident ultrasonic energy has been assumed to follow a far-field type radiation pattern.¹¹ The most popular methods, such as tip-diffraction¹² and time-of-flight diffraction methods,¹³ involve tracking signals in time that are diffracted from the crack tip. However, the assumption of far-field behavior of the source is not necessarily appropriate for ultrasonic inspection in certain geometries, particularly for samples on the order of 25 mm or less in thickness.¹⁴ Other models have also been used to predict the crack diffraction pattern, such as the elastodynamic Kirchhoff theory¹⁵ and those that follow the Sommerfeld theory of diffraction.¹⁶ The former still relies on far-field assumptions, and the latter is solvable exactly for only a semi-infinite half-plane. In addition, neither theory is able to account for the frequency dependence of the diffracted signal. A number of improvements to the geometrical theories include the solution of a crack opening displacement to account for differences due to crack shape.^{17,18} However, these models often still require the use of the far-field assumption in order to calculate a practical solution. The laser generation/EMAT detection system described in this work will be used to characterize ideal cracks for which a far-field assumption cannot be made, i.e., plates measuring less than 25 mm in thickness. It will also be shown that straightforward signal processing using Fourier transform methods can be useful in sizing cracks by examining the frequency content of diffracted signals rather than by predicting the diffraction pattern.

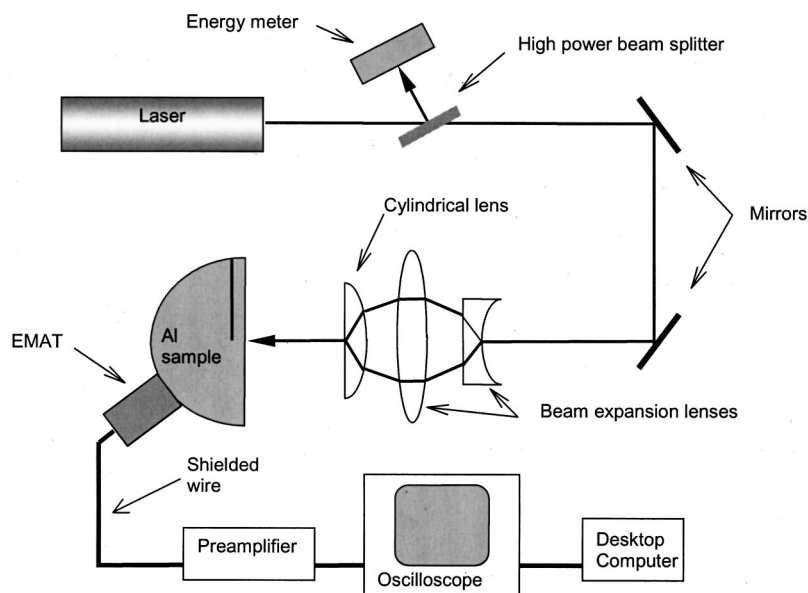
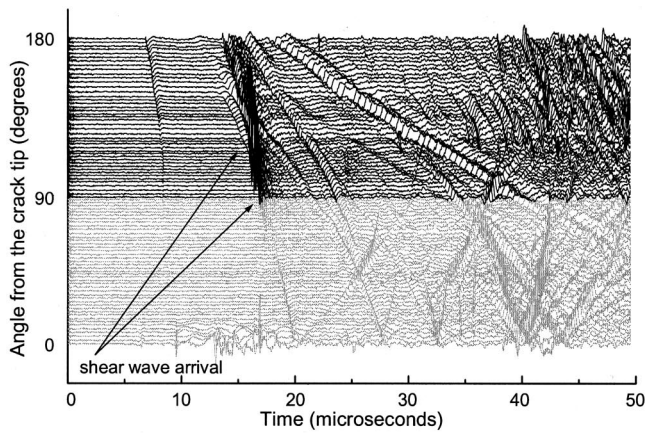
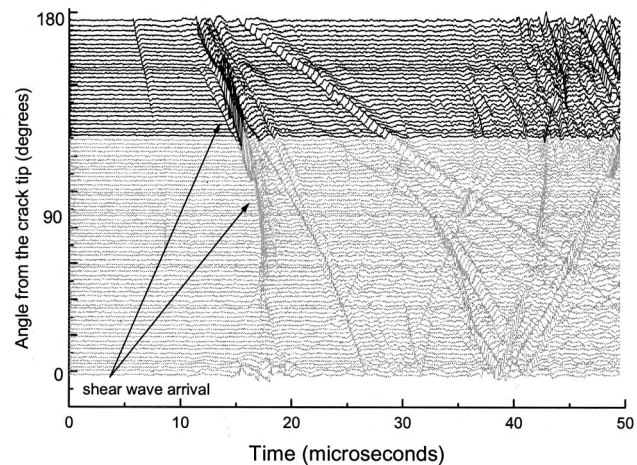


FIG. 2. Experimental setup for measuring ultrasonic crack diffraction in aluminum half-cylinder.



(a)



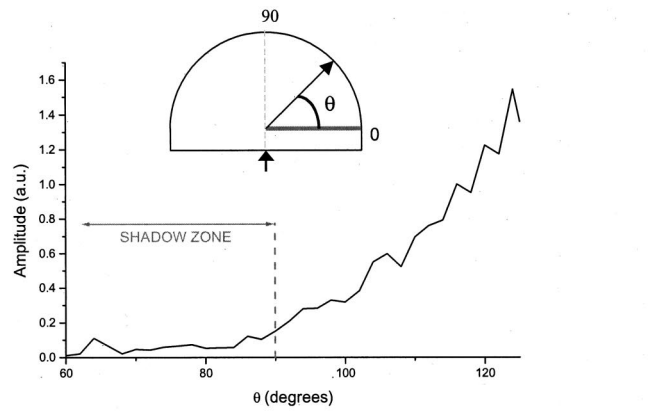
(b)

FIG. 3. Waveform scans in aluminum half-cylinder for (a) epicentral placement of source and (b) off-axis placement. Waveforms in gray indicate the angular range of the geometrical shadow zone of the EDM slot for each source configuration.

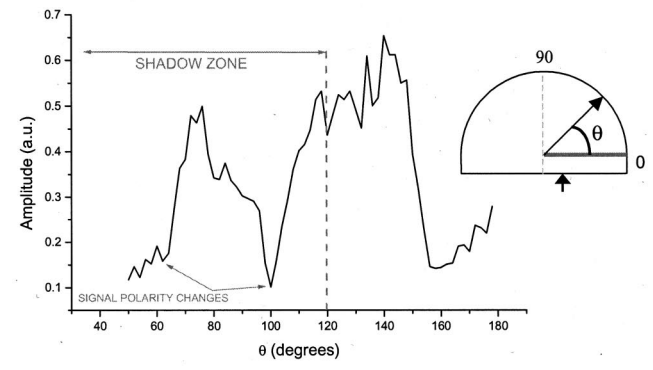
II. EXPERIMENTAL TECHNIQUE AND RESULTS

A. Diffraction from an ideal crack

To examine the diffraction of ultrasound from a line source at an ideal crack, or semi-infinite half-plane, scans were made on an aluminum half-cylinder with a slot made by a wire electrodischarge machine (EDM), approximately $280\ \mu\text{m}$ wide, machined along the radius. The laser line source was used in two different positions, shown in Fig. 1. In the first configuration, the laser line source was aligned with the crack tip along the y -axis. In the second configuration, the line source was offset by $7.5\ \text{mm}$ in the x -direction, corresponding to an incident angle of 120° at the crack tip, a peak in the amplitude for a laser-generated line source in aluminum. The experimental setup is shown in Fig. 2. The laser used to generate the ultrasound was a Q -switched, pulsed Nd:YAG ($1.064\ \mu\text{m}$). The laser beam was expanded with a planoconcave spherical lens followed by a double convex lens, and focused to a line with a cylindrical lens onto the center of the flat face of the aluminum half-cylinder. The laser line was approximately $80\ \text{mm}$ long, and $250\ \mu\text{m}$ wide. Pulse duration was $20\ \text{ns}$. The energy incident on the surface of the aluminum was measured to be $1\ \text{mJ}$ or less.



(a)



(b)

FIG. 4. Amplitude the direct shear arrival for (a) epicentral placement of source and (b) off-axis placement. The geometrical shadow zone is shown for both cases.

The EMAT footprint measured $25.4\ \text{mm}$ by $3\ \text{mm}$ with the long dimension of the EMAT oriented along the long dimension of the laser line. The vertical polarization of the EMAT receiver corresponded to the vertical polarization of the laser-generated shear wave. The EMAT was measured to be sensitive to ultrasonic signals up to $10\ \text{MHz}$. The signal received by the EMAT was sent through a shielded differential cable to a series of impedance matching preamplifiers before being recorded by a digital oscilloscope. The signals were transferred to a desktop computer for storage and analysis. The EMAT receiver was scanned along the circumference of the cylinder from 0° to 180° , in 2° increments. Waveform scans for both source configurations are shown in Fig. 3. Note that waveforms in gray indicate the angular range of the geometric shadow zone of the EDM slot for the two source configurations. The direct shear wave arrival, noted for each source configuration, is the primary signal of interest. The amplitude of the shear arrival, which occurs before $20\ \mu\text{s}$ for both configurations, is shown in Fig. 4. Note that in Fig. 3 signals that arrive later than $20\ \mu\text{s}$ correspond to wave arrivals resulting from multiple reflections within the cylinder and the arrival of the surface wave that travels along the circumference of the cylinder.

For the first source configuration, angles measuring 0° to 90° correspond to the geometric shadow zone behind the crack. Concentrating on the direct shear arrival before $20\ \mu\text{s}$, Fig. 4(a) shows that the majority of the ultrasonic energy is recorded at angles where the incident wave never interacts

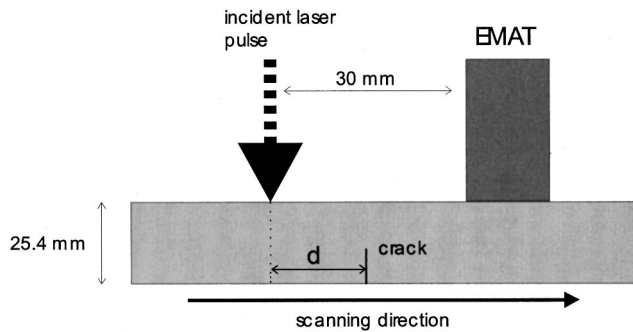


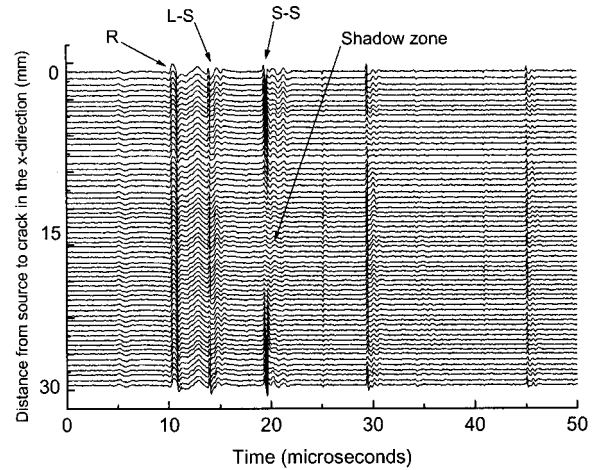
FIG. 5. Diagram of aluminum plate showing slot, source/EMAT placement, and scanning direction.

with the crack tip, as expected, from 90° to 180° . However, a small, but measurable diffracted wave is present between approximately 84° and 90° . This appears to be a genuine effect as mathematical models have shown that diffraction of ultrasound at the tip of an ideal crack will produce diffracted waves propagating in all directions.^{10,17} Additional ultrasonic sources may also come from tip diffraction of the Rayleigh wave generated on the surface of the crack face by the incident ultrasonic wave.¹⁹

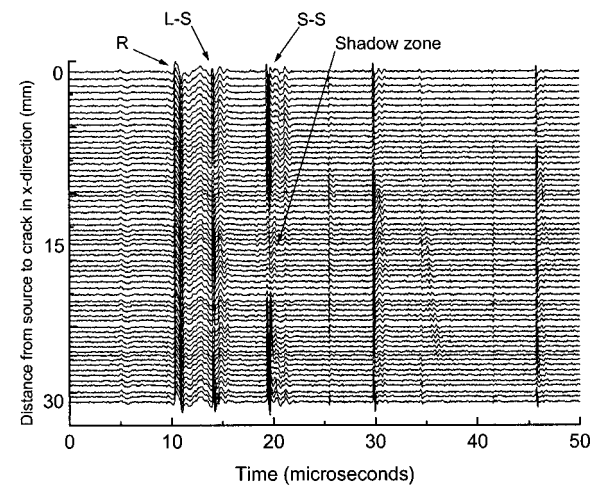
The amplitude of the direct shear wave arrival for the second source configuration is shown in Fig. 4(b). In this case, more ultrasonic energy interacts with the crack tip since the direction of the source to the crack tip coincides with the peak in amplitude for a laser generated ultrasonic source in aluminum, at 60° and 120° . The shadow zone is defined by the angular range from 0° to 120° . As before, a significant amount of energy never interacts with the crack, and the incident wavefield propagates unhindered between 120° and 180° . However, a sizeable diffracted shear wave is detected in the shadow zone between approximately 60° and 120° , shown clearly in both Fig. 3(b) and Fig. 4(b). For this case, the shadow zone boundary is not readily apparent. Another interesting feature of the shear wave arrival is a reversal in signal polarity from the undiffracted signal between 62° and 100° . A single reversal in polarity for the diffracted wave in the shadow zone is anticipated, however, the angle at which the polarity change first occurs and the fact that it changes back is unexpected. Previously reported hybrid systems were unable to show these effects as a result of design limitation in the sensor/receiver configuration,⁷ a large receiver footprint,⁸ or a complicated wavefront amplitude pattern for the ultrasonic source.⁹

B. Crack sizing measurements on aluminum plates

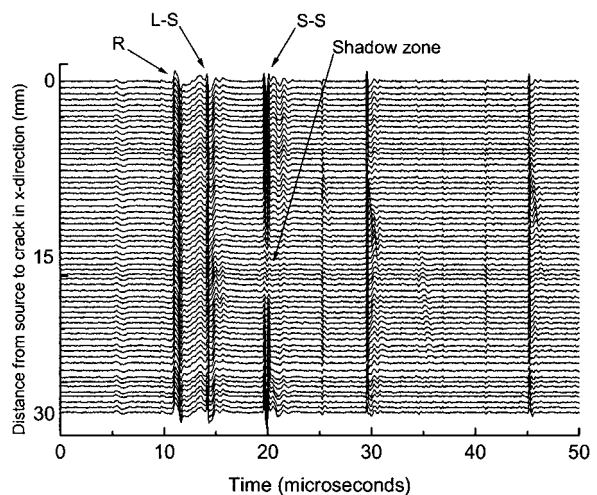
In order to examine the viability of a laser line/broadband EMAT system in sizing cracks, experiments were conducted on aluminum plates milled with slots. Three different slot depths were examined: 2.54 mm (0.1 in.), 5.08 mm (0.2 in.), and 7.62 mm (0.3 in.). Each plate measured $127.0\text{ mm} \times 254.0\text{ mm} \times 25.4\text{ mm}$. The slots were machined across the plates, perpendicular to the long dimension. The experimental setup used was similar to that shown in Fig. 2 with the half cylinder replaced by a plate. Each plate was scanned with the line source and EMAT on one side of the



(a)



(b)



(c)

FIG. 6. Waveform scans for aluminum plates with milled slots measuring (a) 7.62 mm (0.3 in.) (b) 5.08 mm (0.2 in.), and (c) 2.54 mm (0.1 in.). The arrival of the surface wave, R , the mode-converted longitudinal arrival, $L-S$, and the shear arrival, $S-S$, are shown, as well as the geometrical shadow boundary.

plate, and the slot on the opposite side. The plate was translated while the source and EMAT remained stationary, as shown in Fig. 5. Given the geometry of the aluminum plates, a distance of 30 mm between the source and the center of the

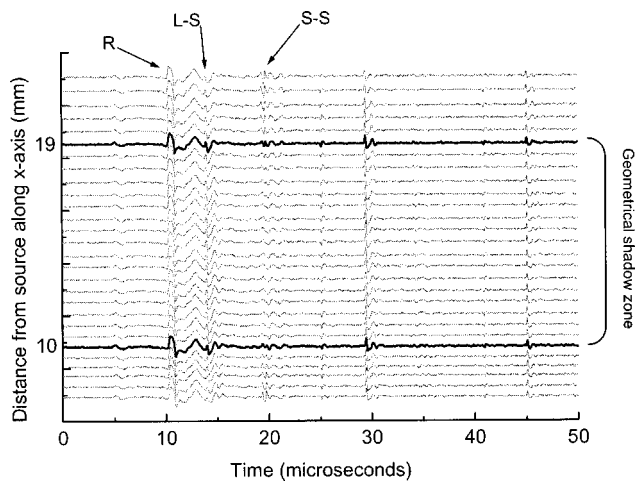
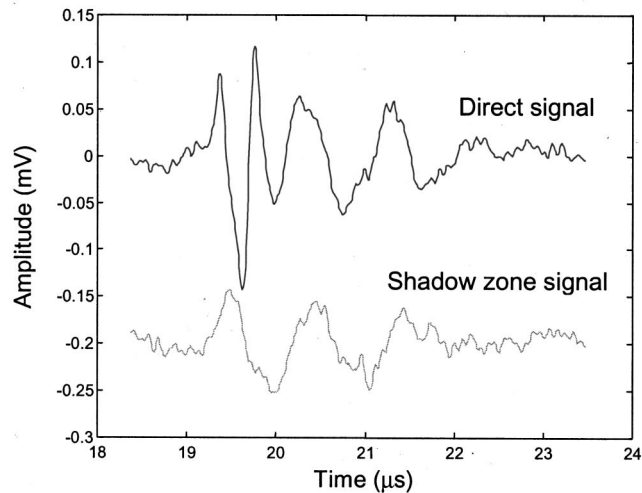


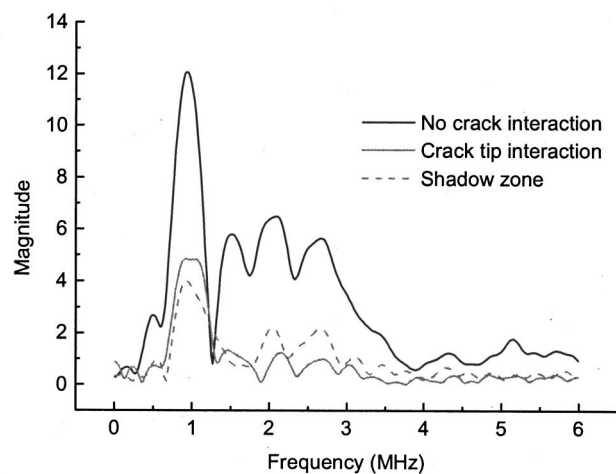
FIG. 7. Detail of Fig. 6(a). Waveforms in bold indicate geometric shadow boundary.

EMAT wires corresponds to the optimum placement for reception of the strongest signal from the backwall reflection. The results of the scans for each plate are shown in Fig. 6. Similarities between all of the plate scans are immediately evident. For each scan, the first strong signal at approximately $10 \mu\text{s}$ corresponds to the Rayleigh surface wave, *R*, traveling between the source and the receiver. The second signal at approximately $14 \mu\text{s}$ corresponds to a longitudinal wave that mode converts to a shear wave, *L-S*, at the back wall of the plate. This signal will never interact with the crack because of the propagation and reflection angles of the primary longitudinal and the mode-converted shear waves in aluminum relative to the laser and EMAT positions. The third signal at approximately $19 \mu\text{s}$ is the shear wave that reflects off the backwall, *S-S*, i.e., the signal that interacts with the crack. This signal diminishes toward the middle of the scan for each plate corresponding to the shadow zone; however, it does not disappear completely. The geometrical portion of the incident wave is shadowed by the slot, yet a diffracted wave is still produced by the interaction of the incident wave with the slot tip. Closer examination of the data from the 7.62 mm slot scan, shown in Fig. 7, shows that the diffracted wave energy makes the geometric shadow boundary difficult to interpret. A relatively sharp shadow boundary is critical to determining the size of the slot.

In Fig. 8, the frequency spectrum of diffracted signals from the shadow zone of the 7.62 mm slot scan is compared to that from a direct signal. Visual examination of the two time signals in Fig. 8(a) shows that the frequency content is different. The upper signal was taken from a direct waveform outside the shadow zone boundary. The lower signal was taken from inside the shadow zone. This difference is confirmed in Fig. 8(b) by comparing the Fourier spectra of the two signals along with a signal from a wave that interacts directly with the crack tip, i.e., a signal that should define the shadow zone. The diffracted energy lacks the high frequency content centered at 2.1 MHz found in the direct signal. Possible contributors to the frequency dependence are the influence of the reception angle along the surface of the plate, and the shape of the crack tip.



(a)



(b)

FIG. 8. (a) Detail of shear arrivals for direct and shadow zone signals in Fig. 6(a), and (b) corresponding frequency spectra of both signals with the frequency spectrum of the crack tip signal.

III. DISCUSSION

The waveform scans on the slotted half-cylinders, shown in Fig. 3, illustrate that a diffracted wave is detected in the geometrical shadow zone of a crack. For both source configurations, diffracted energy is detectable into the geometrical shadow zone of the crack. In addition, the amplitude of the ultrasonic energy drops off gradually, rather than sharply. The effect is more pronounced in the results for the offset source configuration. In this case, more energy was incident on the crack tip, thus producing a stronger diffracted wave. The ramifications of the results for both cases are clear. A sizeable amount of energy can be diffracted into the shadow zone depending on the source configuration and measurement geometry as shown by ultrasonic diffraction models and the results of these experiments. A sharp shadow boundary cannot be expected for diffraction of ultrasound by a crack and, thus, there will be a systematic error in crack measurement calculations if only time domain signals are analyzed.

From the experiments on the aluminum plates, it would

TABLE I. Linear distance along surface of plate corresponding to the shadow region of the crack and estimated error in measurements.

Slot size	Δd (calculated)	Δd (measured)	Measured slot size	% Error
7.62 mm (0.3 in.)	8.8 mm	8.0 mm	6.90 mm	9.56
5.08 mm (0.2 in.)	5.86 mm	4.5 mm	3.88 mm	23.62
2.50 mm (0.1 in.)	2.88 mm	3.0 mm	2.59 mm	3.60

appear that measuring a crack using ultrasonic time domain signals will consistently undersize cracks given the lack of a sharp shadow zone. However, analysis of the results of the 7.62 mm plate scans in Fig. 8 show that signal processing using Fourier analysis may provide a better method for crack measurement. While ray tracing methods are still useful for defect detection, more sophisticated signal processing methods such as described here must be used for separation of diffracted signals from the geometric signals so that defects can be sized.

A theoretical resolution limit for sizing cracks can be calculated by examining the geometry of the plate/crack system and considering a ray tracing approach for the propagating ultrasonic shear waves. If we assume that a laser line source sends an ultrasonic shear wave at an angle of 30° from the surface normal into a 25.4 mm (1 in.) aluminum plate, the geometrically propagating rays that interact with the crack can be calculated (shown in Fig. 10). The horizontal distance between the source and the crack is calculated for the distance from which the first back wall reflection is blocked by the crack tip d_1 , and the distance from which the direct ray is blocked by the crack tip, d_2 . Subtraction of d_1 from d_2 , Δd , gives a linear distance along the surface of the plate which is directly proportional to the size of the crack. Table I gives Δd expected for each slot size, or depth. For a 25 mm thick aluminum plate, every millimeter in slot depth corresponds to 1.16 mm in linear distance along the surface of the aluminum plate. Thus

$$\frac{\Delta d}{1.16} = l, \quad (1)$$

where l is the slot depth. The distance, Δd , will vary depend-

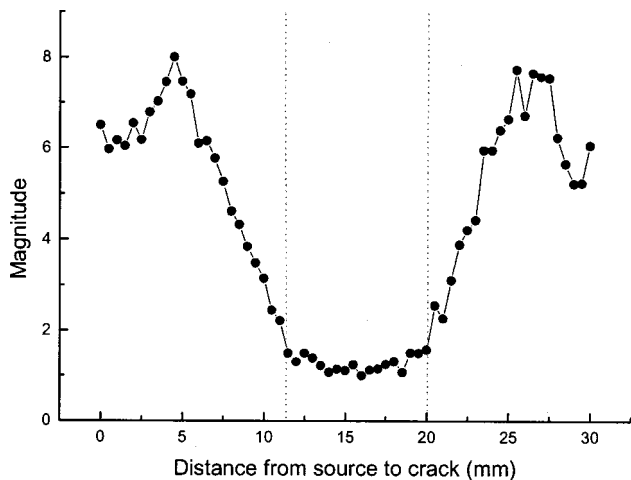


FIG. 9. Amplitude of 2.1 MHz component for frequency spectrum of each S-S wave arrival in Fig. 6(a).

ing on the material properties of the plate since the propagation angle of the maximum amplitude for a shear wave is dependent on Poisson's ratio. The measured values for each slot using the time-domain data, shown in Table I, are taken from Fig. 6. Error in the measurement comes from several sources, mostly dependent on the EMAT design. Even though the maximum sensitivity is found at the center of the EMAT, the detector still has a finite, albeit small, width. Signals will be received at the edges as well as at the center of the detector. Thus the cracks are likely to be undersized as shown in the error estimates calculated in Table I. In addition, selection of a representative shadow zone boundary signal is highly subjective. Signal shapes are not necessarily uniform along the length of the plate. Ideally, the waveform with the lowest reflected shear amplitude would be selected.

These sources of error may be eliminated by examining the frequency spectrum of each waveform. The results shown in Fig. 8(b) suggest that selective filtering of frequencies lower than 1.5 MHz may aid in finding the shadow zone. This is equivalent to filtering out the diffracted wave. Thus only the geometric, or ray tracing, signal will remain. In fact, if the frequency spectrum of each S-S signal in Fig. 6(a) is calculated, and the maximum in amplitude at 2.1 MHz is plotted, as in Fig. 9, it is found that the minimum corresponds very closely to the actual crack dimensions. Using this data, $\Delta d = 8.5$ mm which corresponds to a measured slot size of 7.33 mm. Compared to the actual slot size, 7.62 mm, as in Fig. 10 this represents a measurement error of 3.8%, a marked improvement over using the time domain signals. This hybrid laser/EMAT system coupled with frequency analysis of the signals will give a more accurate crack sizing measurement, particularly for plates that will not satisfy the far-field condition for ultrasonic inspection, i.e., those on the order of 25 mm or thinner.

IV. CONCLUSION

This work has shown that a hybrid laser generation/EMAT detection system coupled with frequency analysis of

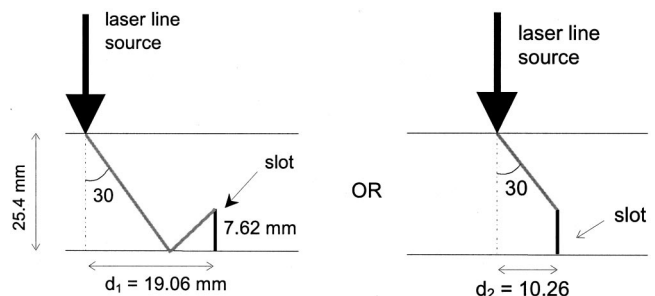


FIG. 10. Ray tracing diagram for 7.62 mm slot.

the time domain signals can be effective for characterizing the diffraction of ultrasound at cracks. The resolution in time and frequency of the EMAT detector was able to show the diffraction of ultrasound in all directions at the crack tip as predicted by ultrasonic crack diffraction models. It was also able to show a difference in the frequency content of direct and shadow zone signals.

These preliminary measurements point to two subjects that require further investigation. The first topic is crack shape and width. All experiments in this report were conducted on relatively wide slots whose sides do not touch. Real cracks are likely to have faces in intimate contact. This may be another source of frequency dependence of the diffracted wave. In addition, the shape of the crack tip may play a significant role, particularly with regard to frequency dependence. Thus the frequency content of the signal may potentially be used for measuring other effects such as stress concentration at the crack tip and crack tip shape.

ACKNOWLEDGMENTS

This work was supported by the Center for Nondestructive Evaluation at The Johns Hopkins University and McDer-mott Technologies, Inc. The authors would also like to thank Professor Robert E. Green, Jr. for his contributions.

¹D. E. Bray and R. K. Stanley, *Nondestructive Evaluation* (CRC Press, Boca Raton, 1997).

²J. Krautkramer and H. Krautkramer, *Ultrasonic Testing of Materials* (Springer Verlag, New York, 1990).

³P. A. Doyle and C. M. Scala, "Crack depth measurement by ultrasonics: A review," *Ultrasonics* **16**, 164 (1978).

⁴C. B. Scruby and L. E. Drain, *Laser Ultrasonics: Techniques and Applications* (Adam Hilger, Bristol, 1990).

⁵J. B. Spicer and S. L. Wallace, "Laser ultrasonic monitoring of aluminium alloy microstructural evolution." *J. Mater. Sci.* **33**, 3899–3906 (1998).

⁶H. M. Frost, "Electromagnetic-Ultrasonic Transducers: Principles, Practice, and Applications." *Phys. Acoust.* **14**, 179 (1979).

⁷D. A. Hutchins, C. Saleh, M. Moles, and B. Farahbakhsh, "Ultrasonic NDE using a concentric laser/EMAT system." *J. Nondestruct. Eval.* **9**, 247 (1990).

⁸D. A. Oursler and J. W. Wagner, "Narrow-band hybrid pulsed laser/EMAT system for noncontact ultrasonic inspection using angled shear waves," *Mater. Eval.* **53**, 593 (1995).

⁹S. Dixon, C. Edwards, and S. B. Palmer, "A laser-EMAT system for ultrasonic weld inspection," *Ultrasonics* **37**, 273 (1999).

¹⁰J. R. Bernstein and J. B. Spicer, "Line source representation for laser-generated ultrasound in aluminum," *J. Acoust. Soc. Am.* **107**, 1352 (2000).

¹¹J. Blitz and G. Simpson, *Ultrasonic Methods of Non-destructive Testing* (Chapman Hall, London, 1996).

¹²K. Harumi, Y. Ogura, and M. Uchida, Eds., *Ultrasonic Defect Sizing: Japanese Tip Echo Handbook* (Japanese Society for Non-Destructive Inspection, Japan, 1989).

¹³J. P. Charlesworth and J. A. G. Temple, *Engineering Applications of Ultrasonic Time-of Flight Diffraction* (Wiley, New York, 1989).

¹⁴J. R. Bernstein, "Ultrasonic crack diffraction in metals: Investigations using laser generated ultrasonic shear waves and broadband EMAT detection," Ph.D. Dissertation, The Johns Hopkins University, Baltimore, 1999.

¹⁵R. K. Chapman, "A system model for the ultrasonic inspection of smooth planar cracks," *J. Nondestruct. Eval.* **9**, 197 (1990).

¹⁶A. T. de Hoop, "Representation theorems for the displacement in an elastic solid and their application to elastodynamic diffraction theory," Ph.D. dissertation, Technische Hogeschool, Delft, Holland, 1958.

¹⁷J. D. Achenbach, A. K. Gautesen, and H. McMaken, *Ray Methods for Waves in Elastic Solids* (Pitman Books, London, 1982).

¹⁸P. Bovik and A. Bostrom, "A model of ultrasonic nondestructive testing for internal and subsurface cracks," *J. Acoust. Soc. Am.* **102**, 2723 (1997).

¹⁹A. K. Gautesen, J. D. Achenbach, and H. McMaken, "Surface-wave rays in elastodynamic diffraction by cracks." *J. Acoust. Soc. Am.* **63**, 1824–1831 (1978).

Performance of a low-frequency, multi-resonant broadband Tonpilz transducer

Dhilsha Rajapan

*Tests and Measurements Laboratory, Marine Instrumentation, National Institute of Ocean Technology
Campus, Pallikaranai, Chennai-601 302, Tamilnadu, India*

(Received 18 December 2000; accepted for publication 10 January 2002)

The underwater performance of a high-power multi-resonant Tonpilz transducer with a nearly flat frequency response and a power handling capability of 2 kW (peak) is reported here. A maximum transmitting voltage response (TVR) value of 156 dB *re*: 1 $\mu\text{Pa/V}$ at 1 m has been achieved at 3 kHz with a specially designed matching coil. A maximum receiving sensitivity (RS) of -164 dB *re*: 1 $\text{V}/\mu\text{Pa}$ at 3 kHz has been measured without using a matching coil. The horizontal half-power beam width of the transducer at 4 kHz is 101 degrees with a directivity index of 4 dB. This transmitter can be used for oceanographic applications such as subbottom profiling as well as long-range underwater communication. © 2002 Acoustical Society of America. [DOI: 10.1121/1.1456927]

PACS numbers: 43.38.Ar, 43.38.Fx, 43.58.Vb [SLE]

I. INTRODUCTION

Wide bandwidth waveforms are necessary in applications where high resolution or high bit rates are required such as data transmission, marine sediment analysis, and underwater communication.¹⁻³ Different designs have been reported in the literature in achieving a broadband underwater transducer.⁴⁻⁹ The possibilities of achieving broadband Tonpilz transducers utilizing different vibrational modes, while still retaining the simple conventional configurations, have been investigated by several authors theoretically in the medium frequency (above 20 kHz) range.⁷⁻⁹ A rarely used method is the use of multi-resonance in a device through a careful design of the head mass.⁹ For a given acoustic transmitter face diameter and material, the quality factor Q is proportional to the mass of the head. Q is reduced by reducing the thickness of the head along with configuration changes (such as tapering the head structure). Since the specific acoustic impedance of the ceramic is higher than that of water, a better impedance match would be achieved if the area of the radiating face is significantly larger than that of the piezoelectric ceramic materials. Actually, this leads to a design with a tapered (mushroom) head mass.

A practical realization of a high-power, multi-mode optimized Tonpilz transducer in the low-frequency regime, and its underwater performance (experimental results), are reported in this article. A circular head mass made of aluminum with a front face diameter of 158 mm has been selected on an experimental basis in the present case. The head mass is moulded with an ethylene propylene rubber for water-tight encapsulation as well as good impedance matching with the water medium. A ratio of 1:4 has been adopted for the head to tail mass (made of brass) for optimum performance. A prestress bolt made of steel with a diameter of 12 mm was used. Indigenous, locally available PZT-4 (thickness drive) ceramic rings of inner diameter 19.5 mm and 6 mm thickness were utilized in the fabrication of this transducer. In order to avoid the effect of loading on the supporting structure, the transducer assembly was decoupled from the encapsulation casing structure (PVC) by using an annular rubber dia-

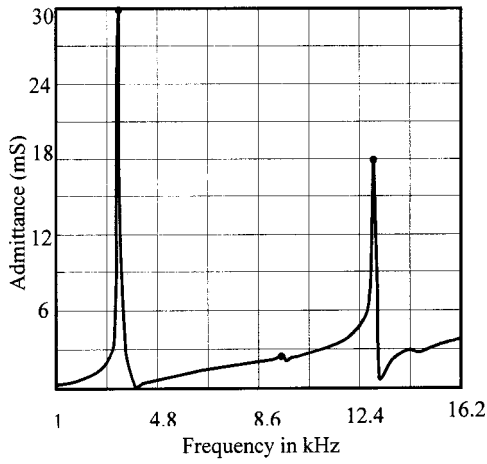
phragm with the outer part clamped rigidly to the housing. In addition, an O-ring seal is provided between the head mass and the casing. The specific design is intended to be protected by a patent.

II. MEASUREMENTS OF ELECTRICAL AND ACOUSTICAL PARAMETERS

The in-air and underwater impedance, resistance, and admittance of the transducer as a function of frequency was carried out from 2 to 16 kHz utilizing an LF Impedance Analyzer (HP 4194A). The methods of measurements for the underwater evaluation of the transducer have been carried out, as given by Bobber,¹⁰ in an Acoustic Test Facility (ATF) at 3 m water depth. The underwater parameters such as transmitting voltage response (TVR) and receiving sensitivity (RS) were carried out using an impulse method in the frequency range 2–10.25 kHz. A dynamic signal analyzer has been used for the impulse technique. The measurement error is estimated to be ± 1 dB. The horizontal directivity measurements at fixed frequencies and the source level (SL) measurements were carried out by tone burst method. After initial measurement of TVR, RS, etc., a matching coil was designed exclusively for optimizing the underwater parameters for using this transducer for oceanographic application like acoustic subbottom profiling (ASP).

III. RESULTS AND DISCUSSION

In-air admittance of a multi-resonant transducer without a matching coil is shown in Fig. 1. The in-air, resonances are designed to be around 3.50 and 13 kHz, respectively, and this was achieved as seen in the figure. The first peak in the admittance corresponds to the fundamental resonance, whereas the third one corresponds to a flapping or flexural mode. The fundamental mode is dominant over the other modes. A small resonance around 9.5 kHz is also observed and this could be due to a contribution from the prestress bolt. The transmitting voltage responses of the transducer, measured without and with a matching coil, are given in Fig.



X1 = 3.4 kHz, Y1 = 29.7mS
 X2 = 9.4 kHz, Y2 = 2.6 mS
 X3 = 12.9 kHz, Y3 = 18 mS

FIG. 1. Variation of admittance versus frequency for a multi-resonant transducer.

2. The dotted curve represents the TVR plots without a matching coil. A TVR of 143 dB *re*: 1 μ Pa/V at 1 m at 3 kHz is achieved whereas the value could be enhanced to 156 dB *re*: 1 μ Pa/V at 1 m with a matching coil. The TVR values at \sim 9 kHz are almost equal in magnitude to that at 3 kHz. TVR falls down rapidly around 10 kHz. Qingshan Yao *et al.*⁹ has observed such a behavior due to a contribution by the stress bolt and the screw joints at the head and tail masses. Hence the reason for this is being studied experimentally by increasing the bolt diameter used for providing an optimum prestress. Typical measured receiving sensitivity (RS) of the transducer is shown in Fig. 3. A maximum sensitivity of -164 dB *re*: 1 V/ μ Pa at 3 kHz has been achieved without using a matching coil. Unlike the TVR, the receiving sensitivity falls down rapidly above 8.3 kHz. This behavior may also be due to a contribution by the bolt resonance. The same transducer can be used as a transceiver in the anticipated applications if the skew-type behavior of the receiving sensitivity can be eliminated. The increase in bandwidth and higher TVR values indicate a substantial improvement in the effective coupling factor k_{eff} .^{6,11} This is in principle deter-

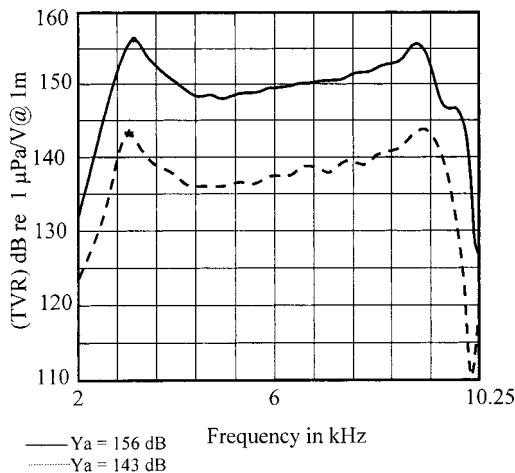


FIG. 2. Transmitting voltage response (TVR) of the transducer.

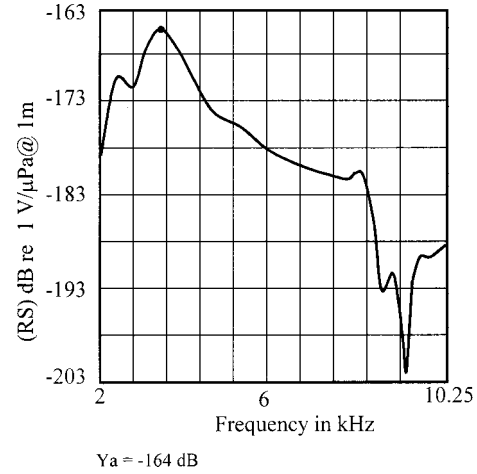


FIG. 3. Typical receiving sensitivity (RS) of the transducer.

mined by an improvement in the structural design of the Tonpilz while multiple resonance is incorporated. Thus there exists a possibility of improving the transducer performance by improving the design while using an active material with the same electro-mechanical coupling coefficient k_{33} . The material coupling factor k_{33} is different from whole transducer coupling factor k_{eff} . It is to be mentioned that this point was first mentioned by W. P. Mason in his approximation and was discussed in detail by Moffett *et al.*¹¹

A source level (SL) of 191 dB *re*: 1 μ Pa at 1 m has been experimentally measured for an electrical power drive level of 1.43 kW (rms) at 3 kHz with a distortion in the signal of the order of 9% with a matched coil. The variation in the SL over the frequency range was nearly 3 dB and this is mainly due to the change in the frequency and hence the change in the power handling due to a variation in the impedance. Horizontal directivity measurements showed a half-power beam width of 101 degrees at 4 kHz and 60 degrees at 8 kHz, respectively. Typical directivity pattern measured at 4 kHz is shown in Fig. 4. The directivity at low frequencies should be nearly omni-directional due to the larger wavelength and a

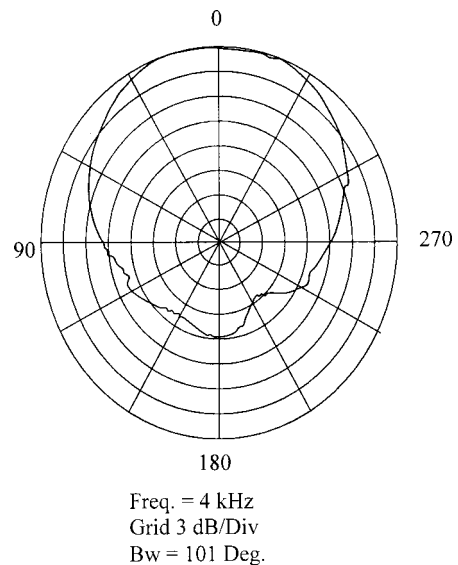


FIG. 4. Horizontal directivity pattern of the transducer at 4 kHz.

fixed aperture at the transmitting face of the transducer. The directivity indices are 4 and 7 dB at the two higher frequencies, respectively. The power handling capacity of the transducer is 2 kW (peak). This transducer is portable, light weight (~12 kg in air, inclusive of casing) and with the capability of delivering high powers which was not possible with the conventional Tonpilz designs. Typical values of SL and RS for commercially available transducers used for similar purposes are 147 dB *re*: 1 $\mu\text{Pa}/\text{V}$ at 1 m and -175 dB *re*: 1 V/ μPa , respectively. The half-power beam width at 7 kHz for such a commercially available transducer is 80 degrees. However, estimations on efficiencies are yet to be done, since the conventional method of obtaining it from admittance loci cannot be used in the present case, due to the multi-resonant behavior.

IV. CONCLUSIONS

A high-power wideband transducer having usable operational frequencies in the range 2–10 kHz has been achieved utilizing a multi-resonant Tonpilz design. It is believed that the prestress bolt and its screw joints play a major role in the performance of the transducer. Further research is concentrated on the optimum design of the stress bolt to extend the bandwidth of operation. A theoretical finite element modeling (FEM) utilizing ANSYS as well as an experimental study are required to increase the frequency range up to 16 kHz and for further optimization in the performance. The design of an optimum matching coil for achieving higher acoustic levels also forms part of the future work.

ACKNOWLEDGMENTS

The author is grateful to Professor M. Ravindran, Director, NIOT for his keen interest and permitting him to take up this work. He also thanks Professor D. Srinivasan, who was always a source of inspiration, and Shri. A. S. Ramamoorthy for his advice at various stages and constant encouragement

through out this work. The author thanks the Director, N.P.O.L, for extending the Acoustic Test Facility. The underwater performance evaluation could not have been possible without the wholehearted support from Acoustic Measurements, group of N.P.O.L, Kochi. Thanks are also due to everyone in the instrumentation group, for their support. Special mention is deserved to P. M. Rajeshwari of NIOT for her skillful technical assistance in realizing the design feasibility as well as in the measurements. This work is supported by NIOT.

- ¹R. W. Timme, A. M. Young, and J. E. Blue, "Transducer Needs for Low Frequency Sonar," in *Power Transducers for Sonics and Ultrasonics*, edited by B. F. Hamonic, O. B. Wilson, and J. N. Decarpigny (Springer, Berlin, 1991), pp. 3–13.
- ²R. Person, "Transducer Needs for Oceanography," in *Power Transducers for Sonics and Ultrasonics*, edited by B. F. Hamonic, O. B. Wilson, and J. N. Decarpigny (Springer, Berlin, 1991), pp. 14–21.
- ³R. F. W. Coates, "The design of transducers and arrays for underwater data communication," *IEEE J. Ocean. Eng.* **16**(1), 123–135 (1991).
- ⁴S. C. Thompson, M. P. Johnson, E. A. McLaughlin, and J. F. Lindberg, "Performance and recent developments with doubly resonant wide band transducers," in *Transducers for Sonics and Ultrasonics*, edited by M. D. McCollum *et al.* (TECHNOMIC, U.S.A., Lancaster, Pennsylvania, 1993), pp. 239–249.
- ⁵D. Boucher, "New Solutions for Low Frequency Sonar Projectors," in *Transducers for Sonics and Ultrasonics*, edited by M. D. McCollum *et al.* (TECHNOMIC, U.S.A., Lancaster, Pennsylvania, 1993), pp. 17–37.
- ⁶D. Stansfield, *Underwater Electroacoustic Transducers, A Handbook for Users and Designers* (Bath U. P., Bath, I.O.A., 1990).
- ⁷D. W. Hawkins and P. T. Gough, "Multiresonance design of tonpilz transducer using finite element method," *IEEE Trans. Ultrason. Ferroelectr. Freq. Control* **43**, 782–790 (1996).
- ⁸J. L. Butler, J. R. Cipolla, and W. D. Brown, "Radiating head flexure and its effect on transducer performance," *J. Acoust. Soc. Am.* **70**, 500–503 (1981).
- ⁹Q. Yao and L. Bjorno, "Broadband Tonpilz Underwater Acoustic Transducers Based on Multimode Optimization," *IEEE Trans. Ultrason. Ferroelectr. Freq. Control* **44**, 1060–1065 (1997).
- ¹⁰R. J. Bobber, *Underwater Electroacoustic Measurements* (Naval Research Laboratory, Washington D.C., 1970; reprinted by Peninsula, Los Altos, CA, 1988).
- ¹¹M. B. Moffett and W. J. Marshall, Jr., (ONR) Report AD-A284 309, US Navy, Undersea Warfare Center, Newport, RI, June 1994.

Generation of an acoustically bright zone with an illuminated region using multiple sources

Joung-Woo Choi and Yang-Hann Kim^{a)}

Center for Noise and Vibration Control (NOVIC), Department of Mechanical Engineering, Korea Advanced Institute of Science and Technology (KAIST), Science Town, Taejeon-shi 305-701, Korea

(Received 20 March 2001; accepted for publication 10 January 2002)

This article addresses the way in which we can generate an “acoustically bright zone” in a space. The bright zone is defined as the volume where we can have higher acoustic energy than in other space. A method is proposed to generate the bright zone by controlling multiple monopole sources. Two kinds of cost functions involved with acoustic brightness are defined. One is the ratio of the brightness of a zone to the input power, and the other expresses the “contrast” between the bright zone and the other space. Through eigenvalue analysis, the optimal volume velocity distribution of the monopoles has been obtained. © 2002 Acoustical Society of America.

[DOI: 10.1121/1.1456926]

PACS numbers: 43.38.Hz, 43.20.-f [SLE]

I. INTRODUCTION

Acoustic potential energy determines the magnitude of a sound perception. Many researchers have tried to make a “zone of quiet,¹” where the acoustic potential energy is low, using multiple control sources and sensors. We call this active noise control. In contrast to the active noise control situation, we sometimes want to increase the acoustic energy in a desired space. For example, we may want to transmit specific information to a region of interest or would like to make a region where we have better sound or musical quality. In contrast to the quiet zone, we can define the zone of high acoustic potential energy as an “acoustically bright zone.” This article deals with a method to generate an acoustically bright zone using multiple control sources.

Among the problems related to the generation of an acoustically bright zone in general, for example, control sources locations and directivity, this study focuses on two specific cases. One is the constraint that has to do with the input power, and the other one is associated with the definition of a bright zone.

One constraint associated with the problem has to do with the fact that the input power is limited. Therefore, maximizing the acoustic potential energy in a desired or target zone has to be achieved under the given or allowable input power. Concerning the definition of the bright zone, there could be many possible ways. However, if we want to have the bright zone compared with the neighboring region, then our problem is to make the best possible contrast—the potential energy difference—under the given input power without changing the location and number of control sources.

To solve these two problems, we define two kinds of zone (Fig. 1). One is the total zone of interest V_t , which means that the potential energy outside V_t is out of our interest. The other zone is an acoustically bright zone V_b , where the receivers wish to get high acoustic potential energy. We also assume that V_t always includes the bright zone V_b . Leftover in V_t is the acoustically dark (quiet) zone that is related with the second problem.

In practice, we can use many different kinds of sources as the control sources. However, for simplicity, we assume that only monopole sources are available. The number of sources is assumed to be finite and the locations of the sources are arbitrary in space. Therefore, the problem we have now is to find the best possible way to make the bright zone, which has finite volume, by using a finite number of sources and finite effort.

II. PROBLEM DEFINITION

Figure 2 shows a system with arbitrary boundary condition. The $\hat{p}(\vec{x})$ represents the complex magnitude of pressure generated by the control sources that radiate sound of frequency ω . The total number of control sources is K .

Each control source is located at the position, $\vec{x}_c^{(i)}$ ($i = 1, \dots, K$) and has a volume velocity $\hat{q}_c(x_c^{(i)})$. Then the pressure $\hat{p}(\vec{x})$ can be written in terms of Green’s function $\hat{G}(\vec{x}|\vec{x}_c^{(i)})$. That is,

$$\hat{p}(\vec{x}) = \sum_{i=1}^K \hat{G}(\vec{x}|\vec{x}_c^{(i)}) \hat{q}_c(\vec{x}_c^{(i)}). \quad (1)$$

Let us define a matrix, which represents Green’s function between measurement positions $\vec{x}_m^{(j)}$ ($j = 1, \dots, M$) and control source positions $\vec{x}_c^{(i)}$ ($i = 1, \dots, K$) as

$$\mathbf{G}(\vec{\mathbf{x}}_m|\vec{\mathbf{x}}_c) = \begin{bmatrix} \hat{G}(\vec{x}_m^{(1)}|\vec{x}_c^{(1)}) & \cdots & \hat{G}(\vec{x}_m^{(1)}|\vec{x}_c^{(K)}) \\ \vdots & \ddots & \vdots \\ \hat{G}(\vec{x}_m^{(M)}|\vec{x}_c^{(1)}) & \cdots & \hat{G}(\vec{x}_m^{(M)}|\vec{x}_c^{(K)}) \end{bmatrix}. \quad (2)$$

The vector expression, $(\vec{\mathbf{x}}_m, \vec{\mathbf{x}}_c)$ is used to express that the matrix represents the relation between the multiple measurement positions $\vec{\mathbf{x}}_m = [\vec{x}_m^{(1)} \cdots \vec{x}_m^{(M)}]$ and the multiple control source positions $\vec{\mathbf{x}}_c = [\vec{x}_c^{(1)} \cdots \vec{x}_c^{(K)}]$.

Then, Eq. (1) can be rewritten as

$$\hat{p}(\vec{x}) = [\hat{G}(\vec{x}|\vec{x}_c^{(1)}) \cdots \hat{G}(\vec{x}|\vec{x}_c^{(K)})] \times [\hat{q}_c(\vec{x}_c^{(1)}) \cdots \hat{q}_c(\vec{x}_c^{(K)})]^T = \mathbf{G}(\vec{x}|\vec{\mathbf{x}}_c) \mathbf{q}_c. \quad (3)$$

^{a)}Electronic mail: yhkim@sorak.kaist.ac.kr

We have now expressed the cause and effect relation between sources and sound pressure at the position of interest, in terms of selected acoustic and geometrical variables (Fig. 2). The next problem has to do with how we express or define “acoustical brightness.” The first choice to express the overall acoustical brightness of a zone will be space-averaged potential energy density, as a first approximation. The acoustic potential energy density is proportional to the square of pressure complex magnitude, and that can be written as

$$e_b = \frac{1}{V_b} \int_{V_b} \hat{p}(\vec{x})^* \hat{p}(\vec{x}) dV. \quad (4)$$

In terms of matrices defined in Eq. (3), this can be re-written as, using a Hermitian operator H ,

$$e_b = \mathbf{q}_c^H \left(\frac{1}{V_b} \int_{V_b} \mathbf{G}(\vec{x}|\vec{x}_c)^H \mathbf{G}(\vec{x}|\vec{x}_c) dV \right) \mathbf{q}_c = \mathbf{q}_c^H \mathbf{R}_b \mathbf{q}_c, \quad (5)$$

where

$$[\mathbf{R}_b]_{(r,s)} = \frac{1}{V_b} \int_{V_b} \hat{G}(\vec{x}|\vec{x}_c^{(r)})^H \hat{G}(\vec{x}|\vec{x}_c^{(s)}) dV.$$

Each element of \mathbf{R}_b represents the spatial correlation of the pressure field in the bright zone produced by each control source. Similarly, the average potential energy density of V_t is given by

$$e_t = \mathbf{q}_c^H \mathbf{R}_t \mathbf{q}_c, \quad (6)$$

where

$$\mathbf{R}_t = \frac{1}{V_t} \int_{V_t} \mathbf{G}(\vec{x}|\vec{x}_c)^H \mathbf{G}(\vec{x}|\vec{x}_c) dV.$$

Now, we are able to express the acoustic potential energy density in terms of selected variables. Next we must define the brightness and the contrast of the zone in which we have interest.

III. SOLUTION METHOD

A. Brightness problem

The first problem which we will address now is to make maximum brightness in a zone using given input power.

The input power (J_0) can be written as

$$J_0 = \mathbf{q}_c^H \mathbf{q}_c. \quad (7)$$

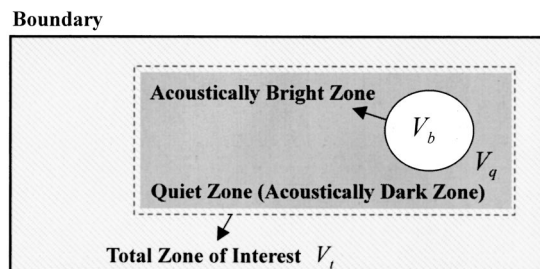


FIG. 1. Schematic of acoustic zones.

This also expresses the “control effort” consumed to generate the acoustically bright zone. Then the problem can be defined as

$$\text{maximize: } e_b = \mathbf{q}_c^H \mathbf{R}_b \mathbf{q}_c, \quad (8)$$

$$\text{constrained to: } J_0 = \mathbf{q}_c^H \mathbf{q}_c. \quad (9)$$

The above equations [Eqs. (8) and (9)] can be written in rather compact form by introducing the Lagrangian multiplier² α :

$$\text{maximize } J = \mathbf{q}_c^H \mathbf{R}_b \mathbf{q}_c + \alpha (J_0 - \mathbf{q}_c^H \mathbf{q}_c). \quad (10)$$

Taking derivatives with respect to \mathbf{q}_c and α , we can get the stationary point of J :

$$\mathbf{R}_b \mathbf{q}_c = \alpha \mathbf{q}_c, \quad J_0 = \mathbf{q}_c^H \mathbf{q}_c. \quad (11)$$

It is well known that this constrained optimization problem shares the same solution with the maximization problem of the following ratio,³ that is,

$$\alpha = \frac{e_b}{J_0} = \frac{\mathbf{q}_c^H \mathbf{R}_b \mathbf{q}_c}{\mathbf{q}_c^H \mathbf{q}_c}. \quad (12)$$

The ratio α represents the quantity of acoustic potential energy density generated in the bright zone by unit input power. Let us denote this ratio as the first cost function. This function has a maximum when the volume velocity vector \mathbf{q}_c equals the eigenvector corresponding to the maximum eigenvalue of \mathbf{R}_b . It is noteworthy that if we measure the Green’s function between the source positions and the bright zone V_b , then the correlation matrix \mathbf{R}_b is readily available. Therefore we can find the optimal volume velocity vector \mathbf{q}_c with the maximum value α_{\max} , using Eq. (12).

As an extreme case, we may consider a case of which V_b is given by a point located at \vec{x}_b (point focusing). The correlation matrix \mathbf{R}_b corresponding to a bright “point” will be

$$\mathbf{R}_b = \mathbf{G}(\vec{x}_b|\vec{x}_c)^H \mathbf{G}(\vec{x}_b|\vec{x}_c), \quad (13)$$

and the optimal solution can be readily found by

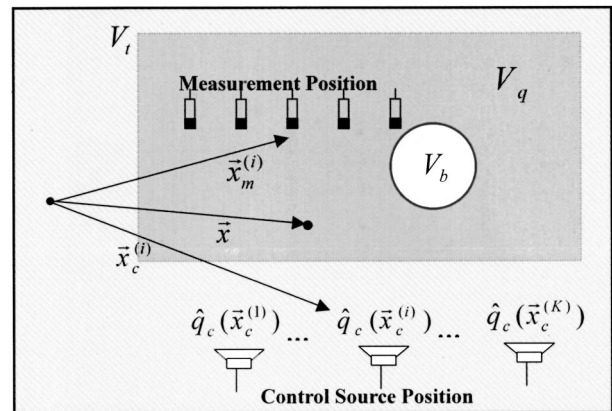


FIG. 2. Definitions of acoustic variables: V_b : volume of acoustically bright zone, V_q : volume of acoustically dark zone, V_t : volume of total zone of interest, $\vec{x}_c^{(i)}$: position of the i th control source, $\vec{x}_m^{(i)}$: position of the i th sensor, and $\hat{q}_c(\vec{x}_c^{(i)})$: volume velocity of the i th control source.

$$\mathbf{q}_\alpha = \sqrt{\frac{J_0}{\alpha_{\max}}} \mathbf{G}(\vec{x}_b | \vec{x}_c)^H, \quad (14)$$

where

$$\alpha_{\max} = \mathbf{G}(\vec{x}_b | \vec{x}_c) \mathbf{G}(\vec{x}_b | \vec{x}_c)^H = \sum_i |G(\vec{x}_b | \vec{x}_c^{(i)})|^2.$$

Since the optimal vector also obeys the acoustical reciprocity [$\mathbf{G}(\vec{x}_b | \vec{x}_c) = \mathbf{G}(\vec{x}_c | \vec{x}_b)^T$], the resultant potential energy field can be rewritten as

$$\begin{aligned} e(\vec{x}) &= \frac{J_0}{\alpha_{\max}} |\mathbf{G}(\vec{x} | \vec{x}_c) \mathbf{G}(\vec{x}_b | \vec{x}_c)^H|^2 \\ &= \frac{J_0}{\alpha_{\max}} |\mathbf{G}(\vec{x}_c | \vec{x})^H \mathbf{G}(\vec{x}_c | \vec{x}_b)|^2. \end{aligned} \quad (15)$$

This gives the same potential energy field that can be obtained by using “matched field processing,⁴” or “time reversal mirror.^{5,6}” Both of these methods utilize the fact that the reemission of the received signal from a point source [$\mathbf{G}(\vec{x}_b | \vec{x}_c)^H$] generates a focused sound field at the source location. The first problem that we have addressed leads to the classical focusing method when the bright zone is “a point.”

It is noteworthy that the maximum eigenvalue α_{\max} essentially means that the more controllable sources are used, the more acoustical potential energy we can generate at the point \vec{x}_b with the same input power [except when $\mathbf{G}(\vec{x}_b | \vec{x}_c^{(i)}) = 0$ for the i th source].

B. Contrast problem

The second problem we have to solve is to maximize the contrast between the bright zone and the other zone.

The corresponding cost function can be defined as

$$\beta = \frac{e_b}{e_t} = \frac{\mathbf{q}_c^H \mathbf{R}_b \mathbf{q}_c}{\mathbf{q}_c^H \mathbf{R}_t \mathbf{q}_c}. \quad (16)$$

This function essentially determines the ratio of the acoustic potential energy density in the bright zone to the zone of interest. As long as the pressure fields produced by each control source are linearly independent within the total zone of interest, the Hermitian matrix $\mathbf{R}_t = (1/V_t) \times \int_{V_t} \mathbf{G}(\vec{x} | \vec{x}_c)^H \mathbf{G}(\vec{x} | \vec{x}_c) dV$ has a full rank of K and is invertible.

The volume velocity vector that maximizes β is given by the following form:

$$(\mathbf{R}_t^{-1} \mathbf{R}_b) \mathbf{q}_\beta = \beta_{\max} \mathbf{q}_\beta. \quad (17)$$

That is, it is equal to an eigenvector corresponding to the maximum eigenvalue of $\mathbf{R}_t^{-1} \mathbf{R}_b$. Thus, if the pressure fields produced by each control source can be measured within V_t , it is possible to construct the correlation matrix \mathbf{R}_t and \mathbf{R}_b . Then the optimal volume velocity distribution can be calculated.

The acoustic potential energy of the zone of interest is equal to the sum of potential energy of the bright zone and the dark zone. Introducing β' as a ratio of brightness of the dark zone to the brightness of the zone of interest,

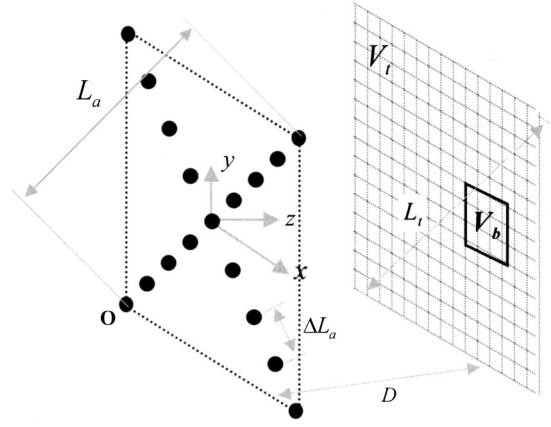


FIG. 3. Simulation setup: L_a : aperture size of monopole array, ΔL_a : distance between monopoles, L_t : aperture size of zone of interest, D : distance between zone of interest and monopole array, V_t : size of total zone of interest, and V_b : size of the bright zone.

$$\beta' = \frac{e_q}{e_t}, \quad (18)$$

the following relation can be obtained:

$$\beta \frac{V_b}{V_t} + \beta' \frac{V_q}{V_t} = 1. \quad (19)$$

Note that the weighted sum of β and β' is always constant. Therefore, if β is maximized, then the acoustical brightness ratio of the dark zone to the zone of interest is minimized. That is, the maximum contrast between the bright zone and the dark zone can be achieved.

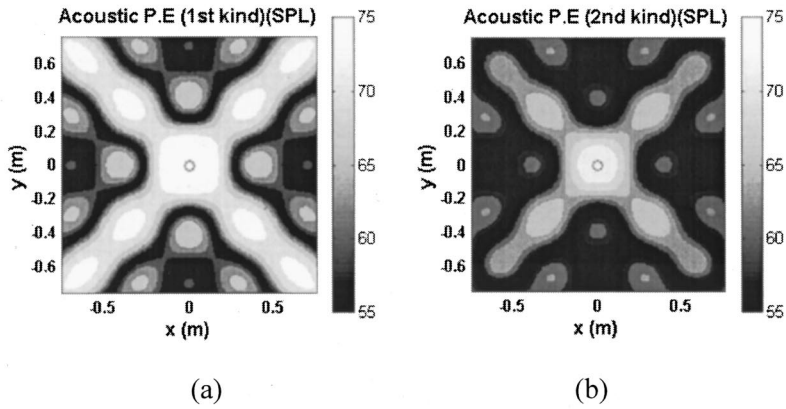
Also note that the solution of the contrast problem is independent of control effort. That is, the difference of sound pressure level between V_b and V_t (or V_b and V_q) is only determined by the “direction” of the volume velocity vector. By examining the value α and $\alpha' = \mathbf{q}_c^H \mathbf{R}_q \mathbf{q}_c / \mathbf{q}_c^H \mathbf{R}_c \mathbf{q}_c$, one can determine whether the contrast maximization is accomplished by making the bright zone brighter, or by making the total zone darker.

The drawback of this optimization is that brightness of the bright zone cannot be guaranteed. For example, consider a case where the control sources produce similar pressure field in V_t . Then the minimum eigenvalue of \mathbf{R}_t is nearly zero and, if the control sources are excited so that the volume velocity vector belongs to the null space of \mathbf{R}_t , the cost function β grows to infinity. As a result, the maximization process tends to minimize the brightness of V_t rather than to maximize the brightness of V_b . Thus it can take much more input power to increase the brightness of the bright zone than

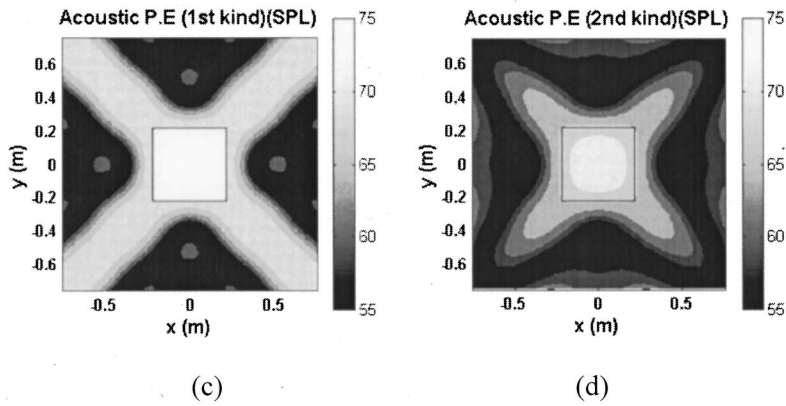
TABLE I. Simulation parameters.

	Case I	Case II	Case III
Bright zone	point	$(0.4 \times 0.4 \text{ m}^2)$	$(0.8 \times 0.8 \text{ m}^2)$
$f = 3.43 \text{ kHz}$, $K = 21$,	$\tilde{L}_t = L_t /$	$\tilde{L}_a = L_a /$	$\Delta \tilde{L}_a = 0.49$
	$\lambda = 21.21$,	$\lambda = 212.13$,	

Case I



Case II



Case III

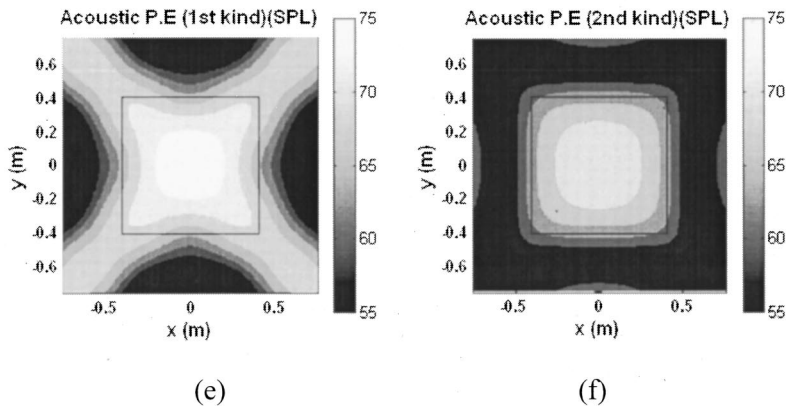


FIG. 4. Simulation results for various bright zone area. (a), (c), and (e) First kind optimization. (b), (d), and (f) Second kind optimization. (a) and (b) Case 1. (c) and (d) Case II. (e) and (f) Case III.

the first kind optimization (even though the contrast is maximum). Because the input power is always limited in a practical situation, the pressure field generated by each source must be linearly independent in the zone of interest to acquire an adequate brightness in the bright zone.

C. Simulation results and interpretation

Although this method guarantees the optimized solution, the resultant brightness or contrast of a system fully depends on the Green's function of the selected system. To verify the proposed method, a 2-D simulation was performed in free field for its simplicity. Figure 3 is a schematic diagram showing

the simulation condition. Control sources (monopoles) are arranged on the same plane with shape of X. Since the simulation was performed in free field, free space Green's function

TABLE II. Simulation results.

		Case I	Case II	Case III
Optimized by α	$\alpha_{n,\max}$ (dB)	13.12	9.36	6.24
	β (dB)	10.57	6.81	3.77
Optimized by β	α_n^a (dB)	7.37	4.59	2.20
	β_{\max} (dB)	11.54	7.87	4.80

^a $\alpha_n = \alpha/e_0$, where $e_0 = (\rho_0\omega/4\pi D)^2$.

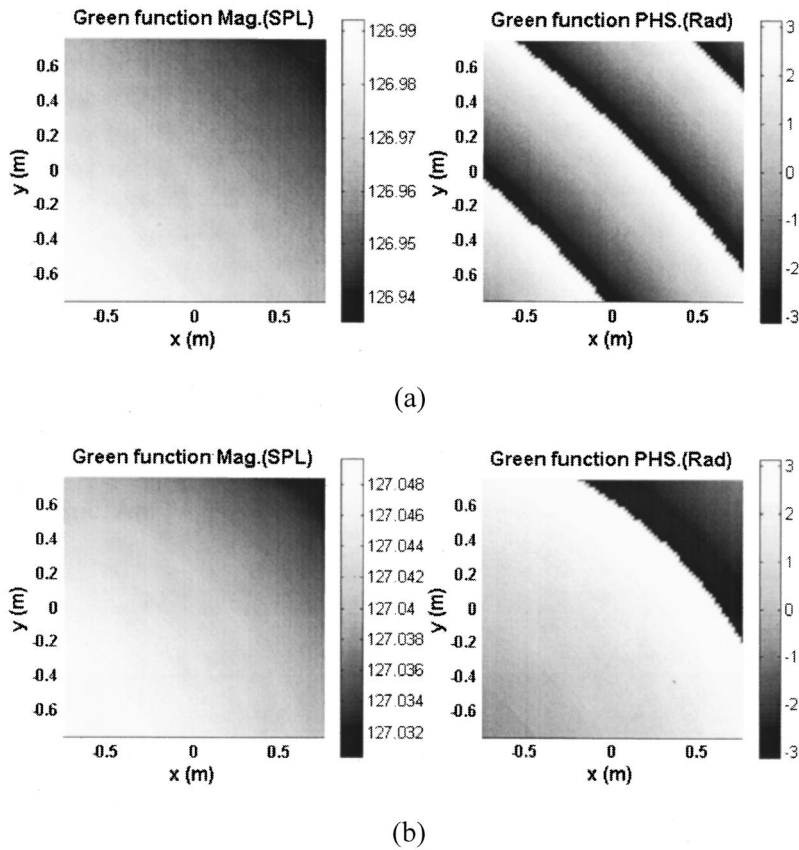


FIG. 5. Magnitude and phase of the Green's function. (a) Green's function of a monopole located at $(x,y) = (-4.5, -4.5)(m)$. (b) Green's function of a monopole located at $(x,y) = (-3, -3)(m)$.

$$G(\vec{x}|\vec{x}_0) = \hat{c} \frac{e^{jkR}}{R} \quad \text{where} \quad R = |\vec{x} - \vec{x}_0|, \quad \hat{c} = \frac{-j\rho_0\omega}{4\pi}, \quad (20)$$

was used and all monopoles were excited by a frequency of 3.4 kHz. Total zone of interest is a plane having an area of V_t and located in the distance of D from the 2-D array. The aperture size of array is L_a and the aperture size of zone of interest is L_t . Specific values of the simulation parameters are summarized in Table I.

We began with examining a point focusing case. The acoustically bright point is desired at the center of V_t . Figure 4 shows the resultant potential energy field and Table II shows values of the cost functions. Figure 4(a) is the result of the first kind of optimization and Fig. 4(b) is of the second kind of optimization. To nondimensionalize, the first kind cost function α is divided by $e_0 = (\rho_0\omega/4\pi D)^2$. This constant is the potential energy density that one monopole source of a unit input power generates in the distance of D .

When the volume velocity distribution was optimized by the first kind of cost function, the value of normalized cost function (α_n) is over 13 dB. This means that the potential energy density of the bright point is 13 dB higher than that generated by one monopole source with the same input power. The second kind of cost function has a value over 10 dB. This means that the acoustic potential energy density of the bright point is 10 dB higher than that of the interested zone. Similarly, after the second kind of optimization, β is over 11 dB, but the α_n decreases to 7 dB. This tells us that more input power is required for the second kind of optimi-

zation to obtain the same brightness as first kind optimization.

As the bright zone is enlarged (cases II and III in Fig. 4), the first kind cost function decreases. Actually, from Eq. (14), the result of point focusing depends on the magnitude of the Green's function at that point. But in this simulation, the magnitude of the Green's function is almost constant for all points within V_t (Fig. 5). Therefore, the resultant potential energy density of point focusing does not vary with the location of bright point. But for the case of zone, the pressure fields generated by each source are averaged out over the zone. Therefore, the point focusing is easier than the generation of bright zone in this situation.

The second kind of cost function also decreases as the size of bright zone increases. This tendency can be explained by the fact that β_{\max} cannot be greater than V_t/V_b from Eq. (19) (when $\beta' = 0$).

IV. CONCLUSIONS

We proposed a method to make an acoustically bright zone. This was accomplished by controlling the multiple monopole sources that radiate single frequency sound. For different applicative purpose, two kinds of solutions were obtained. The first was for maximizing the brightness of a desired zone, and the second was for maximizing the contrast between two different zones. The optimal volume velocity of each monopole source was determined through an eigen value analysis. As an extreme case, it was shown that the optimal brightness solution converges to the existing fo-

cusing method when the bright zone reduces to a point. In addition, 2D simulations were performed and the resultant potential energy fields show remarkable improvement in brightness and contrast.

ACKNOWLEDGMENTS

This study was partly supported by the NRL (National Research Laboratory) project of KISTEP (Korea Institute of Science and Technology Evaluation and Planning) and the BK21 (Brain Korea 21) project initiated by Ministry of Education and Human Resources Development of Korea.

¹P. A. Nelson and S. J. Elliott, *Active Control of Sound* (Academic, New York, 1992), p. 310.

²A. D. Belegundu and T. R. Chandrupatla, *Optimization Concepts and Applications in Engineering* (Prentice Hall, Englewood Cliffs, NJ, 1999), pp. 146–148.

³L. Meirovitch, *Principles and Techniques of Vibrations* (Prentice–Hall, Englewood Cliffs, NJ, 1997), pp. 232–249.

⁴A. B. Baggeroer, W. A. Kuperman, and P. N. Michalevsky, “An Overview of Matched Field Methods in Ocean Acoustics,” *IEEE J. Ocean. Eng.* **18**, 401–424 (1993).

⁵C. Dorme and M. Fink, “Focusing on transmit-receive mode through inhomogeneous media: the time reversal matched filter approach,” *J. Acoust. Soc. Am.* **98**, 1155–1162 (1995).

⁶M. Tanter, J.-L. Thomas, and M. Fink, “Time reversal and the inverse filter,” *J. Acoust. Soc. Am.* **108**, 223–234 (2000).

Experimental study of vibrational behavior of laminated annular disks

Huan Wang

Department of Mechanical Engineering, TaiZhou Polytechnical College TaiZhou, JiangSu 225300, People's Republic of China

(Received 29 June 2000; accepted for publication 31 October 2001)

The purpose of this paper is to present an experimental study of the vibrational behavior of laminated annular disks, and effects of laminations on the vibrations of the disks. The vibrations of a series of solid annular disks were calculated using the finite-element method in order to provide a basis for comparison with experimental data. An extensive range of experiments was performed on both a series of solid disks and a series of laminated disks under a range of normal clamping pressures. Based on the calculated and experimental results, it was found that the vibrational behavior of the laminated disks was dominated by that of the individual disk, of which the laminated disks were composed. Laminations had great effects on the vibrational behavior of the laminated disks and the effects depended upon the mode type, the clamping pressure, and the number of disk assembly. Laminations increased damping and reduced the amplitude of frequency response function for both the transverse modes and in-plane modes of disks. The resonant frequency of transverse modes shifted higher because of the effects of laminations. For the in-plane vibrational modes, the effects on the resonant frequency could be neglected and the resonant frequency could be considered to be a constant. © 2002 Acoustical Society of America. [DOI: 10.1121/1.1448313]

PACS numbers: 43.40.At [PJR]

I. INTRODUCTION

In order to reduce electromagnetic acoustic noise in an electrical machine, it is important to understand the vibrational behavior of the stator so as to avoid resonant of the stator when excited by the electromagnetic forces generated within the machine. An accurate determination of vibrational modes of stators is, therefore, essential in the design of quiet electrical machines. Over the years, several analyses have been developed. However, in the vibrational study of electrical machine stators, it was found that the vibrational behavior of a realistic stator was quite different from that of a solid thick cylinder, which was often used as an analytical model of a stator in the past. The most significant finding was that only a few predicted vibrational modes, generally those with no vibrational node in the axial direction, i.e., the in-plane vibrational modes could be confirmed by experiment for the realistic stator.^{1,2} In order to explain this phenomenon, the effects of teeth, windings, frame, impregnation, and temperature on the vibrations of stators were investigated by Watanabe,² and Singal.³ And it was also found that the phenomenon could not be explained by such influences alone. It is well known that in order to prevent eddy current losses in stators, they are designed with a laminated structure. Stators are actually composed of laminated annular disks with teeth. These laminations cut off the elastic connection between adjacent disks, and allow some micro or macro slip to occur between them. This interface probably has a great effect on the vibrations of laminated disks, and is likely the major reason for their vibrational behavior being quite different from that of the corresponding solid model. Hence, a study of the effect of laminations upon vibrations is essential to an understanding of the vibrational behavior of laminated annular disks, and in the vibrational analysis of realistic stators.

The vibrations of laminated structures were investigated by several authors in the past. The effect of interlaminar damping on the vibrations of laminated circular plates was investigated experimentally by Beards.⁴ The vibrational behavior of an actual laminated stator of an electrical machine was studied experimentally by Williams.¹ A comprehensive investigation of the effects of clamping pressure on the vibrational behavior of laminated stators was reported by Watanabe.² Most of the effort devoted to the study of the frictional interface has been directed to frictional joints,⁵ beams,⁶ turbine blades,⁷ and plates.⁸ Compared with a solid structure, the vibrational analysis of a laminated structure with internal slip is much more complicated because of both the mutual effects of the adjacent laminations and the complexity of interlaminar slip. A thorough understanding of the mechanism of the effects of laminations is still limited. Therefore, research work is generally restricted either to static analysis or to simple dynamic models. A widely accepted model for interface friction, especially one that would adequately represent laminated annular disks with interlaminar slip, has not been found in the literature covering vibrational analysis.

In this paper, the natural frequencies and mode shapes of a series of solid annular disks of varying axial thickness were first studied using the finite-element method. The reason for this study was to obtain data, which could be used to confirm the validity of the modal analysis techniques, and to confirm that no modes were missed in experiment. This was important, as the experimental study of the same series of solid annular disks was followed by a series of laminated models tested under a range of normal clamping pressures. Based on the calculated and experimental results, the effects of lami-

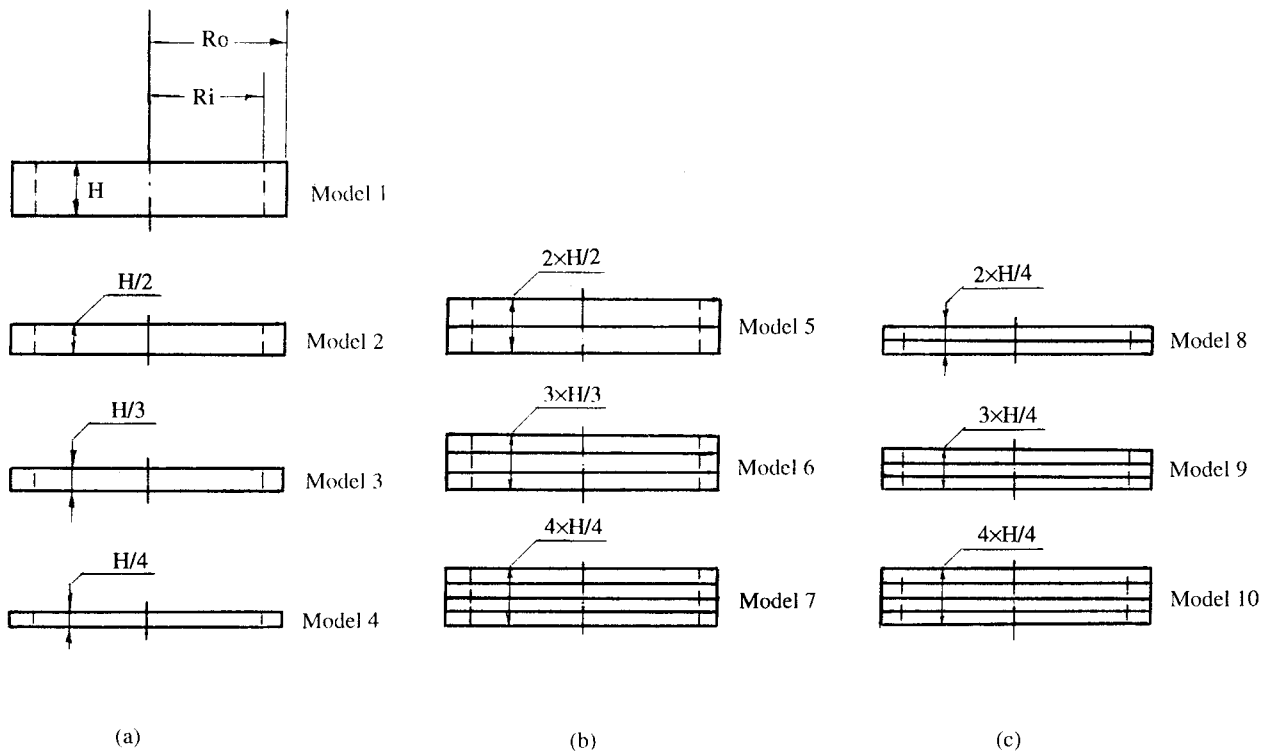


FIG. 1. Calculated and experimental models. (a) Solid models; (b) and (c) laminated models.

nations on vibrations, and the vibrational behaviors of laminated annular discs are presented.

II. FINITE ELEMENT ANALYSIS OF SOLID MODELS

The vibrations of an annular disk are conventionally classified into in-plane vibrations and transverse vibrations. In this paper, the finite-element method was used to calculate the natural frequencies and mode shapes of all the modes of solid disks. There were four calculated disk models shown in Fig. 1(a). The radial dimensions of all the models are the same: inside radius $R_i = 139.5$ mm, outside radius $R_o = 190.0$ mm. The axial thickness of model 1 is $H = 28.5$ mm. All the calculated models were modeled as collections of three-dimensional block elements with eight nodes per element and with three translational degrees of freedom per node. The four models were divided into the same total number of elements in order to have a common comparison basis. It was found that for the calculated frequency range 0–10 kHz, once the element number was over 48 in the circumferential direction, the improvement in the accuracy of the frequency predictions was very limited with any further increase in the element number. Hence, a total of 48 elements was used for each model in the calculation. The software ANSYS⁹ was used to perform the finite-element analysis. The equation of motion used was

$$\mu U_{i,mm} + (\lambda + \mu) U_{m,mi} + F_i = \rho U_{i,tt}, \quad (1)$$

where U is the displacement component, F is the applied force, λ is the Lamé coefficient, μ is the shear modulus of elasticity, ρ is the material density, and $i, m = x, y, z$. If the weighted residual method is applied to Eq. (1), then

$$\int_{\Omega} W [\mu U_{i,mm} + (\lambda + \mu) U_{m,mi} + F_i - \rho U_{i,tt}] d\Omega = 0. \quad (2)$$

The corresponding equation of motion for free vibrations is

$$\mathbf{M}\ddot{\mathbf{U}} + \mathbf{K}\mathbf{U} = 0, \quad (3)$$

where

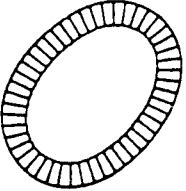
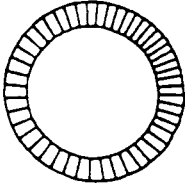
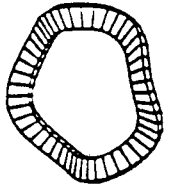
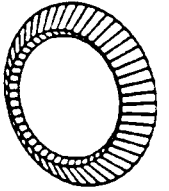
$$\mathbf{M} = \int_{\Omega} \rho W U_i d\Omega,$$

$$\mathbf{K} = \int_{\Omega} [\mu W_{,m} U_{i,m} + (\lambda + \mu) W_{,i} U_{m,m}] d\Omega,$$

where \mathbf{M} is the mass matrix, \mathbf{K} is the stiffness matrix, and W is a weighting function.

The samples of calculated mode shapes and natural frequencies in the frequency range 0–10 kHz are shown in Table I, and also plotted in Fig. 2. From the calculated results, it can be seen that the in-plane vibrational modes can be divided into pure radial modes and circumferential modes. For the former, the median surface remains unstretched. For the latter, the median surface is stretched, as can be seen in parts A and B of Table I, respectively. The natural frequencies of the in-plane modes are almost constant for all of the models, i.e., they are independent of axial thickness, as can be seen in Fig. 2. For the calculated models, the transverse vibrations can also be divided into two subcategories: transverse modes with nodal radii and transverse modes with a nodal circle, as shown in parts C and D of Table I, respectively. The natural frequencies of the transverse modes are dependent upon the axial thickness of the model. The thicker the model, the higher the frequency, as shown in Fig. 2.

TABLE I. Natural frequency and mode shape.

Mode shape	n	Frequency (Calculated / <i>experimental</i> Hz)			
		Model 1	Model 2	Model 3	Model 4
	2*	1141 / 1136	1141 / 1136	1141 / 1136	1141 / 1136
	3	3068 / 3016	3067 / 3016	3067 / 3016	3067 / 3016
	4	5531 / 5384	5529 / 5384	5528 / 5384	5528 / 5384
	5	8370 /	8368 /	8366 /	8366 /
	6		out of range		
	0	5023 / 5056	5023 / 5056	5023 / 5056	5023 / 5056
	1*	6953 /	6953 /	6953 /	6953 /
	2	656 / 648	339 / 344	228 / 240	172 / 192
	3	1807 / 1776	940 / 936	635 / 640	481 / 488
	4*	3377 / 3304	1789 / 1760	1216 / 1208	925 / 912
	5	5314 / 5144	2884 / 2800	1975 / 1920	1509 / 1456
	6	7573 /	4225 / 4040	2918 / 2800	2241 / 2140
	7		5813 / 5456	4055 / 3800	3128 / 2827
	8		7650 /	5395 / 5072	4183 / 3736
	9			6949 /	5416 / 5088
	10	out of range		8729 /	6814 /
	11				8476 /
		0*	2479 / 2496	1374 / 1336	937 / 888
1		3708 / 3600	2187 / 2104	1511 / 1456	1148 / 1040
2		6089 / 5776	3714 / 3560	2592 / 2504	1983 / 1856
3		8756 /	5448 / 5160	3842 / 3680	2967 / 2744
4			7331 /	5223 / 4896	4090 / 3688
5			9370 /	6782 / 6176	5371 / 4704
6		out of range		8512 /	6834 / 5760
7				8501 /	

n: the circumferential mode order.

*: The mode illustrated

III. EXPERIMENTAL MODELS, SETUP, AND PROCEDURE

In order to verify the calculated results and more importantly, to study the influence of laminations, experimental modal analysis was performed on a number of experimental models. There were ten experimental models. The radial dimensions of all ten models were the same, as can be seen in Fig. 1. The ten models were divided into three groups. Group

(a) had four solid models 1–4, which were exactly the same as the calculated models 1–4. This group was used to confirm the calculated results obtained above. In group (b), models 5, 6, and 7 were formed by pressing several of either solid models 2, 3, and 4 together to make the total axial thickness the same as that of solid model 1. Group (b) was used mainly to compare the vibrational behavior of each laminated model with that of the corresponding solid model in group (a), in

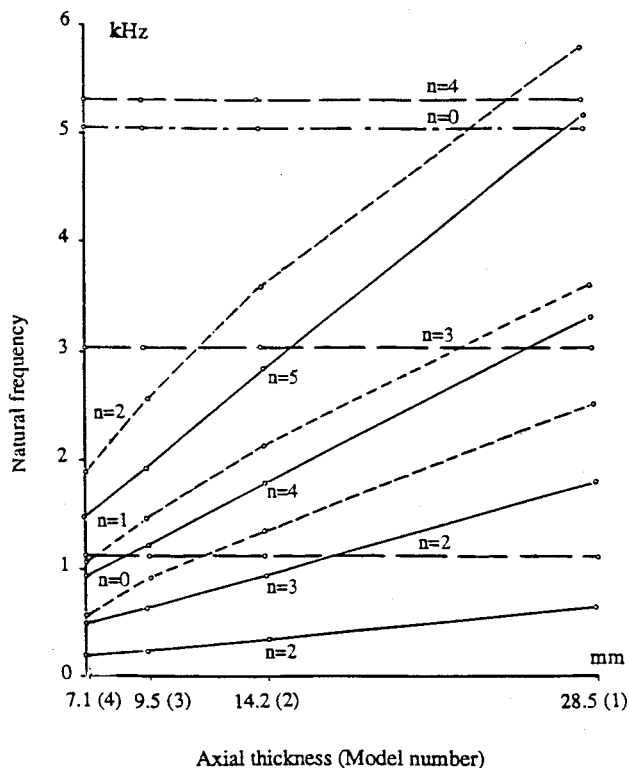


FIG. 2. Variation in the resonant frequency of the different modes, with axial thickness, for solid models 1, 2, 3, and 4. --- In-plane pure radial modes, --- in-plane circumferential modes, ——— transverse modes with nodal radii, -.- transverse modes with a nodal circle.

order to investigate the effects of laminations on vibrational behavior. In group (c), models 8, 9, and 10 were formed by pressing two, three, or four of model 4 together, respectively. Group (c) was mainly used to investigate the effect of the number of laminations and clamping pressure on the vibrations. Model 10 was exactly the same as model 7. For the convenience of explanation, two different model numbers were used for the same model in groups (b) and (c), respectively.

All the experimental models were made of mild steel. The contacting surfaces of the laminated models had a fine-turned and lapped finish, then uniformly abraded with fine glass beads. To connect the contacting surfaces of the middle disks, small holes were made in these disks. In order to obtain an even clamping force over the whole of the contacting surfaces, a fine equalizing circumferential groove was also cut on the contacting surfaces, as can be seen in Fig. 3. A soft tape covered the inside and outside seams to form an edge

seal. The air between the contacting surfaces was partially withdrawn by means of a vacuum pump, and the difference between the internal and atmospheric pressures was used to provide the clamping force. By changing the amount of vacuum between the contacting surfaces, the clamping pressure could be adjusted within the required range. Compared with other clamping measures, such as using bolts, the advantage of using atmospheric pressure for clamping is that the effects of the bolts on the vibrations can be eliminated, allowing for the observation of the effects of laminations alone. A schematic diagram of the experimental setup is shown in Fig. 4.

For experimental solid models 1 to 4, frequency response functions in both the radial and axial directions were measured at each measurement point. Altogether, 128 frequency response functions were measured per model since each model was divided into 16 equal segmental elements. From the 128 frequency response functions, the corresponding natural frequencies, damping factors, and mode shapes were obtained.

Experiments were also performed on laminated models 5 to 10. Each model was again divided into 16 equal segmental elements. The air between the contacting surfaces of the laminations was evacuated until the air pressure fell to 0.9 atm., i.e., the clamping pressure acting on the models was 0.1 atm. This pressure was maintained until all 128 frequency response functions in both the radial and axial directions had been measured, and transferred to the modal analysis system. The clamping pressure was then increased in increments of 0.1 atm., and the procedure repeated for nine different clamping pressures investigated.

IV. EXPERIMENTAL RESULTS

The experimental results for the solid models are also shown in Table I (in italics). It can be seen from the table that the experimental results verified the calculated results. The natural frequencies of the in-plane vibrations are independent of the axial thickness of the model. The natural frequencies of the transverse vibrations are dependent upon the axial thickness of the model, and increase as the axial thickness of the model increases.

For the laminated disks, the most important observation from the experimental results is that although the thickness of each of the composite models 5 to 7 is exactly the same as that of model 1, their vibrational behavior is quite different from that of model 1. Figures 5(a) and (b) show the fre-

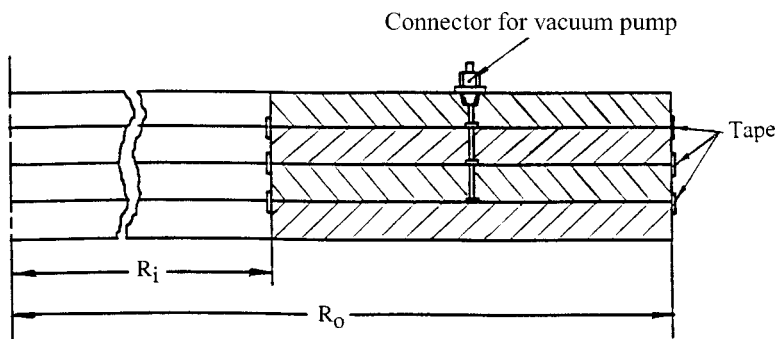


FIG. 3. Half cross section of laminated model 7.

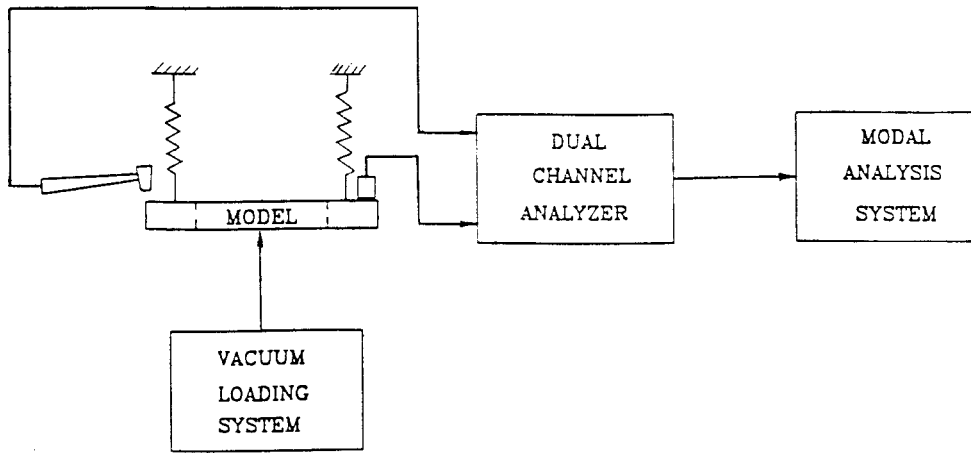


FIG. 4. Experimental setup.

frequency response function magnitudes of model 5 for a clamping pressure of 0.1 atm. measured in the transverse and radial directions, respectively. For comparison, the frequency response functions of models 1 and 2 are also plotted in the figure. From Fig. 5(a) it can be seen that the vibrational behavior of model 5, in the transverse direction, is quite different from that of model 1, although their dimensions are exactly the same. From Fig. 5(a) it can also be seen that the frequency response function of model 5 is close to that of model 2. This means that the vibrational behavior of laminated model 5 is dominated by that of the individual parts, i.e., model 2, from which it is built. The same conclusions were obtained for all the laminated models 6 to 10. In the case of the in-plane modes, shown in Fig. 5(b), the three

models (1, 2, and 5) exhibit the same vibrational behavior. Again, this was found to be the case with models 6 to 10. Therefore, it is suggested that the vibrational behavior of a realistic stator may be dominated by that of an individual lamination, of which the stator is composed.

In order to explain the phenomenon, the hypothetical vibrational deformations of model 8 are shown in Fig. 6. For the transverse modes, because the dimensions of these two disks are exactly the same, their vibrational deformations are the same. Since $R1$ is not equal to $R2$, a gap always exists between the contacting surfaces, as can be seen in Fig. 6(a). Under a clamping pressure, the two disks contact only along a narrow circumferential band, and most of the common surfaces are separated by the gap. Each disk basically forms a

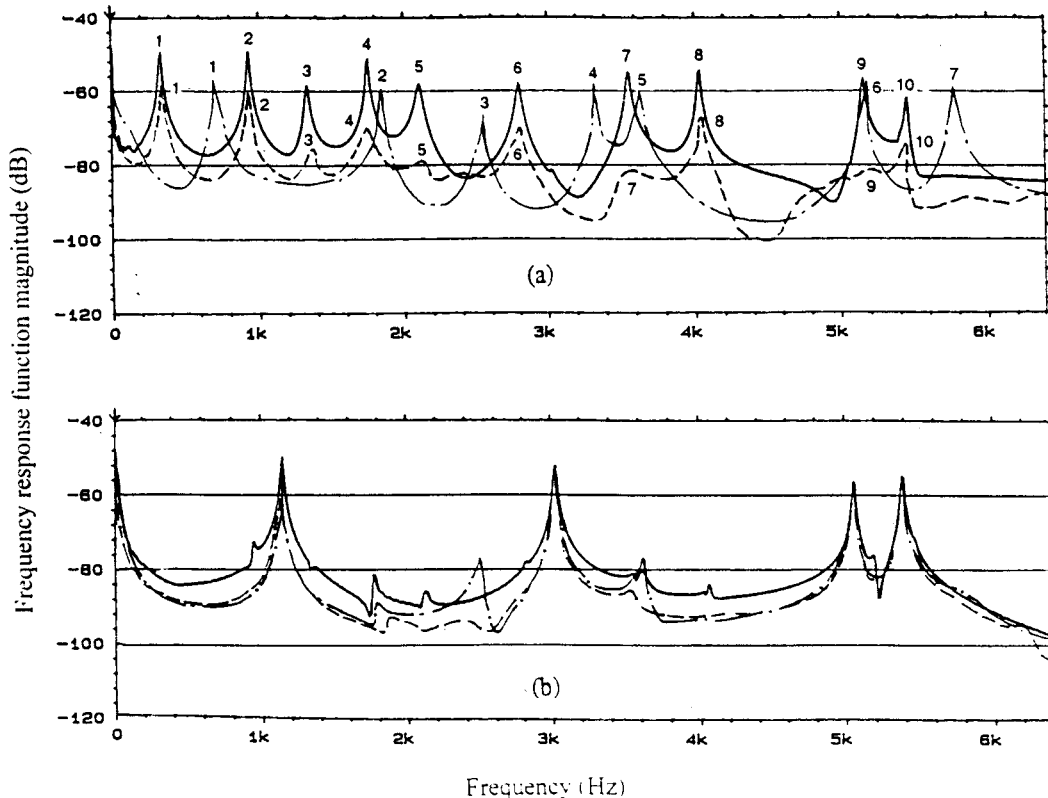


FIG. 5. Frequency response functions of models 1, 2 and 5. (a) Transverse vibrations; (b) in-plane vibrations. --- Model 1, ——— model 2, - - - model 5.

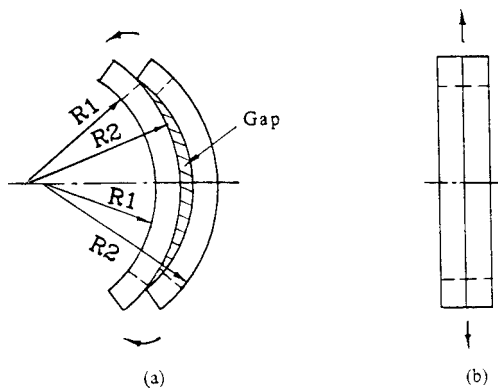


FIG. 6. Vibrations of model 8. (a) Transverse vibration; (b) in-plane vibration.

self-contained system, and the vibrational behavior of each disk dominates the vibrational behavior of the disk assembly. Adjacent disks provide boundary conditions, both elastic and frictional, for each other. The vibrational behavior of the disk assembly, hence, is not exactly the same as that of an individual disk under free-boundary conditions. For the in-plane modes, laminations cut off the elastic connection between the disks, and each disk basically forms a self-contained system. Therefore, the vibrations of the disk assembly are dominated by the individual vibrations of each disk. Since the two disks vibrate in phase with each other in the radial direction, there are no relative displacements and a gap does not exist between their common surfaces. Because of the in-phase displacements, the whole disk assembly always vibrates as one in the radial direction, and the assembly can be treated as a solid annular disk. This means that, compared with the transverse modes, laminations have little or no effect on the vibrations of the in-plane modes. From the discussion above, it can be concluded that the vibrational behavior of the laminated disks is dominated by that of the individual disk, from which the laminated disks are composed. The vibrations of

an individual disk should be the study basis for the vibrations of a disk assembly.

On the other hand, because of the boundary condition changes of an adjacent disk, laminations do have some effects on the vibrational behavior of the disk assembly, as discussed below.

- (1) Resonant frequency shift of the transverse modes. From Fig. 5(a), it can be seen that although the frequency response function of the laminated model 5 is close to that of the solid model 2, all of the resonant frequencies for the transverse modes of model 5 shift higher than the corresponding modes of model 2. Figure 7 shows the changes, which occur in the resonant frequencies with different clamping pressures and different disks numbers. In Fig. 7, the values corresponding to 0 atm. are the natural frequencies of models 2, 3, and 4, respectively. It can be seen that the resonant frequencies for those transverse vibrational modes with nodal radii increase as the clamping pressure increases, and are dependent upon the number of disks. The resonant frequencies of the transverse vibrational modes with a nodal circle also appear to increase, as can be seen for models 5 and 6, but all of them disappear quickly. From Fig. 5(b) and Fig. 7 it can be seen that, for the in-plane vibration modes, there is no resonant frequency shift. This means that the resonant frequency of an in-plane vibrational mode is almost a constant under different clamping pressures. This frequency is also independent of model (1 to 10 inclusive). Hence, it can be concluded that the resonant frequencies of the in-plane vibrational modes are independent of whether the model is solid or comprised of several disks. Such modes are dependent only upon the radial dimensions of the disk.
- (2) Decrease in frequency response function magnitude. Figure 8 shows the decrease in the magnitude of the frequency response function of models 8, 9, and 10 from

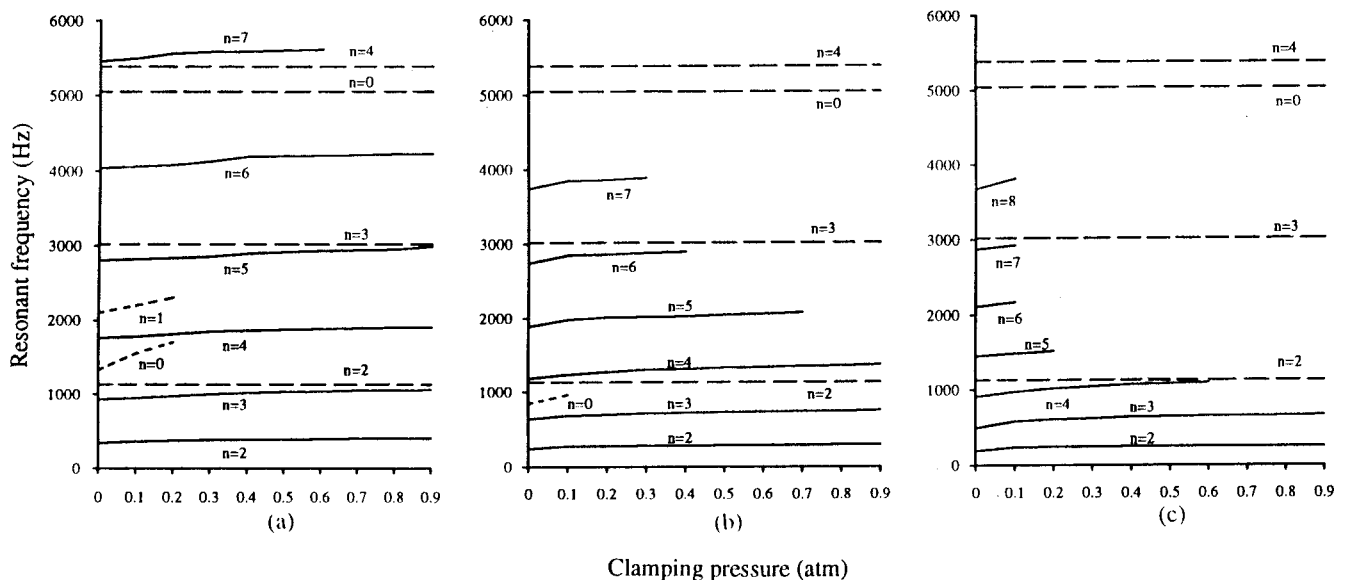


FIG. 7. Variation in resonant frequencies of various modes with clamping pressure. (a) Model 5; (b) model 6; (c) model 7. --- In-plane modes, ——— transverse modes with nodal radii, - - - transverse modes with a nodal circle.

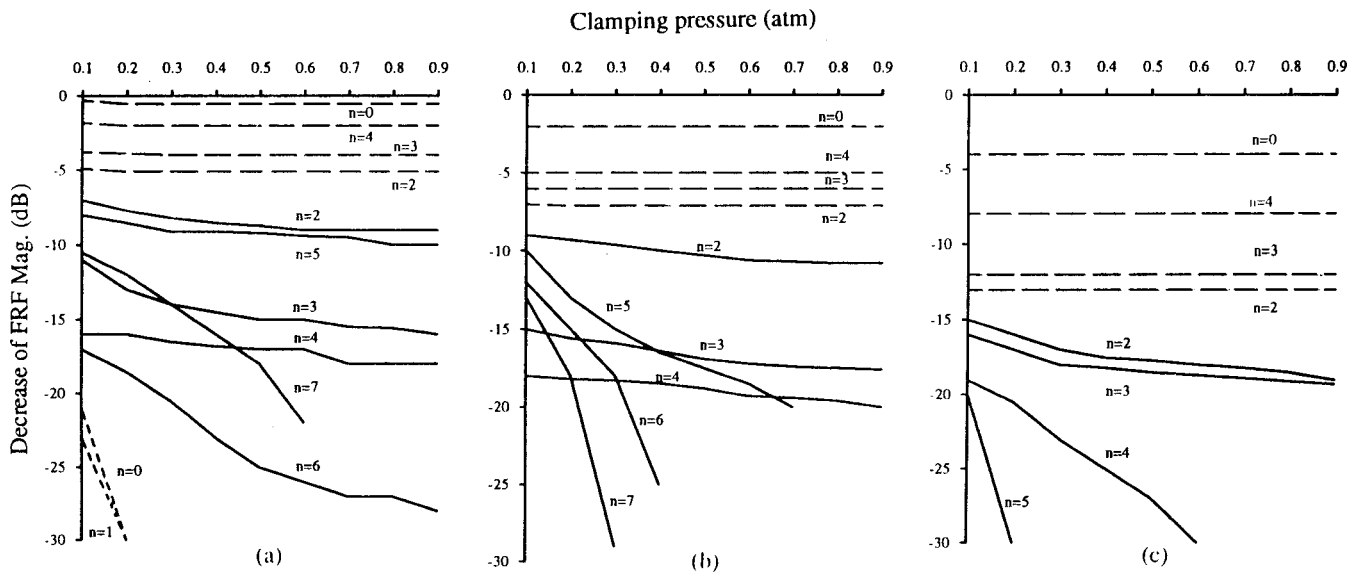


FIG. 8. Reduction in frequency response function magnitude of various modes with clamping pressure. (a) Model 8; (b) model 9; (c) model 10. --- In-plane modes, ——— transverse modes with nodal radii, -.- transverse modes with a nodal circle.

that of the solid model 4. It can be seen from the figure that the magnitude of the frequency response functions of all the laminated models are smaller than those of the solid models. The degree of the reduction varies with the type of mode. Generally, the reductions in the in-plane vibrational modes are much less than those for the transverse vibrational modes of a given model. For the transverse vibrational modes, the reductions where a nodal circle exists are much larger than for those modes with nodal radii. Once the clamping pressure is over 0.1 atm., none of the transverse vibrational modes, with a nodal circle, can be detected in any of the laminated models. In the case of the in-plane vibrational modes, the magnitude of the frequency response function does not change with clamping pressure. Comparing model 8 with models 9 and 10, it can be seen that as the number of disks increases, there is a corresponding decrease in frequency response function magnitude for the in-plane modes. This dependency of frequency response function magnitude upon the number of laminations reflects the number of frictional surfaces where energy is dissipated. Hence, the magnitude of the frequency response function for the in-plane vibrational modes is independent of the clamping pressure but dependent on the number of disks of which the model is composed. The magnitude of the transverse vibration modes is dependent on both the clamping pressure and the number of disks.

- (3) Variation in damping factor with clamping force. The damping in the experimental laminated models has two forms: the damping of the disk material and the damping by the interlaminar friction between the disks. The former is substantially proportional damping under small deformations. The latter is generally amplitude dependent.⁸ Since the vibrational behavior of a laminated disk model is dominated by that of the individual disk and all the measurable equivalent damping factors are small, the laminated disks can be regarded as quasi-linear, and modal analysis techniques are used in this

paper. The experimental damping factors were the equivalent proportional damping factors because experimental modal analysis is based on a linear model. Figure 9 shows the numerical values of the change in the damping factors of models 8, 9, and 10 over that of the solid model 4 under different clamping pressures. This numerical value is referred to as the difference in the damping factor. It can be seen that laminations cause positive differences, which are dependent upon the type of mode. For all modes, as the number of disks increases, generally the damping factor increases for a given clamping pressure. This is because the number of contacting surfaces, where energy can be dissipated by frictional force, increases. Variations in the damping factor with clamping force differ for different kinds of modes. The change in damping factor for the in-plane vibrational modes is small, and almost constant with increasing clamping pressure. The effect of clamping pressure changes is most significant in the case of those transverse vibrational modes with a nodal circle. The damping factor of such modes increases rapidly such that when the clamping pressure is over 0.1 atm., most of these modes cannot be detected. A possible hypothesis to explain the rapid damping increase of the transverse modes with a nodal circle is based on the conjectured deflected shapes of adjacent laminae. As the curvature at such an interface changes from convex to concave (positive to negative), relative sliding must occur. Whether this is localized or distributed over the whole contacting surface, it will give rise to large frictional dissipative forces, which increase with increasing contact pressure. For the transverse vibration modes with nodal radii, the damping factor initially increases as the clamping pressure increases, and the increments in damping factor are nonlinear.

- (4) It should be noted that a realistic electric machine stator is composed of several parts, and stator laminations are pressed together by bolts. Because of the effects of bolts, impregnation, the mutual effects between parts, etc., the

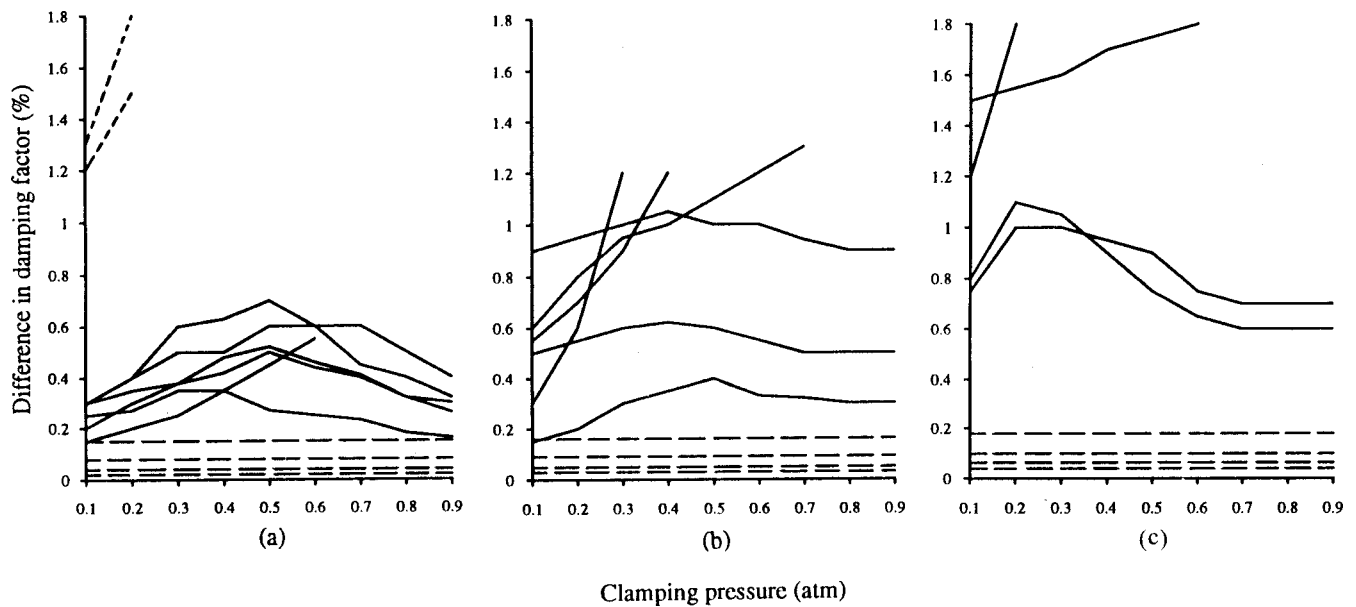


FIG. 9. Increase in damping factors of various modes with clamping pressure. (a) Model 8; (b) model 9; (c) model 10. --- In-plane modes, ——— transverse modes with nodal radii, -·- transverse modes with a nodal circle.

vibrational behavior of a realistic stator is more complicated than that of simple laminated disks. Hence, the experimental results in this paper can only partly explain the vibrational behavior of a realistic stator.

V. CONCLUSIONS

The vibration behavior of a laminated disk is dominated by the vibration behavior of the individual component of which the disk is comprised. The influence of laminations on the transverse vibration modes is much stronger than that on the in-plane vibration modes. For the transverse vibration modes, the presence of laminations causes a resonant frequency shift, an increase in the damping factor, and a reduction in magnitude of the frequency response function. The effects on those transverse modes with a nodal circle are greater than for the transverse modes with nodal radii. All the effects are dependent upon both the clamping pressure and the number of disks. For the in-plane vibration modes, the presence of laminations causes an increase in the damping factor and a reduction in the magnitude of the frequency response function, both of which are dependent on the number of laminations. The presence of laminations has no effect on the value of the resonant frequency.

ACKNOWLEDGMENTS

The author wishes to thank The National Sciences and Engineering Research Council of Canada (NSERC) for financial support.

- ¹K. Williams, R. K. Singal, and S. P. Verma, "Vibrations of long and short laminated stators of electrical machines. II. Results for long stators," *J. Sound Vib.* **129**, 15–29 (1989).
- ²S. Watanabe, S. Kenjo, K. Ide, F. Sato, and M. Yamamoto, "Natural frequencies and vibration behavior of motor stators," *IEEE Trans. Power Appar. Syst.* **PAS-102**, 949–956 (1983).
- ³R. K. Singal, K. Williams, and S. P. Verma, "The effect of windings, frames and impregnation upon the resonant frequencies and vibrational behavior of an electrical machine stator," *J. Exp. Mech.* **30**, 270–280 (1990).
- ⁴C. F. Beards and I. M. A. Imam, "The damping of plate vibration by interfacial slip between layers," *J. Machine Tool Design Res.* **18**, 131–137 (1978).
- ⁵C. F. Beards and J. L. Williams, "The damping of structure vibration by rotational slip in joints," *J. Sound Vib.* **53**, 333–340 (1977).
- ⁶E. H. Dowell and H. B. Schwartz, "Forced response of a cantilever beam with a dry friction damper attached. I. Theory," *J. Sound Vib.* **91**, 255–291 (1983).
- ⁷C. H. Menq, J. Bielak, and J. H. Griffin, "The influence of microslip on vibration response. I. A new microslip model," *J. Sound Vib.* **107**, 279–307 (1986).
- ⁸C. F. Beards and D. A. Robb, "The use of frictional damping to control the vibration of the plates in structure," *International Conference on Recent Advances in Structural Dynamics*, pp. 749–760 (1980).
- ⁹ANSYS, Swanson Analysis System Inc., Houston (1996).

Maximum likelihood estimation of structural wave components from noisy data

Peter J. Halliday

Ford Motor Company, MD X7 Experimental Vehicle Building, 20800 Oakwood Boulevard, Dearborn, Michigan 48124-4076

Karl Grosh

Department of Mechanical Engineering, University of Michigan, Ann Arbor, Michigan 48109-2125

In this paper, a general framework is developed for determining the underlying parameters of general signal models through the application of maximum likelihood estimation theory for functions whose variables separate. This method extends previous work in sinusoidal and exponential estimation to include models with other functional bases, such as exponential functions with nonconstant amplitudes and Bessel functions. Nonuniform spatial sampling is also possible with this technique. The maximum likelihood method is applied to the identification of wave components along one-dimensional structural elements. Results are given which demonstrate the viability and accuracy of the technique estimating exponential and Bessel function model parameters from noisy simulation data. © 2002 Acoustical Society of America.

[DOI: 10.1121/1.1456518]

PACS numbers: 43.40.At, 43.40.Le [CBB]

I. INTRODUCTION

In the analysis of structural acoustic systems it is desirable to have a robust and flexible method for analyzing wave phenomena along the structure and in the surrounding fluid. Accurate knowledge of the waves present on a structure is instrumental to the exponential determination of structural intensity, dispersion relations, and material properties. In this paper, a flexible maximum likelihood method is developed for the identification of wave-component models of spatial response. Wave-component models are comprised of functions of complex wave-number-like quantities and associated wave amplitudes. In a maximum likelihood method, the square error of the difference between the prediction of a parametric model and the actual data is directly minimized. This technique, like other identification techniques, enables the identification of the parameters of the model (e.g., wave numbers of a spatial exponential model). Through the approach used here, the choice of basis functions available for the underlying model is expanded over traditional approaches, enabling very nearly an arbitrary functional basis for the spatial representation. Therefore, identification of functions other than sinusoidal and exponential, such as Bessel functions or more complicated functional combinations, is possible. A further advantage of this method is that the least-squares parameter estimation is obtained via a two-step process where the wave number parameters are found first, followed by the corresponding wave amplitudes.

Previous work in wave-component identification has focused on the estimation of constant amplitude sinusoidal and exponential signals. One popular technique is Prony's method, which has been applied to identify wave numbers when the displacement field is assumed to be exponential. A succinct presentation of the technique is given by Hildebrand (1956). However, the presence of measurement noise severely diminishes the capabilities of the method. Kumeresan *et al.* (1984) proposed the inclusion of more than the ex-

pected number of exponentials in an attempt to fit noisy data. Further work in this area was done by Grosh and Williams (1993), who also used an overdetermined model order and developed methods for extracting the physical parameters of the model. The limitations of Prony's method are the implicit reliance upon exponential signals and the requirements of uniform spatial sampling (or the approximation thereof) via the application of spline interpolation or another such technique which introduces some level of error into the solution. Also, this technique cannot be applied to estimate other important functional dependencies, such as Bessel functions or polynomials. In addition to Prony's method, there are other effective techniques for the estimation of exponential and sinusoidal functional dependencies; many of these methods also rely on model order overdetermination. Surveys of some of these methods are presented in Marple, 1987; Kay, 1988.

Maximum likelihood estimation provides an alternative to traditional techniques like Prony's method and its variants for the identification of exponential and nonexponential signals in noise. Because of their importance, exponential models have been the focus of most (but not all) work on maximum likelihood estimation. Evans and Fischl developed techniques for solving the least squares problem for exponential function estimation (Evans and Fischl, 1973). Golub and Pereyra (1973) and Guttman *et al.* (1973) focused on minimizing least-squares error for a class of problems where the variables separate for very general functional parametric models. Tufts and Kumeresan contributed computationally efficient maximum likelihood methods for fitting sinusoids in a noisy field (Tufts and Kumeresan, 1982, 1980a, 1980b, 1981). Parthasarathy and Tufts used maximum likelihood techniques to estimate damped sinusoids in noise via an algorithm based on Newton's method (Parthasarathy and Tufts, 1985). Bresler and Macovski (1985, 1986) applied maximum likelihood estimation to the problem of fitting exponential models to observed data in a constrained nonlinear minimi-

zation to find the coefficients of the characteristic polynomial. Other groups that have been active in the area of using nonlinear least-squares methods for fitting sinusoids and exponentials include Osborne and Smyth, 1995, and Kaufman *et al.*, 1994.

Maximum likelihood identification theory is not specific to sinusoidal and exponential identification. In this paper, previous work is extended to the identification of general spatial structural models from noisy data. A framework is developed which admits complex wave components, general functional bases, and nonuniform spatial sampling. Some computational efficiency is achieved through the use of separable nonlinear least-squares theory (Golub and Pereyra, 1973) reducing the dimensionality of the nonlinear minimization problem and enabling a separate solution of the linear portion. Minimization of the square error is accomplished through a derivative-based approach which extends the work of Golub and Pereyra (1973) to allow complex wave numbers and include second derivative information in the algorithm. The resulting method converges quickly and performs well with noisy data without relying on model-order over-determination for noise rejection. Convergence of the minimization procedure assures at least local optimality of the model fit, unlike other techniques such as Prony's method. The maximum likelihood method is applied to simulations of beams with uniform cross-sectional and material properties where the initial estimate is found by a Prony-based algorithm. The method is also applied to simulations of beams with linearly tapering thickness using an initialization algorithm developed herein and a maximum likelihood parametric model based on Bessel functions with nonuniform spatial amplitudes. The effects of various noise levels and spatial samplings are also studied.

II. MAXIMUM LIKELIHOOD/NONLINEAR LEAST-SQUARES ESTIMATION

The maximum likelihood method minimizes the squared-error functional of the difference between a measured signal and a parametric model. In this study, solution of the minimization of the squared error results in a problem that separates the underlying model parameters into two sets, one for which the minimization problem is linear and the other for which the minimization problem is nonlinear. This class of problems is denoted as separable nonlinear least-squares problems. A simple example of such a separable problem is the exponential model, where the least-squares problem is linear in the wave amplitudes and nonlinear in the wave numbers. By separating the error in this fashion, the parameters that give rise to a nonlinearity in the minimization problem are found first through an iterative process followed by a linear least-squares fit for the remaining parameters. A general formulation for finding the parameters that minimize the least-squares error between measured signals and functional solutions with separable variables follows.

A. The maximum likelihood error functional

The separable nonlinear least-squares problem is described next. The maximum likelihood error functional is written as

$$\chi(\mathbf{a}, \boldsymbol{\gamma}) = \sum_{j=1}^N \left[s_j - \sum_{k=1}^w \sum_{l=1}^{n_k} a_{kl} \phi_{kl}(x_j, \gamma_k) \right]^2. \quad (1)$$

In this equation, the assumed solution form is written in terms of the basis functions, $\phi_{kl}(x_j, \gamma_k)$, which depend on position, x_j , and wave number, γ_k . For each of the w wave number parameters present in the assumed solution, γ_k , there may be up to n_k spatial functions which depend on this parameter. The goal is to find the vector $\mathbf{a} \in \mathbb{C}^{n \times 1}$, where $n \equiv \sum_{k=1}^w n_k$, and $\boldsymbol{\gamma} \in \mathbb{C}^{w \times 1}$ that minimize χ . The functions are evaluated at N positions, x_j , that correspond to a measurement taken at that position, denoted by s_j . Finally, each function will have a corresponding amplitude, a_{kl} .

A matrix of the basis functions evaluated at each position is defined such that $[\Phi]_{jm} \equiv \phi_{kl}(x_j, \gamma_k)$, where $m = l + \sum_{k'=0}^{k-1} n_{k'}$, $l = 1, 2, \dots, n_k$, and $n_0 \equiv 0$. Further, the measured data are collected in the vector $\mathbf{s} = \{s_1, \dots, s_N\}^T$ and the wave amplitudes form the vector $\mathbf{a} = \{a_1, \dots, a_n\}^T$. Using these definitions, the error functional, Eq. (1), can be rewritten as

$$\chi(\mathbf{a}, \boldsymbol{\gamma}) = \|\mathbf{s} - \Phi(\boldsymbol{\gamma})\mathbf{a}\|^2. \quad (2)$$

If the wave numbers are known or estimated, then an associated estimate of the wave amplitudes is determined in a least-squares sense as

$$\mathbf{a}^{\text{LS}} = \Phi^\dagger \mathbf{s}, \quad (3)$$

where the pseudoinverse of the function matrix, $\Phi^\dagger \equiv (\Phi^H \Phi)^{-1} \Phi^H$, minimizes the least-squares problem $\Phi \mathbf{a} = \mathbf{s}$ (Golub and Loan, 1989). The superscript H denotes the complex conjugate transpose of a matrix. The least-squares approximation, \mathbf{a}^{LS} , is substituted into Eq. (2) and the error may now be written solely in terms of the wave numbers as

$$\chi_2(\boldsymbol{\gamma}) = \|\mathbf{s} - \Phi(\boldsymbol{\gamma})\Phi^\dagger(\boldsymbol{\gamma})\mathbf{s}\|^2. \quad (4)$$

The importance of this substitution is that the maximum likelihood error is written only in terms of wave numbers. Thus, minimization of the error is accomplished first by determining the wave components on which there is a nonlinear dependence. Further, there will be no coupling of derivatives of the error functional with respect to the amplitudes and wave numbers. Such coupling would complicate the procedure.

Defining the projection onto the column space of the function matrix as $\mathbf{P}_\Phi \equiv \Phi \Phi^\dagger$ and the orthogonal projection as $\mathbf{P}_\Phi^\perp \equiv \mathbf{I} - \mathbf{P}_\Phi$, the error can be written in a compact form and the corresponding minimization problem becomes (Golub and Pereyra, 1973)

$$\min_{\boldsymbol{\gamma} \in \mathbb{C}^{w \times 1}} \chi_2(\boldsymbol{\gamma}) = \min_{\boldsymbol{\gamma} \in \mathbb{C}^{w \times 1}} \|\mathbf{P}_\Phi^\perp \mathbf{s}\|^2. \quad (5)$$

B. Minimization of error

The maximum likelihood error functional of Eq. (5) lends itself to a variety of minimization techniques. The approach used in this study is to determine the critical points of the error functional and check for their character. To this end, a gradient-based method has been applied to obtain the results presented later.

When complex wave numbers are admitted, derivatives of χ_2 with respect to the wave numbers are nonanalytic due to the inclusion of the complex conjugate in the error functional. However, if the wave numbers are parameterized such that $\gamma_j = \alpha_j + \beta_j i$, derivatives may be taken with respect to the real and imaginary parts of each wave number. This technique effectively doubles the number of wave number parameters, but renders the resulting problem solvable.

1. Algorithm

The maximum likelihood problem consists of minimizing the error functional as in Eq. (5). A multidimensional Gauss–Newton–Raphson technique using Hessian information is employed to locate the possibly local zeros of the gradient of the squared error (Press *et al.*, 1992). For many structural vibration problems, calculation of the derivatives necessary in order to obtain the Hessian matrix is straightforward. Therefore, an analytic minimization algorithm to provide updates of wave component estimates is used. A description of the initialization algorithm is deferred until the problem is specified.

A necessary condition for a minimum is that the gradient of the error with respect to the wave number parameters, whose components are $[\nabla\chi_2]_p \equiv \partial\chi_2/\partial\gamma'_p$ where $\gamma' \equiv [\alpha^T \beta^T]^T$, be zero. A Taylor series expansion of the error about the current wave number estimate is taken such that

$$\frac{\partial\chi_2(\gamma' + \delta\gamma')}{\partial\gamma'_j} = \frac{\partial\chi_2(\gamma')}{\partial\gamma'_j} + \sum_{k=1}^N \frac{\partial^2\chi_2(\gamma')}{\partial\gamma'_j\partial\gamma'_k} \delta\gamma'_k + \mathcal{O}(\delta\gamma'^2), \quad (6)$$

or in direct notation

$$\nabla\chi_2(\gamma' + \delta\gamma') = \nabla\chi_2(\gamma') + \mathbf{H} \cdot \delta\gamma' + \mathcal{O}(\delta\gamma'^2), \quad (7)$$

where $[\mathbf{H}]_{pq} \equiv \partial^2\chi_2(\gamma')/\partial\gamma'_p\partial\gamma'_q$ is the Hessian matrix; the brackets here denote the components of the matrix. Assuming that $\nabla\chi_2(\gamma' + \delta\gamma') = 0$, the wave number estimate is updated by

$$\gamma'_{\text{new}} = \gamma'_{\text{old}} + \delta\gamma' = \gamma'_{\text{old}} - \mathbf{H}^{-1} \nabla\chi_2. \quad (8)$$

The entire process is repeated until the error falls within a desired tolerance, ϵ .

The steps of the algorithm used in this study are outlined as follows.

Step (1) Set $t=0$.

Step (2) Determine an initial estimate of the wave numbers, γ^0 , through an appropriate technique.

Step (3) Compute the current error, $\chi_2(\gamma')$. If $t>0$ and $1 - [\chi(\gamma')/\chi(\gamma'^{-1})] < \epsilon$, then skip to step (7).

Step (4) Compute first and second derivatives of the error with respect to the real and imaginary parts of the wave numbers.

Step (5) Update $\gamma'^{+1} = \gamma' + \delta\gamma$.

Step (6) Increment $t = t + 1$ and return to step (3).

Step (7) Calculate the wave amplitudes.

2. Derivatives of the error functional

To minimize the maximum likelihood error functional analytically, derivative information is required. Golub and Pereyra (1973) showed that the gradient of the maximum likelihood error functional, Eq. (5), is

$$\nabla\chi_2(\gamma) = \mathbf{s}^H \mathbf{D}(P_\Phi^\perp) \mathbf{s} = -2\mathbf{s}^H \mathbf{P}_\Phi^\perp \mathbf{D}[\Phi(\gamma)] \Phi^\dagger(\gamma) \mathbf{s} \quad (9)$$

for real wave numbers. Here, the notation $\mathbf{D}(\Phi)$ refers to the Fréchet derivative with respect to the wave numbers ($[\mathbf{D}(\Phi)]_{jmp} \equiv \partial[\Phi]_{jm}/\partial\gamma_p$) (Dieudonné, 1960). This calculation of the gradient capitalizes on some useful properties of the projector (where \mathbf{P} represents either \mathbf{P}_Φ or \mathbf{P}_Φ^\perp)

$$\mathbf{P}^H = \mathbf{P}, \quad (10a)$$

$$\mathbf{P}^2 = \mathbf{P}, \quad (10b)$$

$$\mathbf{P}\mathbf{P}^\dagger\mathbf{P} = \mathbf{P}, \quad (10c)$$

$$(\mathbf{P}\mathbf{P}^\dagger)^T = \mathbf{P}\mathbf{P}^\dagger, \quad (10d)$$

which can be shown from the definition of the projector operators. The relationship

$$\mathbf{D}(\mathbf{P}_\Phi^\perp) = \mathbf{D}(\mathbf{I} - \mathbf{P}_\Phi) = -\mathbf{D}(\mathbf{P}_\Phi), \quad (11)$$

where \mathbf{I} is the identity matrix of the same dimension as \mathbf{P}_Φ is also required. The key result of this derivation is that the derivative of the error depends only on the Fréchet derivative of the function matrix, Φ , not derivatives of the more complicated projector matrix.

However, when the wave numbers are not purely real, the complex derivatives required are nonanalytic due to the dependence of χ on the conjugate of the γ . Thus, the wave numbers must be parameterized in terms of their real and imaginary components and derivatives are taken with respect to those terms. Modifying the definition of the Fréchet derivative to be $[\mathbf{D}(\Phi)]_{jmp} = (\partial[\Phi]_{jm})/(\partial\gamma'_p)$, Eq. (9) can still be used to calculate the gradient.

To determine the critical points of the gradient, first and second derivatives of the error functional with respect to the real and imaginary parameters of the wave numbers are required. The second derivative (or Hessian) matrix, \mathbf{H} , is calculated analytically as

$$\begin{aligned} \mathbf{H} = & -\mathbf{s}^H [\mathbf{P}_\Phi^\perp \mathbf{D}^2(\Phi) \Phi^\dagger - 2\mathbf{D}(\mathbf{P}_\Phi) \mathbf{D}(\Phi) \Phi^\dagger \\ & + \{\mathbf{P}_\Phi^\perp \mathbf{D}^2(\Phi) \Phi^\dagger - 2\mathbf{D}(\mathbf{P}_\Phi) \mathbf{D}(\Phi) \Phi^\dagger\}^H + 2\{\mathbf{D}(\mathbf{P}_\Phi)\}^2] \mathbf{s}. \end{aligned} \quad (12)$$

Proof: The maximum likelihood error functional, Eq. (5), can be written as

$$\chi_2 = \|\mathbf{P}_\Phi^\perp \mathbf{s}\|^2 = (\mathbf{P}_\Phi^\perp \mathbf{s})^H \mathbf{P}_\Phi^\perp \mathbf{s} = \mathbf{s}^H \mathbf{P}_\Phi^\perp \mathbf{s}. \quad (13)$$

Since the data vector, \mathbf{s} , is independent of the parameters, differentiation affects only the orthogonal projector matrix, \mathbf{P}_Φ^\perp , and $\mathbf{H} = \nabla^2\chi_2 = \mathbf{s}^H \mathbf{D}^2[\mathbf{P}_\Phi^\perp] \mathbf{s}$. Thus, the second derivative of the projector, $\mathbf{D}^2(\mathbf{P}_\Phi)$, is required.

The second derivative of the projector may be written as

$$\begin{aligned}\mathbf{D}^2(\mathbf{P}_\Phi) &= \mathbf{D}^2(\mathbf{P}_\Phi^2) \\ &= \mathbf{D}[\mathbf{D}(\mathbf{P}_\Phi)\mathbf{P}_\Phi + \mathbf{P}_\Phi\mathbf{D}(\mathbf{P}_\Phi)] \\ &= \mathbf{D}^2(\mathbf{P}_\Phi)\mathbf{P}_\Phi + 2[\mathbf{D}(\mathbf{P}_\Phi)]^2 + \mathbf{P}_\Phi\mathbf{D}^2(\mathbf{P}_\Phi).\end{aligned}\quad (14)$$

Note that

$$\begin{aligned}\mathbf{D}^2(\Phi) &= \mathbf{D}^2(\mathbf{P}_\Phi\Phi) \\ &= \mathbf{D}[\mathbf{D}(\mathbf{P}_\Phi)\Phi + \mathbf{P}_\Phi\mathbf{D}(\Phi)] \\ &= \mathbf{D}^2(\mathbf{P}_\Phi\Phi) + 2\mathbf{D}(\mathbf{P}_\Phi)\mathbf{D}(\Phi) + \mathbf{P}_\Phi\mathbf{D}^2(\Phi).\end{aligned}\quad (15)$$

Rearranging this equation gives

$$\mathbf{D}^2(\mathbf{P}_\Phi)\Phi = \mathbf{P}_\Phi^+\mathbf{D}^2(\Phi) - 2\mathbf{D}(\mathbf{P}_\Phi)\mathbf{D}(\Phi).\quad (16)$$

Post-multiplication of Eq. (16) by the pseudoinverse of the function matrix, Φ^\dagger , yields

$$\mathbf{D}^2(\mathbf{P}_\Phi)\mathbf{P}_\Phi = \mathbf{P}_\Phi^+\mathbf{D}^2(\Phi)\Phi^\dagger - 2\mathbf{D}(\mathbf{P}_\Phi)\mathbf{D}(\Phi)\Phi^\dagger.\quad (17)$$

Next, the first and third terms on the right-hand side of Eq. (14) are obtained by using Eq. (17) and the relation $[\mathbf{D}^2(\mathbf{P}_\Phi)\mathbf{P}_\Phi]^H = \mathbf{P}_\Phi\mathbf{D}^2(\mathbf{P}_\Phi)$. The second term on the right-hand side of Eq. (14) is found by identifying $[\mathbf{D}(\mathbf{P}_\Phi)]$ from Eq. (9). The proof is completed by substituting these results into the expression for the Hessian, provided sufficient differentiability exists for the function matrix. This derivation is similar to that for the first derivative shown by Golub and Pereyra (1973).

3. Remark

Minimization of the maximum likelihood error functional may alternatively be accomplished by determining a search direction, \mathbf{g} , and setting up a corresponding iterative one-dimensional minimization problem where the error is minimized along the search direction

$$\min_{\theta \in \mathbb{R}} \chi_2(\boldsymbol{\gamma} - \theta\mathbf{g}).\quad (18)$$

Here, the real parameter, θ , determines the step size. Typically the search direction will be along the gradient of the error functional, which may be calculated either numerically or analytically.

The solution of this minimization problem may be arrived at through the use of a bisection or Golden section scheme, either of which requires only function evaluations, or a derivative-based technique such as a Gauss–Newton or secant method for zeroing the first derivative with respect to the real parameter θ (Dennis and Schnabel, 1983).

Alternatively, a Levenberg–Marquardt technique (Press *et al.*, 1992) could be employed which requires calculation of the gradient of the original function, but estimates higher derivatives. This may be preferable for a problem where the basis functions are complicated or not easily differentiable to higher order. Further, global search algorithms may also be used, especially in the case where initial estimates may be difficult to obtain.

III. APPLICATION TO UNIFORM BEAMS

The maximum likelihood technique for wave-component analysis of structural vibrations can be applied to

any system where the amplitudes and functions of wave numbers are separable. One such case is the propagation of waves along a uniform beam, which is simulated herein.

A. Analytic solution

For harmonic vibrations of a beam with uniform material and cross-sectional properties, the transverse displacement is assumed to be of the form

$$y = \sum_{k=1}^2 (a_{2k-1}e^{i\gamma_k x_j} + a_{2k}e^{i\gamma_k x_j})e^{-i\omega t}.\quad (19)$$

If a Bernoulli–Euler beam model is applied, the two wave numbers present in Eq. (19) will be determined by

$$\gamma = \left[\frac{\rho A}{EI} \omega^2 \right]^{1/4},\quad (20)$$

with the positive values being used and $\gamma_2 = i\gamma_1$. When accuracy over a broader frequency range is desired, the Timoshenko kinematic hypothesis yields better results. Here, the wave numbers will satisfy

$$\frac{EI}{\rho A} \gamma^4 - \frac{I}{A} \left(1 + \frac{E}{G\kappa} \right) \gamma^2 \omega^2 - \omega^2 + \frac{\rho I}{GA\kappa} \omega^4 = 0.\quad (21)$$

Once again, the positive roots are used for γ_1 and γ_2 . In this study, Timoshenko theory is assumed for uniform beams.

B. Uniform beam function matrix

To minimize the maximum likelihood error and improve upon the initial estimate, the function matrix, Φ , must be defined to satisfy the form specified in Eq. (1) and the assumed solution form of Eq. (19). For uniform beams, the function matrix is constructed of exponential functions at discrete data points

$$[\Phi]_{jm} = \begin{cases} e^{i\gamma_1 x_j} & \text{for } m=1 \\ e^{-i\gamma_1 x_j} & \text{for } m=2 \\ e^{i\gamma_2 x_j} & \text{for } m=3 \\ e^{-i\gamma_2 x_j} & \text{for } m=4. \end{cases}\quad (22)$$

However, there is no requirement on the spacing of the data points. This allows for refinement of data around discontinuities in order to improve upon the estimation of evanescent waves.

C. Initial estimate

The initial estimate of the wave numbers required by step (2) of the algorithm is provided by the overdetermined modified extended Prony technique (OMEP) developed by Grosh and Williams (1993). OMEP is a fairly robust method which is computationally efficient and requires few iterations, but does have some limitations.

For clean data or data taken with a high signal-to-noise ratio, the OMEP performs very well in estimating the propagating and evanescent waves as long as there are a sufficient number of data points per spatial period. However, as the signal-to-noise ratio decreases, the estimation of the evanescent wave deteriorates until an SNR of 25 dB when errors in

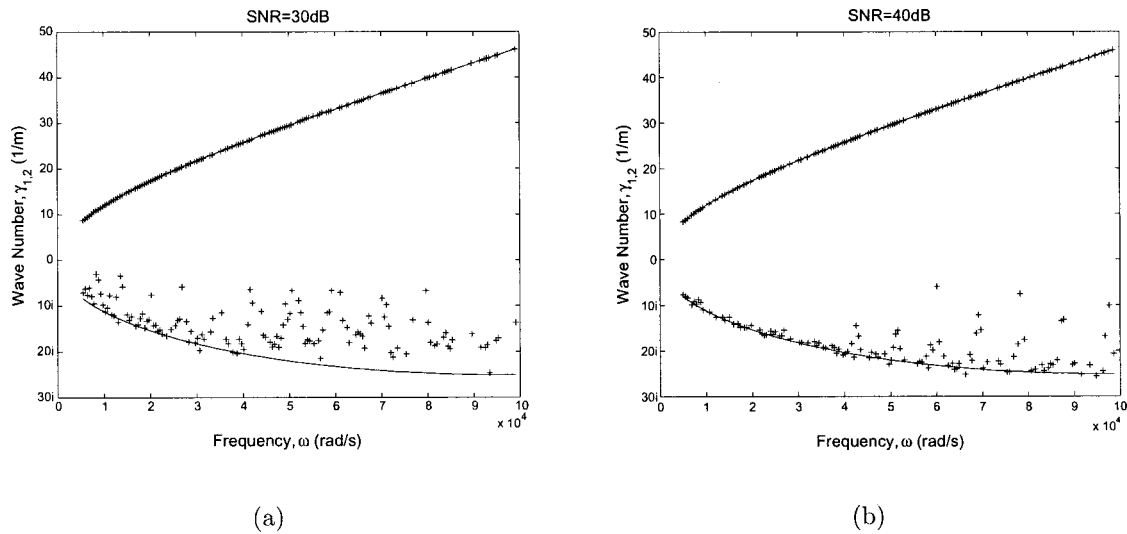


FIG. 1. Experimental (+) and analytic (—) dispersion curves for semi-infinite beam after application of the OMEP technique with (a) SNR=30 dB and (b) SNR=40 dB.

estimating the evanescent wave number are on the order of 100%. This may be attributed to the fact that the evanescent waves are very localized—and because more so as frequency increases—which results in their affecting only a few data points. Therefore, high noise levels combined with limited data lead to large errors in predictions of the evanescent waves. Due to the reliance on evenly spaced data inherent to Prony techniques, an inordinately large number of data points would be required to combat this problem using OMEP alone (although an algorithm based on two different sets of even spacing is possible).

D. Results for uniform beams

To test the combination of OMEP and maximum likelihood techniques, numerical experiments were performed. A clean signal was created by analytically solving for the waves present on a 1.000-m beam using Timoshenko theory.

Uniformly distributed, spatially varying noise was added to the signal at each frequency. The signal-to-noise ratio was calculated by

$$\text{SNR} = 10 \log_{10} \left(\frac{\sum_{j=1}^N |y_j|^2}{\sum_{j=1}^N |n_j|^2} \right), \quad (23)$$

where n_j is the noise added to the clean signal y_j at a position x_j . The beam in question had an elastic modulus $E = 2.1 \times 10^{11}(1 + 0.001i)$ Pa, density $\rho = 7800 \text{ kg/m}^3$, a rectangular cross section with thickness 0.050 m, and a shear correction factor $\kappa = 0.833$.

The initial wave number estimates were performed using OMEP on data taken at intervals of 0.020 m along the length of the beam. For a basis of comparison, results from applying the OMEP technique to the data to obtain the dispersion relations are shown in Fig. 1. Plotted are the real parameter of the predominantly real wave number and the imaginary

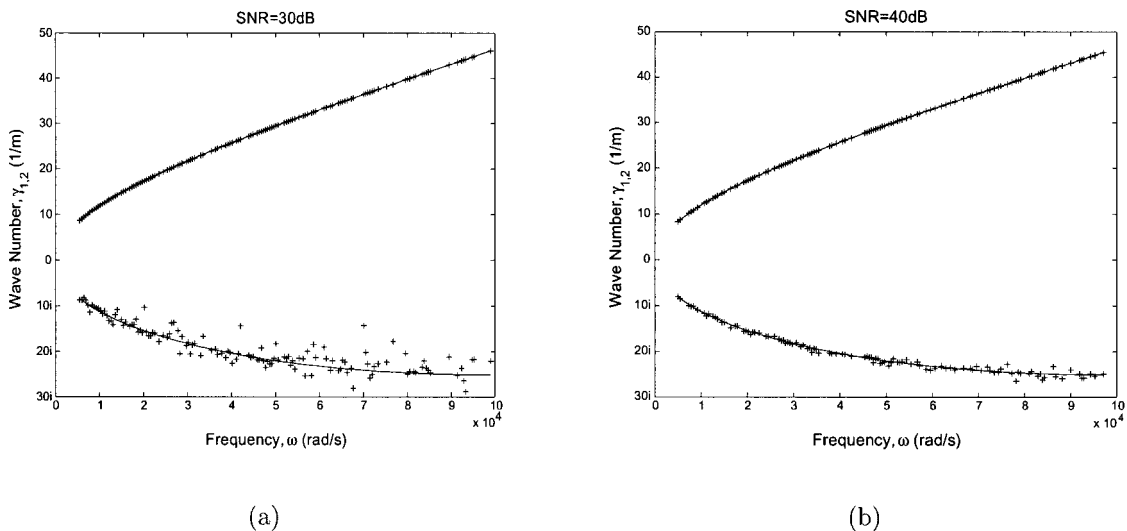


FIG. 2. Experimental (+) and analytic (—) dispersion curves for semi-infinite beam after application of the maximum likelihood technique with (a) SNR=30 dB and (b) SNR=40 dB.

TABLE I. Comparison of error in the evanescent wave number with different spatial samplings at a signal-to-noise ratio of 30 dB. Initial mean error from OMEP was 26.3% with a standard deviation of 19.6%.

Fine spacing (m)	Coarse spacing (m)	Mean error	Standard dev.
0.002	0.040	5.5%	7.9%
0.001	0.040	5.2%	6.9%
0.020	0.020	6.7%	8.6%
0.002	0.020	2.8%	7.0%
0.001	0.020	4.5%	5.2%

parameter of the primarily imaginary wave number. For the beams used in this study, the other parameters are three orders of magnitude smaller and thus less significant.

Results obtained through use of the maximum likelihood technique are presented in Fig. 2. In this case, the data were refined at the ends of the beam such that a data point was taken every 0.002 m for the first and last 0.020 m, and at intervals of 0.020 m over the rest of the beam.

It is seen in Fig. 1(a) that the propagating (primarily real) wave number is estimated accurately by the OMEP method even at a signal-to-noise ratio of 30 dB. However, the evanescent field is not as well determined. The mean error $[(1/N)\sum_{j=1}^N(\gamma_j^{\text{est}} - \gamma_j)/\gamma_j]$ in the evanescent wave number is 26.3%, with a standard deviation in the error of 19.6%. This highlights the presence of a noise bias error in the OMEP estimate (Kumaresan and Tufts, 1982). Since energy is input into beams where evanescent fields are important, such misestimation of the nonpropagating wave fields may be important in power-flow computations. After application of the maximum likelihood algorithm to this estimate, the average mean error is improved to 2.8%, with a standard deviation of 7.0%. Thus, the maximum likelihood estimate greatly reduces both the noise bias error and the standard deviation. This reduction can be seen in Fig. 2(a).

At a signal-to-noise ratio of 40 dB, the OMEP technique estimates the evanescent component with better accuracy, as is seen in Fig. 1(b). After application of maximum likelihood to this data—as shown in Fig. 2(b)—the mean error in the evanescent wave number is improved from 6.6% to 0.3% and the standard deviation from 12.3% to 1.6%.

An advantage of the maximum likelihood technique is that nonuniform spatial sampling is allowed. As was previously discussed, the evanescent waves affect small regions around discontinuities. Therefore, it is desirable to include extra data points in these regions. Further, fewer data points may be used in uniform areas where the propagating waves dominate. A set of trials was performed for 30-dB signal-to-noise level data with fine spacing in the first and last 0.020 m of the beam and coarse spacing over the rest. The initial estimates were calculated as before with data spaced at 0.020-m intervals. Results are shown in Table I for various spacings with the error shown.

Estimates tend to show that the most improvement typically occurs when the spacing is finest. However, the degradation in performance for coarser spacing is not so great as to preclude use of those results when more data points may not be available. Thus, with the maximum likelihood tech-

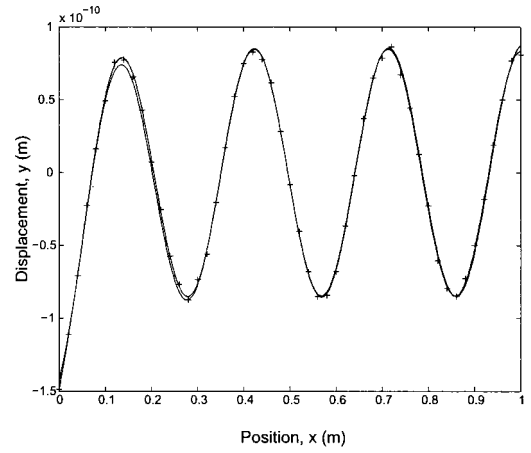


FIG. 3. Transverse displacement along a uniform beam with noisy data (+). Best fits after OMEP estimate (- -) and maximum likelihood (· · ·) compared to exact displacement (—).

niques the number of data points used may be reduced without severely affecting the accuracy of the prediction. Such a reduction in the size of the problem will lead to major computational time savings for applications with large data sets.

Figure 3 shows estimates of the transverse displacement of the uniform beam based on the OMEP and maximum likelihood estimates at 3×10^4 rad/s. While the OMEP estimate provides a good fit of the data to the actual signal, the maximum likelihood estimate delivers better results, particularly at the ends of the beam and in the first peak in the displacement at the left or $x=0$ end. This is due to a 30% improvement in the estimate of the primarily complex wave number at this frequency. The signal-to-noise ratio in this case was 30 dB. The mean-squared error

$$e^{\text{MS}} = \frac{\sum_{j=1}^N |s_j - \sum_{k=1}^w \sum_{l=1}^{n_k} a_{kl} \phi_{kl}(x_j, \gamma_k)|^2}{\sum_{j=1}^N |s_j|^2}, \quad (24)$$

is small for both estimation methods, but improved from 2.5% to 1.5% in this example.

IV. APPLICATION TO TAPERED BEAMS

Another class of structural members for which the maximum likelihood technique is clearly applicable is for beams whose thicknesses vary linearly. This problem clearly demonstrates the effectiveness of maximum likelihood estimation for problems with nonexponential bases.

A. Analytic solution

Assuming a Bernoulli–Euler kinematic hypothesis for the beam, the governing ordinary differential equation is

$$[EI(x)y_{,xx}]_{xx} - \rho A(x)\omega^2 y = 0, \quad 0 < x < L \quad (25)$$

for harmonic response with no forcing along the length. If the relative thickness of the beam is defined as $\xi(x) \equiv 1 + [(\tau - 1)/L]x$, where τ is the ratio of the thickness at $x = L$ to the thickness at $x = 0$, then a change of variables is performed to attain the following form:

$$\xi^2 y_{,\xi\xi\xi\xi} + 6\xi y_{,\xi\xi\xi} + 6y_{,\xi\xi} - \gamma^4 y = 0, \quad 1 < \xi < \tau, \quad (26)$$

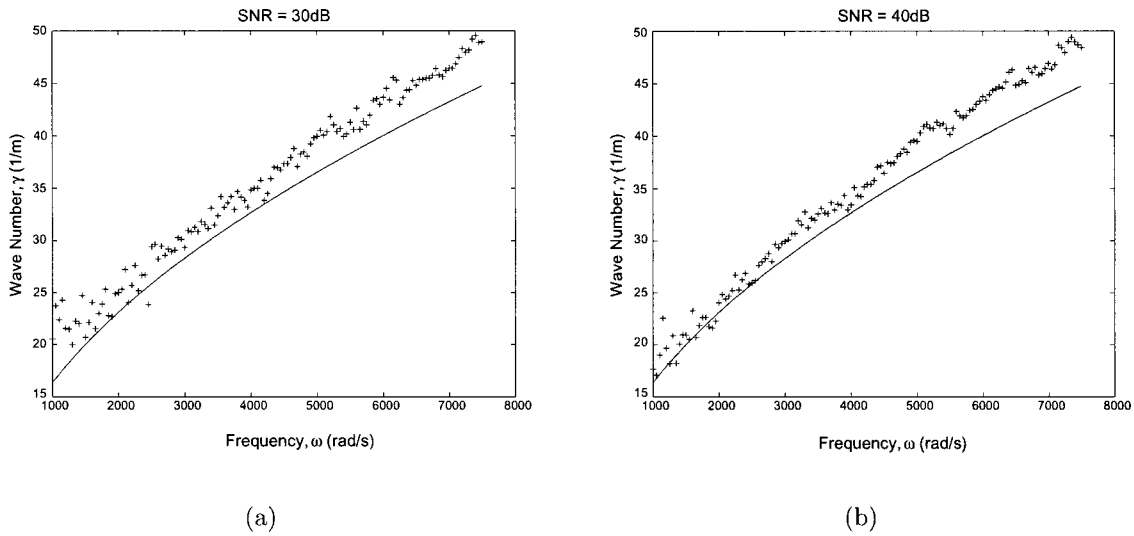


FIG. 4. Experimental (+) and analytic (—) dispersion curves for tapered beam after application of the polynomial estimation technique with (a) SNR=30 dB and (b) SNR=40 dB.

where $\gamma^4 = \rho \omega^2 [A(0)L^4/EI(0)]$. The general solution form for this differential equation is found in terms of Bessel functions of the first kind

$$y = \xi^{-1/2} [a_1 J_1(2\gamma \xi^{1/2}) + a_2 Y_1(2\gamma \xi^{1/2}) + a_3 I_1(2\gamma \xi^{1/2}) + a_4 K_1(2\gamma \xi^{1/2})], \quad (27)$$

as was shown by Auciello and Nolé (1998).

B. Tapered beam function matrix

The maximum likelihood technique may be applied to tapered beams starting from an initial estimate of the wave number. The function matrix will be constructed from Bessel functions in the same manner that exponentials were used for uniform beams.

$$[\Phi]_{jm} = \begin{cases} \xi_j^{-1/2} J_1(2\gamma \xi_j^{1/2}) & \text{for } m=1 \\ \xi_j^{-1/2} Y_1(2\gamma \xi_j^{1/2}) & \text{for } m=2 \\ \xi_j^{-1/2} I_1(2\gamma \xi_j^{1/2}) & \text{for } m=3 \\ \xi_j^{-1/2} K_1(2\gamma \xi_j^{1/2}) & \text{for } m=4. \end{cases} \quad (28)$$

Here, $1 \leq \xi \leq \tau$.

C. Initial estimate

An initial estimate of the tapered beam wave number is arrived at through use of a polynomial fit to the data, which is in turn substituted into the governing differential equation. This estimate is made using a least-squares fit of a polynomial in ξ to a section of data and the governing differential equation. It was determined empirically that an eighth-order polynomial fit over two spatial periods provides a good estimate.

In this estimate, the matrix problem

$$\mathbf{s} = \Psi \mathbf{c}, \quad (29)$$

is set up where $[\Psi]_{jr} = \xi_j^{r-1}$ and \mathbf{c} is the vector of polynomial coefficients. Thus, the problem is cast as a set of j polynomials with undetermined coefficients. The coefficient

vector is approximated by $\mathbf{c} \approx \Psi^\dagger \mathbf{s}$. The resulting polynomial is then substituted into the governing ODE, Eq. (26), to solve for an estimated value of the wave number at each data point

$$(\gamma_j^{\text{est}})^4 = \frac{\xi_j^2 y_{j,\xi\xi\xi\xi} + 6\xi_j y_{j,\xi\xi\xi} + 6y_{j,\xi\xi}}{y_j}, \quad 1 \leq j \leq h. \quad (30)$$

Since the wave number γ is the only unknown in the equation upon substitution of the polynomial, a discrete set of estimates is made at the h data points. The discrete estimates are averaged to provide the zeroth-order estimate for the maximum likelihood iterations. This finite difference approximation to the differential equation acts as the generator for the Bessel functions from which to estimate the wave number of the Bessel function. For Bessel function models different from Eq. (30) a generating differential equation appropriate for the model may be used for the initial estimate.

D. Results of tapered beam analysis

To test the maximum likelihood technique for wave-component estimation on the tapered beam, much of the same procedure was used as in the uniform beam case. Clean data were generated by analytically solving for the waves present based on the assumed solution of Eq. (27). The beam model also was assumed to have an elastic modulus $E = 2.1 \times 10^{11}(1 + 0.001i)$ Pa, and density $\rho = 7800$ kg/m³. The length of the beam was 1.000 m with a thickness which tapered from 0.010 to 0.015 m. Data were taken at intervals of 0.010 m along the entire length of the beam. Uniformly distributed noise was added to the clean signal at every frequency of interest.

Initial estimates of the wave numbers were made from data constructed at signal-to-noise ratios of 30 and 40 dB. The real parameters of these estimates are displayed in Fig. 4, along with the analytical solution as a function of angular frequency. The maximum likelihood technique was applied to the data starting from the polynomial estimate. Results of this trial are shown in Fig. 5. It can be seen that for both of

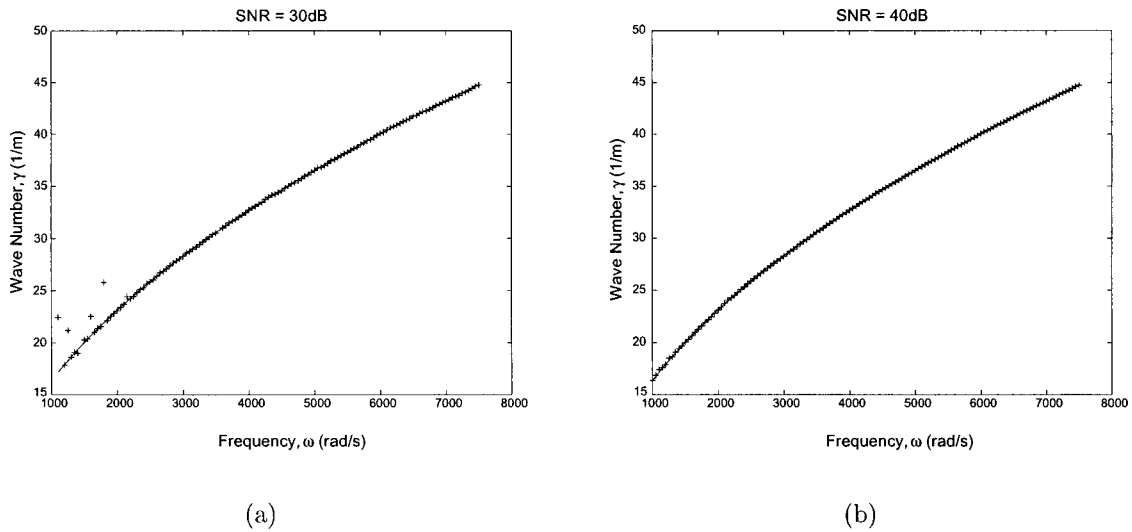


FIG. 5. Experimental (+) and analytic (—) dispersion curves for tapered beam after application of the maximum likelihood technique with (a) SNR=30 dB and (b) SNR=40 dB.

these signal-to-noise ratios, the maximum likelihood results are very close to the true values for the wave numbers. For the signal-to-noise ratio of 30 dB, the polynomial estimate had a mean error of 8.0%, which was improved to 0.6% upon application of the maximum likelihood technique. The standard deviation of the error was improved from 3.8% to 0.4% for the same case. For the 40-dB signal-to-noise level, the mean error was improved from 6.7% to 0.2% and the standard deviation from 3.4% to 0.04%.

Figure 6 demonstrates the typical improvement of the displacement estimate along the length of the beam when the wave number identified is improved through the use of maximum likelihood. The displacement estimate based upon the polynomial estimate of the wave number shows a significant phase shift from the actual displacement curve. The displacement fit using the improved wave number estimate is significantly improved and is practically indistinguishable from the actual displacement. This figure was generated based on data at 7000 rad/s with an SNR=30 dB.

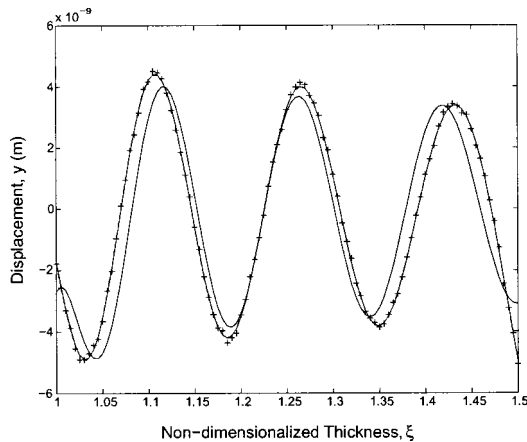


FIG. 6. Transverse displacement along a tapered beam with noisy data (+). Best fits after polynomial estimate (---) and maximum likelihood (···) compared to exact displacement (—).

V. GLOBAL MINIMIZATION AND NOISE EFFECTS

Noise affects the parameter estimation process in two ways. First, the maximum likelihood point shifts in parameter space, and second, the noise can give rise to poor initial estimates. For low signal-to-noise ratios, the maximum likelihood point wanders away from the noise-free parameters that were used to generate the data. This effect is especially apparent for the evanescent root of the uniform beam studied previously and shown in Fig. 7. Here, the parameters which yield a global minimum of the maximum likelihood error for the uniform beam—found through a grid search around the analytic solution—are plotted for signal-to-noise ratios of 20 and 25 dB. For these signal-to-noise ratios, a global minimization procedure is needed rather than a local gradient-based approach because the initial estimates provided by the OMEP technique are not sufficiently close to the true maximum likelihood point. At this SNR, the OMEP technique tends to estimate the propagating wave number accurately, but returns a second wave number which is nonphysical in nature. When the initial estimate falls outside of a convex basin around the global minima, the gradient-based approach may converge to a local minima rather than the global minima. However, the global maximum likelihood point does provide a best estimate of the wave numbers even for noise levels where other methods, like Prony-based techniques, fail to give a reasonable estimate.

If the noise is uncorrelated to the signal, averaging can reduce the deleterious effects of noise. As few as ten data sets provide a good deal of improvement to the averaged signal. If the noise is colored and the spectrum can be measured, then noise rejection techniques may be applied (Garth and Bresler, 1996; Zou and Lu, 1997).

VI. CONCLUSIONS

This work provides a robust method for estimating wave components on beam-like structures from noisy transverse vibration measurements. With a moderately accurate initial

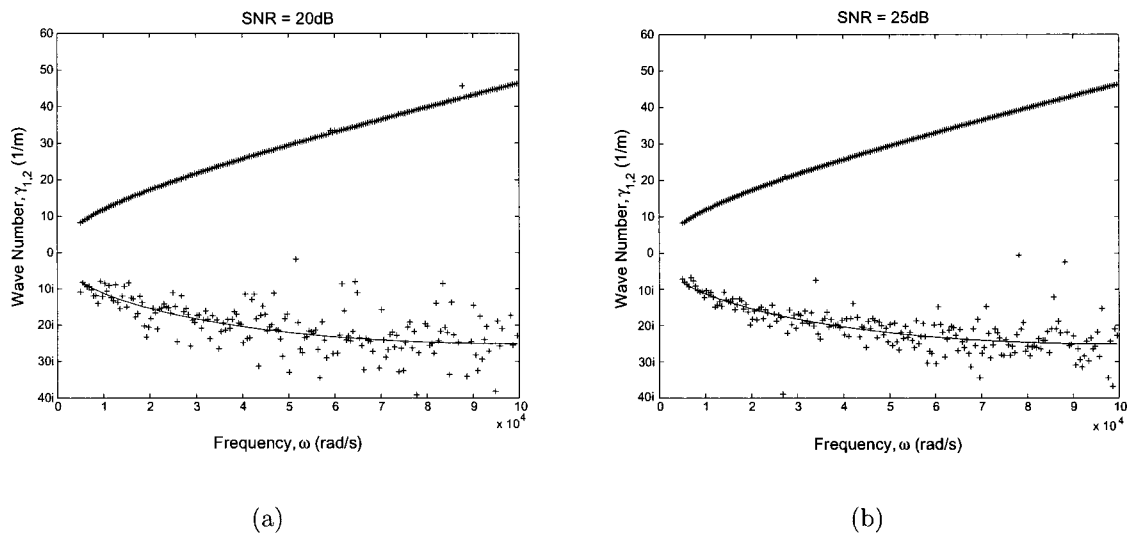


FIG. 7. Global minima of the maximum likelihood error (+) and analytic (—) dispersion curves for uniform beam with (a) SNR=20 dB and (b) SNR=25 dB.

prediction of the wave numbers present, the maximum likelihood technique applied herein returns a very accurate estimate of the wave components. While the initial estimates may be accurate enough for some applications, even a small error in the wave number can cause significant errors in the displacement. For structural intensity or energy loss measurements, these errors can be great enough as to preclude accurate results, thereby necessitating the maximum likelihood improvements.

The method discussed in this work may be applied to other structural acoustic problems where the solutions have variables which separate. These extensions include, but are not limited to, two-dimensional systems such as plates and membranes, and approximate solutions for other beams with slowly varying properties. Further, these identification techniques can provide a first step in measuring structural intensity and estimating unknown material properties.

Auciello, N. M., and Nolé, G. (1998). "Vibrations of a cantilever tapered beam with varying section properties and carrying a mass at the free end," *J. Sound Vib.* **214**(1), 105–119.

Bresler, Y., and Macovski, A. (1985). "Exact maximum likelihood estimation of superimposed signals in noise," in *Proceedings-ICASSP, IEEE International Conference on Acoustics, Speech and Signal Processing*, pp. 1824–1827.

Bresler, Y., and Macovski, A. (1986). "Exact maximum likelihood parameter estimation of superimposed exponential signals in noise," *IEEE Trans. Acoust., Speech, Signal Process.* **34**(5), 1824–1827.

Dennis, J. E., Jr., and Schnabel, R. B. (1983). *Numerical Methods for Unconstrained Optimization and Nonlinear Equations* (Prentice Hall, Englewood Cliffs, NJ).

Dieudonné, J. (1960). *Foundations of Modern Analysis* (Academic, New York).

Evans, G., and Fischl, R. (1973). "Optimal least squares time-domain synthesis of recursive digital filters," *IEEE Trans. Audio Electroacoust.* **21**(1), 61–65.

Garth, L. M., and Bresler, Y. (1996). "A comparison of optimized higher order spectral detection techniques for non-Gaussian signals," *IEEE Trans. Signal Process.* **44**(5), 1198–1213.

Golub, G. H., and Loan, C. F. V. (1989). *Matrix Computations* (The Johns Hopkins University Press, Baltimore).

Golub, G. H., and Pereyra, V. (1973). "The differentiation of pseudo-inverses and nonlinear least squares problems whose variables separate," *SIAM (Soc. Ind. Appl. Math.) J. Numer. Anal.* **10**(2), 413–432.

Grosh, K., and Williams, E. G. (1993). "Complex wave-number decomposition of structural vibrations," *J. Acoust. Soc. Am.* **93**, 836–848.

Guttman, I., Pereyra, V., and Scolnik, H. D. (1973). "Least squares estimation for a class of nonlinear models," *Technometrics* **15**(2), 209–218.

Hildebrand, F. B. (1956). *Introduction to Numerical Analysis* (McGraw-Hill, New York).

Kaufman, L., Sylvester, G., and Wright, M. (1994). "Structured linear least-squares problems in system identification and separable nonlinear data fitting," *SIAM J. Control Optim.* **4**, 847–871.

Kay, S. M. (1988). *Modern Spectral Estimation* (Prentice-Hall, Englewood Cliffs, NJ).

Kumaresan, R., and Tufts, D. W. (1982). "Estimating the parameters of exponentially damped sinusoids and pole-zero modeling in noise," *IEEE Trans. Acoust., Speech, Signal Process.* **30**(6), 833–840.

Kumaresan, R., Tufts, D. W., and Scharf, L. L. (1984). "A Prony method for noisy data: Choosing the signal components and selecting the order in exponential signal models," *Proc. IEEE* **72**(2), 1354–1355.

Marple, S. L., Jr. (1987). *Digital Spectral Analysis with Applications* (Prentice-Hall, Englewood Cliffs, NJ).

Osborne, M. R., and Smyth, G. K. (1995). "A modified Prony algorithm for exponential function fitting," *SIAM J. Sci. Comput. (USA)* **16**, 119–138.

Parthasarathy, S., and Tufts, D. W. (1985). "Maximum-likelihood estimation of parameters of exponentially damped sinusoids," *Proc. IEEE* **73**(10), 111–124.

Press, W. H., Teukolsky, S. A., Vetterling, W. T., and Flannery, B. P. (1992). *Numerical Recipes in FORTRAN 77*, 2nd ed. (Cambridge University Press, Cambridge).

Tufts, D. W., and Kumaresan, R. (1982). "Estimation of frequencies of multiple sinusoids: Making linear prediction perform like maximum likelihood," *Proc. IEEE* **70**(9), 975–989.

Tufts, D. W., and Kumaresan, R. (1980a). "Improved spectral resolution," *Proc. IEEE* **68**(2), 419–420.

Tufts, D. W., and Kumaresan, R. (1980b). "Improved spectral resolution II," in *Records of the IEEE International Conference on Acoustics, Speech and Signal Processing*, pp. 592–597.

Tufts, D. W., and Kumaresan, R. (1981). "A two-dimensional technique for frequency-wavenumber estimation," *Proc. IEEE* **69**(11), 1515–1517.

Zou, L., and Lu, J. (1997). "Linear associative memories with optimal rejection to colored noise," *IEEE Trans. Circuits Syst.* **44**(12), 990–999.

Comparison of moments and couple-generating forces near discontinuities in structural-acoustic systems

W. Steve Shepard, Jr.

Department of Mechanical Engineering, The University of Alabama, Box 870276, Tuscaloosa, Alabama 35487

(Received 23 May 2001; revised 11 December 2001; accepted 7 January 2002)

In modeling vibration isolators in structural-acoustic systems, the isolator's dynamic properties are often treated as acting only in the axial direction as moments are often neglected. Furthermore, the size, or scale, of the isolator is often neglected and the isolator is assumed to act at single points on the connected structures. Previous work has shown that concentrated moments can be particularly important when located near a fixed support or a structural discontinuity. This research extends that work to examine the importance of moment scale effects for a system containing a distributed structural discontinuity with its own scale. Moment scale effects are examined by determining the difference in radiated acoustic power for a simple system that is excited by a couple-generating distributed force and a concentrated moment. The distributed force produces a couple that is equivalent to the concentrated moment. As a result, only the scale is being examined. Particular interest occurs when the excitation is located near the structural discontinuity. Based on the cases studied here, moment scale is shown to be important at lower frequencies when the excitation is located near the edges of the discontinuity. At higher frequencies, any overlap of the excitation and discontinuity may warrant the need to consider moment scales. © 2002 Acoustical Society of America. [DOI: 10.1121/1.1456515]

PACS numbers: 43.40.Dx, 43.40.Rj [JGM]

I. INTRODUCTION

Vibration isolators are often used to isolate mechanical vibrations from some primary structure, as shown in Fig. 1. This application could be found in an office building or a shipboard environment. In many system-level analyses, the isolator is often modeled as a simple spring connected to each structure at a single mathematical point. The size of the contact region between the isolator and the primary structure, denoted by Δ_C in the figure, is often neglected in most analyses. Furthermore, moments due to rotations of the supported structure are usually neglected. Previous research, though, has shown that the presence of moments in the vicinity of structural discontinuities can have a dramatic impact on the system response. Although many issues related to rotational effects have been examined previously, the influence of the moment's physical size, also called the scale Δ_C , in the context of a fluid-loaded system containing a discontinuity with its own physical size, Δ_D , has not been investigated. The goal of this work, therefore, is to examine moment scale effects in the context of a structural-acoustic system containing a distributed discontinuity.

The importance of including moments in system dynamic models has previously been studied. Sanderson conducted an analytical and experimental study to investigate the impact of neglecting rotational effects when modeling isolators connected at a point.¹ Depending on the ratio of isolator stiffness to foundation stiffness, it was shown that the rotational degrees of freedom may be important at all frequencies. Sanderson and Petersson noted the increase of rotational velocities in beam- and plate-like structures at higher frequencies.¹⁻³ As a result, moments can be especially

important in these types of structures at higher frequencies. Goyder discussed the behavior of power flow associated with a moment excitation.⁴ For a force excitation, the power flow into a beam or plate structure tends to remain constant or decrease with frequency. For a moment, though, the power flow into these structures tends to increase with frequency. Other work has examined the impact of concentrated moments that are located near structural discontinuities. Petersson showed that when a moment is located near a structural discontinuity, the power flow in the structure can be important even at low frequencies.² This behavior could be especially important when designing isolators to be used in building or shipboard environments as these isolators tend to be located near structural stiffening components. Research on moment effects near discontinuities was recently extended by Shepard.⁵ In that work, the radiated acoustic power was computed for an axial force excitation. Then, the impact of adding a concentrated moment was examined. The system considered in that study, which was finite in the direction of wave propagation, was fluid-loaded and contained a distributed mass continuity. That study concluded that concentrated moments generally have the largest impact on the radiated acoustic power when located in the vicinity of the mass discontinuity. This work, like the others discussed above, was limited to addressing concentrated moments that act at a single point.

Some basic research on the spatial modeling requirements for isolators has also been conducted. Pinnington examined changes in the predicted structural response when using a continuous uniform isolator as opposed to a lumped isolator.⁶ That numerical and experimental work investigated

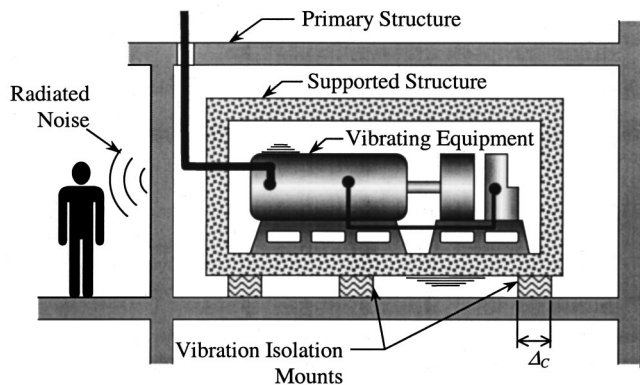


FIG. 1. Example vibration-isolation system with an isolation mount of scale Δ_C .

a finite supported structure connected to an infinite beam via a continuous uniform locally reacting spring. The performance metric of interest was the power transmitted through the isolator into an infinite structure. One conclusion was that at lower frequencies a distributed isolator could accurately be represented using a lumped parameter model (i.e., single connection point). The work of Petersson discussed above was also extended to compare the effects of a distributed moment on the response of a semi-infinite plate structure.⁷ This work was later continued by Fulford and Petersson⁸ to examine various issues related to moment modeling in isolators. Unlike a realistic isolator, though, the shape of the structure used to generate the moment distribution was annular in nature to facilitate a closed-form solution. Since a ring shaped contact region was used to facilitate a solution, the results of this work may not extend to analyses where the isolator contact region is circular or rectangular. Furthermore, the primary structures considered in these analyses were infinite in the direction of wave propagation and the power consideration solely focused on power transmitted into the structure.

Other works have considered the spatial scale effects of various attached substructures. It has been shown that the system response predicted using continuous substructure models can often differ from the predicted response when using discrete (i.e., lumped parameter) subsystems.^{9,10} Other studies have considered how the scale, or geometric size, of a distributed feature impacts the response of a simple system.¹¹⁻¹⁵ Examples of attached substructures include a simple mass or a spring-mass subsystem. Most of these efforts, though, only considered locally reacting subsystems with no rotational effects.

An example of when combined moment and scale effects may be important is the excitation of a common low-frequency mode that often occurs in a cylindrically shaped isolator, such as the one shown in Fig. 2. For this mode, a nodal plane is parallel to the line of action. As a result, the net force transmitted to the base is zero while a couple is generated on the below-mount structure due to the fact that the net forces on either side of the nodal plane have opposing phases. When this type of behavior occurs, the size of the isolator, denoted by scale Δ_C in the figure, may be important. The onset of these mode types for acoustically soft isolators

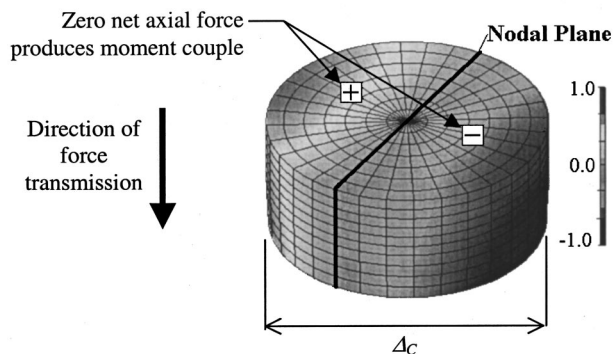


FIG. 2. Couple producing mode for a vibration isolator of scale Δ_C .

often occurs at frequencies that are not very high. As a result, moment scale effects may be important at relatively low frequencies in system-level analyses.

Many of the works that considered moments, as described above, examined primary systems that had an infinite dimension in at least one of the directions of wave propagation. These efforts were usually conducted for an *in vacuo* system and radiated acoustic power was not considered. Nevertheless, one is often interested in the amount of acoustics power that is radiated into an adjoining fluid. Furthermore, it is important to understand moment scale effects in the context of a fluid-loaded system containing a discontinuity where cross coupling is present. Both Petersson² and Shepard⁵ noted the importance of concentrated moments when structural coupling is present. Nevertheless, one cannot currently make any general conclusions from these works regarding the influence of moment scale on the predicted response of structural-acoustic systems.

This work compares the structural-acoustic response of a simple fluid-loaded plate system when a distributed couple-generating force of scale Δ_C is replaced by a concentrated moment of equal magnitude. The plate system, which radiates acoustic energy, is simply supported in a rigid baffle. For a portion of the study, the system will also contain a distributed mass discontinuity that is located away from the edge supports. As a result, the impact of a distributed force couple in the vicinity of a distributed discontinuity can be examined. The primary response metric of interest is the acoustic power radiated from the plate surface.

The following section provides a brief overview of the modeling associated with the plate system and the distributed mass discontinuity. Because it is desired to observe scale effects within the context of a fluid-loaded system containing a distributed discontinuity, no closed-form solution is readily available. The numerical modeling approach for the structure is based on Hamilton's principle while the acoustic modeling is based on the acoustic surface variational principle.^{16,17} A very brief overview of the plate and mass modeling is provided here for completeness although details associated with the modeling can be found in other works.^{5,12} Details associated with the derivation of the couple-generating force distribution as well as the concentrated moment excitation descriptions are provided in a later section. Note that while a concentrated excitation has been considered in another work,⁵ a distributed couple-generating excitation representa-

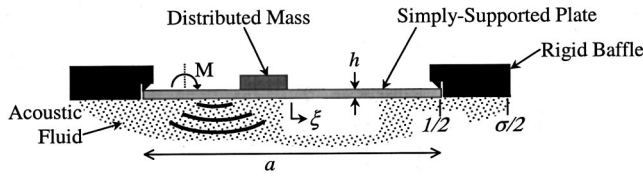


FIG. 3. Moment excited structural-acoustic plate system containing distributed mass discontinuity.

tion has not previously been considered. Finally, the numerical results for a few sample cases are discussed.

II. SYSTEM MODELING

A sketch of the system to be considered is shown in Fig. 3. This figure shows a cross section of the semi-infinite plate of width a . The nondimensional location on the plate is given by $\xi = x/a$ where $-1/2 \leq \xi \leq 1/2$. This portion of the paper is only concerned with the modeling of the acoustic fluid and structure.

The density of the acoustic fluid is ρ . The mass per unit surface area of the plate is $\rho_s h$, h is the plate thickness, ρ_s is the plate density, and the subscript s refers to steel. The characteristic wave speed for the structure, $c_s = \sqrt{D/\rho_s h a^2}$, depends on the plate bending stiffness, $D = Eh^3/(12(1-\nu^2))$, where E is the elastic modulus and ν is Poisson's ratio.

The surface response is represented by an M -term Ritz expansion¹¹ as

$$w(\xi, t) = a \sum_{j=1}^M \phi_j(\xi) q_j(t), \quad -\frac{1}{2} \leq \xi \leq \frac{1}{2}. \quad (1)$$

where

$$\phi_j = \sin[j\pi(\xi + 1/2)] \quad (2)$$

satisfy the geometric boundary conditions. The normal surface velocity is $v_n(\xi, t) = (-ika)w(\xi, t)$, where $ka = a\omega/c$ is the nondimensional wave number in the fluid, ω is the angular frequency, and c is the sound speed in the fluid. The harmonic time dependence, $\exp(-i\omega t)$, has been dropped to simplify notation. The surface pressure is expressed using an N -term expansion

$$p(\xi) = \sum_{l=1}^N \psi_l(\xi) p_l, \quad -\frac{\sigma}{2} \leq \xi \leq \frac{\sigma}{2}, \quad (3)$$

where the baffle size is denoted by σ and

$$\psi_l = \sin[l\pi(\xi/\sigma + 1/2)]. \quad (4)$$

The pressure is assumed to be zero beyond the distance $\xi = \sigma/2$ (see Refs. 14 and 18) with $\sigma = 5$.

The locally-reacting mass discontinuity is evenly distributed over a width Δ_D centered at $\xi = \xi_0$, as shown in Fig. 4. For this mass

$$m(\xi) = \frac{m_{\text{rat}}}{\Delta_D} [u(\xi - (\xi_0 - \Delta_D/2)) - u(\xi - (\xi_0 + \Delta_D/2))], \quad (5)$$

where $u(\xi)$ represents the unit step function, and m_{rat} is the amount of attached mass relative to the plate mass¹²

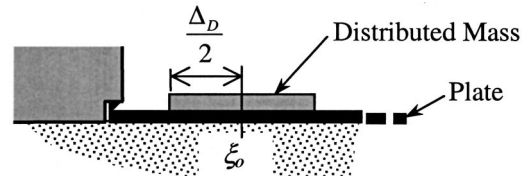


FIG. 4. Locally reacting distributed mass discontinuity of width Δ_D located at $\xi = \xi_0$.

$$m_{\text{rat}} = \frac{m_{\text{added}}}{\rho_s h a}. \quad (6)$$

Using the variational principle (SVP) to obtain the acoustic relationships and Lagrange's equation to obtain the structural relationships, an $M + N$ square system of coupled equations relating the surface pressure coefficients $\{p\}$, the surface response coefficients, $\{w\}$, and the excitation vector $\{F^e\}$, is obtained^{11,12}

$$\begin{bmatrix} [A] & -2\pi(ka)^2[R]^T \\ [R] & [D] \end{bmatrix} \begin{Bmatrix} \{p\} \\ \{w\} \end{Bmatrix} = \begin{Bmatrix} \{0\} \\ \{F^e\} \end{Bmatrix}, \quad (7)$$

where the superscript T refers to the matrix transpose. Detailed expressions for the individual terms can be found in Ref. 12. Fluid radiation is described by the $[A]$ matrix, fluid-structure coupling is described by the $[R]$ matrix, and the $[D]$ matrix describes the structural dynamics of the plate and the attached mass.

For the example cases presented below, the material and geometric properties are those for a plate submerged in seawater¹⁹

$$a/h = 25, \quad \rho_s/\rho = 7.58, \quad c_s/c = 3.84(h^2/12)^{1/2}.$$

In these examples, the highest frequency considered is $ka = 20$. The number of spatial functions used to describe the surface response, Eq. (1), and the surface pressure, Eq. (3), are $M = 20$ and $N = 100$, respectively. To ensure numerical convergence, it is necessary that the higher index coefficients have magnitudes much smaller than the coefficient with the largest magnitude. For example, at $ka = 20$ the displacement coefficients, q_j , for $j \geq 12$ are at least 30 dB smaller than the maximum valued coefficient. As a result, convergence is assured. For a more detailed discussion on convergence, see Ref. 14.

For a given structural configuration, Eq. (7) can be solved for the modal coefficients, p_l and w_j , once the excitation vector $\{F^e\}$ is defined. Then the surface displacement and pressure can be constructed from Eqs. (1) and (3), respectively. The derivation of $\{F^e\}$ for the excitations that will be considered is given in the following section.

Once the surface response is computed, the nondimensional radiated acoustic power per unit depth is¹⁴

$$\phi_{\text{rad}} = \frac{1}{2} \text{Re}(-ika\{p\}^T [R]^T \{q\}^*), \quad (8)$$

where $*$ denotes the complex conjugate. Although the primary response metric of interest here is the radiated acoustic power, other metrics could also be examined, such as the acoustic radiation modes.²⁰ Methods of using these modes

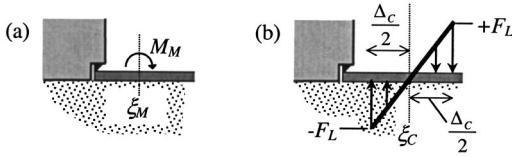


FIG. 5. Harmonic excitations, (a) line moment at $\xi = \xi_M$, and (b) couple-generating distributed line force of magnitude F_L and width Δ_C centered at $\xi = \xi_C$.

and other performance metrics have already been implemented in other works.¹²

III. HARMONIC EXCITATION DESCRIPTIONS

As noted above, the response of the system for a lumped moment excitation will be compared to the response found using a spatially distributed couple-generating force of equal magnitude. Examples of these two excitations are shown in Fig. 5. For the line-moment excitation shown in Fig. 5(a), all of the moment is concentrated at a single location ξ_M . This excitation will be used to compute a reference system response. For the force couple shown in Fig. 5(b), a force is spatially distributed over a width Δ_C centered about ξ_C . The force, which produces no net axial force, will be used to determine the impact of moment scales. The amplitude of the distributed excitation, F_L , will be varied so that as Δ_C is changed the total couple generated by the distribution remains constant. Details related to the modeling of these excitations follow.

For the lumped moment excitation with magnitude M_M located at $\xi = \xi_M$, Fig. 5(a), the forcing function is given by⁵

$$M(\xi) = M_M \delta(\xi - \xi_M) \quad (9)$$

and the corresponding terms of the excitation vector, $\{F^e\}$ in Eq. (7), are

$$F_j^e = M_M \phi_j'(\xi_M). \quad (10)$$

The derivative $\phi' = d\phi/d\xi$ follows directly from Eq. (2). These terms are used in Eq. (7) to compute the system response for a lumped moment excitation.

For a general force excitation $f(\xi)$, the terms of the excitation vector are given by¹¹

$$F_j^e = \int_{-1/2}^{1/2} f(\xi) \phi_j(\xi) d\xi. \quad (11)$$

For the forcing function shown in Fig. 5(b), the spatial distribution can be described by

$$f(\xi) = \begin{cases} \frac{2F_L}{\Delta_C}(\xi - \xi_C) & \text{for } (\xi_C - \Delta_C/2) \leq \xi \leq (\xi_C + \Delta_C/2) \\ 0 & \text{otherwise} \end{cases}. \quad (12)$$

It follows that the terms of the excitation vector become

$$F_j^e = \frac{2F_L}{\Delta_C} \int_{\xi_C - (\Delta_C/2)}^{\xi_C + (\Delta_C/2)} (\xi - \xi_C) \phi_j(\xi) d\xi \quad (13)$$

for the distributed couple-generating force. These terms are used in Eq. (7) to compute the system response for a distrib-

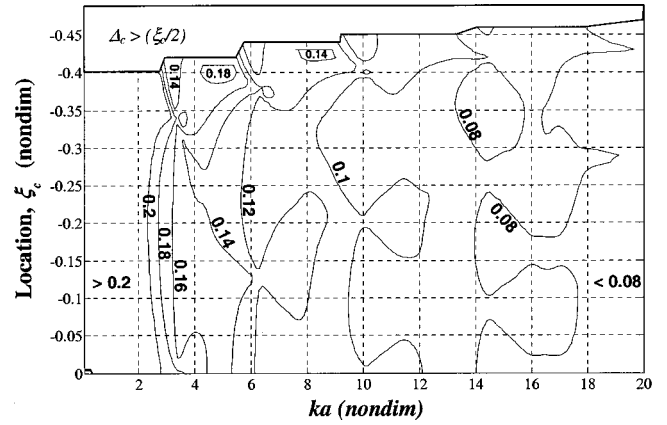


FIG. 6. Force couple scale, Δ_C , required to produce a ± 0.5 dB difference in radiated power for various locations ξ_C . No discontinuities.

uted couple. In order for this distributed force to generate a couple equivalent to the concentrated moment excitation given by Eq. (9) with $\xi_M = \xi_C$, it is required that

$$F_L = \frac{6M_M}{\Delta_C^2}. \quad (14)$$

In the example cases that follow, the difference in the system response due to a point moment excitation and a distributed couple excitation with scale Δ_C will be examined. Since it is only desired to examine the impact of moment scales, the distributed couple amplitude F_L will be maintained by Eq. (14) as Δ_C is changed for a given M_M . For example, if the scale of the force distribution is increased by a factor of 2, then the amplitude of the distribution will be decreased by a factor of 4 so that the couple is the same as that generated by the point moment. Since one excitation acts at a point while the other acts over a finite region of the plate, the response due to these excitations may be quite different.

IV. NUMERICAL EXAMPLES

Prior to addressing the impact of a moment and couple-generating force on the radiated acoustic power near a discontinuity, it is interesting to observe the impact of these excitations in a clean plate system (i.e., $m_{\text{rat}}=0$). The first few fluid-loaded resonances for this clean system occur around $ka=0.20, 1.4, 3.5, 6.4, 10, 14.4,$ and 19.3 (see Ref. 14). Figure 6 shows the couple scale, Δ_C , needed to produce a 0.5 dB change in the radiated acoustic power from the point moment excitation. The power is first computed using a point moment excitation at ξ_C as described in Eq. (9). The power is then computed for an equivalent strength distributed couple as described in Eq. (12) at the same location, $\xi_M = \xi_C$. The value of Δ_C required to produce a ± 0.5 dB change in the radiated power from the point excitation is shown in the figure. Note that when the excitation is located near the edge of the plate, $\xi_C = -0.5$, the value of Δ_C required may be larger than that physically possible, as the distributed couple cannot extend beyond the edges of the plate. This truncated data has been omitted from the plot. Note also that this plot is symmetric about $\xi_C = 0$. As can be seen in the figure, at low frequencies a large couple scale is

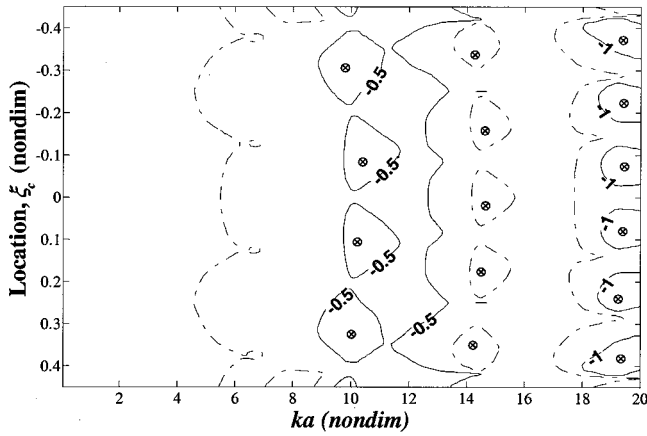


FIG. 7. Difference in radiated power for a clean system with $\Delta_c=0.10$. (— 0.50 dB increment; - - - 0.25 dB increment; \otimes and \odot see text.)

needed to generate a change in power. As the frequency increases, the scale of the couple needed to change the radiated power decreases. When the distributed couple is located near a minimum in the surface response, then the required couple scale decreases. For example, at approximately $ka=10$ a minimum in the surface response occurs near $\xi=-0.1$ since the $j=5$ term in Eq. (1) dominates the surface response of the plate. As a result, a relatively small couple scale produces a large change in power. At $ka=10$ and $\xi=-0.2$, though, the excitation is located near a maximum in the surface response, which is a region of minimum slope. Consequently, a larger scale is needed to result in an appreciable change in radiated power. These observations are not too surprising, as moments in general are known to have a larger impact when they are located near minimums in the surface response. As can be seen in the figure, the fluid-loaded resonances tend to delineate the general regions where the required couple scale decreases. It is worth noting that this plot applies for all values of M_M so long as M_M and F_L are related through Eq. (14). This is due to the fact that a relative comparison of power is being made and that the system is linear.

The change in radiated acoustic power for a clean plate with a fixed couple distribution width is shown in Fig. 7 for $\Delta_c=0.10$, $\xi_M=\xi_C$, and a range of excitation locations. This difference, or change, in power can be mathematically represented as

$$\text{dB} = 10 \log_{10} \left(\frac{\varphi(F_L, \Delta_C)}{\varphi(M_M)} \right), \quad (15)$$

where the three variables are related through Eq. (14). This difference represents the error in the predicted power when a distributed couple is replaced by the simpler concentrated moment representation. For this and all subsequent figures, the contour lines are shown at 0.25 dB increments. Furthermore, the solid lines represent values that are multiples of ± 0.50 dB and the intermediate values, which are in odd increments of ± 0.25 dB, are represented as dotted-dashed lines. The \otimes symbol in the enclosed region denotes values that are less than the surrounding region (i.e., more negative) and the \odot symbol denotes values that are larger than the surrounding region (i.e., less negative). Additionally, for all

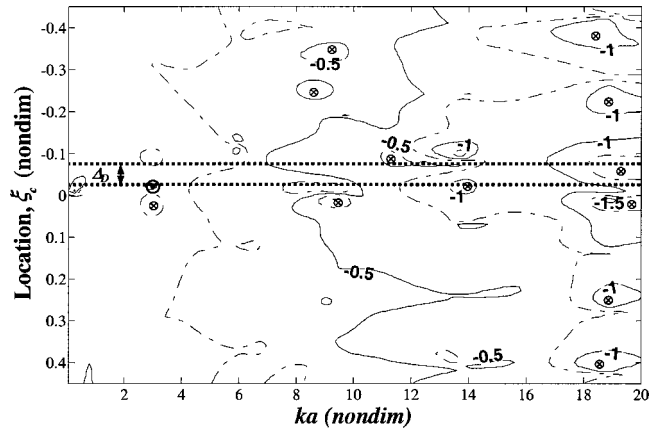


FIG. 8. Difference in radiated power for a system with $\Delta_c=0.10$. Mass discontinuity of $m_{\text{rat}}=0.40$, $\Delta_D=0.05$, located at $\xi_0=-0.05$ (discontinuity region denoted by \cdots).

power comparisons $\xi_M=\xi_C$. Since the system is linear and a relative comparison of power is being made, this and all subsequent figures apply for any value of M_M . Due to the size of couple distribution, with $\Delta_c/2=0.05$, the location ξ_C is limited to those values where the distribution is entirely on the plate, $-0.45 \leq \xi_C \leq 0.45$. Generally, the difference in power increases as frequency increases. At lower frequencies, there is basically no difference in the radiated power when a distributed couple-generating force of scale $\Delta_c=0.10$ is replaced by a concentrated moment. At higher frequencies, the difference in power for these two excitations increases. The general trend is for the point moment to generate a higher radiated acoustic power as most of the values in the figure are less than zero. When the distributed couple is located near a minimum in the surface response, such as for $ka=10$, $\xi=\pm 0.30$, and $\xi=\pm 0.10$, the general trend is to cause a more noticeable decrease in power from the concentrated moment case. Likewise, when the excitations are located near a maximum in the surface response, such as for $ka=10$ and $\xi=\pm 0.20$, the difference in radiated power is generally not as large. Similar behavior can be observed at higher frequencies. In the cases considered thus far, the plate system has been clean. As noted above, there is particular interest in the impact of a distributed force in a system containing a distributed discontinuity. A few example cases for this type of system will now be considered.

Figure 8 shows the difference in radiated power for a system that includes a distributed mass of $m_{\text{rat}}=0.40$, $\Delta_D=0.05$, located at $\xi_0=-0.05$. The other system parameters are the same as those used for Fig. 7. In Fig. 8 and all subsequent figures, the straight dark dashed lines are used to denote the locations of the mass distribution edges. Because the mass of the system has been altered, the fluid-loaded system resonances have a slightly lower value than those listed above. When the excitation is located away from the discontinuity, the general behavior is the same as that discussed for Fig. 7. When the excitation is located near the discontinuity, though, the behavior is somewhat different. At low frequencies, when the center of the couple distribution is near the edge of the discontinuity with only a partial overlap, the impact of replacing the distributed couple with a concen-

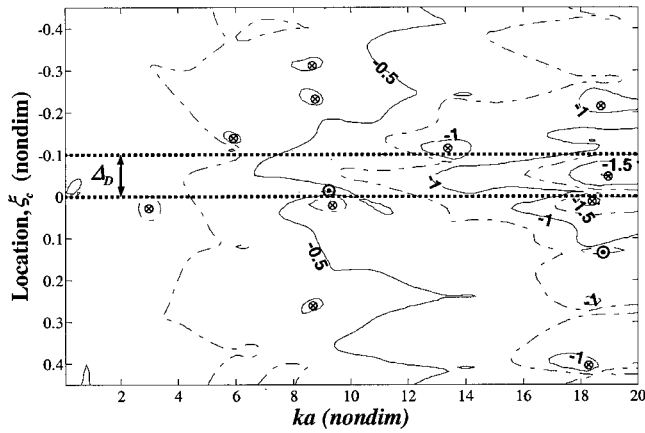


FIG. 9. Difference in radiated power for a system with $\Delta_c=0.10$. Mass discontinuity of $m_{\text{rat}}=0.40$, $\Delta_D=0.10$, located at $\xi_0=-0.05$.

trated moment is to produce a more noticeable change in radiated power. Near $ka=6$ and $ka=9$ a distributed couple located near the discontinuity can produce a power that is more than 0.5 dB different from the concentrated moment power. This is in contrast to Fig. 6 where a slightly larger scale Δ_c was required. Consequently, the addition of a distributed mass discontinuity has slightly enhanced the impact of the couple-generating force distribution at these two frequencies. At higher frequencies, there is also a noticeable difference in radiated power when the force distribution is in the vicinity of the discontinuity. Near $ka=19$, there is an impact when the center of the distribution overlaps the discontinuity. For other discontinuity locations, such as $\xi_0=-0.20$, the behavior at both low and high frequencies, although not shown, is similar to that shown in Fig. 8. Furthermore, the behavior at low frequencies is the same for smaller discontinuity widths, such as $\Delta_D=0.01$. For this more localized discontinuity, the behavior at higher frequencies only varies slightly from that shown in Fig. 8.

When the scale of the discontinuity is increased, the impact of replacing a distributed couple with a concentrated excitation at higher frequencies is even more pronounced, as shown in Fig. 9 for $\Delta_D=0.10$. For this case, the scales of the discontinuity and force distribution are equal. The other system parameters are the same as for Fig. 8. Recall that the total mass of the discontinuity is the same as for the previous case. Only the region of the distribution and mass density have changed. As in the previous case, the impact at lower frequencies is pronounced when the center of the force distribution is close to the edge of the discontinuity. The influence of replacing a distributed couple with a concentrated moment for a larger discontinuity becomes even more pronounced at higher frequencies, such as near $ka=16$.

When the scale of the discontinuity is further increased, such as for $\Delta_D=0.15$ and $\xi_0=-0.20$ in Fig. 10, the region of locations ξ_c where an appreciable radiated power difference is observed at higher frequencies further increases. Note that when the scale of the discontinuity Δ_D is changed, there is a slight change in the fluid-loaded resonances. As can be seen in the figure, the impact at higher frequencies occurs over a broader range of excitation locations ξ_c for frequencies above $ka=10$. There can be an appreciable change in

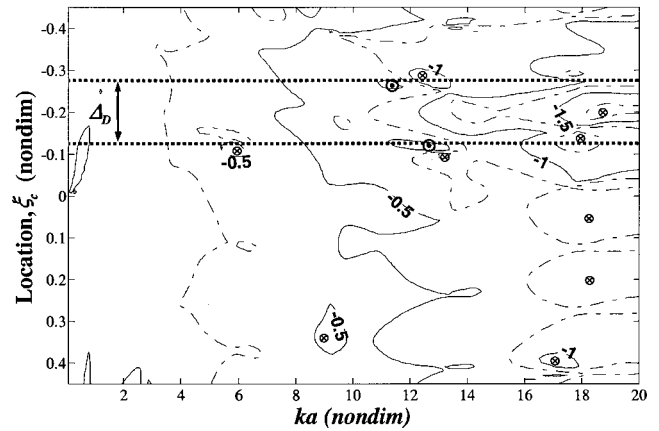


FIG. 10. Difference in radiated power for a system with $\Delta_c=0.10$. Mass discontinuity of $m_{\text{rat}}=0.40$, $\Delta_D=0.15$, located at $\xi_0=-0.20$.

radiated power for this case between the fluid-loaded resonances. Although not shown, the behavior when ξ_c is near ξ_0 is similar for the same discontinuity at other locations, such as $\xi_0=-0.05$.

The difference in radiated power for a more localized discontinuity and a broader couple distribution is shown in Fig. 11. This case is for a discontinuity distributed over $\Delta_D=0.07$ and $\Delta_c=0.12$ with $m_{\text{rat}}=0.40$ and $\xi_0=-0.15$. As before, when the distributed force is located near the edge of the discontinuity, the difference in power at lower frequencies can be greater than for other locations. At higher frequencies, though, almost any degree of overlap between the distributed force excitation and the discontinuity results in a much greater change in acoustic power. It is interesting to note that for the seventh fluid-loaded resonance, which occurs around $ka=19$, the term that dominates the plate response has a quarter-wavelength that is approximately equal to the size of the discontinuity, $\Delta_D=0.07$. Near $ka=19$, there are large values of power difference when the excitation is located near the edges of the discontinuity. For this case, the size of the force distribution is approximately equal to a quarter-wavelength for a fluid-loaded plate resonance around $ka=3.5$. As shown in the figure, there can be a noticeable change in the power at frequencies above $ka=3.5$

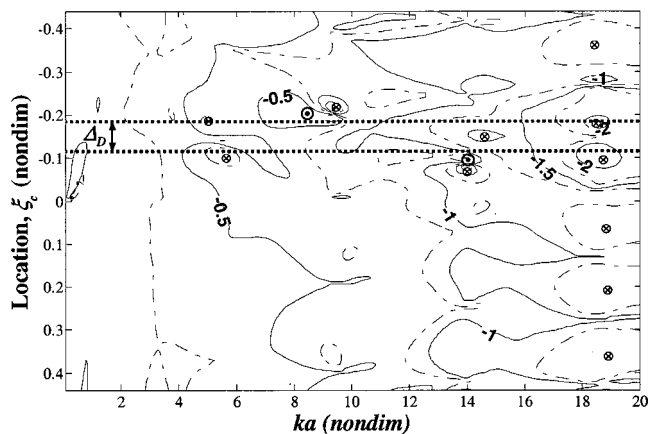


FIG. 11. Difference in radiated power for a system with $\Delta_c=0.12$. Mass discontinuity of $m_{\text{rat}}=0.40$, $\Delta_D=0.07$, located at $\xi_0=-0.15$.

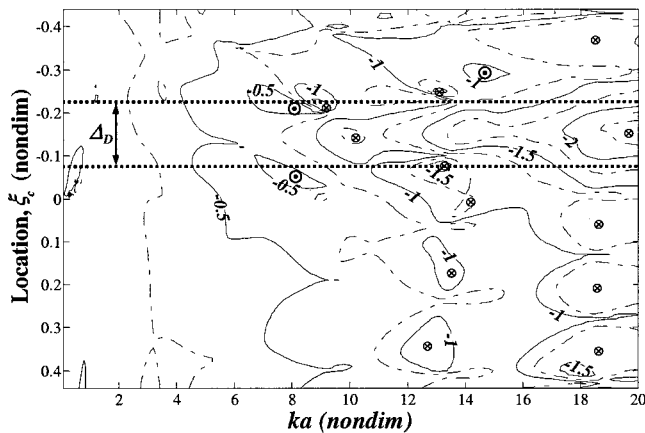


FIG. 12. Difference in radiated power for a system with $\Delta_C=0.12$. Mass discontinuity of $m_{rat}=0.40$, $\Delta_D=0.15$, located at $\xi_0=-0.15$.

when the center of the force distribution is near the edges of the discontinuity. Nevertheless, for ka greater than 10, almost any overlap between the couple and the discontinuity can result in an appreciable difference in power from the concentrated moment solution.

Finally, Fig. 12 shows the difference in radiated power for a more distributed discontinuity of $\Delta_D=0.12$. All of the other system parameters are the same as for the previous figure. The most apparent difference from the previous figure occurs for frequencies greater than $ka=10$. The impact of a distributed couple at higher frequencies increases with the amount of overlap between the excitation and the discontinuity. For the previous figure, this was not necessarily the case. In that figure, the scale of the mass discontinuity was less than that of the distributed excitation. When the excitation was centered over the mass, extending beyond both sides, the impact was not as great as when the excitation was centered near the edge of the discontinuity and extended beyond only one side. This behavior is likely due to the fact that when the excitation is centered over the mass, any inertial forces of the mass would only provide a slight impact on the excitation. When the center of the excitation is near the edge of the mass, however, the inertial reactions tend to reduce the moment generated by the distributed excitation making it appear more like an axial force. Of course, it is difficult to make general conclusions from this behavior based on the limited results presented here. For the current case of Fig. 12, the excitation can only extend beyond the discontinuity on one side since the discontinuity scale is larger than the excitation scale. Therefore, an impact for this case is observed for any overlap at higher frequencies. The influence at lower frequencies is not quite so apparent when the center of the force distribution is located near the edge of the discontinuity. This is likely due to the decrease in mass density of the discontinuity and inertial effects. Nevertheless, the impact, although not as dramatic as Fig. 11, is present near $ka=6$. At this frequency, the difference in power near the edge of the discontinuity is greater than for locations away from the discontinuity or when centered over the discontinuity. It is worth noting that for frequencies between the fluid-loaded resonances, the impact at locations away from the more distributed discontinuity is not as great as for the

more localized discontinuity. For example, with $\Delta_D=0.07$, Fig. 11, the difference in power between $ka=14$ and $ka=16$ and $0.20 \leq \xi_C \leq 0.40$ is generally higher than for the same range of frequencies and locations for $\Delta_D=0.15$ in Fig. 12. The difference, although present, is not very large. The behavior is not as apparent when comparing Figs. 8 and 9. As a result, it is difficult to make any conclusions regarding this behavior based on the figures.

V. SUMMARY

This research has focused on the examination of moment scale effects for systems containing a structural discontinuity with its own scale. The system considered was a semi-infinite fluid-loaded plate that radiates acoustic energy. The discontinuity considered here was a distributed locally reacting line mass. To investigate moment scale effects, the structural-acoustic response of the system was first computed using a concentrated moment at various excitation locations. Then, the concentrated moment was replaced by an equivalent strength couple-generating distributed force with a specified scale (i.e., size). The primary response metric of interest was the difference in the radiated acoustic power for the system response due to these two excitations. This difference in power is essentially the error one would obtain in a response prediction by replacing a distributed couple by the simpler concentrated moment representation.

Several example system configurations were considered. Based on the example cases considered here, the impact of a distributed couple depends primarily on the excitation frequency and the excitation location relative to the discontinuity location. At relatively low excitation frequencies, the use of a distributed force couple has the largest impact when the excitation center is located near the edge of the discontinuity. At higher frequencies, there are two excitation locations of concern. When the excitation is located near a minimum in the system response, such as near a node, the impact of replacing a distributed couple by a concentrated moment tends to be greater than when located near a maximum in the response. This observation is not surprising. When the excitation is located in the vicinity of a distributed discontinuity, replacing a distributed couple with a concentrated moment tends to result in a larger error in the predicted power. The errors in power can be large when the excitation is located near the edge of the discontinuity as well as with significant overlap between the force distribution and the discontinuity.

¹M. A. Sanderson, "Vibration isolation: Moments and rotations included," *J. Sound Vib.* **198**, 171–191 (1996).

²B. A. T. Pettersson, "Structural acoustic power transmission by point moment and force excitation, Part I: Beam- and frame-like structures," *J. Sound Vib.* **160**, 43–66 (1993).

³B. A. T. Pettersson, "Structural acoustic power transmission by point moment and force excitation, Part II: Plate-like structures," *J. Sound Vib.* **160**, 67–91 (1993).

⁴H. G. D. Goyder and R. G. White, "Vibrational power flow from machines into built-up structures, Part III: Power flow through isolation systems," *J. Sound Vib.* **68**, 97–117 (1980).

⁵W. S. Shepard, Jr., "The impact of moments near discontinuities in structural-acoustic systems," *J. Vib. Acoust. Trans. ASME* (submitted).

⁶R. J. Pinnington, "Vibrational power transmission from a finite source beam to an infinite receiver beam via a continuous complaint mount," *J. Sound Vib.* **137**, 117–129 (1990).

- ⁷B. A. T. Petersson, "Efficiency of annularly distributed moment and force excitation regarding structural acoustic power transmission to plate-like structures," *J. Sound Vib.* **176**, 625–639 (1994).
- ⁸R. A. Fulford and B. A. T. Petersson, "The role of moments on the vibration transmission in built-up structures," *J. Sound Vib.* **227**, 479–510 (1999).
- ⁹D. Feit and S. Johnson, "Scattering by a mass inhomogeneity on a fluid-loaded elastic plate," *J. Acoust. Soc. Am.* **90**, 2309 (1991).
- ¹⁰D. Feit and J. M. Cuschieri, "Scattering of sound by a fluid-loaded plate with a distributed mass inhomogeneity," *J. Acoust. Soc. Am.* **99**, 2686–2700 (1996).
- ¹¹J. H. Ginsberg, K. A. Cunefare, and H. Pham, "Spectral description of inertial effects in fluid-loaded plates," *J. Vibr. Acoust.* **117**, 206–212 (1995).
- ¹²W. S. Shepard, Jr. and K. A. Cunefare, "Sensitivity of structural acoustic response to attachment feature scales," *J. Acoust. Soc. Am.* **102**, 1612–1619 (1997).
- ¹³W. S. Shepard, Jr., K. A. Cunefare, and J. H. Ginsberg, "Identifying critical elastic scales in structural-acoustic models," *J. Vibr. Acoust.* **120**, 455–460 (1998).
- ¹⁴W. S. Shepard, Jr., Ph.D. thesis, Georgia Institute of Technology, 1996.
- ¹⁵K. A. Cunefare, W. S. Shepard, Jr., and J. H. Ginsberg, "Spectral investigation of spatial scales associated with substructures on a fluid-loaded plate," *J. Acoust. Soc. Am.* **95**, 2846 (1994).
- ¹⁶X. F. Wu, M.S. thesis, Georgia Institute of Technology, 1984.
- ¹⁷X. F. Wu and A. D. Pierce, "Uniqueness of solutions to variationally formulated acoustic radiation problems," *J. Vibr. Acoust.* **112**, 263–267 (1990).
- ¹⁸J. H. Ginsberg and P. Chu, "Asymmetric vibration of a heavily fluid-loaded circular plate using variational principles," *J. Acoust. Soc. Am.* **91**, 894–906 (1992).
- ¹⁹S. Alper and E. B. Magrab, "Radiation from the forced harmonic vibrations of a clamped circular plate in an acoustic fluid," *J. Acoust. Soc. Am.* **48**, 681–691 (1970).
- ²⁰M. N. Currey and K. A. Cunefare, "The radiation modes of baffled finite plates," *J. Acoust. Soc. Am.* **98**, 1570–1580 (1995).

Global damping of noise or vibration fields with locally synthesized controllers

Jing Yuan^{a)}

Department of Mechanical Engineering, The Hong Kong Polytechnic University, Hunghom, Kowloon, Hong Kong

(Received 14 May 2001; revised 21 November 2001; accepted 7 January 2002)

A locally synthesized controller (LSC) is one that uses a local feedback signal in a noise or vibration field (VF) to synthesize the actuation signal. The global damping of a VF by available LSCs requires sensor–actuator collocation. This study presents a LSC for the global damping of a VF without requiring sensor–actuator collocation, which is important to noise control applications where a sensor may be placed away from an actuator to avoid the near field effects. It is proven that the LSC damps the entire VF instead of just a local feedback loop. This is different from other LSCs that may control local feedback loops without damping the VFs. A decentralized control law is presented here to extend the LSC to a decentralized damping system using multiple actuators. © 2002 Acoustical Society of America. [DOI: 10.1121/1.1456516]

PACS numbers: 43.40.Vn, 43.50.Ki [JGM]

I. INTRODUCTION

This study investigates active control of noise and vibration in the low frequency ranges. Both the noise and vibration fields will share the abbreviation “VF,” which stands for a vibration field, since sound is the vibration of air and a noise field can be modeled with modal theory or transfer functions like a vibration field. The scope of this study is active damping of a VF by feedback control—an important feature not possessed by feedforward controllers. While one may combine feedback and feedforward control to utilize the advantages of both strategies, concentrating on feedback control would keep a better focus on the main scope.

The well-known modal theory enables a control engineer to decouple the dynamics of a VF into m second-order differential equations when the model is properly truncated.¹ Most feedback controllers for VFs are based on modal space feedback,^{2,3} though some researchers use physical state feedback⁴ to avoid estimating the modal states. These controllers use global states of the VFs to synthesize the actuation signals. They are named “globally synthesized controllers” (GSCs) to distinguish them from the “locally synthesized controller” (LSC) whose actuation signal is synthesized from a local feedback signal.

It is believed that the number of actuators should equal the number of modes to be attenuated for active damping of a VF. An optimization method is available to reduce the number of actuators.⁵ Recent studies showed the possibility of using one actuator to attenuate multiple modes simultaneously.^{6–8} These GSCs require exact model parameters to calculate the feedback gains. The model parameters, such as mode functions, are not always available as discussed in Banks *et al.*⁹ Some of the GSCs avoid the mode functions by means of the multiple spring-mass^{4,7} or finite element⁸ models, but still depend on other parameters such as mass and stiffness of the finite elements, etc.

LSCs, which are much less model dependent, may be needed if model parameters are not available, or not accurate enough, for VFs with irregular geometric shapes and boundary conditions. The first LSC for active damping may be traced back to Olson and May.¹⁰ Clark and Cole¹¹ presented a direct rate feedback LSC for the same purpose, which requires sensor–actuator collocation. Many LSCs use high gains to suppress the feedback signals. This will drive the closed-loop poles toward zeros of the open-loop transfer functions.¹² It requires that open-loop transfer functions be minimum phase, which is true for collocated sensor–actuators but is not necessarily true otherwise. Driving the poles of a closed loop toward the open-loop zeros does not damp the VF, as explained in Sec. III.

This study presents a LSC to damp an entire VF while relaxing the minimum phase restriction. This is important for noise control in which case transfer functions are very likely nonminimum phase. The pole placement control is applied to modify eigenvalues of a VF. A designer can select closed-loop poles instead of driving them toward open-loop zeros. The LSC is based on a transfer function available by either on-line or off-line identification, and hence may be adaptive to deal with parameter drifting.¹³ While structural systems tend to be fairly stable, it is not uncommon for parameters of a noise field to drift with time. Being able to adapt with respect to possible parameter drifting is an advantage of the LSC. For best focus, this paper analyzes the global damping effect of the LSC. Stability and robustness of the adaptive version are discussed in a separate paper.¹³

The implementation of active control for a VF will involve filters in the system. A popular way to analyze the filter effects is to use truncated models,^{4,6–8} which is equivalent to the use of *ideal filters* to cut-off the uncontrolled modes and leave the controlled modes intact. This study takes a new approach in the LSC design. The actuator, sensor, and filter dynamics are described by transfer functions. Both the controlled and uncontrolled modes are studied analytically to address the concern of possible spillover in the presence of

^{a)}Electronic mail: mmjyuan@polyu.edu.hk

realistic filters. The LSC design procedure may be modified, when necessary, to design decentralized LSCs for active damping of a VF using multiple actuators. All features of the LSC will be explained analytically and numerically in this paper.

II. MATHEMATICAL MODEL

The dynamics of a VF, subject to the excitation of an actuator, can be described by a general second-order equation

$$(\mathbf{M}s^2 + \mathbf{K})\mathbf{q} = \mathbf{b}f + \mathbf{d}, \quad (1)$$

where \mathbf{M} , $\mathbf{K} \in R^{m \times m}$ are the mass and stiffness matrices; $\mathbf{q} \in R^m$ is the generalized displacement vector; $\mathbf{b} \in R^m$ the actuator location vector; $\mathbf{d} \in R^m$ the disturbance vector and f a scalar control signal. Matrices \mathbf{M} and \mathbf{K} are symmetric and positive definite, but not necessarily diagonal or band diagonal. The equation is expressed in the Laplace transform domain. One may derive it with different approaches, such as the finite element method, multiple spring-mass modeling, Rayleigh–Ritz approximation, or modal analysis with a proper truncation. This study uses the properties of Eq. (1) for analysis only. Unless stated specifically, model parameters are used here with assumed *existence*, but not *availability*.

If Eq. (1) is derived by modal analysis, then \mathbf{q} is the modal state vector. The local feedback signal is given by

$$y = \mathbf{h}^T \mathbf{q}, \quad (2)$$

where $\mathbf{h}^T = [\varphi_1(x_s), \dots, \varphi_m(x_s)]$ and $\varphi_i(x_s)$ is the i th eigenfunction sampled at the sensor location x_s . Similarly, the actuator location vector is $\mathbf{b}^T = [\varphi_1(x_a), \dots, \varphi_m(x_a)]$ with $\varphi_i(x_a)$ taken at the actuator location x_a . If Eq. (1) represents a multiple spring-mass system, then $\mathbf{h} = \mathbf{e}_i$ and $\mathbf{b} = \mathbf{e}_j$ where

$$\mathbf{e}_i = \underbrace{[0 \ \cdots \ 0]_{i-1 \text{ zeros}}} \underbrace{[1 \ 0 \ \cdots \ 0]_{m-i \text{ zeros}}}^T.$$

The underlying assumption is that the sensor and the actuator are attached to the i th and j th bodies, respectively.

For vibration control, it is common to collocate the sensor with the actuator so that $\mathbf{h} = \mathbf{b}$. For noise control, however, the sensor may be placed away from the actuator to avoid the near field. Therefore \mathbf{h} is not necessarily \mathbf{b} . The normalized version of \mathbf{h} may be denoted as \mathbf{h}_n . Its null space is spanned by $m-1$ unit length and orthogonal basis $\{\boldsymbol{\zeta}_1 \cdots \boldsymbol{\zeta}_{m-1}\}$ with $\mathbf{h}^T \boldsymbol{\zeta}_i = 0$ for $1 \leq i \leq m-1$. The existence of these vectors implies the existence of an orthogonal matrix $\mathbf{H} = [\mathbf{h}_n \boldsymbol{\zeta}_1 \cdots \boldsymbol{\zeta}_{m-1}]$, such that $\mathbf{x} = \mathbf{H}^T \mathbf{q}$ and $\boldsymbol{\Lambda}(s) = \mathbf{H}^T (\mathbf{M}s^2 + \mathbf{K}) \mathbf{H}$. Therefore Eq. (1) is equivalent to

$$\boldsymbol{\Lambda}(s)\mathbf{x} = \boldsymbol{\beta}f + \boldsymbol{\eta}, \quad (3)$$

where $\boldsymbol{\beta} = \mathbf{H}^T \mathbf{b}$ and $\boldsymbol{\eta} = \mathbf{H}^T \mathbf{d}$. While Eq. (3) describes a multivariable system, the LSC is based on a single-input single-output (SISO) local plant. The feedback signal, given by Eq. (2), is actually $y = hx_1$ where $h = \|\mathbf{h}\|$. The Cramer's rule suggests

$$y = hx_1 = h \frac{\det[\boldsymbol{\Lambda}_1(s), \boldsymbol{\beta}]f + \det[\boldsymbol{\Lambda}_1(s), \boldsymbol{\eta}]}{\det[\boldsymbol{\Lambda}(s)]}, \quad (4)$$

where $[\boldsymbol{\Lambda}_1(s), \boldsymbol{\beta}]$ and $[\boldsymbol{\Lambda}_1(s), \boldsymbol{\eta}]$ are matrices obtained by replacing the first column of $\boldsymbol{\Lambda}(s)$ with vectors $\boldsymbol{\beta}$ and $\boldsymbol{\eta}$, respectively.

Before LSC design, a control engineer may apply a probing signal $f = F_a(s)u$ to excite the VF, where $F_a(s)$ is the actuator filter and u is a pseudorandom noise. The feedback sensor measures $v = F_s(s)y$ that will be used to identify the transfer function. Here $F_s(s)$ represents the sensor filter. Polynomials $\det[\boldsymbol{\Lambda}(s)]$ and $\det[\boldsymbol{\Lambda}_1(s), \boldsymbol{\beta}]$ have degrees $2m$ and $2m-2$, respectively. Many algorithms¹⁴ are available to identify an autoregressive and moving-average plant like Eq. (4). Any one of these algorithms may be applied to obtain

$$v(s) = \frac{h \det[\boldsymbol{\Lambda}_1(s), \boldsymbol{\beta}]N_s(s)N_a(s)u(s) + \epsilon}{\det[\boldsymbol{\Lambda}(s)]D_s(s)D_a(s)} \quad (5a)$$

where

$$\epsilon = hN_s(s)D_a(s)\det[\boldsymbol{\Lambda}_1(s), \boldsymbol{\eta}] \quad (5b)$$

represents the effect of disturbance filtered by the sensor; $N_s(s)$, $N_a(s)$, $D_s(s)$, and $D_a(s)$ are the numerators and denominators of filter transfer functions $F_s(s)$ and $F_a(s)$, respectively.

Both Eqs. (4) and (5) are valid models of a SISO local plant for a specific actuator and feedback sensor loop. The latter includes actuator and sensor dynamics $f = F_a(s)u$ and $v = F_s(s)y$. Model parameters of a VF are not necessarily available, but the numerator and denominator of Eq. (5) can be identified from measurement data. These polynomials may share some common roots. Therefore one may express

$$h \det[\boldsymbol{\Lambda}_1(s), \boldsymbol{\beta}]N_s(s)N_a(s) = N(s)C(s), \quad (6a)$$

$$\det[\boldsymbol{\Lambda}(s)]D_s(s)D_a(s) = D(s)C(s), \quad (6b)$$

where $C(s)$ is a common divisor, and $N(s)$ and $D(s)$ are coprime factors for the numerator and denominator of Eq. (5a).

Equation (6) enables one to express Eq. (5a) as

$$v(s) = \frac{N(s)}{D(s)}u(s) + \frac{\epsilon(s)}{D(s)C(s)}.$$

The coprime pair $N(s)$ and $D(s)$ makes a controllable feedback loop transfer function,¹⁴ which is identified when $\epsilon = 0$ and denoted by

$$\frac{v(s)}{u(s)} = \frac{N(s)}{D(s)} = T(s).$$

Common divisor $C(s)$, according to control theory,¹⁴ contains poles of uncontrollable modes to be “canceled out” in $T(s)$. It is important to know which modes are controllable by $T(s)$ in order to select sensor–actuator locations. If the roots of $D(s)$ are distinct, then the partial fraction expansion theory¹⁵ implies

$$T(s) = \frac{N(s)}{D(s)} = M(s) + \sum_{k=1}^n \frac{c_k}{s^2 + \omega_k^2}, \quad (7a)$$

where $M(s)$ contains terms contributed by poles of actuator–sensor filters and ω_k is the k th resonant frequency of the controllable modes. If $D(s)$ has a pair of second-order roots $\pm j\omega_n$, then one has another partial fraction expansion

$$T(s) = \frac{N(s)}{D(s)} = M(s) + \sum_{k=1}^{n-1} \frac{c_k}{s^2 + \omega_k^2} + \frac{sc_{n1} + c_{n2}}{(s^2 + \omega_n^2)^2}. \quad (7b)$$

Similar expansions can be derived for the cases where $D(s)$ has one or more high-order roots. In any events, the right-hand side of Eq. (7) contains resonant peaks of controllable modes. These peaks are visible via an off-line fast Fourier transform analyzer connected to both ends of the feedback loop. A count of the resonant peaks helps one to identify the modes controllable by a specific loop from the actuator to the sensor.

For active control of a VF, controllability depends on the actuator location while observability depends on the sensor location. Both GSCs and LSCs face the problem of selecting actuator and sensor locations. A controllability or observability check of a GSC requires exact model parameters. For a LSC, such a check is much easier, thanks to the hint of Eq. (7). The first step is to use a probing device to select the feedback sensor location, where the sensor should be able to measure a selected or maximum number of resonant peaks excited by the disturbance. Empirically, this is a spot in a VF where vibration or noise is most significant. The actuator should then collocate with the feedback sensor wherever possible. Otherwise, one should select an actuator location near the feedback sensor such that it excites a selected or maximum number of resonant peaks measurable by the feedback sensor. This is possible by trial and error without knowing exact model parameters of the VF.

Physically, the forming of a resonance depends on two conditions: (1) there exists a path for the vibration energy to bounce in a VF; and (2) the phase condition of a round trip along an energy path is in favor of energy accumulation at a resonant frequency. Vibration energy distribution along the bouncing paths corresponds to mode functions of the modal theory. The above-mentioned experimental procedure enables a control engineer to place the actuator and feedback sensor in the intersection of energy paths for multiple resonant peaks. This is physically equivalent to a controllability check for a GSC that requires model parameters. If a LSC absorbs vibration energy at these resonant frequencies in the selected location, it will weaken the resonant conditions of the corresponding energy paths. This implies global damping to the VF. Section III will explain analytically how this is possible.

III. LSC DESIGN AND ANALYSIS

The pole-placement control strategy may be applied to design the LSC. A prototype polynomial $P(s)$ is used to prescribe the closed-loop poles. The control law is given by

$$u = \frac{R(s)}{S(s)} \nu, \quad (8)$$

where polynomials $R(s)$ and $S(s)$ are solved from a Bezout equation¹⁴

$$P(s) = D(s)S(s) + N(s)R(s). \quad (9a)$$

One may denote $P(s) = p_0 s^{4n-3} + p_1 s^{4n-4} + \dots + p_{4n-4} s + p_{4n-3}$ and apply similar notations to $D(s)$, $S(s)$, $N(s)$,

and $R(s)$ whose degrees are $2n$, $2n-3$, $2n-2$, and $2n-1$, respectively. Then Eq. (9a) has a matrix-vector expression

$$\begin{bmatrix} p_0 \\ p_1 \\ \vdots \\ p_{4n-4} \\ p_{4n-3} \end{bmatrix} = \begin{bmatrix} d_0 & \cdots & 0 & n_0 & \cdots & 0 \\ \vdots & \ddots & 0 & \vdots & \ddots & 0 \\ d_{2n} & \vdots & d_0 & n_{2n-2} & \vdots & n_0 \\ 0 & \ddots & \vdots & 0 & \ddots & \vdots \\ 0 & \cdots & d_{2n} & 0 & \cdots & n_{2n-2} \end{bmatrix} \begin{bmatrix} s_0 \\ \vdots \\ s_{2n-3} \\ r_0 \\ \vdots \\ r_{2n-1} \end{bmatrix} \quad (9b)$$

where the matrix, known as the Sylvester resultant,¹⁴ is non-singular since $N(s)$ and $D(s)$ are coprime. Coefficients of $S(s)$ and $R(s)$ can be solved from Eq. (9b) for the controller transfer function (8). Substituting Eqs. (8) and (9a) into Eq. (5a), one can express the closed-loop SISO system as

$$\nu = \frac{S(s)}{C(s)P(s)} \epsilon,$$

where the prototype polynomial $P(s)$ becomes a part of the closed-loop denominator. Its roots are placed as closed-loop poles of the local SISO system.

The irreducible part of Eq. (6b) may be expressed as $D(s) = D_a(s)D_s(s)\prod_k(s^2 + \omega_k^2)$, where $D_s(s)$ and $D_a(s)$ are the filter denominators and $\prod_k(s^2 + \omega_k^2)$ represents the resonant poles. One may use $P(s) = D_a(s)D_s(s)\prod_k(s^2 + \zeta_k s + \omega_k^2)$ to damp the resonant peaks and keep the filter denominators $D_s(s)$ and $D_a(s)$ in the closed loop. In view of Eq. (5b), one may write

$$\nu = \frac{S(z)\det[\mathbf{\Lambda}_1(s), \boldsymbol{\eta}]}{C(s)\prod_k(s^2 + \zeta_k s + \omega_k^2)} F_s(s).$$

Although the roots of $C(s)$, which correspond to uncontrollable modes, remain poles of the closed-loop SISO system, these components will be blocked by a filter $F_s(s)$ —the numerator $N_s(s)$ in Eq. (5b) will combine with the denominator $D_s(s)$ in $P(s)$ to form $F_s(s)$ and remove any signals in its stop band.

The LSC design does not require exact model parameters. Only the numerator and denominator of Eq. (5) are involved that are available by identification. While actuator and sensor dynamics are taken into explicit account in terms of $N_s(s)$, $N_a(s)$, $D_s(s)$, and $D_a(s)$, these are hidden in the numerator $N(s)$ and denominator $D(s)$ of the local transfer function. There is no restriction on the types of the sensor and actuator filters, as long as they are represented by stable transfer functions whose exact forms need not be known.

Attention is now directed to the global effect of the LSC. One may wonder how the LSC introduces global damping to a VF. Consider, for example, a duct with cross section much smaller than the wavelengths of the noise source. This is a one-dimensional noise field. Its resonant is due to an impedance mismatch in both ends, which allows acoustic energy to bounce around and accumulate. If the impedance of either end of the duct matches the characteristic imped

ance of the duct, then the resonant peaks can be attenuated. This means global damping is possible by a local (passive) control.

The LSC has been shown able to damp the resonant peaks at a local point. Since this is the intersection of multiple energy paths, local damping weakens the resonant conditions and prevents global energy accumulation. Its global effect is investigated here analytically. In view of $f = F_a(s)u$ and $v = F_s(s)y$, Eq. (8) implies

$$f = -G(s)y,$$

where

$$G(s) = \frac{R(s)N_s(s)N_a(s)}{S(s)D_s(s)D_a(s)}. \quad (10)$$

The actuator and sensor dynamics have been included in the controller transfer function $G(s)$ explicitly. Substituting Eq. (10) into Eq. (3), one obtains

$$\Lambda^*(s)\mathbf{x} = [\Lambda(s) + hG(s)\boldsymbol{\beta}\mathbf{e}_1^T]\mathbf{x} = \boldsymbol{\eta}, \quad (11)$$

where $y = \mathbf{h}^T\mathbf{q} = hx_1 = h\mathbf{e}_1^T\mathbf{x}$ has been substituted. The modi-

fication introduced by $hG(s)\boldsymbol{\beta}\mathbf{e}_1^T$ only changes the first column of $\Lambda(s)$. Hence

$$\Lambda^*(s) = \begin{bmatrix} \alpha_{11}(s) + hG(s)\beta_1 & \alpha_{12}(s) & \cdots & \alpha_{1m}(s) \\ \alpha_{21}(s) + hG(s)\beta_2 & \alpha_{22}(s) & \cdots & \alpha_{2m}(s) \\ \vdots & \vdots & \ddots & \vdots \\ \alpha_{m1}(s) + hG(s)\beta_m & \alpha_{m2}(s) & \cdots & \alpha_{mm}(s) \end{bmatrix}, \quad (12)$$

where β_k is the k th element of vector $\boldsymbol{\beta}$.

The global effect of the LSC is reflected in $\det[\Lambda^*(s)]$, which is the characteristic equation of the closed-loop VF. One may express $\det[\Lambda^*(s)]$ with respect to the first column of $\Lambda^*(s)$. It reads

$$\det[\Lambda^*(s)] = \sum_{k=1}^m (-1)^{k+1} [\alpha_{k1}(s) + hG(s)\beta_k] \det[\Lambda_{1k}(s)],$$

where $\Lambda_{1k}(s)$ is a matrix obtained by removing the first column and the k th row from either $\Lambda(s)$ or $\Lambda^*(s)$. The above-given expression suggests

$$\begin{aligned} \det[\Lambda^*(s)] &= \det[\Lambda(s)] + hG(s)\det[\Lambda_1(s), \boldsymbol{\beta}] = \frac{\det[\Lambda(s)]D_s(s)D_a(s)S(s) + h\det[\Lambda_1(s), \boldsymbol{\beta}]N_s(s)N_a(s)R(s)}{D_s(s)D_a(s)S(s)} \\ &= \frac{C(s)[D(s)S(s) + N(s)R(s)]}{D_s(s)D_a(s)S(s)} = \frac{C(s)P(s)}{D_s(s)D_a(s)S(s)}, \end{aligned} \quad (13)$$

where Eqs. (10), (6), and (9a) have been substituted sequentially in deriving the last equation.

One may understand the global damping of the LSC by comparing $\det[\Lambda(s)]$ and $\det[\Lambda^*(s)]$. These are, respectively, open- and closed-loop characteristic equations of the VF. Roots of these polynomials are eigenvalues of the VF before and after the application of the LSC. Therefore damping ratios of $\det[\Gamma(s)]$ and $\det[\Gamma^*(s)]$ are, respectively, damping ratios of the VF before and after the application of the LSC. It is not difficult to see, from Eqs. (6b) and (13), that

$$\begin{aligned} \det[\Lambda(s)] &= \frac{C(s)D(s)}{D_s(s)D_a(s)}, \\ \det[\Lambda^*(s)] &= \frac{C(s)P(s)}{D_s(s)D_a(s)S(s)}. \end{aligned}$$

Roots of $P(s)$ replace roots of $D(s)$ to be the closed-loop eigenvalues of the VF. With $P(s)$ preselectable, a control engineer may select the damping ratio of $P(s)$ to tune the global damping ratio for the closed-loop VF. This is, of course, limited to the controllable modes. Roots of the common divisor $C(s)$ correspond to those modes uncontrollable by $T(s)$. Damping ratios of $C(s)$ remain unchanged due to the physical constraint of actuator–sensor locations.

An analytical implication of Eq. (13) is that the LSC introduces global damping to the controlled modes without

affecting the uncontrolled modes. It manages to avoid spillover by taking account of $N_s(s)$, $N_a(s)$, $D_s(s)$, and $D_a(s)$ in its local design stage. To the best knowledge of the author, this is the first attempt to investigate both controlled and uncontrolled modes analytically and realistically in a controller design for a distributed system. It is different from a GSC design where the uncontrolled modes are usually ignored in calculating the GSC gain matrix.^{4,6–8}

Other LSCs do not necessarily damp the VF globally. Take the high-gain LSC for example, its modal models are $(s^2\mathbf{I} + \mathbf{K})\mathbf{q} = \mathbf{d}$ and $(s^2\mathbf{I} + \mathbf{K} + g\mathbf{b}\mathbf{h}^T)\mathbf{q} = \mathbf{d}$, respectively, for the open- and closed-loop of a VF when the open-loop damping is negligible. Here \mathbf{K} is diagonal with elements $\{\omega_i^2\}$; g is the LSC gain. In order for the closed loop to be stable, $\mathbf{K} + g\mathbf{b}\mathbf{h}^T$ must be positive definite, which is true for collocated sensor–actuator ($\mathbf{h} = \mathbf{b}$) but not necessarily true otherwise. This is consistent with the conclusion of the local transfer function approach.¹² Let $\{\lambda_i\}$ be the eigenvalues of $\mathbf{K} + g\mathbf{b}\mathbf{h}^T$, then it is not difficult to see $\det(s^2\mathbf{I} + \mathbf{K} + g\mathbf{b}\mathbf{h}^T) = \prod(s^2 + \lambda_i)$. Comparing with $\det(s^2\mathbf{I} + \mathbf{K}) = \prod(s^2 + \omega_i^2)$, one can see that a high-gain LSC does not damp the VF, though it suppresses the sensed signals¹² in a local feedback loop.

The analysis is based on the continuous model (1) in the Laplace transform domain. Practically, Eq. (5) is usually identified as a discrete-time model in the Z -transform domain.¹⁴ A strictly rigorous approach would be converting

the VF model to its discrete-time version and reaching the same conclusion. That may introduce unnecessary distractions since the discrete-time model is slightly more complicated and the conversion may introduce new symbols. Since the continuous-time model is physically and mathematically equivalent to its discrete-time version and the conclusion is the same, using the continuous model may keep a better focus here. Practically, it is recommended to use the discrete-time model to design the LSC. When the number of modes to be damped is large and the resonant frequencies span a wide range, the roots of $N(s)$ and $D(s)$ would spread along the imaginary axis in a wide range if one works with a continuous model. With a discrete-time model, however, the imaginary axis of the s plane is mapped to the unit circle in the z plane. The roots of $N(z)$ and $D(z)$ should be near the unit circle. As a result, the condition number of the Sylvester resultant can be improved and numerical errors can be reduced.

IV. DECENTRALIZED DESIGN OF LSCs

A VF may need active damping by multiple actuators mounted in different locations, probably because several modes share the same resonant frequency or the actuators have limited power. Cross coupling of the actuation signals is inevitable, which causes difficulties in controller design. For active control of a VF by multiple actuators, currently available methods depend on the exact model parameters to deal with the problem of cross coupling between actuators and feedback sensors. These are centralized design methods. This paper presents a simple decentralized design procedure for active damping of a VF by multiple actuators.

The idea is to add a LSC to a VF that has been controlled by a stable active controller. The existing controller may be designed with any available schemes in the literature, including the LSC scheme presented earlier. The dynamic model of the VF, subject to the existing controller and the additional LSC, may be expressed as

$$[\mathbf{M}s^2 + \mathbf{K} + \mathbf{G}(s)]\mathbf{q} = \mathbf{b}f + \mathbf{d}, \quad (14)$$

where $\mathbf{G}(s)$ represents the gain of the existing controller. Other symbols remain the same as in Eq. (1). Since the existing controller may be designed by a scheme different from LSC, $\mathbf{G}(s)$ is not necessarily available. However, it is important to assume that the existing controller is *stable* such that roots of $\det[\mathbf{M}s^2 + \mathbf{K} + \mathbf{G}(s)]$ are all in the negative half of the s plane.

The normalized version of \mathbf{h} is still denoted as \mathbf{h}_n . Its null space is still spanned by $m-1$ unit length and orthogonal basis $\{\zeta_1 \cdots \zeta_{m-1}\}$ with $\mathbf{h}^T \zeta_i = 0$ for $1 \leq i \leq m-1$. The existence of these vectors implies the existence of an orthogonal matrix $\mathbf{H} = [\mathbf{h}_n \zeta_1 \cdots \zeta_{m-1}]$, such that $\mathbf{x} = \mathbf{H}^T \mathbf{q}$ and $\Gamma(s) = \mathbf{H}^T [\mathbf{M}s^2 + \mathbf{K} + \mathbf{G}(s)] \mathbf{H}$. Therefore Eq. (14) is equivalent to

$$\Gamma(s)\mathbf{x} = \boldsymbol{\beta}f + \boldsymbol{\eta}, \quad (15)$$

where $\boldsymbol{\beta} = \mathbf{H}^T \mathbf{b}$ and $\boldsymbol{\eta} = \mathbf{H}^T \mathbf{d}$ remains the same as in Eq. (3). The feedback signal may be expressed as

$$y = hx_1 = h \frac{\det[\Gamma_1(s), \boldsymbol{\beta}]f + \det[\Gamma_1(s), \boldsymbol{\eta}]}{\det[\Gamma(s)]}, \quad (16)$$

where $[\Gamma_1(s), \boldsymbol{\beta}]$ and $[\Gamma_1(s), \boldsymbol{\eta}]$ are matrices obtained by replacing the first column of $\Gamma(s)$ with vectors $\boldsymbol{\beta}$ and $\boldsymbol{\eta}$, respectively. Parameters of Eqs. (14)–(16) are not necessarily available.

The LSC design procedure, presented in Sec. II, may be repeated here. A control engineer uses a probing signal $f = F_a(s)u$ to excite the VF while the feedback sensor measures $v = F_s(s)y$, which will be used to identify the transfer function. Only this time, the existing controller must be *turned on* so that a local plant model

$$\nu(s) = \frac{h \det[\Gamma_1(s), \boldsymbol{\beta}]N_s(s)N_a(s)u(s) + \epsilon}{\det[\Gamma(s)]D_s(s)D_a(s)} \quad (17)$$

can be identified from measurement data. Although Eq. (17) looks similar to Eq. (5), it is different because potential coupling effects of the existing controller are identified by Eq. (17). The additional LSC depends on Eq. (17) to avoid cross coupling with the existing controller. While identifying Eq. (17), a control engineer may adjust the actuator and sensor locations to excite and measure selected modes. These should be modes not controlled by the existing controller.

The numerator and denominator of Eq. (17) may share some common roots. Therefore one should express

$$h \det[\Gamma_1(s), \boldsymbol{\beta}]N_s(s)N_a(s) = N_e(s)C_e(s), \quad (18a)$$

$$\det[\Gamma(s)]D_s(s)D_a(s) = D_e(s)C_e(s), \quad (18b)$$

where the roots of common divisor $C_e(s)$ correspond to vibration modes not controllable or observable by the additional LSC. $N_e(s)$ and $D_e(s)$ are coprime polynomials. The control law of the additional LSC is given by

$$u = -\frac{R_e(s)}{S_e(s)}\nu, \quad (19)$$

where polynomials $R_e(s)$ and $S_e(s)$ are solved from a different Bezout equation

$$P_e(s) = D_e(s)S_e(s) + N_e(s)R_e(s), \quad (20)$$

where $P_e(s)$ is a prototype polynomial assigned to the additional LSC. Substituting Eqs. (19) and (20) into Eq. (17), one can express the closed-loop local system as

$$\nu = \frac{S_e(s)}{C_e(s)P_e(s)}\epsilon,$$

where $P_e(s)$ becomes a part of the closed-loop denominator. Similar to the arguments of Sec. III, Eq. (19) implies

$$f = -G_e(s)y,$$

where

$$G_e(s) = \frac{R_e(s)N_s(s)N_a(s)}{S_e(s)D_s(s)D_a(s)}. \quad (21)$$

Substituting Eq. (21) into Eq. (15), one obtains

$$\Gamma^*(s)\mathbf{x} = [\Gamma(s) + hG_e(s)\boldsymbol{\beta}\boldsymbol{\eta}^T]\mathbf{x} = \boldsymbol{\eta},$$

where

$$\mathbf{\Gamma}^*(s) = \begin{bmatrix} \gamma_{11}(s) + hG(s)\beta_1 & \gamma_{12}(s) & \cdots & \gamma_{1m}(s) \\ \gamma_{21}(s) + hG(s)\beta_2 & \gamma_{22}(s) & \cdots & \gamma_{2m}(s) \\ \vdots & \vdots & \ddots & \vdots \\ \gamma_{m1}(s) + hG(s)\beta_m & \gamma_{m2}(s) & \cdots & \gamma_{mm}(s) \end{bmatrix}.$$

One may derive, similar to the derivation of Sec. III,

$$\begin{aligned} \det[\mathbf{\Gamma}^*(s)] &= \det[\mathbf{\Gamma}(s)] + hG(s)\det[\mathbf{\Gamma}_1(s), \boldsymbol{\beta}] \\ &= \frac{C_e(s)P_e(s)}{D_s(s)D_a(s)S_e(s)}, \end{aligned}$$

where $P_e(s)$ has been placed as a part of the closed-loop characteristic equation. This implies global damping to the selected modes not controlled by the existing controller.

The above mentioned derivation can be generalized to the case where $\mathbf{G}(s)$ represents the feedback gains of several existing controllers. This makes it possible to add LSCs to a VF one by one for active damping using multiple actuators. Each time a new LSC is added to the VF, its actuator and feedback sensor location should be chosen in such a way that the local plant is controllable and observable with respect to a set of modes uncontrolled by the previous controllers.

V. A NUMERICAL EXAMPLE

A numerical example is presented here to demonstrate how global damping is possible by a LSC. The VF is a one-dimensional cantilever beam satisfying the Bernoulli–Euler equation

$$EI \frac{\partial^4 w}{\partial x^4} + \rho \frac{\partial^2 w}{\partial t^2} = d(x, t) + f(x, t),$$

where w is the vibration displacement; x and t are spatial and temporal variables; ρ is the mass density; E is the Young's modulus of elasticity, and I the moment of inertia of the cross-sectional area with respect to the neutral axis. The disturbance and the LSC control forces are denoted by $d(x, t)$ and $f(x, t)$, respectively. The eigenfunctions of the beam are given by

$$\begin{aligned} \varphi_i(x) &= [\cosh(\lambda_i x) - \cos(\lambda_i x)] \\ &\quad - \mu_i [\sinh(\lambda_i x) - \sin(\lambda_i x)], \end{aligned}$$

where

$$\mu_i = \frac{\cos(\lambda_i L) + \cosh(\lambda_i L)}{\sin(\lambda_i L) + \sinh(\lambda_i L)}$$

depends on λ_i —the i th root of $\cos(\lambda_i L)\cosh(\lambda_i L) + 1 = 0$. The eigenvalue λ_i also determines the i th mode frequency $\omega_i = (\lambda_i L)^2 \sqrt{EI/\rho L^4}$, where $L = 1$ and $\sqrt{EI/\rho L^4} = 0.05$ are assumed. Such a choice does not lose generality since implementation of the LSC is carried out with a discrete-time model in the Z -transform domain. One can always select the sampling frequency such that the resonant frequencies of the modes are properly spaced in the unit circle. This demonstration uses a continuous model just to be consistent with the previous sections.

Theoretically the LSC is able to damp as many modes as the actuator and feedback sensor can excite and observe.

Practically, however, most active control devices are applied to the low frequency ranges because high-order modes are absorbed more effectively with inexpensive passive methods. For this reason, the model is truncated to the first five modes with $\omega_1 = 0.7706$, $\omega_2 = 2.4982$, $\omega_3 = 5.2124$, $\omega_4 = 8.9135$ and $\omega_5 = 13.6015$ (rad/s). If fitted into Eq. (1), these parameters make \mathbf{K} diagonal, \mathbf{M} identity, and $\det(\mathbf{M}s^2 + \mathbf{K}) = \prod_{k=1}^5 (s^2 + \omega_k^2)$. The actuator and feedback sensor are collocated near the middle of the beam such that $f(x, t) = \delta(x - 0.58L)f(t)$, or $\mathbf{b} = \mathbf{h} = [\varphi_1(0.58), \dots, \varphi_5(0.58)]^T$. A local transfer function is derivable as $T(s) = N(s)/D(s) = \sum_{k=1}^5 \varphi_k^2(0.58)/s^2 + \omega_k^2$.

A prototype polynomial $P(s) = (s + 2)^6 \prod_{k=1}^5 (s^2 + 0.08\omega_k s + \omega_k^2)$ is used to prescribe closed-loop poles for the local system, which are also closed-loop poles of the entire beam, as to be demonstrated in this example. The Sylvester resultant, defined in Eq. (9b), may be numerically ill conditioned when the resonant frequencies spread in a wide range. For this reason, a real multiple pole $(s + 2)^6$ is added to $P(s)$ to reduce possible numerical errors in solving $P(s) = D(s)S(s) + N(s)R(s)$ for the LSC gain

$$G(s) = \frac{R(s)}{S(s)}.$$

If one designs the LSC with a discrete-time model, however, the real pole may not be necessary because the condition number for the Sylvester resultant will be much better.

In order to see the global damping effect, a monitor sensor could be placed anywhere along the beam to measure the vibration spectrum. A possible location is $x_m = 0.98L$ —near the free end of the cantilever beam. The disturbance is acting at $x_d = 0.78L$, which is physically between the LSC actuator and the monitor sensor. The location vectors are $\mathbf{m} = [\varphi_1(0.98), \dots, \varphi_5(0.98)]^T$, and $\mathbf{d} = [\varphi_1(0.78), \dots, \varphi_5(0.78)]^T$ respectively. Let $y_m(s)$ denote the vibration signal of the monitor sensor and assume a broadband random disturbance source $d(s) = 1$, then the spectra of $y_m(s)$ are given by

$$y_m(s) = \mathbf{m}^T [\mathbf{M}s^2 + \mathbf{K} + \mathbf{b}\mathbf{b}^T G(s)]^{-1} \mathbf{d},$$

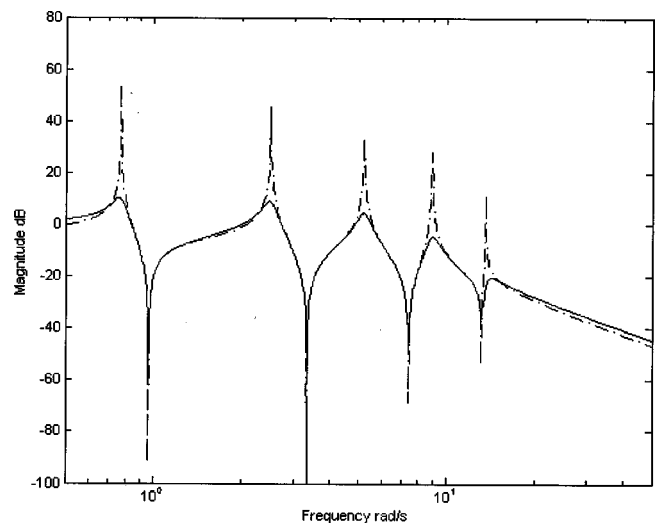


FIG. 1. Vibration spectra with (solid line) and without (dash-dot line) LSC damping, measured near the free end of the beam.

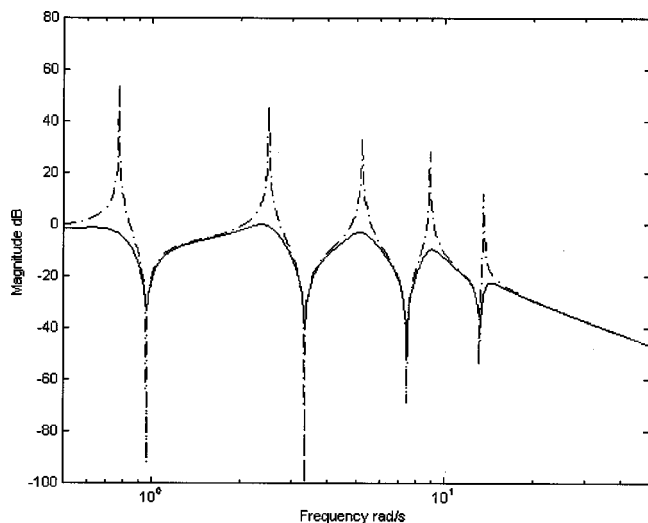


FIG. 2. Vibration spectra with (solid line) and without (dash-dot line) GSC damping, measured near the free end of the beam.

$$y_m(s) = \mathbf{m}^T [\mathbf{M}s^2 + \mathbf{K}]^{-1} \mathbf{d}$$

for the cases with and without LSC damping, respectively. These spectra are plotted in Fig. 1 for comparison. Although the LSC is designed for a local system, its damping effect on the monitor signal, measured near the free end of the beam, is obvious. For the same beam, a linear quadratic optimal GSC is designed using the exact modal parameters. Figure 2 plots the global damping effects of the GSC. Generally, the performance of a GSC is better than that of a LSC at the expense of exact modal parameters. A GSC is always the first choice if exact modal parameters are available. The LSC is recommended if these parameters are not available, or not accurate enough, for VFs with irregular geometric shapes and boundary conditions.

One may select other locations for the monitor sensor. This means different choices of $\mathbf{m} = [\varphi_1(x_m), \dots, \varphi_5(x_m)]^T$. If substituted into the above-given equations, similar damping effects can be obtained as shown in Figs. 3 and 4. Altering the locations of the disturbance source and the monitor

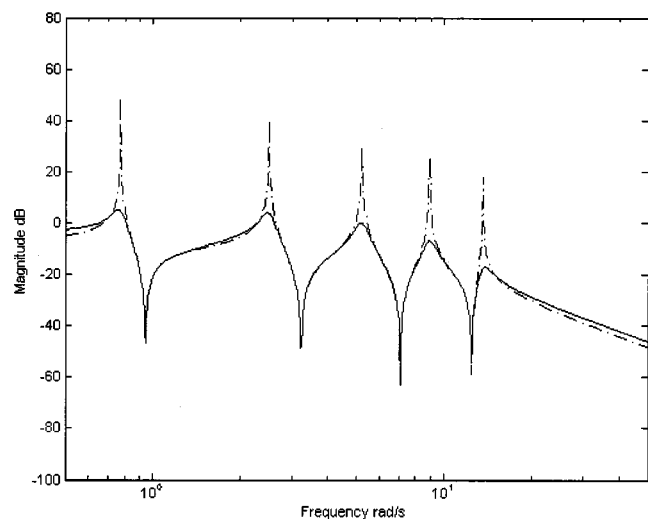


FIG. 3. Vibration spectra with (solid line) and without (dash-dot line) LSC damping, measured near the middle of the beam.

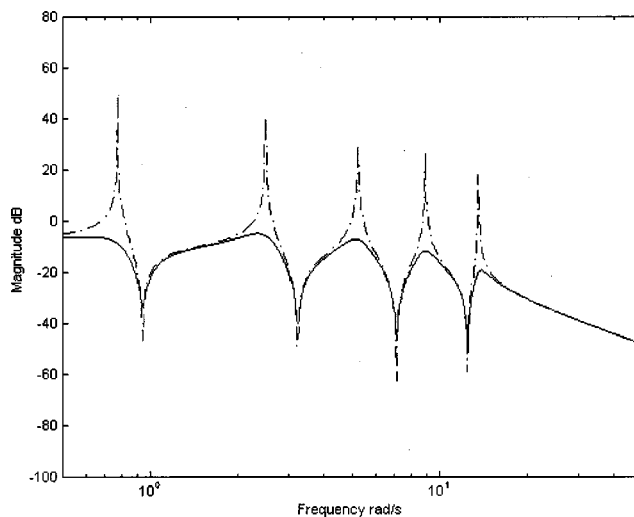


FIG. 4. Vibration spectra with (solid line) and without (dash-dot line) GSC damping, measured near the middle of the beam.

sensor changes the values of location vectors \mathbf{m} and \mathbf{d} , respectively. It does not affect the global damping effects since the eigenstructure of $\mathbf{M}s^2 + \mathbf{K} + \mathbf{b}\mathbf{b}^T G(s)$ is determined by the LSC gain $G(s)$ and the location vector \mathbf{b} (for the actuator and feedback sensor).

VI. CONCLUSION

This study investigates, analytically and numerically, the global damping of a VF by means of a single LSC. A positive conclusion has been reached with an easy procedure for the LSC design and implementation. The LSC has many positive features. It does not require detailed dynamic model of the VF. One may use available system identification techniques to estimate a local transfer function, check its controllability, and design the LSC. Unlike other available controllers that ignore uncontrolled modes when computing the feedback gains, the LSC design deals with both controlled and uncontrolled modes plus sensor and actuator dynamics. The design procedure allows one to design and implement, when necessary, multiple LSCs to damp the resonant peaks of a VF selectively.

ACKNOWLEDGMENT

The work described in this paper was substantially supported by a grant from the Research Grants Council of the Hong Kong Special Administration Region (Project No. PolyU 5175/01E).

¹L. Meirovitch, *Dynamics and Control of Structures* (Wiley, New York, 1990).

²J. S. Vipperman and R. L. Clark, "Multivariable feedback active structural acoustic control using adaptive piezoelectric sensor/actuators," *J. Acoust. Soc. Am.* **105**, 219–225 (1999).

³S. Griffin, C. Hansen, and B. Cazzolato, "Feedback control of structurally radiated sound into enclosed spaces using structural sensing," *J. Acoust. Soc. Am.* **106**, 2621–2628 (1999).

⁴K. Seto, M. Ren, and F. Doi, "Feedback vibration control of a flexible plate at audio frequencies by using a physical state-space approach," *J. Acoust. Soc. Am.* **103**, 924–934 (1998).

⁵R. E. Lindberg and R. W. Longman, "On the number and placement of

- actuators for independent modal shape control," J. Guid. Control Dyn. **2**, 215–221 (1984).
- ⁶N. Rizet, M. Brissaud, P. Gonnard, J.-C. Bera, and M. Sunyach, "Modal control of beam flexural vibration," J. Acoust. Soc. Am. **107**, 2061–2067 (2000).
- ⁷K. Seto, M. Ren, and F. Doi, "Modeling and feedback structural acoustic control of a flexible plate," Trans. ASME, J. Vib. Acoust. **123**, 18–23 (2001).
- ⁸T. Samejima, "Modifying modal characteristics of sound fields by state feedback control," J. Acoust. Soc. Am. **110**, 1408–1414 (2001).
- ⁹H. T. Banks, Z.-H. Luo, L. A. Bergman, and D. J. Inman, "On the existence of normal modes of damped discrete-continuous systems," ASME Trans. J. Appl. Mech. **65**, 980–989 (1998).
- ¹⁰H. F. Olson and May, "Electronic sound absorber," J. Acoust. Soc. Am. **25**, 1130–1136 (1953).
- ¹¹R. L. Clark and D. G. Cole, "Active damping of enclosed sound fields through direct rate feedback," J. Acoust. Soc. Am. **97**, 1710–1716 (1995).
- ¹²R. L. Clark and G. P. Gibbs, "Analysis, testing and control of a reverberant sound field within the fuselage of a business jet," J. Acoust. Soc. Am. **105**, 2277–2286 (1999).
- ¹³J. Yuan, "Improving an adaptive controller for non-minimum phase plants," Automatica (to be published).
- ¹⁴G. C. Goodwin and K. S. Sin, *Adaptive Filtering, Prediction and Control* (Prentice–Hall, Englewood Cliffs, NJ, 1984).
- ¹⁵K. Ogata, *Modern Control Engineering* (Prentice–Hall, Englewood Cliffs, NJ, 1997).

Analysis of noise barrier overlap gaps

Lloyd A. Herman^{a)} and Craig M. Clum^{b)}

Department of Civil Engineering, Ohio University, Athens, Ohio 45701

(Received 25 May 1998; revised 17 December 2001; accepted 21 December 2001)

Sound propagation through the gap produced by two parallel vertical barriers with overlapped ends is formulated for traffic noise sources. The analysis identifies both source and receiver regions according to the mechanisms that influence noise propagation in the vicinity of an overlap gap. A method to account for the contributions from the various source regions for a given receiver location is described. The derived method can be implemented using various equations for sound propagation. The results of using equations approved by the United States Federal Highway Administration for traffic noise propagation are given. Uncalibrated predictions are compared with field measurements for up to 30 receiver positions from each of four overlap gaps. The relative importance of contributions from reflected rays to the noise levels at receiver positions is given. The analysis confirms the initial hypothesis that a commonly used strategy of overlapping barriers by an amount equal to two or three times the overlap width is useful for controlling line-of-sight propagation but ignores the substantial effect of reflections. © 2002 Acoustical Society of America. [DOI: 10.1121/1.1453448]

PACS numbers: 43.50.Gf, 43.50.Lj [MRS]

I. INTRODUCTION

Noise barrier performance can be affected by discontinuities that interrupt the barrier along its length. The term overlap gap as used in this article refers to a specific type of discontinuity created where two parallel screens of finite height above a plane are offset in their horizontal alignment and overlapped a finite amount to produce a gap. The lengths of each screen are much greater than the perpendicular distances between either the screens and the source or the screens and the receiver. The effect of such a gap on the propagation of noise from randomly spaced, moving point sources of varying heights above the plane on one side of the screens to receivers at fixed locations on the opposite side of the screens, which is considered in this article, has a direct application to the performance of traffic noise barriers where overlap gaps are created to accommodate the need for maintenance access, drainage and barrier alignment changes at the transitions between excavation and embankment sections of a roadway.

In practice, efforts to reduce barrier performance degradation, due to the presence of discontinuities, have typically involved strategies to reduce line-of-sight propagation paths from the source to the receiver by extending the barriers to form an overlap. Reasonable overlap lengths eliminate most line-of-sight paths except those from sources located at greater distances from the gap, which tend not to contribute significantly to receiver noise levels. Rules-of-thumb typically suggest a 2:1 or 3:1 ratio of the overlap length (the amount the barriers extend past one another) to the overlap width (the perpendicular distance between the barriers).^{1,2} However, these strategies fail to account for the effect of any reflections that might occur within the overlap gap, which

have been modeled for barriers having similar overlap geometries at on/off highway ramp areas.³

The analysis undertaken in this study stemmed from the hypothesis that reflections in an overlap gap area make significant contributions to receiver levels to the extent that substantial degradation to barrier performance could occur using the conventional rule-of-thumb approach. The analysis presented in this article is intended to increase quantitatively the understanding of noise propagation in the area of an overlap gap. The analysis gives the equations and procedures needed to formulate algorithms that when coupled with suitable equations for sound propagation and sound source reference levels can be used to predict noise levels for receivers located near a barrier overlap gap. Further, the analysis method can be used to both identify the location of each reflection in an overlap gap for a variety of barrier configurations as well as to determine the effect of sound absorbing materials that might be used for specified portions of barrier surfaces to control reflections.

II. ANALYSIS AND GEOMETRICAL RELATIONSHIPS

A. Approach

Any approach to the analysis of reflections at overlap barrier gaps, even with the simplest geometry, is substantially more complex than the analysis of reflections from single or parallel barriers, where the barrier geometry does not change with respect to the source. While the overlap gap consists of parallel barriers in the overlap area, the source is not located between the barriers, and the orientation of the gap relative to a vehicle noise source constantly changes as the vehicle moves along the roadway. Therefore, a three-dimensional analysis is required rather than the two-dimensional analysis often used for parallel barriers.

The analysis is based on ray acoustics rather than the finite element or boundary element methods for a number of reasons. Computation time is a primary concern for the task

^{a)}Electronic mail: Lloyd.Herman@ohio.edu

^{b)}Current address: Development Consultants Group, 3305 Breckinridge Blvd., Suite 102, Duluth, GA 30096.

of determining the sound level contribution in eight octave frequency bands, at 10 receivers, for three classes of vehicles moving along as many as 10 traffic lanes. Also for this reason, image sources, which have been used to investigate the effect of reflections in other studies⁴⁻⁷ are used rather than ray tracing, although this requires a number of simplifying assumptions about barrier configuration. Second, the basic concepts of ray acoustics conform well to the many geometrical calculations required for the analysis, particularly the identification of reflection locations and the quantification of the relative significance of propagation mechanisms for various source-receiver combinations. Finally, ray acoustics conforms well to the equations of propagation used for final implementation of the analysis as required by the Federal Highway Administration for use on federally funded highway projects.

B. Assumptions

The following simplifications, assumptions, and limitations are used in the development of the method.

- (1) Reflections are assumed to be specular, and only energy contributions from the rays and image rays are added.
- (2) The effect of diffraction for noise flanking the ends of a barrier is neglected.
- (3) The attenuation for rays diffracted by the top edge of both barriers (double-diffraction) is based on the barrier offering the greatest attenuation.
- (4) Contributions from rays that may reach the receiver through ground reflections are not included.
- (5) All receivers must be lower than the top edge of both barriers.
- (6) The ground is assumed to be acoustically hard.
- (7) All barriers are considered to be parallel to the line of the noise source.
- (8) All barriers are free-standing walls, not earth berms.
- (9) The overlap width is greater than the longest wavelength of interest.

C. Ray paths

The possible paths through which noise may propagate to a receiver at an overlap gap site are characterized as follows:

- (1) Direct propagation
- (2) Simple diffraction
- (3) Double diffraction
- (4) Multiple reflected rays (MRR)
- (5) Multiple reflected diffracted rays (MRDR)
- (6) Diffracted multiple reflected rays (DMRR).

Direct propagation of a sound wave does not involve any barrier attenuation. The sound wave travels through the gap directly to the receiver from the source. Simple diffraction occurs when sound waves from the source are diffracted by the top edge of either the near barrier (the barrier closest to the community side of the highway) or the far barrier before reaching the receiver. Double diffraction occurs when

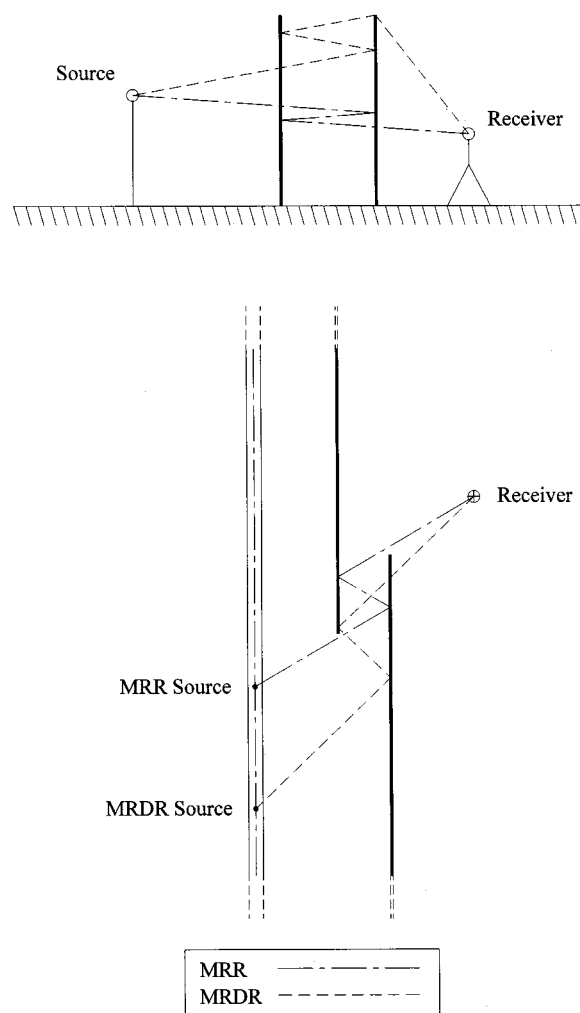


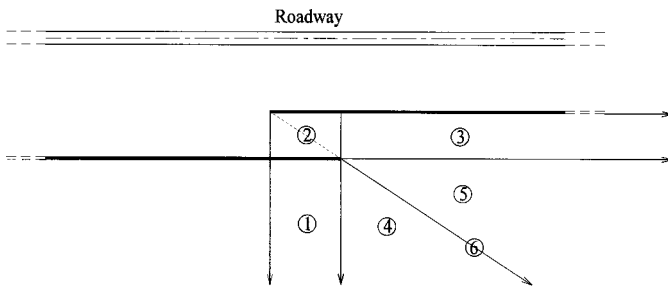
FIG. 1. Multiple reflected rays and multiple reflected diffracted rays.

sound waves are diffracted by the top edges of both barriers before reaching the receiver.

The last three paths represent sound waves that are reflected from one or both noise barriers before reaching the receiver. MRDR and MRR paths are shown in Fig. 1. The DMRR path would appear as the MRDR path if the source and receiver positions were reversed in the figure. These paths require special analysis to determine their contribution to levels at receivers located near a gap, as well as the effect of sound absorbing materials that may be used on portions of barrier surfaces.

Multiple reflected rays (MRR) are reflected sound waves that reach the receiver without being diffracted by the top edge of a noise barrier. With each reflection a portion of the sound wave's energy is lost. Also, a MRR must travel greater distances than a direct ray to reach the receiver.

Multiple reflected diffracted rays (MRDR) and diffracted multiple reflected rays (DMRR) are similar to MRR. A MRDR is also reflected from one or both noise barriers then diffracted by the top edge of the near barrier before reaching a receiver. Similarly, a DMRR is first diffracted by the top edge of the far barrier then reflected between the walls within the overlap area. These rays contribute less to receiver levels than their corresponding single barrier attenu-



Note: Case 6 is located on the line drawn between the ends of the far and near barriers.

FIG. 2. Overlap gap receiver locations.

ated rays due to energy losses from longer pathlengths and reflection losses. DMRR generally have an even smaller effect than MRDR since a much small number exist for most barrier geometries.

D. Overlap gap receiver locations

The analysis is performed to determine sound levels for receivers located in each of the six zones shown in Fig. 2. Receivers outside of these zones can be analyzed using noise prediction methods for single barriers.

The size of each of these zones can vary from site to site, depending on the geometries of the gap. The mechanisms that can influence the path of propagation for rays that reach each receiver are listed by case (i.e., receiver zone location) in Table I.

E. Determination of source regions

For each receiver case, the ray paths and the corresponding mechanisms that influence the propagation of noise depend on the section of the source (i.e., roadway) being considered. The source regions can vary greatly in size depending on the orientation of the receiver with respect to the roadway and overlap gap. An analysis must be performed to establish these source regions for each receiver. The source regions are bounded by end points, as shown for case 1 receivers in Fig. 3. For example, the end point of the intersection of the perpendicular line from the overlap end of the far barrier with the roadway is the boundary point for multiple reflected rays (MRR). To the right of this point, no reflective path from the source to the receiver can exist.

The identification of these various source regions for each receiver case allows the subdivision of the source to

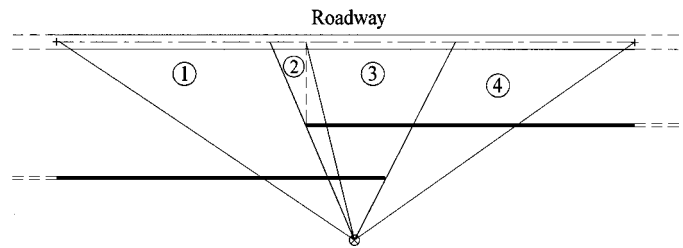


FIG. 3. Case 1 for source regions.

facilitate the computation of noise levels, since the paths may be influenced by different mechanisms for each sub-source.

F. Source segmentation

A well-defined point for the origin of a ray must be specified to determine whether or not the ray can reach a receiver for a given gap configuration. The source (i.e., roadway) can be represented by a series of finite elements. The energy centroid for each finite element is taken as the point of ray origin. However, the energy centroid is not located at the center of the element except for the element closest to the receiver (at the intersection of a perpendicular line from the source path to the receiver). By contrast, successive elements will appear to rotate slightly, relative to the receiver, as progress is made along the source path from the closest position toward either endpoint of the source path. One end of the element will be closer to the receiver than the other, so that the actual energy centroid will be shifted from the center of the element to a position closer to the receiver. The segment lengths can be described by equal angle divisions rather than equal length divisions. Through this segmentation process, a particular source region may be divided into several hundred elements. The horizontal and vertical propagation angles for each ray are calculated from the mid-angle point of the element, which was found to be a good approximation for the location of the energy centroid.

G. Image ray analysis

Image sources are used for reflected rays to facilitate the computation process as shown in Fig. 12. Ray paths will have both horizontal and vertical components. For analysis, the components are treated separately where the perpendicular distance is determined under horizontal propagation and the vertical propagation angles and the elevations of reflections are determined under vertical propagation. The rela-

TABLE I. Propagation mechanisms that influence overlap gap receivers.

Propagation mechanism	Receiver case					
	1	2	3	4	5	6
Direct propagation		X	X		X	
Simple diffraction	X	X	X	X	X	X
Double diffraction	X			X		
Diffracted Multiple Reflected Rays (DMRR)		X	X	X	X	X
Multiple reflected rays (MRR)		X	X	X	X	X
Multiple reflected diffracted rays (MRDR)	X			X		X

tionships to determine these parameters must be developed for each receiver case and for the characteristic propagation types involving reflections as listed in Table I. The derivation of equations to analyze case 1 receivers for multiple reflected diffracted rays is given as an example in the Appendix.

Cases 4, 5, and 6 can be analyzed using a similar approach. However, the image source for cases 2 and 3, in which the receiver is within the gap, is located either on the roadway side of the gap or on the receiver side depending on whether the last reflection occurs at the far barrier or the near barrier.

The equations given in the Appendix yield all possible reflections for a given source segment and receiver location. However, several steps must be added to the process to limit the rays selected for analysis. First, the use of source elements of finite size limits the number of sources for rays. Second, a limitation is placed on the number of image sources. Even though the required equivalency of the angle of incidence and angle of reflection gives a discrete number of reflections, the process described above yields an infinite number of image sources without an imposed limit upon the process. For the range of gap widths studied, it was found that after five or six reflections the intensity of reflected rays was reduced by the attenuation mechanisms of geometric spreading, molecular absorption and wall absorption to the point that the summation of all ray contributions were within 0.1 dB of the result obtained with a much greater reflection limit.

Not only does an imposed reflection limit reduce computation time, but it also tends to reduce the number of reflections that occur near the top edge of a barrier. When a sound wave reflects near an edge, a portion of the wave is diffracted by the edge. An analysis using a method such as the one described by de Jong *et al.*⁸ can be used to quantify the portions reflected or diffracted for a precise analysis.

In the absence of a precise analysis, the total energy of the ray will be associated with the reflection, producing a tendency to over-predict. However, an imposed reflection limit in the range of 5 to 10 reflections, limits the analysis to the larger vertical propagation angles, which corresponds to reflection locations that are typically 0.5 m or more from the top edge of the barrier, as observed by Bowlby.⁹

Third, an analysis must also be made to determine whether it is possible for a ray to actually reach a given receiver. For a reflected ray to reach a receiver, it must enter the overlap gap. Rays that do not enter the gap can only be reflected from the near or far walls toward the roadway. The near barrier must overlap the far barrier by a sufficient amount in order for the next-to-the-last reflection for the *i*th image ray to reach a receiver, for cases 4, 5, and 6 as well as cases 2 and 3 for even-numbered image rays. The check for sufficient barrier length must also be made for cases 2 and 3 for the last reflection if image rays are odd-numbered.

The horizontal and vertical propagation angles for each image source are used to identify the location of each reflection for all rays qualified for analysis. Upon reflection, a portion of the energy associated with the ray will be lost, depending on the barrier material. Barriers composed of sound absorbing materials may dissipate most of the energy,

TABLE II. Overlap gap geometry for field measurement sites.

Gap site	Elevation (m)				Gap overlap length (m)	Gap overlap width(m)
	Far barrier		Near barrier			
	Bottom	Top	Bottom	Top		
Cincinnati #1	251.3	256.3	250.5	256.6	32.5	15.6
Cincinnati #2	246.1	251.2	246.3	252.1	28	18
Columbus	274.9	281.0	274.3	280.7	30.5	9.1
Dayton	275.1	277.2	275.2	279.2	21.3	7.3

particularly in certain frequency bands. On the other hand, concrete, steel or wood barriers may dissipate very little of the waves' energy. To account for the energy absorbed, a wall absorption coefficient, which depends upon the wall material, is associated with each reflection location similar to the method used by Hurst.¹⁰

III. EVALUATION OF ANALYSIS METHOD

A. Source specification and noise propagation equations

The analysis method was evaluated by applying it to several overlap gap configurations at existing traffic noise barrier sites to predict sound levels for receivers located in the receiver zones described above. In order to carry out the prediction, the traffic noise source must be specified and equations must be implemented to account for the various attenuation mechanisms, which affect each ray. Since this analysis was ultimately to be incorporated into a computer program to aid designers for highway projects, the U.S. Federal Highway Administration's Reference Energy Mean Emission Levels and the equations for traffic noise propagation^{9,11} were selected for use with the analysis method. This approach to evaluation was chosen to provide an overall gage of performance even though a pure evaluation of the analysis method is precluded, since inaccuracies in the method could not be isolated from inaccuracies inherent in the reference levels and equations of propagation.

B. Field procedure

The overlap gap sites selected for field measurements were located at four traffic noise barrier projects on interstate highways in Ohio. Three of the noise barrier projects used pre-cast concrete walls and the fourth project used steel walls. The dimensions of the overlap gaps are given in Table II.

The American National Standard, "Methods for Determination of Insertion Loss of Outdoor Noise Barriers," and "Measurement of Highway-Related Noise" were followed where appropriate for all measurements.^{12,13} All measurements were performed with dry pavement and no precipitation. No measurements were performed when the wind speed was greater than 4.5 m/s. Most measurements were conducted when the wind speed was calm or less than 1.0 m/s. All noise levels were measured as the equivalent continuous sound pressure level (Ref. 20 micro-Pa), A-weighted, the squared sound pressure being obtained with fast (*F*) exponentially weighted time averaging.

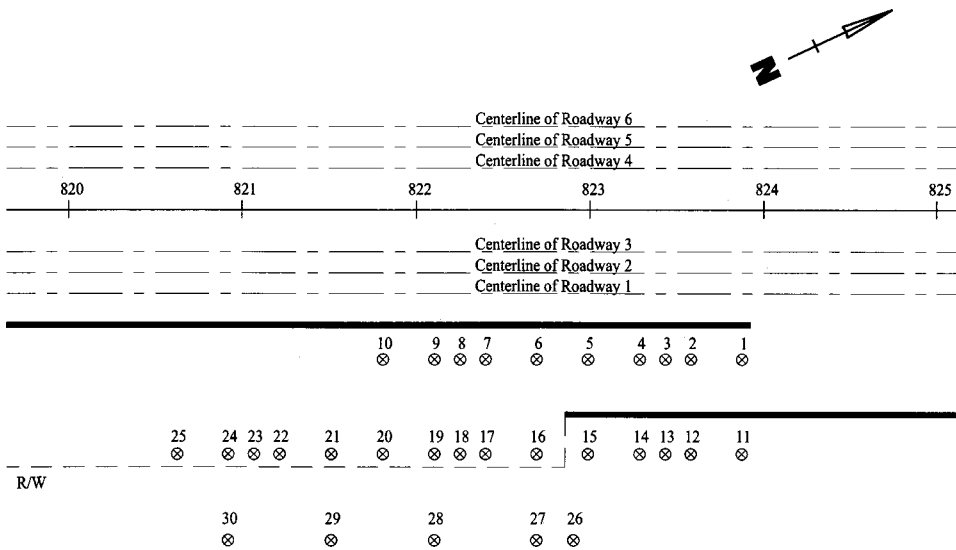


FIG. 4. Cincinnati overlap gap #1 roadway, barrier and receiver microphone locations. Drawn to scale with the distance between centerline stations numbers being 30.48 m (100 ft).

The measurement microphones were located in a grid so that data from each of the receiver cases (except case 6, which is a line) could be obtained at each measurement site. The microphone array is drawn to scale for one of the sites as shown in Fig. 4, where each numbered centerline station in the figure represents a distance of 30.48 m (100 ft). While this pattern was typical for all sites, variations in both the terrain and the geometry of the barriers precluded using the identical microphone positions at each site. Therefore, a given microphone number does not represent the same receiver region at all sites. The 30 microphone positions were not occupied simultaneously, since only five sound level meters were available. However, traffic data used to characterize the noise source was acquired for each measurement interval. The numbers and average speeds of vehicles were collected by traffic lane and by vehicle classification (autos, medium trucks, and heavy trucks). Therefore, predictions for each measurement position are based on the actual traffic observed during the noise level measurement.

IV. RESULTS

A. Effect of overlap gaps on noise barrier performance

Additional sound level predictions were made for the source and overlap gap geometry of the Cincinnati 1 site to gain a perspective of the overall effect of a typical gap. Three predictions were made, using a typical source description, for 70 receivers, which were located on a grid. The first prediction was made for a noise barrier without a gap. The second prediction was made for the barrier with the overlap gap, but the contribution from reflected rays was not included in the sound level predicted for each receiver. The third prediction was the same as the second except the contribution from reflected rays was included. Noise level contour lines shown in Fig. 5 were plotted from the predictions to illustrate the effect of the gap. The degradation in barrier effectiveness indicated by the difference between the contours in Fig. 5(b) and Fig. 5(c) supports the initial hypothesis of this study. The commonly used strategy of overlapping

barriers by an amount equal to two or three times the overlap width is useful for controlling line-of-sight propagation but ignores the substantial effect of reflections.

The errors discussed in Sec. IV C. are applicable to the absolute levels represented by the contours in Fig. 5(c). However, the errors associated with the relative differences in levels between the contours in Figs. 5(a)–(c) would be

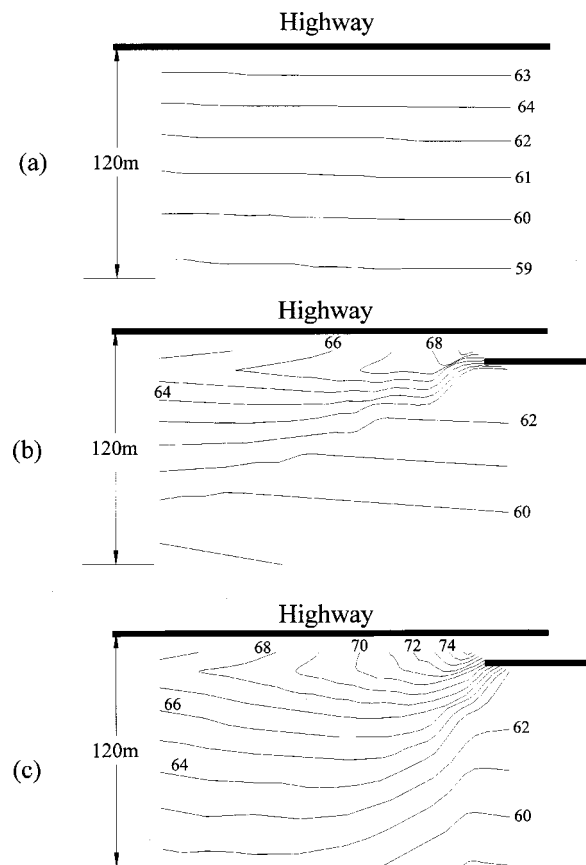


FIG. 5. A comparison of single barrier versus overlap gap noise contours. Predicted contours are shown for the single barrier in (a), for a gap not accounting for reflections in (b), and for a gap accounting for reflections in (c).

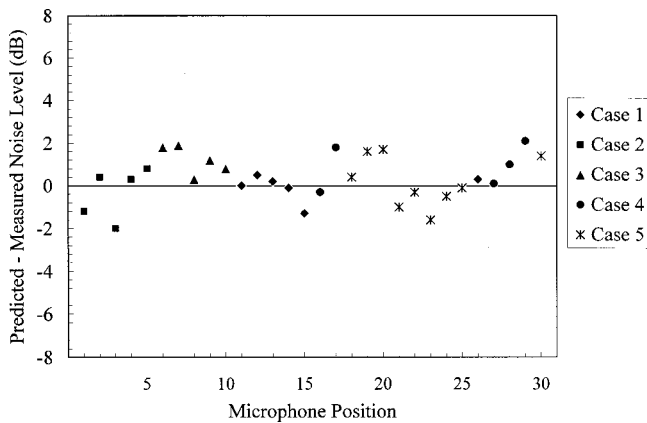


FIG. 6. Noise level difference by receiver case versus microphone position. (Cincinnati #1).

less those for the absolute values, since a portion of the overall prediction bias would be canceled for the differences.

B. Prediction versus measurements

The specific traffic-correlated measurements and predictions are compared for each site in Figs. 6–9. The microphone numbers follow a similar pattern from site to site (refer to Fig. 4), but they are not identical. No specific correlation between prediction error and microphone position is observed except for the Cincinnati 2 site shown in Fig. 7. The ground elevation at this site slopes downward away from the highway such that microphones 18 and 19 in the second row of receivers and microphones 22, 23, and 24 were progressively lower in elevation and therefore were exposed to lower levels due to increased shielding by the barriers. Since the analysis method assumed level ground, the pattern of progressively increasing over-prediction resulted for these receivers.

The single barrier prediction, which ignores the presence of the gap, was used to predict noise levels for each of the receiver microphones to determine the relative importance of including the gap for various receiver cases. As a result of not accounting for the gap, the measured levels for all sites were underestimated by an average of 10.4 dB for case 2 receivers, 5.6 dB for case 3 receivers, 1.5 dB for case 4

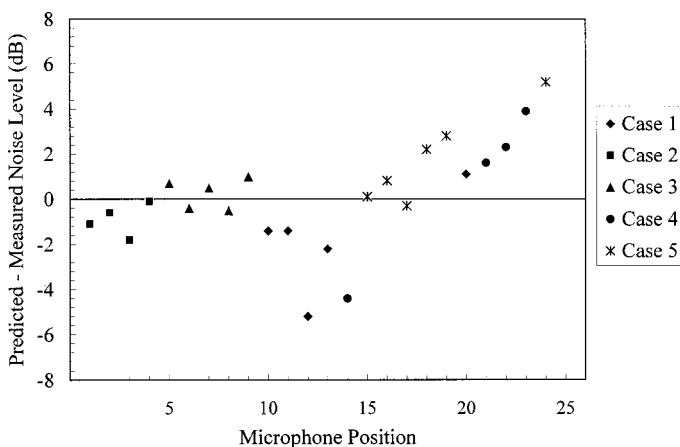


FIG. 7. Noise level difference by receiver case versus microphone position. (Cincinnati #2).

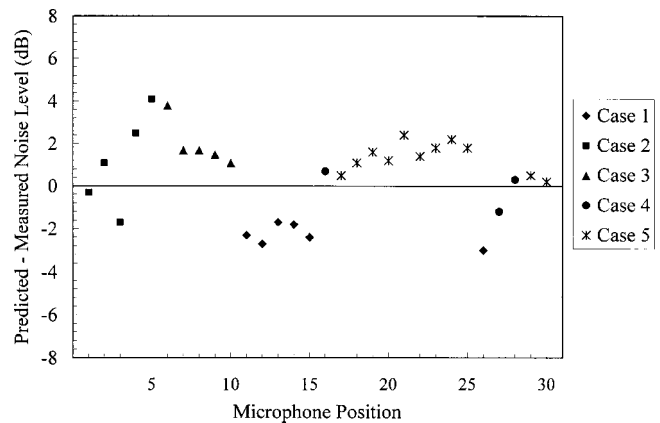


FIG. 8. Noise level difference by receiver case versus microphone position. (Columbus).

receivers and 3.1 dB for case 5 receivers. No significant underestimation was obtained for receiver case 1 measurements.

The prediction errors for all four sites are grouped by receiver case in Fig. 10. The mean prediction error is +1.0 dB for case 1 receivers, which were located on the community side of the overlap region of the gap and shielded by both barriers. The Dayton Case 1 receivers are over-predicted more than the other sites. The ends of the barriers at the Dayton site were stepped-down (for aesthetic purposes) more gradually than the other sites, which provides less shielding for the receivers than would be predicted due to the assumption of a full barrier height at the ends of the barriers. The mean prediction error for case 2 receivers, which were located within the overlap area, is also +1.0 dB. The range of errors for the Columbus overlap gap case 2 receivers is the largest not only for case 2 but also for all cases. The stepped-down treatment of the barrier ends was also prominent at this site and may have caused some of the scatter in the data. The mean prediction error for case 3, 4, and 5 receivers, was +2.3 dB, +2.1 dB, and +2.2 dB, respectively. Both the greater distance to most of these receivers and the greater number of direct rays that contributed to these receivers may have resulted in an over-prediction due to ground attenuation that was not accounted for in the equations used for propagation.

Overall, the average difference between predicted and

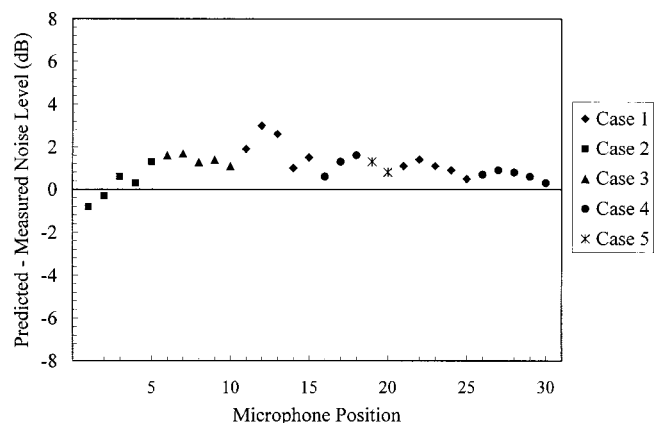


FIG. 9. Noise level difference by receiver case versus microphone position. (Dayton).

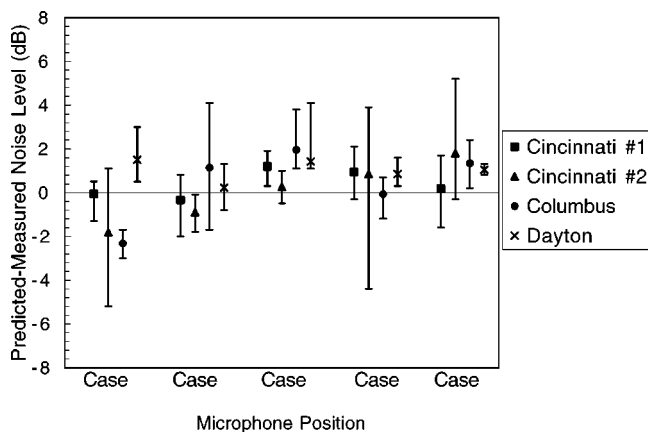


FIG. 10. Mean and range of noise level difference by receiver case for all sites.

measured noise levels for all receivers at all sites is 1.7 dB with a standard deviation of 1.2 dB. As mentioned above, errors in the analysis method cannot be isolated from errors in the equations of propagation. The Federal Highway Administration equations of propagation as implemented in the STAMINA 2.0 noise model have been found to over-predict noise levels by an average of 2 to 3 dB for first row receivers at sites with barriers,^{11,14} due in part to errors in the prediction of ground attenuation.¹⁵

C. Potential sources of error

In addition to the site features noted above several other factors could have contributed to the differences between predicted and measured noise levels. The diffraction of rays that flank the ends of the barriers, and double diffraction at the top edges of the two barriers in the overlap region were not taken into account. Based on the field measurements, the actual noise levels were usually greater than the predicted levels for receivers located close to the end of (but shielded by) the near barrier, which may indicate the presence of rays that flank the ends of the barriers. On the other hand, actual noise levels should be reduced slightly where double diffraction was present compared to predicted levels, which include the effect of diffraction at one wall only (the barrier offering the most attenuation due to diffraction). Note, approaches such as those of Pierce¹⁶ or Foss¹⁷ could be implemented to improve accuracy for contributions from these rays.

Ground of finite impedance was not considered in the analysis for several reasons. While the ground effect can be significant even for sites with barriers¹⁸ the combination of barriers and the primary interest of the study in relatively short receiver distances tends to produce reflection angles of incidence at the ground that do not approach grazing incidence, a requisite factor for higher levels of ground absorption.¹⁹ It has long been recognized that nonlevel ground introduces a complexity to ground attenuation prediction to all but preclude its accurate determination.²⁰ Further, nonuniform surface impedances compound this complexity. While methods have been suggested to account for terrain variations having a simple cross-section and a point source,^{8,21} or to analyze nonuniform surface impedances on flat ground,²² the additional computation time required to

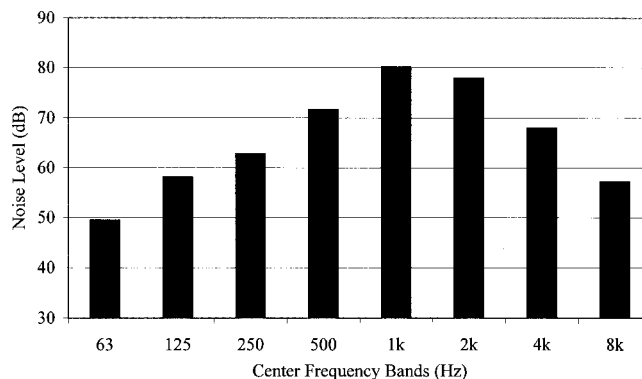


FIG. 11. Typical traffic noise source spectrum at measurement sites.

account for ground of finite impedance and nonlevel terrain with continuously varying cross-sections could not be justified for either the evaluation or the implementation of the gap analysis method developed in this study. Nevertheless levels for more distance receivers may have been reduced by ground absorption as noted in Sec. IV B.

The compromise introduced by ignoring ground of finite impedance is more relevant for the comparison of predictions with measured values than for applications of the analysis method in which the differences between overlap gap barriers and a single barrier are of the importance. For such applications the predicted ground attenuation would be similar in both cases and therefore canceled in the comparison.

The assumption of specular reflections has been shown to be valid for typical noise barrier surfaces²³ and is valid when the gap size is large compared with the wavelength of interest. The Dayton overlap gap had the smallest dimensions, with the overlap width being only slightly larger than the wavelength for the lowest predicted frequency (63 Hz). A typical traffic noise source spectrum measured near the Cincinnati barriers is given in Fig. 11. While the over-prediction for case 4 receivers (characterized by having the most contributing reflections of all cases) at the Dayton site was less than two of the sites with larger gap widths, this source of error could become an issue for more serious compromises to the assumption of specular reflections.

Due to the geometrical complexities of the problem, all barriers and roadways were treated as if they were straight lines parallel to one another. None of the actual noise barrier sites had this exacting geometry.

Two sites, Cincinnati #1 and #2, had median barriers approximately one meter in height, which were not considered in the analysis. Median barriers act as an additional noise barrier, which would shield portions of the noise from vehicles in the far lanes, while reflecting noise from near lane vehicles.

Errors exist in the specification of the traffic noise source.²⁴ The Federal Highway Administration equation assumes that each vehicle within a classification has the same source height. Further, the source heights are intended to be composite source heights representing the various components from each vehicle. This is an approximation that could

result in significant changes in the predicted noise levels when considering the number of rays examined for a typical analysis. In addition, the reference levels are specified for speeds up to 110 km/h, which is less than some of the vehicle speeds that occurred during field measurements.

V. CONCLUSIONS

Sound propagation through the gap produced by two parallel vertical barriers with overlapped ends was formulated for traffic noise sources. It was found that the source for ray paths could be located by using angular-based source segmentation, which effectively models the source position relative to the receiver during vehicle pass-bys. The barrier overlap gap analysis identifies the propagation paths for each source and receiver region associated with an overlap gap. The paths are characterized by direct, single diffracted, double diffracted, multiple reflected, multiple reflected diffracted, and diffracted multiple reflected rays.

The overlap gap analysis method was evaluated by applying it to several overlap gap configurations at existing traffic noise barriers sites to predict levels for receivers at locations where field measurements were made. The Federal Highway Administration reference levels and equations for traffic noise propagation were incorporated to quantify the source and account for the attenuation mechanisms affecting each ray reaching a receiver. Overall, the average difference between predicted and measured noise levels for all receivers was between 1 and 2 dB with a standard deviation of 1 dB. While the error associated with the analysis method cannot be isolated from the error associated with the Federal Highway Administration equations and reference levels, the results of the evaluation indicate that the method is suitable for overlap gap analysis for gaps with dimensions in the range of those used in this study, considering the limitations and assumptions imposed upon the method. Further, the method is reliable for studying the effect of changes in gap geometry or sound absorbing surfaces, which are based on the differences in before and after levels (in which most bias errors would be canceled) rather than the absolute levels.

Results from the application of the analysis method supports the initial hypothesis that reflections, particularly reflected rays that are not diffracted, in an overlap gap area make significant contributions to receiver levels for typical configurations. Thus, the conventional approach to overlap gap design, which considers only line-of-sight propagation, is shown to be inadequate, allowing substantial degradation to barrier performance.

ACKNOWLEDGMENTS

The authors gratefully acknowledge the Ohio Department of Transportation and the Federal Highway Administration for sponsoring the research described in this article.

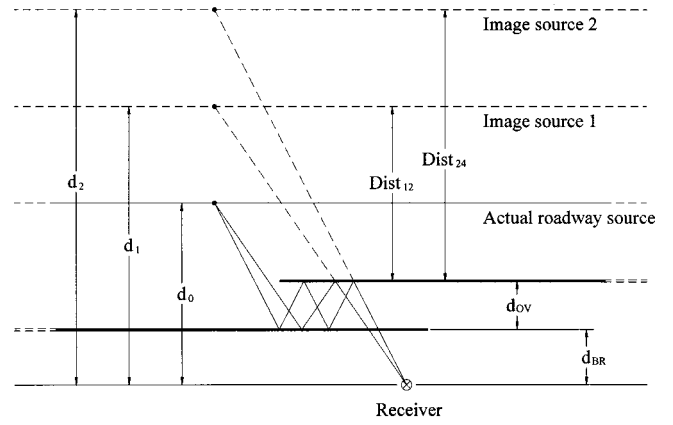


FIG. 12. Horizontal propagation of case 1 MRDR.

APPENDIX: EQUATIONS TO ANALYSE CASE 1 RECEIVERS

1. Case 1 MRDR: Horizontal propagation

With each reflection, the perpendicular distance between the image source and the receiver increases as shown in Fig. 12. This horizontal distance, the image source distance, is determined for case 1 MDRR by the following equations:

$$\begin{aligned} d_1 &= d_0 + (2 \times d_{OV}), \\ d_2 &= d_0 + (4 \times d_{OV}), \\ d_i &= d_0 + (2 \times i) d_{OV}, \end{aligned} \quad (A1)$$

where d_i is the perpendicular distance from the i th image source to the receiver, d_0 is the perpendicular distance from the roadway source to the receiver, and d_{OV} is the overlap gap width.

The formulation of the vertical propagation for case 1 MRDR requires that the horizontal perpendicular distance be computed from the image source to the respective barrier where each reflection occurs. Equation (A2) is the result of this procedure:

$$\begin{aligned} \text{Image source 1} & \begin{cases} \text{Reflection 1: } \text{Dist}_{11} = d_0 - d_{BR}, \\ \text{Reflection 2: } \text{Dist}_{12} = d_0 - d_{BR} + d_{OV}; \end{cases} \\ \text{Image source 2} & \begin{cases} \text{Reflection 1: } \text{Dist}_{21} = d_0 - d_{BR}, \\ \text{Reflection 2: } \text{Dist}_{22} = d_0 - d_{BR} + d_{OV}, \\ \text{Reflection 3: } \text{Dist}_{23} = d_0 - d_{BR} + 2d_{OV}, \\ \text{Reflection 4: } \text{Dist}_{24} = d_0 - d_{BR} + 3d_{OV}; \end{cases} \\ \text{Dist}_{ij} &= d_0 d_{BR} + (j - 1) d_{OV}, \end{aligned} \quad (A2)$$

where Dist_{ij} is the perpendicular distance from the i th image source to the j th reflection, d_0 is the perpendicular distance from the roadway source to the receiver, d_{BR} is the perpendicular distance from the near barrier to the receiver, and d_{OV} is the overlap gap width.

2. Case 1 MRDR: Vertical propagation

The height of each reflection increases before the ray is diffracted by the near barrier to the receiver. Figure 13 shows

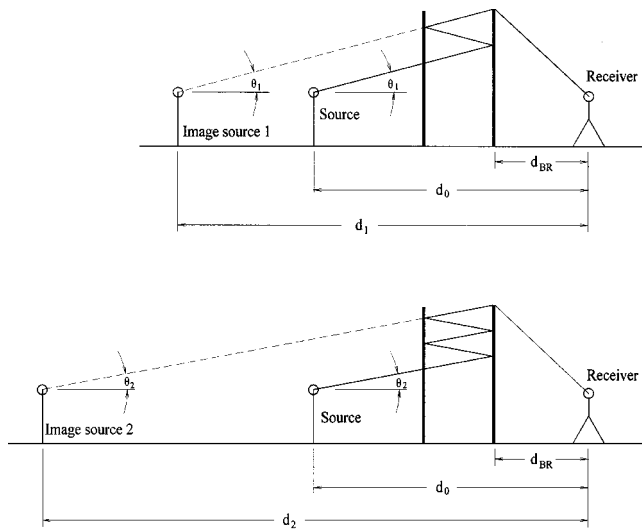


FIG. 13. Vertical propagation of case 1 MRDR.

the vertical propagation of the image ray for two source images. The derivation of the equation to calculate the vertical propagation angle follows:

$$\begin{aligned}\tan \theta_1 &= \frac{Z_N - Z_S}{d_1 - d_{BR}}, \\ \tan \theta_2 &= \frac{Z_N - Z_S}{d_2 - d_{BR}}, \\ \tan \theta_i &= \frac{Z_N - Z_S}{d_i - d_{BR}},\end{aligned}\quad (\text{A3})$$

where θ_i is the vertical angle of the i th image ray from the horizontal, Z_N is the elevation of the top of the near barrier, Z_S is the elevation of the source (vehicle-class dependent), d_i is the perpendicular distance from the i th image source to the receiver, as determined from Eq. (A1), and d_{BR} is the perpendicular distance from the near barrier to the receiver.

Equation (A3) can be used to compute the vertical propagation angle of each ray. However, it is of greater interest to be able to compute the elevation of a ray at each point that it strikes a barrier and is either reflected or diffracted. This computation makes it possible to verify whether or not a ray can reach a receiver. Further, once the location of each reflection is known, a specific absorption coefficient may be assigned to account for the attenuation due to sound absorbing materials that may be present on a given barrier surface. The height of each reflection relative to some arbitrary datum, not necessarily the source, can be expressed as

$$Z_{R_{ij}} = (Z_N - Z_S) \left(\frac{\text{Dist}_{ij}}{d_i - d_{BR}} \right) + Z_S, \quad (\text{A4})$$

where $Z_{R_{ij}}$ is the elevation of the j th reflection from the i th image source, Z_N , elevation of the top of the near barrier, Z_S

is the elevation of the source (vehicle-class dependent), Dist_{ij} is the perpendicular distance from the i th image source to the j th reflection, as determined from Eq. (A2), d_i is the perpendicular distance from the i th image source to the receiver, as determined from Eq. (A1), and d_{BR} is the perpendicular distance from the near barrier to the receiver.

- ¹M. A. Simpson, "Noise barrier design handbook," National Technical Information Service, Springfield, VA, Report FHWA-RD-76-58, 1976.
- ²Organization for Economic Cooperation and Development, "Roadside noise abatement," Paris, Road Transport Research, IRRD No. 870922, 1995.
- ³V. Lee, S. Slutsky, E. Ken, R. Michalove, and W. McColl, "Barrier overlap analysis procedure." *Transp. Res. Rec.* 1255, 1990.
- ⁴M. Gensane and F. Santon, "Prediction of sound fields in rooms of arbitrary shape: validity of the image sources method," *J. Sound Vib.* **63**, 97-108 (1979).
- ⁵J. Borish, "Extension of the image model to arbitrary polyhedra," *J. Acoust. Soc. Am.* **75**, 1827-1836 (1984).
- ⁶A. L'Espérance, "The insertion loss of finite length barriers on the ground," *J. Acoust. Soc. Am.* **86**, 179-183 (1989).
- ⁷W. Bowlby and L. F. Cohn, "IMAGE-3: Computer-aided design for parallel highway noise barriers," *Transp. Res. Rec.* **937**, 52-62 (1983).
- ⁸B. A. de Jong, A. Moerkerken, and J. D. van der Toorn, "Propagation of sound over grassland and over an earth barrier," *J. Sound Vib.* **86**, 23-46 (1983).
- ⁹W. Bowlby and L. F. Cohn, "A model for insertion loss degradation for parallel highway noise barriers," *J. Acoust. Soc. Am.* **80**, 855-868 (1986).
- ¹⁰C. J. Hurst, "Sound transmission between absorbing parallel planes," *J. Acoust. Soc. Am.* **67**, 206-213 (1980).
- ¹¹R. A. Harris, L. F. Cohn, and C. D. Grant, "Using the STAMINA 2.0 computer program to calculate contours of the one-hour-average sound levels from highway traffic noise," *Noise Control Eng. J.* **43**, 173-179 (1995).
- ¹²Acoustical Society of America, American National Standard S12.8-1998 "Methods for determination of insertion loss of outdoor barriers" (Acoustical Society of America, New York, 1998).
- ¹³C. S. Y. Lee and G. G. Fleming, "Measurement of highway-related noise," National Technical Information Service, Springfield, VA, Final Report, FHWA-PD-96-046, 1996.
- ¹⁴L. A. Herman and W. Bowlby, "Case history: an evaluation of STAMINA 2.0 based on I-440 field measurements," *Noise Control Eng. J.* **45**, 52-59 (1997).
- ¹⁵L. A. Herman, "An evaluation of STAMINA 2.0 using the ORNAMENT ground attenuation algorithm," *J. Acoust. Soc. Am.* **100**, 3460-3464 (1996).
- ¹⁶A. D. Pierce, "Diffraction of sound around corners and over wide barriers," *J. Acoust. Soc. Am.* **55**, 941-955 (1974).
- ¹⁷R. N. Foss, "Double barrier noise attenuation and a predictive algorithm," *Noise Control Eng. J.* **13**, 83-91 (1979).
- ¹⁸T. Isei, T. F. W. Embleton, and J. E. Piercy, "Noise reduction by barriers on finite impedance ground," *J. Acoust. Soc. Am.* **67**, 46-58 (1980).
- ¹⁹T. F. W. Embleton, J. E. Piercy, and G. A. Daigle, "Effective flow resistivity of ground surfaces determined by acoustical measurements," *J. Acoust. Soc. Am.* **74**, 1239-1244 (1983).
- ²⁰T. F. W. Embleton, J. E. Piercy, and N. Olson, "Outdoor sound propagation over ground of finite impedance," *J. Acoust. Soc. Am.* **59**, 267-277 (1976).
- ²¹K. B. Rasmussen, "On the effect of terrain profile on sound propagation outdoors," *J. Sound Vib.* **98**, 35-45 (1985).
- ²²S. N. Chandler-Wilde and D. C. Hothersall, "Sound propagation above an inhomogeneous impedance plane," *J. Sound Vib.* **98**, 475-491 (1985).
- ²³W. Bowlby, L. F. Cohn, and R. A. Harris, "A review of studies of insertion loss degradation for parallel highway noise barriers," *Noise Control Eng. J.* **28**, 40-53 (1987).
- ²⁴S. A. L. Glegg and J. R. Yoon, "Determination of noise source heights, Part II," *J. Sound Vib.* **143**, 39-50 (1990).

Relationship between low-frequency aircraft noise and annoyance due to rattle and vibration

Sanford Fidell^{a)}, Karl Pearsons^{b)}, Laura Silvati^{c)}, and Matthew Sneddon^{d)}
BBN Technologies, A Part of Verizon, 21128 Vanowen Street, Canoga Park, California 91303

(Received 6 February 2001; revised 3 October 2001; accepted 26 November 2001)

A near-replication of a study of the annoyance of rattle and vibration attributable to aircraft noise [Fidell *et al.*, *J. Acoust. Soc. Am.* **106**, 1408–1415 (1999)] was conducted in the vicinity of Minneapolis–St. Paul International Airport (MSP). The findings of the current study were similar to those reported earlier with respect to the types of objects cited as sources of rattle in homes, frequencies of notice of rattle, and the prevalence of annoyance due to aircraft noise-induced rattle. A reliably lower prevalence rate of annoyance (but not of complaints) with rattle and vibration was noted among respondents living in homes that had been treated to achieve a 5-dB improvement in A-weighted noise reduction than among respondents living in untreated homes. This difference is not due to any substantive increase in low-frequency noise reduction of acoustically treated homes, but may be associated with installation of nonrattling windows. Common interpretations of the prevalence of a consequential degree of annoyance attributable to low-frequency aircraft noise may be developed from the combined results of the present and prior studies. © 2002 Acoustical Society of America. [DOI: 10.1121/1.1448339]

PACS numbers: 43.50.Qp, 43.50.Lj, 43.50.Jh [MRS]

I. INTRODUCTION

The annoyance of transportation noise is commonly assessed in the United States for environmental disclosure and policy analysis purposes by means of a relationship published by the Federal Interagency Committee on Noise (FICON, 1992). Day–night average sound level (DNL), a time-weighted average sound level devised as a generic descriptor of long-term, cumulative environmental noise exposure (EPA, 1974), is the customary predictor variable for relationships such as FICON's. As noted by Job (1988) and others, this relationship between a measure of cumulative noise exposure and the prevalence of annoyance, as well as its predecessors and successors (e.g., relationships described by Schultz, 1978; Fidell, Barber, and Schultz, 1991; and Miedema and Vos, 1998), leave much of the variance in annoyance prevalence rates unexplained.

As an A-weighted metric, DNL discriminates heavily against low-frequency noise—a reasonable strategy as a generality, given the disparity of direct contributions of low- and high-frequency noise to annoyance (Kryter and Pearsons, 1963). Secondary emissions of light architectural elements of residences (e.g., rattling windows, ductwork, and doors) and of household paraphernalia (e.g., pictures, mirrors, and bric-a-brac) may be annoying, however, even when the low-frequency sources that induce such rattling are not directly annoying. Thus, some of the apparent underestimation by

FICON of the annoyance of aircraft noise exposure as measured outdoors that Miedema and Vos (1998) and others note might be associated with the annoyance of indoor secondary emissions.

Efforts to relate the annoyance of rattle to low-frequency environmental noise sources have concentrated on the noise of high-energy impulses, such as those reviewed by CHABA (1996). Schomer and Neathammer (1998) have documented the ability of helicopters to cause annoying rattle in residences, however, and Fidell *et al.* (1999) have described a relationship between an event-based metric of low-frequency aircraft noise and annoyance due to rattle and vibration. The latter association between nonimpulsive noise of aircraft ground operations and annoyance is distinguishable from that between cumulative, A-weighted aircraft noise exposure and annoyance.

DNL values due to aircraft operations are often considerably lower in runway sideline neighborhoods than in neighborhoods near extended runway centerlines, because A-weighted noise exposure gradients orthogonal to runways are steep, and because runway sideline areas at large airports are not often exposed to the noise of large numbers of low-altitude aircraft overflights. Large jet transports nonetheless create substantial noise at low frequencies in areas adjacent to runways during takeoff run and application of reverse thrust. Thus, low-frequency noise to which DNL is insensitive can produce secondary emissions that may be annoying both in their own right, and to the extent that they may call further attention to aircraft noise events. The present study was undertaken as an empirical test of whether differences in lifestyle and housing construction in different climates affected the generality or applicability of the findings of Fidell *et al.* (1999).

^{a)}Current address: Fidell Associates, 23139 Erwin Street, Woodland Hills, CA 91367.

^{b)}Current address: Pearsons Psychoacoustics, 22689 Mullholland Drive, Woodland Hills, CA 91367.

^{c)}Current address: Fidell Associates, 23139 Erwin Street, Woodland Hills, CA 91367.

^{d)}Current address: Wavefront Scientific, 4442 York Boulevard, Suite 10, Los Angeles, CA 90041.

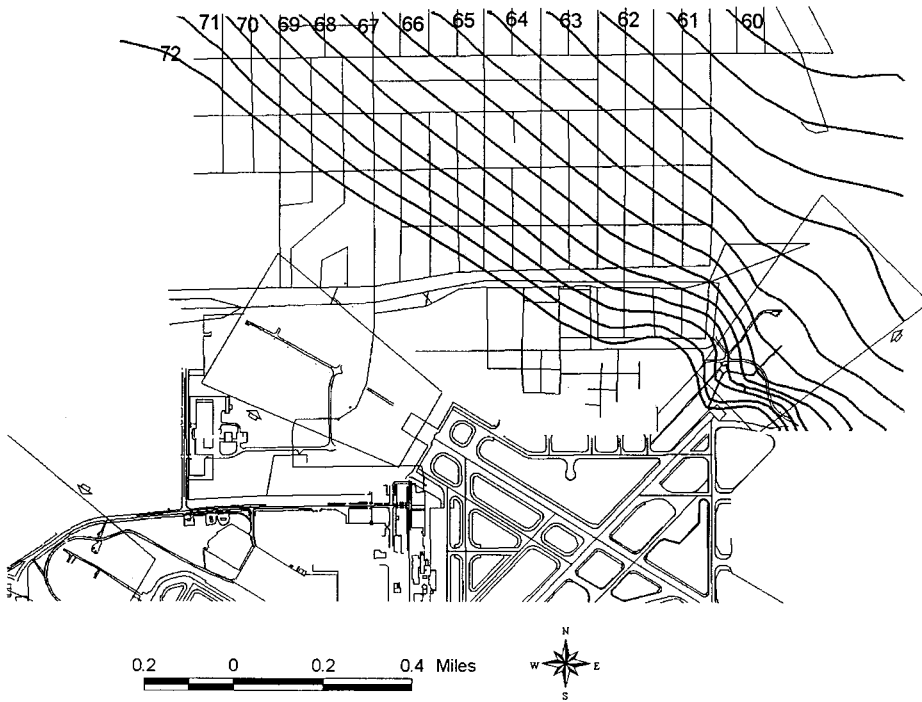


FIG. 1. INM 6.0 prediction of DNL contours in the interviewing area at MSP.

II. METHOD

A. Selection of interviewing area

A residential area to the north of the intersection of Runways 4/22 and 12/30 at MSP was identified as a neighborhood of low-density housing (primarily single-family detached wood-frame dwellings) that is not directly overflowed at low altitude, but that is close enough to runway sidelines to be exposed to low-frequency aircraft noise. Surface traffic noise in this area is that produced on a grid of two-lane secondary streets. A multilane thoroughfare north of the run-

way intersection is depressed below grade level throughout much of the southerly portion of the interviewing area.

Version 6.0 of the Federal Aviation Administration's INTEGRATED NOISE MODEL (INM) software was used to calculate DNL and maximum C-weighted aircraft single-event level contours from operational information provided by the Metropolitan Airports Commission. Contours computed at 1-dB intervals were overlaid on a base map of residences to identify street address ranges with similar expected aircraft noise, as shown in Figs. 1 and 2 for DNL and C-weighted maximum sound levels, respectively.

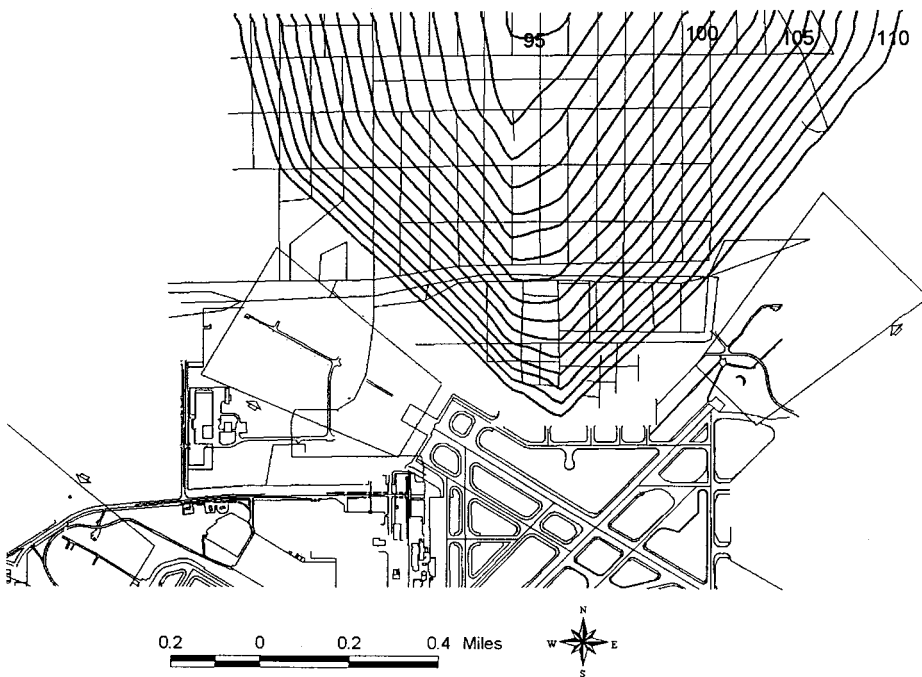


FIG. 2. INM 6.0 prediction of C-weighted maximum contours in the interviewing area at MSP.

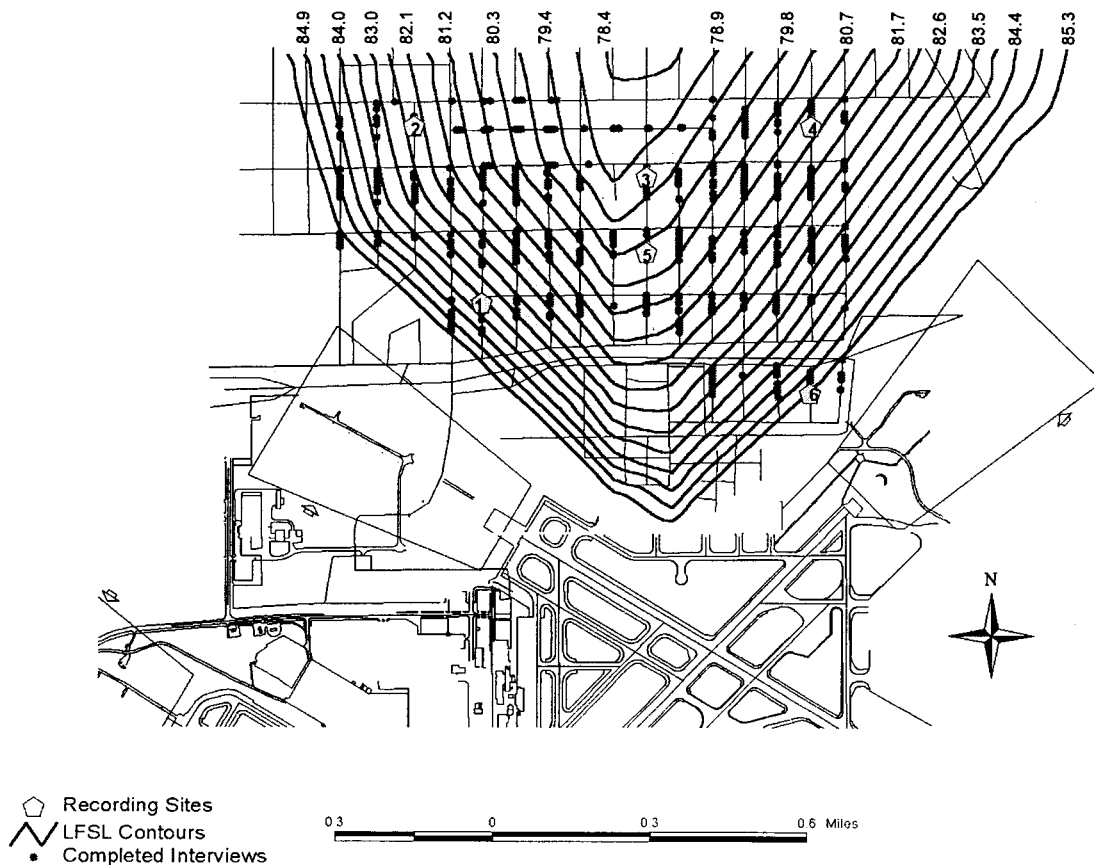


FIG. 3. Noise measurement and completed interview sites, with estimated LFSL contours.

B. Measurement of low-frequency aircraft noise levels

Unattended wideband digital recordings were made at six sites within the interviewing area (as shown in Fig. 3) to characterize low-frequency sound levels due to aircraft operations. These measurements were made during 12 daylight and evening hours per day over the course of 4 days to yield a total of 288 h of recordings for subsequent analysis of low-frequency aircraft noise events.

C. Sampling and interviewing procedures

A sampling frame of 1003 households with listed telephone numbers was assembled from digital reverse directories and an MSP-provided database of residences that had received airport-sponsored acoustic insulation treatments. Potential respondents were identified by simple random selection from the sampling frame at the time of interviewing. On 10 June 1999, 12 centrally supervised telephone interviewers began ten contact attempts: an initial attempt, followed by nine callbacks at different times of day over an 8-day interviewing period. The opinions of one English-speaking, verified adult household member were sought from each selected household. All interviewers read a training manual and underwent half an hour of training, including practice interviews, prior to conducting interviews.

D. Questionnaire

A brief, structured questionnaire composed of two open-response items and several closed-response category items

was administered. The wording and order of questionnaire items was taken from that of Fidell *et al.* (1999). Two items were added to the end of the questionnaire about awareness and satisfaction with the airport-sponsored acoustic-insulation program. Respondents were constrained to reply to questions about intensity of annoyance by selecting one of the following response categories: “not at all annoyed,” “slightly annoyed,” “moderately annoyed,” “very annoyed,” or “extremely annoyed.” The latter two response categories were considered to represent a consequential (or “high”) degree of annoyance.

The interview was introduced as a study of neighborhood living conditions. The first explicit mention of noise occurred in item 4 (“*Would you say that your neighborhood is quiet or noisy?*”), following preliminary questions about duration of residence, and about the most and least-favored aspects of neighborhood living conditions. The next two items inquired about annoyance with street traffic noise and aircraft noise. Respondents were next asked whether airplanes made vibrations or rattling sounds in their homes. Respondents who had noticed rattling in their homes were asked five additional questions about how annoyed they were with the rattling sounds, how often they noticed the rattling sounds, what objects rattled in their homes, whether they had tried to do anything to reduce the rattling in their homes, and whether they had ever complained to the airport about the rattling.

TABLE I. Disposition of telephone interview contact attempts.

	Final status
Total telephone numbers in sampling frame	1003
Nonsample ^a	143
Noncontacts ^b	248
Refusals	117
Completed interviews	495
Completion rate ^c	0.809

^aIncludes disconnects, nonresidential telephones, fax machines, modern lines, wrong addresses, changed numbers, and non-English-speaking households.

^bIncludes busy, no answer, not available, call blocked, or answering machine after ten contact attempts.

^cCompletion rate calculated as: completed interviews ÷ [completed interviews + refusals].

III. RESULTS

A. Summary of results of interviewing

Table I summarizes the mechanics of data collection. Interviews were completed at 495 residences, as shown in Fig. 3, for an interview completion rate of 81%. The bulk (79%) of the nonsample telephone numbers were disconnected and changed telephone numbers. Failure to complete an interview was due mostly to refusals and noncontacts after ten attempts. The average length of the interview was 6 min. Of the completed interviews, 177 were conducted in households that had been acoustically treated, and 318 were conducted in households that had not been so treated.

B. Measurements of low-frequency aircraft sound levels

Panel A of Fig. 4 is a spectrogram of a typical time-

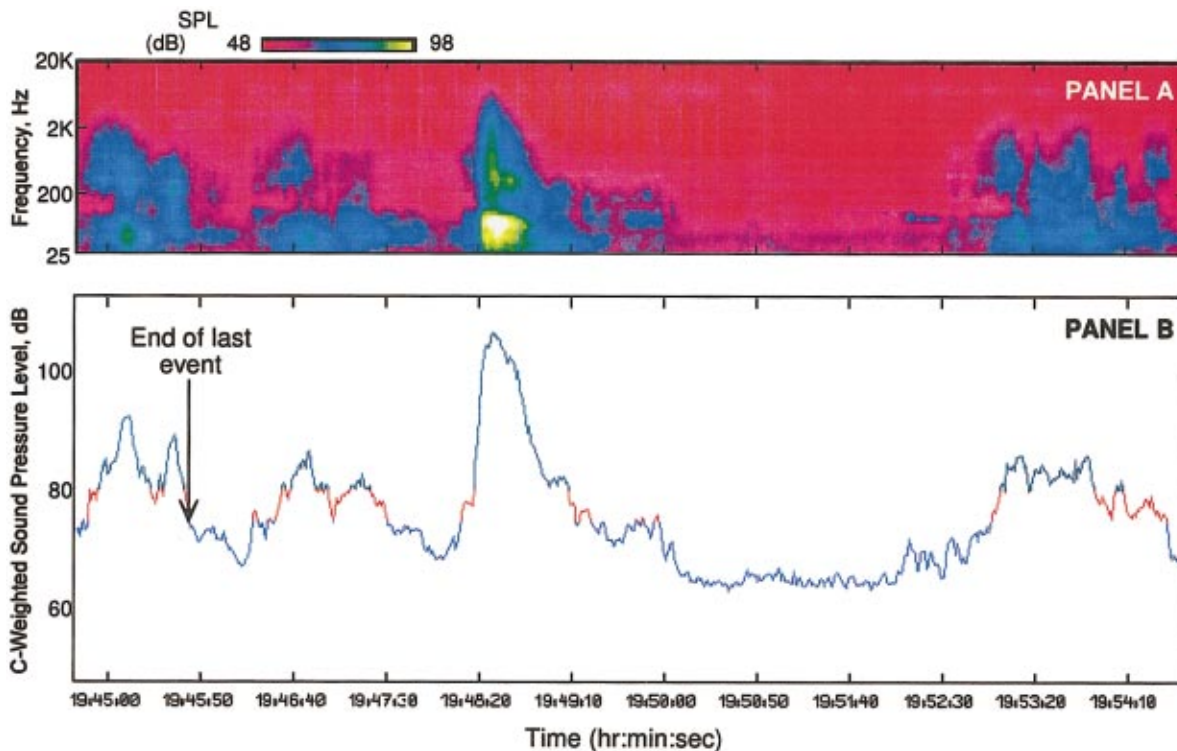


FIG. 4. Typical time history [panel (B)] and spectrogram [panel (A)] of aircraft noise events recorded at a site within the interviewing area.

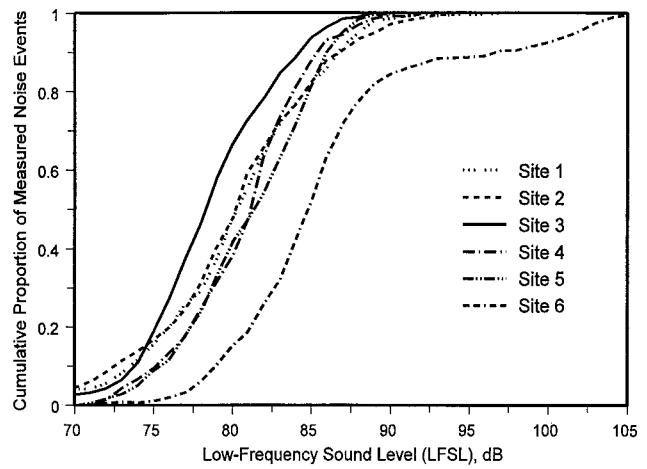


FIG. 5. Cumulative distributions of low-frequency sound levels of aircraft noise events at six measurement sites within the interviewing area.

history segment as recorded in the interviewing area, color-coded to help identify the low-frequency content of the noise events. The concentration of low-frequency energy shortly after the peak of the prominent noise event in the time-history trace shown in panel (B) is characteristic of an aircraft noise event. The noise event that occurred about 5 min later, which lacks the characteristic concentration of low-frequency noise, is a vehicle pass-by on a nearby street. The color-coding of the time-history trace distinguishes C-weighted levels between 75 and 80 dB (a range of levels within which the likelihood of rattle due to low-frequency noise increases notably) from higher and lower levels.

Statistical distributions of low-frequency sound level (LFSL) values for screened aircraft noise events were computed as described by Fidell *et al.* (1999) at the time of the

TABLE II. Summary of distributions of low-frequency sound levels measured at the C-weighted maxima of aircraft noise events at six sites within the interviewing area.

Site	C-Max (per INM)	Mean (dB)	Median (dB)	<i>n</i>	σ (dB)	L_{10} (dB)	L_5 (dB)	L_1 (dB)
1	106.2	81.3	83.2	654	7.5	89.2	90.0	91.5
2	103.4	81.8	83.0	504	7.2	90.1	91.0	93.1
3	96.3	77.5	78.0	493	5.5	84.1	85.3	86.9
4	100.6	81.6	82.1	220	3.9	86.1	88.1	89.9
5	97.9	82.0	82.3	378	4.0	87.0	87.8	89.1
6	110.2	86.9	85.9	411	6.5	97.9	102.8	104.9

maximum C-weighted single-event level, by summing the energy in the one-third-octave bands centered at 25 through 80 Hz, inclusive. Figure 5 displays cumulative LFSL distributions for these aircraft noise events at each of the six measurement sites.

C. Estimation of LFSL values for individual respondents

Table II summarizes maximum C-weighted levels predicted by INM 6.0 and LFSL distribution information for each measurement site. A linear regression equation relating average measured LFSL values to INM-predicted maximum C-weighted aircraft noise levels ($L_{FSL} = 0.46 * L_{C_{max}} + 34.8$ dB) was applied to maximum C-weighted values calculated for the street address of each completed interview. The regression accounts for 65% percent of the variance in the measured LFSL values. The LFSL value assigned to each respondent's street address was the arithmetic mean of the maxima of measured LFSL values of aircraft noise events in excess of 75 dB. (Since the bulk of the aircraft noise event maxima exceeded 75 dB, the average LFSL value of the event maxima in excess of 75 dB differed little from the average of aircraft noise events with LFSL values in excess of 60 dB.) Note that the LFSL value so estimated is *not* the greatest single aircraft noise event level at a respondent's home, but rather a lower value consistent with the "few times a day" to "few times an hour" modal responses to the frequency of notice questions in the current and LAX surveys. Figure 3 shows INM-produced maximum C-weighted noise level contours relabeled with estimated LFSL values.

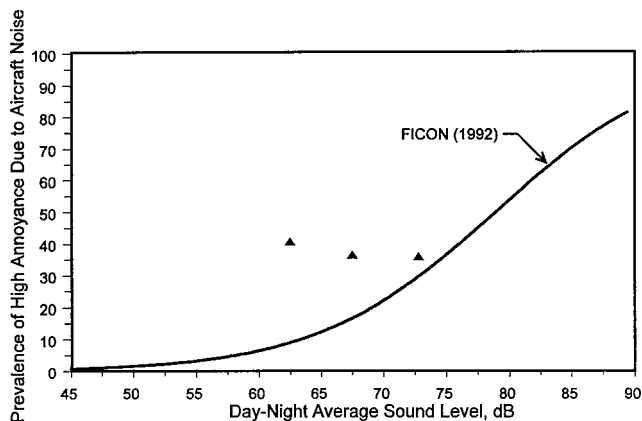


FIG. 6. Relationship between DNL and prevalence of a consequential degree of aircraft noise-induced annoyance.

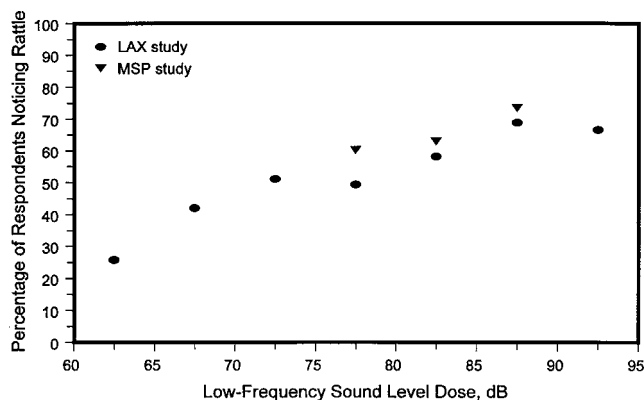


FIG. 7. Percentage of respondents noticing aircraft-induced rattle in LAX and MSP surveys as a function of LFSL.

D. Responses to primary questionnaire items

The questionnaire items of principal concern were items 6 through 10. Item 6 ("While you're at home are you bothered or annoyed by aircraft noise in your neighborhood?") inquired about respondents' annoyance due to aircraft noise in general. Three groups of respondents with similar noise exposure (± 2.5 dB) were formed: $60.0 \leq L_{dn} \leq 65$ dB, $65 \leq L_{dn} \leq 70$, and $70 \leq L_{dn} \leq 75$ dB. Of the 157 respondents with the least noise exposure, 64 (40.1%) described themselves as highly annoyed by aircraft noise; 96 of 263 respondents (36.5%) in the group with intermediate exposure described themselves as highly annoyed by aircraft noise; and 27 of 75 respondents (36%) in the group with the greatest noise exposure described themselves as highly annoyed by aircraft noise. Figure 6 compares these annoyance prevalence rates, plotted at the midpoints of the noise exposure intervals, with the FICON (1992) dosage-response relationship.

Item 7 ("Do airplanes make vibrations or rattling sounds in your home?") inquired about notice of aircraft-induced secondary emissions. More than half of the respondents (58% in acoustically insulated homes and 65% in non-insulated homes) reported that airplanes made rattling sounds in their homes. Of those respondents who noticed rattle, 67% in acoustically insulated homes and 79% in noninsulated homes reported annoyance in some degree due to vibrations or rattling sounds (item 8), while 35% and 45% of these respondents, respectively, reported that they were very or

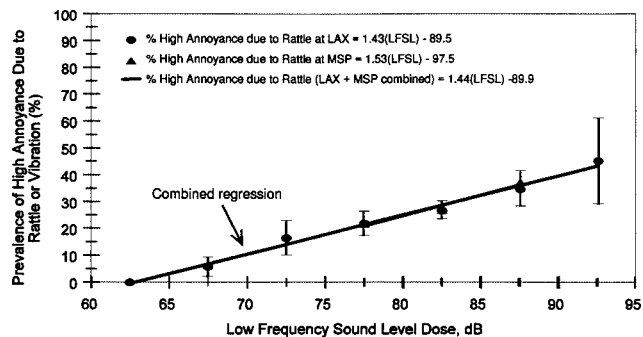


FIG. 8. Relationship between low-frequency sound levels of aircraft at two airports and prevalence of annoyance due to vibrations or rattling sounds. Error bars mark the width of 90% confidence intervals of the underlying data sets.

TABLE III. Observed prevalence of annoyance with rattle at midpoints of LFSL exposure intervals.

Midpoint of LFSL interval (dB)	Percent of respondents highly annoyed by rattle	
	LAX	MSP
62.5	0%	
67.5	5.8%	
72.5	16.3%	
77.5	21.5%	21.6%
82.5	26.2%	26.6%
87.5	34.1%	36.8%
92.5	44.4%	

highly annoyed. Figure 7 compares the percentages of respondents who reported noticing rattling sounds in the MSP and LAX surveys as a function of LFSL.

Item 9 (“*About how often do you notice vibrations or rattling sounds in your home made by airplanes?*”) inquired about frequency of notice of rattling noises. About 30% of all respondents who noticed rattling sounds in their homes reported that they noticed vibrations or rattling sounds several times an hour. About 14% of all respondents who noticed rattling sound in their homes reported noticing rattle once an hour. Item 10 (“*What sorts of things vibrate or rattle in your home?*”) inquired about the sources of rattling noises. The most common source of rattle, reported by 61% of all respondents, was windows. Other commonly reported sources of rattle included walls (16%) and pictures (14%).

Items 12 and 13 (“*Have you ever complained to the airport about vibrations or rattling sounds in your home made by airplanes?*” and “*Have you ever complained to the airport about aircraft noise in general?*”) inquired about complaints due to rattling noises and aircraft noise in general. Less than a third of the respondents who reported rattling sounds in their homes had complained to the airport about them. Less than a quarter of all respondents in both acoustically insulated and noninsulated homes had complained to the airport about aircraft noise in general.

IV. DISCUSSION

A. Relationship between LFSL and the prevalence of annoyance due to rattle

Figure 8 shows linear regressions for grouped data (see Table III) within 5-dB LFSL intervals and the prevalence of aircraft-induced rattle and vibration for the combined data sets. The linear regression accounts for 93% of the variance in the combined data set. The error bars plotted at the midpoints of the 5-dB LFSL intervals show the upper and lower bounds of 90% confidence intervals on the proportions of highly annoyed respondents in the combined LAX and MSP data sets.

B. Geographic association of prevalence of high annoyance due to low-frequency aircraft noise and runway sideline distances

Three decades of contouring A-weighted aircraft noise at major airports has led to widespread appreciation of expo-

sure gradients and distances along extended runway centerlines at which annoyance due to overflights may be expected. This information is of considerable utility for purposes such as land-use planning and estimation of the magnitude of potential aircraft noise mitigation projects. Comparable information about low-frequency sound levels and their effects is not as well appreciated. It is therefore of some interest to note runway sideline distances at which low-frequency noise effects are likely to be observed in residential areas, even though the geographic association itself is inherently non-causal. The information summarized in such a geographic association is intended to complement rather than supplant the dosage-response analysis illustrated in Fig. 8. Although the relationship is necessarily site-specific to some degree, it may nonetheless be of interest for general planning purposes at large airports contemplating runway expansion projects.

Figure 9 plots the prevalence of high annoyance with rattle or vibration with respect to runway sideline distance intervals. The relationships displayed in Fig. 9 were developed in three steps. First, the distance was determined from each household at which an interview was completed to the centerline (or extended centerline, as necessary) of the nearest runway at LAX or MSP. Second, the distances from households to runway centerlines were grouped in 500-ft. intervals. Third, the percentage of respondents describing themselves as very or extremely annoyed by aircraft-induced rattle and vibration was calculated for each distance interval.

Although the geographic association between sideline distance from runways and their extended centerlines and the prevalence of annoyance due to rattle has obvious limitations, it does *not* rely upon measurement or estimation of any acoustic quantities, and is independent of the distance from homes to points of brake release or thrust reverser application, and of fleet mix, propagation, and residential construction factors. The independence of this association from acoustic quantities and aircraft operational factors is important for two reasons. First, the association reflects the net effect of all of the interacting influences of low-frequency source levels and acoustic propagation into residences, as well as the potential influences of nonacoustic factors. Second, it is not heir to any of the uncertainties of acoustic measurement or aircraft operation.

C. Effects of acoustic insulation on annoyance and complaints about rattle

The prevalence of high annoyance due to vibrations or rattling sounds was 20.3% among respondents living in acoustically insulated homes and 29.2% in noninsulated homes. This difference ($\chi^2_{(df=1)} = 4.7, p = 0.03$) was unlikely to have arisen by chance alone. Since the noise exposure of respondents living in acoustically treated homes was greater than that of respondents living in untreated homes (mean $L_{dn} = 71$ and 65 dB, respectively), it is apparent that the treatments afforded some reduction in annoyance due to secondary emissions. Noise reduction measurements reported in Fidell *et al.* (2000) show that standard acoustic insulation treatments provided to single-family homes at MSP have no appreciable effect on their noise reductions at frequencies

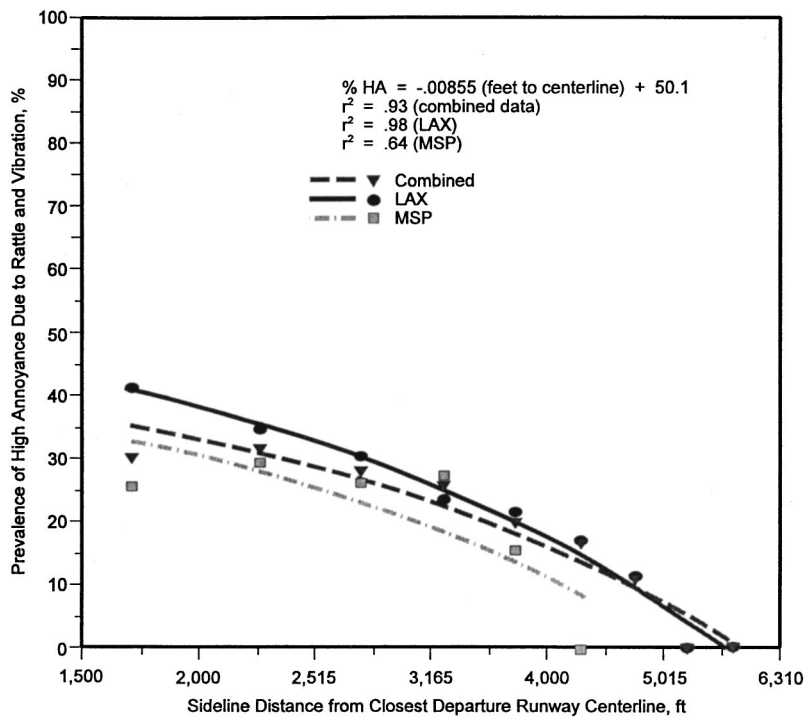


FIG. 9. Relationships between runway sideline distances and prevalence of annoyance due to rattle and vibration.

below about 100 Hz. The reduction in annoyance due to rattle is therefore likely to be attributable to the relatively recent installation of tightly fitted (nonrattling) windows as part of the standard acoustic treatment package.

Respondents who had noticed aircraft-induced rattling sounds in their homes were asked whether they had complained to the airport about them. Of the respondents living in acoustically insulated homes who had noticed rattle, 24.3% had complained to the airport about the rattling sounds in their homes, whereas 32.7% of the respondents in noninsulated homes had complained to the airport. This difference was not statistically significant ($\chi^2_{(df=1)} = 2.3$, $p = 0.13$). The percentages of respondents in acoustically insulated and noninsulated homes who had complained to the airport about aircraft noise in general were 19% and 24%, respectively. This difference was not statistically significant ($\chi^2_{(df=1)} = 1.6$, $p = 0.21$).

D. Potential nonacoustic influences on annoyance judgments

Self-reports of annoyance attributed to rattle and vibration are as susceptible to nonacoustic influences as self-reports of annoyance due to other forms of aircraft noise exposure. Fields (1993) has analyzed an extensive literature on demographic, attitudinal, and situational factors that may affect such reports. Fidell, Schultz, and Green (1988) and Baird, Harder, and Preis (1997) have suggested various other nonacoustic factors that may influence self-reports of annoyance. No effort was made in the present study to identify any such specific effects.

V. CONCLUSIONS

Figure 8 summarizes findings about the prevalence of annoyance associated with rattle and vibration due to low-frequency aircraft noise in runway sideline neighborhoods near two large civil airports. Until refined by further information, this relationship can complement interpretations of the annoyance of A-weighted aircraft noise. The geographic association summarized in Fig. 9 may also be of interest for general land-use planning purposes.

ACKNOWLEDGMENTS

This study was sponsored by the City of Richfield, Minnesota and the Minneapolis Metropolitan Airports Commission (MAC). Mr. Richard Horonjeff and Mr. Andrew Harris of Harris Miller Miller & Hanson supervised field measurements and data reduction of aircraft noise levels at three sites, and conducted low-frequency noise reduction measurements of homes in the interviewing area. The present findings about low-frequency sound levels in the interviewing area are based on further analyses of the acoustic measurements contained in the report of the Low-Frequency Noise Expert Panel of the Richfield-MAC Noise Mitigation Agreement of 17 December 1998 (Fidell, Harris, and Sutherland, 2000).

- Baird, J. C., Harder, K., and Preis, A. (1997). "Annoyance and community noise: Psychophysical model of dose-response relationships," *J. Environ. Psych.* **17**, 333–343.
- Committee on Hearing, Bioacoustics, and Biomechanics (CHABA) (1996). "Community Response to High-Energy Impulsive Sounds: An Assessment of the Field Since 1981," *Report of Working Group 102 of the National Research Council Committee on Hearing, Bioacoustics, and Biomechanics* (National Academy, Washington, D.C.).

- Environmental Protection Agency (EPA) (1974). "Information on Levels of Environmental Noise Requisite to Protect Public Health and Welfare with an Adequate Margin of Safety," EPA/ONAC 550/9-74-004.
- Federal Interagency Committee on Noise (FICON) (1992). "Federal Agency Review of Selected Airport Noise Analysis Issues," Report for the Department of Defense, Washington, D.C.
- Fidell, S., Harris, A. S., and Sutherland, L. (2000). "Findings of the Low-Frequency Noise Expert Panel of the Richfield-MAC Noise Mitigation Agreement of 17 December 1998," Report to the City of Richfield, Minnesota, and the Minneapolis Metropolitan Airports Commission. There was *not* unanimous agreement by the authors on all material in the Report.
- Fidell, S., Silvati, L., Pearsons, K., Lind, S., and Howe, R. (1999). "Field study of the annoyance of low-frequency runway sideline noise," *J. Acoust. Soc. Am.* **106**(3), 1408–1415.
- Fidell, S., Barber, D., and Schultz, T. J. (1991). "Updating a dosage-effect relationship for the prevalence of noise-related annoyance," *J. Acoust. Soc. Am.* **89**, 221–233.
- Fidell, S., Schultz, T. J., and Green, D. M. (1988). "A theoretical interpretation of the prevalence rate of noise-induced annoyance in residential populations," *J. Acoust. Soc. Am.* **84**, 2109–2113.
- Fields, J. M. (1993). "Effect of personal and situational variables on noise annoyance in residential areas," *J. Acoust. Soc. Am.* **93**, 2753–2763.
- Job, R. F. S. (1988). "Community response to noise: A review of factors influencing the relationship between noise exposure and reaction," *J. Acoust. Soc. Am.* **83**, 991–1001.
- Kryter, K. D., and Pearsons, K. S. (1963). "Some effects of spectral content and duration on perceived noise level," *J. Acoust. Soc. Am.* **35**, 866–883.
- Miedema, H., and Vos, H. (1998). "Exposure-response relationships for transportation noise," *J. Acoust. Soc. Am.* **104**, 3432–3445.
- Schomer, P. D., and Neathammer, R. D. (1998). "The role of helicopter noise-induced vibration and rattle in human response," *J. Acoust. Soc. Am.* **81**, 966–976.
- Schultz, T. J. (1978). "Synthesis of social surveys on noise annoyance," *J. Acoust. Soc. Am.* **64**, 377–405.

Synthesis of a robust broadband duct ANC system using convex programming approach

Mingsian R. Bai and Pingshun Zeung

Department of Mechanical Engineering, National Chiao-Tung University, 1001 Ta-Hsueh Road, Hsin-Chu 30010, Taiwan, Republic of China

(Received 24 July 2000; revised 27 August 2001; accepted 17 January 2002)

A robust active controller using spatially feedforward structure is proposed for broadband attenuation of noise in ducts. To meet the requirements of performance and robust stability in the presence of plant uncertainties, an H_2 cost function and an H_∞ constraint are employed in the synthesis of the controller. The design is then converted into a convex programming problem using Q -parametrization and frequency discretization. An optimal controller that satisfies the quadratic cost functions and linear inequality constraints can be found by sequential quadratic programming. The optimal controller was implemented via a digital signal processor (DSP) and verified by experiments. Experiment results showed that the system attained 16.5 dB maximal attenuation and 5.9 dB total attenuation in the frequency band 200–600 Hz. © 2002 Acoustical Society of America. [DOI: 10.1121/1.1460926]

PACS numbers: 43.50.Ki [MRS]

I. INTRODUCTION

Active noise control (ANC) offers numerous advantages, e.g., compact size and low-frequency performance, over conventional passive technologies. Although the adaptive feedforward control, e.g., the filtered-X algorithm is widely used, fixed controllers based on optimal control and robust control are gaining research attention in the field of ANC. Many design techniques have been applied to the duct ANC problem for synthesizing fixed controllers. Hong *et al.*¹ and Wu *et al.*² investigated the duct ANC problem using the linear quadratic Gaussian (LQG) control. Along the same line, robust controllers are designed using combined pole placement and loop shaping method.³ Using model matching approach, Bai and Wu⁴ solved the problem via linear programming in the l_1 -norm and l_2 -norm vector space. In earlier research, Bai and Chen⁵ developed the H_2 and H_∞ model matching principle to deal with the same problem. Moreover, to suppress narrow-band noise, an internal model-based active noise control system has been proposed.⁶ In the work of Bai and Lin,⁷ H_∞ robust control theory was used to compare three control structures: feedback control, feedforward control, and hybrid control in terms of performance, stability, and robustness.

In ANC applications to date, feedforward control has been a most effective approach. However, a nonacoustical reference required by feedforward control is usually unavailable in many applications. The *spatially feedforward* control structure shown in Fig. 1 appears to be a more viable approach in dealing with such situations, especially when broadband attenuation is sought. The term, spatially feedforward structure, stems from the fact that the ANC system in Fig. 1 includes an acoustic feedback path and is thus not a purely feedforward structure. In this case, stability and robustness problems will arise and the achievable performance will also be degraded. For the spatially feedforward structure, the zero spillover controller⁸ or the Roure's controller⁹ can be used. However, these controllers may be noncausal

and require special modifications, e.g., direct truncation of impulse response, before practical implementation. Therefore, an optimization method combining an H_2 performance objective with an H_∞ constraint is proposed for the design of a spatially feedforward controller for duct. Using this approach, nominal performance can be achieved under the H_∞ constraint of robust stability.

Much work has been addressed in the literature^{10–15} on the mixed H_2/H_∞ control. The controllers can be synthesized by the Riccati equation approach, the convex optimization approach or the dynamic game approach, etc. In Ref. 15, a duct ANC system was developed using mixed H_2/H_∞ control. The work incorporated an H_∞ -constrained, LQG feedback controller with an internal model to attenuate a narrow-band disturbance. The controller is synthesized analytically by solving the Riccati equations. In contrast to their approach, a numerical optimization approach, convex programming, applied within a general framework originally suggested by Boyd¹⁶ is employed in this paper for achieving broadband noise reduction in a spatially feedforward structure. Then, Q -parametrization^{17,18} is used to formulate all stabilizing controllers. The resulting Q -parametrization represented by a finite impulse response (FIR) filter transforms the design problem into a convex optimization problem in frequency domain. The approach suggested by Boyd¹⁶ is used in this work, where the optimal controller is found using *sequential quadratic programming*.^{19,20} Common causes of plant uncertainties are modeling errors, measurement noises, and the perturbations in physical conditions. A comprehensive investigation on the effect of different physical conditions on ducts such as flow, temperature, lining, and radiation impedance, can be found in Ref. 21. However, in this paper, we shall focus on primarily the uncertainty resulting from modeling error on which the robust stability constraint is based.

This paper is organized as follows. First, the convex programming and Q -parametrization are presented in the

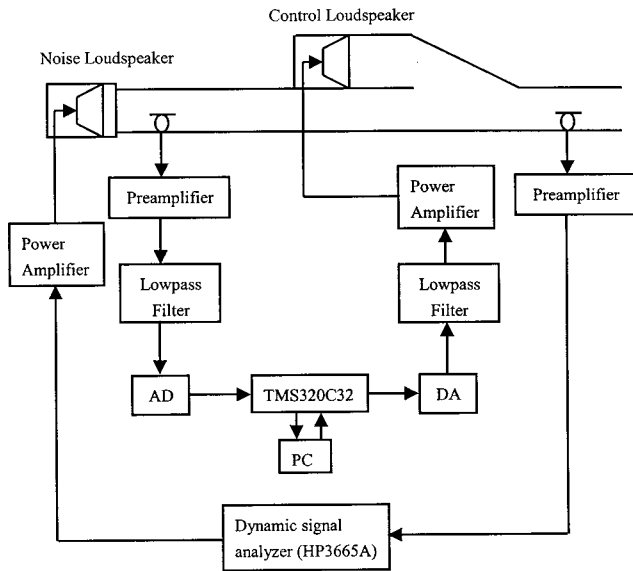


FIG. 1. Experimental setup of the ANC problem.

context of performance and robustness analysis. Then, the calculated controller is implemented as a FIR filter on a TMS320C32 digital signal processor (DSP). Finally, the proposed ANC system will be justified by experimental investigations and the results will be discussed.

II. ZERO SPILLOVER CONTROLLER AND ROURE'S CONTROLLER

Consider a standard control framework, with K the feed-forward controller, G the plant, w the exogenous input, z the controlled variables, u the control force, and y the measurement as illustrated in Fig. 2. Thus, the general input–output relation of the augmented plant can be expressed as follows:

$$\begin{bmatrix} z(k) \\ y(k) \end{bmatrix} = \begin{bmatrix} G_{zw}(z)G_{zu}(z) \\ G_{yw}(z)G_{yu}(z) \end{bmatrix} \begin{bmatrix} w(k) \\ u(k) \end{bmatrix}, \quad (1)$$

where $G_{yu}(z)$, $G_{zu}(z)$, $G_{zw}(z)$, and $G_{yw}(z)$ are properly partitioned transfer matrices of G . They are represented in Figs. 3(a)–(d). The closed loop transfer function can be expressed as

$$\begin{aligned} T_{zw}(z) &= [G_{zw}(z) - (G_{zw}(z)G_{yu}(z) \\ &\quad - G_{zu}(z)G_{yw}(z))K(z)][1 - G_{yu}(z)K(z)]^{-1} \\ &= F(z)S_0(z), \end{aligned} \quad (2)$$

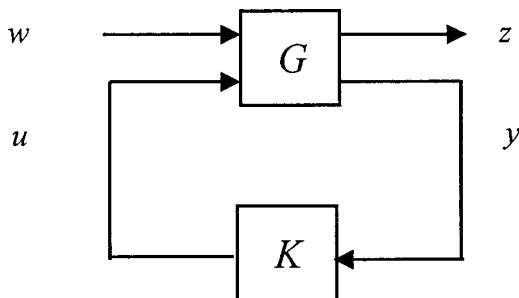


FIG. 2. The generalized control framework of the ANC system.

where

$$F(z) \equiv G_{zw}(z) - [G_{zw}(z)G_{yu}(z) - G_{zu}(z)G_{yw}(z)]K(z) \quad (3)$$

is the *spillover function* and

$$S_0(z) \equiv [1 - G_{yu}(z)K(z)]^{-1} \quad (4)$$

is the *sensitivity function*.

The block diagram of the duct system of Fig. 1 is shown in Fig. 4(a), using the notations of Eq. (1). In terms of frequency response functions, letting the spillover function represented in Eq. (3) be zero leads to the so-called *zero spillover controller*:⁸

$$K_{ZSP}(e^{j\omega}) = \frac{G_{zw}(e^{j\omega})}{G_{zw}(e^{j\omega})G_{yu}(e^{j\omega}) - G_{zu}(e^{j\omega})G_{yw}(e^{j\omega})}, \quad (5)$$

where the digital frequency $\omega = \Omega T$ with Ω being the analog frequency and T the sampling interval. On the other hand, the Roure's controller that is equivalent to the zero spillover controller can be obtained by dividing the numerator and the denominator of Eq. (5) by $G_{yw}(e^{j\omega})$:

$$\begin{aligned} K_{ZSP}(e^{j\omega}) &= \frac{-G_{zw}(e^{j\omega})/G_{yw}(e^{j\omega})}{G_{zu}(e^{j\omega}) - G_{yu}(e^{j\omega})G_{zw}(e^{j\omega})/G_{yw}(e^{j\omega})} \\ &= \frac{-H_0(e^{j\omega})}{H_2(e^{j\omega}) - H_1(e^{j\omega})H_0(e^{j\omega})} \\ &\equiv K_{\text{Roure}}(e^{j\omega}), \end{aligned} \quad (6)$$

where $H_0(e^{j\omega}) \equiv G_{zw}(e^{j\omega})/G_{yw}(e^{j\omega})$ is the frequency response function between the performance microphone and the measurement microphone, $H_1(e^{j\omega}) \equiv G_{yu}(e^{j\omega})$ is the frequency response function between the measurement microphone and the control speaker, and $H_2(e^{j\omega}) \equiv G_{zu}(e^{j\omega})$ is the frequency response function between the performance microphone and the control speaker. The block diagram of the Roure's controller is shown in Fig. 4(b).

It is noted that in the Roure's controller the frequency response function $H_0(e^{j\omega})$ can be directly measured without knowing the disturbance w . The impulse response of the Roure's controller is then obtained by inverse Fourier transform of $K_{\text{Roure}}(e^{j\omega})$. However, this procedure generally results in noncausal filters. Roure adopted a simple but effective approach to overcome this difficulty. He chose to truncate the noncausal part directly and implemented the controller with a FIR filter.

III. DESIGN OBJECTIVE AND CONSTRAINT

The aforementioned Roure's method provides a straightforward means to obtain an implementable (proper, stable, and causal) controller. Unlike Roure's approach that requires the closed loop transfer function $T_{zw}(z)$ be strictly zero, we seek to recast the problem into an optimization problem: find an implementable controller such that the following cost function of performance,

$$\|T_{zw}(z)W_1(z)\|_2^2, \quad (7)$$

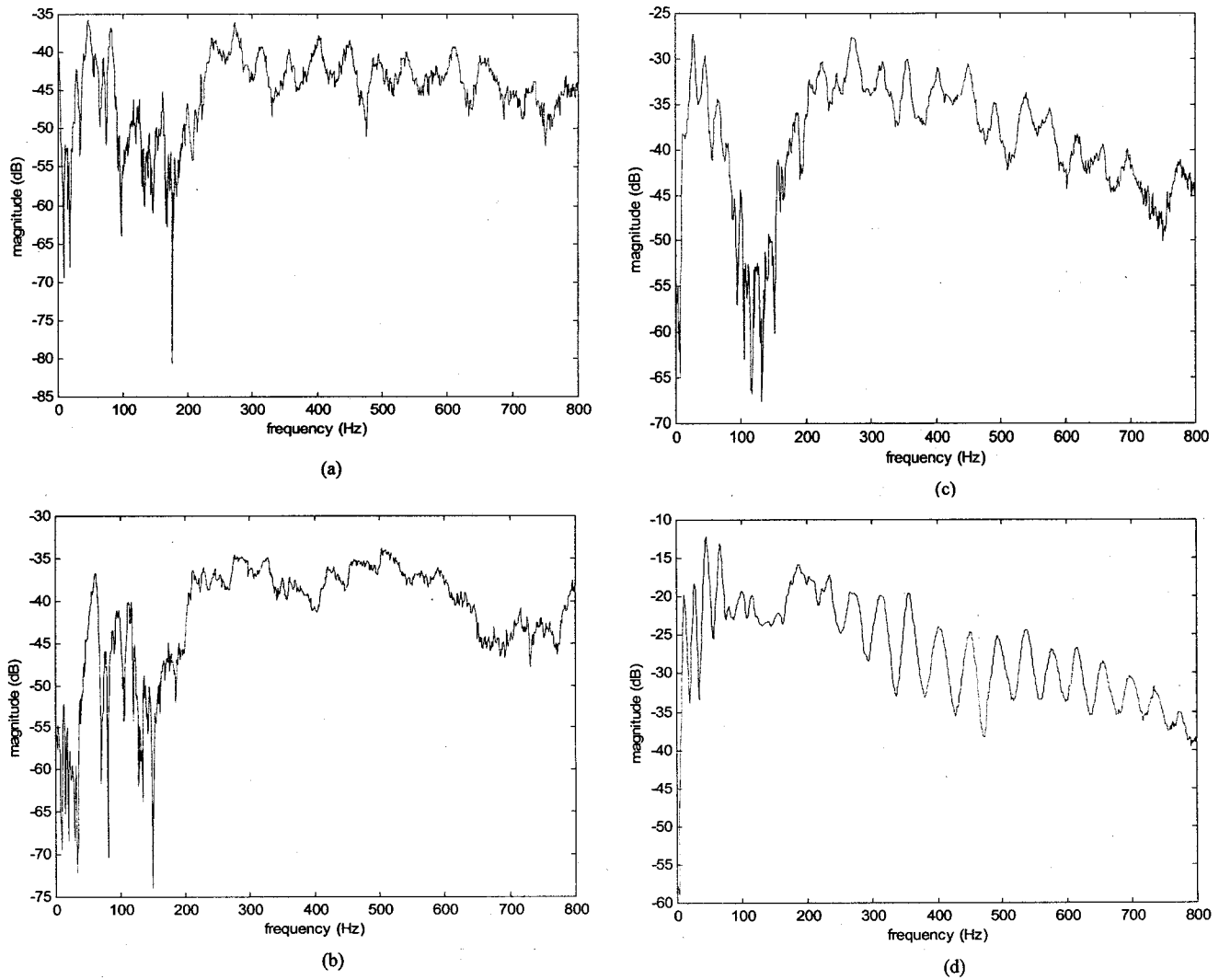


FIG. 3. The frequency responses of the nominal duct system. (a) The frequency response of G_{yu} ; (b) the frequency response of G_{zu} ; (c) the frequency response of G_{zw} ; and (d) the frequency response of G_{yw} .

is minimized, where

$$\|T_{zw}(z)\|_2 \triangleq \left(\frac{1}{2\pi} \int_{-\pi}^{\pi} |T_{zw}(e^{j\omega})|^2 d\omega \right)^{1/2} \quad (8)$$

represents the two-norm²² in discrete-time domain and $W_1(z)$ is a weighting function that is generally a low-pass function.

In addition to performance consideration, robust stability is another important issue. Robust stability is understood as the robustness of stability of the closed loop ANC system against plant uncertainties and perturbations frequently encountered in practical applications. One way of coping with system uncertainties and perturbations is to use an adaptive controller, whereas this paper adopted an alternative strategy—a robust controller which requires simpler implementation than the adaptive counterpart. To this end, a robust stability constraint is incorporated into the aforementioned optimization problem. Assume the following perturbed plant model,²³

$$G_p(z) = G_{yu}(z)[1 + \Delta(z)], \quad (9)$$

where $G_{yu}(z)$ is the nominal plant, $\Delta(z)$ is the multiplicative uncertainty, and G_p represents the physical plant. The uncertainty $\Delta(z)$ is assumed to be bounded by $|\Delta(z)| < W_2(z)$. The uncertainty considered here is primarily the difference between the plant model and the real plant beyond the control bandwidth, which may cause excessive control output at high frequency. Therefore, it is important for the controller to be robust against this type of uncertainty. It can be shown by *small-gain theorem* that the condition of robust stability takes the form

$$\|T_0(z)W_2(z)\|_{\infty} < 1, \quad (10)$$

where $T_0(z) = 1 - S_0(z)$ is the *complementary sensitivity function* [$S_0(z)$ is as defined in Eq. (4)] and $W_2(z)$ is a weighting function that is generally a high-pass function to be determined from the plant uncertainty.

In summary, the ANC problem can be written in the language of optimization as follows:

$$\min_K \|T_{zw}(z)W_1(z)\|_2^2 \quad (11)$$

subject to

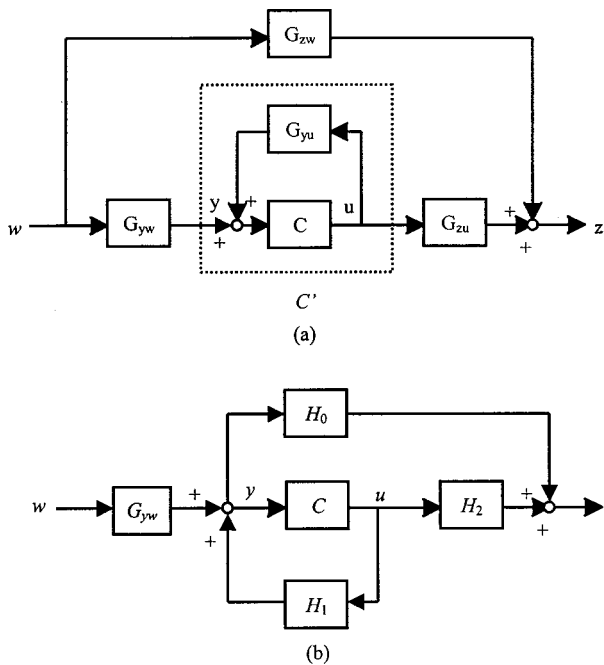


FIG. 4. Two equivalent spatially feedforward controllers. (a) Block diagram of zero spillover controller; (b) block diagram of the Roure's controller.

$$\|T_0(z)W_2(z)\|_\infty < 1. \quad (12)$$

The control problem described in Eqs. (11) and (12) is a mixed norm problem that can be solved by a convex programming technique to be presented in the next section.

IV. CONVEX PROGRAMMING USING Q-PARAMETRIZATION

In this section, the formulation in Eqs. (11) and (12) will be converted to a convex programming problem and solved by using a technique originally suggested by Boyd.¹⁶ The key step of the conversion to a convex problem is the so-called Q -parametrization¹⁷ to Youla's parametrization.¹⁸ Assume that the plant G_{yu} is stable. According to the method, the controllers that stabilize the closed loop system can be parametrized by a proper and stable transfer function $Q(z)$ as follows:

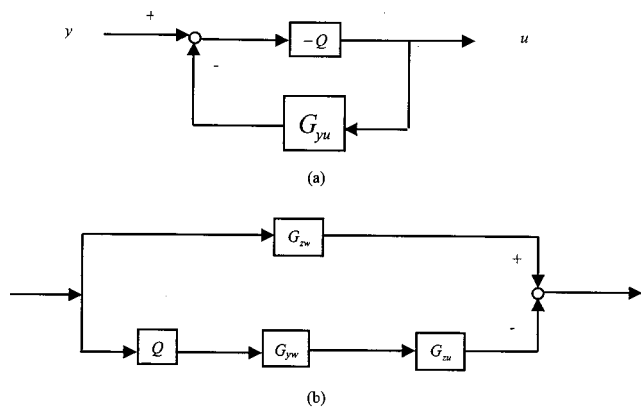


FIG. 5. Block diagrams of Q -parametrization. (a) The internal model controller; (b) the model matching problem obtained from Q -parametrization.

$$K(z) = \frac{-Q(z)}{1 - Q(z)G_{yu}(z)}. \quad (13)$$

The block diagram is shown in Fig. 5(a). More precisely, the resulting closed loop system will guarantee to be stable if the controller is selected in the form of Eq. (13) with a proper and stable $Q(z)$. The latter requirement is easily achieved in discrete time domain by choosing $Q(z)$ to be a FIR filter. In addition, the controller design in Eq. (13) is also known as the *internal model controller* because it has a "built in" nominal plant model G_{yu} .

At this point, the optimization problem has been formulated in frequency domain via Q -parametrization. To solve the problem, an approach proposed by Boyd and Helton²⁴ was employed in the paper. The same method was also successfully used by Rafaely²⁵ and Elliott who have done pioneering work to solve an ANC problem for a headrest. This method first discretizes the frequency response function by uniformly sampling the unit circle, and then solves the optimization problem by convex programming.

Substituting Eq. (13) into Eqs. (11) and (12), $T_{zw}(z)$ and $T_0(z)$ can be parametrized in terms of a proper and stable function $Q(z)$:

$$T_{zw}(z) = G_{zw}(z) - Q(z)G_{yw}(z)G_{zu}(z),$$

$$T_0(z) = Q(z)G_{yu}(z).$$

Thus minimization of $\|T_{zw}\|_2$ is tantamount to a model matching problem depicted in Fig. 5(b). Note that both $T_{zw}(z)$ and $T_0(z)$ are affine functions of $Q(z)$. By frequency discretization, the cost function and constraint function of the optimization problem now take the following form:

$$\min_{\mathbf{q}} \frac{1}{N} \sum_{k=0}^{N-1} |[G_{zw}(k) - Q(k)G_{yw}(k)G_{zu}(k)]W_1(k)|^2 \quad (14)$$

subject to

$$|Q(k)G_{yu}(k)W_2(k)| < 1, \quad k=0,1,\dots,N-1, \quad (15)$$

where $\mathbf{q} = (q_0 q_1 \dots q_{m-1})^T$ being the coefficient vector of the FIR filter Q with length m are the design variables and N is the number of frequency samples. Only the acoustic feedback path $G_{yu}(k)$ has to do with robust stability constraints. It should be noted that those gains of the transfer functions such as $G_{yu}(z)$, $G_{zw}(z)$, $G_{yw}(z)$, and $G_{zu}(z)$ are assumed to be time invariant for our application where the temperature is not changed much. To summarize, the optimization in Eq. (15) is comprised of the design variable \mathbf{q} , the cost function in quadratic form, and the constraint function in linear inequality form.

Define the following Hessian matrix²⁶

$$\mathbf{H}_s = \begin{bmatrix} \frac{\partial^2 f}{\partial x_1^2} & \frac{\partial^2 f}{\partial x_1 \partial x_2} & \dots & \frac{\partial^2 f}{\partial x_1 \partial x_n} \\ \frac{\partial^2 f}{\partial x_2 \partial x_1} & \frac{\partial^2 f}{\partial x_2^2} & \dots & \frac{\partial^2 f}{\partial x_2 \partial x_n} \\ \vdots & \vdots & \ddots & \vdots \\ \frac{\partial^2 f}{\partial x_n \partial x_1} & \frac{\partial^2 f}{\partial x_n \partial x_2} & \dots & \frac{\partial^2 f}{\partial x_n^2} \end{bmatrix}. \quad (16)$$

Because the Hessian matrix of the function in Eq. (14) is positive definite, the function is a strictly convex function.²⁶ Furthermore, the design specification in Eq. (15) is a convex specification because it is norm-bounded.²⁷ Since the cost function and the constraint function are both convex, Eqs. (14) and (15) represent a convex problem. A local minimum of a convex problem is also a global minimum.

The method used in this work to compute the optimal controller by solving the optimization problem in Eqs. (14) and (15) was sequential quadratic programming²⁶ which is provided as a MATLAB command *constr* in optimization toolbox. However, other programming methods such as semidefinite programming²⁷ can be used. Because the function *constr* was based on the sequential programming that accepts only linear constraints, the single robust stability constraint in Eq. (12) has been replaced with N linear inequality constraints in Eq. (15).

V. CONTROLLER IMPLEMENTATION AND EXPERIMENTAL INVESTIGATION

A duct made of plywood shown in Fig. 1 is used for verifying the proposed ANC method. The length of the duct is 440 cm and the cross section is 25×25 cm². There is 10 cm between the primary source speaker and the measurement microphone. To reduce the undesirable acoustic feedback, we use the backward control loudspeaker facing the open end of the duct. The distance between the measurement microphone and the control speaker is 235 cm to ensure causality of the controller. The distance between the control speaker and the performance microphone is 110 cm. A floating point DSP, TMS320C32 equipped with four 16-bit analog IO channels, is utilized to implement the controller. The sampling frequency is chosen to be 2 kHz. Considering the cutoff frequency of the duct (approximately 700 Hz) and the poor response of speaker at low frequency, we chose control bandwidth from 200 to 600 Hz. It should be noted that a loudspeaker should be mounted near the primary noise source for identification of the frequency response functions $G_{yw}(e^{j\omega})$ and $G_{zw}(e^{j\omega})$ because the noise source (a fan, for example) is generally unmeasurable in practice.

A digital spatially feedforward controller is designed to reject the noise in the duct. The ANC system is as shown in Fig. 1. Figure 3(a) shows the measured frequency response function $G_{yu}(e^{j\omega})$. To weight performance as in Eq. (14), the weighting function $W_1(z)$ is chosen as a low-pass filter with cutoff frequency 600 Hz and unity gain, as shown in Fig. 6(a).

To weigh the robust stability as in Eq. (15), on the other hand, the weighting function $W_2(z)$ is determined from the

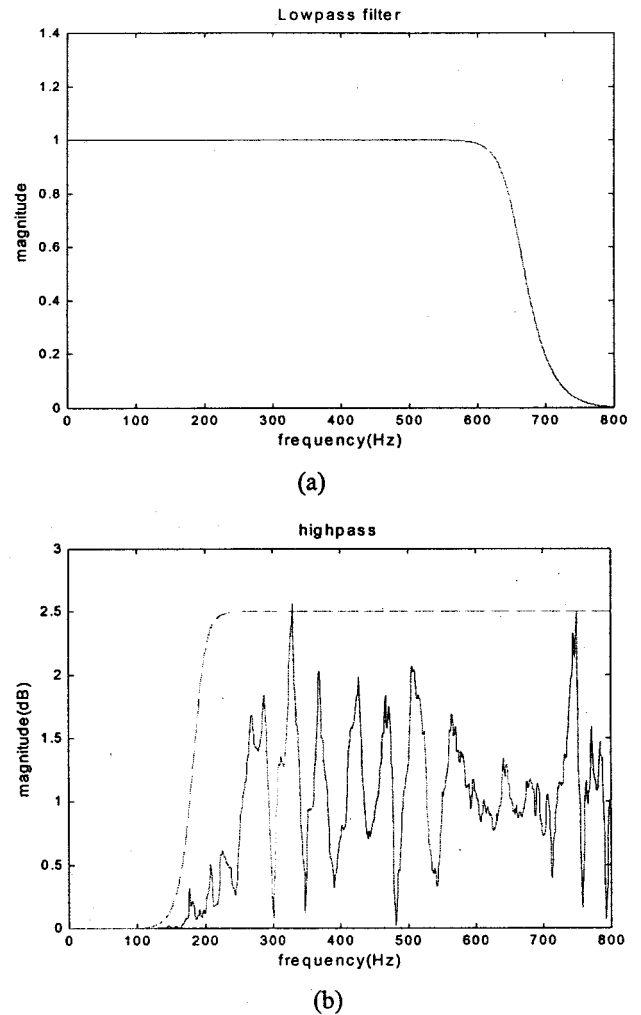


FIG. 6. Two weighting functions used in the implementation. (a) The weighting function W_1 ; (b) — — —, the weighting function W_2 ; —, the uncertainty of the nominal plant.

uncertainty definition in Eq. (9). The frequency responses of the nominal plant in 0–800 Hz and in 0–1600 Hz are measured. The former is taken as the nominal plant, while the latter the actual plant. By using the MATLAB command *invfreqz*, transfer functions of the nominal and true plant are calculated. Then the weighting function $W_2(z)$ is selected according to the following equation:

$$\left| \frac{G_p(e^{j\omega})}{G_{yu}(e^{j\omega})} - 1 \right| \leq |W_2(e^{j\omega})| \quad \forall \omega, \quad (17)$$

where $G_p(e^{j\omega})$ is the frequency response function of the actual plant and $G_{yu}(e^{j\omega})$ is the frequency response function of the nominal plant. Figure 6(b) shows the calculated uncertainty bounded by the weighting function W_2 which is a high-pass filter with gain 2.5 and cutoff frequency 200 Hz.

The optimization problem formulated in Eqs. (14) and (15) with the design variables \mathbf{q} of 128 coefficients (initially set to be zeros) was solved numerically by using the MATLAB function *constr*. The unit circle was uniformly sampled at 2048 points. For the control bandwidth 200–600 Hz, only 801 constraints need to be considered. In the choice of parameters, sufficiently large number of frequency samples²⁸ N and long FIR filter Q are generally required to ensure an

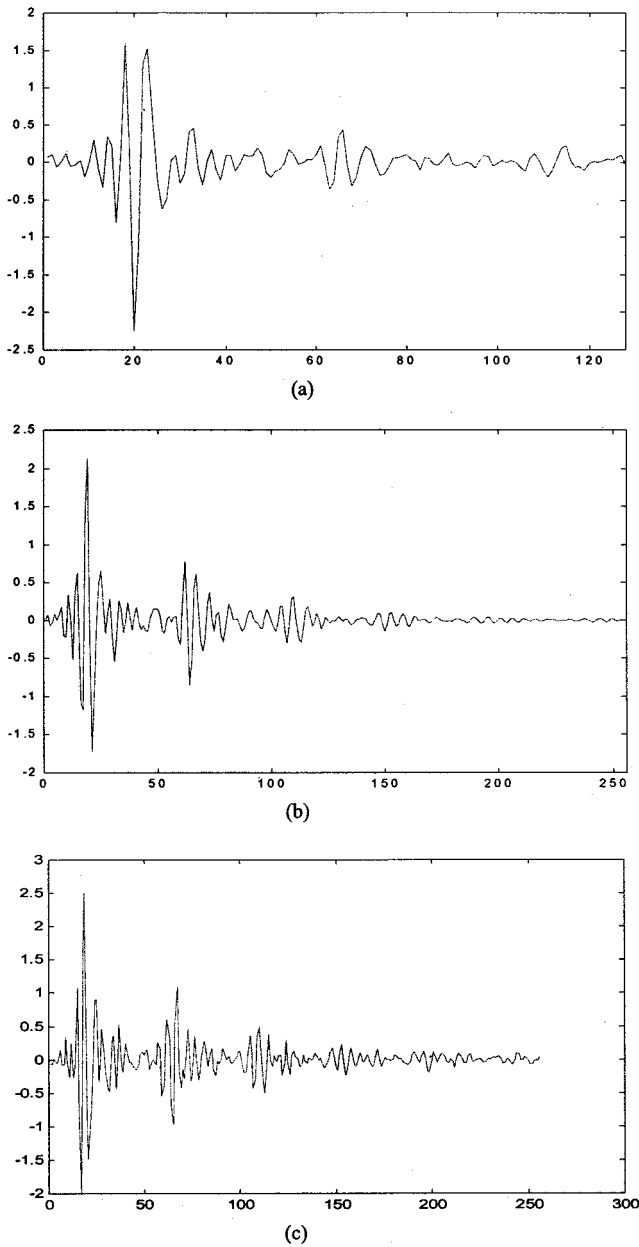


FIG. 7. The calculation result of Q -parametrization and the impulse responses of convex programming controller and Roure's controller. (a) The coefficient vector \mathbf{q} ; (b) the impulse response of the convex programming controller; and (c) the impulse response of Roure's controller.

accurate discrete approximation of the continuous problem. Titterton and Olkin²⁹ suggested increasing the length of \mathbf{q} and the length of N until the impulse response of \mathbf{q} sufficiently decays such that any further increase of length would not result in significant improvement.

Figure 7(a) shows the coefficient vector of the control filter \mathbf{q} with 128 coefficients. As can be seen in the figure, the impulse response decays almost completely. Any further increase in filter length will not provide significant improvement. The calculated coefficient vector \mathbf{q} is then substituted into Eq. (13) to obtain the optimal controller that is in turn converted to a FIR filter of length 256. Figure 7(b) shows the calculated impulse response of the controller. The resulting controller is then implemented on the platform of the DSP. An experiment is undertaken to verify the ANC system. The

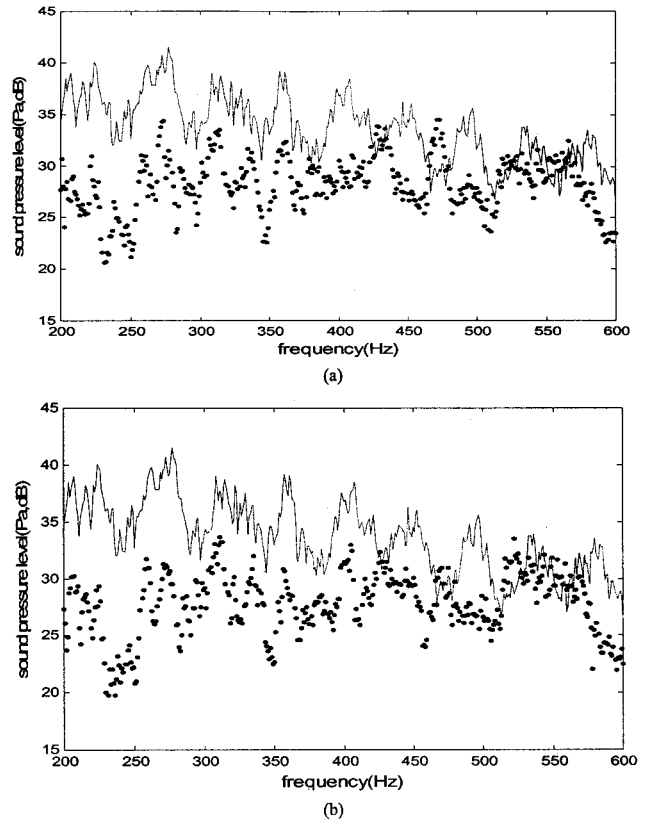


FIG. 8. Active control results of the feedforward controllers. (a) Noise reduction using Roure's controller; (b) noise reduction using the convex programming controller. —, control off; · · · ·, control on.

result of control in terms of pressure spectra measured at the performance microphone is shown in Fig. 8(b). The total attenuation within the control bandwidth is 5.9 dB.

Roure's controller is also implemented for comparison with the mixed norm controller. Roure's controller is calculated from Eq. (6), based on the measurable frequency response functions $H_0(e^{j\omega})$, $H_1(e^{j\omega})$, and $H_2(e^{j\omega})$. The impulse response of Roure's controller is shown in Fig. 7(c). Using Roure's controller, the experimental result is shown in Fig. 8(a) with a total attenuation 5.4 dB. Detailed comparison between the mixed norm controller and Roure's controller is summarized in Table I.

VI. CONCLUSIONS

This paper presents a spatially feedforward design for active control of noise in a duct. As opposed to earlier methods that compute optimal controllers analytically, this method utilizes a frequency domain convex programming technique. This approach is effective in that it guarantees to

TABLE I. Comparison of ANC methods.

Items	Roure's controller	Convex programming controller
Control bandwidth	200–600 Hz	200–600 Hz
FIR filter length	256	256
Maximal attenuation	15.5 dB	16.5 dB
Total band attenuation	5.4 dB	5.9 dB

find the global minimum solution. In comparison to conventional LQG or H_∞ design, where experience is required for choosing appropriate weighting functions, all the functions required in our method can be derived directly from measured data. The convex programming method, in conjunction with Q -parametrization and frequency discretization, proved to be useful in ANC application for several reasons. First, the chosen uncertainty model derived from measured data was found to be a reasonable model for construction of constraints in optimization. This is an advantage over other “trial and error” design methods such as LQG in which we are unable to determine explicitly the weighting functions from measured data. Second, the design problem is a convex problem whose solution can easily be found using commercially available software such as MATLAB optimization toolbox. Third, optimization can be focused on performance since closed-loop stability has already been ensured by Q -parametrization.

To summarize, this research has two potential contributions to the area of ANC. First, we have shown that the controller obtained from convex programming approximates well the idea spatially feedforward controller. It yields comparable performance as the zero spillover controller and the Roure controller which use a direct truncation of the non-causal impulse response of the ideal controller. The proposed approach achieves nominal performance subject to the H_∞ -constraint on closed-loop robust stability. Second, the procedures involved in the analysis and implementation phases are presented in detail. Experimental verifications of the proposed ANC system were conducted for a duct problem. In particular, technical issues such as how to choose the plant uncertainty model and the performance index are addressed.

ACKNOWLEDGMENTS

The work was supported by the National Science Council in Taiwan, Republic of China, under Project No. NSC 87-2212-E009-022.

- ¹J. Hong, J. C. Akers, R. Venugopal, M. N. Lee, A. G. Sparks, P. D. Washabaugh, and D. S. Bernstein, “Modeling, identification, and feedback control of noise in an acoustic duct,” *IEEE Trans. Control Syst. Technol.* **4**, 283–291 (1996).
- ²Z. Wu, V. K. Varadan, and V. V. Varadan, “Time-domain analysis and synthesis of active noise control systems in ducts,” *J. Acoust. Soc. Am.* **101**, 1502–1511 (1997).
- ³J. C. Carmona and V. M. Alvarado, “Active noise control of a duct using robust control theory,” *IEEE Trans. Control Syst. Technol.* **8**, 930–938 (2000).
- ⁴M. R. Bai and T. Y. Wu, “Study of the acoustic feedback problem of active noise control by using the l_1 and l_2 vector space optimization approaches,” *J. Acoust. Soc. Am.* **102**, 1004–1012 (1997).
- ⁵M. R. Bai and H. P. Chen, “Development of a feedforward active noise control system by using the H_2 and H_∞ model matching principle,” *J. Sound Vib.* **201**, 189–204 (1997).

- ⁶M. R. Bai and T. Y. Wu, “Simulation of an internal model-based active noise control system for suppressing periodic disturbances,” *ASME J. Vib. Acoust.* **120**, 111–116 (1998).
- ⁷M. R. Bai and H. H. Lin, “Comparison of active noise control structures in the presence of acoustical feedback by using the H_∞ synthesis technique,” *J. Sound Vib.* **206**, 453–471 (1997).
- ⁸J. Hong and D. S. Bernstein, “Bode Integral Constraints, Colocation, and Spillover in Active Noise and Vibration Control,” *IEEE Trans. Control Syst. Technol.* **6**, 111–120 (1998).
- ⁹A. Roure, “Self-adaptive Broadband Active Sound Control System,” *J. Sound Vib.* **101**, 429–441 (1985).
- ¹⁰D. S. Bernstein and W. M. Haddad, “LQG control with an H_∞ performance bound: A Riccati equation approach,” *IEEE Trans. Autom. Control* **34**, 293–305 (1989).
- ¹¹P. P. Khargonekar and M. A. Rotea, “Mixed H_2/H_∞ control: A convex optimization approach,” *IEEE Trans. Autom. Control* **36**, 824–837 (1991).
- ¹²C. W. Scherer, “Multiobjective H_2/H_∞ control,” *IEEE Trans. Autom. Control* **40**, 1050–1062 (1995).
- ¹³Y. Theodor and U. Shaked, “Output-feedback mixed H_2/H_∞ control-A dynamic game approach,” *Int. J. Control* **64**(2), 263–279 (1996).
- ¹⁴C. W. Scherer, “Mixed H_2/H_∞ control,” in *Proc. European Contr. Conf. (ECC95)* (1995), pp. 173–216.
- ¹⁵J. Y. Lin and Z. L. Luo, “Internal model-based LQG/ H_∞ design of robust active noise controllers for acoustic duct system,” *IEEE Trans. Control Syst. Technol.* **8**, 864–872 (2000).
- ¹⁶P. B. Boyd, V. Balakrishnan, C. H. Barrat, N. M. Khraishi, X. Li, D. G. Meryer, and S. Norman, “A new CAD method and associated architectures for linear controllers,” *IEEE Trans. Autom. Control* **33**, 268–283 (1988).
- ¹⁷D. C. Youla, J. J. Bongiorno, and H. A. Jabr, “Modern Wiener-Hopf design of optimal controllers. Part I: The single-input-output case,” *IEEE Trans. Autom. Control* **21**, 3–13 (1976).
- ¹⁸M. Morari and E. Zafriou, *Robust Process Control* (Prentice-Hall, Englewood Cliffs, NJ, 1989).
- ¹⁹E. Gill, W. Murray, and M. H. Wright, *Practical Optimization* (Academic, New York, 1981).
- ²⁰A. Grace, *Matlab Optimization Toolbox*, The Math Works, Inc. (1995).
- ²¹M. R. Bai and H. H. Lin, “Plant uncertainty analysis in a duct active noise control problem by using the H_∞ theory,” *J. Acoust. Soc. Am.* **104**, 237–247 (1998).
- ²²P. A. Nelson and S. J. Elliott, *Active Control of Sound* (Academic, London, 1992).
- ²³J. C. Doyle, B. A. Francis, and A. R. Tannenbaum, *Feedback Control Theory* (MacMillan, New York, 1992).
- ²⁴J. W. Helton and A. Sideris, “Frequency response algorithms for H_∞ optimization with time domain constraints,” *IEEE Trans. Autom. Control* **34**, 427–434 (1989).
- ²⁵B. Rafaely and S. J. Elliott, “ H_2/H_∞ output feedback design for active control,” ISVR, Univ. Southampton, U.K., Tech. Memo 800 (July 1996).
- ²⁶J. S. Arora, *Introduction to Optimum Design* (McGraw-Hill, New York, 1989).
- ²⁷S. Boyd, L. Vandenberghe, and M. Grant, “Efficient convex optimization for engineering design,” in *Proc. IFAC Symp. Robust Contr. Design, Rio de Janeiro, Brazil* (Sept. 1994).
- ²⁸B. Rafaely and S. J. Elliott, “ H_2/H_∞ active control of sound in a headset: Design and implementation,” *IEEE Trans. Control Syst. Technol.* **7**, 79–84 (1999).
- ²⁹P. J. Titterton and J. A. Olkin, “A practical method for constrained optimization controller design: H_2 or H_∞ optimization with multiple H_2 and/or H_∞ constraints,” in *Proc. 29th IEEE Asilomar Conf. Signals, Syst., Comput.* (1995), pp. 1265–1269.

Experimental evaluation of leaky least-mean-square algorithms for active noise reduction in communication headsets^{a)}

David A. Cartes, Laura R. Ray,^{b)} and Robert D. Collier

Thayer School of Engineering, Dartmouth College, 8000 Cummings Hall, Hanover, New Hampshire 03755

(Received 1 March 2001; revised 14 November 2001; accepted 1 December 2001)

An adaptive leaky normalized least-mean-square (NLMS) algorithm has been developed to optimize stability and performance of active noise cancellation systems. The research addresses LMS filter performance issues related to insufficient excitation, nonstationary noise fields, and time-varying signal-to-noise ratio. The adaptive leaky NLMS algorithm is based on a Lyapunov tuning approach in which three candidate algorithms, each of which is a function of the instantaneous measured reference input, measurement noise variance, and filter length, are shown to provide varying degrees of tradeoff between stability and noise reduction performance. Each algorithm is evaluated experimentally for reduction of low frequency noise in communication headsets, and stability and noise reduction performance are compared with that of traditional NLMS and fixed-leakage NLMS algorithms. Acoustic measurements are made in a specially designed acoustic test cell which is based on the original work of Ryan *et al.* [“Enclosure for low frequency assessment of active noise reducing circumaural headsets and hearing protection,” *Can. Acoust.* **21**, 19–20 (1993)] and which provides a highly controlled and uniform acoustic environment. The stability and performance of the active noise reduction system, including a prototype communication headset, are investigated for a variety of noise sources ranging from stationary tonal noise to highly nonstationary measured F-16 aircraft noise over a 20 dB dynamic range. Results demonstrate significant improvements in stability of Lyapunov-tuned LMS algorithms over traditional leaky or nonleaky normalized algorithms, while providing noise reduction performance equivalent to that of the NLMS algorithm for idealized noise fields. © 2002 Acoustical Society of America. [DOI: 10.1121/1.1448314]

PACS numbers: 43.50.Ki, 43.60.Qv, 43.50.Hg [MRS]

I. INTRODUCTION

Current research in active noise reduction (ANR) for communication headsets focuses on using digital feedforward technology based on least-mean-square (LMS) optimization. References 1–3 provide substantial experimental evidence that digital feedforward technology has the potential to improve performance of ANR headsets over state-of-the-art, commercially available, feedback systems. This is particularly true with respect to low frequency noise, which cannot be adequately attenuated passively by the headset structure—typically 10 dB at 100 Hz, and for which feedback ANR systems exhibit limited performance, e.g., 15 dB between 100 and 250 Hz. The goal of Refs. 1–3 was to document *feasibility* of feedforward ANR applied to communication headsets using DSP technology that was available at that time.

References 1 and 2 use the filtered-X normalized least-mean-square (FXNLMS) algorithm and a dual sample-rate system to demonstrate active noise reduction of up to 26 dB in response to band limited (80–750 Hz) white noise in flat plate testing of a prototype feedforward ANR communication headset. The filtered-X algorithm, first derived in Refs. 4

and 5, is used in systems where, like the communication headset, the transfer function of the path between the reference input and the LMS filter output must be precisely modeled. In communication headsets this path represents the combined transfer functions of several components such as microphones, amplifiers, and speakers, which may exhibit temporal variation, and whose frequency response functions must be accounted for in shaping the cancellation signal. Using the FXNLMS algorithm, ANR performance of 10–30 dB has also been demonstrated at frequencies up to 250 Hz for band limited (10–1000 Hz) noise from a helicopter at the location of the aircrew.³ For the helicopter noise experiments, ANR performance at the critical blade passage frequency (16 Hz) was reported to be as high as 26 dB.³

The work presented in Refs. 1–3 fulfills the objective of proving feasibility of feedforward ANR systems for communication headsets. In practice, however, traditional feedforward LMS algorithms have significant stability and performance deficiencies caused by nonstationary reference inputs, finite precision arithmetic, and measurement noise associated with quantization and electronic amplifiers. In particular, the dynamic range of real-world noise fields under which feedforward ANR in communication headsets must operate results in time-varying signal-to-noise ratios (SNR) on the measured reference input.

In response to these stability and performance issues, the family of LMS algorithms developed over the past two decades includes leaky variants. As with the well-known NLMS algorithm, where adaptation of the *step size* addresses

^{a)}Portions of this work were presented at the 2001 American Control Conference, D. Cartes, L. R. Ray, and R. D. Collier, “Lyapunov Tuning of the Leaky LMS Algorithm for Single-Source, Single-Point Noise Cancellation.”

^{b)}Author to whom correspondence should be addressed; electronic mail: Laura.Ray@Dartmouth.edu

speed of convergence, the *leakage factor* addresses stability deficiencies that arise from nonstationary inputs, low SNR, and finite-precision arithmetic. Thus, the leaky LMS filter is a valid approach to improving the stability of feedforward ANR in communication headsets, in which stability is an issue due to real-world noise environments. The FXNLMS algorithm used to demonstrate feedforward ANR in Refs. 1–3, while assuring convergence when the secondary path transfer function is non-negligible, increases the output power and may cause distortion in the secondary path through nonlinear behavior of the cancellation speaker.⁶ The leakage factor can be combined with the FXNLMS algorithm with a resultant increase in stability in the presence of finite precision and measurement noise, and a limit on output power to avoid distortion. However, a constant leakage factor reduces ANR performance for acoustic noise which exhibits temporal variations over a very large dynamic range because such a leakage factor must be chosen to retain stability during worst-case SNR, resulting in significant performance reductions during high SNR conditions. Moreover, in combining the leaky LMS algorithm with *any* of the family of LMS algorithms, tuning the leakage parameter remains a highly empirical process.

In Ref. 7, the authors introduce a Lyapunov tuning method for choosing a combination of adaptive step size and leakage factor that addresses both stability and performance in the face of one of the factors that necessitates the use of a leaky LMS algorithm, namely measurement noise on the measured reference input due to quantization and analog noise. For highly nonstationary, impulsive noise fields, in which measurement noise is non-negligible and SNR is time-varying, maintaining stability at minimal performance degradation is crucial. The Lyapunov tuning method results in a *time-varying* adaptive leakage factor and step size combination which maintains stability for low SNR on the measured reference input, while minimizing performance reduction for both high and low SNR.⁷ In addition, the Lyapunov tuning method eliminates the need for empirical tuning of leaky NLMS filters.

This paper focuses on experimental evaluation of Lyapunov-tuned LMS algorithms for ANR in a prototype communication headset. Issues addressed in experimental evaluation include providing a highly controlled acoustic environment for low frequency performance measurements, testing prototype communication headsets over a large dynamic range to study stability and performance behavior, and comparing Lyapunov-tuned NLMS filters to traditional fixed-leaky, NLMS (LNLMS) filters in order to demonstrate stability and ANR performance improvements. For experimental evaluation, a low frequency acoustic test chamber was designed and constructed, based on the original work of Ref. 8, to provide a precisely controlled acoustic environment with a flat frequency response from 0 to 200 Hz. The prototype was tested within this chamber for noise sources ranging from highly stationary tonal noise to highly nonstationary F-16 noise. Tonal noise was generated locally, while the last three noise sources were taken from a compilation of noise files issued by the North Atlantic Treaty Organization (NATO).⁹ These sound files provide a standard set of both

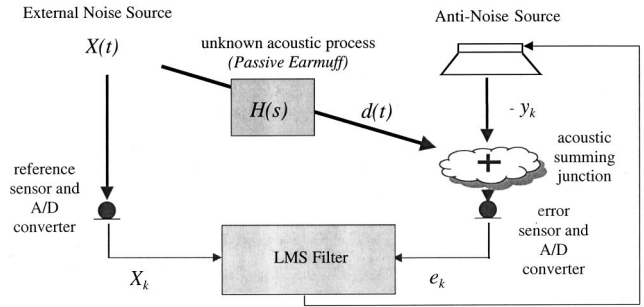


FIG. 1. Feedforward active noise cancellation system.

military and nonmilitary noise sources for research in auditory acoustics. In order to verify that a Lyapunov-tuned, adaptive, leaky NLMS filter works over a large dynamic range, experiments were performed for source signals at two sound pressure levels—80 and 100 dB, providing SNR on the measured reference input of approximately 35 and 55 dB, respectively, based on measured ambient noise levels. In addition, simulation analysis was performed to examine the stability of Lyapunov-tuned LMS algorithms at a SNR of 15 dB. This paper focuses on the results, which demonstrate the use of the Lyapunov tuning method to propose and evaluate candidate tuning laws that result in superior stability and performance characteristics over traditional NLMS algorithms or constant leakage parameter LNLMS algorithms.

The contributions of this paper are: (1) an experimentally verified tuning method for determining and evaluating candidate leakage and step size parameter combinations that maintain acceptable stability of the LMS family of algorithms at minimal performance degradation, and (2) application of this method to enhance performance of adaptive feedforward noise cancellation in communication headsets. Though the focus of this paper is on tuning LNLMS algorithms, the resulting tuning parameters can also be used in combination with other members of the LMS family, such as the FXNLMS.

The paper is organized as follows. Section II summarizes the Lyapunov-tuned candidate LMS algorithms developed by the authors in Ref. 7. Section III describes the acoustic test chamber, prototype communication headset, and measurement and analysis procedure. Section IV presents the results of experimental testing, and Sec. V presents additional simulation analysis performed to verify the Lyapunov tuning method.

II. THE LYAPUNOV TUNING METHOD

A block diagram of a traditional feedforward LMS algorithm denoting signal definitions is shown in Fig. 1. The LMS algorithm recursively selects a weight vector $W_k \in R^n$ to minimize the squared error between d_k and the adaptive filter output $y_k = W_k^T X_k$, where $X_k \in R^n$ is the sampled reference input and $d_k \in R^1$ is the output of the unknown continuous acoustic process at time t_k , which in the present application is the passive noise attenuation of a headset. The Wiener solution, or optimum weight vector is

$$W_o = E[X_k X_k^T]^{-1} E[X_k d_k]. \quad (1)$$

$E[X_k X_k^T]$ is the autocorrelation of the input signal and $E[X_k d_k]$ is the cross correlation between the input vector and process output. The unbiased, recursive LMS weight vector filter is

$$W_{k+1} = W_k + \mu e_k X_k, \quad (2)$$

where $e_k = d_k - W_k^T X_k$. The mean weight vector resulting from Eq. (2) converges to the Wiener solution in the ideal situation of stationary inputs, infinite signal-to-noise ratio, and infinite precision arithmetic, given an appropriate step size. In response to nonstationary inputs, finite-precision arithmetic, nonpersistent excitation, and low signal-to-noise ratio, the leaky LMS algorithm and its step-size normalized versions “leak off” excess energy associated with weight drift. This results in a biased recursive weight update equation

$$W_{k+1} = \lambda W_k + \mu e_k X_k, \quad (3)$$

where λ is the leakage factor.¹⁰ The leakage factor prevents convergence of the weight vector to the Wiener solution and hence results in reduced performance over the unbiased LMS algorithm. The Lyapunov tuning method seeks *time varying* tuning parameters λ_k and μ_k that maintain stability of Eq. (3) and maximize performance in the presence of measurement noise. With noise $Q_k \in R^n$ corrupting the reference signal X_k , and with time varying leakage and step size parameters, λ_k and μ_k , the LNLMS weight update equation of Eq. (3) becomes

$$W_{k+1} = \lambda_k W_k + \mu_k (W_o^T X_k - W_k^T (X_k + Q_k)) (X_k + Q_k). \quad (4)$$

Note that in practice, the quantity $X_k + Q_k$ represents the measured, noise-corrupted reference input, and thus is known, while the individual quantities X_k and Q_k are unknown. The quantity $d_k = W_o^T X_k$ represents the output of the unknown process. While the individual samples of Q_k are unknown, it is assumed that the measurement noise variance σ_q^2 or a worst-case SNR is known. The variance or worst-case SNR can be determined through testing of electronic equipment when no reference input is present, and from knowing the quantization error associated with finite-precision analog-to-digital converters.

For stability at maximum performance, time-varying parameters λ_k and μ_k that are functions of measurable quantities are determined, such that stability conditions on a candidate positive-definite Lyapunov function V_k are satisfied for all k in the presence of noise Q_k on reference input X_k . The conditions on V_k for uniform asymptotic stability are (i) $V_k \geq 0$, and (ii) $V_{k+1} - V_k \leq 0$.¹¹ If $V_{k+1} - V_k > 0$, the system may or may not be stable, and therefore no stability claim or disproof can be made for such cases. Thus the objective of Lyapunov tuning is to define tuning parameters that guarantee that conditions (i) and (ii) are met for the largest possible subspace of R^n .

Lyapunov tuning proceeds by first defining a positive definite Lyapunov function of a scalar projection \tilde{w}_k of the weight vector:

$$V_k = \tilde{w}_k^T \tilde{w}_k, \quad (5)$$

where

$$\tilde{W}_k = W_k - W_o, \quad \tilde{w}_k = \tilde{W}_k^T u_k, \quad u_k = \frac{(X_k + Q_k)}{\|X_k + Q_k\|}.$$

λ_k and μ_k are to be selected such that Lyapunov difference

$$V_{k+1} - V_k = ((\phi_k^2 - 1)A^2 + \gamma_{1_k}^2 + \gamma_{2_k}^2 B^2 + 2\phi_k \gamma_{1_k} A + 2\phi_k \gamma_{2_k} AB + 2\gamma_{1_k} \gamma_{2_k} B) W_o^T u_k u_k^T W_o \quad (6)$$

is negative for the largest possible subspace of R^n , where

$$\phi_k = \lambda_k - \mu_k (X_k + Q_k)^T (X_k + Q_k), \quad (7)$$

$$\gamma_{1_k} = \lambda_k - 1, \quad (8)$$

$$\gamma_{2_k} = -\mu_k (X_k + Q_k)^T (X_k + Q_k), \quad (9)$$

$$A = \frac{\tilde{W}_k^T u_k}{W_o^T u_k}, \quad (10)$$

$$B = \frac{W_o^T \alpha_k}{W_o^T u_k}, \quad (11)$$

$$\alpha_k = \frac{Q_k}{\|X_k + Q_k\|}. \quad (12)$$

The expression for the Lyapunov function difference $V_{k+1} - V_k$ in Eq. (6) takes the n -dimensional vector space of W_k and projects it to a two-dimensional space that is a function of scalars A and B . The parameter A represents the output error ratio between the actual output $y_k = W_k^T (X_k + Q_k)$ of a noise corrupted system and the ideal output $W_o^T (X_k + Q_k)$ of a noise corrupted system converged to the Wiener solution. B represents the output noise ratio, or portion of the ideal output that is due to noise vector Q_k . Physically, these parameters are inherently bounded based on (i) the maximum output that a real system is capable of producing, and (ii) signal-to-noise ratio. Though bounds are difficult to determine in practice, at high SNR, B approaches zero, and when the weight vector converges to the Wiener solution, $A = 0$. Thus, high SNR implies that both A and B approach zero. With low excitation or low signal-to-noise ratio, larger instantaneous magnitudes of A and B are possible, but it is improbable that these constants are persistently much greater than unity in practice.

Since several terms are positive in Eq. (6), *each individual* term of Eq. (6) cannot be guaranteed to be negative. Thus, the approach taken by the Lyapunov tuning method is to define the region of stability around the Wiener solution in terms of A and B . Hence, A and B provide a convenient parametrization of the multidimensional weight vector stability analysis problem that enables visualization of the region of stability of the weight update equation in two dimensions. In Ref. 7, the *structure* of $V_{k+1} - V_k$ of Eq. (6) is used to propose parameters λ_k and μ_k as functions of measurable quantities in order to simplify the analysis of Eq. (6) and subsequently determine conditions on any remaining scalar parameters such that $V_{k+1} - V_k \leq 0$ for the largest region possible around the Wiener solution. This region is defined by

parameters A and B , which provide measures to graphically display the stable region and to visualize performance/stability tradeoffs introduced for candidate leakage and step size parameters.

Two candidate adaptive leakage parameter and adaptive step size combinations are proposed in Ref. 7 for such parametrization, and an additional candidate adaptive leakage parameter and step size combination is taken directly from the literature to serve as a baseline for comparison to Lyapunov tuned candidates. The latter candidate uses a traditional choice for leakage parameter as presented in Ref. 12 in combination with a traditional choice for adaptive step size from Ref. 13 and is denoted here as candidate 1:

$$\lambda_k = 1 - \mu_k \sigma_q^2, \quad (13)$$

$$\mu_k = \frac{\mu_o}{(X_k + Q_k)^T (X_k + Q_k)}. \quad (14)$$

σ_q^2 is the variance of noise Q_k corrupting X_k . To determine the remaining scalar parameter, μ_o , we perform a scalar optimization to select the value of μ_o that minimizes

$$\mu_k = \frac{2(X_k + Q_k)^T (X_k + Q_k) + 4\sigma_q^2}{2((X_k + Q_k)^T (X_k + Q_k))^2 + 8\sigma_q^2 (X_k + Q_k)^T (X_k + Q_k) + 8\sigma_q^4}. \quad (15)$$

The final candidate appeals directly to the structure of Eq. (6) to determine an alternate parametrization as a function of μ_o as follows:

$$\mu_k = \frac{\mu_o \lambda_k}{(X_k + Q_k)^T (X_k + Q_k)}, \quad (16)$$

$$\lambda_k = \frac{X_k^T X_k - Q_k^T Q_k}{(X_k + Q_k)^T (X_k + Q_k)}. \quad (17)$$

The expression for λ_k in Eq. (17) cannot be measured, but it can be approximated as

$$\lambda_k = \frac{(X_k + Q_k)^T (X_k + Q_k) - 2L\sigma_q^2}{(X_k + Q_k)^T (X_k + Q_k)} \quad (18)$$

for $\|X_k\| > \|Q_k\|$. L is the filter length. The optimum μ_o for this candidate, which is again found by scalar optimization subject to worst-case conditions on A and B , is $\mu_o = 1/2$.

Note that these candidate tuning laws present varying degrees of use of the Lyapunov tuning method to parametrize expressions for λ_k and μ_k in terms of measurable quantities or design parameters such as filter length. Candidate 1 fixes the functional form of λ_k and μ_k , resulting in a single remaining parameter, namely the fixed step size μ_o . Candidate 2 allows for a new structure for the adaptive step size μ_k to be determined through minimization of the Lyapunov function difference $V_{k+1} - V_k$. Finally, candidate 3 results directly from seeking an alternate parametrization of λ_k and μ_k based on the Lyapunov function choice of Eq. (5). Further details regarding the Lyapunov tuning method are provided in Refs. 7 and 14. While it is conceivable that other candi-

$V_{k+1} - V_k$. The scalar optimization results are evaluated for projected worst case values of A and B . This results in a value of μ_o that makes $V_{k+1} - V_k$ most negative for worst case deviations of weight vector W_k from the Wiener solution and for worst case effects of measurement noise Q_k . Maximizing performance while retaining acceptable stability forms the basis behind this optimization procedure, as minimizing the gradient of the Lyapunov function results in fastest convergence to steady state. For the candidate adaptive leakage parameter and step size combination of Eqs. (13) and (14), this procedure results in $\mu_o = 1/3$, which is consistent with the choice for μ_o from Ref. 13.

The second candidate also retains the traditional leakage factor of Eq. (13), but finds an expression for μ_k as a function of $X_k + Q_k$ and σ_q^2 directly by performing a scalar optimization to minimize $V_{k+1} - V_k$ with respect to μ_k for projected worst-case values of A and B . In essence, this candidate uses the parametrization of the Lyapunov function provided by fixing the leakage factor expression, but provides an alternate expression for the step size parameter. This results in

date tuning rules could be derived from the initial Lyapunov function choice or from an alternate choice of Lyapunov function, these three are chosen to illustrate stability and performance tradeoffs that can be elicited through Lyapunov analysis.

Evaluation of Eq. (6) as a function of A and B reveals insights on the stability and performance of each candidate tuning law. The $V_{k+1} - V_k$ vs A and B surface is shown in Fig. 2 for SNR=35 dB and for each candidate, along with the plane $V_{k+1} - V_k = 0$ that identifies the region of guaranteed stability. This stability region, which is defined by the extent of the surface that lies below $V_{k+1} - V_k = 0$, is largest for candidate 3, followed by candidate 1, while candidate 2 shows the smallest stability region overall. Performance is indicated both by the magnitude and gradient of the $V_{k+1} - V_k$ vs A and B surface, with a larger gradient denoting more aggressive performance. For example, in the limiting case of $V_{k+1} - V_k = 0$ for every value of A and B , as would be the case for $\lambda_k = 1$ and $\mu_k = 0$, the system is uniformly asymptotically stable, and the gradient $V_{k+1} - V_k$ is zero. However, no convergence results, as $W_{k+1} = W_k$ for this set of parameters. Based on the gradient of the $V_{k+1} - V_k$ surface, in rank order, candidate 2 is expected to have the most aggressive performance, followed by candidates 3 and 1. These tradeoffs point to candidate 3 as the best choice of the three candidate tuning rules. Candidate 3 provides greater stability and performance than the traditional choice of λ_k and μ_k given by candidate 1 and greater stability than candidate 2.

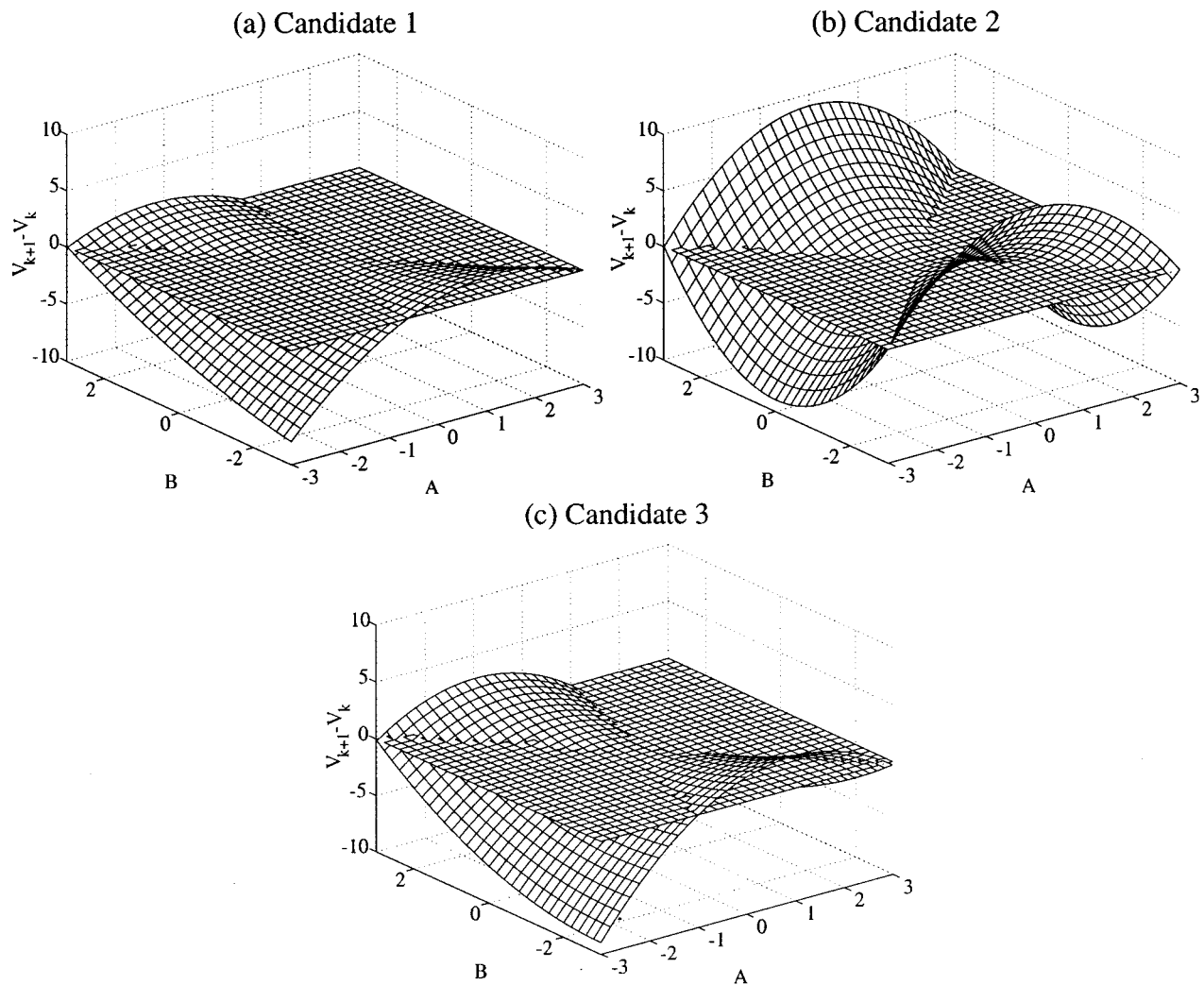


FIG. 2. Lyapunov difference $V_{k+1} - V_k$ vs A and B surface for candidate Lyapunov tuned leaky LMS algorithms.

III. EXPERIMENTAL APPARATUS AND TEST PROCEDURE

The three Lyapunov tuned candidate adaptive leaky NLMS algorithms are analyzed and compared experimentally with three traditional fixed parameter NLMS and LNLMS algorithms at two sound pressure levels—80 and 100 dB—representing signal-to-noise ratio environments of 35 and 55 dB, respectively. The purpose behind such comparisons is to highlight the stability and performance gains of adaptive LNLMS filters achieved through Lyapunov tuned, time-varying leakage factor and step size combinations over fixed leakage factor LNLMS filters. Comparisons are made for four acoustic noise sources ranging from stationary tonal noise to highly nonstationary F-16 aircraft noise. Results for the two extremes of these noise sources—tonal noise and F-16 noise—are presented here. The full set of results for all four noise sources is given in Ref. 14. Comparisons are made with a modified prototype communication headset mounted on a flat plate in a custom designed low frequency acoustic test cell that provides a controlled acoustic environment. This section documents design and acoustical characteristics of the test cell, the prototype headset construction, and the measurement and analysis procedures.

A. Low frequency test cell

The low frequency acoustic test cell is designed to provide a flat frequency response from 0 to 200 Hz for sound pressure levels of up to 140 dB. The design and experimental verification of the test chamber, which is based on the original work of Ref. 8, is described in detail in Ref. 14. Figure 3 provides photographs of the assembled and disassembled test chamber, with a prototype headset mounted in its base. A 15.24-cm-diam Rockford Fosgate model FNQ1406, 100 W speaker provides the sound source. A calibrated B&K 4190 precision microphone is mounted axially in the base plate near where the ear would be located inside of the headset when worn. A second precision microphone is mounted radially through the cylinder wall to simultaneously measure the reference sound pressure level in the test cell. With a prototype headset in the test cell, these two microphones allow simultaneous, calibrated measurement of the sound pressure levels outside and inside the headset, and they also serve to calibrate the reference and error microphones of the prototype headset.

The test chamber is mounted on two layers of packing material separated by a 35 kg brass plate to minimize noise due to structural vibration. The predicted and measured fre-

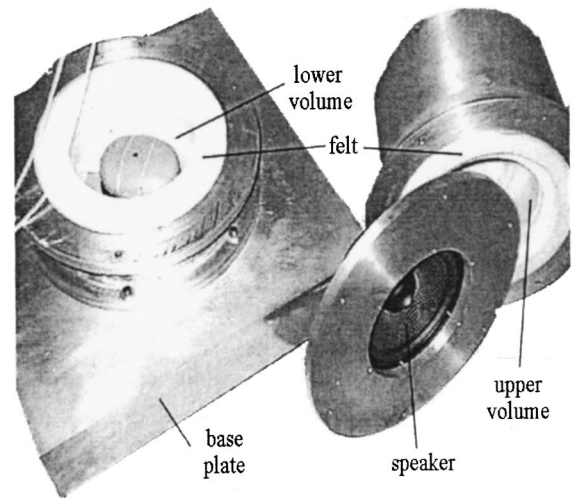
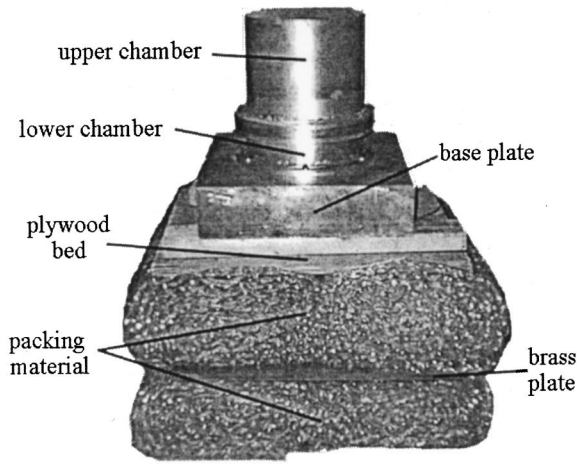


FIG. 3. Unassembled and assembled test cell with prototype earmuff mounted on base plate.

quency response of the test cell at the B&K microphone mounted in the flat plate at its base is shown in Fig. 4.

B. Prototype headset

The prototype headset is depicted schematically in Fig. 5, along with pertinent transfer functions. $H_1(s)$ represents the transfer function of the test cell, reference microphone, and its amplifier. $H_2(s)$ represents the transfer function of the cancellation path, which includes the cancellation speaker and its amplifier, the acoustic path between the speaker and the error microphone, and the error microphone and its amplifier. $H_3(s)$ is the unknown transfer function of the passive headset, which is to be found using the LMS filter, and $H_4(s)$ is the acoustic feedback path from the cancellation speaker to the reference microphone.

The reference and error microphones are Panasonic WM-34B electret microphones. The error microphone is slightly recessed from the cancellation speaker, and the reference microphone is located on the outside periphery of the headset dome. When mounted on the flat plate in the test

cell, the prototype's reference microphone is located 0.6 cm from the precision microphone in the side of the test cell, and the error microphone is located 2.5 cm above the precision microphone in the base of the test cell. A Sennheiser HD570 cancellation speaker is used due to its rated low frequency characteristics and relatively low distortion. Figure 6 shows the experimentally determined speaker transfer function, which is the major contributor to $H_2(s)$ in Fig. 5. Figure 6 shows a relatively flat speaker transfer function, with a low frequency roll off at approximately 50 Hz, and a notch at 100 Hz.

The cancellation speaker distortion was evaluated in the test cell during ANR of single tones at 50, 100, 150, and 200 Hz, at sound pressure levels of 80 and 100 dB. These tests were performed at a sample frequency of 10 kHz, weight update rate of 5 kHz, and a filter length of 200, using the NLMS algorithm. At 100 dB SPL, total harmonic distortion was measured to be 0.7%, 1.8%, 0.6%, and 0.3%, respectively, for the four input frequencies. At 80 dB, total harmonic distortion is less than 0.3% at all frequencies. In addition, the feedback path transfer function [$H_4(s)$ in Fig. 5]

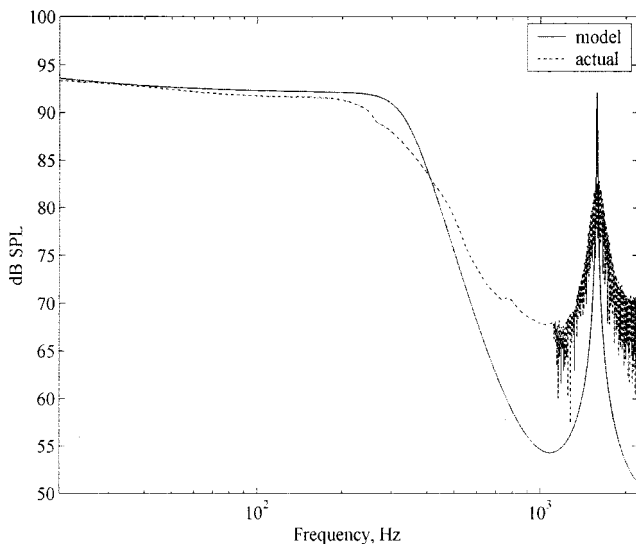


FIG. 4. Predicted and measured test cell frequency response.

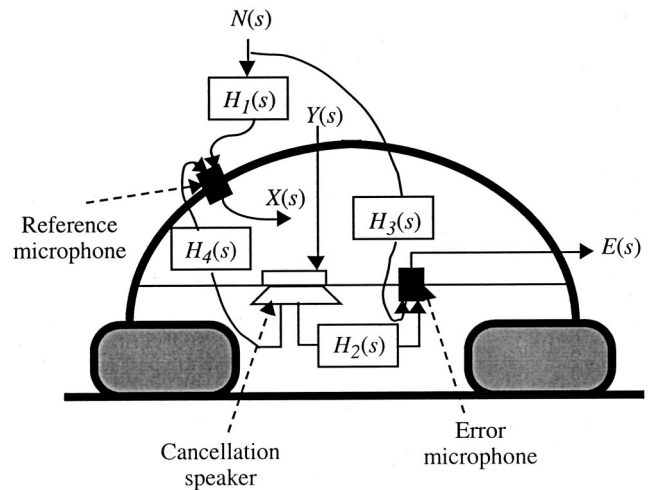


FIG. 5. Schematic of ANR earmuff, including pertinent transfer functions.

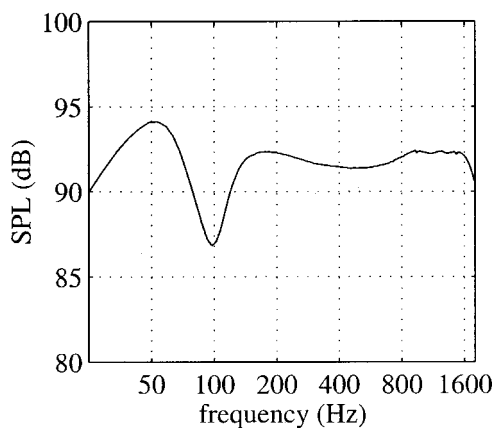


FIG. 6. Experimentally determined cancellation speaker transfer function.

was measured during these experiments. In all cases, the magnitude response of the feedback path presents a minimum of 35 dB attenuation and is therefore considered an insignificant contribution to the reference signal X_k .

C. Noise sources

Four noise sources with increasing degrees of nonstationarity were selected for evaluation of candidate algorithms: (1) a sum of pure tones at the 1/3 octave center band frequencies between 50 and 200 Hz, (2) Lynx helicopter noise, (3) Pink noise, and (4) F-16 aircraft noise. Results for the two extremes—tonal noise and F-16 noise—are presented in this paper. Tonal noise represents the easiest of the four noise sources to cancel using ANR, and F-16 noise represents an extremely challenging source for which to achieve high performance ANR while maintaining stability of the weight update equation. Performance for the remaining two noise sources falls between that of the two noise sources presented here.

All sources are band limited at 50 Hz to maintain a low level of low frequency distortion due to the cancellation speaker roll off and 200 Hz, the upper limit for a uniform sound field in the low frequency test cell. Figure 7 shows the

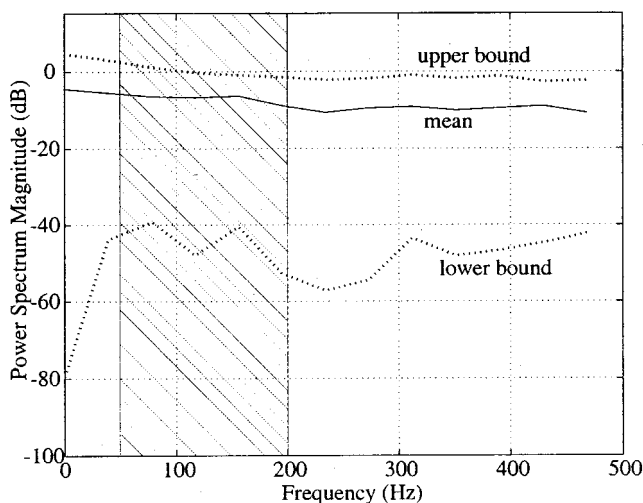


FIG. 7. Representative power spectrum of F-16 aircraft noise used in experimental evaluation of Lyapunov tuned leaky LMS algorithms. Shaded area denotes band limited range used for experiments.

power spectral density for the F-16 noise used for testing, along with measured bounds on the power spectrum, which denote the degree of nonstationarity.

D. Measurement and analysis procedure

The three candidate Lyapunov tuned leaky LMS algorithms are evaluated and compared to (i) empirically tuned, fixed leakage parameter LNLMS algorithms, and (ii) an empirically tuned NLMS algorithm. These algorithms assume that the cancellation path transfer function is constant, and that the gain of the cancellation path is well known. In Fig. 5, the cancellation path is represented by $H_2(s)$ and the portion of $H_1(s)$ associated with the reference microphone and its amplifier. In practice, the transfer function of this path is generally slowly time varying due to factors such as amplifier drift, temperature variations, and variations in mounting of the prototype headset within the test cell. In order to accommodate for slowly time varying transfer functions in the secondary path, the frequency response amplitude of the microphone and cancellation speaker and their amplifiers are adjusted prior to each experiment such that the frequency response magnitude of the cancellation path is unity and is reasonably flat. To do so, the calibrated microphones in the base and side of the test cell are used to adjust the amplifier gains for the reference and error microphones. The speaker amplifier is also adjusted such that the speaker transfer function is approximately unity. By band limiting the noise source, as explained previously, and by making these adjustments prior to each set of experiments, the need for compensation of the cancellation path is avoided. Once adjustments are made, the cancellation path transfer function remains relatively constant for the duration of the experiments, which is a period of 2–3 h. All experimental data are collected during this time period, to ensure accurate comparisons between traditional and Lyapunov tuned leaky LMS algorithm performance. All LMS algorithms are implemented in Simulink and run on a dSPACE 1103 DSP board, which contains 16 bit A/D and 12-bit D/A converter channels for input and output, as well as processing capabilities for algorithm implementation.

The amplitude of the noise source is established to evaluate algorithm performance over a 20 dB dynamic range, i.e., at average sound pressure levels of 80 and 100 dB. These sound pressure levels are measured at the B&K microphone mounted in the base of the test cell and thus reflect the SPL *inside* the headset after passive attenuation of the reference noise and before active noise reduction. All SPL measurements use C weighting. Measurements over a 20 dB dynamic range test the ability of the traditional and Lyapunov tuned leaky LMS algorithms to adapt to different signal-to-noise ratios, based on source sound pressure levels of 80 and 100 dB, which represent signal-to-noise ratios on the measured reference input of approximately 35 and 55 dB, respectively. The quantization noise magnitude is $610e-6$ V, based on a 16 bit round-off A/D converter with a ± 10 V range and one sign bit, and the average noise floor of the test cell as measured at the error microphone is 49 dB. A filter length of 250 and weight update frequency of 5 kHz are used. Each noise cancellation test is repeated four times for

TABLE I. Experimentally determined tuning parameters for three candidate adaptive LNLMS algorithms.

LMS algorithm and sound pressure level (SPL)	Mean leakage factor (tones)	Standard deviation of leakage factor $\times 10\,000$ (tones)	Mean leakage factor (F-16)	Standard deviation of leakage factor $\times 10\,000$ (F-16)
LNLMS(80) 80 dB	0.999 930 6	0 (constant)	0.999 930 6	0 (constant)
LNLMS(100) 100 dB	0.999 988 305	0 (constant)	0.999 988 305	0 (constant)
Candidate 1 80 dB	0.999 999 813 0	0.000 035 40	0.999 999 874 9	0.000 156 3
100 dB	0.999 999 998 3	0.000 000 071	0.999 999 998 6	0.000 004 67
Candidate 2 80 dB	0.999 999 407 7	0.000 054 41	0.999 999 558 4	0.001 308 12
100 dB	0.999 999 994 7	0.000 000 241	0.999 999 997 2	0.000 005 60
Candidate 3 80 dB	0.999 732 404 8	0.123 289 85	0.999 739 378 4	0.528 805 03
100 dB	0.999 997 367 6	0.000 000 24	0.999 997 892 7	0.004 826 22

each SPL and noise source. Ensemble average results of the four trials are reported here. All ANR results are presented as measured at the error microphone of the prototype headset.

In the first part of the comparative study, *empirically* tuned NLMS and LNLMS filters with constant leakage parameter and the traditional adaptive step size of Eq. (14) are used with the F-16 noise source. These algorithms are tuned

to maximize performance for F-16 noise at 100 dB SPL and subsequently applied *without change* to all other noise sources at both 100 and 80 dB SPL. A second constant leakage parameter LNLMS filter is *empirically* tuned for the F-16 noise at 80 dB and subsequently applied to all other test conditions. These two empirically tuned algorithms are denoted LNLMS(100) and LNLMS(80), respectively. For both

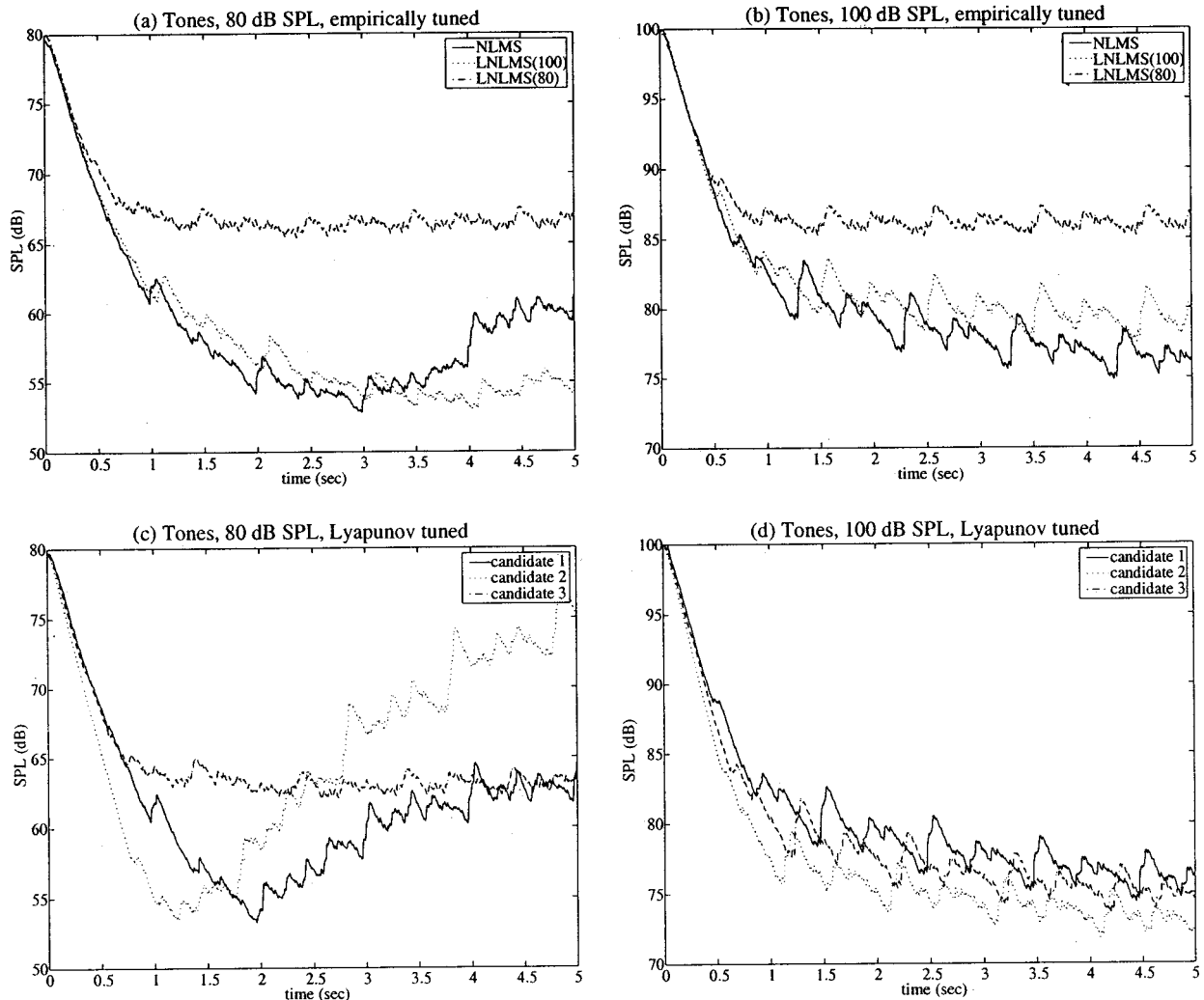


FIG. 8. ANR performance of the NLMS, LNLMS(100), LNLMS(80), and three candidate Lyapunov tuned LMS algorithms acting on a sum of pure tones at 80 and 100 dB.

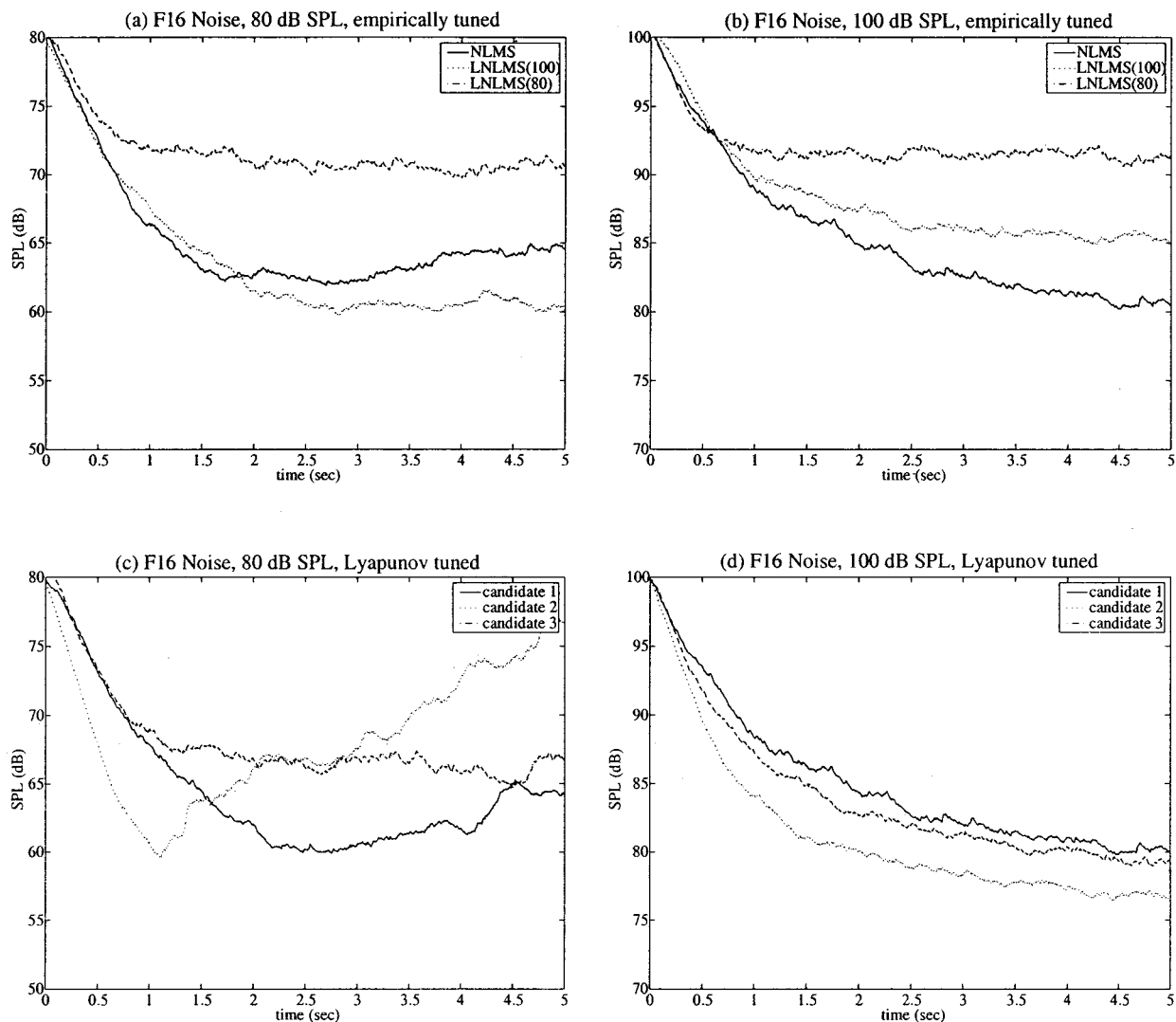


FIG. 9. ANR performance of the NLMS, LNLMS(100), LNLMS(80), and three candidate Lyapunov tuned LMS algorithms acting on F-16 noise at 80 and 100 dB.

filters, $\mu_o = 1/3$, and the respective leakage parameters are given in Table I. At 100 dB SPL, SNR is high enough to minimize the possibility of instability due to measurement noise on the reference input; hence, to maintain stability at 100 dB SPL, the LNLMS(100) filter has a leakage factor that is closer to unity than that of the LNLMS(80) filter. However, in a commercial ANR system, the reference noise SPL is not known *a priori*, thus the leakage factor must be chosen based on *worst case* SNR in order to prevent instability. Thus, if the fixed leaky NLMS filter were to be implemented in a commercial product, stability demands would necessitate using the LNLMS(80) filter, which provides the “worst-case” or smallest fixed leakage factor that retains stability at *both* SNR conditions. Thus, in the experimental test procedure, application of the algorithm tuned for a specific SPL to cancellation of noise *not* matching the tuning conditions demonstrates the loss of performance that results for constant tuning parameters.

The Lyapunov based tuning approach aims to retain stability *and* performance in the presence of any noise source, ranging from stationary tones to highly nonstationary

F-16 noise over the 20 dB dynamic range, i.e., at both 80 and 100 dB SPL. Therefore, a successful Lyapunov tuned candidate theoretically should provide better performance than the LNLMS(80) filter at low SNR, while maintaining performance equal to or exceeding that of the LNLMS(100) filter at high SNR.

IV. EXPERIMENTAL COMPARISON OF EMPIRICALLY TUNED AND LYAPUNOV TUNED ALGORITHMS

Figures 8 and 9 show the results of the NLMS, LNLMS(80), LNLMS(100), and the three candidate Lyapunov tuned LMS algorithms acting on the sum of tones and F-16 noise, respectively. The results presented in Figs. 8 and 9 represent an ensemble average of performance of four trials for each algorithm on 5 s noise samples, for tonal noise and F-16 noise, respectively, and both sound pressure levels.

Beginning with results for pure tones in Fig. 8, the NLMS is unstable when applied to the 80 dB noise source. This is indicated by the drift in SPL after convergence, which is caused by weight vector instability associated with mea-

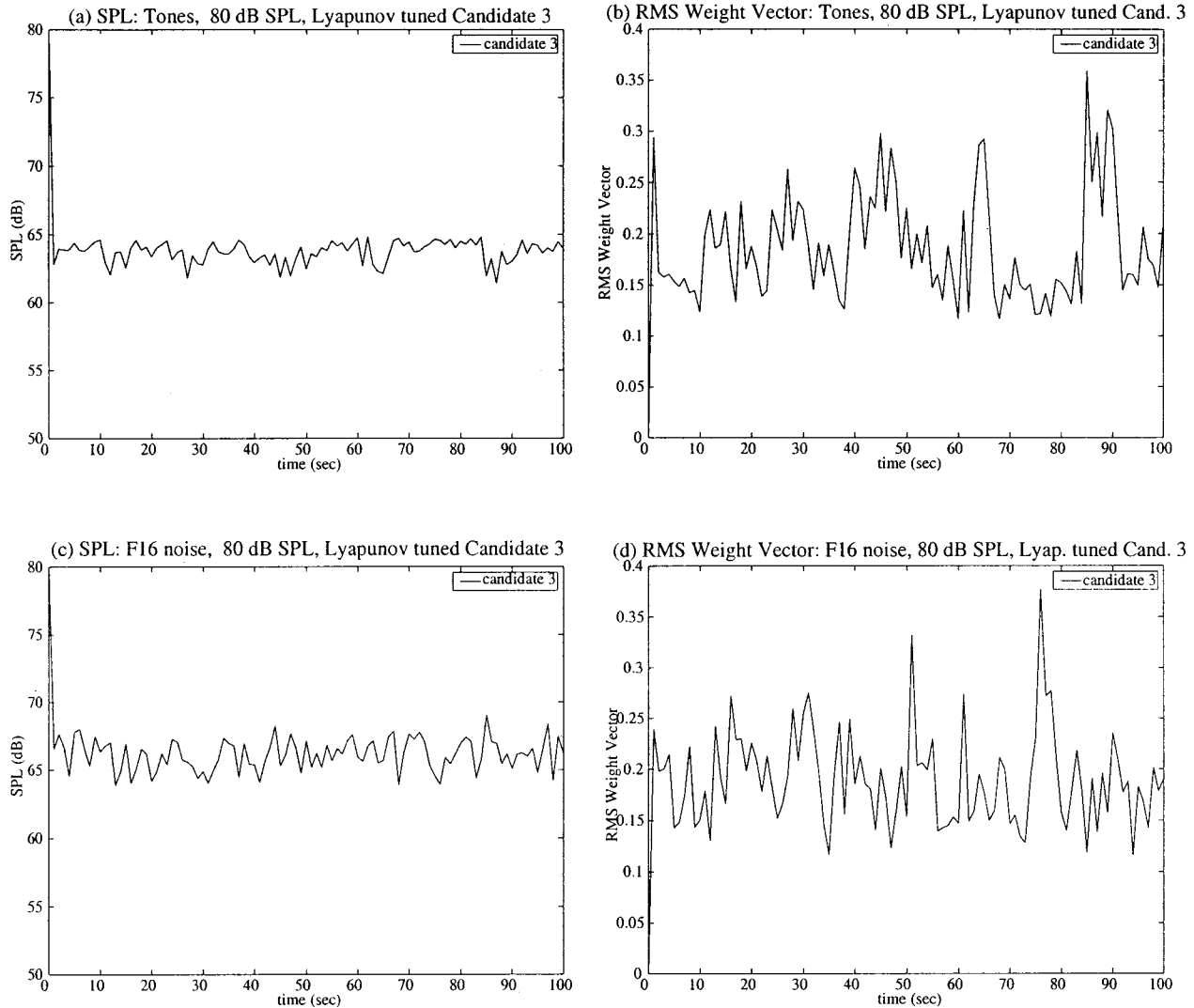


FIG. 10. ANR performance and filter weight performance of Lyapunov tuned candidate 3 acting on 100 s samples of a sum of pure tones and F-16 noise at 80 dB.

surement noise. The LNLMS(100) also is unstable, albeit the weight drift is slower than for the NLMS algorithm. Instability of the NLMS algorithm indicates that a leaky LNLMS algorithm is indeed required, and instability of the LNLMS(100) indicates that a fixed leakage parameter providing optimal performance for 100 dB F-16 noise simply is not large enough to retain stability for the 80 dB tonal noise source. The LNLMS(80) is empirically tuned to retain stability at 80 dB for F-16 noise, but it results in a performance loss of approximately 12 dB over the minimum SPL achieved during transient convergence of the NLMS filter. Of the Lyapunov tuned LMS algorithms [Fig. 8(c)], candidates 1 and 2 are also unstable at 80 dB SPL, while candidate 3 retains stability and provides a steady-state noise reduction exceeding that of the LNLMS(80). For 100 dB SPL tonal noise, all algorithms are stable, although a reduction in performance over that of the NLMS algorithm results for the empirically tuned LNLMS(100) and LNLMS(80) algorithms, as indicated by the steady-state SPL. The Lyapunov tuned algorithms each retain noise reduction performance comparable to that of the NLMS algorithm, indicating that for the higher SPL, the time varying leakage parameter is

closer to unity, on average. Instability of candidates 1 and 2 at 80 dB SPL is due to the fact that SNR conditions for this level were purposely chosen to violate assumptions on A and B for optimization of fixed step size μ_o in Eqs. (14) and (15). This was done in order to test the stability limits of each candidate.

In ranking the stability and performance characteristics of each candidate, as predicted, candidate 2 provides the most aggressive performance; it exhibits the fastest transition to steady state of the Lyapunov tuned algorithms, as noted from Fig. 8(d). Candidate 2 also exhibits the poorest stability of the three candidates as indicated by the response to the 80 dB source in Fig. 8(c). Here, the weight drift is fastest for candidate 2, followed by candidate 1, while candidate 3 remains stable under all conditions tested. These experimental results confirm the analytic results derived from Fig. 2 that rank candidate 3 as the algorithm of choice for maintaining both stability and performance.

For F-16 noise, stability and performance results, which are shown in Fig. 9, are similar. In all cases, the NLMS algorithm, LNLMS(100), and first two candidate Lyapunov tuned LMS algorithms are unstable for each 80 dB noise

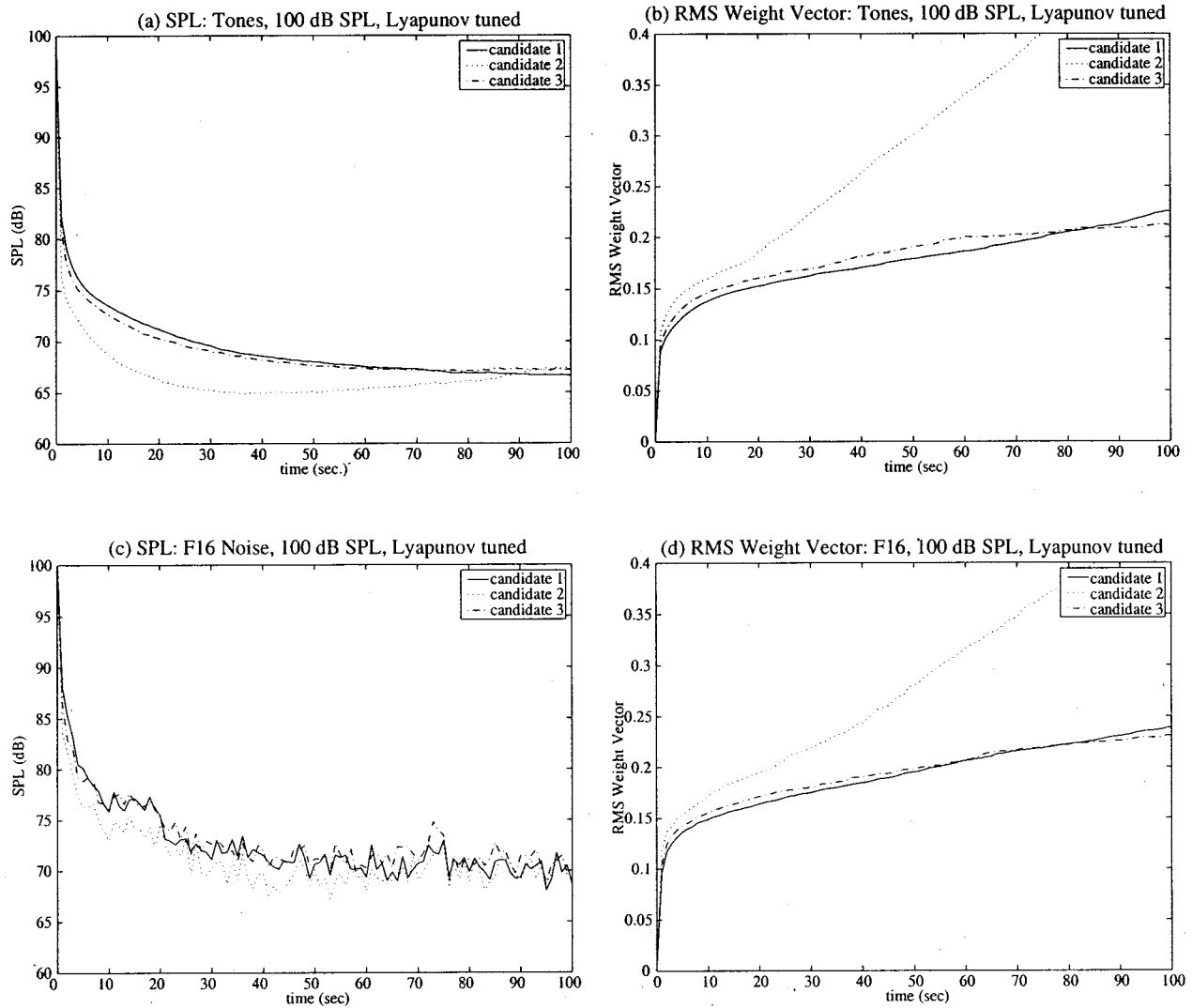


FIG. 11. ANR performance and filter weight performance of Lyapunov tuned candidates 1–3 acting on 100 s samples of a sum of pure tones and F-16 noise at 100 dB.

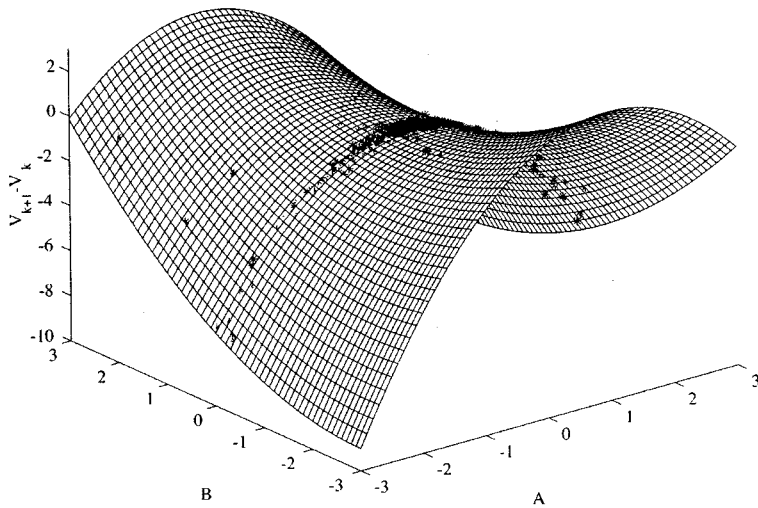
source. LNLMS(80) and candidate 3 are stable for each 80 dB noise source, and candidate 3 outperforms the fixed leakage parameter LNLMS(80). For each 100 dB noise source, all algorithms are stable, with the exception of the NLMS, which exhibits a slow weight vector instability that is imperceptible in the 5 s sample. However, both the LNLMS(80) and LNLMS(100) exhibit significant performance reduction over the NLMS algorithm, while the candidate Lyapunov tuned algorithms retain performance comparable to the NLMS algorithm.

Performance gains of Lyapunov tuned candidates over the fixed leakage parameter LNLMS algorithms are confirmed by the experimentally determined mean and variance of the leakage factor for each candidate, as shown in Table I. The Lyapunov tuned LMS algorithms are more aggressively tuned and operate closer to the Wiener solution ($\lambda = 1$), providing better performance than constant leakage factor algorithms. The experimental results provide evidence that stability and performance gains are achieved in the reduction of both stationary and highly nonstationary noise for an optimized combination of both adaptive step size and adaptive

leakage factor without requiring empirical tuning.

The stability of Lyapunov tuned LMS algorithms is further investigated for the stationary tones and nonstationary F-16 noise sources by examining steady-state noise attenuation and filter weights for a single 100 s noise sample. For the 80 dB noise sources, for which candidate 3 is stable for 5 s noise samples, stability is also evident for 100 s samples, as indicated in Fig. 10. Figures 10(a) and (c) show that average steady-state ANR performance of at least 15 dB is maintained, and Figs. 10(b) and (d) show that no weight drift is evident for the 100 s noise samples. For the 100 dB noise source, Figs. 11(a) and (c) show that all three candidates reach a steady-state ANR performance of at least 30 dB, a significant improvement over the lower SNR condition. A slow weight drift is apparent for candidates 1 and 2, while candidate 3 asymptotically approaches steady state. Overall noise reduction performance of 30 dB for the more difficult nonstationary F-16 source is only 3 dB lower than the 33 dB noise reduction for pure tones. Thus, minimal performance degradation is incurred as the LMS filter attempts to cancel a source whose statistics can vary rapidly with time.

(a) Tones, SNR = 35 dB



(b) F-16 noise, SNR = 35 dB

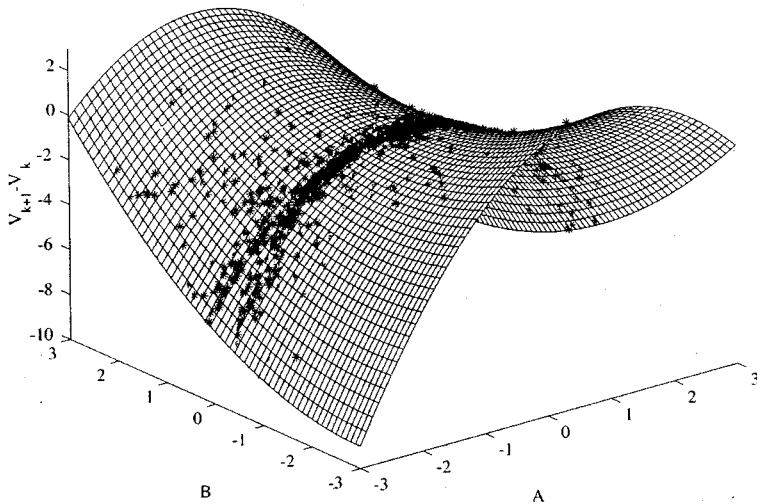


FIG. 12. $V_{k+1} - V_k$ for 1 s simulation (5000 points) of candidate 3 with archived reference and measurement noise sequence at 35 dB SNR. An asterisk denotes actual operating point on the surface.

V. SIMULATION OF LYAPUNOV TUNED CANDIDATES FOR INDUCED, LOW SNR

The Lyapunov tuning method presents stability bounds as a function of scalar constants A and B defined in Eqs. (11) and (12). These scalar constants, along with a Lyapunov function of the projected weight vector difference \tilde{w}_k collapse the n -dimensional weight vector space to a two-dimensional space, such that stability and performance tradeoffs of candidate tuning laws can be visualized in a three-dimensional plot of $V_{k+1} - V_k$ vs A and B . To evaluate the use of scalar parameters in the analysis of stability of LMS algorithms, a simulation was performed in which A and B can be determined for each time step, and in which stability and performance for very low SNR was measured. The

simulation was performed in addition to experimental results presented in Sec. IV, because actual measurement noise sequences are known during simulation, allowing for computation of A and B at each time step, but noise sequences are not known during an actual experiment. Thus, simulation allows visualization of the region of operation of candidate Lyapunov tuned algorithms in the parameter space defined by A and B .

In the simulation, the unknown acoustic transfer function of the headset ($H_3(s)$ in Fig. 5) is modeled by a finite impulse response filter which represents the passive attenuation of the headset. The acoustic noise sources are input to this simulated system to provide the signal d_k which is to be canceled. The candidate LMS algorithm acts on a noisy mea-

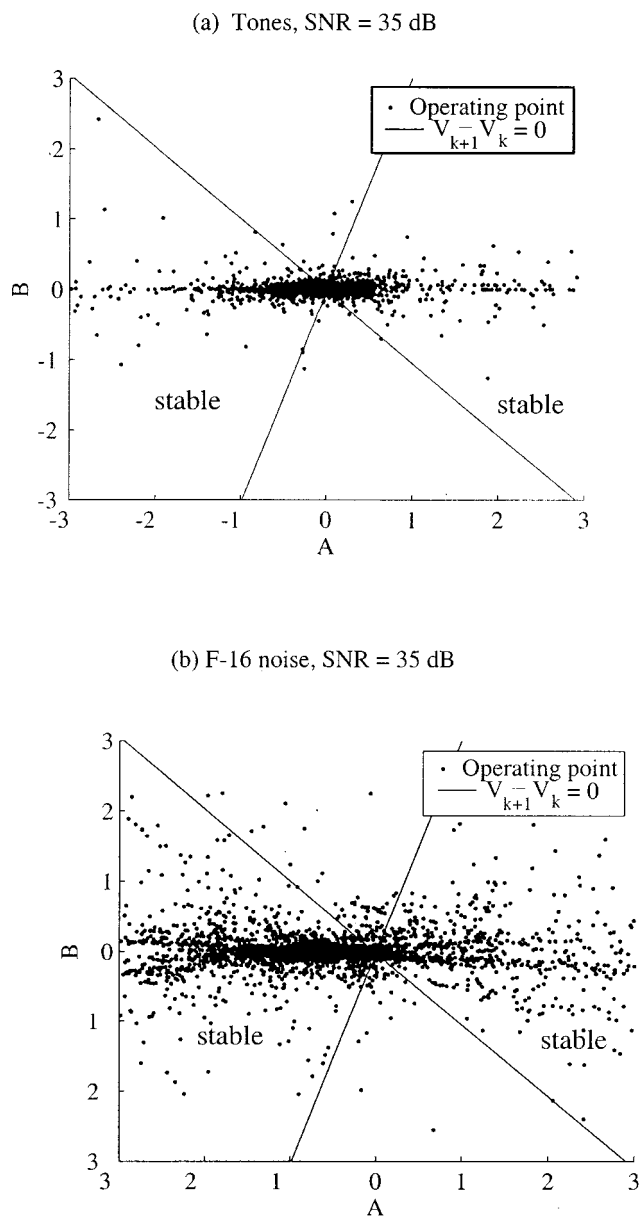


FIG. 13. Two-dimensional view of $V_{k+1} - V_k$ vs A and B for candidate 3 with archived reference and measurement noise sequence at 35 dB SNR.

sured source sequence $X_k + Q_k$, as in the actual experimental evaluation. However, in simulation, the noise sequence Q_k is known *a priori*, as is the Wiener solution, which is the finite impulse response filter representing the passive system. The noise sequence Q_k is generated by recording a time history of the actual test cell noise floor, and scaling this measured sequence to represent a desired SNR for the simulation. The scaled noise sequence is added to the acoustic noise source to generate $X_k + Q_k$. Tonal noise and band limited F-16 noise are used as the noise sources.

Figure 12 shows the results of simulation analysis, presented as a three-dimensional plot of $V_{k+1} - V_k$ vs A and B , showing 5000 samples of the actual system operating points for 35 dB SNR. Points satisfying $V_{k+1} - V_k \leq 0$ represent stable operating conditions, while for $V_{k+1} - V_k > 0$, the system may or may not be stable. From the simulation, it is evident that a *majority* of the instantaneous operating points

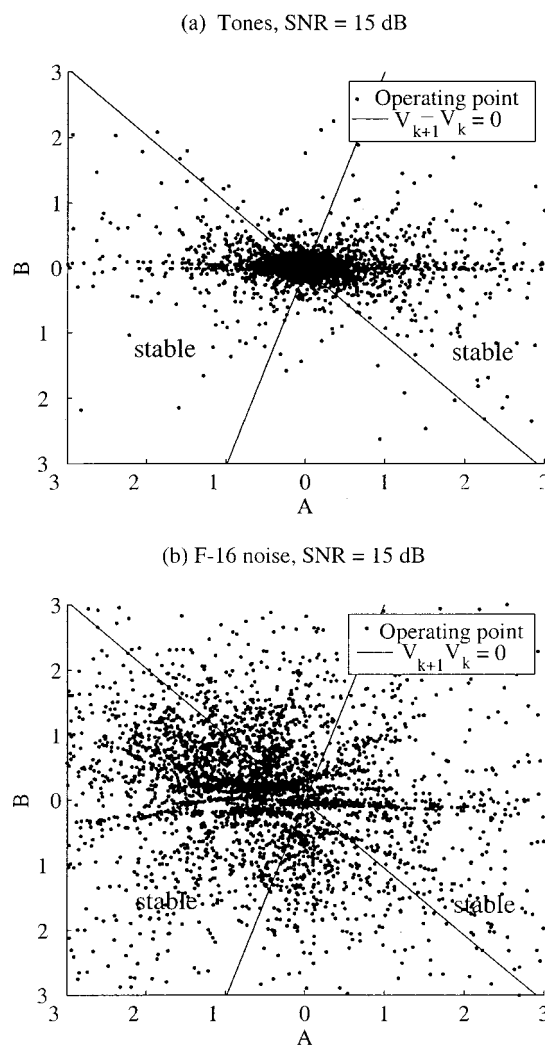


FIG. 14. Two-dimensional view of $V_{k+1} - V_k$ vs A and B for candidate 3 with archived reference and measurement noise sequence at 15 dB SNR.

are guaranteed to be stable for both pure tones and F-16 noise, with fewer excursions to larger values of A and B , or away from the Wiener solution ($A=0, B=0$), for stationary tonal noise than for nonstationary F-16 noise. Additional insight is gained by viewing Fig. 12 as a two-dimensional plot, as shown in Fig. 13. Here, the plane $V_{k+1} - V_k = 0$ is defined by solid lines, and the stable region is denoted. Figure 14 shows the same results for a lower SNR of 15 dB. Figures 13 and 14 show a “cluster” of operating points near the Wiener solution, with occasional excursions to larger values of A and B caused by measurement noise. The cluster is nearer to the Wiener solution for 35 dB SNR than for 15 dB SNR, since the bias in the steady-state weight vector due to the leakage factor increases with decreased SNR. In addition, for F-16 noise, variation or scatter in the operating points is greater than for tonal noise, as would be expected for nonstationary noise. Simulation analysis such as that presented in Figs. 13 and 14 aids in visualizing the relative effects of nonstationarity and measurement noise on stability and performance of Lyapunov tuned algorithms.

To further aid in the analysis, we define P , the probability of operating *outside* of the guaranteed stability boundary, i.e., the probability that $V_{k+1} - V_k > 0$. For pure tones P

TABLE II. Probability of $V_{k+1} - V_k > 0$ for simulation of candidate 2 and candidate 3 in response to pure tones and F-16 noise and archived measurement noise on the reference input.

Noise source	P , candidate 2	P , candidate 3
Pure tones		
35 dB SNR	0.0328	0.1162
15 dB SNR	0.2018	0.1704
F-16 noise		
35 dB SNR	0.0502	0.0379
15 dB SNR	0.3274	0.2556

$=0.1162$ and 0.1704 for 35 and 15 dB, respectively, indicating the expected reduction in stability as SNR decreases, and for F-16 noise, $P=0.037$ and 0.2556 , respectively, for 35 and 15 dB SNR. For F-16 noise, a significant bias away from the Wiener solution is indicated by a center of the cluster of points far from $A=B=0$, as compared to tonal noise. As a consequence, the F-16 simulation at 35 dB SNR has a *lower* overall P , although excursions in operating points away from $A=B=0$ are more frequent, as would be expected for this nonstationary noise source.

Confirming the experimental evaluation, simulation results of candidate 3 compared with other candidate algorithms indicate that it retains the best stability properties, while candidate 2 retains more aggressive performance at a sacrifice to stability. Table II provides a summary of the probabilities of exceeding $V_{k+1} - V_k = 0$ for candidates 2 and 3. Here, with the exception of pure tones at 35 dB, the probability of exceeding the guaranteed stability boundary is larger for candidate 2, indicating this stability sacrifice. The gradient of the $V_{k+1} - V_k$ vs A and B surface of candidate 2 compared with candidate 3, as shown in Fig. 2, contributes to a *lower* P for the 35 dB SNR and pure tones. However, the same phenomenon generally contributes to the reduction in stability for this algorithm. That is, equal excursions away from $A=B=0$ for each candidate result in a larger value of $V_{k+1} - V_k$ for candidate 2 than for candidate 3, increasing the likelihood of instability for candidate 2. In all simulation results, the weight update equation was stable, even though the probability of exceeding the stability boundary was non-zero. Thus, Lyapunov analysis errs on the conservative side when predicting stability.

VI. CONCLUSION

Experimental evaluation of Lyapunov tuned leaky LMS algorithms in a prototype ANR communication headset demonstrates the use of Lyapunov tuning for *a priori* evaluation of stability and performance tradeoffs in time-varying leakage and step size LMS algorithms. The comparative study conducted in a low frequency acoustic test cell for a measured range of 50–200 Hz shows that LNLMS filters with adaptive leakage parameter and step size can provide im-

proved stability at low SNR, while retaining low frequency performance comparable to an NLMS algorithm at high SNR. Lyapunov tuned candidate 3, which results from a non-traditional step-size and leakage parameter combination obtained through a novel parametrization of the Lyapunov function difference, demonstrated the best overall stability and performance characteristics in both measured and simulated ANR experiments. Flat plate active noise reduction measurements over the 50–200 Hz range show that candidate 3 retains stability at 80 dB reference input levels, while demonstrating average steady-state performance of 33 and 30 dB, respectively, in the reduction of pure tones and band limited F-16 noise at 100 dB SPL.

ACKNOWLEDGMENTS

This research is supported in part by United States Air Force Contract No. F41624-99-C-6006 through a subcontract with Create, Inc. The authors are grateful to the Air Force Research Laboratory Human Effectiveness Directorate, Wright Patterson Air Force Base, Dayton, OH, for the support. The authors also thank Dr. Anthony Brammer of the National Research Council of Canada for insight and suggestions on development of the low frequency acoustic test cell.

- ¹G. J. Pan, A. J. Brammer, R. Goubran, J. G. Ryan, and J. Zera, "Broadband active noise reduction in communication headsets," *Can. Acoust.* **22**, 113–114 (1994).
- ²A. J. Brammer and G. J. Pan, "Opportunities for active noise control in communication headsets," *Can. Acoust.* **26**, 32–33 (1998).
- ³A. J. Brammer, G. J. Pan, and R. B. Crabtree, "Adaptive feedforward active noise reduction headset for low-frequency noise," *Proceedings of Active '97 - Symposium on Active Control of Sound and Vibration*, 1997, pp. 365–372.
- ⁴J. C. Burgess, "Active adaptive sound control in a duct: A computer simulation," *J. Acoust. Soc. Am.* **70**, 715–726 (1981).
- ⁵B. Widrow, D. Shur, and S. Shaffer, "On adaptive inverse control," *Proceedings of the 15th Asilomar Conference*, 1981, pp. 185–189.
- ⁶S. M. Kuo and D. R. Morgan, *Active Noise Control Systems* (Wiley, New York, 1996).
- ⁷D. Cartes, L. R. Ray, and R. D. Collier, "Lyapunov tuning of the leaky LMS algorithm for single-source, single-point noise cancellation," *Proceedings of the American Control Conference*, 2001, pp. 3600–3605.
- ⁸J. G. Ryan, E. A. G. Shaw, A. J. Brammer, and G. Zhang, "Enclosure for low frequency assessment of active noise reducing circumaural headsets and hearing protection," *Can. Acoust.* **21**, 19–20 (1993).
- ⁹H. J. Steeneken and F. W. Geirtsen, "Description of the RSG-10 Noise Database," TNO Human Factors Institute, Soesterberg, The Netherlands, 1988.
- ¹⁰R. P. Gitlin, H. C. Meadows, and S. B. Weinstein, "The tap-leakage algorithm: An algorithm for the stable operation of a digitally implemented fractionally spaced equalizer," *Bell Syst. Tech. J.* **61**, 1817–1839 (1982).
- ¹¹J. E. Slotine and W. Li, *Applied Nonlinear Control* (Prentice-Hall, Englewood Cliffs, NJ, 1991).
- ¹²S. Haykin, *Adaptive Filtering Theory* (Prentice-Hall, Englewood Cliffs, NJ, 1996).
- ¹³S. B. Gelfand, Y. Wei, and J. V. Krogmeier, "The stability of variable step-size LMS algorithms," *IEEE Trans. Signal Process.* **47**, 3277–3288 (1999).
- ¹⁴D. Cartes, "Lyapunov tuning and optimization of feedforward noise reduction for single-point, single-source cancellation," Ph.D. dissertation, Thayer School of Engineering, Dartmouth College, 2001.

Wheel/rail noise generation due to nonlinear effects and parametric excitation

Anders Nordborg^{a)}

*The Marcus Wallenberg Laboratory for Sound and Vibration Research, Kungl Tekniska Högskolan,
100 44 Stockholm, Sweden*

(Received 16 June 1998; revised 16 January 2002; accepted 22 January 2002)

Two models are developed, one in the time domain and another in the frequency domain, to explain when a wheel/rail noise generation model requires the inclusion of discrete supports, parametric excitation, and the nonlinear contact spring. Numerical simulations indicate the inclusion of discrete supports to describe low frequency response, and also at higher frequencies, especially where the rail is very smooth or has a corrugation/wavelength corresponding to the pinned-pinned frequency. With a corrugation, it may become essential to include the nonlinear contact spring, as contact loss occurs at high corrugation amplitudes. As nonlinearity causes force generation over a broad frequency range, some contributions excite wheel resonances, resulting in high radiation levels, that require the inclusion of wheel/rail nonlinear effects and parametric excitation for accurate prediction. © 2002 Acoustical Society of America. [DOI: 10.1121/1.1459463]

PACS numbers: 43.50.Lj, 43.40.Cw, 43.50.Ed, 43.40.At [PJR]

I. INTRODUCTION

The most comprehensive and widely used wheel/rail noise model is that developed by Remington and Thompson.¹⁻⁴ It is linear, time invariant, performed in the frequency domain, with a validated standard deviation of up to 5 dB, in third-octave bands. They consider roughness only as an excitation mechanism, while suggesting that prediction errors are due to uncertainties in the real roughness level combined with the actual rail/wheel contact position across the rail surface. The conclusion that such an approximation suffices to adequately describe railway noise generation may be premature, requiring evidence from more advanced descriptions of the generation mechanisms. Alternative excitation mechanisms include nonlinearities and parametric excitation due to changing rail and contact receptance with position. In exciting the whole wheel/rail system, a broad insight into force generation would be most helpful in improving noise abatement!

For continuously supported track, nonlinear wheel/rail contact effects are mostly unimportant, unless the roughness level is very high or the static load is very small.⁵ Real tracks, however, are discretely supported. It is strongly believed^{6,7} that in modifying the contact force, the discrete supports are responsible for corrugation formation on rail surfaces. Of course, it is the same contact force that excites rails and wheels into vibration and noise radiation. Therefore, a realistic rail model should include discrete supports. Two distinct properties are associated with the discrete supports: the sleeper-passing frequency f_s , and the pinned-pinned frequency f_{pp} . The wheels pass the sleepers with the sleeper-passing frequency $f_s = v/l$, where v is the speed and l the sleeper distances. At the pinned-pinned frequency f_{pp} , the bending wavelength of the rail is precisely two sleepers distant $\lambda_{pp} = 2l$, with nodes at the sleeper positions.

In order to investigate when it is necessary to include discrete supports, parametric excitation, and the nonlinear contact spring, two models are presented: one in the time domain and the other in the frequency domain. With each it is possible to either include or exclude a certain property, e.g., discrete supports. Numerical simulations then suggest when this property must be included in the model to accurately describe force generation.

The time domain model, inspired by Heckl's proposal,⁸ and by Ilias's and Ripke's wheel/rail interaction models,^{7,9} determines the vertical rail deflection by time integrating Green's function of the rail together with force impulses from the wheel/rail contact. Nonlinear Hertzian contact mechanics can be used, less realistic, however, than a discretized contact region allowing for rough surfaces. The wheel is a rigid mass.

The frequency domain model, a simpler version of that developed in Refs. 10 and 11, yields the response by solving a discretized integral equation. Due to the parametric excitation, there is a coupling between different frequency components; the coupling coefficients are essentially the Fourier coefficients of expansion of the varying receptance along the track, described by the track Green's function.

In fact, both models are equivalent formulations of the same problem, once in the time domain and once in the frequency domain. Green's function yields the solution in both cases.

Numerical simulations show that it is necessary to include discrete supports in rail modeling to describe the response at low frequencies, determined by the sleeper-passing frequency f_s , and around the pinned-pinned frequency f_{pp} , usually around 1 kHz—in particular if the rail is very smooth or has a corrugation with a wavelength corresponding to the pinned-pinned frequency. If the rail has a corrugation it may also be necessary to include the nonlinear contact spring, since loss of contact occurs for great corrugation amplitudes, e.g., if the corrugation amplitude r_0 is greater than 15 μm

^{a)}Electronic mail: anders.nordborg@fkt.kth.se

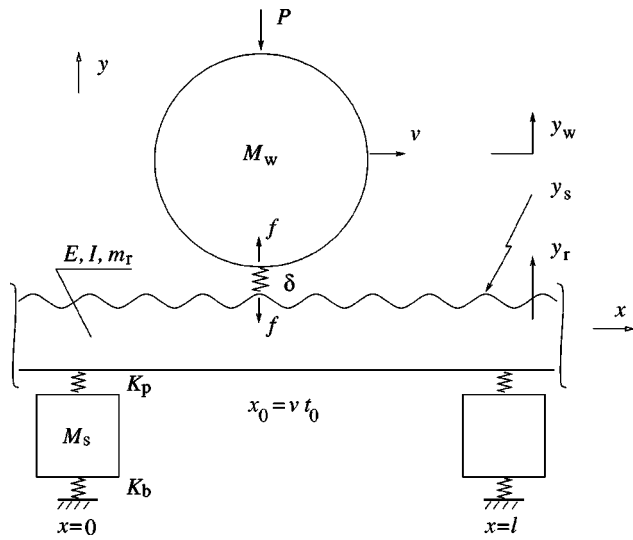


FIG. 1. Time domain wheel/rail interaction model.

when the preload P is 65 kN (for the parameters used in this paper). Nonlinearity causes force generation over a broad frequency range. It may for instance be expected that high frequency contributions will excite wheel resonances, resulting in high noise radiation levels, that require wheel/rail nonlinear effects and parametric excitation for accurate predictions.

II. THEORY

A. Time domain model

A wheel with mass M_w and preload P rolls with forward velocity v over a rail (Fig. 1). The rail has mass m_r per unit length, bending stiffness EI , and a corrugation $y_s = r_0 \sin(2\pi/\lambda_0)x$ on the running surface. The coordinate axis for x points in the forward running direction, and for y upwards in the vertical direction. A perfectly smooth rail implies that $y_s = 0 \mu\text{m}$. The rail is periodically supported at discrete points with spacings l . Each support consists of a spring-mass-spring combination: K_p denotes pad stiffness with loss factor η_p , M_s sleeper mass, and K_b ballast stiffness with loss factor η_b . The compression in the wheel-rail contact region, $\delta_{\text{lin}} = y_r + y_s - y_w$, is a function of vertical rail, y_r , and wheel, y_w , deflections plus the deviation from a perfect running surface, y_s . The contact force f , caused by the compression, excites the wheel (upwards) and the rail (downwards). Since this is a time-domain model, rail and wheel deflections, plus the contact force are calculated at each discrete point $x_0 = n\Delta x$, where n is an integer and Δx the space increment, with the corresponding time increment $\Delta t = \Delta x/v$.

1. Rail

The vertical rail deflection, $y_r(x_0, t_0)$, at the moving point, $x_0 = vt_0$ (under the wheel), is a convolution of the rail Green's function, $g(x, x_0; t, t_0)$, and the contact force $f(x, t)$,

$$y_r(x_0, t_0) = \int \int g(x, x_0; t, t_0) f(x, t) dx dt.$$

After discretization, and using that the contact force moves forward, $f(x, t) = f(t) \delta(x - vt)$,

$$y_r(t_0) = \sum_{k=0}^{K-1} g(x_0 - k\Delta x, x_0; t_0 - k\Delta t, t_0) \times f(t_0 - k\Delta t) \Delta t, \quad (1)$$

where k is an integer. Note that the force point, $x = x_0 - k\Delta x$, is expressed relative to the response point, x_0 . Previous calculations¹² (Appendix B) have provided Green's function in the frequency domain, $G_\omega(x, x_0)$, here first made conjugate symmetric, $G_{-\omega} = G_\omega^*$ (the asterisk denoting complex conjugate), to ensure reality and causality, and then transformed to the time domain by a discrete Fourier transform, $g(x, x_0; t, t_0) = \text{DFT}^{-1}[G_\omega(x, x_0)]$. The force, $f(t_0 - k\Delta t)$, known in the past where $k > 0$, must be found by iterative improvements for the very last time step, $k = 0$. The total number of points, K , must be so great that the impulse from the most distant point, $x_0 - (K-1)\Delta x$, has decayed to a negligible amplitude before it arrives at the response point, x_0 .

2. Wheel

The wheel model is the simplest possible: a rigid mass, M_w , acted upon vertically by a constant preload force, P , plus the contact force, f . Numerically, e.g., with Runge-Kutta, solving the ordinary differential equation $M_w \ddot{y}_w(t) = f(t) - P$ (the dots denoting time derivatives) gives the vertical displacement y_w .

3. Contact

This paragraph essentially follows Refs. 7 and 9. The compression of the wheel/rail contact

$$\delta_{\text{lin}} = y_r + y_s - y_w, \quad (2)$$

a function of the contact force. Being unknown at the current time step, it can be approximated first with its most recent value, $f(t_0) \leftarrow f(t_0 - \Delta t)$. According to Hertz, the compression distance is a nonlinear function of the contact force f ,

$$\delta_H = \left[\frac{2f(1-\nu)}{G\sqrt{R_a}} \right]^{2/3} \alpha_\delta. \quad (3)$$

Of course, $f \geq 0$ always; $f = 0$ implies loss of wheel-rail contact, $\delta_{\text{lin}} \leq 0$. Here G is the shear modulus, ν Poisson's ratio, and R_a one of the radii of curvature at the contact point. The function α_δ depends on the elliptical shape of the contact area (Fig. 2). Now, solving

$$\delta_{\text{lin}} - \delta_H(f) = 0,$$

iteratively, yields the Hertzian contact force f . It is then possible to iterate, with the successive force improvements $f(t_0) \leftarrow f$, until the error $|f(t_0) - f| < \epsilon$, ϵ being a small number. The contact force f plus rail and wheel deflections, y_r and y_w , are now known at the current time step.

B. Frequency domain model

The presentation in this section (also found in Ref. 13), essentially a simpler version of that found in Ref. 10, de-

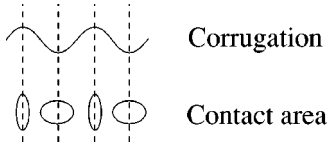


FIG. 2. Contact area variations.

scribes, in three steps, the mathematical framework of the frequency domain model for parametric excitations due to varying contact and track stiffnesses. First, the equation of motion for a mass on a time-varying spring is derived. Second, a continuously supported beam is inserted under the spring. Third, discrete supports are substituted for the continuous foundation under the beam.

1. Mass on a time-varying spring

A rigid mass M moves vertically on a time-varying spring k and a damper c (Fig. 3). Expressing the stiffness in terms of receptance $\alpha(t) = 1/k$, the equation of vertical motion $y(t)$ of the mass becomes

$$\alpha(t) \left[M \frac{d^2 y(t)}{dt^2} + c \frac{dy(t)}{dt} \right] + y(t) = b(t),$$

where $b(t)$ is an external base displacement excitation. The time variation of $\alpha(t)$ provides the internal parametric excitation. Fourier expansions of $\alpha(t)$, $b(t)$, and $y(t)$:

$$\alpha(t) = \sum_{n=-\infty}^{\infty} a_n e^{-i\Omega_n t},$$

$$b(t) = \sum_{n=-\infty}^{\infty} b_n e^{-i\Omega_n t},$$

$$y(t) = \sum_{n=-\infty}^{\infty} y_n e^{-i\Omega_n t},$$

yield the system

$$y_m = - \sum_{n=-\infty}^{\infty} a_{m-n} \alpha_{M,c}^{-1}(\Omega_n) y_n + b_m, \quad (4)$$

or $y = Ay + b$ in matrix form, where $-\alpha_{M,c}^{-1}(\Omega_n) = M\Omega_n^2 + ic\Omega_n$. Equation (4) defines the mathematical framework of the frequency domain model for parametric excitations.

2. Wheel on a time-varying contact spring and a continuously supported, corrugated rail

A wheel with vertical receptance $\alpha_{\text{veh}}(\omega) = -1/M_w \omega^2$ and static preload P (including the wheel mass) traverses, with speed v , a corrugated, continuously supported rail (Fig. 15). The track input receptance as “seen” from the wheel consists of Hertzian contact spring receptance $\alpha_H(t)$ and rail receptance $\alpha_r(\omega)$ (Appendix A) in series,

$$\alpha_{H,r}(t, \omega) = \alpha_H(t) + \alpha_r(\omega) = \sum_{n=-\infty}^{\infty} a_n(\omega) e^{-i\Omega_n t}.$$

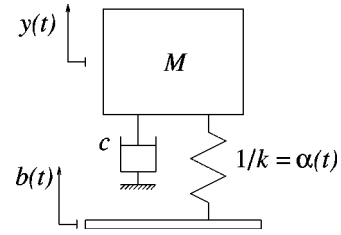


FIG. 3. Mass on a time-varying spring.

(NB: Variables t and Ω_n are a transform pair, while ω is a constant.) The coefficients $a_n(\omega)$ go into matrix A of system (4), or

$$y_m = - \sum_{n=-\infty}^{\infty} a_{m-n}(\Omega_n) \alpha_{\text{veh}}^{-1}(\Omega_n) y_n + b_m. \quad (5)$$

To solve system (5) the coefficients of the external excitation vector, b_m , and of the track receptance, $a_{m-n}(\Omega_n)$, must be known. Define the vertical surface deviation due to the corrugation as having the (idealized) form

$$\begin{aligned} b_{\text{corr}}(t) &= -2r'_0 \cos \Omega_\nu t \\ &= -r'_0 e^{-i\Omega_\nu t} - r'_0 e^{i\Omega_\nu t}. \end{aligned}$$

The corrugation amplitude $2r'_0$ equals r_0 from the time domain model (Sec. II A), $2r'_0 = r_0$. The excitation circular frequency $\Omega_\nu = 2\pi v/\lambda_0$, ν the index for this frequency, and λ_0 is the corrugation wavelength. That is, there is a trough at $t = 0$ ($x = 0$). Due to contact area variations (Fig. 2), the contact receptance has minima in the troughs and maxima on the peaks:

$$\begin{aligned} \alpha_H(t) &= \bar{\alpha}_H - 2\tilde{\alpha}_H \cos \Omega_\nu t \\ &= -\tilde{\alpha}_H e^{-i\Omega_\nu t} + \bar{\alpha}_H - \tilde{\alpha}_H e^{i\Omega_\nu t}, \end{aligned} \quad (6)$$

where $\bar{\alpha}_H$ is the average contact receptance, $\tilde{\alpha}_H$ its (also ideal) variation. The external excitation is a combination of the corrugation and the deflection variation under the static load P ,

$$b = b_{\text{corr}} + b_{\text{stat}}, \quad (7)$$

with nonzero components for $m = \pm \nu$, where $b_{\text{corr}, \pm \nu} = -r'_0$ and $b_{\text{stat}, \pm \nu} = -Pa_\nu$, $a_\nu = -\tilde{\alpha}_H$. It follows from Eq. (5) that the diagonal of the matrix $A_{\text{diag}} = A_{m,m} = -a_0(\Omega_m) \alpha_{\text{veh}}^{-1}(\Omega_m)$ [where $a_0(\Omega_m) = \bar{\alpha}_H + \alpha_r(\Omega_m)$], i.e., the ratio between the average track receptance as “seen” by the wheel, and the wheel receptance. Neglecting internal parametric excitation, but including external roughness excitation changes Eq. (5), short form $y = Ay + b$, to the simpler rolling noise generation presumption

$$y = A_{\text{diag}} y + b_{\text{corr}}, \quad (8)$$

which for a certain circular frequency Ω_ν takes the well-known form

$$y(\Omega_\nu) = \frac{b_{\text{corr}}(\Omega_\nu)}{1 + a_0(\Omega_\nu)/\alpha_{\text{veh}}(\Omega_\nu)},$$

the same as that used in most railway noise generation frequency models (e.g., Refs. 1–4).

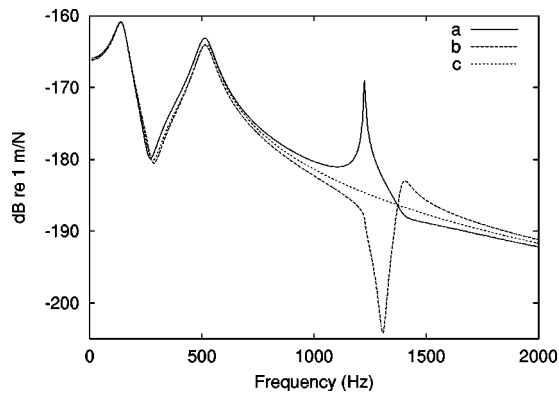


FIG. 4. Vertical rail receptance magnitude: (a) periodic supports, excitation between two sleeper positions; (b) periodic supports, excitation above a sleeper position; (c) continuous supports. Pinned-pinned resonance at 1224 Hz; pinned-pinned antiresonance at 1305 Hz.

3. Wheel on a time-varying contact spring and a periodically supported, corrugated rail

Now, the wheel traverses a corrugated, periodically supported, rail (Fig. 17), with the varying point receptance $\alpha_p(x, \omega)$ (Appendix B). The rail surface has the same corrugation and contact receptance variation as before, expressed as a function of the space variable $x = vt$, $\alpha_H(x) = \bar{\alpha}_H - 2\bar{\alpha}_H \cos k_v x$, where $k_v = 2\pi/\lambda_0 = \Omega_v/v$. The total track input receptance as “seen” by the wheel, $\alpha_{H,p}(x, \omega) = \alpha_H(x) + \alpha_p(x, \omega)$, with the Fourier coefficients

$$a_n(\omega) = \frac{1}{l} \int_0^l \alpha_{H,p}(x, \omega) e^{ik_n x} dx \quad (9)$$

(where l is the sleeper distances, $k_n = 2\pi n/l = \Omega_n/v$) to be inserted into matrix A of system (5), $y = Ay + b$. Since $\alpha_{H,p}(x, \omega)$ is an even function of x , $a_{-n}(\omega) = a_n(\omega)$. The solution of Eq. (5) with these track Fourier coefficients yields the deflection amplitudes of the wheel, when traversing the corrugated, sleeper-supported rail.

TABLE I. Rail parameters.

Parameter	Value	Description
v	60 m/s	Wheel velocity
M_w	600 kg	Wheel mass
P	65 kN	Wheel preload (including wheel mass)
R_w	0.46 m	Wheel radius
R_r	0.3 m	Rail head radius
E	2.1×10^{11} N/m ²	Rail modulus of elasticity
η_r	0.004	Rail loss factor
I	22.5×10^{-6} m ⁴	Rail moment of area inertia
m_r	60 kg/m	Rail mass per unit length
M_s	150 kg	(Half) sleeper mass
l	0.6 m	Sleeper spacing
K_p	300×10^6 N/m	Pad stiffness
η_p	0.15	Pad loss factor
T	0 Nm/rad	Torsional support stiffness
K_b	150×10^6 N/m	Ballast stiffness (under a half sleeper)
η_b	0.4	Ballast loss factor

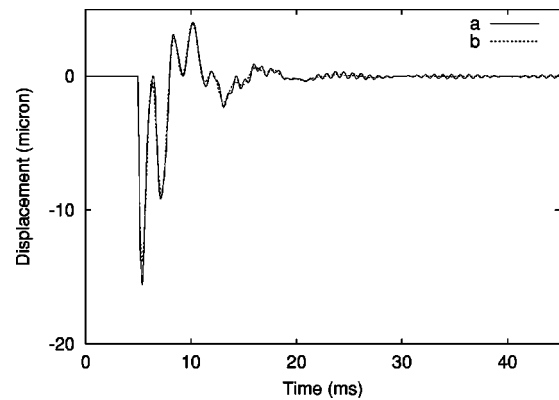


FIG. 5. Moving Green's function, $v=60$ m/s impulse force, $f(t) = 5 - 65 \delta(t-t_0)$ kN, $t_0=5$ ms (sleeper positions at 0,10,20,..., ms). Two rail models: (a) periodic supports; (b) continuous supports.

III. NUMERICAL RESULTS AND DISCUSSION

A. Rail receptance

The calculations assume parameters according to Table I, unless otherwise stated. Euler beam theory is used, with a reduction of the moment of inertia for a UIC 60 rail to 75% of its tabulated value (30.0×10^{-6} m⁴), thus extending the useful frequency region for vertical rail vibrations up to and above 2 kHz.^{12,14}

Figure 4 shows vertical rail point receptance calculated with two different models: a periodically supported (Fig. 17) and a continuously supported (Fig. 15) track model. For the periodically supported track, the receptance for two different excitation positions are calculated: between two support positions and above a support position. As a result of having reduced the moment of inertia to 75% of its tabulated value, the pinned-pinned resonance occurs a little above 1200 Hz, which is lower than the 1400 Hz obtained with 100% of the tabulated value. The pinned-pinned antiresonance occurs at about 1300 Hz.

Hitting the rail with an impulse force, following the vertical displacement at a position, moving with velocity v in the x direction, produces the moving Green's function [Eq. (1)]. Figure 5 shows the moving ($v=60$ m/s) Green's functions for periodically and continuously supported rails. For the periodic rail, the impact excitation occurs precisely between two support positions. The model with periodic sup-

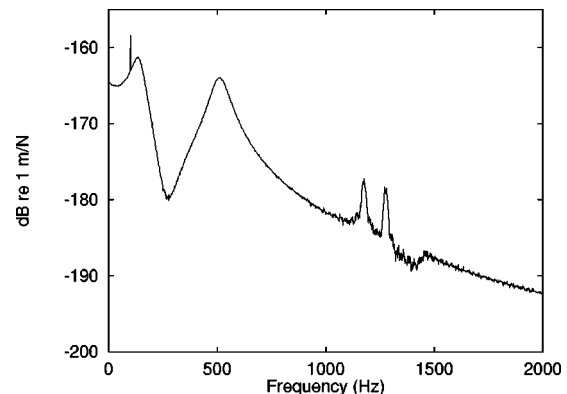


FIG. 6. Moving rail receptance. Velocity $v=60$ m/s. Static force, 65 kN. Random force, 65 kN.

TABLE II. Wheel and contact model parameters.

Parameter	Value	Description
v	60 m/s	Wheel velocity
M_w	600 kg	Wheel mass
P	65 kN	Wheel preload (including wheel mass)
R_w	0.46 m	Wheel radius
R_r	0.3 m	Rail head radius
r_0	25 μm	Corrugation amplitude
λ_0	4.60 cm	Corrugation wavelength

ports has a response at the pinned–pinned frequency, clearly seen as a high frequency component after about 15 ms; otherwise the moving Green’s function from the two models are almost identical.

Figure 6 shows the vertical rail point receptance for periodically supported rail, when a static plus a random moving force excite the rail, obtained using the time-domain moving Green’s function [Fig. 5 and Eq. (1)]. Forward velocity causes the receptance peak at the pinned–pinned frequency, $f_{pp}=1244$ Hz, to split. The new peaks are approximately located at $f_{pp}(1 \pm M)$, where the Mach number $M=v/c_B$, c_B is the bending wave velocity. Since, by definition, the bending wavelength $\lambda_B=2l$ at f_{pp} , $f_{pp}M=f_s/2$, where $f_s=v/l=100$ Hz for $v=60$ m/s, is the sleeper passing frequency, the shifted peaks appear approximately at $f_{pp} \pm f_s/2$. Apart from splitting the f_{pp} peak, forward velocity together with the static load, also cause a peak at the sleeper-passing frequency f_s . The height of the peak is proportional to the static load. Clearly, the moving rail receptance differs from the stationary one at the sleeper-passing frequency and around the pinned–pinned frequency.

B. Time domain model

The calculations assume parameters according to Table I and II, unless otherwise stated. The first calculation (Figs. 7 and 8) simulates a wheel rolling on a corrugated, continuously supported rail (Fig. 15). The contact model is linear and time invariant, not accounting for parametric excitation. The generated contact force has one frequency component only, at the corrugation passing frequency, $f_0=1300$ Hz.

The next calculation simulates a wheel rolling on a corrugated, sleeper-supported rail (Fig. 1). The contact model

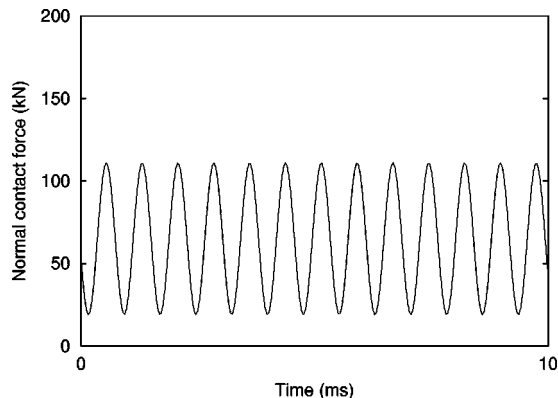


FIG. 7. Normal contact force for wheel rolling over a corrugated, continuously supported rail. Fully linear contact model.

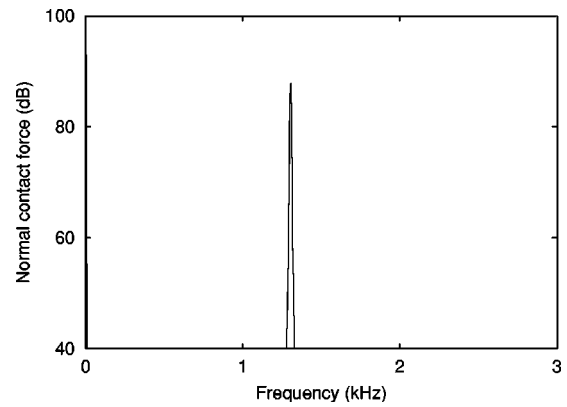


FIG. 8. Normal contact force spectrum for wheel rolling over a corrugated continuously supported rail. Fully linear contact model. Peak at the corrugation-passing frequency $f_0=1300$.

now accounts for the nonlinear relation between force and deflection/compression (3), as well as parametric excitation in the contact region due to variations of the shape of the contact ellipse (Fig. 2). The corrugation wavelength $\lambda_0=4.60$ cm corresponds to the antiresonance of the pinned–pinned mode, located at 1300 Hz (Fig. 4), a “worst case,” but not an unrealistic situation. The corrugation amplitude $r_0=25$ μm .

Because of the discrete supports, the contact force amplitude varies extensively through the sleeper spans (Fig. 9). In the middle of a span, contact loss occurs, causing the contact force to vanish, allowed by the nonlinear contact model. The distance between rail and wheel (Fig. 10), plus the deviation of the rail surface, equals the compression of the wheel/rail contact (2).

The contact force spectrum (Fig. 11) has three main regions. First, at low frequencies, the discrete sleeper supports cause an excitation at the sleeper-passing frequency $f_s=v/l=100$ Hz, plus at its harmonics. Second, corrugation causes an excitation peak at the corrugation-passing frequency $f_0=v/\lambda_0=1300$ Hz, accompanied by smaller peaks 100 Hz apart due to modulation by the sleeper-passing frequency. Third, contact loss and parametric excitation within the contact region, due to shape variations of the contact ellipse, cause an excitation of twice the corrugation-passing fre-

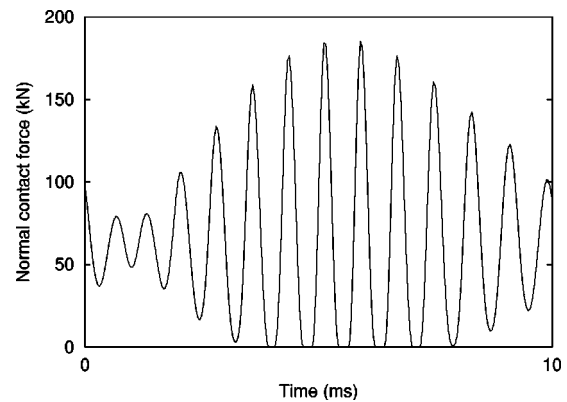


FIG. 9. Normal contact force for wheel rolling one sleeper span over a corrugated rail. Sleeper positions at 0 and 10 ms. Contact model accounting for nonlinearities and parametric excitation.

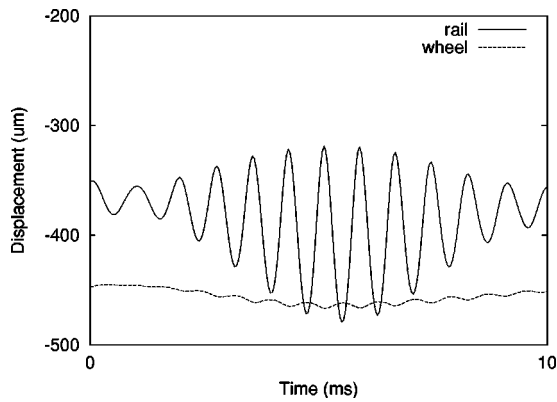


FIG. 10. Rail and wheel deflection for wheel rolling one sleeper span over a corrugated rail. Sleeper positions at 0 and 10 ms. Contact model accounting for nonlinearities and parametric excitation.

quency $2f_0 = 2600$ Hz, which is also modulated by sleeper passings.

Comparison of Figs. 11 and 8 clearly enhances the importance of including discrete supports, parametric excitation, and a nonlinear contact spring. The linear, time invariant model (Fig. 8) has a response at one frequency only, while the improved model (Fig. 14) exhibits responses over a broad frequency range. It may for instance be expected that contributions above 2 kHz excite wheel resonances, resulting in high noise radiation levels that require the inclusion of wheel/rail nonlinear effects and parametric excitation for reliable prediction!

C. Frequency domain model

If no wheel/rail contact loss occurs, nonlinearities are small, and the frequency domain model (Sec. II B) accounting for parametric excitation should be appropriate; reducing the corrugation amplitude to $15 \mu\text{m}$ or increasing the wheel preload to 100 kN guarantees wheel/rail contact (shown by simulations not included here).

The external excitation vector b , Eq. (7), (Fig. 12) represents an equivalent roughness spectrum for a corrugated, sleeper-supported rail. The broadband parts of the spectra correspond to a rough and a smooth rail, respectively. The rough rail has a roughness level of 10 dB per 1/3 octave

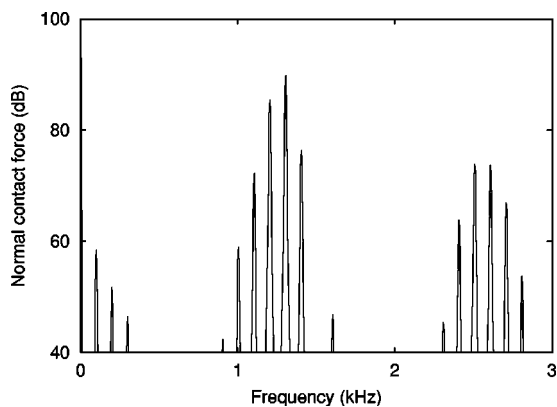


FIG. 11. Normal contact force spectrum for wheel rolling over a corrugated sleeper-supported rail. Contact model accounting for nonlinearities and parametric excitation.

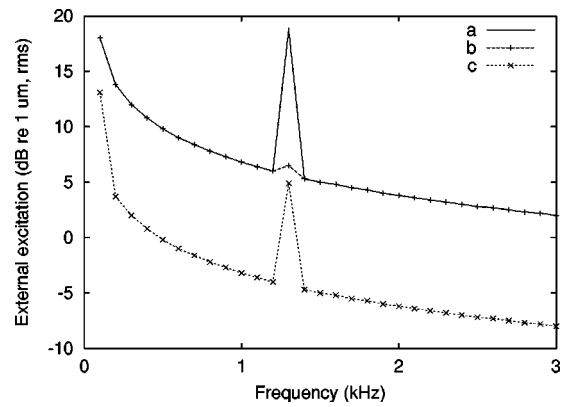


FIG. 12. Equivalent roughness spectrum (external excitation). Three rail surfaces: (a) roughness level $L_{r_0} = 10$ dB, corrugation amplitude $r_0 = 15 \mu\text{m}$, contact receptance variation, 5%; (b) roughness level $L_{r_0} = 10$ dB, corrugation amplitude $r_0 = 3 \mu\text{m}$, contact receptance variation, 0%; (c) roughness level $L_{r_0} = 0$ dB, corrugation amplitude $r_0 = 3 \mu\text{m}$, contact receptance variation, 1%.

bands, and the smooth rail a level of 0 dB per 1/3 octave bands, according to the formula $L_{r_0} = 10 \log(r_0^2/r_{\text{ref}}^2)$ (dB), where $r_{\text{ref}} = 1 \mu\text{m}$, rms. Since the frequency resolution here is a constant 100 Hz, the spectra fall off with frequency.

The increased levels at low frequencies are due to varying receptance through the sleeper spans. The peaks at 1.3 kHz are caused by the corrugation with a wavelength λ_0 of 4.6 cm, and an amplitude r_0 of either 3 or $15 \mu\text{m}$. Contact area variations (Fig. 2) cause a contact receptance variation, of 5%, 0%, or 1%.

Figure 13 shows contributions to the response caused by parametric excitation due to discrete sleeper supports and contact receptance variations, i.e., the difference between the levels calculated by Eq. (5), including parametric excitation, and by the approximation (8), excluding parametric excitation. Similarly, as for the time domain model (Fig. 11), there is response at low frequencies due to sleeper passings, and around the pinned–pinned frequency at 1.3 kHz. However, the response around twice the corrugation-passing frequency $2f_0 = 2.6$ kHz due to contact area variations is missing here,

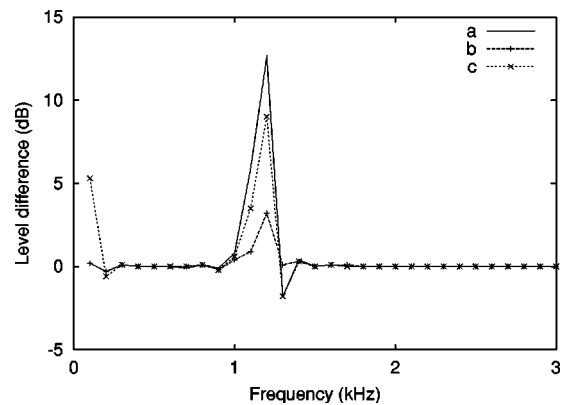


FIG. 13. Parametric excitation contributions: (a) roughness level $L_{r_0} = 10$ dB, corrugation amplitude $r_0 = 15 \mu\text{m}$, contact receptance variation, 5%; (b) roughness level $L_{r_0} = 10$ dB, corrugation amplitude $r_0 = 3 \mu\text{m}$, contact receptance variation, 0%; (c) roughness level $L_{r_0} = 0$ dB, corrugation amplitude $r_0 = 3 \mu\text{m}$, contact receptance variation, 1%.

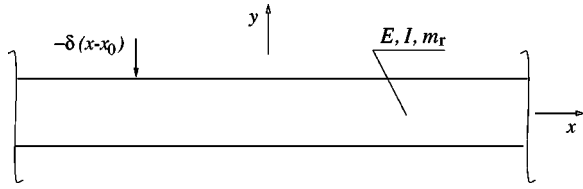


FIG. 14. Infinite beam, excited by a unit point force.

since it is shadowed by the response caused by the broadband part of the roughness spectrum. Obviously, parametric excitation becomes important at low frequencies for smooth rails, and around the pinned–pinned frequency for corrugated rails. Precisely at the corrugation-passing frequency $f_0 = 1.3$ kHz, the response with the model accounting for parametric excitation is a little smaller than that predicted by the pure roughness excitation model, because the deflection variation under the static load P and the surface deviation partly cancel each other out [see Eq. (7)].

IV. CONCLUSIONS

Two models describing wheel/rail noise generation have been developed: one in the time domain and the other in the frequency domain. With each model, it is possible to either include or exclude a certain property, e.g., discrete supports, parametric excitation, and the nonlinear contact spring. Numerical simulations then suggest when this property must be included in the model to accurately describe the force generation.

It is necessary to include discrete supports in rail modeling to describe the response at low frequencies, determined by the sleeper-passing frequency f_s , and around the pinned–pinned frequency f_{pp} , usually around 1 kHz—in particular if the rail is very smooth or has a corrugation with a wavelength corresponding to the pinned–pinned frequency. If the rail has a corrugation it may also be necessary to include the nonlinear contact spring, since loss of contact occurs for great corrugation amplitudes (e.g., if the corrugation amplitude r_0 is greater than $15 \mu\text{m}$ when the preload P is 65 kN, for the parameters used in this paper). Nonlinearity causes force generation over a broad frequency range. It may for instance be expected that high-frequency contributions excite wheel resonances, resulting in high noise radiation levels, that for accurate prediction require wheel/rail nonlinear effects and parametric excitation to be included.

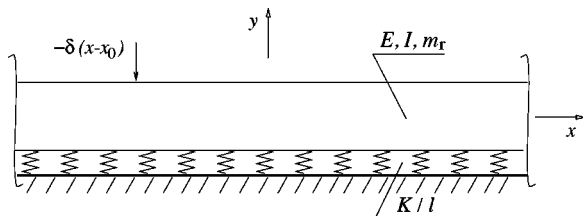


FIG. 15. Continuously supported rail, excited by a unit point force.

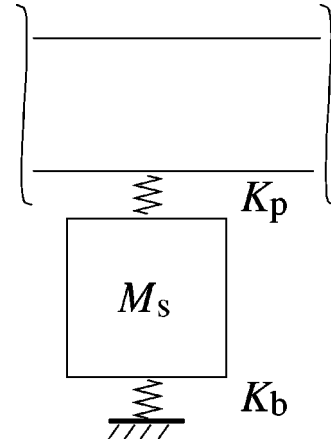


FIG. 16. Rail support: pad stiffness K_p , sleeper mass M_s , and ballast, stiffness K_b .

APPENDIX A: GREEN'S FUNCTION FOR A CONTINUOUSLY SUPPORTED RAIL

A unit point force $\delta(x-x_0)$ excites an infinite beam (Fig. 14), with mass per unit length m_r , and bending stiffness $B = E(1-i\eta_r)I$, where Young's modulus is E , moment of area inertia I , and η_r the loss factor. The equation of motion in the frequency domain is

$$B \left[\frac{d^4}{dx^4} - \frac{m_r \omega^2}{B} \right] G(x|x_0) = \delta(x-x_0), \quad (\text{A1})$$

with the wave number

$$k = \sqrt[4]{\frac{m_r \omega^2}{B}}.$$

A Fourier transform in the x direction, defined by

$$Y(x) = \frac{1}{2\pi} \int_{-\infty}^{\infty} \hat{Y}(\kappa) e^{i\kappa x} d\kappa,$$

$$\hat{Y}(\kappa) = \int_{-\infty}^{\infty} Y(x) e^{-i\kappa x} dx,$$

reduces Eq. (A1) to

$$\hat{G}(\kappa; x_0) (\kappa^4 - k^4) = \frac{1}{B} e^{-i\kappa x_0}.$$

An inverse transform,

$$G(x|x_0) = \frac{1}{B} \frac{1}{2\pi} \int_{-\infty}^{\infty} \frac{e^{i\kappa(x-x_0)}}{\kappa^4 - k^4} d\kappa,$$

yields Green's function

$$G(x|x_0) = \frac{1}{4Bk^3} (ie^{ik|x-x_0|} - e^{-k|x-x_0|}). \quad (\text{A2})$$

Now, the rail is continuously supported (Fig. 15). Pad stiffness K_p (loss factor η_p), (half) sleeper mass M_s , and ballast stiffness K_b (loss factor η_b)—evenly spread out along the track—comprise the rail foundation. For discrete supports (Fig. 16), the dynamic stiffness at each support point would be

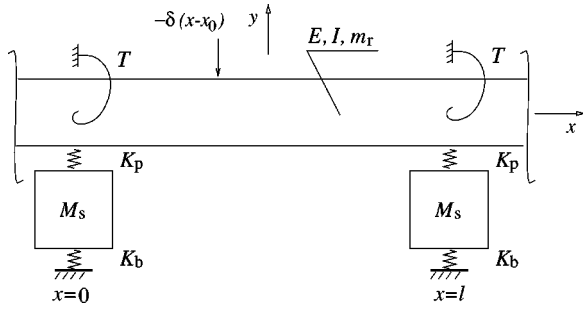


FIG. 17. Discretely supported rail, excited by a unit point force.

$$K = \frac{K_b(1 - i\eta_b) - M_s\omega^2}{1 + \frac{K_b(1 - i\eta_b) - M_s\omega^2}{K_p(1 - i\eta_p)}}$$

Here, however, when “smeared out” under the rail, the stiffness per unit length is K/l , where l is the nominal sleeper distance for a corresponding sleeper-supported rail. The equation of motion defining Green’s function (A1) changes to

$$B \left[\frac{d^4}{dx^4} - \frac{m_r\omega^2}{B} + \frac{K/l}{B} \right] G(x|x_0) = \delta(x - x_0),$$

so the wave number becomes

$$k = \sqrt[4]{\frac{m_r\omega^2 - K/l}{B}}.$$

Otherwise, Green’s function (A2) remains unchanged. The point input receptance for the continuously supported rail [$\alpha_r(\omega) = G(x_0|x_0)$],

$$\alpha_r(\omega) = \frac{1}{4Bk^3}(i - 1).$$

APPENDIX B: GREEN’S FUNCTION FOR A PERIODICALLY SUPPORTED RAIL

References 11 and 12 in detail derive Green’s function for a periodically supported beam, where the support reaction forces are restrained in the vertical. This section (also found in Ref. 15, repeated here for completeness) roughly outlines the derivation adding a rotational degree of freedom to the support reaction (Fig. 17). By including the rotational springs, the solution remains the same, apart from some new terms in the dispersion relation.

1. Support forces

A translational spring at position x by definition reacts with the vertical force $-KY(x)$ on the beam, where $Y(x)$ is the vertical beam displacement at x . The dynamic support stiffness, K , is a complex function, including friction and inertia. Similarly, the complex rotational spring stiffness T reacts on the beam with the moment $M(x) = -TY'(x)$, where the prime denotes a derivative in the x direction, corresponding to the vertical force $M'(x) = -TY''(x)$.

2. Free vibration

The equation of motion, in the frequency domain, for the periodically supported beam is

$$\frac{d^4 Y(x)}{dx^4} - k^4 Y(x) + \left[\frac{K}{B} Y(x) + \frac{T}{B} \frac{d^2 Y(x)}{dx^2} \right] \sum_{n=-\infty}^{\infty} \delta(x - nl) = 0, \quad (B1)$$

where

$$k = \sqrt[4]{\frac{m_r\omega^2}{B}}.$$

$B = EI$ is the bending stiffness, m_r the rail mass per length, l the period length, and n an integer. A Fourier transform in the x direction, defined by

$$Y(x) = \frac{1}{2\pi} \int_{-\infty}^{\infty} \hat{Y}(\kappa) e^{i\kappa x} d\kappa,$$

$$\hat{Y}(\kappa) = \int_{-\infty}^{\infty} Y(x) e^{-i\kappa x} dx,$$

reduces Eq. (B1) to

$$\kappa^4 \hat{Y}(\kappa) - k^4 \hat{Y}(\kappa) + \frac{K}{B} \sum_{n=-\infty}^{\infty} Y(nl) e^{-i\kappa nl} + \frac{T}{B} \sum_{n=-\infty}^{\infty} Y''(nl) e^{-i\kappa nl} = 0,$$

where the prime denotes derivative in the x direction. Using Floquet’s theorem

$$Y(x + nl) = Y(x) e^{ng}, \quad (B2)$$

it is possible to reach

$$\hat{Y}(\kappa) = \frac{-\frac{K}{B} Y(0) \sum_{n=-\infty}^{\infty} e^{ng} e^{-i\kappa nl}}{\kappa^4 - k^4} + \frac{-\frac{T}{B} Y''(0) \sum_{n=-\infty}^{\infty} e^{ng} e^{-i\kappa nl}}{\kappa^4 - k^4}.$$

After having evaluated the inverse Fourier integrals and infinite sums,^{11,12} the solution to this is

$$Y(x, g) = -[KY(0) + TY''(0)] Y_h(x, g), \quad (B3)$$

where the homogeneous solution

$$Y_h(x, g) = \frac{1}{4Bk^3} [\alpha_1(x, g) - \alpha_2(x, g)],$$

with the functions

$$\alpha_1(x, g) = \frac{\sin k(l-x) + e^g \sin kx}{\cos kl - \cosh g},$$

$$\alpha_2(x, g) = \frac{\sinh k(l-x) + e^g \sinh kx}{\cosh kl - \cosh g}.$$

3. Dispersion relation

Putting $x=0$ into Eq. (B3), and its second derivative, yields

$$\begin{pmatrix} 1 + KY_h(0,g) & TY_h(0,g) \\ KY_h''(0,g) & 1 + TY_h''(0,g) \end{pmatrix} \begin{pmatrix} Y(0) \\ Y''(0) \end{pmatrix} = 0,$$

in matrix form. Evaluation of the determinant yields the dispersion relation,

$$\begin{aligned} & \cosh^2 g + \left[\frac{K}{4Bk^3} (\sinh kl - \sin kl) \right. \\ & \left. + \frac{T}{4Bk} (\sinh kl + \sin kl) - (\cosh kl + \cos kl) \right] \cosh g \\ & + \frac{K}{4Bk^3} (\cosh kl \sin kl - \cos kl \sinh kl) \\ & - \frac{T}{4Bk} (\cosh kl \sin kl + \cos kl \sinh kl) \\ & + \cosh kl \cos kl = 0. \end{aligned}$$

There are four solutions, two for right, and two for left traveling waves, with the propagation coefficients, $g_{1,2}^r$, chosen so that all solutions decay away from the excitation point, according to Floquet (B2).

4. Forced vibration

Consider a unit force which excites the beam at $x=x_0$ in the interval $[0, l]$,

$$\begin{aligned} & B \left[\frac{d^4}{dx^4} - k^4 + \sum_{n=-\infty}^{\infty} \delta(x-nl) \left(\frac{K}{B} + \frac{T}{B} \frac{d^2}{dx^2} \right) \right] G(x|x_0) \\ & = \delta(x-x_0), \end{aligned}$$

where $G(x|x_0)$ is Green's function. A linear combination of homogeneous solutions, Eq. (B3), which may be rewritten,

$$Y(x,g) = c[\alpha_1(x,g) - \alpha_2(x,g)],$$

where c is a frequency dependent coefficient, constitute Green's function:

$$G(x|x_0) = \begin{cases} c_1^r Y_1^r(x, g_1^r) + c_2^r Y_2^r(x, g_2^r) & \text{for } x \geq x_0, \\ c_1^l Y_1^l(x, g_1^l) + c_2^l Y_2^l(x, g_2^l) & \text{for } x \leq x_0. \end{cases} \quad (\text{B4})$$

Matching derivatives at the force point finally determines Green's function. The point input receptance for the periodically supported rail $\alpha_p(x, \omega) = G(x_0|x_0)$.

5. Matching of excitation point boundary conditions

Equation (B4) determines Green's function; matching derivatives at the force point $x=x_0$ leads to

$$\begin{pmatrix} a_{11} & a_{12} & a_{13} & a_{14} \\ a_{21} & a_{22} & a_{23} & a_{24} \\ a_{31} & a_{32} & a_{33} & a_{34} \\ a_{41} & a_{42} & a_{43} & a_{44} \end{pmatrix} \begin{pmatrix} c_1^r \\ c_2^r \\ c_1^l \\ c_2^l \end{pmatrix} = \frac{1}{Bk^3} \begin{pmatrix} 0 \\ 0 \\ 0 \\ 1 \end{pmatrix}.$$

The matrix coefficients a_{ij} consist of the functions

$$\begin{aligned} \alpha_1(x,g) &= \frac{\sin k(l-x) + e^g \sin kx}{\cos kl - \cosh g}, \\ \alpha_2(x,g) &= \frac{\sinh k(l-x) + e^g \sinh kx}{\cosh kl - \cosh g}, \\ \beta_1(x,g) &= \frac{e^g \cos kx - \cos k(l-x)}{\cos kl - \cosh g}, \\ \beta_2(x,g) &= \frac{e^g \cosh kx - \cosh k(l-x)}{\cosh kl - \cosh g}, \end{aligned}$$

evaluated at the excitation point $x=x_0$ as follows:

$$\begin{aligned} a_{11} &= \alpha_1(x_0, g_1^r) - \alpha_2(x_0, g_1^r), \\ a_{31} &= -\alpha_1(x_0, g_1^r) - \alpha_2(x_0, g_1^r), \\ a_{12} &= \alpha_1(x_0, g_2^r) - \alpha_2(x_0, g_2^r), \\ a_{32} &= -\alpha_1(x_0, g_2^r) - \alpha_2(x_0, g_2^r), \\ a_{13} &= -\alpha_1(x_0, g_1^l) + \alpha_2(x_0, g_1^l), \\ a_{33} &= \alpha_1(x_0, g_1^l) + \alpha_2(x_0, g_1^l), \\ a_{14} &= -\alpha_1(x_0, g_2^l) + \alpha_2(x_0, g_2^l), \\ a_{34} &= \alpha_1(x_0, g_2^l) + \alpha_2(x_0, g_2^l), \\ a_{21} &= \beta_1(x_0, g_1^r) - \beta_2(x_0, g_1^r), \\ a_{41} &= -\beta_1(x_0, g_1^r) - \beta_2(x_0, g_1^r), \\ a_{22} &= \beta_1(x_0, g_2^r) - \beta_2(x_0, g_2^r), \\ a_{42} &= -\beta_1(x_0, g_2^r) - \beta_2(x_0, g_2^r), \\ a_{23} &= -\beta_1(x_0, g_1^l) + \beta_2(x_0, g_1^l), \\ a_{43} &= \beta_1(x_0, g_1^l) + \beta_2(x_0, g_1^l), \\ a_{24} &= -\beta_1(x_0, g_2^l) + \beta_2(x_0, g_2^l), \\ a_{44} &= \beta_1(x_0, g_2^l) + \beta_2(x_0, g_2^l). \end{aligned}$$

¹P. J. Remington, "Wheel/rail rolling noise. I. Theoretical analysis," *J. Acoust. Soc. Am.* **81**, 1805–1823 (1987).

²P. J. Remington, "Wheel/rail rolling noise. II. Validation of the theory," *J. Acoust. Soc. Am.* **81**, 1824–1832 (1987).

³D. J. Thompson, B. Hemsworth, and N. Vincent, "Experimental validation of the TWINS prediction program for rolling noise. 1. Description of the model and method," *J. Sound Vib.* **193**, 123–135 (1996).

⁴D. J. Thompson, P. Fodiman, and H. Mahé, "Experimental validation of the TWINS prediction program for rolling noise. 2. Results," *J. Sound Vib.* **193**, 137–147 (1996).

⁵T. X. Wu and D. J. Thompson, "Theoretical investigation of wheel/rail non-linear interaction due to roughness excitation," *Veh. Syst. Dyn.* **34**, 261–282 (2000).

⁶K. Hempelmann, "Short pitch corrugation on railway rails: A linear model for prediction," Ph.D. thesis, Technische Universität Berlin, 1994, Fortschritt-Berichte VDI Reihe 12 Nr. 231.

⁷H. Ilias, "Nichtlineare Wechselwirkungen von Radsatz und Gleis beim Überrollen von Profilstörungen (Nonlinear wheel-rail interaction of a wheelset rolling on a track with profile deviations)," Ph.D. thesis, Technische Universität Berlin, 1996, Fortschritt-Berichte VDI Reihe 12 Nr. 297.

⁸M. Heckl, "Proposal for a railway simulation program," in *A Workshop on*

- Rolling Noise Generation* (Institute für Technische Akustik, Technische Universität Berlin, October 1989), pp. 128–148.
- ⁹B. Ripke, “Hochfrequente Gleismodellierung und Simulation der Fahrzeug-Gleis-Dynamik unter Verwendung einer nichtlinearen Kontaktmechanik (High-frequency track modeling and simulation of vehicle-track dynamics using a nonlinear contact mechanics),” Ph.D. thesis, Technische Universität Berlin, 1994, Fortschritt-Berichte VDI Reihe 12 Nr. 249.
- ¹⁰A. Nordborg, “Vertical rail vibrations: parametric excitation,” *Acust. Acta Acust.* **84**(2), 289–300 (1998).
- ¹¹A. Nordborg, “Vertical rail vibrations: Noise and structure-borne sound generation,” Ph.D. thesis, Kungl Tekniska Högskolan, Stockholm, 1995.
- ¹²A. Nordborg, “Vertical rail vibrations: Pointforce excitation,” *Acust. Acta Acust.* **84**, 280–288 (1998).
- ¹³A. Nordborg, “Parametric excitations of a wheel rolling on a corrugated, sleeper-supported track,” in *INTER-NOISE 97-Budapest*, Vol. II, pp. 119–122, August 1997.
- ¹⁴J.-F. Hamet, “Railway Noise: Use of the Timoshenko model in rail vibration studies,” *Acust. Acta Acust.* **85**, 54–62 (1999).
- ¹⁵A. Nordborg, “Rail/wheel parametric excitation: Laboratory and field measurements,” *Acust. Acta Acust.* **85**, 355–365 (1999).

Acoustic and dynamic mechanical properties of a polyurethane rubber

Peter H. Mott^{a)} and C. Michael Roland
Chemistry Division, Naval Research Laboratory, Washington, DC 20375-5320

Robert D. Corsaro
Acoustics Division, Naval Research Laboratory, Washington, DC 20375-5320

(Received 13 June 2001; accepted for publication 17 January 2002)

Acoustical and dynamic mechanical measurements were carried out on a commercial polyurethane rubber, DeSoto PR1547. The sound speed and attenuation were measured over the range from 12.5 to 75 kHz and 3.9 to 33.6 °C. Shear modulus was measured from 10^{-4} to 2 Hz and -36 to 34 °C. The peak heights of the shear loss tangent varied with temperature, demonstrating thermorheological complexity. At higher temperatures, time-temperature superpositioning could be applied, with the shift factors following the Williams-Landel-Ferry equation. From the combined acoustical and mechanical measurements, values for the dynamic bulk modulus were determined. Moreover, superposition of the bulk modulus data was achieved using the shift factors determined from the dynamic mechanical shear measurements. Finally, this work illustrates the capability and the working rules of acoustical measurements in a small tank. [DOI: 10.1121/1.1459465]

PACS numbers: 43.58.Dj, 43.35.Mr [SLE]

I. INTRODUCTION

To understand the relaxation processes of polymers above the glass transition temperature T_g , it is necessary to determine how molecular motions, kinematically coupled to produce both bulk (volume) and shear relaxations, are governed by the structure of the chain molecules. Bulk viscoelastic behavior is fundamentally different from the shear properties. Bulk relaxations reflect very local motions of the polymer molecules, and are thus insensitive to long-range structural features, such as entanglements and crosslinks.¹ On the other hand, at low frequency and/or high temperature, the terminal dynamics associated with shear flow involve much longer lengths of the chain, with entanglements having a pronounced effect.

Direct measurement of the dynamic bulk modulus at frequencies above 1 kHz is difficult. Early measurements were made by Philippoff and Brodnyan² using a piston-cylinder arrangement with mercury as the confining fluid. This determination was limited to frequencies below 5 Hz. Marvin and collaborators^{3,4} measured the dynamic bulk modulus over a wider frequency range for a soft elastomer, constructing master curves encompassing a broad range of reduced frequency. Dubbelday and co-workers^{5,6} employed this data reduction technique to determine bulk modulus shift factors for four different elastomers; unfortunately, PR1541 polyurethane was not evaluated. More recently, Holownia and James⁷ developed a differential pressure technique and Willis *et al.*^{8,9} employed interferometry to obtain dynamic bulk modulus data. All these direct methods are limited to relatively low frequencies, usually less than 5 kHz.

Because of the practical difficulties with the above techniques, indirect measurements of the bulk modulus are sometimes employed. For example, Litovitz and co-workers¹⁰ determined the dynamic bulk compliance by subtracting the

shear from the longitudinal complex compliance, both measured ultrasonically, for low molecular weight glass-forming liquids. DiMeglio and Wang¹¹ have introduced a variational algorithm to find dynamic elastic moduli from acoustical measurements of butyl rubbers. Another interesting technique, introduced by Piquette,¹² used acoustic scattering to obtain the bulk and shear moduli of rubbery spheres.

In this article we report the sound speed c and attenuation coefficient α for a low-loss polyurethane elastomer. The measurements, performed in a small laboratory tank, were carried out over the frequency range from 12.5 to 75 kHz at temperatures from 3.9 to 33.6 °C. We also obtained dynamic mechanical shear data on the same material, at lower frequencies over a broader temperature range. When combined, these data provide an estimate of the dynamic bulk modulus.

Also described herein are some working rules for using large-area transducers in small tanks. These were developed two decades ago, at a time when facilities were under development to evaluate the acoustic properties of new materials for underwater applications. These working rules were derived from practical experience and have not been previously documented.

II. EXPERIMENT

A. Sample preparation and shear measurements

The proper sample thickness is governed by many factors. For acoustical measurements, increasing the sample thickness provides higher measurement resolution. However, in very thick samples, internal reflections and waveguide behavior can decrease the accuracy and measurement window available (discussed shortly). Other practical considerations include material cost, difficulty of fabrication, and the increased likelihood that thick samples will include defects.

For the present study we selected a thickness of 52 mm. The two-part amber PR1547 polyurethane (PRC-DeSoto International) was mixed according to the manufacturer's pro-

^{a)}Electronic mail: phm@xbl.nrl.navy.mil

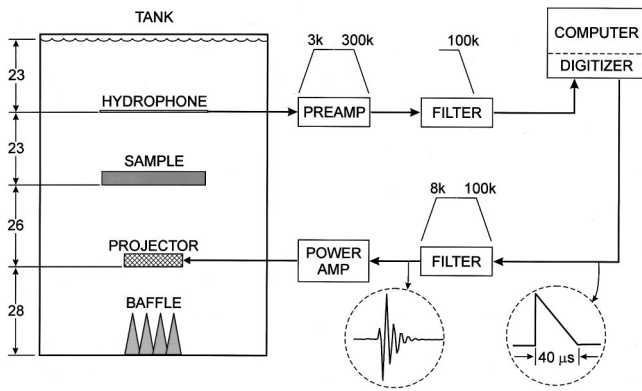


FIG. 1. Schematic of the sound speed experimental apparatus. The vertical placements within the tank—baffle, projector, sample, hydrophone, and water surface—are given in cm. The sample was $35 \times 35 \times 5.2 \text{ cm}^3$. See text for further discussion.

cedure. To reduce the likelihood of entrapping air bubbles, the specimen was cast as a four-layer composite, with each layer added in turn, degassed, and cured overnight at 80°C before adding the next layer. Samples prepared for dynamic mechanical measurements were cut from a 4.5-mm-thick sheet, cured similarly. The Shore A durometer of the material was 80, consistent with the manufacturer's specifications.

Characterization of the isothermal shear dynamic properties of the material was performed using a Bohlin VOR rheometer with parallel plate geometry. A cylindrical sample, 12 mm diameter \times 4.5 mm height, was glued to the plates with cyanoacrylate adhesive. The applied torque was continually adjusted over the frequency scan to maintain a 28 kPa shear stress. The maximum torsional strain did not exceed 0.6%, which is well within the limits of linearity. To prevent debonding during the measurements, the sample was subjected to a small compressive load (5.2 kPa). Typically, the shear moduli are repeatable to within 10%.

B. Sound speed apparatus

A schematic of the sound speed apparatus and measurement system is given in Fig. 1. The tank was cylindrical (0.724 m diameter \times 1.01 m tall), and its acoustical characteristics and use for reflectivity measurements have been described previously.¹³ The temperature of the ion-exchanged water was controlled by a Neslab refrigerated recirculator, which was allowed to equilibrate overnight.

The projector and hydrophone were both directive large area devices. The sound projector was the F33 standard¹⁴ (from Underwater Sound Reference Division, Naval Undersea Warfare Center). The hydrophone was $30 \times 30 \text{ cm}^2$, constructed from poly(vinylidene fluoride) (PVDF) sheets (Kynar film, from Measurement Specialties, Inc.) with silver ink electrodes. This hydrophone was fabricated from three layers of PVDF,¹⁵ but is operationally equivalent to a four-layer design arranged as a dual differential bimorph. Each bimorph is of a conventional type used to suppress the signal generated by bending. Pairing these bimorphs places electrical ground planes on the exterior surfaces, thus providing electrical shielding. As usual for PVDF hydrophones,¹⁶ a thin aluminum shim layer is included to suppress lateral modes.

Large-area thin-film PVDF transducers have been in routine use in various laboratories for many years, both as projectors and hydrophones. Because of their inherent area averaging response and their favorable acoustic transparency, they have found use in material property and structural acoustical studies. Two of the largest such arrays presently in use are the $71 \times 71 \text{ cm}^2$ array of Morse,¹⁷ and the $285 \times 76 \text{ cm}^2$ array at NRL. Such hydrophones typically operate over a very broad frequency bandwidth, often extending to 500 kHz. Their frequency response is reasonably flat over most of their operating range, but calibration is required to identify select frequency regions which may contain geometry dependent features. They are typically stable and relatively temperature and pressure independent. Their chief drawback is their rather low sensitivity, typically near $-215 \text{ dB re: } 1 \mu\text{Pa}$. This restricts their use to relatively high signal levels.

C. Sample placement

The locations of the projector, hydrophone, and sample were chosen to provide a maximum echo-free time window within the height constraint of the tank. The sound projector is positioned about one-quarter of the way from the tank bottom; the hydrophone was similarly located about one-quarter of the way from the top water surface (see Fig. 1). The sample, placed at the midpoint, could be removed or inserted without disturbing the position of the hydrophone.

For the above geometry, the first arriving interfering echoes have paths corresponding to projector-bottom-projector, sample-projector-sample, hydrophone-sample-hydrophone, and hydrophone-surface-hydrophone. All of these have path lengths nominally 42 cm greater than that of the direct signal (including the sample thickness). Hence these interfering echoes arrive approximately $250 \mu\text{s}$ after the direct signal.

If the measurement time window is small, it can be the determining factor governing the lowest frequency at which reliable data can be obtained. This low-frequency limit is set by the nominal working requirement that (without special processing) the measurement time window be sufficient to include at least 1.5 waves plus the time required for one round-trip within the sample. In practice, due to ring-down transients of the projector, it is desirable to have a measurement time window that is long enough to include the observable end of the signal of interest. For the impulse-type source signals used here, this requirement becomes nominally the duration of three waves at the lowest frequency of interest.

For the above case, the available $250\text{-}\mu\text{s}$ time window would therefore allow measurements to frequencies as low as 12 kHz using the three-wave guidance.

D. Sample size and edge diffraction

There is a considerable body of theoretical literature related to the influence of a lateral finite sample size on reflectivity and insertion loss measurements.^{18,19} A summary of

established practice is contained in a recent report by Piquette.²⁰ These treatments typically concentrate on the interference signal arriving from the edge-diffracted wave, and use idealized cases such as point or plane-wave source and receiver. While applicable in the standard test arrangements used in underwater evaluation facilities, they provide only coarse guidance in cases of closely spaced finite-size transducer elements.

Simple point transducers cannot be used at low frequencies in the current (relatively small) facility. We briefly consider this case of point transducers as a starting point due to their common use in small tanks at high frequencies, and occasionally their improper use in such tanks at low frequencies. The lowest frequency that can be used with a test article in transmission is typically limited by the arrival of an edge-diffracted wave. For the case of point source and point receiver, the arrival time of this wave can be calculated from the geometry. For the separation distances and sample size used here, the earliest edge-diffracted wave would arrive 75 μs after the direct wave. (Due to the square sample geometry, additional edge-diffracted components would arrive with progressively lower amplitude for up to 140 μs after the direct wave.) Using the above three-wave rule for the available time window gives a lowest usable frequency of only 40 kHz. Even extending to the 1.5-wave rule allows measurements only as low as 20 kHz.

Since the time window of the measurement will therefore include edge-diffracted waves, it becomes important to ensure that the magnitude of their contribution is negligible. This is encouraged by using large-area transducers, which suppress off-axis contributions due to their directivity. Additionally, since the magnitude of a diffracted wave is related to the impedance mismatch, it is helpful to use test samples having a specific acoustic impedance not much different from that of water.

The improvement attainable with large-area transducers is predictable, but somewhat complicated. It involves initially calculating the signal received at the surface of the hydrophone. This double integral can be performed in a more computationally efficient manner by approximating the actuator and sensor areas as disks, such that one can use the variable transform approach of Archer-Hall and Gree.²¹ The approach finds that the pressure at any field point from a disk radiator, P_1 , can then be expressed by the single integral

$$P_1 = P_\sigma \left\{ \begin{array}{l} \left[\begin{array}{l} 0, \quad b > a \\ \frac{1}{2}, \quad b = a \\ 1, \quad b < a \end{array} \right] e^{-ikz} \\ + \frac{1}{\pi} \int_0^\pi e^{-iks} \left(\frac{ab \cos \theta - a^2}{a^2 + b^2 - 2ab \cos \theta} \right) d\theta \end{array} \right\}, \quad (1)$$

where P_σ is the pressure at the surface, a is the radius of the projector, b and z are distances between the field point and the disk radiator along the disk radial and normal directions, respectively, k is the wave number, and θ is the azimuth angle. The quantity s is defined as

$$s \equiv \sqrt{a^2 + b^2 + z^2 - 2ab \cos \theta}. \quad (2)$$

The pressure sensor output is then found by integrating this field over the area of the sensor,

$$\bar{P} = \frac{2}{a^2} \int_0^a b P_1 db. \quad (3)$$

For transmission estimates, the process is then repeated using the appropriate sample aperture, as developed by N. Yen.²² (For reflectivity estimates, the approach is similar but an image method is used.)

The above procedure is too complicated for routine laboratory use. Instead some simple “rules-of-thumb” have been developed by experimentalists when collecting data with such finite-size transducers. These were arrived at from direct observations of laboratory data, on a wide range of materials. Such tests were conducted in various tank facilities, including the facilities located at the Naval Research Laboratory (Washington, DC), the Underwater Sound Reference Division (Orlando, FL), and the Naval Surface Warfare Center (Crane, IN).

These working rules are intended only as guidance in initial selection of sample size, and certainly do not guarantee valid data over the given frequency range. They are as follows, where the size referred to is the smallest (lateral) width, and λ is the wavelength of sound in water. For insertion loss measurements on flat samples at normal sound incidence, typically the sample should be at least 4λ in width. If the impedance of the sample is not too different from that of water and the loss is not very high, then the amplitude of the edge-diffracted wave will be small relative to the transmitted wave. In combination with directional hydrophones, reliable sound speed data can then be obtained for sample sizes as small as 3λ .

Based on the above, the current $35 \times 35 \text{ cm}^2$ sample size and directive transducers should permit sound speed data to frequencies nominally as low as 12.7 kHz. These recommendations of minimum sample size are provided as rough guides, and only apply to the usual test arrangements, and data collection and analysis procedures. They do not apply to more computationally extensive techniques. They are supported by the observation that data accuracy on known samples typically appears noticeably degraded as these limits are exceeded.

E. Data sampling

The laboratory data acquisition system available was a Powerlab (ADInstruments, Inc.) used in connection with a desktop computer (PowerMac G3). This system has a maximum sampling rate of only 200 kHz, and this rate is available only in the single-channel mode. This permits sampling at 2.5 points per cycle at 80 kHz, the highest signal frequency of interest in this study. While the sampling theorem indicates that this rate is entirely satisfactory, some care is required when sampling this close to the Nyquist limit.

The source signal is a 40 μs sawtooth pulse, generated by the digitizer. The rapid rise time of this signal provided a reasonably uniform excitation over the frequency band of interest; the slow return ramp reduced turn-off transients.

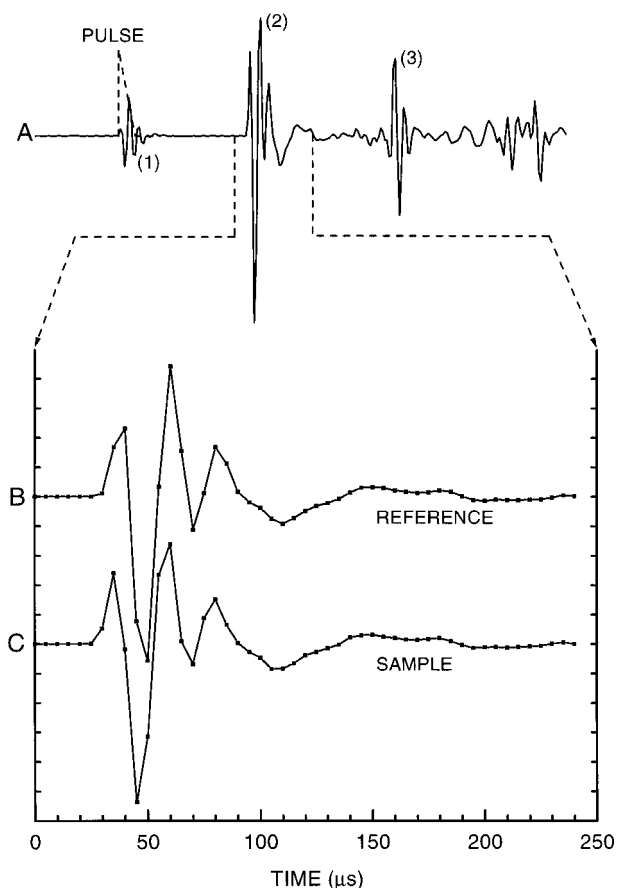


FIG. 2. Time records for a representative sound speed measurement. Trace A is the complete record, with the first pulse (1) coincident with saw-tooth excitation pulse (indicated by the dashed line). The next pulse (2) is the received direct signal, which is shown on an expanded scale as traces B (with sample in place) and C (with sample removed). The following pulse (3) is the reflection from the upper water surface.

This pulse then passed through an 8–100-kHz band-pass filter, which removed out-of-band signals, including particularly low-frequency off-sets. This filtered signal was amplified and applied to the projector. The hydrophone output was directed through a differential preamplifier and a 12-dB/oct 100-kHz low-pass filter.

Each signal is averaged over 128 pulses by the acquisition system. Low-pass filtering also occurred in other system elements (preamplifier, projector, etc.) and was sufficient to prevent aliasing at the sample rate used. Since the source signal is synchronized to the digitizing or sampling rate, an additional timing reference channel is not needed.

F. Sound speed data analysis

A series of representative time records for a single measurement is shown in Fig. 2. Trace A is the complete record with the sample in place. The dashed line represents the 40- μ s sawtooth excitation pulse. The first received pulse, coincident with the excitation, is electrically induced. The second pulse is the sound transmitted through the sample. The third pulse is the reflection from the upper surface of the water (identified by disturbing the surface), and subsequent pulses are reflections from other surfaces. Traces B and C compare the second pulse, with the sample and without (la-

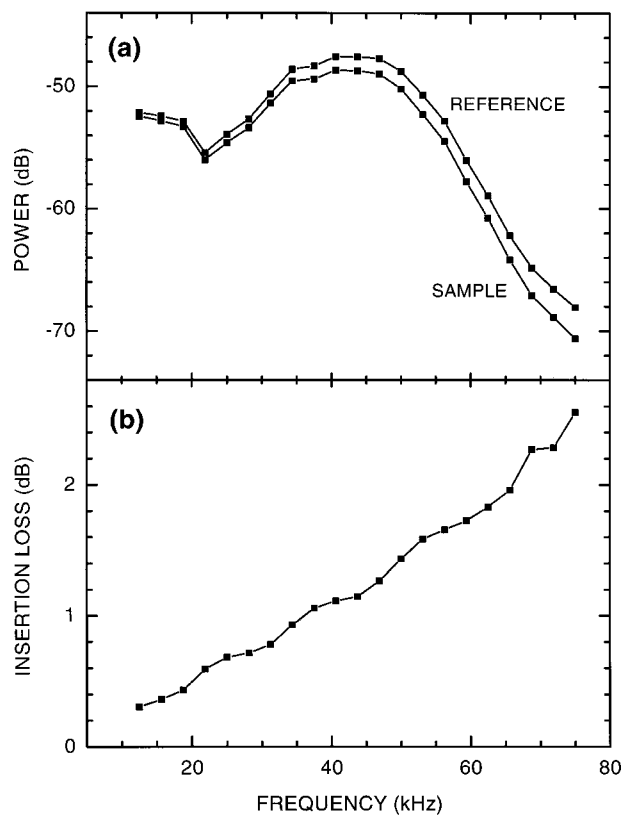


FIG. 3. (a) Fourier transform (power spectrum) of traces B and C of Fig. 2. (b) Insertion loss, defined as the difference between the two curves above.

beled “reference”); the difference between the two signals is subtle, but accurately resolvable by the instrumentation used.

The Fourier transform of traces B and C are shown in Fig. 3(a). The time window of the transform was made as wide as possible, without including extraneous reflections. The frequency response is governed by the signal, the characteristics of the transducers, and the filters.

The difference in the magnitudes of these spectra in decibels is the insertion loss [Fig. 3(b)], or when expressed as a simple ratio is the transmissibility. This was used to evaluate the attenuation coefficient α . In the usual procedure for evaluating α from transmissibility, the reflectivity is also measured, and the attenuation coefficient is then obtained only after correcting the transmissibility for the loss due to reflections. In this case, however, the measured sound speed, density, and attenuation indicate a value for the specific acoustic impedance that is reasonably close to that of water. The resulting reflection loss is then a negligible component in the calculation.

The speed of sound in this sample is calculated from the phase difference between these two spectra using

$$c = \frac{1}{1/c_w + \phi/360ft}, \quad (4)$$

where ϕ is the phase difference, in degrees, between the reference and the sample signals, f is the frequency in Hz, and t is the sample thickness. The sound speed in water c_w is given by²³

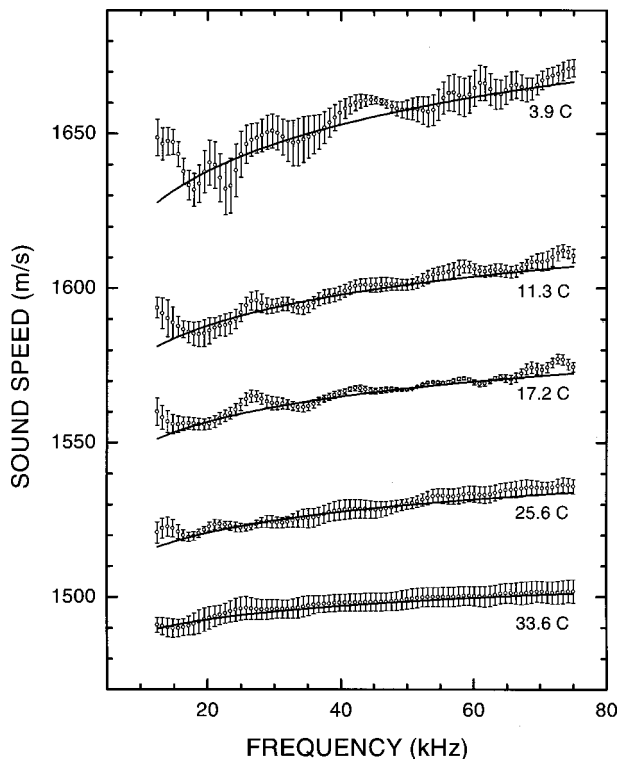


FIG. 4. Sound speed (average of four measurements) determined from phase difference [Eq. (4)]; the error bars represent one standard deviation. The solid lines are the fit from the attenuation data (Fig. 5) and the Kramers–Kronig relation [Eq. (6)].

$$c_w = 1402.7 + 4.88T - 0.0482T^2 + 1.35 \times 10^{-4}T^3 \text{ (in m/s)}, \quad (5)$$

where T is the temperature in Celsius.

III. RESULTS AND DISCUSSION

A. Sound speed and attenuation

Figure 4 shows the measured sound speed. The data points represent the average of the individual measurements (four per temperature), and the error bars are one standard deviation. (The smooth curves are not fits to the data, as described below.) As the temperature increases, both the magnitude and the frequency dependence of c are observed to decrease.

Sound attenuation values are shown in Fig. 5, where again the points are averages, and the error bars represent one standard deviation. The lines are linear least-squares fits to the data, constrained to pass through the origin. As the temperature increases, the slope of the frequency-dependence decreases. Table I summarizes these results; the uncertainty represents one standard deviation.

The internal consistency of these results can be verified from the Kramers–Kronig relations,^{24,25} which, for small dispersion, reduces to the following expression for the attenuation coefficient:²⁶

$$\alpha(f) = \frac{\pi^2 f}{c^2} \frac{dc}{df}. \quad (6)$$

Taking the ratio α/f to be a constant (namely A , the slope of straight lines of Fig. 5), Eq. (6) is integrated to yield

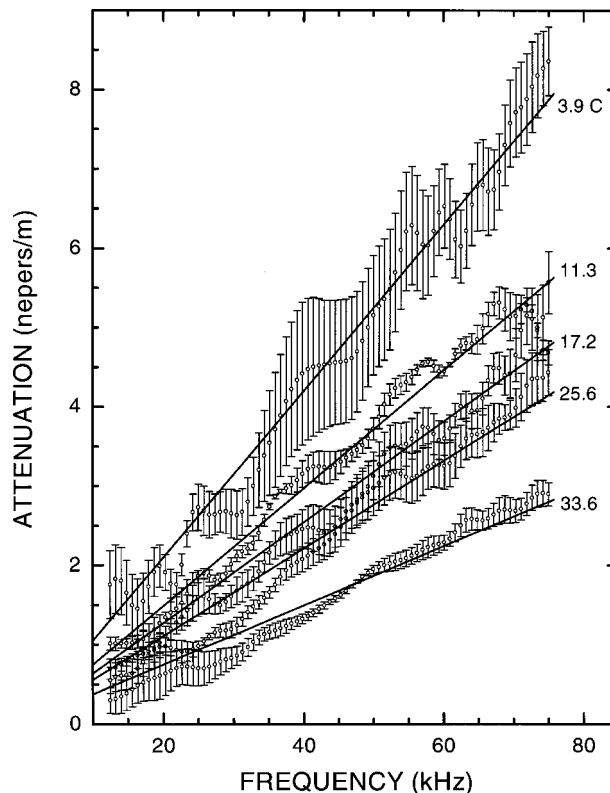


FIG. 5. Sound attenuation at the indicated temperatures. Circles represent the average of four trials, and the error bars indicate one standard deviation. The solid lines are linear least square fits constrained to pass through the origin.

$$c(f) = \frac{c_0}{1 - (Ac_0/\pi^2)\ln(f/f_0)}, \quad (7)$$

where c_0 is the sound speed at an arbitrary reference frequency, $f_0 = 43$ kHz. The values of c_0 , along with the uncertainty, were derived from a straight line fit through the data displayed in Fig. 4, and are listed in Table I. The resulting Kramers–Kronig curves are drawn in Fig. 4, and the agreement with the data is seen to be excellent. This agreement provides support for the sample size “rules-of-thumb” discussed above.

B. Shear modulus

The complex shear modulus, G^* , and loss tangent ($\tan \delta_G \equiv G''/G'$, the ratio of the loss to the storage moduli) were obtained over the temperature range of -36 °C to 34 °C, at frequencies from 10^{-4} to 2 Hz with the Bohlin VOR rheometer. The results are shown in Fig. 6.

TABLE I. Sound speed parameters.

Temperature (°C)	Attenuation slope ($\times 10^{-6}$ nepers/(m/s))	Sound speed ^a (m/s)
3.9	104.93 ± 0.68	1654.5 ± 1.61
11.3	74.30 ± 0.51	1598.9 ± 0.76
17.2	63.55 ± 0.52	1565.7 ± 0.61
25.6	55.27 ± 0.53	1528.3 ± 0.31
33.6	37.34 ± 0.35	1497.5 ± 0.42

^aFrom a linear fit to Fig. 4, at 43.0 kHz.

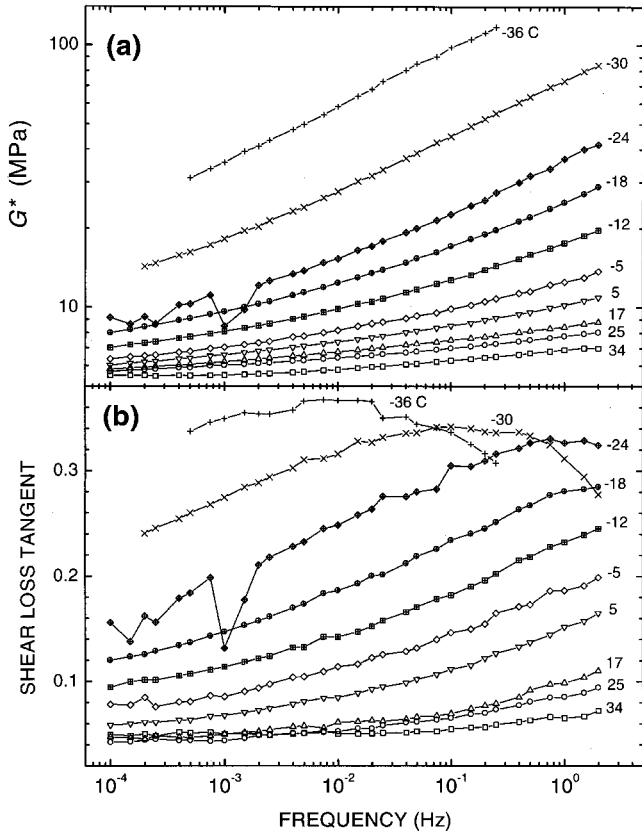


FIG. 6. The dynamic shear modulus (a) and tangent of the phase angle (b), at the indicated temperatures.

Temperature–frequency shift factors, a_T , were determined by superposition of the loss tangent data. These same shift factors were used, along with small vertical shifting, to construct the master curve for the dynamic modulus shown in Fig. 7.

Deviations from the time–temperature superposition principle are evident in the loss tangent data at higher frequencies. These deviations become evident in the softening (glass–rubber transition) zone of the viscoelastic spectrum, due to intrusion of the local segmental relaxation, which has a different temperature dependence than the chain modes probed at lower frequency. The result is a systematic increase in the height of the loss tangent as temperature decreases. Such thermorheological complexity has been seen previously in a variety of polymers, including 1,4-polyisoprene,²⁷ polystyrene,²⁸ poly(vinyl acetate),²⁹ polypropylene glycol,³⁰ poly(phenylmethyl siloxane),³¹ polybutadiene,³² polyisobutylene,³³ and atactic polypropylene.^{34,35} The breakdown of time–temperature superposition is a consequence of both local segmental motion and the polymeric chain modes contributing to the dynamics in this region of the spectrum.

For reduced frequencies below the transition zone (i.e., temperatures higher than the transition zone), the time–temperature superposition principle provides a good description of the data. In this region, the shift factors were fit to the Williams–Landel–Ferry (WLF) equation,³⁶

$$\log a_T = \frac{-C_1(T - T_0)}{C_2 + T - T_0}. \quad (8)$$

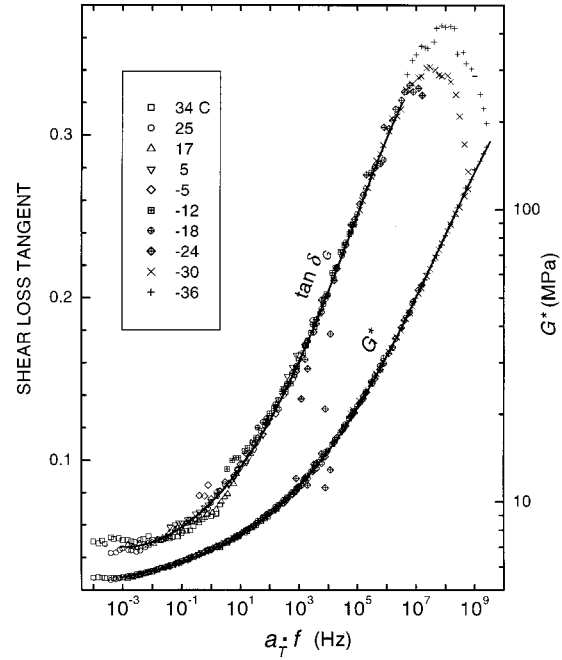


FIG. 7. Master curves of the complex shear modulus and loss tangent. The solid lines are fifth-order polynomial fits. The breakdown in time–temperature superposition is evident in the loss tangent at high frequencies.

The obtained parameters, C_1 and C_2 , the reference temperature T_0 , and previously reported WLF parameters for PR1547 polyurethane³⁷ (converted to the same reference temperature) are listed in Table II. Figure 8 displays $\log a_T$ as a function of temperature. The present shift factors agree with the earlier results at higher temperatures, but deviate below about 5 °C. This is not unexpected, since the previous measurements only extended down to –5 °C. As the comparison in Fig. 8 makes clear, extrapolation of shift factors to temperatures beyond the measured range can entail large error.

C. Bulk modulus

The frequency-dependent bulk modulus, B^* , can be found from the sound speed, attenuation, and dynamic shear modulus, using the relations³⁸

$$M^* \approx M' = \rho c^2, \quad (9)$$

$$\tan \delta_M = \frac{\alpha c}{\pi f}, \quad (10)$$

and

$$B^* = M^* - \frac{4}{3}G^*, \quad (11)$$

where ρ is the density, M^* is the complex longitudinal modulus, and $\tan \delta_M (=M''/M')$ is analogous to the shear loss tangent. The temperature-dependent density was deter-

TABLE II. Williams–Landel–Ferry (WLF) equation parameters.

	This study	Reference 37
C_1	7.391	4.2241
C_2 (C)	119.6	72.6
T_0 (C)	34	34

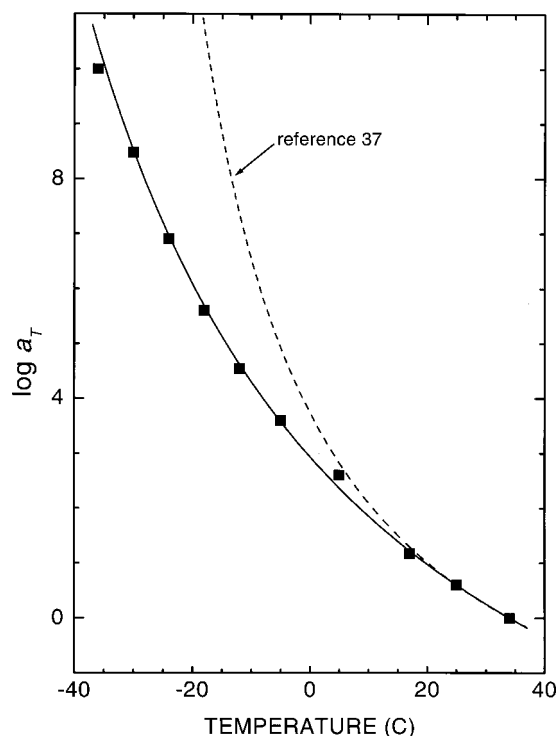


FIG. 8. Time-temperature shift factors ($\log a_T$), corresponding to the master curves in Fig. 7. Also included as the dashed line is the WLF equation fit to this same material reported by Capps (Ref. 37).

mined by combining the room temperature value (manufacturer specifications: 1050 kg/m^3) with the thermal expansion coefficient. The latter was found from the variation of the sample gap during the shear experiments, $1.28 \pm 0.05 \times 10^{-3} \text{ C}^{-1}$, over for the temperature range -36 to $34 \text{ }^\circ\text{C}$. The frequency-dependent values of M' were calculated from the sound speed data shown in Fig. 4, with $\tan \delta_M$ deduced from the attenuation measurements shown in Fig. 5. To determine the storage and loss components of the dynamic bulk modulus [Eq. (11)], the corresponding values of G were taken from polynomial fits to the shear master curves, as shown in Fig. 7. The calculated values of the bulk storage, B' , and loss, B'' , moduli are shown in Fig. 9. At the lowest temperature, $3.9 \text{ }^\circ\text{C}$, the data are less reliable due to the breakdown in time-temperature superposition noted in Fig. 7. The magnitudes of the shear moduli are approximately 1% of the bulk moduli, as expected for an incompressible material. However, the shear modulus has a stronger frequency dependence, giving rise to the slopes of the lines in Fig. 9.

As suggested by previous work,^{1,3,4} the horizontal shift factors for the dynamic shear modulus were used to generate master curves for $\tan \delta_B$ ($=B''/B'$) and the complex bulk modulus. These results are shown in Fig. 10. The vertical shifting used to superimpose B^* increased linearly from 0.875 to unity over the temperature interval. Again, due to the breakdown in time-temperature superpositioning, the data are less reliable at the higher reduced frequencies (corresponding to the lowest measurement temperature, $3.9 \text{ }^\circ\text{C}$).

In general, published data on bulk modulus shift factors are limited.³⁻⁶ The near equivalence of the shift factors for bulk and shear deformations suggests that similar molecular mechanisms govern both. On the other hand, thermorheo-

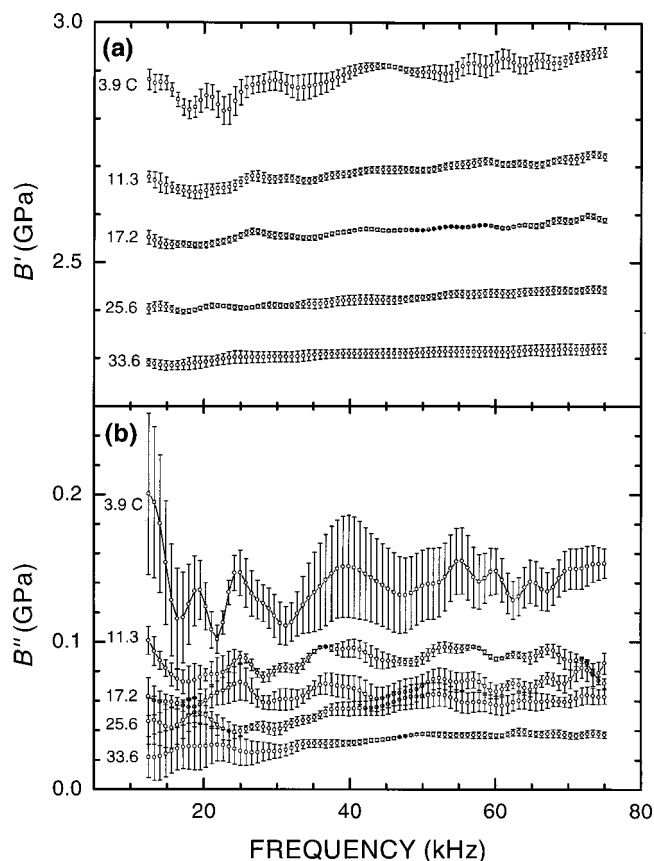


FIG. 9. Calculated bulk storage (a) and loss (b) moduli, at the indicated temperatures, found by combining the sound speed (Fig. 4), attenuation (Fig. 5), and the shear master curves (Fig. 7), using Eqs. (9)–(11). The points are the averages of four trials, and the error bars mark one standard deviation.

logical complexity, demonstrated by the varying $\tan \delta_G$ peak heights in Fig. 7, indicates that the local segmental motions and polymeric chain modes have a different temperature dependence. This implies that the chain modes, not the local segmental motions, underlie relaxation of the bulk modulus, at least over the range of experimental temperatures and frequencies probed herein. These differences in temperature dependence are not evident over a relatively narrow frequency range, such as in Fig. 10.

Comparisons between the time scales of relaxation for different processes have been carried out for a few polymers.³⁹⁻⁴³ Much of this work is focused on the volumetric effects of physical aging below T_g , where the material is not at its equilibrium density. Above T_g , Bero and Plazek³⁹ found that the time-temperature shift factors agree between volume and creep for both constant cooling rate and constant temperature jump experiments. Thus, the agreement of the dynamic bulk and shear moduli shift factors is in accord with related experimental results.

IV. CONCLUSIONS

Sound speed and attenuation were measured for a commercial polyurethane, DeSoto PR1547, over the range from 12.5 to 75 kHz and 3.9 to 33.6 $^\circ\text{C}$; the complex shear moduli were measured from 10^{-4} to 2 Hz and -36 to $34 \text{ }^\circ\text{C}$. The accuracy of the former was affirmed from consistency with

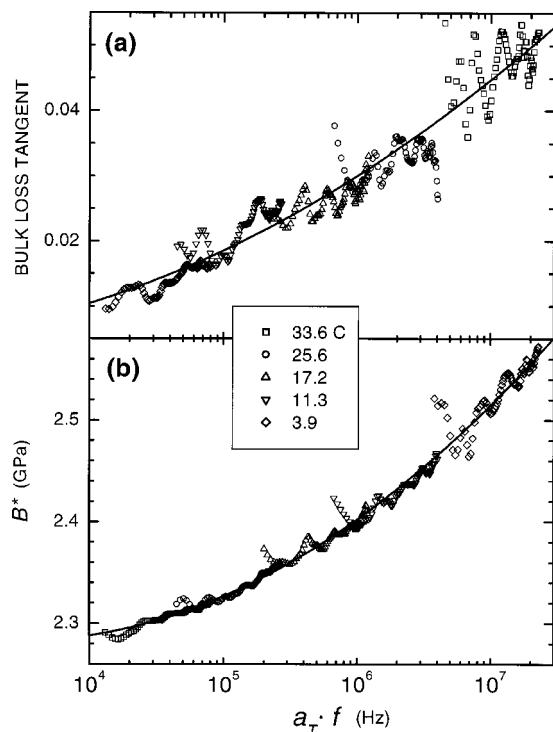


FIG. 10. Master curves of the bulk loss tangent (a) and complex bulk modulus (b) (data adapted from Fig. 9). The error bars are not shown for clarity. The horizontal shift factors a_T for the loss tangent were taken from the shear modulus, Fig. 8.

the Kramers–Kronig relation. By combining the sound speed and dynamic mechanical data, master curves were constructed for the complex bulk moduli. Although there was apparent agreement between the shift factors for bulk and shear deformation, this is probably due to the narrow range of measurement frequencies. This work illustrates the capability and some of the working rules associated with acoustical measurements in a small tank, as well as the use of such data to deduce material properties.

ACKNOWLEDGMENTS

We thank Dr. P. G. Santangelo for his insights and assistance with the dynamic mechanical measurements, and Dr. K. L. Ngai, Dr. G. B. McKenna, and Dr. D. L. Plazek for useful discussions. This work was supported by Advanced Acoustic Concepts of Columbia, MD and the Office of Naval Research.

- ¹J. D. Ferry, *Viscoelastic Properties of Polymers*, 3rd ed. (Wiley, New York, 1980), Chap. 11.
- ²W. Philippoff and J. Brodnyan, "Preliminary results in measuring dynamic compressibilities," *J. Appl. Phys.* **26**, 846–849 (1955).
- ³J. E. McKinney, S. Edelman, and R. S. Marvin, "Apparatus for the direct determination of the dynamic bulk modulus," *J. Appl. Phys.* **27**, 425–430 (1956).
- ⁴J. E. McKinney, H. V. Belcher, and R. S. Marvin, "The dynamic compressibility of a rubber-sulfur vulcanizate and its relation to free volume," *Trans. Soc. Rheol.* **4**, 347–362 (1960).
- ⁵J. Burns, P. S. Dubbelday, and R. Y. Ting, "Dynamic bulk modulus of various elastomers," *J. Polym. Sci., Part B: Polym. Phys.* **28**, 1187–1205 (1990).
- ⁶P. S. Dubbelday and J. Burns, "Dynamic bulk modulus of soft elastomers," *J. Wave-Material Interaction* **5** and **6**, 181–210 (1991).
- ⁷B. P. Holownia and E. H. James, "Determination of dynamic bulk modulus of elastomers using pressure measurement," *Rubber Chem. Technol.* **66**, 749–753 (1993).

- ⁸R. L. Willis, T. S. Stone, Y. H. Bertholot, and W. M. Madigosky, "An experimental-numerical technique for evaluating the bulk and shear dynamic moduli of viscoelastic materials," *J. Acoust. Soc. Am.* **102**, 3549–3555 (1997).
- ⁹R. L. Willis, L. Wu, and Y. H. Bertholot, "Determination of the complex Young and shear dynamic moduli of viscoelastic materials," *J. Acoust. Soc. Am.* **109**, 611–621 (2001).
- ¹⁰R. Meister, C. J. Marhoeffer, R. Sciamanda, L. Cotter, and T. Litovitz, "Ultrasonic viscoelastic properties of associated liquids," *J. Appl. Phys.* **31**, 854–870 (1960).
- ¹¹A. DiMeglio and L. S. Wang, "A variational method for the identification of viscoelastic parameters from experimental data," *J. Acoust. Soc. Am.* **108**, 2746–2753 (2000).
- ¹²J. C. Piquette, "Determination of the complex dynamic bulk modulus of elastomers by inverse scattering," *J. Acoust. Soc. Am.* **77**, 1665–1673 (1985).
- ¹³M. P. Hagelberg and R. D. Corsaro, "A small pressurized vessel for measuring the acoustic properties of materials," *J. Acoust. Soc. Am.* **77**, 1222–1228 (1985).
- ¹⁴I. D. Groves, "Twenty years of underwater electroacoustic standards," Naval Research Laboratory Formal Report, No. FR-07735 (1975).
- ¹⁵K. W. Ng, "Transducer structure," US Patent 5,367,500, issued 22 November 1994.
- ¹⁶H. Wang, Q. M. Zhang, L. E. Cross, and A. O. Sykes, "Clamping effect on the piezoelectric properties of poly(vinylidene fluoride-trifluoroethylene) copolymer," *Ferroelectrics* **150**, 255–266 (1993).
- ¹⁷S. F. Morse, P. L. Marston, and G. Kaduchak, "High-frequency back-scattering enhancements by thick finite cylindrical shells in water at oblique incidence," *J. Acoust. Soc. Am.* **103**, 785–794 (1998).
- ¹⁸A. J. Rudgers and C. A. Solvold, "Apparatus-independent acoustical-material characteristics obtained from panel-test measurements," *J. Acoust. Soc. Am.* **76**, 926–934 (1984).
- ¹⁹J. C. Piquette, "Direct measurements of edge diffraction from soft underwater acoustic panels," *J. Acoust. Soc. Am.* **95**, 3090–3099 (1994).
- ²⁰J. C. Piquette, "Conventional oblique-incidence panel test procedures," Naval Undersea Warfare Center-NPT Technical Memorandum 01-035 (2001).
- ²¹J. A. Archer-Hall and D. Gee, "A single integral computer method for axisymmetric transducers with various boundary conditions," *NDT Int.* **13**, 95–101 (1980).
- ²²N. Yen, private communication.
- ²³L. E. Kinsler, A. R. Frey, A. B. Coppens, and J. V. Sanders, *Fundamentals of Acoustics*, 3rd ed. (Wiley, New York, 1982), p. 107, Eq. 5.22.
- ²⁴R. Kronig, "On the theory of dispersion of x-rays," *J. Opt. Soc. Am.* **12**, 547–557 (1926).
- ²⁵R. Kronig and H. A. Kramers, "Zur theorie der absorption und dispersion in den Röntgenspektren (Theory of absorption and dispersion in x-ray spectra)," *Z. Phys.* **48**, 174–179 (1928).
- ²⁶M. O'Donnell, E. T. Jaynes, and J. G. Miller, "Kramers–Kronig relationship between ultrasonic attenuation and phase velocity," *J. Acoust. Soc. Am.* **69**, 696–701 (1981).
- ²⁷P. G. Santangelo and C. M. Roland, "Temperature dependence of mechanical and dielectric relaxation in *cis*-1,4-polyisoprene," *Macromolecules* **31**, 3715–3719 (1998).
- ²⁸D. J. Plazek, "Temperature dependence of viscoelastic behavior of polystyrene," *J. Phys. Chem.* **69**, 3480–3487 (1965).
- ²⁹D. J. Plazek, "Temperature-dependence of the viscoelastic behavior of poly(vinyl acetate)," *Polymer J.* **12**, 43–53 (1980).
- ³⁰K. L. Ngai, A. Schonhals, and E. Schlosser, "An explanation of anomalous dielectric-relaxation properties of poly(propylene glycol)," *Macromolecules* **25**, 4915–4919 (1992).
- ³¹D. J. Plazek, C. Bero, S. Neumeister, G. Floudas, G. Fytas, and K. L. Ngai, "Viscoelastic properties of amorphous polymers. 3. Low-molecular-weight poly(methylphenylsiloxane)," *Colloid Polym. Sci.* **272**, 1430–1438 (1994).
- ³²L. I. Palade, V. Verney, and P. Attane, "Time-temperature superposition and linear viscoelasticity of polybutadienes," *Macromolecules* **28**, 7051–7057 (1995).
- ³³D. J. Plazek I.-C. Chay, K. L. Ngai, and C. M. Roland, "Viscoelastic properties of polymers. 4. Thermorheological complexity of the softening dispersion in polyisobutylene," *Macromolecules* **28**, 6432–6436 (1995).

- ³⁴D. J. Plazek and D. L. Plazek, "Viscoelastic behavior of atactic polypropylene," *Macromolecules* **16**, 1469–1475 (1983).
- ³⁵P. G. Santangelo, K. L. Ngai, and C. M. Roland, "Temperature dependence of relaxation in polypropylene and poly(ethylene-co-propylene)," *Macromolecules* **29**, 3651–3653 (1996).
- ³⁶M. L. Williams, R. F. Landel, and J. D. Ferry, "Mechanical properties of substances of high molecular weight. 19. The temperature dependence of relaxation mechanisms in amorphous polymers and other glass-forming liquids," *J. Am. Chem. Soc.* **77**, 3701–3707 (1955).
- ³⁷R. N. Capps, "Dynamic Young's moduli of some commercially available polyurethanes," *J. Acoust. Soc. Am.* **73**, 2000–2005 (1983).
- ³⁸J. Jarzynski, "Mechanisms of Sound Attenuation in Materials," in *Sound and Vibration Damping with Polymers*, edited by R. D. Corsaro and L. H. Sperling, ACS Symposium Series 424 (American Chemical Society, Washington, DC, 1990).
- ³⁹C. A. Bero and D. J. Plazek, "Volume-dependent rate-processes in an epoxy-resin," *J. Polym. Sci., Part B: Polym. Phys.* **29**, 39–47 (1991).
- ⁴⁰C. G. Robertson, J. E. Monat, and G. L. Wilkes, "Physical aging of an amorphous polyimide: enthalpy relaxation and mechanical property changes," *J. Polym. Sci., Part B: Polym. Phys.* **37**, 1931–1946 (1999).
- ⁴¹S. L. Simon, J. W. Sobieski, and D. J. Plazek, "Volume and enthalpy recovery of polystyrene," *Polymer* **42**, 2555–2567 (2001).
- ⁴²G. B. McKenna, Y. Leterrier, and C. R. Schultheisz, "The evolution of material properties during physical aging," *Polym. Eng. Sci.* **35**, 403–410 (1995).
- ⁴³M. M. Santore, R. S. Duran, and G. B. McKenna, "Volume recovery in epoxy glasses subjected to torsional deformations—the question of rejuvenation," *Polymer* **32**, 2377–2381 (1991).

High power ultrasound standard

George S. K. Wong and Lixue Wu

Acoustical Standards, Institute for National Measurement Standards, National Research Council, Ottawa, Ontario KIA 0R6, Canada

(Received 30 November 2000; accepted for publication 17 January 2002)

A sensitive radiation force balance for laboratory measurement of ultrasonic power is presented. The principle of the system is based on measuring the ultrasonic radiation force exerted on a conical float suspended in water. Technical details of the implementation of the economically attractive system are described. The operation of the system is automated with the aid of the IEEE-488 bus and a desktop computer. Design aspects that affect measurement uncertainty are investigated. A theoretical model for the measurement of ultrasonic power with a conical reflector target is discussed. The expanded uncertainty (95% confidence level) of the above radiation force conical float system is estimated to be between 5% to 10%. [DOI: 10.1121/1.1459464]

PACS numbers: 43.58.Vb, 43.58.Pw, 43.35.Yb [SLE]

LIST OF SYMBOLS

A	water attenuation	P_i	power of the incident beam, W
a	attenuation coefficient of water	P_0	acoustic power, W
c	speed of sound in water, m/s	R	reflectivity factor, dimensionless
c_t	sound speed in the material of the target, m/s	r, h	distances, m
d	distance, m	t_{90}	temperature defined by the International Temperature Scale of 1990, Celsius
e_r	correction factor for a reflecting target, dimensionless	T	temperature, Celsius
e_a	correction factor for an absorbing target, dimensionless	θ	angle, degrees
$D(\phi, \theta)$	transducer normalized directivity function	θ_i	beam incident angle, degrees
E_i	time average density of the incident beam	$(180-2\alpha)$	apex of cone angle of a reflecting target, degrees
E_r	time average density of the reflected beam	ϕ	angle in the horizontal plane, degrees
F_n	radiation force, N	ψ	refracting angle related to the incident angle ($\alpha - \theta_i$)
F_r	radiation force with a reflecting target, N	Ω	solid angle, rad^2
F_a	radiation force with an absorbing target, N	γ^2	E_r/E_i
g	acceleration due to gravity, m/s^2	k	constant factor related to the total acoustic power P_0
m	mass reading taken by the electronic balance		
P	power, W		

I. INTRODUCTION

There are several techniques for implementation¹ of high-power ultrasound measurements. One of the most precise methods is based on laser interferometry:¹ A target made of a thin membrane is immersed in water. The power generated by a test transducer is assessed by measuring interferometrically the displacement of the membrane due to impingement of the ultrasound beam. The uncertainty of such a method is approximately 3%. (Unless otherwise stated, uncertainty refers to approximately the 95% confidence level.) A less precise but economically attractive technique is the tethered float.² A conical float is immersed in water. The float is attached to finely made silver chains. Similar to hydrometers, the submerged position of the float in water is adjustable by the length of the overhang tethers that are immersed in water. The ultrasound beam, generated by a test transducer

that is fixed in a vertical position, impinges on the float, causing the latter to sink deeper until there is a balance between the weight of the tethers and the ultrasound power generated. By calibrating the vertical displacement of the float with known weights placed on the float, one can deduce the ultrasound power generated by measuring the change in vertical displacement of the submerged target. The uncertainty of the tethered float is approximately 15% to 20%, depending on the technique used to measure the displacement. There is a variety of other implementations²⁻⁴ that employ targets made of various absorbing materials and operate in conjunction with electronic balances for the measurement of the impinging force generated by a transducer. The aim here is to describe an economically attractive high-power ultrasound standard that has an uncertainty within the range from 5% to 10% for the measurement of ultrasound power in the range of 0.1 to 1 watts.

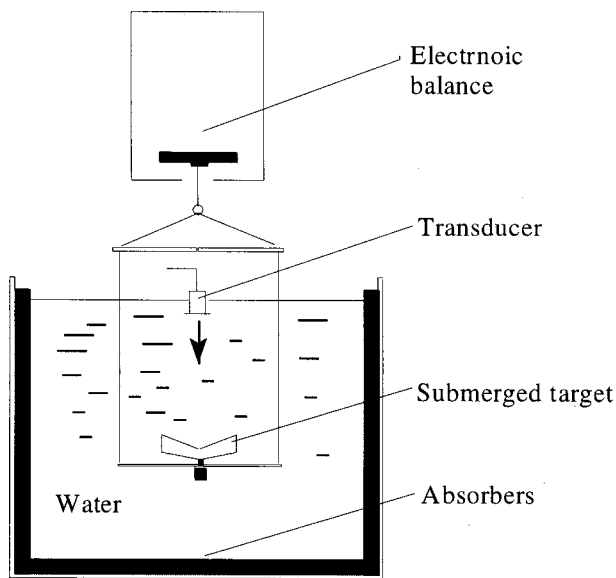


FIG. 1. Schematic diagram of the ultrasound power measuring balance.

II. THEORETICAL ANALYSIS

The schematic representation of the ultrasound balance is shown in Fig. 1. A conical target (that was part of a tethered float system) submerged in water was suspended with thin wires from a small hook at the bottom of an electronic balance. The test transducer with its active surface submerged in water was positioned coaxially above the target. The radiation force generated by the transducer impinging on the target was measured by the electronic balance. Additional lateral absorbers that lined the wall of the water tank reduced multipath reflection.

In the above arrangement, there are two assumptions: (1) the ultrasonic beam is a plane wave; and (2) the target is large enough that the entire ultrasonic beam is intercepted. The radiation force F of the normal incident beam is then related to acoustic power P_0 as⁴

$$F = mg = P_0 R / c, \quad (1)$$

where m is the mass reading taken from the electronic balance, g is the acceleration due to gravity at the site at which the electronic balance was calibrated, c is the speed of sound in water, and R is the reflectivity factor.

The target reflectivity factor R depends on the specific acoustic impedance for the particular incident beam geometry with respect to the submerged target. The numerical values for R are 1 and 2, for a perfect absorber target and a perfect reflector target, respectively. For the arrangement shown in Fig. 1, the reflectivity factor R of the cone reflector used in the measurement system is $2 \cos^2 \alpha$, where α is 25° .

A. Radiation forces acting on a conical target

As indicated by Beissner,⁴ although the corrections to the reflectivity R have been derived theoretically for the absorbing and the plane-reflecting targets and for a focused beam for absorbing targets,⁵ similar corrections for the conical target have not been dealt with adequately in the literature. In the following, the relationship between the ultra-

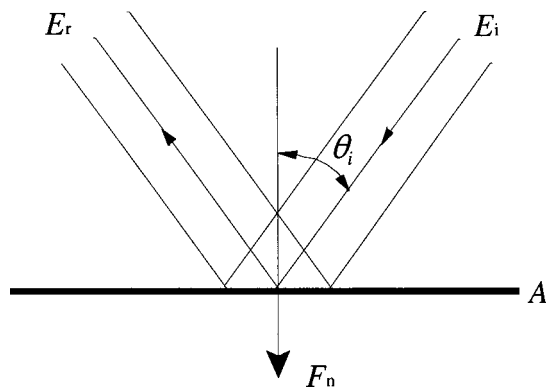


FIG. 2. Ultrasound beam of plane compression wave striking a plane reflecting surface A.

sound power, the reflectivity factor R , that includes the diffraction of the ultrasonic beam, the reflection coefficient of the material of the target, and the finite size of the target, is formulated.

The ultrasonic beam that is decomposed into many infinitesimal sectors of an infinitesimal cross section is assumed to propagate in a straight line. The beam strikes a plane interface A of two different media at an angle θ_i with respect to the normal of the interface (see Fig. 2). The radiation pressure p per unit area and normal to surface A is given by⁶

$$p = E_i (1 + \gamma^2) \cos^2 \theta_i, \quad (2)$$

where γ is the reflection coefficient defined as $\gamma^2 = E_r / E_i$, and the time average of the energy densities in the incident and reflected beam are E_i and E_r , respectively. For a plane wave, the power P_i of the incident beam is related to E_i by $E_i = P_i / c$, and c is the speed of sound in water. Therefore, the normal radiation force F_n acting on A can be written as

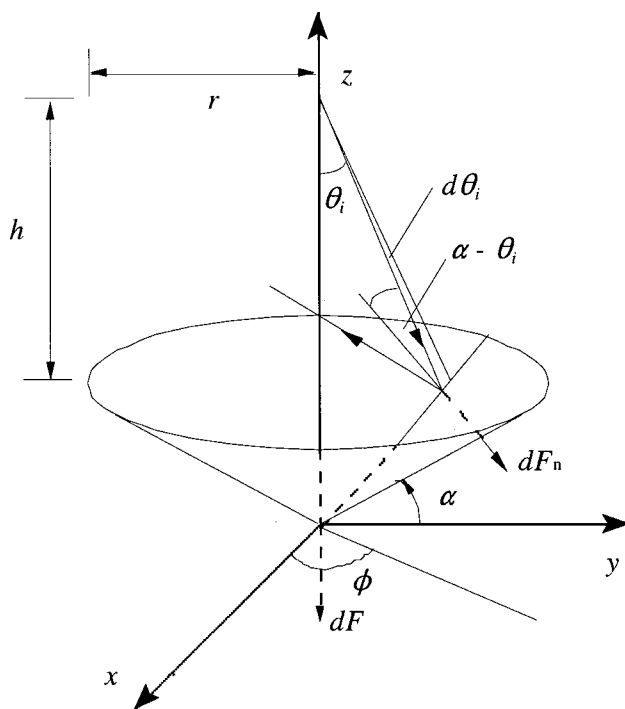


FIG. 3. Geometric illustration for theoretical consideration.

$$F_n = (1 + \gamma^2) \cos \theta_i P_i / c. \quad (3)$$

An illustration of the geometric relation used in the derivation is shown in Fig. 3. A cone reflector that has a radius r with a cone angle of $(180^\circ - 2\alpha)$ is located at a distance h from the source transducer and placed coaxially in the far field region. Consider an infinitesimal sector at ϕ and θ_i , where the ultrasound beam with power dP impinges on the cone reflector at an incident angle $(\alpha - \theta_i)$. The radiation force dF_n generated by the sector of the beam normal to the cone surface is given by

$$dF_n = (1 + \gamma^2) \cos(\alpha - \theta_i) \frac{dP}{c}. \quad (4)$$

The component dF of the radiation force dF_n pointing along the beam axis is calculated from

$$F = \frac{P_0 \cos^2 \alpha}{c} \cdot \frac{\int_0^{2\pi} \int_0^{\tan^{-1}(r/h)} (1 + \gamma^2(\theta_i)) \cos(\alpha - \theta_i) |D(\phi, \theta_i)|^2 \sin \theta_i d\theta_i d\phi}{\cos \alpha \int_0^{2\pi} \int_0^{\tan^{-1}(r/h)} |D(\phi, \theta_i)|^2 \sin \theta_i d\theta_i d\phi}, \quad (8)$$

where the reflection coefficient is given by

$$\gamma(\theta_i) = \frac{Z \cos(\alpha - \theta_i) - Z_t \cos \psi}{Z_t \cos(\alpha - \theta_i) + Z \cos \psi}, \quad (9)$$

where Z and Z_t are the characteristic acoustic impedance for water and for the target material, respectively, ψ is the refraction angle related to the incident angle $(\alpha - \theta_i)$ through Snell's law, and c_i is the sound speed in the target material. Note that the above equation is applicable to the condition of an absorbing target when $\alpha = 0^\circ$.

The new equation can be rewritten for reflecting and absorbing targets as follows:

For reflecting targets

$$e_r = \frac{\int_0^{2\pi} \int_0^{\tan^{-1}(r/h)} (1 + \gamma^2(\theta)) \cos(\alpha - \theta) |D(\phi, \theta)|^2 \sin \theta d\theta d\phi}{2 \cos \alpha \int_0^{2\pi} \int_0^{\tan^{-1}(r/h)} |D(\phi, \theta)|^2 \sin \theta d\theta d\phi}, \quad (12)$$

and

$$e_a = \frac{\int_0^{2\pi} \int_0^{\tan^{-1}(r/h)} (1 + \gamma^2(\theta)) \cos(\alpha - \theta) |D(\phi, \theta)|^2 \sin \theta d\theta d\phi}{\cos \alpha \int_0^{2\pi} \int_0^{\tan^{-1}(r/h)} |D(\phi, \theta)|^2 \sin \theta d\theta d\phi}. \quad (13)$$

Assuming that a piston-type transducer is placed in an infinite rigid baffle, the correction factors to be applied to the sound power measured as a function of transducer radius for different perfect targets with infinite large size are shown in Fig. 4. It can be seen that the numerical results, $e_r > 1$ and $e_a < 1$, are in agreement with the hypothesis of the reflectivity factor R . This is discussed in more detail in the following section.

$$dF = (1 + \gamma^2) \cos(\alpha - \theta_i) \cos \alpha \frac{dP}{c}. \quad (5)$$

The power dP is expressed as

$$dP = k |D(\phi, \theta_i)|^2 d\Omega = k |D(\phi, \theta_i)|^2 \sin \theta d\phi d\theta, \quad (6)$$

where $D(\phi, \theta)$ is the normalized directivity function of the transducer and k is the constant factor related to the total acoustic power P_0 as follows:

$$P_0 = k \int_0^{2\pi} \int_0^{\pi/2} |D(\phi, \theta_i)|^2 \sin \theta d\phi d\theta_i. \quad (7)$$

Thus, the total force F acting on the cone reflector along the beam axis is calculated from the following expression with the double integral over the whole cone of the ultrasonic beam interacting with the cone reflector:

$$F_r = \frac{2P_0 \cos^2 \alpha}{c} e_r, \quad (10)$$

and for absorbing targets

$$F_a = \frac{P_0 \cos^2 \alpha}{c} e_a. \quad (11)$$

Similarly, the correction factors, respectively, for each case are:

B. Ultrasonic power measurements with two different targets

Three requisite conditions are assumed in the above derivation: (1) the normal incidence beam is a plane wave; (2) there is perfect materials at the interface between water and target (total reflection for reflectors and no reflection for absorbers); and (3) the target is large enough to eliminate

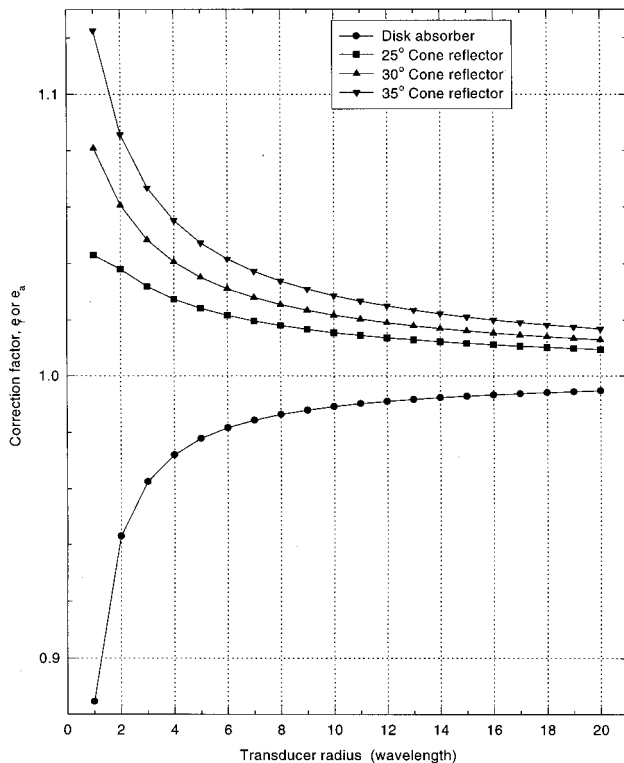


FIG. 4. Correction factors as a function of transducer radius.

an edge effect. In practice, the above conditions are only approximate assumptions. It has been shown that when the radius of the aperture of the transducer is much greater than the wavelength of the ultrasonic wave⁴ the assumption of plane waves is a good approximation. To investigate the validity of the remaining assumptions, an experiment with the arrangement shown in Fig. 1 is performed. Based on the mass readings of the balance, ultrasonic powers are calculated with Eq. (1) for the conical reflector and the absorbing disk target. Figure 5 shows, under similar environmental conditions and with identical measuring instruments, the measured ultrasonic power for the two targets. It is noted that there is a discrepancy between the power measured by the cone reflector (90-mm diameter with a cone angle of 130 deg) and the disk absorbing target. Since the cone-reflecting target and the absorbing target both operate with the same measuring system, and systematic uncertainties are common to both target arrangements, the relatively smaller measurement discrepancy (shown in Fig. 5) between the cone reflector and the disk absorber at the far-field region is most likely due to uncertainties of the approximations in the derivation of the reflectivity factor R . It is obvious that for $R = 2 \cos^2(\alpha)$, the assumption for $\alpha = 25^\circ$ is too small for the cone reflector and $\alpha = 0^\circ$ is too large for the disk absorber. Intuitively, if the diffraction of the ultrasonic beam is taken into consideration and the reflection coefficient of the material of the target is included in the derivation, it is possible to reduce the discrepancy through increasing R for reflecting targets and decreasing R for absorbing targets.

III. SYSTEM IMPLEMENTATION

The implementation of the measurement system is based on the fact that the incident acoustic energy acting on a re-

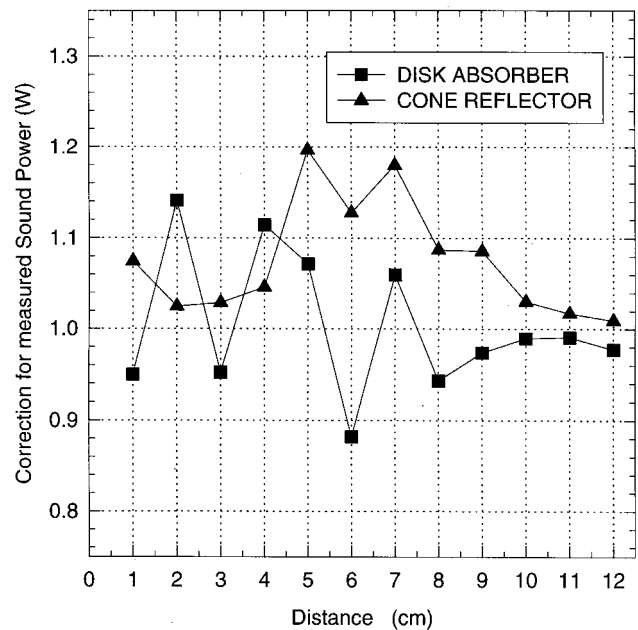


FIG. 5. Ultrasound power measurement with a cone reflector (90-mm diameter and a cone angle of 130 deg), and a disk absorber (100-mm diameter, 12.7-mm-thick Wallgone).

flecting or an absorbing target transfers its momentum to the target. This momentum is measured as a force that is directly proportional to the spatial- and temporal-averaged acoustic power.

A. Conical float

The heart of the NRC ultrasound power measurement system is a conical float target (Fig. 6) that has been used in a tethered float system. The tethered float, is supplied by NPL, UK. The construction of the float is a thin-walled, air-backed, concave metal cone with a base diameter of 90 mm and apex angle of 130° . The concave cone serves as a reflector with its apex directed away from the transducer. The half-cone angle of 65° is necessary to comply with boundary conditions designed for the tethered float system. When a coaxial radiation force is applied the concave reflector has the advantage of self-centering with respect to the ultrasound beam. The small weight shown in Fig. 6 makes it possible to adjust the initial reading and the selection of an optimum range for the electronic balance. If necessary, a disk made of absorbing material can be placed on the top of the float to convert the system to an absorbing target. Thin wires that suspend the float have a nominal diameter of 0.01 in. The three suspension wires for the float are coated with plastics to reduce the water surface tension.

B. Ultrasound transducer positioning

Misalignment and tilt of the conical float target with respect to the vertical axis affects ultrasound power measurements. The vertical position of the transducer has to be adjusted carefully to obtain good measurements. A precision positioning system has been designed to provide fine adjustments for translation and rotation in the Y axis (horizontal; see Fig. 3), and the Z axis (vertical). The reference trans-

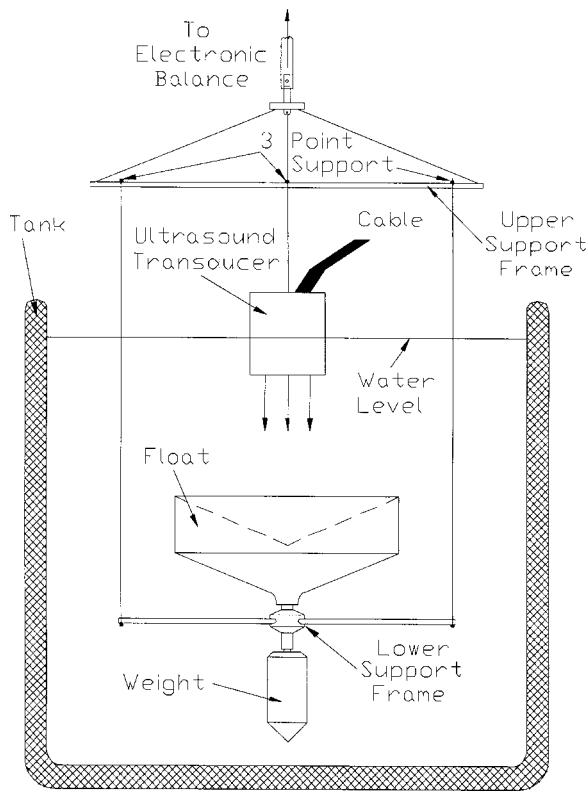


FIG. 6. General arrangement of the conical-float balance system for ultrasound power measurement.

ducer (NIST standard ultrasound source SRM 1855-37) is positioned with the aid of a hollow metal tube. Before placement of the transducer, a mirror was placed at a 45-deg angle on top of the tube for sight and to align the relative position between the vertical axis of the tube and the apex of the cone reflector located below. After installation of the reference transducer, the distance between the transducer active surface and the top surface of the submerged cone reflector is measured by sighting lines marked at the outer circumference of the transparent water tank. The uncertainty of the distance between the transducer and the surface of the cone reflector is estimated to be 1 mm.

C. Ultrasound absorbers

Lateral absorbers that lined the water tank inner surfaces are used to reduce multipath reflections in the water tank. For the following experiment, it was found that 6.4-mm thick Nitrile (American Biltrile), a commercially available rubber, can be used to augment the previously used absorber material known as Wallgone, that is no longer available commercially. Experiment has shown that when operating at 2 MHz and with 6.4-mm-thick Nitrile lining, the reflection coefficient is approximately 1%, which is comparable to the reflection coefficient of Wallgone of similar thickness.

D. Reflecting targets versus absorbing targets

Both reflecting and absorbing targets have their advantages and disadvantages. While absorbing targets are rela-

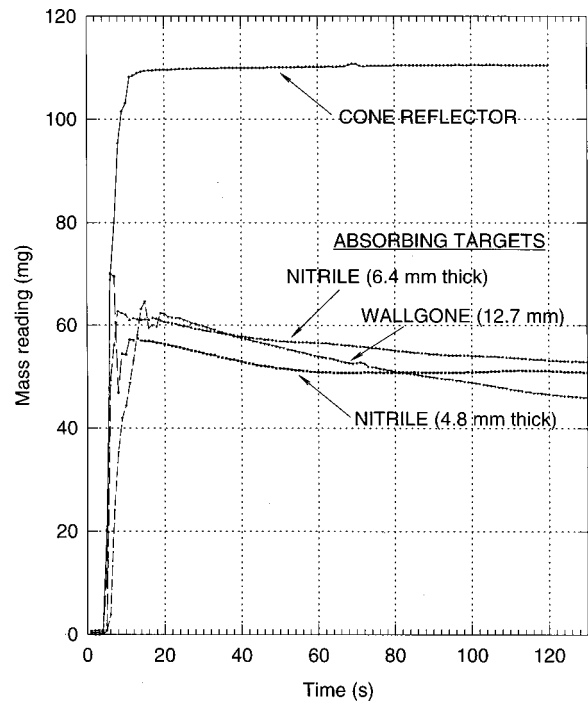


FIG. 7. Mass reading drift with conical reflector and absorbing targets.

tively insensitive to misalignment, the alignment of a cone reflector with respect to the transducer vertical axis must be adjusted carefully. For a 130° cone reflector, every 1° departure of the float alignment from the vertical axis increases the uncertainty in the measured ultrasound power by 1.7%. On the other hand, good absorbing targets will minimize the above positioning error. However, during operation, absorbing targets are affected by heat built up on their surface layers. In general, imperfect absorption of acoustic energy can cause standing waves between the transducer and the absorbing target, and can lead to large uncertainty in ultrasound power measurement.

The variation of the electronic balance mass readings as a function of time for the 130° conical float reflector and three types of 100-mm-diameter absorbing targets are shown in Fig. 7. The readings are sampled at 1-s intervals for a period of 2 min. It can be seen that for the absorbing targets the mass readings drift by approximately 5% per 10 s. This is mainly due to heat build-up, which causes the target volume to expand in the absorbing targets. The readings taken with the conical float are relatively stable.

E. Supporting structure of the measuring system

External vibration is one of the most serious problems encountered in the operation of electronic balances. Vibration also generates water surface waves, which cause roughness of the water surface and create random nonspecular reflections that may influence the radiation force measured. The measuring system, shown in Fig. 6, is mounted on a 5-cm-thick steel plate resting on a 10-cm-thick granite table that is supported by air pads (Fig. 8). A shielding cage covering the entire system reduces thermal air currents in the surrounding area.

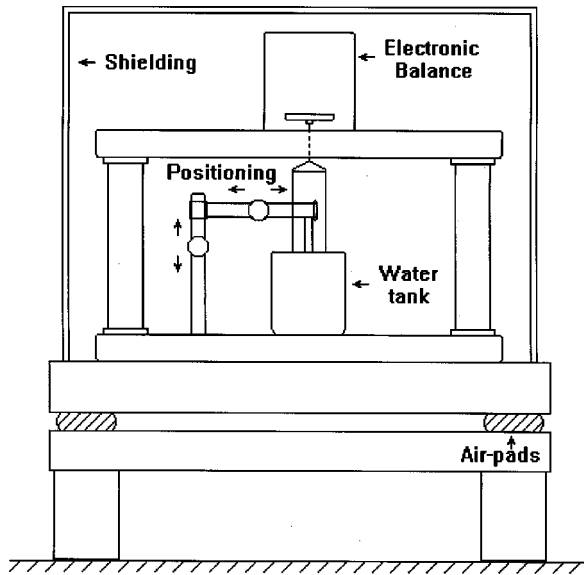


FIG. 8. Supporting structure of the ultrasound power measuring system.

F. Computer control

The schematic diagram of the control instrument arrangement is shown in Fig. 9. The system consists of an oscillator (model HP3326A, Hewlett-Packard), a rf power amplifier (model EIN 240L, Electronic Navigation Industries, Inc.), a dc voltmeter (model 8506A, John Fluke MFG Co.), a wideband true rms voltmeter (model 8920A, John Fluke MFG Co.), an electronic balance (model AT201, Mettler Instruments AG), a printer and a desktop computer. A precision quartz thermometer (model F250, Automatic Systems Laboratories, Inc.), not shown, is included in the system. The IEEE-488 general purpose interface bus (GPIB) controlled all signal-generating and measuring devices. A variable attenuator (model 940-114-33-1, Lucas Weinschel) was used to match the impedance between the RF power amplifier and the test transducer. The printer recorded the measurement results.

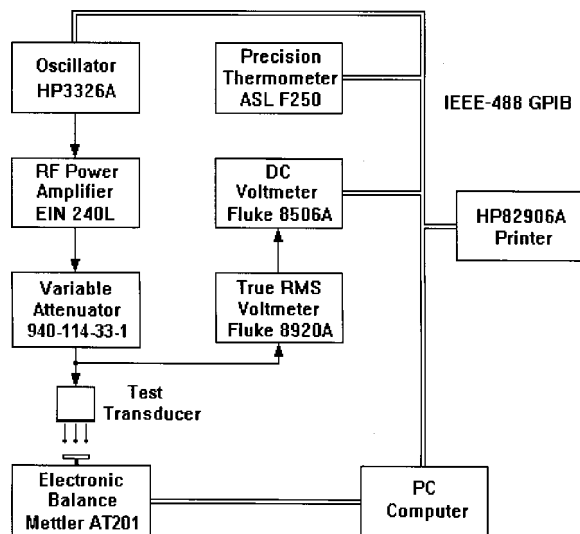


FIG. 9. Schematic arrangement of measuring instruments.

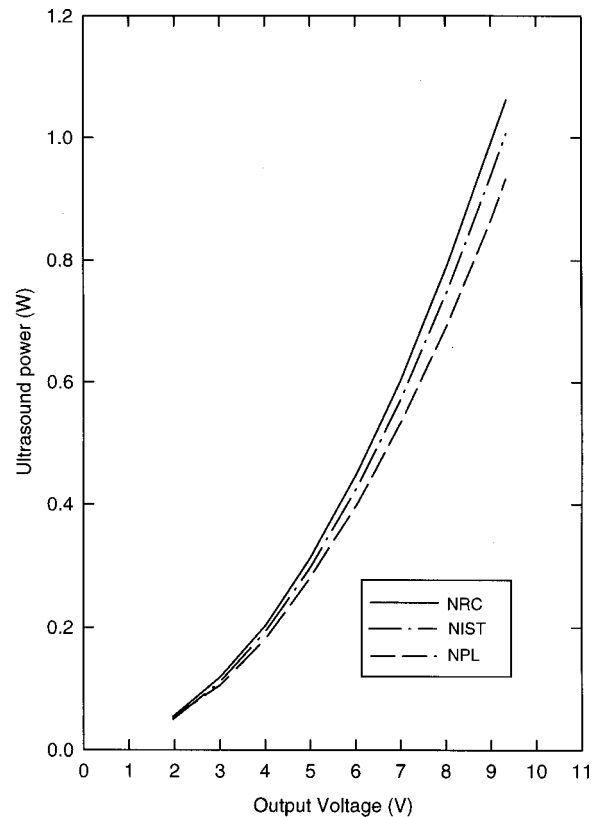


FIG. 10. With the NIST reference transducer (SRM 1855-37) as a transfer standard, measurement comparisons between the NRC conical-float system and the NPL precision ultrasound power balance NPL/AC941024) were made at 1.584 MHz.

IV. MEASUREMENTS

The performance of the above NRC ultrasound power measuring system was compared with the ultrasound power generated by the above NIST reference transducer^{7,8} (NIST standard ultrasound source SRM 1855-37). The NIST reference transducer has been calibrated at frequencies from 1.584 to 20 MHz for output power up to 1 W. The power generated by the above reference transducer was also measured with a portable NPL precision ultrasonic power balance (NPL/AC941024) that has been calibrated by NPL at a frequency of 0.928 MHz for power up to 1 W. The NIST reference transducer has a dc/rf splitter that provides a dc voltage corresponding to the ultrasound power generated.

Distilled and degassed water was left overnight for temperature stabilization and then degassed before the measurement. A light source with an optical fiber to isolate thermal disturbance provides the illumination to observe and facilitate the removal of any air bubbles trapped on the surface of the transducer and submerged target. The electronic balance for the system was calibrated before and after measurements by placing known standard weights on the balance pan.

The NIST reference standard transducer was utilized as a transfer standard during comparison measurements between the above NRC conical float ultrasound power balance and between the above NPL ultrasonic power balance. Figure 10 shows the ultrasound power measured at 1.584 MHz by

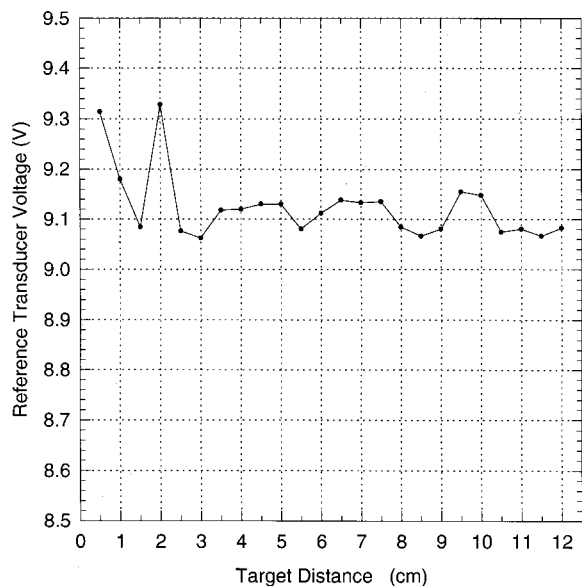


FIG. 11. Variation of transducer dc voltage due to different target distances.

the above balance systems referenced to the dc voltage generated by the NIST transducer. At 1 W, with the NIST transducer as the reference (center curve), the deviations of the measured ultrasound power between the NRC balance (top curve) and the NPL balance (lower curve) are approximately 4.6% and -6.5% , respectively. At the 0.4-W range, the above deviations are approximately 5.6% and -6.6% , respectively, as shown in Fig. 10.

V. MEASUREMENT UNCERTAINTIES

Some possible factors that contributes to uncertainty of the measurement are as follows.

A. Target distance

Beissner⁹ discussed the theory for the acoustic radiation pressure in the near-field for an ideal flat absorber of infinitely large size. In order to reduce uncertainties due to acoustic absorption in water, streaming, and the diverging structure of the sound field, it is recommended that the target be placed as near as possible to the transducer.⁹ However, at the extreme near-field a continuously vibrating, baffled, circular plane piston transducer has been shown to be very different from a plane progressive wave.¹⁰ It was found that by placing a finite-size target in the near-field the radiation impedance of the transducer changes and affects the radiated ultrasonic power generated. The variation of the dc voltages due to impedance variations of the NIST reference transducer at different target distances is shown in Fig. 11. At the near-field, the impedance variation is evident from the variation of dc voltages. From Fig. 11, the target distance selected for the above measurements with a conical float target was 11.5 cm at the far field. For the following measurements, corrections had been applied to the ultrasound power measured for water attenuation and sound-field diffraction. Acoustic streaming effect,⁴ if any, is negligible for frequencies below 2 MHz.

B. Mass measurement

Mass reading is affected by the volume change of the float and other submerged components. Volume changes of the float occur because of thermal expansions due to temperature change. The buoyancy effect on the mass reading for the system is about $3 \text{ mg}/^\circ\text{C}$. Since over the duration of a measurement the water temperature change is within $\pm 0.06^\circ\text{C}$, the uncertainty budget for mass reading due to thermal expansion of the float is approximately $\pm 0.18 \text{ mg}$. The electronic balance for the system has a linearity of $\pm 0.12 \text{ mg}$ over a measuring range of 200 g. The conical float arrangement, including the suspension wires, weighs approximately 50 g when submerged in water. The maximum mass readings due to ultrasonic power, after “tare” of the balance, are approximately 150 mg, the uncertainty contribution due to balance nonlinearity is estimated to be approximately $\pm 0.03 \text{ mg}$.

There is a small displacement of $0.5 \mu\text{m}$ per gram of the balance load. The volume change of the suspension wires that in turn modify the buoyancy of the float arrangement should be considered. For 1-W acoustic power, that is approximately equivalent to a load increase of 0.11 g; the buoyancy change is equivalent to about 0.0001 mg for wires with a nominal diameter of 0.01 in.

C. Water attenuation

Water attenuation A can be calculated using the equation $A = \exp(-2\alpha f^2 d)$, where α is the attenuation coefficient of water and d is the distance between the transducer and the cone reflector. An equation for calculating α at a temperature T is obtained by fitting Pinkerton’s measurement data¹¹ to a polynomial. The distance d is determined from the measured distance between the face of the transducer and the top surface of the cone reflector. The uncertainty in the distance measurement is $\pm 1 \text{ mm}$. The total uncertainty was then calculated by differentiating the equation $A = \exp(-2\alpha f^2 d)$ with respect to T and d . The relative uncertainty of the attenuation calculation including the measurement standard uncertainty of Pinkerton’s¹¹ data is less than 1.5%.

D. Water temperature and sound speed

The sound speed in water was calculated with the first term (zero salinity for pure water) of the UNESCO equation and by utilizing the coefficients for temperature t_{90} given by Wong and Zhu.¹² Since the temperature change during the experiment was within $\pm 0.06^\circ\text{C}$, the uncertainty budget contributed by sound speed is 0.02%.

Heating effects due to water attenuation of the ultrasonic beam are considered: For a 11.5-cm column of water that has the same diameter (2.54 cm) as the transducer, the temperature rise is approximately 0.001°C per s when the transducer is operating at 1 W. Since the tank is filled with 16 L of water, and the ultrasound power “on” time for a balance reading was less than 10 s, the expected uncertainty budget due to heating effects is less than 0.004%.

TABLE I. Uncertainty budget for the NRC ultrasound power measuring system.

	Source	Uncertainty %
Mass measurement	Microbalance	± 0.1
	Temperature	± 0.2
	Suspension wires	± 0.0001
Speed calculation	Formula from Ref. 11	± 0.001
	Temperature	± 0.02
	Pressure	± 0.0001
Water attenuation	Fisher's formula	± 0.02
	Temperature	± 0.007
	Distance	± 0.01
Target	Reflection coefficient	± 0.4
	Misalignment	± 1.6
	Cone tip	± 0.5
	Multiple reflection	± 0.2
Transducer beam pattern	Practical limitation (nonpiston, etc.)	± 1.0
	Gravitational acceleration	± 0.001
Random	INMS mass standards lab. Standard deviation (3 measurements)	± 3.0

E. Reflection coefficient

The actual reflection coefficient of the cone reflector is unknown. Since the cone is made of an alloy that is dominated by steel, the specific acoustic impedance of steel is used in calculating the reflection coefficient. The estimated uncertainty for the reflection coefficient is ± 0.01 .

F. Misalignment

The cone reflector is sensitive to misalignment and tilt. Although the positioning system and the optical mirror provide a precision alignment between the transducer center and the cone apex, some misalignment is detected. This is evident from the small transversal movement of the cone reflector when the ultrasonic power is turned off. The misalignment is due to the following factors: (1) The acoustic center of the transducer is not located at the geometric center of the transducer; (2) the ultrasonic beam diameter is not of circular symmetry; (3) the cone angle may not be uniform; (4) the lengths of the suspension wires are not equal. The error due to the misalignment can be calculated numerically from the tilt uncertainty and the noncoaxial error using Eq. (9) for the reflection coefficient. The tilt uncertainty of 1.6% is estimated from the resolution of the apex image in the mirror.

G. Multiple reflections

Due to imperfect absorbers that lined the wall of the water tank, the multiple reflected ultrasonic waves may reflect back to the conical target. Since all the interfaces (water/air and water/rubber) are smooth, the reflected waves are coherent to the direct path wave, and this may produce constructive and destructive interference at the cone reflector. Multiple reflections can be minimized by proper determination of the distance between the tank wall absorber and the edge of the float. Using the acoustic ray method and considering only the main beam, the maximum distance between

the tank wall absorber and the edge of the float can be calculated such that the third reflection (float to absorber to water surface) of the outermost ray does not impinge on the edge of the float. Multiple reflections can be further reduced by placing absorbers on the water surface (leaving a small window for cavitation observation).

H. Transducer beam pattern

A piston vibration and infinite rigid baffle has been assumed for the calculation of a theoretical beam pattern. The uncertainty due to the beam-pattern approximation was investigated with the NPL's beam profile measurement system.¹³ The actual beam pattern of the NIST transducer is measured and the reflection factor R is calculated using the measured directivity function. The uncertainty is estimated at $\pm 1.0\%$.

I. Gravitational acceleration

The gravitational acceleration g is $9.806\,16\text{ m/s}^2$, which is based on the value supplied by the INMS mass standards laboratory. The uncertainty is estimated to be $\pm 0.0001\text{ m/s}^2$.

J. Calculation of total uncertainty

The overall sound-power measurement uncertainties including those discussed above are summarized in Table I. The uncertainty of 5.0% at a confidence level of 95% was computed with the method give by Ziskin.¹⁴

VI. CONCLUSIONS

A system for the absolute measurement of ultrasonic power in the range of 0.1 to 1 W is described. The principle of the system is based on measuring the ultrasonic radiation force exerted on a conical float suspended in water. The system is automated with the aid of the IEEE-488 bus under the control of a desktop computer. Various issues related to measurement accuracy are discussed. The estimated uncertainty at a confidence level of 95% is between 5% to 10%, depending on the power at which the measurements are made.

¹B. Zeqiri, "Overview of measurement techniques," in *Output Measurements for Medical Ultrasound*, edited by R. C. Preston (Springer, London, 1991), pp. 35–56.

²F. Davidson, "Ultrasonic power balances," in Ref. 1, pp. 75–90.

³IEEE Guide for Medical Ultrasound Field Parameter Measurements, IEEE Standard 790–1989.

⁴K. Beissner, "Measurement techniques, Part A: Radiation force and force balances," in *Ultrasonic Exosimetry*, edited by M. C. Ziskin and P. A. Lewin (CRC Press, Boca Raton, 1993).

⁵J. Wu, "Calculation of acoustic radiation force generated by focused beams using the ray acoustics approach," *J. Acoust. Soc. Am.* **97**(5), 2747–2750 (1995).

⁶F. E. Borgnis, "Acoustic radiation pressure of plane-compressional waves at oblique incidence," *J. Acoust. Soc. Am.* **24**, 468–469 (1952).

⁷S. E. Fick, F. R. Breckenridge, C. E. Tschiegg, and D. G. Eitzen, "An Ultrasonic absolute power transfer standard," *J. Res. Natl. Bur. Stand.* **89**, No. 2 (1984).

⁸S. E. Fick, "The NIST power reference source," in Ref. 4.

⁹K. Beissner, "Acoustic radiation pressure in the near field," *J. Sound Vib.* **93**, No. 4, 537–548 (1984).

- ¹⁰K. Beissner, "On the plane-wave approximation of acoustic intensity," *J. Acoust. Soc. Am.* **71**, 1406–1411 (1982).
- ¹¹J. M. M. Pinkerton, "A pulse method for the measurement of ultrasonic absorption in liquids: Results for water," *Nature (London)* **160**, 128–129 (1947).
- ¹²G. S. K. Wong, and S. Zhu, "Speed of sound in seawater as a function of salinity, temperature, and pressure," *J. Acoust. Soc. Am.* **97**, 1732–1736 (1995).
- ¹³R. C. Preston, "The NPL ultrasound beam calibrator," *IEEE Trans. Ultrason. Ferroelectr. Freq. Control* **35**, No. 2, 122–139 (1988).
- ¹⁴M. C. Ziskin, "Measurement uncertainty in ultrasonic exosimetry," in Ref. 4.

Sources of DPOAEs revealed by suppression experiments, inverse fast Fourier transforms, and SFOAEs in impaired ears

Dawn Konrad-Martin,^{a)} Stephen T. Neely, Douglas H. Keefe, Patricia A. Dorn, Emily Cyr, and Michael P. Gorga

Boys Town National Research Hospital, 555 North 30th Street, Omaha, Nebraska 68131

(Received 18 June 2001; revised 2 January 2002; accepted 7 January 2002)

DPOAE sources are modeled by intermodulation distortion generated near the f_2 place and a reflection of this distortion near the DP place. In a previous paper, inverse fast Fourier transforms (IFFTs) of DPOAE filter functions in normal ears were consistent with this model [Konrad-Martin *et al.*, *J. Acoust. Soc. Am.* **109**, 2862–2879 (2001)]. In the present article, similar measurements were made in ears with specific hearing-loss configurations. It was hypothesized that hearing loss at f_2 or DP frequencies would influence the relative contributions to the DPOAE from the corresponding basilar membrane places, and would affect the relative magnitudes of SFOAEs at frequencies equal to f_2 and f_{DP} . DPOAEs were measured with $f_2=4$ kHz, f_1 varied, and a suppressor near f_{DP} . L_2 was 25–55 dB SPL ($L_1=L_2+10$ dB). SFOAEs were measured at f_2 and at 2.7 kHz (the average f_{DP} produced by the f_1 sweep) for stimulus levels of 20–60 dB SPL. SFOAE results supported predictions of the pattern of amplitude differences between SFOAEs at 4 and 2.7 kHz for sloping losses, but did not support predictions for the rising- and flat-loss categories. Unsuppressed IFFTs for rising losses typically had one peak. IFFTs for flat or sloping losses typically have two or more peaks; later peaks were more prominent in ears with sloping losses compared to normal ears. Specific predictions were unambiguously supported by the results for only four of ten cases, and were generally supported in two additional cases. Therefore, the relative contributions of the two DPOAE sources often were abnormal in impaired ears, but not always in the predicted manner. © 2002 Acoustical Society of America. [DOI: 10.1121/1.1455024]

PACS numbers: 43.64.Ha, 43.64.Jb [BLM]

I. INTRODUCTION

Distortion product otoacoustic emissions (DPOAEs) are produced by intermodulation distortion caused by the basilar membrane's nonlinear response to a two-tone stimulus (f_1 and f_2 , where $f_1 < f_2$), which occurs near the f_2 place. The $2f_1 - f_2$ distortion product may provide energy for additional emissions, in the form of coherent reflections or stimulus frequency otoacoustic emissions (SFOAEs) arising at the basilar membrane place tuned to the DP frequency (f_{DP}) (Kim, 1980; Kemp and Brown, 1983; Shera and Guinan, 1999; Knight and Kemp, 2000). Minor structural abnormalities causing an impedance mismatch along the basilar membrane forward-transmission path represent a possible physical basis for these reflection sites. Theoretically, they would be most effective when located near the characteristic place associated with a forward-traveling wave in a healthy ear (Shera and Zweig, 1993). According to this two-source model for DPOAE generation, cochlear status at both f_2 and DP places affects DPOAE measurements.

Several studies have attempted to isolate components of the DPOAE arising from the f_2 and DP places in normal ears. In particular, studies have shown that removing the DP-place contribution (by presenting a suppressor-tone near the f_{DP}), reduces or eliminates DPOAE fine structure in the

frequency-domain representation of responses obtained using continuous tones for primaries (Kemp and Brown, 1983; Heitmann *et al.*, 1998; Dreisbach, 1999; Dreisbach and Siegel, 1999; Mauermann *et al.*, 1999a; Talmadge *et al.*, 1999; Kalluri and Shera, 2001; Konrad-Martin *et al.*, 2001). Suppressing the reflection component of the DPOAE also was shown to remove excursions in DP level and phase in the time-domain representation of responses obtained using a pulsed-primary paradigm (Talmadge *et al.*, 1999).

A recent study compared measurements of the DP-place component of the DPOAE to SFOAEs obtained at the f_{DP} (Kalluri and Shera, 2001). The DP-place component of the DPOAE was derived by complex subtraction of the DPOAE measured in the presence of a suppressor (placed near the f_{DP}) from the DPOAE measured in the absence of the suppressor. Both the DPOAE data and the SFOAE data were collected while the stimulus frequency was varied in small steps. The slope of the phase plotted as a function of stimulus frequency (and the latency derived from this slope) was similar for the DP-place component of the DPOAE and the SFOAE at the f_{DP} . Greater similarity was achieved when an extra tone was presented along with the SFOAE stimulus in order to mimic the f_1 primary present in the DPOAE paradigm. These observations support the hypothesis that the DPOAE measured in the ear canal contains a reflection component at the f_{DP} .

Other studies examining derived DPOAE latencies also have provided evidence for the two-source model of DPOAE generation (e.g., O'Mahoney and Kemp, 1995; Moulin and

^{a)} Author to whom correspondence should be addressed. Current address: Dept. of Communication Disorders and Sciences, Rush University, 1653 W. Congress Parkway, Room 1015 Armour, Chicago, IL 60612. Electronic mail: Dawn_Konrad-Martin@rush.edu

Kemp, 1996; Stover *et al.*, 1996). Recently, we collected DPOAE level and phase data in normal ears using a fixed- f_2 paradigm, in which f_1 was varied (Konrad-Martin *et al.*, 2001). Data were collected with and without a suppressor tone, placed near and tracking with the f_{DP} in order to suppress the reflection component coming from the DP place. These two sets of data were converted into an equivalent time representation using inverse fast Fourier transform (IFFT) techniques. For low-to-moderate stimulus levels, it was possible to resolve at least two main components (peaks) in the derived time-domain response constructed from data obtained in the absence of a suppressor. Introducing the suppressor reduced or eliminated later peaks in the IFFT, whereas the earliest peak was less affected by the suppressor. The elimination of later peaks by the suppressor was accompanied by a reduction in DPOAE fine structure. Similar effects on fine structure were obtained using time-domain windowing in order to eliminate energy after the first IFFT waveform peak. These data were interpreted as indicating that the earliest IFFT peak represents the f_2 -place component and that the second IFFT peak is a reflection arising near the DP place, initiated by the intermodulation distortion at the f_2 place that traveled in the forward direction to the DP place. IFFT peaks beyond the second peak were thought to represent higher-order reflections (from the DP place) of the two initial components.

The aim of this article was to further test the two-source model of DPOAE generation by making measurements in ears with hearing loss. DPOAE measurements were made using the experimental paradigm and IFFT analysis described earlier. Subjects with particular hearing-loss configurations were chosen in an effort to manipulate the generator sources contributing to the DPOAE measured in the ear canal. It was hypothesized that the relative contributions of the f_2 and f_{DP} sources to the DPOAE recorded in the ear canal would depend on the magnitude and configuration of hearing loss (Mauermann *et al.*, 1999b; Stover *et al.*, 1999). It was predicted that in ears with normal hearing at f_2 and hearing loss at f_{DP} (“rising losses”), DPOAEs would be more likely to be dominated by the f_2 -place component. In contrast, it was predicted that in ears with hearing loss at f_2 and normal hearing at f_{DP} (“sloping losses”), DPOAEs, if present, would have a relatively large contribution from the DP place. Finally, it was predicted that for mild flat losses in the frequency regions corresponding to f_2 and f_{DP} , the relative contributions from DPOAE sources would resemble those observed in normal ears at equivalent stimulus levels, although absolute response levels would be reduced.

In order to complement the DPOAE data, SFOAEs were measured using continuous tones presented at the f_2 used during DPOAE measurements and at the average f_{DP} produced by the f_1 sweep used to construct DPOAE filter functions. It was hypothesized that, to a first approximation, hearing-loss induced alterations in the relative contributions of the two-source DPOAE would be reflected in alterations of the normal pattern of SFOAE levels at f_2 and f_{DP} .

II. METHODS

A. Stimuli

DPOAEs were obtained using custom-designed software (EMAV, Neely and Liu, 1993). A fixed- f_2 stimulus paradigm was used, in which $f_2 > f_1$. For L_2 's ranging from 25 to 55 dB SPL, f_2 was fixed at 4 kHz and f_1 was varied in 31-Hz steps ($f_2/f_1 = 1.02 - 1.4$). L_1 was set to $L_2 + 10$ dB. A suppressor-tone (f_3), placed 15.6 Hz below f_{DP} , was always present and tracked with f_1 . The suppressor level (L_3) was varied from 0 to 75 dB SPL.

SFOAEs were obtained (without a suppressor tone) using the double-evoked method (Keefe, 1998). For each SFOAE measurement, three equal-duration, equal-frequency stimuli were presented (s_1, s_2, s_{12} , where $s_{12} = s_1 + s_2$). The levels of the stimuli also were equal ($L_1 = L_2$, thus $L_{12} = L_1 + 6$ dB). The corresponding responses are p_1, p_2 , and p_{12} , and the derived SFOAE response p_d is calculated by $p_d = p_{12} - (p_1 + p_2)$. This technique extracts the nonlinear response component that is presumably of cochlear origin.

The stimuli for SFOAEs were continuous tones presented at 4 kHz (equivalent to the f_2 used in the DPOAE paradigm) and 2.7 kHz (which corresponds to the f_{DP} when $f_2 = 4$ kHz and $f_2/f_1 = 1.2$). Test levels varied from 20 to 60 dB SPL in 5-dB steps and three repetitions of each SFOAE measurement were obtained in all but two subjects. For two subjects (who were unable to complete all test sessions), a single input-output (I/O) function was generated at each test frequency, and the stimulus level was varied in 10 dB steps.

B. Measurement system

Detailed descriptions of DPOAE (Konrad-Martin *et al.*, 2001) and SFOAE (Keefe, 1998) measurements have been described previously. For DPOAEs, primary frequencies were generated using separate D/A channels of a signal processing board (Turtle Beach, Fiji), and presented through separate loudspeakers coupled to the ear canal via a probe-microphone system (Etymotic Research, ER-10C), which also recorded the response. The channel containing f_2 also was used to deliver the suppressor tone. For SFOAEs, stimuli were generated by two D/A converters of a signal processing board (CAC, DSP32) and were presented through separate sound sources using a different ER-10C probe-microphone system. Both ER-10C systems were modified by removing a 20-dB attenuator that precedes the input to each loudspeaker.

C. IFFT analysis

DPOAEs were measured for 33 f_1 frequencies, providing data at DP frequencies ranging from 1750 to 3813 Hz. These data were converted to complex values and used as input to an IFFT. The IFFT envelope was calculated as the IFFT of the “spectrum” constructed by placing $2f_1 - f_2$ DPOAE measurements elicited by the f_1 sweep into their correct frequency positions within a buffer. For a linear system, the IFFT of its frequency response is its impulse response. Because the ear is a nonlinear system, the IFFT of

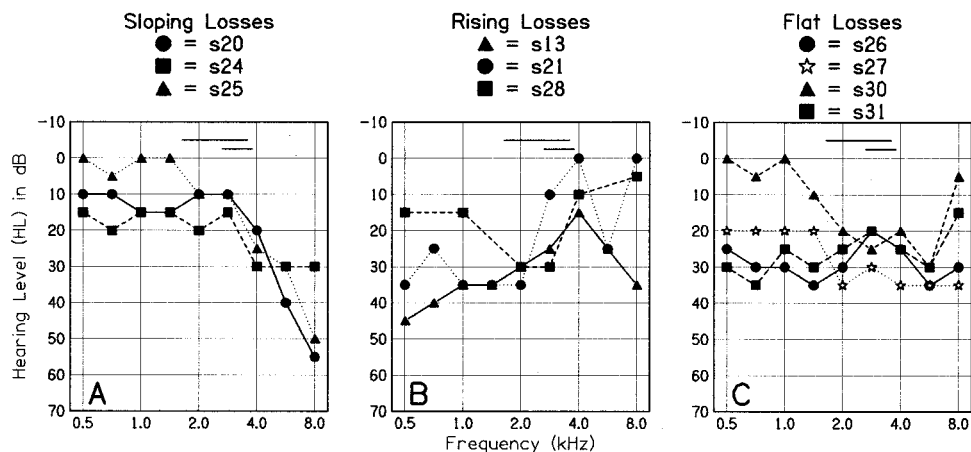


FIG. 1. Audiograms for the ten subjects with hearing loss by general hearing-loss category, which was defined over the frequency range encompassing 2–4 kHz. Panel (a): sloping losses. Panel (b): rising losses. Panel (c): flat losses. Bars near the tops of the audiograms specify the f_1 range used in the DPOAE measurements (2.9–3.9 kHz), and the corresponding f_{DP} values (1.8–3.8 kHz). The symbol used to designate a given subject in this figure refers to the same subject for subsequent figures.

the present DPOAE data is not exactly an impulse response. Nevertheless, the IFFT still preserves a direct correspondence between the slope of the phase in the frequency domain and delay in the time domain. Furthermore, there is evidence that IFFT delays are in agreement with latencies predicted by cochlear models (Konrad-Martin *et al.*, 2001). Even though the IFFT analytic signal has no direct physical correspondence, empirical evidence suggests that it provides useful information about DPOAE sources.

D. Subjects

Nine adults and one teenager with mild-to-moderate sensorineural hearing loss at f_2 and/or f_{DP} served as subjects. Efforts were made to include subjects with audiometric configurations that were likely to restrict the presumed DPOAE sources to the f_2 site (rising losses, with normal hearing at 4 kHz), or to result in reduced intermodulation distortion from the f_2 site, combined with normal reflection at the f_{DP} place (sloping losses, with normal hearing below 4 kHz). DPOAE data obtained in hearing-impaired subjects were compared to data obtained in nine normal-hearing subjects (pure-tone thresholds ≤ 15 dB HL for octave and half-octave frequencies from 0.25 to 8 kHz), which were presented in a previous paper (Konrad-Martin *et al.*, 2001). Additional DPOAE measurements were made in six of the nine normal-hearing subjects when $L_2 = 55$ dB SPL and $L_1 = 65$ dB SPL, a condition that was not included in the previous paper. In addition, SFOAE I/O functions were obtained in seven of the subjects with hearing loss and in six of the normal-hearing subjects. All subjects had normal middle-ear function as confirmed by tympanometric measurements performed prior to each test session using a 226-Hz probe tone. Figure 1 shows audiograms for subjects in sloping (a), rising (b), and flat (c) hearing-loss categories. Each of these hearing-loss categories is defined over the local frequency range encompassing 2–4 kHz. Audiometric thresholds and other identifying information for the hearing-impaired subjects are given in Table I.

III. RESULTS

A. Filter functions

Figure 2 shows DPOAE magnitudes in the form of “filter functions” for representative subjects with normal hear-

ing and with hearing loss. The first two columns show data for a normal-hearing subject at a sensation level (SL) similar to the SL shown for the impaired ears (column 1) and at an absolute SPL equivalent to the SPLs shown for two of the impaired ears (column 2). The remaining three columns provide data from individual subjects in each of three hearing-loss categories. The top row (all five columns) represents control conditions where the suppressor had no effect. The middle and bottom rows represent conditions in which the suppressor produced small and large effects in ears with normal hearing (see Konrad-Martin *et al.*, 2001).

These DPOAE responses, plotted as a function of f_{DP} , had fine structure (variations in DP level as a function of small changes in f_{DP}). As shown previously, increasing L_3 reduced the amount of fine structure in normal ears, suggesting that this feature of the response results from the disparate phase responses of distortion and reflection components (e.g., Heitmann *et al.*, 1998; Mauermann *et al.*, 1999a, 1999b; Talmadge *et al.*, 1999; Kalluri and Shera, 2001; Konrad-Martin *et al.*, 2001). Fine structure, although present, was reduced relative to overall response level when higher-level primaries were used in a subject with normal hearing [compare panels (a) and (d) in the figure]. At $L_2 = 45$, the high-level suppressor all but eliminated fine structure from the response.

Filter functions in ears with hearing loss also contained fine structure (columns 3–5). However, the degree of fine

TABLE I. Audiometric thresholds, hearing-loss category (S=sloping, R=rising, F=flat), and age for ten subjects with hearing loss. Thresholds in boldface type indicate the individuals whose data are presented as examples in subsequent figures.

HL	ID	Age	Audiometric thresholds (dB HL)								
			500	750	1000	1500	2000	3000	4000	6000	8000
S	20	64	10	10	15	15	10	10	20	40	55
S	24	60	15	20	15	15	20	15	30	30	30
S	25	68	0	5	0	0	10	10	25	30	50
R	13	77	45	40	35	35	30	25	15	25	35
R	21	35	35	25	35	35	35	10	0	25	0
R	28	39	15		15		30	30	10		5
F	26	65	25	30	30	35	30	20	25	35	30
F	27	34	20	20	20	20	35	30	35	35	35
F	30	12	0	5	0	10	20	25	20	30	5
F	31	40	30	35	25	30	25	20	25	30	15

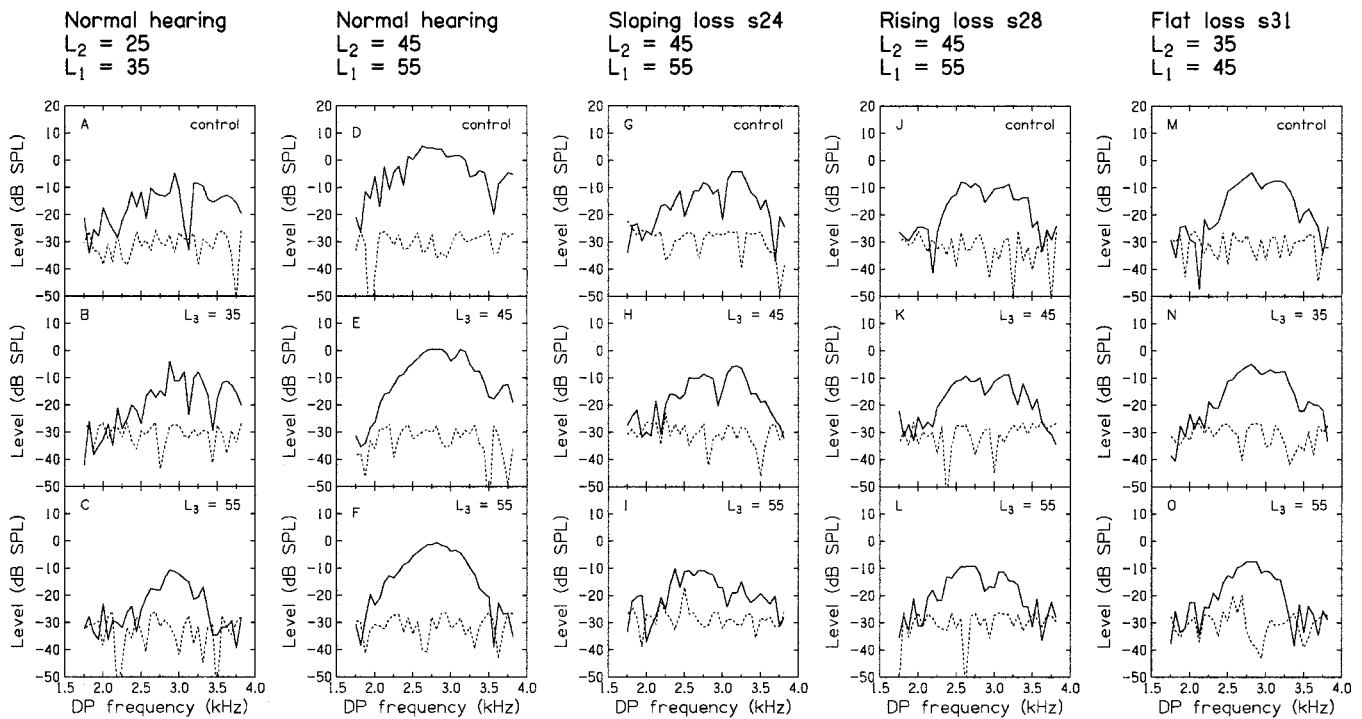


FIG. 2. Frequency-domain representations of DPOAEs in normal and impaired ears. Solid lines indicate DPOAE level as a function of f_{DP} . Dashed lines indicate the noise floor. Columns 1 and 2 represent data for a normal ear at a low and moderate stimulus level, respectively. Column 3 represents data for a subject with a sloping hearing loss, L_2 is 45 dB SPL, which is near threshold for this subject. Column 4 presents data for a subject with a rising loss, and column 5 shows data for a subject with a flat hearing-loss configuration. For each column, going down by row indicates an increase in suppressor level (L_3). Identification numbers are indicated for the hearing-impaired subjects.

structure was reduced for the ear with a rising loss [panel (j)] compared to data from normal ears [panels (a) and (d)], regardless of primary level. Further, L_3 did not remove the fine structure for the ear with rising loss. The unsuppressed filter function obtained in an ear with sloping loss [panel (g)] had more fine structure compared to the ear with rising loss [panel (j)] and the ear with a flat loss [panel (m)]. The ear with sloping loss had more fine structure compared to responses in a normal ear at an equivalent SPL [panel (d)], but had similar fine structure compared to responses in a normal ear at a similar SL [panel (a)]. It was shown previously that the relative contribution from the DP place in normal ears is greater for low-level primaries (Konrad-Martin *et al.*, 2001). These findings are consistent with the prediction that the sloping hearing loss configuration results in a relatively greater contribution to the DPOAE from the DP-place component. Taken together, these observations are consistent with the view that DPOAE fine structure in normal ears is at least partly related to interference between the two DPOAE sources (e.g., Mauermann *et al.*, 1999a).

Consistent with previous reports (Brown and Gaskill, 1990; Harris *et al.*, 1989), the unsuppressed filter functions in normal ears [Fig. 2, panels (a) and (d)] had a peak near $f_{DP} = 2.7$ kHz, which was equivalent to a primary frequency ratio (f_2/f_1) of 1.22. Ears with mild hearing loss also tended to have maximum DPOAE levels near $f_2/f_1 = 1.22$, although filter functions in some ears with sloping and rising losses had peaks that were skewed toward lower or higher f_{DP} 's [for example, see panel (g)], which means that the largest responses were not necessarily observed when $f_2/f_1 = 1.22$. This was more evident for stimulus levels near threshold,

whereas, at higher levels, the maximum DPOAE response was more likely to occur when f_2/f_1 was approximately 1.2.

B. IFFT envelopes

Figure 3 shows time-domain representations of DPOAEs (energy as a function of time) in the same subjects for whom DPOAE filter functions were shown in Fig. 2. Energy (in arbitrary units) is calculated as the squared amplitude of the IFFT response. Column 1 shows IFFT envelopes for low-level primaries in a normal ear. The unsuppressed IFFT envelope in this subject contained more than one peak [Fig. 3, panel (a)]. Introducing a suppressor just below the f_{DP} reduced or eliminated peaks in the IFFT envelope, other than the first [panel (c)] (see also Konrad-Martin *et al.*, 2001). The earliest peak was affected comparatively less by the suppressor, suggesting that peaks beyond the first are due to a secondary source at the DP place. Column 2 shows the effect of increasing L_2 to 45 dB SPL on IFFT envelopes for a normal ear. Note that the y-axis range is expanded for this column compared to the other columns in this figure to accommodate the large normal response for this stimulus level. As shown previously (Konrad-Martin *et al.*, 2001), the relative amplitudes of the initial and subsequent peaks in the unsuppressed IFFT envelope varied with primary level in ears with normal hearing. Later energy comprised a greater proportion of the total DPOAE energy when L_2 was near threshold [panel (a)] while early energy dominated IFFT responses at moderate stimulus levels [panel (d)]. One interpretation of these data is that the generator at the DP place saturates at a relatively low input level, where the

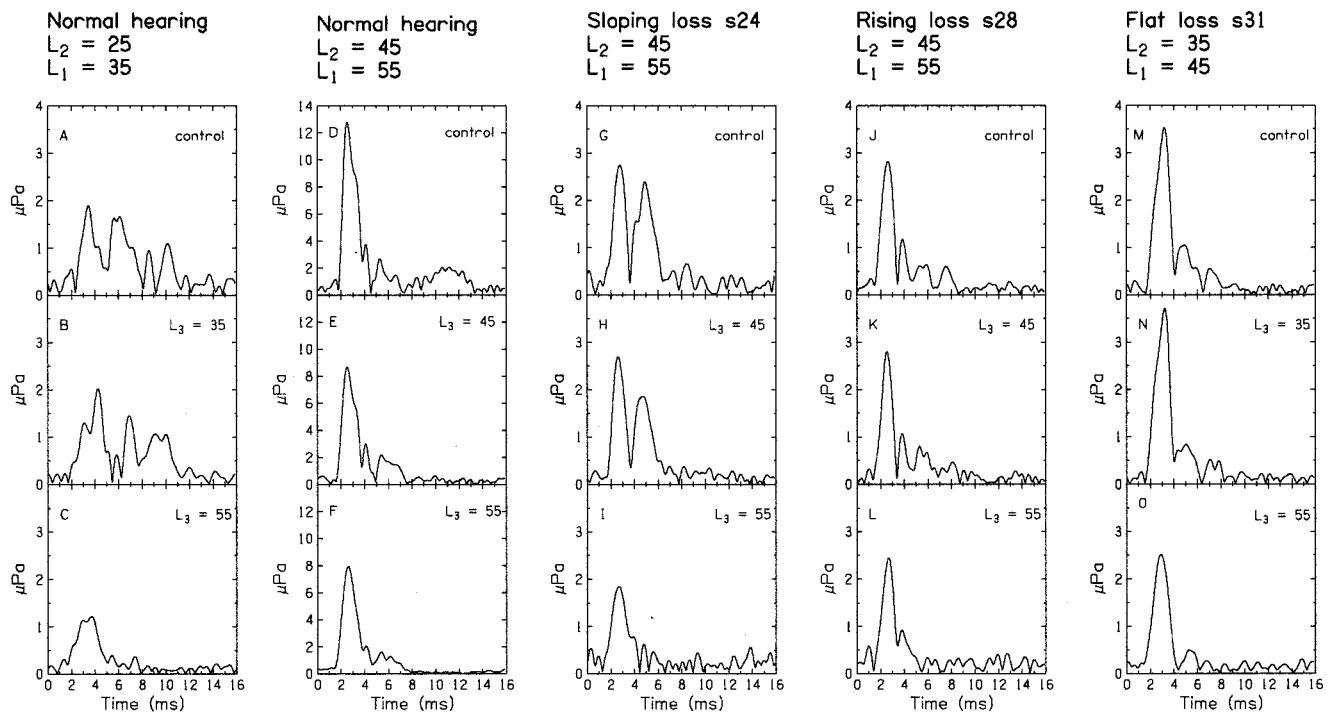


FIG. 3. Time-domain representations of DPOAEs in normal and impaired ears, following the format of Fig. 2.

“input” is the intermodulation distortion arising near the f_2 place and propagating to the DP place. In contrast, intermodulation distortion (near the f_2 place) apparently has not saturated for these stimulus levels. It is also possible that increasing the stimulus level increases suppression of the DP-place component by L_1 , particularly for closely-spaced primary frequencies (small f_2/f_1 ratios), where the DP place component is thought to dominate the DPOAE response (Knight and Kemp, 2000).

Figure 3, column 3, shows time-domain representations of DPOAEs in a subject with sloping hearing loss. L_2 is 45 dB SPL, which is at a relatively low sensation level for this subject. IFFT envelopes obtained in this subject had two peaks in the control and moderate- L_3 conditions, and one peak in the high- L_3 condition. The earliest IFFT peak shown in panel (g) had a lower magnitude compared to the normal ear when primaries are presented at the same L_2 [panel (d)]. The magnitude of the second IFFT peak in the impaired ear was similar to that of the second peak in the normal ear, but reduced relative to the first peak in the normal ear. Stated differently, later energy represented a relatively larger proportion of the response in the impaired ear compared to the normal ear at equivalent stimulus levels. Note that the relative amplitudes of the first and second IFFT peaks in the ear with sloping loss were similar to those in the normal ear at a similar sensation level (i.e., when L_2 was 25 dB SPL for the normal ear, and L_2 was 45 dB SPL for the impaired ear).

Figure 3, column 4, shows time-domain representations of DPOAEs in a subject with a rising hearing loss. The unsuppressed IFFT envelope shown for this subject [panel (j)] was dominated by a single, early peak. Later peaks were small relative to the initial peak in this subject. As a consequence, the suppressor had little effect on the IFFT. At this stimulus level, the magnitude of the earliest IFFT peak also

was small compared to IFFTs in normal ears [contrast panels (j) and (d)]. However, the magnitude of the earliest IFFT peak was similar to that shown for a normal ear when $L_2 = 25$ dB SPL [panel (a)]. This comparison shows that the DP-place component was small in the ear with a rising loss compared to a normal ear, even under conditions in which the initial intermodulation distortion appeared to be similar.

Figure 3, column 5, shows time-domain representations of DPOAEs in a subject with flat hearing loss. L_2 was 35 dB SPL, which was the lowest level that evoked a response in this ear. Unsuppressed IFFT envelopes for this ear were dominated by an early peak [panel (m)], in contrast to results obtained in normal ears for stimuli presented at an equivalent sensation level [panel (a)]. The envelope shapes were more similar to those obtained in a normal ear when L_2 was 45 dB SPL [panel (d)].

C. Effect of hearing loss on early and late DPOAE energy

Figure 4 shows the effect of hearing loss on early and late DPOAE energy (expressed as SPL in dB). Because we did not know the ear canal impedance, energy is an estimate (in arbitrary units) calculated from the mean of the squared amplitude of the IFFT waveform. Energy in the unsuppressed IFFT waveforms was partitioned into early and late energy with the aid of conditions in which a high-level suppressor tone eliminated all but the earliest peak. For ears with hearing loss, the point at which the suppressed response receded into the noise floor was used to determine the dividing point between early and late portions of the waveform. Each symbol in this figure is used to represent data from an individual subject with hearing loss (refer to Fig. 1 for the corresponding audiogram for each subject). Open versions of

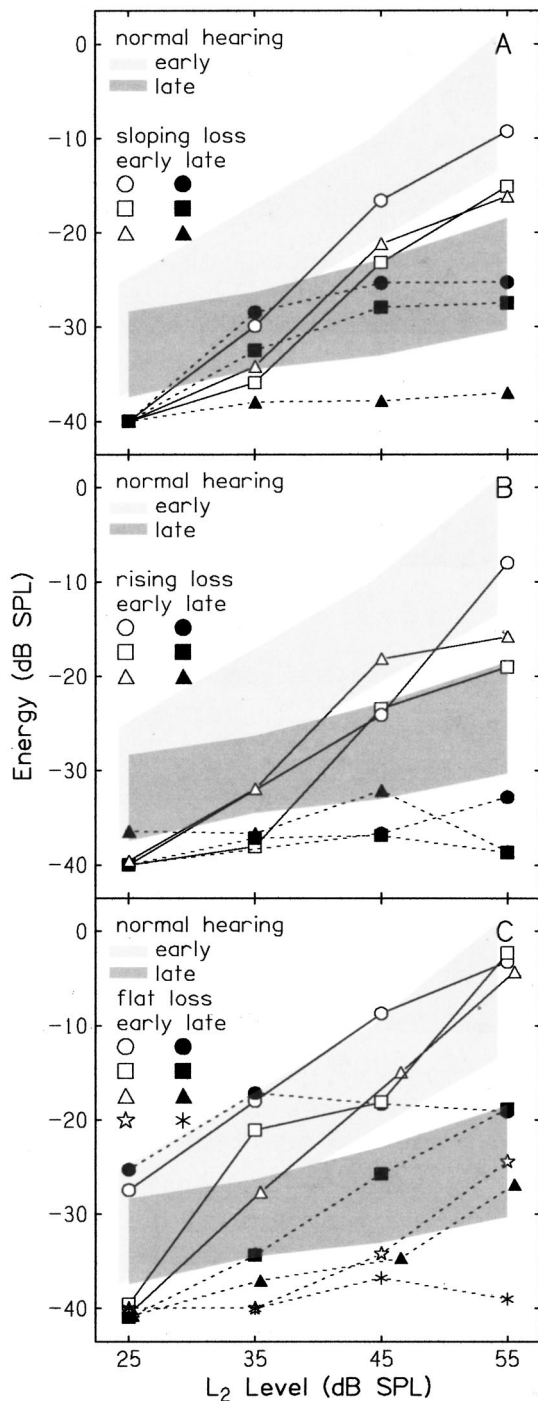


FIG. 4. Energy in the initial and subsequent IFFT peaks in normal and hearing-impaired subjects. Open symbols indicate energy in the initial peak (early energy) and closed symbols indicate energy in subsequent peaks (late energy) in the IFFT. Values are given for individual hearing-impaired subjects with sloping, rising, and flat hearing losses. Gray fill: Mean data ± 1 s.d. for normal-hearing subjects are shown in each panel for comparison. Data collection was terminated when filter functions were in the noise floor. Filter functions in the noise floor resulted in energy values (in dB) of approximately -40 dB. Therefore, points on the curves, which correspond to stimulus levels below the response threshold, were set to an arbitrary value of -40 dB.

the symbol represent energy in the earliest peak of the IFFT, whereas filled versions of the same symbol represent energy in later portions of the IFFT. Mean data (± 1 s.d.) from normal-hearing subjects (Konrad-Martin *et al.*, 2001) are

shown as shaded areas in each panel for comparison. As described previously (Konrad-Martin *et al.*, 2001), the average time point obtained across all normal-hearing subjects was used to divide IFFT envelopes in normal ears. This represents a slight difference in the methodology as compared to that used for subjects with hearing loss, as time points for ears with hearing loss were not averaged across subjects. Once conditions were reached for which the signal-to-noise ratios (SNRs) of filter function data were ≤ 6 dB, testing was terminated, because the measurements were considered unreliable. For the purposes of the analyses shown in Fig. 4, these conditions were assigned energy levels of -40 dB.

For a normal ear, early energy increased with increases in L_2 at a faster rate than later energy, as could be expected from the data shown in Fig. 3, panels (a) and (d). For one of three ears with sloping loss [Fig. 4, panel (a), subject 24, square symbols], the pattern of results as a function of primary level was shifted toward the right of the figure compared to the pattern obtained in normal ears. In other words, compared to normal ears, a higher L_2 was required for early energy to dominate the response, as predicted. For one ear with sloping loss (subject 20, circles), IFFT responses were borderline normal at 35 dB SPL and normal at 45 and 55 dB SPL. For this subject, pure-tone thresholds were 20 dB HL at 4 kHz and 10 dB HL at 2 kHz. The small difference between thresholds at 2 and 4 kHz apparently was not enough to alter the contribution of DPOAE sources. In contrast to predictions, one ear with sloping loss had little contribution from the DP place regardless of stimulus level (subject 25, triangles). This subject had a steeply sloping loss, with good low-frequency hearing.

As predicted for ears with rising hearing loss [Fig. 4, panel (b)], late energy was of low amplitude compared to normal ears for all subjects at all stimulus levels with the exception of subject 13 (triangles), when L_2 was 45 dB SPL. Late energy did not increase with increases in the level of the f_2 -place component, meaning the response was dominated by energy in the initial IFFT peak. Additionally, a slightly higher L_2 was required to produce early energy levels similar to those in normal ears. Of the three ears with rising hearing loss, two had elevated pure-tone thresholds at 6 kHz. Therefore, while the DP-place component was thought to be reduced in subjects with rising losses, damage at higher-frequency regions of the cochlea may have diminished the DPOAE arising near the f_2 place.

Results for ears with flat hearing loss [Fig. 4, panel (c)] did not conform to a single pattern. In one subject with flat hearing loss and audiometric thresholds around 25 dB HL (subject 26, circles), DPOAE responses in general, and responses linked to the DP place component, in particular, were large compared to those obtained in normal ears at equivalent stimulus levels. This example of a situation in which OAE level is a poor indicator of audiometric status highlights the notion that, while OAEs generally perform well as indicators of audiometric status, test performance is imperfect (e.g., Gorga *et al.*, 1997, 2002). On the other hand, this example calls into question our assumption that the sensorineural hearing loss in this subject is primarily due to outer hair cell dysfunction. Responses in another ear with flat

loss (subject 31, squares) fell roughly within the normal range, for levels of 35 dB SPL or greater. This result was not completely unexpected due to the mild degree of hearing loss. In two other ears with flat losses (subject 30, triangles, and subject 27, asterisks), responses were shifted toward higher L_2 's compared to responses in normal ears. The most convincing predicted effect of flat hearing loss on DPOAEs was present for subject 27 (asterisks), in which only relatively high-level stimuli ($L_2=45$, and $L_2=55$ dB SPL) elicited a response above the noise floor. Audiometric thresholds in this subject were among the poorest of all of the subjects at 4 kHz (35 dB HL).

Taken together, the IFFT data indicate that six of ten ears with hearing loss conformed to predictions presented in the Introduction for most (but not all) stimulus levels presented. Only four ears with hearing loss were unambiguously consistent with the predictions. The general category that supported predictions most strongly was the rising hearing loss group [Fig. 4, panel (b)].

D. SFOAE results

SFOAE data were obtained at two frequencies: the f_2 used during DPOAE measurements (4 kHz) and the average DP frequency (2.7 kHz) produced by the f_1 sweep. It was hypothesized that the relative contributions of the two DPOAE sources would be reflected in a change in the pattern of SFOAEs at f_2 and f_{DP} compared to that obtained in normal ears.

Figure 5 shows SFOAE levels at 2.7 and 4 kHz as a function of stimulus level in two representative normal ears and in six ears with hearing loss (two ears per hearing-loss category). Thus, each panel contains a total of four curves. For both normal ears [panel (a)], SFOAE levels were smaller at 2.7 kHz compared to 4 kHz at most stimulus levels. A notch in the 4-kHz I/O function for one of the normal ears (open circles) was repeatable across three measurements. For two ears with sloping loss [panel (b)], SFOAE levels at 2.7 kHz were equal to or larger than those measured at 4 kHz, which is the predicted effect based on the sloping hearing loss. For ears with rising losses [panel (c)], SFOAE levels, although variable, tended to be smaller at 2.7 kHz compared to 4 kHz, which is the predicted effect based on the rising hearing loss. For two ears with flat hearing losses [panel (d)], relative SFOAE levels at 2.7 and 4 kHz were similar to the responses obtained in normal ears, as predicted. In contrast to predictions, absolute SFOAE levels in two ears with flat losses were similar to those obtained in normal ears at all stimulus levels (subject 26), or once threshold was reached (subject 31). Similarly, DPOAEs obtained in these two ears with flat hearing loss were similar to or larger than those obtained in normal ears [refer to Fig. 4, panel (c)]; thus, these ears produced unexpected SFOAE and DPOAE results.

The data presented in Fig. 5 are summarized in Fig. 6, which shows the difference in dB between the SFOAEs levels at 4 and 2.7 kHz. The difference was calculated by converting from dB to amplitude, taking the ratio of the ampli-

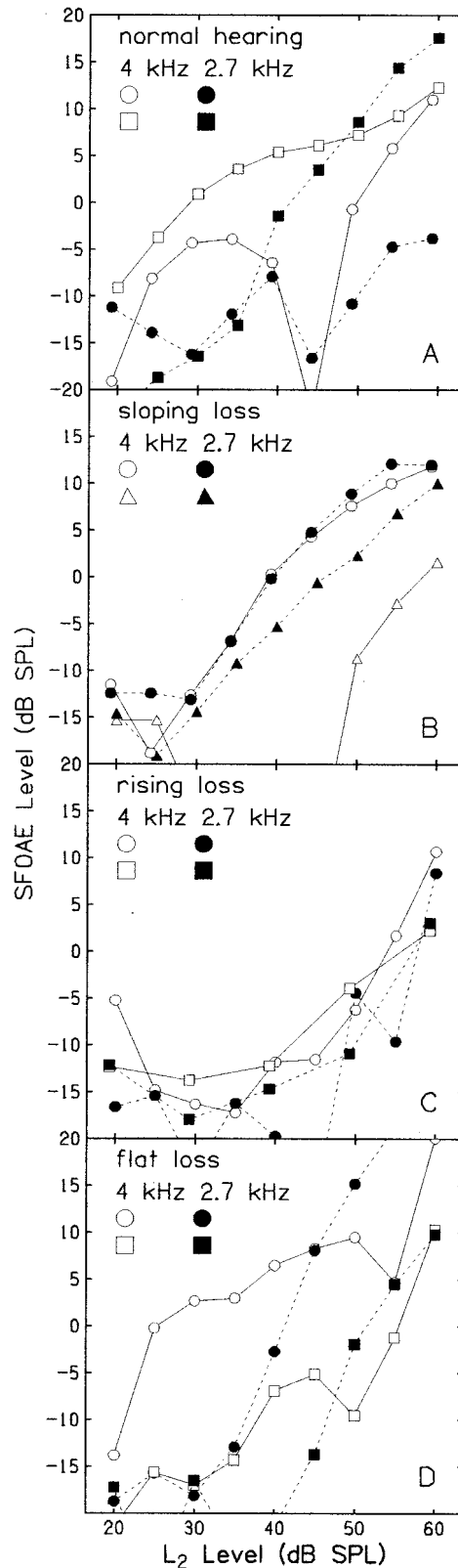


FIG. 5. SFOAEs at 2.7 and 4 kHz as a function of level in normal and hearing-impaired subjects. Panel (a): Data from two normal-hearing subjects. Panel (b): Data from two subjects with sloping losses. Panel (c): Data from two subjects with rising losses. Panel (d): Data from two subjects with a flat loss. Open symbols indicate 4-kHz data. Closed symbols indicate 2.7-kHz data.

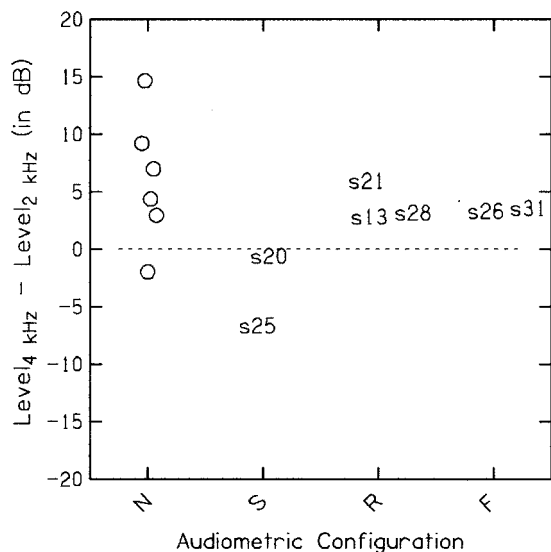


FIG. 6. The difference in dB between SFOAEs at 4 kHz and 2.7 kHz, summed across L_2 . The dashed line at 0 dB corresponds to equal SFOAE levels at 4 and 2.7 kHz. SFOAE data were obtained in a subset of subjects: Seven of the subjects with hearing loss and six of the normal-hearing subjects. Identification numbers for hearing-impaired subjects are given.

tudes at the two frequencies, averaging this ratio across all L_2 's, and then converting back to dB. The dashed line at 0 dB is given as a point of reference, corresponding to equal SFOAE levels at 4 and 2.7 kHz. For five of six normal ears, the average SFOAE level at 4 kHz was large compared to the average level at 2.7 kHz, meaning that a positive SFOAE difference was common in normal ears.

Results in ears with sloping loss showed a trend in the predicted direction: there was a reduction in the difference between 4- and 2.7-kHz responses compared to the mean difference in normal ears. We expected and found that in ears with rising losses, SFOAEs at 4 kHz were greater in amplitude than those at 2.7 kHz. In contrast to predictions, however, the observed difference was similar to, or reduced compared to the mean difference found in normal ears. One possible explanation for this is that SFOAEs corresponding to the f_2 frequency also were somewhat diminished. Subjects 13 and 21 had some hearing loss at frequencies above 4 kHz, suggesting that impaired regions of the cochlea may have influenced OAE levels arising from the f_2 place. Consistent with this explanation, the f_2 -place component of DPOAEs (as viewed using IFFT techniques) was decreased in ears with rising loss compared to those obtained in normals ears (Fig. 4). Finally, ears with flat losses also showed a positive SFOAE difference. This is consistent with the hypothesis that relative magnitudes at f_2 and f_{DP} would be similar to those observed in normal ears, although the difference in ears with flat losses was slightly less positive than the mean difference observed in normal ears. Variability in the SFOAE difference for normal ears was greater than the variability between normal and impaired groups. Therefore, it is likely that most differences across groups would not be of statistical significance. In summary, comparing the average level differences between SFOAEs at 4 and 2.7 kHz in normal ears to those obtained in hearing-loss groups did not support

predictions, with the possible exception of the group with sloping loss.

IV. DISCUSSION

A. Summary

In a previous paper, we showed that activity at the DP place could be selectively suppressed by a third tone, presumably eliminating the reflection component of the DPOAE, while leaving the initial intermodulation distortion component intact (Konrad-Martin *et al.*, 2001). In the present article, frequency-selective hearing loss as determined by pure-tone audiometry was used in an effort to manipulate contributions to the DPOAE from f_2 and DP places. In all cases, stimulus levels (L_1 , L_2 , and L_3) were chosen that were well below the levels that would produce system distortion. This stimulus-level limitation required that subjects be chosen who had no more than a mild hearing loss at f_2 , resulting in relatively small threshold differences between subjects with normal and impaired hearing. While subjects were sorted into general hearing-loss categories, individual differences within categories may still exist. In spite of these limitations, DPOAE results were unambiguously consistent with predictions based on the two-source model for DPOAE generation for four of ten cases, and were generally consistent with predictions in two additional cases. Predictions were most strongly supported in ears with rising hearing loss compared to ears with sloping and flat hearing loss. Thus, the present article extends previous work by showing that relative contributions from DPOAE sources differ in subjects with normal hearing compared to subjects having dissimilar auditory thresholds at the f_2 and DP frequencies (although not always in a predictable manner).

B. Relationship between audiometric thresholds, DPOAEs, and SFOAEs

Correlations between emission levels (DPOAE and transient OAE) and audiometric thresholds have been demonstrated in ears with normal middle-ear function (Moulin *et al.*, 1994; Gorga *et al.*, 1997, 2002; Bonfils *et al.*, 1988; Hussain *et al.*, 1998). However, correlations are imperfect due to variability in OAE levels generated by ears having similar pure-tone thresholds. There is also imprecision inherent in the measurement of pure-tone thresholds in both stimulus frequency and response level. Thus, configuration of hearing loss may not be an accurate description of cochlear status in all cases. A possible example of this in the context of the present study is an ear with flat hearing loss (subject 26), in which DPOAE and SFOAE results were consistent with each other, although both sets of data were unexpected, given the hearing loss. Results in this subject were similar to corresponding measurements obtained in normal ears. Thus, for this subject, pure-tone thresholds may not have been an accurate indicator of cochlear status. Data in this subject also raise the possibility that the hearing loss was not due to OHC damage.

In the present study, pure-tone thresholds varied for individual subjects within general categories of hearing loss. Some of these variations may have been responsible for data

not conforming to the predictions described in the Introduction. For example, one of the subjects with sloping loss had normal hearing below 2000 Hz, while the other two had thresholds that were close to the border of clinically significant hearing loss below 2000 Hz. Therefore, while the audiometric results are consistent with the f_2 -place component being affected in ears with sloping loss, in two of three subjects, audiometric results would also be consistent with observations that the DP-place component of the DPOAE was also reduced relative to normal.

A correlation exists between DPOAE levels for a given f_2 frequency, and hearing loss at frequencies higher than f_2 (Dorn *et al.*, 1999). In the present study, two of three subjects with rising loss had elevated pure-tone thresholds at 6000 Hz. Therefore, while we expected the DP-place component to be reduced in these subjects, audiometric data are consistent with the possibility that DPOAE components arising near the f_2 place may have been diminished, given the correlation observed by Dorn *et al.* (1999).

SFOAE results in the present study supported predictions of the pattern of level differences between SFOAEs at 4 and 2.7 kHz for the sloping-loss category of hearing loss, but they did not support predictions for the rising-loss and flat-loss categories. Differences between SFOAE and DPOAE results might be related to complex nonlinear interactions occurring during DPOAE measurements, between the traveling-wave response to the primaries and the distortion products. For example, the response to the primaries may have suppressed the DP-place component of the $2f_1$ - f_2 DPOAE. Such interactions would not be expected to be present for single tones, such as in the SFOAE measurement paradigm. This hypothesis is supported by the results of a recent study in which SFOAE behavior more closely resembled that of the DP-place component of the DPOAE when the SFOAE stimulus was presented with an additional tone that mimicked the f_1 primary in the DPOAE paradigm (Kalluri and Shera, 2001). Moreover, the IFFT calculation combines DPOAE responses across a range of frequencies, whereas, the SFOAE responses were measured at a single frequency within this range.

Agreement between OAE results and audiometric thresholds may have been improved if middle-ear transmission characteristics for individual subjects had been taken into account. Differences in middle ear transmission characteristics across subjects may have resulted in increased variability in the DPOAE and SFOAE data obtained in normal and impaired ears.

C. Source of DPOAE fine structure

In normal ears, DPOAE fine structure decreases in level with increasing stimulus level when $f_2 = 4$ kHz (e.g., He and Schmiedt, 1993). This decrease in fine structure has been shown to accompany a shift in the relative magnitudes of early and late energy in the time representations (IFFT envelopes) of DPOAE filter functions (Konrad-Martin *et al.*, 2001). That is, late energy was shown to be a smaller proportion of the total ear-canal DPOAE energy as stimulus level was increased. In the present study, DPOAE fine structure was reduced by frequency-specific hearing loss at the

DP place (Mauermann *et al.*, 1999b), although the effect was small and variable across subjects. These observations may be consistent with the hypothesis that DPOAE fine structure is a by-product of interference between multiple sources (e.g., Heitmann *et al.*, 1998; Mauermann *et al.*, 1999a).

D. Source of DPOAE filter function shape

The maximum DPOAE level in normal ears is obtained when a primary ratio (f_2/f_1) of about 1.2 is used, and even among normal ears, is known to vary across individuals and with stimulus frequency and level (Harris *et al.*, 1989; Gaskill and Brown, 1990). In a previous study (Stover *et al.*, 1999), ears with steeply rising hearing-loss configurations (impaired hearing at the f_{DP} and normal hearing at f_2) had a high-pass filter-function shape, suggesting that the characteristic filter-function shape in normal ears is due to interaction between DPOAE sources. In the present study, there was variability in the f_2/f_1 ratio that produces maximal DPOAE amplitude in ears with mild hearing loss, including those ears with rising hearing loss. Therefore, the present data do not support the hypothesis that the characteristic filter-function shape (in particular, the dip in the response near small f_2/f_1 ratios) is due to the interaction between DPOAE sources, as was suggested by Stover *et al.* (1996). Moreover, in a previous study (Konrad-Martin *et al.*, 2001, Fig. 3), the typical filter-function shape was present even when late energy (which was linked to the DP place) was removed by editing the response in the time domain. Thus, it would appear that the characteristic (bandpass) filter-function shape does not require a contribution from the DP place.

V. CONCLUSIONS

DPOAEs were measured in subjects with frequency-specific hearing loss, such that predictions based on the two-source model of DPOAE generation could be tested. DPOAE data were collected in the form of “filter functions,” from which amplitude and phase information was used to derive an IFFT waveform. IFFT waveforms were interpreted in relation to previous data from normal-hearing subjects (Konrad-Martin *et al.*, 2001). Hearing loss restricted in frequency to the DP place tended to reduce the reflection component of the DPOAE, whereas hearing loss that included both the intermodulation place (close to where f_2 was represented) and the DP place tended to produce abnormal, although unpredictable IFFT results. Predictions based on a two-source model were supported by the IFFT waveforms in only a subset of subjects. SFOAEs were also measured, at stimulus frequencies chosen to approximate both the intermodulation place (4 kHz) and the average reflection place (2.7 kHz) from the DPOAE measurements. With the possible exception of sloping losses, SFOAE results in ears with hearing loss did not match predicted amplitude differences between SFOAEs at 4 and 2.7 kHz. Possible explanations for the lack of generalizability of the present results may be due to the small number of subjects (related to the difficulty in finding subjects with well-defined, mild hearing losses) and the assumption that the pure-tone audiogram provides an accurate measurement of cochlear status in all cases. More data

are needed to explore the relationships between DPOAE and SFOAE responses across different configurations of hearing loss.

ACKNOWLEDGMENTS

This work was supported by the NIH (RO1 DC02251, RO1 DC03784, and T32 DC00013). We would like to thank two anonymous reviewers for their helpful comments and suggestions on an earlier version of this manuscript.

- Bonfils, P., Piron, J.-P., Uziel, A., and Pujol, R. (1988). "A correlative study of evoked otoacoustic emission properties and audiometric thresholds," *Arch. Otolaryngol.* **112**, 272–277.
- Brown, A. M., and Gaskell, S. A. (1990). "Measurement of acoustic distortion reveals underlying similarities between human and rodent mechanical responses," *J. Acoust. Soc. Am.* **88**, 840–849.
- Dorn, P. A., Piskorski, P., Gorga, M. P., Keefe, D. H., and Neely, S. T. (1999). "Predicting audiometric status from distortion product otoacoustic emissions using multivariate analyses," *Ear Hear.* **20**, 149–163.
- Dreisbach, L. E. (1999). "Characterizing the $2f_1-f_2$ distortion-product otoacoustic emission and its generators measured from 2 to 20 kHz in humans," Ph.D. thesis, Northwestern University.
- Dreisbach, L. E., and Siegel, J. H. (1999). "Level and phase relationships of distortion-product otoacoustic emission sources with varied primary frequency ratios in humans," Midwinter Meeting of the Assoc. for Res. in Otolaryngol. Abs., Vol. 392, p. 98.
- Gaskell, S. A., and Brown, A. M. (1990). "The behavior of the acoustic distortion product, $2f_1-f_2$, from the human ear and its relation to auditory sensitivity," *J. Acoust. Soc. Am.* **88**, 821–837.
- Gorga, M. P., Neely, S. T., and Dorn, P. A. (2002). "Distortion product otoacoustic emissions in relation to hearing loss," in *Otoacoustic Emissions: Clinical Applications*, 2nd ed., edited by M. S. Robinette and T. J. Glattke (Thieme Medical, New York), pp. 243–272.
- Gorga, M. P., Neely, S. T., Ohlrich, B., Hoover, B., Redner, J., and Peters, J. (1997). "From laboratory to clinic: A large scale study of distortion product otoacoustic emissions in ears with normal hearing and ears with hearing loss," *Ear Hear.* **18**, 440–455.
- Harris, F. P., Lonsbury-Martin, B. L., Stagner, B. B., Coats, A. C., and Martin, G. K. (1989). "Acoustic distortion products in humans: systematic changes in amplitude as a function of f_2/f_1 ratio," *J. Acoust. Soc. Am.* **85**, 220–229.
- He, N.-J., and Schmeidt, R. A. (1993). "Fine structure of the $2f_1-f_2$ acoustic distortion product: Changes with primary level," *J. Acoust. Soc. Am.* **94**, 2659–2669.
- Heitmann, H. J., Waldmann, B., Schnitzler, H. U., Plinkert, P. K., and Zenner, H.-P. (1998). "Suppression of distortion product otoacoustic emissions (DPOAE) near $2f_1-f_2$ removes dp-gram fine structure—evidence for a secondary generator," *J. Acoust. Soc. Am.* **103**, 1527–1531.
- Hussain, D. M., Gorga, M. P., Neely, S. T., Keefe, D. H., and Peters, J. (1998). "Transient evoked otoacoustic emissions in patients with normal hearing and in patients with hearing loss," *Ear Hear.* **19**, 434–439.
- Kalluri, R., and Shera, C. A. (2001). "Distortion-product source unmixing: A test of the two-mechanism model for DPOAE generation," *J. Acoust. Soc. Am.* **109**, 622–637.
- Keefe, D. (1998). "Double-evoked otoacoustic emissions. I. Measurement theory and nonlinear coherence," *J. Acoust. Soc. Am.* **103**, 3489–3498.
- Kemp, D. T., and Brown, A. M. (1983). "An integrated view of cochlear mechanical nonlinearities observable from the ear canal," in *Cochlear Mechanics*, edited by E. de Boer and M. A. Viergever (Delft U.P., Delft), pp. 75–82.
- Kim, D. O. (1980). "Cochlear mechanics: Implications of electrophysiological and acoustical observations," *Hear. Res.* **2**, 297–317.
- Knight, R. D., and Kemp, D. T. (2000). "Indications of different distortion product otoacoustic emission mechanisms from a detailed f_1, f_2 area study," *J. Acoust. Soc. Am.* **107**, 457–473.
- Konrad-Martin, D., Neely, S., Keefe, D., Dorn, P., and Gorga, M. (2001). "Sources of distortion product otoacoustic emissions revealed by suppression experiments and inverse fast Fourier transforms in normal ears," *J. Acoust. Soc. Am.* **109**, 2862–2879.
- Mauermann, M., Uppenkamp, S., van Hengel, P. W. J., and Kollmeier, B. (1999a). "Evidence for the distortion product frequency place as a source of distortion product otoacoustic emission (DPOAE) fine structure in humans. I. Fine structure and higher-order DPOAE as a function of the frequency ratio f_2/f_1 ," *J. Acoust. Soc. Am.* **106**, 3473–3483.
- Mauermann, M., Uppenkamp, S., van Hengel, P. W. J., and Kollmeier, B. (1999b). "Evidence for the distortion product frequency place as a source of distortion product otoacoustic emission (DPOAE) fine structure in humans. II. Fine structure for different shapes of cochlear hearing loss," *J. Acoust. Soc. Am.* **106**, 3484–3491.
- Moulin, A., Bera, J.-C., and Collet, L. (1994). "Distortion product otoacoustic emissions and sensorineural hearing loss," *Audiology* **33**, 305–326.
- Moulin, A., and Kemp, D. T. (1996). "Multicomponent acoustic distortion product otoacoustic phase in humans. II. Implications for distortion product otoacoustic emissions generation," *J. Acoust. Soc. Am.* **100**, 1640–1662.
- Neely, S. T., and Liu, Z. (1993). "EMAV: Otoacoustic emission averager," Tech. Memo No. 17 (Boys Town National Research Hospital, Omaha).
- O'Mahoney, C. F., and Kemp, D. T. (1995). "Distortion product otoacoustic emission delay measurement in human ears," *J. Acoust. Soc. Am.* **97**, 3721–3735.
- Shera, C. A., and Guinan, J. J. (1999). "Evoked otoacoustic emissions arise by two fundamentally different mechanisms: A taxonomy for mammalian OAEs," *J. Acoust. Soc. Am.* **105**, 782–798.
- Shera, C. A., and Zweig, G. (1993). "Order from chaos: Resolving the paradox of periodicity in evoked otoacoustic emission," in *Biophysics of Hair Cell Sensory Systems*, edited by H. Duifhuis, J. W. Horst, P. van Dijk, and S. M. van Netten (World Scientific, Singapore), pp. 54–63.
- Stover, L. J., Neely, S. T., and Gorga, M. P. (1996). "Latency and multiple sources of distortion product otoacoustic emissions," *J. Acoust. Soc. Am.* **99**, 1016–1024.
- Stover, L. J., Neely, S. T., and Gorga, M. P. (1999). "Cochlear generation of intermodulation distortion revealed by DPOAE frequency functions in normal and impaired ears," *J. Acoust. Soc. Am.* **106**, 2669–2678.
- Talmadge, C. L., Long, G. R., Tubis, A., and Dhar, S. (1999). "Experimental confirmation of the two-source interference model for the fine structure of distortion product otoacoustic emissions," *J. Acoust. Soc. Am.* **105**, 275–292.

Pure-tone threshold estimation from extrapolated distortion product otoacoustic emission I/O-functions in normal and cochlear hearing loss ears

Paul Boege and Thomas Janssen^{a)}

Hals-Nasen-Ohrenklinik, Technische Universität München, Ismaningerstrasse 22, D-81675 Munich, Germany

(Received 8 August 2001; revised 22 January 2002; accepted 24 January 2002)

A new method for direct pure-tone threshold estimation from input/output functions of distortion product otoacoustic emissions (DPOAEs) in humans is presented. Previous methods use statistical models relating DPOAE level to hearing threshold including additional parameters e.g., age or slope of DPOAE I/O-function. Here we derive a DPOAE threshold from extrapolated DPOAE I/O-functions directly. Cubic $2f_1-f_2$ distortion products and pure-tone threshold at f_2 were measured at 51 frequencies between $f_2=500$ Hz and 8 kHz at up to ten primary tone levels between $L_2=65$ and 20 dB SPL in 30 normally hearing and 119 sensorineural hearing loss ears. Using an optimized primary tone level setting ($L_1=0.4L_2+39$ dB) that accounts for the nonlinear interaction of the two primaries at the DPOAE generation site at f_2 , the pressure of the $2f_1-f_2$ distortion product p_{DP} is a linear function of the primary tone level L_2 . Linear regression yields correlation coefficients higher than 0.8 in the majority of the DPOAE I/O-functions. The linear behavior is sufficiently fulfilled for all frequencies in normal and impaired hearing. This suggests that the observed linear functional dependency is quite general. Extrapolating towards $p_{DP}=0$ yields the DPOAE threshold for L_2 . There is a significant correlation between DPOAE threshold and pure-tone threshold ($r=0.65$, $p<0.001$). Thus, the DPOAEs that reflect the functioning of an essential element of peripheral sound processing enable a reliable estimation of cochlear hearing threshold up to hearing losses of 50 dBHL without any statistical data. © 2002 Acoustical Society of America. [DOI: 10.1121/1.1460923]

PACS numbers: 43.64.Jb, 43.64.Kc, 43.64.Yp [BLM]

I. INTRODUCTION

Predicting pure-tone threshold from DPOAE I/O-functions could be a valuable addition to current established audiometric methods. Previous works used statistical models relating DPOAE level to hearing threshold including additional demographic parameters to predict normal versus abnormal pure-tone threshold (Kimberly *et al.*, 1994). However, referring to the literature, there is almost no physiological evidence that supports the expectation that DPOAEs can predict pure-tone threshold directly (Kimberley *et al.*, 1997). Solely, Gorga *et al.* (1997) suggested that the audiometric threshold could be predicted from DPOAEs.

By relating the DPOAE level and growth rate of DPOAE I/O-functions to pure-tone threshold, a correlation much stronger than reported before can be found (Janssen *et al.*, 1998; Kummer *et al.*, 1998) when using an optimum primary tone level setting (Kummer *et al.*, 2000). Here, we further analyze optimum DPOAE I/O-functions to answer two questions. First, do DPOAE I/O-functions reflect basilar membrane responses known from animal data (e.g., Ruggero *et al.*, 1997) and, if so, what is the relationship between input and output and can it easily be described by a simple mathematical approximation? Second, is it possible to derive DPOAE threshold from DPOAE I/O function and how close is its correspondence to hearing threshold?

In this study we recorded DPOAE I/O-functions over a wide primary tone level range and at a high frequency resolution in 30 normal and 119 sensorineural hearing loss ears. DPOAE I/O-functions of the normally hearing volunteers have been compared to the basilar membrane I/O-functions from animals (Ruggero *et al.*, 1997) to demonstrate the similarity of the basilar membrane and the DPOAE growth when DPOAEs are elicited by a primary tone setting which accounts for the different compression of the two primaries at the DPOAE generation site, at f_2 .

We will show that the $2f_1-f_2$ distortion product pressure p_{DP} is a linear function of the primary tone level L_2 and therefore DPOAE threshold can easily be derived from the semi-log DPOAE I/O-function by extrapolation using linear regression analysis. We will further show that there is a close correspondence between DPOAE threshold and pure-tone threshold in most of the normal and impaired ears tested.

We therefore suggest DPOAEs to reflect intrinsic sound processing mechanisms at the threshold of hearing enabling an objective estimation of hearing loss in cochlear impairment. In comparison to other methods [e.g., auditory brainstem responses (ABR)] extrapolated DPOAE I/O-functions provide a fully automatic method for assessing hearing loss.

II. METHODS

A. Subjects

Thirty normal-hearing subjects (right ears only) and 119 ears out of 92 patients (59 right and 60 left ears) suffering

^{a)} Author to whom correspondence should be addressed. Electronic mail: t.janssen@lrz.tum.de

from sensorineural hearing loss were measured in this study. The normal-hearing subjects (18 females and 12 males) were aged between 12 and 33 years (mean 24 years). According to clinical audiometry their hearing loss was lower than 20 dB at octave frequencies from 0.125 to 8 kHz. The patients (35 females and 84 males) were aged between 20 and 60 years (mean 39 years). Among the sensorineural hearing loss ears there were 23 without and 96 with tinnitus. Hearing losses ranged from 20 to 80 dB HL. The hearing loss was due to acoustic trauma, Ménière disease, head trauma as well as sudden and progressive hearing loss of unknown etiology. ABRs were recorded and the I-V interpeak interval was measured to exclude a retrocochlear pathology (see Stockard *et al.*, 1980). In severe hearing-loss cases, where ABR wave-I could not be detected and, correspondingly, the I-V interpeak interval was not available, computer tomography (CT) was performed. In all cases neither ABR nor CT revealed a retrocochlear process. All ears had normal middle ear function proved by tympanometry.

B. DPOAE measurement

The measurements of $2f_1 - f_2$ DPOAE were performed at 51 frequencies between $f_2 = 488$ and 8008 Hz with a constant f_2/f_1 ratio ($f_2 > f_1$) of 1.2 using Cub^eDis™ instrumentation (Mimosa Acoustics, NJ). For details, see Kummer *et al.* (1998, 2000). Up to ten stimulus levels from $L_2 = 65$ to 20 dB SPL have been applied, whereby $L_1 - L_2$ increased with decreasing primary tone level according to the equation $L_1 = 0.4 \cdot L_2 + 39$ dB. This parameter paradigm was used to account for the nonlinear interaction of the two primaries at the DPOAE generation site at the f_2 -place. DPOAEs were accepted as valid for signal-to-noise ratios exceeding 6 dB.

C. DPOAE off-line analysis to obtain DPOAE pressure I/O-functions for the estimation of DPOAE threshold

From the DPOAE levels recorded, DPOAE pressure I/O-functions were reconstructed by plotting the DPOAE sound pressure $p_{DP} = p_0 10^{(L_{DP}/20)}$ dB with $p_0 = 20$ μ Pa against the primary tone level L_2 . Finding a linear dependency between the DPOAE pressure p_{DP} and the primary tone level L_2 a simple fit was performed using linear regression analysis. For estimating the DPOAE threshold an extrapolation of the DPOAE pressure I/O-function was performed. The point of intersection of the extrapolated regression line with the L_2 coordinate was calculated and served as an estimated DPOAE threshold level L_{EDPT} . The estimated DPOAE threshold level $L_{EDPT}(f_2)$ was compared to the psycho-acoustic pure-tone threshold $L_t(f_2)$.

D. High-resolution pure-tone threshold measurement

For a reliable comparison the psycho-acoustic pure-tone threshold L_t was recorded immediately after the DPOAE measurement at all 51 f_2 frequencies with the same in-the-ear probe without changing the probe fit. L_t was obtained by using a computer-controlled method of sound pressure level adjustment. The volunteer or patient was instructed to decrease or increase the f_2 -tone sound pressure level by button

press or release as long as he had a hearing sensation or as soon as he had no sensation, respectively. The sound pressure level was changed in steps of 1 dB with a velocity of ± 5 dB/s over a period of 30 s for each f_2 . L_t was estimated from an average of the reversal points of the f_2 -tone sound pressure level within the flat run of the adjustment (usually from the fifth second). The associated standard deviation estimates the error of L_t to be 3.9 dB in average over all measured ears.

To avoid artificial distortion produced by the probe maximum tone level was restricted to 65 dB SPL. Measurements were performed in a double-walled sound-proof room. DPOAE measurement took up to 35 min, threshold measurement up to 25 min per ear.

E. Comparison between DPOAE pressure I/O-function and basilar membrane I/O-function

In order to compare DPOAE pressure I/O-function and basilar membrane I/O-function the data of Ruggero *et al.* (1997) have been used where basilar membrane responses to single tones were measured with laser velocimetry. The velocity spectra measured at one place in the cochlea was interpreted here as a velocity distribution over the location for one frequency. To qualitatively estimate the basilar membrane I/O-function for the cubic distortion $2f_1 - f_2$ the basilar membrane velocity v_{DP} was approximated by superposition of the two independent responses v_1 and v_2 for the single tones f_1 and f_2 neglecting any interaction.

III. RESULTS

A. DPOAE pressure depends logarithmically on the f_2 primary tone sound pressure when using the primary tone level setting $L_1 = 0.4 \cdot L_2 + 39$ dB

Using the primary tone level setting $L_1 = 0.4 \cdot L_2 + 39$ dB in most of the I/O-functions a logarithmic dependency of the distortion product sound pressure p_{DP} on the sound pressure p_2 of the f_2 primary tone was found. In semi-logarithmic scale this gives a linear dependency between p_{DP} and the primary tone level L_2 . In Fig. 1 the DPOAE sound pressure p_{DP} (upper panel) and the DPOAE sound pressure level L_{DP} (lower panel) of the same I/O-function are plotted as a function of the primary tone level L_2 . The linear fit to the data (solid line) proves the logarithmic dependency of p_{DP} on p_2 . The correlation coefficient r^2 gives a measure of the accuracy of the linear fit. For correlation coefficients close to one the measurement data can be described by the two parameters a and b of the linear fit:

$$p_{DP}(L_2) = a \cdot (L_2 - b). \quad (1)$$

Parameter a gives the slope of the linear DPOAE pressure I/O-function, which is constant over L_2 in contrast to the varying slope of the DPOAE level I/O-function (compare upper and lower panel in Fig. 1). The second parameter b represents the threshold value for L_2 , where the DPOAE pressure is zero.

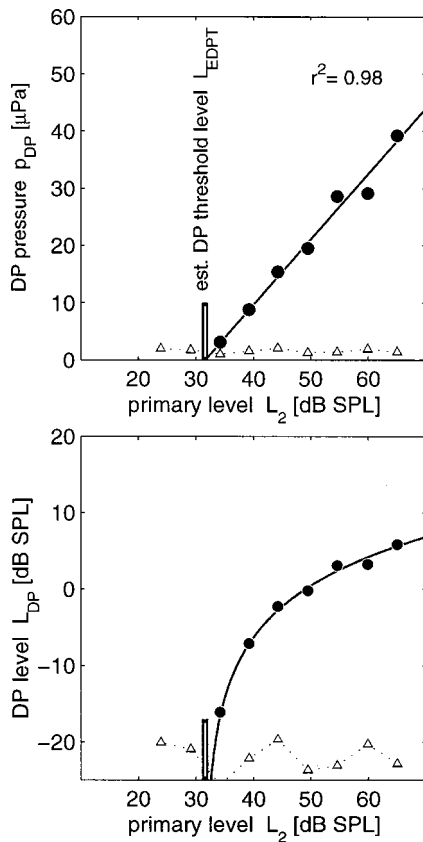


FIG. 1. DPOAE I/O function at $f_2 = 1709$ Hz for subject S.I. (right ear). In the upper panel the DPOAE sound pressure p_{DP} is plotted as a function of the primary tone level L_2 (semi-logarithmic scale) and in the lower panel the same data is plotted as DPOAE level L_{DP} as a function of L_2 (log-log scale). Filled circles (DPOAE values) and open triangles (noise floor) give the measurement values. The solid line shows the fitted linear function ($r^2 = 0.98$) in both scales together with the estimated DPOAE threshold level L_{EDPT} (vertical bar) revealing logarithmic relationship of the DPOAE pressure to the primary tone pressure.

B. DPOAE pressure I/O-function with $L_1 = 0.4L_2 + 39$ dB is similar to Ruggero *et al.*'s basilar membrane I/O-function

The basilar membrane response data of Ruggero *et al.* (1997) are interpreted here as a spatial velocity distribution along the basilar membrane over the location x for one frequency at different stimulus levels L . The original data were interpolated with respect to x and L . The left panel in Fig. 2 shows the velocity v of the basilar membrane plotted over the location x for stimulus levels L ranging from 20 to 90 dB SPL where x_{CF} is the location of the characteristic frequency (CF). In the right panel of Fig. 2 the same data are plotted as velocity I/O-functions $v(L)$ over stimulus level L for various locations relative to CF. At the CF place x_{CF} (filled circles) the velocity shows a linear dependence to the stimulus level L , which means a logarithmic dependence to the stimulus sound pressure p as proved by the linear behavior in the semi-logarithmic plot. For locations above x_{CF} ($x = 1.2x_{CF}$) and below x_{CF} ($x = 0.4x_{CF}$, $0.6x_{CF}$, and $0.8x_{CF}$) the velocity I/O-functions show a completely different dependency on the stimulus level. In a linear plot of velocity v versus stimulus pressure p (not shown here) this dependency is identified as close to linear.

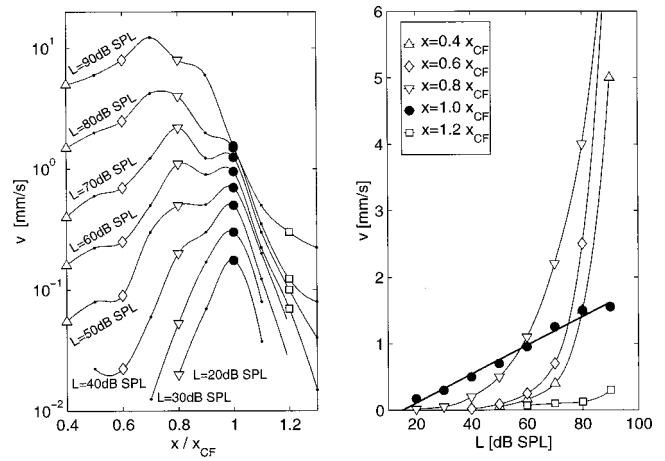


FIG. 2. The left panel shows the basilar membrane velocity data from Ruggero *et al.* (1997) interpreted as a velocity distribution over location x for one frequency for stimulus intensities from 20 to 90 dB SPL in steps of 10 dB. x_{CF} is the location of the characteristic frequency (CF). The right panel illustrates the I/O-functions in a semi-logarithmic scale at different locations. Filled circles give the I/O-functions at x_{CF} revealing logarithmic relationship of the basilar membrane response to stimulus sound pressure.

To model the growth of the cubic distortion produced by two stimuli with frequencies f_1 and f_2 and levels L_1 and L_2 the basilar membrane velocity was approximated by superposition of the two independent responses for single tones of frequency f_1 and f_2 , respectively. This very rough approximation is sufficient here, since we are only interested in the qualitative behavior of the distortion product amplitude at the place x_{CF2} as a function of level L_2 for certain settings of L_1 .

In Fig. 3 the velocity v_2 is plotted over the normalized location x/x_{CF2} for stimulus levels from $L_2 = 20$ dB to $L_2 = 80$ dB in 20-dB steps (solid line) with the place of the CF of the f_2 stimulus as reference. The velocity distribution v_1 of the f_1 stimulus (dashed line) is inserted in the f_2 location plot by shifting it by a factor of 1.2 [corresponding to the frequency ratio of the DPOAE primary tones ($f_2/f_1 = 1.2$)]. In the left column of Fig. 3 the stimulus level L_1 is adjusted for each L_2 such that it gives an equivalent response $v_1(L_1) = v_2(L_2)$ for both stimuli at x_{CF2} whereas in the right column the responses of the two stimuli are plotted for $L_1 = L_2$.

The superposition of the responses with frequency f_1 and f_2 is calculated in a first-order approximation as the mean value of the single responses $v_{DP} = (v_1 \cdot v_2)^{1/2}$. The shaded areas in Fig. 3 show the resulting velocity distribution for the different level settings. In general maximum distortion is suggested to be produced at locations on the basilar membrane where both responses interact maximally, i.e., where they have equal amplitudes. This is true in the simple approximation v_{DP} of the distortion product velocity in Fig. 3. The place of maximum interaction is close to x_{CF2} (open and filled circles in Fig. 3). In the left column of Fig. 3 the responses v_1 , v_2 to the stimuli and the approximation v_{DP} to the cubic distortion coincide at location x_{CF2} (filled circles) giving the maximum value of v_{DP} . When plotting these velocity values over stimulus level L_2 the growth of $v_{DP}(L_2)$ is linear in the semi-logarithmic scale (see Fig. 4, filled circles).

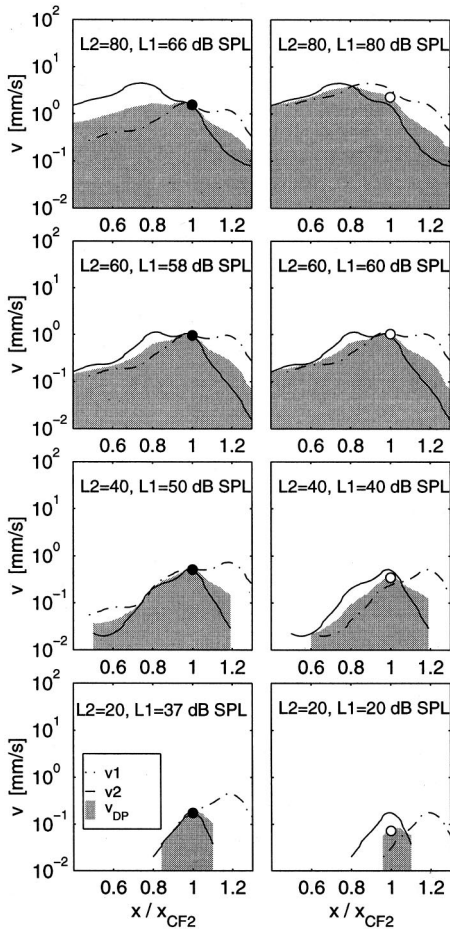


FIG. 3. The left column shows the velocity distribution v_1 (dashed line) and v_2 (solid line) of two tones corresponding to frequencies f_2 and $f_1 = 1.2 \cdot f_2$ and the overlap of two tones calculated by $v_{DP} = (v_1 \cdot v_2)^{1/2}$ (shaded area) for the $L_1 > L_2$ condition. For $L_2 = 20, 40, 60, 80$ dB SPL the level L_1 is adjusted to give equal response $v_1(L_1) = v_2(L_2)$ at $x = x_{CF2}$. Note that location is normalized by x_{CF2} here. In the right column v_1 , v_2 , and v_{DP} for the $L_1 = L_2$ condition are plotted. In the $L_1 > L_2$ condition the overlap at x_{CF2} coincides with v_2 (filled circles) in contrast to the $L_1 = L_2$ condition (open circles).

Thus, the growth of the cubic distortion shows the same behavior as the single tone response $v(L)$ at x_{CF} in Fig. 2.

In contrast to this, when plotting the maximum values of the approximated velocity v_{DP} of the cubic distortion for the $L_1 = L_2$ condition over stimulus level L_2 (open circles in Fig. 4) the growth is not linear and is similar to the growth of the single tone response $v(L)$ in Fig. 2 at locations below x_{CF} .

This demonstrates that for an appropriate L_1 stimulus setting with increasing level difference $L_1 - L_2$ (like the primary tone level setting $L_1 = 0.4L_2 + 39$ dB used in this study for eliciting DPOAE) the growth of the cubic distortion $v_{DP}(L_2)$ does correspond to the compressive growth of a single tone response at the place of its CF. The similarity of the compressive growth of the basilar membrane response to the cubic distortion with the DPOAE pressure growth measured in normal-hearing ears (compare Figs. 4 and 1) proves that DPOAEs are capable to reflect nonlinear cochlear sound processing when using a primary tone level setting for eliciting DPOAE that accounts for the different compression of the two primaries at the f_2 place.

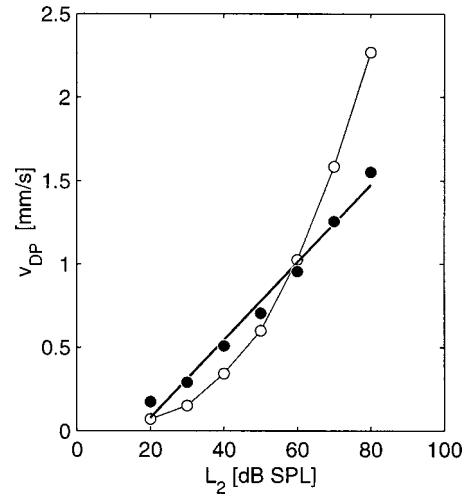


FIG. 4. I/O-functions derived from the overlap v_{DP} at x_{CF2} in Fig. 3. The open circles show the values of v_{DP} for the $L_1 = L_2$ condition, filled circles for the $L_1 > L_2$ condition. This illustrates that when L_1 is adjusted to fulfill $v_1(L_1) = v_2(L_2)$ at $x = x_{CF2}$ the overlap v_{DP} resembles the logarithmic growth of v_2 response corresponding to the DPOAE pressure growth (see Fig. 1).

C. DPOAE threshold can be estimated by means of extrapolated DPOAE pressure I/O-functions

Following the linear fit in Eq. (1) the DPOAE pressure I/O-functions measured with the $L_1 = 0.4 \cdot L_2 + 39$ dB primary tone level setting can be described by a logarithmic function of the primary-tone sound pressure p_2 :

$$p_{DP}(p_2) = a \cdot \log(p_2/b). \quad (2)$$

The parameters can be determined by a simple linear fit to

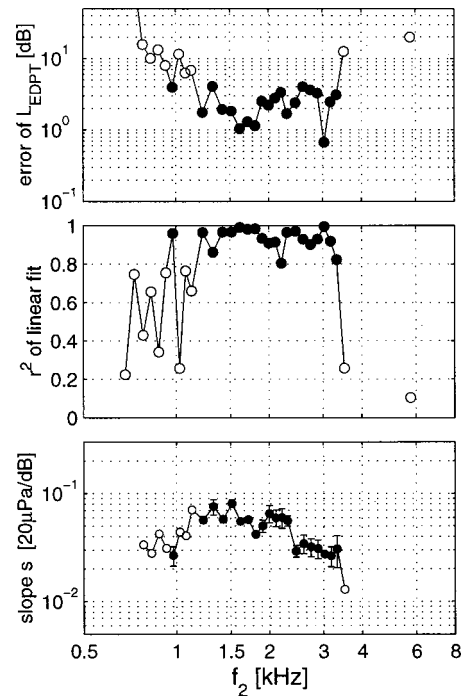


FIG. 5. For subject S.I. the threshold estimation error (upper panel), the value for r^2 from the linear regression (center panel), and the slope of the fitted DPOAE I/O-functions (bottom panel) are plotted over f_2 . Full circles mark I/O-functions fulfilling the linear regression criteria.

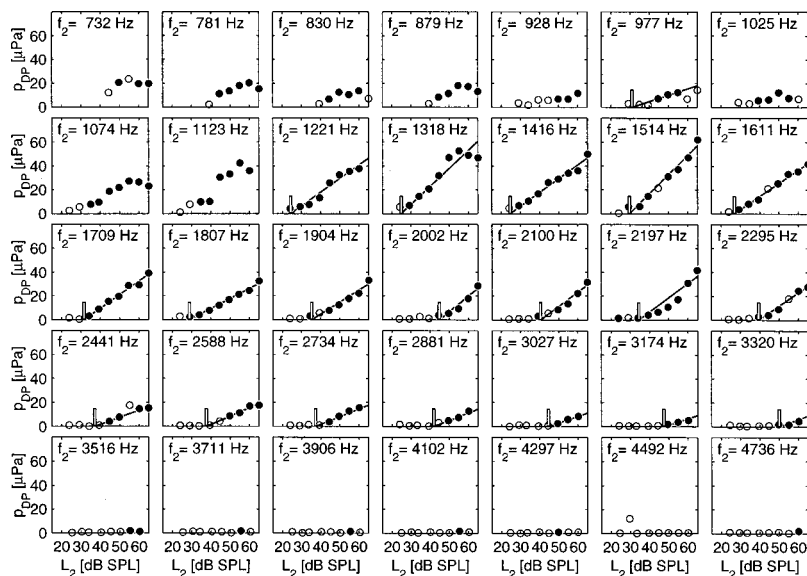


FIG. 6. The DPOAE pressure I/O-functions for subject S.I. are shown for f_2 from 700 to 4800 Hz. Filled circles show DPOAE values with a signal-to-noise ratio greater than 6 dB. For all I/O-functions fulfilling the criteria as in Fig. 5 the fitted linear function (solid line) and the estimated DPOAE threshold L_{EDPT} (vertical bar) are shown.

the I/O-functions in a semi-logarithmic scale:

$$p_{DP}(L_2) = s \cdot (L_2 - L_{EDPT}), \quad (3)$$

with $L_2 = 20 \text{ dB} \cdot \log(p_2/20 \mu\text{Pa})$ and the two fit parameters threshold

$$L_{EDPT} = 20 \text{ dB} \cdot \log(b/20 \mu\text{Pa})$$

and slope

$$s = (a/20) \mu\text{Pa}/\text{dB}.$$

The threshold L_{EDPT} is an extrapolated value equivalent to the primary tone level L_2 that would give a zero DPOAE sound pressure p_{DP} . In Fig. 1 the vertical bar marks the estimated DPOAE threshold level L_{EDPT} in both panels.

Before the fit parameter L_{EDPT} is compared to the pure-tone threshold L_T measured at the f_2 frequencies the quality of the linear fit following Eq. (3) is investigated at different f_2 frequencies.

D. Criteria to accept DPOAE threshold data

The accuracy of the DPOAE threshold estimation is mainly determined by the degree of linearity between the measured DPOAE pressure p_{DP} and the primary tone level L_2 .

We calculated the correlation coefficient r^2 , the standard error of L_{EDPT} which provides a measure of the uncertainty of the DPOAE threshold estimated from the linear regression, and the slope s and set up empirical criteria for accepting or rejecting a fit, i.e.,

$$\begin{aligned} r^2 &\geq 0.8, \\ \text{standard error of } L_{EDPT} &< 10 \text{ dB}, \\ s &\geq 0.1 \mu\text{Pa}/\text{dB}. \end{aligned} \quad (4)$$

These criteria allowed us to filter out a minority of measured I/O-functions that were nonmonotonic or had very small slopes resulting in a very inaccurate extrapolation. Further, only DPOAE pressure I/O-functions with at least three data points were fitted. It should be emphasized that only DPOAE

levels with an signal-to-noise ratio exceeding 6 dB were accepted as valid data points.

In Fig. 5 for one subject (S.I.) the standard error of L_{EDPT} , the correlation coefficient r^2 , and the slope s are plotted as a function of f_2 . Filled circles mark the values fulfilling the criteria (4) while open circles show values at frequencies where at least one of the criteria was not reached. Figure 6 shows the corresponding DPOAE I/O-functions. The filled circles mark the distortion product sound pressure p_{DP} in μPa for the applied primary tone levels L_2 for signal-to-noise ratios greater than 6 dB where open circles mark values of p_{DP} for signal-to-noise ratios below 6 dB. I/O-functions fulfilling the criteria (4) have a solid line indicating the linear regression and a vertical bar marking the DPOAE threshold L_{EDPT} .

E. Prediction of pure-tone threshold from DPOAE threshold

In Fig. 7 the estimated DPOAE threshold L_{EDPT} and the pure-tone threshold L_T for subject S.I. are plotted as a function of the frequency f_2 . There is good agreement between the objective and subjective measures. For the DPOAE

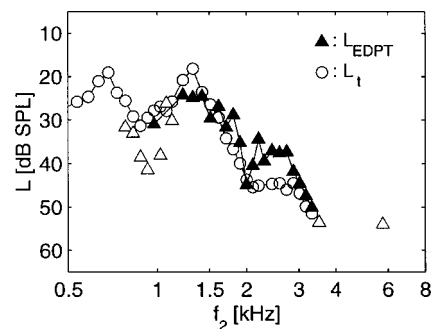


FIG. 7. The pure tone threshold L_T (open circles) and the estimated DPOAE threshold level L_{EDPT} (triangles) for subject S.I. are plotted as a function of f_2 . Filled triangles mark DPOAE threshold values extrapolated from I/O-functions fulfilling the linear regression criteria, while open triangles show DPOAE thresholds not being accepted by these criteria. There is a good agreement between objectively and subjectively assessed threshold.

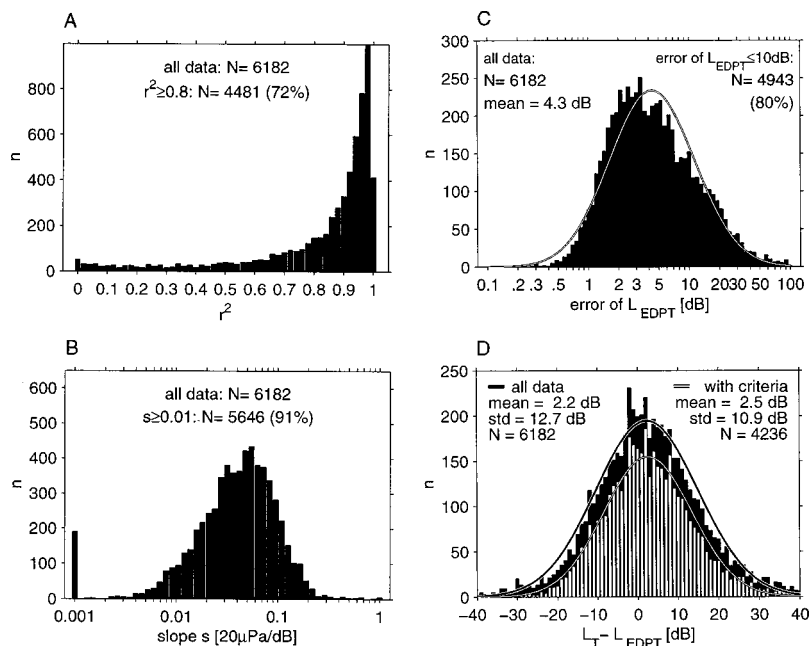


FIG. 8. Group data from 30 normally hearing and 119 sensorineural hearing loss ears. Panel (a) shows the distribution of r^2 of the linear fit for the total of $N = 6182$ I/O-functions measured and the number of I/O-functions ($N = 4481$) meeting the criterion in (4) for r^2 , which is 91% of all I/O-functions. Analog to panel (a) the distribution of the slope s and the DPOAE threshold estimation error is illustrated in panels (b) and (c), respectively. In panel (b) all I/O-functions with slopes less than or equal to 0.01 have been counted together. Panel (d) gives the corresponding distribution of the difference between pure-tone threshold and DPOAE threshold. The mean difference amounts to 2.5 dB, its standard deviation being 10.9 dB when analyzing the data fulfilling the linear regression criteria.

threshold filled triangles show the values of L_{EDPT} where the linear fit does fulfill the criteria (4), open triangles correspond to I/O-functions not fulfilling the criteria. DPOAEs at hearing thresholds of more than 55 dB could not be measured. Thus, no data are available for f_2 above 3320 Hz. For f_2 lower than 732 Hz the signal-to-noise ratio was too small and therefore no reasonable fitting was possible.

F. Pooled data

From the 30 normal-hearing ears and the 119 sensorineural hearing loss ears a total of 6182 DPOAE I/O-functions was available. The distribution of the correlation coefficient r^2 of the linear fit for all 6182 I/O-functions shows that the majority of the I/O-functions (72%) have values above 0.8 [Fig. 8(a)]. This proves the linearity of the I/O-functions in almost all 149 measured ears and suggests that the underlying logarithmic relationship of p_{DP} and p_2 is quite general.

Figures 8(b) and (c) illustrate the distribution of the slope s and the standard error of L_{EDPT} , respectively. The fitted Gaussian function in Fig. 8(c) gives a mean value of 4.3 dB for the standard error of L_{EDPT} . Out of all 6182 I/O-functions 91% have a slope s equal or larger than 0.01 and in 80% the error of L_{EDPT} is smaller or equal to 10 dB. The set of all three criteria [see (4)] is fulfilled for 4236 DPOAE I/O-functions (70% of the total). Figures 8(a)–(d) thereby show that the criteria in (4) include the majority of the data.

Figure 8(d) shows the distribution of the difference between L_{EDPT} and L_T . For all 6182 I/O-functions as well as for the 4236 I/O-functions fulfilling the criteria a Gaussian distribution fitted to the data gives a mean difference of 2.2 and 2.5 dB, respectively. The standard deviations were 12.7 and 10.9 dB, respectively. Thus, the difference of pure-tone threshold and DPOAE threshold is not greater than the standard error of the DPOAE threshold. DPOAE I/O-functions fulfilling the criteria (4) yielded a smaller deviation.

On the other hand, when looking at a single prediction of pure-tone threshold from DPOAE threshold the standard error of 10.9 dB gives the standard deviation of the resulting difference from the mean difference in all 149 ears. Neglecting the mean error of 2.5 dB, the standard deviation of 10.9 dB is a measure of the average prediction error of pure-tone threshold from DPOAE threshold.

The pure-tone threshold is compared to the estimated DPOAE threshold in Fig. 9. Data for all frequencies and all 149 ears are shown, that fulfill the criteria (4). The close relationship between DPOAE threshold and pure-tone threshold is clearly demonstrated by the linear regression having a slope close to 1 with a correlation coefficient $r = 0.65$ showing high significance ($p < 0.001$), thereby revealing an almost 1:1 relationship of the DPOAE threshold and the pure-tone threshold.

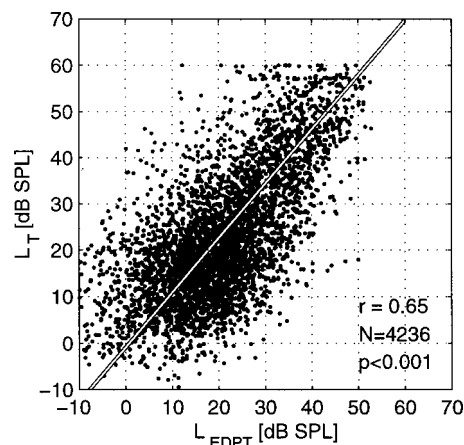


FIG. 9. The pure-tone threshold L_T is plotted versus the DPOAE threshold L_{EDPT} for all $N = 4236$ I/O-functions fulfilling the linear regression criteria. L_T and L_{EDPT} correlate significantly. The regression line demonstrates an almost 1:1 relationship between DPOAE and hearing threshold.

IV. DISCUSSION

A. Dependency of the DPOAE pressure on the f_2 primary tone pressure

It is evident that distortion product otoacoustic emissions arise from a frequency-selective compressive nonlinearity in basilar membrane mechanics (see Robles and Ruggero, 2001) mainly due to outer hair cells (Neely and Kim, 1983) which are thought to amplify basilar membrane motion for increasing sensitivity and frequency selectivity of the hearing organ. It is assumed that DPOAEs mainly originate in the region of maximum overlap of both primary tones that is near the f_2 place (Kummer *et al.*, 1998).

Equal primary tone responses at the f_2 place (not equal primary tone levels!) are therefore thought to be optimal conditions for DPOAE generation. It has been shown that with decreasing primary tone level maximum DPOAE levels are yielded when using a parameter setting with increasing primary tone separation $L_1 - L_2$ (Gaskill and Brown, 1990; Whitehead *et al.*, 1995; Kummer *et al.*, 2000). This can be explained on the basis of characteristics of basilar membrane vibration. With respect to the f_2 place the basilar membrane response to the f_2 primary tone is most compressive whereas it is almost linear to the f_1 primary tone (see Fig. 2). Thus, for yielding maximum overlap at the f_2 place the f_2 response has to be smaller than the f_1 response at low intensities, whereas at high intensities f_1 and f_2 responses have to be more equal (see Fig. 3 from bottom to top, left column). Optimal primary tone level separations with fixed f_2/f_1 ratio which results in maximum DPOAE levels thus have been shown to be close to $L_1 = L_2$ at high stimulus level, but continuously increased with decreasing stimulus level towards $L_1 > L_2$ (Gaskill and Brown, 1990; Whitehead *et al.*, 1995; Kummer *et al.*, 2000). It was found that the systematic dependence of the maximum DPOAE level is almost independent on frequency and may well be approximated by a linear equation such as $L_1 = 0.4 \cdot L_2 + 39$ dB (Kummer *et al.*, 2000).

The good qualitative and even quantitative correspondence between the reconstructed basilar membrane response to the cubic distortion (Fig. 4) and the human DPOAE I/O-function using the $L_1 = 0.4 \cdot L_2 + 39$ dB setting (Fig. 1) emphasizes the major importance of the f_2 place for DPOAE generation and confirms the assumption that optimal conditions for DPOAE generation are equal primary tone responses at the f_2 place. The fact that two-tone suppression was ignored appears not to confound this approach.

Using the $L_1 = 0.4 \cdot L_2 + 39$ dB primary tone setting DPOAE I/O-functions reflect the compressive nonlinearity of the basilar membrane response. As well in the animal data as in the human DPOAE data the compression is most prominent at high intensities having similar rates of growth of about 0.2 dB/dB (Ruggereo *et al.*, 1997; Kummer *et al.*, 1998; Janssen *et al.*, 1998).

In most of the DPOAE I/O-functions (70%) of our 149 ears measured, a strong logarithmic dependency of the DPOAE sound pressure on the f_2 primary tone sound pressure was found. The fact that linear regression analysis yielded correlation coefficients higher than 0.9 in the major-

ity of the DPOAE I/O-functions [see Fig. 8(a)] proves a close logarithmic relationship between stimulus (p_2) and otoacoustic emission (p_{DP}) in general. Due to this logarithmic relationship a simple fit of the data was possible by simply performing linear regression analysis in a semi-log plot (p_{DP} vs L_2).

For correlation coefficient above 0.8, DPOAE I/O-functions can easily be described by only two parameters, i.e., the slope of the I/O-function and the intersection of the extrapolation line with the L_2 axis (see Figs. 1 and 6). The slope is a measure of compression and the intersection with the L_2 axis, i.e., the estimated DPOAE sound pressure at the threshold of hearing, is a measure for the sensitivity of cochlear sound processing. This statement is suggested to be true under the assumption that DPOAE I/O-functions obtained with the $L_1 = 0.4 \cdot L_2 + 39$ dB primary tone setting do really reflect the transfer function of the outer hair cell amplifier. The fact that the growth of the cubic distortion can be approximated by calculating the mean value of the f_1 and f_2 basilar membrane response supports this assumption.

DPOAE I/O-functions recorded by using a primary tone setting which accounts for the different compression of the two primaries at the f_2 place obviously make it possible to detect cochlear responses at stimulus levels close to hearing threshold.

B. Relationship between DPOAE threshold and hearing threshold

Optimal stimulus conditions for DPOAE generation are one important key to exploit the potential of DPOAEs in clinical diagnostics. DPOAE I/O-functions make it possible to extrapolate to a DPOAE threshold, which may be interpreted as a correlate of cochlear hearing (see Fig. 1). The significant correlation ($p < 0.001$) between the estimated DPOAE threshold and the behavioral threshold (Fig. 9) proves the close relationship between otoacoustic emissions and the threshold of hearing. As it can be seen from our data this seems to be true also for cochlear impaired hearing. The 1:1 relationship between hearing loss and DPOAE loss (see Fig. 9) supports the assumption that DPOAEs directly reflect dysfunction of cochlear signal processing and shows that the primary tone setting based on data from normal-hearing subjects appeared to be also effective in impaired hearing.

Kimberley *et al.* (1994) used discriminant analysis for pure-tone threshold estimation from DPOAEs that attempts to define groups on the basis of linear combinations of attributes common to all groups. Discrimination functions were used to present weighted linear combinations of the attributes. A relative good prediction performance could be achieved with the use of only two variables, that is, DPOAE level elicited with a stimulus level of 60 dB SPL and subject age. However, this test provides only classification in normal or elevated pure-tone thresholds. A direct quantitative evaluation of hearing loss could not be achieved.

Janssen *et al.* (1997) used a linear regression model with the DPOAE level obtained at different primary tone levels between $L_2 = 20$ and 65 dB using the $L_1 = 0.4 \cdot L_2 + 39$ dB primary tone setting and the slope of the DPOAE I/O function as predictive parameters. When comparing estimated

and behavioral thresholds the predicted mean square error was 12 dB. When using only the DPOAE level as predicting parameter the predicted error was worse. The need for an extensive database restricts this method for general application. This finding underlines the importance of close to threshold DPOAE measurements and gave the idea to extrapolate DPOAE I/O-functions for estimating pure-tone threshold.

C. Validity of the prediction of hearing threshold by means of DPOAE

The accuracy of the DPOAE threshold L_{EDPT} due to the linear extrapolation is described by the standard error of L_{EDPT} . This error depends on the correlation coefficient r^2 describing the degree of linearity between the pressure p_{DP} and the level L_2 , and on how far $p_{DP}(L_2)$ is extrapolated out of the measurement interval of L_2 to $p_{DP}(L_{EDPT})=0$. Therefore, the slope s of $p_{DP}(L_2)$ was subject to a criterion, too, as it contributes to the accuracy of the extrapolation. The criteria (4) were set up empirically to account for the limitations of the linear model for $p_{DP}(L_2)$, which cannot be used to describe I/O-functions that show nonmonotonic behavior. However, a majority of 70% of all measured I/O-functions met the criteria, proving that the linear dependency is quite general. It should also be mentioned that applying the criteria does not change the overall correspondence of DPOAE threshold and hearing threshold in our data as can be seen from Fig. 8(c).

The interindividual variation of the distortion product level L_{DP} only allows qualitative estimation of hearing threshold from L_{DP} (see Sec. IV B). Looking at Eq. (3) might show why the method presented in this paper improves this situation. When assuming the linear form of $p_{DP}(L_2)$ in Eq. (3) to be general at the place of the DPOAE generation in the cochlea, then the interindividual variation of the p_{DP} for ears with identical hearing thresholds and identical DPOAE thresholds will be caused by an individual factor multiplied on p_{DP} . In Eq. (3) only the slope s will be changed by this factor, not the threshold L_{EDPT} . Such a interindividual variability in p_{DP} (e.g., caused by middle-ear transfer function) is only reflected in one of the two parameters describing the I/O-function, in the slope s .

The actually measured DPOAE sound pressure can also include an additive term to Eq. (3) (e.g., the contribution from the place of a second source in the cochlea). Such a term can explain the nonmonotonic I/O-functions that have been filtered out by our empirical criteria. In test experiments not shown here we applied a third primary tone (see Heitman *et al.*, 1998) to suppress the second DPOAE generation place in the cochlea and found reduced nonmonotonic behavior of certain I/O-functions that enabled the estimation of the DP threshold for these I/O-functions.

However, keeping in mind that DPOAEs do reflect the nonlinear compression characteristics in the cochlea but cannot give information about inner hair cell function or further neural processing, the DPOAE threshold should not be expected to be identical to subjective hearing threshold, but to supply additional information as a mechanical analog.

An important technical problem is the calibration of the probe. For the current work the probe transducers were calibrated in the ear canal before each measurement with a chirp response based on a manufacturer supplied microphone sensitivity. The sound pressure measured with the microphone at the probe tip therefore varies from one measurement to the next due to different ear canal geometry and changes of the probe characteristics. Providing an accurate, frequency-dependent calibration of the probe transducers and thereby of the stimulus sound pressure seems to be essential for the method presented in this paper to yield true quantitative results for the DPOAE threshold.

Finally, we did not evaluate the dependency of the slope s on probe and ear-canal characteristics. Ignoring this technical difficulty and again keeping in mind that DPOAEs reflect the nonlinear compression characteristics in the cochlea, one could expect the slope s to give a mechanical analog to the growth of subjective loudness. In this context it is interesting to note that Eq. (2) corresponds to Fechner's proposal that perceived magnitude should be a logarithmic function of physical magnitudes (Hartmann, 2000). Both the DPOAE I/O-function and the basilar membrane response at CF show this behavior. In contrast to this the subjective loudness does not follow Fechner's proposal (Hartmann, 2000), further pointing out that the DPOAE I/O-functions supply additional information from an intermediate stage of sound processing.

It should be emphasized that the estimation of DPOAE threshold with our new method is performed solely on individual data. No statistical data are needed. Further, no human expert is necessary to decide whether there is a DPOAE or not. This is in contrast to ABR threshold estimation where there is still a lack for automatic identification. The only disadvantage over ABR is that DPOAEs cannot evaluate severe hearing losses because DPOAEs are capable of assessing outer hair cell sound processing only when it is restricted to 50 or 60 dB sound level. Eliciting DPOAEs with higher sound levels than 65 dB SPL as used in our measurements may assess hearing loss of higher degree. However, high sound levels produce artificial distortion. To overcome this problem there are two ways, either manufacturing electroacoustic transducers with lower distortion or getting knowledge on artificial distortion overlying biological distortion (Dorn *et al.*, 2001).

V. CONCLUSION

Using the primary tone level setting $L_1=0.4 \cdot L_2 + 39$ dB that accounts for the different compression of the two primaries at the DPOAE generation site, at f_2 , in most of the DPOAE I/O-functions a logarithmic dependency of the distortion product sound pressure p_{DP} on the sound pressure p_2 of the f_2 primary tone was found. In a semi-logarithmic scale this gives a linear dependency between p_{DP} and the primary tone level L_2 .

The linearity of the DPOAE I/O-functions $p_{DP}(L_2)$ is sufficiently fulfilled in all ears and thus enables a reliable DPOAE threshold estimation by simply extrapolating the I/O-functions using linear regression analysis.

A surprisingly small mean difference between estimated DPOAE threshold and pure-tone threshold (2.2 dB for all

data and 2.5 dB for the data fulfilling our empirical criteria for an optimum fit, respectively) with a relatively small standard deviation (12.7 and 10.9 dB, respectively) was found.

This suggests, first, that the found logarithmic dependency of p_{DP} from p_2 is quite general and might give a functional description of the compression characteristic of the outer hair cells. Second, the threshold of DPOAE I/O-functions seems to reflect an important factor for hearing threshold related to outer hair cell physiology. An almost 1:1 relationship of DPOAE threshold and pure-tone-threshold is found for 70% of all measured I/O-functions. The fact that not all DPOAE threshold estimations yield a close correspondence to pure-tone threshold can be interpreted that in these cases there is a contribution to the DPOAE threshold not being related to pure-tone threshold, which has to be investigated. However, since we did apply the same fixed criteria to all I/O-functions, the results presented here do already allow a pure-tone threshold estimation with a small prediction error. Third, the similarity between optimum DPOAE I/O-function and basilar membrane velocity I/O-functions for single tones at CF might help us to understand the correspondence of the DPOAE threshold and the subjective pure-tone threshold.

In conclusion, the ability of the presented method to directly predict pure-tone threshold by means of extrapolated DPOAE I/O-functions seems robust enough to improve the clinical potential of DPOAEs. We therefore suggest the DPOAE threshold as an objective measure of hearing threshold while one still has to keep in mind other sources of hearing impairment as inner hair cell or retrocochlear damage.

ACKNOWLEDGMENT

This work was supported by the Deutsche Forschungsgemeinschaft (Ja 597/5-2).

Dorn, P. A., Konrad-Martin, D., Neely, S. T., Keefe, D. H., Cyr, E., and Gorga, M. P. (2001). "DPOAE Input-output functions in normal and impaired human ears," *Assoc. Res. Otolaryngol. Abs.*, No. 28.

Gaskill, S. A., and Brown, A. M. (1990). "The behavior of the acoustic

distortion product, $2f_1 - f_2$, from the human ear and its relation to auditory sensitivity," *J. Acoust. Soc. Am.* **88**, 821–839.

Gorga, M. P., Neely, S. T., Ohlrich, B., Hoover, B., Redner, J., and Peters, J. (1997). "From laboratory to clinic: a large scale study of distortion product otoacoustic emissions in ears with normal hearing and ears with hearing loss," *Ear Hear.* **18**, 440–455.

Hartmann, W. (2000). *Signals, Sound and Sensation*, Series in Modern Acoustics and Signal Processing (Springer, New York), ISBN 1-56396-283-7.

Heitmann, J., Waldmann, B., Schnitzler, H.-U., Plinkert, P. K., and Zenner, H.-P. (1998). "Suppression of distortion product otoacoustic emissions (DPOAE) near $2f_1 - f_2$ removes DP-gram fine structure—Evidence for a secondary generator," *J. Acoust. Soc. Am.* **103**, 1527–1531.

Janssen, T., Kummer, P., and Arnold, W. (1998). "Growth behavior of the $2f_1 - f_2$ distortion product otoacoustic emission in tinnitus," *J. Acoust. Soc. Am.* **103**, 3418–3430.

Janssen, T., Boege, P., Kummer, P., Scholz, M., and Arnold, W. (1997). "Reconstruction of hearing thresholds by means of DPOAE," *Audiol. Akust.* **4**, 178–190.

Kimberley, B. P., Brown, D. K., and Allen, J. B. (1997). "Distortion Product Emissions and Sensorineural Hearing Loss," in *Otoacoustic Emissions: Clinical Applications*, edited by M. S. Robinette and T. J. Glatke (Thieme, New York), pp. 181–204.

Kimberley, B. P., Hernadi, I., Lee, A. M., and Brown, D. K. (1994). "Predicting pure-tone thresholds in normal and hearing impaired ears with distortion product emission and age," *Ear Hear.* **15**, 199–209.

Kummer, P., Janssen, T., and Arnold, W. (1998). "The level and growth behavior of the $2f_1 - f_2$ distortion product otoacoustic emission and its relationship to auditory sensitivity in normal hearing and cochlear hearing loss," *J. Acoust. Soc. Am.* **103**, 3431–3444.

Kummer, P., Janssen, T., Hulin, P., and Arnold, W. (2000). "Optimal $L_1 - L_2$ primary tone level separation remains independent of test frequency in humans," *Hear. Res.* **146**, 47–56.

Neely, S. T., and Kim, D. O. (1983). "An active cochlear model showing sharp tuning and high sensitivity," *Hear. Res.* **9**, 123–130.

Robles, L., and Ruggero, M. (2001). "Mechanics of the mammalian cochlea," *Physiol. Rev.* **81**, 1305–1352.

Ruggero, M. A., Rich, N. C., Recio, A., and Narayan, S. S. (1997). "Basilar-membrane responses to tones at the base of the chinchilla cochlea," *J. Acoust. Soc. Am.* **101**, 2151–2163.

Stockard, J. J., Stockard, J. E., and Sharbrough, F. W. (1980). "Brainstem auditory evoked potentials in neurology: Methodology, interpretation, clinical application," in *Electrodiagnosis in Clinical Neurology*, edited by M. Aminoff (Churchill Livingstone, New York), pp. 370–413.

Whitehead, M. L., McCoy, M. J., Lonsbury-Martin, G. K., and Martin, G. K. (1995). "Dependence of distortion-product otoacoustic emissions in primary tone level in normal and impaired ears. I. Effects of decreasing L_2 below L_1 ," *J. Acoust. Soc. Am.* **97**, 2346–2358.

Rhythmic masking release: Contribution of cues for perceptual organization to the cross-spectral fusion of concurrent narrow-band noises^{a)}

Martine Turgeon,^{b)} Albert S. Bregman, and Pierre A. Ahad

Psychology Department, McGill University, 1205 Dr. Penfield Avenue, Montreal, Quebec, Canada

(Received 9 March 2000; revised 27 October 2000; accepted 29 December 2001)

The contribution of temporal asynchrony, spatial separation, and frequency separation to the cross-spectral fusion of temporally contiguous brief narrow-band noise bursts was studied using the Rhythmic Masking Release paradigm (RMR). RMR involves the discrimination of one of two possible rhythms, despite perceptual masking of the rhythm by an irregular sequence of sounds identical to the rhythmic bursts, interleaved among them. The release of the rhythm from masking can be induced by causing the fusion of the irregular interfering sounds with concurrent “flanking” sounds situated in different frequency regions. The accuracy and the rated clarity of the identified rhythm in a 2-AFC procedure were employed to estimate the degree of fusion of the interfering sounds with flanking sounds. The results suggest that while synchrony fully fuses short-duration noise bursts across frequency and across space (i.e., across ears and loudspeakers), an asynchrony of 20–40 ms produces no fusion. Intermediate asynchronies of 10–20 ms produce partial fusion, where the presence of other cues is critical for unambiguous grouping. Though frequency and spatial separation reduced fusion, neither of these manipulations was sufficient to abolish it. For the parameters varied in this study, stimulus onset asynchrony was the dominant cue determining fusion, but there were additive effects of the other cues. Temporal synchrony appears to be critical in determining whether brief sounds with abrupt onsets and offsets are heard as one event or more than one. © 2002 Acoustical Society of America. [DOI: 10.1121/1.1453450]

PACS numbers: 43.66.Dc, 43.66.Lj, 43.66.Mk, 43.66.Rq [DWG]

I. INTRODUCTION

A. Multiple cues in sound-source determination

Many scientists have studied the question of how the auditory system parses the acoustic signal so as to provide the animal with a useful perceptual description of the activity of individual sound sources (Bregman, 1990, 1993; Darwin and Carlyon, 1995; Hartmann, 1988; Moore, 1989; Yost, 1991). Bregman (1990) has proposed that the auditory parsing process is governed by ecologically valid heuristics that have evolved to exploit the acoustical properties of causally related sound-producing events. There has been converging empirical evidence that the auditory system is built to extract these regularities from the acoustic signal for the purpose of sound-source determination. This has been reviewed by several researchers (Bregman, 1990; Darwin and Carlyon, 1995; Yost and Sheft, 1993; Yost, 1991).

No auditory grouping¹ cue operates in isolation; rather cues act together; sometimes reinforcing each other, and sometimes competing with each other to provide the groupings of components upon which the most valid perceptual description of the acoustic signal can be built. That cues can have combined effects is a recognized fact and stimulated empirical work some 20 years ago (Bregman, 1978; Breg-

man and Pinker, 1978; Dannenbring and Bregman, 1978; Steiger and Bregman, 1982); until recently, there has been relatively little subsequent work done on auditory organization in the presence of multiple cues. One of the main goals of the present study was to further explore the perceptual outcome when factors known to either promote the segregation or the fusion² of complex sounds, act together.

Apart from the recognition of multiple cues in sound-source determination, there has been a growing recognition of the importance of cross-spectral analysis (Yost and Sheft, 1993). A variety of paradigms have been employed to investigate the cross-spectral integration¹ of acoustical information: profile analysis (Green, 1988), modulation detection interference or MDI (Hall and Grose, 1991; Yost *et al.*, 1989), comodulation masking release or CMR (Grose and Hall, 1993; Hall *et al.*, 1984), comodulation detection difference or CDD (McFadden and Wright, 1990), and more recently, comodulation masking protection or CMP (Gordon, 1997). All of those paradigms are based upon an analysis of energy across frequency channels, though they differ as to the task, stimuli and measurements used to explore cross-spectral integration. For instance, while in CMR the detection of a sinusoidal target signal masked by a modulated noise within the same frequency band is improved by the presence of comodulated flanker noises situated in different frequency bands, in MDI the discrimination of the depth of modulation of such a target can be impaired by the presence of comodulated sinusoidal maskers of different frequencies. Despite these methodological differences, these paradigms provide converging evidence that the auditory system is sensitive to

^{a)}This research was presented as part of the first author's Ph.D. thesis to the Psychology Department of McGill University.

^{b)}Reprints are available from Martine Turgeon at “Behavioural Brain Sciences Centre, School of Psychology, The University of Birmingham, Edgbaston, Birmingham B15 2TT, UK,” where she is currently affiliated. Electronic mail: M.Turgeon@Bham.ac.uk

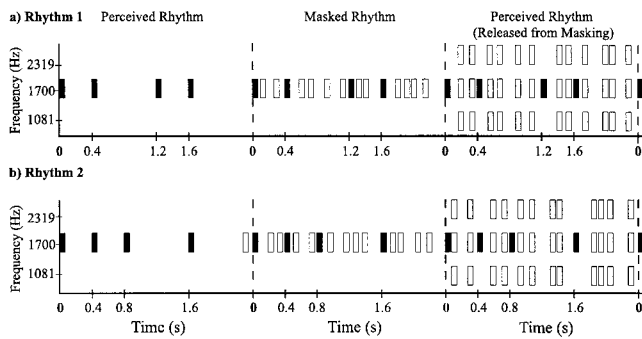


FIG. 1. Temporal structures of sequences in rhythmic masking release (RMR). Rhythms 1 and 2 consist of 3.5 replications of the succession of intervals shown at the left of panel (a) and (b), respectively. They are composed of different temporal arrangements of 48-ms noise bursts separated by two possible intervals: 384 and 768 ms. To camouflage perceptually the rhythm, two irregular “maskers” are added in the 384-ms interval and four in the 768-ms one [see middle of panels (a) and (b)]. The rhythm is masked because no acoustic property distinguishes the regular from the irregular sounds. The rhythm can be released from masking when “flankers” of different frequencies are added simultaneously to the maskers, as shown on the right of panels (a) and (b). Hearing the rhythm depends on the fusion of the irregular maskers and flankers.

across-frequency correlations in the time-varying patterns of intensity.

B. RMR to study cross-spectral fusion in the context of multiple cues

The present study uses the rhythmic masking release (RMR) paradigm (Bregman and Ahad, 1996, Demonstration 22; Turgeon and Bregman, 1997) to look directly at the link between cross-spectral integration and perceptual fusion. In RMR, perceptual fusion depends on the use of relations among the components of the signal in different frequency regions, such as simultaneous onsets and offsets. Figure 1 schematizes the temporal structure of the stimuli used in the present study. Similar stimuli were used in a preliminary RMR experiment (Turgeon, 1999). The results of that experiment are useful to introduce the RMR paradigm. They also provide some predictions as to what should be perceived under different conditions of the present study. When a regular sequence of narrowband noise bursts is played in isolation, a simple rhythm is heard. Such rhythms are perceived upon repeating the successions of short and long intervals shown in the left of panels (a) and (b) of Fig. 1. While alternating the short and long intervals shown in the top pattern (a) evokes a rhythm with pairs of bursts (Rhythm 1 in the present study); cycling the succession of short, long, long, and short intervals shown in the bottom pattern (b) evokes a rhythm with triplets of bursts alternating with a single burst (Rhythm 2 in the present study). In both examples, sounds that are closer together in time perceptually group together (Handel, 1989).

If an irregular sequence of identical sounds is intermingled among those of the regular one, the rhythm is no longer heard (white bars of the same frequency as the dark bars). This is because no acoustic property distinguishes the regular bursts from the irregular ones. We refer to the camouflaging bursts as “maskers;” while they do not mask the regular bursts, they do mask their sequential organization,

that is, the rhythm.³ Together, the rhythmic bursts and the maskers form the “masked-rhythm sequence” (dark and white bars in the middle portion of Fig. 1). In the rightmost portion, narrowband noise “flankers” are added. These are synchronous with the irregular maskers, but located in other frequency regions (white bars at the top and bottom of the masked rhythm sequence). The prior RMR study has shown that this causes the rhythm to be “released from masking” (Turgeon, 1999). The release was explained by the fusion of the maskers and flankers that have simultaneous onsets. The emergent perceptual properties of the masker-flanker complexes (e.g., a global timbre different from that of each rhythmic pulse) allow the listener to distinguish these irregularly spaced bursts from the regularly-spaced ones. Hence, the accurate perception of the rhythm is contingent upon the fusion of the two irregular sequences of maskers and flankers into a single sequence of masker-flanker complexes.

II. EXPERIMENT 1. TEMPORAL LIMITS AND RELATIVE CONTRIBUTION OF CUES TO THE CROSS-SPECTRAL FUSION OF NOISE BURSTS PRESENTED BINAURALLY

Experiment 1 explored the contribution of four acoustical properties to diotic and dichotic fusion: temporal asynchrony (Dannenbring and Bregman, 1978; Darwin and Ciocca, 1992), amplitude modulation (Bregman *et al.*, 1985; Grose and Hall, 1993) frequency separation (Brochard *et al.*, 1999; Turgeon, 1994) and dichotic presentation (Hukin and Darwin, 1995; Kidd *et al.*, 1994). There is evidence that each of these properties influences the cross-spectral integration of information in a number of phenomena: (i) Temporal asynchrony has been shown to affect MDI by Hall and Grose (1991), binaural MDI by Sheft and Yost (1997), CMR by Grose and Hall (1993) and McFadden (1986), CMP by Gordon (1997), and localization by Woods and Colburn (1992). (ii) The correlation of envelope modulation across frequency has been related to CMR by Grose and Hall (1993), to dichotic CMR by Schooneveldt and Moore (1987), to MDI by Yost *et al.* (1989), and to binaural MDI by Sheft and Yost (1997). (iii) The frequency separation between the signal and the flanking bands decreases CMR (Schooneveldt and Moore⁴). (iv) Similarly, the contralateral presentation of the flanking bands relative to the signal decreases CMR (Schooneveldt and Moore, 1987) and reduces MDI slightly (Sheft and Yost, 1997).

In this study, the asynchrony of onset and offset between pairs of narrow-band flanker bursts symmetrically placed relative to each masker burst was manipulated. Because the maskers and flankers had the same duration, the onset asynchrony was equal to the offset asynchrony; hence only the magnitude of the stimulus onset asynchrony (SOA) will be mentioned. The ecological validity of temporal synchrony for sound-source determination combined with the converging evidence that it is a very powerful grouping cue (Darwin and Carlyon, 1995), including a prior RMR experiment (Turgeon, 1999), led us to the following hypotheses: (i) Synchronous maskers and flankers should fully fuse to yield RMR independently of their frequency separation (ΔF), whether or not the flankers are presented in the same or contralateral

ear as the maskers; (ii) SOA should significantly decrease fusion for both the diotic and dichotic presentation of concurrent maskers and flankers; and (iii) SOA, ΔF and contralateral presentation should reinforce each other in favoring the segregation (i.e., diminishing the fusion) of the concurrent maskers and flankers.

Another important goal was to estimate the temporal asynchrony required to abolish the fusion of concurrent sounds situated in different frequency regions. For convenience, we refer to such an asynchrony as “SOA threshold,” though we do not suggest that it applies to synchrony per se; it is rather an “event-segregation threshold,” that is, the SOA necessary to perceive brief sounds close together in time, as separate events. A last objective was to compare the cross-spectral fusion resulting from correlated amplitude fluctuations at different temporal scales, namely the slow amplitude changes at the macro scale of the whole sequence (i.e., onsets and offsets) with the faster ones at the micro scale within each sequential component (AM).

Grose and Hall (1993) wanted to know whether a correlated pattern of AM was sufficient to induce CMR. Although it was shown to induce CMR when the onsets of correlated masking and flanking bands were simultaneous, the CMR was considerably decreased when they were asynchronous; in fact, a 50-ms SOA between the on-signal band and the flanking bands completely abolished CMR. Note that the asynchronous bands were comodulated during their period of overlap. These results are consistent with those of McFadden (1986) who found that SOAs between 3-to-15 ms abolished CMR. This suggests that the effect of a common AM in CMR is contingent upon the perceptual fusion evoked by sounds that come on synchronously or slightly asynchronously. From these CMR results, as well as those of a prior RMR experiment (Turgeon, 1999), the rhythm was expected to be released from masking whenever the irregular maskers and flankers were fully temporally overlapping, despite the combined action of many segregating cues: different ears of presentation and large ΔF 's. Though uncorrelated AM within the brief overlapping portions of the masker and flanker bursts was expected to diminish their fusion, and hence RMR, it was not expected to abolish it.

A. Methods

1. Subjects

There were 18 listeners who were naive to the purpose of the experiment. All listeners had normal hearing for the 250–8000 Hz frequency range, as assessed through a short air-conductance audiometric test.

2. Stimulus generation and presentation

All stimuli were synthesized and presented by a PC-compatible 486 computer, using MITSYN Version 8.1 signal processing software (Henke, 1990) and a 16-bit digital-to-analog converter. The rate of output was 20 000 samples per second. Signals were low-pass filtered at 5 kHz using a flat amplitude (Butterworth) response with a roll-off of 48 dB octave. Listeners sat in a sound-attenuating test chamber and listened to stimuli presented through Sony NR-V7 head-

phones. Stimuli were presented diotically, dichotically or monaurally, depending on condition. The rms level fluctuated slightly across the sequence due to random sampling of the noise components. The level of a 1-kHz pure tone equal in intensity to the mean rms of the noise bursts of the masked-rhythm sequence and of the flankers (measured as a pair) was calibrated at 60 dB SPL, using a General Radio Company Type 1565-B (“B” weighting, slow). The experiment was run on-line with the help of a MAPLE Version 2.0 program (Achim *et al.*, 1995) using ASYST Version 4.00 software.

3. Structure of sequences

Listeners were asked to discriminate two rhythms, presented as a sequence of noise bursts. These were made more difficult or impossible to discriminate by the insertion of maskers placed randomly in the time intervals between them. These were identical in all respects to the rhythmic components. Both of the rhythms were formed of the same set of long and short time intervals, but in a different arrangement. One cycle of each rhythm is shown in the left portion of panels (a) and (b) of Fig. 1. The long intervals were twice the duration of the shorter ones (short=384 ms; long=768 ms). Whereas Rhythm 1 repeated the sequence of intervals, short, long, short, and long, three and one-half times, Rhythm 2 repeated the sequence short, long, long, and short, three and one-half times. Figure 1 shows that there were two random maskers in the short interval, and four, in the long one. The temporal positions of the maskers were random from cycle to cycle. Except in the case of the no-flanker controls, these maskers were accompanied by noise bursts (“flankers”) situated in other frequency regions (see the white bars above and below the central sequence in the right portion of Fig. 1). The rhythm started at a variable time after the start of the irregular masking and flanking noise bursts and ended at a variable time before the irregular maskers and flankers stopped, keeping the total duration of the sequence constant across trials. This ensured that correct rhythm identifications did not result from the use of attentionally driven strategies exploiting local cues (e.g., listen for the short interval at the beginning of the sequence).

4. Structure of individual bursts

All the noise bursts (forming the masked-rhythm sequence and flankers) were 48-ms long, including a 8-ms quarter-sine onset and a 8-ms reversed-quarter-sine offset. Each burst was obtained by multiplication of an independent 1-to-100 Hz, 48-ms-long, nominally flat noise sample by a pure tone. This procedure yielded a 200-Hz-wide nominally flat noise band centered at the frequency of the tone. Each independent noise sample was created by the summation of closely spaced sinusoids (1-Hz apart) in randomly selected phases. The rhythmic and masker bursts were centered at 1700 Hz. The flankers were two 200-Hz-wide noise bands 48 ms in duration, equally distant from the central masking band. The ΔF between the maskers and each of the two flankers was either 619 Hz or 1238 Hz. Hence, the maskers

and flankers were always in different critical bands, as measured in equal rectangular bandwidths (Glasberg and Moore, 1990).

The amplitude fluctuation within each masker, due to the randomness of noise, could both be either correlated with that of its corresponding flanker burst, or not. The maskers and flankers that had correlated envelopes were obtained by using the same noise sample. This sample was multiplied by sinusoids of different frequencies to obtain masker and flanker bursts with different center frequencies. The random intensity changes were correlated throughout the overlapping portion of asynchronous maskers and flankers. This was produced by the method used to synthesize them. This involved the starting of the noise samples for the masker and flanker bursts at the same time, while triggering the gain control for the intensity of the delayed burst, only after the asynchrony time of a given condition. Different noise samples were used to obtain uncorrelated maskers and flankers. The order of presentation of the noise samples within the regular and irregular sequences was randomly varied across trials. Furthermore, a masker burst could be delayed or advanced relative to its two temporally adjacent flanking bands (there was an equal likelihood of each for any masker and flanker bursts). The amount of overlap between the maskers and flankers varied from full to none; that is, the SOA was either 0, 12, 24, 36, or 48 ms. The masked rhythm and the flankers could either be presented together to both ears (diotic) or separately to the two ears (dichotic). While for the former, the no-flanker control was diotic, for the latter, it was monotic.

5. Procedure

The listeners had to judge which of the two rhythms was embedded in the sequence and how clearly it was heard on a 5-point scale. They were instructed to use the lowest clarity rating of “1” when guessing. The other values of the scale corresponded to the following degrees of perceived clarity of the identified rhythm: “2” stood for “very unclear,” “3” for “unclear,” “4” for “clear,” and “5” for “very clear.” Listeners were familiarized with the procedure and brought to a high level of performance on non-masked sequences. They were then trained on masked sequences. To yield a stable performance, there were two practice sessions that provided feedback about accuracy of rhythm identification. Feedback continued to be provided throughout the subsequent sessions. The order of presentation of the different conditions was randomized across trials, except for the diotic and dichotic ones, which alternated across sessions. For the dichotic sessions, the listeners were instructed to direct their attention to one ear, namely that of the masked rhythm.

6. Design

a. Independent variables. The center frequencies of the masking and flanking bands were either 619 or 1238 Hz apart. The maskers and flankers were either presented in both ears or spatially separated through dichotic presentation; their asynchrony was 0, 12, 24, 36, or 48 ms. The temporal envelope of each masker was either correlated or not, with that of its overlapping flanker bursts. This was thus a 2×2

$\times 5 \times 2$ within-subject design with eight replications per cell. A no-flanker condition was added to verify that the rhythm was masked in the absence of any flanker.

b. Dependent variables. The accuracy of rhythm identification as well as the perceived clarity of the identified rhythm served as a measure of the fusion¹ of the flankers and maskers. This was based on the assumption that fusion was not all-or-none, but that higher degrees of fusion would lead to greater ease in distinguishing the rhythmic bursts from the irregular ones. We used the sensitivity measure of d' (MacMillan and Creelman, 1991, p. 8) and estimated SOA thresholds from the fitting of psychometric functions to proportion-correct (PC) scores (Weibull, 1951). We also used a measure that weighted the accuracy by the rated clarity of the identified rhythm; this weighted-accuracy scale (WA) was more sensitive to the effect of weak cues than were “pure objective measures of accuracy.” For instance, while the PC and d' scores did not show any significant difference for rapid envelope correlations, the WA scores revealed some significant ones for nearly synchronous stimuli. Because it captured weak effects well, WA was used to evaluate the relative weight of cues in favoring fusion. On the other hand, the fitting of Weibull functions to PC scores were more suited to evaluate the temporal limits for sound-event segregation. Lastly, the detection measure, d' , provided a conservative index of the most critical properties in cross-spectral fusion, since those were the ones most likely to affect the discriminability of the rhythm (signal). Individual response biases were also estimated (MacMillan and Creelman, 1991, p. 32).

B. Results and discussion

1. Measure of sensitivity to the target rhythm

Rhythm detectability and response bias (d' and c) were computed according to standard detection theory procedures.⁵ The WA scores were obtained by multiplying the absolute clarity rating of the listener on a 5-point scale by +1 when the rhythm was correctly identified, and by -1, when it was not. This yielded a scale ranging from -5 to +5. Because there were two units separating -1 from +1 (versus 1 unit between all other adjacent values of the scale), 0.5 was subtracted from the original clarity ratings to yield an equal-interval weighted-accuracy scale ranging from a -4.5 (incorrect “very clear”) to +4.5 (correct “very clear”). This equal-interval scale was required for the analysis of variance (ANOVA) of the WA scores, in the present case, a 4-way within-subject ANOVA. Note that none of the statistical assumptions to perform that ANOVA was violated, including that of the normal distribution of the WA scores.

Each individual subject's SOA threshold was determined from the best-fitting “Weibull” function (Weibull, 1951). Figure 2 shows Weibull psychometric functions for subject CB for the diotic conditions with a 619-Hz ΔF [continuous curve in panel (a)] and a 1238-Hz ΔF [dashed curve in panel (a)] and for the dichotic conditions with a 619-Hz ΔF [continuous curve in panel (b)] and a 1238-Hz ΔF [dashed curve in panel (b)]. Each of these functions minimizes the mean square estimate of error for the proportion of correct (PC) rhythm identifications as a function of SOA. For each con-

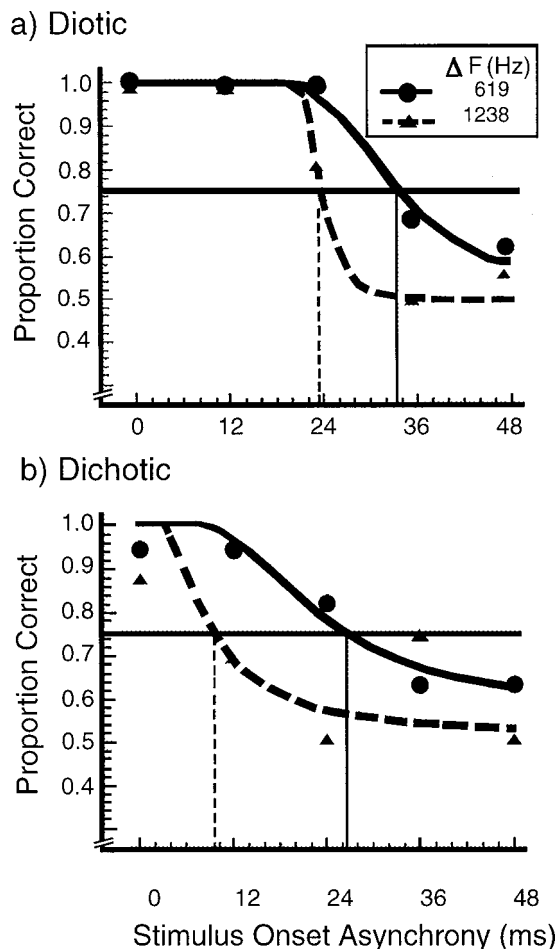


FIG. 2. Onset asynchrony (SOA) psychometric functions for subject CB for $\Delta F=619$ Hz (solid lines) and for $\Delta F=1238$ Hz (dashed lines), for diotic (a) and dichotic (b) conditions. SOA thresholds are taken as values yielding a proportion correct of 0.75.

dition, the mean of the within-subject Pearson-coefficient correlation (r) between the fitted function and the data points was at least 0.92. The threshold estimates were thus based on reasonably good fits of the PC data. Because there was very little difference between the PC scores obtained for the maskers and flankers with a correlated and uncorrelated envelope (mean PC of 0.72 and 0.69, respectively), the Weibull function was estimated from the PC scores collapsed across the two levels of envelope correlation.

The mean PC score obtained for the presentation of the masked rhythm alone (i.e., the no-flanker control) was 0.518, and the standard error (SE) for the 18 subjects was 0.015. The mean d' was 0.132, with a SE of 0.129 [see Fig. 3(b); the size of the SE corresponds to that of the cross symbol]. This performance was close to chance levels; hence, in the absence of flankers, the rhythm was perceptually masked. Given the continuous feedback about rhythm-identification accuracy, these results demonstrate that no attentionally driven strategies were able to overcome masking.

There was no evidence for individual bias towards either of the two rhythms ($0.5 < c < 0.5$), except for one listener who was biased towards Rhythm 2 ($c < -1$). Given that there was no consistent response bias for 17 out of 18 listen-

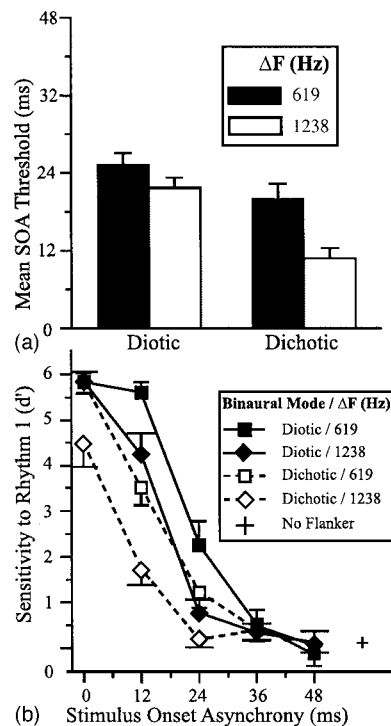


FIG. 3. (a) Mean onset asynchrony (SOA) thresholds for rhythm discrimination as a function of ΔF and binaural mode (ear of presentation). (b) Rhythm sensitivity as a function of ΔF and binaural mode. Higher thresholds and higher d' values represent higher degrees of fusion of the maskers and flankers. Data have been collapsed across the two levels of envelope correlation. Standard errors (SE) are shown; for the no-flanker control, its size corresponds to that of the cross symbol.

ers, it appears that the power of the statistical comparisons was not diminished by response bias.

2. Temporal resolution for event perception and rhythm discriminability

The threshold estimates of listener CB (see Fig. 2) were representative of those found for the 18 listeners. Panel (a) of Fig. 3 shows that the largest mean SOA threshold of 25.3 ms (SE=1.8 ms) was obtained for the diotic condition with the smaller 619-Hz ΔF . This was followed by the diotic condition with the larger ΔF of 1238 Hz (mean=21.8 ms, SE=1.5 ms), the dichotic condition with the 619-Hz ΔF (mean=20.1 ms, SE of 2.3 ms) and the dichotic condition with the 1238-Hz ΔF (mean=10.8 ms, SE=1.6 ms). Since a larger SOA threshold indicates that it was easier for the flanker to capture the masker into a common perceptual unit, it is concluded that cross-spectral fusion diminished with frequency separation as well as with the difference in the lateralization induced by dichotic presentation. The largest mean SOA threshold of 25.3 ms suggests that within the range of conditions of this experiment; an asynchrony of 25 ms triggers the perception of temporally contiguous sounds as separate events. However, smaller asynchronies can abolish their fusion in the presence of other cues, such as frequency separation and/or dichotic presentation. This is compatible with the near chance level of performance found for SOAs of at least 24 ms [see Figs. 3(b) and 4].

Figure 4 shows the WA scores as a function of SOA with ΔF [panel (a)], and envelope correlation and dichotic pre-

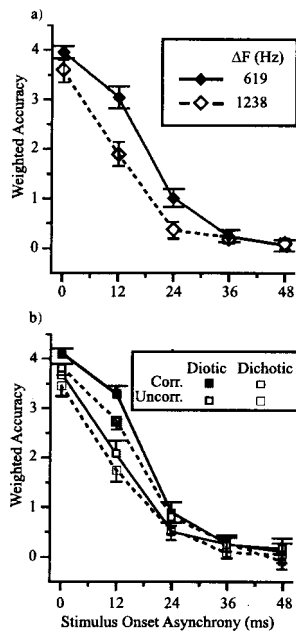


FIG. 4. Mean weighted accuracy (WA) as a function of SOA for maskers and flankers. (a) The parameter is ΔF , and the data have been collapsed across the two levels of envelope correlation and presentation (diotic/dichotic). (b) The parameters are presentation mode and envelope correlation, and the data have been collapsed across the two ΔF 's. Higher WA scores represent higher degrees of fusion of the maskers and flankers. The error bars represent ± 1 SE.

sensation [panel (b)] as parameters. As can be seen, the WA scores exhibit the same general trends as the rhythm-discrimination measure (d') shown in panel (b) of Fig. 3. However, while rapid correlated amplitude changes weakly increased fusion for periods of 36 and 48 ms of overlap [see solid versus dotted line at SOAs of 0 and 12 ms in Fig. 4(b)], they did not make the rhythm more discriminable than did their uncorrelated counterparts, as estimated by both PC and d' scores. Accordingly, the results in Fig. 3 have been collapsed across the two within-burst envelope correlations.

3. Relative contribution of cues to fusion: Description of the trends for WA scores

a. Interaction effects. Figure 4 shows that the weak effect of correlation of rapid intensity changes within individual bursts depended on SOA (only present for synchronous or nearly synchronous stimuli), on a large ΔF and on dichotic presentation. This is consistent with the four-way significant interaction, at the 5% level [$F(4,68)=2.78$, $p=0.03$]. Similarly, that the effect of ΔF depended on both the SOA value and dichotic presentation [see Fig. 3(b)] is reflected by the significant three-way interaction between these factors [$F(4,68)=3.85$, $p=0.007$]. Frequency separation interacted with both SOA [$F(4,68)=18.07$, $p<10^{-5}$] and the mode of presentation [$F(1,17)=25.36$, $p=0.0002$]. There was also a two-way interaction between SOA and the mode of presentation [$F(4,68)=12.08$, $p<10^{-5}$]. This indicates that the difference in WA between the diotic and dichotic stimuli depended on the value of SOA: though there was a difference in WA at 0 ms; it was larger at 12-ms SOA and was basically absent at 36-ms and 48-ms SOAs; this held at both ΔF 's [see Panels (a) and (b)]

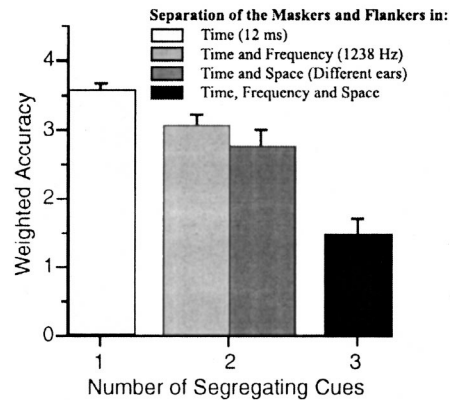


FIG. 5. Synergetic action of cues favoring segregation: a small SOA of 12 ms, dichotic presentation, and a large ΔF of 1238 Hz. The degree of fusion of the maskers and flankers separated by a 12-ms SOA decreases as the number of cues favoring segregation increases from one (white bar at left), to two (middle cluster of two bars) to three (black bar at right). For each listener, the mean WA scores were obtained from data collapsed across the two levels of envelope correlation.

of Fig. 4]. The fact that neither ΔF , nor dichotic presentation had an effect at SOAs of 36 and 48 ms is probably due to their near chance-level performances; that is, these asynchronies by themselves appear to abolish fusion. The results suggest that the effect of ΔF depended on the presence of other cues diminishing fusion: an asynchrony and/or dichotic presentation. Similarly, dichotic presentation, was not sufficient, unaided by asynchrony and/or a large ΔF , to abolish the fusion of simultaneous or nearly simultaneous sounds.

b. Main effects. Figure 4 shows that WA decreased with SOA [$F(4,68)=381.22$, $p<10^{-5}$]. This held for the diotic [$p<10^{-5}$] and the dichotic [$p<10^{-5}$] presentation of the masked rhythm and flankers. This suggests that SOA strongly affected fusion. Overall, WA also decreased with ΔF [$F(1,17)=62.45$, $p<10^{-5}$]; this held for the diotic [$p=0.004$] and dichotic stimuli [$p<10^{-5}$]. This figure also shows that cues reinforced each other in diminishing fusion.

Figure 5 provides another way to look at the interaction between cues which appear to weakly diminish fusion: a small temporal separation of 12 ms, a large frequency separation of 1238 Hz and spatial separation through dichotic presentation. In the absence of frequency and/or spatial separation, a 12-ms asynchrony only weakly diminished fusion (white bar); this is shown by its mean WA of 3.5, indicating that the correctly identified rhythm was rated on average as “clear.” Adding one of these cues (second set of bars), and the two of them (black bar) progressively diminished fusion more, to the point of almost abolishing it. The black bar shows a mean WA around 1.5, that is, when three cues acted together, the correctly identified rhythm was rated on average as “very unclear.” This suggests that a group of cues can have a synergetic action in diminishing fusion, though each by itself diminished fusion only weakly.

III. EXPERIMENT 2. TEMPORAL LIMITS AND RELATIVE CONTRIBUTION OF CUES TO THE CROSS-SPECTRAL FUSION OF NOISE BURSTS PRESENTED IN FREE FIELD

Experiment 2 was designed to generalize the results of experiment 1 to free field presentation. Using the RMR para-

digm, it explored the effects of temporal asynchrony, rapid envelope correlation and frequency separation (ΔF) on fusion. In addition, it manipulated the angular separation of their sources ($\Delta\theta$) and estimated temporal thresholds for event perception in a semi-circular speaker array.

In experiment 1, almost perfect rhythm identifications were obtained for synchronous masker and flanker bursts that were dichotically presented over headphones, had uncorrelated envelopes and were widely separated in frequency. Based on those results, it was expected that temporal coincidence would fuse the masker and flanker bursts, independently of values of the other cues. Experiment 1 also led us to expect that a SOA of 10–25 ms would lead to their perception as separate events, causing the rhythm to remain perceptually camouflaged. Compared to the slow intensity changes induced by temporal synchrony, the rapid ones within individual bursts were expected to have a negligible effect on fusion. It was also expected that ΔF and $\Delta\theta$ would weakly, but consistently, interfere with the perception of the rhythm; when present together, they should reinforce each other in diminishing fusion.

A. Methods

There were 18 normal-hearing listeners; 7 of them had also participated in experiment 1. The synthesis and presentation of the stimuli, as well as the procedure were the same as for experiment 1, except for a few points exposed below. The stimuli were presented from an array of 13 loudspeakers, situated in the sound-attenuated chamber of Dr. R. Zatorre, at the Montreal Neurological Institute (see Fig. 6). Listeners sat one meter away from each loudspeaker. The axis of the diameter of the semicircle, passing through the two end speakers (i.e., from 0 to 180 deg) passed through the axis of the two ears.

The mean rms level for the rhythmic and masking bursts and for the two flankers (measured as a pair) was calibrated to be equal to that of a 1-kHz tone presented over the central speaker and measured as 60 dB SPL at the central position of the listener's head. Due to the constraints of the available space and to keep the listeners' heads immobile, it was neither possible for them to record their responses directly into the computer after each trial, nor to read the computer screen for feedback and initiate new trials. Instead, the experimenter sat three meters away from the listener, behind the speaker array and close to the computer screen. From that position, she entered the listener's verbal response after each trial, read out the computer's feedback about whether or not the rhythm was correctly identified, and initiated each new trial. The listeners could neither see the speakers nor the experimenter during testing. At the beginning of each trial, a 1-kHz warning tone was played through the speaker of the masked rhythm, so that listeners could pay attention to its location. The listeners' heads remained fixed facing the central speaker, even when their attention was directed to other speakers.

Experiment 2 presented a new set of noise samples over loudspeakers, rather than over headphones as in experiment 1. Furthermore, while in experiment 1, the masker pulses could either precede or follow the corresponding flanker

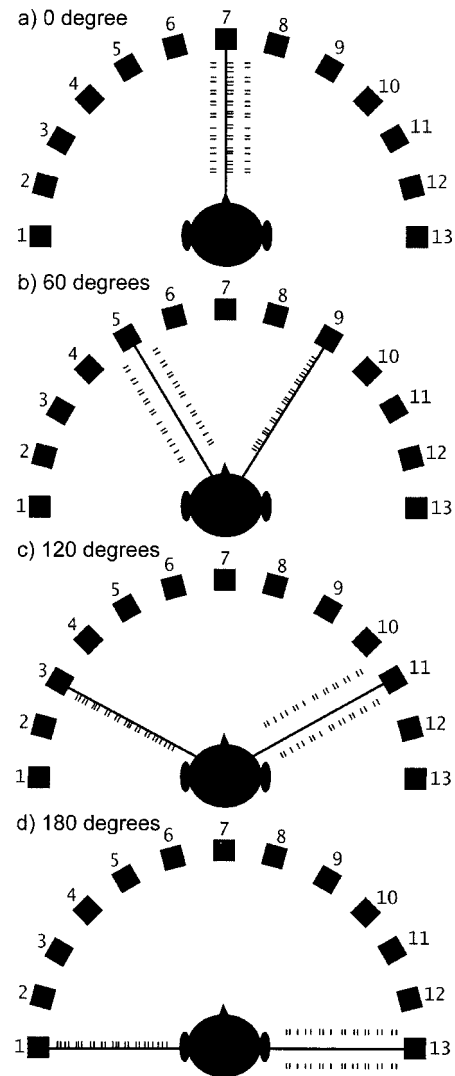


FIG. 6. Semi-circular array of 13 speakers used for the free-field presentation of the stimuli. The masked rhythm (illustrated by the single row of pulses) and the flankers (represented by the double row of pulses) could be presented in the central speaker of the array (a) or at various angular separations ($\Delta\theta$'s), namely, 60 deg (b), 120 deg (c), or 180 deg (d). For each $\Delta\theta$, the speakers of the masked speaker and flankers were symmetrically placed relative to the central speaker.

pulses, in experiment 2, the maskers always preceded the asynchronous flankers. Figure 6 shows that the masked rhythm and flankers could either be both presented in the central speaker [panel (a)] or at various angular separations ($\Delta\theta$) from it: 60, 120, and 180 deg [panels (b), (c), and (d)]. For each $\Delta\theta$, the masked rhythm and flankers came from speakers that were symmetrically placed relative to the central axis. The choice of which signal to present on each side of the array was counterbalanced across trials. There was a no-flanker control for each of the four $\Delta\theta$'s, in which the masked-rhythm sequence alone was either presented in the central speaker or at 30, 60, or 90 deg to the left or to the right of it. The different conditions were randomly presented across trials.

B. Results and discussion

1. Measures of sensitivity to the target rhythm

The degree of fusion of the maskers and flankers was assessed in the same way as for experiment 1. Because the

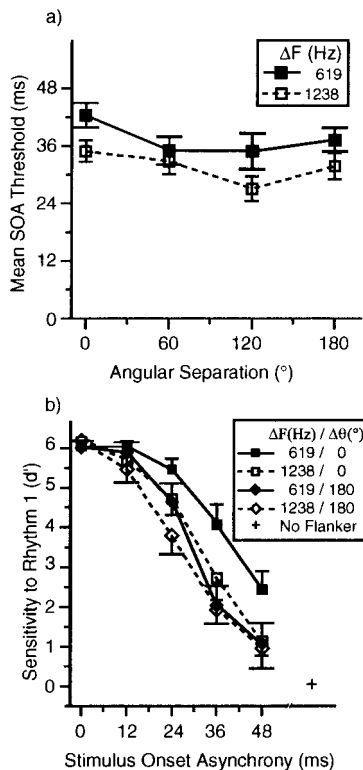


FIG. 7. (a) Mean onset asynchrony (SOA) thresholds for rhythm discrimination as a function of ΔF and $\Delta\theta$. (b) Rhythm sensitivity as a function of ΔF and $\Delta\theta$. Higher thresholds and higher d' values represent higher degrees of fusion of the maskers and flankers. Data have been collapsed across the two levels of envelope correlation. Standard errors (SE) are shown; for the no-flanker control, its size corresponds to that of the cross symbol.

mean PC scores, computed across listeners was 0.86 for correlated and 0.82 for uncorrelated AM (i.e., they differed by only 0.04), the Weibull functions were estimated from the PC scores collapsed across the two levels of envelope correlation. For each $\Delta\theta$ -by- ΔF condition, the mean, across listeners, of the within-subject Pearson-coefficient correlations (r) between the fitted function and the data points was at least 0.9.

2. No-flanker controls, performance range and response bias in rhythm-detection accuracy

The no-flanker control yielded a mean PC of 0.520 (SE of 0.018) and a mean d' of 0.059 [SE of 0.089 shown by the size of the cross symbol in Fig. 7(b)]. This very near chance-level performance verified that the rhythm was masked in the absence of flankers. On the other hand, synchrony fused spatially and spectrally distributed noise bursts. For each 0-ms SOA condition, the mean d' was larger than 4.65.

There was no systematic response bias for 17 listeners (i.e., $-0.2 > c < 0.2$). One listener had a slight bias towards Rhythm 1 for the conditions with and without flankers, the c values being -0.45 and -0.38 , respectively. Given that 95% of the listeners had very small c values, the power of the statistical comparisons was probably not diminished by response bias.

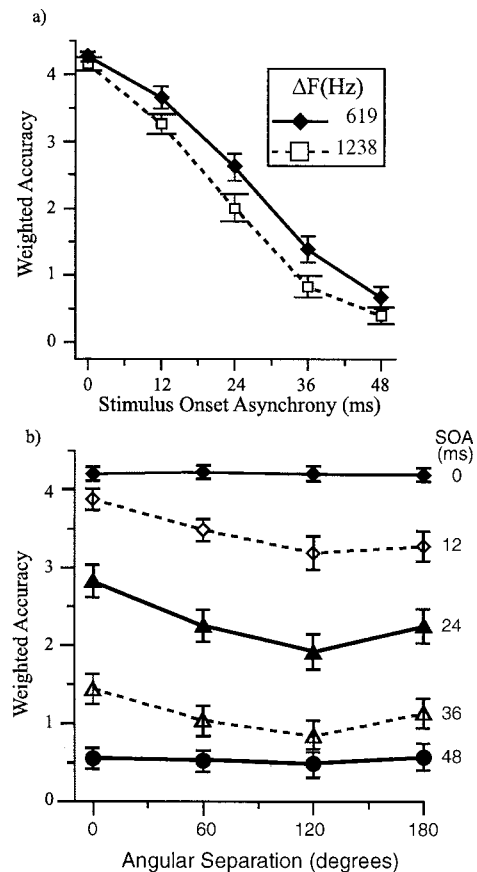


FIG. 8. Relative contribution of cues to the fusion of brief noise bursts separated in frequency and in space. Higher WA scores represent higher degrees of fusion. (a) WA as a function of SOA for the two ΔF 's collapsed across the two levels of envelope correlation and the four $\Delta\theta$'s. (b) WA as a function of $\Delta\theta$, with SOA as the parameter; data are collapsed across the two levels of envelope correlation and the two ΔF 's. The error bars represent ± 1 SE.

3. Temporal resolution for event perception and rhythm discriminability

The SOA-threshold estimates graphed in Fig. 7(a) show that a SOA between 25 and 45 ms (i.e., from one SE below the lowest mean threshold to one above the highest one) abolished fusion. The asynchrony required for the temporal resolution of brief noise bursts depended on how far apart they were in frequency [filled versus empty squares in Fig. 7(a)]. This was also the case in experiment 1 over headphones [black versus white bars in Fig. 3(a)]. This first experiment also showed higher thresholds for sounds presented in both ears versus different ears [left versus right bars in Fig. 3(a)]. This is consistent with the effect of spatial separation ($\Delta\theta$) on thresholds in this second experiment [Fig. 7(a)]. However, post-hoc pairwise comparisons showed that the effect of $\Delta\theta$ in diminishing fusion (i.e., lowering thresholds) was all-or-none: whether or not sounds came from the same speaker mattered, but how far apart the speakers were in space did not.

4. Relative contribution of cues: Description of the main trends for WA scores

Figure 8 shows a monotonic decrease in WA scores with increases in SOA [$F(4,68) = 324.46$, $p < 10^{-5}$]. On the

other hand, frequency separation (ΔF), spatial separation ($\Delta\theta$), and envelope correlation affected only weakly fusion. Their combined effect was not sufficient to overcome the powerful effect of synchrony on fusion. The lowest mean WA among the 0-ms SOA conditions was 4. It was obtained for both the 120 and 180 deg $\Delta\theta$'s with a 1238-Hz ΔF and uncorrelated envelopes; this value falls between 3.5 and 4.5 which correspond, respectively, to a "clear" and "very clear" rating of the correct rhythm. The effect of ΔF , $\Delta\theta$, and uncorrelated envelopes was clearest for the cases of partial fusion that were observed when the maskers and the flankers were partly overlapping (see Fig. 8). When the fusion of the maskers and flankers was complete, as at 0-ms SOA, or absent, as at 48-ms SOA, the contribution of a much weaker cue might be too small for its effect on fusion to be observable. This interpretation is consistent with the two-way interaction SOA-by- ΔF [$F(4,68)=4.18$, $p=0.005$] and SOA-by- $\Delta\theta$ [$F(12,204)=5.23$, $p<10^{-5}$] showing that the effects of both ΔF and $\Delta\theta$ depended on the value of SOA.

5. Unexpected effect of a sequential cue on fusion

Overall, the thresholds found when noise-burst stimuli were presented in a free field were higher than those found when they were presented over headphones [compare Figs. 3(a) and 7(a)]. A higher threshold means that fusion still took place at larger SOAs, fusion improving performance in the RMR task. The higher performance of the free-field presentation relative to that over headphones was also reflected by higher absolute mean WA scores across all conditions. This resulted in ceiling performance at 0-ms SOA and in near chance-level performance at 36-ms and 48-ms SOAs. The authors suspected that the common magnitude and direction of SOA in the global sequences of experiment 2—the two flanker bands were always delayed from the temporally adjacent masker by a given SOA—contributed to fusion over and above the local magnitude of SOA. To test whether such a sequential cue favored fusion, a post hoc analysis compared the performance at 48-ms SOA against that for the no-flanker control. Since there was no overlap between the maskers and flankers at that largest SOA, a higher degree of fusion could only be due to sequential cues. For each $\Delta\theta$, the 48-ms SOA condition yielded a higher WA than that obtained for the no-flanker control: the mean WA was almost equal across $\Delta\theta$'s, varying from 0.50 to 0.57; for the no-flanker control, it was only 0.03. The mean PC of 0.64 and d' of 0.74, obtained at 48-ms SOA were also larger than the PC of 0.51 and d' of 0.06 obtained for the no-flanker control. This can be contrasted with the near chance level of performance observed for the bi-directional 48-ms SOA condition of experiment 1, namely, mean PC of 0.54 and d' of 0.25. Post hoc comparisons between the 48-ms SOA and the no-flanker conditions were highly significant [$p<10^{-5}$] for WA, PC, and d' . This suggests that a constant direction of SOA affected the scores. It is also possible that an unforeseen difference between the free-field and binaural contexts affected performance.

C. Discussion

1. Relative contribution of temporal, spatial, and spectral separation to the segregation of temporally contiguous sound events

a. Strong effect of cross-spectral correlation of slow-varying intensity changes on fusion. The simultaneity of onsets and offsets across the masker and flanker bursts resulted in a slow pattern of correlated intensity changes across frequency regions. Given that such a pattern was nonperiodic (i.e., resulting from irregularly-spaced sounds), it did not have a frequency of modulation per se. However, one can say that overall it was slow, in that it resulted from sequences in which the temporal density of the irregular masker and flanker sounds was low, namely one per 192-ms interval. This is equivalent to 5.2 sounds/s and as such is comparable to a frequency of amplitude modulation of 5 Hz. When temporal synchrony, favoring fusion, competes with frequency separation and spatial separation (through presentation in different ears or loudspeakers), favoring segregation (i.e., diminishing fusion), synchrony played the determinant role, producing strong fusion (see Figs. 3, 4, 7, and 8). This powerful effect of synchrony is consistent with past results in the literature (see Darwin and Carlyon, 1995 for a review).

b. Very weak effect of cross-spectral correlation of fast-varying intensity changes on fusion. The slow correlation in intensity changes induced by temporal synchrony can be contrasted with that obtained through within-bursts envelope correlation. The latter is much more rapid and takes place over much shorter periods varying from 12 ms (36-ms SOA) to 48 ms (0-ms SOA) of temporal overlap. Such brief overlaps follow from the use of sounds of a constant 48-ms duration. The differences in WA resulting from envelope correlation were only observed at 0-ms and 12-ms SOA [solid versus dashed lines in Fig. 4(b)]. These results suggest that slow, but not fast intensity changes affect cross-spectral fusion. However, the fastest modulation in the envelope spectrum being nominally 100 Hz (i.e., the width of the common noise modulator), there might have been too few samples of the common amplitude envelope for the auditory system to reliably detect it. Future experiments should use noise bursts of a longer duration to determine whether there is a minimum number of cycles of the correlated waveform necessary to induce fusion. However, to truly compare the effect of the fast-varying amplitude changes of a local event to the slower ones of the global sequence on fusion, SOA should be manipulated independently from the duration of the sounds.⁶

c. Weak effect of large frequency separations on fusion. The weak, but consistent effect of frequency separation (ΔF) in this study replicates that found in a prior RMR experiment, with very similar stimuli (Turgeon, 1999). This experiment presented diotically and dichotically 200-Hz-wide noise bursts, the flanker bands being either 400, 550, 700, or 850 Hz remote in frequency from the masker bands centered at 1500 Hz. Furthermore, the role of ΔF in RMR is compatible with its effect on comodulation masking release or CMR (Hall *et al.*, 1984): though it did not abolish fusion, it reduced the degree of fusion of temporally overlapping, but asynchronous sounds (see Figs. 3 and 7). This effect has some ecological validity since causally related concurrent

sounds are more likely to cluster in frequency than causally unrelated ones. For instance, in many species, the sounds produced by a male and a female tend to be more distributed in frequency than those produced by a single female (the sounds produced by a female being typically in higher frequency registers than those of a male). However, being rich sounds, they are likely to partly overlap in frequency; hence the auditory system would still have to somehow separate the spectrally overlapped portions.

d. Weak effect of large spatial separations on fusion: Different ears versus different speakers. The weak but consistent effect of spatial separation in diminishing fusion suggests that it is used by the mammalian brain for sound-source determination. This is consistent with its role in promoting the identification of non-speech auditory patterns (Kidd *et al.*, 1998) and in the localization of concurrent sounds, as shown by studies on the concurrent minimum audible angle in a free field (Perrott, 1984) and in simulated space (Divenyi and Oliver, 1989). Taken together, these results suggest that spatial separation influences sound segregation (“how many”), identification (“what”), and localization (“where”), though it is not sufficient to segregate brief, concurrent, frequency-separated sounds (i.e., abolish their fusion). Figure 8 shows that unlike an asynchrony of 48 ms, which yielded a near-chance level of performance at each frequency and spatial separations (i.e., WA near 0), large spatial separations of 120 and 180 deg did not prevent the rhythm from being partly released from masking in the absence of an asynchrony of at least 36 ms. However, as Yost *et al.* (1996) have proposed, the separation of sources might play a more important role when more than two concurrent sounds are present. Further research should compare the contribution of spatial separation under conditions of varying number of concurrent sounds.

Figure 8 shows that the clearest effect of $\Delta\theta$ on the segregation of noise bursts is the contrast between sounds coming from the same speaker (a $\Delta\theta$ of 0 deg) or from different ones ($\Delta\theta$'s larger than 0 deg). These results suggest that the magnitude of the angular separation of sound sources is irrelevant for the segregation of sounds close together in time. A comparison between Figs. 3(a) and 7(a) suggests another important conclusion: the spatial disparity provided by dichotic presentation has more impact on the temporal resolution of brief concurrent sounds, than that provided by the spatial separation of their sound sources in a free field. It might be that dichotic separation is more efficient for sound segregation because it is an extreme case of interaural differences for sounds happening simultaneously, the stimulation of one sound being delivered to one ear only, while that of the other sound(s) is delivered to the other ear only. The free-field testing is more akin to real-world situations in which each of many individual sounds stimulates both ears,⁷ though at slightly different times and intensities, allowing for the computation of the location of each source. We suggest that when drawing conclusions about the contribution of spatial disparities, one should not consider dichotic presentation as reflecting ecologically valid differences in the location of sound sources. Even when two sound sources are close to different ears, a sound coming from one of them usually

stimulates the two ears, albeit with larger binaural differences in intensities and time of arrival than if sources were closer to the midline axis. For this reason, the separation of sound sources in a free field is considered as more representative of the true contribution of spatial separation to sound-source segregation. This contribution is weak when two sources are simultaneously active. Further experimentation should determine whether these conclusions apply to sounds of a longer duration, as well as to temporally contiguous but non overlapping sounds.

2. Binaural fusion is not spectrally limited for the purpose of sound-source determination

Taken together, the results from dichotic RMR and CMR provide evidence for a process that performs a cross-spectral analysis of the low-rate amplitude changes. It is suggested that this analysis generalizes to the way in which acoustic information that is spread out over the spectrum or over space will contribute to the perception of either a single sound or more than one sound. Contrary to this suggestion, some experiments have concluded that binaural fusion has clear spectral limits (Perrott and Barry, 1969; van den Brink *et al.*, 1976). Perrott and Barry (1969) have shown that the fusion of concurrent pure tones presented to the different ears is contingent upon them having less than a critical difference in frequency, which is proportional to the frequency of the tones themselves (approximately 4% of the latter). Other experiments on the concurrent minimum audible angle (CMAA) in simulated space (Divenyi and Oliver, 1989) and in a free field (Perrott, 1984) have demonstrated that the auditory system has a very poor spatial resolution (as much as 60 deg) for spectrally overlapping concurrent sounds as well as for spectrally nonoverlapping sounds that are close in frequency. Assuming that poor spatial resolution is linked to poor perceptual segregation, this provides supportive evidence that the binaural segregation of spectrally overlapping sounds requires a wide spatial separation. This interpretation is further reinforced by the work of Scharf *et al.* (1976) which suggests that the segregation of two components in space is most likely to occur when their spectral patterns show little or no overlap. Given that fusion is the absence of segregation,¹ if sounds are not segregated in space, as in CMAA, they must be fused, at least partly. Therefore, together, the results on binaural fusion and on the CMAA provide evidence that the sound-source determination of concurrent sounds is somehow spectrally limited. How can these results be reconciled with the results obtained with the RMR and CMR paradigms, which together provide evidence for a cross-spectral binaural analysis underlying sound-source determination?

The present research suggests that sounds coming from different locations in space can be perceived as a single environmental event, without their being spectrally matched (spectral matching being typical of sounds arising from a common natural source). This is consistent with past observations which mention that spectrally remote sounds can evoke a single image, though it is typically not well localized and described as “diffuse” (Perrott and Barry, 1969; Thurlow and Elfner, 1959). In the present study, the observations

of the authors suggest that the fusion of the maskers and flankers which were perceived as being causally related, but were spectrally and spatially remote, produced the localization of the masker-flanker complexes to either a virtual source, or to the veridical source of the flankers. The different tasks used in the RMR paradigms, CMAA studies, and other studies of binaural fusion might have been looking at different types of fusion: (i) The fusion of spectrally overlapping components distributed in space through binaural cross-correlation localization mechanisms (Jeffress, 1972; Lindemann, 1986); and (ii) The fusion of spectrally nonoverlapping components through independent pre-attentive grouping processes.¹ When fusion is defined as the perception, as a single sound event, of many frequency components that might or might not be distributed in space, there does not seem to be any spectral limit for fusion. On the other hand, the perception of a single sound event at a definite location in the environment (“what is where”) appears to be spectrally limited (Divenyi and Oliver, 1989; Perrott, 1984; Scharf *et al.*, 1976).

3. Implications of the results for the psychophysical limits of event perception

The two RMR experiments suggest that the asynchrony needed for the segregation of brief sound events with abrupt onsets and offsets is about 20-to-40 ms; however, it can be lowered by the synergetic action of other simultaneous-grouping cues such as frequency and spatial separation, as well as sequential ones, such as a constant direction of asynchrony. The range of asynchrony thresholds is in general agreement with the literature on auditory grouping showing that an asynchrony of 30–40 ms is required for removing a partial from contributing to the overall timbre (Bregman and Pinker, 1978), to the lateralization (Hill and Darwin, 1993) or to the vowel identity (Darwin, 1981) of a complex sound. If timbre, vowel quality, and perceived lateralization are assumed to be properties of perceptually segregated sounds, one should expect this close correspondence. The 20-to-40 ms asynchrony in these phenomena is about an order of magnitude higher than the 2–3 ms required for the cross-spectral detection of an asynchrony (Green, 1973) and an order of magnitude lower than the 200–300 ms asynchrony preventing a partial from contributing to the pitch of a complex tone (Darwin and Ciocca, 1992). The fact that a just detectable asynchrony is not sufficient to segregate temporally overlapping sounds in different parts of the spectrum is compatible with the observation that listeners report only a single click while reliably detecting very small asynchronies (Green, 1973). At the other extreme, the discrepancy between the temporal limits for pitch and for event perception might indicate different underlying neural mechanisms. The temporal limits for event perception should be further investigated, especially as they relate to other spectro-temporal regularities known to influence auditory organization, both of local properties of a sequence (e.g., duration and rate of onset and offset of each sound) and global ones (e.g., tempo, distribution of silent intervals). Further experiments should also look at how time-varying intensity changes interact with spectral

regularities influencing the computation of pitch and the fusion of the tonal sounds forming harmonic and inharmonic complexes (Roberts and Brunstrom, 1998).

4. Implications of the results for the probabilistic approach to event perception

In complex world environments, many sources of acoustic evidence typically converge upon a common perceptual interpretation: sounds come from the same spatial location, start and stop at the same time and undergo common spectro-temporal changes. The present study created competition among alternative auditory organizations. Such ambiguous stimuli unveil the relative importance of grouping cues. In this study, despite the combined effect of frequency and spatial separation in favoring segregation, simultaneous sounds fused strongly enough to perceptually release the rhythm from masking. The possibility that temporal synchrony is “weighted” more strongly than frequency and spatial separation taken together has ecological validity. Temporal coincidence is a highly reliable and robust property of the components of biologically relevant sounds. Although it is likely for sounds coming from different sources to have some degree of temporal overlap, it is highly unlikely that they happen to start and stop at exactly the same time. On the other hand, frequency separation is not as reliable a cue since concurrent sounds coming from a common biological source typically occupy different frequency regions (Yost and Sheft, 1993); conversely those coming from different sources can overlap in frequency. Similarly, causally related sounds need not have a sharply focused location, because they go through and around some surfaces and are reflected by others. Because of these properties of the acoustic world, onset synchrony and deviations from it are more informative to a biological system than either the frequency or the spatial separation of acoustic components. This might explain why asynchrony contributed more to sound segregation than other cues did in the present study. Such a weighted contribution might, however, be dependent on the particular methodology of RMR studies as well as the parameters values used in these experiments. Experiments with other tasks and stimuli should look at the issue to determine to what extent these results are generalizable to the perceptual organization of complex sounds.

ACKNOWLEDGMENTS

This research was supported in part, by a grant from the National Sciences and Engineering Research Council of Canada (NSERC) to A. S. Bregman and in part by the FCAR program of the Province of Quebec. We are grateful for the technical assistance of Pierre A. Ahad of the McGill Auditory laboratory. We also want to thank Dr. Robert Zatorre for having allowed us to do the free-field testing in his laboratory at the Montreal Neurological Institute.

¹Glossary of terms: *Auditory grouping* involves the perceptual organization of sound components into coherent perceptual units. These units can be isolated sound events (e.g., a hand clap) or sequences of them (e.g., a melody), also known as streams. The term “grouping” typically encompasses both the *fusion* of *n* sound components (usually concurrent ones)

into a single event and their *segregation* as n distinct sounds (sequential or concurrent ones). *Pre-attentive auditory grouping* results from biologically implemented processes exploiting environmental regularities with adaptive value; this is independent of acquired knowledge, not under the control of attentional mechanisms and can be contrasted with attentionally driven grouping (Bregman, 1990). *Cross-spectral integration* is the summing up of time-varying intensity changes across frequency-selective channels; the information might or might not be weighted equally in different channels. *Cross-spectral fusion* happens when cross-spectral integration leads to the perception of multiple frequency components as a single sound event.

²We conceive of fusion and segregation as being the two extremes of a continuum: at one extreme, many sound components are fused, that is, they are perceived as one sound event; at the other extreme, they are segregated, that is, perceived as separate sound events. There are intermediate cases of *partial fusion* on this continuum in which many sound components can be perceived as many sound events or as a single one with global properties different from those of its parts. For such ambiguous percepts, what is heard depends on attentional factors and/or cognitive expectations, such as trying to hear out the individual notes of a chord versus the whole chord. Although segregation is assumed to be inversely correlated with fusion, for clarity purposes, the results have been described mainly, in terms of “degrees of fusion,” such as complete fusion, partial fusion, no fusion (i.e., segregation). This is not to imply that we take a position about whether or not fusion is the default for simultaneous sounds. In the statements of hypotheses and interpretation of results, we refer to both “fusion” and “segregation;” the use of each term being justified by how a cue is typically described in the literature (e.g., a segregation cue, in the case of onset asynchrony and a fusion cue, in the case of a common fundamental frequency).

³In RMR, a sequence is masked but its individual sounds are not. This type of masking can be distinguished from that due to peripheral signal-to-noise constraints (Zwicker, 1970). Such *energetic masking* takes place between temporally overlapping sounds that are either spectrally overlapping or close in frequency (e.g., when a noise burst perceptually masks a simultaneously present sinusoidal signal situated in the same frequency region, as in CMR). The *sequential masking* in RMR is more akin to *informational masking* (IM) in which the signal and maskers are perceptually segregated objects (Kidd *et al.*, 1994). Unlike IM, in which the release from masking can be due to spectral or temporal regularities among the subset of sequential target components that are not shared by the masking ones, in RMR, no sequential property distinguishes the components of the target rhythm from those of the masking sequence (i.e., apart from their regular vs irregular arrangement). Rather, the rhythm is released from masking by spectro-temporal regularities relating the concurrent maskers and flankers that cause them to fuse perceptually.

⁴This effect of frequency separation between the on-signal masking band and the flanking bands might be inflated by within-channel processes, such as “dip listening” (Schooveveldt and Moore, 1987).

⁵Sensitivity to Rhythm 1 (d') and response biases (c) were estimated for each subject from signal detection theory. In terms of Z (i.e., the inverse of the normal distribution function), d' is defined as $Z(H) - Z(F)$ and c , as $0.5 * [Z(H) + Z(F)]$; where “ H ” is the proportion of Hits and “ F ” is the proportion of False Alarms. In the present experiments, “ H ” was the proportion of correctly identified Rhythm 1 and “ F ,” that of falsely identified Rhythm 1 (i.e., Rhythm 2 was present). To avoid values of infinity in the computation of d' , proportions of 1 were converted into 0.999; this yields a d' value of 6.18. Hence, we used a d' value of 0 as the chance-level performance, and a d' of 6.18 as the perfect performance. When the frequency of response to Rhythm 1 across all trials is equal to that of Rhythm 2, the response bias statistic (c) equals zero (i.e., False Alarm and Miss rates are equal). A positive or a negative c indicates a higher tendency to respond “Rhythm 1” or “Rhythm 2,” respectively.

⁶The lack of discriminability of fast-varying amplitude correlations might be responsible for the lack of an RMR effect. Another concern is that the period of within-burst correlation decreased with asynchrony. Consequently, part of the SOA effect might reflect the reduction of fine-scale envelope correlation. This follows from the constant duration of the bursts, which allowed for a wider range in the selection of the silent intervals between irregular bursts. Despite the possible contribution of the correlated-envelope duration to the overall effect of SOA (half of the masker-flanker events being correlated), there was a clear effect of SOA on fusion. SOA had a strongly significant effect [$p < 10^{-5}$], both for the conditions of this experiment, and in a prior experiment in which the maskers and flankers were always uncorrelated (Turgeon, 1999).

⁷There are some rare exceptions to this generalization; for instance, the sound produced when there is an insect in one ear stimulates only the receptors in that ear.

- Achim, A., Bregman, A. S., and Ahad, P. A. (1995). “Manager of Auditory Perception and Linguistic Experiments (MAPLE).” Montreal QC., Canada: Auditory Perception Laboratory, Dept. of Psychology, McGill University.
- Bregman, A. S. (1978). “Auditory streaming: Competition among alternative organizations,” *Percept. Psychophys.* **23**, 391–398.
- Bregman, A. S. (1990). *Auditory Scene Analysis: The Perceptual Organization of Sound* (MIT Press, Cambridge, MA).
- Bregman, A. S. (1993). “Auditory scene analysis: Hearing in complex environments,” in *Thinking in Sounds: Cognitive Aspects of Human Audition*, edited by S. McAdams and E. Bigand (Oxford University Press, Oxford), pp. 10–36.
- Bregman, A. S., and Ahad, P. (1996). “Demonstrations of Auditory Scene Analysis: The perceptual organization of sound,” (Compact disk and booklet, pp. 41–42), Auditory Perception Laboratory, Psychology Dept., McGill University.
- Bregman, A. S., and Pinker, S. (1978). “Auditory streaming and the building of timbre,” *Can. J. Psychol.* **32**, 19–31.
- Bregman, A. S., Abramson, J., Doehring, P., and Darwin, C. J. (1985). “Spectral integration based on common amplitude modulation,” *Percept. Psychophys.* **37**, 483–493.
- Brochard, R., Drake, C., Botte, M.-C., and McAdams, S. (1999). “Perceptual organization of complex auditory sequences: Effect of number of simultaneous subsequences and frequency separation,” *J. Exp. Psychol., Hum. Percept. Perform.* **25**, 1742–1759.
- Dannenbring, G., and Bregman, A. S. (1978). “Streaming vs fusion of sinusoidal components of complex tones,” *Percept. Psychophys.* **24**, 369–376.
- Darwin, C. J. (1981). “Perceptual grouping of speech components differing in fundamental frequency and onset-time,” *Q. J. Exp. Psychol.* **33**, 185–207.
- Darwin, C. J., and Carlyon, R. (1995). “Auditory grouping,” in *The Handbook of Perception and Cognition, Volume 6, Hearing*, 2nd ed., edited by B. C. J. Moore (Academic, London), pp. 387–424.
- Darwin, C. J., and Ciocca, V. (1992). “Grouping in pitch perception: Effects of onset asynchrony and ear of presentation of a mistuned component,” *J. Acoust. Soc. Am.* **91**, 3381–3390.
- Divenyi, P. L., and Oliver, S. K. (1989). “Resolution of steady-state sounds in simulated auditory space,” *J. Acoust. Soc. Am.* **85**, 2042–2052.
- Glasberg, B. R., and Moore, B. C. J. (1990). “Derivation of auditory filter shapes from notch-noise data,” *Hear. Res.* **47**, 103–138.
- Gordon, P. C. (1997). “Coherence masking protection in brief noise complexes: Effects of temporal patterns?” *J. Acoust. Soc. Am.* **102**, 2276–2283.
- Green, D. M. (1973). “Temporal acuity as a function of frequency,” *J. Acoust. Soc. Am.* **54**, 373–379.
- Green, D. M. (1988). *Profile Analysis: Auditory Intensity Discrimination* (Oxford University Press, New York).
- Grose, J. H., and Hall III, J. W. (1993). “Comodulation masking release: Is comodulation sufficient?” *J. Acoust. Soc. Am.* **93**, 2896–2902.
- Hall III, J. W., and Grose, J. H. (1991). “Some effects of auditory grouping factors on modulation detection interference (MDI),” *J. Acoust. Soc. Am.* **90**, 3028–3035.
- Hall III, J. W., Haggard, M. P., and Fernandes, M. A. (1984). “Detection in noise by spectro-temporal pattern analysis,” *J. Acoust. Soc. Am.* **76**, 50–56.
- Handel, S. (1989). “Rhythm,” Chapter 5, in *Listening: An Introduction to the Perception of Auditory Events* (MIT Press, Cambridge, MA).
- Hartmann, W. M. (1988). “Pitch perception and the organization and integration of auditory entities,” in *Auditory Function: Neurobiological Bases of Hearing*, edited by G. W. Edelman, W. E. Gall, and W. M. Cowan (Wiley, New York), pp. 623–645.
- Henke, W. L. (1990). *MITSYN Languages* (Belmont, MA).
- Hill, N. I., and Darwin, C. J. (1993). “Lateralization of a perturbed harmonic: Effects of onset asynchrony and mistuning,” *J. Acoust. Soc. Am.* **100**, 2352–2364.
- Hukin, R. W., and Darwin, C. J. (1995). “Effects of contralateral presentation and of interaural time differences in segregating a harmonic from a vowel,” *J. Acoust. Soc. Am.* **98**, 1380–1387.
- Jeffress, L. A. (1972). “Binaural signal detection: Vector theory,” in *Foundations of Modern Auditory Theory, Vol. II*, edited by J. V. Tobias (Academic, New York).

- Kidd, G., Mason, C., Rohdla, T. L., and Deliwala, P. S. (1998). "Release from masking due to spatial separation of sources in the identification of nonspeech auditory patterns," *J. Acoust. Soc. Am.* **104**, 422–431.
- Kidd, G., Mason, C., Deliwala, P. S., Woods, W. S., and Colburn, H. S. (1994). "Reducing informational masking by sound segregation," *J. Acoust. Soc. Am.* **95**, 3475–3480.
- Lindemann, W. (1986). "Extension of a binaural cross-correlation model by contralateral inhibition. I. Simulation of lateralization for stationary signals," *J. Acoust. Soc. Am.* **80**, 1608–1622.
- Macmillan, N. A., and Creelman, C. D. (1991). *Detection Theory: A User's Guide* (MIT Press, Cambridge, MA).
- McFadden, D. M. (1986). "Comodulation masking release: Effects of varying the level, duration, and time delay of the cue band," *J. Acoust. Soc. Am.* **80**, 1658.
- McFadden, D. M., and Wright, B. A. (1990). "Temporal decline of masking and comodulation detection differences," *J. Acoust. Soc. Am.* **88**, 711–724.
- Moore, B. C. J. (1989). *An Introduction to the Psychology of Hearing*, 3rd ed. (Academic, New York).
- Perrott, D. R. (1984). "Concurrent minimum audible angle: A re-examination of the concept of auditory spatial acuity," *J. Acoust. Soc. Am.* **75**, 1201–1206.
- Perrott, D. R., and Barry, S. H. (1969). "Binaural fusion," *J. Aud. Res.* **9**, 263–269.
- Roberts, B., and Brunstrom, J. M. (1998). "Perceptual segregation and pitch shifts of mistuned components in harmonic complexes and in regular in-harmonic complexes," *J. Acoust. Soc. Am.* **104**, 2326–2338.
- Scharf, B., Florentine, M., and Meiselman, C. H. (1976). "Critical band in auditory lateralization," *Sens. Processes* **1**, 109–126.
- Schooneveldt, G. P., and Moore, B. C. J. (1987). "Comodulation masking release (CMR): Effects of signal frequency, flanking band frequency, masker bandwidth, flanking band level, monotic versus dichotic presentation of the flanking band," *J. Acoust. Soc. Am.* **82**, 1944–1956.
- Sheft, S., and Yost, W. A. (1997). "Binaural modulation detection interference," *J. Acoust. Soc. Am.* **102**, 1791–1798.
- Steiger, H., and Bregman, A. S. (1982). "Competition among auditory streaming, dichotic fusion and diotic fusion," *Percept. Psychophys.* **32**, 153–162.
- Thurlow, W. R., and Elfner, L. F. (1959). "Pure-tone cross-ear localization effects," *J. Acoust. Soc. Am.* **31**, 1606–1608.
- Turgeon, M. (1999). Chapter 2 in: *Cross-spectral auditory grouping using the paradigm of rhythmic masking release: Doctoral dissertation*, McGill University, Montreal, Qc., Canada.
- Turgeon, M. (1994). *The influence of log-frequency parallel gliding upon perceptual fusion*. Master's thesis, McGill University, Montreal, Qc., Canada.
- Turgeon, M., and Bregman, A. S. (1997). "'Rhythmic Masking Release: A paradigm to investigate auditory grouping resulting from the integration of time-varying intensity levels across frequency and across ears,'" *J. Acoust. Soc. Am.* **102**, 3160.
- van den Brink, G., Sintnicolaas, K., and van Stam, W. S. (1976). "Dichotic pitch fusion," *J. Acoust. Soc. Am.* **59**, 1471–1476.
- Weibull, W. A. (1951). "A statistical distribution function of wide applicability," *J. Appl. Mech.* **18**, 292–297.
- Woods, W. S., and Colburn, H. S. (1992). "Test of a model of auditory object formation using intensity and interaural time difference discrimination," *J. Acoust. Soc. Am.* **91**, 2894–2902.
- Yost, W. A. (1991). "Auditory image perception and analysis: the basis for hearing," *Hear. Res.* **56**, 8–18.
- Yost, W. A., and Sheft, S. (1993). "Auditory perception," in *Human Psychophysics*, edited by W. A. Yost, A. N. Popper, and R. F. Fay (Springer-Verlag, New York), pp. 193–236.
- Yost, W. A., Dye, Jr., R. H., and Sheft, S. (1996). "A simulated 'Cocktail Party' with up to three sound sources," *Percept. Psychophys.* **58**, 1026–1036.
- Yost, W. A., Sheft, S., and Opie, J. (1989). "Modulation interference in detection and discrimination of amplitude modulation," *J. Acoust. Soc. Am.* **86**, 2138–2147.
- Zwicker, E. (1970). "Masking and psychological excitation as consequences of the ear's frequency analysis," in *Frequency Analysis and Periodicity Detection in Hearing*, edited by R. Plomp and G. F. Smoorenburg (AW Sijthoff, The Netherlands), pp. 376–394.

Assessing auditory distance perception using virtual acoustics

Pavel Zahorik^{a)}

Waisman Center, University of Wisconsin-Madison, Madison, Wisconsin 53705

(Received 27 March 2001; revised 14 January 2002; accepted 14 January 2002)

In most naturally occurring situations, multiple acoustic properties of the sound reaching a listener's ears change as sound source distance changes. Because many of these acoustic properties, or cues, can be confounded with variation in the acoustic properties of the source and the environment, the perceptual processes subserving distance localization likely combine and weight multiple cues in order to produce stable estimates of sound source distance. Here, this cue-weighting process is examined psychophysically, using a method of virtual acoustics that allows precise measurement and control of the acoustic cues thought to be salient for distance perception in a representative large-room environment. Though listeners' judgments of sound source distance are found to consistently and exponentially underestimate true distance, the perceptual weight assigned to two primary distance cues (intensity and direct-to-reverberant energy ratio) varies substantially as a function of both sound source type (noise and speech) and angular position (0° and 90° relative to the median plane). These results suggest that the cue-weighting process is flexible, and able to adapt to individual distance cues that vary as a result of source properties and environmental conditions.

© 2002 Acoustical Society of America. [DOI: 10.1121/1.1458027]

PACS numbers: 43.66.Qp, 43.66.Pn, 43.66.Yw [LRB]

I. INTRODUCTION

Compared to directional localization, relatively little is known about human perception of sound source distance. It is clear that for a complete description of perceived three-dimensional auditory space, distance is no less important than direction. Rigorous study of auditory distance perception is often difficult, however, because of inherent complexities of the stimulus. Changes in sound source distance often result in changes to multiple acoustic properties of the sound reaching a listener's ears, properties which themselves may be affected by factors other than source distance. In many cases, properties of the sound source itself and of the acoustic environment may be confounded with the acoustic changes resulting from distance changes. The perceptual processes subserving distance localization therefore likely analyze and sensibly combine multiple sources of acoustic information, or cues, in order to produce stable estimates of sound source distance. Perhaps a result of the potentially unreliable nature of distance cues, the accuracy with which sound source distance is judged has often times been found to be quite poor (Békésy, 1949; Bronkhorst and Houtgast, 1999; Coleman, 1968; Holt and Thurlow, 1969; Loomis *et al.*, 1998; Mershon *et al.*, 1989; Nielsen, 1993).

At least four possible acoustic distance cues have been proposed for conditions where both listener and sound source are stationary (Mershon and King, 1975). These may be briefly described as follows.

Intensity. In general, sound intensity at the listener's position decreases when the distance between listener and fixed-power sound source is increased. The precise nature of this intensity change, however, depends on both environmental characteristics and various properties of the sound source, including acoustic power and radiation patterns. Under ideal

conditions (a point source in an acoustic free field), intensity loss as a function of distance obeys an inverse-square law, which implies a 6-dB intensity loss for each doubling of distance. Notable departures from this function occur when the acoustic environment contains surfaces that reflect sound. In these conditions, the rate of loss of intensity as a function of distance is decreased. It is also important to note that source distance and source power are completely confounded in measures of intensity at the ear. As a result, the auditory system is presumably forced to rely on assumptions about source power in order to use intensity reliably as a distance cue. This fact has led, in part, to the suggestion that the accuracy of distance judgments may be improved if the sound source is familiar to the listener (Coleman, 1962; McGregor, Horn, and Todd, 1985), because this familiarity may aid in assumptions relating to the acoustic power of the source.

Direct-to-reverberant energy ratio. In environments with sound reflecting surfaces, the ratio of energy reaching a listener directly (without contact with reflecting surfaces) to energy reaching the listener after reflecting surface contact (reverberant energy) decreases systematically with increases in source distance. In rooms, change in direct-to-reverberant energy ratio results primarily from the effect of the inverse-square law on the direct portion of the sound field, because the energy in the later-arriving reflected portion of the sound field may be well approximated by a diffuse sound field, which is defined to have uniform energy over varying source positions. For a given room, reverberant energy as a function of time is determined principally by the size of the room and the acoustic properties of the reflecting surfaces of the room. Many outdoor environments also produce reverberation, and hence a direct-to-reverberant energy ratio cue that varies with distance (Richards and Wiley, 1980).

Spectrum. At least two circumstances cause systematic

^{a)}Electronic mail: zahorik@waisman.wisc.edu

changes in the at-the-ear spectrum as a function of distance. For distances greater than approximately 15 m (Blauert, 1983), the sound-absorbing properties of air significantly modify the sound source spectrum. In general, these absorbing properties of air attenuate high frequencies the most, although the effect is relatively small: on the order of 3- to 4-dB loss per 100 meters at 4 kHz (Ingard, 1953). A second type of spectral change occurs in sound-reflective environments where the spectrum that reaches the ear may be affected by the acoustic properties of the reflective surfaces. As distance increases, the proportion of reflected energy increases, thereby potentially changing the at-the-ear spectrum systematically. Like the intensity cue, spectral cue changes with distance are confounded with changes in the sound source spectrum. As a result, sound source familiarity may also enhance the utility of this cue.

Binaural differences. When sound sources are in the acoustic near-field, binaural differences in both intensity and time are no longer independent of radial distance, as they are for far-field planar waves. These differences, often referred to as differences resulting from acoustic parallax, are maximal along the interaural axis, and decrease to zero on the median plane. For example, Hartley and Fry (1921) have shown that interaural intensity differences (IID) for a sound source (1860-Hz sinusoid) on the interaural axis can differ for distances between 87.5 and 17.5 cm by as much as 20 dB (values derived using a spherical head model). Interaural time differences (ITD) changes with distance have been shown to be less salient than those for IID (Brungart and Rabinowitz, 1999; Duda and Martens, 1998).

Among the most important unanswered questions regarding the perception of sound source distance concerns the way in which information from these multiple acoustic cues is sensibly combined and processed. Because of the complexity of the stimulus, past experiments have typically chosen to manipulate only one of these acoustic cues at a time, while either removing or holding constant all other cues. Although this approach retains strict experimental control, the resulting stimulus may bear little resemblance to that encountered in natural situations, in which multiple distance cues are available to the listener. The recent advances in virtual acoustic technology (Møller *et al.*, 1995; Wightman and Kistler, 1989) make it possible to avoid this trade-off, as precise stimulus control is available under stimulus conditions that are ostensibly identical to those occurring in natural environments. As such, the use of virtual acoustic technology is ideally suited for examining listeners' use of multiple distance cues in a natural environment.

This article describes a series of experiments that examines listeners' abilities to judge sound source distance in a room environment, and specifically the ways in which listeners combine and weight multiple distance cues. Virtual acoustic technology is extensively used, both as a method for precisely quantifying the acoustic stimulus reaching the listeners' ears, and as a means of realistic and accurate stimulus presentation. The rest of the article is divided into three sections. The first (Sec. II) describes the measurement procedure that quantifies the at-the-ear stimulus for a variety of distances in a representative room environment. These measure-

ments are then evaluated in terms of potential acoustic cues to distance. Section III describes an experiment in which psychophysical distance functions are measured for virtual sound source stimuli constructed from the individualized measurements described in Sec. II. These stimuli allow all of the acoustic distance cues present in the real room environment to vary as they would naturally. The last section (Sec. IV) describes an experiment in which certain distance cues present in the virtual sound source stimulus are manipulated simultaneously. This experiment addresses the relative salience of various acoustic distance cues in a room environment.

II. ACOUSTICAL ANALYSIS OF POTENTIAL SOURCE DISTANCE CUES

One of the major limitations of past work on auditory distance perception has been the quantification and control of the stimulus reaching the listener's ears. To overcome this limitation, the current work employs modern virtual acoustic techniques to measure impulse responses of an acoustic system that contains: a listener, a room environment thought (*a priori*) to be rich in acoustic distance cues, and a sound source that can be varied in distance from the listener. The methods used to measure these impulse responses, which will be referred to as *binaural room impulse responses* (BRIRs), are fundamentally similar to those used for anechoic measures (e.g., Møller *et al.*, 1995; Wightman and Kistler, 1989), but require longer excitation periods to fully capture the response of the room environment. Because these impulse responses are essentially complete representations of the proximal stimulus reaching the listener's two ears, all acoustic distance cues are represented within them and may therefore be precisely quantified.

A. Methods

1. Environment

A small auditorium (264-person seating capacity) located within the Waisman Center at the University of Wisconsin—Madison served as the test environment. This room was chosen based on the following characteristics: (a) its size; (b) its reverberation characteristics; and (c) its availability for the purposes of this experiment. The auditorium had a total volume of approximately 830 m³ and total surface area of approximately 653 m². Its shape was complex, with sloping floor (-6°) and ceiling (11°), as well as nonparallel sections of the side walls. The main floor (not including stage area) was approximately rectangular: 14 m long by 12.2 m wide. The majority of floor surfaces were carpeted, excluding seating areas and the stage, which were covered in tile and wood, respectively. The ceiling was covered with acoustical tile and the walls were composed primarily of painted drywall material.

The sound source consisted of a small, high-quality loudspeaker (Realistic Minimus 3.5) with a 90-mm full-range driver. This loudspeaker was mounted on a tripod that could be easily moved up and down one aisle of the auditorium. Twelve distances extending from a fixed origin point near the end of one aisle were examined: 0.30, 0.43, 0.61, 0.86, 1.22, 1.72, 2.44, 3.45, 4.88, 6.90, 9.75, and 13.79 m.

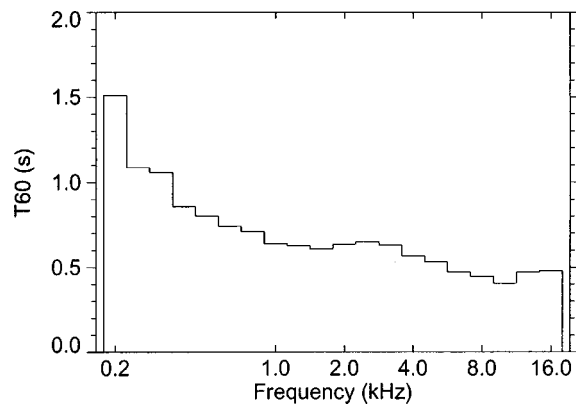


FIG. 1. Reverberation time, T_{60} , for the test environment (a medium-sized auditorium) as a function of frequency. Results have been averaged across the 12 distances measured with a reference microphone.

The loudspeaker was always oriented with its driver facing the origin. In order to accommodate the farthest distance, the loudspeaker had to be placed on the auditorium's stage (approximately 1.5 m from the front edge). At this position, the loudspeaker height was decreased in order to account for the 0.38-m height of the stage. For all other positions, no attempt was made to adjust the loudspeaker height to compensate for the floor slope.

Figure 1 displays measured reverberation time (T_{60}) as a function of frequency for this environment. These measurements were made with a reference microphone (Brüel & Kjør $\frac{1}{2}$ -in. microphone, cartridge type 4133) using methods similar to those described by Schroeder (1965).

2. Participants

Nine paid volunteers (8 female and 1 male, ages 20–28) participated in the binaural impulse-response measurements. None of the participants had any prior exposure to the auditorium where the measurements took place. These participants also served as listeners in all subsequent experiments.

3. Measurement technique and apparatus

Binaural room impulse responses (BRIRs) were measured using methods fundamentally similar to those described in detail by Møller *et al.* (1995), although much longer excitation periods were used to capture the response of the room. Miniature electret microphones (Sennheiser KE4-211-2) were inserted into each participant's ear canals such that the microphone diaphragm was at the position of the canal entrance, and an acoustic seal was formed between the microphone and canal wall using Etymotic Research ER-13R-2 ring seals (a blocked-meatus configuration). Two impulse-response measurements were made with the loudspeaker positioned (ear height for the 0.30-m source, approximately 1.25 m from the floor surface) at each of the 12 distances. For one measurement the seated participant faced the loudspeaker (0° azimuth), for the other the listener was rotated 90° such that the loudspeaker was opposite the right ear (90° azimuth). All measurements were made with the loudspeaker driven with a fixed power level that produced approximately 80 dB SPL at 0.30 m with the participant removed.

A technique using a maximum-length sequence (MLS) excitation signal, a type of pseudorandom noise, was used to measure all impulse responses (Rife and Vanderkooy, 1989). Generally, this technique excites the system under evaluation periodically with an MLS signal, while recording the results and then averaging these results periodically. The system's impulse response is computed by cross correlating the averaged response with the raw MLS. This technique offers a number of advantages over past impulse-response measurement techniques in terms of excitation signal generation, stability of required computations, and signal-to-noise ratio (Rife and Vanderkooy, 1989). In situations where nonstationary noise disturbances exist, a weighted average of responses to the excitation signal periods may be used to further improve signal-to-noise ratio. Nielsen (1998) has shown that weighting response periods by the reciprocal of the mean-squared level in each period can substantially improve signal-to-noise ratio in conditions of high-level nonstationary disturbances. This weighted averaging procedure was used for all impulse responses in this application.

Specifically developed software was used to implement the MLS technique on Tucker–Davis Technologies (TDT) hardware (DD1 2-channel D/A and A/D, AP2 array processor card with optical link to the DD1) with two simultaneous recording channels and the ability to average recording periods in real time. For all measurements, a 15th-order MLS (32 767 points) was used. D/A and A/D conversion was effected with 16-bit precision at a sampling frequency of 50.0 kHz. Forty-four periods of the MLS signal were presented, with the results of the final 40 periods averaged (weighted) in real time. The responses to the first four periods were not recorded in order to insure steady-state system excitation for the final 40 periods. Microphone outputs were fed first to custom-built amplifiers, then into TDT MA2 microphone amplifiers to provide an additional 10 dB of gain prior to TDT DD1 A/D input. The output of the DD1 D/A was fed to a Crown D-75 amplifier with fixed gain driving the movable loudspeaker. The computed impulse responses were stored in floating-point format on a Pentium-class PC used to control the TDT hardware.

It should be noted that a different technique for impulse-response measurement was initially utilized in the present study. This method, using a Golay code stimulus (Foster, 1986; Zhou and Green, 1992) was found to have serious shortcomings when used to measure systems that are to a small degree time-variant, such as binaural recordings from humans. These disturbances, caused by such factors as small head movements, resulted in impulse-response artifacts when using the Golay technique (Zahorik, 2000). Given these problems, the Golay technique was abandoned in favor of the MLS technique.

Headphone (Beyerdynamic DT 990 Pro) impulse responses when coupled to the ears of a given participant were also measured. These measurements were collected for the generation of virtual sound sources to be used in subsequent experiments. Since it is important that the microphone position in the ear canal is the same for both BRIR measurements and these ear-coupled headphone IR measurements, both were obtained during the same measurement session. Param-

eters of the MLS recording system were different in this application, because the headphone IRs are much shorter than the room IRs. Two hundred ten repetitions of a 9th-order MLS (511 points) were presented at a 50-kHz sampling rate, averaging the final 200 repetitions. The playing/recording equipment chain was the same as for the BRIR measurements, except for a TDT headphone buffer (HB1) and 40 dB of attenuation provided by a Hewlett-Packard 350C attenuator placed between the D/A and headphone buffer. In order to assess headphone placement variability on the participant's ears, three replication measurements were collected in which the participant removed and replaced the headphones between replications.

Reference measurements were also made for each of the 12 distances with the participant absent, using a Brüel & Kjær $\frac{1}{2}$ -in. condenser microphone (omnidirectional cartridge type 4133) placed at the position normally occupied by the center of the participant's head, oriented to point to the loudspeaker source. These measurements were used to both evaluate system noise, as well as for level calibration purposes. The microphone's amplified output (Brüel & Kjær model 2609 amplifier) was fed to the TDT DD1 A/D. Impulse-response measurements were made for each distance using the MLS system previously described. Noise measurements were also collected by simply turning off the excitation signal to the loudspeaker. As a result, the noise measurements reflect the average of 40 recording periods, having, in theory, a mean level of $10 \log(40)$ dB less than an unaveraged noise measurement.

4. Procedure

Each participant was met outside the auditorium and briefed on the measurement procedure. After placing microphones in the ears, the participant was blindfolded and led into the auditorium, where he/she was seated in a chair positioned at the zero point. Participants were instructed to remain as quiet and motionless as possible during the course of a given measurement. If the operator detected any noticeable participant motion or unusual environmental noise during a measurement, that measurement was discarded and another collected at the same position. Measurements were obtained from the 12 distances and 2 angular orientations followed by the series of headphone measurements. Upon completion of measurements, participants were led out of the auditorium and blindfolds removed. Hence, the participants were at no time allowed to examine the auditorium visually. Auditory experience with the acoustic environment was also minimized, given the attenuation provided by the sealed-canal microphone placement. The total time required to complete the measurement for each participant was approximately 30 min.

5. Post-processing

Signal-to-noise ratio present in the room was determined from the reference measurements. Figure 2 displays the magnitude spectra of measured impulse responses for three instances of room excitation: measurement signal at the closest distance (0.30 m), measurement signal at the farthest dis-

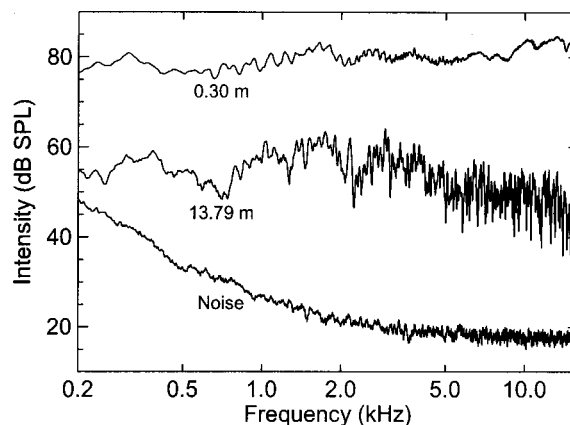


FIG. 2. Magnitude spectra of the sound source signal at 13.79 m, signal at 0.3 m, and the noise alone as measured with a reference microphone and averaged 40 times.

tance (13.79 m), and no measurement signal (noise alone). The y-axis scale is based on an observed average sound pressure of 80 dB SPL at the closest distance. The noise is greatest at the low frequencies, which is caused primarily by the air-handling system in the auditorium. As a result, signal-to-noise at the low frequencies was poorest, with the smallest ratio—on the order of 7 dB at 200 Hz—existing when the signal is farthest away. Over much of the frequency range, however, signal-to-noise ratios even for the farthest signal are greater than 30 dB. The closest signal produces the best signal-to-noise ratios: 45 to 60 dB over the range of 0.5 to 10 kHz. It should be emphasized that these are *averaged* results. The actual SPL of the unaveraged noise was approximately 16 dB higher.

Poor signal-to-noise ratio was, therefore, a substantial issue in the present measurements, especially at low frequencies for distant sound sources. Two standard approaches for increasing signal-to-noise ratio were not practical in this situation. Increases in excitation level would have risked nonlinear loudspeaker operation as well as potential participant fatigue/discomfort. Significant increases in the number of excitation signal-averaging periods would have caused increases in measurement time, and as a result increased the chances of measurement contamination resulting from participant motion. An alternative method of post-processing the BRIR measurements was therefore used in an attempt to minimize noise contamination in regions of poor signal-to-noise ratio, particularly the later portions of the response where much of the reverberant energy has decayed away. This noise contamination may be seen as a change in slope of the cumulative energy decay functions (Schroeder, 1979). An example of this is shown in Fig. 3, where the slope of the measured decay (dark curve) becomes substantially more shallow at around 200 ms.

Because both the noise and the diffuse reverberant signal have essentially Gaussian probability-density functions (independent in each ear), the noise may be treated as though it were simply reverberation with a different (and incorrect) decay rate. Imposing the proper decay rate onto the noise will in theory result in a close approximation to an uncontaminated impulse response. This decay rate correction must

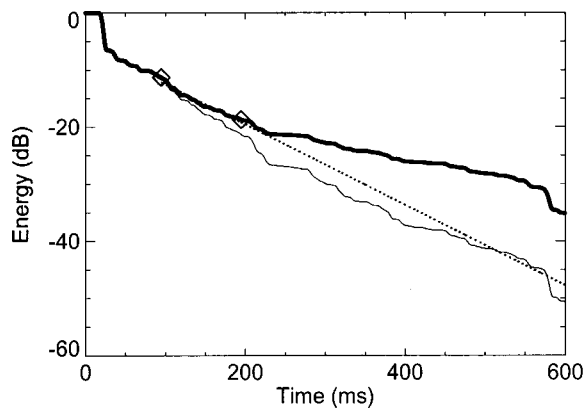


FIG. 3. Energy decay function (dark curve) for the frequency band centered at 635 Hz (participant SRQ, left ear, 4.88-m source distance). The dotted line is a linear fit to the decay function region between the two diamond symbols. The light curve is the derived decay function after application of the exponential decay time-windowing procedure.

be done in a frequency-dependent manner, however, because reverberation decay rate is known to be frequency dependent (as seen in the T_{60} measure of Fig. 1).

To implement this style of noise reduction, BRIRs were first passed through a bank of bandpass filters (zero-phase FIR) with 1/3-octave-band center-frequency spacing from 0.2 to 16 kHz. Cumulative energy decay curves were then computed for each frequency band, followed by a linear fit of the decay curve in dB, from 80 to 180 ms after the direct-path arrival. The dotted line in Fig. 3 shows the linear fit in dB to the decay curve in the region between the diamond symbols (80 to 180 ms post direct-path arrival). An exponentially decaying time window was then constructed based on the slope of this linear fit and applied to the corresponding impulse response from each frequency band. The light curve in Fig. 3 shows the decay curve for the windowed result. For 1/3-octave bands ≤ 400 Hz, slopes of the fitted decay functions were increased by 30% in order to ensure that most low-frequency components of the impulse response would decay sufficiently within its 655-ms period. Windowed results from all frequency bands were then summed in the time domain to recompose a *windowed* version of the original impulse response. Figure 4 displays decay contours as a function of frequency before [Fig. 4(a)] and after [Fig. 4(b)] application of this windowing procedure. It may be seen that the windowing procedure is effective at removing the later nonlinearly decaying (in dB) noise contamination. All subsequent use of BRIRs refer to measurements that have been modified by this post-processing stage.

6. Potential limitations

At least two potential limitations of the described methods for measuring and processing the BRIRs should be noted. First, the 1/3-octave filtering and reconstruction operations used in this post-processing procedure did impose a degree of ripple to the frequency spectrum of the processed result, due to the overlapping passbands in the filters. Second, the measurement and subsequent post-processing both caused distortion of the low-frequency decay of reverberant energy. The measurement period should ideally have been

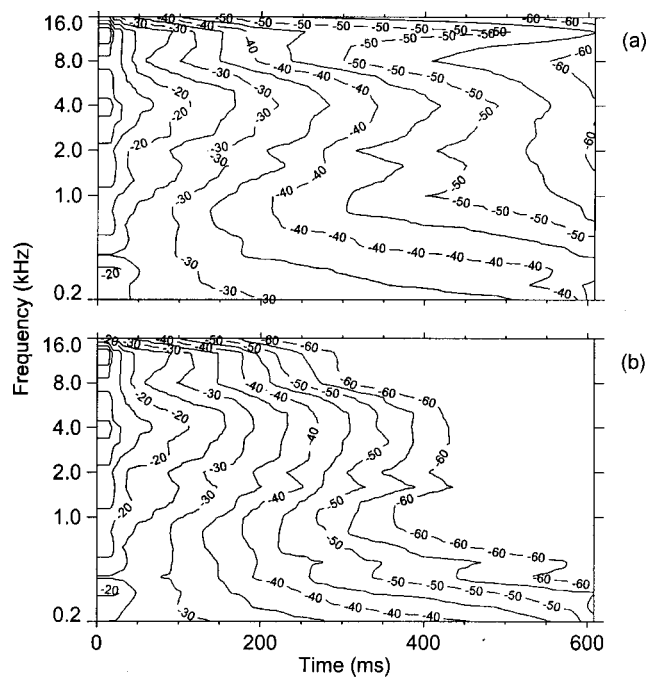


FIG. 4. Energy decay function contours for a BRIR measured from 4.88 m (participant SRQ, left ear) before (a) and after (b) application of the frequency-dependent time-windowing procedure.

extended to fully capture all low-frequency decay components, although technical and noise-level limitations prevented this. In an attempt to minimize these effects, the post-processing stage was specifically designed to increase the rates of reverberant energy decay below 400 Hz.

Both of these limitations were not believed to significantly impact the current application, principally because direct psychophysical comparisons were not made between the real and simulated environments. The amount of frequency ripple imposed by the filterbank was both reasonably small (within ± 3 dB) and constant across all processed BRIRs. It could therefore be easily attributed to a property of the sound source itself, such as a loudspeaker response. Similarly, the artificially increased decay of low-frequency reverberation can be thought to represent an environment that was slightly more damped in the low frequencies than the physical measurement environment. Clearly, other applications may require further attention to these issues.

B. Results

Analyses of potential acoustic cues to distance were performed on the post-processed BRIRs, for each of the 12 distances and 9 participants. For each analysis, results were averaged across participants ($n=9$), in order to focus on acoustical aspects that change with source distance change, and to remove the small acoustical idiosyncrasies resulting from individual participant characteristics.

1. Intensity: Monaural and binaural

Figure 5 displays relative intensity changes as a function of source distance for the two angular orientations (0° and 90° azimuth). Intensity was computed based on each entire

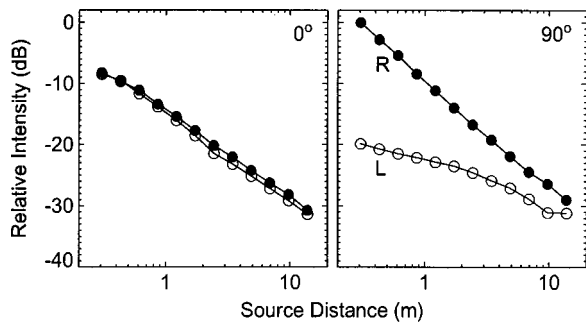


FIG. 5. Average ($n=9$) relative intensity change as a function of source distance for angular orientations of 0° (left panel) and 90° (right panel) azimuth. Solid symbol curves show data for the right (R) ear. Open symbols show data for the left (L) ear. Intensity decay rate for L and R ears at 0° is approximately -4 dB per doubling of source distance. Decay rate for L and R ears at 90° is approximately -2 and -5 dB per doubling distance.

BRIR. As a result, the relative intensity values represent both direct-path energy as well as reverberant energy, explaining why the intensity change per distance doubling in all cases is less than the 6 dB predicted by an inverse square law. The binaural differences in intensity change between the left and right ears for the 90° orientation may also be explained by reverberant energy. As the source distance is increased, direct-path energy, which causes the large intensity differences between the two ears for the 90° orientation, will decrease. Therefore, the diffuse reverberant energy, which excites both ears equally, will account for a greater proportion of the total energy at the farther distances. For the closest distances, additional near-field effects may also contribute to the interaural intensity differences at 90° .

From these results, it is likely that relative intensity is a salient distance cue for this environment. Intensity changes were both systematic and quite large—changes for this environment that corresponded to a doubling of source distance were on the order of 3 to 5 times best estimates of an intensity jnd (just-noticeable difference) (Jesteadt, Wier, and Green, 1977). Binaural differences in intensity for source directions displaced from the median plane can also provide listeners with additional distance information.

2. Direct-to-reverberant energy ratio

The ratio of direct to reverberant energy was computed for each of the BRIRs by a simple time-windowing procedure. The start of the direct-path portion of the impulse response was first determined by finding the first time at which energy was greater than 20 dB above the noise floor. Because anechoic (direct-path only) head-related transfer functions are known to have impulse-response lengths on the order of 2.5 ms (Møller *et al.*, 1995), the direct-path portion of the BRIRs was defined to be 2.5 ms in duration. The reverberant portion of the BRIRs was defined to be the remainder of the IR following the 2.5-ms direct-path portion. Direct-to-reverberant energy ratio is simply the ratio of total energies in each of these regions of the BRIRs.

This time-window duration was effective at separating the direct path from reflections for all but the farthest sound sources where the delay between the direct path and the floor

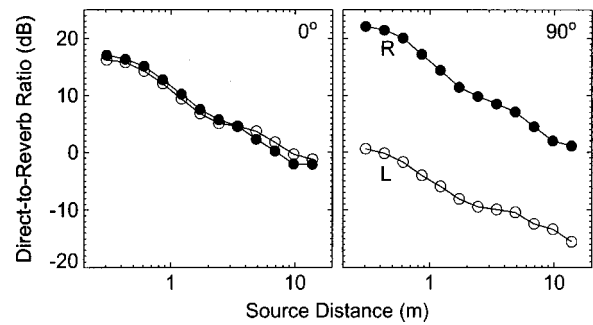


FIG. 6. Average ($n=9$) direct-to-reverberant energy ratio change as a function of source distance for angular orientations of 0° (left panel) and 90° (right panel) azimuth. Solid symbol curves show data for the right (R) ear. Open symbols show data for the left (L) ear. Direct-to-reverberant energy ratio decay rate for all cases is approximately -3 to -4 dB per doubling source distance.

reflection was very small. Given the absorption properties of the carpeted floor, the energy contribution of the floor reflection was quite small, however.

Figure 6 displays direct-to-reverberant energy ratios as a function of source distance for the two angular orientations (0° and 90° azimuth). The decrease in ratios is due primarily to the decrease in direct-path energy (which decreases by 6 dB per distance doubling), given that reverberant energy is acoustically diffuse, and therefore relatively constant within rooms. In the present room environment, reverberant energy was found to decrease by approximately 1 dB per doubling of source distance.

Although the observed changes in direct-to-reverberant energy appear to be substantial, there are at present no relevant psychophysical results (i.e., no jnd measures) with which to compare this variation.

3. Spectrum

Change in spectral shape of the BRIRs with varying distance was examined via a $1/3$ -octave-band analysis, which was the same as that implemented for measurement post-processing. Figure 7 displays average magnitude spectra ($n=9$) for the two ears and two angular orientations. In order to remove effects of overall level (see Fig. 5), each spectrum

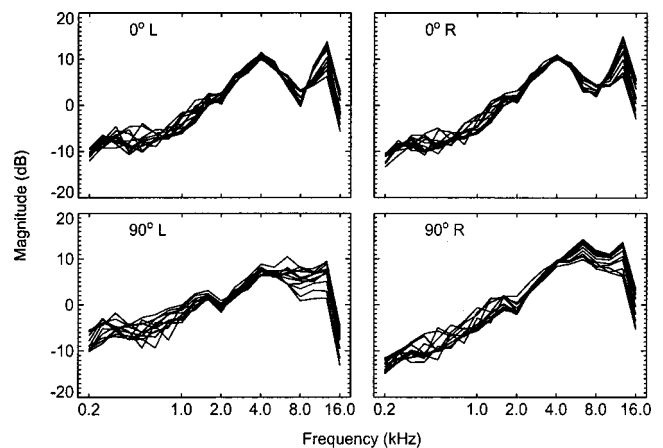


FIG. 7. Average ($n=9$) $1/3$ -octave-band BRIR spectral shape with the mean magnitude for each distance removed. Azimuth angle (0° or 90°) and ear (L or R) are displayed in each panel.

has been normalized by its mean magnitude. The only systematic changes in source spectrum with increasing distance are the slight decreases in high-frequency energy, which decrease by at most 9 dB over the full range of source distances, or roughly 1.6 dB per distance doubling. These small changes observed in spectral shape suggest that it is unlikely to be a salient distance cue in this situation, given known sensitivity to spectral shape changes under conditions where source distance is fixed (Green and Mason, 1985).

III. APPARENT SOURCE DISTANCE

This section describes an experiment in which psychophysical distance functions were estimated for nine listeners, using a direct scaling procedure on the virtual sound source stimuli constructed from the individualized measurements described in the previous section. All of the acoustic distance cues present in the real room environment were present in the virtual display, and varied as they would naturally. Because both source direction (Gardner, 1969; Holt and Thurlow, 1969; Mershon *et al.*, 1989), and familiarity (Coleman, 1962; McGregor *et al.*, 1985) with the source stimulus may provide listeners with additional distance cue information, these factors were manipulated in the experiment.

A. Methods

1. Participants

Nine paid volunteers (8 female and 1 male, ages 20–28) participated as listeners. All had participated previously in the binaural room impulse-response (BRIR) measurements, and had normal pure-tone thresholds, as verified by audiometric screening at 15 dB HL.

2. Stimulus generation and presentation

Virtual sound source stimuli were generated using the blocked-meatus BRIR and headphone impulse-response (IR) measurements collected for each listener (see Sec. II) following the technique described by Møller *et al.* (1995). As part of this technique, 32 768-coefficient FIR filters were constructed from the post-processed BRIR measurements for each individual listener ($n=9$) and spatial location: 12 distances (0.3–13.79 m) and 2 angular orientations (0° and 90°). Similarly, headphone equalization filters were constructed based on the individual headphone IRs. In an attempt to minimize the acoustic effects of headphone placement variability, an average (rms) of the three headphone measurement replications was computed based on each measurement's smoothed (20% of a critical bandwidth) magnitude spectrum. The averaged spectrum was then inverted and bandpass filtered between 0.2 and 16 kHz and defined to have linear phase, in order to construct a 256-coefficient finite impulse response (FIR) equalization filter. To simulate loudspeaker reproduction of a given input signal in an auditorium room environment for a given listener at a given spatial location, a BRIR filter for the given listener and location along with that listener's headphone equalization filters were applied to the input signal and presented over headphones (Beyerdynamic DT 990 Pro) using Tucker-Davis Technologies hardware (PD1) for D/A conversion (16-bit, 50 kHz).

Two types of source signals were used in these experiments: a noise burst and a speech syllable. The noise burst was Gaussian with 50-ms duration and was gated on/off with a cosine-squared window of duration 2.5 ms up/down. The speech sample was an anechoic recording of a male speaker uttering the syllable /da/ at a conversational level, 1 m from the recording microphone. Levels in the virtual display were adjusted such that the natural anechoic level of the speech syllable was preserved at a distance of 1 m.

3. Procedure

Listeners were seated in a sound-attenuating booth and asked to judge the apparent egocentric distance in feet of virtual sound sources presented in a random order via a direct scaling procedure. The unit of feet was chosen because all listeners, except listener SSI, indicated that they were most comfortable with reporting distances in British units. Listener SSI preferred SI units, and therefore responded in meters. A response of zero (feet or meters) was reserved for those sources that appeared to originate from a location within the listener's head. Listeners were instructed to close their eyes during the self-paced source presentation. Responses were made (with eyes open) on a computer terminal with a numeric keypad, using a minimum precision of two decimal places. Stimulus type (noise or speech) and source angular position (0° or 90°) were the same within a block of 120 trials (10 repetitions per source distance). Four blocks of trials, corresponding to the combinations of stimulus type and angular source position, were run in a single 2-h session.

B. Results

All listener's judgments of apparent source distance were transformed to meters and plotted as a function of virtual source distance for each of the four stimulus conditions: noise 0° , noise 90° , speech 0° , and speech 90° . These results, which are assumed to be good estimates of perceived distance, are displayed in Figs. 8–11, with separate panels in each figure for individual listeners. Within each panel, point symbols represent responses on individual trials. A small degree of random variation in the x dimension was introduced when displaying these data, so as to avoid symbol occlusion for like responses across trials. The square symbols are geometric means of responses for each distance. Linear fits (on logarithmic coordinates) to the geometric means are shown in each panel, along with their corresponding slopes in the lower right corner of each panel. No zero responses were reported, indicating that in all cases listeners perceived sources to be externalized from the head.

Since the proportion of variance accounted for by the linear fit on logarithmic coordinates is generally quite high (R^2 ranging from 0.7 to 0.9), it may be concluded that the data are well approximated by a compressive power function of the form

$$\psi_r = k \phi_r^a,$$

where ψ_r is perceived distance, ϕ_r is physical source distance, a is the power-law exponent, and k is a constant. On the logarithmic coordinates of Figs. 8–11, a is equivalent to

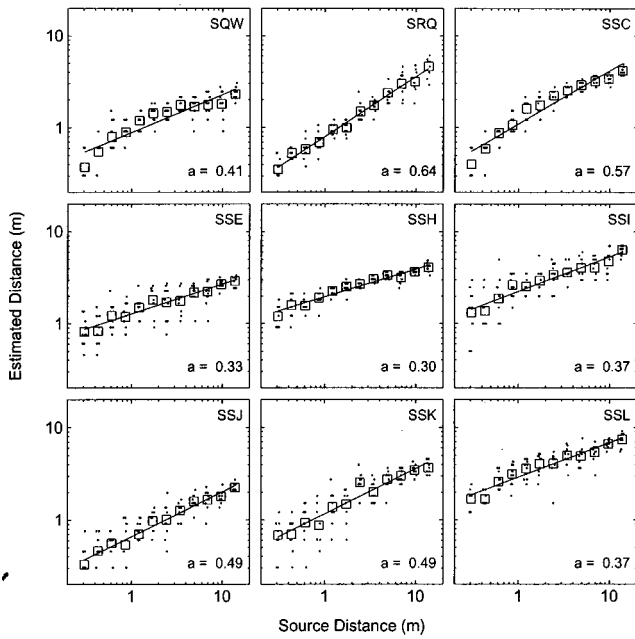


FIG. 8. Individual apparent distance judgments as a function of physical distance for the noise-burst stimulus at 0° azimuth. Each panel displays data for one listener. Point symbols represent individual trial data. The square symbols are geometric means. A linear fit to the data on log-log coordinates is also displayed, with slope (a) shown in the lower right.

the slope of linear fit, and $\log(k)$ the intercept. The average value of a was approximately 0.39 (s.d.=0.13) across all listeners and stimulus conditions, which is substantially less than the veridical value of 1.0. The average value of k was approximately 1.32 (s.d.=0.56), slightly higher than the veridical $k=1$. These results suggest that listeners tend to make large underestimates of source distance for most sources, and that the amount of underestimation is related exponentially to the actual source distance. Very close sources, however,

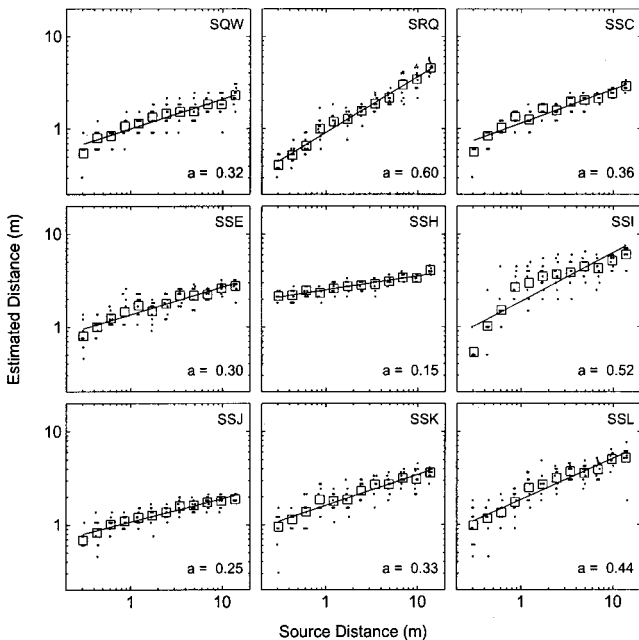


FIG. 9. Individual apparent distance judgments as a function of physical distance for the noise-burst stimulus at 90° azimuth.

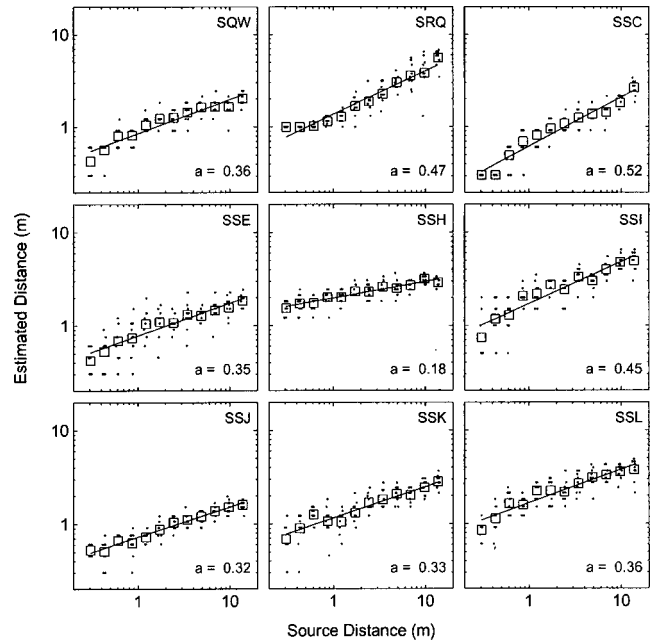


FIG. 10. Individual apparent distance judgments as a function of physical distance for the speech stimulus at 0° azimuth.

are actually (on average) overestimated, because values of k are greater than 1.

At least two lines of evidence suggest that these observed errors are in fact perceptual errors, and do not result merely from the method of response. First, similar response methods have been used to study visual distance perception that result in near-perfect accuracy under full-cue conditions (see Da Silva, 1985, for a summary of relevant literature). Second, for auditory distance, other response methods have been shown to produce results very similar to those collected using methods analogous to the direct scaling procedure implemented here (Loomis *et al.*, 1998).

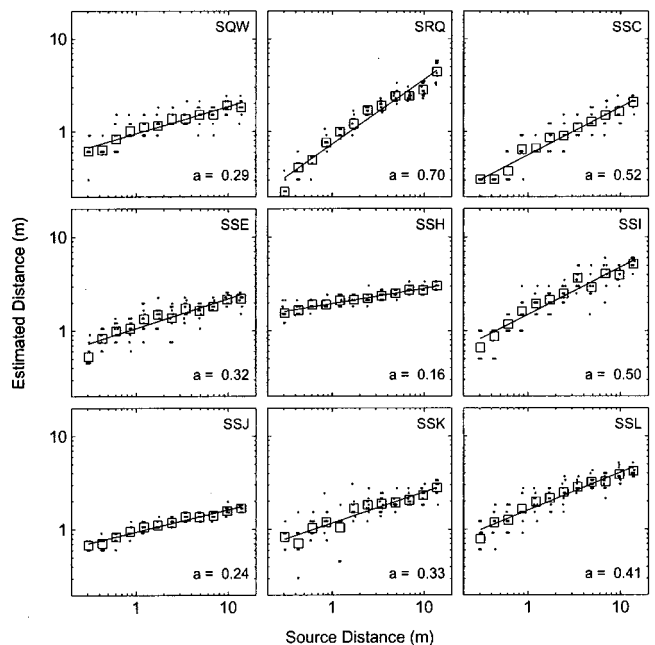


FIG. 11. Individual apparent distance judgments as a function of physical distance for the speech stimulus at 90° azimuth.

Although all listeners tended to underestimate most sound source distances, substantial differences existed in the amount of underestimation. The standard deviation of computed exponents within an experimental condition ranged from 0.10 to 0.17. This result is not surprising, given the known individual variability in judgment of visual target distance. Da Silva (1985) reports exponent standard deviations ranging from 0.09 to 0.18 for judgment of visual target distances using both magnitude estimation and ratio estimation methods.

Because consistent effects of angular orientation and stimulus type were not immediately observable in Figs. 8–11 as a result of individual listener variability, two repeated-measures analyses of variance (ANOVAs) were used to examine these effects more closely. One ANOVA had the fitted exponents, a , as its dependent measure. Since ANOVA has been shown to be robust with respect to violations of its normality assumption (Pearson, 1931), the fact that the a population is potentially non-normally distributed does not likely affect the outcome of the analysis. The other ANOVA had the constant values, $\log(k)$, as its dependent measure. Both ANOVAs treated angular orientation and stimulus type as within-subjects factors. In order to hold experiment-wise alpha level at the chosen criterion level of 0.05, alpha must be split for evaluation of each separate ANOVA, because the two dependent measures are not logically independent. No statistically significant differences between angular orientations or stimulus types were found for either dependent measure at the 0.025 significance level. The values of a were found to be significantly less than 1 on average, $F(1,8) = 257.89$, $p < 0.0001$; and the values of $\log(k)$ were found to be significantly greater than zero on average, $F(1,8) = 59.79$, $p < 0.0001$, indicating that k was significantly larger than the veridical value of 1.

An additional aspect of the data may be seen by visual inspection of Figs. 8–11. For many listeners, change in perceived distance appears to increase more rapidly for near sources (less than approximately 1.2 m) than for far sources (e.g., Fig. 9, listener SSI). The cause of these results is at present unknown, although it appears unlikely to be stimulus based. None of the physical cue measures reported in the previous section showed qualitatively different effects for near and far sources. Additionally, near-field binaural cues (which were not explicitly measured) were also unlikely to have caused these patterns of results because they were observed at source directions on the median plane for certain listeners (e.g., Fig. 8, listener SQW).

In summary, psychophysical distance functions were found to be well approximated by compressive power functions, suggesting that most source distances are underestimated. Although a substantial amount of individual variability was observed, the psychophysical functions do not appear to be systematically affected by either source signal type or source direction.

IV. LISTENER WEIGHTING OF ACOUSTIC CUES

The goal of this experiment is to evaluate the relative importance listeners place on individual acoustic distance cues under naturalistic stimulus conditions. Since multiple

acoustic parameters covary with physical sound source distance in most, if not all, naturally occurring environments, it is of interest to know how listeners combine the information from these multiple cues to arrive at a single distance percept. For the environment examined in this article, intensity and direct-to-reverberant energy ratio appear to be the acoustic parameters that vary most with source distance (see Sec. II). As such, listeners' use of these two cues is highlighted. Of additional interest is how cue use may change with varying source angle or source signal type.

This basic question, how it is that complex stimulus information is combined to form a single percept, has been the motivation for considerable study. Among the more famous early inquiries were those made by Brunswik (1952). This program of study involved correlating measures of naturally occurring physical parameters in the environment with perceptual responses, in an attempt to determine the perceptual weight placed on each physical parameter. Though innovative, this method experienced problems when all physical parameters were highly correlated with each other (causing problems of multicollinearity; Cohen and Cohen, 1983). More modern techniques experimentally apply small amounts of independent random perturbation to each physical parameter of interest (Berg, 1989, 1990; Berg and Green, 1990; Lutfi, 1995; Lutfi and Oh, 1997; Stellmack *et al.*, 1997; Willihnganz *et al.*, 1997). Because these perturbations are small, departures from natural stimulation are argued to be minimal. This is one of the principal advantages of this technique over more conventional factorial designs, which result in many stimulus presentations with highly unnatural combinations of cues.

In this technique, perceptual weights are estimated by examining the relation between responses and physical parameter perturbations. Estimation procedures using a maximum-likelihood criterion based on a presumed model (Ahumada and Lovell, 1971; Berg, 1989) and a least-squares criterion (Lutfi, 1995; Lutfi and Oh, 1997) have both been used. Because fewer assumptions are required by the latter procedure (Lutfi, 1995), it was used in the current experiments, correlating the trial-to-trial perturbation values for intensity and direct-to-reverberant energy ratio with apparent distance responses to determine the perceptual weight placed on each distance cue.

The experiment described here quantifies the relative perceptual weight listeners place on the intensity, I , and direct-to-reverberant energy ratio, ν , when making distance judgments under three different stimulus conditions. The first condition presented a noise-burst signal with equal degrees of perturbation applied to the naturally occurring values of I and ν cues at each distance. The second condition was the same as the first, except that the source signal was a speech syllable. The final condition attempts to verify that the magnitudes of perturbation applied to each cue do not affect the derived perceptual weights. In this condition, the noise-burst signal was presented with different degrees of perturbation were applied to I and ν . All stimulus conditions examined source positions at both 0° and 90° azimuth. Additionally, because it is possible that I and ν weights change with changing distance, these interactions were also evaluated.

A. Methods

1. Participants

Seven paid volunteers (all female, ages 20–28) participated as listeners in the first and second conditions of the experiment. Five of these listeners also participated in the third verification conditions. All listeners participated previously in the binaural room impulse-response (BRIR) measurements, as well as in the baseline experiments used to determine psychophysical distance functions.

2. Stimulus generation and presentation

Virtual sound source stimuli were constructed using methods previously described (see Sec. III), with individualized BRIRs (post-processed) and individualized headphone equalization filters used for all listeners. As before, BRIRs from 12 different distances and two angular orientations were used (see Sec. II). Perturbations of the I and ν cues were performed on each BRIR from trial to trial in the following way. Intensity was perturbed by scaling the BRIRs. Scale values were computed using samples drawn from a normal distribution with zero mean (relative to the given natural cue value at each distance) and $\sigma_I = 3$ dB. Direct-to-reverberant energy ratio, ν , was perturbed by scaling only the direct-path portion of the BRIRs, which was defined to extend from the first point in the impulse response with appreciable energy to a point 2.5 ms later (see Sec. II for details). These scale values were also computed using samples drawn from a normal distribution with zero mean. For the first two stimulus conditions, this distribution had $\sigma_\nu = 3$ dB. The final verification condition set $\sigma_\nu = 6$ dB. Perturbation values for I and ν were drawn independently, with each being applied equally to left- and right-ear BRIRs. It should be stressed that on any one trial, actual cue values for I and ν may be thought to consist of two parts: the nominal cue value present in each BRIR (see Figs. 5 and 6), and the additional perturbation value. Therefore, perturbation distribution means were effectively centered on the nominal values of the I and ν cues for each distance. The values for perturbation standard deviation, $\sigma_I = \sigma_\nu = 3$ dB, were chosen to span approximately a doubling of source distance (see Figs. 5 and 6). As such, the potential for wildly conflicting I and ν cue values was small. The same noise-burst and speech signals used in the previous baseline experiment (Sec. III) were used as stimuli in the present experiments.

3. Procedure

The procedure was identical to that described for the previous apparent source distance experiment (Sec. III), except that the number of blocks of trials completed for each stimulus condition was increased. The first condition used the noise-burst stimulus and source angles of either 0° or 90° azimuth. Source azimuth was the same within a block of 120 trials (10 repetitions per source distance). Both I and ν were independently perturbed from trial to trial, with $\sigma_I = \sigma_\nu = 3$ dB. A total of eight blocks of trials was collected from each listener, four blocks for each source angle. The second condition proceeded identically, except that the speech syllable stimulus was used. The third verification condition also

proceeded in the same way, using the noise-burst stimulus with $\sigma_I = 3$ dB and $\sigma_\nu = 6$ dB. Approximately eight 2-h sessions were required for each listener to complete all three experiments.

B. Weighting procedure

The general weighting procedure used here was very similar to that proposed by Lutfi (1995), with one major difference. The current experiments employed a continuous response type, whereas Lutfi (Lutfi, 1995; Lutfi and Oh, 1997) as well as others (Ahumada and Lovell, 1971; Berg, 1989) have all applied weighting analyses to binary response data. In practice, this detail had little effect on the way the analysis was performed, which was simply a multiple regression analysis on standardized scores.

From the previous apparent distance experiments, it was shown that a power function relates perceived distance to physical sound source distance. This power function was equivalently expressed as a linear function relating logarithmically transformed perceived distances to physical distances (as in Figs. 8–11). This linear function may be expressed in terms of the following simple regression equation:

$$response' = B_r X_{r'} + C + \varepsilon,$$

where $response'$ represents the predicted log-transformed responses, and $X_{r'}$ the log-transformed physical distances. B_r is the function's slope parameter, C is a logarithmic constant, and ε an error term. For the current experiments, additional terms for explanation of response variance from the independent perturbations applied to I and ν (in units of decibels) were required. Certain interaction terms for I and ν cues with source distance (log-transformed) were also included, in order to evaluate changes in these cue weights with source distance. Predicted responses may now be characterized by the following multiple regression equation:

$$response' = B_r X_{r'} + B_I X_I + B_\nu X_\nu + B_{I \times r'} X_I X_{r'} + B_{\nu \times r'} X_\nu X_{r'} + C + \varepsilon.$$

The interaction terms of $I \times \nu$ and $I \times \nu \times r'$ were not included in this weighting equation, because in subsequent analyses, these terms were found to produce statistically non-significant weights in all cases. This result was expected given the independence of the I and ν perturbations.

Since the predictor variables were not all in the same units and do not all have the same variance, it is difficult to directly interpret the values of B_i in terms of perceptual weights. For these reasons, all variables were standardized (converted to z scores) prior to the multiple regression. Standardized predicted responses are therefore given by the relation

$$Z_{response'} = \beta_r Z_{r'} + \beta_I Z_I + \beta_\nu Z_\nu + \beta_{I \times r'} Z_I Z_{r'} + \beta_{\nu \times r'} Z_\nu Z_{r'} + \varepsilon.$$

This is the weighting equation utilized for all analyses in this section, where the β_i weights are all partial correlations between the given term (either log-distance, or cue perturbation value, or interaction) and the log-transformed responses. Partial correlation, which conceptually is the correlation be-

tween a given predictor variable and the dependent variable while holding contributions of all other predictor variables constant, is required in this application, because the interaction terms are not independent of the other predictor variables (Lutfi, 1995).

Weights, β_i , were determined for each listener individually, with R^2 , the proportion of total variance accounted for, being used as a measure of how well the weighting equation fits the data. The desired number of trials per condition was determined through a power analysis, with 480 trials allowing for detection of $\beta_i=0.1$ with 90% power and $\alpha=0.05$, assuming a population $R^2=0.6$ (Cohen and Cohen, 1983).

In an attempt to more precisely quantify the effects of the I and ν cue perturbations on response accuracy, simple power-function fits to the data were also computed as described in Sec. III. These fits were then compared (within listeners) to the baseline conditions (Sec. III) in which no artificial perturbation was applied to any of the distance cues. The fitted exponents were expected to be slightly smaller than the baseline values, because the additional I and ν cue perturbations added some degree of uncertainty to the stimulus and this uncertainty likely causes a slight regression towards a mean perceived distance.

C. Results

Figures 12 and 13 display the individual listener weights for the noise and speech stimulus conditions ($\sigma_I=\sigma_\nu=3$ dB), respectively, each with separate analyses for 0° [Figs. 12(a) and 13(a)] and 90° degrees [Figs. 12(b) and 13(b)]. A number of observations apply to all results shown in Figs. 12 and 13. First, it is observed that r' weights are always very large and positive. This result is expected given the relatively small amounts of experimentally imposed perturbation driving the additional weights. Second, I and ν weights are always negative. This is a result of the inverse relation between the I and ν cues and source distance. Third, all weighting equations represent good fits to the response data, explaining approximately 70% of the total variance, R^2 .

Considerably more interesting is the way weighting strategies appear to change for different source signals or source directions. To evaluate these changes fully, multiple repeated-measures ANOVAs were performed treating each correlation weight as a dependent variable. Because the sampling distribution of nonzero correlations is skewed, however, weights were transformed via Fisher's z' transform (Cohen and Cohen, 1983)

$$z' = \frac{1}{2}[\log_e(1 + \beta_i) - \log_e(1 - \beta_i)],$$

prior to the ANOVAs. In an attempt to hold experiment-wise $\alpha=0.05$, α was split between the dependent variable analyses in the following way. Since I and ν perturbation values were chosen independently, each was evaluated at a nonsplit level of $\alpha=0.05$. The remaining dependent variables were each evaluated at the $\alpha=0.05/3=0.0167$ level. Both angular source position (0° or 90°) and stimulus type (noise or speech) were treated as within-subjects factors for all analyses.

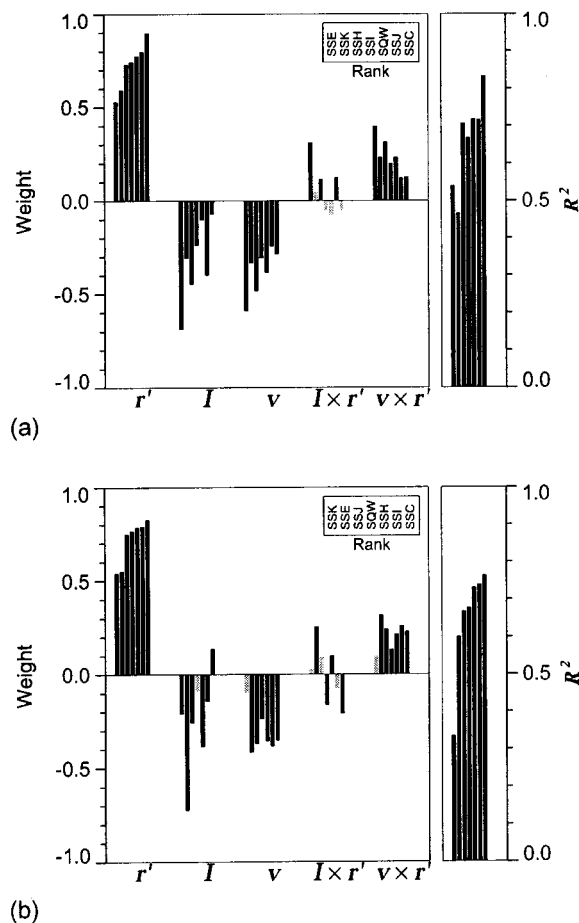


FIG. 12. Individual listener weights for the noise-burst stimulus ($\sigma_I=\sigma_\nu=3$ dB), with the 0° azimuth results displayed in the top panel (a), and 90° azimuth results in the bottom panel (b). The order of individual listener weights from left to right is displayed in the upper right corner of each panel. This rank from left to right is determined by the r' weight from lowest to highest. Each bar corresponds to the weight for one listener and one cue. Lightly shaded bars represent weights that are nonsignificantly ($p > 0.05$) different from zero. The proportion of variance explained by the weighting model for each listener, R^2 , is displayed on the right side of both panels.

A number of differences in the weights between experimental conditions may be seen. First, the ν weight changes significantly between noise and speech stimulus types, $F(1,6)=24.478$, $p=0.003$ ($\eta^2=0.803$), with greater weight (in absolute value) being placed on the ν cue for the noise-burst stimulus (Fig. 12) than for the speech stimulus (Fig. 13). Second, the $\nu \times r'$ weight also changes significantly between the stimulus types, $F(1,6)=13.010$, $p=0.011$ ($\eta^2=0.684$). For the noise-burst stimulus (Fig. 12), nearly all $\nu \times r'$ weights were significantly different from zero. By rearranging terms in the raw-score weighting equation

$$Z_{\text{response}'} = B_{r'}X_{r'} + (B_I + B_{I \times r'}X_{r'})X_I + (B_\nu + B_{\nu \times r'}X_{r'})X_\nu + C + \varepsilon,$$

it is clear that significant $\nu \times r'$ weight implies that the ν weight increases (in absolute value) with increasing source distance. This result was not observed for the speech stimulus (Fig. 13), which produced very few significant $\nu \times r'$ weights. Third, I weights are significantly different for

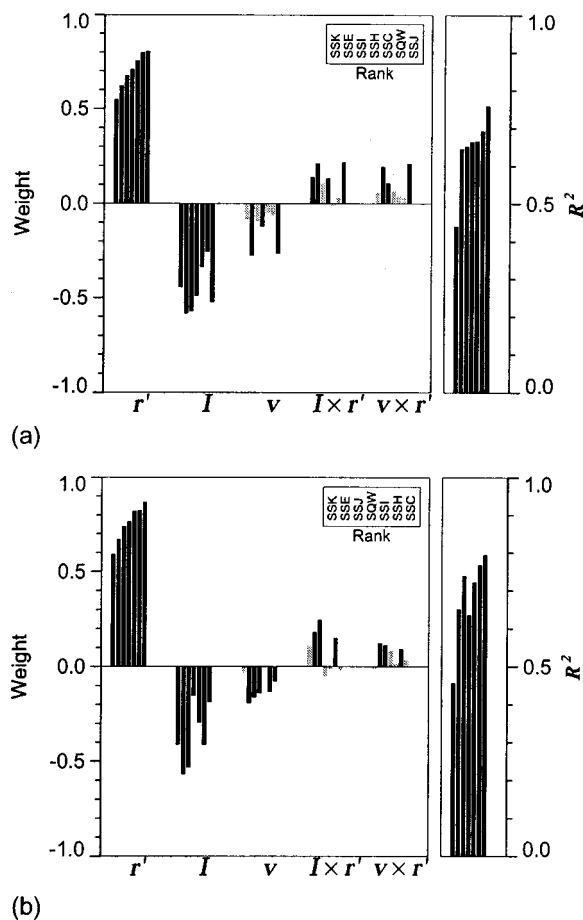


FIG. 13. Individual listener weights for the speech stimulus ($\sigma_I = \sigma_v = 3$ dB), with the 0° azimuth results displayed in the top panel (a), and 90° azimuth results in the bottom panel (b). The order of individual listener weights from left to right is displayed in the upper right corner of each panel. This rank from left to right is determined by the r' weight from lowest to highest. Each bar corresponds to the weight for one listener and one cue. Lightly shaded bars represent weights that are nonsignificantly ($p > 0.05$) different from zero. The proportion of variance explained by the weighting model for each listener, R^2 , is displayed on the right side of both panels.

source angles of 0° and 90° azimuth, $F(1,6) = 12.423$, $p = 0.012$ ($\eta^2 = 0.674$), with I weight generally higher for 0° [Figs. 12(a) and 13(a)] and lower for 90° [Figs. 12(b) and 13(b)].

Since simple power-function fits to the data were also performed, these results may be compared, within the same listeners, to those described in Sec. III. Specifically, the slopes relating log-transformed perceived distance to log-transformed physical distance were compared (which are equivalent to power-function exponents). As predicted, slopes were shallower in the weighting experiments than for the unperturbed baseline conditions, $t(29) = 3.752$, $p = 0.001$. The slope decrement was only approximately 20% on average, however. Hence, it is concluded that the naturalistic stimulus conditions of the previous experiments have not been unduly sacrificed in the name of experimental cue manipulation and experimental design. It is also important to note that, just as in the baseline experiments, slopes did not change significantly within listeners when either source type,

$F(1,6) = 1.053$, $p = 0.344$, or source orientation was changed, $F(1,6) = 1.414$, $p = 0.279$.

Results of the third control experiment, in which $\sigma_I = 3$ dB and $\sigma_v = 6$ dB, verified that precise choices of σ do not affect the resulting weighing patterns. Multiple repeated-measures ANOVAs were used to compare the results of the third control experiment to the first experiment. No statistically significant differences were found. Because of the standardization of scores, the differences in σ do not affect the weighting procedure itself. This result demonstrates, however, that a listener's responses are also unaffected by differences in perturbation σ . Hence, within a reasonable range, the precise choices for σ_I and σ_v are probably irrelevant.

In summary, the perceptual weights assigned to intensity and direct-to-reverberant distance cues were found to change substantially as a function of source signal type, source direction, and to a lesser extent, source distance. The ecological validity of this result is strengthened by the fact that the weights were determined under conditions of largely natural combinations of cues (i.e., small cue perturbation values).

V. GENERAL DISCUSSION

The results of the experiments reported in this article demonstrate that: (1) listener's judgments of apparent sound source distance produce consistent patterns of error under a variety of stimulus conditions, including different source signals (speech or noise) and different source directions (0° or 90° azimuth). (2) The manner in which listeners process, or perceptually weight two principal distance cues (intensity and direct-to-reverberant ratio) varies substantially across the same stimulus conditions. These results taken together point to an auditory distance perception process that, though adept at modifying its cue integration rules in response to varying stimulus conditions, consistently produces distance percepts that are in error when compared to physical states of affairs. At least two questions remain, however. (1) How do the errors reported in the current experiments relate to errors that have been reported in past studies? (2) How might the perceptual weighting process shown here generalize to other stimulus and environmental conditions?

A. Apparent distance: Relation to past results

Almost without exception, past studies of auditory distance perception have reported that listeners tend to underestimate the true physical distance to a source of sound. Although the results of the present experiments are consistent with this general statement, it is of interest to more closely compare the nature and degree of underestimation with relevant past results. To do this, past studies were identified in which more than two far-field source distances were used and listeners made judgments of apparent distance. Table I summarizes the results of all known past experiments that satisfy these two criteria. For each study, the reported data were fit with power functions. Parameters of the fitted functions are also displayed in Table I.

High values of R^2 were obtained in all cases, indicating that power functions represent good fits to the data. The average exponent, a , from these studies was 0.59, with s.d. = 0.24, and average constant, k , was 1.66 (s.d. = 0.92). This

TABLE I. Summary of results from past auditory distance perception studies in which more than two source distances were presented, and listeners made judgments of apparent distance. Each study is described by environment in which the experiment took place, source stimulus type, source azimuth angle (θ), as well as range and number (n) of distances presented. Power functions of the form $\psi_r = k \phi_r^a$ (where ψ_r is perceived distance and ϕ_r is the physical source distance) were fit to the published data. Parameters of the fitted functions (a and k), along with R^2 are displayed for each study.

	ID	Environment	Stimulus	θ	Range (m)	n	a	k	R^2	Notes
Békésy (1949)	1	Anechoic	Live speech	0°	1–10	7	0.76	1.02	0.94	
Coleman (1968)	2	Damped room	LP filtered (10.56 kHz) impulse	0°	2.44–7.92	10	0.38	3.11	0.94	
	3	Damped room	LP filtered (7.68 kHz) impulse	0°	2.44–7.92	10	0.39	3.38	0.93	
Holt and Thurlow (1969)	4	Outdoors	Noise burst ^a	90°	9.75–19.2	4	0.75	1.46	0.97	
Mershon and Bowers (1979)	5	Room	Noise ^a	0°	0.55–8	5	0.65	1.38	0.87	b
	6	Room	Noise ^a	90°	0.55–8	5	0.65	1.46	0.89	b
	7	Room	Noise ^a	0°	0.55–8	5	0.59	1.40	0.89	c
	8	Room	Noise ^a	90°	0.55–8	5	0.74	1.44	0.94	c
Mershon <i>et al.</i> (1989)	9	Reverberant room	Pulse train	0°	0.75–6	4	0.67	2.63	0.61	
	10	Reverberant room	Pulse train	Variable	0.75–6	4	0.65	1.88	0.94	
	11	Damped room	Pulse train	0°	0.75–6	4	0.47	0.40	0.66	
	12	Damped room	Pulse train	Variable	0.75–6	4	0.68	0.39	0.59	
	13	Reverberant room	Pulse train	Variable	0.75–6	4	0.90	1.76	0.62	d
	14	Reverberant room	Pulse train	Variable	0.75–6	4	0.55	2.64	0.88	e
	15	Damped room	Pulse train	Variable	0.75–6	4	0.77	0.24	0.51	d
	16	Damped room	Pulse train	Variable	0.75–6	4	0.38	0.66	0.29	e
Nielsen (1991)	17	Listening room	Speech ^a	0°	1–5	4	0.57	1.78	0.95	f
	18	Anechoic	Speech ^a	0°	1–5	4	-0.12	1.48	0.54	f
	19	Classroom	Speech ^a	0°	1–5	4	0.59	1.70	0.96	f
	20	Listening room	Speech ^a	-45°	1–2.82	3	0.36	2.15	0.97	f
	21	Anechoic	Speech ^a	45°	1–5	4	0.05	1.60	0.96	f
	22	Classroom	Speech ^a	45°	1–5	4	0.55	1.85	0.98	f
	23	Listening room	Speech	0°	1–5	4	0.76	1.38	0.98	
	24	Listening room	Guitar	0°	1–5	4	0.70	1.11	0.98	
	25	Listening room	Pop music	0°	1–5	4	0.95	1.04	0.95	
	26	Listening room	Noise	0°	1–5	4	0.94	0.93	0.95	
Speigle and Loomis (1993)	27	Outdoors	Pulse train	0° to 90°	2–6	3	0.29	3.14	0.96	g
Ashmead, Davis and Northington (1995)	28	Outdoors	Noise burst (random intensity)	0°	5–19	15	0.50	4.04	0.76	h
	29	Outdoors	Noise burst (random intensity)	0°	5–19	8	0.60	3.04	0.97	i
Loomis <i>et al.</i> (1998)	30	Outdoors	Synthesized speech	0°	4–16	4	0.78	1.02	0.99	
	31	Outdoors	Synthesized speech	-120° to 120°	4–16	3	0.79	0.83	>0.99	g
Bronkhorst and Houtgast (1999)	32	Damped room	Noise burst ^a	0°	1–3	5	0.86	0.90	0.97	
	33	Reverberant room	Noise burst ^a	0°	1–3	5	0.44	1.66	0.98	

^aConstant at-the-ear intensity.

^bFirst presentation.

^cSecond presentation.

^dLow S/N.

^eHigh S/N.

^fAveraged across source level.

^gAveraged across θ .

^hExperiment 1.

ⁱExperiment 2.

result suggests that, although the average exponent observed in past studies is generally higher than those observed here, interexperiment exponent variability is quite large. As a result, both the exponents and constants observed in the current experiments may arguably be considered similar to those observed in the past, because average distance exponent and constant values observed here are within 1 standard deviation of the past studies. Of additional note, the only experiments listed in Table I to use virtual acoustic methods were those of Bronkhorst and Houtgast (1999). One of these experiments, conducted under reverberant conditions (ID 33), produced an exponent value of 0.44, which is very similar to the average exponent of 0.39 observed in the current experiments.

These results showing that far physical distances are underestimated and near distances are overestimated are consistent with an influence of a perceptual organization factor known as *specific distance tendency* (Gogel, 1969; Mershon

and King, 1975). This factor describes a tendency towards a specific “default” value of perceived distance under conditions where all distance cues are removed. An estimate of this distance tendency may be computed by determining the point at which perceived distance is equivalent to physical distance. Assuming that a power function does closely approximate the underlying distance psychophysical function, and using the average exponent and constant resulting from the current experiments, the value of specific distance tendency is estimated to be approximately 1.5 m. This value is in good agreement with average source distance estimates that have been reported under anechoic conditions using a noise-burst sound source with fixed level, conditions where distance is in theory indeterminate (Wightman and Kistler, 1997; Zahorik, Kistler, and Wightman, 1994).

To evaluate the effects of differing stimulus conditions on perceived distance, the past experiments shown in Table I were grouped according to environmental factors (either re-

verberant or nonreverberant), source stimulus factors (either familiar or unfamiliar), and source angular positions (either median plane or nonmedian plane). Environments listed in Table I as “room,” “reverberant room,” “listening room,” or “classroom” were classified as reverberant. All other environments were nonreverberant. Sound source types listed as “live speech,” “speech,” “synthesized speech,” “guitar,” or “pop music” were classified as familiar. All other source types were labeled as unfamiliar. Finally, source azimuth angles listed as 0° were classified as median-plane positions (no 180° positions existed), and all other positions were considered nonmedian plane. Differences between these groups for both exponent, a , and constant, k , values were examined via two full-factorial ANOVAs. These analyses revealed no statistically significant differences between any of the stimulus condition groups, or their interactions for either dependent variable.

When results from additional distance perception studies that did not meet the selection criteria for Table I are also considered, some disagreement may be noted as to the effects of source stimulus familiarity as well as source angular position on distance perception accuracy. Both Coleman (1962) and McGregor *et al.* (1985) report increased distance judgment accuracy for familiar sources. These results are at odds with those of Nielsen (1991) that show no significant differences in apparent distance judgments between four types of stimuli, both familiar and unfamiliar (see ID numbers 23–26 in Table I). Similarly, results from certain studies show that judgment error is related to source direction for both near-field (Brungart, Durlach, and Rabinowitz, 1999) and far-field sources (Gardner, 1969; Holt and Thurlow, 1969; Mershon *et al.*, 1989). Results from other studies do not show this relationship in either the near-field (Simpson and Stanton, 1973) or the far-field (Cochran, Throop, and Simpson, 1968; Mershon and Bowers, 1979; Nielsen, 1993).

B. Acoustic cue combination

Perhaps implicit in the cue-weighting results reported in this article is a general framework for combining information from multiple cues in order to arrive at a unitary distance percept. Consider a framework in which each of the individual distance cues available to the listener produces its own distance estimate, estimates which are then combined and weighted according to the “quality” of distance information they provide for the given situation. Quality is determined by two factors: content of the auditory scene, and consistency of the distance estimate for a given cue with those estimates from other cues. As a result, not only are cues that are unavailable or unreliable in a given scene weighted less, but cues that produce distance estimates that are highly discrepant from the other cue estimates are also down-weighted. This general framework for cue combination is essentially identical to that proposed by Landy *et al.* (1995) for visual depth perception.

In the current experiments, such a cue combination framework could perhaps explain the changes in the perceptual weights placed on different acoustic distance cues. For example, the intensity cue was found to be weighted more heavily than the direct-to-reverberant cue for the speech sig-

nal (Fig. 13). This implies, based on the hypothesized cue combination framework, that intensity is a more reliable cue than direct-to-reverberant ratio in this situation. This implication seems plausible, given that speech is a familiar signal, and prior knowledge of natural speech levels may be used to decrease and possibly eliminate ambiguity present in the intensity cue (Brungart and Scott, 2001). In contrast, direct-to-reverberant ratio depends on potentially more variable and complicated acoustic information about the environment. For unfamiliar signals, the intensity cue may become less reliable than direct-to-reverberant energy ratio, given the lack of natural level information available. The patterns of weights for the noise-burst signal (Fig. 12) are consistent with this notion.

This cue combination framework could also accommodate distance perception in varying acoustic environments or over differing source ranges. For the acoustic environment in which the current experiments were conducted, intensity and direct-to-reverberant ratio were the primary cues available to listeners. Other environments and situations may warrant the use of different cues. For example, when sources are very far away, changes in high-frequency energy with distance become increasingly large, and therefore likely receive significant perceptual weight in these circumstances. Similarly, very close distances in anechoic space produce substantial changes in the binaural cues as distance is varied, and therefore also likely receive significant weight. These examples of the extremely variable nature of distance information present in the acoustic stimulus underscore the importance of flexibility in combining information from various acoustic distance cues to produce distance percepts that are unitary and stable, although often underestimates of physical source distance.

ACKNOWLEDGMENTS

I would like to thank Fred Wightman and Doris Kistler for their invaluable discussions and suggestions, Kathy Hoopes for her assistance in behavioral data collection, and Bob Lutfi, Rick Jenison, Jim Dannemiller, and John Brugge for providing helpful comments on an earlier version of this work. Financial support was provided by the NIH-NIDCD Nos. (P01 DC00116-23), ONR (N00014096-1-0675), NASA (Cooperative Agreement No. NCC2-542), and NIH-NEI (No. 1F32EY07010-01).

- Ahumada, A., and Lovell, J. (1971). “Stimulus features in signal detection,” *J. Acoust. Soc. Am.* **49**, 1751–1756.
- Ashmead, D. H., Davis, D. L., and Northington, A. (1995). “Contribution of listeners’ approaching motion to auditory distance perception,” *J. Exp. Psychol. Hum. Percept. Perform.* **21**, 239–256.
- Békésy, G. v. (1949). “The moon illusion and similar auditory phenomena,” *Am. J. Psychol.* **62**, 540–552.
- Berg, B. G. (1989). “Analysis of weights in multiple observation tasks,” *J. Acoust. Soc. Am.* **86**, 1743–1746.
- Berg, B. G. (1990). “Observer efficiency and weights in a multiple observation task,” *J. Acoust. Soc. Am.* **88**, 149–158.
- Berg, B. G., and Green, D. M. (1990). “Spectral weights in profile listening,” *J. Acoust. Soc. Am.* **88**, 758–766.
- Blauert, J. (1983). *Spatial Hearing* (MIT Press, Cambridge, MA), p. 118.
- Bronkhorst, A. W., and Houtgast, T. (1999). “Auditory distance perception in rooms,” *Nature (London)* **397**, 517–520.

- Brungart, D. S., Durlach, N. I., and Rabinowitz, W. M. (1999). "Auditory localization of nearby sources. II. Localization of a broadband source," *J. Acoust. Soc. Am.* **106**, 1956–1968.
- Brungart, D. S., and Rabinowitz, W. M. (1999). "Auditory localization of nearby sources. Head-related transfer functions," *J. Acoust. Soc. Am.* **106**, 1465–1479.
- Brungart, D. S., and Scott, K. R. (2001). "The effects of production and presentation level on the auditory distance perception of speech," *J. Acoust. Soc. Am.* **110**, 425–440.
- Brunswik, E. (1952). *The Conceptual Framework of Psychology* (University of Chicago Press, Chicago).
- Cochran, P., Throop, J., and Simpson, W. E. (1968). "Estimation of distance of a source of sound," *Am. J. Psychol.* **81**, 198–206.
- Cohen, J., and Cohen, P. (1983). *Applied Multiple Regression/Correlation Analysis for the Behavioral Sciences* (Erlbaum, Hillsdale, NJ).
- Coleman, P. D. (1962). "Failure to localize the source distance of an unfamiliar sound," *J. Acoust. Soc. Am.* **34**, 345–346.
- Coleman, P. D. (1968). "Dual role of frequency spectrum in determination of auditory distance," *J. Acoust. Soc. Am.* **44**, 631–634.
- Da Silva, J. A. (1985). "Scales for perceived egocentric distance in a large open field: Comparison of three psychophysical methods," *Am. J. Psychol.* **98**, 119–144.
- Duda, R. O., and Martens, W. L. (1998). "Range dependence of the response of a spherical head model," *J. Acoust. Soc. Am.* **104**, 3048–3058.
- Foster, S. (1986). "Impulse response measurements using Golay codes," in *IEEE, 1986, Conference on Acoustics, Speech, and Signal Processing (ICASSP)* (IEEE, New York), Vol. 2, pp. 929–932.
- Gardner, M. B. (1969). "Distance estimation of 0 degrees or apparent 0 degree-oriented speech signals in anechoic space," *J. Acoust. Soc. Am.* **45**, 47–53.
- Gogel, W. C. (1969). "The sensing of retinal size," *Vision Res.* **9**, 1079–1094.
- Green, D. M., and Mason, C. R. (1985). "Auditory profile analysis: Frequency, phase, and Weber's Law," *J. Acoust. Soc. Am.* **77**, 1155–1161.
- Hartley, R. V. L., and Fry, T. C. (1921). "The binaural location of pure tones," *Phys. Rev.* **18**, 431–442.
- Holt, R. E., and Thurlow, W. R. (1969). "Subject orientation and judgment of distance of a sound source," *J. Acoust. Soc. Am.* **46**, 1584–1585.
- Ingard, U. (1953). "A review of the influence of meteorological conditions on sound propagation," *J. Acoust. Soc. Am.* **25**, 405–411.
- Jesteadt, W., Wier, C. C., and Green, D. M. (1977). "Intensity discrimination as a function of frequency and sensation level," *J. Acoust. Soc. Am.* **61**, 169–177.
- Landy, M. S., Maloney, L. T., Johnston, E. B., and Young, M. (1995). "Measurement and modeling of depth cue combination: In defense of weak fusion," *Vision Res.* **35**, 389–412.
- Loomis, J. M., Klatzky, R. L., Philbeck, J. W., and Golledge, R. G. (1998). "Assessing auditory distance perception using perceptually directed action," *Percept. Psychophys.* **60**, 966–980.
- Lutfi, R. A. (1995). "Correlation coefficients and correlation ratios as estimates of observer weights in multiple-observation tasks," *J. Acoust. Soc. Am.* **97**, 1333–1334.
- Lutfi, R. A., and Oh, E. L. (1997). "Auditory discrimination of material changes in a struck-clamped bar," *J. Acoust. Soc. Am.* **102**, 3647–3656.
- McGregor, P., Horn, A. G., and Todd, M. A. (1985). "Are familiar sounds ranged more accurately?," *Percept. Mot. Skills* **61**, 1082.
- Mershon, D. H., Ballenger, W. L., Little, A. D., McMurtry, P. L., and Buchanan, J. L. (1989). "Effects of room reflectance and background noise on perceived auditory distance," *Perception* **18**, 403–416.
- Mershon, D. H., and Bowers, J. N. (1979). "Absolute and relative cues for the auditory perception of egocentric distance," *Perception* **8**, 311–322.
- Mershon, D. H., and King, E. (1975). "Intensity and reverberation as factors in the auditory perception of egocentric distance," *Percept. Psychophys.* **18**, 409–415.
- Møller, H., Sørensen, M. F., Hammershøi, D., and Jensen, C. B. (1995). "Head-related transfer functions of human subjects," *J. Audio Eng. Soc.* **43**, 300–321.
- Nielsen, J. L. (1998). "Improvement of signal-to-noise ratio in long-term MLS measurements with high-level nonstationary disturbances," *J. Audio Eng. Soc.* **45**, 1063–1066.
- Nielsen, S. H. (1991). "Distance perception in hearing," Ph.D. thesis, Aalborg University, Denmark.
- Nielsen, S. H. (1993). "Auditory distance perception in different rooms," *J. Audio Eng. Soc.* **41**, 755–770.
- Pearson, E. S. (1931). "The analysis of variance in cases of non-normal variation," *Biometrika* **23**, 113–131.
- Richards, D. G., and Wiley, R. H. (1980). "Reverberations and amplitude fluctuations in the propagations of sound in a forest: Implications for animal communication," *Am. Nat.* **115**, 381–399.
- Rife, D. D., and Vanderkooy, J. (1989). "Transfer-function measurement with maximum-length sequences," *J. Audio Eng. Soc.* **37**, 419–444.
- Schroeder, M. R. (1965). "New method of measuring reverberation time," *J. Acoust. Soc. Am.* **37**, 409–412.
- Schroeder, M. R. (1979). "Integrated-impulse method measuring sound decay without impulses," *J. Acoust. Soc. Am.* **66**, 497–500.
- Simpson, W. E., and Stanton, L. D. (1973). "Head movement does not facilitate perception of the distance of a source of sound," *Am. J. Psychol.* **86**, 151–159.
- Speigle, J. M., and Loomis, J. M. (1993). "Auditory distance perception by translating observers," in *Proceedings of the IEEE Symposium on Research Frontiers in Virtual Reality* (IEEE, New York), pp. 92–99.
- Stellmack, M. A., Willihnganz, M. S., Wightman, F. L., and Lutfi, R. A. (1997). "Spectral weights in level discrimination by preschool children: Analytic listening conditions," *J. Acoust. Soc. Am.* **101**, 2811–2821.
- Wightman, F. L., and Kistler, D. J. (1989). "Headphone simulation of free-field listening. I. Stimulus synthesis," *J. Acoust. Soc. Am.* **85**, 858–867.
- Wightman, F. L., and Kistler, D. J. (1997). "Monaural sound localization revisited," *J. Acoust. Soc. Am.* **101**, 1050–1063.
- Willihnganz, M. S., Stellmack, M. A., Lutfi, R. A., and Wightman, F. L. (1997). "Spectral weights in level discrimination by preschool children: Synthetic listening conditions," *J. Acoust. Soc. Am.* **101**, 2803–2810.
- Zahorik, P. (2000). "Limitations in using Golay codes for head-related transfer function measurement," *J. Acoust. Soc. Am.* **107**, 1793–1796.
- Zahorik, P., Kistler, D. J., and Wightman, F. L. (1994). "Sound localization in varying virtual acoustic environments," in *Proceedings of the Second International Conference on Auditory Display, ICAD 1994*, Santa Fe, NM, edited by G. Kramer, pp. 179–186.
- Zhou, B., and Green, D. M. (1992). "Characterization of external ear impulse responses using Golay codes," *J. Acoust. Soc. Am.* **92**, 1169–1171.

Glottal flow through a two-mass model: Comparison of Navier–Stokes solutions with simplified models

M. P. de Vries, H. K. Schutte, A. E. P. Veldman, and G. J. Verkerke

Artificial Organs, Biomedical Engineering, Ant. Deusinglaan 1, 9713 AV Groningen, The Netherlands

(Received 29 July 1999; accepted for publication 12 September 2000)

A new numerical model of the vocal folds is presented based on the well-known two-mass models of the vocal folds. The two-mass model is coupled to a model of glottal airflow based on the incompressible Navier–Stokes equations. Glottal waves are produced using different initial glottal gaps and different subglottal pressures. Fundamental frequency, glottal peak flow, and closed phase of the glottal waves have been compared with values known from the literature. The phonation threshold pressure was determined for different initial glottal gaps. The phonation threshold pressure obtained using the flow model with Navier–Stokes equations corresponds better to values determined in normal phonation than the phonation threshold pressure obtained using the flow model based on the Bernoulli equation. Using the Navier–Stokes equations, an increase of the subglottal pressure causes the fundamental frequency and the glottal peak flow to increase, whereas the fundamental frequency in the Bernoulli-based model does not change with increasing pressure.

© 2002 Acoustical Society of America. [DOI: 10.1121/1.1323716]

PACS numbers: 43.70.Aj [AL]

LIST OF SYMBOLS

CQ	closed quotient	k_1	lower spring stiffness
\mathbf{F}	vector representing external forces on the fluid	r_1	lower damper
F_0	fundamental frequency	m_2	upper mass
U_g	glottal peak flow	k_2	upper spring stiffness
p	pressure	r_2	upper damper
p_s	subglottal pressure	k_c	coupling stiffness
\mathbf{u}	vector with the velocity components	k_{col1}	lower collision spring stiffness
ν	kinematic viscosity of the fluid	k_{col2}	upper collision spring stiffness
u	horizontal velocity of fluid	x_1	deflection of m_1
ν	vertical velocity of fluid	x_2	deflection of m_2
m_1	lower mass	ζ_1	lower damping ratio
		ζ_2	upper damping ratio

I. INTRODUCTION

To understand the process of voice production, several authors have investigated the pressure–flow relationship in the glottis (e.g., van der Berg *et al.*, 1957; Scherer and Titze, 1983; Alipour *et al.*, 1996; Guo and Scherer, 1993; Liljencrants, 1991). These examinations were all performed in a static glottis. Other investigations include the dynamic behavior of the voice source, which has been experimentally studied by Shadle *et al.* (1999) and Mongeau *et al.* (1997). Numerical modeling of the interaction between the oscillating vocal folds and the airflow in the glottis is performed using a simplified description of the vocal fold combined with a simplified description of the airflow (e.g., Ishizaka and Flanagan, 1972; Pelorson *et al.*, 1994; Story and Titze, 1995; Herzel *et al.*, 1995; Lous *et al.*, 1998). With these so-called lumped parameter models, glottal waves are produced as a result of a flow-induced oscillation of the vocal folds. Generally, in these lumped parameter models, the pressure and flow in the glottis are related by the Bernoulli equation. To apply this Bernoulli equation, assumptions concerning the physical characteristics of the fluid, air in our case, have to

be made. The use of the Bernoulli equation is allowed when the flow is assumed to be steady, laminar, nonviscous, and incompressible. In a cross section, pressure and velocity are usually assumed to be constant. In reality, pressure and velocity vary over a cross section. The velocity even has a transverse component that is ignored. Each of the assumptions, mentioned before, introduces an error and the resulting accumulation of errors results in an inaccurate description of the flow. To improve the flow calculations, a more accurate flow description has to be used. This is possible by using the two-dimensional Navier–Stokes equations. These equations describe the nonsteady and viscous behavior of a fluid under an external load. In this study, Navier–Stokes equations are implemented having only the assumption of incompressibility.

Although solving the Navier–Stokes equations is very time consuming, today's computing power ensures acceptable calculation times. Therefore, in the last decade, the Navier–Stokes equations already have been used in research concerning voice production. Alipour *et al.* (1996), Guo and Scherer (1993), and Liljencrants (1991) presented data using the Navier–Stokes equations in a static model of the vocal

folds. The pressure–flow relationships resulting from these investigations in the static glottis are related to the dynamic situation during phonation.

Recently, Alipour and Titze (1996) combined the incompressible Navier–Stokes equations with a dynamic finite-element method (FEM) model of the vocal folds and simulated phonation in this way. In their model, the finite-element method model of the vocal fold and the model of the Navier–Stokes equations exchange information, resulting in glottal waves. A disadvantage of this model is that it is only possible to prescribe a subglottal flow rate instead of an initial pressure. A preceding Bernoulli solution is needed in their model to approximate the flow rate that occurs at physiological subglottal pressures.

When the lumped parameter models of the vocal folds (Ishizaka and Flanagan, 1972; Herzel *et al.*, 1995; Pelorson *et al.*, 1994) are compared with the model of Alipour and Titze (1996), it can be seen that the glottal airflow description, based on the Bernoulli equation in the lumped parameter models, is replaced by the Navier–Stokes equations in the Alipour and Titze model, and the description of the vocal folds by a number of masses, springs, and dampers in the lumped parameter models is replaced by an FEM model. In the present study we will present a model composed of a lumped parameter model of the vocal folds combined with a Navier–Stokes model of the glottal flow. In this way, the need for assumptions concerning the viscous losses, as is needed in studies using a Bernoulli-based equation, is not necessary: as a consequence of the use of Navier–Stokes equations, viscous effects are included. We will give a comparison between results obtained using the Navier–Stokes equations with results obtained using the Bernoulli-based model. For the model of the vocal fold, we will use a lumped parameter model, i.e., the two-mass model. In this way, only one of the two steps presented by Alipour and Titze (1996) has been performed. This study is meant to be a step between the low-order models (the lumped parameter models) and the high-order models. Also, a new model of the aerodynamics is presented in which it is possible to prescribe the subglottal pressure.

II. MATERIALS AND METHODS

A model of one vibrating vocal fold has been developed, composed of a two-mass model describing the vocal fold and the Navier–Stokes equations describing the glottal flow. Due to symmetry, only one vocal fold is considered. First, the two-mass model simulating the vocal fold will be described, followed by the Navier–Stokes equations describing the aerodynamics. The interaction between the two-mass model and the Navier–Stokes equations will be described in a following section.

A. Two-mass model of the vocal folds

A two-mass model describes one vocal fold by two coupled oscillators (e.g., Ishizaka and Flanagan, 1972; Herzel *et al.*, 1995; Pelorson *et al.*, 1994; Lous *et al.*, 1998). Each oscillator consists of a mass, a spring, and a damper (Fig. 1). Mass m_1 , spring stiffness k_1 , and damper r_1 represent the lower part of the vocal fold. Mass m_2 , spring stiff-

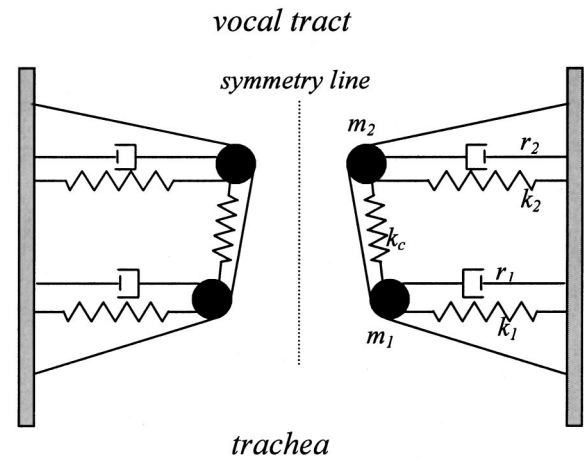


FIG. 1. Two-mass model.

ness k_2 , and damper r_2 represent the upper part. The two masses are coupled by a spring with stiffness k_c . The two masses, m_1 and m_2 , are permitted to move only in a lateral direction. The deflections of m_1 and m_2 are x_1 and x_2 , respectively. In the two-mass model, symmetry with respect to a plane parallel to the main flow axis is assumed; therefore, only one vocal fold is considered. When the vocal fold approaches the symmetry line within a very short distance, collision springs with stiffness k_{col1} and k_{col2} are activated and have an influence on the masses m_1 and m_2 , respectively, in the contralateral direction (e.g., Ishizaka and Flanagan, 1972; Pelorson *et al.*, 1994). In this way, the effective spring stiffness during collision changes. As a consequence of this way of modeling the collision, the glottal opening is allowed to have a small negative value.

In this study, we use two sets of values of the masses and springs. The first set of values consists of values used by Ishizaka and Flanagan (1972), which are also used by several other researchers (e.g., Herzel *et al.*, 1995; Steinecke and Herzel, 1995). The second set of values consists of values proposed by de Vries *et al.* (1999). This new set of parameters is based on a finite-element method (FEM) study of the mechanic behavior of a vocal fold. The values of the masses and springs are substantially smaller than the values used in previous studies. The parameter values for both sets are listed in Table I.

TABLE I. Parameter values for the two-mass model: Ishizaka and Flanagan parameters and de Vries parameters.

	I&F parameters	de Vries parameters
m_1 lower mass (g)	0.125	0.024
m_2 upper mass (g)	0.025	0.020
k_1 lower spring stiffness (N/m)	80	22
k_2 upper spring stiffness (N/m)	8	14
k_c coupling spring stiffness (N/m)	25	10
ζ_1 damping ratio (g/s)		0.1
ζ_2 damping ratio (g/s)		0.6
l_g glottal length (cm)		1.3
k_{col1} collision spring stiffness (N/m)		$3k_1$
k_{col2} collision spring stiffness (N/m)		$3k_2$

B. Aerodynamics

To obtain oscillation of the vocal folds, aerodynamic forces have to act on the two masses. In the present study, the aerodynamic forces result from the pressure distribution along the glottal surface as determined by the Navier–Stokes equations. For the computation of the aerodynamic part of this model, the incompressible two-dimensional Navier–Stokes equations are used. These equations are based on two conservation laws.

(1) Conservation of mass

$$\nabla \cdot \mathbf{u} = 0, \quad (1)$$

where \mathbf{u} is the vector with the velocity components.

(2) Conservation of momentum

$$\frac{\partial \mathbf{u}}{\partial t} + \nabla p = \mathbf{R}, \quad (2)$$

with

$$\mathbf{R} = -(\mathbf{u} \cdot \nabla) \mathbf{u} + \nu (\nabla \cdot \nabla) \mathbf{u} + \mathbf{F}.$$

In Eq. (2), p is the pressure, ν is the kinematic viscosity of the fluid, and \mathbf{F} is the vector representing external forces on the fluid.

The term $\partial \mathbf{u} / \partial t$ in Eq. (2) is discretized in time with a forward Euler method using time step ∂t . This results in

$$\nabla \cdot \mathbf{u}^{n+1} = 0, \quad (3)$$

$$\frac{\mathbf{u}^{n+1} - \mathbf{u}^n}{\partial t} + \nabla p^{n+1} = \mathbf{R}^n, \quad (4)$$

where $n+1$ is the new time step and n is the present time step. These terms can be rearranged as

$$\mathbf{u}^{n+1} = \mathbf{u}^n + \partial t \mathbf{R}^n - \partial t \nabla p^{n+1}. \quad (5)$$

This can be substituted into Eq (3), which results in the Poisson equation for the pressure

$$(\nabla \cdot \nabla) p^{n+1} = \nabla \cdot \left(\frac{\mathbf{u}^n}{\partial t} + \mathbf{R}^n \right). \quad (6)$$

Spatial discretization of the Navier–Stokes equations is performed in a Cartesian grid. This grid can be refined at places of particular interest. The three degrees of freedom of each cell in the grid are the velocity in the direction of the main flow u , the velocity perpendicular to the main flow v , and the pressure p . The velocity in the direction of the main flow u is defined on the right edge of a cell, the velocity perpendicular to the main flow v is defined on the upper edge of a cell, and the pressure p is defined in the center of a cell. This staggered way of placing the variables is known as the marker-and-cell (MAC) method (Harlow and Welsh, 1965). The numerical advantage of this method is the uniqueness of the pressure.

The equations stated above have to be completed by boundary conditions. At the laryngeal wall, the tangential velocity is set to zero, simulating the sticking of the fluid to the wall, the so-called no-slip condition, and the perpendicular velocity is set to zero, simulating the impermeability of the wall. At the inlet, the subglottal pressure is prescribed.

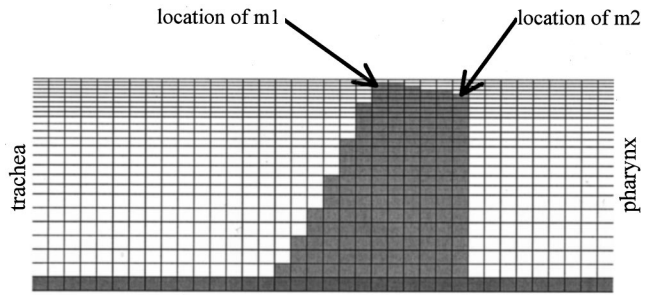


FIG. 2. Nonuniform grid with model of the vocal fold.

The outlet conditions combine a prescribed pressure with zero normal derivatives of the velocities. Since in the two-mass model only one vocal fold is modeled because of the symmetry assumption along the glottis, the aerodynamics is assumed to be symmetric along the glottis. At this symmetry line, the velocity perpendicular to the symmetry line is set to zero and the derivative of the axial velocity to its perpendicular coordinate is set also to zero.

The model of the aerodynamics makes use of adaptive time steps: within every time step, a routine checks for the time step to be small enough to give reliable results. The routine tries to calculate for the optimal time step for the present situation. This adaptive time step is profitable in the present research because the aerodynamic grid is changing during the simulation as a consequence of the moving vocal fold. In this way, a stable and fast solution is obtained. During the simulations presented in this study, the time step varied between 32.0E-6 and 0.5E-6 s. An exhaustive validation of an expanded version of the model of the aerodynamics is presented by Veldman *et al.* (1999).

To be able to compare the results using Navier–Stokes equations with results using simplified models, simulations with a glottal flow model based on Bernoulli are also used. The model used for comparison has been presented before by Lous *et al.* (1998).

C. Interaction

Interaction between the vocal fold and the aerodynamics takes place at the surface that is defined by the location of the two masses (Fig. 2). The masses are connected by rigid, massless plates. This configuration is also used by Lous *et al.* (1998), where they describe a two-mass model that uses the Bernoulli equation. In this configuration, sharp edges at the locations of the masses are present.

The interaction between the two-mass model and the aerodynamic model occurs in the grid of the aerodynamics. The cells of the grid in which a part of the two-mass model is present are supposed to be filled by a nonfluid material. In this way, a distinction is made between cells that are filled with air (aerodynamic cells) and cells that are not filled with air (mechanic cells). In the aerodynamic cells, the Navier–Stokes equations are calculated. The mechanic cells provide the boundary conditions for the aerodynamic cells. In the grid, information concerning the pressure of the airflow is transferred to the two-mass system, and information about

the position and the velocity of the two masses is transferred to the aerodynamic model in every time step.

The pressure distribution along the vocal-fold surface resulting from the Navier–Stokes calculations has to be translated to two point forces that act on the two masses. These forces are not directly available from the aerodynamic model, but are derived from the pressures in the aerodynamic cells adjacent to the vocal fold. The pressure values of the cells that contain air and that are also adjacent to the cells that contain a part of the vocal fold are multiplied by the area of the concerning cell, which corresponds to the length of the cell multiplied by the glottal length. These pressure forces are calculated in all fluid cells adjacent to the vocal-fold cells, so the complete glottal surface is considered. The pressure forces are distributed over the two masses in such a way that they form a statically equivalent system. The resulting new positions and velocities of the two masses are calculated and transferred to the aerodynamic model by defining a new distribution of aerodynamic cells and mechanic cells in the grid. The velocities of the mechanic cells at the glottal surface are calculated by interpolation of the velocities of the two masses. In this way, a dynamic boundary condition for the aerodynamic cells is defined, which is used in the next time step of the calculations of the Navier–Stokes equations. In this way, a realistic description of the interaction is obtained.

The two-mass model is by definition a two-dimensional model. Therefore, the aerodynamics is also considered to be two-dimensional. To obtain results as glottal flow and aerodynamic forces, the third dimension is simulated by assuming a uniform distribution of the aerodynamic quantities along the length of the vocal fold. According to measurements performed by Baer (1981), the length of the vocal fold is modeled by a length of 1.3 cm. In this way, boundary effects that occur at the anterior and posterior glottal commissure are neglected.

To determine the numerical validity of the model, the number of cells has been varied until a grid was obtained for which a doubling of the number of cells does not result in a noticeable difference in the glottal waves. The grid is made nonuniform by taking smaller cells in the neighborhood of the glottis, because in this region larger velocity gradients and pressure gradients can be expected.

To obtain glottal waves, different values for the subglottal pressure P_s were applied. In a previous study (de Vries *et al.*, 1999), the properties of glottal waves that are produced at a pressure of 6 cm H₂O were compared to normal values. We also used the value of 6 cm H₂O in this study, which is chosen after Holmberg *et al.* (1989), where they derived average values for several quantities concerning phonation in males and females. The normal value of the subglottal pressure of 4.3 cm H₂O, determined by Schutte (1980), has not been used because no glottal waves were obtained at that pressure for the specific set of model parameters used in our study. Properties of the glottal waves produced with the presented numerical model will be considered at $P_s=0.6$ kPa, which is almost equal to 6 cm H₂O. In this

TABLE II. Properties of the glottal waves produced using the Navier–Stokes equations compared to normal values; these results were obtained using the de Vries parameters because the use of the Ishizaka and Flanagan parameters does not result in glottal waves.

	Two-mass+ Bernoulli	Two-mass+ Navier-Stokes	Normal phonation	
			Female	Male
Fundamental frequency F_0 (Hz)	187	165	207	119
glottal peak flow U_g (1/s)	0.25	0.48	0.14	0.23
closed quotient CQ(-)	0.30	0.30	0.26	0.39

way, properties of the glottal waves can be compared easily.

The glottal waves produced with the new model are analyzed and will be compared with the glottal waves produced by lumped parameter models using the Bernoulli-based model by comparing the fundamental frequency, glottal peak-flow rate, and closed quotient.

To obtain information about the phonation threshold pressure and the range of self-sustained oscillation, subglottal pressure was increased during the simulations by 8.0 kPa per second until a value of 2 kPa was reached. Simulations have been performed with an initial glottal gap of 0.0, 0.05, 0.01, and 0.25 mm. The initial shape of the glottis during these simulations was uniform, no diverging, and converging initial shapes are simulated.

III. RESULTS

Using a grid with 128×30 cells, the condition of stable solutions is satisfied. Therefore, this grid is used in all the simulations.

Using the parameters sets of Ishizaka and Flanagan and de Vries, different results were obtained. Using the Ishizaka and Flanagan parameter values, no self-sustained oscillation is obtained for subglottal pressures between 0.0 and 2.0 kPa and different initial glottal gaps. The de Vries parameters show self-sustained oscillation for a wide range of subglottal pressures and initial glottal gaps. Therefore, the following results are all produced using the de Vries parameters.

The properties of glottal waves resulting from a simulation with subglottal pressure of 0.6 kPa have been determined. Glottal waves with a closed phase could only be obtained using an initially closed glottis when a subglottal pressure of 0.6 kPa was applied. Comparisons of the properties of the glottal waves with the properties of the glottal waves produced using the Bernoulli-used model instead of the Navier–Stokes equations are summarized in Table II. For comparison, values for normal phonation according to Holmberg *et al.* (1989) are listed. From this table, it can be seen that the fundamental frequency appears to be lower by using the Navier–Stokes equations than by using the model based on the Bernoulli equation.

The glottal peak flow of the glottal waves produced using the Navier–Stokes equations is a factor of 2 higher than the glottal peak flow of the glottal waves produced using the Bernoulli-based model. This value is also higher than the

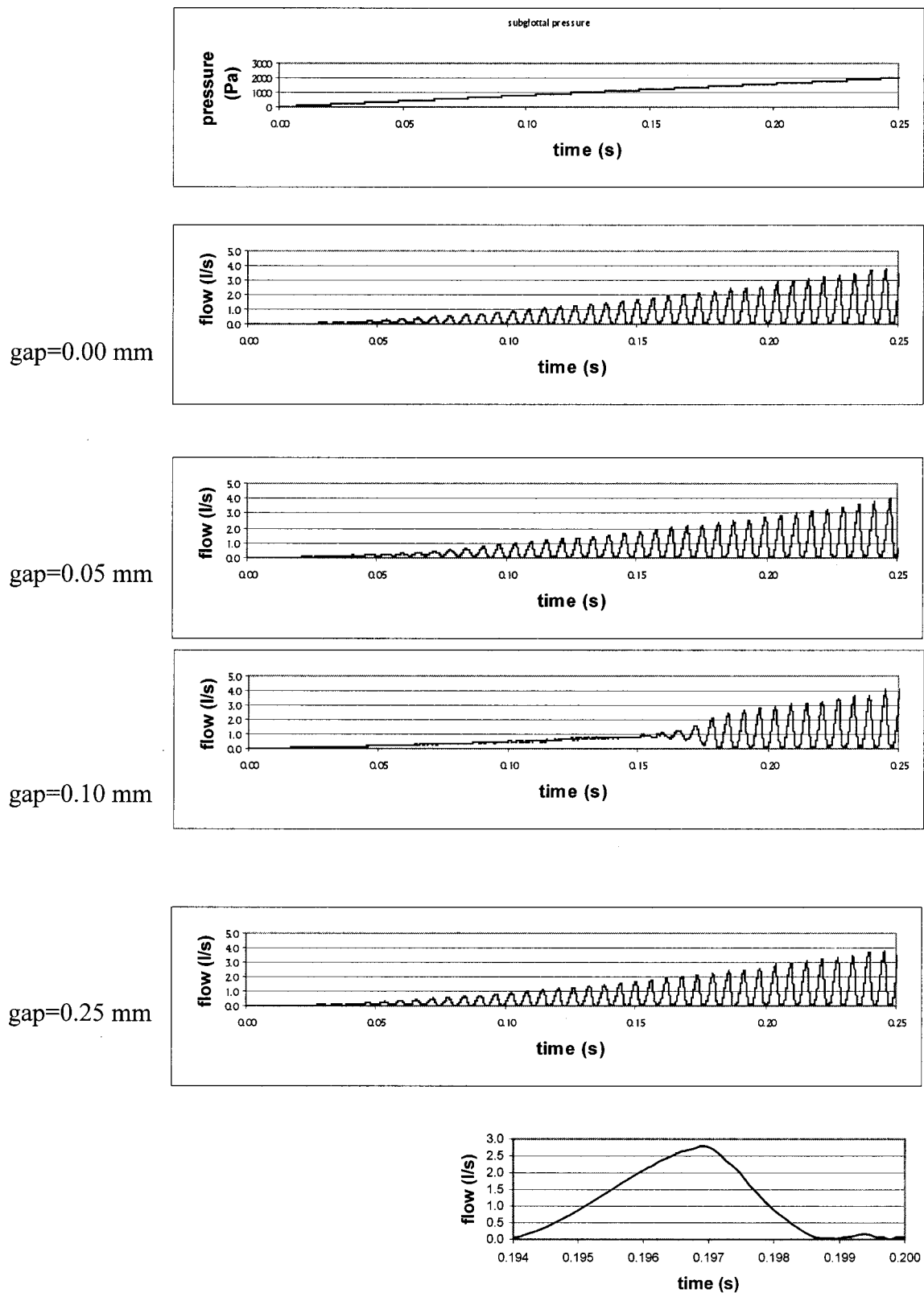


FIG. 3. Glottal waves for different initial glottal openings and rising subglottal pressure; at the bottom right, a close-up of one glottal wave (0.1-mm glottal gap) is shown.

normal value in female and male phonation, as shown in Table II.

Application of Navier–Stokes instead of the Bernoulli-based model does not influence the value of the closed quotient.

Results of an increase of subglottal pressure in the model using different values for the initial glottal gap are shown in Fig. 3. It can be seen that, using a different initial glottal gap, oscillation starts at a different subglottal pressure. The pressure at which self-sustained oscillation occurs

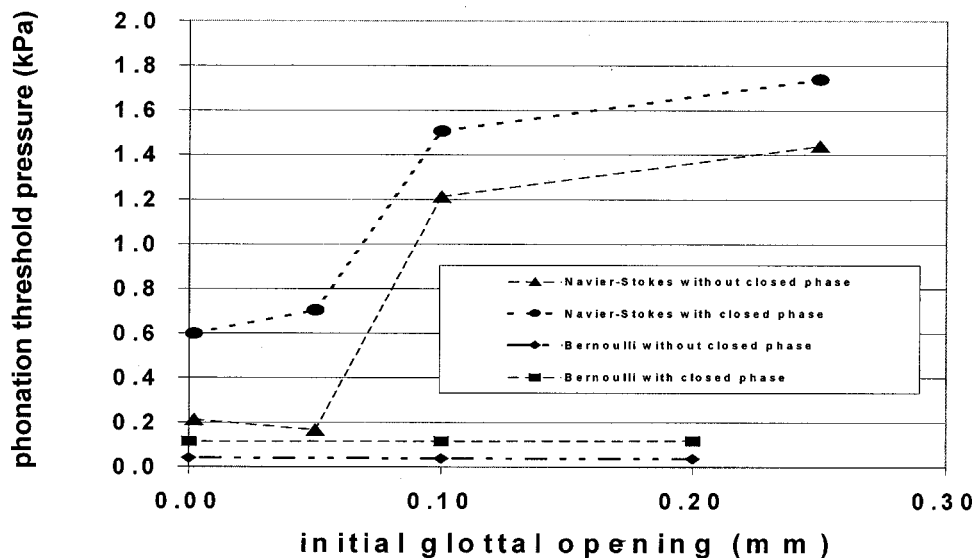


FIG. 4. Phonation threshold pressure for different initial glottal opening.

(phonation threshold pressure) is shown in Fig. 4. At this phonation threshold pressure, a sinus-like waveform is obtained. Increasing the pressure above the phonation threshold pressure results in a more than proportional increase of the amplitude of the oscillation, resulting in glottal waves that are not sinus-like but which have a closed quotient. The pressure at which glottal waves with a closed quotient are obtained, is also plotted in Fig. 4. The phonation threshold pressure obtained is higher using the Navier–Stokes than when using the Bernoulli-based model (Fig. 4) for all initial glottal gaps. Titze (1988) studied the phonation threshold pressure for different initial glottal gaps; for a uniform glottis with an initial glottal gap of 0.1 mm, he determined a value of approximately 0.9 kPa, which is close to the value obtained using the Navier–Stokes equations of 1.2 kPa. The value obtained with the Bernoulli-based model is almost 0.1 kPa, which is much lower.

The rate of change of the fundamental frequency as a function of the subglottal pressure (dF_0/dP_s) is derived by dividing the difference between F_0 at 0.6 kPa ($F_0 = 165$ Hz) and at 1.6 kPa ($F_0 = 168$ Hz) by the difference in pressure ($1.6 - 0.6 = 1.0$ kPa). Over this pressure range, dF_0/dP_s is determined to be 3 Hz/kPa, which is almost equal to 0.3 Hz/cm H₂O. This value is substantially lower than the 2.5 Hz/cm H₂O determined by Ishizaka and Flanagan (1972) using their two-mass model. Using the glottal flow model that is based on the Bernoulli equation, the frequency remains unchanged when subglottal pressure is varied.

To demonstrate the variations in glottal flow during a glottal cycle, Fig. 5 shows the velocity component along the main flow direction in an open phase and in a closed phase, as determined during a simulation with the de Vries parameters with an initial glottal opening of 0.5 mm and a subglottal pressure of 0.8 kPa, resulting in a mean flow of 430 ml/s.

IV. DISCUSSION

In this study it is demonstrated that it is possible to achieve self-sustained oscillation with a two-mass model of the vocal folds in combination with a Navier–Stokes de-

scription of the glottal flow. The results show that the choice of the set of parameter values is crucial to achieve phonation: no self-sustained oscillation is obtained using the parameter values of Ishizaka and Flanagan (1972), while the use of the parameter values of de Vries *et al.* (1999) results in the production of acceptable glottal waves. This could be caused by the fact that the parameter values of Ishizaka and Flanagan are larger than those of de Vries. Probably the values of the masses and springs that represent the vocal folds are overestimated by Ishizaka and Flanagan, as suggested by Lous *et al.* (1998). In the case of an overestimation of the mechanic influence of the vocal folds, they predominate the dynamic behavior of the vocal folds.

The properties of the glottal waves produced using the Navier–Stokes equations differ from those produced using the Bernoulli-based model. Because applying the Navier–Stokes equations lowers the fundamental frequency, it can be

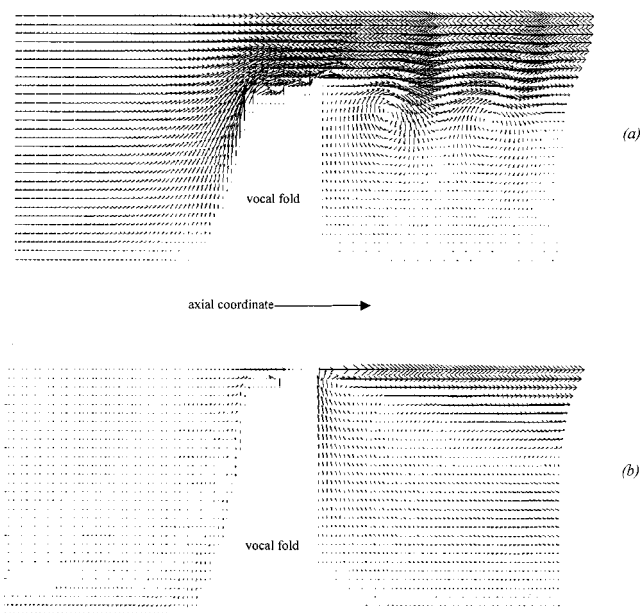


FIG. 5. Vector plot of velocities of maximum open phase (a) and closed phase (b).

stated that an increase in the effective mass of the vocal folds has been achieved. So, the lowering in the fundamental frequency might be partially explained by the influence of inertia effects which are present in the Navier–Stokes equation and absent in the Bernoulli equation. To which extent this effect contributes to the lowering is a question that will be answered in a forthcoming study.

The fact that the glottal peak flow is increased by a factor of 2 by applying the Navier–Stokes equations instead of the Bernoulli-based model can be explained by the fact that the viscous losses are described in a different manner: in the Bernoulli-based model, viscous effects are calculated using a fixed separation point for a convergent and divergent glottis. In the Navier–Stokes equations, the viscous effects in the main flow and in the boundary layer are described much more accurately, which can have a significant influence on the value of the glottal peak flow. The closed quotient of the glottal waves produced using the Navier–Stokes equations does not differ from the closed quotient produced using the Bernoulli-based model. The combination of a higher glottal peak flow with an equal closed quotient results in a higher glottal airflow velocity in the Navier–Stokes simulations than from the Bernoulli-based model. This also can be due to a different description of the viscous effects in both aerodynamic models.

The phonation threshold pressure depends on the initial glottal gap. This is in correspondence with Titze (1988), who stated that a tighter adduction of the vocal folds results in a lower phonation threshold pressure. The fact that a sinus-like oscillation occurs at a lower pressure using a gap of 0.05 mm can be explained by the fact that the initially closed glottis has to be opened first. The transition of a sinus-like oscillation to oscillation with a closed phase has also been demonstrated in normal phonation (Schutte and Seidner, 1988).

The value of the maximum jet velocity as shown in Fig. 5 corresponds very well with Alipour *et al.* (1996). In an excised larynx, they measured a supraglottal jet velocity of about 40 m/s at almost the same mean flow rate, namely 470 ml/s.

In the model presented in this paper, we are able to apply a subglottal pressure without using the Bernoulli equation to approximate the subglottal pressure for a given flow field, in contrast to Alipour and Titze (1996) and Guo *et al.* (1993). In comparison with Alipour and Titze (1996) we can state that, despite of our simple mechanical description of the vocal folds, we obtain glottal waves that are at least as realistic as in their study.

In our study, we assume the vocal folds to be sharp-edged because we do not apply any rounding to the geometry of the vocal fold. This choice is made because of the uncertain measures for rounding of the vocal folds that are available. Instead of the recommendations by Alipour and Titze (1999), no bulging of the vocal-fold surface is applied. If bulging is applied, the small pulses of air in the closed phase (which occur at higher pressure, as shown in Fig. 3) would probably be avoided. From this point of view, rounding of the vocal fold at the edges and bulging of the

vocal-fold surface would be a possible improvement for the mechanical model.

ACKNOWLEDGMENT

This research was supported by the Technology Foundation.

- Alipour, F., Scherer, R., and Knowles, J. (1996). "Velocity distributions in glottal models," *J. Voice* **10**(1), 50–58.
- Alipour, F., and Titze, I. R. (1996). "Combined simulation of two-dimensional airflow and vocal fold vibration," in *Vocal Fold Physiology*, edited by P. J. Davis and N. H. Fletcher (Singular, San Diego), pp. 17–29.
- Alipour, F., and Titze, I. R. (1999). "Vocal fold bulging effects on phonation using biophysical computer model," NCVS Status Progress Report **13**, 105–114.
- Baer, T. (1981). "Observation on vocal fold vibration: Measurement of excised larynges," in *Vocal Fold Physiology*, edited by K. Stevens and M. Hirano (University of Tokyo, Japan), pp. 119–133.
- de Vries, M. P., Schutte, H. K., and Verkerke, G. J. (1999). "Determination of parameters for lumped parameter models of the vocal folds using a finite element method approach," *J. Acoust. Soc. Am.* **106**, 3620–3628.
- Guo, C. G., and Scherer, R. C. (1993). "Finite element simulation of glottal flow and pressure," *J. Acoust. Soc. Am.* **94**, 688–700.
- Harlow, F. H., and Welsh, J. E. (1965). "Numerical calculation of time-dependent viscous incompressible flow of fluid with free surface," *Phys. Fluids* **8**, 2182–2189.
- Herzel, H., Berry, D., Titze, I. R., and Steinecke, I. (1995). "Nonlinear dynamics of the voice: Signal analysis and biomechanical modelling," *Chaos* **5**(1), 30–34.
- Holmberg, E. B., Hillman, R. E., and Perkell, J. S. (1989). "Glottal airflow and transglottal air pressure measurements for male and female speakers in low, normal, and high pitch," *J. Voice* **3**(4), 294–305.
- Ishizaka, K., and Flanagan, J. L. (1972). "Synthesis of voiced sounds from a two-mass model of the vocal cords," *Bell Syst. Tech. J.* **51**, 1233–1267.
- Liljencrants, I. (1991). "Numerical simulations of glottal flow," in *Vocal Fold Physiology*, edited by J. Gauffin and B. Hammarberg (Raven, New York), pp. 99–104.
- Lous, N. J. C., Hofmans, G. C. J., Veldhuis, R. N. J., and Hirschberg, A. (1998). "A symmetrical two-mass vocal-fold model coupled to vocal tract and trachea, with application to prosthesis design," *Acta Acust. (China)* **84**(6), 1135–1150.
- Mongeau, L., Franchek, N., Coker, C. H., and Kubli, R. A. (1997). "Characteristics of a pulsating jet through a small modulated orifice, with application to voice production," *J. Acoust. Soc. Am.* **102**, 1121–1133.
- Pelorsson, X., Hirschberg, A., van Hassel, R. R., Wijnands, A. P. J., and Auregan, Y. (1994). "Theoretical and experimental study of quasisteady-flow separation within the glottis during phonation. Application to a modified two-mass model," *J. Acoust. Soc. Am.* **96**, 3416–3431.
- Scherer, R. C., and Titze, I. R. (1983). "Pressure-flow relationships in a model of the laryngeal airway with a diverging glottis," in *Vocal Fold Physiology*, edited by P. J. Davis and N. H. Fletcher (Singular, San Diego), pp. 179–193.
- Schutte, H. K. (1980). "The efficiency of voice production," Ph.D. thesis, University of Groningen.
- Schutte, H. K., and Seidner, W. W. (1988). "Registerabhängige Differenzierung von Elektrolottogrammen. Sprache-Stimme-Gehör," **12**, 59–62.
- Shadle, C. H., Barney, A., and Davies, P. O. A. L. (1999). "Fluid flow in a dynamic mechanical model of the vocal folds and tract. Implications for speech production studies," *J. Acoust. Soc. Am.* **105**, 456–466.
- Steinecke, I., and Herzel, H. (1995). "Bifurcations in an asymmetric vocal-fold model," *J. Acoust. Soc. Am.* **97**, 1874–1884.
- Story, B. H., and Titze, I. R. (1995). "Voice simulation with a body-cover model of the vocal folds," *J. Acoust. Soc. Am.* **97**, 1249–1260.
- Titze, I. R. (1988). "The physics of small-amplitude oscillation of the vocal folds," *J. Acoust. Soc. Am.* **83**, 1536–1552.
- van den Berg, J. W., Zantema, J. T., and Doornenbal, P. (1957). "On the air resistance and the Bernoulli effect of the human larynx," *J. Acoust. Soc. Am.* **29**, 626–631.
- Veldman, A. E. P., and Verstappen, R. W. C. P. (1999). "Higher-order discretization methods for CFD," *Nieuw archief voor de wiskunde* **17**(2), 195–204.

American and Swedish children's acquisition of vowel duration: Effects of vowel identity and final stop voicing^{a)}

Eugene H. Buder

The University of Memphis, School of Audiology and Speech–Language Pathology, 807 Jefferson Avenue, Memphis, Tennessee 38105

Carol Stoel-Gammon

University of Washington, Department of Speech and Hearing Sciences, 1417 N.E. 42nd Street, Seattle, Washington 98105-6246

(Received 6 August 2001; accepted for publication 30 January 2002)

Vowel durations typically vary according to both intrinsic (segment-specific) and extrinsic (contextual) specifications. It can be argued that such variations are due to both predisposition and cognitive learning. The present report utilizes acoustic phonetic measurements from Swedish and American children aged 24 and 30 months to investigate the hypothesis that default behaviors may precede language-specific learning effects. The predicted pattern is the presence of final consonant voicing effects in both languages as a default, and subsequent learning of intrinsic effects most notably in the Swedish children. The data, from 443 monosyllabic tokens containing high-front vowels and final stop consonants, are analyzed in statistical frameworks at group and individual levels. The results confirm that Swedish children show an early tendency to vary vowel durations according to final consonant voicing, followed only six months later by a stage at which the intrinsic influence of vowel identity grows relatively more robust. Measures of vowel formant structure from selected 30-month-old children also revealed a tendency for children of this age to focus on particular acoustic contrasts. In conclusion, the results indicate that early acquisition of vowel specifications involves an interaction between language-specific features and articulatory predispositions associated with phonetic context. © 2002 Acoustical Society of America.

[DOI: 10.1121/1.1463448]

PACS numbers: 43.70.Ep, 43.70.Kv, 43.70.Fq [AL]

I. INTRODUCTION

A. Rationale

The durational patterns of natural human speech are determined by both physiological disposition and language learning. A fundamental question remains: In what measure and priority do each of these influences govern specific segment duration patterns? Examples of such patterns include both the *intrinsic* variations associated with vowel identity and the *extrinsic* variations associated with phonetic context. Probably the most definitive and natural “experiments” addressing the sources of these patterns are provided by the investigation of speech acquisition in language environments in which the intrinsic and extrinsic influences differ.

In this article, we present data describing the acquisition of vowel durations by young children learning American English (AE) and Swedish (Sw) in order to examine the relative roles of intrinsic and extrinsic influences in these two lan-

guages. Specifically, we report results describing 24- and 30-month-old AE and Sw children's acquisition of high front vowels in monosyllabic words ending in voiced and unvoiced stop consonants. The primary purpose is to explore the hypothesis that in early stages of language learning, children adhere to certain predisposed speech patterns regardless of maternal language. With more exposure to their language and increased ability to control phonetic aspects of production, children's output conforms more closely to adult language-specific patterns. Following a review of background literature pertaining to intrinsic and extrinsic influences on vowel duration, this introduction closes with three central hypotheses concerning duration measures and an exploratory hypothesis regarding the extension of the rationale to formant measures.

B. Background

1. Intrinsic vowel length

Within a language, vowel length is affected by a variety of factors in context-free environments. These “intrinsic” factors include articulatory differences (high vowels are generally shorter than low vowels; central vowels are shorter than peripheral vowels) and phonological factors, particularly in languages in which vowel length is phonemic. In describing Germanic languages, the terms “tense” and “lax” are often used to describe the relationship between vowels that share some articulatory features, but differ in quality and/or quantity. The “tense” member of the pair is higher or more “close,” and generally more peripheral than the “lax”

^{a)}Portions of this work were presented in Stoel-Gammon, C., Buder, E. H., and Kehoe, M. M. (1995). “Acquisition of vowel duration: A comparison of Swedish and English,” in *The Proceedings of the XIIIth International Congress of Phonetic Sciences*, edited by K. Elenius and P. Branderud (KTH and Stockholm University, Stockholm), pp. 30–37, and in Stoel-Gammon, C., and Buder, E. H. (1998). “The effects of postvocalic voicing on the duration of high front vowels in Swedish and American English: Developmental data,” in *Proceedings 16th International Congress on Acoustics and 135th Meeting of the Acoustical Society of America*, edited by P. K. Kuhl and L. A. Crum (Acoustical Society of America, Woodbury, NY), pp. 2989–2990.

member; it is also longer, hence the use of “long” and “short” in classifying these vowels (Catford, 1977; Lehiste, 1970; Lindau, 1978). As an articulatory label, the tense-lax distinction is controversial as it refers to different aspects of articulation in different languages (Clark and Yallop, 1995; Maddieson and Ladefoged, 1985). In general terms, vowels designated as tense are said to involve a greater degree of deviation from a neutral vocal tract configuration (Jakobson *et al.*, 1952).

In American English, /i/ and /ɪ/, the high front vowels of interest in this study, are characterized by both quality and quantity differences. The “tense” member of the pair (/i/) is higher, fronter and longer than its “lax” counterpart. According to House (1961), the lax-to-tense (or short-to-long) duration ratio is 0.71, a relatively unmarked length distinction compared to some other languages. Perceptual tests suggest that quality differences play the primary role in distinguishing these vowels: When listeners are presented with a production of the word “heat” that has vowel quality of /i/ and the vowel length of /ɪ/, it is heard as “heat” and not “hit” (Giegerich, 1992).

In contrast to English, Swedish is a language in which vowel length plays a prominent role in the phonological system. Swedish has a large vowel inventory comprised of 18 vowels typically described as nine “long-short” pairs. Although quality differences in pairs do exist, they are generally assumed to be secondary to the length difference (Elert, 1964; Fant, 1973; Hadding-Koch and Abramson, 1964). According to Elert (1964), the average short-to-long ratio of vowel pairs in Swedish is 0.65. For the high front vowels of interest in the present study, quality differences are minimal and vowel identity depends almost exclusively on durational differences (see Fant, 1973, especially Chap. 5, “Formant frequencies of Swedish vowels,” and Chap. 12, “Notes on the Swedish vowel system”).

Given the different phonetic and phonological roles played by vowel length in American English and Swedish, we might expect different learning patterns from children acquiring the two languages. Presumably, American children would pay more attention to the quality differences between vowel pairs, whereas children acquiring Swedish would attend to the quantity differences. These predictions may also be affected by the extrinsic vowel length differences described in the following section.

2. Extrinsic vowel length

In addition to durational differences that are intrinsic to a vowel, phonetic context plays an important role in vowel length. Analyses of American English have shown that final consonant voicing is the primary influence on the duration of a preceding vowel (Denes, 1955; House and Fairbanks, 1953; Lisker, 1957; Peterson and Lehiste, 1960). In English, the effect of final consonant voicing is strong, with vowels preceding voiced consonants nearly twice as long as vowels preceding voiceless cognates (House, 1961). As noted by Chen (1970), many languages exhibit the same effect documented for English vowels, although the effects of final-consonant voicing vary in terms of degree. This finding has

led some researchers to suggest that the durational difference is universal and physiologically determined (Chen, 1970; Elert, 1964).

One explanation for the observed phenomenon is that the vowel-to-consonant transition in the case of voiceless consonants is more forceful, and hence quicker, because of the greater aerodynamic control required to establish an oral cavity seal when the glottal valve is open (Chen, 1970; de Jong, 1991). However, Löfqvist and Gracco (1997) examined lip and jaw kinematic data during labial stop closures and found no consistent effects associated with voicing differences, casting doubt on this particular explanation. The notion that extrinsic effects are somehow “automatic” has also been critiqued on phonological grounds. Keating (1985) points out that in a small number of languages, including Polish, Czech, and Saudi Arabic, there is no interaction between vowel length and consonant voicing and argues that context-sensitive patterns of vowel duration are language specific and must be learned. In Swedish, the effects of final consonant voicing are small, as might be expected in a language with a phonemic vowel length contrast. For adult Swedish, Elert (1964) reported an average voiceless-to-voiced ratio of 0.97, indicating that vowel length remains essentially unchanged in spite of differences in final consonant voicing.

Given the near universal occurrence of longer vowels before voiced obstruents, it seems reasonable to assume that this pattern is the more basic pattern and that it may have motoric underpinnings that predispose children to this extrinsic lengthening effect. If this is the case, we would predict that children learning a language that conforms to the basic, or “unmarked,” pattern would learn the pattern with ease, as if it were the starting point for learning. In contrast, children learning a language that has a more unusual, or “marked,” pattern would be slower to acquire that pattern, as it would require moving further from the neutral, unmarked predisposition. Thus, in a comparison of English and Swedish, we would predict that children acquiring Swedish would have difficulty suppressing the tendency to produce lengthened vowels before voiced stops, whereas children acquiring English would simply conform to the unmarked pattern. This notion is elaborated further below.

3. Acquisition of vowel quality and quantity

The majority of studies focusing on the acquisition of vowels have involved children acquiring American English. A review of perceptual (i.e., transcription based) investigations yields a basic consensus that quality differences between vowel pairs, particularly the pair of high front vowels under investigation, are present in the speech of most children by the age of 3 years (Stoel-Gammon and Herrington, 1990; Templin, 1957). In a longitudinal study of six children aged 22–30 months, Otomo and Stoel-Gammon (1992) reported that the vowel /i/ exhibited a high proportion of correct productions at 22 months (73%), rising to 91% by 30 months, while correct production of its short/lax counterpart /ɪ/ averaged only 28% at 22 months, rising to 40% at 30 months. At 22 months, the most frequent substitution for /i/ was [ɪ] and vice versa; at 26 and 30 months, the most fre-

quent substitution for /I/ was [ɛ], another short/lax vowel. Otomo and Stoel-Gammon (1992) did not discuss the role of quantity in the children's substitution patterns.

Acoustic investigations of extrinsic vowel duration have also focused primarily on English. In a review of studies completed by the early 1980s, Wardrip-Fruin stated that "children under six make little use of vowel duration difference as cues to voicing in final stops." (Wardrip-Fruin, 1982, p. 187). In spite of this conclusion, other researchers were concurrently reporting that children as young as 3 years of age utilized vowel duration in both perception and production as a cue to following consonant voicing (Krause, 1982b). Furthermore, it was found that the length of children's vowel durations preceding voiced stops continued to increase with age (Krause, 1982a). A developmental learning effect in production appears to augment the physiological disposition in American English, apparently compensating for final stops that are unreleased and therefore without intrinsic duration. Naeser's data (1970) showed that, at 22 months, extrinsic and intrinsic ratios of American children were comparable to those of adult speakers with a reported extrinsic ratio of 0.50 and an intrinsic ratio of 0.74. At 34 months, however, the ratios Naeser obtained were less adult-like, with an extrinsic ratio of 0.62 and an intrinsic ratio of 0.64. Greenlee's data (1978), from children at 26 months, yielded ratios that exhibited minimal differences between extrinsic and intrinsic ratios: The extrinsic ratio was 0.66 and the intrinsic ratio was 0.68. Finally, a report by Raphael and colleagues (Raphael *et al.*, 1980) indicated that 3- to 4-year-old children exhibited ratios close to those of adults with extrinsic ratios around 0.55 and intrinsic ratios around 0.72.

Preliminary analyses of a subset of the data reported here (Stoel-Gammon and Buder, 1998) revealed that 24-month-old American children exhibited shortening of high front vowels preceding voiceless stops, although the ratio was larger than for the adult data reported in House (1961). Intrinsic shortening was also observed in the same group of 24-month-old children, although, here again, the durational differences were smaller than those found in adult speech. Analyses of a subset of the data from Swedish participants revealed that, at 24 months, these children exhibited both intrinsic and extrinsic shortening. The pattern for intrinsic duration differences mirrored that found in the adult language; the pattern for extrinsic durations was markedly stronger. As noted previously, vowel duration is phonemic in Swedish and phonetically conditioned changes in duration, such as those created by differences in final consonant voicing, are minimal in adult speech.

4. From universal to language-specific phonetic patterns

The preliminary finding that Swedish children exhibited a pattern of extrinsic shortening even though this pattern is not found in the target language is central to the issue of phonetic and phonological acquisition (Stoel-Gammon and Buder, 1998; Stoel-Gammon *et al.*, 1995). It leads us to the prediction that children begin with "universal" or "default" patterns in the early stages of language acquisition and subsequently develop language-specific phonetic patterns of

their mother tongue. The idea that children's early word productions are based on "default" or "unmarked" patterns has support from studies of other aspects of phonological development. For example, it is well documented that, in the early stages of meaningful speech (and in babble as well), children from all language-learning environments tend to produce voiceless unaspirated stops, presumably the "default" form. Thus, French children are said to "devoice" stops in words with (pre)voiced stops (Allen, 1985), and American children are said to "voice" target voiceless aspirated stops (Macken and Barton, 1980). In fact, children from both language groups are producing voiceless unaspirated stops, the default type; with increased articulatory and phonatory control, they learn to produce stops with the language-specific characteristics of their maternal tongue.

In her review of intrinsic and extrinsic vowel duration effects, Keating (1985) proposed that even the most universal phonetic patterns must be incorporated into a phonological level of production. Most pertinent to the present study, she acknowledged the possibility (attributing the idea to Stampe, 1973, as an implication of his concepts of "natural phonology") that "a child begins acquisition with a set of phonetic processes and replaces some of them with rules on the basis of learning" (Keating, 1985, p. 128). This is essentially the guiding principle of the present study, in which we propose to detect this "replacement" phenomenon by comparing the acquisition of vowel duration in two different language environments that place differing emphasis on intrinsic versus extrinsic patterns.

Clear AE-Sw adult target differences can also be found in the vowel quality domain. In the high-front vowel space, the tense/lax contrast of the Swedish system appears to rest almost entirely on a quantity contrast while the cognate vowels of American English differ more considerably in quality as well (Fant, 1973, Ch. 5). Theoretical arguments have been advanced for predisposed distributions of vowels in the quality domain, such as Stevens' quantal theory (Stevens, 1989), Lindblom's adaptive dispersion theory (Lindblom, 1992), and principles based on self-organizing processes (de Boer, 2000; Lindblom *et al.*, 1984). If it is indeed found that quantity contrasts dominate children's intrinsic vowel contrasts in Sw but not in AE, further investigation of quality contrasts is motivated in those children. For example, if some Swedish children fail to use a quantity contrast at an age when their peers are otherwise adopting this phonetic pattern, it would be interesting to explore—at the stage at which these quantity contrasts generally become effective—whether their quality contrasts were carrying the contrastive load at that point. Because the primary focus of this report is on the quantity contrasts *per se*, this extension to the quality domain is developed only as an exploratory hypothesis below and applied to selected individuals whose quantity contrasts are typical or atypical of their language group cohorts.

5. Predictions regarding acquisition of vowel duration.

In summary, the set of explanatory principles that we have adopted yields a simple outcome for the acquisition of vowel durations. Over the course of phonological acquisition, Swedish and American children will diverge in their use

of vowel duration patterns. Specifically, a similarity in use of extrinsic shortening at 24 months will yield to the use of more language-specific (i.e., adultlike) patterns at 30 months. These predictions can be explored in a number of ways depending on whether the results are viewed in group or individual summaries, and whether raw durations or shortening ratios based on these durations are examined. It is therefore important to analyze the data at both levels, and in both forms, to fully assess the findings.

The following three hypotheses represent ways to test the predictions regarding length, and an additional hypothesis extends the rationale to the quality domain:

Hypothesis 1: As compared to American children, Swedish children's vowel duration differences due to the extrinsic influence of final consonant voicing will diminish with age.

This hypothesis will be tested at group levels by comparing differences in vowel duration measures within all four subject groups (American and Swedish 24- and 30-month-old children), with the expectation that the Swedish 30-monthers will show diminished differences in vowel durations influenced by the extrinsic effect of final consonant voicing.

Hypothesis 2: As compared to American children, Swedish children's vowel shortening effects due to intrinsic vowel identity will increase with age.

This hypothesis will be tested at individual levels by comparing intrinsic to extrinsic vowel duration ratios within each of the four subject groups.

Hypothesis 3: Intrinsic and extrinsic vowel shortening effects will develop in different directions depending on ambient language.

This hypothesis will be tested at group levels by pooling all children's vowel duration ratios and examining for a language by ratio type interaction that increases from 24 to 30 months of age.

Exploratory hypothesis: Children whose intrinsic duration contrasts are atypical for their language may also be atypical in their quality contrasts.

For example, 30-month-old Swedish children not yet employing a quantity contrast to signal intrinsic vowel identities may instead be employing quality contrasts, while American 30-monthers employing duration to signal the intrinsic vowel identities may not be employing quality to do so.

II. METHODS

A. Participants

The participants in the present investigation were selected from pools of 6–36-month-old subjects involved in a series of studies of early phonological acquisition, including Kehoe *et al.* (1995), Stoel-Gammon and Buder (1998), Stoel-Gammon *et al.* (1994), and Sussman *et al.* (1996). The present study reports cross-language cross-sectional findings based on data from Swedish (Sw) and American English (AE) participants, and two age levels, 24 and 30 months. Prior to 24 months, the children did not produce adequate numbers of tokens to allow statistical assessment of vowel durations; after 30 months, vowel duration ratios were essentially adultlike.

Children were recorded in two 30- to 45-min sessions occurring within 10 days time, with the first session falling within two weeks of the exact targeted age. An inclusion criterion of proficiency greater than the 15th percentile on the MacArthur Inventory of Communicative Development (Fenson *et al.*, 1991) was applied to the AE group. Swedish children who participated in the study showed no evidence of motor, cognitive, or speech delay. Because of multiple screening criteria for token selection, the actual numbers of participants and gender compositions of the final sets varied across the four groups, but each set retained a minimum of five children—further details are provided in Sec. III.

B. Materials and elicitation strategies

The targeted production materials for the present study were CVC tokens with tense/lax (long/short) high front vowels in which the initial consonants were obstruents and the final consonants were stops varying in voice and place. To elicit the target words, children were engaged in activities that prompted spontaneous naming of real objects or objects in specially constructed story books. In all situations, an effort was made through the use of these materials to obtain the maximum number of target materials produced by the child in a “neutral” tone (not whispered, shouted, or sung) without an adult model.

C. Recording

All speech samples were recorded in sound-treated rooms, Sw samples at the Department of Linguistics, Stockholm University, Stockholm, and AE samples at the Department of Speech and Hearing Sciences, University of Washington, Seattle, WA. Recordings were made using Lavalier microphones and transmitted via FM wireless systems (Sennheiser MKE 2 microphones, SK-2012 transmitters, and EM-1005 receivers in Stockholm; Countryman MEMF05 microphones, and HME RX722 and Telex FMR-50 transmitters/receivers in Seattle). The transceivers and microphone capsules were fitted into cloth vests, helping to assure a highly consistent mike-to-mouth distance as well as overall clean, noise-free recordings. The Countryman microphone capsules used had low-profile low-friction housings and were situated within rail-shaped guards inside the vests so that only a small face screen was exposed.

Caregivers also wore microphone and transmitter vests, usually putting them on first in order to reassure the child. Signals from both children and caregivers were recorded in stereo on Panasonic VHS videocassette recorders using high-definition audio tracks (model AG-7450 in Stockholm, model AG-1950 in Seattle; AG-W1 recorders were used at both sites to convert between the American NTSC and European PAL video formats).

D. Glossing, transcribing, and digitizing

Glossing and transcribing the data involved several steps. First, the sessions were glossed in their entirety by a

TABLE I. Numbers of CVC tokens included in the study.

Gender	American English						Swedish					
	30 months			24 months			30 months			24 months		
	/i/stop _{+v}	/i/stop _{-v}	/ɪ/stop _{-v}	/i/stop _{+v}	/i/stop _{-v}	/ɪ/stop _{-v}	/i/stop _{+v}	/i/stop _{-v}	/ɪ/stop _{-v}	/i/stop _{+v}	/i/stop _{-v}	/ɪ/stop _{-v}
Female	7	7	8	4	6	4	5	5	3	3	4	4
Female	7	8	7	5	10	6	4	5	3	2	3	2
Female	2	7	7	3	6	4	3	7	7	4	5	2
Female	3	7	5	3	10	6	2	5	3			
Female							2	3	3			
Male	3	6	9	4	5	3	3	6	5	3	6	4
Male	8	8	6	3	7	5	2	3	3	3	8	1
Male	3	5	2	3	8	6	2	5	2			
Male	8	8	6	8	6	6	5	3	2			
Male							3	4	3			
Totals	41	56	50	33	58	40	31	46	34	15	26	13

native language transcriber. The glossing notes included information on time of occurrence on the tape and whether the child's production appeared to be spontaneous or imitated. Second, the tokens of interest to this study (CVCs with high front vowels) were identified and phonetically transcribed by a native language listener. Tokens produced with unusually high or low arousal (e.g., shouted or whispered) were rejected at this point. In recognition of the effects of phrase final lengthening (Oller, 1972), all CVCs selected for acoustic analysis occurred as single-word productions or at the end of a phrase.

Tokens were played back via the high-definition line level outputs of Panasonic AG-1950 VCRs and digitized at a 20-kHz sampling rate using Kay Elemetrics Computerized Speech Laboratory equipment (hardware Models 3400 or 4300B and software versions 4.x or 5.x). Input gain settings were adjusted on a token-by-token basis to optimize waveform amplitudes for the various recorded signal strengths obtained from children of these young ages, but were generally maintained at low to moderate levels. All gain settings were noted in the data records, and in no cases were overdriven signals (either in the analog recording or the digitization phases) retained for analysis.

E. Acoustic analysis

Vowel durations were analyzed in the Kay Elemetrics Multi-Speech program (Ver. 2.x) by visual inspection of waveforms and spectrograms and segment-by-segment listening. As the first phase of the duration measurement work, tokens were judged spectrographically and rejected if they were unsuitable for duration measurement, e.g., if there was no visible evidence of a final consonant stop-gap. After this final phase of rejections, 443 CVC tokens in which C2 was a stop remained available for study as listed in Table I.¹ As shown in the table, five to ten subjects participated in each age/language category, and the number of tokens measured for each of the vowel/consonant voicing categories was, with one exception, at least two and generally more than two. Given the difficulties encountered in obtaining tokens to meet the selection criteria, maximizing representativeness

via an unbalanced design was deemed preferable to the arbitrary elimination of data (see comments to follow on statistical analysis).

Duration measures proceeded primarily on the basis of formant structure as seen in a moderately broad bandwidth (300 Hz) spectrogram with a 6-kHz range. Because one of the chief difficulties with child speech analysis is voice quality (Buder, 1996), multiple strategies for interpretation of formant structure were required. The goal of such strategies was to detect the times of vocal tract opening out of the word-initial consonant and of vocal tract closing into the word-final consonant. In most cases, a loss of energy in the formant bands was an adequate criterion, but as the energy of voicing was often reduced as well at vowel boundaries due to creaky or breathy phonation it was also important to examine for rapid formant movement. Many instances of strong glottal fry or subharmonic vocal fold vibration were encountered, usually before voiceless terminal consonants, and these were so frequent, even routine in certain children, that they could not be eliminated. In such cases, the vowel offset was marked at the point at which regular (e.g., subharmonic) pulsing ceased, occasionally leaving isolated aperiodic pulses in what was construed to be a stop gap whose onset was marked more by a laryngeal gesture than by supralaryngeal closure.

Consonant imprecision was also a special difficulty regularly encountered in the analysis of such young children's speech. A vowel terminating frication was encountered in some Swedish tokens. This phenomenon appeared to be associated with the highly constricted dynamic vowel gestures that mark Swedish high-front vowels (Fant, 1973, Ch. 5), and the fricated segment was therefore included in the vowel duration (contrary to Krause, 1982a, who, examining AE only, eliminated spirantized intervals preceding stop consonants from the vowel segment).

For formant measures, tokens from four subjects (selected on the basis of their duration measure outcomes as described in Sec. III) were analyzed for F1, F2, and F3 formant frequencies at vowel midpoint. Formant frequency measurement strategies were developed and applied in the Kay Elemetrics Multi-Speech environment (Ver. 2.x) closely

TABLE II. Reliability of formant frequency measures.

	F1	F2	F3
Mean difference (Hz)	13	16	1
SD of differences	6	23	24
SE of differences	41	160	160

following the procedures advocated by Buder (1996). Formant analysts were trained and assessed on a structured set of tokens including representation from both languages and both vowel types.

F. Reliability

Duration measures were made only after the duration analysts had been certified via their performance on an assessment trial of 20 tokens selected for balance across the conditions of the study and including tokens known to be difficult (e.g., requiring application of the principles described in the preceding section). The assessment results of seven analysts as a whole differed on average by only 2.7 ms in absolute value, a statistically insignificant difference as assessed by a repeated measures ANOVA on the analyst effect. Of 206 measurements compared in this way, only 2 were greater than 50 ms (one at -122 ms and one at +76 ms). Despite this level of reliability, virtually every token's measurement was reviewed by a three-person team of listeners who concurred on the duration as heard and as seen in the tagged waveform.

Reliability of formant frequency measures is shown in Table II. As discussed in Kent and Forner (1979) and in Buder (1996), the dispersion statistics of Table II reflect the high degree of measurement variability encountered in young children's high f_0 speech. The measures can nevertheless be regarded as adequate for supporting statistical investigations of perceptually relevant formant differences.

G. Statistical analysis

Because of the variability in numbers of tokens obtained per subject, it was not possible to apply a homogenous statistical criterion to assess the existence and stability of vowel shortening patterns within subjects. A balanced assessment was obtained by pooling the durations within vowel identity and final consonant voicing groups within each age/language group and assessing the duration differences at this level by t -tests. Prior to this and other parametric assessments, however, the raw data were log transformed to convert a positively skewed (skewness of raw durations = 1.33) distribution of durations to one more closely approximating a normal skewness of 0 (skewness of log transformed durations = -0.22).

The ultimate objects of description and comparison for this study were the intrinsic and extrinsic shortening ratios. To obtain these measures for each child, average durations for each child's vowel in each voicing category were calculated and ratio measures of vowel shortening for intrinsic and extrinsic influences based on these average durations were obtained. The application of parametric statistical assessments was still problematic at this level because of the vari-

TABLE III. Results of t -tests comparing durations across consonant voicing and vowel identity categories, pooled within subject groups.

Language	Age (months)	Final consonant voicing			Vowel identity		
		t	df	p	t	df	p
AE	24	-4.09	89	<0.001	2.50	96	<0.05
	30	-8.06	95	<0.001	4.80	104	<0.001
Sw	24	-4.45	39	<0.001	3.24	37	<0.01
	30	-0.83	75	n.s.	6.81	80	<0.001

able numbers of subjects in each group and because of the dependencies between ratios introduced by the participation of the same duration set in both ratios (specifically, the /i/_{stop-v} durations). Expressed in nonparametric terms, the hypothesis could be simply stated as a prediction that the American group would contain a greater than chance number of children whose extrinsic shortening ratios are smaller (i.e., more extreme) than their intrinsic ratios, while Swedish children would display the opposite pattern. The study framework also predicted that 24-month-old Swedish children, in comparison to 30-monthers, would resemble Americans more in their degrees of extreme extrinsic shortening. These hypotheses were easily tested by the Mann-Whitney test, the two-group t -test form of the Kruskal-Wallis one-way analysis of variance.

Nonparametric tests, while sensitive, do not retain the full variability information of original measurement distributions. Also, the most direct expression of the study rationale could be made only in a parametric ANOVA: a language by ratio type interaction was predicted. That is, the difference in extrinsic versus intrinsic shortening ratios would be in different directions depending on the language group, and no main effects (language or ratio type) were expected to be significant. These ANOVAs were run to see whether the predicted trends emerged, understanding that the specific probability estimates associated with these trends would need to be accepted as potentially inaccurate. Finally, the measured formants and duration values for selected children were assessed using t -tests within each subject.

III. RESULTS

The original hypotheses are repeated here followed by findings associated with each hypothesis:

Hypothesis 1: As compared to American children, Swedish children's vowel duration differences due to the extrinsic influence of final consonant voicing will diminish with age.

Table III reports t -test results tending to confirm this prediction. It should be noted that the effect of final consonant voicing for Swedish 30-monthers is the only nonsignificant difference in this set of comparisons. This extrinsic shortening effect is much stronger among the 24-month-old subjects from this language community, even though the statistical power is reduced within this age group due to the smaller number of available tokens. All other durational contrasts were stronger in the older groups as shown by the doubling in size of t statistics from 24 to 30 months for the intrinsic effects in both languages and for the extrinsic effect in American English.

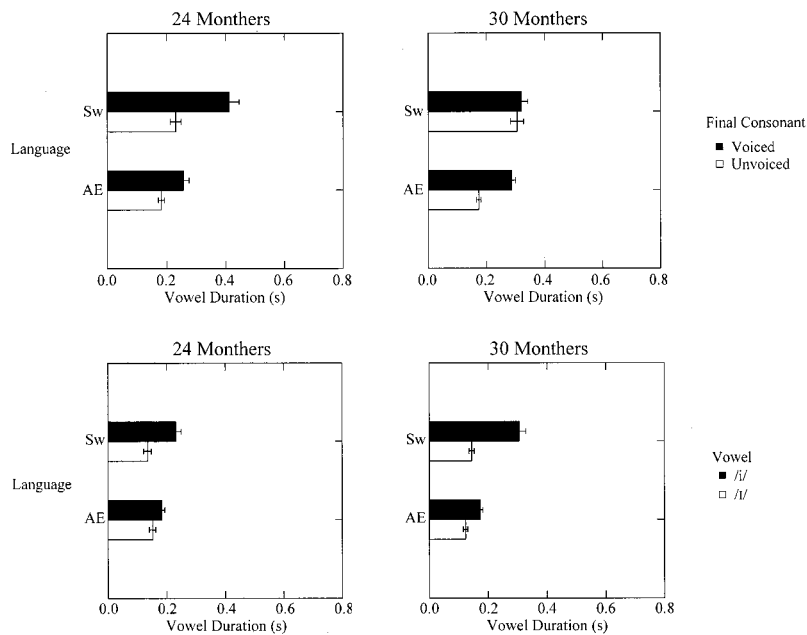


FIG. 1. Vowel duration measures, pooled across subjects within age and language groups, showing extrinsic effects (top panels) and intrinsic effects (lower panels) at 24 months of age (left-hand panels) and 30 months of age (right-hand panels), with standard errors. See Table III for additional detail.

Figure 1 displays the mean durations and variabilities for the groups on which the Table III statistics are based. Again, it is apparent that the major effect of age in either of these language communities is the reduction of the extrinsic final consonant voicing influence in Swedish (top right panel), apparently involving both an increase in the length of vowels before unvoiced stops and a decrease in their duration before voiced stops from 24 to 30 months. In other domains, there appear to be slight trends for lengthening of the appropriate vowel categories with age, especially in the Swedish long vowels. (Note, however, that because these are not longitudinal datasets the trends may not be truly developmental but rather just characteristics of the particular cross-sectional subject pools.) Strictly speaking, *t* statistics should not be compared across varying sample sizes. As

noted above, however, the predicted effect reduction occurred in a relatively large sample.

Hypothesis 2: As compared to American children, Swedish children's vowel shortening effects due to intrinsic vowel identity will increase with age.

The group comparisons that validate hypothesis 1, while compelling, are subject to some interpretive caveats: (1) they do not examine individual patterns of durational contrast, (2) the tests are not strictly independent because many tokens are involved in multiple categories, and (3) they vary considerably in degrees of freedom because of the variable numbers of tokens. A nonparametric assessment of individual durational ratios addresses the first two concerns (1) by summarizing each child's degrees of vowel shortening (as described in Sec. II G) and (2) by examining these shortening

TABLE IV. Shortening ratios by subject, and results of nonparametric analyses of differences between ratios within subject groups.

	American English						Swedish					
	24 Mos.			30 Mos.			24 Mos.			30 Mos.		
Gender	Ext	<>	Int	Ext	<>	Int	Ext	<>	Int	Ext	<>	Int
Female	0.61	<	0.82	0.78	<	0.81	1.02	>	0.47	0.89	>	0.30
Female	0.67	<	0.80	0.64	<	0.81	0.65	>	0.35	0.62	<	0.64
Female	0.73	<	1.02	0.46	<	0.79	0.52	<	0.68	1.28	>	0.27
Female	0.63	<	1.03	0.67	>	0.54				0.79	<	0.92
Female										0.79	>	0.70
Male	0.77	>	0.64	0.64	=	0.64	0.52	<	0.55	1.23	>	0.37
Male	0.48	<	1.16	0.57	<	0.71	0.39	<	0.76	0.71	>	0.67
Male	1.15	>	0.60	0.57	<	0.90				0.69	>	0.50
Male	0.85	>	0.58	0.56	=	0.56				1.01	>	0.42
Male										1.12	>	0.60
χ^2 (approx.) ^a	0.54			2.82			0.01			9.14		
<i>p</i>	0.46			0.09			0.92			0.003		

^aThe χ^2 statistics reported here are approximations based on the results of Mann-Whitney tests that examine the relative rank sums of extrinsic vs intrinsic ratios.

effects, not separate tokens, as observations. The dataset is still not completely balanced from this perspective because unequal numbers of subjects met selection criteria in the various language and age groups. The nonparametric test also involves a substantial loss of power when the observational units are subjects instead of tokens. With these tradeoffs in mind, the following results present a more conservative test of our general framework of predictions by comparing the vowel-shortening effects (intrinsic versus extrinsic) within each group.

Table IV displays individual level data in the form of shortening ratios calculated from each subjects' vowel duration data. The ratios from different conditions are compared for each child; these comparisons are summarized by the symbols "<," ">," or "="." The Mann–Whitney test examines these data by testing the null-hypothesis that when the values are ranked one type does not dominate. An approximation to the χ^2 statistic can be calculated from the results and assessed for statistical significance; four such tests are reported at the bottom of Table IV, one for each age/language group. As can be seen from these results, no differences between the relative ranks of extrinsic and intrinsic ratios show even a trend towards statistical significance in either of the language groups at age 24 months. However, the AE 30-month-old children show a trend, and the Sw children of this age exhibit a strong difference in the relative rankings. Among the eight AE 30-monthers, five exhibit more extreme extrinsic shortening than intrinsic, two show equal degrees of shortening, and only one exhibits more extreme intrinsic shortening. In a clearly opposite pattern, eight of the ten Sw 30-monthers exhibit a more extreme shortening due to intrinsic factors. It is especially striking to observe that in many of these Sw children, the extrinsic ratios are greater than 1.0, indicating that at this stage their vowels are actually longer before voiceless stops than before voiced. In all of those children, the shortening of the phonologically short vowels appears to be very well established.

Hypothesis 3: Intrinsic and extrinsic vowel shortening effects will develop in different directions depending on ambient language.

The picture that has developed in the tests of hypotheses 1 and 2 is one of diverging trends in the two language communities: with age, young AE children strengthen the basic pattern of extrinsic shortening while Sw children lose this extrinsic shortening in favor of intrinsic effects. The clearest way to express this observation at 30 months is in the form of a statistical interaction of ratios crossing the effects of language with type of shortening. Although the p values that are obtained by submitting these ratios to a parametric ANOVA are suspect due to the violated assumptions of both independence and balance in this dataset, it is nonetheless informative to inspect for interaction effects (especially in the light of the more conservative significance levels already implemented in testing hypotheses 1 and 2).

The main and interaction ANOVA effects obtained from ratio data are summarized in Table V and graphed in Fig. 2. The dominant effect is clearly an interaction of language and type for 30-monthers, which, as seen by comparing the intrinsic to extrinsic bars in the right panel of Fig. 2, is due to

TABLE V. Analyses of variance for ratios, by age.

Source	24 monthers		30 monthers	
	<i>df</i>	<i>F</i>	<i>df</i>	<i>F</i>
Language	1	5.16 ^a	1	0.99
Type	1	0.05	1	4.70 ^a
Language×Type	1	0.80	1	15.78 ^b
Error <i>df</i> and (mean square)	22	(0.044)	32	(0.033)

^a $p < 0.05$.

^b $p < 0.01$.

the different directions of the ratio differences across the language groups. Consistent with the previous analyses, this effect seems to be driven primarily by the disappearance of extrinsic shortening in the Swedish 30-monthers. The moderate effects of language among 24-monthers and type among 30-monthers are curious, and not directly interpretable in the present study framework. However, in comparison to the significant interaction found in the 30-monther's data, the lack of a significant interaction among the 24-monthers is evidence that the observed pattern is a learned development due to language exposure.

Exploratory hypothesis: Children whose intrinsic duration contrasts are atypical for their language may also be atypical in their quality contrasts.

The primary results, as laid out in the exposition of the preceding hypotheses, have revealed that for the group of Swedish children, intrinsic vowel identity is the primary, or even sole, determinant of vowel duration. As the adult model for intrinsic vowel tense/lax identity is generally realized in both the quality and quantity domains, most clearly for AE but also for Sw (Elert, 1964; Hoard, 1966), the exploratory hypothesis was designed to assess the impact of quantity acquisition on quality contrasts. This hypothesis was explored in the current dataset by selecting the four 30-month-old children whose intrinsic duration patterns from each language community were most or least well-established.

The statistical stabilities of these children's quantity and quality contrasts are described in Table VI. To maximize power, the formant measures were made for fricative-final as well as stop-final tokens, accounting for the larger degrees of freedom in the quality tests. The basis for selection of these particular children was the presence or absence of the intrinsic quantity contrast as determined by the statistical results in the first column of the table: the "AE Girl" in the first row was distinctive in her language group for exhibiting a strong use of quantity in the vowel contrast, and the Sw girl in the third row of the table, "Sw Girl 1," was distinctive in her group for *not* utilizing quantity in her vowel contrast. The other two subjects in each group were selected because they represented the "typical" patterns: the "AE Boy" utilized quality, not quantity in his vowel contrast, and the second Sw girl, "Sw Girl 2," produced a clear intrinsic quantity contrast. In sum, AE Boy was typical of his language group while AE Girl was not, and Sw Girl 2 was typical of her language group while Sw Girl 1 was not.

Starting with Sw Girl 2, it can be seen that there was no statistically significant difference in any of the formants, suggesting that at this stage Sw Girl 2 was, in fact, relying

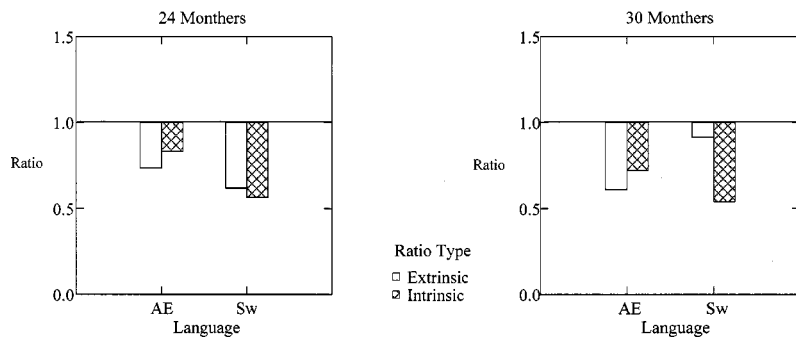


FIG. 2. Vowel ratios, pooled across subjects within age and language groups, showing extrinsic effects and intrinsic effects at 24 months of age (left panel) and 30 months of age (right panel). See Table IV for additional detail.

entirely on the durational difference to signal these distinct vowels. By comparison, Sw Girl 1, who was not employing a durational contrast, was, in fact, employing measurably distinct formant differences to signal the contrast ($F1_{/i/} - F1_{/ɪ/} = 154$ Hz, $F3_{/i/} - F3_{/ɪ/} = 194$ Hz). It appears that an “either/or” strategy might be typical of this stage of phonological acquisition. The AE situation was somewhat less neat, in that the AE Girl with the quantity contrast also displayed a quality contrast ($F1_{/i/} - F1_{/ɪ/} = 245$ Hz, $F2_{/i/} - F2_{/ɪ/} = -997$ Hz, $F3_{/i/} - F3_{/ɪ/} = -531$ Hz), while the AE Boy without a quantity contrast employed a quality contrast that was clear, especially in F1, but perhaps still less robust than his age-mate, at least in F2 and F3 ($F1_{/i/} - F1_{/ɪ/} = 260$ Hz, $F2_{/i/} - F2_{/ɪ/} = -536$ Hz, $F3_{/i/} - F3_{/ɪ/} = 14$ Hz). In general, the pattern observed in these few children is consistent with the idea that children not strongly employing a means of phonetic vowel contrasting favored by their language peers would show instead a tendency to adopt the secondary means.

IV. CONCLUSIONS

The support obtained for each of the three central hypotheses of this study is consistent with the view that certain aspects of vowel duration represent more basic default behaviors, while non-default patterns are learned as a result of exposure to ambient language phonology. In each of the three statistical tests, (1) comparing pooled durations across varying intrinsic and extrinsic conditions, (2) comparing individual shortening ratios due to these conditions for their relative strengths, and (3) comparing the ratio types in a factorial design across languages, the strongest effects resulted from the same phenomenon: a loss of the extrinsic shortening effects in the 30-month-old Sw children. The data

therefore describe the attenuation of an apparently predisposed extrinsic vowel duration influence due to the cognitive acquisition of an intrinsic duration influence, a development that seems driven by the greater linguistic load of the intrinsic influence.

This development may be accompanied in Swedish children by a concurrent strengthening of consonant-intrinsic cues to final stop voicing. Zajdó and Stoel-Gammon (in press) investigated durations of stop-gap closures in the rhyme of CVC tokens, utilizing many of the same tokens as in this study. They reported, again, that the language learners diverged from 24 to 30 months with AE children lengthening the stop-gap before the voiced stop /d/ and Swedish children showing a greater equalization between gaps in voiced and voiceless final stops.

The general scenario, in which children appear to select and differentially prioritize available means of phonetic differentiation to achieve phonological contrasts, was also supported by our exploration of individual 30-monthers’ use of quality contrasts. The finding that a Swedish child lacking a quantity contrast was utilizing a quality contrast is particularly striking given perceptual findings reported by Behne *et al.* (1997) that formant changes are generally ineffective for distinguishing Swedish high front long–short vowels for adult listeners.

In summary, the primary contribution of this study is the comparison of different sources of vowel contrasts in different language environments. This natural developmental “experiment” may also provide support for the idea that duration is naturally correlated with final stop consonant voicing, most likely due to some form of the articulatory disposition hypothesis discussed by Chen (1970) and others (cf. Löfqvist and Gracco, 1997). Despite the general concordance with Keating’s argument (1985) that vowel duration is likely

TABLE VI. *t*-tests on selected individual 30-month-old children’s quantity and quality contrasts.

Language	Child	Quantity				Quality			
		i/ɪ		±voicing		F1	F2	F3	
		<i>t</i>	<i>df</i>	<i>t</i>	<i>df</i>	<i>t</i>	<i>t</i>	<i>t</i>	<i>df</i>
AE	Girl (atypical)	-3.9 ^b	8	-2.13	10	-5.83 ^c	7.60 ^c	2.53 ^a	16
	Boy (typical)	-0.01	5	-1.89	6	-11.01 ^c	3.32 ^b	-0.09	15
Sw	Girl 1 (atypical)	0.06	6	-0.85	5	-2.98 ^a	1.30	-2.51 ^a	8
	Girl 2 (typical)	-8.45 ^c	12	1.30	8	-0.64	-1.74	-0.86	8

Note: Formant statistics are measured from data transformed to the Mel scale.

^a*p* < 0.05.

^b*p* < 0.01.

^c*p* < 0.001.

“phonologized” at an early age, the finding that extrinsic effects are present in a language like Swedish, which is characterized by strong intrinsic durational differences, indicates a more fundamental, possibly prelearned, pattern. The extent to which very young children learning languages such as American English, in which final stop consonants are often unreleased, perceive extrinsic vowel duration effects remains an issue, but some studies have suggested that these effects can be heard by adults even when combined with variations in speech rate (Fitch, 1981).

The idea that this extrinsic effect is an “unmarked” or default state that does not originally require learning may help to explain why it often occurs in languages at measurable levels that are nonetheless barely perceptible (Keating, 1985), why it occurs with such high degrees of contextual variability (Klatt, 1976), and perhaps even why the robust perception of final consonant voicing ultimately relies on additional cues (Hillenbrand *et al.*, 1984; Hogan and Rozsypal, 1980). The contextual variation found by Hogan and Rozsypal indicated that the effect is more robust in the context of fricatives than in stops. The paucity of fricative-final monosyllabic words in Swedish makes this difficult to test in the cross-linguistic framework of the current investigation, but analyses are underway to explore the phenomenon more thoroughly in the acquisition of American English.

ACKNOWLEDGMENTS

This research was supported by grants from the Virginia Merrill Bloedel Hearing Research Center of the University of Washington and from NICHD (R01-HD32065) to the second author. The authors acknowledge the contributions of Karen Williams and Olle Engstrand of Stockholm University who were responsible for collecting the speech samples from the Swedish children, and they also express gratitude for the helpful comments of Anders Löfqvist and two anonymous reviewers.

¹From an initial pool of 1325, approximately 38% were eliminated because the children were not producing satisfactory tokens in all categories. From the remaining pool of 823, another 33% were fricative-final. Of the remaining 551 tokens, approximately 19% were rejected due to problems with measurement.

Allen, G. (1985). “How the young French child avoids the pre-voicing problem for word-initial voiced stops,” *J. Child Lang* **12**, 37–46.

Behne, D. M., Czigler, P. E., and Sullivan, K. (1997). “Perception of vowel duration and spectral characteristics in Swedish,” in *Eurospeech 1997 Proceedings*, edited by N. F. G. Kokkinakis and E. Dermatas (European Speech Communication, Grenoble, France), pp. 2171–2174.

Buder, E. H. (1996). “Experimental phonology with acoustic phonetic methods: Formant measures from child speech,” in *Proceedings of the UBC International Conference on Phonological Acquisition*, edited by J. Bernhardt, J. Gilbert, and D. Ingram, pp. 254–265.

Catford, J. C. (1977). *Fundamental Problems in Phonetics* (Edinburgh University Press, Edinburgh).

Chen, M. (1970). “Vowel length variation as a function of the voicing of the consonant environment,” *Phonetica* **22**, 129–159.

Clark, J., and Yallop, C. (1995). *An Introduction to Phonetics and Phonology*, 2nd ed. (Blackwell, Oxford).

de Boer, B. (2000). “Self-organization in vowel systems,” *J. Phonetics* **28**, 441–465.

de Jong, K. (1991). “An articulatory study of consonant-induced vowel duration changes in English,” *Phonetica* **48**, 1–17.

Denes, P. (1955). “Effect of duration on the perception of voicing,” *J. Acoust. Soc. Am.* **27**, 761–764.

Elert, C.-C. (1964). *Phonological Studies of Quantity in Swedish* (Almqvist & Wiksells, Uppsala).

Fant, G. (1973). *Speech Sounds and Features* (MIT, Cambridge, MA).

Fenson, L., Dale, P., Reznick, S., Thal, D., Bates, E., Hartung, J., Pethick, S., and Reilly, J. (1991). *MacArthur Communicative Development Inventories* (San Diego State Univ., San Diego).

Fitch, H. L. (1981). “Distinguishing temporal information for speaking rate from temporal information for intervocalic stop consonant voicing,” *Haskins Lab Stat. Rep. Spch. Res.* Vol. 65, pp. 1–32.

Giegerich, H. (1992). *English Phonology: An Introduction* (Cambridge University Press, Cambridge).

Greenlee, M. (1978). “Learning the phonetic cues to the voiced-voiceless distinction: an exploration of parallel processes in phonological change,” unpublished doctoral dissertation, University of California-Berkeley, Berkeley, CA.

Hadding-Koch, K., and Abramson, A. S. (1964). “Duration versus spectrum in Swedish vowels: Some perceptual experiments,” *Studia Linguist.* **18**, 94–107.

Hillenbrand, J., Ingrisano, D. R., Smith, B. L., and Flege, J. E. (1984). “Perception of the voiced-voiceless contrast in syllable-final stops,” *J. Acoust. Soc. Am.* **76**, 18–26.

Hoard, J. E. (1966). “Contrastive analysis of English and Swedish phonology,” unpublished Masters Thesis, University of Washington, Seattle, WA.

Hogan, J. T., and Rozsypal, A. J. (1980). “Evaluation of vowel duration as a cue for the voicing distinction in the following word-final consonant,” *J. Acoust. Soc. Am.* **67**, 1764–1771.

House, A. S. (1961). “On vowel duration in English,” *J. Acoust. Soc. Am.* **33**, 1174–1182.

House, A. S., and Fairbanks, G. (1953). “The influence of consonantal environment upon the secondary acoustical characteristics of vowels,” *J. Acoust. Soc. Am.* **25**, 105–113.

Jakobson, R., Fant, G., and Halle, M. (1952). *Preliminaries to Speech Analysis: The Distinctive Features and Their Correlates* (MIT, Cambridge, MA).

Keating, P. A. (1985). “Universal phonetics and the organization of grammars,” in *Phonetic Linguistics—Essays in Honor of Peter Ladefoged*, edited by V. A. Fromkin (Academic, Los Angeles), pp. 115–132.

Kehoe, M., Stoel-Gammon, C., and Buder, E. H. (1995). “Acoustic correlates of stress in young children’s speech,” *J. Speech Hear. Res.* **38**, 338–350.

Kent, R. D., and Forner, L. (1979). “Developmental study of vowel formant frequencies in an imitation task,” *J. Acoust. Soc. Am.* **65**, 208–217.

Klatt, D. H. (1976). “Linguistic uses of segment duration in English: Acoustical and perceptual evidence,” *J. Acoust. Soc. Am.* **59**, 1208–1221.

Krause, S. E. (1982a). “Developmental use of vowel duration as a cue to postvocalic stop consonant voicing,” *J. Speech Hear. Res.* **25**, 388–393.

Krause, S. E. (1982b). “Vowel duration as a perceptual cue to postvocalic consonant voicing in young children and adults,” *J. Acoust. Soc. Am.* **71**, 990–995.

Lehiste, I. (1970). *Suprasegmentals* (MIT, Cambridge, MA).

Lindau, M. (1978). “Vowel features,” *Language* **54**, 541–563.

Lindblom, B. (1992). “Phonological units as adaptive emergents of lexical development,” in *Phonological Development*, edited by C. A. Ferguson, L. Menn, and C. Stoel-Gammon (York, Timonium, MD), pp. 131–164.

Lindblom, B., MacNeilage, P., and Studdert-Kennedy, M. (1984). “Self-organizing processes and the explanation of phonological universals,” in *Explanations for Language Universals*, edited by B. Butterworth, B. Comrie, and O. Dahl (Mouton, Berlin), pp. 181–203.

Lisker, L. (1957). “Closure duration and the intervocalic voiced-voiceless distinction in English,” *Language* **33**, 42–49.

Löfqvist, A., and Gracco, V. L. (1997). “Lip and jaw kinematics in bilabial stop consonant production,” *J. Speech Lang. Hear. Res.* **40**, 877–893.

Macken, M. A., and Barton, D. (1980). “The acquisition of the voicing contrast in English: A study of voice onset in word-initial stop consonants,” *J. Child Lang* **7**, 41–74.

Maddieson, I., and Ladefoged, P. (1985). “‘Tense’ and ‘lax’ in four minority languages of China,” *J. Phonetics* **13**, 433–454.

Naeser, M. A. (1970). “The American child’s acquisition of differential vowel duration,” Technical Report #144, University of Wisconsin, Center for Cognitive Learning, Madison, WI.

Oller, D. K. (1972). “The effect of position in utterance on speech segment duration in English,” *J. Acoust. Soc. Am.* **54**, 1235–1247.

- Otomo, K., and Stoel-Gammon, C. (1992). "The acquisition of unrounded vowels in English," *J. Speech Hear. Res.* **35**, 604–616.
- Peterson, G. E., and Lehiste, I. (1960). "Duration of syllable nuclei in English," *J. Acoust. Soc. Am.* **32**, 693–703.
- Raphael, L. J., Dorman, M. F., and Geffner, D. (1980). "Voicing-conditioned durational differences in vowels and consonants in the speech of three- and four-year old children," *J. Phonetics* **8**, 335–341.
- Stampe, D. (1973). "A dissertation on natural phonology," doctoral dissertation, University of Chicago, Chicago. Also distributed by Indiana University Linguistics Club as Stampe (1979).
- Stevens, K. (1989). "On the quantal nature of speech," *J. Phonetics* **17**, 3–45.
- Stoel-Gammon, C., and Buder, E. H. (1998). "The effects of postvocalic voicing on the duration of high front vowels in Swedish and American English: Developmental data," in *Proceedings of the 16th International Congress on Acoustics and 135th Meeting of the Acoustical Society of America*, edited by P. K. Kuhl and L. A. Crum (Acoustical Society of America, Woodbury, NY), pp. 2989–2990.
- Stoel-Gammon, C., and Herrington, P. B. (1990). "Vowel systems of normally developing and phonologically disordered children," *Clin. Linguist. Phonet.* **4**, 145–160.
- Stoel-Gammon, C., Buder, E. H., and Kehoe, M. M. (1995). "Acquisition of vowel duration: A comparison of Swedish and English," in *The Proceedings of the XIIIth International Congress of Phonetic Sciences*, edited by K. Elenius and P. Branderud (KTH and Stockholm Univ., Stockholm), pp. 30–37.
- Stoel-Gammon, C., Williams, K., and Buder, E. H. (1994). "Cross-language differences in phonological acquisition: Swedish and American /t/," *Phonetica* **51**, 146–158.
- Sussman, H. M., Minifie, F., Buder, E. H., Stoel-Gammon, C., and Smith, J. (1996). "Consonant-vowel interdependencies in babbling and early words: Preliminary examination of a locus equation approach," *J. Speech Hear. Res.* **39**, 424–433.
- Templin, M. C. (1957). *Certain Language Skills in Children* (Univ. of Minnesota, Minneapolis).
- Wardrip-Fruin, C. (1982). "On the status of temporal cues to phonetic categories: Preceding vowel duration as a cue to voicing in final stop consonants," *J. Acoust. Soc. Am.* **71**, 187–195.
- Zajdó, K., and Stoel-Gammon, C. (in press). "The acquisition of rhyme-internal timing in American English versus Swedish: Similarities and differences in speech development," in *Sprachwissenschaft auf dem Weg ins nächste Jahrtausend*, edited by R. Rapp (Peter Lang, Frankfurt).

Gender differences in vocal fold contact computed from electroglottographic signals: The influence of measurement criteria

Maureen B. Higgins^{a)}

Boys Town National Research Hospital, Omaha, Nebraska 68131

Laura Schulte

University of Nebraska at Omaha, Omaha, Nebraska 68182

(Received 7 August 2001; revised 26 December 2001; accepted 20 January 2002)

EGGW is a phonatory parameter that can be derived from electroglottographic (EGG) signals and used to infer the relative degree of vocal fold contact. Vocal fold models predict that men will exhibit medial bulging of their vocal folds during phonation but women will not. These models lead us to expect gender differences in the magnitude of EGGW. Nevertheless, significant gender differences in EGGW for adults with normal voices have not been documented in previous studies when EGGW was computed from criterion lines placed at 25%–40% of the amplitude of the uninverted EGG wave form. We hypothesized that EGGW would better reflect gender differences in vocal fold adductory patterns if EGGW was computed from portions of the wave form that were associated with more vocal fold contact. EGGW was measured for seven men and seven women with normal voices. When EGGW was computed from segments of the wave form that were associated with relatively greater vocal fold contact (i.e., using criterion levels of $\geq 55\%$), findings were consistent with the gender-specific adductory patterns that have been proposed from vocal fold models. Guidelines for appropriate placement of criterion lines when computing EGGW are discussed. © 2002 Acoustical Society of America. [DOI: 10.1121/1.1456517]

PACS numbers: 43.70.Gr, 43.70.Jt [AL]

I. INTRODUCTION

To obtain an electroglottographic (EGG) signal, a small, high frequency current is passed across laryngeal tissue. When the current is transmitted during vocal fold vibration, the EGG signal varies in response to the fluctuations in electrical impedance that are induced by changes in the contact area of the vocal folds (Baken and Orlikoff, 2000; Childers and Krishnamurthy, 1985). Thus, the EGG signal has been used to infer a variety of characteristics related to the degree and timing of vocal fold contact. There are numerous factors that can contribute to less than ideal EGG signals, including poor electrode placement, mucous strands across the vocal folds, excess fat in the area of the electrodes, and vocal pathologies associated with limited vocal fold contact (Childers and Krishnamurthy, 1985; Colton and Conture, 1990). In addition, researchers and clinicians need to be aware of what the EGG signal cannot reveal. For example, the EGG signal often does not show precise landmarks associated with vocal fold opening and closing, it provides little information about the open phase of vibration, and it does not reflect glottal width or area (Baken and Orlikoff, 2000; Colton and Conture, 1990). Nevertheless, the EGG signal can provide valuable information for clinical and research purposes when data are collected and interpreted cautiously (Colton and Conture, 1990).

One measure that can be derived from EGG signals is EGGW or EGG cycle width. This measure has been used to

infer the relative degree of vocal fold contact in studies of both normal and disordered phonation (Arends *et al.*, 1990; Dromey *et al.*, 1995; Fisher *et al.*, 1996; Higgins *et al.*, 1999; Higgins *et al.*, 1994, 1998; Higgins and Saxman, 1991; Howard, 1995; Orlikoff, 1991, 1998; Orlikoff *et al.*, 1997; Robb and Simmons, 1990; Rothenberg and Mahshie, 1988; Sapienza *et al.*, 1998; Scherer *et al.*, 1995). In different studies EGGW has gone by other names including contact quotient (Orlikoff, 1991, 1998; Orlikoff *et al.*, 1997; Robb and Simmons, 1990), EGG duty cycle (Higgins and Saxman, 1991; Rothenberg and Mahshie, 1988), abduction quotient (Higgins *et al.*, 1994), and EGG open quotient (Sapienza *et al.*, 1998). Some researchers have elected to measure EGGW from the uninverted EGG signal, where maximum vocal fold contact would be represented at the top of the wave form (Higgins *et al.*, 1998; Howard, 1995; Orlikoff, 1991, 1998; Orlikoff *et al.*, 1997; Scherer *et al.*, 1995). Others have looked at the inverted signal, so that the open phase of vibration was represented at the top of the wave form (Higgins *et al.*, 1994; Higgins and Saxman, 1991; Robb and Simmons, 1990; Rothenberg and Mahshie, 1988; Sapienza *et al.*, 1998). Often this was done to be consistent with the orientation of glottal air flow signals that were collected simultaneously with the EGG.

To compute EGGW, a horizontal criterion line is placed across a segment of the EGG signal, and the time for two crossings of the line relative to the glottal period is calculated. (Refer to Fig. 1.) The placement of the criterion line for measurement of EGGW has been a somewhat arbitrary decision. Across investigations, criterion lines have been

^{a)}Electronic mail: higgins@boystown.org

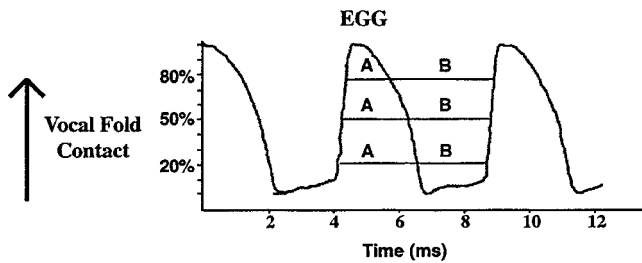


FIG. 1. EGGW is represented as $A/A+B$. Criterion lines placed at 20%, 50%, and 80% of the amplitude of the uninverted EGG signal are shown. The EGG wave form displayed is from an adult normal female.

placed at points representing 25%, 30%, 40%, 50%, 75%, and 80% of the amplitude of the uninverted wave form (Arends *et al.*, 1990; Fisher *et al.*, 1996; Higgins and Saxman, 1991; Orlikoff, 1991; Orlikoff *et al.*, 1997; Robb and Simmons, 1990; Rothenberg and Mahshie, 1988; Sapienza *et al.*, 1998; Scherer *et al.*, 1995). Such widespread variability in measurement criteria has occurred for several reasons. Some researchers were attempting to use the criterion line to differentiate the closed and open phases of the vibratory cycle. However, as noted by Orlikoff (1991, 1998), the specific points of vocal fold opening and closing cannot be identified from the EGG signal. As a result, there has not been agreement about where the criterion line should be placed. In addition, selection of the criterion level often included practical considerations such as avoidance of noise that can occur in segments of the wave form associated with little vocal fold contact (Orlikoff, 1991; Orlikoff *et al.*, 1997; Scherer *et al.*, 1995). Sometimes the criterion line used has been designated by labeling the measurement as EGGW25 for a 25% criterion level or EGGW50 for a 50% criterion level, etc. (Dromey *et al.*, 1995; Fisher *et al.*, 1996; Scherer *et al.*, 1995). Orlikoff (1998) defined EGGW as “the percent of the entire vibratory cycle wherein vocal fold contact area is greater than some ‘minimal level’” (p. 44). The “minimal level” selected is represented by the criterion line. Because of variation in the measurement criteria used to compute EGGW, it has been difficult to make direct comparisons of findings across studies (Robb and Simmons, 1990; Sapienza *et al.*, 1998). Research is needed to provide a better rationale for the placement of the criterion line used to compute EGGW and to facilitate comparison of EGGW data computed with different criterion levels.

By using vocal fold models and simulated EGG signals, Titze (1984, 1989, 1990) demonstrated differences in vocal fold contact patterns for men and women. In particular, Titze suggested that men’s vocal folds adduct with a medial surface bulge resulting in “skirt bulging” of the EGG signal. Such bulging presumably is associated with contraction of the thyroarytenoid muscle during adduction (Alipour and Scherer, 2000). Titze (1989, 1990) stated that a knee in the EGG wave form reflects medial bulging of the vocal folds and is consistent with a rapid change in vocal fold contact. The typical location of the knee is not clear from the literature. In some presentations of EGG signals, it has been displayed in the upper half of the uninverted EGG wave form, a section of the signal that is associated with a relatively large

degree of vocal fold contact (Anastaplo and Karnell, 1988; Titze, 1990). However, in other cases, it appears to be more in the mid-region of the EGG signal (Baer *et al.*, 1983; Titze, 1989). In Titze’s models of vocal fold contact patterns for women, such intermittently accelerated changes in vocal fold contact were not shown. Rather, women appear to have a more linearly convergent glottis. This is consistent with the findings of Baer *et al.* (1983), who found a knee in the EGG signal for their male subject but not their female subject. They suggested that this was the case because the female speaker had a more gradual opening of her glottis.

Orlikoff (1998) noted that the EGG signal reflects vocal fold contact area but not glottal characteristics. Therefore, he suggested that the glottal gaps that are commonly seen for women with normal voices (Biever and Bless, 1989) might not impact the relative degree of vocal fold contact to the point that they would contribute to significant gender differences in EGGW. While this may be the case, it seems reasonable to expect that the medial vocal fold surface bulging described by Titze would affect vocal fold contact area and should contribute to gender differences in EGGW. Nevertheless, as noted by Orlikoff (1998) and Baken and Orlikoff (2000), significant gender differences in EGGW generally have not been found. In fact, Orlikoff *et al.* (1997) found almost identical EGGW values for normal men and women during production of [a].¹

Some other studies provide evidence of at least subtle gender differences in the degree of vocal fold contact as measured from EGG signals. Higgins and Saxman (1991) reported EGGW values for young and aged men and women producing vowels and syllables under four phonatory conditions (normal, soft, loud, and high-pitched + loud phonation). A significant gender effect was seen only for vowel prolongation and only during loud + high pitched phonation when the aged and young speakers were combined. However, there was a clear trend for young men to have smaller EGGW than young women across all conditions, even though the differences were not statistically significant. Because Higgins and Saxman (1991) used an inverted EGG signal, this finding was indicative of more vocal fold contact for young men than young women. Similarly, Higgins *et al.* (1998) reported that gender differences for their EGGW data from men and women approached significance during normal phonation. In this case, the investigators found reduced EGGW for women as compared to men. Because Higgins *et al.* (1998) used a noninverted EGG signal, this finding also was suggestive of more vocal fold contact for men than women.

Variations in EGGW measurement criteria could have contributed to differences in findings from the studies by Higgins and colleagues and Orlikoff *et al.* (1997). Orlikoff *et al.* (1997) computed EGGW with a criterion line placed at 25% of the amplitude of the EGG signal whereas Higgins and colleagues used a 40% criterion line. In an uninverted EGG signal, a 40% criterion line would be in a portion of the wave form that is associated with more vocal fold contact than a 25% criterion line. It may be the case that EGGW is more sensitive to gender differences in vocal fold contact patterns when the measurement is made in a segment of the

vibratory cycle that is associated with more adduction. In other words, the medial bulging and rapid changes in vocal fold contact described by Titze (1984, 1989, 1990) for men's larynges may not be especially evident until there is considerable vocal fold contact.

Recent computer models have focused on the phonatory effects of vocal fold surface bulging. Alipour and Scherer (2000) used bulging parameters ranging from 0.3 to 0.8 in their model to determine how changes in vocal fold bulging affected glottal flow resistance, glottal air flow, and maximum glottal width and area. They positioned their bulging parameter at the vertical midpoint of the glottis. They found that "the bulging parameter may be a relatively strong determinant of the overall glottal flow resistance...if the human actually can or does vary bulging over the 0.3–0.8 range..." (p. 481). Alipour and Scherer (2000) highlighted how computer models of vocal fold vibration could enhance our understanding of the pathophysiology of voice disorders, particularly those related to excess laryngeal muscle tension or vocal fold collision forces. Further work is needed to refine elements of computer models, including the appropriate placement and magnitude of bulging parameters, in order to improve their clinical applicability. Gender-specific models should be developed based on documented differences in phonatory physiology between men and women. A preliminary step toward this aim is determining whether EGG signals from human subjects reflect the gender differences in vocal fold bulging patterns that have been described in modeling studies and if such differences are more evident at certain points in the vibratory cycle.

In the present investigation EGGW was measured at different segments of the EGG wave form for a group of men and women with normal voices. The criterion lines used to compute EGGW ranged from 20% to 80% of the signal amplitude, encompassing the range that has been applied in earlier studies. The primary purpose of the investigation was to determine if significant gender differences in EGGW are more evident in normal speakers when higher criterion levels are used. This information could contribute to the development of more appropriate and consistent measurement criteria for EGGW when gender differences in vocal fold vibratory behaviors are of interest. In addition, these data might support theories of gender-specific vocal fold adductory patterns that have been generated from computer models and assist in the refinement of existing models. A secondary purpose was to provide some data that would facilitate comparison of EGGW findings across studies that employed different measurement criteria.

II. METHOD

A. Participants

Participants were seven men and seven women (aged 24–37 years) with normal voices. Mean ages of the male and female groups were 29.1 years (s.d.=4.5) and 30.6 years (s.d.=4.5), respectively. All of the participants were native speakers of English with no reported history of vocal pathology, neuropathology, smoking, hearing loss, or singing training. The speakers were a subset of the individuals who had

participated in earlier studies related to the within-speaker stability of selected phonatory measures (Higgins *et al.*, 1994) and articulatory influences on phonatory function (Higgins *et al.*, 1998). The present data were derived from some of the productions used in those earlier investigations.

B. Data collection

A SynchroVoice single channel EGG was used, and signals were recorded with an FM tape recorder (Hewlett Packard 3968A Instrumentation Recorder). Electrodes were placed lateral to the thyroid cartilage at the site that resulted in the largest signal amplitude. The electrodes were held in place with an elastic strap. EGG signals were collected four times over a two-week period while the participants repeated [pa] syllables at a rate of three syllables per second using conversational pitch and loudness. We elected to use syllable production rather than sustained vowels in order to assess a speaking task that more closely represented the dynamics of conversational speech. Rate of production was rehearsed with a metronome prior to data collection. On each of the four days the participants produced at least three syllable series with approximately seven syllables per series. EGG signals from all of the participants were evaluated visually by M.B.H. and judged to show very little evidence of noise.

C. Data analysis

Due to articulatory influences, there can be more baseline shift in the EGG signal during syllable production than during sustained vowels. To counteract this, the EGG signal was linear-phase high pass filtered at 20 Hz to stabilize the DC component of the wave form (Rothenberg and Mahshie, 1988). For each of the four days, the second syllable of three series was selected for analysis, resulting in a total of 12 syllables per participant. Syllables were digitized at 20,000 Hz. Ten consecutive EGG cycles surrounding the vowel midpoint were analyzed, always excluding the first and last five cycles. Custom-made software measured the peak-to-peak amplitude of the EGG signal for each cycle. Criterion lines were placed at points representing 20%, 25%, 30%, 35%, 40%, 45%, 50%, 55%, 60%, 65%, 70%, 75%, and 80% of the amplitude of the uninverted signal. EGGW was measured at the time for two crossings of the criterion line (a positive then a negative crossing) relative to glottal period at each of the 13 criterion levels. Figure 1 depicts measurements of EGGW₂₀, EGGW₅₀, and EGGW₈₀ using 20%, 50%, and 80% criterion levels.

D. Measurement reliability

A second judge re-analyzed 10% of the signals. Mean absolute differences between the measures obtained from the judges were very small at all criterion levels. In most cases (82%) mean absolute differences were 0.00, and they were never more than 0.02. Pearson production moment correlations were 0.99–1.0 ($p < 0.01$) for all of the criterion levels.

TABLE I. Means and standard deviations (s.d.) for EGGW measured at different criterion levels for seven men and seven women with normal voices. The criterion level is represented by the number after EGGW. For example, EGGW20 means that the criterion line was placed at 20% of the amplitude of the uninverted EGG signal.

EGGW	Gender	Mean	Intersubject s.d.	Intrasubject s.d.
EGGW20	Male	0.63	0.04	0.03
	Female	0.61	0.05	0.02
EGGW25	Male	0.60	0.04	0.03
	Female	0.58	0.05	0.03
EGGW30	Male	0.58	0.04	0.03
	Female	0.55	0.05	0.03
EGGW35	Male	0.56	0.04	0.03
	Female	0.53	0.05	0.03
EGGW40	Male	0.54	0.04	0.03
	Female	0.50	0.05	0.03
EGGW45	Male	0.52	0.04	0.03
	Female	0.48	0.05	0.03
EGGW50	Male	0.51	0.04	0.03
	Female	0.46	0.05	0.03
EGGW55	Male	0.49	0.04	0.03
	Female	0.43	0.04	0.03
EGGW60	Male	0.47	0.04	0.03
	Female	0.40	0.04	0.03
EGGW65	Male	0.44	0.04	0.03
	Female	0.37	0.04	0.03
EGGW70	Male	0.41	0.04	0.03
	Female	0.34	0.04	0.03
EGGW75	Male	0.38	0.04	0.03
	Female	0.30	0.04	0.02
EGGW80	Male	0.34	0.04	0.03
	Female	0.26	0.04	0.02

E. Statistical analysis

The EGGW data were statistically analyzed using a two-way analysis of variance (ANOVA). Gender was the between-subjects factor and criterion level was the within-subjects factor. An alpha level of 0.05 was used.

III. RESULTS

A. Mean data and gender effects

Averaged data for the male and female groups are displayed in Table I. For all subjects EGGW steadily decreased with criterion lines placed more toward the maximum amplitude of the uninverted signal. A 5% change in criterion line placement typically resulted in a change of about 0.02–0.03.

At each criterion level, the male group had larger EGGWs than the female group. However, this difference became more pronounced at higher criterion levels. For example, at the 20% criterion level there was only a 0.02 difference in EGGW for the men and women (male EGGW20

=0.63, female EGGW20=0.61). At the 80% criterion level, the difference was 0.08 (male EGGW80=0.34; female EGGW80=0.26).

The ANOVA results showed a significant main effect for criterion level [$F(12,144) = 777.7, p < 0.0005$], a significant main effect for gender [$F(1,12) = 5.1, p = 0.4$], and a significant gender \times criterion level interaction [$F(12,144) = 9.9, p = 0.002$]. Because of the significant interaction, simple main effects tests were performed to determine if there were significant gender effects at specific criterion levels. There were no significant gender differences for criterion levels of 20%–50%. All of the higher criterion levels were associated with significant gender effects (EGGW55 [$F(1,12) = 5.5, p = 0.04$]; EGGW60 [$F(1,12) = 7.0, p = 0.02$], EGGW65 [$F(1,12) = 9.5, p = 0.01$]; EGGW70 [$F(1,12) = 12.1, p = 0.005$]; EGGW75 [$F(1,12) = 14.5, p = 0.002$]; EGGW80 [$F(1,12) = 15.5, p = 0.002$]). In all of these cases, EGGW was greater for the male than the female group. Simple main effects tests were performed to determine if there were significant criterion level effects when the data were separated by gender. There was a significant difference across all pairwise level comparisons for males and females ($p < 0.005$), using the Bonferroni adjustment for multiple comparisons.

B. Variability

The intersubject and intrasubject variability of EGGW was examined by computing standard deviations. These data are displayed in Table I. There was not an appreciable difference in intersubject variability based on criterion line placement. Standard deviations of the group data ranged from 0.04 to 0.05 across all criterion line levels. Intrasubject standard deviations also were computed, based on the 12 productions from each speaker. Males had average intrasubject standard deviations of 0.03 across all criterion levels, and women had average intrasubject standard deviations of 0.02–0.03 across all criterion levels.

IV. DISCUSSION

A. Gender effects

As predicted, gender differences were more evident when EGGW was measured with higher criterion levels. Although there were trends for EGGW to be larger for men than women at all criterion levels, differences increased with higher criterion levels and became significant only for criterion levels of 55% or greater. This finding fits well with previous data showing minimal differences in EGGW for men and women when low criterion levels (i.e., 25%) were used (Orlikoff *et al.*, 1997) and results that only approached significance when midlevel criterion line placements (i.e., 40%) were used (Higgins *et al.*, 1998). The EGGW data at higher criterion levels are consistent with the gender-specific adductory patterns predicted from vocal fold models (Titze, 1984, 1989, 1990). It seems that EGGW best reflects these patterns when the measurement is made in a portion of the vibratory cycle that is associated with a relatively large degree of vocal fold contact. Therefore, it seems wisest to use criterion levels of at least 55% in future studies where gender differences in vocal fold contact are of interest.

TABLE II. Comparisons of EGGW values from the present investigation and previous studies of adult normal speakers. In cases where investigators used an inverted EGG signal, the EGGW data reported were converted to be the equivalent of what would have been obtained with an uninverted signal. Mean data from males (*M*) and females (*F*) are presented.

Investigation	Subjects	Speaking task	EGGW	EGGW from present investigation
Higgins and Saxman (1991)	<i>N</i> = 10 males	[bæp] syllables at normal loudness	EGGW40	EGGW40
	<i>N</i> = 10 females Age 20–31 years		<i>M</i> = 0.53 <i>F</i> = 0.48	<i>M</i> = 0.54 <i>F</i> = 0.50
Orlikoff (1991)	<i>N</i> = 10 males Age 26–37 years	Sustained [a] at moderate loudness (70–78 dB SPL)	EGGW25 <i>M</i> = 0.57	EGGW25 <i>M</i> = 0.60
Orlikoff <i>et al.</i> (1997)	<i>N</i> = 8 males Age 30–44 years	Producing [a] in 2 s intervals while alternating between ingressive and egressive phonation	EGGW25 <i>M</i> = 0.54 ^a	EGGW25 <i>M</i> = 0.60
	<i>N</i> = 8 females Age 23–39 years		<i>F</i> = 0.53 ^a	<i>F</i> = 0.58
Sapienza <i>et al.</i> (1998)	<i>N</i> = 10 females Age 20–29 years	[pa] syllables at four intensity levels (70, 75, 80, 85 dB SPL)	EGGW50 <i>F</i> = 0.44–0.47	EGGW50 <i>F</i> = 0.46
			EGGW80 <i>F</i> = 0.26–0.30 ²	EGGW80 <i>F</i> = 0.26

^aSee note 1.

It should be noted that these gender effects apply only to EGG signals from young and middle-aged adults. In a previous study, Higgins and Saxman (1991) found that the trend of more vocal fold contact for men than women actually reversed with aging. During normal phonation, EGGW40 was representative of less vocal fold contact for their aged (≥ 69 years of age) male subjects than their aged female subjects. This raises the question of whether vocal fold surface bulging diminishes with aging for men. Age-related changes in vocal fold tissue, including atrophy of the thyroarytenoid muscle (Kahane, 1987), could contribute to such an effect. Different models may be needed to represent gender-specific adductory behaviors in the young and aged larynx.

B. Comparison to other studies

One goal of the present investigation was to facilitate comparison among studies that used EGGW based on different measurement criteria. In general, our results compare well with those from earlier studies of normal speakers. (Refer to Table II.) For example, Higgins and Saxman (1991) found what they termed “EGG duty cycle” to be 0.52 for young women and 0.47 for young men during production of the syllable [bæp]. Higgins and Saxman (1991) used the equivalent of our 40% criterion line, and their data can be compared to our EGGW40 values. However, we have to convert their EGGW data to take into account that they used an inverted EGG signal. Their converted values of 0.48 for women and 0.53 for men are similar to our EGGW40 values of 0.50 for women and 0.54 for men. Orlikoff (1991) found an average EGGW25 of 0.57 for men producing the vowel [a] with moderate loudness which is comparable to the value

demonstrated by our male speakers (EGGW25=0.60). In another study Orlikoff *et al.* (1997) measured EGGW25 when speakers alternated between inspiratory and expiratory phonation. They found mean values of EGGW25 of 0.54 for men and 0.53 for women during expiratory phonation. These data are lower than our EGGW values of 0.60 for men and 0.58 for women at 25% criterion level, but they show a similarly small gender difference. Sapienza *et al.* (1998) gathered EGGW data from women producing [pa]. They based their criterion line placement on the amplitude of an inverted signal, so their 20% criterion line was actually the equivalent of our 80% criterion line. When we account for this difference and their use of an inverted signal, their EGGW values convert to EGGW80 ranging from 0.26–0.30 and EGGW50 ranging from 0.44–0.47 across different intensity levels. These compare well to our EGGW80 values of 0.26 and EGGW50 values of 0.46 for women. Finally, Scherer *et al.* (1995) used EGG data from four men and three women with normal voices to compute an equation by which EGGW25 data could be predicted from EGGW50 data. Their equation was: Predicted EGGW25=1.067(EGGW50)+0.081. When we apply this equation to our data, the EGGW25 predicted for men is 0.63, as compared to a measured value of 0.60. The EGGW25 predicted for women is 0.57 as compared to a measured value of 0.58. Therefore, our data are in good agreement with the predictions proposed by Scherer *et al.* (1995).

In summary, when the present data are compared to findings from normal speakers across several investigations, there seems to be generally good reliability in EGGW values from different laboratories. Differences that exist may be due to a variety of factors. These could include the speaking task

that was used and the relatively small number of participants in any given study.

C. Implications for selection of EGGW measurement criteria

Scherer *et al.* (1995) correlated EGGW25, EGGW50, and EGGW75 from seven normal speakers. Four of the participants were men and three were women. The correlation between EGGW25 and EGGW50 was 0.82. The correlation between EGGW25 and EGGW75 was 0.71, and the correlation between EGGW50 and EGGW75 was 0.97. Based on these findings, Scherer suggested that EGGW50 and EGGW75 are “essentially redundant” (p. 273). Similarly, Orlikoff *et al.* (1997) noted that various researchers had used different criterion levels (in particular, 25% and 50%) to compute EGGW, but there was no evidence that “this substantially alters the measure or prevents comparison of different data sets, as long as the criterion used is strictly adhered to for each set” (p. 1840).

The present data tell a somewhat different story. That is, there may be some differential sensitivity of specific criterion levels depending upon the research question or population to be studied. To examine gender differences, it appears that it is advantageous to use higher criterion levels that will reflect phonatory behaviors that occur relatively late in the closing phase and relatively early in the opening phase. Sapienza *et al.* (1998) also found that the placement of the criterion line can influence how well EGGW reflects specific phonatory behaviors for normal speakers. They reported EGGW50 and EGGW80² for women producing speech at various intensity levels. Interestingly, they found that changes in EGGW in response to relatively large intensity variations (70 dB vs 85 dB) were more evident when the 80% criterion level was used. Scherer *et al.* (1995) and Orlikoff *et al.* (1997) both noted that criterion lines placed too low in the EGG signal can be in the path of noise or wave form artifacts. Therefore, one would want to be especially careful about choosing to use low criterion levels to measure EGGW in speakers with vocal pathologies associated with limited vocal fold contact or erratic vocal fold behavior. Rothenberg and Mahshie (1988) suggested that a 35% or 50% criterion line might be equally good for examining normal or breathy phonation, but they recommended a 30%–35% criterion line if one was interested in studying hyperadductory behaviors. However, they provided very limited data to support their suggestions.

Another factor to keep in mind when selecting a criterion level is whether it is desirable for the EGGW value obtained to be closely related to other phonatory parameters. Scherer *et al.* (1995) noted that EGGW25 was more highly correlated than EGGW50 or EGGW75 with another measure reflective of vocal fold adduction, namely the abduction quotient described by Titze (1984). Rothenberg and Mahshie (1988) suggested the use of a 50% criterion level if one wanted a close correspondence to open quotient values estimated from glottal air flow signals.

In the present investigation, no criterion level resulted in markedly less intersubject or intrasubject variability. Therefore, there seems to be no advantage in choosing one crite-

tion level over another in an attempt to minimize variability, at least for normal speakers. Rather, the decision to choose an appropriate criterion level from which to measure EGGW should depend on a number of other factors including (1) when the behaviors of interest occur in the vibratory cycle, (2) the strength and regularity of the EGG signals that were obtained, and (3) if it is desirable for the EGGW data obtained to correlate well with other phonatory measures. In any case, it should not be assumed that different criterion levels always would result in similar findings. At least for gender comparisons, the measurement criterion used may significantly affect the results obtained. Future studies should examine how variations in measurement criteria for EGGW influence its sensitivity to changes in the degree of vocal fold adduction (i.e., normal versus breathy versus pressed voice) or specific vocal fold pathologies.

ACKNOWLEDGMENTS

The authors thank Linda Weller, Elizabeth McCleary, and Tamara Field for assistance with data analysis. We also appreciate the help of Tom Creutz, who designed the software program that was used for measurement of EGGW. Finally, we thank Kimberly Fisher, Ph.D. for providing valuable feedback on an earlier version of the manuscript.

¹Orlikoff *et al.* (1997) used a task where participants alternated between egressive and ingressive phonation. The findings reported here were from egressive phonation.

²Sapienza *et al.* (1998) reported that they used a 20% criterion line placement. However, because this was based on the amplitude of an inverted signal, it was the equivalent of an 80% criterion line in an uninverted signal. Therefore, we refer to their measure as EGGW80.

- Alipour, F., and Scherer, R. C. (2000). “Vocal fold bulging effects on phonation using a biophysical computer model,” *J. Voice* **14**, 470–483.
- Anastaplo, S., and Karnell, M. P. (1988). “Synchronized videostroboscopic and electroglottographic examination of glottal opening,” *J. Acoust. Soc. Am.* **83**, 1883–1890.
- Arends, N., Povel, D., Van Os, E., and Speth, L. (1990). “Predicting voice quality of deaf speakers on the basis of glottal characteristics,” *J. Speech Hear. Res.* **33**, 116–122.
- Baer, T., Lofqvist, A., and McGarr, N. S. (1983). “Laryngeal vibrations: A comparison between high-speed filming and glottographic techniques,” *J. Acoust. Soc. Am.* **73**, 1304–1308.
- Baken, R. J., and Orlikoff, R. F. (2000). *Clinical Measurement of Speech and Voice*, 2nd ed. (Singular Thomason Learning, San Diego).
- Biever, D. M., and Bless, D. M. (1989). “Vibratory characteristics of the vocal folds in young adult and geriatric women,” *J. Voice* **3**, 120–131.
- Childers, D. G., and Krishnamurthy, A. K. (1985). “A critical review of electroglottography,” *Crit. Rev. Biomed. Eng.* **12**, 131–161.
- Colton, R. H., and Conture, E. G. (1990). “Problems and pitfalls of electroglottography,” *J. Voice* **4**, 10–124.
- Dromey, C., Ramig, L. O., and Johnson, A. B. (1995). “Phonatory and articulatory changes associated with increased vocal intensity in Parkinson Disease. A case study,” *J. Speech Hear. Res.* **38**, 751–764.
- Fisher, K. V., Scherer, R. C., Guo, C. G., and Owen, A. (1996). “Longitudinal phonatory characteristics after botulinum toxin type A injection,” *J. Speech Hear. Res.* **39**, 968–980.
- Higgins, M. B., McCleary, E. A., and Schulte, L. (1999). “Altered phonatory physiology with short-term deactivation of children’s cochlear implants,” *Ear Hear.* **20**, 426–438.
- Higgins, M. B., Netsell, R., and Schulte, L. (1994). “Aerodynamic and electroglottographic measures of normal voice production: Intrasubject variability within and across sessions,” *J. Speech Hear. Res.* **37**, 38–45.

- Higgins, M. B., Netsell, R., and Schulte, L. (1998). "Vowel-related differences in laryngeal articulatory and phonatory function," *J. Speech Lang. Hear. Res.* **41**, 712–724.
- Higgins, M. B., and Saxman, J. H. (1991). "A comparison of selected phonatory behaviors of healthy aged and young adults," *J. Speech Hear. Res.* **34**, 1000–1010.
- Howard, D. M. (1995). "Variation of electrolaryngographically derived closed quotient for trained and untrained adult female singlers," *J. Voice* **9**, 163–172.
- Kahane, J. C. (1987). "Connective tissue changes in the larynx and their effects on voice," *J. Voice* **1**, 27–30.
- Orlikoff, R. F. (1991). "Assessment of the dynamics of vocal fold contact from the electroglottogram: Data from normal male subjects," *J. Speech Hear. Res.* **34**, 1066–1072.
- Orlikoff, R. F. (1998). "Scrambled EGG: The uses and abuses of electroglottography," *Phonoscope* **1**, 37–54.
- Orlikoff, R. F., Baken, R. J., and Kraus, D. H. (1997). "Acoustic and physiologic characteristics of inspiratory phonation," *J. Acoust. Soc. Am.* **102**, 1838–1845.
- Robb, M. P., and Simmons, J. O. (1990). "Gender comparisons of children's vocal fold contact behavior," *J. Acoust. Soc. Am.* **88**, 1318–1322.
- Rothenberg, M. and Mahshie, J. J. (1988). "Monitoring vocal fold abduction through vocal fold contact area," *J. Speech Hear. Res.* **31**, 338–351.
- Sapienza, C. M., Stathopoulos, E. T., and Dromey, C. (1998). "Approximations of open quotient and speed quotient from glottal air flow and EGG wave forms: Effects of measurement criteria and sound pressure level," *J. Voice* **12**, 31–43.
- Scherer, R. C., Vail, V. J., and Rockwell, B. (1995). "Examination of the laryngeal adduction measure EGGW," in *Producing Speech: Contemporary Issues: for Katherine Safford Harris*, edited by F. Bell-Berti and L. J. Raphael (American Institute of Physics, Woodbury, NY), pp. 269–290.
- Titze, I. R. (1984). "Parameterization of the glottal area, glottal flow, and vocal fold contact area," *J. Acoust. Soc. Am.* **75**, 570–580.
- Titze, I. R. (1989). "Physiologic and acoustic differences between male and female voices," *J. Acoust. Soc. Am.* **85**, 1699–1707.
- Titze, I. R. (1990). "Interpretation of the electroglottographic signal," *J. Voice* **4**, 1–9.

Toward a model for lexical access based on acoustic landmarks and distinctive features

Kenneth N. Stevens^{a)}

*Research Laboratory of Electronics and Department of Electrical Engineering and Computer Science,
Massachusetts Institute of Technology, Cambridge, Massachusetts 02139-4307*

(Received 16 January 2001; accepted for publication 10 January 2002)

This article describes a model in which the acoustic speech signal is processed to yield a discrete representation of the speech stream in terms of a sequence of segments, each of which is described by a set (or bundle) of binary distinctive features. These distinctive features specify the phonemic contrasts that are used in the language, such that a change in the value of a feature can potentially generate a new word. This model is a part of a more general model that derives a word sequence from this feature representation, the words being represented in a lexicon by sequences of feature bundles. The processing of the signal proceeds in three steps: (1) Detection of peaks, valleys, and discontinuities in particular frequency ranges of the signal leads to identification of acoustic landmarks. The type of landmark provides evidence for a subset of distinctive features called articulator-free features (e.g., [vowel], [consonant], [continuant]). (2) Acoustic parameters are derived from the signal near the landmarks to provide evidence for the actions of particular articulators, and acoustic cues are extracted by sampling selected attributes of these parameters in these regions. The selection of cues that are extracted depends on the type of landmark and on the environment in which it occurs. (3) The cues obtained in step (2) are combined, taking context into account, to provide estimates of “articulator-bound” features associated with each landmark (e.g., [lips], [high], [nasal]). These articulator-bound features, combined with the articulator-free features in (1), constitute the sequence of feature bundles that forms the output of the model. Examples of cues that are used, and justification for this selection, are given, as well as examples of the process of inferring the underlying features for a segment when there is variability in the signal due to enhancement gestures (recruited by a speaker to make a contrast more salient) or due to overlap of gestures from neighboring segments. © 2002 Acoustical Society of America.

[DOI: 10.1121/1.1458026]

PACS numbers: 43.71.An, 43.72.Ar, 43.72.Ne [KRK]

I. INTRODUCTION

This article describes a proposed model of the process whereby a listener derives from the speech signal the sequence of words intended by the speaker. The proposed model contains a lexicon in which the words are stored as sequences of segments,¹ each of which is described in terms of an inventory of distinctive features. Acoustic cues are extracted from the signal, and from these cues a sequence of feature bundles is derived. This pattern of estimated feature bundles is matched against the items in the lexicon, and a cohort of one or more sequences of words is hypothesized. A final feedback stage synthesizes certain aspects of the sound pattern that could result from each member of the cohort, and selects the word sequence that provides the best match to the measured acoustic pattern.

This article is concerned primarily with the part of the model that leads to a description of the signal in terms of a sequence of discrete phonological segments, i.e., in terms of bundles of distinctive features. That is, we are attempting to model the speech perception process up to the point where the analog acoustic signal has been interpreted as a sequence of discrete phonological units.

There is ample evidence that words are stored in memory in terms of sequences of segmental units, and that these segmental units are further represented in terms of the values of a set of binary features. That is, the lexical representation is discrete in at least two ways: each word is an ordered sequence of discrete segments, each of which is represented by a discrete set of categories. Some of this evidence comes from acoustic studies of sounds produced by various manipulations of the vocal tract, showing certain distinctive and stable acoustic patterns when the vocal tract is in particular configurations or performs particular maneuvers. These combinations of acoustic and articulatory patterns are based on the physics of sound generation in the vocal tract, including theories of coupled resonators, the influence of vocal-tract walls on sound generation, and discontinuities or stabilities in the behavior of sound sources (Stevens, 1972, 1989, 2001). Evidence for features also comes from quantal aspects of auditory responses to sound, such as responses to acoustic discontinuities and to closely spaced spectral prominences (Chistovich and Lublinskaya, 1979; Delgutte and Kiang, 1984). There is further evidence that these features are grouped together in a hierarchical structure (Clements, 1985; McCarthy, 1988; Halle, 1992; Halle and Stevens, 1991). The aim of the acoustic processing of the speech signal, then, is to uncover the features intended by the speaker, so that these

^{a)}Electronic mail: stevens@speech.mit.edu

features can be matched against the lexicon, which is also specified in terms of segments and features.

In contrast to the discretely specified phonological representation of an utterance, the acoustic signal that is radiated from the mouth of a speaker is continuous. It is an analog signal that is generated by continuous movements of a set of articulatory and respiratory structures. As has been observed, however, the relations between the articulatory and the acoustic representations of speech have certain quasi-discrete or quantal characteristics that are exploited in speech production (Stevens, 1972, 1989). These quantal attributes help to simplify the process of uncovering the discretely specified segmental and categorical representations that are building blocks of words.

In this article we first examine how the acoustic signal provides evidence for the presence of the discrete segmental units, and we review the inventory of segmental features and their defining or primary acoustic and articulatory correlates (Sec. II). A formal structure for storing words in the lexicon is then described (Sec. III). We then observe (in Sec. IV) that in running speech there are several factors that combine to create variability in the acoustic representation of the segments and features. These factors introduce additional cues for the features depending on the context in which they occur. It is argued that this variability can be reduced by selecting acoustic cues that are closely tied to articulation, since the variability can be traced to modifications in articulation that are governed by well-defined principles. The process of estimating the discretely specified underlying segments and their features from analysis of the continuous speech signal is then outlined (Sec. V).

II. SEGMENTS AND THEIR FEATURE REPRESENTATIONS

The distinctive features describe the contrasts between words in language. That is, a change of the binary value of a feature for a segment in a word has the potential of generating a different word. For example, the word pairs seat and sheet or bat and pat differ by a single feature in the first segment. As discussed below, each distinctive feature is assumed to have a defining articulatory action and a corresponding defining acoustic correlate.

A. Segments and articulator-free features

There is a set of features that classify segments into broad classes—classes that can be described roughly as vowels and some general classes of consonants. These are called articulator-free features since they do not specify a particular articulator that is activated to produce the segment (Halle, 1992). Rather, they refer to general characteristics of constrictions within the vocal tract and the acoustic consequences of producing these constrictions.

Probably the most fundamental distinction in speech is between vowels and consonants. Vowels are produced with a relatively open vocal tract, so that air can flow freely through the tract without obstruction and without significant pressure drop across any narrowing that may be present in the supraglottal airway. True consonants, on the other hand, are pro-

duced with a significant narrowing of the airway in the oral cavity.

Acoustically, vowels have greater intensity than consonants. The first formant frequency is generally higher in vowels than in consonants because the oral cavity is relatively open for vowels and there is a narrow constriction in the oral region for consonants. The generation of true consonants involves a sequence of two steps: the formation of a narrowing in the oral cavity, and the subsequent release of that narrowing. By definition, true consonants cause a particular type of discontinuity in the acoustic signal at one or both of these times of closing and releasing. The acoustic discontinuity is a consequence of a rapid change in the pressures and flows within the vocal tract—either a rapid increase or decrease in pressure behind the constriction in the oral cavity (to produce obstruent consonants) or an abrupt switching of the airflow to a different path within the oral and nasal cavities without an increase in intraoral pressure (to produce sonorant consonants). In the case of sonorant consonants, it is possible to produce the requisite acoustic discontinuity only by creating a complete closure of an oral articulator in the midline of the oral cavity. For obstruent consonants, however, an acoustic discontinuity can be formed either by making a complete closure in the midline or by creating a partial closure that is narrow enough to cause a pressure increase and to create continuous flow through the constriction.

One of the ways that true consonants differ from vowels (in addition to the presence of the acoustic discontinuity noted above) is that the spectrum amplitude in the low and midfrequency regions in the consonant region is weaker than the corresponding spectrum amplitude in the adjacent vowels. A reduced spectrum amplitude of this kind can also be produced without generating a constriction that is sufficient to cause an acoustic discontinuity. Segments produced in this way are glides. In English, they include /w/ and /j/, which are produced by raising the tongue dorsum to produce a narrowing between the dorsum and the palate, and, in the case of /w/, a rounding of the lips. The consonant /h/ is also a glide, and the reduced amplitude is produced by spreading the glottis without creating a significant narrowing in the vocal tract above the glottis.

In summary, then, there are three broad classes of segments: vowels, glides, and consonantal segments. Production of a vowel causes a maximum in the low- and midfrequency spectrum amplitude. An acoustic discontinuity occurs at the times when a consonantal constriction is formed or released. And the acoustic correlate of a glide is a reduction in low- and midfrequency spectrum amplitude but without acoustic discontinuities. Evidence for these three kinds of segments within an utterance is provided by landmarks in the signal: a peak in low-frequency amplitude for a vowel, a minimum in low-frequency amplitude, without acoustic discontinuities, for a glide, and two acoustic discontinuities for a consonant, one of which occurs at the consonant closure and one at the consonant release. Figure 1(a) displays a spectrogram of a sentence, and shows the placement of vowel and consonant landmarks; examples of glide landmarks are shown in Fig. 1(b). In Fig. 1(a), the arrows at the top of the spectrogram

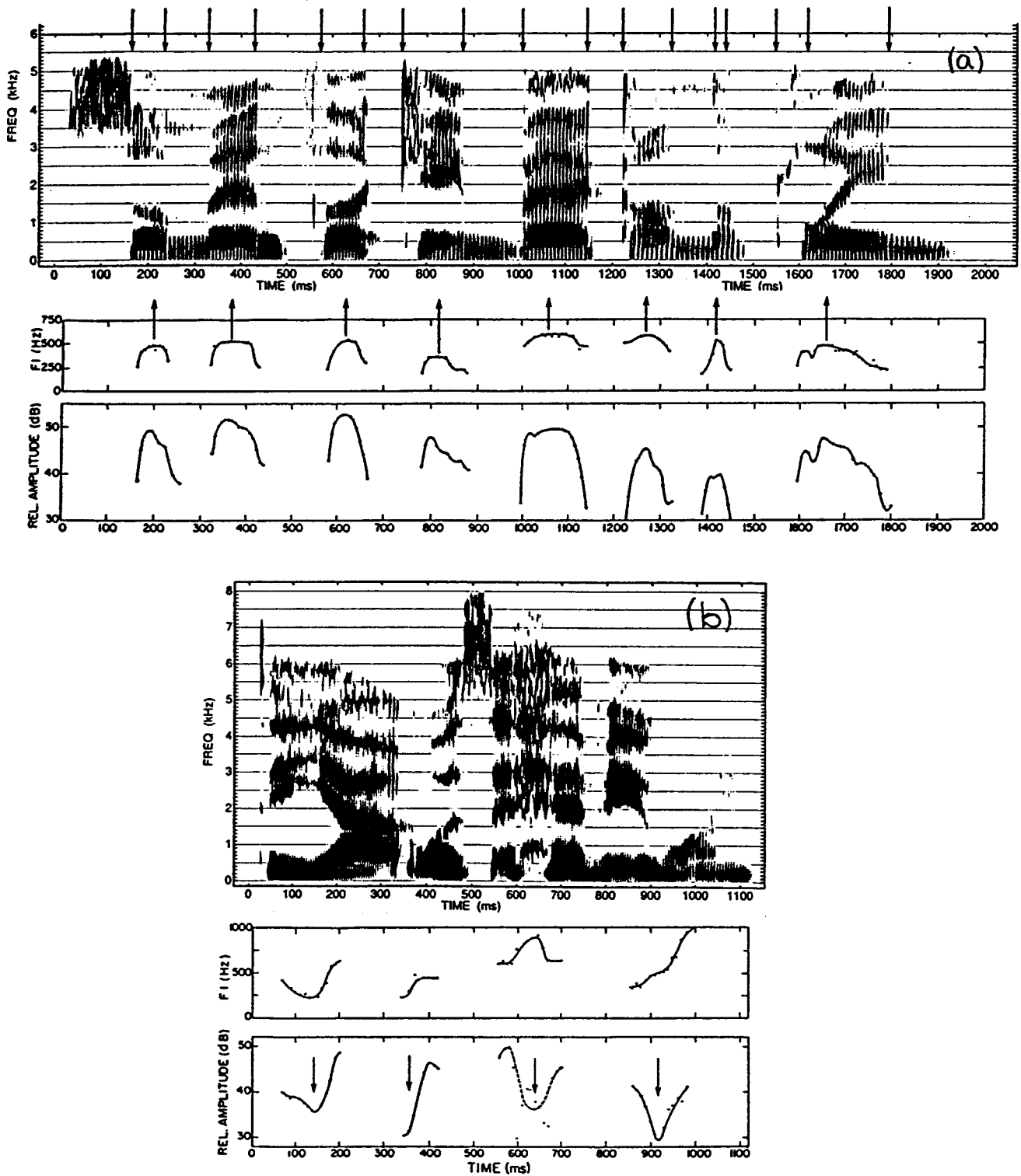


FIG. 1. (a) Shown at the top is a spectrogram of the sentence *Samantha came back on the plane*, produced by an adult male speaker. The plot immediately below the spectrogram gives the frequency of F_1 versus time during the vocalic regions, measured at 7.5-ms intervals. At the bottom is a plot of the relative amplitude of the first-formant prominence during the vocalic regions. Each point on this amplitude plot and on the plot of frequency of F_1 is measured from a spectrum which is obtained by averaging a 10-ms sequence of spectra, each of which is calculated using a 6.4-ms Hamming window. The arrows below the spectrogram indicate vocalic landmarks and the arrows at the top identify consonantal landmarks. See text (from Stevens, 1998). (b) The spectrogram is the sentence *The yacht was a heavy one*, produced by a female speaker, illustrating acoustic attributes of glides. The first-formant frequency in the vicinity of the glides is shown immediately below the spectrogram. The plot at the bottom is the amplitude of the F_1 prominence. The arrows at the amplitude minima for the glides identify the glide landmarks. The irregularities in the amplitude for /h/ are smoothed with the dashed line. Measurements are made at 10-ms intervals using the procedures described in the legend for part (a) (from Stevens, 1998).

TABLE I. Articulator-free features for some consonants in English.

	t,d	s,z	θ,ð	n
Continuant	–	+	+	–
Sonorant	–			+
Strident		+	–	

identify acoustic discontinuities due to consonant closures or releases. The two panels below the spectrogram are plots of the first-formant frequency versus time and the amplitude of the F1 spectral prominence versus time during the vowels. Vowel landmarks are indicated by the arrows near the times when F1 is a maximum, which is close to the time when the low-frequency amplitude is a maximum. For the four glides in Fig. 1(b), the arrows identify times when the amplitude of the F1 prominence is a minimum.

In the case of consonantal segments, we have observed that two further subclassifications can be assigned. A consonant can be formed with a complete closure in the oral cavity in the midline (designated by the articulator-free feature [–continuant]) or with a partial closure that permits a fricative consonant to be produced with continuous turbulence noise (designated as [+continuant]). For [–continuant] segments, there is a further subdivision into [+sonorant] (no increase in pressure behind the consonant closure) and [–sonorant] (increased intraoral pressure).

Still another articulator-free feature is used to implement a contrast for [+continuant] consonants produced with the tongue blade. With appropriate shaping of the cavity anterior to the constriction, and by directing the air stream against the lower teeth, the resulting sound spectrum of the fricative consonant at high frequencies has a much greater spectrum amplitude than the adjacent vowel in the same frequency range. Such a consonant is designated as [+strident], whereas a fricative with weak high-frequency noise is [–strident].

For consonantal segments, then, there are three articulator-free features: continuant, sonorant, and strident. Table I gives a classification of representative consonants in terms of these features. It is noted that the feature [sonorant] is distinctive only for [–continuant] consonants, whereas [strident] is distinctive only for [+continuant] consonants. We adopt here a convention of not designating a feature value when that value is redundant, i.e., can be predicted from the other features.

B. Articulator-bound features and their acoustic correlates

We turn now to a description of features that specify which articulators are active when the vowel, glide, or consonant landmarks are created, and how these articulators are shaped or positioned. Descriptions of the primary articulatory and acoustic correlates of these features have been given in a number of publications (Chomsky and Halle, 1968; Keyser and Stevens, 1994), and we will simply summarize those descriptions here.

There are seven articulators that can potentially be active in producing phonetic distinctions in language. These

TABLE II. Seven articulators and the features that specify phonetic distinctions that can be made with each articulator. The articulators are divided into three groups: those that can form a constriction in the oral cavity, those that control the shape of the airway in the laryngeal and pharyngeal regions, and the aspect of vocal-fold adjustment relating to stiffness.

lips	[round]
tongue blade	[anterior]
	[distributed]
	[lateral]
	[rhotic]
tongue body	[high]
	[low]
	[back]
soft palate	[nasal]
pharynx	[advanced tongue root]
glottis	[spread glottis]
	[constricted glottis]
vocal folds	[stiff vocal folds]

are (1) the lips, (2) the tongue blade, (3) the tongue body, (4) the soft palate, (5) the pharynx, (6) the glottis, and (7) adjustments of the tension of the vocal folds. These articulators can be manipulated in one or more ways to generate segments that are distinctive (i.e., that could potentially distinguish between words). Each of these ways of manipulating an articulator is described by a feature, which can have a plus or minus value. The articulators and the features associated with them are listed in Table II.

In Table II, the articulators are classified into three groups. The first group, consisting of the lips, the tongue blade, and the tongue body, involve adjustments of the configuration of the oral cavity. The soft palate, the pharynx, and the glottis form the second group, and manipulations of these articulators control the vocal-tract shape in the laryngeal and pharyngeal regions. The third class in Table II describes adjustments of the stiffness or slackness of the vocal folds, and these adjustments are not involved directly in changing the shape of the airway. Not all of the features in Table II are distinctive in English, and this is not an exhaustive list of the universal distinctive features that are used across languages.

Vowels and glides are specified completely by a listing of articulator-bound features. In general, the major features for vowels are the features specifying the position of the tongue body—the features [high], [low], and [back]. In English, additional features that describe contrasts for vowels are [round] and [advanced tongue root].² The features that distinguish between glides can involve any of the top six articulators in Table II. In English (and in most, if not all, languages), the inventory of glides is considerably smaller than the inventory of vowels or consonants.

A listing of the features for some vowels and glides is given in Table III. Note that the feature [round] is unspecified for front vowels, and the feature [spread glottis] is the only one that is specified for the glide /h/. Some vowels in English are diphthongs, such as the vowels in *hide* and *boy*. We represent these diphthongs as sequences of two segments, the second of which is a glide. An example of the feature representation for the diphthong /aj/ is given in Table III. Our convention for the offglides of such diphthongs is to leave as

TABLE III. Listing of the features for some vowels and glides in English.

	i	ε	æ	ɑ	ʌ	u	w	j	h	ɔj
High	+	-	-	-	-	+	+	+		-+
Low	-	-	+	+	-	-	-	-		+ -
Back	-	-	-	+	+	+	+	-		+ -
Round				-	-	+	+			
Advanced tongue root	+	-	-	-	-	+	+	+		-
Spread glottis									+	

unspecified the value of the feature [advanced tongue root] but to mark this offglide as a glide.

To fully describe a consonant, it is necessary to designate which primary articulator is used to form the constriction that produces the acoustic discontinuities or discontinuity that constitutes the landmark. Only three articulators can produce these consonantal landmarks: the lips, the tongue blade, and the tongue body. These articulators produce constrictions in the oral cavity. Associated with each articulator there is a set of one or more articulator-bound features. For a given primary articulator, some of these features must be specified. In addition to designating a primary articulator and its features, it is usually necessary to specify the features associated with secondary articulators. In English, these features are [nasal] and [stiff vocal folds]. (In some other languages, the features [spread glottis] and [constricted glottis] are used distinctively.)

A listing of articulators and articulator-bound features for some consonants in English, together with articulator-free features already given, is displayed in Table IV. Features that are redundant or do not contribute to a distinction in English for a given segment are left blank.

The articulator-bound features in Tables II–IV are identified with particular articulators and with the shaping and positioning of those articulators. However, these features also have well-defined acoustic and perceptual correlates. Linguists have argued that the universal set of features that are used to define contrasts in the languages of the world (of which those discussed above for English represent a subset) have the property that for each feature there is a coincidence between the articulatory description for the contrast and a

distinctive acoustic correlate for that contrast. We illustrate this premise with three examples.

When a consonant is produced with a tongue-blade constriction, the constriction can be positioned forward of the alveolar ridge (in which case the defining feature is [+anterior]) or posterior to the alveolar ridge (i.e., [-anterior]). The strident fricatives /s/ and /ʃ/ in English are distinguished by this feature, as Table IV shows. Acoustically, the tongue blade position for /s/ creates a resonance of the cavity anterior to the constriction that is in the range of the fourth or fifth formant for the speaker, giving rise to a spectral prominence in the sound in this frequency range. In the case of /ʃ/, the tongue blade is moved to a slightly more posterior position, and is shaped somewhat differently, so that there is a spectral prominence in the third formant range. Thus the + or - values of the feature [anterior] define the position of the tongue-blade constriction with respect to a landmark on the hard palate. Coincident with this manipulation of the constriction, there are well-defined acoustic (and perceptual) consequences that specify which natural frequency of the vocal tract receives principal excitation from the friction noise source near the constriction.

Another example is the feature [back] for vowels. For [+back] vowels, the tongue body is displaced back to form a narrowing in the pharyngeal or posterior oral cavity. The acoustic consequence is a second-formant frequency that is low and close to the first-formant frequency. Vowels classified as [-back], on the other hand, are produced with the tongue body forward and a high second-formant frequency. A natural dividing line for [+back] and [-back] vowels is the frequency of the second subglottal resonance, which is in

TABLE IV. Listing of articulator-free features, articulators, and articulator-bound features for some consonants in English.

	b	d	g	p	f	s	z	ʃ	m	l
Continuant	-	-	-	-	+	+	+	+	-	-
Sonorant	-	-	-	-					+	+
Strident						+	+	+		
Lips	+			+	+				+	
Tongue blade		+				+	+	+		+
Tongue body			+							
Round	-			-	-				-	
Anterior		+				+	+	-		+
Lateral									-	+
High			+							
Low			-							
Back			+							
Nasal									+	-
Stiff vocal folds	-	-	-	+	+	+	-	+		

the vicinity of 1500–1700 Hz for adults (Cranen and Boves, 1987). When F_2 for a vowel comes close to this resonance, an acoustic perturbation can be created. This subglottal resonance forms a kind of “acoustic berm.” Vowels that are [–back] tend to maintain F_2 above this perturbation; for [+back] vowels, speakers tend to place F_2 below this frequency. There is also evidence that the auditory response to a front vowel, with F_2 high and close to F_3 , is qualitatively different from that for a back vowel (Syrdal and Gopal, 1986). Again we see a coincidence of an articulatory positioning and an acoustic and perceptual consequence of that articulatory manipulation.

A third example is concerned with the features [stiff vocal folds]³ (Halle and Stevens, 1971). When this feature is used to characterize an obstruent consonant, there are two acoustic consequences in the vicinity of the consonant release. For a consonant classified as [–stiff vocal folds] (commonly referred to as a voiced consonant), the vocal folds are slackened, and glottal vibration during the time when there is a reduced transglottal pressure in the consonant interval is facilitated. The increased slackening also carries over into the following vowel, leading to a lowered fundamental frequency near the beginning of the vowel. The opposite effect occurs for a consonant that is [+stiff vocal folds] (i.e., a voiceless consonant). The vocal-fold stiffening inhibits glottal vibration during the obstruent interval. This increased stiffening extends into the following vowel, leading to a raised fundamental frequency near the beginning of the vowel. Again we see a coincidence between the articulatory manipulation for the feature and the acoustic consequences of this manipulation. In this example there is an acoustic correlate of the feature in the constricted interval for the consonant and a different acoustic correlate in the vowel following the consonantal release. (As will be noted later, in certain phonetic or prosodic environments in English, additional gestures may be introduced to enhance the saliency of the contrast between consonants that differ in the feature [stiff vocal folds].)

These and other examples provide support for the view that for each articulator-bound distinctive feature there is a defining articulatory manipulation and a distinctive acoustic pattern that results from this manipulation. We will observe later, however, that, in addition to the defining acoustic attribute for a feature, there may be added articulatory gestures and further acoustic cues that can contribute to identification of the feature, depending on the context in which it appears.

The acoustic correlates of the articulator-bound features depend to some extent on the type of segment—whether it is a vowel, a glide, or a consonant. In general, the acoustic manifestations of these features are most salient in the vicinity of the landmarks. For example, to estimate the values of the features for a vowel or glide, attributes of the acoustic signal in the region that is within a few tens of milliseconds of the vowel or glide landmarks must be examined. In general, the acoustic properties in the vicinity of these landmarks for vowels and glides change in a smooth and continuous manner, and the time course of these changes provides the information needed to uncover the features for these segments. Acoustic information that can help to deter-

mine articulator-bound features for consonants resides in regions that are a few tens of milliseconds on either side of the consonant landmarks. Since the consonant landmarks are defined by acoustic discontinuities, the acoustic properties near one side of a landmark are usually quite different from the properties near the other side of the landmark, as in the example above relating to stiff vocal folds (Stevens, 2000a). The diverse information from these two sets of properties, including the nature of the abrupt changes in certain acoustic properties, must be integrated to determine the intended articulator-bound features.

The features listed in Tables I–IV can be organized in a geometrical, treelike hierarchy to represent more closely their relation to the articulatory structures that are used to implement them. This treelike structure highlights the fact that the various features in Tables I–IV are not simply a list, but are structured into groups. As has been noted elsewhere (Clements, 1985; McCarthy, 1988; Keyser and Stevens, 1994), the phonological patterning of the sounds in language can be described succinctly in terms of these groupings. In the model described in the present article, however, the lexical representations will not utilize this formal hierarchical structure.

III. LEXICAL REPRESENTATION AND PLANNING STAGE

The stored items in the lexicon consist of sequences of segments, each of which is represented by a list of features. The features are of several kinds: membership in one of three broad classes of vowel, glide, and consonant; in the case of vowels and glides, a listing of articulator-bound features; and in the case of consonants, a specification of the articulator-free features (continuant, sonorant, strident), one of three possible primary articulators (tongue body, tongue blade, and lips), and a set of articulator-bound features.

It is also necessary to specify in the lexicon the structure of the syllables. In English, there are particular constraints on the contexts in which consonants can occur. These constraints for a given consonant can be described conveniently in terms of the position of the consonant in the syllable and on the features of the vowel and consonants within the syllable. A conventional way of representing syllable structure in English characterizes the syllable as an onset and a rime, with the rime consisting of a nucleus and a coda (cf. Clements and Keyser, 1983). A consonant or consonant sequence can be appended after the coda as an affix. If there is a glide or a sonorant consonant in the onset or the coda, this segment is always adjacent to the nucleus, or vowel (with rare exceptions, as in the sequences /mju/ or /nju/ in words like *mute* and *new*). With some exceptions, a consonantal segment (i.e., a segment that is implemented with abrupt landmarks) is always adjacent to either a vowel or a glide. (The exceptions are when the consonant is /s/ or is adjacent to /s/, as for the /s/ in *spot* or the /k/ in *desk*. Other exceptions are in affixes following the rime, as in *asked* or *fifth*, where the affixes are always consonants produced with the tongue blade.)

Knowledge of the syllable structure is important during speech production because details of the implementation of a

TABLE V. Lexical representations for the words debate, wagon and help. The syllable structure of each word is schematized at the top (σ =syllable, o=onset, r=rime).

	d	ə	b	e	t		w	æ	g	ə	n		h	ɛ	l	p
Vowel		+		+				+		+				+		
Glide							+						+			
Consonant	+		+	+					+		+				+	+
Stressed		-		+				+		-				+		
Reducible		+		-				-		+				-		
Continuant	-		-	-					-		-				-	-
Sonorant	-		-	-					-		+				+	-
Strident																
Lips			+													+
Tongue blade	+			+							+				+	
Tongue body								+								
Round			-				+									-
Anterior	+			+							+				+	
Lateral															+	
High		+		-			+	-	+	-				-		
Low		-		-			-	+	-	-				-		
Back		-		-			+	-	-	+				-		
Adv. tongue root				+			+	-						-		
Spread glottis													+			
Nasal											+					
Stiff vocal folds	-		-	+					-							+

consonant, including the timing of the articulator movements, are dependent to some extent on its position within the syllable. The timing of implementation of the syllable nucleus or vowel is also influenced by the syllable structure. For a listener, the ability to estimate syllable structure in running speech can be helpful in determining word boundaries, since the onset of a word is always the onset of a syllable in the lexicon.

Words in English containing more than one syllable always mark one of the syllables as carrying primary stress. Furthermore, some vocalic nuclei in a word may be marked in the lexicon as being potentially reducible. Thus, three kinds of vocalic nuclei are identified in the lexicon: stressed, reducible, and neither stressed nor reducible. The acoustic correlates of primary stress and of reduction are not well defined, but some combination of vowel amplitude, duration, fundamental frequency contour, glottal source waveform, and vowel formant pattern contributes to judgments of these attributes. In the lexical representation, the status of a syllable as being stressed, reducible, or neither stressed nor reducible is indicated by two features that are attached to each

vowel. These features are [stress] and [reducible], and three combinations of plus or minus are used. The combination [+stress, +reducible] is not allowed.

Examples of the representation of three words in memory in the proposed lexical access model are given in Table V. A schematic representation of the syllable structure for each word is given at the top of the table. The syllable is marked by σ and the onset and rime by o and r. One of the words has one syllable and the other two have two syllables. In the case of the word wagon, the consonant /g/ is shared between the two syllables of the word. This consonant is said to be ambisyllabic (Clements and Keyser, 1983).

The first three rows of the table below the syllable structure specify the general category of vowel, glide, or consonant. Stress and potential for reduction for the vowels are marked in the next two rows, followed by the three articulator-free features that apply to consonants. The primary articulator for each consonant is given by a “+” placed in one of the next three rows. The remaining rows list the articulator-bound features. The last two features are separated out from the others since they can be considered as

secondary articulator-bound features for consonants in English.

The conventions used for marking the features or descriptors for lexical items in Table V depart somewhat from lexical representations proposed, for example, by Chomsky and Halle (1968) or by Clements (1985). For example, the designation of vowel, glide, or consonant, while marked in the lexicon by “+” in the appropriate row, is not strictly a feature representation. Any one segment is classified by one “+,” and such a segment is automatically not a member of either of the other classes. Similar comments could be made about the use of “+” to specify the primary articulator for a consonant. A consonant (at least in English and in most other languages) can have just one primary articulator.

It is evident that the representation of any one segment of a lexical item is rather sparse. All but one of the segments in Table V are represented in terms of 6 or 7 features (except /h/), whereas the entire list of features in the table numbers 21. The specification of some features is conditional on the values of the articulator-free features and, for consonants, on the designation of the primary articulator. If one requires that each feature be truly distinctive, in the sense that changing the value of the feature creates a potentially different word, then the feature representations in Table V can be made even more sparse. For example, a segment that is [+consonant, +tongue body] is automatically [+high], and for such a segment the features [−low, +back] are not distinctive. Thus the average number of distinctive features for each segment is smaller than the six or seven implied in Table V, especially for consonants.

In the representation of the words debate and wagon in Table V, the reducible syllables are assigned a full set of vowel features. The first syllable in debate has the features for the high front vowel /i/, and the second syllable in wagon has the features for the nonhigh back vowel /ʌ/. These are postulated to be the features underlying the vowels, and the acoustic manifestations of these features would be well defined in some situations if the words were spoken clearly. In this case, the vowels would be implemented as [−reduced]. However, the presence of the feature [+reducible] is an indication that these vowel features are not distinctive in the sense that no minimal pairs are generated when the values of these features are changed. Thus these features do not contribute to identification of the words. In the more common production of these vowels, the durations would be decreased.

In addition to stem morphemes, the lexicon also contains affixes which can be appended to stems to produce new words. This process can lead to modification of certain features in the stem or to different forms for the affix depending on features of segments at or near the stem boundary. Rules for generating these new formatives involve modification of features or groups of features in environments that are also specified in terms of features. An example is the generation of the plural forms of nouns. The process for generating these plural forms can be described as a sequence of two ordered rules. The first rule is to add an unstressed schwa vowel at the ends of words that terminate in strident consonants produced with the tongue blade. The second step in

forming the plural adds /z/ in all cases except when the noun terminates in a voiceless segment, in which case the voiceless /s/ is added. These rules lead to the standard plural forms such as bus/busses, bag/bags, and bat/bats, the plural being represented by the affix /z/ in the first two examples and /s/ in the third example. Similar rules that manipulate features or groups of features apply to a large variety of affixes.

It is assumed that a representation of words in the memory of a speaker or listener takes the form shown in Table V. One type of evidence for this assumption comes in part from the fact that a language user appears to have access to phonological rules of the type just described for appending the plural phoneme to nouns in English. There is a large number of such rules (e.g., Chomsky and Halle, 1968), involving essentially all the features that are contrastive in English, i.e., for which the change in the value of a feature creates a possible new word. The rules can be expressed efficiently in terms of manipulations of these features or groups of features.

When an utterance is to be produced, there is an initial planning process. For a multi-word utterance, a sequence of words, possibly constructed from morpheme sequences, is selected from the lexicon. Retrieval processes and phonological rules operate on the morpheme sequences to produce a sequence of segments and their associated features, which will subsequently be translated into articulatory commands. The syllabification of this segment/feature sequence may be adjusted somewhat from the syllabification in the lexicon. This planning stage also involves prosodic markers in the form of a metrical template which, at a minimum, indicates phrasally prominent syllables, full vowel syllables without phrasal prominence, and reduced syllables. In addition, prosodic specifications for the F0 contour, duration pattern, and amplitude contour of the utterance must be generated, to reflect both word-level and phrase-level prosodic constituents and prominences. The details of these prosodic aspects of the planning stage are not central to the aim of this article, which is concerned instead with the listener’s task of estimating the speaker’s planned sequence of segments and features. These issues about the nature of the planning stage have also been addressed in Levell (1989), Shattuck-Hufnagel (1992), Levell *et al.* (1999).

IV. MULTIPLE ACOUSTIC CUES FOR FEATURES AND THEIR DEPENDENCE ON CONTEXT

A. Articulatory interactions and multiple acoustic cues

From the point of view of the speaker, the array of segments and features in the planning stage provides a sketch of the instructions to the articulators specifying how a word is to be produced. It describes which articulators are to be manipulated and how they are to be shaped and positioned. These movements of the articulators in turn give rise to the sound pattern.

Although each of the distinctive features has certain defining articulatory and acoustic correlates, there are additional acoustic properties that are biproducts of the principal

articulatory and acoustic requirements for the feature. These properties can arise through articulatory actions that are not specified directly by the feature. Some of these actions may be automatic consequences of the primary articulatory gesture for the feature, and others may be introduced to enhance the perceptual contrast defined by the feature when the feature occurs in certain phonetic or prosodic contexts (cf. Keyser and Stevens, 2001). Such enhancing gestures often give rise to new acoustic properties, as well as strengthen the primary acoustic correlate of the feature. Of these enhancing gestures, some are obligatory in the sense that they are required for proper acoustic implementation of the primary acoustic property, whereas others may be optional. These additional articulatory gestures and their acoustic properties are not specified in terms of distinctive features since they do not by themselves define contrasts in the language. They can, however, provide acoustic and perceptual cues that potentially help the listener in the estimation of the distinctive features. This view that enhancing gestures are introduced by a speaker to strengthen a perceptual contrast is consistent with similar views expressed by Diehl (1991), by Kingston and Diehl (1994), and by Diehl *et al.* (2001).⁴

The enhancing gestures are presumably introduced when the defining acoustic correlate for a particular contrast is not sufficiently salient. That is, the use of enhancing gestures is driven by perceptual requirements (Diehl, 1991; Keyser and Stevens, 2001). Since the inventory of features (and contrasts) is language dependent, the gestures that may be used for enhancing the perceptual saliency of a feature may be language dependent. It is possible, then, to observe differences in the acoustic manifestation of the same feature in different languages. Such variability is well documented in the literature (cf. Ladefoged, 1980).

The articulatory actions that are automatic consequences of the implementation of particular features include (1) the stiffening of the vocal folds during the production of a high vowel, leading to a higher fundamental frequency for high vowels than for low vowels (House and Fairbanks, 1953; Whalen *et al.*, 1998); (2) the increased duration of low vowels relative to high vowels (House and Fairbanks, 1953); and (3) the different duration of the frication noise burst at the release of different articulators in producing a stop consonant (Cho and Ladefoged, 1999; Hanson and Stevens, 2000), the duration being shortest for labials, longest for velars, and intermediate for tongue-blade consonants. These (and possible other) consequences of particular feature-related gestures are determined by anatomical and physiological factors over which the speaker has little control.

We consider next some examples of active secondary articulatory gestures that are required if the primary acoustic correlate of a feature is to be realized. In each of these examples, the primary feature is an articulator-free feature. (1) Any consonant that is classified as [–sonorant] must be produced with a closed velopharyngeal port, since by definition pressure is built up in the oral cavity for such a consonant. (2) The production of a consonant that is [+continuant] requires significant airflow through the oral constriction, and usually this airflow can only be achieved when the glottal opening is greater than it would normally be for a vowel. (3)

A [+strident] consonant (in English) is produced by directing the airstream against the lower incisors. This action requires that the tongue blade be shaped in a way that properly directs the jet of air, and therefore requires that the jaw be raised so that the lower incisors are properly positioned to provide an obstacle for the jet. The contrasting [–strident] consonant requires a tongue blade position and shape that avoids an airstream that impinges on the lower incisors downstream from the constriction. For each of these examples, the secondary articulatory gestures have acoustic consequences that can provide cues to aid the listener in uncovering the feature.

Recruitment of articulators that are not directly specified by the features for a segment may also be motivated by the need to enhance the acoustic and perceptual consequences of one of the features of the segment. Some of these enhancement actions are reviewed in Keyser and Stevens (2001). We restrict our discussion here to two examples where the enhancing gesture creates not only a strengthened primary acoustic cue for the feature, but also introduces additional acoustic properties or perceptual cues that can contribute to a listener's estimation of the feature.

There are two primary acoustic correlates of the feature [+stiff vocal folds]. During the consonantal interval (while there is a buildup of intraoral pressure), a segment with the feature [+stiff vocal folds] shows essentially no glottal vibration during the constricted interval for the consonant. The contrasting segment with [–stiff vocal folds] does exhibit glottal vibration at some time during the constricted interval for the consonant. In the initial part of the vowel following the consonant the fundamental frequency is higher for a [+stiff vocal folds] segment than for the [–stiff vocal folds] cognate, reflecting the carryover of vocal-fold stiffness into the following vowel. Several types of gestures are used to enhance the feature [stiff vocal folds] depending on the syllable position of the consonant. In syllable-initial position for a stop consonant before a stressed vowel, aspiration is introduced by maintaining a spread configuration for the glottis for a few tens of milliseconds following the consonant release, leading to a delay in the onset of glottal vibration following the consonant release. This action presumably increases the separation between frication noise at the consonant release and the onset of glottal vibration, and hence enhances the voiceless character of the consonant. The vowel preceding a syllable-final voiceless consonant is often shortened relative to its duration preceding a voiced consonant, particularly if the syllable is phrase-final, thereby reducing the amount of glottal vibration in the syllable and enhancing the perception of the feature [+stiff vocal folds]. Also, when a voiceless stop consonant is in syllable-final position in certain phonetic contexts (particularly for an alveolar consonant), the vocal folds are often adducted to form a glottal closure, leading to an abrupt termination of glottal vibration. This glottalization enhances the voiceless character of the consonant in this syllable-final position (Keyser and Stevens, 2001).

Another articulatory action that can be interpreted as an enhancing gesture is the positioning of the tongue body for a tongue-blade stop consonant. In the case of a [+anterior]

stop consonant in English, for example, the tongue body is adjusted to a somewhat fronted position, presumably to assist in positioning the tongue blade constriction and hence to enhance the contrast with labial consonants, as seen in the spectrum shape of the burst. This tongue-body gesture is reflected in the formant movements in the following vowel. The fronted tongue-body position also leads to formant transitions that are different from those of labial consonants, and therefore contributes to the perceptual saliency of the alveolar consonant.

It is evident, then, that several acoustic cues in combination can lead to identification of a feature and hence of the word for which the feature constitutes a component. In running speech, each of these cues can be present with various degrees of strength, depending on several factors such as speaking style, the syllable position of the segment, and the phonetic and prosodic environment in which the feature occurs. In some environments and for some styles of speaking, all of the cues for a particular feature might be strongly present, and identification of the feature is robust and reliable. In other situations, including speech in noise or in the presence of other distorting influences (such as the degree of casualness), some of the cues may be weak or absent. For example, in rapid speech, the articulatory movements for two adjacent segments may overlap in a way that obscures the acoustic consequences of some of the movements (Browman and Goldstein, 1990). In such cases, identification of the feature from the available cues may be unreliable and may depend strongly on knowledge of the context in which the feature occurs. (See Sec. IV C.) Situations can arise, for example, in which the defining acoustic cues for a feature in some contexts are not available, but cues associated with enhancing gestures remain.

We turn now to a discussion of cases where (1) feature identification is robust, and (2) cues may be severely weakened.

B. Word-initial segments and prominent syllables

There is some evidence that features for consonants in word-initial position exhibit a stronger set of acoustic cues than consonants in other positions (Cutler and Carter, 1987; Manuel, 1991; Gow *et al.*, 1996). This statement is especially true when the word is not a function word, in which the vowel can be reduced. For the most part, these initial consonants are adjacent to vowels, or at least they usually precede vowels, glides, or liquids. Thus there is an opportunity for cues to be present both in the interval preceding the release when the consonant constriction is in place, and in the sonorant or vocalic interval immediately following the release. These cues tend to be modified minimally by a segment at the end of a preceding word. It is not uncommon for some of the cues for features in a word-initial segment to spread their influence to regions of the sound that might normally be associated with the final segment in a preceding word (cf. Zsiga, 1994). In some sense, then, this spreading of cues enhances the identification of the features for the word-initial consonant. Thus, for example, in a sequence like “his five sisters,” voicing in the segment /z/ in *his* or /v/ in *five* may be only weakly represented near the time of closure for

the fricative, because of the influence of the word-initial voiceless /f/ or /s/, respectively. Or, to put it another way, the voicelessness of word-initial /f/ and /s/ is strengthened.

There are, however, exceptions to this word-initial robustness principle. For example, some of the acoustic characteristics of word-initial /ð/ can be influenced by a preceding word-final consonant, so that /ð/ may appear to have the characteristics of a noncontinuant or sonorant consonant (Manuel, 1995). These effects can be observed in sequences like “win those cups,” or “at those classes,” where there may be little direct acoustic evidence for the features [+continuant] and [−sonorant] which are normally associated with /ð/. It is noted, however, that the features [+anterior, +distributed] (i.e., the place features for /ð/) appear to be represented robustly in the signal independent of the context.⁵ Another exception is word-initial /h/ when it occurs before a reduced vowel, as in “will he go.” In casual speech, there may be little or no evidence for /h/ in this phonetic environment.

When there is a word-initial consonant cluster, the same robustness principle applies to the consonant that is immediately adjacent to the vowel. Since there are constraints on the features of the consonant or consonants preceding this vowel-adjacent consonant, the features for these other components of the initial cluster can also be identified reliably (cf. Fujimura, 1997).

In running speech, some syllables are produced with greater prominence than others. This greater prominence is manifested in the sound by increased amplitude, increased vowel duration, and increased duration of the initial consonant. In such a prominent or accented syllable, the cues for the features of the initial consonant or consonants are present in the sound with greater strength and possibly with greater number than are the cues for consonants in other environments. For example, voiceless stop consonants are aspirated in this position, thereby enhancing identification of the feature [+stiff vocal folds], as noted above. And the increased vowel and consonant durations permit a clearer representation of consonantal place of articulation in the vicinity of the consonant release, with minimal influence of vowels and consonants other than the immediately following vowel. The increased vowel duration for an accented syllable also reduces the influence of adjacent consonants and vowels on the formant frequencies near the middle of the vowel. Consequently, the cues for place of articulation for the vowel as well as for the initial consonant are more robust, and the vowel features can be estimated with minimal reliance on contextual information.

It frequently happens, of course, that accented syllables are also word-initial syllables (Cutler and Carter, 1987). In this case, there is more than one reason why the features for initial consonants are represented by robust cues in the sound.

C. Sources of weakening or modification of cues for features

We have just shown that there is a set of environments for consonants and vowels in which cues for the distinctive features tend to be robust. Cues for certain features of seg-

ments in other contexts are subject to weakening or to elimination in running speech. This modification of cues for features of a particular segment generally arises because of the influence of adjacent segments. The articulatory movements needed to implement an adjacent segment may prevent some of the cues for the features from appearing in the signal, or may weaken the cues because of overlap of these movements with those required for the features (Browman and Goldstein, 1990). We discuss here a few examples of such cases in English.

In running speech, it is common to classify the vowels into three categories: accented vowels, full vowels but not accented, and reduced vowels. For example, in the word potato, the first vowel is normally reduced, the second vowel is accented, and the third vowel is a full vowel but nonaccented. Reduced vowels are inherently produced with weakened cues for place features. It is expected that when a vowel is reduced, it is sufficient to specify simply that the vowel is present, with no identification of place features. The more difficult issue is to determine the presence of a reduced vowel. It is normally expected that each vowel or syllabic nucleus in running speech is characterized by a peak in low-frequency amplitude in the waveform, and this peak defines a landmark for the vowel. This peak may be small, however, in the case of a reduced vowel.

Some phonetic environments in which evidence for a reduced vowel may not appear as a separate low-frequency peak in amplitude of the oral acoustic output are listed as follows:

- (1) If a reduced vowel immediately follows another vowel, without an intervening consonant, the presence of the vowel may not be manifested as a low-frequency peak separate from the peak for the preceding vowel. An example is the sequence saw a dog where the sequence /aə/ usually gives rise to only a single peak in low-frequency amplitude, with the peak occurring at the time the mouth opening is largest. The lack of a separate low-frequency amplitude peak can also be observed for a sequence of two vowels when neither vowel is reduced. In an utterance like “he saw eight dogs,” a separate vowel landmark may not be observed in the sequence /ae/. This merging of two vowel landmarks into one cannot occur when the vowel is [–tense], since such vowels must be followed by consonants.
- (2) When a reduced vowel is surrounded by voiceless obstruent consonants, the glottal spreading and vocal-fold stiffening that accompanies the consonants could spread into the vowel, and the vowel would then become voiceless. Examples of this kind of consonant reduction are sometimes observed in words such as potato and classical.
- (3) When a nasal consonant follows a reduced vowel, there are some phonetic environments in which the vowel–consonant sequence reduces to a syllabic nasal. The words button or lesson are examples where such a reduction can occur. In the sequence /ən/ in these examples, the nasalization of the vowel preceding the nasal consonant extends back over the entire length of the vowel and

into the end of the closure for the preceding consonant. This preceding consonant has the same place of articulation as /n/, so that the consonant is terminated by the opening of the velopharyngeal port and is followed immediately by the syllabic nasal. A similar merging can occur when a reduced vowel is followed by a liquid, in which case the peak in low-frequency amplitude occurs within the syllabic /r/ or /l/. The syllabic /r/ could in some cases be considered as a vowel segment (rather than being derived from a sequence /ər/), but in other cases it is a reduction, as in an utterance like come for dinner, where /ər/ in for reduces to syllabic /r/. Similar comments could be made about /l/, for example in the word legal. In all of these cases, it is usually possible to detect a low-frequency amplitude peak or landmark indicating the presence of the syllabic liquid or nasal, and hence to detect that a syllable is present, but there is no direct evidence on the surface for a sequence of a vowel and a consonant.

In reduced vowels, the formant frequencies can be influenced strongly by the consonant context and by the phonetic characteristics of vowels in adjacent syllables. Some influence of context can also be seen in vowels that are not reduced. This influence can be sufficiently strong that estimation of the features underlying a nonreduced vowel must take into account the consonantal context as well as the formant frequencies within the vowel.

As has been observed, the acoustic cues for a consonant are most robust when the consonant is in word-initial position preceding a stressed vowel. For consonants in a number of other phonetic environments, the inventory of cues for the various consonantal features is often more sparse. That is, in some other environments there is less opportunity to generate acoustic cues for the consonant in the vicinity of the times of closure and release for the consonant. The articulatory maneuvers that are specified by the features for the consonant are implemented, but the gestures for nearby segments prevent the acoustic cues for the consonantal features from appearing in the signal. This effect of overlapping gestures is more prevalent when there is an increased speaking rate.

One common omission of a cue for a consonant is an acoustic record of both closing and opening movements when a consonant occurs in a sequence of two or more consonants. For example, in a sequence like up to, the closure for /t/ often occurs before the opening movement for /p/, so that neither the labial release nor the alveolar closure creates an acoustic landmark. There is an articulatory opening and closing gesture for each consonant, but only two landmarks are evident in the sound. It may also happen that the overlap in gestures for the two consonants in a sequence is sufficiently great that the acoustic manifestations for some features of the first consonant are influenced by the second consonant. Thus there can be a weakening of cues for certain features of the first consonant. Examples are the weakening of place cues for a tongue-blade consonant that is followed by a consonant with a different place of articulation (e.g., the sequence note closely) or the weakening of acoustic cues for

voicing of the first consonant in a sequence like his cake (Gow, 2002).

In some versions of words like button or cotton, a cue for the presence of the /t/ following the first vowel may be the glottalization that terminates the vowel. The actual alveolar closure may occur after this glottalization, and consequently there is no direct acoustic evidence of this closure event. The underlying features for the stop consonant (i.e., [-continuant, -sonorant, +tongue blade, +anterior, +stiff vocal folds]) must be inferred from the sequence of three events: the formant movements in the preceding vowel, the glottalization, and the abrupt onset of syllabic /n/ resulting from opening of the velopharyngeal port. All of the gestures for the segments and features are implemented, and sufficient acoustic cues are available to reconstruct the sequence of gestures and hence the segments and features.

Another modification of the acoustic cues for a consonant is the flapping of a coronal stop consonant in certain phonetic environments (Zue and Laferriere, 1979). Examples are in the sequences writer, rider, atom, and bad apple. In these examples, tongue blade contact is made on the hard palate, as specified for the features of an alveolar stop consonant, but the closure and release are so close together that the corresponding acoustic landmarks essentially merge. This reduction in closure time for the consonant may interfere with the implementation of cues for the voicing feature.

These various modifications of the landmarks and acoustic cues for the features of vowels and consonants in English have implications for the lexical access process. It is of some significance that many if not all of the modifications of landmarks and of cues for features are a consequence of influences from other articulatory gestures associated with nearby segments. Usually the articulatory gestures specified by the inventory of features for a segment, including gestures introduced to provide enhancement, are in fact implemented, but the gestural context or the rapidity of the gestures may influence the acoustic end result, leading to reduction in the strength of the cues or of the landmarks or to elimination of acoustic cues or landmarks. Uncovering of the segments and features that underlie the words in an utterance, then, involves using the acoustic data to make inferences about the gestures that the speaker uses to implement these features, since the gestures tend to bear a closer relation to the features than do the acoustic patterns.

V. DERIVING A SEGMENT- AND FEATURE-BASED REPRESENTATION FROM THE SPEECH SIGNAL

A. Introduction: Steps in the derivation

When presented with an utterance, the task of the human listener, or of a speech recognizer that simulates the human listener, is to derive a discrete or symbolic representation similar to that in Table V through appropriate analysis of the acoustic signal, and, ultimately, to derive the sequence of words. In the proposed model, analysis of the acoustic signal leads to extraction of cues that can be interpreted in terms of articulatory movements. From these cues, the segments and features are estimated. We outline in this section the initial process of deriving from the acoustic signal a representation

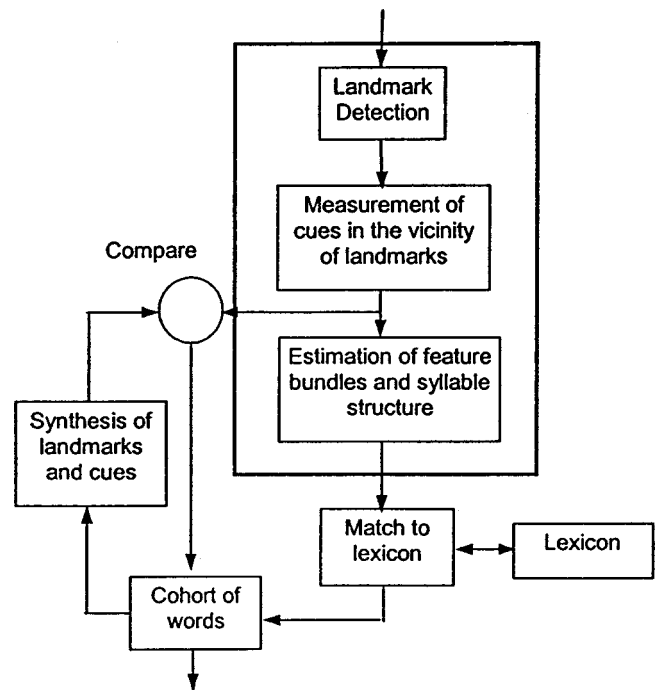


FIG. 2. Block diagram of model of human lexical access. The three components in the box marked by heavy lines are the principal concern of the proposed research (from Stevens, 2000b).

based on segments, features, and syllabic structure, and we illustrate how this derivation proceeds with some examples. Three steps are involved in this process. These steps are schematized by components within the box represented by bold lines in the block diagram in Fig. 2.

In the first step, described in Sec. V B, the locations and types of the basic acoustic landmarks in the signal are established. These acoustic landmarks are identified by the locations of low-frequency energy peaks, energy minima with no acoustic discontinuities, and particular types of abrupt acoustic events. From these acoustic landmarks certain articulatory events can be hypothesized: the speaker produced a maximum opening in the oral cavity, or a minimum opening without an abrupt acoustic discontinuity, or a narrowing in the oral cavity sufficient to create several types of acoustic discontinuity. Estimates of the articulatory-free features are made based on these hypotheses. The second step (Sec. V C) consists of the extraction of acoustic cues from the signal in the vicinity of the landmarks. These cues are derived by first measuring the time course of certain acoustic parameters such as the frequencies of spectral peaks or spectrum amplitudes in particular frequency ranges, and then specifying particular attributes of these parameter tracks. The selection of the acoustic cues is guided by a requirement that they be directly related to the movements or states of various articulators in this time region in the vicinity of the landmarks. The output of this component is a sequence of landmarks, labeled with times and with preliminary estimates of articulator-free features at each landmark, and with the values of a set of acoustic cues attached. Within this component, estimates are also made of the syllable affiliation of the consonants, to the extent that this information is revealed in the acoustic signal. As a part of this second step, the parameters that are derived

from the signal near the landmarks are also examined to determine whether this pattern is consistent with the landmark sequence derived in the initial step of the model. Based on this analysis, new landmarks might be hypothesized, or it might be recognized that some landmarks do not signal the presence of a segment.

In the third step (Sec. V D), the landmarks and acoustic cues derived in the signal processing stage in Fig. 2 are consolidated, and a sequence of feature bundles is derived, as shown by the third block in the figure. The acoustic cues are combined in a way that leads to estimates of the articulator-bound features corresponding to each of the landmarks identified in the first step. A further task in this step is to convert the landmark representation derived in the first step into a representation in terms of underlying segments. For most landmarks there is one-to-one conversion of landmarks to segments for vowels and glides. For consonants, there are two abrupt landmarks (corresponding to an articulatory closure and release). These two landmarks must be converted to a single consonant segment. At this level, the derived segments, the features, and their combinations must be consistent with the patterns that are present in syllables in words in the lexicon, although acoustic evidence for some segments and features may be missing due to casual speaking or external interference, for example, by noise.

The part of the model outside the highlighted box in Fig. 2 looks ahead to the problem of using the estimated segments and features for an utterance, together with the lexicon, to propose a sequence of words. There could be more than one hypothesis concerning the words or word sequences, particularly since there may be a low confidence in the estimates for some features. A final step in the lexical access process would be to test whether each hypothesized sequence is consistent with the original acoustic pattern. This testing involves an internal synthesis of the main acoustic landmarks and cues that would be exhibited by each hypothesized sequence. In particular, the possible sequences of landmarks, together with acoustic parameters around these landmarks, are synthesized. These internally generated landmarks and parameters are matched against the observed landmarks and parameters, and the sequence that gives the best match is selected. The synthesis of the acoustic landmarks and parameters from a hypothesized word or word sequence can be done with full knowledge of the context in which the sequence occurs, and consequently more information is available to help in estimating the landmarks and parameters. In the bottom-up analysis that leads to the hypothesized cohort, this context may not be available, and consequently the feature estimates may be less robust. The process of deriving potential word sequences and the details of the final analysis-by-synthesis step (Stevens and Halle, 1967) are not developed in this article. The derivation of word sequences and their meaning from the acoustic signal also utilizes linguistic knowledge at a level higher than the phonological representation of lexical items. The role of these higher-level sources of linguistic knowledge is not addressed here. The principal concern of this article is the operations in the blocks within the rectangular box in Fig. 2.

B. Detection of acoustic landmarks and estimation of articulator-free features

The initial step in the analysis is to determine the locations of the vowel, glide, and consonant landmarks. Roughly speaking, the vowel landmarks are the places in the signal where there is a maximum in amplitude in a frequency band in the range of the first formant frequency. These places are usually where the first formant frequency is maximally high, and correspond roughly to the times when the oral cavity is maximally open during a syllable. Additional cues for landmark locations come from the fact that there are constraints on the locations of these vowel landmarks. For example, the time between the vowel landmarks is rarely shorter than 120 ms, and, except when there is a pause, is rarely longer than about 350 ms in running speech. Thus there are certain rhythmic aspects of running speech that place some limits on the spacing of the vowel landmarks. The relative amplitude of the maximum for a vowel landmark can be useful for estimating the degree of prominence of the vowel. Examples of the amplitude changes within a vowel have been shown in Fig. 1(a). Procedures for estimating vowel landmarks have been developed and evaluated by Howitt (2000). Earlier work on the detection of syllable nuclei has been reported by Mermelstein (1975).

It has already been observed that any method based on detection of maxima of parameters like amplitude and first-formant frequency will not always generate a landmark for each syllabic nucleus in the underlying representation of running speech. For certain vowel sequences, particularly when one vowel is reduced, only one landmark may be detected. Further analysis of acoustic parameters within the sequence is needed to uncover the presence of more than one vowel. This analysis examines the formant movements primarily of $F1$ and $F2$ on either side of the putative landmark to determine whether the direction and magnitude of these movements are sufficient to suggest the presence of an adjacent vowel. (See Sec. V C.)

The consonantal landmarks are places in the sound where particular types of spectral discontinuities occur. These discontinuities are the result of consonantal closure or release movements by one of the three articulators: lips, tongue blade, and tongue body. The constrictions that give rise to these landmarks are always formed in the oral cavity. A landmark caused by forming a consonantal constriction in the oral cavity has certain types of spectral change that result from rapid changes in the cross-sectional area of the constriction near the landmark.

Other types of acoustic discontinuities can occur as a consequence of closings or openings of the soft palate or laryngeal or pharyngeal movements. These discontinuities have a different acoustic character, and do not qualify as consonantal landmarks in the sense defined here, since they are not produced by a closure or release of one of the oral articulators and therefore do not mark the occurrence of a consonant segment. Further analysis of the signal in the vicinity of the preliminary estimates of consonantal landmark locations is required to separate the bona fide landmarks from these other discontinuities. This analysis examines the formant movements on the vocalic side of each discontinuity.

If these movements are small and/or slow, it is assumed that the discontinuity is not produced by the formation of a closure or release by an oral articulator. The existence of these discontinuities can, however, provide cues for some of the features and for the existence of certain segments. At this stage in the analysis, then, it is assumed that the presence of these “nonconsonantal” discontinuities is marked.⁶

Examples of the locations of the consonantal landmarks are shown at the top of the spectrogram in Fig. 1(a). For certain consonant sequences, an acoustic landmark may not be manifested in the sound for every consonant release and closure, particularly when two stop consonants with different places of articulation occur in sequence.

Each consonantal landmark can readily be further categorized in terms of the articulator-free features that underlie the consonant—the features [sonorant], [continuant], and [strident]. The decision concerning the feature [sonorant] is based largely on the presence or absence of strong vocal-fold vibration on both sides of the landmark, since there is no increase in intraoral pressure, and the pressure across the glottis is the full subglottal pressure. One landmark for a sonorant consonant will always be adjacent to a vowel or a glide. In the case of a landmark produced by a nonsonorant consonant, the consonant is identified as [–continuant] or as [+continuant] depending on whether frication noise is continuous on one side of the landmark. For consonants identified as [+continuant], the main cue for the feature [strident] is the high-frequency amplitude of the frication noise in relation to an adjacent vowel. Some initial progress in developing algorithms for detecting the consonant landmarks and for estimating the associated articulator-free features has been reported by Liu (1996). Extensions of this work for nasal consonants have been reported by Chen (2000).

A glide can occur only immediately adjacent to a vowel in English. Thus if a glide landmark is to be detected it will always occur adjacent to a vowel landmark, with no intervening consonant landmark. In prevocalic position, a glide is usually characterized by a narrowing of the airway in the oral cavity, and hence by a low first-formant frequency, a reduced low-frequency amplitude in relation to the following vowel, and smooth transitions of formant frequencies and of the amplitudes of the formant peaks between the glide and the vowel. Examples of glide landmarks are labeled on the spectrogram in Fig. 1(b). A preliminary algorithm for locating these glide landmarks has been developed by Sun (1996).

Glides can also be implemented immediately following a vocalic nucleus. Such an “offglide” is often seen in diphthongs such as /qj/ and /aw/, where there is a relatively slow and continuous movement of the first and second formant frequencies after the vocalic nucleus /a/. The landmarks for these offglides are placed toward the end of this formant movement where the narrowing of the airway in the oral cavity is most extreme. At the initial landmark-detecting stage, offglides (and some prevocalic glides) may often not be detected through simple measures of amplitude and first-formant frequency. The presence of these glides must be determined at a later stage when articulator-bound features for the vowel are estimated, based on other parameters that are extracted from the signal.

Estimation of the locations of acoustic landmarks is, for the most part, a process that examines local acoustic properties, and is not generally influenced by more remote acoustic events. However, associating these landmarks with underlying segments and their articulator-free features, and postulating segments not directly signaled by the landmarks, may require additional analysis that examines a broader context. (See Sec. V C.)

C. Toward estimation of acoustic cues relevant to articulator-bound features

The detection of a peak landmark or a valley landmark is usually acoustic evidence that a vowel or a glide occurred in the linguistic representation underlying the speaker’s utterance. Acoustic cues that provide evidence for the positions and movements of the articulators that can lead to estimation of the features for a vowel or a glide are expected to be found in the vicinity of these respective landmarks.

The detection of a particular type of abrupt event in the signal is evidence that a closure or narrowing is made by a primary consonant articulator or that a release has been made by such an articulator. Each consonant has an articulatory closure and release (except for consonant sequences produced with the same major articulator). Thus there are two articulatory events when a consonant is produced—a closure and a release—although, as already noted, one of these two events may not always be evident in the signal. Acoustic cues for the articulatory states and movements on which the articulator-bound features for the consonant are based reside in the vicinity of the acoustic landmarks.

The landmarks, then, define the centers or regions in the signal where acoustic parameters are examined, and, based on this examination, cues are extracted. Interpretation of these cues leads to hypotheses as to what the various articulators are doing in the vicinity of the landmarks. We propose here an inventory of acoustic parameters that should be extracted from the signal. The acoustic cues are derived by sampling these parameters (or changes in the parameters) at particular times in the vicinity of landmarks. The parameters fall into ten categories that provide evidence for relevant configurations and movements of the supralaryngeal and laryngeal structures and the state of the respiratory system. Parameters in the first five categories relate to regions of the signal where there is no major constriction in the vocal tract and the sound source is at or near the glottis. We refer to such regions loosely as vocalic regions. Parameters in the next three categories provide information about the supraglottal and laryngeal states during time intervals when there is a consonantal constriction. The ninth category describes parameters that can potentially lead to estimates of changes in subglottal pressure in an utterance, particularly at the initiation and termination of a phrase, and the tenth category is concerned with temporal characteristics based on times at which landmarks are located.

Here is the proposed list of parameters:

- (1) Acoustic parameters related to the position of the tongue body and to lip rounding. These parameters are measured when there is an acoustic source at the glottis,

there is no nasalization, and the vocal tract above the glottis is not sufficiently constricted to create a significant increase in supraglottal pressure. In the vicinity of vowel, glide, and consonant landmarks, these parameters are the formant frequencies and their bandwidths (or, equivalently, the relative amplitudes of the formant prominences). Interpretation of these formant parameters in terms of tongue-body positions and lip rounding may depend on nasalization [item (2) below] and on the glottal configuration [item (5)].

- (2) Parameters that are related to the presence of a velopharyngeal opening in a vocalic region as in (1). These parameters include the amplitude of the F1 prominence in relation to the spectrum amplitude at low frequencies (200–300 Hz) and in the 1000-Hz range (Hattori *et al.*, 1958; Chen, 1997).
- (3) Parameters that describe the spectrum change at times when there is rapid motion of articulators, particularly the lips and the tongue blade. In this same region within which there is an acoustic source at the glottis, there are times that the formant frequencies move very rapidly, particularly near a release or closure for a constant. Cues for the consonant place of articulation reside in these rapid spectral changes, and may be different from those in item (1) above.
- (4) The frequency of glottal vibration. This is the principal parameter indicating vocal-fold stiffness when the vocal folds are vibrating. This parameter is present when the vocal folds are vibrating during a vowel, a glide, or a sonorant consonant.
- (5) Parameters from which the state of the glottis in a vocalic region can be estimated. These parameters include measures of the low-frequency spectrum shape (such as $H1 - H2$, where $H1$ and $H2$ are the amplitudes of the first two harmonics), the spectrum tilt (such as $H1 - A3$, where $A3$ is the amplitude of the third formant prominence), the bandwidth of $F1$ (as inferred from $H1 - A1$), and a measure of the amount of noise in the spectrum at high frequencies (Klatt and Klatt, 1990; Hanson, 1997). These parameters also indicate whether or not there is glottal vibration and whether aspiration noise is present.
- (6) Cues for the place of articulation for an obstruent consonant, as determined from the spectrum shape of the friction noise, and by its amplitude in relation to an adjacent vowel. When there is a raised intraoral pressure, as for an obstruent consonant, friction noise may be generated in the vicinity of the oral constriction, either as a brief burst (for a stop consonant) or as continuous noise (for a fricative).
- (7) Parameters relating to the state of the glottis and of the vocal folds within the region when there is an increased supraglottal pressure. Continued vocal-fold vibration throughout the obstruent region is evidence for slackened vocal folds, while lack of vocal-fold vibration is evidence for stiffened vocal folds near consonant release and for spread or constricted glottis near consonant closure following a vowel.
- (8) Parameters that help to determine the state of the velo-

pharyngeal opening and place of articulation for a nasal consonant, or, for a liquid, the special state of the tongue blade. These parameters are measured during the nasal murmur or the constricted region for a liquid, where there is a low-frequency first formant.

- (9) Parameters providing information concerning the subglottal pressure. These parameters are especially important near the beginning and end of an utterance or adjacent to a pause, where the acoustic cues for certain vowel and consonant articulations are likely to be modulated because of the changing subglottal pressure.
- (10) Parameters based on measurements of the times between landmarks or between landmarks and other events such as onset of glottal vibration. These parameters provide information about timing, and these in turn provide cues for certain features of vowels and consonants.

In the vicinity of a landmark defined by a peak in low-frequency amplitude (a vowel landmark), the acoustic analysis must lead to cues derived from parameters of the type in item (1), with additional help from items (2), (4), and (5) and possibly (8) in the case of syllabic nasals and liquids. The same inventory applies to so-called glide landmarks. In the vicinity of an abrupt landmark that signals a consonantal closure or release, there are cues that are derived from parameters measured in the vocalic region adjacent to the landmark as well as in the region on the other side of the landmark where there is a consonantal constriction (Stevens, 2000a). The cues, then, are based on the types described in items (1)–(5) in the vocalic regions, and (6)–(8) in the constricted regions, depending on the articulator-free features. As noted, cues derived from item (9) are invoked at phrase boundaries. Parameters related to timing [item (10)] form the basis for several cues for vowel and consonant place features and to voicing for consonants.

There are a number of acoustic cues that might be extracted from the parameters listed above in order to contribute to identification of the various features in running speech. The details of these acoustic cues and their effectiveness in identifying the features are beyond the scope of this article. We give one illustration of this cue-selection process, however, by listing some of the cues for one class of features—the features that define the place of articulation for stop consonants. These cues include measures of the first two or three formant frequencies and their movements in the vowel adjacent to the consonant landmark (e.g., Kewley-Port, 1982; Sussman *et al.*, 1991; Manuel and Stevens, 1995); the spectrum amplitude of the release burst at high frequencies relative to midfrequencies (e.g., Fant, 1960, 1973; Stevens, 1998); the spectrum amplitude of the burst in particular frequency ranges in relation to the spectrum amplitude of the vowel immediately adjacent to the landmark (e.g., Ohde and Stevens, 1983); and the duration of the friction noise burst (e.g., Lisker and Abramson, 1964; Fant, 1973; Hanson and Stevens, 2000). All of these cues in one way or another define attributes that are closely related either to (1) the location of the constriction along the oral cavity (e.g., formant transitions for velars and labials, burst spectra for all places

of articulation), (2) the identity of the articulator that forms the constriction (e.g., burst duration and rates of movement of the formants), or (3) an enhancing gesture that characterizes the forward movement of the tongue body adjacent to the landmark for an alveolar consonant (e.g., F_2 and F_3 movements adjacent to the landmark). A similar catalog of cues for other features could be listed.

Derivation of the time course of parameters in the vicinity of landmarks has two functions other than providing a basis for specifying cues that can be combined to estimate distinctive feature values. One of these functions is to allow preliminary estimates of the syllable affiliation of consonants, and the other is to verify or to modify the initial assignment of articulatory-free features to landmarks.

Although syllable affiliation cannot always be estimated with confidence from acoustic analysis, some cues are available in the signal. One example is the delay in onset of glottal vibration following the release of a stop consonant. This delay, together with the presence of aspiration during the delay interval, can be seen in the acoustic parameters that are extracted following the release of the stop consonant. When these attributes are present in the signal, the stop consonant is in syllable-initial position. On the other hand, if the acoustic parameters provide evidence for glottalization at the closure landmark for a stop consonant, the consonant is probably syllable-final. In a vowel preceding the closure landmark for a nasal consonant, nasalization can be observed, and this nasalization begins a few tens of milliseconds preceding the consonant closure if the consonant is syllable final. When the nasal consonant is affiliated with the following vowel, the extent of nasalization in the preceding vowel is considerably less extensive (Krakow, 1993). Differences in the time course of formant parameters and formant amplitude changes can also be observed in syllable-initial and syllable-final liquid consonants (Sproat and Fujimura, 1993).

Tracking of acoustic parameters related to articulation can also provide evidence either for additional segments not detected by simple landmark estimation or for landmarks that are inadvertently inserted but which do not mark the presence of a vowel, consonant, or glide segment. For example, when a sequence of two vowels shows only one low-frequency peak, and hence only one acoustic landmark, the trajectories of the first two formants over a few tens of milliseconds preceding and following the landmark should be sufficient to determine whether or not a sequence of two vowels gave rise to these trajectories. In this case, a second segment is hypothesized, and a “pseudo-landmark” is inserted in the appropriate region.

An example of an inadvertent insertion of a landmark is the production of a glottal stop at the onset of a vowel-initial word (e.g., at the onset of the second word that sometimes occurs in the sequence *two apples*). A glottal onset here might be detected as a landmark representing a consonant release. Further analysis at the beginning of the following vowel would show, however, the presence of glottalization, coupled with the lack of consonantal formant movements immediately following the onset. This acoustic pattern is not the product of the release of a narrowing formed by an oral

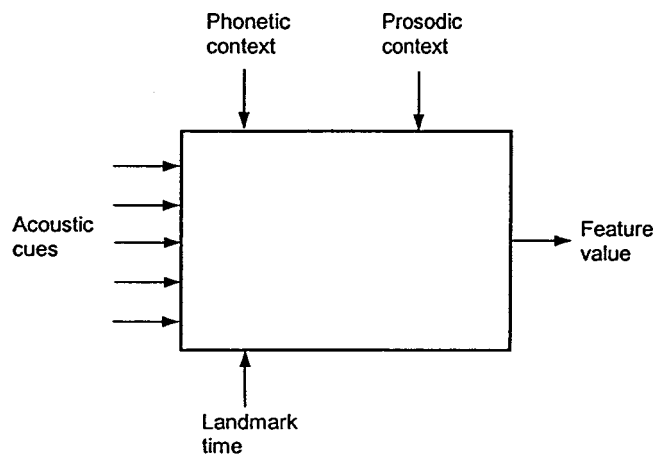


FIG. 3. Schematic representation of a module for estimating an articulator-bound feature (from Stevens, 2000b).

articulator, and hence is not a bona fide consonant landmark. However, the presence of the glottal stop should be noted, since it provides a possible cue for word onset—a cue that can be useful at a higher level when lexical candidates are determined.

D. Estimating the underlying segments and the corresponding articulator-bound features

Once the sequence of landmarks has been identified, and a set of acoustic cues has been evaluated in the vicinity of each landmark, the next step is to transform this graded landmark/cue pattern into a symbolic or quantal description consisting of a sequence of feature bundles. In the vicinity of each landmark, certain acoustic parameters are extracted depending on the type of landmark. The values of these parameters, or the changes that occur in these parameters, provide acoustic cues that are relevant to estimation of the articulator-bound features for the segments. These cues are combined or weighted to obtain estimates of the features. The particular combination of cues and their weighting usually depends on the context in which a landmark occurs. That is, the value of a particular feature (+ or -) associated with a landmark-derived segment depends not only on what the articulators are doing around the time of the landmark but also on the effect of instructions to the articulators from segments that precede or follow the segment that underlies the landmark.

We propose that the estimation of each feature is carried out in a specialized module, as represented schematically in Fig. 3. The inputs to the module are the acoustic cues that are relevant to the feature, and the output is an estimate of the feature as + or -. In addition, the output gives an estimate of the confidence of this value of the feature. (A simple method for specifying the confidence of a feature estimate would use a two-point scale: if a value of + or - for a feature is estimated with high confidence, this value is marked in the output. If the estimate of the feature value has low confidence, no value is entered for this feature.) The module also has inputs that specify the phonetic and prosodic context of the feature for which the model is designed. It is assumed that modules that perform these types of functions

are present in the listener's brain. It is supposed that such modules exist in some elementary form in the child that is learning language, and that experience helps to fill in details such as additional cues and the effects of context, so that the modules become more elaborated based on continued exposure to language.

There is a module of the type shown in Fig. 3 for each articulator-bound feature or group of features. A list of these modules for English includes (1) place of articulation for consonants, (2) the voicing feature for obstruent consonants, (3) the feature [nasal], (4) identification of liquid consonants, (5) the feature [back] for vowels and glides, (6) the features [high] and [low] for vowels, and (7) the feature [advanced tongue root] (or tenseness) for vowels. It is noted that a module is activated for each consonant landmark, although when a consonant is in intervocalic position there are two landmarks for the same consonant. If the feature estimates derived from the modules for the closure and release landmarks are the same (and if the time between landmarks is appropriate for a single segment rather than a geminate), then these two landmarks are merged, and a single segment is proposed. It is possible that the confidence in the feature estimates for this combined segment is greater than the confidence based on each landmark separately. The gain achieved by combining landmarks has been examined for the voicing feature by Choi (1999).

From the listings of features in Tables III–V, it can be seen that, once the articulator-free features associated a landmark have been established, the number of articulator-bound features that is needed to completely specify a segment is relatively small. For example, in the case of consonants that are [–sonorant, –continuant] (i.e., stop consonants), the task of the modules is simply to specify place of articulation ([lips], [tongue blade], or [tongue body]) and the voicing feature ([stiff vocal folds]). Consonants that are [+sonorant] also require just two or three modules to estimate the articulator-bound features. In the case of vowels three modules are necessary, and for glides the number is even fewer. We are dealing, therefore, with a relatively sparse specification of articulator-bound features, and the number of modules that are called into action for a given landmark with its attendant articulator-free features is generally in the range 2 to 4.

The details of each of these modules, including the selection and design of acoustic cues that form possible inputs for each module, are beyond the scope of this article. Some progress toward implementing the modules for some consonant features is reported elsewhere (Choi, 1999; Stevens *et al.*, 1999; Chen, 2000).

VI. SUMMARY AND DISCUSSION

The central concept of the proposed model of lexical access is the representation of words in memory as sequences of segments, each consisting of a bundle of binary distinctive features. Each word in a language generally has just one such representation in the lexicon. The distinctive features define the contrasts in the language: a change in one feature in one segment can potentially generate a different word. Independent of what language is involved, there is a

universal inventory of features that are determined by the properties of the vocal tract as a generator of sounds with perceptually distinctive acoustic properties. Each feature has a defining acoustic and articulatory correlate (although other correlates may also be employed). The features that are used contrastively in a given language are a subset of this universal inventory.

There are two kinds of distinctive features: articulator-free and articulator-bound. Articulator-free features specify classes of articulatory actions but are not tied to particular articulators. They give rise to several types of acoustic landmarks that indicate the presence of segments, and establish regions in the signal where acoustic evidence for the articulator-bound features can be found. Articulator-bound features specify which articulators are involved in producing the landmarks, and how these articulators are positioned and shaped. When the articulator-free features have been established, the number of articulator-bound features that are needed to fill out the bundles of segments is relatively sparse (three to four features, on average).

When a particular articulator-bound feature is specified in a segment within a word that a speaker is producing, variability can occur in the acoustic pattern for that feature. This variability arises for at least two reasons. One type of variability occurs because, in addition to the primary articulatory action specified by the feature, the speaker recruits additional articulatory actions to enhance the perceptual contrast defined by the feature when the segment is in a particular phonetic or prosodic environment. These enhancing gestures may not only strengthen the perceptual salience of the defining acoustic pattern for the feature, but may also introduce additional acoustic properties that can provide a listener with further acoustic cues for the presence of the feature. There may also be other articulatory and acoustic attributes that are biomechanical consequences of implementation of the feature, and that provide additional enhancement to the defining acoustic correlates of the feature. Thus the enhancing gestures can contribute a number of acoustic cues to the identification of a feature depending on the syllable position and the prosodic environment in which the segment occurs. A second type of variability occurs because of overlap in the articulatory gestures that are involved in producing adjacent segments, causing a weakening or obscuring of some of the acoustic cues that would otherwise help to uncover the underlying features.

Estimation of the features from acoustic processing of the speech signal is often straightforward. The defining acoustic properties for the features, together with some additional cues, are evident in the signal, and the effects of overlapping of gestures for nearby segments are minimal. Frequently, however, this is not the case. The listener must be aware of cues for both the defining and the enhancing gestures, and must be able to account for the fact that some of these acoustic cues may be weakened or eliminated due to gestural overlap. From a processing point of view, the inventory of acoustic cues for a feature must be selected to reflect the articulatory actions that created the acoustic pattern, since the enhancements and the overlapping are best defined in terms of articulatory gestures. Once the cues for an

articulator-bound feature have been extracted, these cues must be weighted or combined in some way to yield an estimate of the feature. These combinations of cues must be learned by a speaker of the language.

The lexical-access model described here has several attributes that differ somewhat from those of other models, particularly models that are more data driven. Three of these attributes are listed here.

- (1) There is generally only one representation of each word in the lexicon, and that representation is in terms of bundles of distinctive features. For a given segment, the output of the model is required to postulate a pattern of distinctive features consistent with the patterns that are used in the lexicon. While variability can lead to many ways of producing words, these multiple representations do not appear in the lexicon. Other models tend to deal with variability by proposing several possible pronunciations for words, these pronunciations being specified in terms of acoustic units called phones or phonemelike units (Zue *et al.*, 1990; Rabiner and Juang, 1993; O'Shaughnessy, 2000).
- (2) The analysis of the signal proceeds by identifying a sequence of landmarks, which provide evidence for the sequence of underlying segments. The concept of an acoustic segmentation in which sequences of pieces of the waveform are labeled with phones is not consistent with the proposed model. It is suggested that labeling of an utterance be done at least in terms of landmarks, since it is proposed in the model that landmark identification is a critical first step.
- (3) The selection of acoustic cues in the model is based on the view that variability in articulation is guided by a few principles, and is rather constrained. These acoustic cues are designed to provide information about relevant articulatory states and movements. A spectral representation of the signal based on acoustic patterns that are not specifically oriented to the estimation of articulation is expected to show substantially greater variability than one that is oriented to this goal. Use of such an acoustic representation requires considerable training from a database of utterances in order to describe variability that exists in the acoustic patterns.

In the model proposed here, words in running speech are accessed by assuming a mental representation of words in terms of segments and features, and identifying the words through an analysis that uncovers the segments in the word and the features that define the segments. Such a view of lexical access has not been universally accepted (e.g., Klatt, 1979). A major cause for the skepticism for the proposed approach is the apparent variability in the acoustic manifestation of a feature or of a word, and hence the apparent lack of correspondence between acoustic parameters and the distinctive features. As we begin to acquire an understanding of the sources of variability in the acoustic manifestation of a segment, it is hoped that the link between acoustic patterns and features will become more transparent, and that principles governing variability can be better defined.

Much further research is needed to fill out the details of

the proposed model. For example, while some illustrations of the use of enhancing gestures have been given in Keyser and Stevens (2001), a more thorough study of enhancement both in English and across a variety of languages is needed. Some principles governing the selection of acoustic parameters which must be involved in feature identification have been described here, but it will be necessary to specify in more detail the acoustic cues that are to be derived from these parameters and how these cues should be combined in a variety of listening situations, particularly in noise.

ACKNOWLEDGMENTS

Development of the ideas in this lexical-access model was strongly influenced by discussions with a number of colleagues and students. Acknowledged with special thanks are the contributions of Stefanie Shattuck-Hufnagel, Sharon Manuel, Jay Keyser, Morris Halle, Marilyn Chen, Elizabeth Choi, and Wil Howitt. This research was supported in part by Grant No. DC02978 from the National Institutes of Health.

¹Throughout this article we will frequently use the terms "segment" and "feature." These terms refer strictly to the abstract units in terms of which words are represented in the lexicon of a speaker/listener. The term "segment" does not refer directly to a portion of the speech waveform and does not have temporal characteristics. A "feature" is a linguistic entity, and does not refer directly to an attribute of the acoustic signal. Landmarks provide evidence for underlying segments, and acoustic properties in the vicinity of landmarks provide cues for the features of these segments.

²The feature [advanced tongue root] is used here to distinguish between vowels such as /i/ or /e/ ϵ /. In some formulations, a feature [tense] is used to capture this distinction: /i/ is [+tense] and /e/ is [-tense].

³The feature [stiff vocal folds] is related to the feature fortis/lenis as described by Kohler (1984), but is defined here somewhat differently.

⁴The role of perceptual distinctiveness in shaping the acoustic attributes of segment inventories in language has also been persuasively argued by Lindblom (1990) and by Liljencrants and Lindblom (1972). The discussion of enhancement theory in the present article and in Keyser and Stevens (2001) has attempted to draw on this concept of perceptual saliency while retaining (in somewhat modified form) the traditional view of a universal inventory of distinctive features based on primary articulatory and acoustic correlates.

⁵Strictly speaking, it is not necessary to use the feature [distributed] for /ð/ in English, since /ð/ is distinguished from /s/ by the feature [strident], as noted earlier. The shaping of the tongue blade for /ð/ and /θ/, with a concomitant adjustment of the tongue body to a more backed position than for /s/, can be considered as a gesture that prevents the airstream from impinging on the lower incisors, and hence enhances the distinction between the [+strident] and [-strident] fricatives.

⁶The use of acoustic discontinuities of both types (i.e., those formed by constricting the vocal tract with an oral articulator and those formed in other ways) has been developed by Glass (1988) as an effective way of segmenting the acoustic stream into a sequence of units. This type of acoustic segmentation has been incorporated into the front end of an existing automatic speech recognition system (Zue *et al.*, 1990).

Browman, C. P., and Goldstein, L. (1990). "Tiers in articulatory phonology," in *Papers in Articulatory Phonology I: Between the Grammar and Physics of Speech*, edited by J. Kingston and M. E. Beckman (Cambridge U.P., Cambridge), pp. 341–376.

Chen, M. Y. (1997). "Acoustic correlates of English and French nasalized vowels," *J. Acoust. Soc. Am.* **102**, 2360–2370.

Chen, M. Y. (2000). "Nasal detection module for a knowledge-based speech recognition system," in *Proceedings 6th International Conference on Spoken Language Processing (ICSLP 2000)*, Vol. IV, pp. 636–639, Beijing, China.

- Chistovich, L. A., and Lublinskaya, V. V. (1979). "The 'center of gravity' effect in vowel spectra and critical distance between the formants: Psychoacoustical study of the perception of vowel-like stimuli," *Hear. Res.* **1**, 185–195.
- Cho, T., and Ladefoged, P. (1999). "Variation and universals in VOT: evidence from 18 languages," *J. Phonetics* **27**, 207–229.
- Choi, J.-Y. (1999). "Detection of consonant voicing: A module for a hierarchical speech recognition system," Ph.D. thesis, Massachusetts Institute of Technology, Cambridge, MA.
- Chomsky, N., and Halle, M. (1968). *The Sound Pattern of English* (Harper and Row, New York).
- Clements, G. N. (1985). "The geometry of phonological features," *Phonology Yearbook* **2**, 225–252.
- Clements, G. N., and Keyser, S. J. (1983). *CV Phonology* (MIT, Cambridge, MA).
- Cranen, B., and Boves, L. (1987). "On subglottal formant analysis," *J. Acoust. Soc. Am.* **81**, 734–746.
- Cutler, A., and Carter, D. M. (1987). "The predominance of strong initial syllables in the English language," *Comput. Speech Lang.* **2**, 133–142.
- Delgutte, B., and Kiang, N. Y. S. (1984). "Speech coding in the auditory nerve: IV. Sounds with consonant-like dynamic characteristics," *J. Acoust. Soc. Am.* **75**, 897–907.
- Diehl, R. L. (1991). "The role of phonetics within the study of language," *Phonetica* **48**, 120–134.
- Diehl, R. L., Molis, M. R., and Castleman, W. A. (2001). "Adaptive design of sound systems," in *The Role of Speech Perception in Phonology*, edited by E. Hume and K. Johnson (Academic, San Diego), pp. 123–139.
- Fant, G. (1960). *Acoustic Theory of Speech Production* (Mouton, The Hague).
- Fant, G. (1973). *Speech Sounds and Features* (MIT, Cambridge, MA).
- Fujimura, O. (1997). "Syllable features and the temporal structure of speech," in *Proc. of LP'96: Typology: Prototypes, Item Orderings and Universals*, edited by B. Palek (Charles U.P., Prague), pp. 53–93.
- Glass, J. R. (1988). "Finding acoustic regularities in speech: Applications to phonetic recognition," Ph.D. dissertation, Massachusetts Institute of Technology, Cambridge, MA.
- Gow, Jr., D. W. (2001). "Assimilation and anticipation in continuous spoken word recognition," *J. Memory Lang.* **45**, 133–159.
- Gow, Jr., D. W. (2002). "Does English coronal place assimilation create lexical ambiguity?" *J. Exp. Psychol. Hum. Percept. Perform.* **28**, 163–179.
- Gow, D., Melvold, J., and Manuel, S. Y. (1996). "How word onsets drive lexical access and segmentation: Evidence from acoustics, phonology, and processing," in *Proc. 1996 International Conference on Spoken Language Processing* (University of Delaware and Alfred I. duPont Institute, Philadelphia, PA), pp. 66–69.
- Halle, M. (1992). "Features," in *Oxford International Encyclopedia of Linguistics*, edited by W. Bright (Oxford U.P., New York).
- Halle, M. and Stevens, K. N. (1971). "A note on laryngeal features," MIT Research Laboratory of Electronics Quarterly Progress Report 101, pp. 198–213.
- Halle, M. and Stevens, K. N. (1991). "Knowledge of language and the sounds of speech," in *Music, Language, Speech and Brain*, edited by J. Sundberg, L. Nord, and R. Carlson (MacMillan, London), pp. 1–19.
- Hanson, H. M. (1997). "Glottal characteristics of female speakers: Acoustic correlates," *J. Acoust. Soc. Am.* **101**, 466–481.
- Hanson, H. M., and Stevens, K. N. (2000). "Modeling stop-consonant releases for synthesis," *J. Acoust. Soc. Am.* **107**, 2907(A).
- Hattori, S., Yamamoto, K., and Fujimura, O. (1958). "Nasalization of vowels in relation to nasals," *J. Acoust. Soc. Am.* **30**, 267–274.
- House, A. S., and Fairbanks, G. (1953). "The influence of consonantal environment upon the secondary acoustical characteristics of vowels," *J. Acoust. Soc. Am.* **25**, 105–113.
- Howitt, A. W. (2000). "Automatic syllable detection for vowel landmarks," Ph.D. dissertation, Massachusetts Institute of Technology, Cambridge, MA.
- Kewley-Port, D. (1982). "Measurement of formant transitions in naturally produced stop consonant-vowel syllables," *J. Acoust. Soc. Am.* **72**, 379–389.
- Keyser, S. J., and Stevens, K. N. (1994). "Feature geometry and the vocal tract," *Phonology* **11**, 207–236.
- Keyser, S. J., and Stevens, K. N. (2001). "Enhancement revisited," in *Ken Hale: A Life in Language*, edited by M. Kenstowicz (MIT, Cambridge, MA), pp. 271–291.
- Kingston, J., and Diehl, R. L. (1994). "Phonetic knowledge," *Language* **70**, 419–454.
- Klatt, D. H. (1979). "Speech perception: A model of acoustic-phonetic analysis and lexical access," *J. Phonetics* **7**, 279–312.
- Klatt, D. H., and Klatt, L. C. (1990). "Analysis, synthesis, and perception of voice quality variations among female and male talkers," *J. Acoust. Soc. Am.* **87**, 820–857.
- Kohler, K. J. (1984). "Phonetic explanation in phonology: The feature fortis/lenis," *Phonetica* **41**, 150–174.
- Krakow, R. A. (1993). "Nonsegmental influences on velum movement patterns: Syllables, sentences, stress, and speaking rate," in *Phonetics and Phonology: Nasals, Nasalization, and the Velum*, edited by M. K. Huffman and R. A. Krakow (Academic, San Diego), pp. 87–116.
- Ladefoged, P. (1980). "What are linguistic sounds made of?" *Language* **65**, 485–502.
- Levelt, W. J. M. (1989). *Speaking* (MIT, Cambridge, MA).
- Levelt, W. J. M., Roeloff, A., and Meyer, A. (1999). "A theory of lexical access in speech production," *Brain Behav. Sci.* **22**, 1–75.
- Liljencrants, J., and Lindblom, B. (1972). "Numerical simulation of vowel quality systems: The role of perceptual contrast," *Language* **48**, 839–862.
- Lindblom, B. (1990). "Explaining phonetic variation: A sketch of the H & H theory," in *Speech Production and Speech Modeling*, edited by W. J. Hardcastle and A. Marchal (Kluwer, Dordrecht), pp. 403–439.
- Lisker, L., and Abramson, A. S. (1964). "A cross-language study of voicing in initial stops: Acoustical measurements," *Word* **20**, 527–565.
- Liu, S. A. (1996). "Landmark detection for distinctive feature-based speech recognition," *J. Acoust. Soc. Am.* **100**, 3417–3430.
- Manuel, S. Y. (1991). "Some phonetic bases for the relative malleability of syllable-final versus syllable-initial consonants," in *Proceedings 12th International Congress of Phonetic Sciences, Aix-en-Provence, Vol. V*, pp. 118–121.
- Manuel, S. Y. (1995). "Speakers nasalize /ð/ after /n/, but listeners still hear /ð/," *J. Phonetics* **23**, 453–476.
- Manuel, S. Y., and Stevens, K. N. (1995). "Formant transitions: Teasing apart consonant and vowel contributions," in *Proceedings International Conference on Phonetic Sciences, Stockholm, Vol. 4*, pp. 436–439.
- McCarthy, J. J. (1988). "Feature geometry and dependency: a review," *Phonetica* **45**, 84–108.
- Mermelstein, P. (1975). "Automatic segmentation of speech into syllabic units," *J. Acoust. Soc. Am.* **58**, 880–883.
- Ohde, R. N., and Stevens, K. N. (1983). "Effect of burst amplitude on the perception of stop consonant place of articulation," *J. Acoust. Soc. Am.* **74**, 706–714.
- O'Shaughnessy, D. (2000). *Speech Communications: Human and Machine* (IEEE, New York).
- Rabiner, L., and Juang, B.-H. (1993). *Fundamentals of Speech Recognition* (Prentice-Hall, Englewood Cliffs, NJ).
- Shattuck-Hufnagel, S. (1992). "The role of word structure in segmental serial ordering," *Cognition* **42**, 213–259.
- Sproat, R., and Fujimura, O. (1993). "Allophonic variation in English /l/ and its implications for phonetic implementation," *J. Phonetics* **21**, 291–311.
- Stevens, K. N. (1972). "The quantal nature of speech: Evidence from articulatory-acoustic data," in *Human Communication: A Unified View*, edited by P. B. Denes and E. E. David, Jr. (McGraw-Hill, New York), pp. 51–66.
- Stevens, K. N. (1989). "On the quantal nature of speech," *J. Phonetics* **17**, 3–46.
- Stevens, K. N. (1998). *Acoustic Phonetics* (MIT, Cambridge, MA).
- Stevens, K. N. (2000a). "Diverse acoustic cues at consonantal landmarks," *Phonetica* **57**, 139–151.
- Stevens, K. N. (2000b). "From acoustic cues to segments, features and words," in *Proceedings 6th International Conference on Spoken Language Processing (ICSLP2000)*, Beijing, China, Vol. 1, pp. A1–A8.
- Stevens, K. N. (2001). "The properties of the vocal-tract walls help to shape several phonetic distinctions in language," in *Travaux du Cercle Linguistique de Copenhague*, Vol. XXXI, pp. 285–297.
- Stevens, K. N., and Halle, M. (1967). "Remarks on analysis by synthesis and distinctive features," in *Models for the Perception of Speech and Visual Form*, edited by W. Wathen-Dunn (MIT, Cambridge, MA), pp. 88–102.
- Stevens, K. N., Manuel, S. Y., and Matthies, M. (1999). "Revisiting place of

- articulation measures for stop consonants: Implications for models of consonant production," in Proceedings 14th International Congress of Phonetic Sciences (ICPhS'99, San Francisco), Vol. 2, pp. 1117–1120.
- Sun, W. (1996). "Analysis and interpretation of glide characteristics in pursuit of an algorithm for recognition," MS thesis, Massachusetts Institute of Technology, Cambridge, MA.
- Sussman, H. M., McCaffrey, H. A., and Matthews, S. A. (1991). "An investigation of locus equations as a source of relational invariance for stop place categorization," *J. Acoust. Soc. Am.* **90**, 1309–1325.
- Syrdal, A. K., and Gopal, H. S. (1986). "A perceptual model of vowel recognition based on the auditory representation of American English vowels," *J. Acoust. Soc. Am.* **79**, 1086–1100.
- Whalen, D. H., Gick, B., Kumada, M., and Honda, K. (1998). "Cricothyroid activity in high and low vowels: Exploring the automaticity of intrinsic F_0 ," *J. Phonetics* **27**, 125–142.
- Zsiga, E. C. (1994). "Acoustic evidence for gestural overlap in consonant sequences," *J. Phonetics* **22**, 121–140.
- Zue, V. W., and Laferriere, M. (1979). "An acoustic study of medial /t, d/ in American English," *J. Acoust. Soc. Am.* **66**, 1039–1050.
- Zue, V. W., Glass, J. R., Goodine, D., Phillips, M., and Seneff, S. (1990). "The SUMMIT speech recognition system: Phonological modeling and lexical access," in Proceedings of the IEEE International Conference on Acoustics, Speech, and Signal Processing, pp. 49–52.

Auditory normalization of French vowels synthesized by an articulatory model simulating growth from birth to adulthood

Lucie Ménard,^{a)} Jean-Luc Schwartz, and Louis-Jean Boë
ICP-INPG, UMR CNRS No. 5009, Université Stendhal, Boîte Postale 25, 38040 Grenoble Cedex 9, France

Sonia Kandel
LPE, UMR CNRS No. 5105, Université Pierre Mendès France, Boîte Postale 47, 38040 Grenoble Cedex 9, France

Nathalie Vallée
ICP-INPG, UMR CNRS No. 5009, Université Stendhal, Boîte Postale 25, 38040 Grenoble Cedex 9, France

(Received 27 March 2001; accepted for publication 17 January 2002)

The present article aims at exploring the invariant parameters involved in the perceptual normalization of French vowels. A set of 490 stimuli, including the ten French vowels /i y u e ø o ε œ ɔ a/ produced by an articulatory model, simulating seven growth stages and seven fundamental frequency values, has been submitted as a perceptual identification test to 43 subjects. The results confirm the important effect of the tonality distance between F1 and f_0 in perceived height. It does not seem, however, that height perception involves a binary organization determined by the 3–3.5-Bark critical distance. Regarding place of articulation, the tonotopic distance between F1 and F2 appears to be the best predictor of the perceived front–back dimension. Nevertheless, the role of the difference between F2 and F3 remains important. Roundedness is also examined and correlated to the effective second formant, involving spectral integration of higher formants within the 3.5-Bark critical distance. The results shed light on the issue of perceptual invariance, and can be interpreted as perceptual constraints imposed on speech production. © 2002 Acoustical Society of America. [DOI: 10.1121/1.1459467]

PACS numbers: 43.71.An, 43.71.Es, 43.70.Bk, 43.71.Bp [KRK]

I. INTRODUCTION

Variability involved in vowel production is large. A major source of variability comes from interindividual differences such as the speaker's age and sex. It is well known that vowels produced by speakers with a smaller vocal tract (children and women) have higher formant values (Peterson and Barney, 1952; Hillenbrand *et al.*, 1995; Lee *et al.*, 1999). Furthermore, fundamental frequency decreases during growth. Considering these important variations, traditional vowel characterization by the first three formant values faces several problems. Peterson and Barney (1952) report that formant values of ten American English vowels uttered by men, women, and children partially overlap in the F1/F2 and F2/F3 acoustic spaces. Despite this overlap, perceivers correctly identify each of the ten vowels. The question therefore arises: what are the parameters involved in the identification of distinct phonological categories?

This question is of major importance regarding the issue of language acquisition, especially in the light of the child–adult speech interaction. Indeed, the emergence of native language phonological categories must take into account the possibility for infants to compare, and hence normalize, their own production to the surrounding speech sounds, and we know they are indeed able to do so (Kuhl and Meltzoff, 1996). In this article, an articulatory model simulating non-

uniform vocal tract growth has been exploited in order to create an extended set of synthesized stimuli, while carefully controlling articulatory and acoustic coherence. These stimuli have been designed to cover the extreme possibilities of vocal tract configurations for growing speakers, from birth to adulthood. The remainder of the article is divided into four parts. First, a brief literature review will be presented in Sec. II. The method and the results will then be described in Secs. III and IV. Comparison of our results with the existing normalization theories and related issues will be addressed in the discussion in Sec. V.

II. INVARIANCE AND NORMALIZATION

During the past decades, several studies have attempted to identify and deal with interindividual variability found in vowel production. At the perceptual level, these normalization procedures all aim at reducing intraclass variability and dispersion of some parameters by seeking invariant determinants of each vowel class. But the level at which these determinants are to be extracted is a subject of debate. Indeed, the invariance problem is claimed to exist in the acoustic signal (Stevens, 1996), in the speech gestures at the articulatory level (Liberman and Mattingly, 1985), or as a trade-off between perceptual requirements and production specification (Lindblom, 1996). The present study focuses on acoustic information.

At the acoustic level, attempts in formant variability normalization can be summarized by two main approaches, defined by the kind of information required by the process.

^{a)}Current address: Université du Québec à Montréal, Département de linguistique et de didactique des langues, C. P. 8888, Succursale Centre-Ville, Montréal H3C 3P8, Canada. Electronic mail: menard@icp.inpg.fr

Following Ainsworth's (1975) terminology, we shall distinguish between intrinsic and extrinsic approaches. In the extrinsic framework, the identification of a given vowel uttered by a speaker relies on a frame of reference established from external information provided by the other vowels of the same speaker. Conversely, in the intrinsic approach, the perception of a vowel is based upon information contained within this given vowel, without referring to any external sources. The invariance problem is here solved by a transformation of spectral characteristics into an appropriate scale, giving rise to a better spectral representation. A few hybrid approaches also exist, which combine concepts from the intrinsic as well as extrinsic theories (Fujisaki and Kawashima, 1968; Ainsworth, 1975).

Intrinsic theories involve various spectral parameters. Observed variability in speech production reveals that, when comparing 5-year-old children to adult male, formant frequency values decrease by about 40%, whereas children's fundamental frequency is about 100% higher than adult male's value (based on data reported by Lee *et al.*, 1999). This nonlinear relationship is also found in the shift, along the F1 and/or F2 dimension, of a perceptual category boundary for different f_0 's. In general, the boundary shift is relatively small. Fujisaki and Kawashima (1968) report an increase from 22% up to 29% for F1, for a 1-oct upward shift of f_0 . The difference is even smaller for Slawson (1968) and Ainsworth (1971), for which the increase is only of 10% and 5% in F1, respectively. Nearey (1989), Miller (1953), and Carlson *et al.* (1970) also note rather small changes in F1 boundary. This nonlinearity is dealt with by a conversion of the Hertz scale into a semi-logarithmic scale, usually the "critical band units" (Bark) scale, based on psychoacoustic experiments (Traumüller, 1981; Syrdal and Gopal, 1986; Potter and Steinberg, 1950). A difference is then estimated between adjacent formant peaks and/or F_0 values. This treatment has been related to the characteristics of relative patterns of excitation along the basilar membrane (Potter and Steinberg, 1950). The role of fundamental frequency and formants has been confirmed by Traumüller (1981), Syrdal and Gopal (1986), Carlson *et al.* (1979), and is taken into account in Miller's (1989) model. The "center of gravity effect," introduced after Chistovich *et al.* (1979), is also crucial in some models of auditory processing of vocalic spectral representations. Perceptual integration of close formants is the basis of effective second formant (F_2') models (Carlson *et al.*, 1970, Bladon and Fant, 1978; Mantakas, 1989). Finally, the question remains unsolved as to whether "time-varying features" (Strange, 1989; Nearey, 1989) are involved in the normalization process. The next section contains a brief literature survey of the parameters deemed to be the main determinants of vowel categories.

A. Openness

The role of f_0 in the normalization process for openness identification has been confirmed by Traumüller (1981), Syrdal and Gopal (1986), and Hoemeke and Diehl (1994). In the analysis of the perception of Bavarian one-formant synthesized vowels, Traumüller (1981) shows the strong correlation between perceived height and the value of the F_1-f_0

difference (in Barks). Results suggest that perceptual category boundaries for the five height degrees, for f_0 ranging from 0 to 350–400 Hz, are located around F_1-f_0 boundaries of 1.2, 2.2, 3.2, and 6 Bark. Beyond an f_0 value around 350 Hz, the pattern changes. Indeed, only the distinction between degrees 1 and 2 is preserved at the 1.2-Bark F_1-f_0 boundary. The difference between the intermediate height vowels (degrees 2 and 3) is seldom perceived and distinction between degrees 4 and 5 relies on the first formant value, without any influence of f_0 . Finally, Traumüller (1991) reports that a large intersubject variability exists in the use of f_0 as a perceptual cue for height.

Syrdal and Gopal (1986), after reanalyzing Peterson and Barney's (1952) data, give support to the role of f_0 in the perception of vowel height in ten American English vowels. The authors propose a two-stage model of auditory treatment. At the first stage, a transformation of frequency values into a specific Bark difference occurs. The second, higher-level, stage consists of a binary classification of specific Bark differences, based on the value of 3 Bark, corresponding to the critical distance of the center of gravity effect (Chistovich *et al.*, 1979). Feature extraction occurs at the latter stage.

However, F_1-f_0 is not found to be a better openness predictor than F_1 , for all American front (Hoemeke and Diehl, 1994) and back vowels (Fahey *et al.*, 1996). Indeed, some categories seem better related to F_1 alone.

B. Place of articulation

According to Syrdal and Gopal (1986), the F_3-F_2 difference would account for the perception of the front-back feature, for American English vowels. A good classification is achieved by this parameter, with front vowels corresponding to a value of F_3-F_2 lower than 3 Bark, and back vowels to a value greater than 3 Bark. On the contrary, Fant (1983), for Swedish, distinguishes between front and back vowels on the basis of F_2-F_1 differences, while the difference between F_2 and f_0 would be a correlate of place of articulation for Hirahara and Kato (1992) and Savariaux *et al.* (1999) (for /u/). Finally, Delattre *et al.* (1952) report that formant averaging in the auditory center of gravity process accounts for the fact that back vowels can be represented by a low-frequency single formant, while front vowels are best synthesized with two energy peaks.

C. Rounding

Rounding identification has been less studied. The F_2-f_0 difference has been proposed as a normalized cue for this feature (Fant *et al.*, 1974). F_2' has also been introduced as a major determinant of vowel rounding able to normalize male and female speakers (Mantakas, 1989). According to Traumüller and Lacerda (1987), F_2' is a correlate of perceived rounding for front vowels, in Turkish and Swedish, whereas the difference between F_2' and F_1 better represents this contrast for back vowels. Mantakas (1989) also suggested that f_0 may have a role as a normalizing parameter, resulting in the $F_2'-f_0$ difference.

TABLE I. Feature analysis of French vowels.

	Front		Back
	Unrounded	Rounded	
High	i	y	u
Mid-high	e	ø	o
Mid-low	ɛ	œ	ɔ
Low	a		

D. The French oral vowel system

The previous sections showed that in order to deal with intersubject variability, several parameters were proposed as normalizing factors. The following experiment was designed to determine the main acoustic parameters involved in the perceptual normalization of French vowels uttered by various “synthetic speakers,” from birth to adulthood. To assess the relevance of attested normalizing factors in the identification of French vowels, we synthesized, with an articulatory model integrating nonuniform vocal tract growth, the ten French oral vowels /i y u e ø o ɛ œ ɔ a/ at different growth stages and different f_0 values.

The French phonological system has a double advantage. First, vowel contrasts are realized along three features: height, place of articulation (front/back), and roundedness for front vowels (see Table I). Second, it does not include phonological tense-lax distinctions, and dynamics do not seem to play an important role in vowel identification, apart from classical vowel reduction phenomena. These specifications allow the manipulation of constant spectral parameters, without considering timing and spectral trajectories.

III. METHOD

A. Overview of the model

Stimuli consist of five-formant vowels generated by formant synthesis with the *Variable Linear Articulatory Model* (hereafter VLAM) developed by S. Maeda (Boë and Maeda, 1997), which integrates knowledge acquired from previous articulatory models with the growth data currently available (Goldstein, 1980). The VLAM model was implemented and tested at ICP in an environment originally developed for an articulatory model of adult speech established from cineradiographic data and derived from a statistical analysis guided by knowledge of the physiology of the articulators. This anthropomorphic model has the advantage that it intrinsically takes into account certain articulatory production constraints: the seven control parameters are directly interpretable in terms of functionally organized articulatory blocks (jaw; labial protrusion and aperture; movement of the tongue body, dorsum, and tip; larynx height). The model generates a two-dimensional mid-sagittal section, as well as the corresponding area function (three-dimensional equivalent), from which it is possible to calculate the harmonic response (transfer function), formant frequencies (resonance maxima), and speech signal (Badin and Fant, 1984). The seven parameters P_i , $i \in \{1..7\}$, are adjustable at a value in the range of ± 3.5 standard deviations. The growth process is introduced by modifying the longitudinal dimension of the vocal tract ac-

ording to two scale factors, one for the anterior part of the vocal tract and the other for the pharynx, interpolating the zone in-between.¹ The evolution of the scale factors was calibrated using the data provided by Goldstein (1980), who reports measurements made on cineradiographic images of children. Nonuniform vocal tract growth can be simulated for a male speaker year by year and month by month. Similarly, f_0 values are adjustable. By default, f_0 at each growth stage evolves following the growth data presented by Beck (1996). The model is thus suitable for use in systematic simulation studies as well as for use in phonetics.

B. Stimuli

1. Formant patterns

Vocal tracts representative of the following ages were simulated: 0, 2, 4, 8, 12, 16, and 21 years old. For each growth stage, articulatory-acoustic prototypes for the ten French oral vowels /i y u e ø o ɛ œ ɔ a/ have been determined using the concept of *Maximal Vowel Space* (hereafter MVS, Boë *et al.*, 1989). If the entire input space of command parameters is explored—while satisfying the conditions for vowel production—one can simulate the maximal F1/F2/F3 acoustic space appearing at the output. All possible oral vowels are thus situated within the limits of this space. This kind of extended generation method allows possibilities for maximal distinctiveness to be described precisely, and permits an optimal choice of prototypical realizations.

In the present study, using VLAM, we first generated MVS for a grid of command parameters P_i ($-3.5 < P_i < +3.5$), by a uniform distribution, constraining the minimal intraoral constriction and lip area to be identical for adults and children (constriction area of 0.3 cm² and lip area of 0.1 cm²). For the neonate vowel space, these thresholds were decreased to 0.1 cm² for constriction area and 0.01 cm² for lip area.² The MVS was simulated by setting the model to seven growth stages respectively corresponding to a 4-week-old infant, a 2-, 4-, 8-, and 12-year-old child, a 16-year-old adolescent, and a 21-year-old adult male. Note that we assume each speaker displays the same sensori-motor control capacities.³ According to Goldstein’s (1980) data, the vocal tract configuration of an adult female, in terms of overall length and ratio of the pharyngeal versus oral cavity lengths, corresponds to the vocal tract of a 16-year-old male. It seems thus reasonable to consider this growth stage as representative of an adult female. The following vocal tract length values were obtained, for a neutral articulatory configuration, at each growth stage: 7.70 cm (newborn), 9.92 cm (2 years old), 10.67 cm (4 years old), 11.91 cm (8 years old), 13.52 cm (12 years old), 15.36 cm (16 years old), and 17.45 cm (21 years old). A total of about 7000 vowels for each age were modeled. These MVS are represented in Fig. 1. For the sake of clarity, only the newborn and adult MVS are shown. A comparison of the acoustic data simulated by the model with previous data gathered on children’s speech resulted in a fairly good fit, hence ensuring realistic MVS.

Since the articulatory prototypes had already been determined, for the adult stage, based on typological studies (Vallée, 1994) and inversion, they were used as a starting

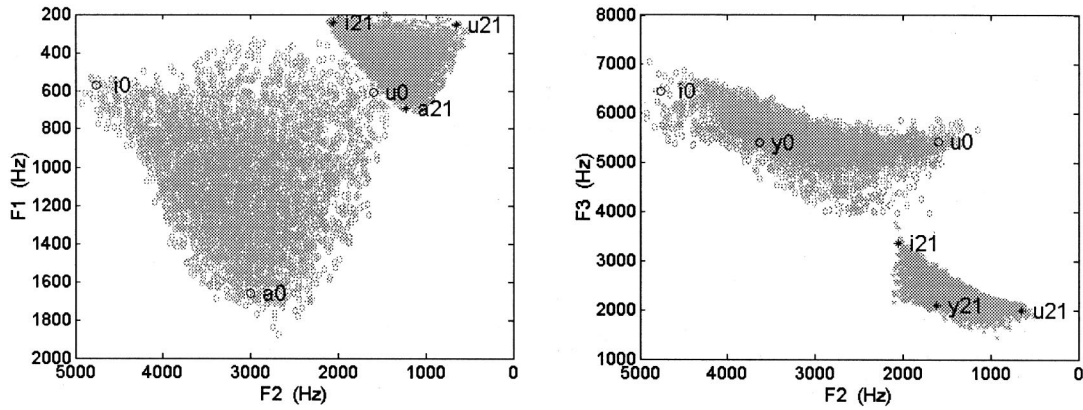


FIG. 1. Maximal vowel spaces for a newborn vocal tract and a 21-year-old adult male vocal tract, in the F1/F2 and F2/F3 spaces, with prototypical focal vowels /i y u a/ (represented by circles and labeled “i0, y0, u0, a0” for the newborn, and represented by stars and labeled “i21, y21, u21, a21” for the adult).

point for the other growth stages. Because of the nonuniform nature of vocal tract growth simulated by our model, the acoustic results of similar articulatory commands from birth to adulthood were located at different relative positions within the MVS (Ménard and Boë, 2000). Therefore, we established articulatory-acoustic prototypes for each growth stage, based on acoustic criteria inspired from the dispersion-focalization theory (DFT, cf. Schwartz *et al.*, 1997). In this theory, it is assumed that vowel systems are shaped by both dispersion constraints increasing mean formant distances between vowels, and by focalization constraints increasing the trend to have focal vowels in the system, that is, vowels with close F1 and F2, F2 and F3, or F3 and F4. First, by comparing the different MVS generated by VLAM, we situated the four focal vowels /i/, /y/, /u/ and /a/, which represent the articulatory-acoustic limits of a speaker, within that space. This method was based on the following acoustic criteria (see Fig. 1):

- (i) [i]: focalization of F3 and F4, resulting in maximal F2 and F3,
- (ii) [y]: focalization of F2 and F3, and minimal F1,
- (iii) [u]: minimal F1 and F2 (focalization of F1 and F2 at their lowest mean position),
- (iv) [a]: maximal F1 (focalization of F1 and F2 at their highest mean position).

The remaining vowels were then situated, on the basis of a

constant relative position in each F1/F2/F3 MVS.

Next, articulatory parameters were retrieved by an iterative inversion method using the pseudo-inverse of the Jacobian matrix (Jordan and Rumelhart, 1992). Since inversion provides several solutions, we retained the articulatory prototypes involving the smallest articulatory distance (in terms of P_i values) compared to the adult male (21 years old) (Ménard and Boë, 2000). Figure 2 groups the set of 70 vowels for the seven growth stages, in the F1/F2 and F2/F3 spaces.

The values of the fourth and fifth formants were finally determined by the articulatory commands retrieved by inversion. Formant bandwidths for the five formants were calculated based on an analog simulation (Badin and Fant, 1984). A cascade formant synthesizer was excited by a glottal waveform generated by the Liljencrants–Fant source model. The resulting signal was digitized at 22 kHz, and had a duration of 600 ms. A fall–rise amplitude contour was applied to the signal.

2. f_0 values

Fundamental frequencies were chosen according to Beck (1996), based on data gathered from children of different ages. f_0 values of 450, 360, 300, 270, 240, 210, and 110 Hz correspond respectively to 0, 2, 4, 8, 12, 16, and 21 year olds. An f_0 value of 210 Hz was chosen for the 16-year-old speaker, representative of an adult female in our analysis. In

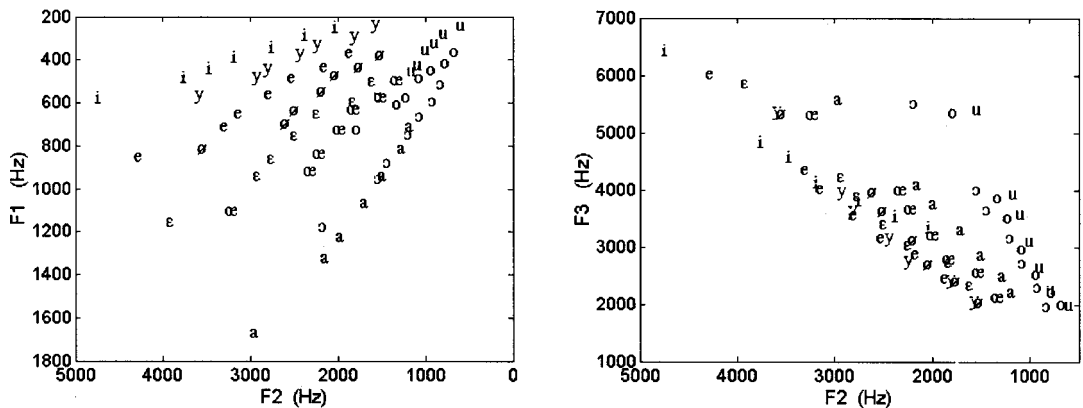


FIG. 2. Representation of the stimuli in the F1/F2 and F2/F3 spaces.

order to separate the influence of vocal tract length and of f_0 values, each of the 70 stimuli was generated with each of the seven frequency values associated to the seven growth stages. As a result, a set of 490 stimuli (10 vowels \times 7 growth stages \times 7 f_0 values) was available.

C. Experimental procedure

Forty-three subjects, aged between 18 and 25 years, participated in the test. The subjects were enrolled in a social science course and did not have any phonetic knowledge. They received course credit for their participation. All subjects reported to have no auditory deficit. The experiment consisted in one occurrence of the 490 stimuli (10 vowels \times 7 growth stages \times 7 f_0 values). Stimuli were presented binaurally via high-quality headphones, on a Power Macintosh 7500/100 (15-in. screen). The subjects' task was to identify, by clicking with the mouse on an icon (out of ten), the perceived vowel among the ten French oral vowels /i y u e ø o ε œ ɔ a/. Each vowel was represented by a monosyllabic word of the structure [fV(C)]: “fil” ([fil]), “fée” ([fe]), “fer” ([fɛʁ]), “fa” ([fa]), “fut” ([fy]), “feu” ([fø]), “fleur” ([flœʁ]), “fou” ([fu]), “fort” ([fɔʁ]), “faux” ([fo]). No time constraints were imposed, but the participants were encouraged to rely only on their immediate appreciation of the vowel identity. Each stimulus was presented only once. No performance feedback was given. The stimuli were randomized across participants. The experiment was preceded by ten practice items (different from those of the identification test) and the subjects had the option of listening to as many occurrences of a stimuli as they desired. The test took place in a sound-treated room and lasted about 40 min.

D. Analysis

1. Analysis of correct identification scores

First, the results were considered according to their correct identification. A stimulus was considered correctly identified if its perceived quality (for instance, /i/) was similar to the experimenters' intention, that is, to the nature of the synthesized vowel. For each f_0 and vocal tract length (represented by a given growth stage), we determined the number of tokens for which the perceived category was identical to the *a priori* phonetic category defined in Fig. 2.

2. Analysis of perceptual invariants

Then, acoustic parameters in relation to perceptual identification were evaluated, without reference to *a priori* phonetic categories displayed in Fig. 2. A stimulus was assigned a vowel category if (and only if) the identification score for this given vowel was greater than 50%. Feature analysis was then performed, by a study of perceptual correlates of height, place of articulation, and rounding.

The treatment of the acoustic data involved two major transformations. First, frequency values, in Hertz, were converted into a Bark scale, using the conversion formula proposed by Schroeder *et al.* (1979): $F_{\text{bark}} = 7 * \text{asinh}(F_{\text{Hz}}/650)$. We also transformed the frequency data following Syrdal and Gopal's (1986) proposed

modifications to represent Traunmüller's (1981) corrected scale. Prior to the Hertz-to-Bark conversion, frequency values were corrected as follows:

- (i) frequency values below 150 Hz are raised to 150 Hz.
- (ii) for frequencies between 150 Hz and 200 Hz:
 $F_c = F - 0.2 (F - 150)$, and
- (iii) for frequencies between 200 and 250 Hz:
 $F_c = F - 0.2 (250 - F)$.

where F_c is the corrected frequency in Hz and F is the original frequency, in Hz. These values will be referred to as the “low-frequency end corrected” values.

$F2'$ was also computed for each vowel, following the model proposed by Mantakas (1989). This model gives a good approximation of F2 and higher formants in the determination of vowel quality (Carlson *et al.*, 1970), using a nonlinear weighted sum of F2, F3, and F4. The algorithm used in this work is described in Fig. 3.

IV. RESULTS

A. Correct identification scores

The number of correct identification scores (Sec. III D 1) were analyzed, irrespective of vowel identity. An analysis of variance (ANOVA), with vocal tract length (7.70 cm—newborn, 9.92 cm—2 years old, 10.67 cm—4 years old, 11.91 cm—8 years old, 13.52 cm—12 years old, 15.36 cm—16 years old, and 17.45 cm—21 years old) and f_0 values (450, 360, 300, 270, 240, 210, and 110 Hz) as within subjects factors, was performed on the correct identification scores and revealed a significant effect of both vocal tract length [$F(6,252) = 153.39$, $p < 0.01$] and f_0 [$F(6,252) = 33.96$, $p < 0.01$] on the percentage of correct identification. An interaction of vocal tract length and f_0 was also significant [$F(36,1512) = 25.26$, $p < 0.01$]. Mean correct identification scores, as a function of growth stage, for the seven f_0 values, are plotted in Fig. 4 (left panel). A noticeable difference in the shape of the curves is observable, with maxima appearing at different f_0 values, for increasing ages. On Fig. 4 (right panel), are displayed the “best” f_0 values (providing maximal identification scores) for each growth stage. We observe the clear decrease of these best f_0 values. If we compare these to the theoretical f_0 values in the model, a small mismatch arises, from 8 years old up to 16 years old.

B. Correlates of perceived vowel features

The previous section focused on the adequacy between perceived and intended stimuli. In this section, we discuss the possible correlates of perceived vowel categories, independently of their *a priori* phonetic identity (see Sec. III D 2). Several analyses of variance (ANOVA) were performed on the data, with the two following within subjects factors, and their associated values: vocal tract length (7.70 cm—newborn, 9.92 cm—2 years old, 10.67 cm—4 years old, 11.91 cm—8 years old, 13.52 cm—12 years old, 15.36 cm—16 years old, and 17.45 cm—21 years old) and f_0 values (450, 360, 300, 270, 240, 210, and 110 Hz).

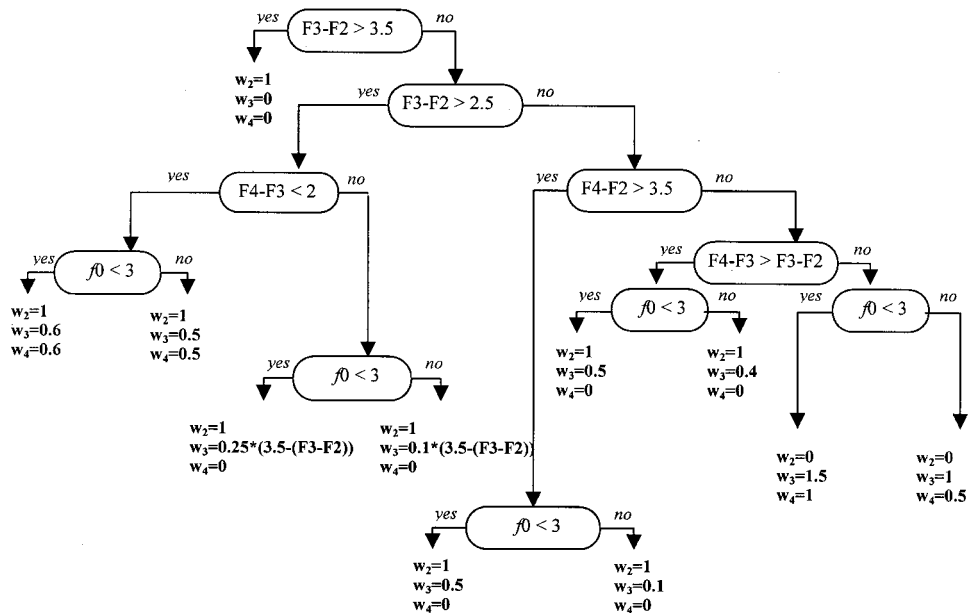


FIG. 3. $F2'$ computation flow chart. $F2'$ is defined by $F2' = (w_2F_2 + w_3F_3 + w_4F_4) / (w_2 + w_3 + w_4)$ (were $w_2 \geq w_3 \geq w_4$, for $w_i \neq 0$). $F2'$ is set at F_2 , if F_3 and F_2 are two widely spaced; the contribution of F_4 is included if F_2 and F_3 are close; if F_2 , F_3 , and F_4 are within 3.5 Bark, $F2'$ is set at the center of gravity of F_2 and F_3 or F_3 and F_4 , depending on the pattern of distances between the three formats; for high f_0 values, the weight of F_3 and F_4 is reduced. All values in Barks.

1. Openness

First, vowels were grouped according to their dominantly perceived openness degree: high (/i y u/), mid-high (/e ø o/), mid-low (/ɛ œ ɔ/), and low (/a/). A repeated measures analysis of variance (ANOVA), with vocal tract length and f_0 values, revealed a main effect of f_0 [$F(6,252) = 302.11; p < 0.01$] and of vocal tract length [$F(6,252) = 1600.07; p < 0.01$] on perceived openness degree. An effect of the interaction of these two factors also arose [$F(36,1512) = 6.46; p < 0.01$]. The importance of the $F1-f_0$ difference (in Barks) in the perception of the openness feature was first evaluated towards its “classification power” and its ability to group perceived vowel height in separate classes. Figure 5 shows the dominantly perceived openness degrees, represented by regions of at least 50% agreement among subjects, in the traditional $F1$ vs $F2$ space, and in the $F1-f_0$ vs $F2$ space. Traunmüller’s (1981) low-frequency end corrected scale was used. Figure 5 (upper panel) depicts the poor normalizing effect of $F1$ alone on openness. As can be seen from Fig. 5 (lower panel), three classes of vowels, classified according to their height, are distinguished by different

values of the $F1-f_0$ tonotopic distance, represented by the dashed lines. High vowels /i y u/ correspond to $F1-f_0$ values below 2 Bark, mid-high vowels /e ø o/ to $F1-f_0$ values ranging from 2 Bark to 4 Bark, and mid-low and low vowels /ɛ œ ɔ a/ to values greater than 4 Bark. It is noteworthy that although a clear distinction exists between high and mid-high vowels, and between mid-high and mid-low vowels, the larger openness degree represented by /a/ is not distinguished from the three mid-low vowels /ɛ œ ɔ/. This fact could be accounted for by the unstable phonological system of our subjects. Indeed, French often lacks the back mid-low vowel /ɔ/ in its inventory. Note that /ɔ/ is nearly absent in the set of perceived vowels. The mid-low back category is thus rarely produced and perceived. As a result, it is possible that the low vowel /a/ is spreading up to the /ɔ/-perceptual zone. Hereafter, the four vowels /ɛ œ ɔ a/ will be grouped in the “low vowels” class.

To assess the validity of the thresholds of 2 and 4 Bark, Table II lists the classification scores of the three groups of perceived vowels (high, mid-high, low), for the 3 $F1-f_0$ classes defined by the 2 and 4-Bark boundaries. Percentages

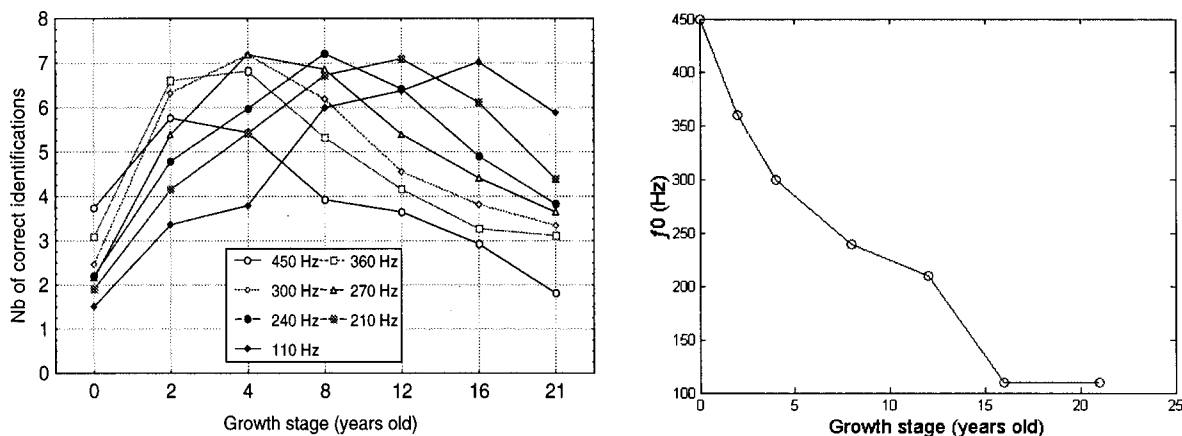


FIG. 4. Number of correct identifications as a function of age, for each f_0 value (left panel) and comparison of perceptually optimal f_0 values as a function of age (right panel).

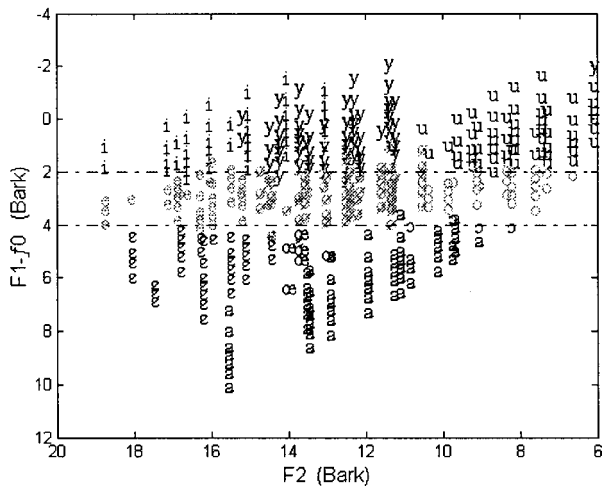
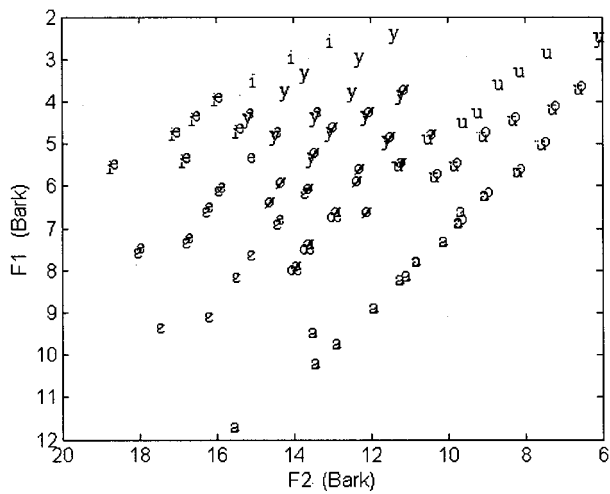


FIG. 5. Dominantly perceived vowel categories, in the F1 vs F2 space (upper panel) (for the sake of clarity, labels were slightly displaced) and F1-f0 vs F2 space (lower panel).

are calculated on the total of vowels actually perceived high, mid-high, and mid-low/low. Original and low-frequency end corrected values are also presented.

Table II shows that whereas the acoustic criteria of

TABLE II. Proportion and number (in parentheses) of vowels of the three perceived openness degrees along the F1-f0 dimension, in Barks.

Perceived height	$x \leq 2$ Bark	4 Bark $> x > 2$ Bark	$x \geq 4$ Bark
Uncorrected values			
High	0.958	0.042	0
/i y u/	(158)	(7)	(0)
Mid-high	0.125	0.820	0.055
/e ø o/	(16)	(105)	(7)
Low	0	0.037	0.963
/ε œ ɔ a/	(0)	(4)	(104)
Low-frequency end corrected values			
High	0.982	0.018	0
/i y u/	(162)	(3)	(0)
Mid-high	0.117	0.867	0.016
/e ø o/	(15)	(111)	(2)
Low	0	0.028	0.972
/ε œ ɔ a/	(0)	(3)	(105)

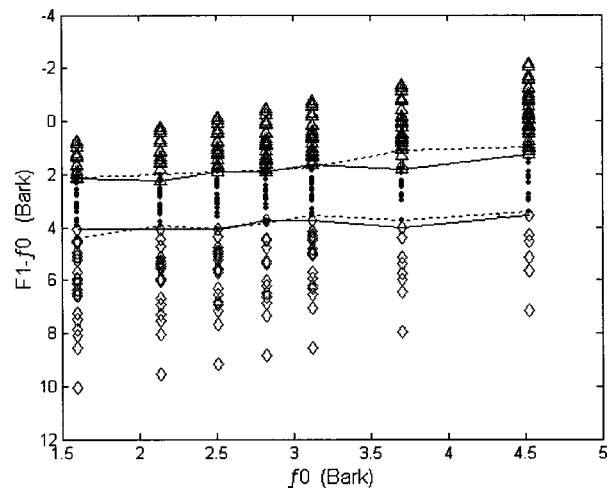


FIG. 6. Representation of dominantly perceived vowels along the F1-f0 dimension, as a function of f_0 (triangles: perceived high /i y u/, dots: perceived mid-high /e ø o/, diamonds: perceived mid-low and low /ε œ ɔ a/). All values in Barks, using low-frequency end corrected scale.

F1-f0 < 2 Bark classifies 98.2% of high vowels, it also includes 11.7% of mid-high vowels. The latter score depicts the rejection power of the criteria. The class of F1-f0 between 2 and 4 Bark classifies 86.7% of mid-high vowels, but includes only 1.8% and 2.8% of high and low vowels, respectively. These preliminary results support the hypothesis that perceived openness is related to the F1-f0 parameter (in Barks), and that [+high] versus [-high] vowels are distinguished by a threshold of 2 Bark, while mid-high versus mid-low and low vowels are distinguished by a threshold of 4 Bark. The use of the low-frequency end corrected values resulted in better classification and rejection scores for all classes of vowels. These results lend some lines of evidence to Traunmüller's (1981) claim about the role of F1-f0 as an invariant correlate of perceived vowel height.

2. f0-dependency limit

In his analysis, Traunmüller (1981) shows that the five openness degrees are distinguished by the F1-f0 parameter, below f_0 values of about 350 Hz. Above this value, intermediate degrees are rarely perceived and the distinction between degree 4 and degree 5 is correlated to F1 only. The author attributes this result to a natural threshold in the auditory perceptual system, related to the well known 3-3.5-Bark critical distance of spectral integration. Above this limit, in his psychoacoustic model, the two lowest partials would no longer be integrated. In order to assess this hypothesis, we plotted our data in the F1-f0 vs f_0 plane, in Fig. 6. Solid lines correspond to the maximal F1-f0 values for perceived mid-low and low vowels. Dashed lines stand for lower and higher F1-f0 values of perceived mid-high vowels.

The 2 and 4-Bark boundaries seem to be effective for all the f_0 range. Despite the slight decrease of the boundaries, this graph contrasts with Traunmüller's (1981) scheme, where boundaries are differently represented along the f_0 continuum. Before ruling out the possibility of a

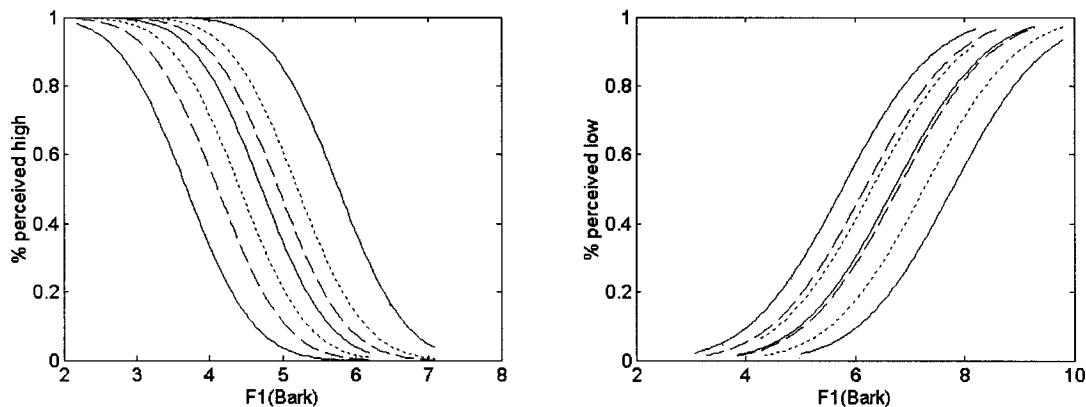


FIG. 7. Probit modeling (by imposed parallelism among the curves) of identification performance for vowel height as a function of F1, for various f_0 values. From left to right: f_0 values of 110, 210, 240, 270, 300, 360, and 450 Hz.

f_0 -dependency limit of the F1- f_0 parameter, a closer investigation of the identification functions was carried out.

Probit statistical analyses were performed on the height perceptual scores as a function of F1 (in Barks), for each set of f_0 values, in order to determine the exact location of the 50% category boundary. The identification functions revealed a significant difference among f_0 sets, lending support to the F1- f_0 invariant. Note that a good fit was obtained by imposing parallelism among the seven functions, displayed in Fig. 7. Figure 8 represents the 50% category boundary along the F1 dimension, as a function of f_0 , for perceived high versus non-high and low versus non-low degrees. Original values, in Barks, and Traummüller (1981) low-frequency end corrected values are compared. Linear regression analyses performed on the two functions respectively provide slope values of 0.65 (high versus mid-high) and 0.66 (mid-high versus low), for raw f_0 values, and 0.71 (high versus mid-high) and 0.73 (mid-high versus low), for corrected f_0 values. Altogether, this confirms the validity of F1- f_0 and of the low-frequency end correction to deal with height perception in French.

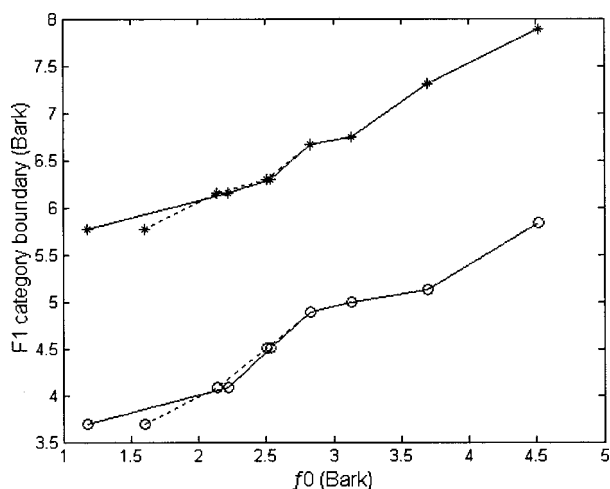


FIG. 8. F1 category boundary for high versus non-high (circles) and low versus non-low (stars) vowels, as a function of f_0 . Solid lines: uncorrected values, dashed lines: low-frequency end corrected values. All values in Barks.

3. Place of articulation

With respect to the front/back feature, perceived vowels were grouped according to their place of articulation: front (/i y e ø ε œ/) and back (/u o ɔ/). A repeated measures analysis of variance (ANOVA), with vocal tract length and f_0 values, revealed a main effect of the vocal tract length factor [$F(6,252)=30.31$; $p<0.01$], but no effect of f_0 . However, an effect of the interaction of these two factors appeared [$F(36,1512)=3.33$; $p<0.01$]. A study of the correlations between the percentage of perceived front vowels and several spectral parameters was then performed. The following parameters were considered, all values in Barks: F2, F2- f_0 , ((F2- f_0)+F1)/2, F2-F1, F3-F2. Except for ((F2- f_0)+F1)/2, all parameters were highly correlated to perceived frontness (F2: $r=0.72$; F2- f_0 : $r=0.68$; F2-F1: $r=0.84$; F3-F2: $r=0.82$). F2-F1 and F3-F2 appear to be the best predictors of perceived place of articulation.

Next, we tested front-back classification based on these parameters. Although F2, F2- f_0 , F2-F1, and F3-F2 provide high scores, F2-F1 performs slightly better (Table III). The stimuli yielding 50% agreement are plotted in Fig. 9, in the F1- f_0 vs F2-F1 and F1- f_0 vs F3-F2 planes. The F2-F1 boundary at 5.5 Bark involves less error, but there is, for the correctly classified vowels, a better separation in terms of F3-F2 (Fig. 9, right panel).

One can conceive the two possible parameters as reflecting two perceptual strategies used by the subjects to identify front and back vowels. On the one hand, listeners could rely on the existence of a low energy concentration, that is, two close formants in the vicinity of F1 and F2, to identify the vowel as a back one. This strategy corresponds to the F2-F1 parameter (Fig. 9, left panel). Above 5.5 Bark, front vowels are perceived and below 5.5 Bark, back vowels are perceived. On the other hand, another perceptual strategy would be based on the existence of two widely spaced energy concentrations in the higher frequency region of the spectrum (F2 and F3), such a pattern denoting a back vowel. This strategy is represented by the F3-F2 parameter (Fig. 9, right panel). Note that Traummüller (1981) also reports that a large intersubject variability is found in the use of these two strategies. In order to adequately represent the use of these cues, F2' was considered, and the difference between F2' and F1

TABLE III. Proportion and number (in parentheses) of vowels of perceived place of articulation classified along the F2, F2- f_0 , F2-F1, and F3-F2 dimensions, in Barks.

Perc. front-back	F2		F2- f_0		F2-F1		F3-F2	
	$x > 11$ Bark	$x < 11$ Bark	$x > 5$ Bark	$x < 5$ Bark	$x > 5.5$ Bark	$x < 5.5$ Bark	$x < 5$ Bark	$x > 5$ Bark
Front /i e ε y ø œ/	0.972 (240)	0.028 (7)	0.972 (240)	0.028 (7)	0.996 (246)	0.004 (1)	0.972 (240)	0.028 (7)
Back /u o ɔ/	0.011 (1)	0.989 (92)	0.054 (5)	0.946 (88)	0.022 (2)	0.978 (91)	0.011 (1)	0.989 (92)

was evaluated. Nevertheless, this parameter did not show any improvement in the classification.

Finally, the variation of the F2-F1 boundary over the entire f_0 range was assessed by probit analysis. Identification functions were plotted, for each f_0 value, for F2-F1 (in Barks). The 50% perceived frontness boundaries were compared in each of the seven f_0 conditions. No significant difference was observed among the f_0 values, as can be seen in Fig. 10. Thus, the F2-F1 achieves full normalization, and f_0 does not seem to play a significant part for frontness identification.

4. Rounding

Regarding the rounding feature, an analysis of variance (ANOVA) of perceived rounding, with vocal tract length and f_0 values as within subjects factors, suggested a main effect of f_0 [$F(6,252)=10.23$; $p < 0.001$] and vocal tract length [$F(6,252)=165.01$; $p < 0.01$], as well as a noticeable effect of the interaction of the two factors [$F(36,1512)=3.91$; $p < 0.01$]. The data were analyzed for perceived vowels for which a rounding distinction was identified (that is, the front vowels /i e ε/ vs /y ø œ/). Only these vowels were considered, since the other ones are not phonologically specified for this feature in French. Several parameters, such as F2-F1, F3-F2, F2', and F2'- f_0 were estimated. F2-F1 and F3-F2 achieve poor performances, as was already seen in Fig. 9.

Despite the large intraclass dispersion for rounded and unrounded vowels, F2' provides good classification scores (Table IV, Fig. 11). Thus, a perceived rounded vowel shows a F2' value lower than 15 Bark, whereas an unrounded vowel corresponds to F2' greater than 15 Bark. To assess the

role of f_0 , the labeling F2' performances were submitted to probit analysis. Figure 12, displaying the seven functions, with imposed parallelism, for each f_0 value, clearly confirms the efficiency of F2', and shows that f_0 is not a normalizing parameter for perceived roundedness.

The validity of the F2' parameter for perceived roundedness is, however, likely restricted to the front vowels, whereas F2'-F1 is shown to be a better correlate of this feature for back vowels (for languages like Turkish, Vietnamese, etc.), according to Traunmüller and Lacerda (1987).⁴ Furthermore, the value of our category boundary (15 Bark, corresponding to 2730 Hz) is to be related to the reference value of 2800 Hz also reported by Traunmüller and Lacerda (1987) in a study of the perceptual correlates of backness and roundedness for two-formant vowels typical of Swedish and Turkish. The invariant description proposed is based on the tonotopic distance between F2' and two reference points. A landmark located at 3 Bark above f_0 , as well as an absolute value of 2800 Hz, serve as references in the model. As discussed by the authors, the existence of the latter reference value at this specific location remains unclear. On the one hand, 2800 Hz could be related to the average F3 of an adult speaker. This hypothesis requires, however, a perceptual numbering of the formants. On the other hand, 2800 Hz is 3 Bark below the spectral attenuation observed in the high-frequency region. The two reference points of 3 Bark above f_0 and 3 Bark below this value thus represent a symmetrical window of spectral onset and offset, used to represent invari-

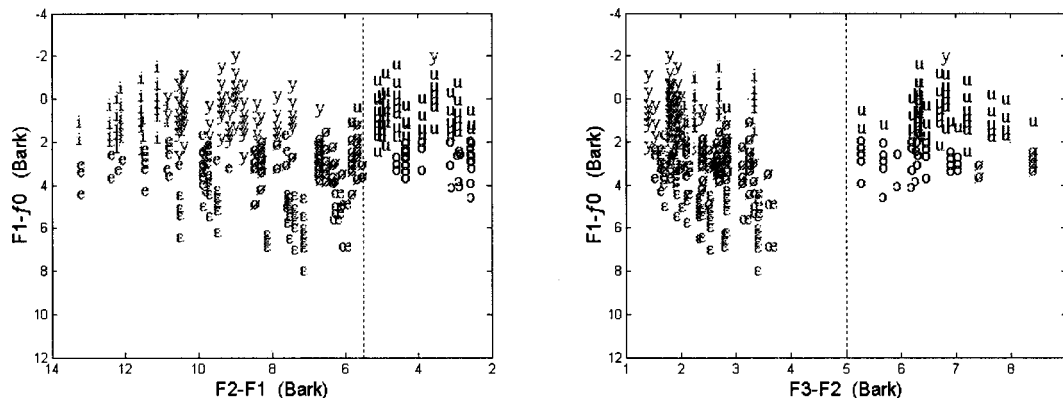


FIG. 9. Dominantly perceived vowels plotted in the F1- f_0 vs F2-F1 space (left panel) and F1- f_0 vs F3-F2 space (right panel). All values in Barks.

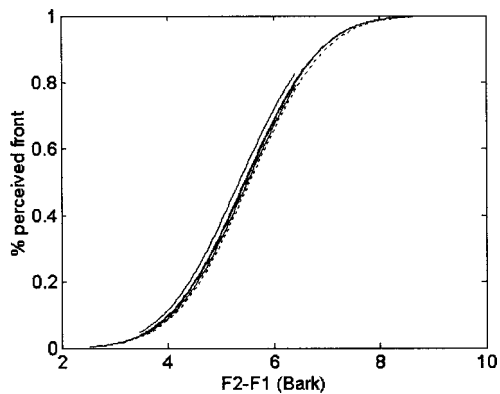


FIG. 10. Probit modeling (by imposed parallelism among the curves) of perceived frontness as a function of $F_2 - F_1$, for all f_0 values.

TABLE IV. Proportion and number (in parentheses) of rounded and unrounded vowels along the $F_2' - f_0$ and F_2' dimensions, in Barks.

Perceived roundedness	$F_2' - f_0$		F_2'	
	$x \leq 12$ Bark	$x > 12$ Bark	$x \leq 15$ Bark	$x > 15$ Bark
Rounded	0.917	0.083	0.967	0.033
/y, ø, œ/	(110)	(10)	(116)	(4)
Unrounded	0.102	0.898	0.031	0.969
/i e ε/	(13)	(114)	(4)	(123)

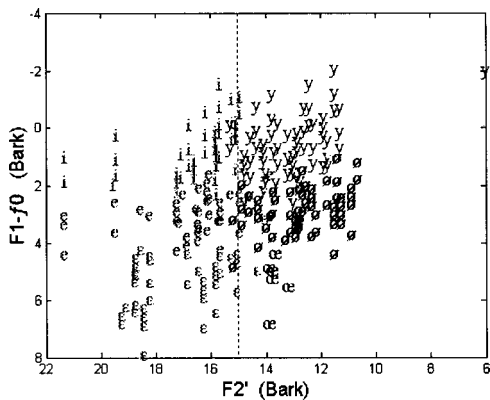


FIG. 11. Dominantly perceived vowels plotted in the $F_1 - f_0$ vs F_2' space. All values in Barks.

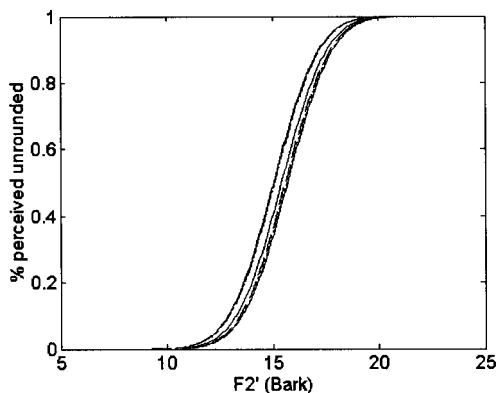


FIG. 12. Probit modeling (by imposed parallelism among the curves) of perceived rounding as a function of F_2' , for each f_0 value. All values in Barks.

TABLE V. Classification matrix for the linear discriminant analysis on 10 classes of vowels (lines: perceived labels; columns: computed labels).

Vowel	%										
	correct	i	e	ε	a	y	ø	œ	u	o	ɔ
i	95.2	40	1	0	0	1	0	0	0	0	0
e	90.2	2	37	0	0	0	2	0	0	0	0
ε	83.8	0	4	31	0	0	2	0	0	0	0
a	95.1	0	0	0	58	0	0	0	0	3	0
y	85.5	5	1	0	0	53	2	0	1	0	0
ø	96.6	0	0	1	0	0	57	0	1	0	0
œ	83.3	0	0	0	0	0	1	5	0	0	0
u	95.1	0	0	0	0	0	1	0	58	12	0
o	92.9	0	0	0	0	0	0	0	2	26	0
ɔ	0	0	0	0	1	0	0	0	0	3	0
%	91.0	47	43	32	59	54	65	5	62	34	0

5. General classification of vowels

Finally, we performed a linear discriminant analysis on the ten classes of perceived vowels. One of each of the following groups of possible classification parameters were provided to the model:

- (i) for height: F_1 , $F_1 - f_0$;
- (ii) for place of articulation (front-backness): F_2 , $F_2 - f_0$, $F_2 - F_1$, $F_3 - F_2$; and
- (iii) for rounding: $F_2' - f_0$, F_2' .

The highest classification scores were achieved by $F_1 - f_0$, $F_2 - F_1$, and F_2' . The resulting classification matrix is tabulated in Table V.

Except for /ɔ/, the good scores confirm that from the traditional four-dimensional acoustic space (F_1 , F_2 , F_3 , and F_4), a three-dimensional “perceptual” space, for French vowels, is provided by the following correlates: $F_1 - f_0$, $F_2 - F_1$, and F_2' . Classification in this algorithm involves, first, a transformation of Hertz values into critical band units (or Bark), and, then, a difference between Bark acoustic parameters, for height and place of articulation. For rounding, a spectral integration mechanism occurs, based on the patterns of distance between F_2 , F_3 , and F_4 . The resulting parameters are then compared to memory stored templates for each phonological category. Note that results give good support to a feature extraction process.

V. DISCUSSION

From this pattern of results, we shall first attempt to come back to the invariance issue. Then, we shall focus on the auditory processing of formants, in particular F_1 , for high f_0 values. At last, we shall discuss what kinds of constraints these perceptual data might provide for the acquisition of control for speech production.

A. Testing Diehl’s three theories of vowel normalization

In Sec. II, several theoretical approaches, dealing with interspeaker variability and vowel normalization, were briefly introduced. In a recent paper, Diehl (2000) discusses three hypotheses about the nature of perceptual boundaries among vowels. Even though our corpus, designed to evaluate

general classification processes, does not allow us to test each of these hypotheses, our results can be considered in the light of these assumptions. The Chistovich/Syrdal hypothesis claims that perceptual invariance operates on a 3–3.5-Bark critical distance, used to perform a binary classification of feature values. According to Traunmüller's (1984) hypothesis, boundaries are related to a weighted combination of tonotopic distance between any adjacent peak, the weight of each distance being inversely correlated to the distance value, up to 6 Bark. Beyond this threshold, the distance is no longer taken into account. According to the third hypothesis (Molis, 1999), perceptual categories would be delimited by relatively linear functions of formant values (in Barks).

Regarding openness, results of our analysis have shown that the difference between F1 and f_0 , in Barks, is a nearly invariant correlate of perceived vowel height. Two boundaries delimited high vowels versus mid-high vowels (2 Bark) and mid-high versus mid-low and low vowels (4 Bark). The data do not support the hypothesis of a universal threshold of 3–3.5 Bark, corresponding to the critical distance of spectral integration, used to perform a binary classification of the [+high] versus [–high] vowels, as reported in Syrdal and Gopal (1986). Our threshold for such a binary classification would correspond to 2 Bark. The F1- f_0 parameter (in Barks) represents also a continuum along which perceived openness can be classified (the greater the value of F1- f_0 , the more open the perceived vowel). Traunmüller (1981) obtained similar results, that is, the distinction between the first and second degrees of openness corresponds to a F1- f_0 boundary of about 1.2 Bark, lower than the critical distance. This difference brings up the question of the universal nature of perceptual boundaries related to openness, assumed by Syrdal and Gopal (1986). Data are more in line with Lindblom's adaptive variability theory (Lindblom, 1996), according to which sound systems of human languages may adaptively exploit acoustical contrasts, provided that they are sufficient for category discriminations. Indeed, the data for French display boundary values along the F1- f_0 dimension that differ from both Bavarian and American English, despite the common use of this acoustic parameter as an invariant correlate of perceived openness.

We now come back to the second hypothesis, by Traunmüller. The prediction is the following. Since for an f_0 value of 110 Hz, F1- f_0 is greater than for stimuli with an f_0 value of 450 Hz, the F1- f_0 parameter could be a poorer predictor of perceived openness for the former set than for the latter. At higher f_0 values, F1- f_0 becomes smaller, and its perceptual weight therefore more important. Linear regressions carried out for each set of f_0 values confirm this assumption. Indeed, r^2 varies from 0.87 to 0.67 for f_0 values ranging from 450 to 110 Hz. On the other hand, for F2-F1 and F3-F2, no relations between the magnitude of the distance and the variance explained was revealed.

Finally, our pattern of data provides good support for the third hypothesis suggested by Molis, based on frequency distances in Barks, for height and front–back contrasts, with F1- f_0 in the first case, and F2-F1 and F3-F2 in the second case. However, the data for rounding suggest that nonlinear formant processing based on F2' and the center of gravity

effect could be of importance also. Altogether, we can confirm that Bark transforms and interfrequency distances are basic for vowel normalization and identification, but we may suggest that for complex feature patterns, as for French rounding, the linear assumption is at the very least debatable.

B. The case of high F0 values

Owing to the low F1 associated with the adult vocal tract, for close vowels, combined with high f_0 values of 450 Hz, the F1- f_0 parameter sometimes results in negative values, as can be observed on previous figures. It might seem theoretically misleading to represent as a perceptual cue the negative difference between F1 and f_0 , that is, to conceive that the energy peak located at F1 is identified despite the lack of harmonics. Furthermore, in the case of f_0 values of 450 Hz, the distance between the two lowest harmonics (3.4 Bark) is within the range of 3–3.5 Bark, representing the critical distance of spectral integration. It could be the case that these two harmonics are no longer integrated and perceived as separate peaks. Other analyses were carried out to evaluate the contribution of several cues in the low-frequency region, which would represent the F1- f_0 parameter. Hoemeke and Diehl (1994) describe a few models used to compute the *effective first formant*, corresponding to the perceived first energy peak, as opposed to the *nominal first formant*, representing the synthesized one. A spectral analysis was performed on the signals with f_0 values of 450 Hz, in order to evaluate the effective first formant in two ways: the most prominent harmonic (H_1) in the vicinity of nominal F1 ($F1eff1$), and the frequency centroid of the first two harmonics H_1 and H_2 ($F1eff2$), that is, an amplitude-weighted sum of frequency values. If we consider the set of dominantly perceived vowels for which f_0 value is 450 Hz, Fig. 13 suggests that the normalized F2-F1 vs F1- f_0 space achieves a better classification for high versus mid-high vowels when F1 is represented by $F1eff1$ (left panel) than when F1 is computed using $F1eff2$ (right panel). Thus, it seems that when H_1 amplitude is very important, a separate peak perception is induced at this location and high vowels are perceived, with F1- f_0 below 2 Bark. When H_2 is more intense, mid-high vowels are perceived and F1- f_0 is within the class defined by the 2- and 4-Bark boundaries. Nevertheless, $F1eff2$ - f_0 operates a better classification for mid-high versus low vowels (Fig. 13, right panel). It remains arguable, however, that these two models represent a good approximation of perceived F1, considering the high correlation between F1- f_0 and perceived height for f_0 values of 450 Hz, reported in Sec. V A.

C. Possible constraints on speech production

Thanks to the articulatory model simulating the extreme limits of vocal tract growth (birth and adulthood), a wide variety of vocal tract lengths was synthesized. Combined with our perceptual results, it seems clear that the three cardinal vowels /i u a/ could be produced with a very small vocal tract, and still be perceived. Obviously, sensorimotor control capabilities prevent the newborn from using his or her articulators to produce such vowels. However, the two

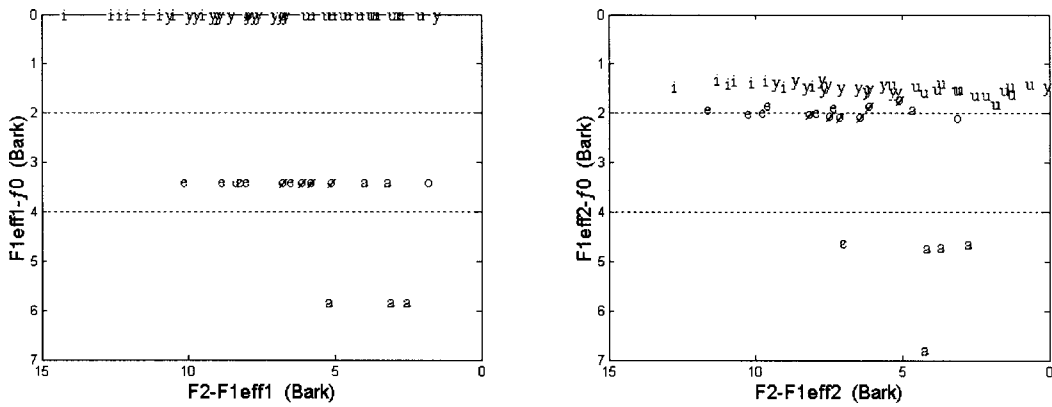


FIG. 13. Dominantly perceived vowels for which $f_0 > 450$ Hz. Two representations are used to compute F1: most prominent harmonic in the vicinity of nominal F1 ($F1_{eff1}$) (left panel) and centroid frequency of the first two harmonics ($F1_{eff2}$) (right panel). All values in Barks.

front rounded vowels /y œ/ and the back ones /o ɔ/, synthesized with a newborn vocal tract, are not perceived by at least 50% of the subjects. Of course, this phenomenon could be explained by poor prototypes, based on acoustic criteria, or by the impossibility of perceiving these particular French vowel categories, as produced by a newbornlike vocal tract. In a perceptual experiment aiming at determining the perceptual categorization of the entire MVS, for five growth stages (newborn, 4, 10, 16, and 21 years old), stimuli have been generated, for a grid of acoustic values covering the F1/F2 and F2/F3 range of each MVS (Ménard and Boë, 2001). Forty French subjects had the task of identifying which of the ten French oral vowels was closest to the stimulus. For the five growth stages, perceived vowels corresponding to 50% agreement among subjects were found for the nine French phonological categories /i y u e ø o ε œ a/, when /o/ and /ɔ/ were grouped together, in order to take into account the unstable opposition between /o/ and /ɔ/, in French. Dispersion ellipses of perceived vowel category, in the newborn vocal tract, are drawn in Fig. 14. Thus, the absence of perceived /y œ/ is likely attributable to poor acoustic prototypes, for our subjects, and the absence of /o ɔ/, to listeners' phonological confusion between the mid vowels /o/ and /ɔ/.

It has been claimed that perceptual goals can explain the covariance of different production strategies, to enhance auditory distinctiveness (Lotto *et al.*, 1997). As regards English vowels normalization, Syrdal and Gopal (1986) interpreted

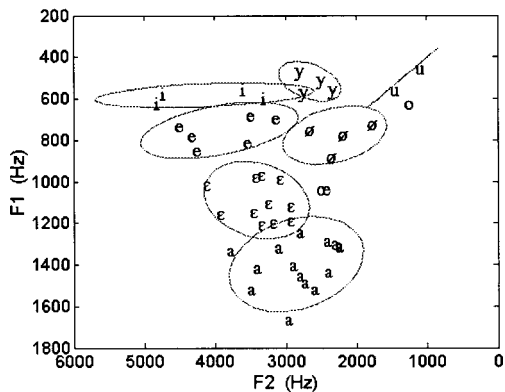


FIG. 14. Dispersion ellipses (± 1.5 s.d.) of the dominantly perceived French vowels, for the maximal vowel space of a newborn.

their boundaries as limits within which formants can be spaced from each other. This can in turn be considered as limiting the production variability and thus representing perceptual constraints on speech production. In the case of height, the 2- and 4-Bark boundaries show that for higher f_0 , the first formant can be very high (above 450 Hz), but as f_0 decreases, F1 must decrease as well, in order to ensure a constant F1- f_0 value. Besides cavity lengthening, a wide variety of articulatory manoeuvres are possible to lower F1, especially for cases where F1 is affiliated to a Helmholtz resonator.

For place of articulation, related to F2-F1, f_0 does not seem to be relevant. Hence, the speaker's task would consist in maintaining widely spaced (greater than 5.5 Bark) or closely spaced (lower than 5.5 Bark) formants for F1 and F2. Since these two formants are mainly affiliated to a Helmholtz resonator of the vocal tract and to the front or back cavity, one must consider here the difference in the ratio of the pharyngeal versus mouth cavity length between children and adults, yielded by nonuniform vocal tract growth. For the same articulatory positions, for front vowels, the modeled baby produces greater F2-F1 since F1 varies less than F2. This F2-F1 value remains over the 5.5-Bark boundary and, following our perceptual correlate, F2 and F1 being widely spaced in front vowels, no articulatory compensation strategies would be perceptually driven for smaller vocal tracts. However, for very back vowels such as /o/ and /ɔ/, for similar articulatory positions, since F2-F1 is greater for the baby compared to the adult, a value close to (or greater than) the 5.5-Bark boundary is realized by the former. Consequently, F2-F1 would have to be decreased for the infant by a different position of the tongue dorsum and tongue body (hence lengthening the cavity affiliated to F2 and lowering F2), and/or by manoeuvres recruited in order to increase F1.

In the case of roundedness, one can expect that the low F2' required for /y/, as opposed to the high F2' for /i/, will limit the extent to which cavities affiliated to F2 and F3 can be shortened or lengthened. Indeed, in the case of /y/, for small vocal tracts, F2 becomes affiliated to the front cavity (the cavity created by the constriction of the tongue towards the palate and the protrusion of the lips), and F3, to the back cavity. For an adult male, two patterns are observed for /y/ (Schwartz *et al.*, 1993): F2 is affiliated to the back or the

front cavity, and, in a complementary way, F3 is associated to the front or the back cavity, respectively. Owing to the long cavities of an adult male, an F2' value below 15 Bark, typical of rounded vowels, is easily achieved for /y/: the front or the back cavity (depending on the type of formant-cavity affiliation pattern) can be lengthened by the lip protrusion gesture in order to reach this value. As a result, F2 and F3 will be located below 15 Bark, both contributing to F2' lower than 15 Bark. However, for children's vocal tract, due to the short cavities, F2 and F3 values in our synthesized /y/ are greater than 15 Bark, resulting in a perceived unrounded vowel. In the model, this was the case for the newborn, and the 4- and 10-year-old growth stages. One can thus postulate that for speakers with this vocal tract configuration, the task of producing front rounded vowels would require that, in order to reach a value below 15 Bark for /y/, F2 has to be sufficiently lowered by compensation articulatory strategies, contributing to decrease F2'. Further investigation, based on an analysis of naturally produced vowels in the light of such constraints, is in process.

VI. CONCLUSION

This article aimed at determining invariant acoustic correlates of French vowels through a study of auditory normalization of growing speakers. Based on a corpus of 490 synthesized vocalic stimuli produced by an articulatory model simulating nonuniform vocal tract growth from birth to adulthood, several vocal tract lengths and f_0 values were generated. Perceptual tests were performed on the stimuli and the data were classified in order to retrieve phonetic features and vocalic categories. It has been shown that the distance between F1 and f_0 , in Barks, is a nearly invariant parameter of perceived vowel height. Furthermore, the front-backness dimension is determined by F2-F1, in Barks. As regards rounding, an attempt to model perceptual data by minor changes to an existing model of the effective second formant F2' gave rather good classification scores. These analyses are of great interest for the development of normalization procedures, and allow the formulation of hypotheses regarding the perceptual constraints on speech production, from a language acquisition and developmental point of view.

ACKNOWLEDGMENTS

This work greatly benefited from the fruitful remarks of two anonymous reviewers. The study was supported by a grant from the Social Sciences and Humanities Research Council of Canada and by funding from the French Ministère de la recherche (ABISPA-cognitive project). Special thanks to Caroline Golansky and Elodie Tournafol for collecting data, and to Marija Tabain for kindly proofreading the manuscript.

¹Note that the model assumes that the tongue is growing proportionally to the palate, since no developmental data are available on this point.

²Reduced thresholds are indeed used by Goldstein (1980), in the simulations of newborn vowel configurations.

³Of course, control capacities are null at 4 weeks old, and still under development at 2 and 4 years old (Kent, 1992), but we explore here how vowels

can be perceived for the entire range of possible variations, despite the possibility of overestimating their magnitude.

⁴This was pointed out by an anonymous reviewer.

- Ainsworth, W. A. (1971). "Perception of synthesized isolated vowels and h_d words as a function of fundamental frequency," *J. Acoust. Soc. Am.* **49**, 1323–1324.
- Ainsworth, W. A. (1975). "Intrinsic and Extrinsic Factors in Vowel Judgments," in *Auditory Analysis and Perception of Speech*, edited by G. Fant and M. A. A. Tatham (Academic, London), pp. 103–113.
- Badin, P., and Fant, G. (1984). "Notes on vocal tract computations," *STL-QPSR* **2–3**, 53–108.
- Beck, J. M. (1996). "Organic variation of the vocal apparatus," in *Handbook of Phonetic Sciences*, edited by W. J. Hardcastle and J. Laver (Blackwell, London), pp. 256–297.
- Bladon, R. A. W., and Fant, G. (1978). "A two-formant model and the cardinal vowels," *STL-QPSR* **1**, 1–8.
- Boë, L.-J., and Maeda, S. (1997). "Modélisation de la croissance du conduit vocal. Espace vocalique des nouveaux-nés et des adultes. Conséquences pour l'ontogenèse et la phylogénèse," *Journées d'Études Linguistiques: "La Voyelle dans Tous ces États,"* Nantes, pp. 98–105.
- Boë, L.-J., Perrier, P., Guérin, B., and Schwartz, J.-L. (1989). "Maximal Vowel Space," in *European Conference on Speech Communication and Technology (Eurospeech)*, Paris, France, pp. 281–284.
- Carlson, R., Granström, B., and Fant, G. (1970). "Some studies concerning perception of isolated vowels," *STL-QPSR* **2–3**, 19–35.
- Carlson, R., Granström, B., and Klatt, D. (1979). "Vowel perception: The relative salience of selected acoustic manipulations," *STL-QPSR* **34**, 19–35.
- Chistovich, L. A., Sheikin, R. L., and Lublinskaya, V. V. (1979). "Centres of Gravity' and Spectral Peaks as the Determinants of Vowel Quality," in *Frontiers of Speech Communication Research*, edited by B. Lindblom and S. Öhman (Academic, London), pp. 143–157.
- Delattre, P., Liberman, A. M., Cooper, F. S., and Gertsman, J. (1952). "An experimental study of the acoustic determinants of vowel color; observations on one- and two-formant vowels synthesized from spectrographic patterns," *Word* **8**, 195–210.
- Diehl, R. L. (2000). "Searching for an Auditory Description of Vowel Categories," *Phonetica* **57**, 267–274.
- Fahey, R. P., Diehl, R. L., and Traunmüller, H. (1996). "Perception of back vowels: effects of varying F1-F0 Bark distance," *J. Acoust. Soc. Am.* **99**, 2350–2357.
- Fant, G. (1983). "Feature analysis of Swedish vowels—A revisit," *STL-QPSR* **2–3**, 1–19.
- Fant, G., Carlson R., and Granström, B. (1974). "The [e]-[ø] ambiguity," in *Proceedings of Speech Communication Seminar*, Stockholm, pp. 117–121.
- Fujisaki, H., and Kawashima, T. (1968). "The Roles of Pitch and Higher Formants in the Perception of Vowels," *IEEE Trans. Audio Electroacoust.* **AU-16**(1), 73–77.
- Goldstein, U. G. (1980). "An articulatory model for the vocal tract of the growing children," Thesis of Doctor of Science, MIT, Cambridge, MA.
- Hillenbrand, J., Getty, L. A., Clark, M. J., and Wheeler, K. (1995). "Acoustic characteristics of American English vowels," *J. Acoust. Soc. Am.* **97**, 3099–3111.
- Hirahara, T., and Kato, H. (1992). "The Effect of F0 on Vowel Identification," in *Speech Perception, Production and Linguistic Structure*, edited by Y. Tohkura, E. Vatikiotis-Bateson, and Y. Sagisaka (Ohmsha/IOS, Tokyo), pp. 89–112.
- Hoemeke, K. A., and Diehl, R. L. (1994). "Perception of vowel height: The role of F1-F0 distance," *J. Acoust. Soc. Am.* **96**, 661–674.
- Jordan, M. I., and Rumelhart, D. E. (1992). "Forward Models: Supervised Learning with a Distal Teacher," *Cogn. Sci.* **16**, 316–354.
- Kent, R. D. (1992). "The Biology of Phonological Development," in *Phonological Development: Models, Research, Implications*, edited by C. A. Ferguson, L. Menn, and C. Stoel-Gammon (York, Timonium, MD), pp. 65–90.
- Kuhl, P. K., and Meltzoff, A. N. (1996). "Infant vocalizations in response to speech: Vocal imitations and developmental change," *J. Acoust. Soc. Am.* **100**, 2425–2438.
- Lee, S., Potamianos, A., and Narayanan, S. (1999). "Acoustics of children's speech: Developmental changes of temporal and spectral parameters," *J. Acoust. Soc. Am.* **105**, 1455–1468.
- Liberman, A. M., and Mattingly, I. G. (1985). "The motor theory of speech perception revisited," *Cognition* **21**, 1–36.

- Lindblom, B. (1996). "Role of articulation in speech perception: Clues from production," *J. Acoust. Soc. Am.* **99**, 1683–1692.
- Lotto, A. J., Holt, L. L., and Kluender, K. R. (1997). "Effect of Voice Quality on Perceived Height of English Vowels," *Phonetica* **54**, 76–93.
- Mantakas, M. (1989). "Application du second formant effectif F² à l'étude de l'opposition d'arrondissement des voyelles antérieures du français," Thèse de Docteur de l'INPG, Systèmes Electroniques, Grenoble.
- Ménard, L., and Boë, L.-J. (2000). "Exploring Vowel Production Strategies from Infant to Adult by Means of Articulatory Inversion of Formant Data," in *International Congress of Spoken Language Processing*, Beijing, China, pp. 465–468.
- Ménard, L., and Boë, L.-J. (2001). "Perceptual categorization of maximal vowel space from birth to adulthood," in *European Conference on Speech Communication and Technology (Eurospeech)*, Aalborg, Denmark, pp. 167–170.
- Miller, D. C. (1953). "Auditory tests with synthetic vowels," *J. Acoust. Soc. Am.* **25**, 114–121.
- Miller, J. D. (1989). "Auditory-perceptual interpretation of the vowel," *J. Acoust. Soc. Am.* **85**, 2114–2134.
- Molis, M. (1999). "Perception of vowel quality in the F₂/F₃ plane," in *Proceedings ICPhS 99*, San Francisco, pp. 171–194.
- Nearey, T. M. (1989). "Static, dynamic, and relational properties in vowel perception," *J. Acoust. Soc. Am.* **85**, 2088–2113.
- Peterson, G. E., and Barney, H. L. (1952). "Control method used in the study of vowels," *J. Acoust. Soc. Am.* **24**, 175–184.
- Potter, R. K., and Steinberg, J. C. (1950). "Toward the specification of speech," *J. Acoust. Soc. Am.* **22**, 807–820.
- Savariaux, C., Perrier, P., Orliaguet, J.-P., and Schwartz, J.-L. (1999). "Compensation strategies for the perturbation of French [u] using a lip tube. II. Perceptual analysis," *J. Acoust. Soc. Am.* **106**, 381–393.
- Schroeder, M. R., Atal, B. S., and Hall, J. L. (1979). "Objective measure of certain speech signal degradations based on masking properties of human auditory perception," in *Frontiers of Speech Communication Research*, edited by B. Lindblom and S. Öhman (Academic, London), pp. 217–229.
- Schwartz, J.-L., Beautemps, D., Abry, C., and Escudier, P. (1993). "Inter-individual and cross-linguistic strategies for the production of the [i] vs [y] contrast," *J. Phonetics* **21**, 411–425.
- Schwartz, J.-L., Boë, L.-J., Vallée, N., and Abry, C. (1997). "The Dispersion-Focalization Theory of vowel systems," *J. Phonetics* **25**, 255–286.
- Slawson, A. W. (1968). "Vowel quality and musical timbre as functions of spectrum envelope and fundamental frequency," *J. Acoust. Soc. Am.* **43**, 87–101.
- Stevens, K. N. (1996). "Critique: Articulatory-acoustic relations and their role in speech perception," *J. Acoust. Soc. Am.* **99**, 1693–1694.
- Strange, W. (1989). "Dynamic aspects of coarticulated vowels spoken in sentence context," *J. Acoust. Soc. Am.* **85**, 2135–2153.
- Syrdal, A. K., and Gopal, H. S. (1986). "A perceptual model of vowel recognition based on the auditory representation of American English vowels," *J. Acoust. Soc. Am.* **79**, 1086–1100.
- Traunmüller, H. (1981). "Perceptual dimension of openness in vowels," *J. Acoust. Soc. Am.* **69**, 1465–1475.
- Traunmüller, H. (1984). "Articulatory and perceptual factors controlling the age- and sex-conditioned variability in formant frequencies of vowels," *Speech Commun.* **3**, 49–61.
- Traunmüller, H. (1991). "The context sensitivity of the perceptual interaction between F₀ and F₁," in *Proceedings of the XIIIth ICPhS*, Aix-en-Provence, France, Vol. 5, pp. 62–65.
- Traunmüller, H., and Lacerda, F. (1987). "Perceptual relativity in identification of two-formant vowels," *Speech Commun.* **6**, 143–157.
- Vallée, N. (1994). "Systèmes vocaliques: de la typologie aux prédictions," Thèse de Doctorat en Sciences du Langage, Université Stendhal, Grenoble.

Quantifying the intelligibility of speech in noise for non-native listeners

Sander J. van Wijngaarden,^{a)} Herman J. M. Steeneken, and Tammo Houtgast
TNO Human Factors, P.O. Box 23, 3769 ZG Soesterberg, The Netherlands

(Received 9 July 2001; accepted for publication 9 January 2002)

When listening to languages learned at a later age, speech intelligibility is generally lower than when listening to one's native language. The main purpose of this study is to quantify speech intelligibility in noise for specific populations of non-native listeners, only broadly addressing the underlying perceptual and linguistic processing. An easy method is sought to extend these quantitative findings to other listener populations. Dutch subjects listening to Germans and English speech, ranging from reasonable to excellent proficiency in these languages, were found to require a 1–7 dB better speech-to-noise ratio to obtain 50% sentence intelligibility than native listeners. Also, the psychometric function for sentence recognition in noise was found to be shallower for non-native than for native listeners (worst-case slope around the 50% point of 7.5%/dB, compared to 12.6%/dB for native listeners). Differences between native and non-native speech intelligibility are largely predicted by linguistic entropy estimates as derived from a letter guessing task. Less effective use of context effects (especially semantic redundancy) explains the reduced speech intelligibility for non-native listeners. While measuring speech intelligibility for many different populations of listeners (languages, linguistic experience) may be prohibitively time consuming, obtaining predictions of non-native intelligibility from linguistic entropy may help to extend the results of this study to other listener populations. © 2002 Acoustical Society of America. [DOI: 10.1121/1.1456928]

PACS numbers: 43.71.Gv, 43.71.Hw [CWT]

I. INTRODUCTION

Most people know from personal experience that “non-native” speech communication is generally less effective than purely “native” speech communication. This is readily verified by listening to foreign-accented speech in one's own language, or by trying to comprehend speech in a foreign language that is not fully mastered. It is also known that the intelligibility of speech depends strongly on the experience with the target language by listeners as well as talkers (e.g., Flege, 1992; Strange, 1995). Especially under adverse conditions (noise, reverberation, background babble), non-native speech communication tends to be less effective (Lane, 1963; Gat and Keith, 1978; Mayo *et al.*, 1997; Nábělek and Donahue, 1984).

Non-native speech has been studied extensively, from the perspective of production as well as perception. Usually, the objective of second-language (L2) speech studies is to contribute to a more profound insight into the complicated processes underlying speech perception. By contrast, our approach starts out by studying the intelligibility effect of non-nativeness in its own right. This information, when properly quantified, is expected to be directly applicable in more engineering-oriented disciplines associated with speech communication (speech intelligibility in room acoustics, design of communication systems). Our findings are also intended to be used for incorporating “the non-native factor” in existing speech intelligibility prediction models, such as the speech transmission index (STI; Steeneken and Houtgast,

1999) and the speech recognition sensitivity model (SRS; Müsch and Buus, 2001). They may also be useful in the field of clinical audiology, where the effects of hearing loss on speech intelligibility may be confounded with the effects of being raised in a “foreign” language.

In this study, the focus will be on the intelligibility effects of non-nativeness from the perspective of speech perception only: we will try to quantify the extent to which a population of L2 learners will suffer reduction of speech intelligibility when listening to a second language.

A great number of variables will influence the speech understanding process for a certain population of non-native listeners. First of all, the relation between the native language and the target (second) language is of importance. Between languages that are relatively similar (in terms of functional phonetic contrasts, phonology, etc.) different effects may be observed than between languages that have very little in common. As already stated above, an important factor is also the population's average experience with the second language (number of years since the language was first learned, intensity of use). Age of acquisition of the second language is another important variable (Flege, 1995; Flege *et al.*, 1997; Mayo *et al.*, 1997), as well as the amount of continued native language use (Meador, 2000). In order to be able to predict the size of any intelligibility effect involving non-native listeners, the population of listeners should be specified in terms of (at least) these factors.

Various studies have produced quantitative results of non-native speech intelligibility for specific subject populations. Florentine *et al.* (1984), for example, reported reduced speech intelligibility in noise for non-native subjects. The

^{a)}Electronic mail: vanwijngaarden@tm.tno.nl

speech-to-noise ratio required for 50% intelligibility of redundant sentences was 4 to 15 dB higher for French learners of the English language than for native English listeners, depending on experience. Florentine (1985) also found that non-native listeners were less able to take advantage of context; the difference between natives and non-natives was smaller for low-predictability sentences than for high-predictability sentences. These findings are supported, for instance, by the experiments of Mayo *et al.* (1997). This is contrary to predictions by Koster (1987), who conducted a series of linguistic experiments with Dutch subjects who were studying to become English teachers. By systematically varying the predictability of a test word through manipulation of its context, he found that the effect of semantic constraints on word recognition was of the same magnitude for native and non-native listeners. A closer investigation of the use of contextual information by non-native listeners is therefore needed.

Experiments concerning non-native speech intelligibility in noise will be described in Sec. II of this article: speech reception threshold (SRT) results are presented, which will allow a broad quantitative comparison between native and non-native speech intelligibility in noise. In Sec. III, this comparison will be refined by looking at the slope of the psychometric function in a sentence recognition task. In Sec. IV we will describe experiments exploring the relation between non-native sentence recognition and redundancy-related measures.

II. INTELLIGIBILITY THRESHOLD OF SPEECH IN NOISE FOR NON-NATIVE LISTENERS

A. Method

An interesting topic in relation to non-native speech perception is the use of word context. This means that speech intelligibility for non-native listeners is best measured using longer phrases (sentences). For measuring sentence intelligibility under the influence of noise, several proven methods are available, among which is the speech reception threshold (SRT; Plomp and Mimpen, 1979). The SRT method, used for all intelligibility experiments described in this article, is an adaptive method that measures the speech-to-noise ratio at which 50% of the tested sentences are perceived correctly. All listeners were Dutch; SRT tests were carried out with the same group of listeners, using sentences in three different languages: Dutch (D), English (E), and German (G).

1. Subjects

In order to allow meaningful interpretation of the intelligibility results obtained through SRT experiments, a well-defined population of test subjects has to be chosen. Mean scores across subjects will only be meaningful if the group of subjects is homogeneous in terms of L2 proficiency, age, level of education, and other factors influencing second-language skills.

Two main groups of subjects were recruited for this experiment. Group I was recruited following fairly strict guidelines. The recruiter used a “checklist” to make sure that only subjects were accepted that matched a set of predefined criteria. Group I consisted of nine tri-lingual Dutch university

students of various disciplines (not including languages or phonetics), aged 18–24 years, who considered English their second language and German their third language. All had first learned both English and German, written and orally, during secondary education (Dutch high school), all starting with English at age 12 or 13, and with German at age 13 or 14. For each individual subject, the self-reported overall proficiency (rated on a 5-point scale) was higher for English (mean rating 3.7) than for German (mean rating 2.9). All individual subjects had a much more frequent use of English than of German: all reported daily use of English (reading and/or listening), while use of the German language was typically weekly to monthly.

Subject group II, consisting of 11 subjects, was matched to group I in terms of age (18–24) and level of education, but without the strict requirements on experience with English and German. Group II subjects were only required to be able to understand spoken and written English and German above a certain minimum level. The spread in German proficiency was therefore larger (mean rating 3.3); the frequency of use of the German language varied from daily to yearly for group II. For English, mean self-reported proficiency and frequency of use of group II turned out to be just as good as of group I (mean rating 3.4). This is probably due to demographic and educational causes: Dutch university students are generally quite proficient in English. The fact that young Dutch people mainly watch English-spoken television with Dutch subtitles may also be part of the explanation.

In addition to the main subject groups I and II, two control groups were recruited: three native German and three American subjects. These control groups were used to verify that the implementation of the SRT test (sentence material and talkers) was equivalent across languages.

2. Procedure

The SRT test gives a robust measure for sentence intelligibility in noise, corresponding to the speech-to-noise ratio that gives 50% correct response of short redundant sentences. In the SRT testing procedure, masking noise is added to test sentences in order to obtain speech at a known speech-to-noise ratio. The standard masking noise spectrum (as applied in the experiments described in this article) is equal to the long-term average spectrum of the test sentences. After presentation of each sentence, the subject responds by orally repeating the sentence to an experimenter. The experimenter compares the response with the actual sentence. If every word in the responded sentence is correct, the noise level for the next sentence is increased by 2 dB; after an incorrect response, the noise level is decreased by 2 dB. The first sentence of a list of 13 sentences is repeated until it is responded correctly, using 4-dB steps. This is done to quickly converge to the 50% intelligibility threshold. By taking the average speech-to-noise ratio over the last ten sentences, the 50% sentence intelligibility threshold (SRT) is obtained.

During the experiments, the subjects (listeners) were seated in a sufficiently silent room. A set of Sony MDR-CD770 headphones was used to present the recorded sentences diotically to the listeners. All subjects participated in a brief training session before taking part in the actual experi-

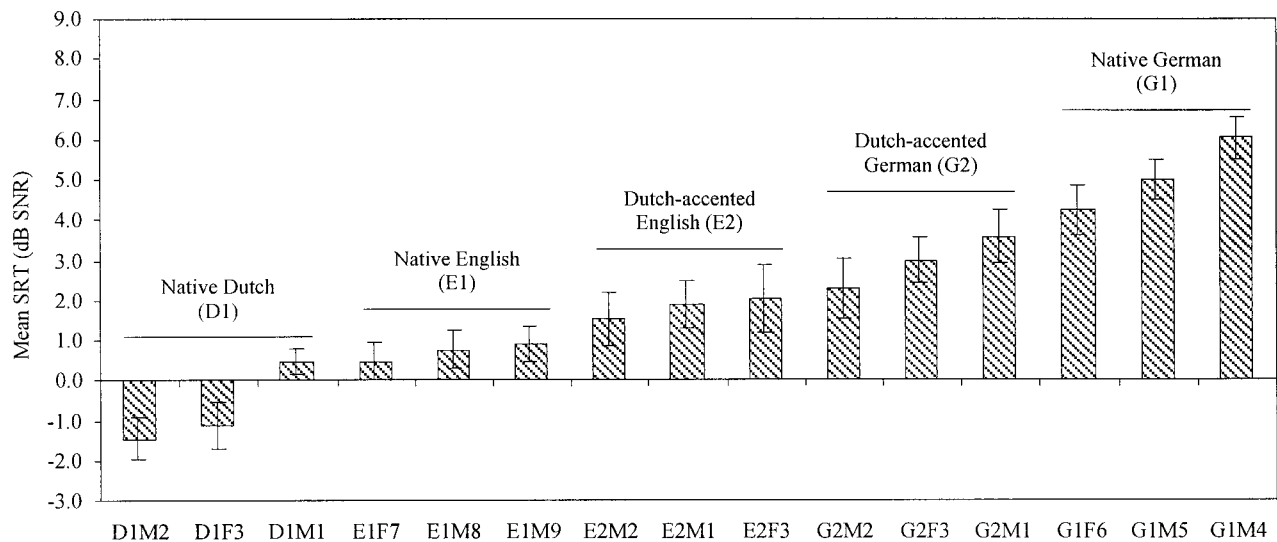


FIG. 1. Mean SRT results of subject group I per individual talker ($N=9$). All listeners were Dutch students, speaking English as a second language and German as a third language. Speech material was in Dutch (D1), English (E1 and E2), and German (G1 and G2). Non-native talkers (E2 and G2) were all Dutch. The talkers are labeled according to language group (e.g., D1), gender (M for male, F for female), and a unique number (1–9) for each talker. The error bars represent the standard error.

ments. None of the subjects had heard or read the test sentences before the experiments; each sentence was used only once with each subject, to avoid memory effects.

3. Stimuli

In order to be able to carry out speech intelligibility tests, suitable speech material has to be collected. A set of 130 standardized Dutch SRT sentences (10 lists of 13 sentences) were “translated” to German and English by native talkers of these languages with phonetic expertise and experience in speech research. This “translation” did not perfectly preserve the literal meaning of the sentences; the aim was to obtain the same context, complexity and length (number of syllables) in all languages. A procedure for obtaining multi-lingual speech databases for SRT tests, which gives equivalent results across languages, was described by van Wijngaarden *et al.* (2001). The sentences were recorded as spoken by native talkers of Dutch, German, and American English (referred to from hereon as D1, G1, and E1). Additionally, Dutch talkers (the same talkers as for the D1 experiment) also recorded English and German sentences (G2 and E2). Recordings were made for a total of nine talkers: three for each native language (two male, one female); because of the fact that the Dutch talkers recorded three sets of sentences (D1, G2, and E2), a total of 15 sets of recorded sentences was collected.

Talkers did not demonstrate any speaking disorders, and were informally estimated to have more or less average clarity of articulation. Influences of regional accents (deviations from the preferred pronunciation in the respective languages), when noticeable at all, were minor.

B. Results

1. Fully native baseline SRT scores

Conclusions regarding the effects of non-nativeness can only be drawn if the SRT implementation that is used is also

independent of language. In other words, we need to make sure that the precautions taken in the “translation” of the test sentences were effective in making the German and English test equal to the original Dutch test. This was verified by conducting “fully native” SRT tests in all three languages (three talkers per language; three English listeners, three German listeners, and 20 Dutch listeners).

The mean SRT was close to -1 dB in all of the languages (-0.8 for Dutch, -1.0 for English, and -1.1 for German). None of the differences in native SRT is statistically significant. This indicates that the performance of the SRT test is language independent.

Compared to SRT results found with thoroughly optimized SRT databases, a mean SRT of -1 dB may seem high. For a nonoptimized SRT test in Dutch (but with specifically selected talkers, which is not the case in the multi-lingual SRT test), Versfeld *et al.* (2000) report a mean SRT of -1.8 dB. The difference can most likely be attributed to the concessions done to keep the recording procedure practical, and the absence of a strict talker selection regime [see van Wijngaarden *et al.* (2001), for more details].

2. SRT scores of group I

Group I, the homogeneous group of nine trilingual Dutch subjects, participated in a SRT experiment in which subjects were presented with Dutch, German, and English speech. In addition to the SRT sentences by (native) G1 and E1 talkers, they were also presented with speech by the three Dutch talkers in German and English (G2 and E2). In this latter case, the overall intelligibility will not only be affected by non-native speech perception, but also by non-native speech production. The results from this experiment, separated by individual talker, are given in Fig. 1.

The talkers in Fig. 1 are grouped by language, and rank ordered according to mean SRT for all nine listeners. The effect of non-native perception of English (difference between D1 and E1 scores) is relatively small; the mean differ-

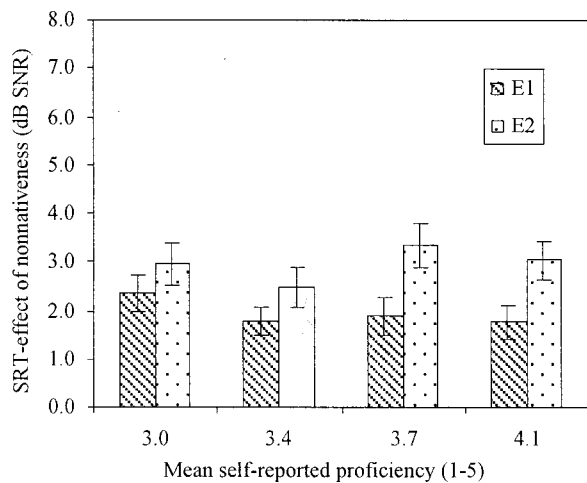


FIG. 2. The effect of non-nativeness (difference between native and non-native SRT) for subgroups of five subjects differing in self-reported proficiency. The non-native language is English. The error bars indicate the standard error (five subjects, three speakers; $N=15$).

ence in SRT is 1.4 dB. The mean difference between D1 and G1 is much larger: 5.8 dB. Different deficits for English and German were to be expected; the difference in proficiency and intensity of use have a clear effect on intelligibility. Compared to earlier results from similar studies in other languages (e.g., Buus *et al.*, 1986; Mayo *et al.*, 1997), the G1 deficit matches expectations, but the E1 deficit is smaller than expected for late bilinguals. The frequent “early” exposure of young Dutch people to English speech on television may be part of the explanation.

It is interesting to compare the scores for E1 (American English talkers) and E2 (Dutch talkers of the English language). The Dutch listeners do not benefit from hearing their “own” non-native accent in a second language: the native English talkers provide a better intelligibility. This is consistent with earlier findings by van Wijngaarden (2001) for the reverse situation (American subjects listening to Dutch sentences). For G1 and G2, the effect is exactly opposite: the Dutch listeners do experience better intelligibility in German if the talkers have a Dutch accent.

3. SRT scores of groups I and II together (group I+II)

The same SRT conditions presented to group I were also tested with group II. By combining the data of groups I and II, analysis based on a larger group of 20 subjects (which we will call “group I+II”) may be carried out, which will be more diverse in terms of their proficiency, at least in German. This allows us to study the effect of proficiency and experience on speech intelligibility.

In Figs. 2 and 3, combined SRT results for group I+II are given. Scores for the 20 subjects were divided into four subgroups of five subjects, according to the self-reported proficiency of the subjects. The leftmost subgroup in each figure is the subgroup with the lowest self-reported proficiency, the rightmost is the one with the highest proficiency. Although Fig. 2 (English) and Fig. 3 (German) are based on scores of the same 20 subjects, the division into subgroups is different. The division enables investigation of the effect of

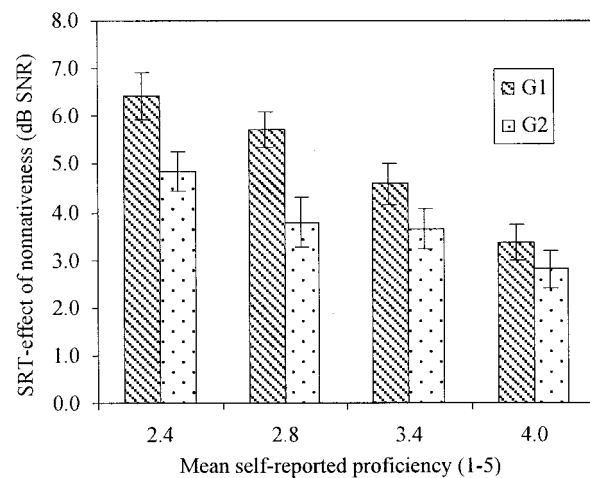


FIG. 3. The effect of non-nativeness (difference between native and non-native SRT) for subgroups of five subjects differing in self-reported proficiency. The non-native language is German. The error bars indicate the standard error (five subjects, three speakers; $N=15$).

proficiency on intelligibility. This is not easily done on the basis of individual proficiency ratings, since these tend to be fairly unreliable.

The results of Figs. 2 and 3 are not simply mean SRT scores on the German and English sentences, but rather the difference of these scores with the scores on the Dutch sentences. This difference is a direct measure of the effect of non-nativeness on speech intelligibility. By taking this difference, a correction is also applied for small differences in (native) Dutch SRT scores between the subgroups.

Figure 2 shows no significant effects of self-reported proficiency. All subjects (also from group II) showed a good command of the English language.

Whereas Fig. 2 does not show any systematic relation between intelligibility and self-reported proficiency, Fig. 3 demonstrates that such a relation can exist. For authentic, unaccented German speech, the intelligibility is higher (the effect of non-nativeness smaller) to the subgroups with higher proficiency ratings. The most proficient subgroup, for example, shows a significantly smaller effect ($p < 0.05$) than all of the other three subgroups for G1 talkers. With the exception of the differences between neighboring subgroups, all other differences for G1 talker in Fig. 3 are also statistically significant ($p < 0.05$; t -tests used to compare the means between subgroups).

The scores for G2 talkers (Dutch-accented German speech) appear to show the same trend. Here, however, the only difference between subgroups that is statistically significant is the difference between the least proficient and the most proficient subgroup ($p < 0.01$).

According to Fig. 2, E1 speech (authentic American English pronunciation) tends to be somewhat more intelligible to non-native Dutch listeners than (accented) English speech by Dutch talkers. This same effect was observed in Fig. 1, and appears to be relatively independent of (small) differences in proficiency.

Figure 3 shows, much the same as Fig. 1, a difference between G1 and G2 intelligibility that is contrary to the difference between E1 and E2. The difference between G1 and

G2 intelligibility appears to decrease with proficiency. The two subgroups with the lower self-reported proficiency differ significantly between G1 and G2; the differences are not significant for the other two (more proficient) subgroups.

It is clear that even subjects that give themselves high ratings for German proficiency have more problems understanding spoken German than the average subject has understanding spoken English. This is observed by comparing the effect of non-nativeness of the most proficient (rightmost) subgroup in Fig. 3 (German) to the least proficient (leftmost) subgroup in Fig. 2 (English); the performance in English appears to be still better than in German, although it is difficult to establish clear statistical proof for this.

Please note that the mean proficiency ratings for the subgroups are only used as relative rankings of proficiency to obtain a division into subgroups. These ratings hold no absolute value; the ratings for English may, for instance, not be directly compared to the ratings for German. The reason for this is that the subjects tend to rate themselves in relation to the performance of their peer group. A more objective measure of proficiency is needed to understand how the results reported in Fig. 3 are related to the results in Fig. 2 (in other words, how the differences in effects between English and German are explained in terms of differences in proficiency). This will be further explored in Sec. IV.

III. STEEPNESS OF THE PSYCHOMETRIC FUNCTION FOR NON-NATIVE SENTENCE INTELLIGIBILITY

A. Methods

The SRT results given in Sec. II characterize the psychometric function of sentence intelligibility by a single value: the SNR for which 50% sentence recognition occurs. However, much speech communication in real life takes place at speech-to-noise ratios corresponding to other levels of sentence intelligibility than 50%. We would therefore like to know the full psychometric function, so that we can predict the SNR necessary to meet any intelligibility criterion. This is especially relevant since the slope of the psychometric function is known to differ between native and non-native listeners (e.g., Mayo *et al.*, 1997).

The straightforward way of obtaining a full psychometric function is by sampling the curve at a fixed set of speech-to-noise ratios. This can be a rather laborious process. There is a theoretical possibility to extract additional information about the psychometric function from standard SRT measurements (Plomp and Mimpen, 1979). Unfortunately, the SRT experiments underlying Figs. 1 and 2 do not include enough individual subject responses at various SNR values to allow an accurate estimate of the steepness of the psychometric function.

A compromise between sampling the entire psychometric function and estimation of the steepness from standard SRT tests was chosen: first the standard SRT was measured, then the percentage of correctly responded sentences was measured directly at four speech-to-noise ratios around the SRT. Next, the psychometric function was fit through these points.

Slopes of the psychometric function will be compared

across languages. In a fully native setting (talker and listener), the SRT in Dutch, English, and German was found to be equal, leading to the conclusion that SRT results can be compared across languages in a straightforward way. For the slope of the psychometric function, this firm baseline was not established, but there are no reasons to expect considerable differences.

1. Subjects, stimuli, and conditions

A new group of 15 trilingual subjects was recruited, matching subject group I (nine subjects) on all relevant parameters. Since SRT subjects must be unacquainted with the sentence material, and the available material was limited to ten lists per language, the subjects from experiment I could not participate in this experiment. For the same reason, the conditions tested in this experiment do not include all talkers from experiment I. The three (baseline) Dutch talkers were included, as well as talker E1M8 (see Fig. 1) to represent the English talkers and talkers G1M5 to represent the German talkers. Dutch talker No. 3 was also included as an L2 talker of German (labeled G2F3 in Fig. 1) and English (E2F3). Material of each talker was presented to 5 subjects out of the group of 15.

2. Procedure

First of all, a standard SRT test was carried out for each subject in each condition. Next, the percentage of correctly repeated sentences was determined at SNR values differing by -4 , -2 , $+2$, and $+4$ dB relative to the SRT. The same criterion was used as in a standard SRT test: the subjects had to be able to correctly repeat the entire sentence for the presentation to be considered "correct." At each SNR value, a single list of SRT sentences (13 sentences) was presented.

Following this procedure, five points of the psychometric function were obtained (including the SRT at 50%) per subject per condition. A cumulative normal distribution was fit through these points using a nonlinear least-squares approach (Gauss-Newton method). Hence, the model assumed for the psychometric function was a cumulative normal distribution. Effectively, two parameters of the distribution were fit: the mean and the standard deviation. The mean of the distribution corresponds to the SRT, while the steepness of the psychometric function at 50% intelligibility is directed related to the standard deviation (Versfeld *et al.*, 2000). The steeper the psychometric function, the stronger the effect of a difference in speech-to-noise ratio on speech intelligibility.

B. Results

The speech reception threshold and the distribution mean obtained by fitting the psychometric function through observation data are essentially different estimates of the same variable: the 50% point of the psychometric function. Both estimates were found to yield very similar results.

The estimated slopes of the psychometric function around 50% intelligibility are given in Fig. 4.

Even at first sight, the steepness of the psychometric function clearly has an inverse relation with the SNR at the 50% point: talkers with higher values of the SRT (50% point)

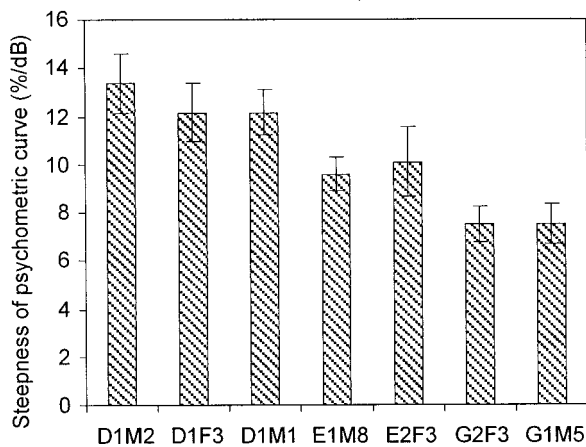


FIG. 4. Estimates of the steepness (slope at the 50% point) of the psychometric function for seven individual talkers. Error bars indicate the standard error of the estimates (five subjects; $N=5$).

have lower steepness, while language appears to be the explaining variable. The statistical significance of the differences in Fig. 4 was investigated by means of a Newman-Keuls test, after finding a significant effect in a one-way ANOVA. None of the differences between talkers speaking the same language was significant. The difference between G2F3 and E2F3, as well as the difference between E1M8 and D1M1, is also not significant. All other differences in Fig. 4 are statistically significant ($p<0.05$).

Clearly, the psychometric function when listening to L2 speech was generally shallower than when listening to L1 (Dutch) speech. For a second language for which the proficiency is lower (German compared to English), the mean of the distribution is not only shifted, but the steepness decreases as well. This is true at least for talkers E1M8 (English) and G1M5 (German); there is no reason to expect a different outcome for other talkers.

In terms of the 50% point of the psychometric function, nonauthentic pronunciation was found to be beneficial to Dutch listeners of German, but not of English (Fig. 1). Similar effects are not found on the slopes of the psychometric function.

IV. RELATIONS BETWEEN ACOUSTIC AND NONACOUSTIC FACTORS

A. The influence of context effects on SRT tests

In the case of non-native listeners, it seems likely that overall speech intelligibility is closely related to the listeners' skills at making use of linguistic redundancy (e.g., Bradlow and Pisoni; Bergman, 1980; Florentine, 1985; Mayo *et al.*, 1997). If this is true, we should be able to predict speech intelligibility from independent estimates of these linguistic skills. For this reason (if not for several others), it is worthwhile to look into methods of measuring listeners' use of linguistic redundancy.

A straightforward measure of linguistic redundancy is obtained through the letter guessing procedure (Shannon and Weaver, 1949), which uses orthographic presentations of sentences to obtain an estimate of linguistic entropy. Other suitable measures, such as the j - and k -factor by Boothroyd

and Nittrouer (1988) and the c -parameters in the context model by Bronkhorst *et al.* (1993), require more complicated and cumbersome experiments.

B. Linguistic entropy (letter guessing procedure)

The letter guessing procedure (LGP) yields a measure of linguistic entropy (LE); this may be seen as the inverse of the effective redundancy through linguistic factors in the speech material. This measure has been used as a measure of individual subjects' linguistic skills (e.g., Van Rooij, 1991). Linguistic entropy has been shown to predict the influence of linguistic factors on speech intelligibility (Müsch and Buus, 2001; Van Rooij, 1991).

Since the procedure is based on orthographic presentations of test sentences, what it measures is by definition nonacoustic. Although it is possible to derive redundancy-related measures from spoken language tests, the LGP has some advantages. Because of the orthographic presentation, there are no individual talker effects, and the influence of speech acoustics is eliminated. Furthermore, redundancy at the subword level is included, since individual letters have to be guessed. For practical reasons, this is hard to achieve in any spoken language test, especially with non-native subjects. The orthographic approach also has clear disadvantages. Some factors that are irrelevant for spoken language intelligibility, such as spelling, are included. Also, some very relevant factors, such as phonological transition rules, are not incorporated in the test. However, it is fair to assume that linguistic entropy according to our definition may serve as an indicator of linguistic factors involved in speech recognition.

1. Subjects and stimuli

The subjects from groups I and II also participated in letter guessing procedure experiments. Although the same sentence material was used as in the SRT test, subjects were presented with each sentence in either the LGP or SRT test, but never saw or heard the same sentence more than once.

2. Procedure

The subject's task was to guess the next letter in an unfinished written sentence, displayed on a computer screen. The subject had to start out with no other information than an indication of the language of the next sentence, and had to guess the first letter using a computer keyboard.

After typing the guessed letter, the subject received visual and auditory feedback ("+" or "-" on the screen, high- or low-pitch sound). The correct letter was displayed on the screen, regardless of what the subject's response was. Next, the subject had to guess the next letter, following the same procedure (but with the added knowledge of what the first letter was). Letter by letter, the correct sentence appeared on the screen, while the subject responses, ignoring the difference between uppercase and lowercase, were stored.

The percentage of correctly guessed letters is a measure of linguistic redundancy. If a subject has no knowledge of the language whatsoever, he will guess each letter in a purely random fashion. Hence, in English he may statistically be expected to guess 1 out of 27 letters right (26 letters and

space). The more redundant the language is to the subject, the fewer letters he is forced to select randomly.

Rather than working directly with the percentage of correctly responded letters, the LGP scores are expressed in terms of linguistic entropy. Entropy, in the context of information theory, is expressed in “bits.” The linguistic entropy L is related to the fraction of correctly responded letters c according to¹

$$L = -\log_2(c). \quad (1)$$

Assuming a 27-letter alphabet (including space), the linguistic entropy associated with pure guessing of a single letter is, according to formula (1), 4.75 bits. This is the upper limit to L . If all letters are immediately guessed correctly, then $L = 0$: the material is perfectly redundant.

As an added measure, subjects were informally checked for their capacity to spell simple words in the tested language. For the letters that are particular to Dutch and German, not existing in English, the subjects were instructed to use similar characters that are usually assigned to replace these letters (e.g., “ss” for German “ß”).

Linguistic entropy will strongly depend on the type of sentences that are used: the more redundant the sentences, the smaller the estimated linguistic entropy. Even words within sentences will differ in terms of LE: semantic constraints will cause words towards the end of a sentence to be more redundant than words at the beginning of a sentence. When LE-estimates are calculated on a word-for-word basis, we expect the average LE as a function of the position of the word within sentences to be a monotonically decreasing function. For individual sentences this will usually not be true; in the phrase “merry Christmas,” for instance, the word “Christmas” is likely to be a local minimum in LE, regardless of the position within a sentence. However, when LE is measured as a function of word position across multiple sentences, differing somewhat in construction and number of words, a monotonically decreasing function seems likely. It also seems fair to assume that the LE decrease between two consecutive words becomes smaller toward the end of the sentence; the more context already exists, the smaller the gain will be by adding one extra word. When we assume that the LE decrease has an inverse proportional relation to word position n ,

$$L_n - L_{n-1} = \frac{\alpha}{n}, \quad (2)$$

where $n \geq 2$ and α is an arbitrary constant, then L will be a function of n of the form

$$L_n = \beta + \alpha \ln n. \quad (3)$$

Here the constant β may be interpreted as the LE of a single word without sentence context; the constant α quantifies the effect of word position within a sentence on word LE. An exception is made for the first word ($n = 1$), for which Eq. (3) is not necessarily expected to hold. Within a set of sentences of a specific structure that is known to the subjects (such as SRT sentences), the predictability of the first word may be much higher than expected from Eq. (3).

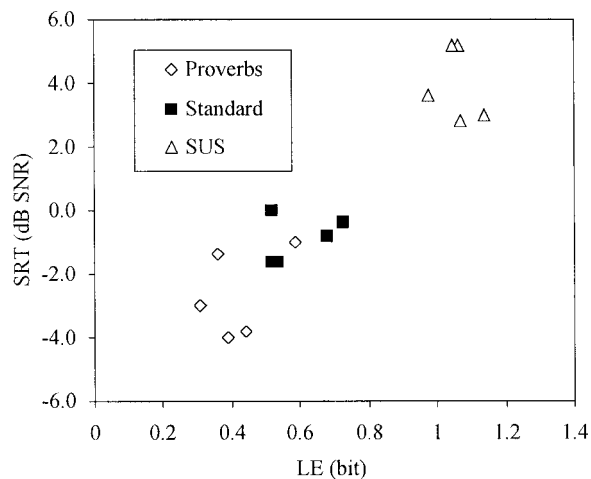


FIG. 5. Relation between SRT and LE, for five individual subjects and three types of SRT sentences. Results are mean values ($N = 2$ for SRT, $N = 13$ for LE). Speech material by the same talker was used for all SRT tests.

Since average LE effects due to word position will predominantly result from semantic constraints, semantic redundancy is in fact what the parameter α measures. By calculating LE as a function of word position across a sufficient number of subjects and sentences, the parameters α and β may be estimated using fixed nonlinear regression. By also estimating the standard errors associated with α and β , statistical significance is investigated by means of t -tests.

C. Results

1. Relation between LE and SRT for native speech communication

Linguistic entropy is the result of an interaction between subject and sentence material. If linguistic entropy estimates are to be used to quantify the effect of linguistic redundancy on SRT, this should also be possible in a fully native setting (Dutch subjects, Dutch language). The difference between subjects is then expected to be relatively small, but the amount of linguistic redundancy in the speech material can be varied systematically. This way, the relation between LE and SRT can be studied without introducing some of the uncertain factors that are automatically introduced when carrying out non-native perception experiments.

An important source of redundancy in natural speech is the use of semantic constraints. The SRT sentences form a homogeneous set in this respect. By constructing new sets of SRT sentences, which are designed to be as similar as possible to the “standard” SRT sentences in every way except semantic redundancy, the effect of semantic redundancy on native speech intelligibility may be evaluated. Similarly, the effect on linguistic entropy is investigated.

Two new sets of Dutch SRT sentences were constructed, one consisting of proverbs (higher than normal redundancy), the other consisting of semantically unpredictable sentences (lower than normal redundancy; Benoit *et al.*, 1996). LGP and SRT experiments were carried out with five native Dutch students, matching subject group II. Individual LE and SRT results are given in Fig. 5.

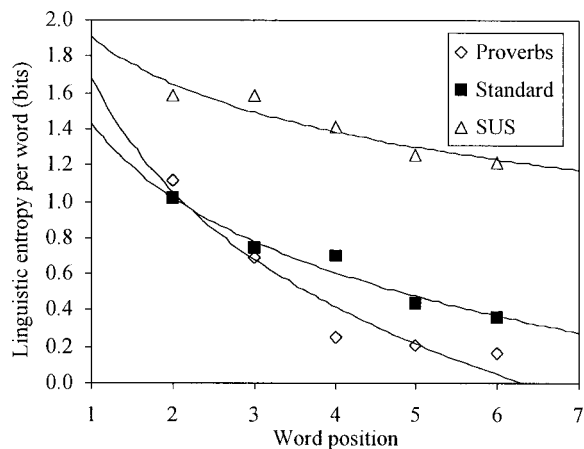


FIG. 6. Word-LE as a function of word position within sentences, for word positions $2 \leq n \leq 6$. The dashed lines are least-squares fits of Eq. (3) to the data for the three different kinds of sentences. Data points are based on five subjects (each 13 sentences) for proverbs and semantically unpredictable sentences, and on nine subjects (each 39 sentences) for the standard SRT sentences.

Figure 5 shows some residual between-subject variance on the SRT scores, not explained by linguistic entropy. Still, the relation between SRT and LE across sentence types is clear. This means that differences in SRT can be predicted, to a certain degree, from linguistic entropy estimates. The mean increase in SRT as a function of LE is 10 dB/bit between the proverbs and the standard sentences. Between the standard sentences and the semantically unpredictable sentences, this slope is also 10 dB/bit.

The linguistic entropy of the three types of sentences was also calculated for individual words as a function of word position; results of this calculation are given in Fig. 6. The very first word of each sentence was not included in this analysis; its baseline predictability is much higher than all the other words, since it is nearly always an article.

Figure 6 shows that LE decreases monotonically with word position, as expected. The estimated values of parameters α and β from Eq. (3) are given in Table I.

If it is true that the three types of sentences differ primarily in semantic constraints, then we expect similar values of β , but different values for α . The differences in α are, as expected, statistically significant. However, the differences in β are also significant. This may indicate that, between the different sentence types, factors other than semantics were also different, such as word choice (mean frequency of occurrence in natural language, mean familiarity). It could also indicate that the assumption expressed by Eq. (2) is not completely justified for words at the beginning of sentences.

TABLE I. Estimated LE parameters from native LGP experiments for three types of sentences.

Sentence type	Slope (α)	Offset (β)	R^2 (explained variance)
Proverbs	-0.91	1.69	0.93
Standard SRT	-0.58	1.41	0.97
SUS	-0.38	1.91	0.88

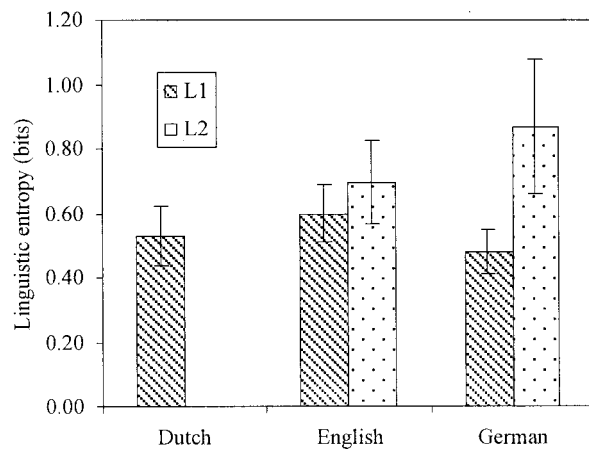


FIG. 7. Mean LGP results of L2 Dutch subjects (group I) and L1 German and American subjects. All L2 results and L1 Dutch results are based on nine listeners (39 sentences per listener, $N=351$); the L1 German and English results are based on three subjects (39 sentences, $N=117$). The error bars indicate the standard deviation.

2. Non-native LE results

With non-active listeners, linguistic entropy was not varied by manipulating the speech material; instead, it varied according to subjects' individual command of their second or third language. The LGP results of subject group I are presented in Fig. 7. Please note that the error bars in Fig. 7 indicate the standard deviation rather than the standard error, because of the large number of observations per language.

All differences in Fig. 7 are highly significant ($p < 0.001$). Unfortunately, and unlike the SRT results, the native (L1) LE scores are also significantly different between languages for L1 subjects. Hence, the LGP test is language dependent, and linguistic entropy estimates may not be compared across languages without applying corrections for differences in the LGP test.

The lowest native LE is found for German, then Dutch, and then English. The reduced entropy for German can be explained from a number of factors. Additional contextual constraints are introduced in German by the use of word gender and case, which is (virtually) not present in English, and of minor influence in Dutch. Moreover, the German convention of spelling nouns with capitalized first letters are also adopted in the feedback given by the LGP test, which also adds some redundancy.

Because of the differences between languages, we will use the "normalized" linguistic entropy from hereon. The normalization is accomplished by subtracting the mean native LE from the observed LE. This should largely eliminate between-language differences.

3. Relation between LE and SRT for non-native listeners

The effects of non-nativeness on LE appear to follow the same patterns as the SRT effects. This suggests that the overall intelligibility is largely determined by linguistic factors. Figure 8 shows the correlation between normalized LE and SRT for the individual subjects of group I+II (20 subjects) in all tested languages.

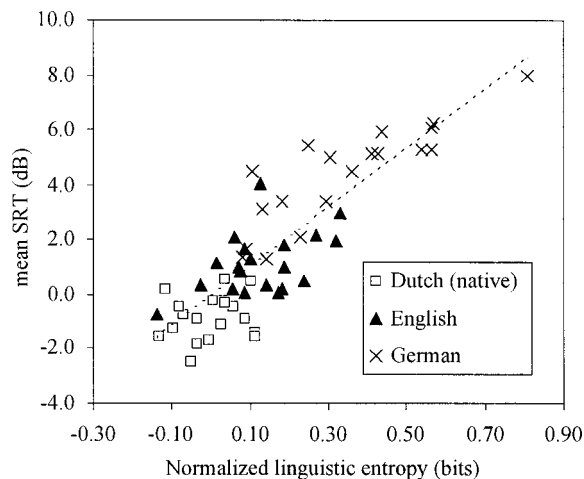


FIG. 8. Correlation between normalized LE and mean SRT (three talkers), for native Dutch and non-native English and German (20 subjects). All talkers were native in the given language. The dashed line is obtained through linear regression ($R^2=0.74$; slope 10.8 dB/bit, intercept -0.15 dB).

The value of the squared correlation coefficient ($R^2 = 0.74$) indicates that roughly 74% of the total variance in SRT scores in Fig. 8 may be explained using normalized linguistic entropy. This indicates that LE scores from letter guessing experiments can be used to obtain a fair prediction of corresponding SRT values.

More may perhaps still be learned from mean word LE as a function of word position, and by estimating the parameters α and β of Eq. (3). For the subjects of group I, we may verify the effect of the known difference in proficiency between (native) Dutch, English, and German (Fig. 9 and Table II).

All differences between the values of α and β in Table II are statistically significant. The influence of semantic constraints on LE, as quantified by slope α , is as could be expected for group I: apparently, the semantic constraints present in German sentences are not used as effectively as in English sentences.

The differences in β are not as easily interpreted, especially since β is higher for English than for German. If we

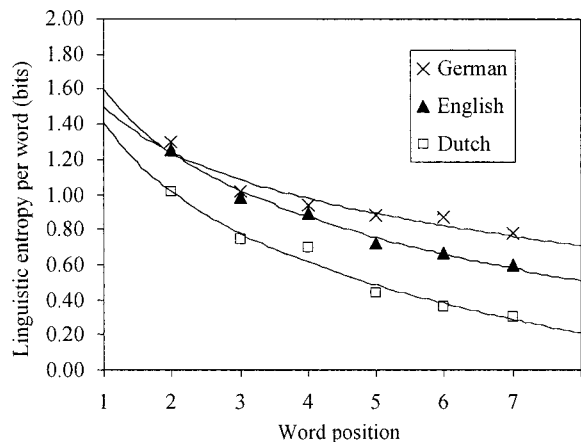


FIG. 9. Group I word-LE as a function of word position within sentences, for word positions $2 \leq n \leq 7$. The dashed lines are least-squares fits of Eq. (3) to the data for three different languages (native Dutch, and non-native English or German).

TABLE II. Estimated LE parameters from LGP experiments with group I subjects.

Sentence type	Slope (α)	Offset (β)	R_2 (explained variance)
Dutch (native)	-0.58	1.41	0.97
English	-0.52	1.60	0.99
German	-0.38	1.50	0.92

assume that β expresses the linguistic entropy of words due to all factors other than semantic constraints, then this also includes the systematic differences between orthographic representations of the different languages. In this light, the fact that β is higher for English than for German does not seem as surprising anymore, but little room is left for interpretation of this parameter. Table II shows that group I subjects benefit more from semantic constraints in English than in German. However, although it appears likely that there is a relation with speech intelligibility, Table II does not provide information about this relation.

By investigating similar curves as given in Fig. 9 for groups of subjects differing in (non-native) speech intelligibility, the relation between the α parameter and the SRT may be established.

For the data presented in Fig. 10, the 20 subjects of group I+II were divided in four subgroups according to their mean SRT when listening to German by G1 talkers. For these subgroups of five subjects, word LE as a function of word position was calculated (Fig. 10 and Table III).

All differences between values of α and all differences between values of β are significant, with the exception of the differences for α and β for the 6.3- and 5.2-dB subgroups. This shows that intelligibility is related to the effective use of semantic constraints (α -parameter), as well as other linguistic factors (β -parameter).

V. DISCUSSION AND CONCLUSIONS

Using the speech reception threshold method, effects of non-native speech perception on speech intelligibility could

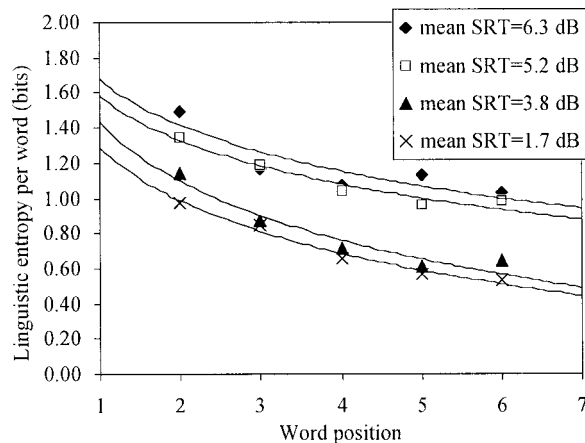


FIG. 10. Non-native German word-LE as a function of word position within sentences, for word positions $2 \leq n \leq 6$. The dashed lines are least-squares fits of Eq. (3) to the data for four subgroups of subject group I+II, differing in mean SRT (G1 speakers). Data points are based on five subjects (each 39 sentences).

TABLE III. Estimated LE parameters from LGP experiments with group I+II subjects (division into subgroups according to mean SRT scores for G1 talkers).

Mean SRT of subgroup (dB)	Slope (α)	Offset (β)	R_2 (explained variance)
6.3	-0.38	1.68	0.80
5.2	-0.36	1.58	0.94
3.8	-0.43	1.43	0.93
1.7	-0.48	1.29	0.98

be quantified for subjects ranging in proficiency from reasonable to excellent. Non-native speech recognition in noise does not just differ in terms of the mean of the psychometric function, but also the slope. To summarize the data given in this article, the average native (stylized) psychometric function and the worst-case non-native psychometric function derived from the experiments are given in Fig. 11.

The mean and slope of the psychometric functions of Fig. 11 can only be interpreted in the context of the specific sentence recognition paradigm used by the SRT test, implemented as described in this article. Other methods of measuring sentence recognition as a function of speech-to-noise ratio, or even other variations on the SRT paradigm, may lead to somewhat different results. For instance, relaxing the requirement that each individual word must be responded correctly will reduce the steepness of the curve. On the other hand, if optimized sets of selected test sentences are used (Versfeld *et al.*, 2000), then steeper psychometric functions will be found.

Despite the fact that there is a degree of dependency of the finding on the test method used, they also hold universal and quantitative meaning. If psychometric functions are known for two different test paradigms, in the same condition, then these curves can be used to transform measurement results from the scale of one test to the other. Hence, the difference between native and non-native intelligibility (given for our worst-case condition by the difference be-

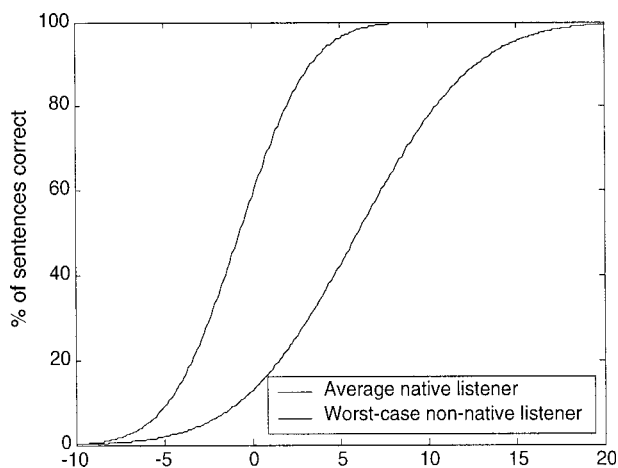


FIG. 11. Psychometric functions of speech reception in noise (percentage of sentences correctly received as a function of speech-to-noise ratio) for the average native listener from the SRT experiments (SRT = -0.7 dB, steepness 12.6%/dB) and the worst-case non-native listener (SRT = 6.0, steepness 7.5%/dB).

tween both curves in Fig. 11) can also be transformed to other intelligibility scales, as long as the corresponding psychometric functions are known as a function of speech-to-noise ratio.

A non-native listener with a degree of command on his second language that is better than that of the worst-case listener presented in Fig. 11 will produce a psychometric function when subjected to a SRT test that is somewhere between the two curves of Fig. 11.

For the listener populations and languages considered in this article, mean intelligibility effects of non-nativeness are sufficiently quantified by the outcome of the experiments. However, for other populations and languages, additional experiments will be needed. Carrying out listening experiments in non-native languages can be a time-consuming and difficult task. Letter guessing tests are easier to carry out, and the resulting linguistic entropy estimates predict speech intelligibility of non-native listeners with reasonable accuracy. This should open up possibilities to obtain (albeit somewhat crude) estimates of non-native listeners' intelligibility effects for a greater number of populations and languages.

As pointed out earlier in this work, the fact that linguistic entropy is a good predictor for intelligibility does not mean that the non-native speech recognition process is fully determined by linguistic factors. Since second-language learners tend to develop oral and written skills simultaneously, general second-language proficiency is an important explaining variable behind both linguistic entropy and SRT scores.

The fact that other than linguistic factors are also important is illustrated by the influence of L2 speech production (accented pronunciation) on L2 speech perception. Dutch listeners who were highly proficient in English experienced somewhat reduced speech intelligibility when listening to English by other non-native Dutch talkers, compared to native English talkers. For the same listeners, who were less proficient in German, the exact opposite was true for the German speech.

The experimental results offer no clear explanation for this discrepancy, but it seems that such an explanation is more likely to be found in the proficiency difference than in language-specific factors. The explanation could be that highly proficient listeners are able to use more subtle phonetic cues in authentically pronounced speech. The allophonic realizations of non-native talkers, even if they match the listeners' native model of phoneme space better, are less effective in transferring information needed in the speech recognition process. For less proficient listeners, these subtle phonetic cues are not as useful; they are unable to accurately categorize allophones using typically L2 phonetic contrasts, and perform better if these L2 allophones are "mapped" to their native phoneme space by non-native talkers.

In view of the results presented in Tables II and III, it seems likely that the contradictory findings by Florentine (1985) and others versus Koster (1987), regarding the use of semantic constraints by non-native listeners, can be explained by differences in their test population's mean proficiency. A high-proficiency population is likely to have "near-

native” use of contextual constraints, while this benefit is reduced for a low-proficiency population.

It is important to note that none of the experiments presented in this article were concerned with subjects of very poor proficiency. The earliest stages of second language learning may involve intelligibility effects beyond our scope of interest. However, people with sufficient command of a second language for practical daily usage will fall into categories somewhere between the two extremes given in Fig. 11. For the listener populations considered in this article, the presented measurement results can be used to assess exactly where between the lines in Fig. 11 we expect the psychometric function for a given population. For other languages and populations, additional data has to be collected. This data can consist of directly measured estimates of speech intelligibility; this is the best and most reliable option, but also the option that is the most difficult and time consuming. Alternatively, listeners’ intelligibility effects can be predicted from measures that are easier to obtain, such as linguistic entropy estimates.

ACKNOWLEDGMENTS

The authors would like to thank Søren Buus and an anonymous reviewer for their very useful comments on an earlier version of this manuscript.

¹Theoretically, linguistic entropy cannot be calculated from the fraction of correctly responded letters only, but needs to be corrected for the feedback (correct/incorrect) given to the subject. For simplicity, this correction is not included.

Benoît, C., Grice, M., and Hazan, V. (1996). “The SUS test: A method for the assessment of text-to-speech synthesis intelligibility using Semantically Unpredictable Sentences,” *Speech Commun.* **18**, 381–392.

Bergman, M. (1980). *Aging and the Perception of Speech* (University Park, Baltimore, MD).

Boothroyd, A., and Nittrouer, S. (1988). “Mathematical treatment of context effects in phoneme and word recognition,” *J. Acoust. Soc. Am.* **84**, 101–104.

Bradlow, A. R., and Pisoni, D. B. (1999). “Recognition of spoken words by native and non-native listeners: talker-, listener-, and item-related factors,” *J. Acoust. Soc. Am.* **106**, 2074–2085.

Bronkhorst, A. W., Bosman, A. J., and Smoorenburg, G. F. (1993). “A model for context effects in speech recognition,” *J. Acoust. Soc. Am.* **93**, 499–509.

Buus, S., Florentine, M., Scharf, B., and Canevet, G. (1986). “Native, French listeners’ perception of American-English in noise,” in *Proc. Internoise 86*, pp. 895–898.

Flege, J. E. (1992). “The intelligibility of English vowels spoken by British and Dutch talkers,” in *Intelligibility in Speech Disorders*, edited by R. D. Kent (Benjamins, Amsterdam).

Flege, J. E. (1995). “Second-language speech learning: theory, findings, and problems,” in *Speech Perception and Linguistic Experience*, edited by W. Strange (York, Baltimore, MD).

Flege, J. E., Bohn, O.-S., and Jang, S. (1997). “Effects of experience on non-native speakers’ production and perception of English vowels,” *J. Phonetics* **25**, 437–470.

Florentine, M., Buus, S., Scharf, B., and Canevet, G. (1984). “Speech reception thresholds in noise for native and non-native listeners,” *J. Acoust. Soc. Am. Suppl. 1* **74**, S84.

Florentine, M. (1985). “Non-native listeners’ perception of American-English in noise,” in *Proc. of Internoise 85*, pp. 1021–1024.

Gat, I. N., and Keith, R. W. (1978). “An effect of linguistic experience; auditory word discrimination by native and non-native speakers of English,” *Audiology* **17**, 339–345.

Koster, C. J. (1987). “Word Recognition in Foreign and Native Language; Effects of Context and Assimilation,” doctoral dissertation, University of Utrecht (Foris, Dordrecht, The Netherlands).

Lane, H. (1963). “Foreign accent and speech distortion,” *J. Acoust. Soc. Am.* **35**, 451–453.

Mayo, L. H., Florentine, M., and Buus, S. (1997). “Age of second-language acquisition and perception of speech in noise,” *J. Speech Lang. Hear. Res.* **40**, 686–693.

Meador, D., Flege, J. E., Mackay, I. R. A. (2000). “Factors affecting the recognition of words in a second language,” *Bilingualism: Language and Cognition* **3**, 55–67.

Müsch, H., and Buus, S. (2001). “Using statistical decision theory to predict speech intelligibility. I. Model structure,” *J. Acoust. Soc. Am.* **109**, 2896–2909.

Nábělek, A. K., and Donahue, A. M. (1984). “Perception of consonants in reverberation by native and non-native listeners,” *J. Acoust. Soc. Am.* **75**, 632–634.

Plomp, R., and Mimpen, A. M. (1979). “Improving the reliability of testing the speech reception threshold for sentences,” *Audiology* **18**, 43–52.

Shannon, C. E., and Weaver, W. (1949). *The Mathematical Theory of Communication* (Univ. of Illinois, Urbana).

Steeneken, H. J. M., and Houtgast, T. (1999). “Mutual dependence of the octave-band weights in predicting speech intelligibility,” *Speech Commun.* **28**, 109–123.

Strange, W. (1995). “Cross-language studies of speech perception: A historical review,” in *Speech Perception and Linguistic Experience*, edited by W. Strange (York, Baltimore, MD).

Van Rooij, J. C. G. M. (1991). “Aging and the perception of speech: auditive and cognitive aspects,” doctoral dissertation, Free University of Amsterdam.

van Wijngaarden, S. J. (2001a). “The intelligibility of non-native Dutch speech,” *Speech Commun.* **35**, 103–113.

van Wijngaarden, S. J., Steeneken, H. J. M., and Houtgast, T. (2001). “Methods and models for quantitative assessment of speech intelligibility in cross-language communication,” in *Proceedings of RTO Workshop on Multi-Lingual Speech and Language Processing*, Aalborg.

Versfeld, N. J., Daalder, J., Festen, J. M., and Houtgast, T. (2000). “Method for the selection of sentence materials for efficient measurement of the speech reception threshold,” *J. Acoust. Soc. Am.* **107**, 1671–1684.

YIN, a fundamental frequency estimator for speech and music^{a)}

Alain de Cheveigné^{b)}

Ircam-CNRS, 1 place Igor Stravinsky, 75004 Paris, France

Hideki Kawahara

Wakayama University

(Received 7 June 2001; revised 10 October 2001; accepted 9 January 2002)

An algorithm is presented for the estimation of the fundamental frequency (F_0) of speech or musical sounds. It is based on the well-known autocorrelation method with a number of modifications that combine to prevent errors. The algorithm has several desirable features. Error rates are about three times lower than the best competing methods, as evaluated over a database of speech recorded together with a laryngograph signal. There is no upper limit on the frequency search range, so the algorithm is suited for high-pitched voices and music. The algorithm is relatively simple and may be implemented efficiently and with low latency, and it involves few parameters that must be tuned. It is based on a signal model (periodic signal) that may be extended in several ways to handle various forms of aperiodicity that occur in particular applications. Finally, interesting parallels may be drawn with models of auditory processing. © 2002 Acoustical Society of America. [DOI: 10.1121/1.1458024]

PACS numbers: 43.72.Ar, 43.75.Yy, 43.70.Jt, 43.66.Hg [DOS]

I. INTRODUCTION

The fundamental frequency (F_0) of a periodic signal is the inverse of its period, which may be defined as the smallest positive member of the infinite set of time shifts that leave the signal invariant. This definition applies strictly only to a *perfectly* periodic signal, an uninteresting object (supposing one exists) because it cannot be switched on or off or modulated in any way without losing its perfect periodicity. Interesting signals such as speech or music depart from periodicity in several ways, and the art of fundamental frequency estimation is to deal with them in a useful and consistent way.

The subjective pitch of a sound usually depends on its fundamental frequency, but there are exceptions. Sounds may be periodic yet “outside the existence region” of pitch (Ritsma, 1962; Pressnitzer *et al.*, 2001). Conversely, a sound may not be periodic, but yet evoke a pitch (Miller and Taylor, 1948; Yost, 1996). However, over a wide range pitch and period are in a one-to-one relation, to the degree that the word “pitch” is often used in the place of F_0 , and F_0 estimation methods are often referred to as “pitch detection algorithms,” or PDA (Hess, 1983). Modern pitch perception models assume that pitch is derived either from the periodicity of neural patterns in the time domain (Licklider, 1951; Moore, 1997; Meddis and Hewitt, 1991; Cariani and Delgutte, 1996), or else from the harmonic pattern of partials resolved by the cochlea in the frequency domain (Goldstein, 1973; Wightman, 1973; Terhardt, 1974). Both processes yield the fundamental frequency or its inverse, the period.

Some applications give for F_0 a different definition, closer to their purposes. For voiced speech, F_0 is usually

defined as the rate of vibration of the vocal folds. Periodic vibration at the glottis may produce speech that is less perfectly periodic because of movements of the vocal tract that filters the glottal source waveform. However, glottal vibration itself may also show aperiodicities, such as changes in amplitude, rate or glottal waveform shape (for example, the duty cycle of open and closed phases), or intervals where the vibration seems to reflect several superimposed periodicities (diphony), or where glottal pulses occur without an obvious regularity in time or amplitude (glottalizations, vocal creak or fry) (Hedelin and Huber, 1990). These factors conspire to make the task of obtaining a useful estimate of speech F_0 rather difficult. F_0 estimation is a topic that continues to attract much effort and ingenuity, despite the many methods that have been proposed. The most comprehensive review is that of Hess (1983), updated by Hess (1992) or Hermes (1993). Examples of recent approaches are instantaneous frequency methods (Abe *et al.*, 1995; Kawahara *et al.*, 1999a), statistical learning and neural networks (Barnard *et al.*, 1991; Rodet and Doval, 1992; Doval, 1994), and auditory models (Duifhuis *et al.*, 1982; de Cheveigné, 1991), but there are many others.

Supposing that it can be reliably estimated, F_0 is useful for a wide range of applications. Speech F_0 variations contribute to prosody, and in tonal languages they help distinguish lexical categories. Attempts to use F_0 in speech recognition systems have met with mitigated success, in part because of the limited reliability of estimation algorithms. Several musical applications need F_0 estimation, such as automatic score transcription or real-time interactive systems, but here again the imperfect reliability of available methods is an obstacle. F_0 is a useful ingredient for a variety of signal processing methods, for example, F_0 -dependent spectral envelope estimation (Kawahara *et al.*, 1999b). Finally, a fairly recent application of F_0 is as metadata for multimedia content indexing.

^{a)}Portions of this work were presented at the 2001 ASA Spring Meeting and the 2001 Eurospeech conference.

^{b)}Electronic mail: cheveign@ircam.fr

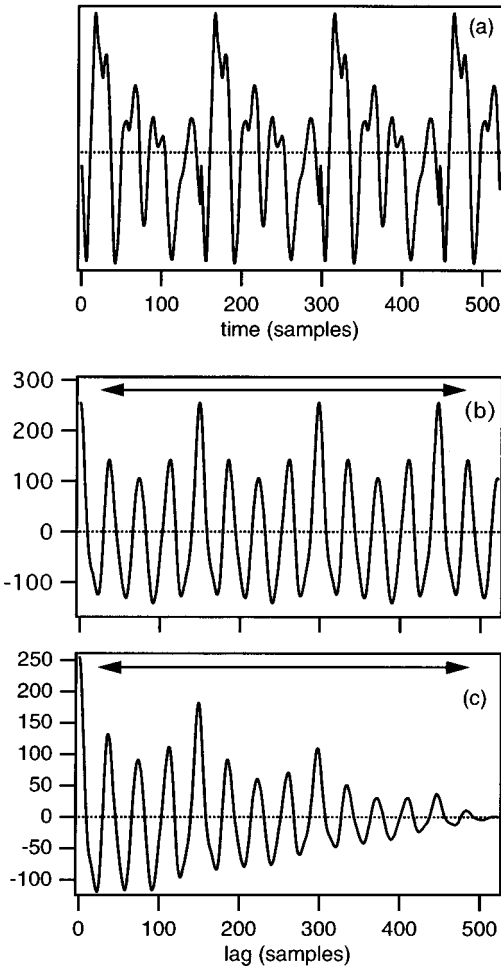


FIG. 1. (a) Example of a speech waveform. (b) Autocorrelation function (ACF) calculated from the waveform in (a) according to Eq. (1). (c) Same, calculated according to Eq. (2). The envelope of this function is tapered to zero because of the smaller number of terms in the summation at larger τ . The horizontal arrows symbolize the search range for the period.

The present article introduces a method for F_0 estimation that produces fewer errors than other well-known methods. The name YIN (from “yin” and “yang” of oriental philosophy) alludes to the interplay between autocorrelation and cancellation that it involves. This article is the first of a series of two, of which the second (Kawahara *et al.*, in preparation) is also devoted to fundamental frequency estimation.

II. THE METHOD

This section presents the method step by step to provide insight as to what makes it effective. The classic autocorrelation algorithm is presented first, its error mechanisms are analyzed, and then a series of improvements are introduced to reduce error rates. Error rates are measured at each step over a small database for illustration purposes. Fuller evaluation is proposed in Sec. III.

A. Step 1: The autocorrelation method

The autocorrelation function (ACF) of a discrete signal x_t may be defined as

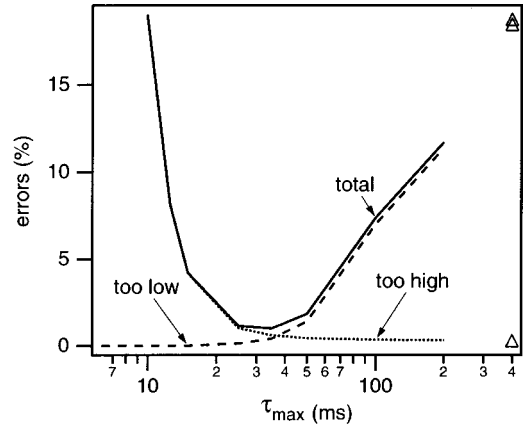


FIG. 2. F_0 estimation error rates as a function of the slope of the envelope of the ACF, quantified by its intercept with the abscissa. The dotted line represents errors for which the F_0 estimate was too high, the dashed line those for which it was too low, and the full line their sum. Triangles at the right represent error rates for ACF calculated as in Eq. (1) ($\tau_{\max} = \infty$). These rates were measured over a subset of the database used in Sec. III.

$$r_t(\tau) = \sum_{j=t+1}^{t+W} x_j x_{j+\tau}, \quad (1)$$

where $r_t(\tau)$ is the autocorrelation function of lag τ calculated at time index t , and W is the integration window size. This function is illustrated in Fig. 1(b) for the signal plotted in Fig. 1(a). It is common in signal processing to use a slightly different definition:

$$r'_t(\tau) = \sum_{j=t+1}^{t+W-\tau} x_j x_{j+\tau}. \quad (2)$$

Here the integration window size shrinks with increasing values of τ , with the result that the envelope of the function decreases as a function of lag as illustrated in Fig. 1(c). The two definitions give the same result if the signal is zero outside $[t+1, t+W]$, but differ otherwise. Except where noted, this article assumes the first definition (also known as “modified autocorrelation,” “covariance,” or “cross-correlation,” Rabiner and Shafer, 1978; Huang *et al.*, 2001).

In response to a periodic signal, the ACF shows peaks at multiples of the period. The “autocorrelation method” chooses the highest non-zero-lag peak by exhaustive search within a range of lags (horizontal arrows in Fig. 1). Obviously if the lower limit is too close to zero, the algorithm may erroneously choose the zero-lag peak. Conversely, if the higher limit is large enough, it may erroneously choose a higher-order peak. The definition of Eq. (1) is prone to the second problem, and that of Eq. (2) to the first (all the more so as the window size W is small).

To evaluate the effect of a tapered ACF envelope on error rates, the function calculated as in Eq. (1) was multiplied by a negative ramp to simulate the result of Eq. (2) with a window size $W = \tau_{\max}$:

$$r''_t(\tau) = \begin{cases} r_t(\tau)(1 - \tau/\tau_{\max}) & \text{if } \tau \leq \tau_{\max}, \\ 0, & \text{otherwise.} \end{cases} \quad (3)$$

Error rates were measured on a small database of speech (see Sec. III for details) and plotted in Fig. 2 as a function of

TABLE I. Gross error rates for the simple unbiased autocorrelation method (step 1), and for the cumulated steps described in the text. These rates were measured over a subset of the database used in Sec. III. Integration window size was 25 ms, window shift was one sample, search range was 40 to 800 Hz, and threshold (step 4) was 0.1.

Version	Gross error (%)
Step 1	10.0
Step 2	1.95
Step 3	1.69
Step 4	0.78
Step 5	0.77
Step 6	0.50

τ_{\max} . The parameter τ_{\max} allows the algorithm to be biased to favor one form of error at the expense of the other, with a minimum of total error for intermediate values. Using Eq. (2) rather than Eq. (1) introduces a natural bias that can be tuned by adjusting W . However, changing the window size has other effects, and one can argue that a bias of this sort, if useful, should be applied explicitly rather than implicitly. This is one reason to prefer the definition of Eq. (1).

The autocorrelation method compares the signal to its shifted self. In that sense it is related to the AMDF method (average magnitude difference function, Ross *et al.*, 1974; Ney, 1982) that performs its comparison using differences rather than products, and more generally to time-domain methods that measure intervals between events in time (Hess, 1983). The ACF is the Fourier transform of the power spectrum, and can be seen as measuring the regular spacing of harmonics within that spectrum. The cepstrum method (Noll, 1967) replaces the power spectrum by the log magnitude spectrum and thus puts less weight on high-amplitude parts of the spectrum (particularly near the first formant that often dominates the ACF). Similar “spectral whitening” effects can be obtained by linear predictive inverse filtering or center-clipping (Rabiner and Schafer, 1978), or by splitting the signal over a bank of filters, calculating ACFs within each channel, and adding the results after amplitude normalization (de Cheveigné, 1991). Auditory models based on autocorrelation are currently one of the more popular ways to explain pitch perception (Meddis and Hewitt, 1991; Cariani and Delgutte, 1996).

Despite its appeal and many efforts to improve its performance, the autocorrelation method (and other methods for that matter) makes too many errors for many applications. The following steps are designed to reduce error rates. The first row of Table I gives the gross error rate (defined in Sec. III and measured over a subset of the database used in that section) of the basic autocorrelation method based on Eq. (1) without bias. The next rows are rates for a succession of improvements described in the next paragraphs. These numbers are given for didactic purposes; a more formal evaluation is reported in Sec. III.

B. Step 2: Difference function

We start by modeling the signal x_t as a periodic function with period T , by definition invariant for a time shift of T :

$$x_t - x_{t+T} = 0, \quad \forall t. \quad (4)$$

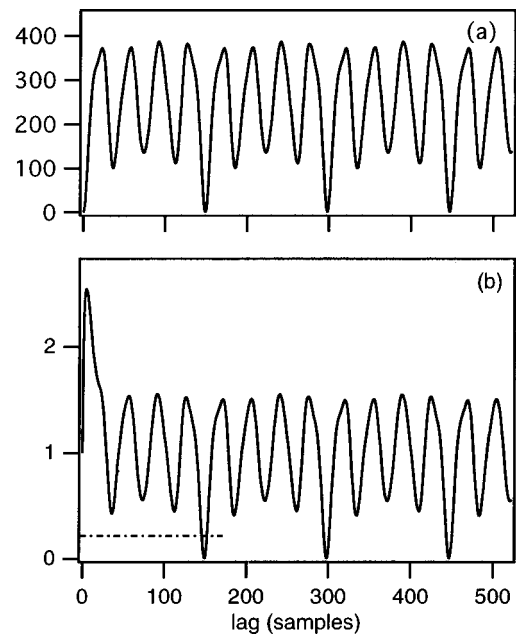


FIG. 3. (a) Difference function calculated for the speech signal of Fig. 1(a). (b) Cumulative mean normalized difference function. Note that the function starts at 1 rather than 0 and remains high until the dip at the period.

The same is true after taking the square and averaging over a window:

$$\sum_{j=t+1}^{t+W} (x_j - x_{j+T})^2 = 0. \quad (5)$$

Conversely, an unknown period may be found by forming the difference function:

$$d_t(\tau) = \sum_{j=1}^w (x_j - x_{j+\tau})^2, \quad (6)$$

and searching for the values of τ for which the function is zero. There is an infinite set of such values, all multiples of the period. The difference function calculated from the signal in Fig. 1(a) is illustrated in Fig. 3(a). The squared sum may be expanded and the function expressed in terms of the ACF:

$$d_t(\tau) = r_t(0) + r_{t+\tau}(0) - 2r_t(\tau). \quad (7)$$

The first two terms are energy terms. Were they constant, the difference function $d_t(\tau)$ would vary as the opposite of $r_t(\tau)$, and searching for a minimum of one or the maximum of the other would give the same result. However, the second energy term also varies with τ , implying that maxima of $r_t(\tau)$ and minima of $d_t(\tau)$ may sometimes not coincide. Indeed, the error rate fell to 1.95% for the difference function from 10.0% for unbiased autocorrelation (Table I).

The magnitude of this decrease in error rate may come as a surprise. An explanation is that the ACF implemented according to Eq. (1) is quite sensitive to amplitude changes. As pointed out by Hess (1983, p. 355), an increase in signal amplitude with time causes ACF peak amplitudes to grow with lag rather than remain constant as in Fig. 1(b). This encourages the algorithm to choose a higher-order peak and make a “too low” error (an amplitude decrease has the opposite effect). The difference function is immune to this par-

ticular problem, as amplitude changes cause period-to-period dissimilarity to increase with lag in all cases. Hess points out that Eq. (2) produces a function that is less sensitive to amplitude change [Eq. (A1) also has this property]. However, using $d(\tau)$ has the additional appeal that this function is more closely grounded in the signal model of Eq. (4), and paves the way for the next two error-reduction steps, the first of which deals with “too high” errors and the second with “too low” errors.

C. Step 3: Cumulative mean normalized difference function

The difference function of Fig. 3(a) is zero at zero lag and often nonzero at the period because of imperfect periodicity. Unless a lower limit is set on the search range, the algorithm must choose the zero-lag dip instead of the period dip and the method must fail. Even if a limit is set, a strong resonance at the first formant (F1) might produce a series of secondary dips, one of which might be deeper than the period dip. A lower limit on the search range is not a satisfactory way of avoiding this problem because the ranges of F1 and F_0 are known to overlap.

The solution we propose is to replace the difference function by the “cumulative mean normalized difference function:”

$$d'_t(\tau) = \begin{cases} 1, & \text{if } \tau=0, \\ d_t(\tau) / \left[(1/\tau) \sum_{j=1}^{\tau} d_t(j) \right] & \text{otherwise.} \end{cases} \quad (8)$$

This new function is obtained by dividing each value of the old by its average over shorter-lag values. It differs from $d(\tau)$ in that it starts at 1 rather than 0, tends to remain large at low lags, and drops below 1 only where $d(\tau)$ falls below average [Fig. 3(b)]. Replacing d by d' reduces “too high” errors, as reflected by an error rate of 1.69% (instead of 1.95%). A second benefit is to do away with the upper frequency limit of the search range, no longer needed to avoid the zero-lag dip. A third benefit is to normalize the function for the next error-reduction step.

D. Step 4: Absolute threshold

It easily happens that one of the higher-order dips of the difference function [Fig. 3(b)] is deeper than the period dip. If it falls within the search range, the result is a subharmonic error, sometimes called “octave error” (improperly because not necessarily in a power of 2 ratio with the correct value). The autocorrelation method is likewise prone to choosing a high-order peak.

The solution we propose is to set an absolute threshold and choose the smallest value of τ that gives a minimum of d' deeper than that threshold. If none is found, the global minimum is chosen instead. With a threshold of 0.1, the error rate drops to 0.78% (from 1.69%) as a consequence of a reduction of “too low” errors accompanied by a very slight increase of “too high” errors.

This step implements the word “smallest” in the phrase “the period is the smallest positive member of a set” (the

previous step implemented the word “positive”). The threshold determines the list of candidates admitted to the set, and can be interpreted as the proportion of aperiodic power tolerated within a “periodic” signal. To see this, consider the identity:

$$2(x_t^2 + x_{t+T}^2) = (x_t + x_{t+T})^2 + (x_t - x_{t+T})^2. \quad (9)$$

Taking the average over a window and dividing by 4,

$$\begin{aligned} 1/(2W) \sum_{j=t+1}^{t+W} (x_j^2 + x_{j+T}^2) \\ = 1/(4W) \sum_{j=t+1}^{t+W} (x_j + x_{j+T})^2 + 1/(4W) \\ \times \sum_{j=t+1}^{t+W} (x_j - x_{j+T})^2. \end{aligned} \quad (10)$$

The left-hand side approximates the power of the signal. The two terms on the right-hand side, both positive, constitute a partition of this power. The second is zero if the signal is periodic with period T , and is unaffected by adding or subtracting periodic components at that period. It can be interpreted as the “aperiodic power” component of the signal power. With $\tau=T$ the numerator of Eq. (8) is proportional to aperiodic power whereas its denominator, average of $d(\tau)$ for τ between 0 and T , is approximately twice the signal power. Thus, $d'(T)$ is proportional to the aperiodic/total power ratio. A candidate T is accepted in the set if this ratio is below threshold. We’ll see later on that the exact value of this threshold does not critically affect error rates.

E. Step 5: Parabolic interpolation

The previous steps work as advertised if the period is a multiple of the sampling period. If not, the estimate may be incorrect by up to half the sampling period. Worse, the larger value of $d'(\tau)$ sampled away from the dip may interfere with the process that chooses among dips, thus causing a gross error.

A solution to this problem is parabolic interpolation. Each local minimum of $d'(\tau)$ and its immediate neighbors is fit by a parabola, and the ordinate of the interpolated minimum is used in the dip-selection process. The abscissa of the selected minimum then serves as a period estimate. Actually, one finds that the estimate obtained in this way is slightly biased. To avoid this bias, the abscissa of the corresponding minimum of the *raw* difference function $d(\tau)$ is used instead.

Interpolation of $d'(\tau)$ or $d(\tau)$ is computationally cheaper than upsampling the signal, and accurate to the extent that $d'(\tau)$ can be modeled as a quadratic function near the dip. Simple reasoning argues that this should be the case if the signal is band-limited. First, recall that the ACF is the Fourier transform of the power spectrum: if the signal x_t is bandlimited, so is its ACF. Second, the ACF is a sum of cosines, which can be approximated near zero by a Taylor series with even powers. Terms of degree 4 or more come mainly from the highest frequency components, and if these are absent or weak the function is accurately represented by

lower order terms (quadratic and constant). Finally, note that the period peak has the same shape as the zero-lag peak, and the same shape (modulo a change in sign) as the period dip of $d(\tau)$, which in turn is similar to that of $d'(\tau)$. Thus, parabolic interpolation of a dip is accurate unless the signal contains strong high-frequency components (in practice, above about one-quarter of the sampling rate).

Interpolation had little effect on gross error rates over the database (0.77% vs 0.78%), probably because F_0 's were small in comparison to the sampling rate. However, tests with synthetic stimuli found that parabolic interpolation reduced fine error at all F_0 and avoided gross errors at high F_0 .

F. Step 6: Best local estimate

The role of integration in Eqs. (1) and (6) is to ensure that estimates are stable and do not fluctuate on the time scale of the fundamental period. Conversely, any such fluctuation, if observed, should not be considered genuine. It is sometimes found, for nonstationary speech intervals, that the estimate fails at a certain phase of the period that usually coincides with a relatively high value of $d'(T_t)$, where T_t is the period estimate at time t . At another phase (time t') the estimate may be correct and the value of $d'(T_{t'})$ smaller. Step 6 takes advantage of this fact, by “shopping” around the vicinity of each analysis point for a better estimate.

The algorithm is the following. For each time index t , search for a minimum of $d'_\theta(T_\theta)$ for θ within a small interval $[t - T_{\max}/2, t + T_{\max}/2]$, where T_θ is the estimate at time θ and T_{\max} is the largest expected period. Based on this initial estimate, the estimation algorithm is applied again with a restricted search range to obtain the final estimate. Using $T_{\max} = 25$ ms and a final search range of $\pm 20\%$ of the initial estimate, step 6 reduced the error rate to 0.5% (from 0.77%). Step 6 is reminiscent of median smoothing or dynamic programming techniques (Hess, 1983), but differs in that it takes into account a relatively short interval and bases its choice on quality rather than mere continuity.

The combination of steps 1–6 constitutes a new method (YIN) that is evaluated by comparison to other methods in the next section. It is worth noting how the steps build upon one another. Replacing the ACF (step 1) by the difference function (step 2) paves the way for the cumulative mean normalization operation (step 3), upon which are based the threshold scheme (step 4) and the measure $d'(T)$ that selects the best local estimate (step 6). Parabolic interpolation (step 5) is independent from other steps, although it relies on the spectral properties of the ACF (step 1).

III. EVALUATION

Error rates up to now were merely illustrative. This section reports a more formal evaluation of the new method in comparison to previous methods, over a compilation of databases of speech recorded together with the signal of a laryngograph (an apparatus that measures electrical resistance between electrodes placed across the larynx), from which a reliable “ground-truth” estimate can be derived. Details of the databases are given in the Appendix. The laryn-

graph F_0 estimate was derived automatically and checked visually, and estimates that seemed incorrect were removed from the statistics. This process removed unvoiced and also irregularly voiced portions (diphony, creak). Some studies include the latter, but arguably there is little point in testing an algorithm on conditions for which correct behavior is not defined.

When evaluating the candidate methods, values that differed by more than 20% from laryngograph-derived estimates were counted as “gross errors.” This relatively permissive criterion is used in many studies, and measures the difficult part of the task on the assumption that if an initial estimate is within 20% of being correct, any of a number of techniques can be used to refine it. Gross errors are further broken down into “too low” (mainly subharmonic) and “too high” errors.

In itself the error rate is not informative, as it depends on the difficulty of the database. To draw useful conclusions, different methods must be measured on the same database. Fortunately, the availability of freely accessible databases and software makes this task easy. Details of availability and parameters of the methods compared in this study are given in the Appendix. In brief, postprocessing and voiced–unvoiced decision mechanisms were disabled (where possible), and methods were given a common search range of 40 to 800 Hz, with the exception of YIN that was given an upper limit of one-quarter of the sampling rate (4 or 5 kHz depending on the database).

Table II summarizes error rates for each method and database. These figures should not be taken as an accurate measure of the intrinsic quality of each algorithm or implementation, as our evaluation conditions differ from those for which they were optimized. In particular, the search range (40 to 800 Hz) is unusually wide and may have destabilized methods designed for a narrower range, as evidenced by the imbalance between “too low” and “too high” error rates for several methods. Rather, the figures are a sampling of the performance that can be expected of “off-the-shelf” implementations of well-known algorithms in these difficult conditions. It is worth noting that the ranking of methods differs between databases. For example methods “acf” and “nacf” do well on DB1 (a large database with a total of 28 speakers), but less well on other databases. This shows the need for testing on extensive databases.

YIN performs best of all methods over all the databases. Averaged over databases, error rates are smaller by a factor of about 3 with respect to the best competing method. Error rates depend on the tolerance level used to decide whether an estimate is correct or not. For YIN about 99% of estimates are accurate within 20%, 94% within 5%, and about 60% within 1%.

IV. SENSITIVITY TO PARAMETERS

Upper and lower F_0 search bounds are important parameters for most methods. In contrast to other methods, YIN needs no upper limit (it tends, however, to fail for F_0 's beyond one quarter of the sampling rate). This should make it useful for musical applications in which F_0 can become very high. A wide range increases the likelihood of “finding” an

TABLE II. Gross error rates for several F_0 estimation algorithms over four databases. The first six methods are implementations available on the Internet, the next four are methods developed locally, and YIN is the method described in this paper. See Appendix for details concerning the databases, estimation methods, and evaluation procedure.

Method	Gross error (%)					
	DB1	DB2	DB3	DB4	Average	(low/high)
pda	10.3	19.0	17.3	27.0	16.8	(14.2/2.6)
fxac	13.3	16.8	17.1	16.3	15.2	(14.2/1.0)
fxcep	4.6	15.8	5.4	6.8	6.0	(5.0/1.0)
ac	2.7	9.2	3.0	10.3	5.1	(4.1/1.0)
cc	3.4	6.8	2.9	7.5	4.5	(3.4/1.1)
shs	7.8	12.8	8.2	10.2	8.7	(8.6/0.18)
acf	0.45	1.9	7.1	11.7	5.0	(0.23/4.8)
nacf	0.43	1.7	6.7	11.4	4.8	(0.16/4.7)
additive	2.4	3.6	3.9	3.4	3.1	(2.5/0.55)
TEMPO	1.0	3.2	8.7	2.6	3.4	(0.53/2.9)
YIN	0.30	1.4	2.0	1.3	1.03	(0.37/0.66)

incorrect estimate, and so relatively low error rates despite a wide search range are an indication of robustness.

In some methods [spectral, autocorrelation based on Eq. (2)], the window size determines both the maximum period that can be estimated (lower limit of the F_0 search range), and the amount of data integrated to obtain any particular estimate. For YIN these two quantities are decoupled (T_{\max} and W). There is, however, a relation between the appropriate value for one and the appropriate value for the other. For stability of estimates over time, the integration window must be no shorter than the largest expected period. Otherwise, one can construct stimuli for which the estimate would be incorrect over a certain phase of the period. The largest expected period obviously also determines the range of lags that need to be calculated, and together these considerations justify the well known rule of thumb: F_0 estimation requires enough signal to cover *twice* the largest expected period. The window may, however, be larger, and it is often observed that a larger window leads to fewer errors at the expense of reduced temporal resolution of the time series of estimates. Statistics reported for YIN were obtained with an integration window of 25 ms and a period search range of 25 ms, the shortest compatible with a 40 Hz lower bound on F_0 . Figure 4(a) shows the number of errors for different window sizes.

A parameter specific to YIN is the threshold used in step 4. Figure 4(b) shows how it affects error rate. Obviously it does not require fine tuning, at least for this task. A value of 0.1 was used for the statistics reported here. A final parameter is the cutoff frequency of the initial low-pass filtering of the signal. It is generally observed, with this and other methods, that low-pass filtering leads to fewer errors, but obviously setting the cutoff below the F_0 would lead to failure. Statistics reported here were for convolution with a 1-ms square window (zero at 1 kHz). Error rates for other values are plotted in Fig. 4(c). In summary, this method involves comparatively few parameters, and these do not require fine tuning.

V. IMPLEMENTATION CONSIDERATIONS

The basic building block of YIN is the function defined in Eq. (1). Calculating this formula for every t and τ is com-

putationally expensive, but there are at least two approaches to reduce cost. The first is to implement Eq. (1) using a recursion formula over time (each step adds a new term and subtracts an old). The window shape is then square, but a triangular or yet closer approximation to a Gaussian shape can be obtained by recursion (there is, however, little reason not to use a square window).

A second approach is to use Eq. (2) which can be calculated efficiently by FFT. This raises two problems. The first is that the energy terms of Eq. (7) must be calculated separately. They are not the same as $r'_t(0)$, but rather the

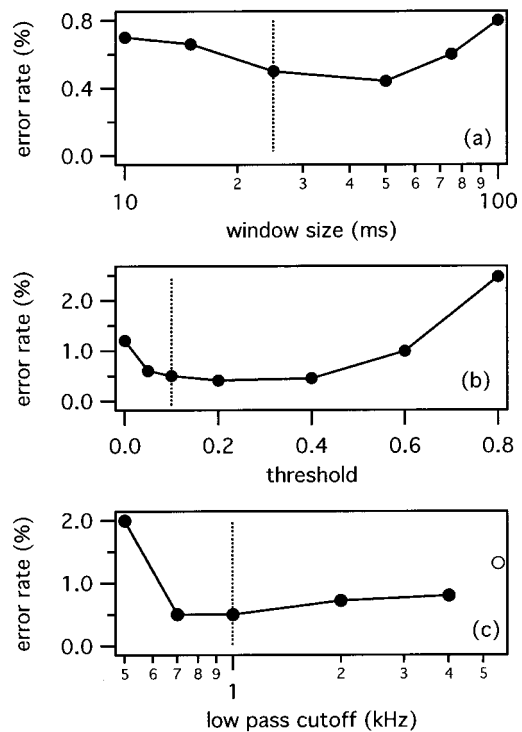


FIG. 4. Error rates of YIN: (a) as a function of window size, (b) as a function of threshold, and (c) as a function of low-pass prefilter cutoff frequency (open symbol is no filtering). The dotted lines indicate the values used for the statistics reported for YIN in Table II. Rates here were measured over a small database, a subset of that used in Sec. III. Performance does not depend critically on the values of these parameters, at least for this database.

sum of squares over the first and last $W - \tau$ samples of the window, respectively. Both must be calculated for each τ , but this may be done efficiently by recursion over τ . The second problem is that the sum involves more terms for small τ than for large. This introduces an unwanted bias that can be corrected by dividing each sample of $d(\tau)$ by $W - \tau$. However, it remains that large- τ samples of $d(\tau)$ are derived from a smaller window of data, and are thus less stable than small- τ samples. In this sense the FFT implementation is not as good as the previous one. It is, however, much faster when producing estimates at a reduced frame rate, while the previous approach may be faster if a high-resolution time series of estimates is required.

Real-time applications such as interactive music tracking require low latency. It was stated earlier that estimation requires a chunk of signal of at least $2T_{\max}$. However, step 4 allows calculations started at $\tau=0$ to terminate as soon as an acceptable candidate is found, rather than to proceed over the full search range, so latency can be reduced to $T_{\max} + T$. Further reduction is possible only if integration time is reduced below T_{\max} , which opens the risk of erroneously locking to the fine structure of a particularly long period.

The value $d'(T)$ may be used as a confidence indicator (large values indicate that the F_0 estimate is likely to be unreliable), in postprocessing algorithms to correct the F_0 trajectory on the basis of the most reliable estimates, and in template-matching applications to prevent the distance between a pattern and a template from being corrupted by unreliable estimates within either. Another application is in multimedia indexing, in which an F_0 time series may have to be down-sampled to save space. The confidence measure allows down-sampling to be based on correct rather than incorrect estimates. This scheme is implemented in the MPEG7 standard (ISO/IEC_JTC_1/SC_29, 2001).

VI. EXTENSIONS

The YIN method described in Sec. II is based on the model of Eq. (4) (periodic signal). The notion of model is insightful: an “estimation error” means simply that the model matched the signal for an unexpected set of parameters. Error reduction involves modifying the model to make such matches less likely. This section presents extended models that address situations where the signal deviates systematically from the periodic model. Tested quantitatively over our speech databases, none of these extensions improved error rates, probably because the periodic model used by YIN was sufficiently accurate for this task. For this reason we report no formal evaluation results. The aim of this section is rather to demonstrate the flexibility of the approach and to open perspectives for future development.

A. Variable amplitude

Amplitude variation, common in speech and music, compromises the fit to the periodic model and thus induces errors. To deal with it the signal may be modeled as a periodic function with time-varying amplitude:

$$x_{t+T}/a_{t+T} = x_t/a_t. \quad (11)$$

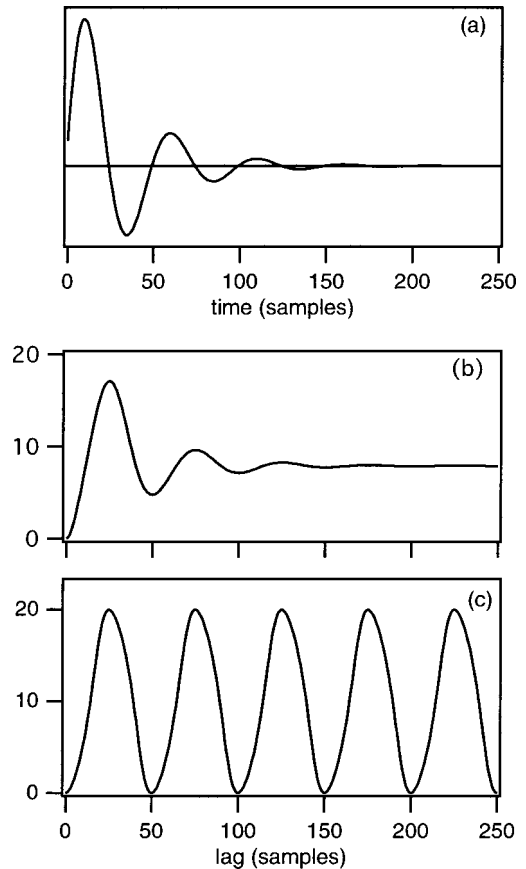


FIG. 5. (a) Sine wave with exponentially decreasing amplitude. (b) Difference function calculated according to Eq. (6) (periodic model). (c) Difference function calculated according to Eq. (12) (periodic model with time-varying amplitude). Period estimation is more reliable and accurate using the latter model.

If one supposes that the ratio $\alpha = a_{t+T}/a_t$ does not depend on t (as in an exponential increase or decrease), the value of α may be found by least squares fitting. Substituting that value in Eq. (6) then leads to the following function:

$$d_t(\tau) = r_t(0) [1 - r_t(\tau)^2 / r_t(0) r_{t+\tau}(0)]. \quad (12)$$

Figure 5 illustrates the result. The top panel displays the time-varying signal, the middle a function $d'(\tau)$ derived according to the standard procedure, and the bottom the same function derived using Eq. (12) instead of Eq. (6). Interestingly, the second term on the right of Eq. (12) is the square of the normalized ACF.

With two parameters the model of Eq. (12) is more “permissive” and more easily fits an amplitude-varying signal. However, this also implies more opportunities for “unexpected” fits, in other words, errors. Perhaps for that reason it actually produced a slight increase in error rates (0.57% vs. 0.50% over the restricted database). However, it was used with success to process the laryngograph signal (see the Appendix).

B. Variable F_0

Frequency variation, also common in speech and music, is a second source of aperiodicity that interferes with F_0 estimation. When F_0 is constant a lag τ may be found for

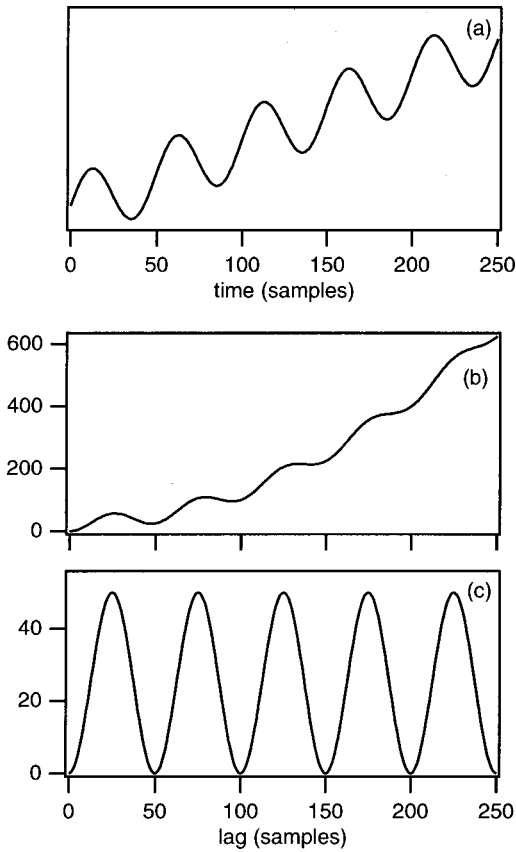


FIG. 6. (a) Sine wave with linearly increasing DC offset. (b) Difference function calculated according to Eq. (6). (c) Difference function calculated according to Eq. (13) (periodic model with DC offset). Period estimation is more reliable and accurate using the latter model.

which $(x_j - x_{j+\tau})^2$ is zero over the whole integration window of $d(\tau)$, but with a time-varying F_0 it is identically zero only at one point. On either side, its value $(x_j - x_{j+\tau})^2$ varies quadratically with distance from this point, and thus $d(\tau)$ varies with the cube of window size, W .

A shorter window improves the match, but we know that the integration window must not be shortened beyond a certain limit (Sec. IV). A solution is to split the window into two or more segments, and to allow τ to differ between segments within limits that depend on the maximum expected rate of change. Xu and Sun (2000) give a maximum rate of F_0 change of about ± 6 oct/s, but in our databases it did not often exceed ± 1 oct/s (Fig. 10). With a split window the search space is larger but the match is improved (by a factor of up to 8 in the case of two segments). Again, this model is more easily satisfied than that of Eq. (4), and therefore may introduce new errors.

C. Additive noise: Slowly varying DC

A common source of aperiodicity is additive noise which can take many forms. A first form is simply a time-varying “DC” offset, produced for example by a singer’s breath when the microphone is too close. The deleterious effect of a DC ramp, illustrated in Fig. 6(b), can be eliminated by using the following formula, obtained by setting the derivative of $d_t(\tau)$ with respect to the DC offset to zero:

$$d_t(\tau) = r_t(0) + r_{t+\tau}(0) - 2r_t(\tau) + \left[\sum_{j=t+1}^{t+W} (x_j - x_{j+\tau}) \right]^2 \quad (13)$$

as illustrated in Fig. 6(c).

Again, this model is more permissive than the strict periodic model and thus may introduce new errors. For that reason, and because our speech data contained no obvious DC offsets, it gave no improvement and instead slightly increased error rates (0.51% vs 0.50%). However, it was used with success to process the laryngograph signal, which had large slowly varying offsets.

D. Additive noise: Periodic

A second form of additive noise is a concurrent periodic sound, for example, a voice or an instrument, hum, etc. Except in the unlucky event that the periods are in certain simple ratios, the effects of the interfering sound can be eliminated by applying a comb filter with impulse response $h(t) = \delta(t) - \delta(t+U)$ where U is the period of the interference. If U is known, this processing is trivial. If U is unknown, both it and the desired period T may be found by the joint estimation algorithm of de Cheveigné and Kawahara (1999). This algorithm searches the (τ, ν) parameter space for a minimum of the following difference function:

$$dd_t(\tau, \nu) = \sum_{j=t+1}^{t+W} (x_j - x_{j+\tau} - x_{j+\nu} + x_{j+\tau+\nu})^2. \quad (14)$$

The algorithm is computationally expensive because the sum must be recalculated for all pairs of parameter values. However, this cost can be reduced by a large factor by expanding the squared sum of Eq. (14):

$$\begin{aligned} dd_t(\tau, \nu) &= r_t(0) + r_{t+\tau}(0) + r_{t+\nu}(0) + r_{t+\tau+\nu}(0) \\ &\quad - 2r_t(\tau) - 2r_t(\nu) + 2r_t(\tau + \nu) \\ &\quad + 2r_{t+\tau}(\nu - \tau) - 2r_{t+\tau}(\nu) - 2r_{t+\nu}(\tau). \end{aligned} \quad (15)$$

The right-hand terms are the same ACF coefficients that served for single period estimation. If they have been precalculated, Eq. (15) is relatively cheap to form. The two-period model is again more permissive than the one-period model and thus may introduce new errors. As an example, recall that the sum of two closely spaced sines is equally well interpreted as such (by this model), or as an amplitude-modulated sine (by the periodic or variable-amplitude periodic models). Neither interpretation is more “correct” than the other.

E. Additive noise: Different spectrum from target

Suppose now that the additive noise is neither DC nor periodic, but that its spectral envelope differs from that of the periodic target. If both long-term spectra are known and stable, filtering may be used to reinforce the target and weaken the interference. Low-pass filtering is a simple example and its effects are illustrated in Fig. 4(c).

If spectra of target and noise differ only on a short-term basis, one of two techniques may be applied. The first is to split the signal over a filter bank (for example, an auditory model filter bank) and calculate a difference function from

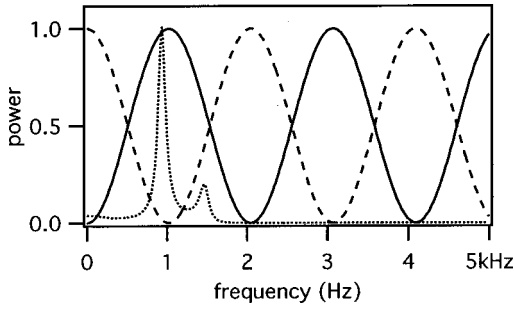


FIG. 7. Power transfer functions for filters with impulse response $\delta_t - \delta_{t+\tau}$ (full line) and $\delta_t + \delta_{t+\tau}$ (dashed line) for $\tau = 1$ ms. To reduce the effect of additive noise on F_0 estimation, the algorithm searches for the value of τ and the sign that maximize the power of the periodic target relative to aperiodic interference. The dotted line is the spectrum of a typical vowel.

each output. These functions are then added to obtain a summary difference function from which a periodicity measure is derived. Individual channels are then removed one by one until periodicity improves. This is reminiscent of Licklider's (1951) model of pitch perception.

The second technique applies an adaptive filter at the input, and searches jointly for the parameters of the filter and the period. This is practical for a simple filter with impulse response $h(t) = \delta(t) \pm \delta(t+V)$, where V and the sign determine the shape of the power transfer function illustrated in Fig. 7. The algorithm is based on the assumption that some value of V and sign will advantage the target over the interference and improve periodicity. The parameter V and the sign are determined, together with the period T , by searching for a minimum of the function:

$$\begin{aligned} dd'_t(\tau, \nu) = & r_t(0) + r_{t+\tau}(0) + r_{t+\nu}(0) + r_{t+\tau+\nu}(0) \\ & \pm 2r_t(\tau) - 2r_t(\nu) \mp 2r_t(\tau + \nu) \\ & \mp 2r_{t+\tau}(\nu - \tau) - 2r_{t+\tau}(\nu) \pm 2r_{t+\nu}(\tau), \end{aligned} \quad (16)$$

which (for the negative sign) is similar to Eq. (15). The search spaces for T and V should be disjoint to prevent the comb-filter tuned to V from interfering with the estimation of T . Again, this model is more permissive than the standard periodic model, and the same warnings apply as for other extensions to that model.

F. Additive noise: Same spectrum as target

If the additive noise shares the same spectral envelope as the target on an instantaneous basis, none of the previous methods is effective. Reliability and accuracy can nevertheless be improved if the target is stationary and of sufficiently long duration. The idea is to make as many period-to-period comparisons as possible given available data. Denoting as D the duration, and setting the window size W to be at least as large as the maximum expected period, the following functions are calculated:

$$d_k(\tau) = \sum_{j=1}^{D-kW} (x_j - x_{j-\tau})^2, \quad k=1, \dots, D/W. \quad (17)$$

The lag (τ) axis of each function is then "compressed" by a factor of $D/W - k$, and the functions are summed:

$$d(\tau) = \sum_{k=1}^{D/W} d_k(\tau/(D/W - k)). \quad (18)$$

This function is the sum of $(D/W)(D/W - 1)/2$ differences. For $\tau \neq T$ each difference includes both a deterministic part (target) and a noise part, whereas for $\tau = T$ they only include the noise part. Deterministic parts add in phase while noise parts tend to cancel each other out, so the salience of the dip at $\tau = T$ is reinforced. Equation (18) resembles (with different coefficients) the "narrowed autocorrelation function" of Brown and Puckette (1989) that was used by Brown and Zhang (1991) for musical F_0 estimation, and by de Cheveigné (1989) and Slaney (1990) in pitch perception models.

To summarize, the basic method can be extended in several ways to deal with particular forms of aperiodicity. These extensions may in some cases be combined (for example, modeling the signal as a sum of periodic signals with varying amplitudes), although all combinations have not yet been explored. We take this flexibility to be a useful feature of the approach.

VII. RELATIONS WITH AUDITORY PERCEPTION MODELS

As pointed out in the Introduction, the autocorrelation model is a popular account of pitch perception, but attempts to turn that model into an accurate speech F_0 estimation method have met with mitigated success. This study showed how it can be done. Licklider's (1951) model involved a network of delay lines (the τ parameter) and coincidence-counting neurons (a probabilistic equivalent of multiplication) with temporal smoothing properties (the equivalent of integration). A previous study (de Cheveigné, 1998) showed that excitatory coincidence could be replaced by inhibitory "anti-coincidence," resulting in a "cancellation model of pitch perception" in many regards equivalent to autocorrelation. The present study found that cancellation is actually more effective, but also that it may be accurately implemented as a sum of autocorrelation terms.

Cancellation models (de Cheveigné, 1993, 1997, 1998) require both excitatory and inhibitory synapses with fast temporal characteristics. The present study suggests that the same functionality might be obtained with fast excitatory synapses only, as illustrated in Fig. 8. There is evidence for fast excitatory interaction in the auditory system, for example in the medial superior olive (MSO), as well as for fast inhibitory interaction, for example within the lateral superior olive (LSO) that is fed by excitatory input from the cochlear nucleus, and inhibitory input from the medial trapezoidal body. However, the limit on temporal accuracy may be lower for inhibitory than for excitatory interaction (Joris and Yin, 1998). A model that replaces one by the other without loss of functionality is thus a welcome addition to our panoply of models.

Sections VID and VIE showed how a cascade of subtractive operations could be reformulated as a sum of autocorrelation terms. Transposing to the neural domain, this suggests that the cascaded cancellation stages suggested by de Cheveigné and Kawahara (1999) to account for multiple pitch perception, or by de Cheveigné (1997) to account for

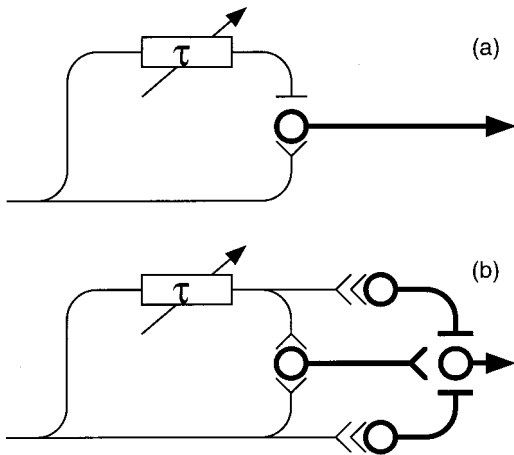


FIG. 8. (a) Neural cancellation filter (de Cheveigné, 1993, 1997). The gating neuron receives excitatory (direct) and inhibitory (delayed) inputs, and transmits any spike that arrives via the former unless another spike arrives simultaneously via the latter. Inhibitory and excitatory synapses must both be fast (symbolized by thin lines). Spike activity is averaged at the output to produced slowly varying quantities (symbolized by thick lines). (b) Neural circuit with the same properties as in (a), but that only requires fast excitatory synapses. Inhibitory interaction involves slowly varying quantities (thick lines). Double “chevrons” symbolize that output discharge probability is proportional to the square of input discharge probability. These circuits should be understood as involving many parallel fibers to approximate continuous operations on probabilities.

concurrent vowel identification, might instead be implemented in a single stage as a neural equivalent of Eq. (15) or (16). Doing away with cascaded time-domain processing avoids the assumption of a succession of phase-locked neurons, and thus makes such models more plausible. Similar remarks apply to cancellation models of binaural processing (Culling and Summerfield, 1995; Akeroyd, 2000; Breebart *et al.*, 2001).

To summarize, useful parallels may be drawn between signal processing and auditory perception. The YIN algorithm is actually a spin-off of work on auditory models. Conversely, addressing this practical task may be of benefit to auditory modeling, as it reveals difficulties that are not obvious in modeling studies, but that are nevertheless faced by auditory processes.

VIII. DISCUSSION

Hundreds of F_0 estimation methods have been proposed in the past, many of them ingenious and sophisticated. Their mathematical foundation usually assumes periodicity, and when that is degraded (which is when smart behavior is most needed) they may break down in ways not easy to predict. As pointed out in Sec. II A, seemingly different estimation methods are related, and our analysis of error mechanisms can probably be transposed, *mutatis mutandis*, to a wider class of methods. In particular, every method is faced with the problem of trading off too-high versus too-low errors. This is usually addressed by applying some form of bias as illustrated in Sec. II A. Bias may be explicit as in that section, but often it is the result of particular side effects of the algorithm, such as the tapering that resulted with Eq. (2) from limited window size. If the algorithm has several parameters, credit assignment is difficult. The key to the success of YIN is

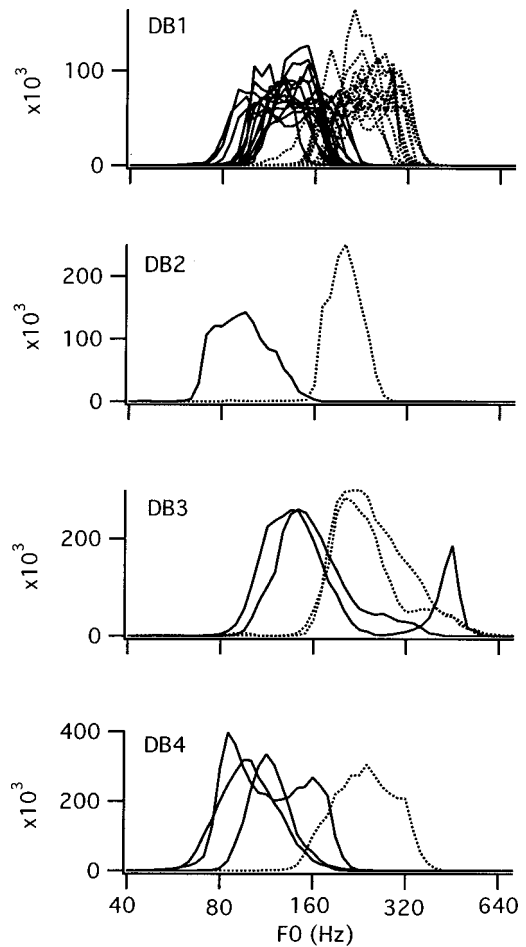


FIG. 9. Histograms of F_0 values over the four databases. Each line corresponds to a different speaker, either male (full lines) or female (dotted lines). The bin width is one semitone ($\frac{1}{12}$ of an octave). The skewed or bimodal distributions of database 3 are due to the presence of material pronounced in a falsetto voice.

probably step 3 that allows it to escape from the bias paradigm, so that the two types of error can be addressed independently. Other steps can be seen as either preparing for this step (steps 1 and 2) or building upon it (steps 4 and 6).

Parabolic interpolation (step 5) gives subsample resolution. Very accurate estimates can be obtained using an interval of signal that is not large. Precisely, to accurately estimate the period T of a perfectly periodic signal, *and* to be sure that the true period is not instead greater than T , at least

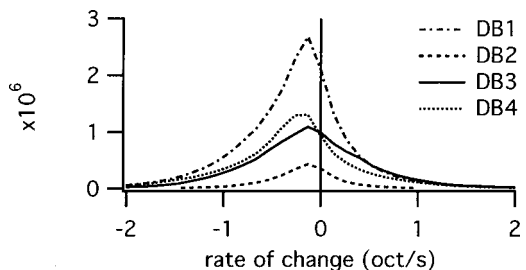


FIG. 10. Histograms of rate of F_0 change for each of the four databases. Each line is an aggregate histogram over all speakers of the database. The rate of change is measured over a 25-ms time increment (one period of the lowest expected F_0). The bin width is 0.13 oct/s. The asymmetry of the distributions reflects the well-known declining trend of F_0 in speech.

$2T+1$ samples of data are needed. If this is granted, there is no theoretical limit to accuracy. In particular, it is not limited by the familiar uncertainty principle $\Delta T \Delta F = \text{const}$.

We avoided familiar postprocessing schemes such as median smoothing (Rabiner and Schafer, 1978) or dynamic programming (Ney, 1982; Hess, 1983), as including them complicates evaluation and credit assignment. Nothing prevents applying them to further improve the robustness of the method. The aperiodicity measure $d'(T)$ may be used to ensure that estimates are corrected on the basis of their reliability rather than continuity *per se*.

The issue of voicing detection was also avoided, again because it greatly complicates evaluation and credit assignment. The aperiodicity measure $d' \tau$ seems a good basis for voicing detection, perhaps in combination with energy. However, equating voicing with periodicity is not satisfactory, as some forms of voicing are inherently irregular. They probably still carry intonation cues, but how they should be quantified is not clear. In a companion paper (Kawahara *et al.*, in preparation), we present a rather different approach to F_0 estimation and glottal event detection, based on instantaneous frequency and the search for fixed points in mappings along the frequency and time axes. Together, these two papers offer a new perspective on the old task of F_0 estimation.

YIN has been only informally evaluated on music, but there are reasons to expect that it is appropriate for that task. Difficulties specific to music are the wide range and fast changes in F_0 . YIN's open-ended search range and the fact that it performs well without continuity constraints put it at an advantage over other algorithms. Other potential advantages, yet to be tested, are low latency for interactive systems (Sec. V), or extensions to deal with polyphony (Sec. VI D). Evaluation on music is complicated by the wide range of instruments and styles to be tested and the lack of a well-labeled and representative database.

What is new? Autocorrelation was proposed for periodicity analysis by Licklider (1951), and early attempts to apply it to speech are reviewed in detail by Hess (1983), who also traces the origins of difference-function methods such as the AMDF. The relation between the two, exploited in Eq. (7), was analyzed by Ney (1982). Steps 3 and 4 were applied to AMDF by de Cheveigné (1990) and de Cheveigné (1996), respectively. Step 5 (parabolic interpolation) is a standard technique, applied for example to spectrum peaks in the F_0 estimation method of Duifhuis *et al.* (1982). New are step 6, the idea of combining steps as described, the analysis of why it all works, and most importantly the formal evaluation.

IX. CONCLUSION

An algorithm was presented for the estimation of the fundamental frequency of speech or musical sounds. Starting from the well-known autocorrelation method, a number of modifications were introduced that combine to avoid estimation errors. When tested over an extensive database of speech recorded together with a laryngograph signal, error rates were a factor of 3 smaller than the best competing methods, without postprocessing. The algorithm has few parameters, and these do not require fine tuning. In contrast to most other methods, no upper limit need be put on the F_0 search range.

The method is relatively simple and may be implemented efficiently and with low latency, and may be extended in several ways to handle several forms of aperiodicity that occur in particular applications. Finally, an interesting parallel may be drawn with models of auditory processing.

ACKNOWLEDGMENTS

This work was funded in part by the Cognitique program of the French Ministry of Research and Technology, and evolved from work done in collaboration with the Advanced Telecommunications Research Laboratories (ATR) in Japan, under a collaboration agreement between ATR and CNRS. It would not have been possible without the laryngograph-labeled speech databases. Thanks are due to Y. Atake and co-workers for creating DB1 and making it available to the authors. Paul Bagshaw was the first to distribute such a database (DB2) freely on the Internet. Nathalie Henrich, Christophe D'Alessandro, Michèle Castellengo, and Vu Ngoc Tuan kindly provided DB3. Nick Campbell offered DB4, and Georg Meyer DB5. Thanks are also due to the many people who generously created, edited, and distributed the software packages that were used for comparative evaluation. We offer apologies in the event that our choice of parameters did not do them justice. Thanks to John Culling, two anonymous reviewers, and the editor for in-depth criticism, and to Xuejing Sun, Paul Boersma, and Axel Roebel for useful comments on the manuscript.

APPENDIX: DETAILS OF THE EVALUATION PROCEDURE

1. Databases

The five databases comprised a total of 1.9 h of speech, of which 48% were labeled as regularly voiced. They were produced by 48 speakers (24 male, 24 female) of Japanese (30), English (14), and French (4). Each included a laryngograph waveform recorded together with the speech.

- (1) DB1: Fourteen male and 14 female speakers each spoke 30 Japanese sentences for a total of 0.66 h of speech, for the purpose of evaluation of F_0 -estimation algorithms (Atake *et al.*, 2000). The data include a “voiced-unvoiced” mask that was not used here.
- (2) DB2: One male and one female speaker each spoke 50 English sentences for a total of 0.12 h of speech, for the purpose of evaluation of F_0 -estimation algorithms (Bagshaw *et al.*, 1993). The database can be downloaded from the URL http://www.cstr.ed.ac.uk/~pcb/fda_eval.tar.gz.
- (3) DB3: Two male and two female speakers each pronounced between 45 and 55 French sentences for a total of 0.46 h of speech. The database was created for the study of speech production, and includes sentences pronounced according to several modes: normal (141), head (30), and fry (32) (Vu Ngoc Tuan and d'Alessandro, 2000). Sentences in fry mode were not used for evaluation because it is not obvious how to define F_0 when phonation is not periodic.

TABLE III. Gross error rates measured using alternative ground truth. DB1: manually checked estimates derived from the laryngograph signal using the TEMPO method of Kawahara *et al.* (1999b). DB2 and DB5: estimates derived independently by the authors of those databases.

Method	Gross error (%)		
	DB1	DB2	DB5
pda	9.8	14.5	15.1
fxac	13.2	14.9	16.1
fxcep	4.5	12.5	8.9
ac	2.7	7.3	5.1
cc	3.3	6.3	8.0
shs	7.5	11.1	9.4
acf	0.45	2.5	3.1
nacf	0.43	2.3	2.8
additive	2.16	3.4	3.7
TEMPO	0.77	2.8	4.6
YIN	0.29	2.2	2.4

- (4) DB4: Two male speakers of English and one male and one female speaker of Japanese produced a total of 0.51 h speech, for the purpose of deriving prosody rules for speech synthesis (Campbell, 1997).
- (5) DB5: Five male and five female speakers of English each pronounced a phonetically balanced text for a total of 0.15 h of speech. The database can be downloaded from <ftp://ftp.cs.keele.ac.uk/pub/pitch/Speech>.

Ground-truth F_0 estimates for the first four databases were extracted from the laryngograph signal using YIN. The threshold parameter was set to 0.6, and the schemes of Secs. VI A and VI C were implemented to cope with the large variable DC offset and amplitude variations of the laryngograph signal. Estimates were examined together with the laryngograph signal, and a reliability mask was created manually based on the following two criteria: (1) any estimate for which the F_0 estimate was obviously incorrect was excluded and (2) any remaining estimate for which there was evidence of vocal fold vibration was included. The first criterion ensured that all estimates were correct. The second aimed to include as many “difficult” data as possible. Estimate values themselves were not modified. Estimates had the same sampling rate as the speech and laryngograph signals (16 kHz for DB1, DB3, and DB4, 20 kHz for database DB2). Figures 9 and 10 show the range of F_0 and F_0 change rate over these databases.

It could be argued that applying the same method to speech and laryngograph data gives YIN an advantage relative to other methods. Estimates were all checked visually, and there was no evidence of particular values that could only be matched by the same algorithm applied to the speech signal. Nevertheless, to make sure, tests were also performed on three databases using ground truth not based on YIN. The laryngograph signal of DB1 was processed by the TEMPO method of Kawahara *et al.* (1999a), based on instantaneous frequency and very different from YIN, and estimates were checked visually as above to derive a reliability mask. Scores are similar (Table III, column 2) to those obtained previously (Table II, column 2). Scores were also measured for DB2 and

DB5, using reference F_0 estimates produced by the authors of those databases using their own criteria. The ranking of methods is similar to that found in Table III, suggesting that the results in that table are not a product of our particular procedures.

2. Reference methods

Reference methods include several methods available on the Internet. Their appeal is that they have been independently implemented and tuned, are representative of tools in common use, and are easily accessible for comparison purposes. Their drawback is that they are harder to control, and that the parameters used may not do them full justice. Other reference methods are only locally available. Details of parameters, availability and/or implementation are given below.

ac: This method implements the autocorrelation method of Boersma (1993) and is available with the Praat system at <http://www.fon.hum.uva.nl/praat/>. It was called with the command “To Pitch (ac)...0.01 40 15 no 0.0 0.0 0.01 0.0 0.0 800.”

cc: This method, also available with the Praat system, is described as performing a cross-correlation analysis. It was called with the command: “To Pitch (cc)... 0.01 40 15 no 0.0 0.0 0.01 0.0 0.0 800.”

shs: This method, also available with the Praat system, is described as performing spectral subharmonic summation according to the algorithm of Hermes (1988). It was called with the command: “To Pitch (shs)...0.01 40 4 1700 15 0.84 800 48.”

pda: This method implements the eSRPD algorithm of Bagshaw (1993), derived from that of Medan *et al.* (1991), and is available with the Edinburgh Speech Tools Library at <http://www.cstr.ed.ac.uk/>. It was called with the command: “pda input_file -o out-put_file -L -d 1 -shift 0.001-length 0.1-fmax 800-fmin 40-lpfilter 1000 -n 0.” Examination of the code suggests that the program uses continuity constraints to improve tracking.

fxac: This program is based on the ACF of the cubed waveform and is available with the Speech Filing System at <http://www.phon.ucl.ac.uk/resource/sfs/>. Examination of the code suggests that the search range is restricted to 80–400 Hz. It provides estimates only for speech that is judged “voiced,” which puts it at a disadvantage with respect to programs that always offer an estimate.

fxcep: This program is based on the cepstrum method, and is also available with the Speech Filing System. Examination of the code suggests that the search range is restricted to 67–500 Hz. It provides estimates only for speech that is judged “voiced,” which puts it at a disadvantage with respect to programs that always offer an estimate.

additive: This program implements the probabilistic spectrum-based method of Doval (1994) and is only locally available. It was called with the command: “additive -0 -S input_file -f 40 -F 800 -G 1000 -X -f0ascii -I 0.001.”

acf: This program calculates the ACF according to Eq. (1) using an integration window size of 25 ms, multiplied by a linear ramp with intercept $T_{\max}=35$ ms (tuned for best performance over DB1), and chooses the global maximum between 1.25 to 25 ms (40 to 800 Hz).

nacf: As “acf” but using the normalized ACF according to Eq. (12).

TEMPO: This program implements the instantaneous frequency method developed by the second author (Kawahara *et al.*, 1999a).

YIN: The YIN method was implemented as described in this article with the following additional details. Equation (1) was replaced by the following variant:

$$r_t(\tau) = \sum_{j=t-\tau/2-W/2}^{t-\tau/2+W/2} x_j x_{j+\tau}, \quad (\text{A1})$$

which forms the scalar product between two windows that shift symmetrically in time with respect to the analysis point. The window size was 25 ms, the threshold parameter was 0.1, and the F_0 search range was 40 Hz to one quarter the sampling rate (4 or 5 kHz depending on the database). The window shift was 1 sample (estimates were produced at the same sampling rate as the speech waveform).

3. Evaluation procedure

Algorithms were evaluated by counting the number of estimates that differed from the reference by more than 20% (gross error rate). Reference estimates were time shifted and downsampled as necessary to match the alignment and sampling rate of each method. Alignment was determined by taking the minimum error rate over a range of time shifts between speech-based and laryngograph-based estimates. This compensated for time shifts due to acoustic propagation from glottis to microphone, or implementation differences. Some estimation algorithms work (in effect) by comparing two windows of data that are shifted symmetrically in time with respect to the analysis point, whereas others work (in effect) by comparing a shifted window to a fixed window. An F_0 -dependent corrective shift should be used in the latter case.

A larger search range gives more opportunities for error, so search ranges must be matched across methods. Methods that implement a voicing decision are at a disadvantage with respect to methods that do not (incorrect “unvoiced” decisions count as gross errors), so the voicing decision mechanism should be disabled. Conversely, postprocessing may give an algorithm an advantage. Postprocessing typically involves parameters that are hard to optimize and behavior that is hard to interpret, and is best evaluated separately from the basic algorithm. These recommendations cannot always be followed, either because different methods use radically different parameters, or because their implementation does not allow them to be controlled. Method “pda” uses continuity constraints and postprocessing. The search range of “fxac” was 80–400 Hz, while that of “fxcep” was 67–500 Hz, and these two methods produce estimates only for speech that is judged voiced. We did not attempt to modify the programs, as that would have introduced a mismatch with the publicly available version. These differences must be kept in mind when comparing results across methods.

Abe, T., Kobayashi, T., and Imai, S. (1995). “Harmonics tracking and pitch extraction based on instantaneous frequency,” Proc. IEEE-ICASSP, pp. 756–759.

Akeroyd, M. A., and Summerfield, A. Q. (2000). “A fully-temporal account of the perception of dichotic pitches,” Br. J. Audiol. **33**(2), 106–107.

Atake, Y., Irino, T., Kawahara, H., Lu, J., Nakamura, S., and Shikano, K. (2000). “Robust fundamental frequency estimation using instantaneous frequencies of harmonic components,” Proc. ICLSP, pp. 907–910.

Bagshaw, P. C., Hiller, S. M., and Jack, M. A. (1993). “Enhanced pitch tracking and the processing of F_0 contours for computer and intonation teaching,” Proc. European Conf. on Speech Comm. (Eurospeech), pp. 1003–1006.

Barnard, E., Cole, R. A., Veal, M. P., and Alleva, F. A. (1991). “Pitch detection with a neural-net classifier,” IEEE Trans. Signal Process. **39**, 298–307.

Boersma, P. (1993). “Accurate short-term analysis of the fundamental frequency and the harmonics-to-noise ratio of a sampled sound,” Proc. Institute of Phonetic Sciences **17**, 97–110.

Breebart, J., van de Par, S., and Kohlrausch, A. (2001). “Binaural processing model based on contralateral inhibition. I. Model structure,” J. Acoust. Soc. Am. **110**, 1074–1088.

Brown, J. C., and Puckette, M. S. (1989). “Calculation of a ‘narrowed’ autocorrelation function,” J. Acoust. Soc. Am. **85**, 1595–1601.

Brown, J. C., and Zhang, B. (1991). “Musical frequency tracking using the methods of conventional and ‘narrowed’ autocorrelation,” J. Acoust. Soc. Am. **89**, 2346–2354.

Campbell, N. (1997). “Processing a Speech Corpus for CHATR Synthesis,” in Proc. ICSP (International Conference on Speech Processing).

Cariani, P. A., and Delgutte, B. (1996). “Neural correlates of the pitch of complex tones. I. Pitch and pitch salience,” J. Neurophysiol. **76**, 1698–1716.

Culling, J. F., and Summerfield, Q. (1995). “Perceptual segregation of concurrent speech sounds: absence of across-frequency grouping by common interaural delay,” J. Acoust. Soc. Am. **98**, 785–797.

de Cheveigné, A. (1989). “Pitch and the narrowed autocoincidence histogram,” Proc. ICMPC, Kyoto, pp. 67–70.

de Cheveigné, A. (1990). “Experiments in pitch extraction,” ATR Interpreting Telephony Research Laboratories technical report, TR-I-0138.

de Cheveigné, A. (1991). “Speech f_0 extraction based on Licklider’s pitch perception model,” Proc. ICPhS, pp. 218–221.

de Cheveigné, A. (1993). “Separation of concurrent harmonic sounds: Fundamental frequency estimation and a time-domain cancellation model of auditory processing,” J. Acoust. Soc. Am. **93**, 3271–3290.

de Cheveigné, A. (1996). “Speech fundamental frequency estimation,” ATR Human Information Processing Research Laboratories technical report, TR-H-195.

de Cheveigné, A. (1997). “Concurrent vowel identification. III. A neural model of harmonic interference cancellation,” J. Acoust. Soc. Am. **101**, 2857–2865.

de Cheveigné, A. (1998). “Cancellation model of pitch perception,” J. Acoust. Soc. Am. **103**, 1261–1271.

de Cheveigné, A., and Kawahara, H. (1999). “Multiple period estimation and pitch perception model,” Speech Commun. **27**, 175–185.

Doval, B. (1994). “Estimation de la fréquence fondamentale des signaux sonores,” Université Pierre et Marie Curie, unpublished doctoral dissertation (in French).

Duifhuis, H., Willems, L. F., and Sluyter, R. J. (1982). “Measurement of pitch in speech: an implementation of Goldstein’s theory of pitch perception,” J. Acoust. Soc. Am. **71**, 1568–1580.

Goldstein, J. L. (1973). “An optimum processor theory for the central formation of the pitch of complex tones,” J. Acoust. Soc. Am. **54**, 1496–1516.

Hedelin, P., and Huber, D. (1990). “Pitch period determination of aperiodic speech signals,” Proc. ICASSP, pp. 361–364.

Hermes, D. J. (1988). “Measurement of pitch by subharmonic summation,” J. Acoust. Soc. Am. **83**, 257–264.

Hermes, D. J. (1993). “Pitch analysis,” in *Visual Representations of Speech Signals*, edited by M. Cooke, S. Beet, and M. Crawford (Wiley, New York), pp. 3–25.

Hess, W. (1983). *Pitch Determination of Speech Signals* (Springer-Verlag, Berlin).

Hess, W. J. (1992). “Pitch and voicing determination,” in *Advances in Speech Signal Processing*, edited by S. Furui and M. M. Sohndi (Marcel Dekker, New York), pp. 3–48.

Huang, X., Acero, A., and Hon, H.-W. (2001). *Spoken Language Processing* (Prentice-Hall, Upper Saddle River, NJ).

ISO/IEC_JTC_1/SC_29 (2001). “Information Technology—Multimedia

- Content Description Interface—Part 4: Audio,” ISO/IEC FDIS 15938-4.
- Joris, P. X., and Yin, T. C. T. (1998). “Envelope coding in the lateral superior olive. III. Comparison with afferent pathways,” *J. Neurophysiol.* **79**, 253–269.
- Kawahara, H., Katayose, H., de Cheveigné, A., and Patterson, R. D. (1999a). “Fixed Point Analysis of Frequency to Instantaneous Frequency Mapping for Accurate Estimation of F_0 and Periodicity,” *Proc. EURO-SPEECH 6*, 2781–2784.
- Kawahara, H., Masuda-Katsuse, I., and de Cheveigné, A. (1999b). “Restructuring speech representations using a pitch-adaptive time-frequency smoothing and an instantaneous-frequency-based F_0 extraction: Possible role of a repetitive structure in sounds,” *Speech Commun.* **27**, 187–207.
- Kawahara, H., Zolfaghari, P., and de Cheveigné, A. (in preparation). “Fixed-point-based source information extraction from speech sounds designed for a very high-quality speech modifications.”
- Licklider, J. C. R. (1951). “A duplex theory of pitch perception,” *Experientia* **7**, 128–134.
- Medan, Y., Yair, E., and Chazan, D. (1991). “Super resolution pitch determination of speech signals,” *IEEE Trans. Acoust., Speech, Signal Process.* **39**, 40–48.
- Meddis, R., and Hewitt, M. J. (1991). “Virtual pitch and phase sensitivity of a computer model of the auditory periphery. I: Pitch identification,” *J. Acoust. Soc. Am.* **89**, 2866–2882.
- Miller, G. A., and Taylor, W. G. (1948). “The perception of repeated bursts of noise,” *J. Acoust. Soc. Am.* **20**, 171–182.
- Moore, B. C. J. (1997). *An Introduction to the Psychology of Hearing* (Academic, London).
- Ney, H. (1982). “A time warping approach to fundamental period estimation,” *IEEE Trans. Syst. Man Cybern.* **12**, 383–388.
- Noll, A. M. (1967). “Cepstrum pitch determination,” *J. Acoust. Soc. Am.* **41**, 293–309.
- Pressnitzer, D., Patterson, R. D., and Krumbholz, K. (2001). “The lower limit of melodic pitch,” *J. Acoust. Soc. Am.* **109**, 2074–2084.
- Rabiner, L. R., and Schafer, R. W. (1978). *Digital Processing of Speech Signals* (Prentice-Hall, Englewood Cliffs, NJ).
- Ritsma, R. J. (1962). “Existence region of the tonal residue. I,” *J. Acoust. Soc. Am.* **34**, 1224–1229.
- Rodet, X., and Doval, B. (1992). “Maximum-likelihood harmonic matching for fundamental frequency estimation,” *J. Acoust. Soc. Am.* **92**, 2428–2429 (abstract).
- Ross, M. J., Shaffer, H. L., Cohen, A., Freudberg, R., and Manley, H. J. (1974). “Average magnitude difference function pitch extractor,” *IEEE Trans. Acoust., Speech, Signal Process.* **22**, 353–362.
- Slaney, M. (1990). “A perceptual pitch detector,” *Proc. ICASSP*, pp. 357–360.
- Terhardt, E. (1974). “Pitch, consonance and harmony,” *J. Acoust. Soc. Am.* **55**, 1061–1069.
- Vu Ngoc Tuan, and d’Alessandro, C. (2000). “Glottal closure detection using EGG and the wavelet transform,” in *Proceedings 4th International Workshop on Advances in Quantitative Laryngoscopy, Voice and Speech Research*, Jena, pp. 147–154.
- Wightman, F. L. (1973). “The pattern-transformation model of pitch,” *J. Acoust. Soc. Am.* **54**, 407–416.
- Xu, Y., and Sun, X. (2000). “How fast can we really change pitch? Maximum speed of pitch change revisited,” *Proc. ICSLP*, pp. 666–669.
- Yost, W. A. (1996). “Pitch strength of iterated rippled noise,” *J. Acoust. Soc. Am.* **100**, 3329–3335.

Modeling sound transmission through the pulmonary system and chest with application to diagnosis of a collapsed lung

T. J. Royston^{a)} and X. Zhang
University of Illinois at Chicago, Chicago, Illinois 60607

H. A. Mansy and R. H. Sandler
Rush Medical College, Chicago, Illinois 60612

(Received 7 July 2001; accepted for publication 21 December 2001)

A theoretical and experimental study was undertaken to examine the feasibility of using audible-frequency vibro-acoustic waves for diagnosis of pneumothorax, a collapsed lung. The hypothesis was that the acoustic response of the chest to external excitation would change with this condition. In experimental canine studies, external acoustic energy was introduced into the trachea via an endotracheal tube. For the control (nonpneumothorax) state, it is hypothesized that sound waves primarily travel through the airways, couple to the lung parenchyma, and then are transmitted directly to the chest wall. In contradistinction, when a pneumothorax is present the intervening air presents an added barrier to efficient acoustic energy transfer. Theoretical models of sound transmission through the pulmonary system and chest region to the chest wall surface are developed to more clearly understand the mechanisms of intensity loss when a pneumothorax is present, relative to a baseline case. These models predict significant decreases in acoustic transmission strength when a pneumothorax is present, in qualitative agreement with experimental measurements. Development of the models, their extension via finite element analysis, and comparisons with experimental canine studies are reviewed. © 2002 Acoustical Society of America. [DOI: 10.1121/1.1452742]

PACS numbers: 43.80.Cs, 43.80.Ev, 43.80.Qf, 43.20.Bi [FD]

I. INTRODUCTION

Pneumothorax (PTX), a collapsed lung, is a relatively common and potentially lethal condition that can occur as a complication of pulmonary pathology or arise spontaneously.¹ In critically ill patients, the diagnosis of PTX takes on additional importance. This is particularly true for patients receiving positive pressure ventilatory support given the increased risk of tension PTX and associated dire hemodynamic consequences.

A recent consensus conference from the American College of Chest Physicians has estimated that there are more than 20 000 primary and secondary pneumothoraces each year and that the cost of managing this condition is almost \$130 mil.¹ Because PTX is potentially life threatening, can be very fast paced, and is usually easily treatable, physicians are loath to miss the diagnosis. Hence, the number of diagnostic procedures to evaluate suspected PTX is several fold higher than the actual PTX incidence.

At present the diagnosis of PTX involves a combination of history, physical examination, and chest imaging procedures, typically a chest x-ray. The chest x-ray is usually sufficient for making a diagnosis of PTX; but, in the setting of critical illness, it may be difficult to obtain adequate positioning and end-expiratory timing to enhance detection of the air in the pleural space. Furthermore, critically ill patients may not be movable to a computed tomography (CT) machine to allow enhanced detection of PTX. In addition, chest

radiographs and CT imaging are not likely to be readily available in remote or low-technology settings. Radiographic procedures are also expensive and pose a small but definite risk from radiation exposure.

The central hypothesis of the current study is that PTX leads to characteristic acoustic transmission changes in the pulmonary system. A diagnostic methodology based on this hypothesis may lead to inexpensive devices providing accurate, portable, rapid, and safe PTX diagnosis. However, there are many possible configurations and approaches that one might consider using, such as the type, number, and locations of acoustic sources and receivers. Because of the numerous possible configurations and conditions, development of a clinically useful diagnostic technique for PTX, and other lung pathologies for that matter, would be catalyzed by the existence of an accurate computer simulation model that would decrease the number of animal and human subject tests and expedite the design optimization process.

The objective of the work presented here is to summarize *initial* experimental data on the acoustic transmission changes associated with PTX in a dog model and to develop *initial simplified* theoretical and computational finite element simulations of sound propagation in the pulmonary and chest region that help explain experimental observations and, with some refinement, may eventually aid in optimization of diagnostic techniques.

Objectives: Consequently, the objectives of the research summarized in this article are as follows:

- (1) Review pilot experimental studies on dogs to investigate the feasibility of an acoustic diagnosis of PTX.

^{a)} Author to whom correspondence should be addressed; electronic mail: troyston@uic.edu

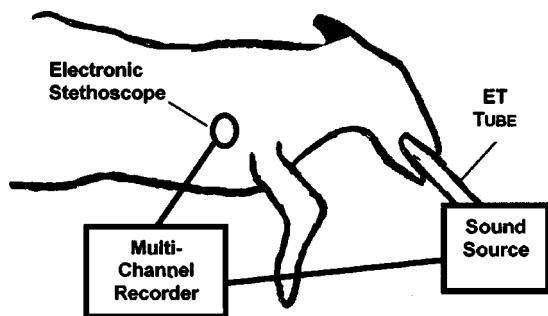


FIG. 1. Schematic of experimental dog studies.

- (2) Develop a one-dimensional (1D) axisymmetric theoretical model to better understand sound transmission in the torso region and how it may be affected by a PTX.
- (3) Implement the 1D theoretical model in a computational finite element analysis (FEA) framework.
- (4) Extend the FEA model to two dimensions (2D) to assess the importance of nonaxisymmetric features that are present in a typical PTX case.

II. EXPERIMENTAL STUDY

Methods. All experiments were approved by the Institutional Animal Care and Use Committee and carried out in the operating theater of the Comparative Research Center of Rush-Presbyterian-St Luke's Medical Center. A schematic of the experimental setup is shown in Fig. 1. Fifteen female mongrel dogs under general anesthesia with endotracheal intubation were studied in the left lateral decubitus (right-side-up) position with their skin closely shaved. Ventilator-delivered tidal volumes were 20 ml/kg with 12 breaths/min; before each acoustic test, the ventilator was briefly stopped for 15 s at end expiration.

Sound was introduced by a speaker (DA-1, Electro-Voice, Buchanan, MI) driven by broadband noise from a dynamic signal analyzer (model 35670, HP, Loveland, CO) through a power amplifier (model PM-125, Carver Professional, Portland, OR). The speaker input contained all frequencies from 20 to 1600 Hz with uniform amplitude within ± 1 dB. An electronic stethoscope (Labtron Electromax, Hauppauge, NY) measured the sound transmitted to the chest at the right mid-clavicular line at the third rib. The static load applied on the stethoscope was kept at 250–300 g as monitored by a load cell (ELF-T3E-2L, Entran, Fairfield, NJ) connected to a digital voltmeter. This load was chosen such that it provides enough coupling to the chest surface without significantly affecting stethoscope performance. Using the fast Fourier transform, spectral content was calculated with a frequency resolution of 8 Hz. Mean spectral values were determined by averaging results from multiple time response windows.

In general, stethoscopes have frequency-dependent sensitivity and their response may vary with mounting conditions.^{2,3} The primary interest in the present study is the relative difference in measurements between normal (no PTX) and PTX conditions; so, sensitivity variation with frequency is acceptable and identical mounting conditions were maintained. Nonetheless, some additional tests of the elec-

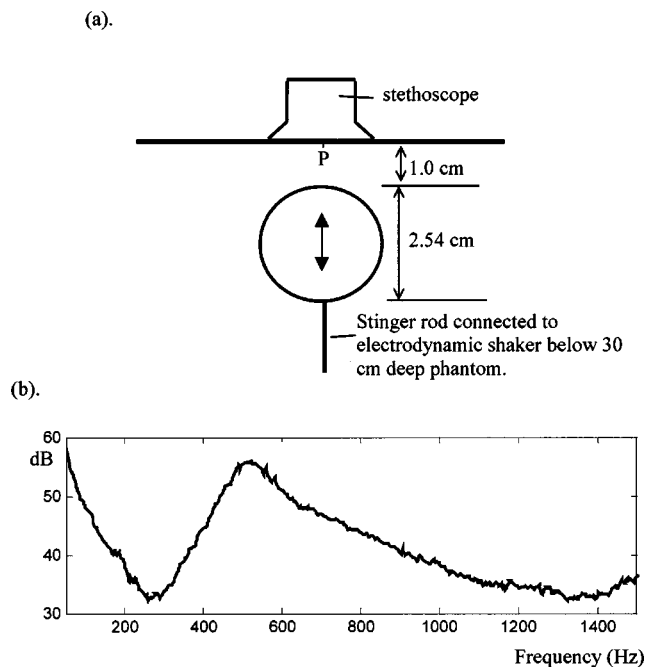


FIG. 2. Stethoscope calibration. (a) Experimental schematic. Stethoscope mounted on viscoelastic halfspace with embedded finite vertical dipole source. (b) Frequency response of stethoscope in dB volts referenced to 1 m/s vertical surface velocity at point *P* measured using laser Doppler vibrometer with stethoscope removed.

tronic stethoscope were performed to gain some insight into how measurements may be colored by stethoscope dynamics. In Fig. 2, results are shown for tests on a biological soft tissue-mimicking phantom; material properties for this phantom are available in the literature.⁴ The phantom is driven by a buried rigid sphere oscillating vertically and driven by an electrodynamic shaker through a stinger (Bruel & Kjaer model 4808 Vibration Shaker driven by model 2712 Power Amplifier). Measurement at the surface of the phantom is made using the stethoscope under study and a noncontacting laser Doppler vibrometer (LDV; Polytec PI, model CLV 800), both directly over the central vertical axis of the source (LDV measurements required adhering a small piece of reflective tape on the phantom surface at point *P*). In Fig. 2(b) the response of the stethoscope relative to the LDV is shown. With respect to a noncontacting, nominally zero impedance velocity sensor (the LDV), the stethoscope exhibits frequency-weighting of the measurement, with a peak response around 500 Hz and otherwise an attenuation with frequency of less than 30 dB up to 1500 Hz. LDV measurements of the vertical velocity of the sphere itself, which were possible since the phantom was translucent, confirmed that the unloaded phantom surface velocity (measured by the LDV) closely matched the rigid sphere velocity. Also, frequency response measurements using as input an accelerometer (PCB Impedance Head 288D01) mounted on the stinger below the sphere [see Fig. 2(a)] and as output either the LDV or stethoscope had nominally perfect coherence (unity) throughout the presented frequency range of 50–1500 Hz. In summary, it is concluded that the stethoscope exhibits some frequency-dependent sensitivity, at least relative to a noncontacting surface velocity measurement.

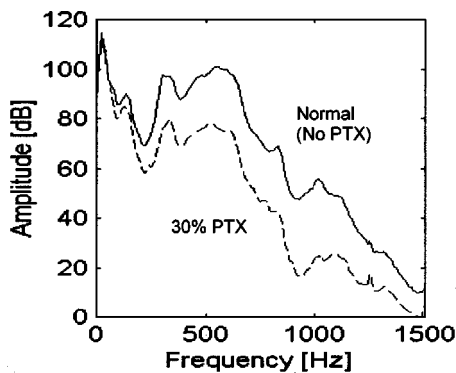


FIG. 3. Average of the spectra of sounds transmitted from the mouth to chest wall of the 15 animals for the control (solid line) and 30% pneumothorax (dashed line) states. A large drop is apparent in acoustic transmission due to pneumothorax at frequencies above ~ 300 Hz compared to the small change in amplitude in the 0–250 Hz range ($p=0.00006$). Note that the amplitude axis is logarithmic, so that the changes are a factor of 10–100.

Following baseline acoustic measurements on the dogs, a PTX state was created by inserting a 5 mm thoracoscopic trocar (Endopath Dilating Tip, model 355, Ethicon, Cincinnati, OH) into the pleural space via a small incision in the seventh intercostal space in the right mid-axillary line. The obturator was removed leaving the thoracoscopic cannula in place. A video endoscope was inserted through a trocar confirming the control state. Then air was introduced via the cannula using a syringe attached to a three-way stopcock to produce a 30% PTX, approximately. The thoracoscopic was inserted intermittently to confirm the location and degree of PTX. This was followed by performing the acoustic tests as described previously.

Results. An average of the spectra of the chest responses is shown in Fig. 3 for all subjects. At low frequencies ($f < 100$ Hz), spectral values were comparable in the two states. However, clear attenuation due to pneumothorax was detected at higher frequencies ($f > 300$ Hz) in all animals. In addition to the general trend of increased attenuation with increasing frequency, some spectral “peaks and valleys” can be seen. These are evident in both the normal and PTX conditions, suggesting that they occur somewhat independently of the PTX. While a portion of the attenuation and antiresonance and resonance trends can be attributed to the stethoscope itself, as discussed previously, not all of the spectral fluctuations nor the greater than 80 dB drop from 500 to 1500 Hz could result only from the stethoscope.

Alternative explanations for some of the resonant behavior can be found in prior studies. According to Fredberg and Moore,⁵ one possibility is that measured resonant behavior is due to the airway structure of the lung (including the endotracheal tube in this case); but, it would need to be dominated by the larger airways of the lung—the trachea, mainstem bronchi, and first few generations with substantial cartilage—as smaller airways collapse when a PTX is present. On the other hand, it is suggested that this resonant behavior is dominantly determined by chest wall dynamics, since the air cavity presence did not significantly alter their frequency, and one might hypothesize that the PTX should significantly affect the resonant behavior of the lung itself. Similar frequency values and insensitivity to lung contents

have been previously reported in a canine model.⁶ The theoretical study discussed in Sec. III will attempt to answer this, as well as other, questions.

III. MODELING SOUND TRANSMISSION THROUGH THE RESPIRATORY SYSTEM

A. Background

In modeling the transmission of sound introduced at the mouth to sensors mounted on the chest wall, the transmission path may be viewed as having two main components: (1) initial transmission in air through the tracheobronchial airway tree and (2) coupling to and transmission through the surrounding biological tissues to reach the chest surface—namely the parenchyma, free air pocket (in the case of a PTX), surrounding muscle and rib cage regions, and outer soft tissue region.

There have been numerous acoustic modeling investigations that focus on the first part, the tracheobronchial airway tree, with some also considering coupling to and modes of wave propagation in the parenchyma.^{5,7–13} Many have considered acoustic *impedance* of the tree, air excitation, and response measurement at the mouth or just below the glottis or some combination of these locations with and without endotracheal intubation, and/or resulting pressure distributions throughout the tree and parenchyma, itself. In these cases, it has been shown that a 1D branching waveguide representation of the trachea and bronchial airways with compliant walls reasonably approximates most of the dynamic behavior up to several kHz. At higher frequencies the 1D quasiplanar wave propagation assumption begins to lose validity in the larger airways. Also, from about 100 Hz to 10 kHz, wave propagation in the parenchyma away from the larger airways is reasonably approximated using a closed cell bubble swarm approach with gas elasticity and tissue density dominating. Below 100 Hz vibratory wave propagation in the parenchyma is more a function of the elastic and inertial properties of the solid tissue only and the acoustic response of the bronchial tree can be reasonably approximated as a capacitive load.¹⁴ To the best of the author’s knowledge, the effect of a PTX on acoustic impedance or transmission through the tracheobronchial tree and parenchyma has not been studied.

There have also been several studies that have focused attention on modeling the second part, transmission through the surrounding biological tissues to reach the chest surface.^{15,16} Usually a very simplified geometry and homogenized material properties are assumed. For example, Wodicka *et al.*¹⁵ assumes an axisymmetric cylindrical geometry and models the parenchyma using the closed cell bubble swarm approach that shows qualitative agreement with experiments, at least from 100 to 600 Hz. In this model, the outer tissue regions of the chest are treated simply as a mass load on the parenchyma. In Vovk *et al.*¹⁶ an axisymmetric layered model for the torso region is used that includes annular regions for the parenchyma, rib cage region, soft outer tissue, and skin.

In the present work, which represents a first step at better understanding the effect of PTX on sound *transmission*,

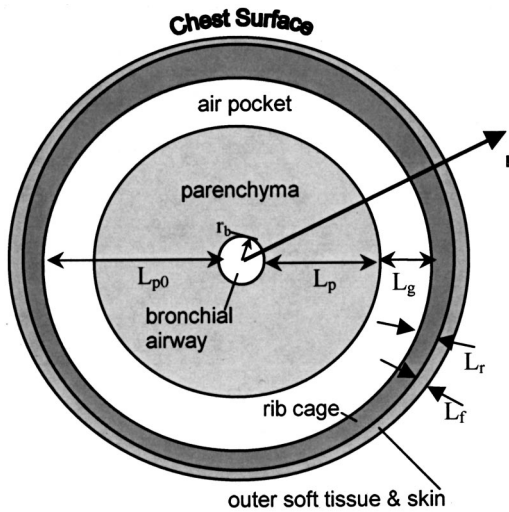


FIG. 4. Schematic of simple model of sound propagation through the chest with pneumothorax.

simplifications of both airway and tissue structures are imposed; their effect on model predictions are discussed. In the model developed in this article, *transmission* from the airways to the chest surface is the focus, *not* airway acoustic impedance. (The reasons for this approach, in part, have to do with the fact that a PTX does not alter the larger airways, which have significant cartilage in their walls, and its effect on the smaller airways is not quantitatively well known; so, how it changes acoustic impedance is unclear and is the subject of the authors' future research. But, one would expect the transmission path to be substantially altered, acoustically, by a PTX due to the presences of a free air gap.) In order to simulate sound transmission with *quantitative* accuracy, both the complexities of the tracheobronchial airway tree and the various tissue regions of the torso need to be modeled in detail. It is noted that, to the best of the authors' knowledge, while there are numerous acoustic airway studies that explicitly model the tracheobronchial airway tree in detail and how it is affected by different lung pathologies (though not PTX), there are no studies that attempt to simulate in detail the tissue pathway to the chest beyond that of the layered axisymmetric description of Vovk *et al.*¹⁶ mentioned previously. The article of Wodicka *et al.*¹⁵ considers the entire path by using a simplified acoustic circuit model for the airway tree and separately considers sound propagation through an axisymmetric torso, as mentioned previously. The effect of increased intrathoracic water density is simulated, showing increased sound transmission, in qualitative agreement with measurements on congested subjects. To the best of the au-

thors' knowledge, there are no theoretical modeling studies of any level of detail that consider the acoustic effects of a PTX on either impedance or transmission.

B. 1D model of transmission to the chest surface neglecting airway tree complexity

Consider the path that sound takes from the respiratory airways to the chest wall surface. This is simplistically represented in Fig. 4 with average dimensions provided in Table I. When no pneumothorax is present, there are three acoustically distinct tissue layers that sound energy located in the bronchial airways must pass through to reach the chest surface: the parenchyma, bone-muscular rib cage region, and outer muscular-fatty soft tissue region. When a pneumothorax is present, a fourth acoustically distinct layer will exist, an air space between the parenchyma and rib cage region. It is acknowledged that this is a substantial simplification of the actual situation. In particular, tracheobronchial airway structural complexity has been ignored and the airway is modeled as a single central cylindrical chamber. Also, nonaxisymmetries and axial variations in the parenchyma, bone, muscle, and soft tissue regions are ignored.

An acoustic model for sound transmission in the normal (no PTX) case using an axisymmetric model similar to that of Fig. 4 can be found in Wodicka *et al.*¹⁵ The salient features are summarized here and extended to the case of a partially or fully collapsed parenchyma, as occurs under the PTX condition. The parenchyma is approximated as air bubbles in water. Since the sound wavelengths λ_p (compression waves) in the frequency range of the experiment, up to 1500 Hz, are significantly longer than the average alveolar radius r_0 , the magnitude of the thermal losses are much larger than those associated with scattering or viscous effects. These thermal losses arise since the bubble compressions and expansions are polytropic; they are more adiabatic at the center of the bubble and isothermal where the air and tissue are in contact. Thus, the work performed on the bubble by the wave during compression is greater than the work performed by the air during expansion, resulting in a net heat flow into the liquid. While a single bubble has little effect on sound transmission, the composite attenuation of many bubbles is significant.

Consider a harmonic acoustic pressure of $P_0 e^{j\omega t}$ acting on the inner boundary of the parenchyma, where P_0 is the amplitude, $j = \sqrt{-1}$, ω denotes the circular frequency in radians/second, and t denotes time in seconds. Given the assumption that the system is acoustically linear, it is sufficient to consider the case of harmonic excitation to determine the system's response to arbitrary inputs with arbitrary

TABLE I. Average dimensions for the healthy adult male human^a and mongrel dog.^b

Adult male	Mongrel dog	Description
$L_{p0} = 10$ cm	$L_{p0} = 8$ cm	Thickness of parenchyma when no pneumothorax is present
$L_r = 2$ cm	$L_r = 1$ cm	Thickness of bone-muscular rib cage region
$L_f = 1$ cm	$L_f = .5$ cm	Thickness of outer muscular-fatty soft tissue layer
$L_g = 0$ cm	$L_g = 0$ cm	Air pocket only exists when a pneumothorax is present

^aReference 16.

^bAuthors' measurements.

spectral content. Given plane wave propagation in the “ r ” direction due to an initial pressure amplitude of P_0 at $r=0$ the expression for pressure as a function of distance “ r ” and time “ t ” is

$$\mathbf{p}(r, t) = P_0 e^{-\alpha_p[\omega]r} e^{j(\omega t - k_p r)}. \quad (1)$$

Attenuation due to dissipative (thermal) effects is accounted for in the coefficient $\alpha_p[\omega] = N\sigma[\omega]/2$ Np/cm $\cong 4.343N\sigma$ dB/cm ($20 \log_{10}[e^{-N\sigma/2}]$). Here, N is the number of bubbles (alveoli) per unit volume in the parenchyma and $\sigma[\omega]$ is the extinction cross section for each bubble. The real part of the wave number is denoted by k_p and the traveling wave has a phase speed c_p that is denoted by $c_p = \omega/k_p$. If we define a complex (bold type) thermodynamic speed of sound \mathbf{c}_p and wave number \mathbf{k}_p , these would be related to the phase speed and attenuation through the following formulas:¹⁷

$$\mathbf{k}_p[\omega] = k_p - j\alpha_p[\omega], \quad (2a)$$

$$\begin{aligned} \mathbf{c}_p[\omega] &= \omega/\mathbf{k}_p[\omega] \\ &= c_p \left(1 + j \left(\frac{\alpha_p[\omega]c_p}{\omega} \right) \right) / \left(1 + \left(\frac{\alpha_p[\omega]c_p}{\omega} \right)^2 \right). \end{aligned} \quad (2b)$$

These parameters, in turn, can be related to material properties as

$$\mathbf{c}_p[\omega] = (\mathbf{B}_p[\omega]/\rho_p)^{1/2}, \quad (3a)$$

$$\mathbf{B}_p[\omega] = B_p + j\omega(4/3)\mu_{2p}. \quad (3b)$$

Here, B_p is the bulk modulus of the parenchyma, ρ_p is its density, and μ_{2p} is the shear viscosity coefficient. In a finite element code, such as ANSYS®, if a fluid element, such as FLUID79, is used, then either the fluid’s bulk viscosity η_{bp} or damping ζ_{bp} are specified along with the bulk modulus B_p such that

$$\mathbf{B}_p[\omega] = B_p + j\omega\eta_{bp} = B_p(1 + j\omega\zeta_{bp}). \quad (4)$$

Thus, in order to express an approximately equivalent set of material parameters in ANSYS for harmonic analysis using the FLUID79 element, one could use the following formulas if it is assumed that $(\alpha_p[\omega]c_p/\omega)^2 \ll 1$: $\rho_p \equiv$ parenchyma composite material density (“mp, rho” in ANSYS), $B_p = c_p^2\rho_p \equiv$ parenchyma composite material bulk modulus (“mp, ex” in ANSYS), $\zeta_{bp} = 2\alpha_p[\omega]c_p/\omega^2 \equiv$ parenchyma composite material bulk damping (“mp, damp” in ANSYS).

For a healthy adult human parenchyma N is about 5.3×10^4 cm⁻³ and the volume fraction of tissue material to gas is $h_0 \approx 0.25$.¹⁵ These values are used in this study as different species- and gender-dependent values were unavailable and differences are expected to be minimal. The chosen value of h_0 will have a noticeable effect on a number of properties, including wave speed and attenuation. With all other parameters unchanged, as an example, increasing h_0 to 0.35 decreases wave speed from 2305 to 2094 cm/s, a change of about 10%. The sensitivity of attenuation to h_0 increases with frequency from being almost negligible at 100 Hz, where as at 500 Hz changing h_0 from 0.25 to 0.35 decreases attenuation from about 20 to 10 dB for plane waves traveling

10 cm. A value of $h_0 = 0.35$ could represent excess fluid in the lung (congestion).¹⁵ For a PTX, the parenchyma shrinks in volume experiencing an increase in effective composite density while maintaining the same number of alveoli, which consequently will have smaller diameters. Thus, a general expression for N as a function of percent pneumothorax $P_{n\%}$ is $N = 5.3 \times 10^4 / (1 - (1 - h_0) \times P_{n\%}/100)$. An expression for $\sigma[\omega]$ is:¹⁵

$$\sigma[\omega] = 16\pi^2 r_0^4 \rho_{tp} c_{tp} R[\omega] / [R[\omega]^2 + (\omega M - (1/\omega C))^2], \quad (5)$$

where c_{tp} is the compression wave phase speed in the soft biological tissue constituting the parenchyma as determined by density ρ_{tp} and bulk modulus B_{tp} ; r_0 refers to the equilibrium radius of the bubbles that represent the alveoli. The terms C , $R[\omega]$, and M refer to the effective mechanical compliance, resistance, and mass of the oscillating alveoli bubbles. Expressions for them are: $C = 1/(12\pi r_0 \kappa P)$, $R = 2\pi r_0^2 \gamma B[\omega] (6P\rho_{tp}/\kappa)^{1/2}$, and $M = 2\pi r_0^3 \rho_{tp}$. Here, κ is the polytropic constant that describes the compression and it is a function of r_0 , the compression wavelength and the thermal characteristics of the air and tissue. For an r_0 value of 1.5×10^{-4} m, κ is approximately equal to unity at lower frequencies, indicating isothermal conditions and reaches 1.03 at 600 Hz;¹⁵ a fixed value of 1 is used in this study. Also, P denotes the ambient pressure (assumed to be atmospheric), $\gamma = 1.4$ is the ratio of specific heats for air under adiabatic conditions, and $B[\omega]$ is a dimensionless damping constant, which is dependent on thermal effects. It is a non-linear function of frequency ω . According to the analysis presented in Ref. 15 (culminating in Fig. 6 of Ref. 15) the following formula for $B[\omega]$ is used for $h = 0.25$: $B[\omega] \approx 8.85 \times 10^{-5} \times (\omega/2\pi)$. To satisfy continuity r_0 will be a function of the percent PTX $P_{n\%}$ by volume. For the healthy parenchyma, $r_0 \approx 1.5 \times 10^{-4}$ m. A PTX-dependent expression then is $r_0 = 0.015 \times (1 - (P_{n\%}/100))^{1/3}$ cm. Thus, given $P_{n\%}$, a frequency-dependent attenuation coefficient can be determined for compression wave (sound) propagation through the parenchyma.

For the parenchyma, values for density ρ_p and wave speed c_p are based on the following:

$$\rho_p = (1 - h)\rho_{gp} + h\rho_{tp}, \quad (6a)$$

$$K_p = (1 - h)K_{gp} + hK_{tp} \quad (6b)$$

$$c_p = [1/(\rho_p K_p)]^{1/2}. \quad (6c)$$

Here, K denotes volumetric compliance, the subscript g denotes the gas (air) phase and subscript t denotes the tissue phase. The volume fraction of tissue material h is dependent on the volume percent PTX $P_{n\%}$ as indicated previously. Typical material parameter values are:¹⁵ $\rho_{gp} = 1.14$ kg/m³ (air), $\rho_{tp} = 1000$ kg/m³ (tissue), $K_{gp} = 1/(P\kappa)$ (air), and $K_{tp} = 4.35 \times 10^{-10}$ m²/N (tissue).

If no pneumothorax is present, then the parenchyma is in direct contact with the bone-muscular tissue of the rib cage region. Considering the axisymmetric model of Fig. 4, given that the inner airway wall pressure is $P_0 e^{j\omega t}$, one has the following equations, boundary conditions, and Helmholtz equation for acoustic pressure $\mathbf{p}_p[r, \omega] e^{j\omega t}$ and acoustic particle velocity $\mathbf{w}_p[r, \omega] e^{j\omega t}$ in the parenchymal region, expressed in terms of the velocity potential $\varphi_p[r, \omega] e^{j\omega t}$:

$$j\omega\varphi_p[r=r_b, \omega] = \mathbf{p}_p[r=r_b, \omega] = P_0, \quad (7a)$$

$$\begin{aligned} \frac{\partial}{\partial r}\varphi_p[r=r_b+L_{p0}, \omega] \\ = \mathbf{w}_p[r=r_b+L_{p0}, \omega] = \frac{\partial}{\partial r}\varphi_r[r=r_b+L_{p0}, \omega] \\ = \mathbf{w}_r[r=r_b+L_{p0}, \omega], \end{aligned} \quad (7b)$$

$$\begin{aligned} j\omega\varphi_p[r=r_b+L_{p0}, \omega] &= \mathbf{p}_p[r=r_b+L_{p0}, \omega] \\ &= j\omega\varphi_r[r=r_b+L_{p0}, \omega] \\ &= \mathbf{p}_r[r=r_b+L_{p0}, \omega], \end{aligned} \quad (7c)$$

$$\left\{ \frac{1}{r} \frac{\partial}{\partial r} \left(r \frac{\partial}{\partial r} \right) + \mathbf{k}_p^2 \right\} \varphi_p = 0 \quad \text{in the region } r_b < r < r_b + L_{p0}. \quad (7d)$$

Note, subscript r denotes the rib cage region. The solution form of the cylindrical Helmholtz equation consists of Bessel functions:

$$\varphi_p[r, \omega] = A_p J_0(\mathbf{k}_p r) + B_p N_0(\mathbf{k}_p r). \quad (8)$$

Here, J_0 denotes the zeroth-order ordinary Bessel function of the first kind and N_0 denotes the zeroth-order Bessel function of the second kind (Neuman function).

If a PTX is present, then one must account for the air layer between the parenchyma and rib cage region. In the simplistic axisymmetric model being developed here, the air will be modeled as an additional annular fluid region within the ribcage shell. For air at atmospheric pressure,¹⁸ body temperature (37 °C), and 100% humidity, the density is $\rho_a = 1.14 \times 10^{-3} \text{ g/cm}^3$ and the phase speed of compression waves is $c_a = (\gamma P / \rho_g)^{1/2}$. A viscosity value of $\eta_a = 1.86 \times 10^{-5} \text{ N/m}^2$ is used. Equations (7b)–(7d) and (8) will be replaced by the following:

$$\begin{aligned} \frac{\partial}{\partial r}\varphi_p[r=r_b+L_p, \omega] &= \mathbf{w}_p[r=r_b+L_p, \omega] \\ &= \frac{\partial}{\partial r}\varphi_a[r=r_b+L_p, \omega] \\ &= \mathbf{w}_a[r=r_b+L_p, \omega], \end{aligned} \quad (9a)$$

$$\begin{aligned} j\omega\varphi_p[r=r_b+L_p, \omega] &= \mathbf{p}_p[r=r_b+L_p, \omega] \\ &= j\omega\varphi_a[r=r_b+L_p, \omega] \\ &= \mathbf{p}_a[r=r_b+L_p, \omega], \end{aligned} \quad (9b)$$

$$\begin{aligned} \frac{\partial}{\partial r}\varphi_a[r=r_b+L_{p0}, \omega] &= \mathbf{w}_a[r=r_b+L_{p0}, \omega] \\ &= \frac{\partial}{\partial r}\varphi_r[r=r_b+L_{p0}, \omega] \\ &= \mathbf{w}_r[r=r_b+L_{p0}, \omega], \end{aligned} \quad (9c)$$

$$\begin{aligned} j\omega\varphi_a[r=r_b+L_{p0}, \omega] &= \mathbf{p}_a[r=r_b+L_{p0}, \omega] \\ &= j\omega\varphi_r[r=r_b+L_{p0}, \omega] \\ &= \mathbf{p}_r[r=r_b+L_{p0}, \omega], \end{aligned} \quad (9d)$$

$$\left\{ \frac{1}{r} \frac{\partial}{\partial r} \left(r \frac{\partial}{\partial r} \right) + \mathbf{k}_p^2 \right\} \varphi_p = 0 \quad \text{in the region } r_b < r < r_b + L_p, \quad (9e)$$

$$\left\{ \frac{1}{r} \frac{\partial}{\partial r} \left(r \frac{\partial}{\partial r} \right) + \mathbf{k}_a^2 \right\} \varphi_a = 0 \quad \text{in the region } r_b + L_p < r < r_b + L_{p0}. \quad (9f)$$

Here L_p refers to the thickness of the parenchyma when a PTX is present and is approximately given by the following expression: $L_p = \sqrt{L_{p0}^2 - (L_{p0}^2 - r_b^2)(1 - h_0)(P_n\%/100)}$. The solution form of the cylindrical Helmholtz equations consist of Bessel functions:

$$\varphi_p[r, \omega] = A_p J_0(\mathbf{k}_p r) + B_p N_0(\mathbf{k}_p r), \quad (10a)$$

$$\varphi_a[r, \omega] = A_a J_0(\mathbf{k}_a r) + B_a N_0(\mathbf{k}_a r). \quad (10b)$$

In this axisymmetric model, the rib cage and inter-rib muscles are replaced by a visco-elastic annular region, subject to the following boundary condition and that of Eqs. (7c) and (7d) or (9c) and (9d), as well as the Helmholtz equation:

$$\begin{aligned} \frac{\partial}{\partial r}\varphi_r[r=r_b+L_{p0}+L_r, \omega] &= \mathbf{w}_r[r=r_b+L_{p0}+L_r, \omega] \\ &= \frac{\partial}{\partial r}\varphi_f[r=r_b+L_{p0}+L_f, \omega] \\ &= \mathbf{w}_f[r=r_b+L_{p0}+L_f, \omega], \end{aligned} \quad (11a)$$

$$\begin{aligned} j\omega\varphi_r[r=r_b+L_{p0}+L_r, \omega] &= \mathbf{p}_r[r=r_b+L_{p0}+L_r, \omega] \\ &= j\omega\varphi_f[r=r_b+L_{p0}+L_f, \omega] \\ &= \mathbf{p}_f[r=r_b+L_{p0}+L_f, \omega], \end{aligned} \quad (11b)$$

$$\left\{ \frac{1}{r} \frac{\partial}{\partial r} \left(r \frac{\partial}{\partial r} \right) + \mathbf{k}_r^2 \right\} \varphi_r = 0 \quad \text{in the region } r_b + L_{p0} < r < r_b + L_{p0} + L_r. \quad (11c)$$

Here, the subscript f denotes the outer tissue layer and \mathbf{k}_r denotes the complex wave number, which is given by the following:

$$\mathbf{k}_r = \omega / \mathbf{c}_r, \quad (12a)$$

$$\mathbf{c}_r = (\mathbf{B}_r[\omega] / \rho_r)^{1/2}, \quad (12b)$$

$$\mathbf{B}_r[\omega] = B_r + j\omega(4/3)\mu_{2r}. \quad (12c)$$

Here, B_r is the bulk modulus of the rib cage region, ρ_r is its density, and μ_{2r} is the shear viscosity coefficient. In a finite element code, such as ANSYS, if a fluid element, such as FLUID79, is used, then either the fluid's bulk viscosity η_{br} or damping ζ_{br} are specified along with the bulk modulus B_r and density ρ_r such that

$$\mathbf{B}_r[\omega] = B_r + j\omega\eta_{br} = B_r(1 + k\omega\zeta_{br}). \quad (13)$$

Alternatively, in a finite element code, like ANSYS, a solid element, such as SOLID45 (three-dimensional model) or

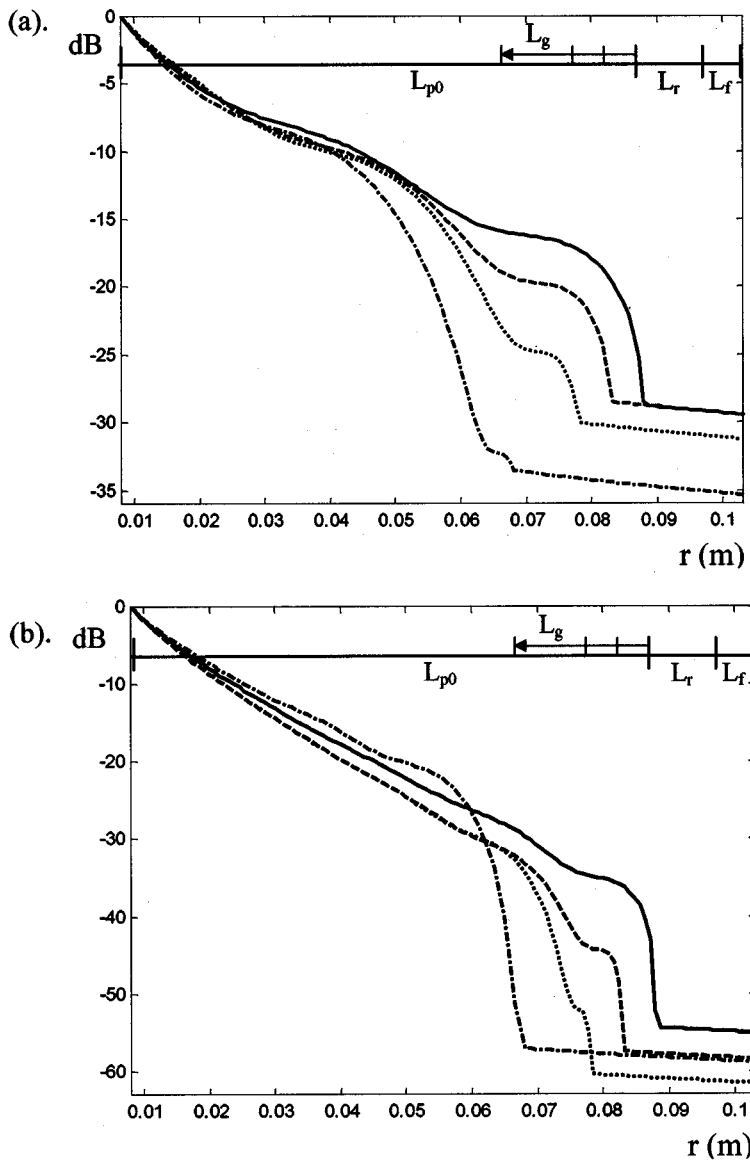


FIG. 5. Theoretical results as a function of radial position for acoustic intensity with an anechoic outer boundary: (a) 300 Hz and (b) 600 Hz. Results normalized to the input intensity at the bronchial airway wall. Key: (—) no PTX ($L_g=0$ cm), (---) 16.3% axisymmetric PTX ($L_g=0.5$ cm), (-.-) 31.6% axisymmetric PTX ($L_g=1$ cm), (-.-) 58.9% axisymmetric PTX ($L_g=2$ cm).

PLANE42 (axisymmetric or 2D planar model), may be specified. In this case, four material parameters need to be specified: E_r ≡ Young's modulus, ζ_r ≡ linear viscous damping coefficient, ν_r ≡ Poisson's ratio, and ρ_r ≡ density. More generally, the viscoelastic parameters can be specified in terms of the two complex Lamé constants: $\lambda = \lambda_1 + j\omega\lambda_2$ and $\mu = \mu_1 + j\omega\mu_2$. Here, λ_1 , λ_2 , μ_1 , and μ_2 denote volume elasticity, volume viscosity, shear elasticity, and shear viscosity. Expressions for E_r , ζ_r , ν_r , B_r and ζ_{br} in terms of the Lamé constants are as follows:¹⁹

$$\mathbf{E}_r = E_r(1 + j\omega\zeta_r) = \frac{\mu(3\lambda + 2\mu)}{\lambda + \mu}, \quad (14a)$$

$$\mathbf{B}_r = B_r(1 + j\omega\zeta_{br}) = \lambda + \frac{2}{3}\mu, \quad (14b)$$

$$\nu_r = \frac{1}{2} \frac{\lambda}{\lambda + \mu}. \quad (14c)$$

For soft biological tissues,²⁰ e.g., muscle, fat, and connective tissue, $\mu_1 \ll \lambda_1$, $\lambda_1 \approx 2.6$ GPa (same as water) and $\lambda_2 \approx 0$. In the simple model used in this study, the rib cage region is approximated with the following material parameters: λ_{1r}

$= 2.6$ GPa, $\lambda_{2r} = 0$, $\mu_{1r} = 10$ kPa, $\mu_{2r} = 20$ Pa s, and $\rho_r = 1500$ kg/m³. These values are based on taking the average of values reported for soft biological tissue and hard (bony) tissue in Refs. 15 and 16.

Like the rib cage region, the outer fatty tissue layer is treated as a visco-elastic annular region, subject to one of the following boundary conditions and that of Eqs. (11a) and (11b), as well as the Helmholtz equation:

$$\begin{aligned} \frac{\partial}{\partial r} \varphi_f[r = r_b + L_{p0} + L_r + L_f, \omega] \\ = \mathbf{w}_f[r = r_b + L_{p0} + L_r + L_f, \omega] \\ = 0 \quad (\text{fixed outer boundary}), \end{aligned} \quad (15a)$$

$$\begin{aligned} j\omega \varphi_f[r = r_b + L_{p0} + L_r + L_f, \omega] \\ = \mathbf{p}_f[r = r_b + L_{p0} + L_r + L_f, \omega] \\ = 0 \quad (\text{free outer boundary}), \end{aligned} \quad (15b)$$

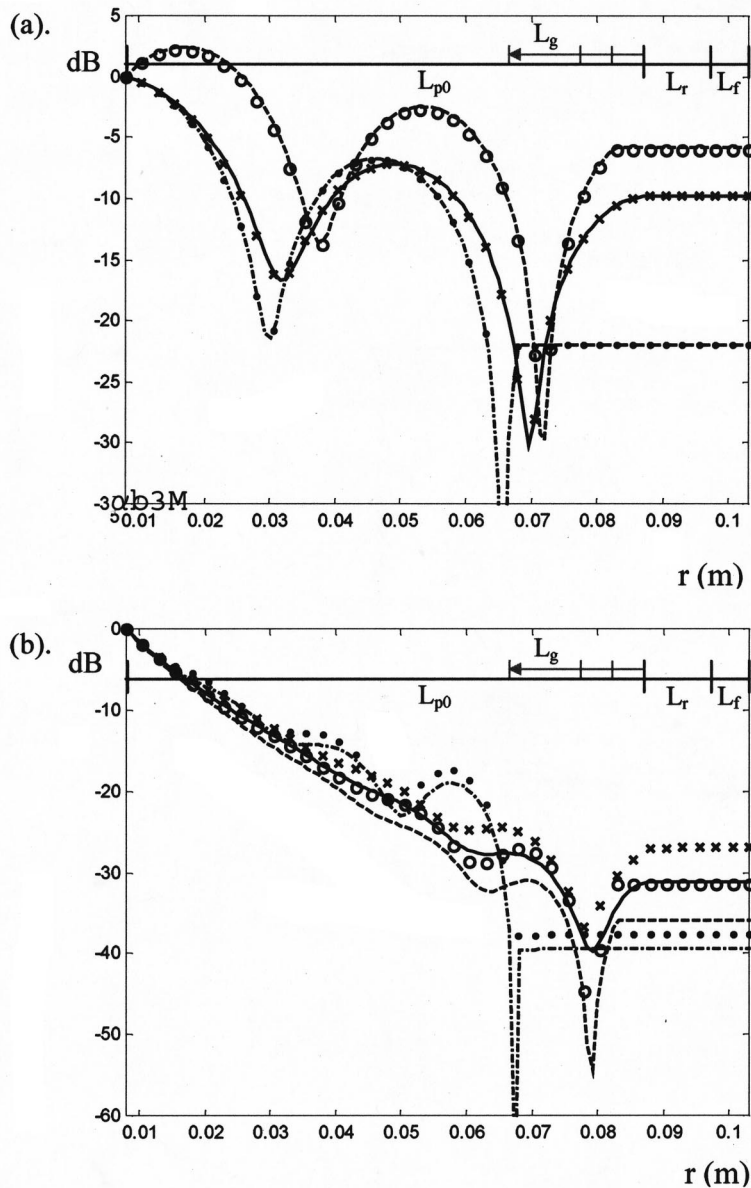


FIG. 6. Theoretical and finite element results as a function of radial position for acoustic pressure with a fixed outer boundary: (a) 300 Hz and (b) 600 Hz. Results normalized to the input pressure at the bronchial airway wall. Key for theoretical results: (—) no PTX ($L_g = 0$ cm), (---) 16.3% axisymmetric PTX ($L_g = 0.5$ cm), (-.-) 58.9% axisymmetric PTX ($L_g = 2$ cm). Key for FEA results: (\times) no PTX ($L_g = 0$ cm), (\circ) 16.3% axisymmetric PTX ($L_g = 0.5$ cm), (\bullet) 58.9% axisymmetric PTX ($L_g = 2$ cm).

$$\left\{ \frac{1}{r} \frac{\partial}{\partial r} \left(r \frac{\partial}{\partial r} \right) + \mathbf{k}_f^2 \right\} \varphi_f = 0$$

$$\text{in the region } r_b + L_{p0} + L_r < r < r_b + L_{p0} + L_r + L_f. \quad (15c)$$

For either of the above-given boundary conditions, the solution form is

$$\varphi_f[r, \omega] = A_f J_0(\mathbf{k}_f r) + B_f N_0(\mathbf{k}_f r), \quad (16)$$

However, if an anechoic outer boundary condition is used (e.g., assuming a perfect impedance match between a skin surface-based sensor and the outer tissue layer), then Eq. (15a) or (15b) is not used, but the solution form has one less unknown coefficient and is given by the following in place of Eq. (16):

$$\begin{aligned} \varphi_f[r, \omega] &= A_f H_0^2(\mathbf{k}_f r), \\ \text{where } H_0^2(\mathbf{k}_f r) &= J_0(\mathbf{k}_f r) - j N_0(\mathbf{k}_f r). \end{aligned} \quad (17)$$

Here, H_0^2 denotes a Hankel function (Bessel function of the third kind). For the chosen convention to denote harmonic motion ($e^{+j\omega t}$) the superscript "2" Hankel function is needed to denote outgoing ($+r$ direction) waves only. Material parameter values for this region are based on the literature^{19,20} and are as follows: $\lambda_{1r} = 2.6$ GPa, $\lambda_{2r} = 0$, $\mu_{1r} = 2.5$ kPa, $\mu_{2r} = 5$ Pa s, and $\rho_r = 1000$ kg/m³.

For a given excitation frequency ω and amplitude P_0 in the bronchial airway, a given outer boundary condition (fixed, free or anechoic), and a given PTX volume percentage $P_{n\%}$, Eqs. (1)–(17) can be used to find the steady state response, in terms of velocity potential φ , tissue particle velocity \mathbf{w} , and acoustic pressure \mathbf{p} as a function of radial position $r_b < r < r_b + L_{p0} + L_r + L_f$. Additionally, alternative but equivalent means of expressing the various material properties are provided such that this axisymmetric theoretical model can also be solved numerically using finite element analysis (FEA). The advantage of this is that FEA can then be used to investigate more realistic and complex, nonaxi-

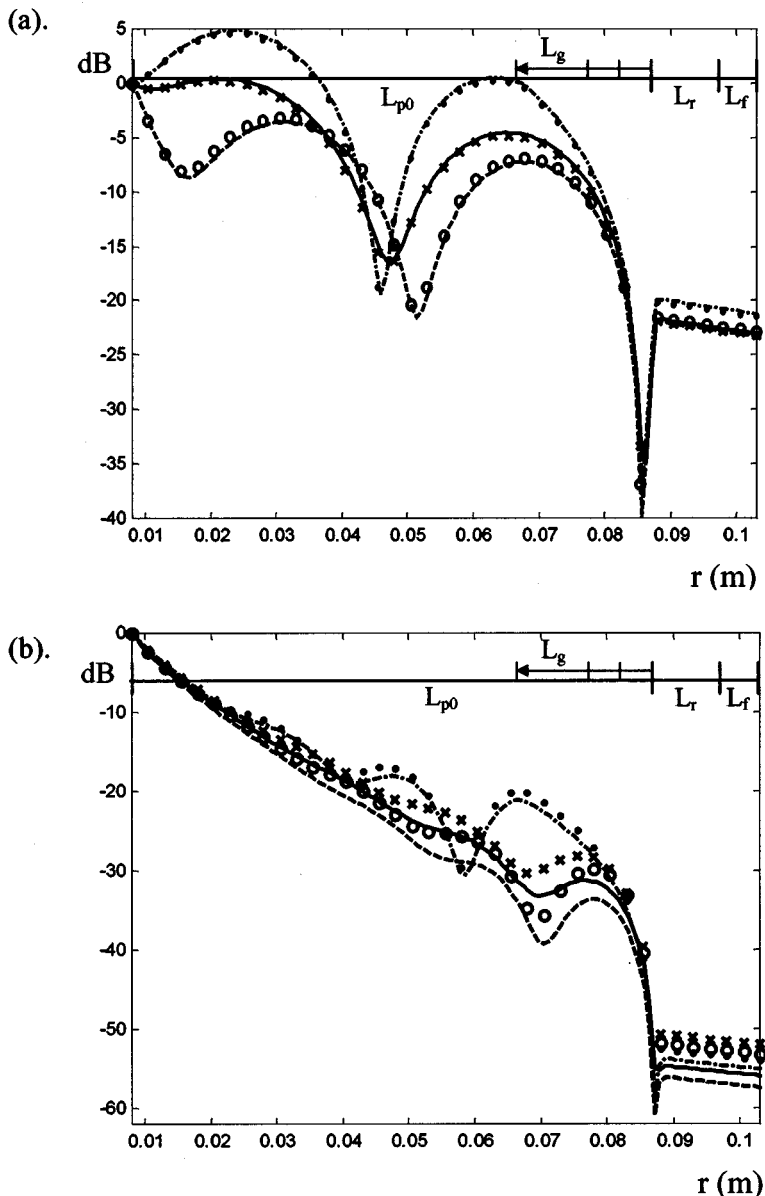


FIG. 7. Theoretical and finite element results as a function of radial position for acoustic velocity with a free outer boundary: (a) 300 Hz and (b) 600 Hz. Results normalized to the input velocity at the bronchial airway wall. Key for theoretical results: (—) no PTX ($L_g = 0$ cm), (---) 16.3% axisymmetric PTX ($L_g = 0.5$ cm), (-·-) 58.9% axisymmetric PTX ($L_g = 2$ cm). Key for FEA results: (×) no PTX ($L_g = 0$ cm), (○) 16.3% axisymmetric PTX ($L_g = 0.5$ cm), (●) 58.9% axisymmetric PTX ($L_g = 2$ cm).

symmetric and axially varying geometries. Finally, the acoustic intensity at a point can be calculated using

$$I[r, \omega] = \frac{1}{2} \text{Real}\{\mathbf{p}[r, \omega] \times \mathbf{w}[r, \omega]^*\}, \quad (18)$$

where the asterisk denotes the complex conjugate.

The above-mentioned model makes many assumptions. In particular, it assumes that the vibratory energy travels only in the radial direction (axisymmetry). This, of course, is not true. Especially at lower frequencies, it is believed that alternate structural paths around the parenchyma will effectively couple the interior to the chest wall. Additionally, since this model does not account for the complexities of the tracheo-bronchial airway network, it does not account for the fact that higher frequency sound couples from the airways to the surrounding tissue more efficiently as one moves further down the branching airway network.^{21,22} Nonetheless, the assumptions applied here have been qualitatively confirmed experimentally at least in the range of 100–600 Hz.⁵ Additionally, Butler *et al.*¹⁴ have shown that, below 100 Hz, the closed-cell bubble model loses validity. Solid tissue elastic-

ity, instead of gas compressibility, is the dominant elastic component in determining compression wave propagation in the parenchyma. With respect to the high frequency limit, this model should be reasonable only if the sound wavelength is significantly greater than the average radius of the alveoli, which is 0.015 cm for an average adult.¹⁵ Compression wave speed in the parenchyma (using the bubble swarm model) is about 2300 cm/s. At 1500 Hz, the sound wavelength is 1.5 cm, which is significantly greater than 0.015 cm. Even at 5000 Hz the wavelength will approximately be 0.46 cm, which is still 30 times the alveoli average radius; so, this type of model may even be reasonable well beyond 600 Hz.

C. Predictions based on the theoretical model (and its numerical implementation via FEA)

The above-mentioned model was used to analyze the effect of a pneumothorax (PTX) on sound propagation from the bronchial airway to the skin surface. A number of cases

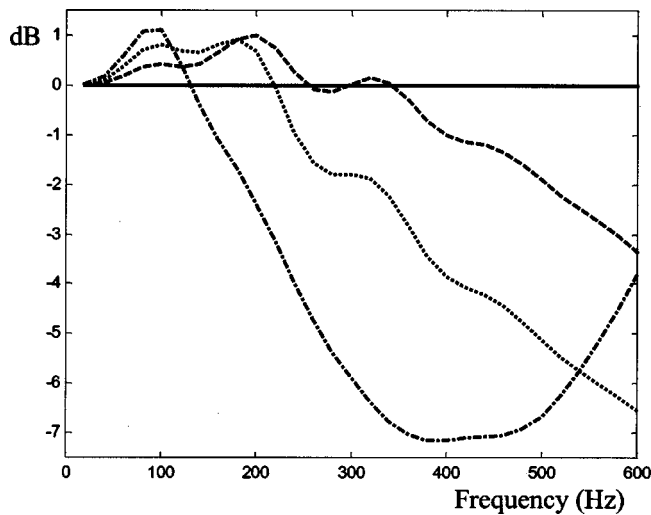


FIG. 8. Acoustic intensity loss through the torso for specific pneumothorax cases relative to the acoustic intensity loss through the torso for the normal (no pneumothorax) case. Using 1D theoretical model with anechoic outer boundary. Key: (---) 16.3% axisymmetric PTX ($L_g=0.5$ cm), (···) 31.6% axisymmetric PTX ($L_g=1$ cm), (-·-) 58.9% axisymmetric PTX ($L_g=2$ cm).

were considered. Selected results are shown in Figs. 5–9 and discussed in the following. Results are given in decibels; so, for acoustic pressure or velocity 20 dB is a 10 to 1 change, whereas 10 dB denotes a 10 to 1 change in acoustic intensity. Note, for Figs. 6 and 7, both the analytical solution of the theoretical model and its approximate solution via FEA (ANSYS) are shown. Good agreement between the two, particularly at 300 Hz, validates the FE implementation of the theory, which is then used in the next section to consider more complex, nonaxisymmetric geometries. Note, for the 1D studies, use of fluid versus solid elements, as discussed in the previous section, for the rib cage region and outer tissue region did not alter results. However, trends showed that a greater element resolution (smaller element size) was needed as frequency increased. The 1D FE model consisted of FLUID79 elements for each region—parenchyma, air, rib cage, and outer tissue. Axisymmetric harmonic response

analysis was performed, which yields the steady state response to a harmonic pressure excitation at the bronchial airway wall. Finite elements all had length and height dimensions of 0.025 mm, under a plane strain assumption in the axial direction.

In Figs. 5–7, results are shown at 300 and 600 Hz for three different types of boundary conditions on the outer chest surface. In Fig. 5, an anechoic boundary condition is used and the acoustic intensity as a function of radial position is shown for the normal and three different PTX conditions. (If the acoustic sensor on the chest surface was closely matched in impedance with the outer tissue layer and had sufficient energy dissipation to prevent reflections, one would consider it as anechoic.) For the larger axisymmetric PTX's, those greater than 30% by volume ($L_g \geq 1$ cm), greater attenuation is observed relative to the normal condition at both frequencies. For a smaller axisymmetric PTX, less than 20% by volume ($L_g \leq 0.5$ cm), the increased attenuation at the chest surface is only observed in the higher frequency case. In Fig. 8, the trends as a function of frequency are given in more detail for the same three PTX cases and boundary condition as Fig. 5. It seems that as the PTX becomes smaller, there is an increase in the frequency at which clear separation occurs from the normal case. In Fig. 9, greater detail is provided for intensity attenuation as a function of radial position and in terms of a range of axisymmetric pneumothorax denoted by percent volume, at the specific frequency of 300 Hz. Overall, these predicted decreases in acoustic intensity at the chest surface are *qualitatively* in agreement with the experimental electronic stethoscope measurements but are quantitatively smaller than experiment. There are several possible reasons for this. The geometry of the real case is more complex, being nonaxisymmetric and nonaxial. And, this model is not accounting for how a PTX collapses the bronchial airway network that insonifies the parenchyma in the first place. One would expect this to have an added attenuation effect.

In comparing Figs. 5–7, it is observed that while decreases in intensity seem to reliably predict the PTX, variations in surface velocity when the chest surface is free or

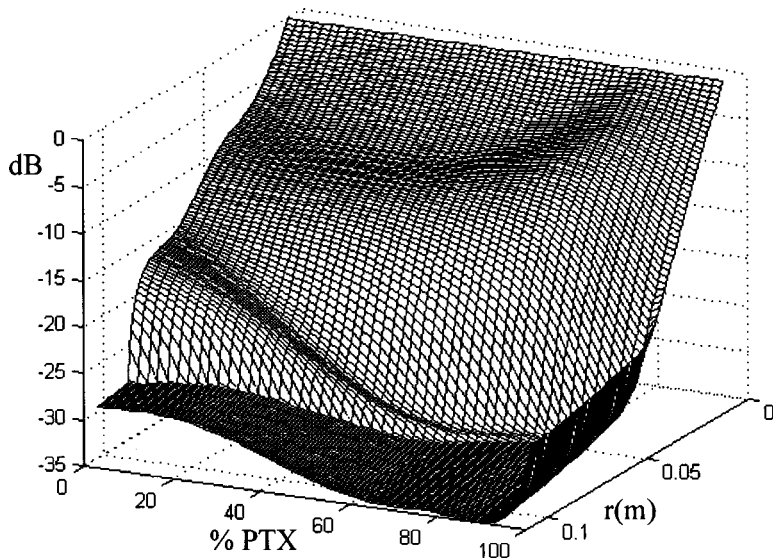


FIG. 9. Acoustic intensity normalized to acoustic intensity input as a function of percent pneumothorax depth and depth below the chest surface in the 1D theoretical model. Anechoic outer boundary condition. Excitation frequency is 300 Hz.

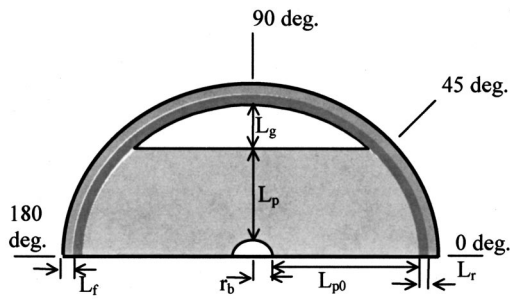


FIG. 10. Schematic of two-dimensional (2D) finite element model. Model symmetric about $\theta=90^\circ$.

variations in the surface pressure when the chest surface is fixed are not as reliable. This suggests that the choice of acoustic sensor, in terms of its impedance relative to the chest surface, will be important in PTX detection. Results in Figs. 6 and 7 may seem counterintuitive. In Fig. 6, it is seen that with a fixed chest wall, acoustic pressure levels in the

pocket, rib cage region, and outer tissue region are roughly constant. One might expect that there should be a substantial drop in pressure between the air pocket and rib cage region, given the large impedance mismatch. However, note that, relative to the parenchyma, attenuation in the other three regions is very small. The air, itself, could be visualized as a lossless annular spring since it is compressible and its mass is so low and the outer tissue regions, with their relatively high bulk moduli and densities, could be considered as an annular rigid mass that is essentially held fixed in place, thus making inertial effects in the outer three regions negligible. Under these conditions, a force (or pressure) applied to the inner surface of the air pocket by the parenchyma will be felt the same throughout the air pocket, rib cage, and outer tissue regions. With negligible inertial and dissipative effects, the outer three regions are behaving quasistatically. Continuing with this analogy, for the case of a free outer surface, in Fig. 7, the outer tissue regions are acting like a rigid mass bouncing on the parenchyma and air pocket springs in series. Dis-

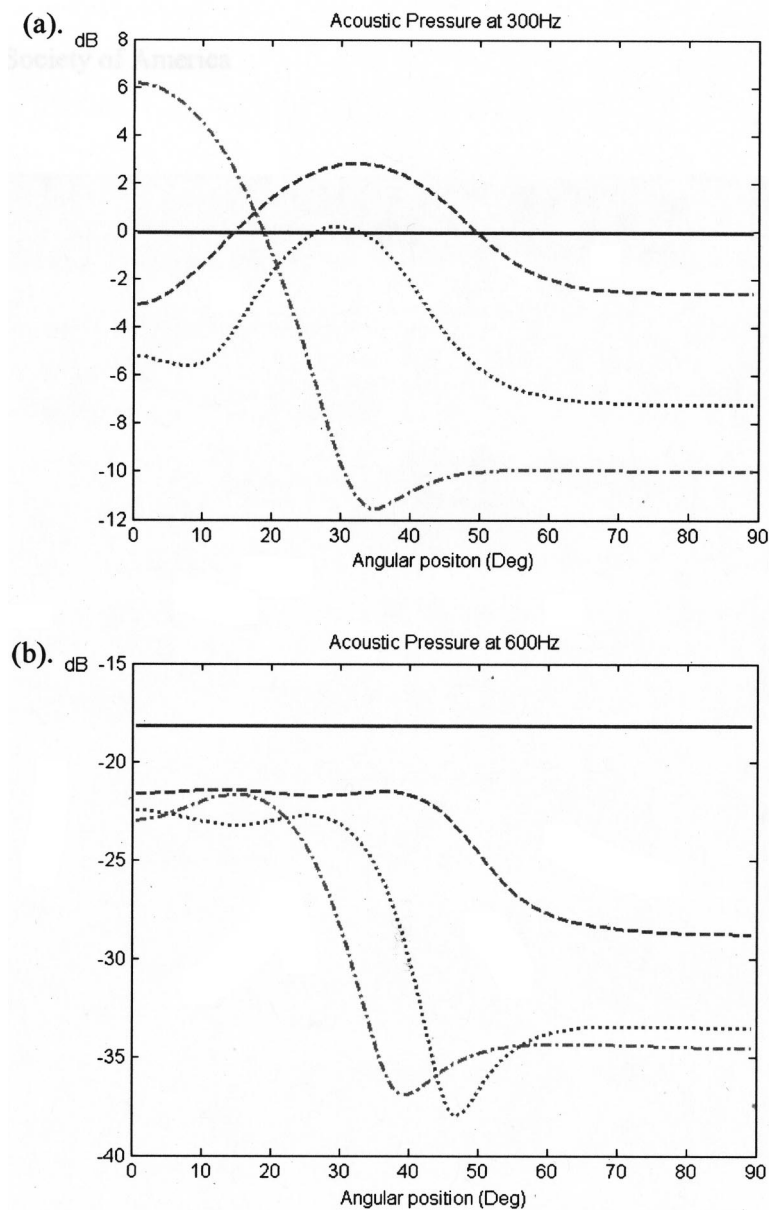


FIG. 11. Acoustic pressure at the surface normalized to acoustic pressure input in the bronchial airway as a function of angular position for the 2D FE model (See Fig. 10). Exterior surface is fixed: (a) 300 Hz and (b) 600 Hz. Key: (—) no PTX ($L_g=0$ cm), (---) 13% PTX ($L_g=2$ cm), (-.-) 23% PTX ($L_g=3$ cm), (-.-) 34% PTX ($L_g=4$ cm).

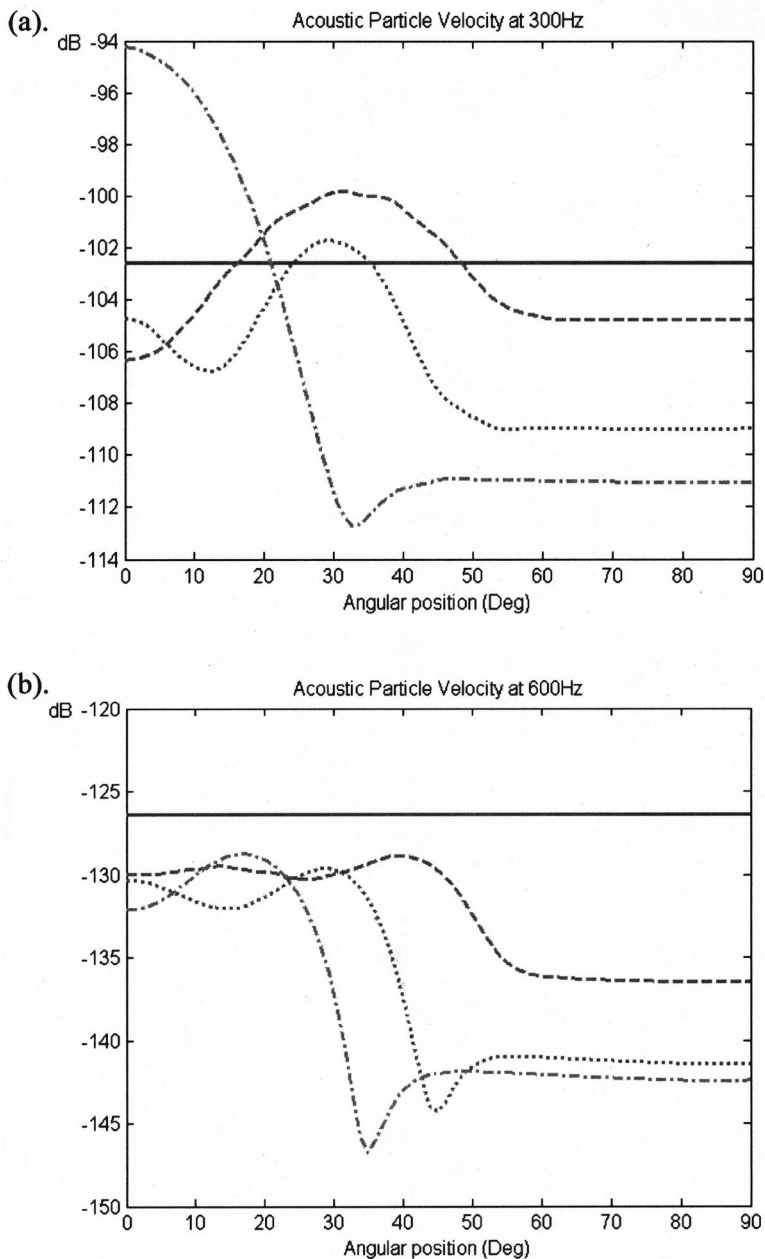


FIG. 12. Radial acoustic particle velocity at the surface as a function of angular position θ for the 2D FE model (See Fig. 10) and for 1 Pa acoustic pressure input in the bronchial airway. Exterior surface is free: (a) 300 Hz and (b) 600 Hz. Key: (—) no PTX ($L_g = 0$ cm), (---) 13% PTX ($L_g = 2$ cm), (- - -) 23% PTX ($L_g = 3$ cm), (· · ·) 34% PTX ($L_g = 4$ cm).

placement throughout the two outer tissue regions is uniform. But, it is a continuous function of radial position throughout the parenchyma and air pocket regions.

D. Extension of numerical finite element model to two dimensions

Description of model. Next, the FE model was extended to a nonaxisymmetric two-dimensional (2D) model that is shown in Fig. 10. Now, the PTX air pocket is nonaxisymmetric and values of L_g correspond to smaller percent PTX's by volume. Actual PTX's will generally have a shape somewhere between that of the 1D axisymmetric model and this 2D model. In this model SOLID42 elements had to be used for the outer tissue layer and rib cage region. A contained fluid FLUID79 element was used to model parenchyma and the acoustic FLUID29 element was used to model the air pocket. The material properties are all the same as described in the

1D models. Harmonic analysis was used. As we know from the previous part, the damping coefficient ζ_{bp} of the parenchyma is a function of frequency; the model was analyzed using the correct damping coefficient at every frequency point between 100 and 600 Hz in 5 Hz increments.

Predictions based on model. In Fig. 11, using the 2D model of Fig. 10, acoustic pressure at the chest surface at 300 and 600 Hz is shown as a function of angular position with a fixed boundary condition on the chest surface. With this 2D model, it seems that smaller pneumothoraxies by percent volume are detectable based on acoustic pressure attenuation. Also, the model suggests that, at least for larger air pockets, one does not need to be directly over the air pocket to get some kind of indication of its presence, as the response is altered at all angles. Like the 1D model, a clearer differentiation between the normal (no PTX) and PTX states exists at the higher frequency. However, directly over the PTX (90°) the 2D model predicts a greater attenuative effect due

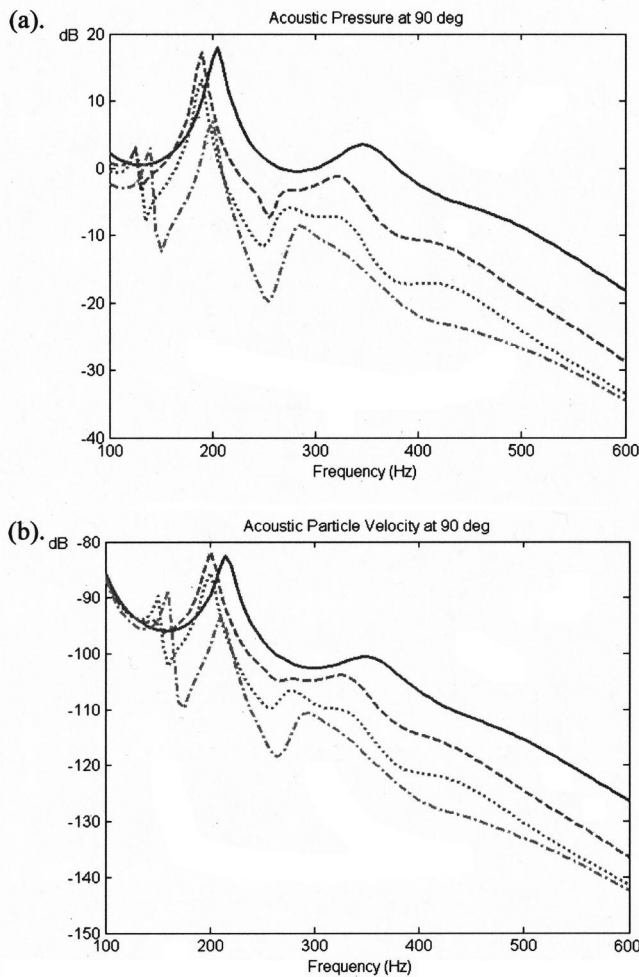


FIG. 13. Radial response at the surface at 90° as a function of frequency and normalized to 1 Pa input pressure in the bronchial airway for the 2D FE model (see Fig. 10). (a) Acoustic pressure with exterior surface fixed. (b) Acoustic particle velocity with exterior surface free. Key: (—) no PTX ($L_g = 0$ cm), (---) 13% PTX ($L_g = 2$ cm), (-.-) 23% PTX ($L_g = 3$ cm), (···) 34% PTX ($L_g = 4$ cm).

to a PTX than does the 1D model, which is in better agreement with experiment. In Fig. 12, acoustic particle velocity at the chest surface is shown for a free boundary condition. Overall, similar trends are observed as were observed for the fixed chest wall case of Fig. 11.

Figure 13 shows a comparison of measurements made directly over the PTX at 90° for the normal case and the cases of a PTX of 13%, 23%, and 34% by volume. These results are qualitatively similar to experimental measurements in that some resonant behavior of the chest wall is present for both the normal and PTX cases. Very similar results, though with less relative attenuation for the PTX cases, are predicted using the 1D model and comparable PTX conditions, suggesting that this is associated primarily with radial dynamics. Beyond 600 Hz up to 1500 Hz no additional resonant behavior was observed; responses continue to attenuate more with increased frequency along the trajectories evident in the 500–600 Hz range. Like in the experiment the PTX, while producing a broadband attenuative effect, does not greatly alter the quality of the resonance.

Modal analysis of both the 1D and 2D models indicate that the observed resonant frequencies are very close to the natural frequencies of the undamped system for mode shapes that are dominated by radial motion of the parenchyma, with the ribcage region and outer tissue layers acting as a mass load. In fact, from the perspective of a pressure input at the inner airway wall of Fig. 4 or 10, the resonant frequencies correspond to peaks in the input mobility, the ratio of radial velocity at the airway wall to applied pressure. So, it is accurate to characterize these resonances as those primarily of the parenchyma (and PTX free air region, if present) that is free at its inner radius and mass-loaded at its outer radius. When a PTX is present, the percentage of solid tissue and gas in the parenchyma–air region is not changed, only redistributed. It seems that this redistribution does not significantly alter the resonant behavior in this model; but, due to the more extreme impedance mismatches at radial boundaries, attenuation is increased. This same phenomenon appears to occur in the experiment. However, the experiment consists of a substantially more complex lung structure with more complicated resonant behavior, which could account for the quantitative differences between it and the model predictions.

In Figs. 14 and 15, the 1D theory (which matches the 1D FEA results) is compared with the 2D FEA results for the case of fixed and free outer boundaries. (In the 2D model, circumferential motion is constrained at the $\theta = 0$ and 180° boundaries, but radial motion is unconstrained; with these conditions these boundaries should not introduce nonaxisymmetry if only radial motion is present.) Results are shown at 300 Hz in the same format as Figs. 6(a) and 7(a), the acoustic pressure (fixed outer boundary) or velocity (free outer boundary) along a radial path from the bronchial airway wall to the outer surface of the chest. For the 1D axisymmetric model, there is, of course, only one radial path. For the 2D FE model, three paths are shown: $\theta = 30^\circ$, 60° , and 90° . In Figs. 14(a) and 15(a) agreement between 1D and 2D models is good, with purely axisymmetric responses. However, some discrepancy exists in pressure predictions in Fig. 14(a) when PLANE42 elements are used in the 2D model for the rib cage and outer tissue regions as opposed to FLUID79 elements, which are used for all regions in the 1D model. When FLUID79 elements are used for all regions in the 2D model, there is exact agreement with the 1D model. Perhaps shear viscoelasticity, not accounted for in the fluid elements, may have some additional attenuative effect. For Figs. 14(b) and 15(b), a PTX of $L_g = 2$ cm is present; it is axisymmetric (see Fig. 4) for the 1D model and nonaxisymmetric (see Fig. 10) for the 2D model. Substantial differences are now found in the results, even between the 1D theory and the path along $\theta = 90^\circ$. Most notably, it is observed in the 2D model that there are distinct jumps in acoustic pressure and particle velocity across changing tissue and gas boundaries. Indeed, this may seem more intuitive in that one would expect a significant change in acoustic pressure and particle velocity across these boundaries, and an associated drop in intensity. The 1D model does not capture this behavior, suggesting that it is related to nonradial scattering of acoustic energy. While attenuation predictions for the 1D and 2D models look comparable for the case of $L_g = 2$ cm, it is noted that this corre-

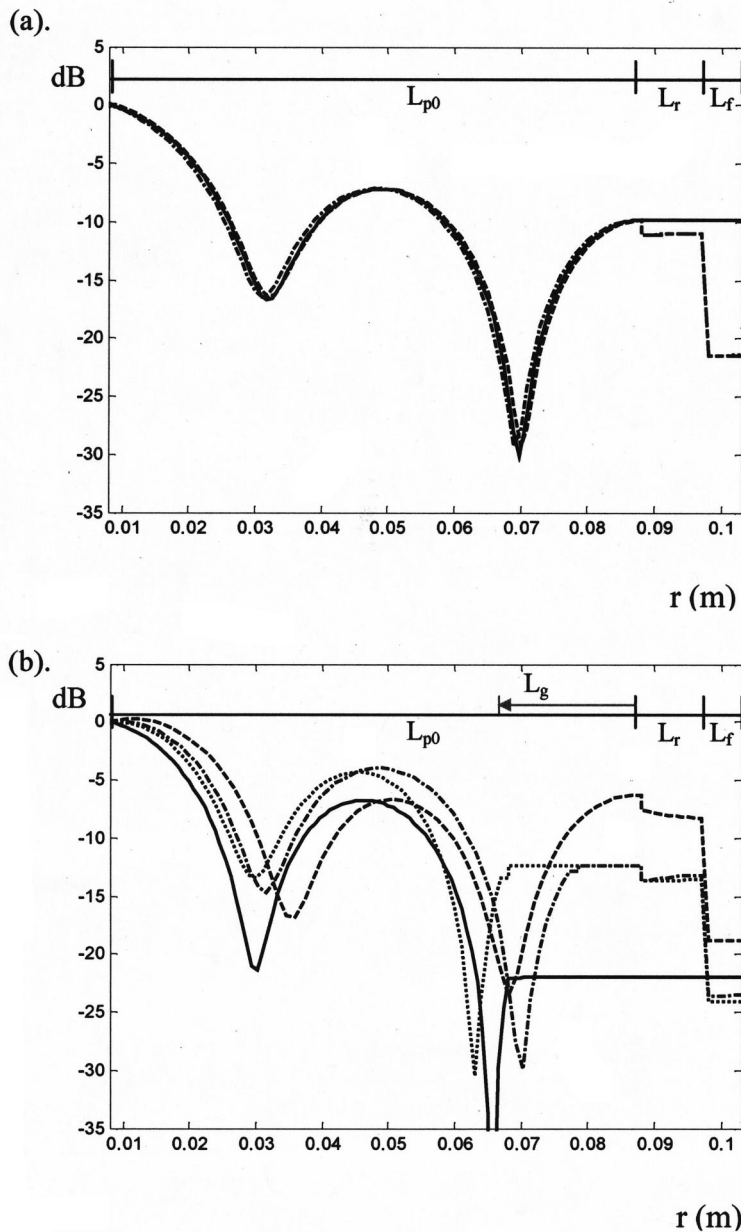


FIG. 14. 1D theory and 2D finite element results as a function of radial position for acoustic pressure with a fixed outer boundary at 300 Hz. Results normalized to the input pressure at the bronchial airway wall. (a) No PTX ($L_g = 0$ cm). Key: (—) 1D theory and 2D FEA along $\theta = 30^\circ, 60^\circ, 90^\circ$ using FLUID79 elements for all tissue layers, (---) 2D FEA along $\theta = 30^\circ, 60^\circ, 90^\circ$ using PLANE42 elements for rib cage and outer tissue layers. (b) PTX present ($L_g = 2$ cm): 1D theory—axisymmetric PTX, 2D FEA—nonaxisymmetric PTX (using PLANE42 elements for rib cage and outer tissue region). Key: (—) 1D theory, (---) 2D FEA along $\theta = 30^\circ$, (-.-) 2D FEA along $\theta = 60^\circ$, (-.-) 2D FEA along $\theta = 90^\circ$.

sponds to a 59% axisymmetric PTX (1D model) and only a 13% nonaxisymmetric PTX (2D model). By accounting for nonaxisymmetry, greater attenuation is predicted for comparable percent PTXs, which is more in agreement with experiment.

IV. CONCLUSION

Summary. Experimental studies were performed on canine subjects to investigate the effect of a pneumothorax (a collapsed lung) on sound transmission from the airway to the chest wall; the results suggest possible clinical utility, at least for pneumothoraxies on the order of 30% (by volume). The following acoustic trends were observed: (1) significant increased attenuation of higher frequency (>200 Hz) sounds occur with pneumothorax; and (2) transmission of low-frequency (<200 Hz) sounds appear to be minimally affected by pneumothorax.

In order to better understand precisely what causes these changes to aid in improvement of diagnostic procedures in the future, several simplified theoretical and computational models were developed to simulate sound transmission to the chest surface. An axisymmetric theoretical model was constructed by extending previous models^{15,16} to the pneumothorax condition. Simulation results obtained from the theoretical model qualitatively agreed with experimental findings. Specifically, for larger pneumothorax conditions, greater than 20% by volume, decreased sound intensity is observed at the chest surface, particularly as frequency increases above 200 Hz. For smaller pneumothoraxies, less than 20% by volume, theoretical and experimental results are inconclusive, in terms of identifying a trend in sound intensity. In the theoretical development presented in this article, it was found that, despite the high rate of sound attenuation, particularly in the parenchyma, it is important to consider multiple reflections (standing wave patterns) in wave transmission. The

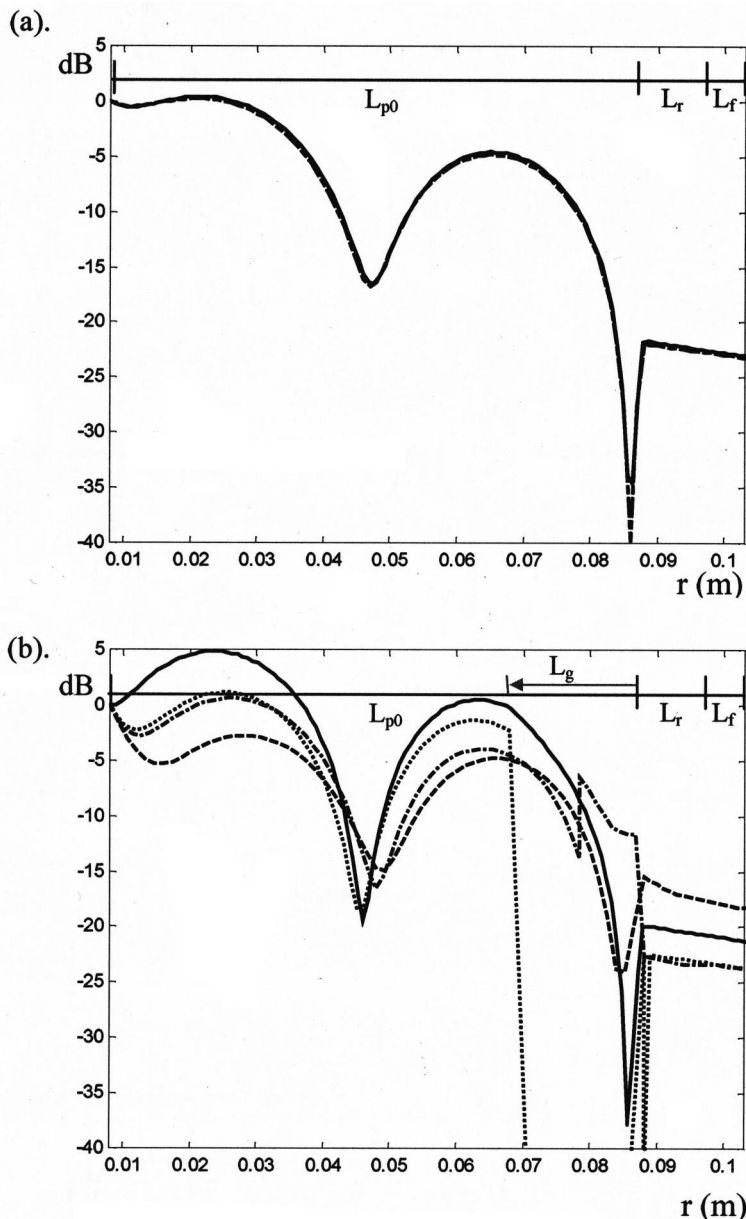


FIG. 15. 1D theory and 2D finite element results as a function of radial position for acoustic velocity with a free outer boundary at 300 Hz. Results normalized to the input velocity at the bronchial airway wall. (a) No PTX ($L_g = 0$ cm). (b) PTX present ($L_g = 2$ cm): 1D theory—axisymmetric PTX, 2D FEA—nonaxisymmetric PTX (using PLANE42 elements for rib cage and outer tissue region). Key: (—) 1D theory (---) 2D FEA along $\theta = 30^\circ$ (-.-) 2D FEA along $\theta = 60^\circ$ (-.-.-) 2D FEA along $\theta = 90^\circ$.

larger differences between the normal and pneumothorax condition observed in the experimental canine studies may be caused by the collapse of the outer branches of the bronchial airway tree, which is not explicitly accounted for in the simplified theoretical modeling. Additionally, due to more complex geometry, there may be more nonradial scattering of sound than predicted by the simple axisymmetric theory that could result in increased attenuation. (Nonaxisymmetric 2D finite element simulations support this hypothesis, indicating greater attenuation for comparable percent PTXs.) Simulations also suggested that the acoustic impedance of the sensor placed on the chest surface may play a significant role in determining diagnostic ability.

To complement and extend the theoretical developments, computational finite element (FE) implementations of the theory, one and two dimensional (1D and 2D), were also developed. The 1D model showed good agreement with the theoretical study, validating the FE implementation. The 2D model showed many similar trends to the 1D model and

experiment, highlighting the importance of radial wave propagation, resonance, and relative impedances at boundaries in the parenchyma and PTX free air region, if present. However, it was found that nonradial vibro-acoustic wave propagation is significant when nonaxisymmetries are introduced into the geometry, even when the excitation source is still axisymmetric. Chest surface responses with direct radial paths to the bronchial airway that avoid air pockets were altered by the presence of a pneumothorax (air pocket) at other circumferential angles. Significant changes in acoustic pressure and particle velocity occurred across tissue and gas boundaries that were not predicted by the 1D representation and resulted in greater attenuation; this is more in agreement with experiment.

Limitations and future research. The above-mentioned theoretical and computational models predict the response at the chest wall relative to sound excitation of the parenchyma using simplistic geometric approximations. In addition to their geometric simplicity they do not account for the dy-

namics of the bronchial airways themselves, and trachea, and whether or not there is intubation. It is of interest to also understand the acoustics of these airways in order to predict what sound is applied to the parenchyma via introduction at the mouth or through an endotracheal tube and how specific measurements of sound transmitted to the chest surface and/or reflected back through the bronchial airways and trachea/endotracheal tube to the mouth may be used to delineate pneumothorax from other conditions, aiding in specificity of diagnosis. Consequently, research currently being conducted by the authors includes: (1) developing a nonaxisymmetric, nonaxial theoretical model to provide more meaningful information; (2) using more precise FE modeling based on detailed geometries of canines and humans; (3) extending detailed “acoustic circuit” models of the trachea—bronchial airway network that are available in the literature^{5,7-13} to the case of PTX and other potentially confounding lung pathologies in order to provide more realistic simulations of acoustic excitation to the parenchyma via the mouth or an endotracheal tube; (4) integrating these same “acoustic circuit” models from the literature, or simplified versions of them, into a comprehensive finite element model of sound propagation in the lung and chest region; and (5) careful experimental studies of the acoustic properties of the various biological materials of the torso region by themselves and *in vivo* in order to determine more accurate material property values and to have more comprehensive experimental information with which to compare theoretical and computational models, specifically for the low audible frequency range, up to 3000 Hz.

ACKNOWLEDGMENTS

The financial support of the National Institutes of Health (NCRR Grant No. 14250 and NHLBI Grant No. 61108) is acknowledged. The help of M. Hacklin, A. Howdysshell, and S.-H. Kim with the animal experiments is appreciated.

¹M. H. Bauman, C. Strange, J. E. Heffner, R. Light, T. J. Kirby, J. Klein, J. D. Luketich, E. A. Panacek, and S. A. Sahn, “Management of spontaneous pneumothorax: An American College of Chest Physicians Delphi Consensus Statement,” *Chest* **19**, 590–602 (2001).

²H. Pasterkamp, S. S. Kraman, and G. R. Wodicka, “Respiratory sounds: Advances beyond the stethoscope,” *Am. J. Respir. Crit. Care Med.* **156**, 974–87 (1997).

³M. Abella, J. Formolo, and D. G. Penney, “Comparison of the acoustic properties of six popular stethoscopes,” *J. Acoust. Soc. Am.* **91**, 2224–2228 (1992).

⁴T. J. Royston, H. A. Mansy, and R. H. Sandler, “Excitation and propagation of surface waves on a viscoelastic half-space with application to medical diagnosis,” *J. Acoust. Soc. Am.* **106**, 3678–86 (1999).

⁵J. J. Fredberg, and J. A. Moore, “Distributed response of complex branching duct networks,” *J. Acoust. Soc. Am.* **63**, 954–961 (1978).

⁶R. L. Donnerberg, C. K. Druzgalski, R. L. Hamlin, G. L. Davis, R. M. Campbell, and D. A. Rice, “Sound transfer function of congested canine lung,” *Br. J. Dis. Chest* **74**, 23–31 (1980).

⁷K. Ishizaka, M. Matsudaira, and T. Kaneko, “Input acoustic-impedance measurement of the subglottal system,” *J. Acoust. Soc. Am.* **60**, 190–197 (1976).

⁸J. J. Fredberg, “Spatial considerations in oscillation mechanics of the lung,” *Fed. Proc.* **39**, 2747–2754 (1980).

⁹A. C. Jackson, C. A. Giudanella, and H. L. Dorkin, “Density dependence of respiratory system impedances between 5 and 320 Hz in humans,” *J. Appl. Physiol.* **67**, 2323–2330 (1989).

¹⁰H. Hudde and H. Slatky, “The acoustical input impedance of excised human lungs: Measurements and model matching,” *J. Acoust. Soc. Am.* **86**, 475–492 (1989).

¹¹R. H. Habib, B. Suki, J. H. Bates, and A. C. Jackson, “Serial distribution of airway mechanical properties in dogs: Effects of histamine,” *J. Appl. Physiol.* **77**, 554–566 (1994).

¹²J. P. Mansfield and G. R. Wodicka, “Using acoustic reflectometry to determine breathing tube position and patency,” *J. Sound Vib.* **188**, 167–188 (1995).

¹³P. Harper, S. S. Kraman, H. Pasterkamp, and G. R. Wodicka, “An acoustic model of the respiratory tract,” *IEEE Trans. Biomed. Eng.* **48**, 543–550 (2001).

¹⁴J. P. Butler, J. L. Lehr, and J. M. Drazen, “Longitudinal elastic wave propagation in pulmonary parenchyma,” *J. Appl. Physiol.* **62**, 1349–1355 (1987).

¹⁵G. R. Wodicka, K. N. Stevens, H. L. Golub, E. G. Cravalho, and D. C. Shannon, “A model of acoustic transmission in the respiratory system,” *IEEE Trans. Biomed. Eng.* **36**, 925–934 (1989).

¹⁶I. V. Vovk, V. T. Grinchenko, and V. N. Oleinik, “Modeling the acoustic properties of the chest and measuring breath sounds,” *Acoust. Phys.* **41**, 667–676 (1995).

¹⁷L. E. Kinsler, A. R. Frey, A. B. Coppens, and J. V. Sanders, *Fundamentals of Acoustics*, 3rd ed. (Wiley, New York, 1982).

¹⁸J. L. Flanagan, *Speech Analysis: Synthesis and Perception* (Springer, New York, 1972).

¹⁹X. Zhang, T. J. Royston, H. A. Mansy, and R. H. Sandler, “Radiation impedance of a finite circular piston on a viscoelastic half-space with application to medical diagnosis,” *J. Acoust. Soc. Am.* **109**, 795–802 (2001).

²⁰H. E. von Gierke, H. L. Oestreicher, E. K. Franke, H. O. Parrack, and W. W. von Wittern, “Physics of vibrations in living tissues,” *J. Appl. Physiol.* **4**, 886–900 (1952).

²¹G. R. Wodicka, A. Aguirre, P. D. DeFrain, and D. C. Shannon, “Phase delay of pulmonary acoustic transmission from trachea to chest wall,” *IEEE Trans. Biomed. Eng.* **39**, 1053–1058 (1992).

²²S. Lu, P. C. Doerschuk, and G. R. Wodicka, “Parametric phase-delay estimation of sound transmitted through intact human lung,” *Med. Biol. Eng. Comput.* **33**, 293–298 (1995).